Landslide Hazards Assessment and Uncertainties

by

Karim S. Karam

Bachelors of Engineering in Civil and Environmental Engineering, Imperial College of Science, Technology and Medicine, (1997)
Masters of Engineering in Civil and Environmental Engineering, Imperial College of Science, Technology and Medicine, (1998)
Master of Science in Civil and Environmental Engineering, Massachusetts Institute of Technology, (2000)

Submitted to the Department of Civil and Environmental Engineering in Partial Fulfillment of the Requirements for the Degree of

Doctor of Philosophy
in the field of Geotechnical and Geoenvironmental Engineering
at the
Massachusetts Institute of Technology
September 2005

Signature of Author: _____
Department of Civil and Environmental Engineering
June 15, 2005

Certified by: _____
Herbert H. Einstein
Professor of Civil and Environmental Engineering
Thesis Supervisor

Certified by: _____
Daniele Veneziano
Professor of Civil and Environmental Engineering
Thesis Supervisor

Accepted by _____
Andrew Whittle
Chairman, Departmental Committee on Graduate Studies

Landslide Hazards Assessment and Uncertainties

by
Karim S. Karam

Submitted to the Department of Civil and Environmental Engineering
on June 15, 2005, in partial fulfillment of the Requirements for
the Degree of Doctor of Philosophy in the field of Geotechnical and Geoenvironmental Engineering

ABSTRACT

Landslides are natural phenomena which are difficult to predict because their initiation depends on many factors and on the interaction between these factors. The annual number of causalities caused by landslides is in the thousands, and infrastructural damage is in the billions of dollars. To satisfy the increasingly urgent societal demand for protection against landslides, it is necessary to systematically assess and manage landslide hazard and risk. This can be done using principles of decision making under uncertainty.

We develop an advanced combined hydrologic – stability model that is better capable of assessing landslide hazards than current models used in landslide analyses. This model allows one to evaluate landslide hazards deterministically. We use the model to study landslide failure mechanisms, and classify these according to the manner in which a slope gets saturated during rain. We showed that slopes with great depths to bedrock and shallow depths to the water table, tend to fail by saturation from below, resulting in deep seated landslides, and slopes with deep lying water tables tend to fail by saturation from above, resulting in shallow landslides.

Landslide hazards include, by definition, uncertainties which can be expressed probabilistically. Uncertainties arise from parameters and from models. We develop efficient techniques to formally incorporate parameter uncertainties into the combined hydrologic – stability model, and hence into the hazard assessment procedure. We then show that landslide hazards are significantly influenced by the joint probability distribution of the soil strength parameters and the strength submodel(s) used in the stability models, and by the soil characteristic curve submodel(s) used in the hydrologic models.

This study leads to a better understanding of landslide mechanisms and to advanced models that assess landslide hazards more accurately than current models. The results of parameter uncertainty investigations show which parameters are most important in landslide analyses, and hence where it is worthwhile to obtain more information. The results of model uncertainty investigations show which models are most important in landslide analyses, and hence where further research needs to be undertaken.

Thesis Supervisor: Herbert Einstein
Title: Professor of Civil and Environmental Engineering

Thesis Supervisor: Daniele Veneziano
Title: Professor of Civil and Environmental Engineering

ACKNOWLEDGEMENTS

I would like to start by thanking our Lord, Jesus Christ, for the infinite gifts he has provided me with, especially the gift of life itself which I so often take for granted. I know He was, and still is with me every day of my life.

I would like to express my deep appreciation and admiration for Professor Herbert Einstein, who has been so much more than my academic advisor throughout my stay at MIT. Professor Einstein has provided me with unconditional guidance, advice and love, and it has been an honor working with him. I would also like to thank Professor Daniele Veneziano, whom I have thoroughly enjoyed working with. It has been a real pleasure working with Professor Veneziano on both this thesis, and the Probability and Statistics class. I feel privileged to have worked with Professors Einstein and Veneziano, two great men, who have left an ever lasting impression on my life.

I would also like to thank Cynthia Stewart, who has helped tremendously during my stay at MIT, by providing me with advice at both the logistical and academic levels. Cynthia was the person I could always rely on for help.

My friends, who have made my years at MIT some of the best of my life. I would like to especially thank:

Rita, who put up with me and my ways in both the ups, but particularly the downs. Rita was always there for me, many times going out of her way, to provide me with unconditional love and support. Bassam and Ralph, great friends: Bassam for the excellent, yet sometimes absurd, conversations about probability and statistics as well as other topics. The discussions we had on the Gibrat and Pareto probability distributions are now classics. Ralph who could always be counted on for a good time. The summer days of ordering Venti's on Newbury Street, and discussions, sometimes heated, on cowboy boots and best tanning lotions, though past, I will never forget. Nisrine for all her kindness, and for providing me with great escapes from MIT making life more enjoyable. Jean-Claude and Rania for being wonderful friends, despite ... forget it! Ziad for the countless hours of fun and laughter, though not always, playing FIFA on the Playstation. Alice, who puts the spark in the geotech department, and who was always there to listen as I let off some heat. Sheila, for the entertaining conversations we had on football, and though an avid Arsenal supporter, I still believe she will see the light and join the Chelsea ranks soon. My office mates, Louie and Songyoon for putting up with my messiness, sometimes at their expense. Louie in particular who endured more than his fair share of my eccentricity, and who helped bring back memories of high school. Pong, who was always in for hilarious conversations. I would also like to mention my colleagues Maria, Erdem, Kartal and Georgios.

Through my assisting with teaching some classes, I have had the pleasure of meeting some wonderful people over the years. They are too many to name in person, but they know who they are, and I would like to thank all of them.

I have left the people I owe the most to until the end. I have been blessed with a wonderful family, who has provided me with unconditional love and affection throughout my life. I could have never done this without each and every one of you, and I thank you all.

Dad and mum, Simon and Arlette, who I owe my life to. Simon, for his infinite wisdom, and advice both academically and socially. You're my idol. I dream of being half the man you are, and I hope to get there one day. Arlette, my amazing mother, who has provided me with never ending love and affection for all I can remember. For her great advice on prioritizing issues in life, most of which I hope I have followed. I could never be where I am without you, and I hope I am the eldest son you always wanted me to be.

Lyne, for the wonderful person she is, and for all the entertainment and support she provided me with. Marianne, who I have been fortunate enough to live with during the past couple of years. Man, I missed on so much 'cause you're awesome! Kika, for being such a wonderful sister, it's your turn next, and I hope I'll be able to live with you as well.

Lastly, my brother, Jad, I said it in 2000, I will say it again here, you and I are one.

TO SIMON, ARLETTE, LYNE, JAD, MARIANNE AND KIKA

THANK YOU!

TABLE OF CONTENTS

LIST OF FIGURES

LIST OF TABLES

CHAPTER 1

INTRODUCTION

Landslides are natural phenomena which are difficult to predict because their initiation depends on many factors. The complexity of the phenomena is increased given that these factors and the interaction between them are uncertain. The consequences of landslides are, unfortunately, quite obvious. These consequences can be localized, such as the La Conchita, California event on January 12, 2005, or widespread as they occur nearly regularly during the rainy season in California or associated with hurricanes such as Hurricane Mitch in Honduras and Nicaragua in May - October 1998. Given these detrimental consequences, and to satisfy the increasingly urgent societal demand for protection against landslides, it is necessary to systematically assess and manage landslide hazard and risk. Landslide hazards and risks can be systematically assessed using the principle of decision making under uncertainty. This has been discussed in Einstein (1988, 1997).

Figure 1.1 is a graphical representation of decision making under uncertainty as proposed by Raiffa and Schlaiffer (1964) and Stael v. Holstein (1974). This process is actually also the standard decision making process used in engineering in which one determines parameters, includes them in models and makes decisions based on the model results. The updating cycle (Figure 1.1) can, amongst other things, represent the observational method in geotechnical engineering (Terzaghi, 1961; Peck, 1969; Einstein, 1988).

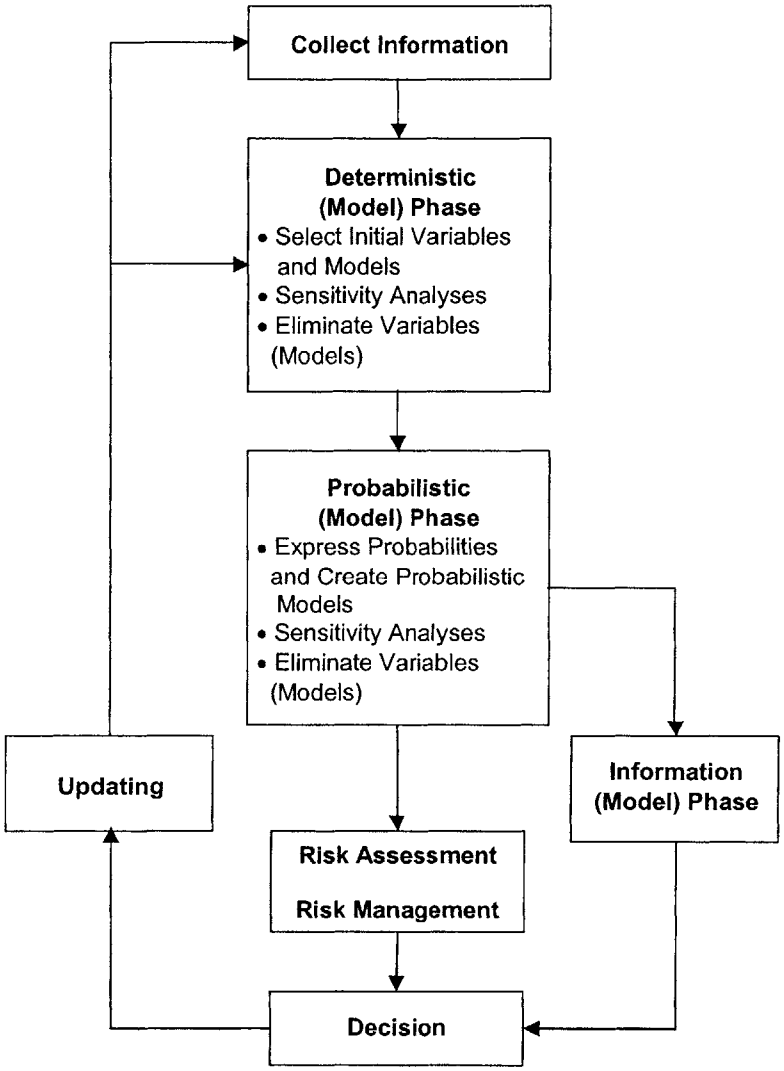

Figure 1.1. The Decision Analysis Cycle

This study attempts to evaluate landslide hazards (as opposed to risks which would require assessment of consequences), and is therefore mainly concerned with the first two phases of the decision making process. The first is the deterministic (model) phase, and the second is the probabilistic (model) phase.

1.1. DETERMINISTIC (MODEL) PHASE

In the deterministic phase, one selects initial variables, and creates deterministic models. Models used in landslide analyses include models for hydrologic analyses, and models for stability analyses.

Hydrologic models range in complexity, from simple one-dimensional infiltration models e.g. Green and Ampt (1911); Lumb (1975), to pore pressure diffusion models e.g. Reid et al. (1998), Ng et al. (1998); Iverson (2000) to one – dimensional e.g. Philip (1969); Bras and Protopapas (1990), two – dimensional e.g. Freeze (1971) and three-dimensional finite difference e.g. Schwartz (1992) and finite element models e.g. CHASM, Wilkinson et al. (2000); HYSWASOR, Dirksen et al. (1992); SEEP/W, Geo-Slope International Ltd. (1998). On a catchment basin scale, several physically based water balance models have been developed e.g. Okimura and Ichikawa (1985); Montgomery and Dietrich (1994); Burton and Bathurst (1994); Wu and Siddle (1995); Wilson and Wieczorek (1995); TRIGRS, Baum et al. (2002). Detailed hydrologic models that consider what happens once the water penetrates into the ground are for instance those by Campbell (1975), for rising water table and those for advancement of a saturation front from the surface of the slope e.g. Lumb (1975); Ho and Fredlund (1982); Brand et al. (1984); Pradel and Raad (1995); Fourie (1996); Lim et al. (1996); Ng at al. (1998); Rahardjo et al. (2001). Recent studies have considered the effects of infiltration on partial saturation of soils, e.g. Cho et al. (2002); Liaug et al. (2003); Rezaur et al. (2003); Chen et al. (2004).

Stability models combine strength model(s) with geometric and equilibrium representations.

Stability models are largely based on the Limit Equilibrium Method which is well established and extensively used in geotechnical engineering. Limit Equilibrium models range in complexity from one dimensional e.g. Infinite Slope Model (Skempton and DeLory, 1957), to two dimensional e.g. Bishop's Simplified (Bishop, 1959), and Rigorous (Bishop, 1960), Janbu's Simplified (Janbu, 1959), and Morgenstern and Price (1962), and three dimensional (Azzouz and Baligh, 1997) models. More advanced, finite

element models include two - e.g. Wilson and Fredlund (1996), and three - dimensional e.g. SLOPE/W (Geo-Slope International Ltd., 1998) models.

Strength models include those for saturated soil and unsaturated soil. The strength of saturated soils is well understood, and strength models based on the effective stress principle (Terzaghi, 1936) exist, e.g. Coulomb's Frictional Model. The strength of unsaturated soils is, however, not well understood, and models that attempt to describe unsaturated strength include the Independent State Variable Model (Fredlund et al., 1978) and models based on the extended effective stress principle (Bishop, 1959). The vast majority of stability models that have incorporated unsaturated strength, e.g. Fredlund and Krahn (1977), Rahardjo et al., (1995) have used the Independent State Variable Model (Fredlund et al., 1978).

Until recently, few of the aforementioned models (hydrologic and stability) have gained widespread use in landslide analyses. The Green and Ampt (1911) hydrologic model has been widely used in landslide analyses because of its simplicity, and the ability to relate the rate of infiltration to measurable soil properties such as its porosity, hydraulic conductivity, and the moisture content. The Infinite Slope (Skempton & DeLory, 1957) stability model has been the most widely used stability model because of its simplicity, and because the assumption it is based on, namely that the depth to length ratio in a slope is small, can be justified for the majority of landslides, particularly shallow landslides.

The problem with these models, both hydrologic and stability, is that they are too simplistic to accurately represent reality. For example, the Green and Ampt (1911) Model can only be used to predict moisture content advancement rather than pore pressure distributions which are what is needed in landslide analyses. The pressures, therefore, have to be inferred from the moisture distribution by making some simplifying yet serious assumptions. Similarly, the Infinite Slope Model, because of the assumption of one dimensionality, make it too simple to be used in accurate landslide analyses. This is because one cannot adequately account for the effects of changes in the initial (negative) pressures on stability with a one dimensional model.

The problems with these models have been recently recognized by researchers in the field, and more advanced models, both hydrologic and stability have been developed

and used in landslide analyses. Notably, Geo-Slope International Ltd. (1998) developed the SEEP/W and SLOPE/W finite element models, and since their development, these have been used extensively in landslide analyses e.g. Rahardjo et al. (1998), Ng, (2000), Lacasse et al., (2003).

Although these models (SEEP/W and SLOPE/W) are more rigorous than other models, there are several reasons for which better models still need to be developed, which include:

(a) Assumptions and Simplifications:

The models do not allow one to alter and question some of the fundamental underlying assumptions. These assumptions are those made in the models themselves and/or in models (or submodels) used within these models, e.g. soil characteristic curves in hydrologic models, and soil strength models in stability models. In particular, the unsaturated strength model used in the SLOPE/W model is the Independent State Variable model developed by Fredlund et al. (1978). While this model has been extensively used since its development there has been a shift, in recent years, to the original effective stress model proposed by Bishop (1959), e.g. Geiser (2000).

(b) Landside Mechanisms:

Landslide mechanisms remain poorly understood. This is partly due to the complexity of the phenomena, and the many factors that affect it, and partly due to the widespread use of simple models to represent them. There exists an interrelationship between understanding the mechanisms of landslides and developing the models required to do so. In order to better understand the mechanisms, models that are better suited for landslide analyses need to be developed. Although the SEEP/W and SLOPE/W are more advanced models than the majority of other models, they do not allow one to perform a comprehensive landslide mechanism review. Also, only very few studies have used these models to study the mechanisms of landslides, e.g. Liaung et al. (2003).

(c) Probabilistic Analyses:

The SEEP/W and SLOPE/W models do not allow one to formally incorporate uncertainties in parameters for probabilistic analyses. This is discussed further in the next section.

Because of what has just been stated, there remains a need to develop advanced hydrologic and stability models (and hence combined models) to more accurately assess landslide hazards, and discuss the underlying assumptions of these assessments. There also is a need to gain a better understanding of the mechanisms of landslides, and these two needs are interrelated as mentioned in (b) above. These needs are addressed in the first part of this study in which an advanced combined model to assess hazards deterministically is developed. The advanced model is then used to perform a comprehensive study on the mechanisms of landslides. Some of the proposed mechanisms have been previously suggested in the literature, and some are new. The latter can account for some of the landslides observed in the field, where the mechanisms of failure were so far not well understood.

1.2. PROBABILISTIC (MODEL) PHASE

In the probabilistic phase, one expresses probabilities and creates probabilistic models. Probabilistic models in hydrologic analyses include, for example those by Protopapas and Bras (1998), Dillah (1998), Wu and Siddle (2000). Probabilistic models for stability analyses include, for example those by Ang and Tang (1974), Low and Tang (1997), Li and Lumb (1978), Chowdhury (1980), Hassan and Wolff (2000), Malkawy et al. (2001). While, as stated above, several probabilistic models have been created in each of the fields of hydrologic and stability modeling, few probabilistic models exist for combined modeling e.g. Wu et al. (2000), Hassan (2001). As a result, only few models have been developed to assess landslide hazards probabilistically, e.g. Hassan (2001), Wu (2003). Furthermore, nearly all these studies consider parameter uncertainty (their inherent spatial and temporal, and from their measurements) as the only source of uncertainty. Only a very few studies have looked at model uncertainty, although it is an issue that has been recognized in recent studies e.g. Einstein and Karam (2001); Lacasse et al. (2003).

There is, therefore, a need to create a probabilistic model in which one systematically incorporates uncertainties in both hydrologic and stability analyses, and hence in combined analyses. Such a model will enable one to probabilistically assess landslide hazards. This is addressed in the second part of this study. Efficient and innovative techniques are developed to perform reliability based and probabilistic, using the Monte Carlo method, landslide hazards assessments, while maintaining the same deterministic model developed in the first part. The probabilistic model is then used to assess the effects of model uncertainty on landslide hazards.

In view of what has been stated above, this study is organized as follows:

In Chapter 2, deterministic models for hydrologic and stability analyses are created. When combined, these models allow one to estimate landslide hazards deterministically. Chapter 3 makes use of the combined model developed in Chapter 2 to perform a comprehensive study on landslide mechanisms. Landslides are classified depending on the manner in which a slope gets saturated during a rainfall event, namely by: saturation from below by a rising water table, or saturation from above by infiltrating rainwater. The mechanisms by which landslides occur by saturation from above are then studied in detail since these are not well understood. In Chapter 4, the sources of uncertainties that enter landslide analyses are described. Sensitivity analyses are performed to evaluate the relative importance of various hydrologic and stability parameters. Parameters that significantly affect the results are retained for probabilistic analyses, whereas those with little effect are dropped. In Chapter 5, uncertainties in parameters described by their probability distributions are formally incorporated into the hazards assessment, thereby creating probabilistic models. These probabilistic models allow one to assess landslide hazards probabilistically. Probabilistic sensitivity analyses are then performed, and these allow one to determine the relative significance of uncertainties in parameters on landslide hazards. Chapter 6 deals with model uncertainty, since it is the least studied source of uncertainty and most difficult to capture. The effects of model uncertainty on landslide hazards, both deterministic and probabilistic are assessed. This allows one to evaluate the relative importance of uncertainties from the models used in landslide analyses. Chapter 7 summarizes the results of the study, and provides recommendations for future work.

CHAPTER 2

DETERMINISTIC LANDSLIDE HAZARDS ASSESSMENT

In this chapter, landslide hazards are assessed within a deterministic framework. This represents the first phase of the decision analysis cycle.

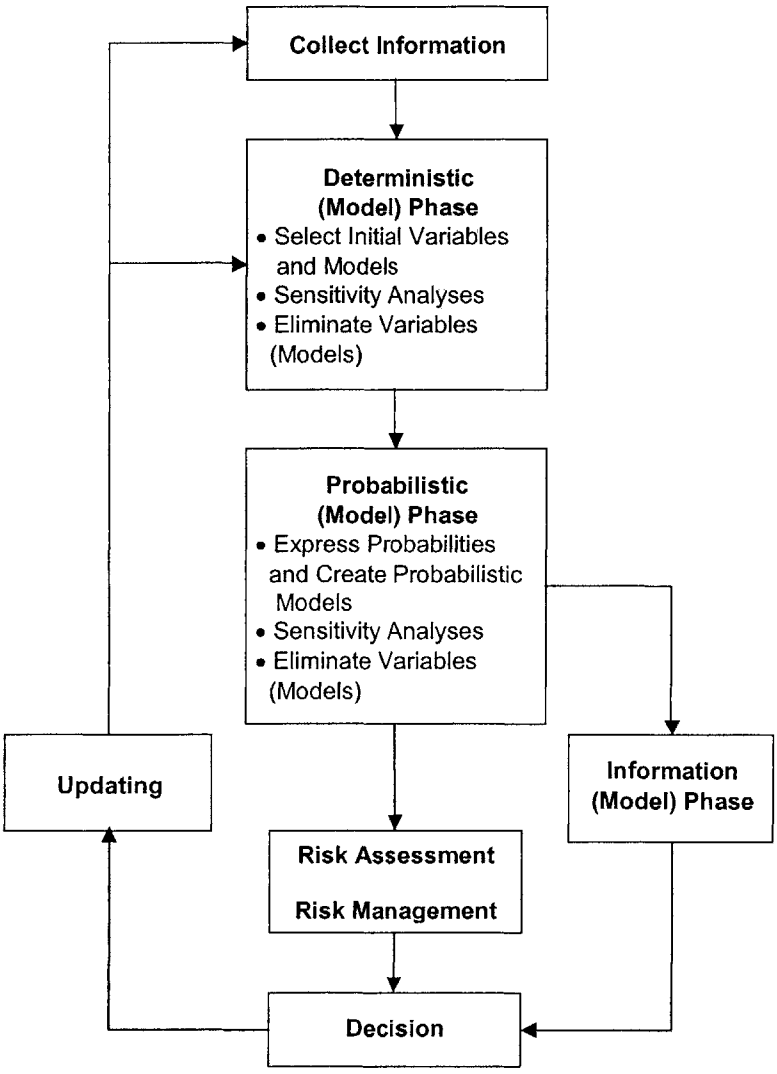

Figure 2.1. The Decision Analysis Cycle

The chapter is divided into 3 parts as follows:

In Part 2-1, the hydrologic response of a soil to a rainfall event is described. The variably saturated flow model is derived, and a finite difference solution to the pressure based form of the model is presented. An infiltration model is thus developed that is capable of predicting the variation of pore pressures with depth below the ground surface and time.

In Part 2-2, the stability of a slope is assessed using the Janbu Generalized Procedure of Slices (1973). Techniques are developed whereby the critical failure surface in a slope can be located.

In Part 2-3, a combined hydrology-stability model is developed by combining the infiltration model developed in Part 1 with the stability model developed in Part 2. The combined model allows one to determine the Factor of Safety in a slope as a function of time. By doing so, landslide hazards are assessed in a deterministic framework.

PART 2-1:

HYDROLOGY MODEL

The hydrologic response of a slope to rainfall is very complex, and depends on a great number of factors, both on local and catchment basin scales. Figure 2.2 illustrates some of these factors.

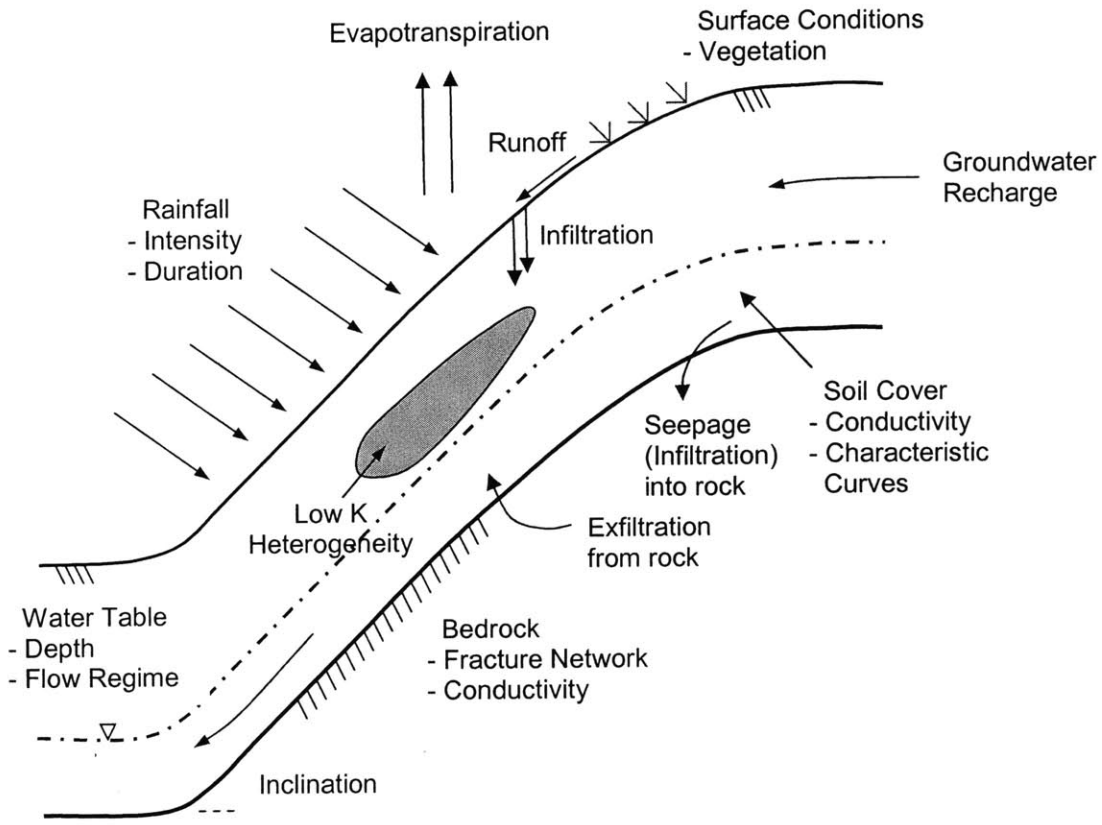

Figure 2.2. Some Factors Affecting Hydrologic Response of Slope to Rain

As it rains onto a slope some of the incident rainwater will infiltrate into the slope and some will run off the surface. This distribution of rainwater will depend on the rainfall characteristics and the hydraulic properties of the soil. Since the soil near the ground surface is usually unsaturated, the process of infiltration involves flow processes through the unsaturated zone. Unsaturated soils exhibit great spatial and temporal variations in

properties with changes in moisture content, rendering the infiltration process very complex. Various models have been developed to estimate the rate of infiltration, which range from simple one-dimensional (Green and Ampt, 1911), to two and three dimensional finite difference (Philips, 1972), and finite elements models (Freeze, 1981). The vast majority of these models are moisture content based, in that they estimate the variation of subsurface moisture with time. This is because they have been, for the most part, developed for use in agricultural studies. Landslide analyses, and stability models in particular, require the determination of pressure variations with time. Though these can be somewhat inferred from the soil characteristic curves if the soil remains unsaturated, they have to be assumed if the soil gets saturated. For this reason, a more adequate model is developed in this part of the chapter. Unsaturated soil properties, and soil characteristic curves are first introduced. The governing equation for variably saturated flow is derived, and the boundary conditions required for its solution are described. A one dimensional finite difference scheme is developed to solve the pressure based form of the one dimensional water flow equation. A one dimensional analysis is sufficiently accurate since infiltration into unsaturated soil is predominantly vertical (Philips, 1965; Romano et al., 1998). The numerical scheme is then illustrated through examples that will illustrate concepts that are important in landslide analyses.

2-1.1. UNSATURATED SOIL PROPERTIES

In unsaturated soil, both the moisture content, θ , and the hydraulic conductivity K, are functions of the pressure head, ψ. The θ-ψ and K - ψ curves are known as the soil characteristic curves. Various models have been developed to estimate the characteristic curves of a soil e.g. Gardner (1956), Brooks and Corey (1966), Bresler et al. (1978), van Genuchten (1980). In this study, the model proposed by van Genuchten (1980) is used. The van Genuchten (1980) model is given by:

$$S_e = 1 \qquad \psi \geq 0 \qquad [2.1]$$

$$S_e = \frac{1}{\left(1+\left(\delta|\psi|\right)^n\right)^m} \qquad \psi < 0 \qquad [2.2]$$

$$K = K_s \qquad \psi \geq 0 \qquad [2.3]$$

$$K = K_s S_e^{0.5}\left[1-\left(1-S_e^{1/m}\right)^m\right]^2 \qquad \psi < 0 \qquad [2.4]$$

where:

K_s is the saturated conductivity of the soil

δ and n are empirical coefficients

$m = 1 - \frac{1}{n}$

$S_e = \frac{\theta - \theta_r}{\theta_s - \theta_r}$

θ_s is the saturated moisture content

θ_r is the residual moisture content, defined as the moisture content at which a decrease in the pressure head does not produce a significant change in moisture content (see Figure 2.4).

Consider the soil with the parameters shown in Table 2.1.

Saturated Conductivity, K_s (m/s)	θ_s (m^3/m^3)	θ_r (m^3/m^3)	n	δ	$m = 1 - \frac{1}{n}$
2.31E-05	0.47	0.11	1.24	0.011	0.193548

Table 2.1. Soil Hydraulic Parameters

Figure 2.3 shows the moisture content characteristic curve, also known as the retention curve according to the van Genuchten (1980) model for the soil with parameters in Table 2.1.

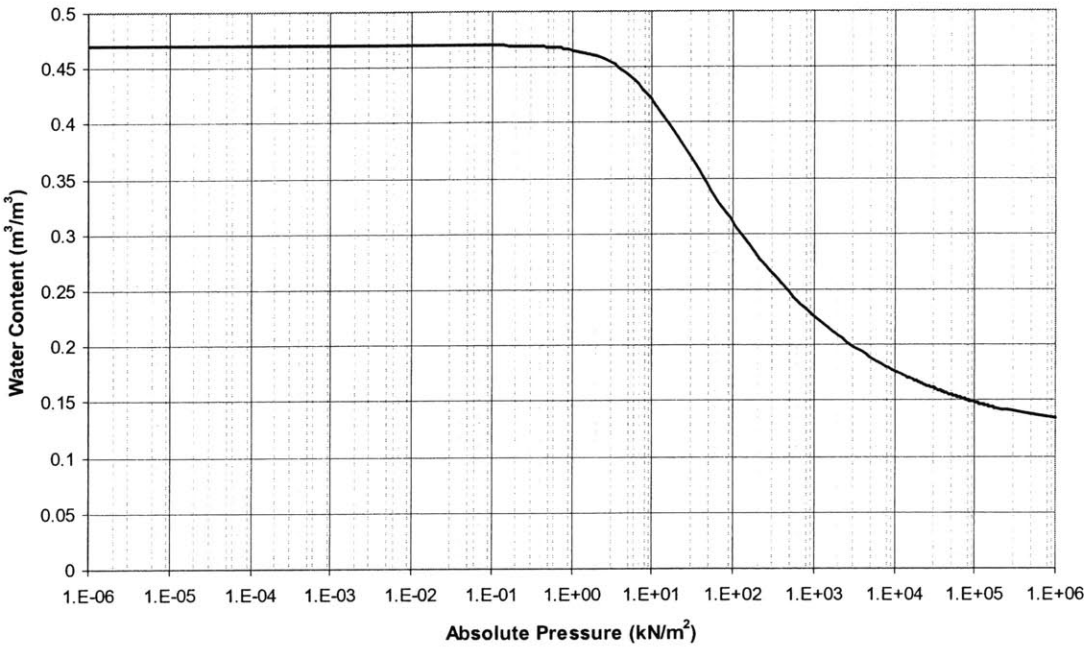

Figure 2.3. Soil Moisture Retention Curve (van Genuchten (1980) model)

Figure 2.4 illustrate, schematically, the transition a soil goes through as it is wetted/dried, and defines the residual moisture content, θ_r, and the air entry pressure, $(u_a - u_w)_{entry}$.

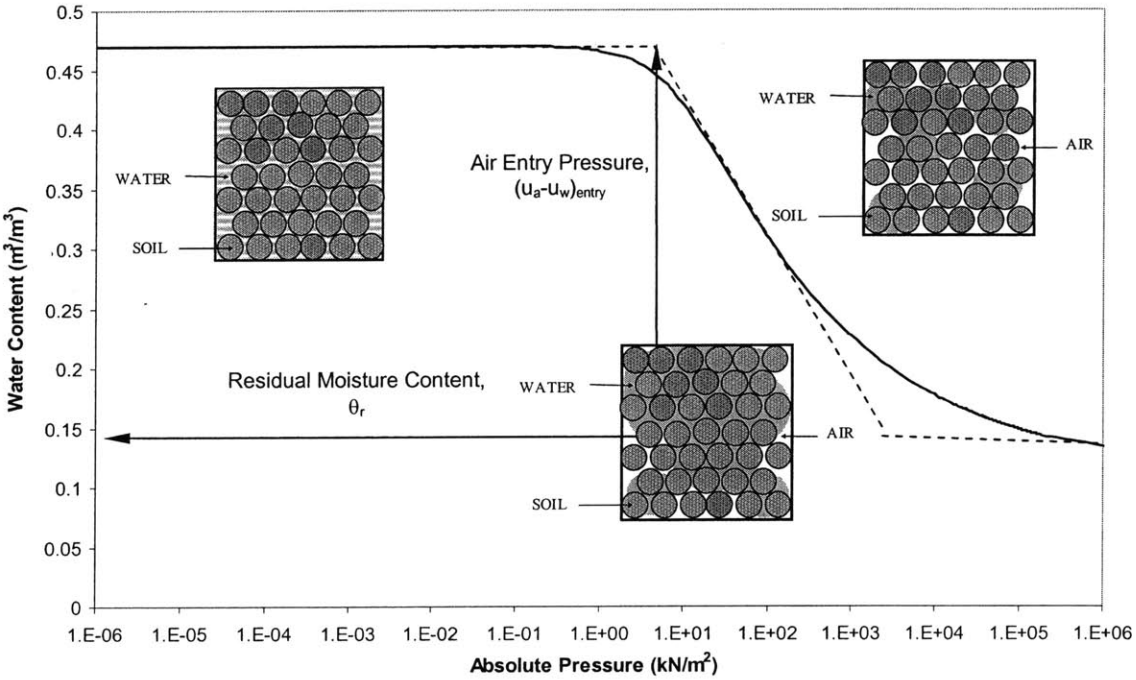

Figure 2.4. Definition of Residual Moisture Content and Air Entry Pressure

The residual moisture content is defined as the moisture content in the soil when it is dry.

The air entry pressure, $(u_a - u_w)_{entry}$, is defined as the pressure below which changes in pressure do not produce significant changes in moisture content (see Figure 2.4). While defined as just stated, the air entry pressure is not a physically measurable quantity. While one can measure the air pressure u_a, and the water pressure u_w, measuring the air entry pressure $(u_a - u_w)_{entry}$ is not possible. Because of this, various methods have been developed to determine the air entry pressure. Figure 2.4 illustrates schematically one such method, which makes use of the slope of the characteristic curve.

Figure 2.5 shows the hydraulic conductivity characteristic curve for the soil with parameters in Table 2.1, using the van Genuchten (1980) model.

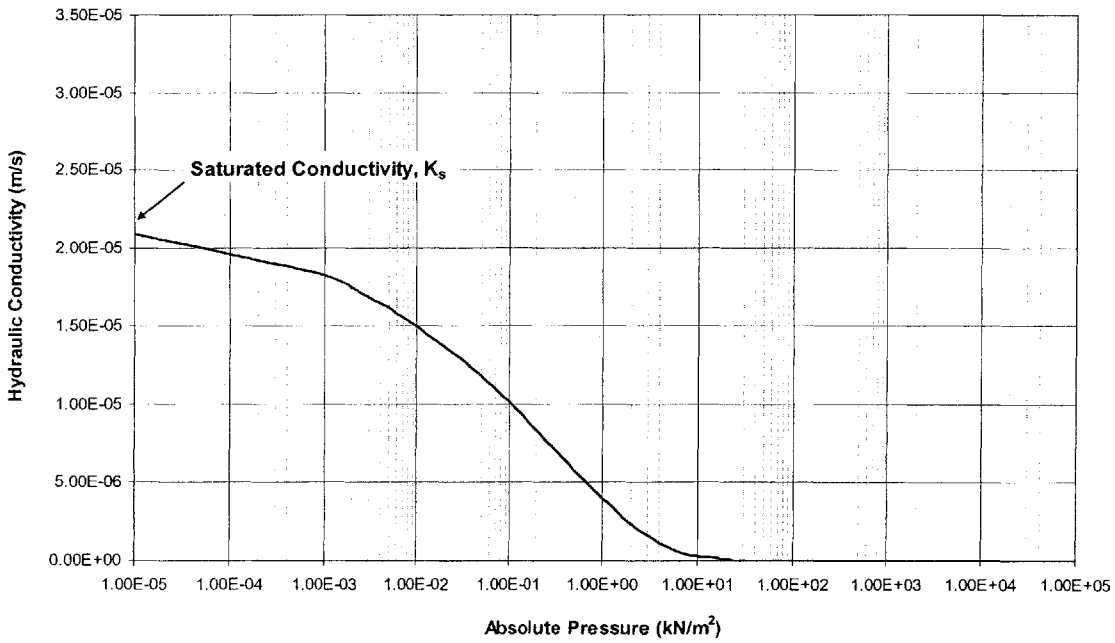

Figure 2.5. Hydraulic Conductivity Function (van Genuchten (1980) model)

In unsaturated soil, both the moisture content and hydraulic conductivity are functional relationships of pressure, as shown in Figures 2.3 and 2.5. Note that the characteristic curves in Figures 2.3 and 2.5 are shown in terms of absolute pressure. These relationships are, however, strictly only applicable when the soil is unsaturated, and pressures are negative. When the soil is saturated, the moisture content is the saturated moisture content of the soil, and the conductivity is the saturated conductivity.

Figures 2.3 and 2.5 show idealized soil characteristic curves that are typically much more complex. Furthermore, experimental studies have shown that these relationships are hysteretic, and follow different wetting and drying paths. This behavior, however, is not considered in this study. The study uses the van Genuchten (1980) model since it has been shown, through numerous laboratory studies, that the model gives good approximate curves (e.g. Tinjum et. 1997; Wang and Benson, 2004; etc).

2-1.2. GOVERNING EQUATION FOR WATER FLOW IN VARIABLY SATURATED MEDIA

Under the assumptions of a homogenous and isotropic soil, and one-dimensional (vertical) single-phase isothermal flow (see Figure 2.6), the conservation of mass of water equation is:

$$S_s S_a(\psi)\left(\frac{\partial \psi}{\partial t}\right) + \frac{\partial \theta}{\partial t} - \frac{\partial q}{\partial z} = 0 \qquad [2.5]$$

where:

- S_s is the specific storage coefficient
- S_a is the degree of saturation
- θ is the volumetric water content
- ψ is the pressure head
- t is time
- q is the soil moisture flux (water flux through the soil)
- z is the vertical coordinate with origin at the soil surface; taken to be positive downwards (see Figure 1)

The $S_s S_a(\psi)\left(\frac{\partial \psi}{\partial t}\right)$ term in Equation [2.5] accounts for the compressibility of the water and of the soil matrix.

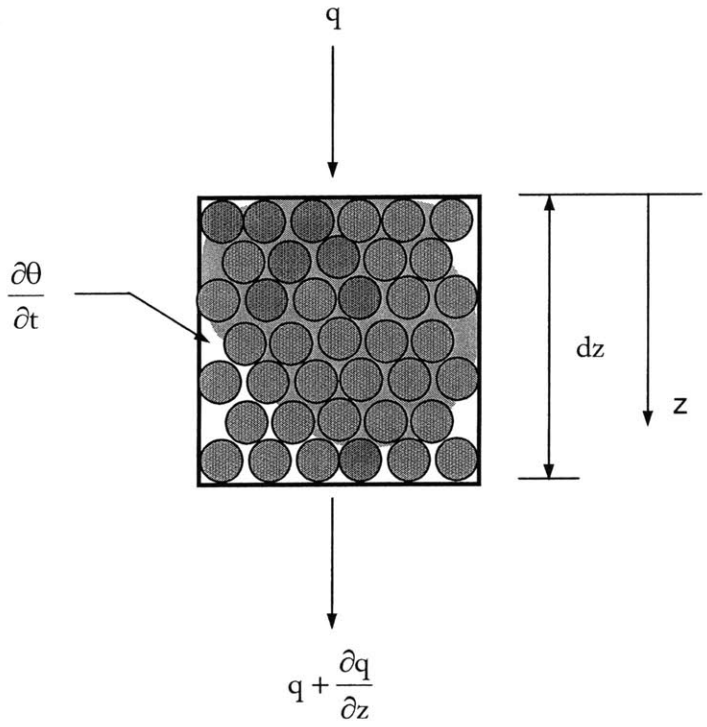

Figure 2.6. Schematic of Conservation of Water Mass Conservation and Sign Convention

Darcy's Law (Darcy, 1856) in one-dimension (see Figure 2.6) is expressed as:

$$q = K(\psi)\frac{\partial h}{\partial z} \qquad [2.6]$$

where:

$K(\psi)$ is the hydraulic conductivity characteristic function of the soil

h is the hydraulic head

Note that the flux in Equation [2.6] is positive because of the sign convention used where positive distances are downwards from the soil surface (see Figure 2.6).

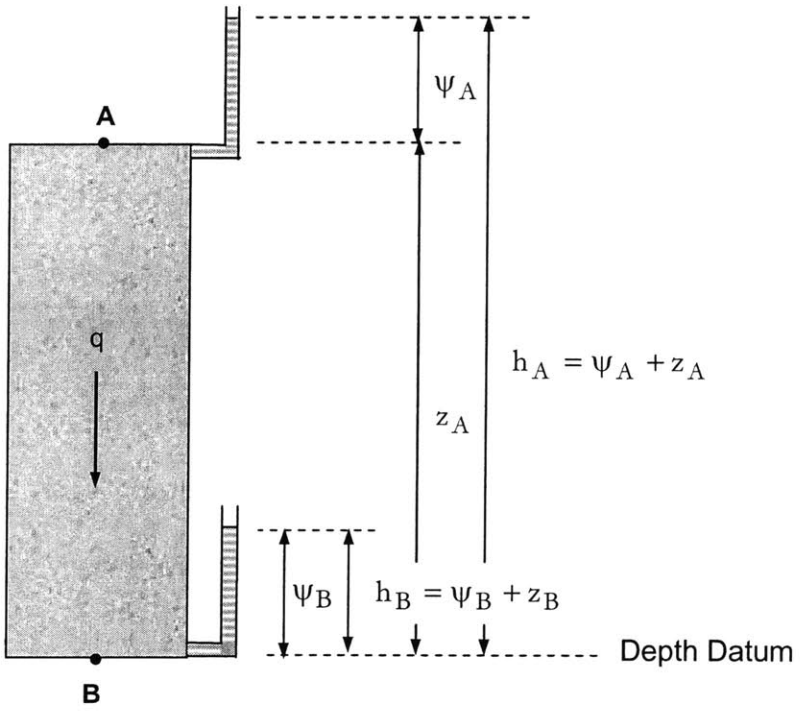

Figure 2.7. Darcy's Law in the Vertical Direction

The hydraulic head, h can be expressed as the sum of the pressure head ψ and the gravitational head, z assuming all other components of head such as kinetic and osmotic head are negligible (see Figure 2.7). Hence,

$$h = \psi + z \qquad [2.7]$$

Differentiating [2.7] with respect to z yields:

$$\frac{\partial h}{\partial z} = \frac{\partial \psi}{\partial z} + 1 \qquad [2.8]$$

Substituting [2.8] into Darcy's Law:

$$q = K(\psi)\left(\frac{\partial \psi}{\partial z} + 1\right) \qquad [2.9]$$

Substituting Equation [2.9] into the conservation of mass of water Equation in [2] gives:

$$\left(S_s S_a(\psi) + \frac{\partial\theta}{\partial\psi}\right)\frac{\partial\psi}{\partial t} = \frac{\partial}{\partial z}\left[K(\psi)\left(\frac{\partial\psi}{\partial z} + 1\right)\right] \qquad [2.10]$$

Defining $C(\psi) = \frac{d\theta}{d\psi}$, the slope of the $\theta(\psi)$ soil moisture retention curve as the specific moisture capacity, Equation [2.10] can be rewritten as:

$$\left(S_s S_a(\psi) + C(\psi)\right)\frac{\partial\psi}{\partial t} = \frac{\partial}{\partial z}\left[K(\psi)\left(\frac{\partial\psi}{\partial z} + 1\right)\right] \qquad [2.11]$$

Equation [2.11] is the governing equation for water flow in variably saturated soils and is commonly referred to as the compressible pressure-head based form of Richards Equation (Richards, 1931).

(A) UNSATURATED FLOW

In unsaturated soils, changes in moisture content θ, are accompanied by changes in the pressure head ψ, through the $\theta(\psi)$ relationship displayed on the soil characteristic curve (see Section 2-2.1). The slope of the $\theta(\psi)$ characteristic curve, $C(\psi)$ is non zero (see Figure 2.3 for example) and represents the unsaturated storage property of a soil. The hydraulic conductivity of unsaturated soils is also a functional relationship of moisture content and can be related to the pressure head through the $K(\psi)$ soil characteristic curve (see Figure 2.5 for example). The compressibility of the water, expressed in the specific storage term, is insignificant in relation to the specific moisture capacity and since $S_a(\psi) < 1$, Equation [2.11] is frequently approximated by:

$$C(\psi)\frac{\partial\psi}{\partial t} = \frac{\partial}{\partial z}\left[K(\psi)\left(\frac{\partial\psi}{\partial z} + 1\right)\right] \qquad [2.12]$$

(B) SATURATED FLOW

In saturated soils, the moisture content θ is equal to the porosity of the soil, which is a constant, so that the specific moisture capacity $C(\psi) = 0$. The hydraulic conductivity of the soil is independent of moisture content (hence pressure head), and is equal to the saturated conductivity of the soil. For generality, the saturated conductivity is assumed to be a function of the depth, z below the ground surface, so that in saturated conditions, $K(\psi) = K_s(z)$. Equation [2.11] thus becomes:

$$S_s \frac{\partial \psi}{\partial t} = \frac{\partial}{\partial z}\left[K_s(z)\left(\frac{\partial \psi}{\partial z} + 1 \right) \right] \qquad [2.13]$$

The solution to Equation [2.11], and hence [2.12] and [2.13] requires the specification of a set of boundary and initial conditions, as well as the soil characteristic curves and the saturated conductivity function $K_s(z)$. Initial conditions usually take the form of an initial soil moisture content profile or equivalently, an initial pressure head distribution. The boundary conditions relevant to the study of rainwater infiltration are discussed in the following section.

2-1.3. BOUNDARY CONDITIONS

2-1.3.1. TOP BOUNDARY CONDITIONS

The boundary conditions at the surface of the soil can be of the following different types:

(A) KNOWN/SPECIFIED FLUX

The first type of boundary condition is where the flux at the soil surface is known and defined by the climatic and soil conditions. The climatic conditions impose a potential flux given as:

$$q^*(0,t) = p + r - (e + i) + \kappa \qquad [2.14]$$

where:

$q^*(0,t)$	is the potential flux at the surface at a time, t
e	is the evaporation flux
p	is the precipitation flux
i	is the interception flux, which is the flux intercepted from the runoff from higher altitudes that enters the ground at the surface (see Figure 2.8)
r	is the irrigation flux
κ	is a parameter introduced to account for all other fluxes

Following the sign convention in Figure 2.6, fluxes into the ground are positive. The different fluxes in Equation [2.14] are shown schematically in Figure 2.8.

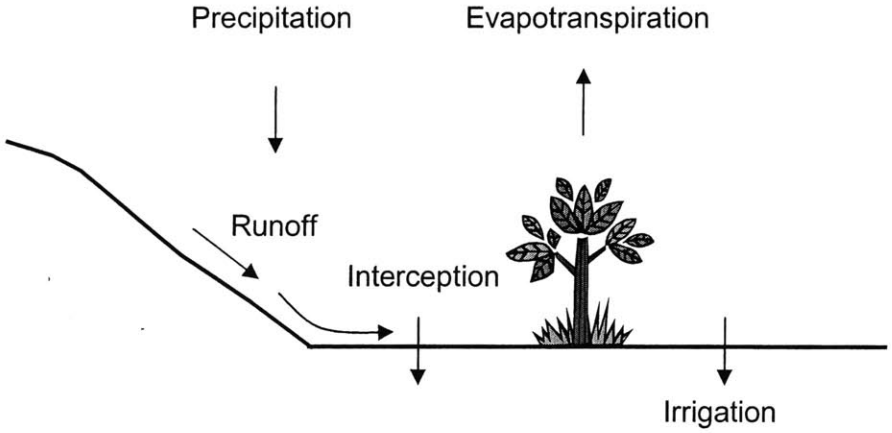

Figure 2.8. Schematic of Various Fluxes at Ground Surface

The potential flux in Equation [2.14] is the maximum possible flux that can enter the soil at the surface. This however, is not necessarily the actual flux that enters the soil. This is because the actual flux infiltrating into the soil is limited by the ability of the soil to

transmit water. The upper bound to the rate soil can transmit water is known as the infiltration capacity or potential infiltration rate of the soil (Horton, 1933) and is given by:

$$q(0,t) = K(\psi)\left[\frac{\partial \psi}{\partial z} + 1\right]_{z=0} \qquad [2.15]$$

A schematic showing the typical variation of potential infiltration with time, and hence increasing moisture content is shown in Figure 2.9.

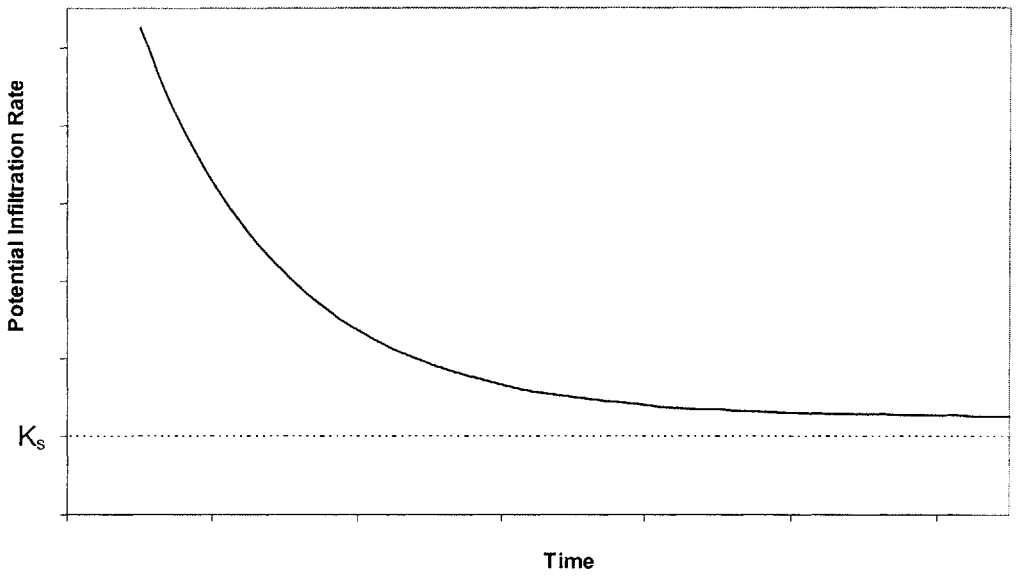

Figure 2.9. Schematic of Potential Infiltration Rate versus Time

Therefore, at any time t, the actual infiltration flux into the soil is given by the smaller of the potential flux in [2.14] and the infiltration capacity of the soil in [2.15]. It is the minimum because of the sign convention used in this study, where fluxes into the soil are taken to be positive. So, the actual infiltration flux is given by:

$$q_t(t) = \min[q(0,t), q^*(0,t)] \qquad [2.16]$$

where:

$q_t(t)$ is the actual flux at the soil surface

During evaporation the fluxes are out of the soil, both $q^*(0,t)$ and $q(0,t)$ are negative (out of the soil), and a minimum pressure head is usually specified at the surface corresponding to dry air conditions:

$$\psi_t = \psi_{min} \text{ and } \theta_t = \theta(\psi_{min}) = \theta_r \qquad [2.17]$$

where:

θ_r is the residual soil moisture content as defined in Section 2-2.1.

The actual flux is now given by:

$$q_t(t) = \max[q(0,t), q^*(0,t)] \qquad [2.18]$$

If $q^*(0,t)$ and $q(0,t)$ have opposite signs, then:

$$q_t(t) = 0 \qquad [2.19]$$

To illustrate the behavior of the fluxes at the soil surface, consider a time varying imposed flux as shown in Figure 2.10.

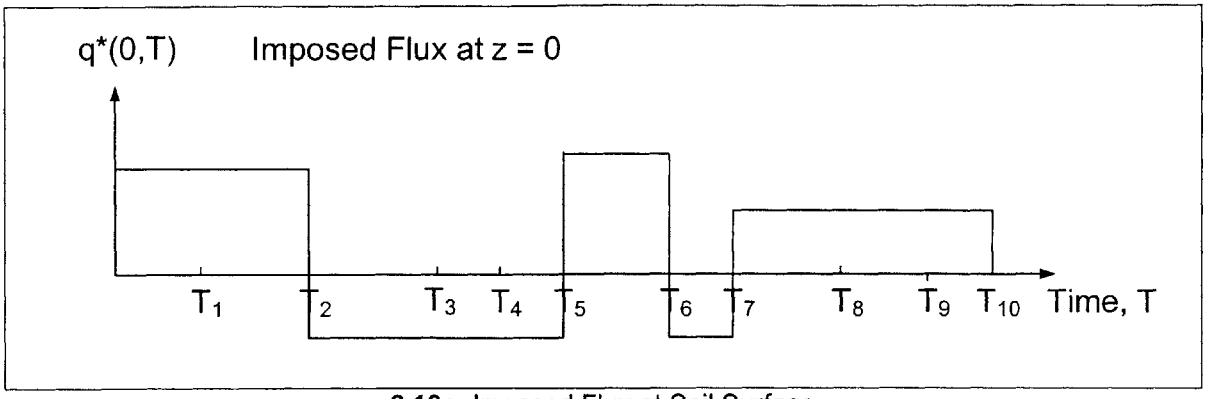

2.10a. Imposed Flux at Soil Surface

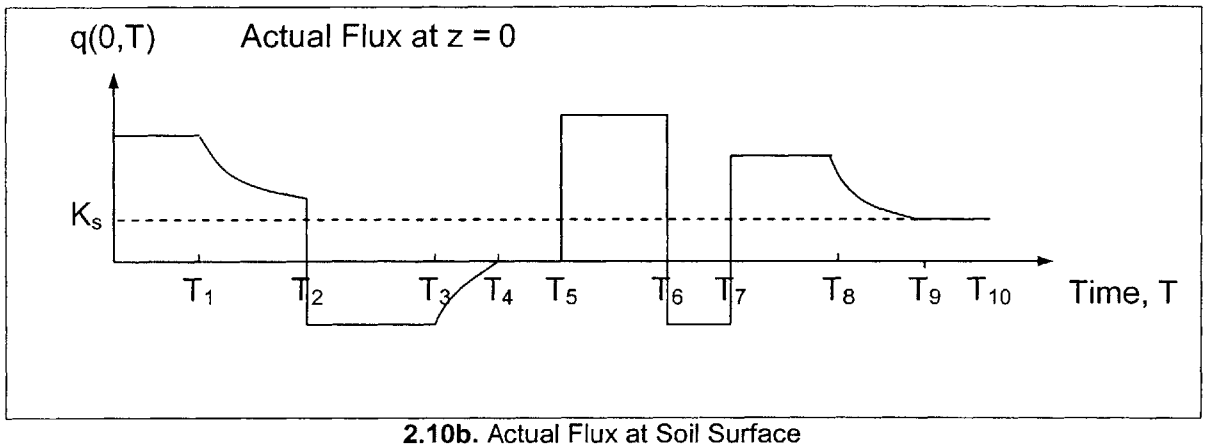

2.10b. Actual Flux at Soil Surface

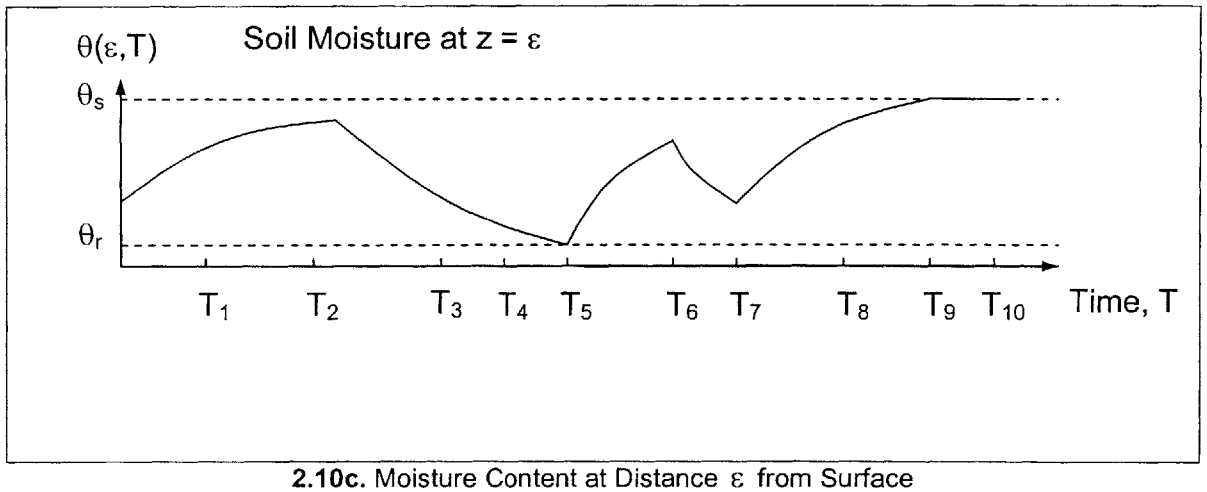

2.10c. Moisture Content at Distance ε from Surface

Figure 2.10. Modeling a Known Flux Boundary Condition at the Soil Surface

Explanation of Figure 2.10:

$0 \leq t \leq T_2$

For all times $0 \leq t \leq T_2$ the imposed flux at the soil surface $q^*(0,t)$ is positive, and infiltration into the soil occurs. Initially, the soil is assumed to have low moisture content as shown in Figure 2.10c. Therefore, the infiltration capacity of the soil is high, and is greater than the imposed flux. The actual flux as given in Equation [2.18] is equal to the imposed flux as shown in Figure 2.10b. All the water infiltrates into the soil increasing the moisture content. Figure 2.10c shows this at a small distance ε below the ground surface. With increasing moisture content, the infiltration capacity of the soil decreases until it becomes equal to the imposed flux at time T_1. For all times $T_1 \leq t \leq T_2$ the actual flux is equal to the infiltration capacity of the soil (see Figure 2.10b). The moisture content at ε continues to increase. All excess water either ponds on the surface or is observed as surface runoff.

$T_2 \leq t \leq T_5$

For times $T_2 \leq t \leq T_5$, the imposed flux $q^*(0,t)$ is negative and evaporation occurs. The infiltration (negative now) or evaporative capacity of the soil is high since the moisture content is high at times slightly greater than T_2. The actual infiltration (evaporation) rate is therefore equal to the imposed flux from T_2 to T_3 because the infiltration (evaporative) capacity is greater than the imposed flux. Water evaporates from the soil as shown in Figure 2.10c, and as this takes place the infiltration (evaporative) capacity decreases. At a time T_3 the infiltration (evaporative) capacity becomes equal to the imposed flux, and for $T_3 \leq t \leq T_4$ the actual flux is equal to the infiltration (evaporative) capacity of the soil. The moisture content continues to decrease as shown in Figure 2.10c. At T_4, the infiltration (evaporative) capacity of the soil becomes positive, and since the imposed flux is negative, the actual flux is zero since no upwards flow is possible. The moisture content at ε decreases until the residual moisture content is reached at time T_5. In essence therefore, what happens in times between $T_2 \leq t \leq T_5$ is similar to what happens for $0 \leq t \leq T_2$ expect that fluxes are negative and evaporative.

$T_5 \leq t \leq T_6$

For $T_5 \leq t \leq T_6$, the imposed flux is positive and since the infiltration capacity of the soil is very large because of its low moisture content, the actual flux is equal to the imposed flux. The moisture content at ε increases (see Figure 2.10c).

$T_6 \leq t \leq T_7$

For $T_6 \leq t \leq T_7$, the imposed flux is negative and the actual flux is equal to the imposed flux. The moisture content at ε decreases (see Figure 2.10c).

$T_8 \leq t \leq T_{10}$

For $T_8 \leq t \leq T_{10}$, the imposed flux is positive and because of the large infiltration capacity of the soil caused by the low moisture content, the actual flux is equal to the imposed flux. The moisture content at ε increases. At T_8, the infiltration capacity becomes equal to the imposed flux and for $T_8 \leq t \leq T_9$ the actual flux is equal to the infiltration capacity. The moisture content continues to increase until at T_9 saturation is reached (see Figure 2.10c). From this time onwards, the actual flux can only be equal to the saturated hydraulic conductivity (see Figure 2.10b).

(B) KNOWN/SPECIFIED PRESSURE HEAD

Another type of boundary condition at the top of a soil profile is where the pressure head (or equivalently, the soil moisture) is specified. In this case:

$$\psi_t = \text{known} \text{ or } \theta_t = \text{known} \qquad [2.20]$$

where:

ψ_t is the pressure head at the soil surface

θ_t is the moisture content at the soil surface

This condition occurs when the soil profile gets saturated and infiltration becomes governed by pressure head at the surface due to the ponding of surface water.

2-1.3.2. BOTTOM BOUNDARY CONDITIONS

The boundary conditions at the bottom of the soil profile relevant to rainwater infiltration include:

(A) CONSTANT OR TIME VARYING GROUNDWATER TABLE

One type of bottom boundary conditions is where the depth to the water table from the ground surface z_w is known. This is a situation of interest, for example, in the presence of a shallow water table of known depth. Consider Figure 2.11 for example, where the depth to the water table is shallow and known. We define a modeling depth z_m as the depth of the soil layer, from the ground surface, that is to be modeled using an infiltration model. In the case of a shallow water table, the modeling depth z_m is the depth to the water table z_w, which is known (see Figure 2.11). Since, the moisture content of the soil at the water table is equal to the saturated moisture content and by definition, the pressure head is equal to zero, the bottom boundary condition can be specified as:

$$\psi_b = \psi(z = z_w) = 0 \text{ or } \theta_b = \theta(z = z_w) = \theta_s \qquad [2.21]$$

where:

ψ_b is the pressure head at the bottom of the soil profile to be modeled

θ_b is the moisture content at bottom of the soil profile to be modeled

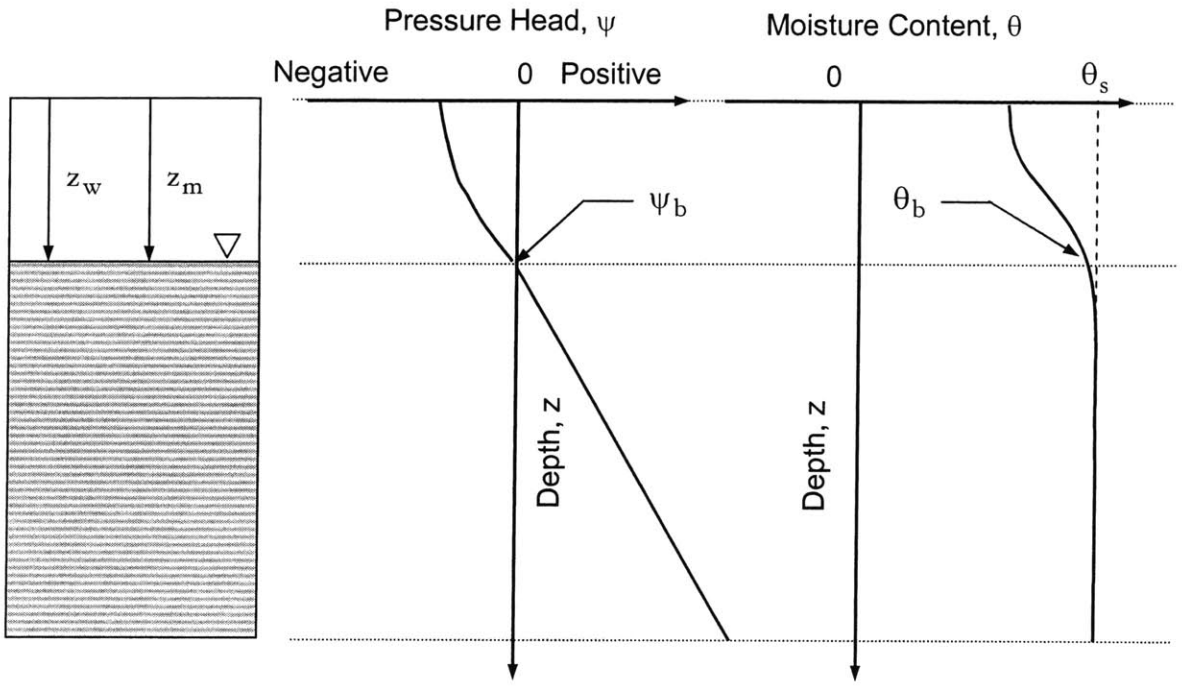

Figure 2.11. Schematic of Bottom Boundary Condition where the Groundwater Level is Shallow and Known

(B) SPECIFIED PRESSURE HEAD

Another type of bottom boundary condition is where the pressure head at the bottom of the soil profile is specified. There is a subtle but important difference between this boundary condition and the one described in (a) above. In (a), the groundwater table depth is known and hence the pressure head at this depth is known. In (b), the pressure head is not known, but assumed and specified. This situation may occur, for example, in the presence of a deep water table. Consider Figure 2.12 for example, where the water table is deep.

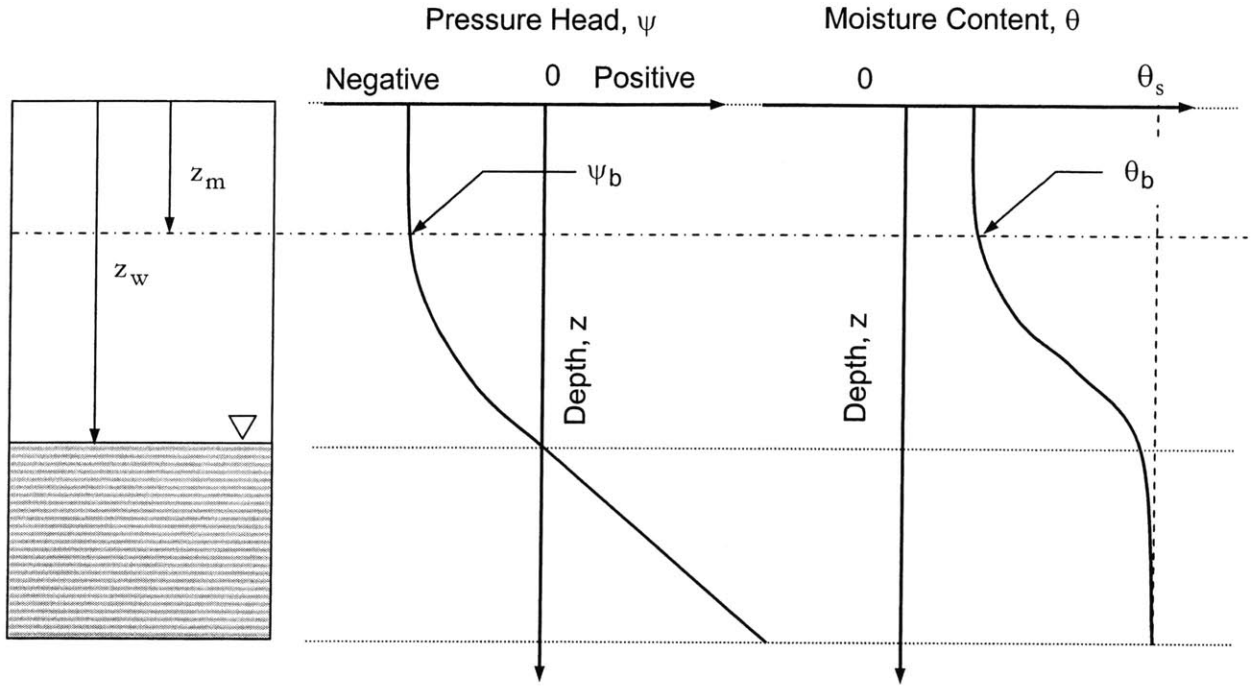

Figure 2.12. Schematic of Bottom Boundary Condition where the Groundwater Level is Deep and Bottom Pressure Head is Specified

Typical moisture content and pressure profiles are shown in Figure 2.12. Figure 2.12 shows that the suction is almost constant up to a certain depth below the ground surface. This is because the maximum suction attainable in the soil is limited by the pore size distribution, grain size distributions, as well as other factors. The modeling depth z_m is therefore less than the water table depth z_w. The bottom boundary condition can be specified as:

$$\psi_b = \psi(z = z_m) = \text{assumed / specified, or}$$
$$\theta_b = \theta(z = z_m) = \text{assumed / specified} \qquad [2.21]$$

where:

ψ_b is the pressure head at the bottom of the soil

θ_b is the moisture content at the bottom of the soil

2-1.4. NUMERICAL SOLUTION OF FLOW EQUATION

Equation [2.11] is a nonlinear partial differential equation for which analytical solutions are limited to few special cases. Numerical methods are, therefore, used to obtain solutions. Finite difference and finite element methods have been used to solve Equation [2.11]. Finite element methods are advantageous for irregular geometries in two and three-dimensional flow domains. In one dimension, finite difference methods are advantageous in that they are relatively easy to visualize and to implement in numerical routines. One dimensional analyses are also sufficiently accurate since infiltration into unsaturated soil is predominantly vertical (Philips, 1965; Romano et al., 1998). Moreover, detailed simulations performed by van Genuchten (1980) showed that finite difference schemes generate more stable solutions than finite element schemes when a steep moisture front is present because of the almost instant decrease in moisture content that are typically associated with steep moisture fronts.

In this study, a finite difference numerical scheme is developed to solve for the pressure based form of the variably saturated flow equation (see Equation [2.11]). The scheme simultaneously solves for flow in saturated and unsaturated soil, and its solution is implemented in a spreadsheet.

Consider a one dimensional vertical unsaturated flow domain, where the governing equation of flow is given by the one dimensional form of Richards' Equation:

$$\frac{\partial \psi}{\partial t} = \left(\frac{1}{C(\psi) + S_s S_a(\psi)} \right) \frac{\partial}{\partial z} \left[K(\psi) \left(\frac{\partial \psi}{\partial z} + 1 \right) \right] \qquad [2.22]$$

where:

$\psi = \psi(z,t) = h - z$ is the pressure head

$C(\psi) = \dfrac{d\theta}{d\psi}$ is the specific moisture capacity

t is the time

$h = h(z,t)$ is the hydraulic head

z is the vertical coordinate, taken to be positive downwards

$\theta(\psi)$ is the volumetric water content

$K(\psi)$ is the hydraulic conductivity function

The finite difference grid for the implicit scheme used in this study is shown in Figure 2.13. The time index is denoted by i and the space index by j.

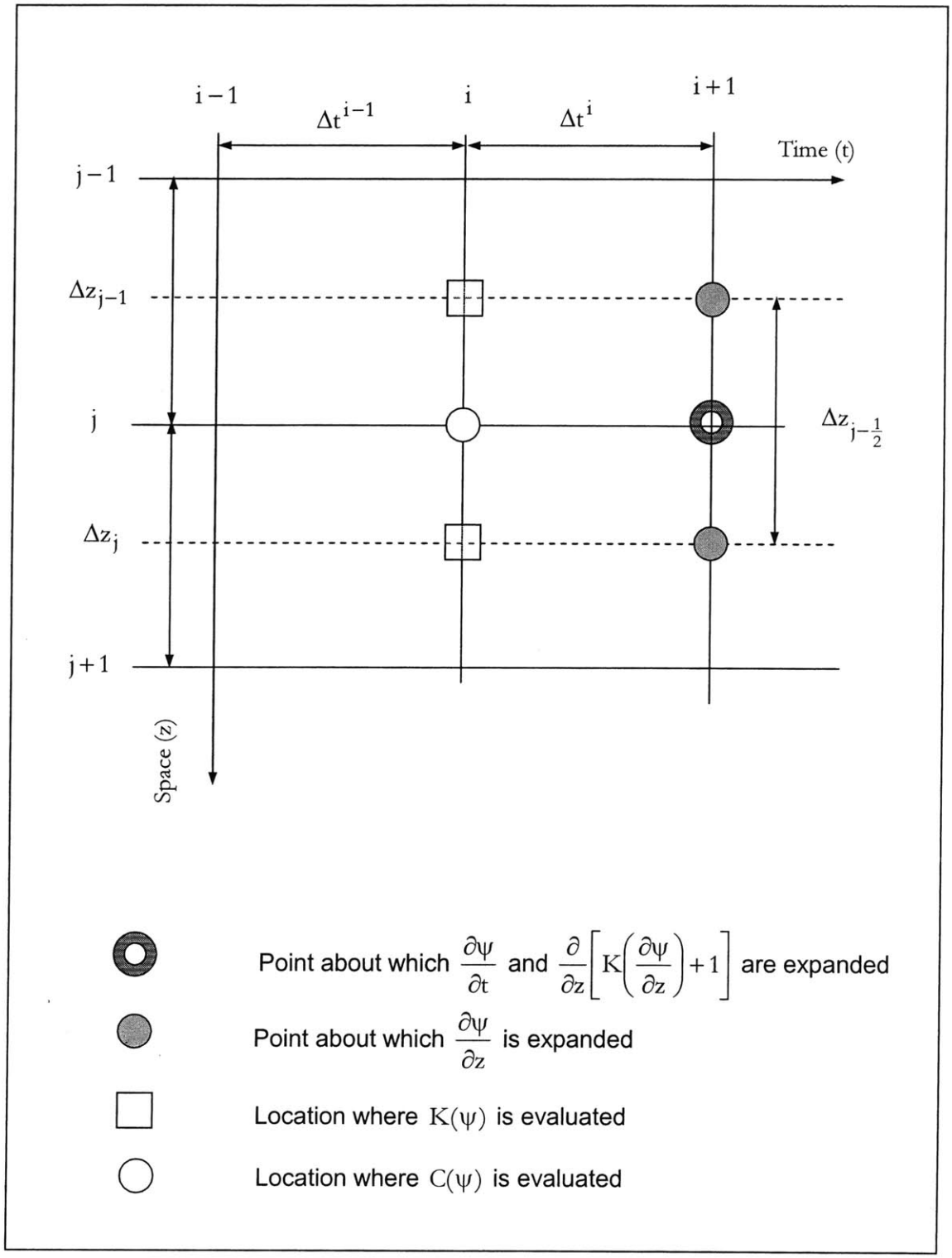

Figure 2.13. Finite Difference Grid, Implicit form for Numerical Solution

The partial differential terms (except for the spatial $\partial\psi/\partial z$ term) in Equation [2.22] are expanded about the point (i+1, j) to give:

$$\frac{\partial \psi}{\partial t} = \frac{\psi_j^{i+1} - \psi_j^i}{\Delta t^i} \qquad [2.23]$$

$$\frac{\partial}{\partial z}\left[K(\psi)\left(\frac{\partial \psi}{\partial z}+1\right)\right] = \frac{1}{\Delta z_{j-1/2}}\left[K\left(\psi^i_{j-1/2}\right)\left(\left(\frac{\partial \psi}{\partial z}\right)^{i+1}_{j-1/2}+1\right) - K\left(\psi^i_{j+1/2}\right)\left(\left(\frac{\partial \psi}{\partial z}\right)^{i+1}_{j+1/2}+1\right)\right] \qquad [2.24]$$

The spatial derivatives are approximated as:

$$\left(\frac{\partial \psi}{\partial z}\right)^{i+1}_{j-1/2} = \frac{\psi^{i+1}_{j-1} - \psi^{i+1}_j}{\Delta z_{j-1}} \qquad [2.25]$$

$$\left(\frac{\partial \psi}{\partial z}\right)^{i+1}_{j+1/2} = \frac{\psi^{i+1}_j - \psi^{i+1}_{j+1}}{\Delta z_j} \qquad [2.26]$$

Since the partial derivatives of Equation [2.26 are expanded about the point $(i+1,j)$, the $C(\psi)$ and $S_a(\psi)$ terms should also be evaluated at the same point. This however, would introduce too many unknowns and the $C(\psi)$ and $S_a(\psi)$ terms are evaluated at the previous time step i.e. at point (i,j). For similar reasons, the $K(\psi)$ terms are also evaluated at the previous time step.

A geometric mean approximation is used to evaluate the $K(\psi)$ terms between spatial nodes (Hoverkamp et al., 1977; Belmans et al., 1983) as:

$$K\left(\psi^i_{j+1/2}\right) = \sqrt{K\left(\psi^i_j\right)K\left(\psi^i_{j+1}\right)} \qquad [2.27]$$

Where the hydraulic conductivities in [2.27] are obtained from the soil characteristic curve, $K(\psi)$.

Substituting Equations [2.23] through [2.27] into Equation [2.22] yields:

$$\frac{\psi_j^{i+1}-\psi_j^i}{\Delta t^i} = \left(\frac{1}{C(\psi_j^i)+S_sS_a(\psi^i)}\right)\frac{1}{\Delta z_{j-1/2}}\left[K\left(\psi_{j-1/2}^i\right)\left(\left(\frac{\psi_{j-1}^{i+1}-\psi_j^{i+1}}{\Delta z_{j-1}}\right)+1\right)-K\left(\psi_{j+1/2}^i\right)\left(\left(\frac{\psi_{j-1}^{i+1}-\psi_{j+1}^{i+1}}{\Delta z_j}\right)+1\right)\right] \quad [2.28]$$

Rearranging Equation [2.28] to move the unknowns ψ_{j+1}^{i+1}, ψ_j^{i+1} and ψ_{j-1}^{i+1} to the left hand side of the equation gives:

$$A_j\psi_{j+1}^{i+1}+B_j\psi_j^{i+1}+D_j\psi_{j-1}^{i+1}=E_j \quad [2.29]$$

where:

$$A_j=-\frac{\Delta t^i K\left(\psi_{j+1/2}^i\right)}{\left(C(\psi_j^i)+S_sS_a(\psi_j^i)\right)\Delta z_{j-1/2}\Delta z_j} \quad [2.30]$$

$$B_j=1+\frac{\Delta t^i K\left(\psi_{j-1/2}^i\right)}{\left(C(\psi_j^i)+S_sS_a(\psi_j^i)\right)\Delta z_{j-1/2}\Delta z_{j-1}}+\frac{\Delta t^i K\left(\psi_{j+1/2}^i\right)}{\left(C(\psi_i^j)+S_sS_a(\psi_j^i)\right)\Delta z_{j-1/2}\Delta z_j} \quad [2.31]$$

$$D_j=-\frac{\Delta t^i K\left(\psi_{j-1/2}^i\right)}{\left(C(\psi_j^i)+S_sS_a(\psi_j^i)\right)\Delta z_{j-1/2}\Delta z_{j-1}} \quad [2.32]$$

$$E_j=\psi_j^i+\frac{\Delta t^i K\left(\psi_{j-1/2}^i\right)}{\left(C(\psi_j^i)+S_sS_a(\psi_j^i)\right)\Delta z_{j-1/2}}-\frac{\Delta t^i K\left(\psi_{j+1/2}^i\right)}{\left(C(\psi_j^i)+S_sS_a(\psi_j^i)\right)\Delta z_{j-1/2}} \quad [2.33]$$

For this one dimensional study, where the soil profile is of finite depth, the depth is divided into n segments creating $n+1$ nodes as shown in Figure 2.14.

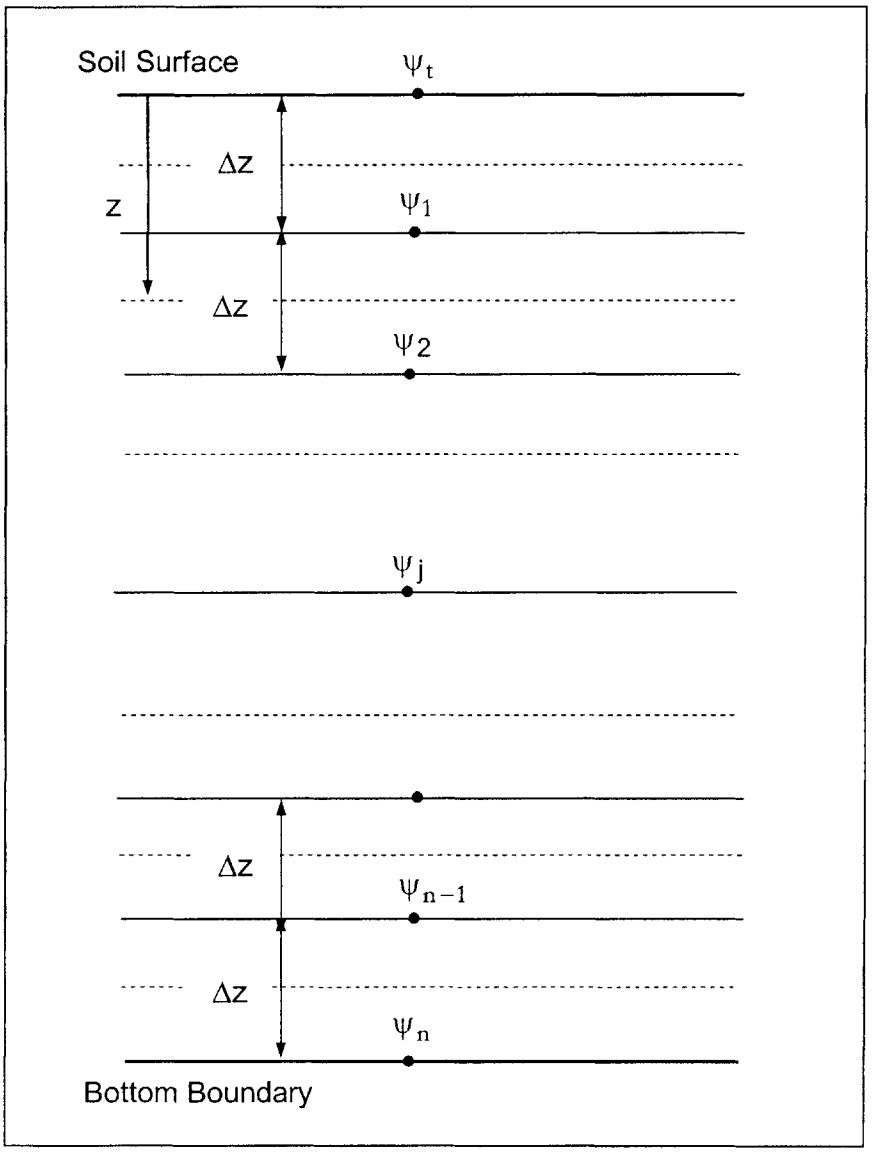

Figure 2.14. Soil Profile Discretization

Equation [2.29] is written at the interior nodes, i.e. $j=1$ through $j=n-1$ (see Figure 2.14). At the top $j=1$ and bottom $j=n$ nodes, boundary conditions are introduced to give rise to two additional equations:

$$A_1\psi_2^{i+1} + B_1\psi_1^{i+1} = E_1 \qquad [2.34]$$

$$B_n\psi_n^{i+1} + D_n\psi_{n-1}^{i+1} = E_n \qquad [2.35]$$

Equation [2.34] is the boundary condition at the top of the soil profile. Note that this boundary condition cannot be specified at exactly the soil surface where $z = 0$, and instead has to be specified at an incremental distance Δz from the surface, and hence at $j = 1$.

Equations [2.29], [2.34] and [2.35] generate a linear system of n equations with n unknowns. These equations are written in matrix form as:

$$\begin{bmatrix} B_1 & A_1 & 0 & \cdots & 0 \\ D_2 & B_2 & A_2 & & \\ 0 & D_3 & B_3 & A_3 & \\ \vdots & & & & \\ & & D_{n-1} & B_{n-1} & A_{n-1} \\ 0 & \cdots & 0 & D_n & B_n \end{bmatrix} \begin{bmatrix} \psi_1^{i+1} \\ \psi_2^{i+1} \\ \vdots \\ \psi_{n-1}^{i+1} \\ \psi_n^{i+1} \end{bmatrix} = \begin{bmatrix} E_1 \\ E_2 \\ \vdots \\ E_{n-1} \\ E_n \end{bmatrix}$$

or

$$A_f(\psi_\kappa, \zeta)\Psi_{\kappa+1} = e(\psi_\kappa, \zeta) \qquad [2.36]$$

where:

$\Psi_{\kappa+1}$ is a column vector of pressure heads at n discrete nodes at time $\kappa + 1$

$A_f(\psi_K, \zeta)$	is a tridiagonal $n \times n$ matrix, i.e. one whose structure has non-zero entries on the leading, and two adjacent diagonals, and zero entries elsewhere
$e(\psi_K, \zeta)$	is an $n \times 1$ vector function
ζ	is a vector with the parameters that control the functions $K(\psi)$ and $C(\psi)$ at each node of the soil profile

Since $A_f(\psi_K, \zeta)$ is a tridiagonal matrix, a direct, fast and simple algorithm, such as the Thomas Algorithm can be used to solve Equation [2.36] for the pressure head distribution $\psi(z,t)$. Details of this are provided in Appendix A. The soil moisture profile $\theta(z,t)$ is then determined from $\psi(z,t)$ and the soil characteristic curve $\theta(\psi)$.

2-1.4.1. NUMERICAL IMPLEMENTATION OF BOUNDARY CONDITIONS

2-1.4.1.1. TOP BOUNDARY CONDITION

(A) KNOWN/SPECIFIED FLUX

The equation for the boundary condition at the soil surface for the case of known flux is derived by first computing q_t using Equation [2.18] as the feasible flux. Then Equation [2.36] with $j = 1$ takes the form:

$$\frac{\psi_1^{i+1} - \psi_1^i}{\Delta t^i} = \frac{1}{\left(C(\psi_1^i) + S_s S_a(\psi_1^i)\right)} \frac{1}{\Delta z_{1/2}} \left[-q_t - K\left(\psi_{3/2}^i\right)\left(\left(\frac{\psi_1^{i+1} - \psi_2^{i+1}}{\Delta z_1}\right) + 1\right)\right] \quad [2.37]$$

or

$$-\left[\frac{\Delta t^i K\left(\psi_{3/2}^i\right)}{\left(C(\psi_1^i) + S_s S_a(\psi_1^i)\right)\Delta z_{1/2}\Delta z_1}\right]\psi_1^{i+1} + \left[1 + \frac{\Delta t^i K\left(\psi_{3/2}^i\right)}{\left(C(\psi_1^i) + S_s S_a(\psi_1^i)\right)\Delta z_{1/2}\Delta z_1}\right]\psi_2^{i+1} =$$

$$\psi_1^i - \left[\frac{\Delta t^i}{\left(C(\psi_1^i) + S_s S_a(\psi_1^i)\right)\Delta z_{1/2}}\right] q_t - \left[\frac{\Delta t^i}{\left(C(\psi_1^i) + S_s S_a(\psi_1^i)\right)\Delta z_{1/2}}\right] K\left(\psi_{3/2}^i\right) \quad [2.38]$$

If we let:

$$A_1 = \left[1 + \frac{\Delta t^i K\left(\psi_{3/2}^i\right)}{\left(C(\psi_1^i) + S_s S_a(\psi_1^i)\right)\Delta z_{1/2}\Delta z_1}\right] \quad [2.39]$$

$$B_1 = 1 - A_1 \quad [2.40]$$

$$D_1 = 0 \quad [2.41]$$

$$E_1 = \psi_1^i - \left[\frac{\Delta t^i}{\left(C(\psi_1^i) + S_s S_a(\psi_1^i)\right)\Delta z_{1/2}}\right] q_t - \left[\frac{\Delta t^i}{\left(C(\psi_1^i) + S_s S_a(\psi_1^i)\right)\Delta z_{1/2}}\right] K\left(\psi_{3/2}^i\right) \quad [2.42]$$

Then Equation [2.38] can be rewritten as:

$$A_1 \psi_2^{i+1} + B_1 \psi_1^{i+1} = E_1 \quad [2.43]$$

Equation [2.43] has exactly the form of Equation [2.29] and the numerical scheme in Appendix A can be implemented.

(B) KNOWN/SPECIFIED PRESSURE HEAD

If we denote the specified pressure head at the surface by $h_{surface}$, the equation for the boundary condition at the soil surface for the case of known pressure head is expressed as:

$$\frac{\psi_1^{i+1} - \psi_1^i}{\Delta t^i} = \frac{1}{\left(C(\psi_1^i) + S_s S_a(\psi_1^i)\right)} \frac{1}{\Delta z_{1/2}} \left[K\left(\psi_{1/2}^i\right)\left(\left(\frac{h_{surface} - \psi_1^{i+1}}{\Delta z_1}\right) + 1\right) - K\left(\psi_{3/2}^i\right)\left(\left(\frac{\psi_1^{1+1} - \psi_2^{i+1}}{\Delta z_1}\right) + 1\right)\right] \quad [2.44]$$

If we let:

$$A_1 = \left[1 + \frac{\Delta t^i K\left(\psi_{3/2}^i\right)}{\left(C(\psi_1^i) + S_s S_a(\psi_1^i)\right)\Delta z_{1/2} \Delta z_1}\right] \quad [2.45]$$

$$B_1 = 1 - A_1 + \frac{\Delta t^i K\left(\psi^i_{1/2}\right)}{\left(C(\psi_1) + S_s S_a(\psi^i_1)\right)\Delta z_{1/2}\Delta z_1} \qquad [2.46]$$

$$D_1 = 0 \qquad [2.47]$$

$E_1 =$

$$\psi^i_1 + \left[\frac{\Delta t^i}{\left(C(\psi^i_1) + S_s S_a(\psi^i_1)\right)\Delta z_{1/2}}\right]\left\{K\left(\psi^i_{1/2}\right) - K\left(\psi^i_{3/2}\right)\right\} - \left[\frac{\Delta t^i}{\left(C(\psi^i_1) + S_s S_a(\psi^i_1)\right)\Delta z_{1/2}\Delta z_1}\right]K\left(\psi^i_{1/2}\right)h_{surface} \qquad [2.48]$$

Then Equation [2.44] can be rewritten as:

$$A_1\psi_2^{i+1} + B_1\psi_1^{i+1} = E_1 \qquad [2.49]$$

Now, Equation [2.49] has the form [2.29] and the numerical scheme in Appendix A can be implemented.

A difficulty that may arise with numerical solutions to the flow problem is that during the application of a specified flux at the soil surface, the top boundary condition may switch from being head controlled to being flux controlled and vice versa. An appropriate procedure for the selection of the top boundary condition may determine the success or failure of a numerical scheme. Figure 2.15 shows the decision procedure for top boundary condition selection.

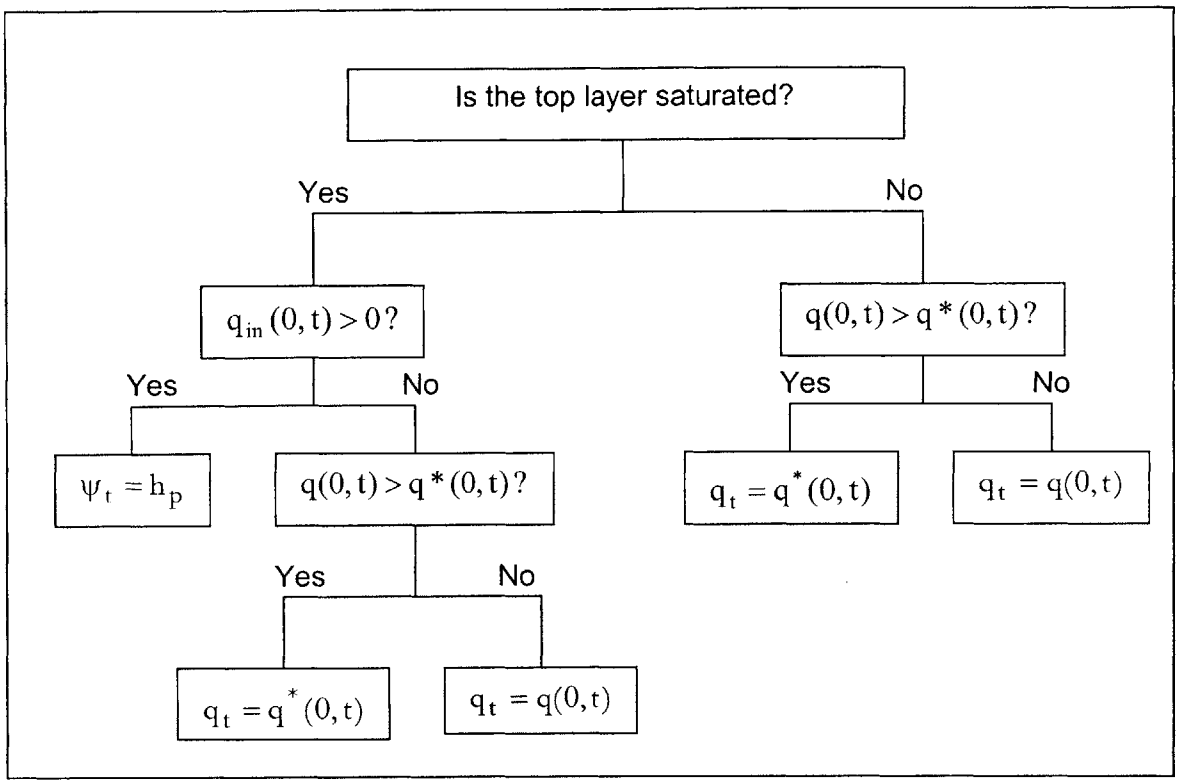

Figure 2.15. Decision Procedure for Selection of Top Boundary Condition

where:

$q*(0,t)$ is the potential flux at the surface at a time, t

$q(0,t)$ is infiltration capacity of the soil at the surface

$q_{in}(0,t)$ is the inflow at the surface and is computed as:

$q_{in}(0,t)$ is given by:

$$q_{in}(0,t) = [q_t(0,t) - q_b(\Delta z,t)]\Delta t^i \qquad [2.50]$$

where:

$q_b(\Delta z,t)$ is the flux at the bottom of the first soil compartment

$q_t(0,t)$ is the actual flux at the top of the soil layer and

$q_t(0,t) = \max[q(0,t), q*(0,t)]$

The first criterion considers if the soil layer at the surface of the profile is saturated or unsaturated at the beginning of every time step. For the first time step, this is determined from the initial (in situ) moisture content profile.

If the soil layer is saturated at the start of the time step, then the second criterion determines whether at the end of the time step the soil layer is still saturated or becomes unsaturated.

If the soil at the surface remains saturated then the top boundary condition is in the form of a specified pressure head $\psi_t = h_p$, where h_p is the ponding depth at the soil surface. If ponding is neglected, the specified top pressure head becomes $\psi_t = 0$.

If the soil becomes unsaturated at the end of the time step then the top boundary condition is in the form of a specified flux where the flux $q_t(0,t)$ is the larger of the applied flux (rainfall intensity) $q(0,t)$ and the potential infiltration rate $q^*(0,t)$.

$$q_t(0,t) = \max[q(0,t), q*(0,t)] \qquad [2.51]$$

If the soil layer at the surface is unsaturated at the beginning of a time step then the top boundary condition is a specified flux which is again the larger of the applied flux (rainfall intensity) $q(0,t)$ and the potential infiltration rate $q^*(0,t)$.

$$q_t(0,t) = \max[q(0,t), q*(0,t)] \qquad [2.52]$$

2-1.4.1.2. BOTTOM BOUNDARY CONDITION

(A) SPECIFIED GROUNDWATER LEVEL z_w

When the groundwater level is at a known or specified depth, z_w, the thickness of the n^{th} compartment of the unsaturated zone varies with time and increasing moisture content because the increase in moisture content causes a rise in the water table level (see Figure 2.16). The thickness of the n^{th} compartment, and hence the water table depth has to be computed at each time step. For equally spaced nodes, the n^{th} compartment thickness is expressed as:

$$\Delta z_n = z_w - n\Delta z \qquad [2.53]$$

The numerical scheme, however, requires that all nodes have constant thickness Δz, and hence the bottom boundary condition cannot be specified at the exact location of the water table. This is overcome by taking the n^{th} node to be at the center of the last compartment, i.e. the node that lies just above the water table in the unsaturated zone (see Figure 2.16). For small Δz, we can assume that the pressure distribution is linear and directly write:

$$\psi_n = -\frac{\Delta z_n}{2} \qquad [2.54]$$

Once ψ_n is specified, the numerical scheme can be implemented.

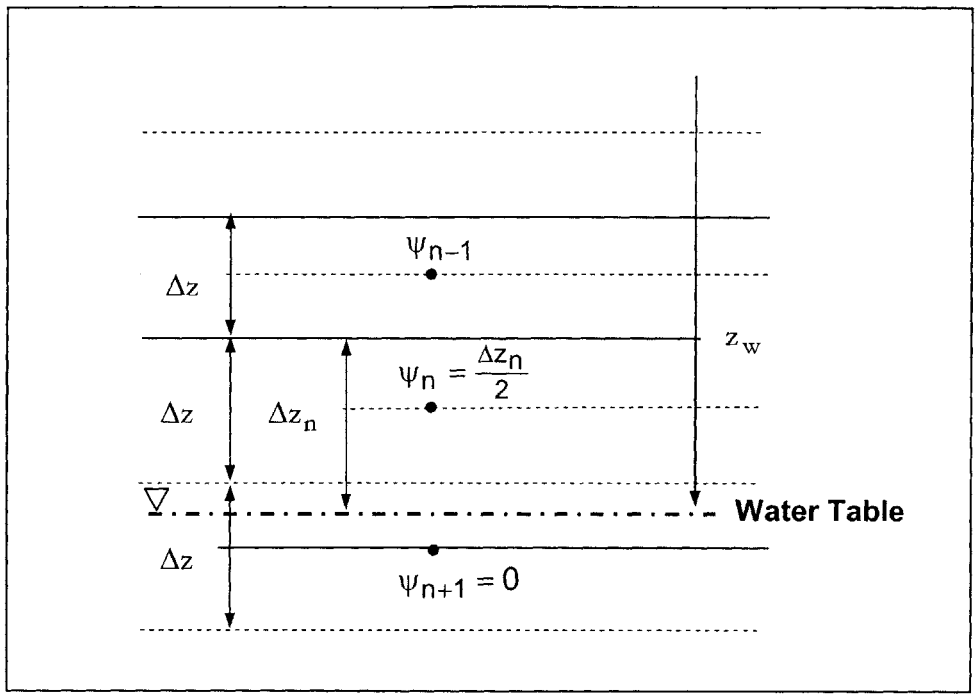

Figure 2.16. Bottom Boundary Condition of a Groundwater Table

(B) KNOWN/SPECIFIED PRESSURE HEAD

When the bottom boundary pressure head is specified, and this not need be zero, the pressure head values at all other nodes can be computed directly.

EQUATIONS FOR BOTTOM BOUNDARY CONDITION

In both cases of a known water table depth, and known or specified pressure head, the bottom boundary condition is in the form of a specified pressure head. We denote this by h_{bottom}. The equations for the boundary condition at the bottom of the soil layer are then given by:

$$\frac{\psi_n^{i+1}-\psi_n^i}{\Delta t^i} = \frac{1}{\left(C(\psi_n^i)+S_sS_a(\psi_n^i)\right)\Delta z_n}\left[K\left(\psi^i_{n-1/2}\right)\left(\left(\frac{\psi_{n-1}^{i+1}-\psi_n^{i+1}}{\Delta z_{n-1}}\right)+1\right)-K\left(\psi^i_{n+1/2}\right)\left(\left(\frac{\psi_n^{i+1}-h_{bottom}^{i+1}}{\Delta z_n}\right)+1\right)\right] \quad [2.55]$$

If we let:

$$A_n=\left[1+\frac{\Delta t^i K\left(\psi^i_{n-1/2}\right)}{\left(C(\psi_n^i)+S_sS_a(\psi_n^i)\right)\Delta z_n\Delta z_{n-1/2}}\right] \quad [2.56]$$

$$B_n=1-A_n+\frac{\Delta t^i K\left(\psi^i_{n+1/2}\right)}{\left(C(\psi_n^i)+S_sS_a(\psi_n^i)\right)\Delta z_{n+1/2}\Delta z_n} \quad [2.57]$$

$$D_n=0 \quad [2.58]$$

$E_n =$

$$\psi_n^i+\left[\frac{\Delta t^i}{\left(C(\psi_n^i)+S_sS_a(\psi_n^i)\right)\Delta z_n}\right]\left\{K\left(\psi^i_{n-1/2}\right)-K\left(\psi^i_{n+1/2}\right)\right\}-\left[\frac{\Delta t^i}{\left(C(\psi_n^i)+S_sS_a(\psi_n^i)\right)\Delta z_{n+1/2}\Delta z_n}\right]K\left(\psi^i_{n+1/2}\right)h_{bottom} \quad [2.59]$$

Then Equation [2.55] can be rewritten as:

$$A_n\psi_n^{i+1}+B_n\psi_{n-1}^{i+1}=E_n \quad [2.60]$$

Equation [2.60] now has exactly the form of Equation [2.29] and the numerical scheme can be implemented.

2-1.4.2. DETAILS OF SPREADSHEET IMPLEMENTATION

The governing equation for variably saturated flow was derived and its solution was given in Section 2-2.2. The flow problem can be solved using an implicit backwards finite difference scheme as is described in Appendix A. In this study, a spreadsheet is used for this purpose, the details of which are outlined in the following steps:

Step 1. Select the number, n of compartments that divide the soil layer (see Figure 2.14)

Step 2. Specify the soil hydraulic properties. These include:

a. Saturated conductivity (or saturated conductivity function $K_s(z)$)
b. Saturated θ_s and residual θ_r moisture contents
c. Specific storage coefficient S_s
d. The parameters needed to compute the soil characteristic curves. These parameters will depend on the model that is used to describe the characteristic curves. The van Genuchten (1980) Model, for example, requires the specification of two parameters n and δ (see Section 2-2.1). Other soil characteristic models will require specification of different parameters. If the characteristic curves are obtained through laboratory measurements, these can be specified directly.

Step 3. Specify the initial conditions in the soil. These most frequently are in the form of an initial moisture content distribution.

Step 4. Enter the formulae for the soil characteristic curves in separate columns for the pressure head and hydraulic conductivity as functions of the soil moisture distribution. Hence, the initial pressure and conductivity distributions are obtained.

Step 5. Enter the formula for the specific moisture capacity $C(\psi)$, $C(\psi) = \frac{d\theta}{d\psi}$.

Step 6. Compute the degree of saturation from:

$$S(\psi) = \frac{\theta(\psi) - \theta_r}{\theta_s - \theta_r} \qquad [2.61]$$

where:

θ_r is the residual soil moisture content

θ_s is the saturated soil moisture content

Step 7. Enter the formula for the geometric mean averaging of the conductivity, and compute both $K\left(\psi^i_{j-1/2}\right)$ and $K\left(\psi^i_{j+1/2}\right)$ as given in Equation [2.27].

Step 8. Enter the Equations for A_j, B_j, D_j and E_j. These are given in Equations [2.30] to [2.33].

Step 9. Specify the Boundary Conditions

Step 10. Compute the final pressure distributions at the end of each time step. The final moisture content profiles are obtained from this and the soil characteristic curves.

Step 11. Repeat steps for as many times intervals as required

2-1.4.2.1. SPREADSHEET IMPLEMENTATION OF TOP BOUNDARY CONDITION SELECTION SCHEME

A scheme is required for the appropriate selection of the top boundary condition which may change from head controlled to flux controlled and vice versa. The decision procedure for this is shown in Figure 2.15, and is implemented in a spreadsheet is as follows:

Assume that the soil near the ground surface is initially unsaturated. This is very frequently the case, unless high antecedent rain has brought the entire soil profile to complete saturation.

Step 1. Compute the potential infiltration rate at the soil surface according to Equation [2.15].

Step 2. The actual infiltration rate (Equation [2.16]) into the soil is determined using the MAX statement in Microsoft Excel that selects the maximum of the potential infiltration rate at the surface and the specified water application flux. The maximum is used as the actual infiltration rate into the soil and appears in the Equation [2.48] for E_1. (Note that the maximum is selected because of the sign convention used which requires both the potential infiltration rate and the rainfall intensity to be negative).

Step 3. The top boundary condition is initially flux controlled with the flux computed as in Step 2.

Step 4. The moisture content in the first soil compartment (near the surface) is computed from the resulting pressure head at the end of a time step and the soil characteristic curves. By dong so, one determines whether the soil is saturated or remains unsaturated at the end of the time step.

Step 5. If the soil at the surface remains unsaturated, then the top boundary condition is flux controlled as in Step 3. Steps 1 to 4 would be repeated in the spreadsheet solution.

Step 6. If the soil at the surface becomes saturated, then the top boundary condition switches from being flux controlled to being head controlled. A value of the top pressure head needs to be specified, and is taken to be zero. This assumes that no ponding takes place.

Steps 5 and 6 are incorporated into the spreadsheet model using the IF statement in Microsoft Excel that appears in the Equations for both B_1 and E_1.

These take the respective forms shown in the Equations [2.62] and [2.63] below:

$$B_1 = \begin{cases} 1 - A_1 + \dfrac{\Delta t^i K\left(\psi_{1/2}^i\right)}{\left(C(\psi_1^i) + S_s S_a(\psi_1^i)\right)\Delta z_{1/2}\Delta z_1}, & \theta_1 = \theta_s \\ 1 - A_1, & \theta_1 < \theta_s \end{cases} \qquad [2.62]$$

$$E_1 = \begin{cases} \psi_1^i + \left[\dfrac{\Delta t^i}{\left(C(\psi_1^i) + S_s S_a(\psi_1^i)\right)\Delta z_{1/2}}\right]\left\{K\left(\psi_{1/2}^i\right) - K\left(\psi_{3/2}^i\right)\right\} - \left[\dfrac{\Delta t^i}{\left(C(\psi_1^i) + S_s S_a(\psi_1^i)\right)\Delta z_{1/2}\Delta z_1}\right] K\left(\psi_{1/2}^i\right) h_{surface}, \theta_1 = \theta_s \\ \psi_1^i - \left[\dfrac{\Delta t^i}{\left(C(\psi_1^i) + S_s S_a(\psi_1^i)\right)\Delta z_{1/2}}\right]\left\{q_t + K\left(\psi_{3/2}^i\right)\right\}, \quad \theta_1 < \theta_s \end{cases}$$

[2.63]

where:

$h_{surface}$ is the pressure head at the soil surface due to ponding and is assumed zero in this study

Step 7. The remainder of the analyses (and equations) remains the same and Steps 1 through 9 are repeated for all time steps.

2-1.5. MODEL VALIDATION

The efficiency and accuracy of the spreadsheet based finite difference numerical scheme is validated with two numerical example analyses from the literature. The first compares the model with a Fortran 90 computer code developed in Protopapas and Bras (1988). The infiltration example devised by Warrick et al. (1971) is used for this. The second compares the model with the finite element model, HYDRUS (Vogel et al, 1978), and the infiltration experiment in Wierenga and Brusseau (1995) is used for this.

Example 1: Warrick et al. (1971)

Warrick et al. (1971) devised a numerical infiltration experiment where water is allowed to infiltrate into a 125 cm deep, homogenous soil profile having the following soil characteristic curve functions:

$$\theta(\psi) = \begin{cases} 0.6829 - 0.09524 \ln|\psi| & \psi \le -29.484 \text{ cm} \\ 0.4531 - 0.02732 \ln|\psi| & -29.484 < \psi \le -14.495 \text{ cm} \end{cases} \quad [2.64]$$

and

$$K(\psi) = \begin{cases} 19.34 \times 10^{-5} |\psi|^{-3.4095} & \psi \le -29.484 \text{ cm} \\ 516.80 |\psi|^{-0.97814} & -29.484 < \psi \le -14.495 \text{ cm} \end{cases} \quad [2.65]$$

where $K(\psi)$ is given in cm/day and ψ in cm.

Equivalently,

$$\psi(\theta) = \begin{cases} \exp\left(\frac{0.6829 - \theta}{0.09524}\right) & \theta \le 0.36 \\ \exp\left(\frac{0.4531 - \theta}{0.02732}\right) & 0.36 < \theta \le 0.43 \end{cases} \quad [2.66]$$

and

$$K(\theta) = \begin{cases} 19.34 \times 10^{-5} \exp\left(\frac{-2.3283 + 3.4095\theta}{0.09524}\right) & \theta \le 0.36 \\ 516.80 \exp\left(\frac{-0.4432 + 0.97814\theta}{0.02732}\right) & 0.36 < \theta \le 0.43 \end{cases} \quad [2.67]$$

These characteristic functions are plotted in Figures 2.17 and 2.18.

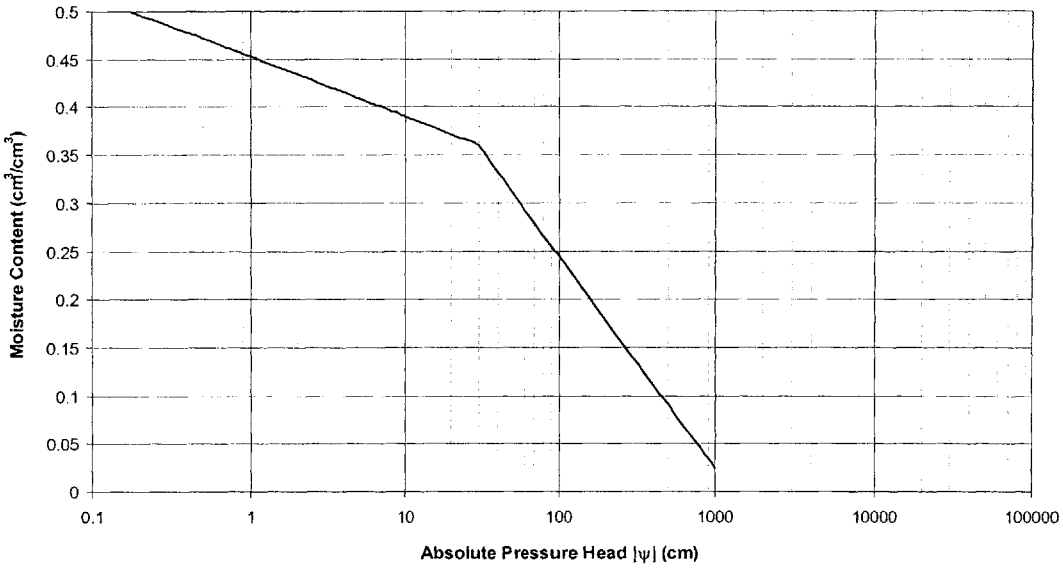

Figure 2.17. Moisture Retention Curve

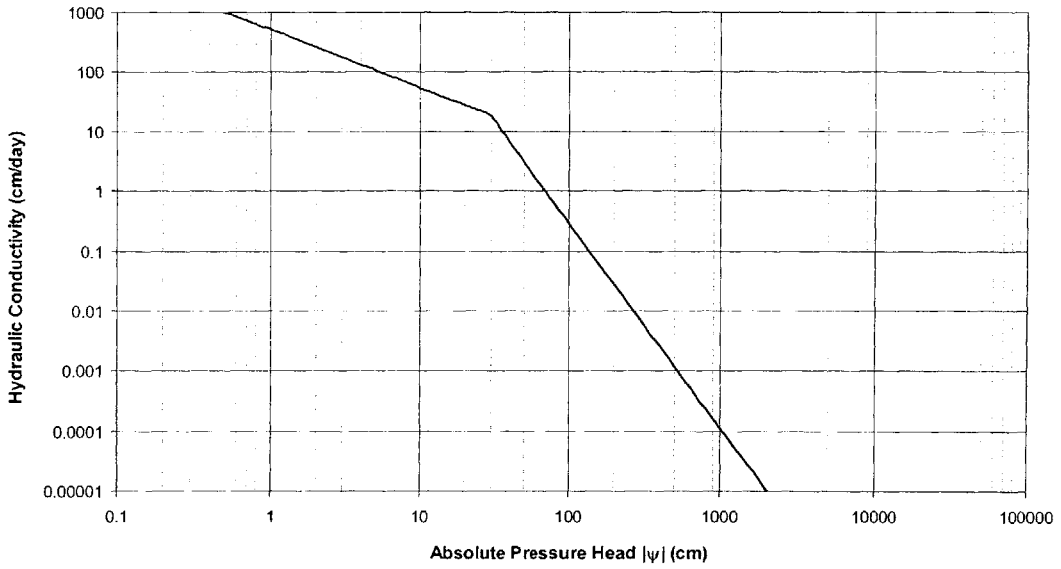

Figure 2.18. Hydraulic Conductivity Curve

The initial conditions are in terms of a stated initial subsurface moisture content distribution as:

$$\theta(z,0) = \begin{cases} 0.15 + 0.0008333|z| & -60 \le z < 0 \text{ cm} \\ 0.20 & -120 < z \le -60 \text{ cm} \end{cases} \qquad [2.68]$$

The boundary conditions are given as:

Top of soil layer: Constant flux

$$q_t = 37.8 \text{ cm/day} \qquad [2.69]$$

Bottom of soil layer: Specified pressure head

$$\psi(-125, t) = -159.19 \text{ cm} \qquad [2.70]$$

The solution obtained by the model developed in this study is shown by the circled symbols in Figure 2.19, and the Protopapas and Bras (1988) solution is shown by the solid line.

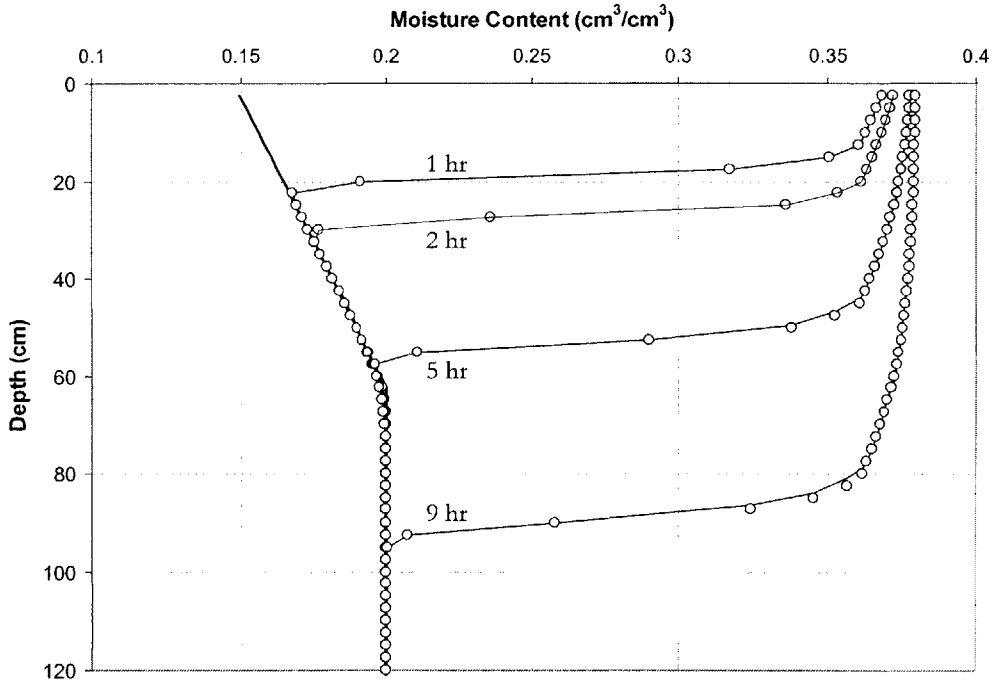

Figure 2.19. Comparison of Soil Moisture Profiles from Spreadsheet Based Finite Difference Scheme (symbols) and from Protopapas and Bras (1988) (solid lines)

Figure 2.19 shows that the results from the spreadsheet model are in very good agreement with those from the Protopapas and Bras (1988) analyses, thereby validating the model.

Example 2: Wierenga and Brusseau (1995) Infiltration Experiment

A second numerical example devised by Wierenga and Brusseau (1995) is used to test the validity of the spreadsheet model. It consists of applying water on top of an initially uniformly moist ($\theta_i = 0.08\,cm^3/cm^3$) homogenous soil. The soil characteristic curves are shown in Figures 2.20 and 2.21.

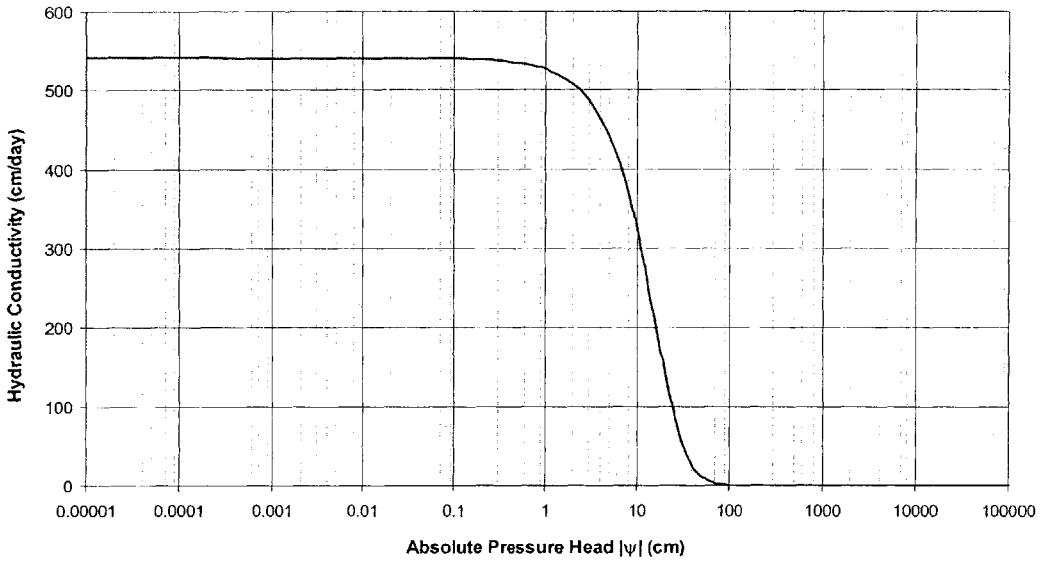

Figure 2.20. Moisture Retention Curve

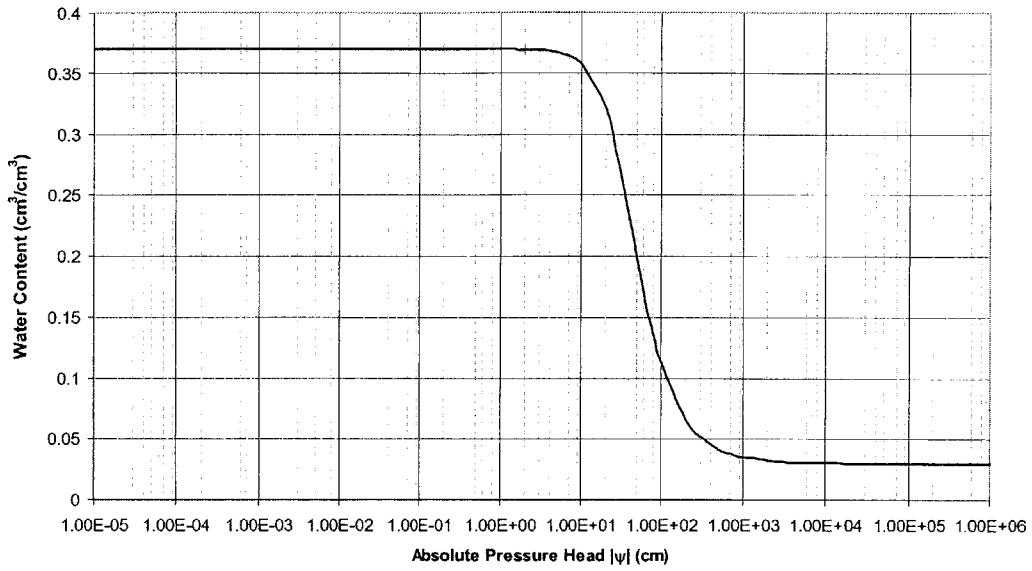

Figure 2.21. Hydraulic Conductivity Curve

Water is applied at a constant rate of 2.5 cm/h for the first 4 hours, followed by a zero application rate. Wierenga and Brusseau (1995) used the HYDRUS (Vogel at al., 1996) computer program, which is designed to simulate one-dimensional water flow, and uses the Galerkin finite element techniques to numerically solve Richards Equation.

Figures 2.22 and 2.23 compare the results obtained by the spreadsheet model with those from Wierenga and Brusseau (1995), in terms of moisture content and pressure head profiles respectively. The results from the spreadsheet model are shown in symbols and those from Wierenga and Brusseau (1995) are shown as solid lines.

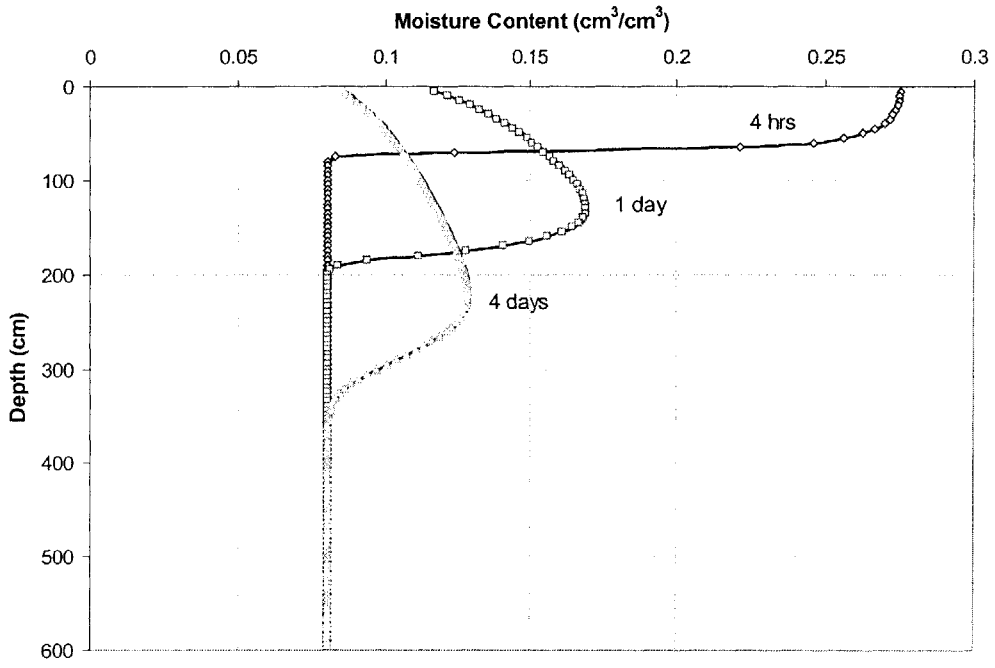

Figure 2.22. Moisture Content Profiles Generated by HYDRUS (solid lines) and the Spreadsheet Based Numerical Scheme (symbols)

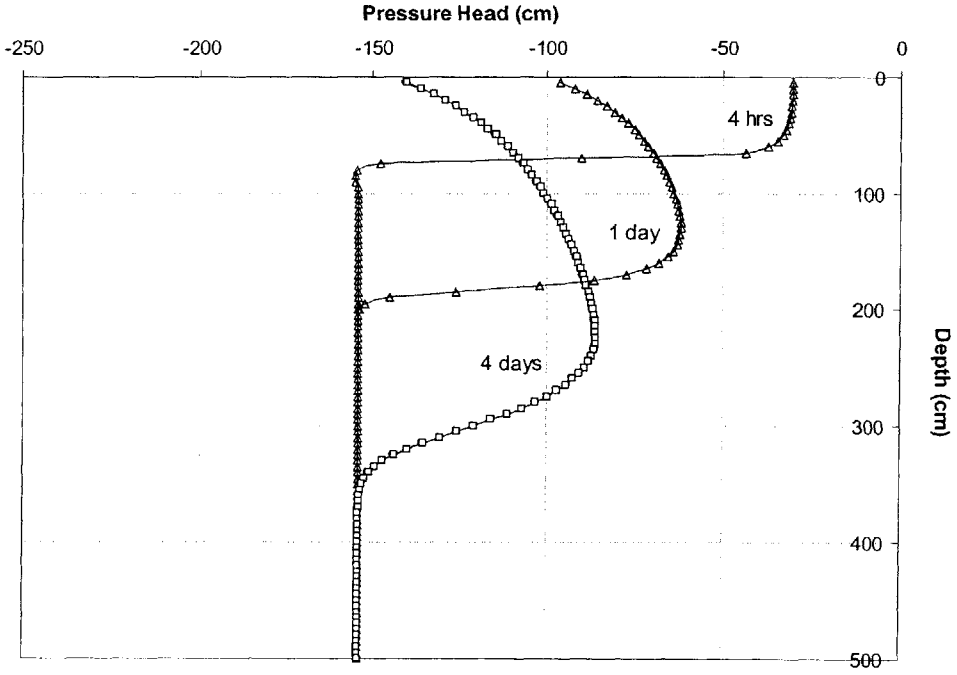

Figure 2.23. Pressure Head Profiles Generated by HYDRUS (solid lines) and the Spreadsheet Based Numerical Scheme (symbols)

The agreement between the HYDRUS (Vogel et al., 1978) program results and the results of the spreadsheet based scheme is excellent.

Both examples in this section verify the spreadsheet based numerical scheme developed in this study to solve the variably saturated flow problem. The spreadsheet based solution has the advantages of being relatively easy to set up, requires no computer coding and utilizes virtually no computer processing time.

2-1.6 MODEL DEMONSTRATION

We illustrate the model using two examples that are relevant to the study of landslides, as will be shown in later chapters. In the first, the water application rate is less than the saturated conductivity of the soil in which case all the water infiltrates into the soil. The water is unable to saturate the soil, and flow takes place in unsaturated soil at a rate equal to the application rate. In the second example, the water application rate is greater than the saturated conductivity of the soil, in which case positive pressures develop as flow takes place in both saturated and unsaturated soil. The infiltration rate is equal to the potential infiltration rate of the soil.

Example 1: Application Rate Less than Saturated Conductivity

Consider a layer of soil of height 5 m, composed of the soil with hydraulic parameters shown in Table 1 in Section 2-1.1. The soil characteristic curves using the van Genuchten (1980) Model were shown in Figures 2.3 and 2.5. An initial and constant moisture content $\theta_i = 0.4$ is assumed throughout the soil layer. A constant application rate of 10 cm/day is applied at the top of the soil column for a duration of 8 hours. The moisture content and pore pressure profiles are at selected times in Figures 2.24 and 2.25 respectively.

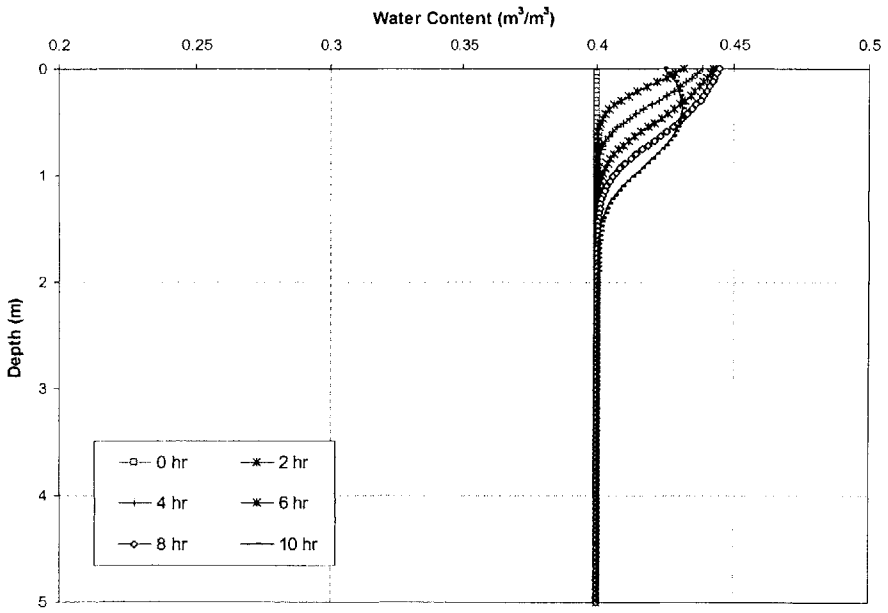

Figure 2.24. Moisture Content Profiles with Time (case when $q < K_s$)

Figure 2.24 shows that saturation is not reached in the soil, throughout water application.

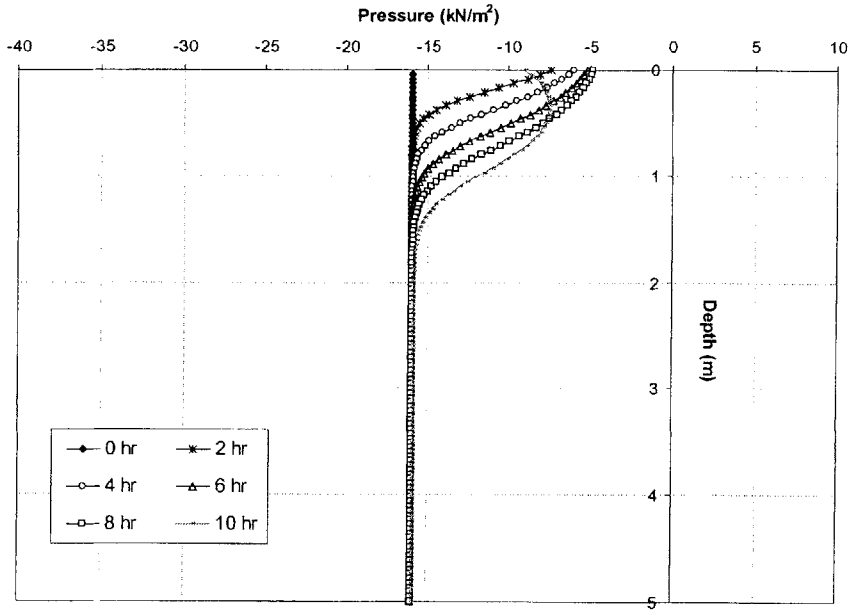

Figure 2.25. Pressure Head Profiles with Time (case when $q < K_s$)

Figure 2.25 shows that the pore pressures remain negative, and flow takes place in unsaturated soil. Figures 2.24 and 2.25 also show that when water application is stopped after 8 hours, moisture (and hence excess pressure) redistribution takes place. This is shown at the time of 10 hours. The rate of redistribution will depend on the soil hydraulic characteristics. This process will continue until all the excess pressures completely dissipate and equilibrium conditions (initial conditions) are restored.

Figure 2.26 shows the rate of infiltration with time.

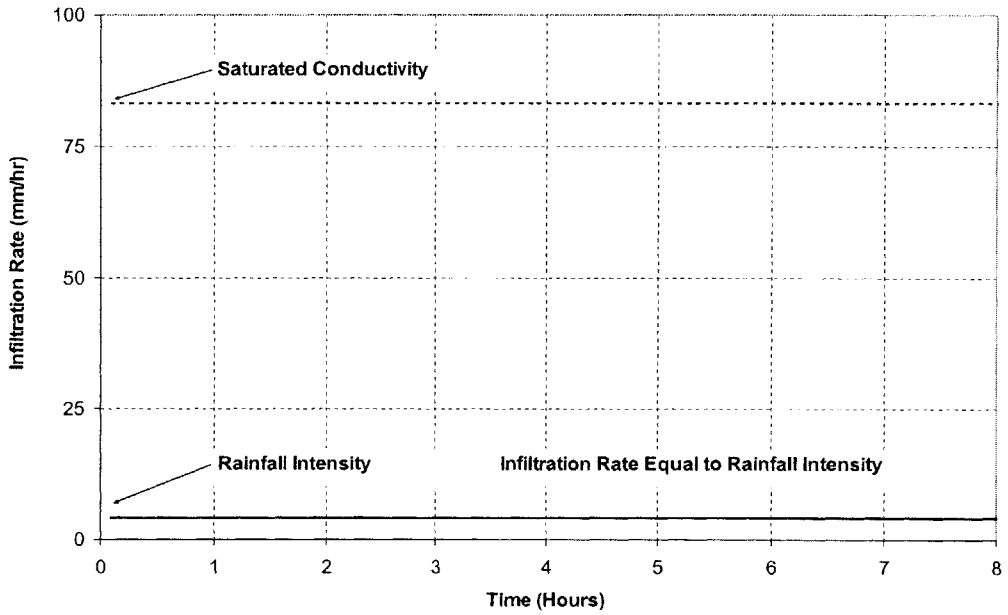

Figure 2.26. Actual Infiltration Rate with Time (case when $q < K_s$)

Figure 2.26 shows that the rate of infiltration remains constant throughout the water application, and is equal to the water application rate. This is because the application rate is less than the potential infiltration rate of the soil, and so all the water infiltrates into the soil.

This example shows that when the water application rate is less than the potential infiltration rate of the soil, all the water infiltrates into the soil, but it is incapable of completely saturating the soil. As flow takes place in unsaturated soil, moisture increases, and pressures increase but remain negative.

Example 2. Application Rate Greater than Saturated Conductivity

In this example, the water application rate is taken to be 375 cm/day for duration of 8 hours. The initial moisture content is taken to be $\theta_i = 0.4$. Figure 2.27 shows the moisture content profiles at selected times, and Figure 2.28 shows the corresponding pore pressure.

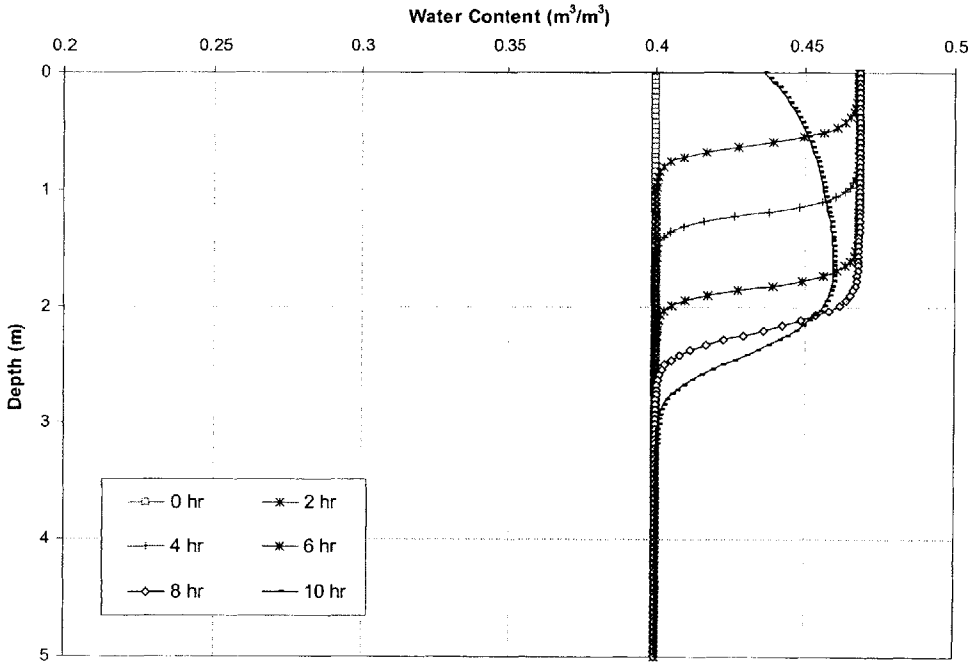

Figure 2.27. Moisture Content Profiles with Time (case when $q > K_s$)

Figure 2.27 shows that saturation is reached at the top of the soil, and this saturated zone travels into the soil layer in the form of a saturating wetting front.

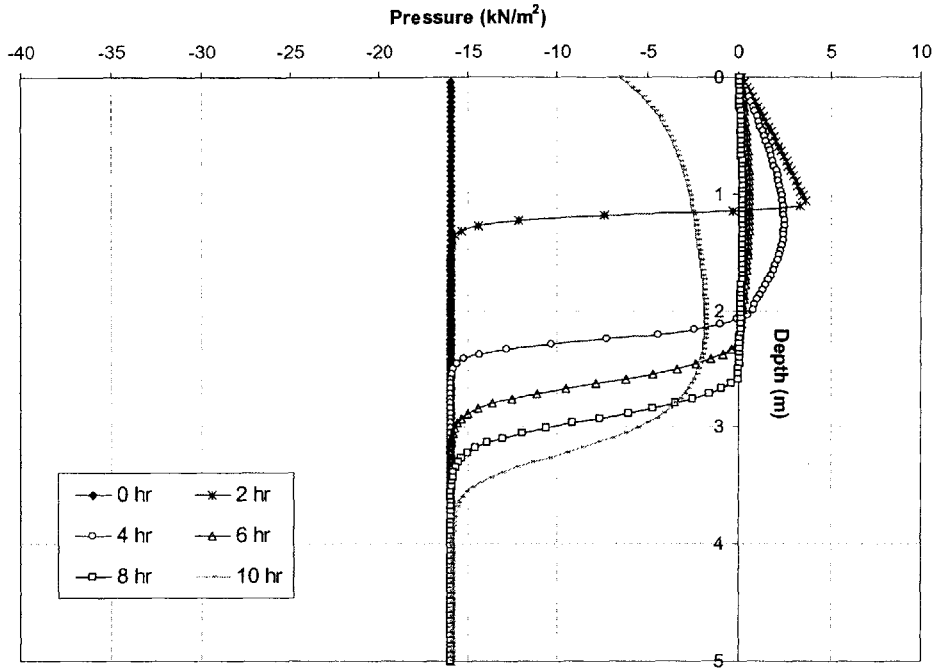

Figure 2.28. Pressure Head Profiles with Time (case when $q > K_s$)

Figure 2.28 shows that positive pressures develop within the infiltrating wetting front as it travels into the soil layer. Figure 2.29 shows the infiltration rate throughout water application.

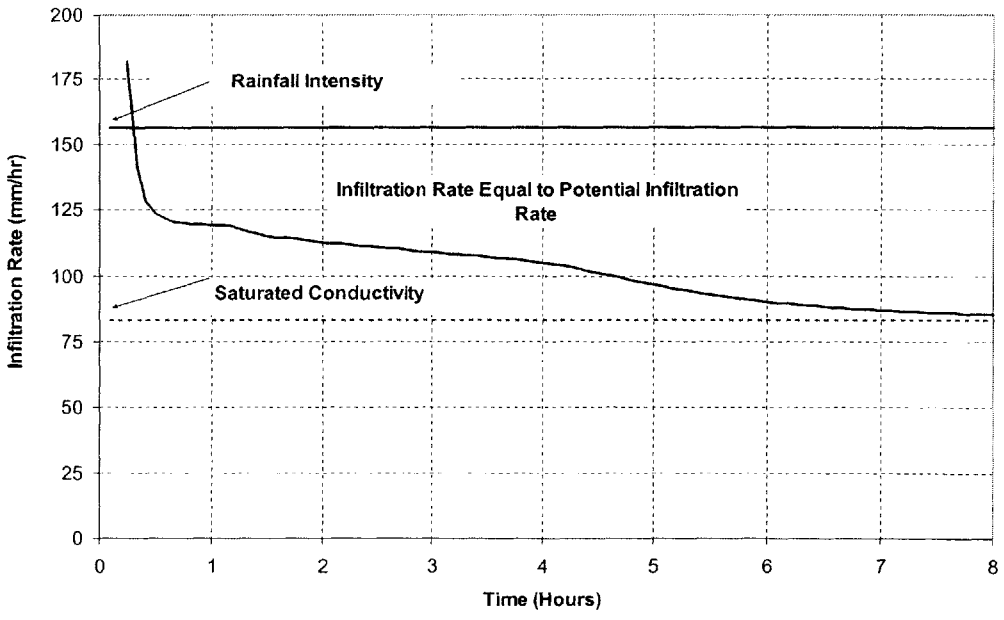

Figure 2.29. Actual Infiltration Rate with Time (case when $q > K_s$)

At early times, since the potential infiltration rate is greater than the rainfall intensity, the actual infiltration rate is equal to the rain intensity. As the potential rate decreases with time, infiltration takes place at this potential rate, which is shown in Figure 2.29. The potential rate of infiltration continues to decrease with time, and water application, tending towards the saturated conductivity of the soil. This decrease in infiltration rate can also be observed in Figure 2.27 which shows the decrease in the rate of wetting front advancement with time. Figure 2.28 also shows this, as pressures, though continue to increase with time, do so at a decreasing rate.

2-1.7. CONCLUSIONS

This part of Chapter 2 discussed unsaturated soil properties, and developed a one dimensional finite difference pressure based solution to the variably saturated flow equation. It was necessary to develop this pressure based procedure since the majority of models solve the moisture based equation, and pressures are what are needed in stability, and hence landslide analyses. The model solves simultaneously for saturated and unsaturated within a spreadsheet environment. Particular attention was paid to the top boundary condition since this may vary during a rainfall event. The model was validated by comparing the results obtained in numerical examples published in the literature. Two examples demonstrated the capabilities of the model, and highlighted some of the characteristics of infiltration processes. One of the biggest shortcomings of the model is that it assumes that rainwater infiltrates into soil as a stable wetting front, and neglects the possibility of fingering and preferential flow that has been shown to develop in both heterogeneous and homogenous soils. This is further discussed in Chapter 5. Nevertheless, the model provides a powerful tool with which one can estimate subsurface pore pressures that are generated during a rainfall event, and will be used in subsequent chapters.

PART 2-2:
STABILITY MODEL

Many Limit Equilibrium models have been developed over the years to analyze the stability of slopes e.g. Bishop Simplified (1955), Bishop Rigorous (1959), Janbu Simplified (1957), Janbu Generalized (1973), Spencer (1973), Morgenstern and Price (1965), Fredlund et al. (1978), Chen (1982), amongst others. These models satisfy different conditions of static equilibrium based on the assumptions that make the problem of slope stability statically determinate. These models are discussed in more detail in Chapter 5.

In this part of Chapter 2, spreadsheet techniques are described by which the stability of slopes can be assessed using the Janbu Generalized Method of Slices (1973). In the Janbu Generalized Method (1973), assumptions are made concerning the point of application of the normal force on a base of a slice, and concerning the point of application of the interslice normal forces. Vertical force equilibrium for each slice, and horizontal force equilibrium for the entire slide mass are satisfied, thereby producing an expression for the Factor of Safety with respect to force equilibrium. The Janbu Method (1973) has been selected for stability analyses in this study, since shallow landslides tend to have shallow, planar failure surfaces, and the model will give reliable results for such geometries (Graham, 1984; Abramson, 1995).

A technique is described whereby the Factor of Safety is computed on a specified failure surface. A method to search for the critical failure surface is then described. The method makes combined use of a spreadsheet's circular iteration option and its optimization tool.

2-2.1. JANBU'S GENERALIZED PROCEDURE OF SLICES (1973)

Consider Figures 2.30a and 2.30b.

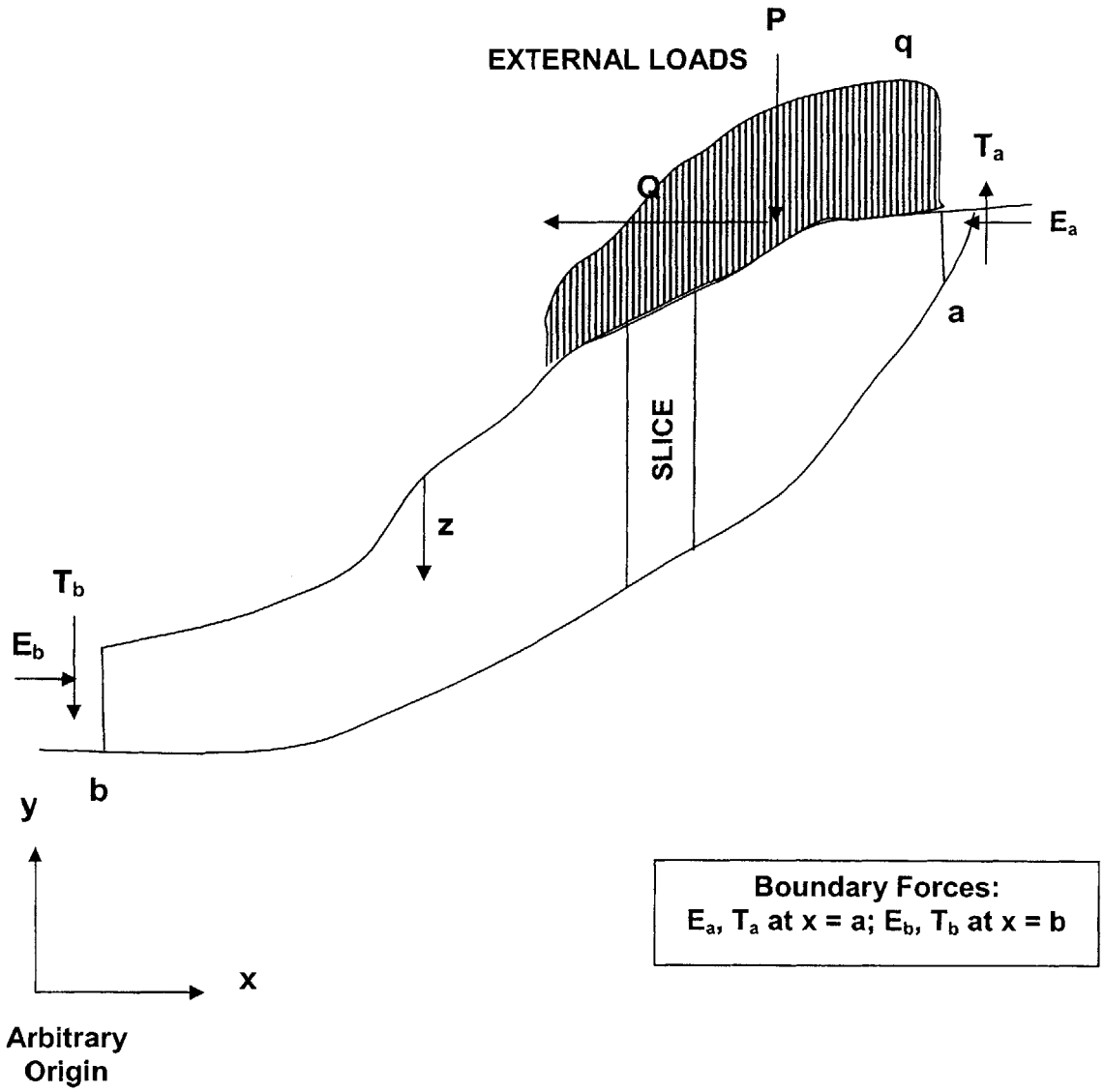

Figure 2.30a. Section through Slope Illustrating Notation used in Janbu's Generalized Procedure

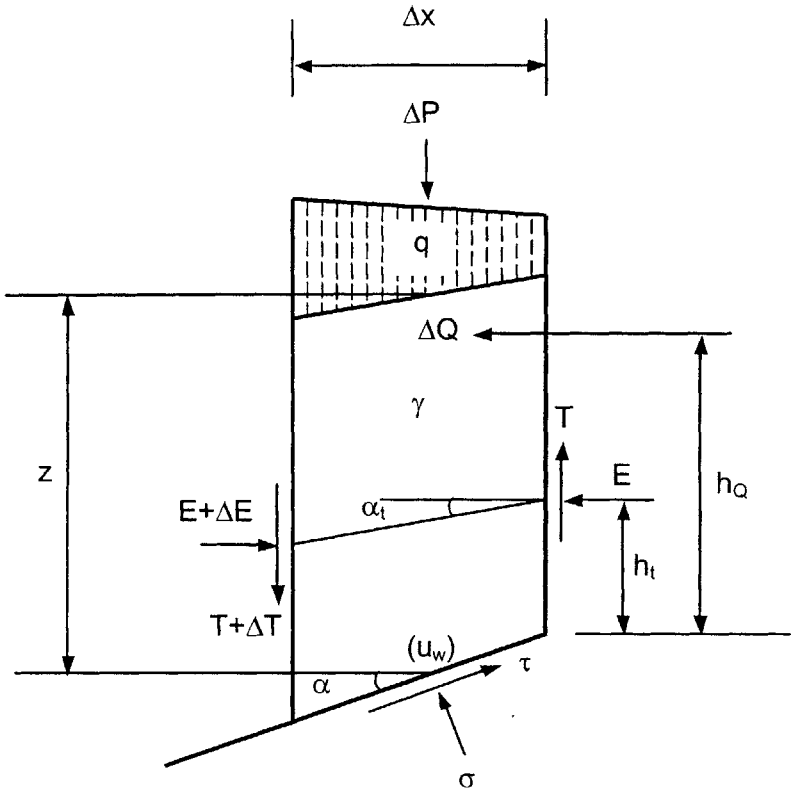

Figure 2.30b. Enlarged Diagram of a Slice

With the notations in Figures 2.30a and 2.30b the equations of equilibrium in the horizontal and vertical directions and the equation of moment equilibrium, neglecting second order terms, of a slice are given by (Janbu, 1973):

$$S = (p + t)\Delta x - \tau \Delta x \tan\alpha \qquad \text{(Vertical Equilibrium)} \qquad [2.70]$$

$$\Delta E = \Delta Q + (p + t)\Delta x \tan\alpha - \tau \Delta x(1 + \tan^2 \alpha) \qquad \text{(Horizontal Equilibrium)} \qquad [2.71]$$

$$T = -E \tan\alpha_t + h_t \frac{\Delta E}{\Delta x} - h_Q \frac{\Delta Q}{\Delta x} \qquad \text{(Moment Equilibrium)} \qquad [2.72]$$

where:

$S = \sigma \Delta x$

σ is the mean total stress normal to the base of a slice

$p = \gamma z + q + \frac{\Delta P}{\Delta x}$ is the total vertical stress acting on a slice

P is an external point load (see Figure 2.30a)

Q is an external point load (see Figure 2.30a)

q is a uniformly distributed external stress (see Figure 2.30a)

$t = \frac{\Delta T}{\Delta x}$

α_t and h_t are defined in the next section, and other parameters are defined in Figures 2.30a and 2.30b

The mobilized shear stress τ at the base of a slice is expressed in terms of the Coulomb strength criterion and the global Factor of Safety F as (Fellenius, 1954):

$$\tau = \frac{c' + (\sigma - u_w) \tan \phi'}{F} \qquad [2.73]$$

where:

c' is the cohesion of the soil

u_w is the mean pore water pressure at a base of a slice

ϕ' is the angle of shearing resistance of the soil

For the overall horizontal equilibrium:

$$\sum_{i=1}^{n} \Delta E = E_b - E_a \qquad [2.74]$$

where E_b and E_a are defined in Figure 2.30a and n is the total number of slices.

From Equations [2.70] through [2.74], Janbu (1973) proposed the set of Equations shown in Figure 2.31 as the working formulae for slope stability analyses by an iterative procedure.

$$B = \Delta Q + (p + t)\Delta x \tan\alpha \qquad [2.75]$$

$$A' = [c' + (p + t - u_w)\tan\phi']\Delta x \qquad [2.76]$$

$$n_\alpha = \frac{1 + \left(1/F\right)\tan\phi' \tan\alpha}{1 + \tan^2\alpha} \qquad [2.77]$$

$$A = A'/n_\alpha \qquad [2.78]$$

$$F = \frac{\sum_{i=1}^{n} A}{E_a - E_b + \sum_{i=1}^{n} B} \qquad [2.79]$$

$$\Delta E = B - A/F \qquad [2.80]$$

$$E = E_a + \sum_{i=1}^{n} \Delta E \qquad [2.81]$$

$$\frac{dE}{dx} \cong \frac{\Delta E}{\Delta x} = \frac{\Delta E_i + \Delta E_{i+1}}{\Delta x_i + \Delta x_{i+1}} \qquad [2.82]$$

$$T = -E\tan\alpha_t + h_t \frac{\Delta E}{\Delta x} - h_Q \frac{\Delta Q}{\Delta x} \qquad [2.83]$$

$$\Delta T = T_i - T_{i-1} \qquad [2.84]$$

$$t = \frac{\Delta T}{\Delta x} \qquad [2.85]$$

$$\tau = \frac{A}{F(1 + \tan^2\alpha)\Delta x} \qquad [2.86]$$

$$\sigma' = p + t - \tau\tan\alpha - u_w \qquad [2.87]$$

Figure 2.31. Janbu's Equations for the Generalized Procedure of Slices (Notation same as Figure 2.30)

2-2.1.1. ASSUMPTIONS

The slope stability problem is statically indeterminate and assumptions have to be made to make it solvable. In the Janbu Generalized Method of Slices (1973) assumptions hare made regarding the line of action of the normal interslice force E for each slice. In Janbu's (1973) formulation this is denoted by the height h_t above the base of a slice (see Figure 2.32). Janbu (1973) assumes that $h_t = \frac{1}{3} h_{i,i+1}$, where $h_{i,i+1}$ is the height of the vertical interface between two adjacent slices i and i + 1 (see Figure 2.32).

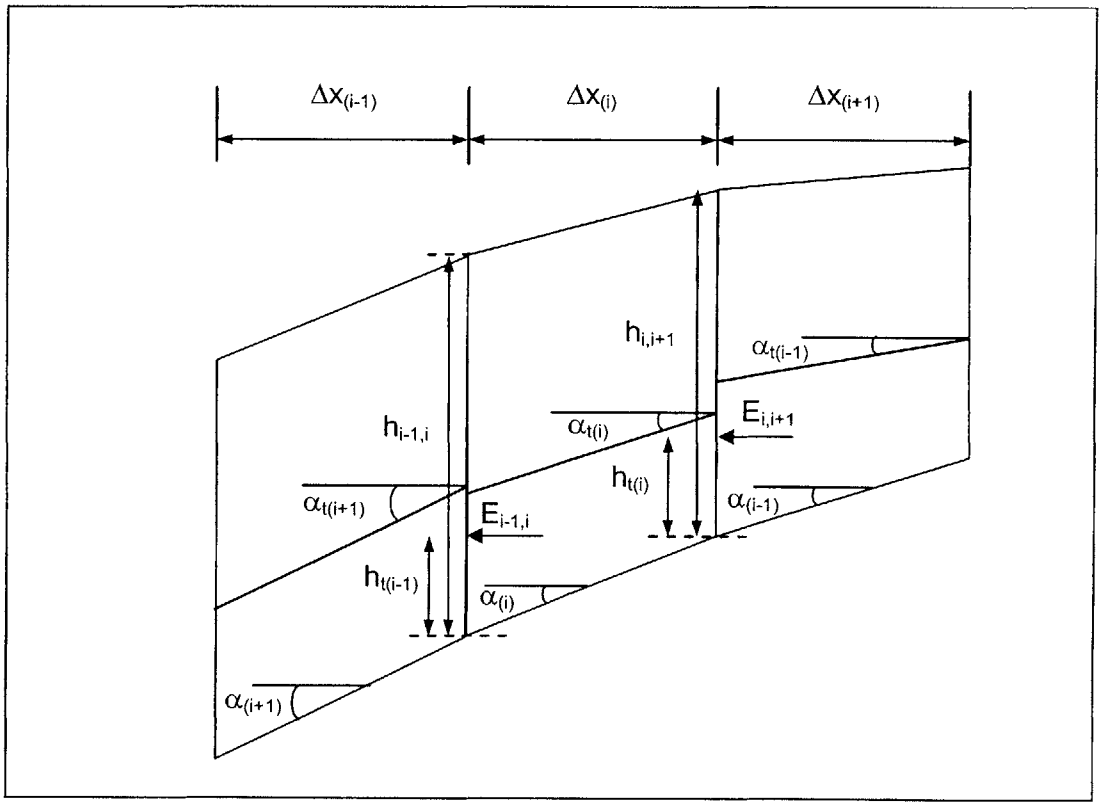

Figure 2.32. Additional Notation used in Janbu Generalized Procedure of Slices

To evaluate the interslice shear force T in Equation [2.83] of Figure 2.31, it is necessary to compute the angle α_t as defined in Figures 2.30b and 2.32. By geometry, each $\tan\alpha_t$ is a function of h_t, Δx and $\tan\alpha$. For a generic slice i, it can be shown that:

$$\tan\alpha_{t(i)} = \frac{(h_{t(i)} - h_{t(i-1)}) + \Delta x_{(i)} \tan\alpha_{(i)}}{\Delta x_{(i)}} \qquad [2.88]$$

The average $\tan\alpha_t$ value adjacent to a particular interface, denoted by $\tan\bar{\alpha}_{t(i)}$ is computed from:

$$\tan\bar{\alpha}_{t(i)} = \frac{1}{2}\left\{\tan\alpha_{t(i)} + \tan\alpha_{t(i+1)}\right\} \qquad [2.89]$$

$$\tan\bar{\alpha}_{t(i)} =$$

$$\frac{1}{2}\left\{\left(\frac{(h_{t(i-1)} - h_{t(i)}) + \Delta x_{(i)} \tan\alpha_{(i)}}{\Delta x_{(i)}}\right) + \left(\frac{(h_{t(i)} - h_{t(i+1)}) + \Delta x_{(i+1)} \tan\alpha_{(i+1)}}{\Delta x_{(i+1)}}\right)\right\} \qquad [2.90]$$

$\tan\bar{\alpha}_{t(i)}$ in Equation [2.90] is then used in Equation [2.83] of Figure 2.31 to compute T.

Having made these assumptions, the stability problem becomes solvable and one can proceed to determine factors of safety for specified failure surfaces.

2-2.2. DETERMINISTIC SLOPE STABILITY ANALYSES FOR A SPECIFIED FAILURE SURFACE

A spreadsheet based procedure is described by which the Factor of Safety for a specified failure surface can be computed using Janbu's Generalized Procedure of Slices (1973). The procedure is largely based on the one proposed by Low and Tang (1997) with some major modifications that are essential to study landslides, and are detailed in subsequent sections of this chapter.

2-2.2.1. BASIC PROCEDURE

The spreadsheet procedure for assessing the stability of a slope using Janbu's Generalized Procedure of Slices (1973) involves solving Equations [2.75] to [2.87] in Figure 2.31. An iterative procedure is required to solve these because the Factor of Safety in Equation [2.79] is a function of A, and hence n_α, and n_α itself is a function of the Factor of Safety (see Equation [2.77] of Figure 2.31).

The procedure is implemented using Microsoft Excel, although other software packages can also be used. The advantage of using spreadsheet procedures over specialized computer programs is that the spreadsheet procedure is relatively easy to set up and computations are very fast. Moreover, the user will have an appreciation of what is being implemented.

The basic input parameters of the model are:

a. The slope geometric properties (topography and/or slope angle)
b. The soil parameters (unit weight and strength)
c. The horizontal (x) and vertical (y) coordinates of a specified failure surface from an arbitrarily set datum (origin)
d. The hydraulic parameters from which the pore pressures on a specified failure surface can be computed
e. The external loads, P and Q, and the boundary forces, E_a and E_b (see Figure 2.30a)

After specifying the input parameters, the Factor of Safety on a specified failure can be computed through an iterative process based on Figure 2.31.

Prior to this, it is necessary to introduce additional notations used in the procedure, and these are shown in Figure 2.33.

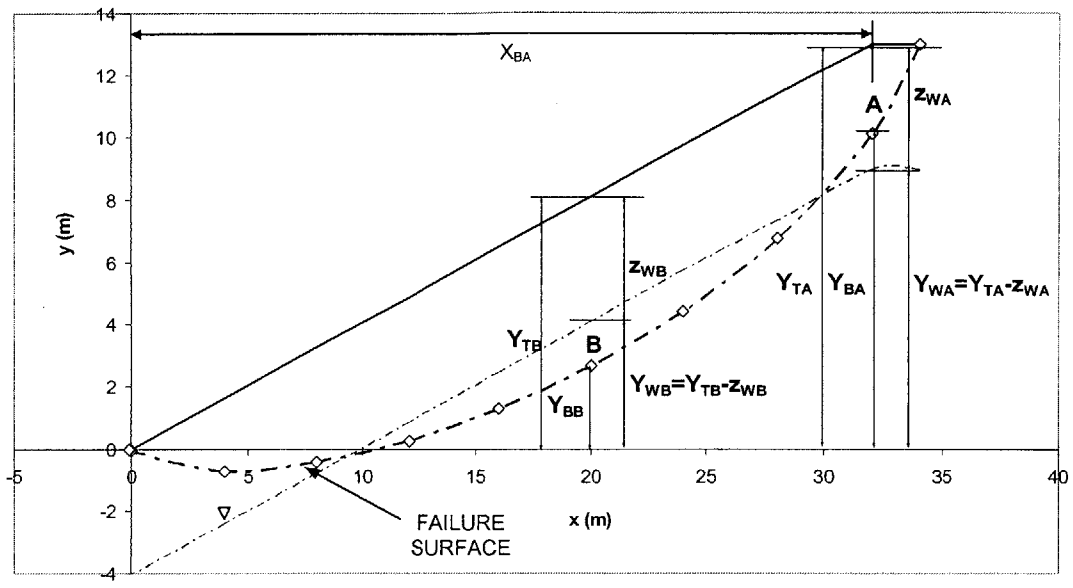

Figure 2.33. Additional Notation used in Spreadsheet Approach

Consider an arbitrary Point A on the specified failure surface. The coordinates of A are (X_{BA}, Y_{BA}). The coordinates of the slope surface at A are $(X_{TA} = X_{BA}, Y_{TA})$, and the coordinates of the water table at A are $(X_{WA} = X_{BA}, Y_{WA})$. If the depth of the water table from the slope surface at A is z_{wA}, then the coordinates of the water table at A are $(X_{BA}, Y_{WA} = Y_{TA} - z_{WA})$.

To illustrate the procedure, consider the slope shown in Figure 2.34.

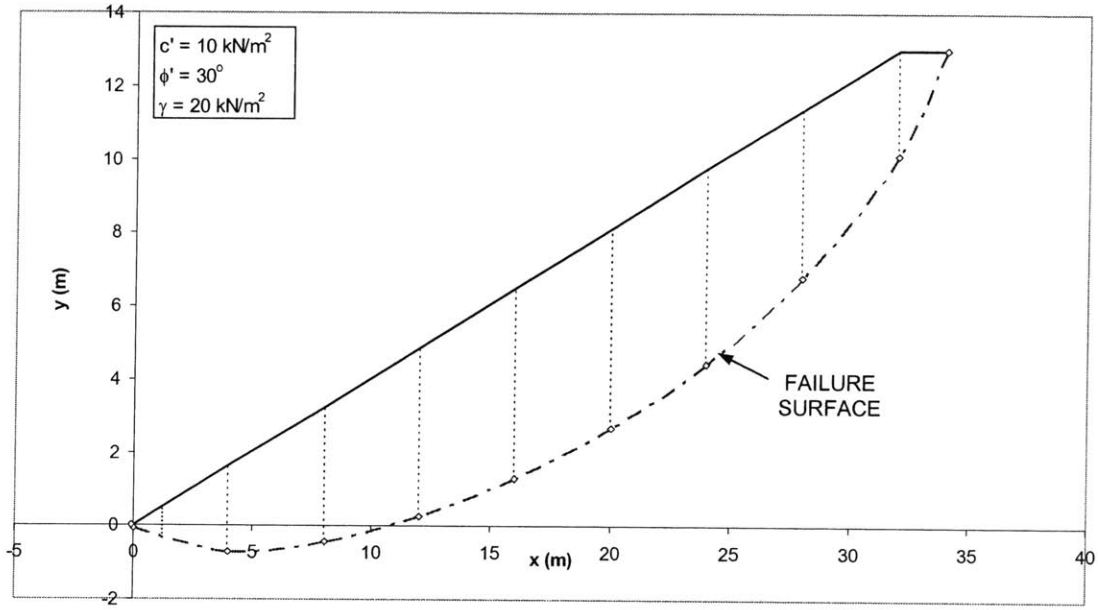

Figure 2.34. Slope Geometry and Soil Properties

We assume the slope is dry, and the pore pressures on the failure surface are zero. We also assume that the external loads and boundary forces are all zero. The spreadsheet procedure is shown in Figure 2.35.

γ	E_a	E_b		c'	tanϕ'
20	0	0		10	0.57

	X_B	Y_B	Y_T	h_{ij}								h_t		
Slice #	34	13	13	0	tan α	Δx	p	u	c'	tanϕ'	ΔQ	0	$\tan\alpha_t$	FACTOR OF SAFETY
1	32	10.123	13	2.8771	1.438561	2	2.877123	0	1	0.67	0	0.959041	0.825921	2.323935728
2	28	6.7786	11.375	4.5964	0.836078	4	7.473558	0	1	0.67	0	1.532145	0.609027	
3	24	4.4395	9.75	5.3104	0.584753	4	9.906881	0	1	0.67	0	1.770149	0.478533	
4	20	2.6612	8.125	5.4638	0.444597	4	10.77428	0	1	0.67	0	1.821279	0.398566	
5	16	1.2818	6.5	5.2182	0.34485	4	10.68207	0	1	0.67	0	1.739412	0.336359	
6	12	0.2499	4.875	4.6251	0.257978	4	9.843383	0	1	0.67	0	1.541716	0.277905	
7	8	-0.428	3.25	3.6781	0.169487	4	8.303241	0	1	0.67	0	1.226031	0.214982	
8	4	-0.705	1.625	2.3299	0.069209	4	6.008026	0	1	0.67	0	0.776644	0.105141	
9	0	-0.065	0	0.0648	-0.16004	4	2.394717	0	1	0.67	0	0.021595	-0.20159	
10	-0.1	0	0	0	-0.64785	0.1	0.064785	0	1	0.67	0	0	-	

					E_a				T_a				
						E			T				
Slice #	B	A'	n_α	A	ΔE	0	ΔE/Δx	0	ΔT	t		τ	σ'
1	7.900921	5.679799	0.46091	12.32302	2.598269	2.598269	1.96435	-0.26207	-0.26207	-0.13104		0.863776	1.503491
2	21.86744	21.52371	0.730445	29.46658	9.187836	11.78611	2.073264	-4.00152	-3.73944	-0.93486		1.865716	4.978813
3	21.60959	28.75991	0.870821	33.02618	7.39828	19.18439	1.415938	-6.67395	-2.67243	-0.66811		2.647539	7.690616
4	18.47397	31.83994	0.941981	33.80105	3.92923	23.11362	0.54543	-8.21892	-1.54497	-0.38624		3.036058	9.038217
5	14.65665	32.476	0.982573	33.05201	0.434217	23.54783	-0.30193	-8.44571	-0.22679	-0.0567		3.177709	9.52954
6	10.42761	31.0818	1.007335	30.85546	-2.84963	20.6982	-1.06798	-7.39865	1.047064	0.261766		3.112187	9.302274
7	5.993587	27.6933	1.019576	27.1616	-5.69417	15.00403	-1.64993	-5.24846	2.150183	0.537546		2.840348	8.359385
8	1.871814	22.12057	1.015091	21.79171	-7.50526	7.49877	-1.86251	-2.23493	3.013528	0.753382		2.333092	6.599936
9	-1.88767	11.90278	0.930041	12.79813	-7.39476	0.104009	-1.82893	-0.01853	2.216406	0.554101		1.342392	3.163651
10	-0.01623	0.116786	0.57281	0.203882	-0.10396	0	-1.03962	0	0.018529	0.185288		0.617953	0.650413
	100.9			234.48									
					E_b				T_b				

X_B and Y_B are the horizontal and vertical coordinates of the specified failure surface from an arbitrarily chosen datum.

Y_T is the vertical coordinate of the slope surface (topography) from an arbitrarily chosen datum

Note that since the slope has been sectioned into 10 slices, there will be 11 points, and hence one needs to specify 11 coordinates. In general, if one chooses n slices to analyze the slope, one would need to specify (n+1) coordinates.

All other parameters were previously defined in Figures 1 and 2. The shaded cells indicate the input parameters, and unshaded cells are automatically computed by the spreadsheet as detailed below.

PROCEDURE:

Step 1. Section the slope into any desired number of slices (ten in this example)

Step 2. Set up a spreadsheet with columns similar to the one shown above

Step 3. Enter the input data

Step 4. Enter a value of 1 in the Factor of Safety cell initially. This is later changed in Step 6 below.

Step 5. Enter formulae for B, A', n_α and A from Figure 2.31. All columns from ΔE to σ' are blank at this time.

Step 6. Enter formulae for the summation of the A and B columns from Figure 2.31.

Step 7. Enter formula for the Factor of Safety from Figure 2.31. Activate the iteration option in Microsoft Excel by clicking on Tools/Options/Calculation/Iterate, and set maximum change to 0.000001. This can be set as desired for accuracy.

Step 8. Enter formulae for the remaining columns (ΔE to σ') from Figure 2.31 in their respective columns.

Step 9. Press the iteration key (F9 in Microsoft Excel) to perform iterations.

Figure 2.35. Spreadsheet Procedure for Janbu Generalized Method of Slices for a Specified Failure Surface

By following Steps 1 to 9 a Factor of Safety of 2.32 is obtained. The iteration is automatic in the spreadsheet.

The following additional notes have to be made with respect to the steps in Figure 2.35 (reference is made to Figure 2.31 for equations):

a. In Step 2, the formula for the Factor of Safety (Equation [2.79] in Figure 2.31) cannot be entered until $\sum A$ and $\sum B$ are defined. An empty cell (which is taken to have a value of zero by Microsoft Excel) is also not permissible because it will lead to division by zero when the formulae for are entered. Hence, a temporary value e.g. 1 should be entered in the Factor of Safety cell.

b. When the formula for the Factor of Safety is finally entered in Step 7, a circular reference is formed, because the Factor of Safety is a function of A, and hence n_α, which is in turn a function of the Factor of Safety. By activating the iteration option, the Factor of Safety value and the four columns B, A', n_α and A will reach convergence. The converged values at this stage are only transitional, since the Equations for ΔE and t have still not been entered (empty cells are taken to be equivalent to zero). These results are not shown in Figure 2.35.

c. In Step 7, in the Tools/Options/Calculation dialog box, the default maximum iteration is 100, which is adequate for most stability problems. However, this number can be set higher as desired. One can also press a key (The F9 key in Microsoft Excel) to test if convergence has been reached.

d. In Step 8, when the formulae for ΔE, $\Delta E/\Delta x$, T and ΔT are entered, the spreadsheet performs normal calculations without iteration since no new circular reference is formed. With the entering of Equation [2.85] in the column t, a second circular reference is introduced and all the columns in the spreadsheet that contain equations are computed until iteration converges in Step 9, as the F9 key is pressed,. The converged final results are shown in Figure 2.35.

2-2.2.2. SITE CONDITIONS

In this section, various additions to the basic procedure described in Section 2-2.2.1. are described. These extensions intend to better describe site conditions, and include slope geometry, strength parameters, and hydraulic conditions. The most important of these are:

(a) Computing pore pressures from the location of a water table, and an assumed subsurface flow regime.
(b) The introduction of unsaturated soil strength in the analyses

These modifications allow one to analyze of the stability of slopes while incorporating unsaturated soil mechanics, which is essential for the study of landslides, particularly shallow landslides. Without these, a comprehensive slope stability analysis for landslide studies cannot be preformed.

2-2.2.2.1. SLOPE GEOMETRY

The geometric properties of the slope (topography) can be obtained directly from a scaled drawing of the slope. The measured coordinates are entered in the X_B and Y_T columns. If a scaled drawing is not available, and for idealized problems, it is frequently assumed that the angle the slope makes to the horizontal, β is constant. By specifying the slope angle, a function can be inserted in the Y_T column of the spreadsheet that automatically computes the Y coordinate of the slope surface as a function of the X coordinate and the specified slope angle. This takes the form:

$$Y_T = X_B \tan\beta \qquad [2.91]$$

Thus, by specifying β and using Equation [2.91], the slope topography is defined.

2-2.2.2.2. PORE PRESSURE DISTRIBUTION

The slope shown in Figure 2.34, was assumed dry. In this section, two methods are outlined by which the effects of pore pressures on a failure surface can be accounted for. The first method assumes a constant pore pressure ratio, r_u along the failure surface. This is the method used by Low and Tang (1997). The second method assumes the presence of a water table at a known depth z_w below the ground surface. From this, and an assumed subsurface flow regime (seepage parallel or non-parallel to slope), the pore pressures on a specified failure surface are determined.

(A) PORE PRESSURE RATIO, r_u

The pore pressure ratio, r_u is defined as:

$$r_u = \frac{u_w}{\gamma_w \bar{h}} \qquad [2.92]$$

where u_w is the pore pressure at the base of a slice, and $\bar{h}$ is the average height of the slice. This average slice height is obtained by first computing the height of each side of a slice by taking the difference between the vertical coordinate of the top of the slope, Y_T and the vertical coordinate of the failure surface, Y_B. The average height of the slice is then obtained by averaging the heights of the sides of the slice. Hence, h is expressed as:

$$\bar{h} = \frac{1}{2}\left\{h_{i,i-1} + h_{i,i+1}\right\} \qquad \text{(see Figure 2.32)} \qquad [2.93]$$

where $h_{i,i-1}$ is the height of the common side between slices i and i - 1, and $h_{i,i+1}$ is the height of the common side between slices i and i + 1. Thus:

$$\bar{h} = \frac{1}{2}\left\{\left(Y_{T_i} - Y_{B_i}\right) + \left(Y_{T_{i+1}} - Y_{B_{i+1}}\right)\right\} \qquad [2.94]$$

By determining the average slice height from Equation [2.94], and by specifying the value of r_u, an equation is introduced in the u_w column of the spreadsheet (see Figure 2.35) that computes the average pore pressure on the base of a slice as:

$$u_w = \bar{h}\, r_u \qquad [2.95]$$

This is done for each slice so that the average pore pressure distribution along the failure surface is defined.

To illustrate this, we revisit the slope shown in Figure 2.34. We assume a constant value $r_u = 0.4$ on the failure surface. The pore pressure distribution along the failure surface is computed and plotted in Figure 2.36a.

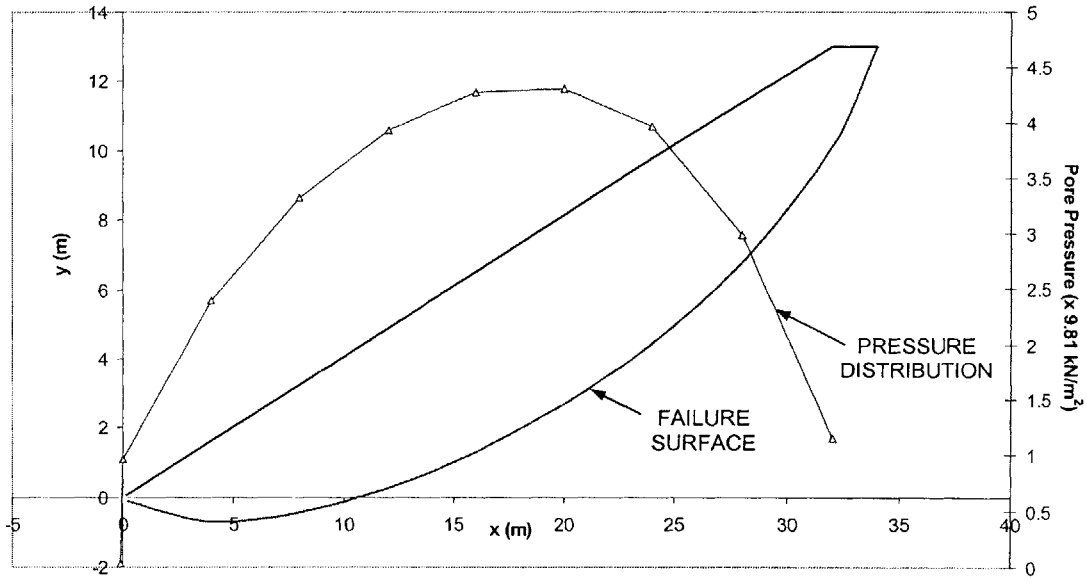

Figure 2.36a. Pore Pressure Distribution on Failure Surface for Constant $r_u = 0.4$

(B) WATER TABLE

A more realistic method to determine the pore pressures on a specified failure surface is to set (if known) or assume (if unknown) a water table at a particular depth z_w below the slope surface, from which the subsurface pore pressures are determined.

When the geometry of the slope is such that its length is significantly greater than its depth, the slope can be regarded as an infinite slope. The water table in an infinite slope typically follows the ground surface. Under steady state conditions, flow takes place parallel to the slope both below and above the water table, and one can show that the steady state pore pressures, assuming full capillarity, vary linearly with depth below the ground surface (see Figure 2.36b) as:

$$u_w = (z - z_w)\gamma_w \cos^2 \beta \qquad [2.96]$$

where:

z is the depth to the failure surface from the ground

z_w is the depth of the water table below the ground surface

Expressing z and z_w in terms of the coordinate system shown in Figure 2.36b, one can express u_{wi}, the pore pressures on the base of slice i as:

$$u_{wi} = ((Y_{Ti} - Y_{Bi}) - (Y_{Ti} - Y_{wi}))\gamma_w \cos^2 \beta \qquad [2.97]$$

and

$$u_{wi} = (Y_{wi} - Y_{Bi})\gamma_w \cos^2 \beta \qquad [2.98]$$

where (see Figure 2.36b):

Y_{Bi} is the y – coordinate of the base of the slice from the origin

Y_{wi} is the y – coordinate of the water table from the origin

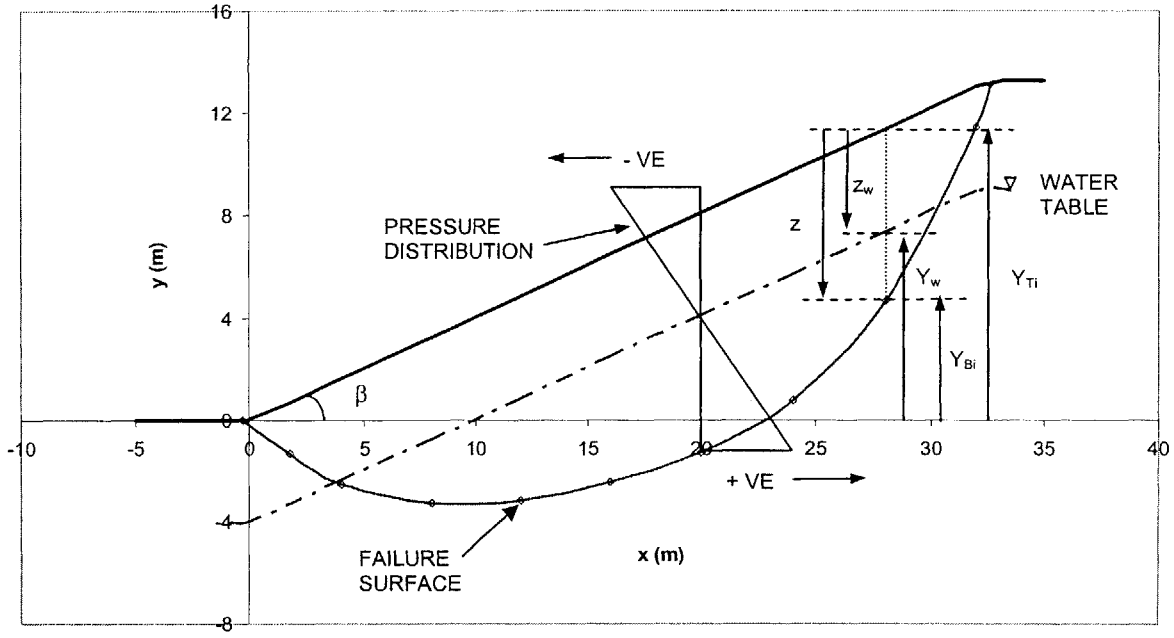

Figure 2.36b. Steady State Pore Pressure Distribution in Infinite Slope (Full Capillarity)

Equation [2.98] for the subsurface pore pressures can be entered into the column u_w of the spreadsheet in Figure 2.35, and the pore pressures along the failure surface are computed accordingly.

2-2.2.2.3. UNSATURATED STRENGTH

The role of suction in increasing the stability of slopes is well known and has been studied in the literature (e.g. see Fredlund et al., 1995; Morgenstern and Krahn, 1997; Ng, 2000). This is of fundamental importance in the study of slope stability, and in particular shallow landslides. Several models to describe the strength of unsaturated soils have been proposed. Two such models are the Effective Stress Model (Bishop, 1959) in conjunction with the Coulomb criterion and the Independent State Variable Model (Fredlund et al., 1978). Models for unsaturated strength are described in Chapter 5. The majority of slope stability studies in the literature that consider unsaturated

strength, and these are not many because unsaturated strength is not well understood, employ the Independent State Variable Model (Fredlund et al., 1978). The reasons for this are described in Chapter 5. In this study, however, we adopt the Effective Stress Model (Bishop, 1959) since it is a more physically based model that can be directly related to soil properties. Other reasons include the recent advancements in experimental procedures, which are described in Chapter 5. These have made it possible for the Effective Stress Model (Bishop, 1959) to better describe unsaturated strength as is done in several more recent studies on unsaturated strength. The model is however yet to be widely employed in stability analyses, and this study will be, one of the first few to adopt model. In this section, we briefly describe the Effective Stress Model, and show how it can be incorporated into stability analyses within the spreadsheet procedure. For a more detailed discussion on unsaturated strength, the models to describe it, and a comparison of these models, reference is made to Chapter 5.

EFFECTIVE STRESS MODEL (Bishop, 1959)

In the Effective Stress Model, the effective stress in the soil is described by an extension to Terzaghi's effective stress principle as (Bishop, 1959).

$$\sigma' = (\sigma - u_a) + \chi(u_a - u_w) \qquad [2.99]$$

where:

σ' is the effective stress

χ is the effective stress parameter

The shear strength, τ can then be evaluated as:

$$\tau = c' + \{(\sigma - u_a) + \chi(u_a - u_w)\} \tan\phi' \qquad [2.100]$$

which is identical to the saturated Coulomb relation where c' and ϕ' are the saturated strength parameters.

χ in Equation [2.99] is an empirical parameter representing the proportion of soil suction that contributes to the effective stress. χ has a value of 1 for saturated soils and 0 for dry soils. Considerable attempts have been made to quantify χ both theoretically and experimentally e.g. Kogho et al., 1993; Modaressi and Abou-Bekr, 1994; Khalili and Khabbaz, 1998). In this study, we employ the relationship proposed by Khalili and Khabbaz (1998) who express χ as:

$$\chi = \left[\frac{(u_a - u_w)}{(u_a - u_w)_{entry}}\right]^{-0.55} \qquad [2.101]$$

where:

$\left[\frac{(u_a - u_w)}{(u_a - u_w)_{entry}}\right]$ is the suction ratio

$(u_a - u_w)_{entry}$ is the air entry suction (as defined in Part 1 of this chapter).

The unsaturated shear strength in Equation [2.100] can be used in Janbu's Generalized Procedure of Slices to assess the stability of slopes by replacing u_w in the u_w column by $\chi(u_a - u_w)$. The effective stress is therefore computed according to Equation [2.99].

An IF statement is used that instructs the spreadsheet to compute the effective stress parameter χ when the failure surface is above the water table and assign a value of χ = 1 when the failure surface is below the water table. This takes the form:

$$\chi = \begin{cases} \left[\frac{(u_a - u_w)}{(u_a - u_w)_{entry}}\right]^{-0.55}, & \text{if the failure surface is in unsaturated soil} \\ 1, & \text{if the failure surface is in saturated soil} \end{cases} \qquad [2.102]$$

2-2.2.2.4. SOIL STRATIFICATION

The spreadsheet procedure has, thus far, been described for a uniform and homogenous subsurface. It is relatively straightforward to include a heterogeneous subsurface into the procedure. There are two main types of stratification, namely parallel to slope, and horizontal. These are shown schematically in Figures 2.37 and 2.38.

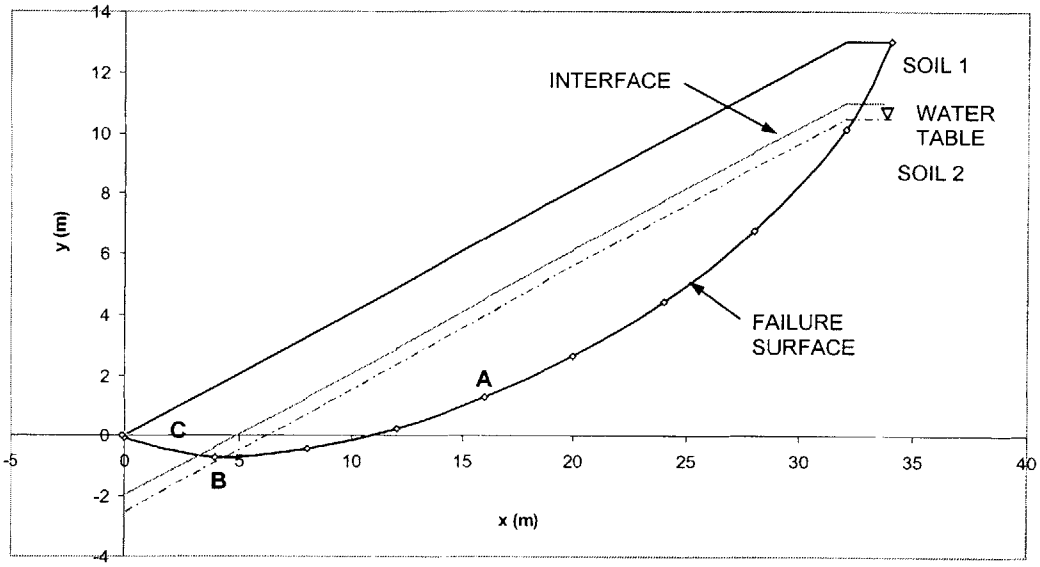

Figure 2.37. Site Conditions and Strength Parameters for Parallel to Slope Stratification

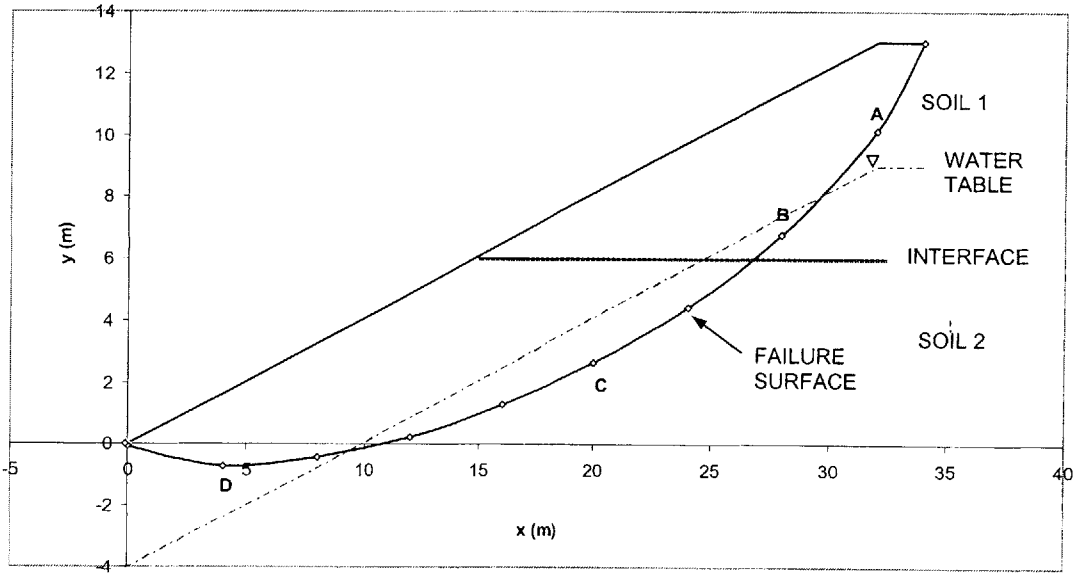

Figure 2.38. Site Conditions and Strength Parameters for Horizontal Stratification

An IF statement is used in the soil strength parameters c' and ϕ' columns that instructs the spreadsheet to use the strength properties of Soil 1 when the failure surface lies in soil 1, and those of soil 2 when the failure surface lies in Soil 2. This takes the form:

$$c' = \begin{cases} c' \text{ of Soil 1}, & \text{if failure surface lies in Soil 1} \\ c' \text{ of Soil 2}, & \text{if failure surface lies in Soil 2} \end{cases}$$

$$\phi' = \begin{cases} \phi' \text{ of Soil 1}, & \text{if failure surface lies in Soil 1} \\ \phi' \text{ of Soil 2}, & \text{if failure surfaces lies in Soil 2} \end{cases} \qquad [2.103]$$

So, for example, for Point C in Figure 2.37, the spreadsheet selects the strength parameters of Soil 1, whereas for Points A and B it selects the strength parameters of Soil 2.

Second IF statements can be used within the IF statement in [2.103] that further instruct the spreadsheet to use either the saturated or unsaturated soil parameters depending on whether the failure surface lies above or below the water table. So, for example, in Figure 2.38, the spreadsheet selects the unsaturated strength parameters of Soil 1 for Point A, the saturated strength parameters of Soil 1 for Point B, the saturated strength parameters of Soil 2 for Point C, and the unsaturated strength parameters of Soil 2 for Point D.

BEDROCK

A special case of stratification, either parallel to slope or horizontal, is the presence of bedrock. This can be accounted for using the same methods described in the previous sections, where the strength parameters of Soil 2, are those of the bedrock. If these strength parameters are known, they can be used directly, and if they are not known, then assuming intact rock, very high values of strength parameters can be used.

Thus far, the subsurface was assumed to be composed of only two soils. Slopes with multi-layered soils can assessed in a very similar way to what was described, using simple modifications in the spreadsheet, which can be extended to include any number of soil layers.

2-2.3. DETERMINISTIC ANALYSES WITH SEARCH FOR THE CRITICAL NON-CIRCULAR SLIP SURFACE

In Section 2-2.2., spreadsheet techniques were described by which the factor of safety was computed for a specified failure surface using Janbu Generalized Method of Slices (1973). In this section, spreadsheet techniques are described by which the critical (minimum factor of safety) deterministic failure surface is located. The problem is set up as an optimization (minimization) problem that is solved using a spreadsheet's optimization tool. The objective function is the factor of safety that is to be minimized by varying the coordinates of an initial trial failure surface, subject to various physical constraints.

The problem is formally set out as follows (with notation as in Figure 2.40):

Objective function:

$$Z : \text{minimize } F \qquad [2.104]$$

where F is the Factor of Safety

By varying:

$$X_{B(1)},\ X_{B(n)} \text{ and } Y_{B(i)} \qquad \text{for } i = 2,...,n-1 \qquad [2.105]$$

where $X_{B(i)}$ $Y_{B(i)}$ are the coordinates of the failure surface, and n is the number of slices the slope is sectioned into.

Subject to:

$$X_{B(1)min} \leq X_{B(1)} \leq X_{B(1)max} \qquad [2.106]$$

$$X_{B(n)min} \leq X_{B(n)} \leq X_{B(n)max} \qquad [2.107]$$

where:

$X_{B(1)min}$, $X_{B(1)max}$, $X_{B(n)min}$ and $X_{B(n)max}$ are physical constraints placed on the X coordinates of the first and n^{th} slice (see Figure 2.40). These are set judgmentally.

$$Y_{B(1)} = Y_{T(1)} \text{ and } Y_{B(n)} = Y_{T(n)} \qquad [2.108]$$

which sets the vertical coordinates of the first and last points on the failure surface to be equal to the ground surface.

$$Y_{B(i)} \leq Y_{T(i)} \qquad \text{for } i = 2,..., n-1 \qquad [2.109]$$

where $Y_{T(i)}$ are the Y coordinates of the slope surface

$$\sigma'_{(i)} \geq 0 \qquad \text{for } i = 1,..., n \qquad [2.110]$$

where $\sigma'_{(i)}$ is the effective stress acting on the bottom of a slice (see Figure 2.40), and this constraints ensures no negative effective stress values are obtained.

This problem is set up and solved using a spreadsheet's built-in optimization tool e.g. Solver in Microsoft Excel as described in Figure 2.39.

Step 1. An initial trial failure surface is selected.
Step 2. The slope is sectioned into any desired number of slices, n.
Step 3. An arbitrary origin is set from which the horizontal (X_B) and vertical (Y_B) coordinates of the failure surface at the interface between two adjacent slices are inserted in the appropriate columns in Figure 2.35.
Step 4. The Y coordinate of the ground surface at the interface between adjacent slices is also measured from the origin and placed into the Y_T column of Figure 2.35. This defines slope topography.
Step 5. The Factor of Safety for the trial failure surface is then computed according to Equation [2.79] of Figure 2.31.
Step 6. Two sets of physical constraints are placed on the minimization problem (see Equations [2.106] to [2.109]).

The first set constrains the boundaries of the failure surface by constraining the coordinates of the crest $(X_{B(1)}, Y_{B(1)})$ and toe $(X_{B(n)}, Y_{B(n)})$ of the failure surface to ensure physically reasonable failure surfaces. The vertical coordinates of these points are set to be equal to the vertical coordinates of the ground surface. The horizontal coordinates of these points are also constrained to limit the horizontal extent of the failure surfaces through which the optimization tool iterates. This would restrict the location of the crest and toe of the slope in a way that has physical meaning. Judgment is required to specify and ensure that these constraints are acceptable. These constraints are shown schematically in Figure 2.40.

The second set of constraints is placed on the effective normal stress σ' acting at the base of each slice. The effective normal stress is computed according to Equation [2.87] of Figure 2.31 and constraints are placed such that these stresses are non-negative.

Step 7. The spreadsheet's built-in optimization tool (Solver in Microsoft Excel) is then invoked to minimize the factor of safety by varying some of the X and Y coordinates of the failure surface. After choosing an initial trial failure surface, and the cells to be varied and the constraints are specified, the spreadsheet optimization tool (Solver in Microsoft Excel) is invoked to search for the critical failure surface on which the factor of safety is minimum.

Step 8. All other columns of Figure 2.35, such as the h_{ij}, $\tan\alpha$, u_w, h_t and $\tan\alpha_t$, are automatically recalculated by the relevant equations in Figure 2 each time the failure surface (X_B, Y_B) is varied.

Figure 2.39. Spreadsheet-Based Optimization Procedure to Determine Critical Failure Surface

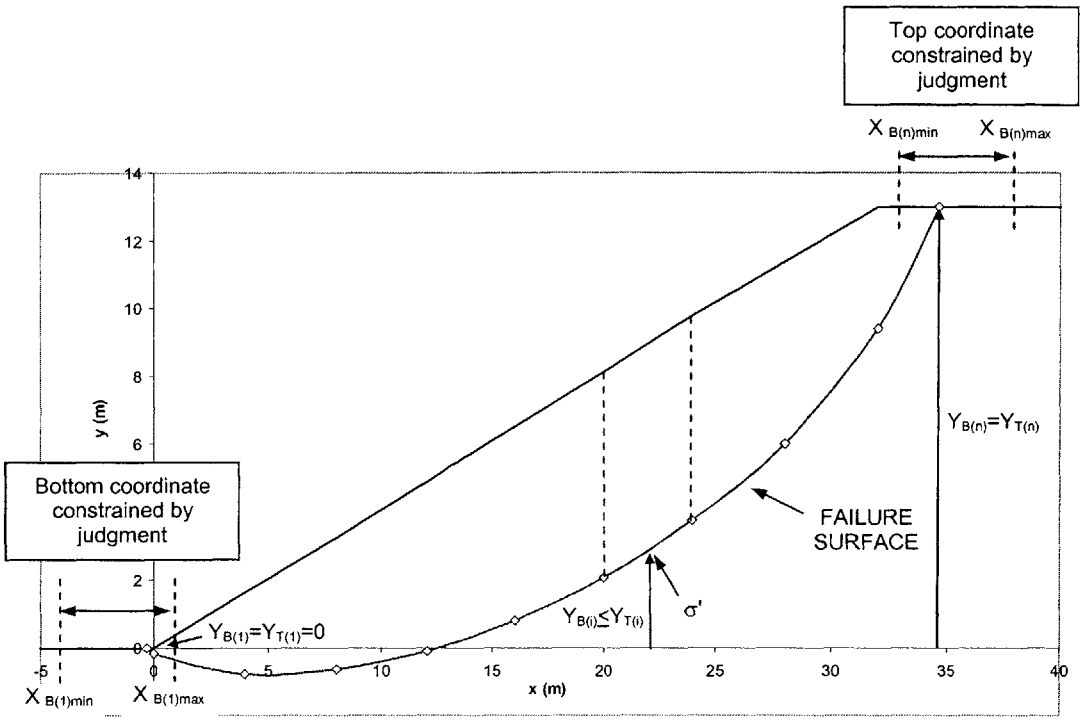

Figure 2.40. Schematic showing Constraints of Spreadsheet Optimization Procedure

To illustrate the spreadsheet optimization procedure, consider the slope shown in Figure 2.41.

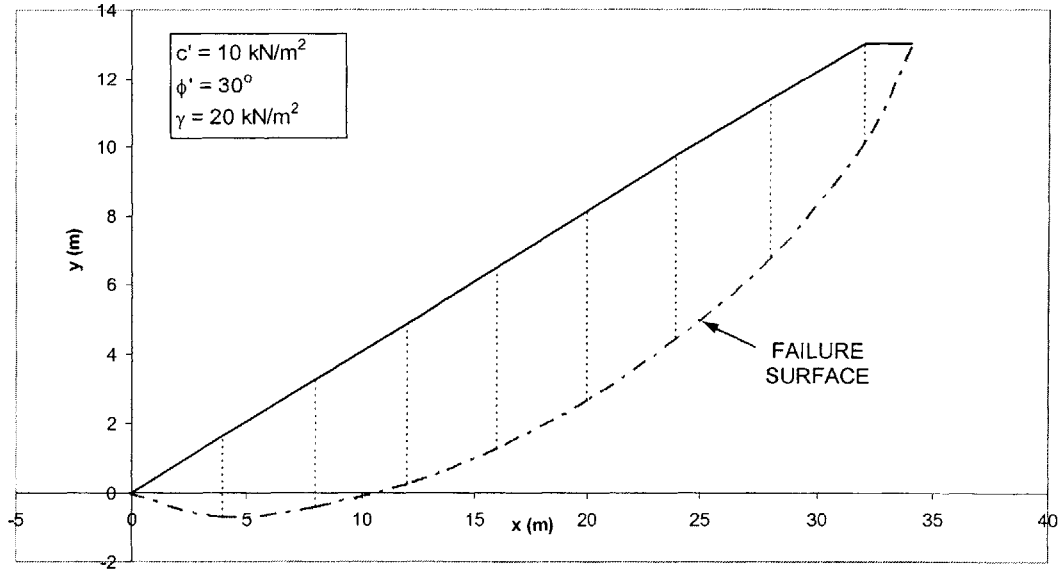

Figure 2.41. Geometric and Strength Properties and Initial Trial Failure Surface

An initial trial failure surface is selected as shown in Figure 2.41.

2-2.3.1. PORE PRESSURE DISTRIBUTION

(A) CONSTANT PORE PRESSURE RATIO

We assume that the pore pressures on a failure surface are determined from a constant pore pressure ratio $r_u = 0.4$, using Equation [2.95]. The Factor of Safety for the initial failure surface, is computed to be 1.47.

The spreadsheet optimization procedure in Figure 2.39 is used to determine the critical failure surface in the slope which is shown in Figure 2.42.

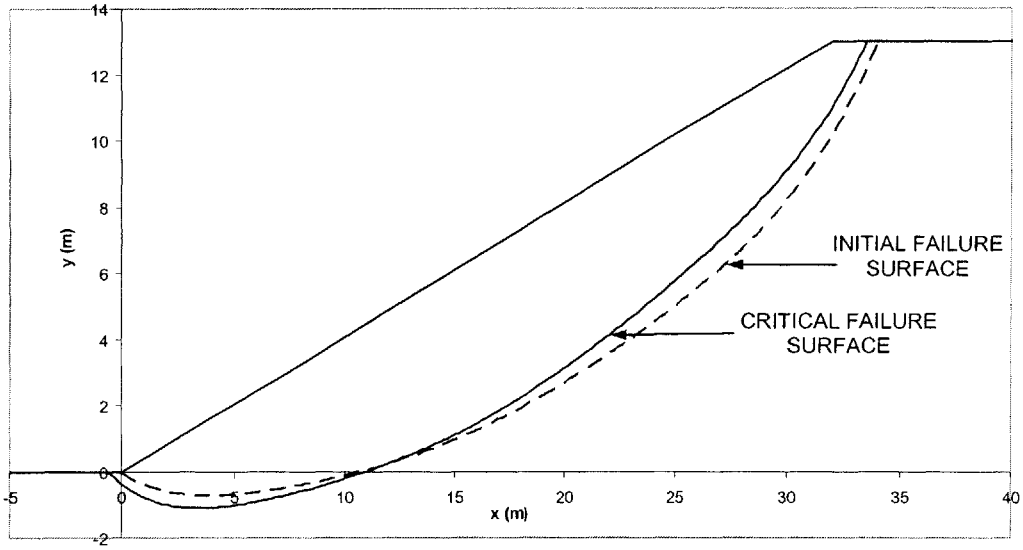

Figure 2.42 Initial and Critical Failure Surfaces for Pore Pressures Obtained from a Constant Pore Pressure Ratio $r_u = 0.4$

A Factor of Safety of 1.45 is computed for the critical surface, and this is the minimum Factor of Safety in the slope.

(B) WATER TABLE

Consider the slope in Figure 2.41, but with a water table located at a depth of 4 m below the ground surface. An initial trial surface is chosen, and is shown in Figure 2.43.

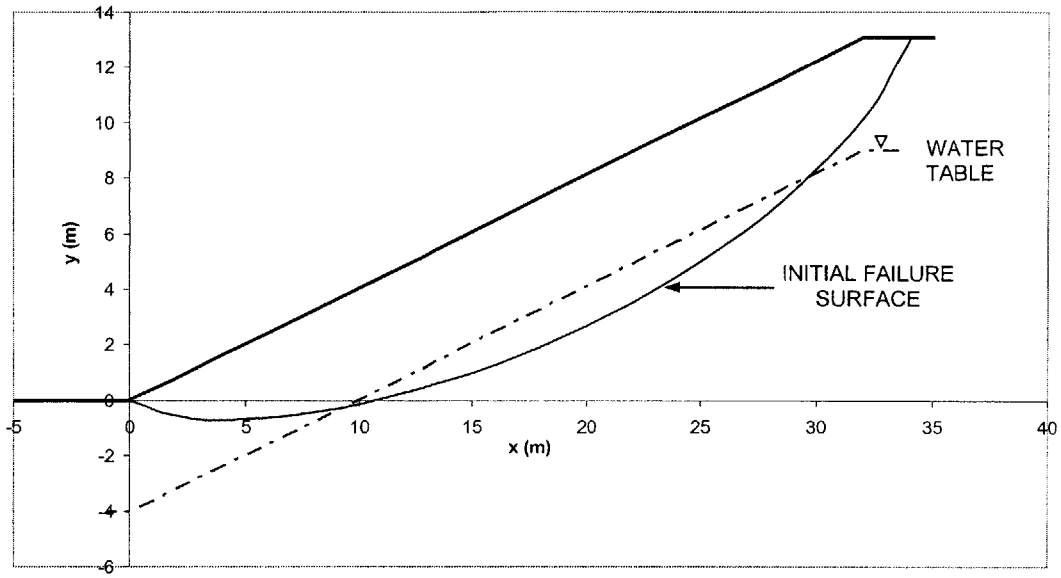

Figure 2.43 Slope Geometry, Hydraulic Condition, and Initial Failure Surface

The Factor of Safety on the initial surface is computed to be 2.37, assuming the Coulomb Model for saturated and unsaturated strength, and full capillarity. The spreadsheet optimization procedure is implemented to locate the critical failure surface and the results are shown in Figure 2.44.

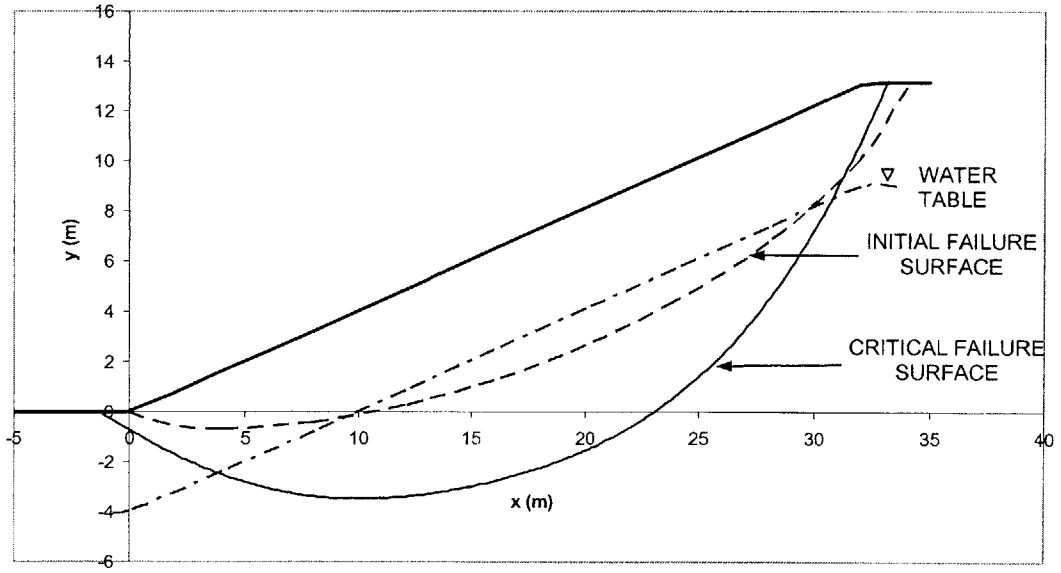

Figure 2.44. Critical Failure Surface for a Water Table at a Depth of 4 m below the Ground Surface Assuming Coulomb Model and Full Capillarity

The Factor of Safety on the critical failure surface is computed to be 2.28, and this is the minimum factor of safety in the slope.

2-2.3.2. UNSATURATED STRENGTH

Unsaturated soil strength is introduced into the optimization procedure by adopting the Effective Stress Model (Bishop, 1959) for unsaturated strength, with an air entry suction, $(u_a - u_w)_{entry} = 0.1 kPa$. The effective stress parameter χ can be computed from the air entry suction according to Equation [2.101] for different values of suction. The spreadsheet optimization procedure is applied, and the critical failure surface is as shown in Figure 2.45.

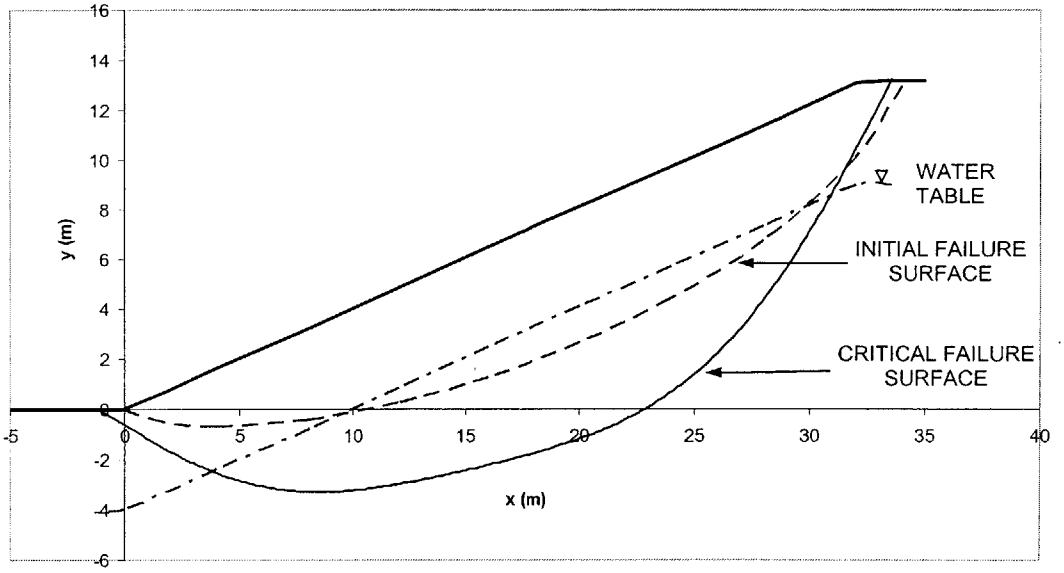

Figure 2.45. Initial and Critical Failure Surfaces adopting the Effective Stress Model (Bishop, 1959) for Unsaturated Soil

A factor of safety of 1.92 is obtained as the minimum factor of safety in the slope on this surface. The value of the Factor of Safety is lower than that when the Coulomb Model (F = 2.37) was assumed because of the lower unsaturated strength. The shapes of the critical surfaces are also different as shown in Figures 2.44 and 2.45.

2-2.3.3. BEDROCK

The search procedure for the critical failure can be extended to account for the presence of an underlying layer of bedrock at a known or given depth below the ground surface. This is done by assigning very high values for the strength parameters of the bedrock assuming it is intact, e.g. $c' = 100kPa$. By doing so, when the optimization tool is invoked to minimize the factor of safety, intermediate failure surfaces that lie within the bedrock are avoided because of the high assigned strength. Consider the slope in Figure 2.46, and assume the presence of bedrock parallel to the slope surface at a depth of 7 m below the ground surface. We adopt the Effective Stress Model (1959) for unsaturated strength with an air entry suction, $(u_a - u_w)_{entry} = 0.1kPa$. A search for the critical failure surface is performed and the results are shown in Figure 2.46.

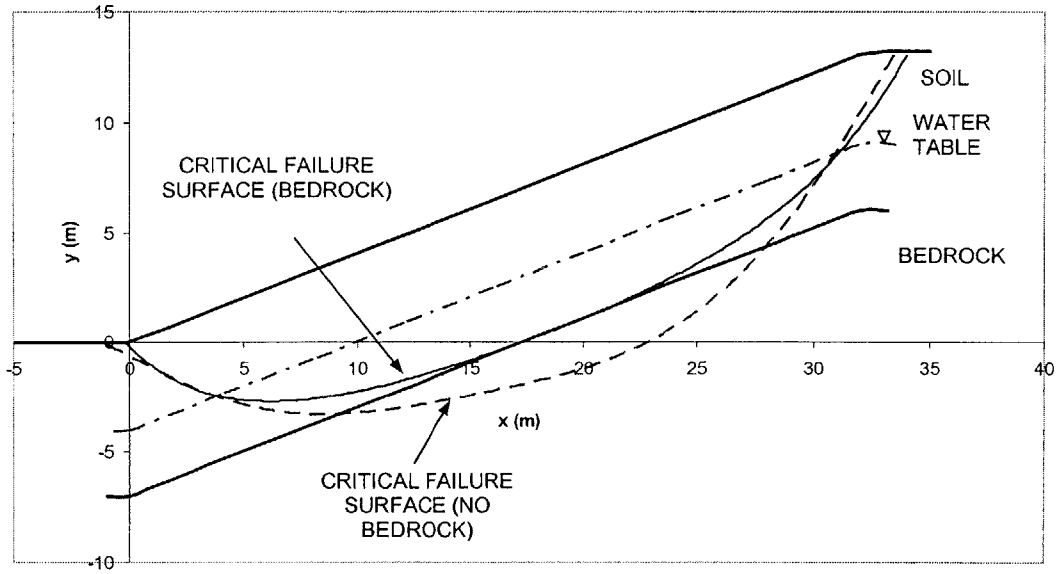

Figure 2.46. Critical Failure Surface in the Presence of Bedrock

A Factor of Safety of 1.98 is obtained as the minimum Factor of Safety in the slope. Figure 2.46 shows that the critical surface lies entirely within the soil layer in the presence of bedrock, at the soil bedrock interface. The assumption is made that the strength parameters of the interface are those of the soil, and hence this result. Figure 2.46 also shows the critical surface in the absence of bedrock. A Factor of Safety of 1.92

was obtained on this surface. The presence of bedrock confines the critical surface to the soil layer, and by doing so, causes the increase in Factor of Safety.

2-2.4. COMMENTS ON THE METHOD OF SLICES

Setting up the problem of locating the critical failure surface as an optimization problem, makes it straightforward to solve using a spreadsheet optimization tool. However, several comments have to be made with regard to numerical difficulties encountered when searching for the critical surface using a stability model based on the Method of Slices, such as the Janbu (1973) Generalized Method (Abramson, 1995; Bromhead, 1994). These include:

1. The possibility that statically inadmissible failure surfaces may be generated as the failure surface geometry is being varied during the optimization process. An initial failure surface may be selected such that the optimization process fails to converge using the Generalized Procedure of Slices. In Microsoft Excel this appears as a "NUM" in the factor of safety cell. To avoid failure surfaces that lead to divergence during iteration, Low and Tang (1997) propose a two stage optimization strategy. In the first stage the formula in the t column (see Figure 2.35) is deleted (taken as zero by Microsoft Excel). A temporary failure surface is obtained by the optimization tool. In doing so, the second circular iteration introduced by t is eliminated, and divergence is prevented. This is followed, in the second stage, by reinstalling the formula in the t column. The final converged failure surface is obtained by the optimization tool.

2. The possibility of obtaining a critical failure surface on which the Factor of Safety is a local minimum during the optimization procedure, but is not the global minimum in the slope, where global refers to the entire subsurface of the slope. This arises because depending on the particular geometric constraints in the optimization problem, and the initial selected trial failure surface, there may be multiple solutions to the problem. This gives rise to non-unique solutions, and during the iterative process the spreadsheet may converge to one of these. Consider Figure 2.47. If the initial trial surface is chosen to be that labeled surface 1, the spreadsheet converges to the critical surface labeled 1, and a Factor of Safety of 2.34 is obtained. If however, initial trial surface 2 is selected, the

resulting critical surface is the one labeled 2, and the Factor of Safety on this surface is 1.92.

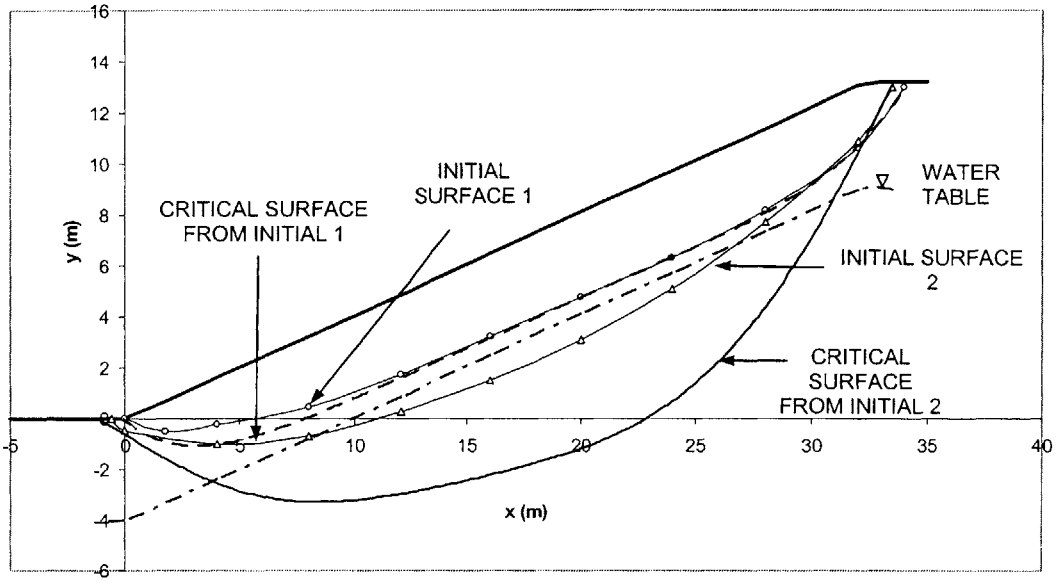

Figure 2.47. Comparison of Different Critical Surfaces Resulting from Different Initial Trial Surfaces

Evidently, because of the lower Factor of Safety, critical failure surface 2 is the critical surface in the slope. This again is a problem that arises when dealing with the Method of Slices, and one way around the problem is to select several initial trial failure surfaces located at different depths below the surface of the slope. Once local critical failure surfaces, if different, are obtained, the factors of safety associated with these can be compared, and thus the global minimum factor of safety failure surface and true critical failure surface can be determined.

3. A third potential problem when dealing with the Method of Slices is that of large angles that bases of slices make to the horizontal. The greater the number of slices used in the analyses, the more accurate the results, but there is the problem of very steep base angles that may give rise to incorrect results. This problem has been recognized in the literature, and as a general guideline it has been suggested that the base angle $\alpha \leq \left(45 + \frac{\phi'}{2}\right)$, where α is the base angle (Bromwell, 1977; Morgenstern, 1978). In Appendix B, we derive, theoretically, the maximum permissible angle in an Infinite Slope

in terms of the slope angle and soil parameters. This has not been previously reported in the literature, and we show that under certain conditions, the widely accepted $\alpha \leq \left(45 + \frac{\phi'}{2}\right)$ may be an unconservative estimate. This problem of maximum permissible angle in the Method of Slices is incorporated into the spreadsheet procedure. When analyzing a specified failure surface, and after the slope is sectioned into the desired number of slices, the spreadsheet automatically computes the base angles of all slices, and reports to the user if an angle is too large for the analysis. This is done by using an IF statement that compares the actual base angle to the maximum angle. This is also incorporated into the search procedure such that if the spreadsheet iterates through failure surfaces with too steep base angles, it will automatically report the problem. The solution to this problem is a compromise on the number of slices used in the analyses, where on the one hand a greater number of slices leads to more accurate numerical results, but on the other hand, may give rise to this problem of maximum angle.

2-2.5. MODEL VALIDATION

Thus far, the analyses have been performed on hypothetical slopes to illustrate the capabilities of the spreadsheet optimization tool to search for the critical failure surface. In this section, we validate the model by back analyzing a failed slope in Walton's Wood, England.

THE LANDSLIDE AT WALTON'S WOOD

In 1963, a landslide occurred at Walton's Wood, about 1½ miles north of Madeley, Staffordshire (Skempton &. Early, 1969). This site was where an embankment for the M6 motorway was to be built. A scaled drawing showing the geology is shown in Figure 2.48. The soil properties as measured at the Imperial Collage laboratories in London are also shown in Figure 2.48.

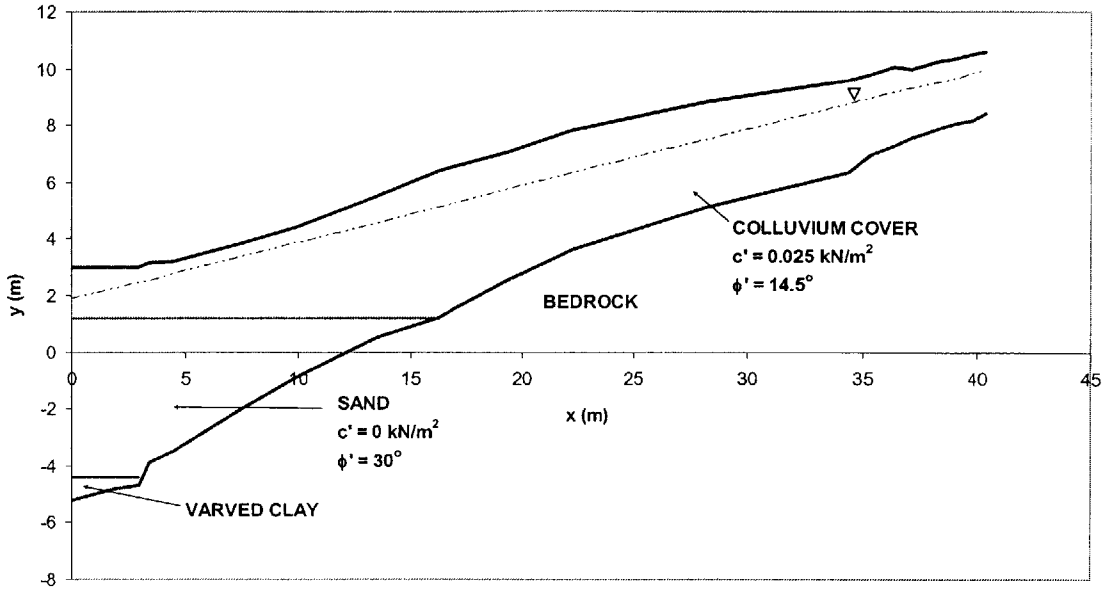

Figure 2.48. Geology and soil properties of the landslide site at Walton's Wood

The first 5 m of the slope is composed of a colluvium cover inclined at an angle of about 11° to the horizontal. The landslide occurred within the colluvium and the actual failure surface is shown in Figure 2.49.

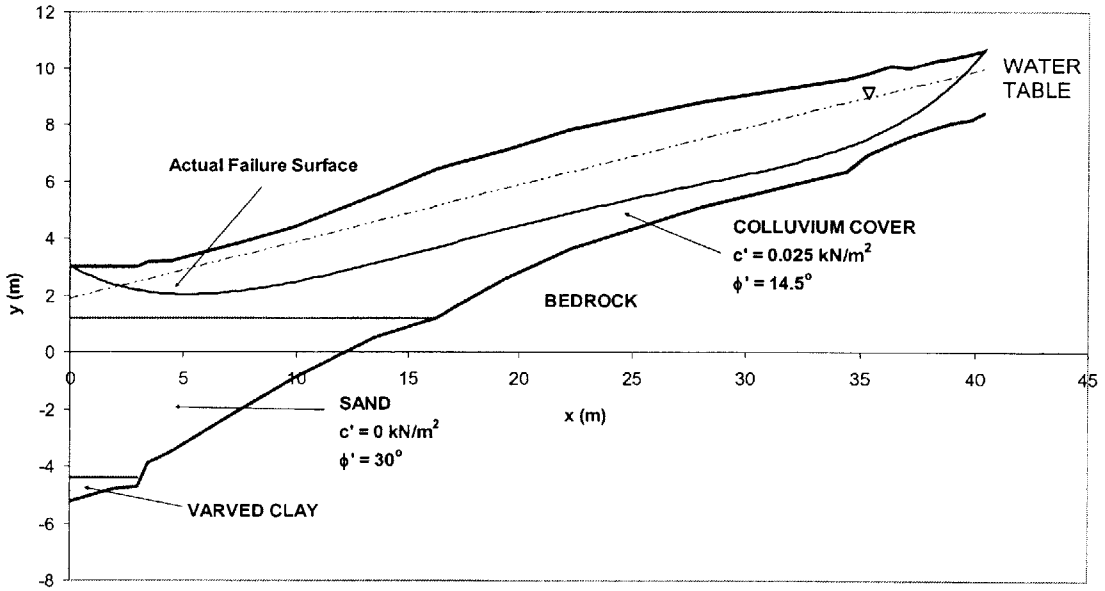

Figure 2.49. Actual Failure Surface of Landslide

The slope topography, location of the water table, and the soil strength parameters are input the spreadsheet. The state of stability of the slope is then analyzed using Janbu's Generalized Procedure of Slices (1973) by searching for the critical failure surface, starting with the initial failure surface shown in Figure 2.50.

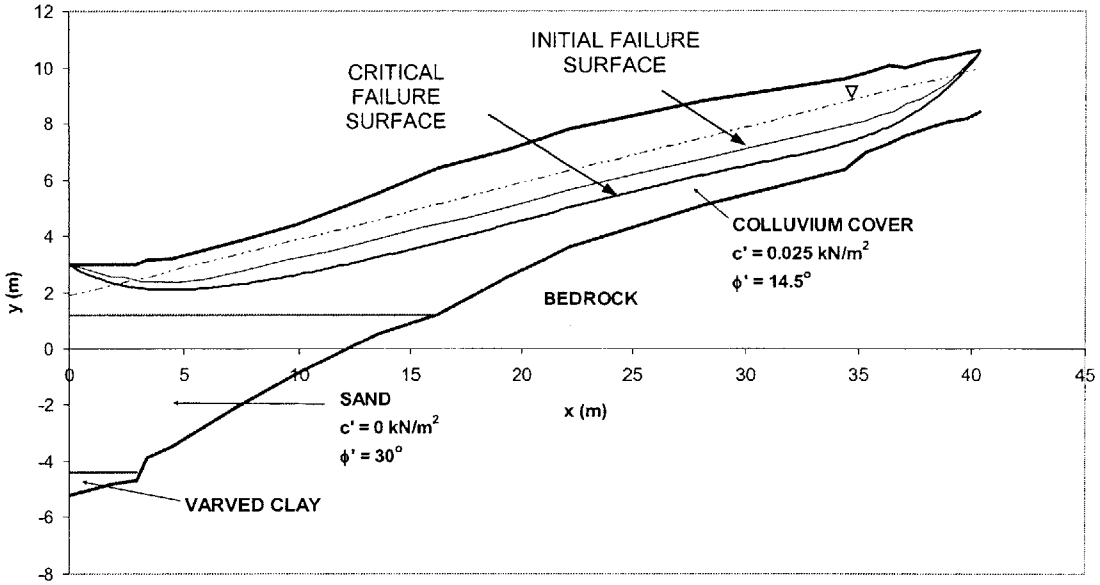

Figure 2.50. Initial Trial and Predicted Failure Surfaces

The resulting predicted critical failure surface is shown in Figure 2.50. Figure 2.51 compares the predicted surface (solid line) with the actual failure surface (dashed line) of the landslide.

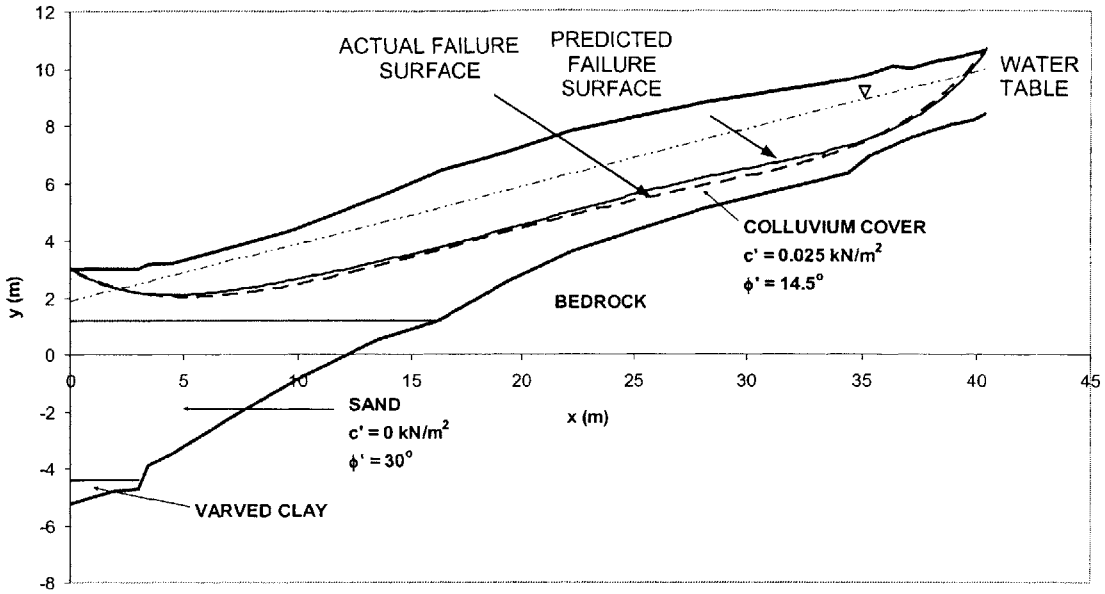

Figure 2.51. Comparison of Predicted Critical Failure Surface and Actual Failure Surface of Landslide

The Factor of Safety for the critical failure surface shown in Figure 2.51 is computed to be 0.99 indicating failure along this surface.

Figure 2.51 shows that the predicted failure surface is in very good agreement with the observed failure surface. Minor discrepancies occur because of the discretiztion of the problem into slices, as well as other factors such as the accuracy of the Generalized Method of Slices (1973).

It should be noted here that this slope has been the subject of extensive studies, and the soil strength parameters have been determined through intensive laboratory tests. This makes it a good example to study, and test the validity of the spreadsheet procedure. Furthermore, since the failure surface is shallow and planar, Janbu's Generalized Procedure of Slices (1973) is well suited to analyze the state of stability.

2-2.6. CONCLUSIONS

This part of Chapter 2 presented methods by which the stability of a slope on a specified failure surface can be assessed using Janbu's Generalized Method of Slices (1973). The method is based on a spreadsheet solution, and details of representing realistic site conditions which include, fundamentally, the incorporation of suction and unsaturated strength. Without these, a comprehensive landslide study is not possible. These include,

A method was presented within the spreadsheet framework by which a search for the critical failure surface, and hence minimum Factor of Safety in a slope can be performed. The method was validated by back analyzing a failed slope at Walton's Wood, and the results are in very good agreement with the actual slide. These methods will be used as the basis for stability analyses in this study.

PART 2-3:

COMBINED MODEL

Various combined hydrology and stability models have been proposed in the literature e.g. Anderson et al, (1990), Wilson and Wieczoreck (1996), Fredlund et al, (1998), Crozier (2000). These, however, suffer from different shortcomings because of the assumptions made in either the hydrologic or stability model, or both. The more advanced infiltration and stability models developed in Parts 2-1 and 2-2 of this chapter allow one to develop a combined model better suited for landslide analyses than the current models being used in the literature. This, in turn, one to better estimate of landslide hazards.

In Part 2-1, the basic flow principles involved during the process of infiltration were described, and a model was developed that solved the pressure based form of the variably saturated flow equation. This model allows one to predict pore pressure profiles with time, given various initial and boundary conditions.

In Part 2-2, the basics of quantitative stability analyses were described, and a model was developed that allows one to determine the state of stability of a slope, in terms of Factor of Safety. This was first done for a specified failure surface, and then a search procedure was described whereby the critical failure surface in the slope could be established.

In this part, the infiltration model is combined with the stability model. The combined model uses the output of the infiltration model (variation of pore pressures with time) as input in the stability model, which allows one to determine Factors of Safety in a slope as a function of time. By doing so, the spatial and temporal hazards of landsliding can be assessed. This is done in the same spreadsheet environment as the infiltration and stability models.

2-3.1. STATE OF STABILITY AT A PARTICULAR TIME FOR SPECIFIED FAILURE SURFACE

The infiltration model developed in Part 2-1 gives the variation of pore pressures with depth (pressure profiles) at successive times given certain initial and boundary conditions. Section 2-2.3.1 described two methods to compute the pore pressures acting along a specified failure surface during steady state conditions, namely from an average pore pressure ratio r_u, or from the known depth z_w of a water table below the ground surface. In this section, the pore pressures are extracted from the infiltration model, and used in the stability model. This allows one to determine the transient state of stability of a slope. An inherent assumption is made in the analyses, namely that any rainfall event occurs with the same intensity on the slope. This implies that the intensity or infiltration flux on the slope surface is the same at any particular time. By making this assumption, one models the infiltration process in one dimension, the vertical dimension, and the resulting pressure distributions apply to all sections along the slope. This effectively eliminates the need to estimate pressures in the horizontal direction and only those in the vertical direction are predicted. This is a reasonable assumption since rainfall events, most frequently, occur on a large area, and would therefore occur on the entire slope, as it is unlikely that rainfall would only take place on a certain section of the slope only.

To do all this, the LOOKUP function in Microsoft Excel is used, which instructs the spreadsheet to look up the depth to the failure surface, and report the value of the pore pressures which are extracted from the hydrology model. The results of the hydrologic analyses can be presented in tabular form, where the pore pressures are expressed as a function of depth (see Figure 2.52a). By doing so, the LOOKUP function in Excel in the stability model (see Figure 2.52b) takes the form:

u_w = LOOKUP("Failure Surface Depth", "Pressure Profile Depth", "Pore Pressures")

Pore pressures from hydrologic analyses input into stability model using the LOOKUP function

Depth	Pore Pressures, u_w (kN/m^2)
0.05	-1.528008654
0.1	-1.483639663
0.15	-1.443789408
0.2	-1.407648898
0.25	-1.37461196
0.3	-1.344213174
0.35	-1.316087856
0.4	-1.289945343
0.45	-1.265550594
0.5	-1.242711204

Figure 2.52a. Results of Hydrology Model at a Particular Time (only shown for small depths upto 0.5m)

	X_B	z_w	Y_{WATER}	X_B	Y_B	Y_T	h_{ij}				
Slice #	16.99992	5	7	17	12	12	0	tan α	Δx	p	u_w
1	16.39	5	7	16.39	10.076	12	1.9239	3.154386	0.609922	1.923929	-1.80511
2	14.15	5	5.5	14.15	8.1648	10.5	2.3352	0.853252	2.24	4.259143	-1.56376
3	12.15	5	4	12.15	6.7673	9	2.2327	0.69873	2	4.567889	-1.62393
4	10.15	5	2.5	10.15	5.4055	7.5	2.0945	0.680926	2	4.327202	-1.705
5	8.15	5	1	8.15	3.8693	6	2.1307	0.7681	2	4.225254	-1.68376
6	6.15	5	-0.5	6.15	2.5929	4.5	1.9071	0.638176	2	4.037805	-1.815
7	4.15	5	-2	4.15	1.0442	3	1.9558	0.774384	2	3.862924	-1.78638
8	2.15	5	-3.5	2.15	0.0484	1.5	1.4516	0.497884	2	3.407461	-2.08228
9	0.15	5	-5	0.15	0.01	0	-0.01	0.019193	2	1.441614	-2.93412
10	-0.10278	5	-5	-0.103	0	0	0	0.03956	0.252783	-0.01	-2.93412

Figure 2.52b. Stability Model Set-Up (Part of)

Figure 2.52. Combined Model Spreadsheet Set-Up

With the notation in Figure 1, the LOOKUP function takes the form:

$$u_W = \text{LOOKUP}((Y_T - Y_B), z, u) \qquad [2.111]$$

where:

- u_W pore pressures acting on failure surface
- Y_T is the vertical coordinate of the slope surface
- Y_B is the y – coordinate of the failure surface
- z column of the depths below the ground surface at which the pore pressures are computed in the hydrologic model (see Figure 2.52a)
- u pore pressures obtained from infiltration model (see Figure 2.52a)

With the function in Equation [2.111] for the pore pressures (in the u_W column of Figure 2.52b), the spreadsheet automatically extracts the appropriate pore pressures from the results of the hydrology model at any particular time, t. The Factor of Safety along the specified surface is then computed as was described in Part 2-2.

To illustrate the procedure consider the slope shown in Figure 2.53.

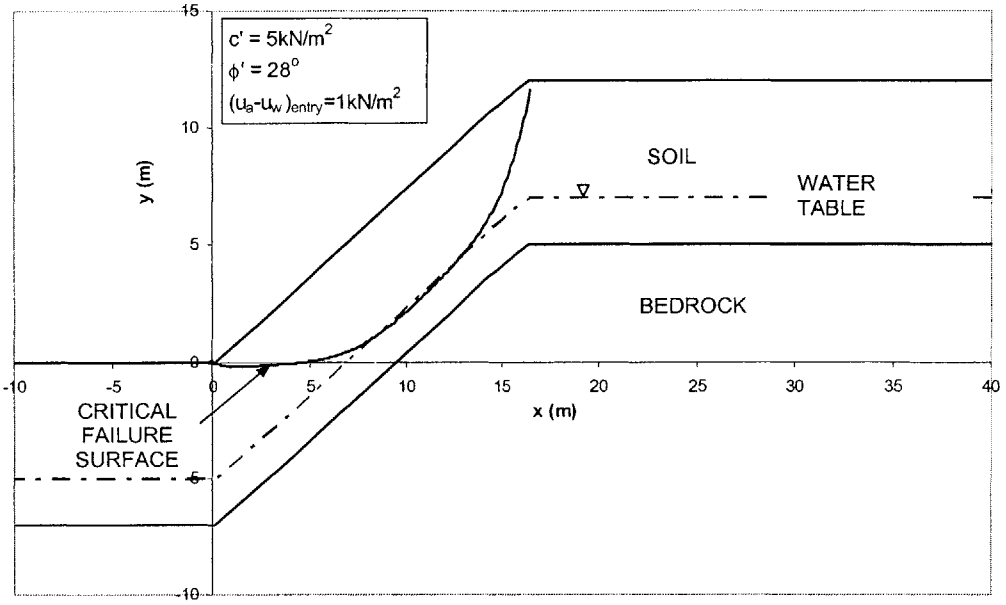

Figure 2.53. Slope Properties and Initial Critical Failure Surface

The slope geometric and soil strength parameters are shown in Figure 2.53. In addition, the soil hydraulic parameters are chosen as:

Saturated moisture content of soil $\theta_s = 0.37$

Residual moisture content of soil $\theta_r = 0.03$

Saturated conductivity $K_s = 300\text{cm/day} = 2.89 \times 10^{-5}\text{m/s}$

Specific storage coefficient $S_s = 0.0025$

The soil characteristic curves (see Part 2-1) are used to describe unsaturated properties. The models developed by van Genuchten (1980) are used (see Part 2-1). The parameters of these models are chosen to be $n = 2.24$ and $\delta = 0.03$. The resulting soil characteristic curves are as shown in Figures 2.54 and 2.55.

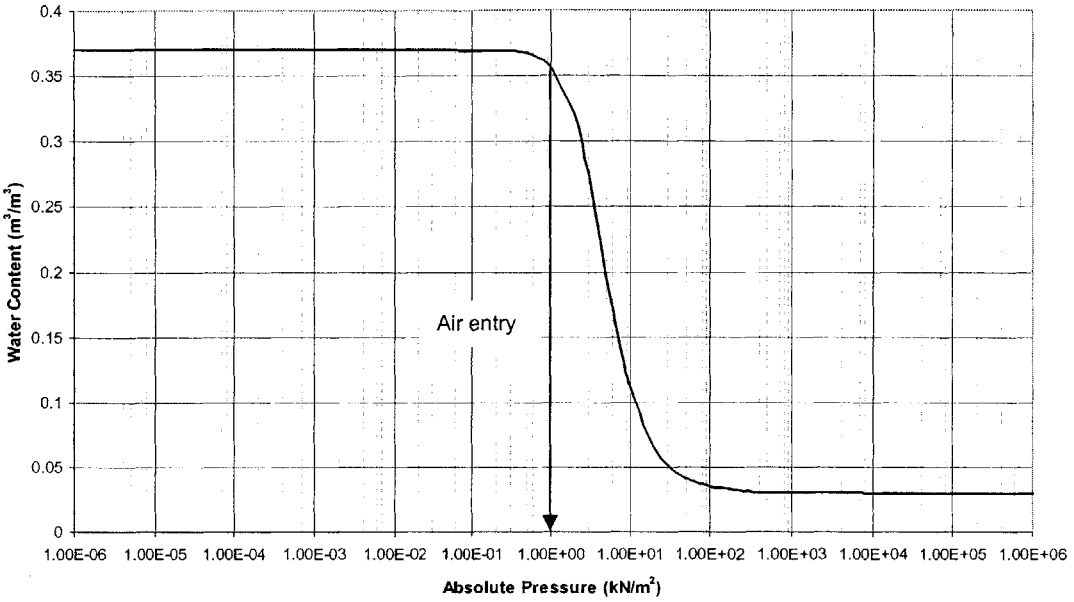

Figure 2.54. Moisture Retention Characteristic Curve

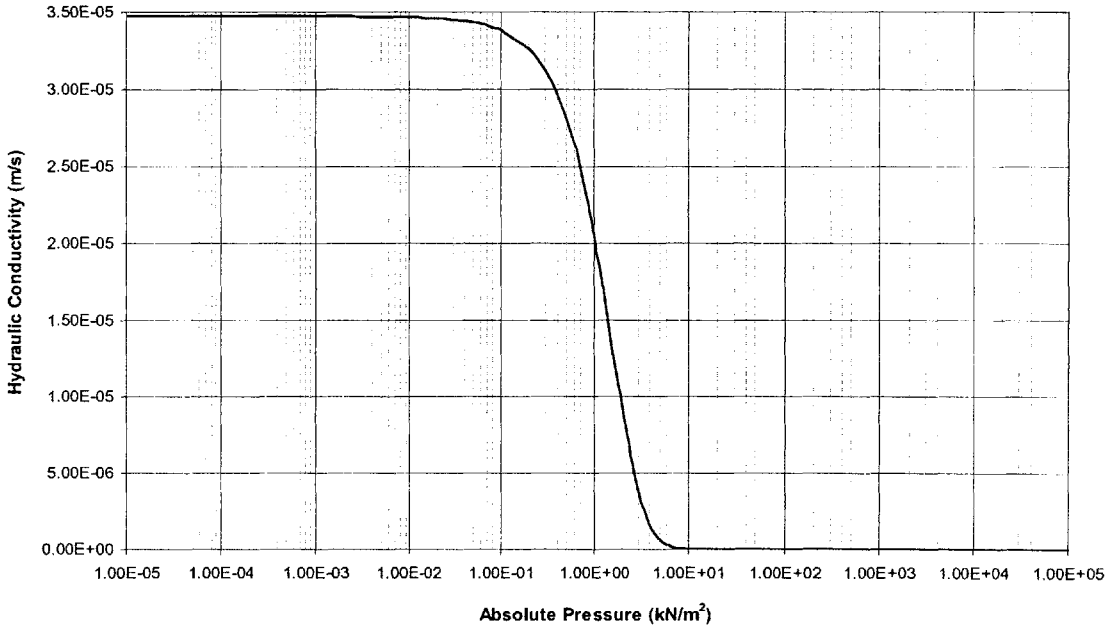

Figure 2.55. Hydraulic Conductivity Characteristic Curve

The air entry pressure (see Part 2-1) is obtained from Figure 2.54, and estimated to be $(u_a - u_w)_{entry} = 1kN/m^2$. A more detailed procedure to do this was provided in Part 1 of this chapter. The air entry pressure is used in the Effective Stress Model (Bishop, 1959) for unsaturated soil strength (see Part 2-2.2).

2-3.1.1. INITIAL STATE OF STABILITY

A failure surface is specified and this is shown in Figure 2.53. Assuming an infinite slope and full capillarity, steady state conditions imply that flow occurs parallel to the slope surface in both the saturated and unsaturated zones. The corresponding pore pressures vary linearly with depth as:

$$u_w = (z - z_w)\gamma_w \cos^2 \beta \qquad [2.112]$$

where:

- u_w is the mean pore water pressures at a depth z below the ground surface
- z_w is the depth of the water table below the ground surface
- γ_w is the unit weight of water
- β is the inclination of the slope to the horizontal

Equation [2.112] results in positive pressures in the saturated zone of the slope below the water table where $z > z_w$, and negative pressures in the unsaturated zone, above the water table where $z < z_w$ (see Figure 2.56). The initial (antecedent) moisture content in the slope can be inferred from Equation [2.112]. Below the water table the moisture content is equal to the saturated moisture content of the soil, and above the water table, the moisture content is less than the saturated value, and is related to the pressures in Equation [2.112] through the soil characteristic curves, e.g. Figure 2.54.

However, in the majority of natural settings/slopes, the initial moisture content distribution, particularly near the surface of the soil is dictated by antecedent rain conditions. During wet seasons, the antecedent (initial) moisture distribution is likely to be greater than that inferred from Equation [2.112]. For this example, we assume a constant antecedent moisture content of $\theta_i = 0.08$ near the surface of the slope, through a depth, we call, z_i (see Figure 2.56) below the ground surface. This corresponds to an initial pressure of about $u_i = -12 kN/m^2$, which is obtained from the soil moisture retention curve (see Figure 2.54). The depth z_i is then obtained as the depth at which

the pore pressures in Equation [2.112] are equal to u_i. The initial pore pressure distribution is then obtained by specifying the value of $u_i = -12kN/m^2$ for all depths smaller than z_i, and evaluating the pressures according to Equation [2.112] for depths greater than z_i. This is illustrated in Figure 2.56.

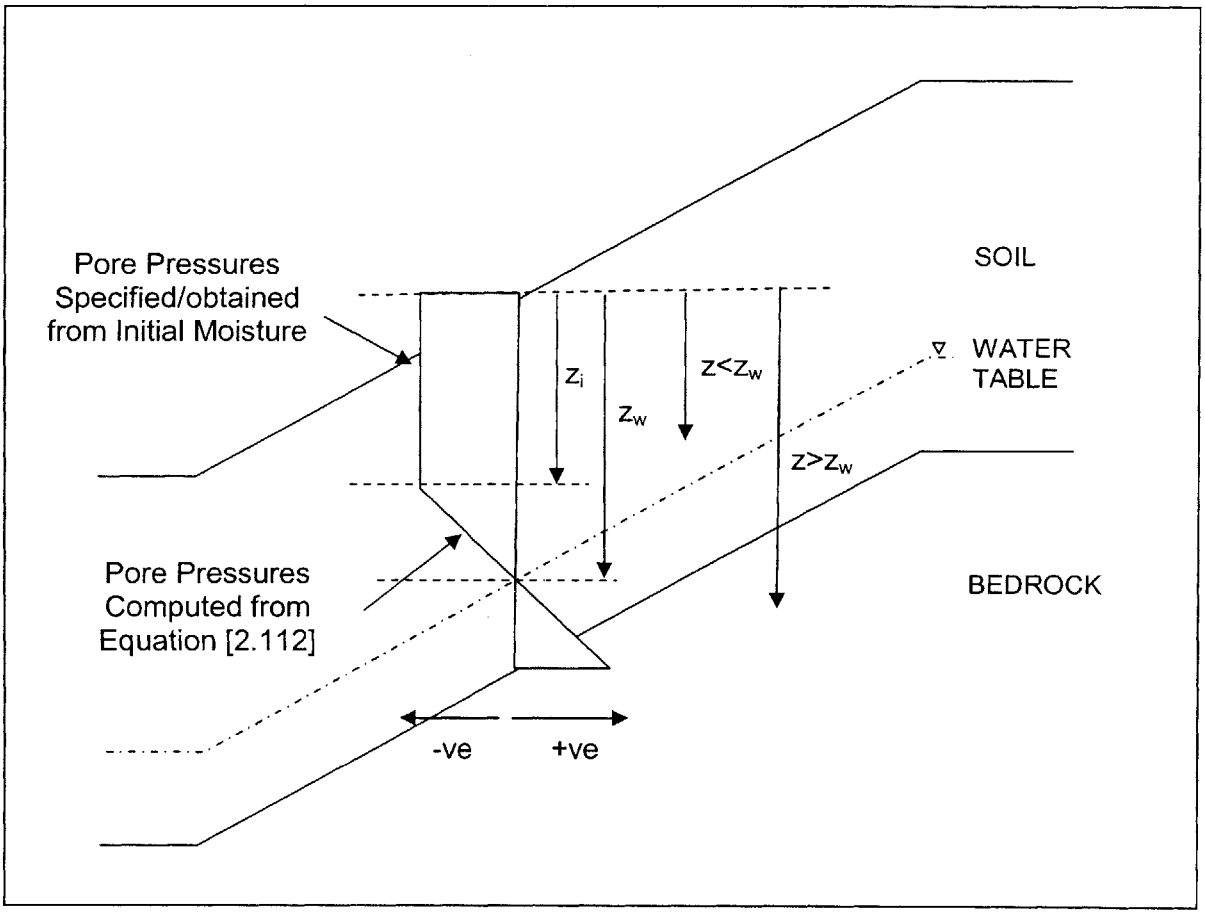

Figure. 2.56. Illustration of Initial Pressure Distribution

In this example, the initial pressure distribution on the failure surface is shown in Figure 2.57 at time t = 0 hrs.

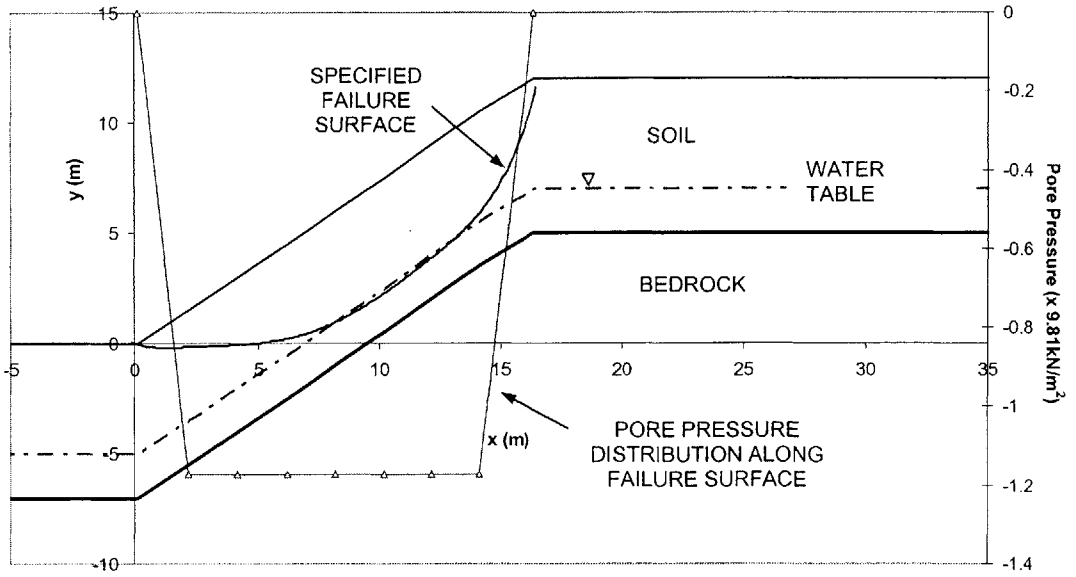

Figure 2.57. Initial Variation of Pore Pressures on Specified Failure Surface (t = 0 hr)

A Factor of Safety of 1.12 is obtained on the specified failure surface shown in Figure 5.27, using the Janbu Generalized Procedure of Slices (1978) and the slope is initially stable.

2-3.1.2. STABILITY DURING/AFTER RAIN

We assume a rainfall event with constant intensity, $I = 165mm/hr$ occurs for duration of 8 hours. Figure 2.58 shows the water content distribution at selected times, prior to, during and after rain, and Figure 2.59 shows the corresponding pore pressure profiles.

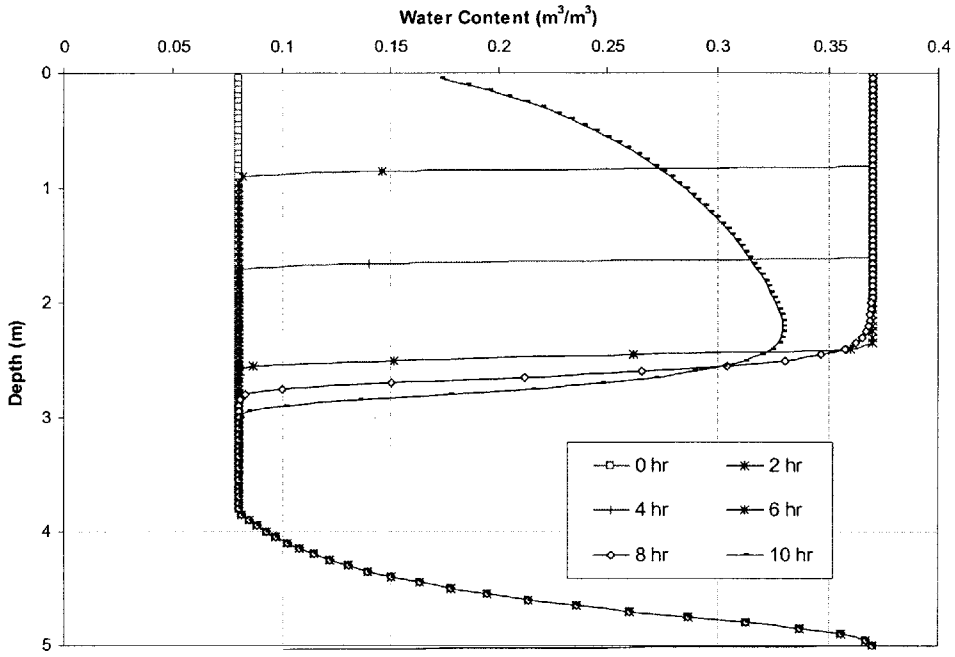

Figure 2.58. Moisture Distribution Profiles at Selected Times

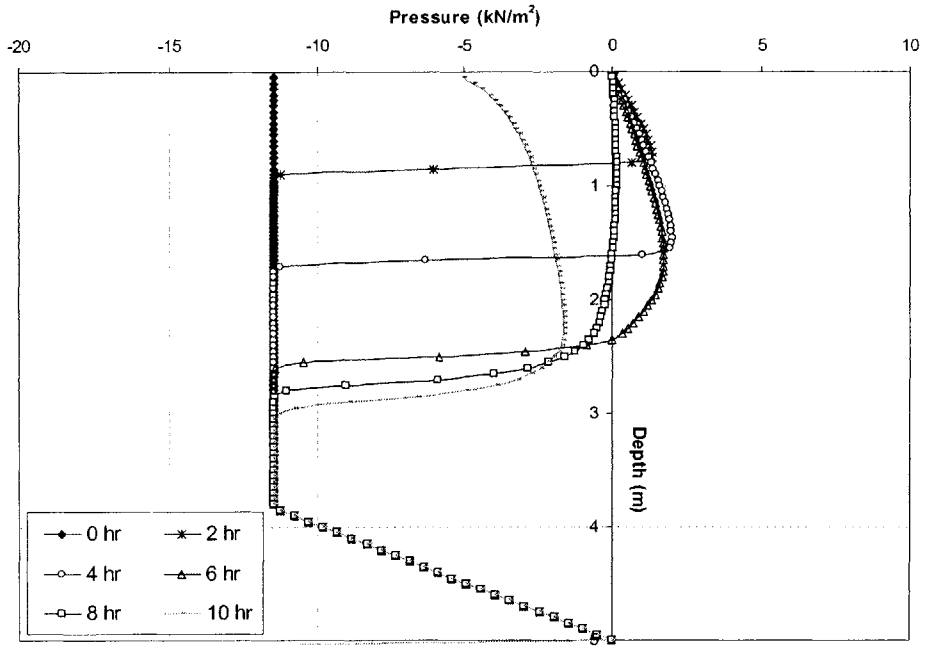

Figure 2.59. Pore Pressure Profiles at Selected Times

Figure 2.58 shows that as the rainwater infiltrates into the slope it saturates the soil above it, as the moisture content is equal to the saturated moisture content. This is because the rain intensity is greater than the saturated conductivity of the soil at the surface. Figure 2.59 shows that positive pressures develop within the infiltration depth at specified times during rain. These pressures continue to build up gradually with increasing rainfall. At times greater than 8 hours, moisture and pressure redistribution takes place.

The state of stability of the slope can be assessed at any particular time. Consider time t = 5 hrs for example. The pore pressures along the specified failure surface are shown in Figure 2.60.

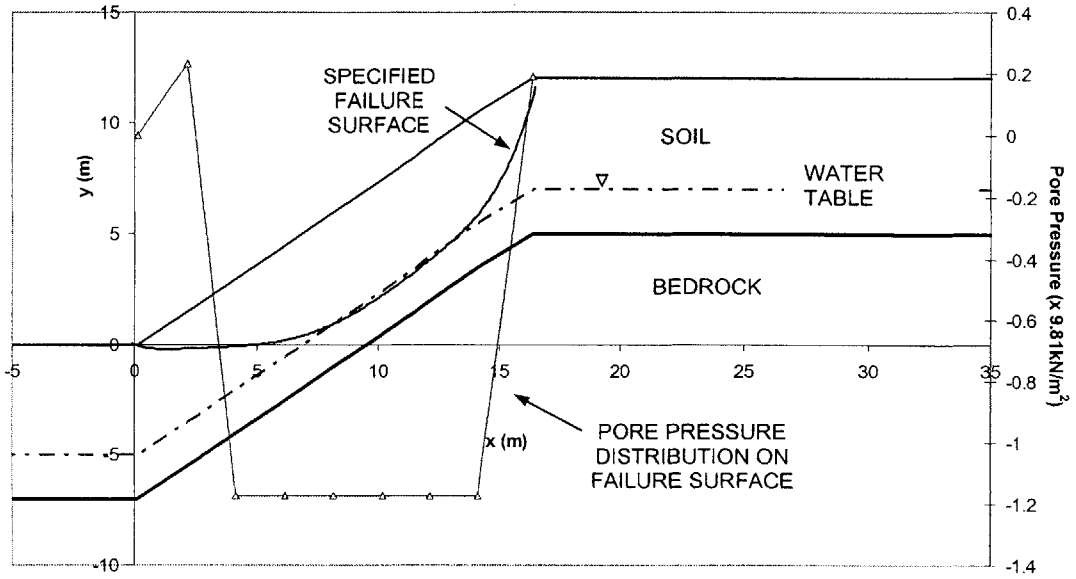

Figure 2.60. Variation of Pore Pressures on Specified Failure Surface at Time t = 5 hrs

Note that the pressures along the failure surface are different from the initial pressures shown in Figure 2.57. The difference occurs in the first few meters below the ground surface where infiltrating rainwater causes an increase in pressures. The state of stability of the slope is assessed and a Factor of Safety of 1.1 is obtained. This is smaller than the initial Factor of Safety on failure surface because of the loss of strength due to the increase in pressures.

In this section, the stability of a slope was assessed at a given time for a specified failure surface. This serves as the basis of the analyses performed in the following sections.

2-3.2. TEMPORAL STABILITY ON A SPECIFIED FAILURE SURFACE

Once the spreadsheet is set up to compute the Factor of Safety on a specified failure surface for a particular time, t, as described in Section 2-3.1, the analyses can be extended to assess stability as a function of time. Stability can be assessed prior, during and after a rainfall event. This is achieved using a VBA code in Microsoft Excel. The code follows the steps shown in Figure 2.61.

Step 1. Compute the Factor of Safety on the failure surface using the pore pressures at time $t = t_0$. This is the initial state of stability.

Step 2. Increment the initial time $t = t_0$, by Δt such that $t_1 = t_0 + \Delta t$.

Step 3. Compute the pore pressure variations at a time $t_1 = t_0 + \Delta t$ for given soil hydraulic parameters, and known characteristics of rainfall, and initial and boundary conditions.

Step 3. Extract the pore pressures along the failure surface at $t_1 = t_0 + \Delta t$ and input these into the stability model.

Step 4. Compute the Factor of Safety at time $t_1 = t_0 + \Delta t$.

Step 5. Repeat Steps 2 to 4 at times $t_i = t_{i-1} + \Delta t$, for $i = 2,...,r$, where r is the final chosen time for analyses.

Figure 2.61. Procedure for Temporal Stability Analyses for a Specified Failure Surface

The results are in the form of a plot of Factor of Safety with time. To illustrate this, we reconsider the slope shown in Figure 2.60, along with the specified failure surface shown in the same figure. We assume a constant intensity $I = 165mm/hr$ rainfall occurs for duration of 8 hours. The moisture content and pore pressure profiles are shown in Figures 2.58 and 2.59 respectively.

The procedure described in Figure 2.61 is then applied to determine the state of stability of the slope as a function of time during and after rain. Figure 2.62 shows the variation of the Factor of Safety along the failure surface with time.

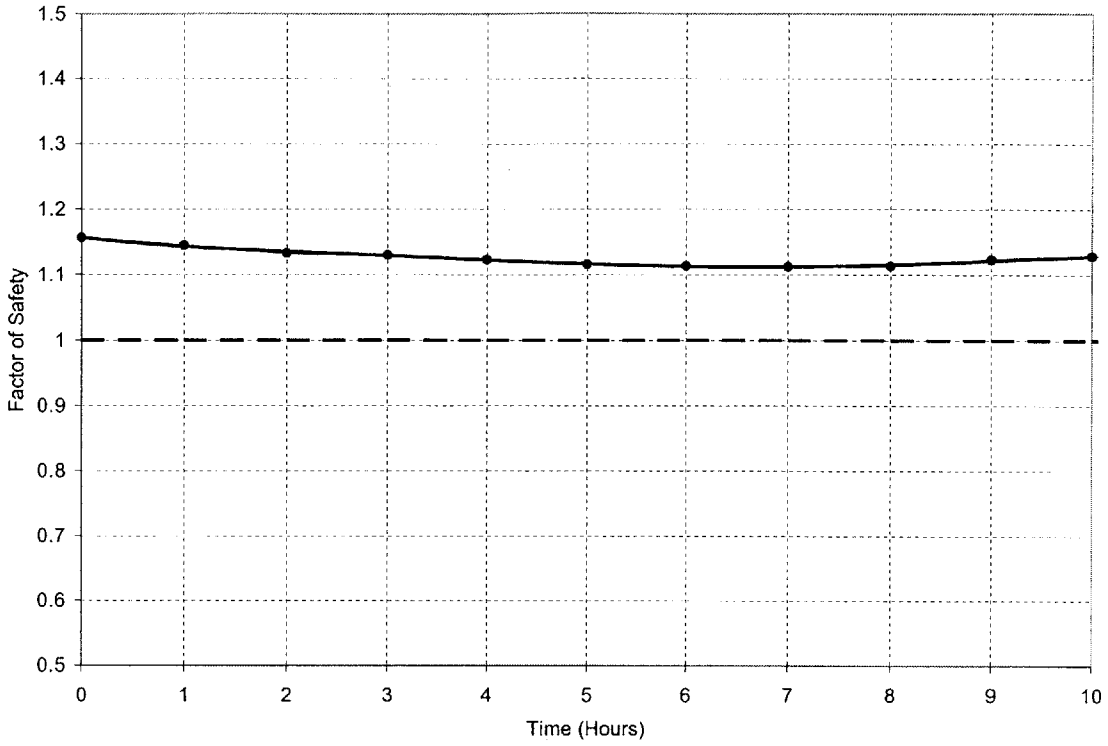

Figure 2.62. Variation of Factor of Safety with Time for a Specified Failure Surface

Figure 2.62 shows that there is a decrease in Factor of Safety with time as the infiltrating rainwater increases the subsurface pressured thereby decreasing soil strength. This decrease in Factor of Safety is not very significant in this example, because of the location of the specified failure surface which is located deep in the slope. The Factor of Safety begins to increase at times greater than 8 hours as rain is stopped, and redistribution takes place.

2-3.3. TEMPORAL STABILITY WITH SEARCH FOR CRITICAL FAILURE SURFACE

The temporal analyses presented in Section 2-3.2 can be extended to include a search for the critical failure surface at each time step. The method for locating the critical surface was described in Part 2-2.3, and involves an optimization procedure. By performing this search at every time step, the critical surface is located and the minimum Factor of Safety in the slope is computed. The procedure for doing this is in Figure 2.63.

Step 1. Compute the Factor of Safety on the failure surface using the pore pressures at time $t = t_0$. This is the initial state of stability.

Step 2. Increment the initial time $t = t_0$, by Δt such that $t_1 = t_0 + \Delta t$.

Step 3. Compute the pore pressure variations at a time $t_1 = t_0 + \Delta t$ for given soil hydraulic parameters, and known characteristics of rainfall, and initial and boundary conditions.

Step 4. Extract the pore pressures along the failure surface at $t_1 = t_0 + \Delta t$ and input these into the stability model.

Step 5. Invoke the spreadsheet's built-in optimization tool (Solver in Microsoft Excel) to locate the critical failure surface at time $t_1 = t_0 + \Delta t$, starting with an initial trial surface.

Step 6. Compute the Factor of Safety is computed on this surface. This is the minimum Factor of Safety in the slope at $t_1 = t_0 + \Delta t$.

Step 7. Repeat Steps 2 to 6 at times $t_i = t_{i-1} + \Delta t$, for $i = 2,...,r$, where r is the final chosen time for analyses.

Figure 2.63. Procedure for Temporal Stability Analyses with Search for Critical Failure Surface

The results are in the form of variation of minimum Factor of Safety in the slope as a function of time. Since the critical surface is located at each time step, these can also be shown. From these results, one can conclude whether a slope will remain stable or fail as a result of a particular rainfall event. In the case where failure takes place, the critical failure surface can be located, and the time to failure from the onset of rain can be determined. The analyses, therefore, allow one to estimate landslide hazards (spatial and temporal).

The procedure described in Figure 2.63 is applied to the slope shown in Figure 2.64. The search for the critical failure surface procedure requires specification of an initial trial surface. For this, a shallow surface is chosen that is located above the water table shown in Figure 2.64.

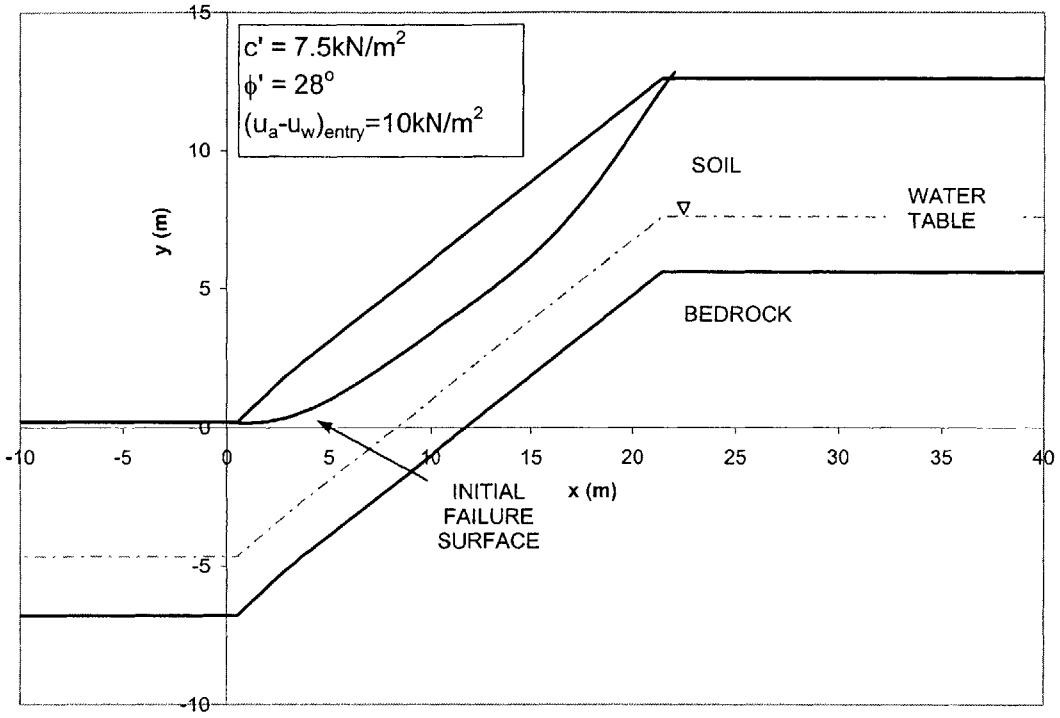

Figure 2.64. Shallow Initial Trial Surface

A plot of the minimum Factor of Safety with time is shown in Figure 2.65.

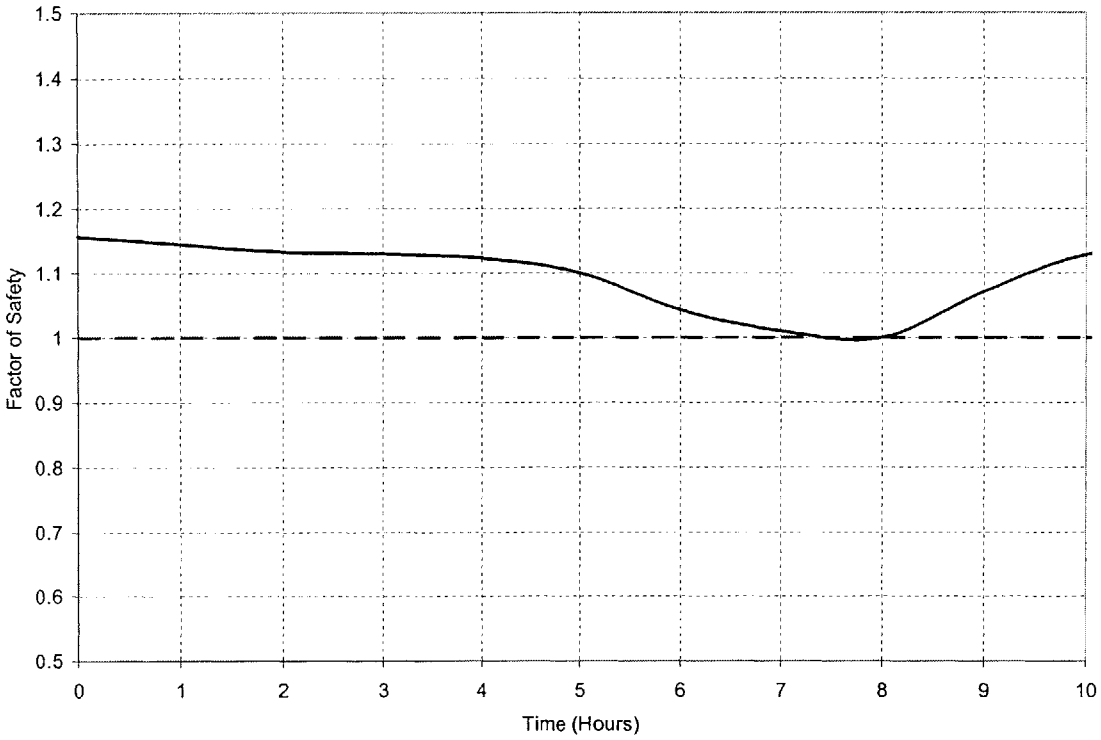

Figure 2.65. Variation of Factor of Safety with Time with Search for Critical Failure Surface Starting from an Initially Shallow Trial Surface

Figure 2.65 shows that the minimum Factor of Safety decreases with time, and is less than one at a time of about 5 hours. This indicates slope failure as a result of rain. The critical failure surfaces obtained at different times are shown in Figure 2.64.

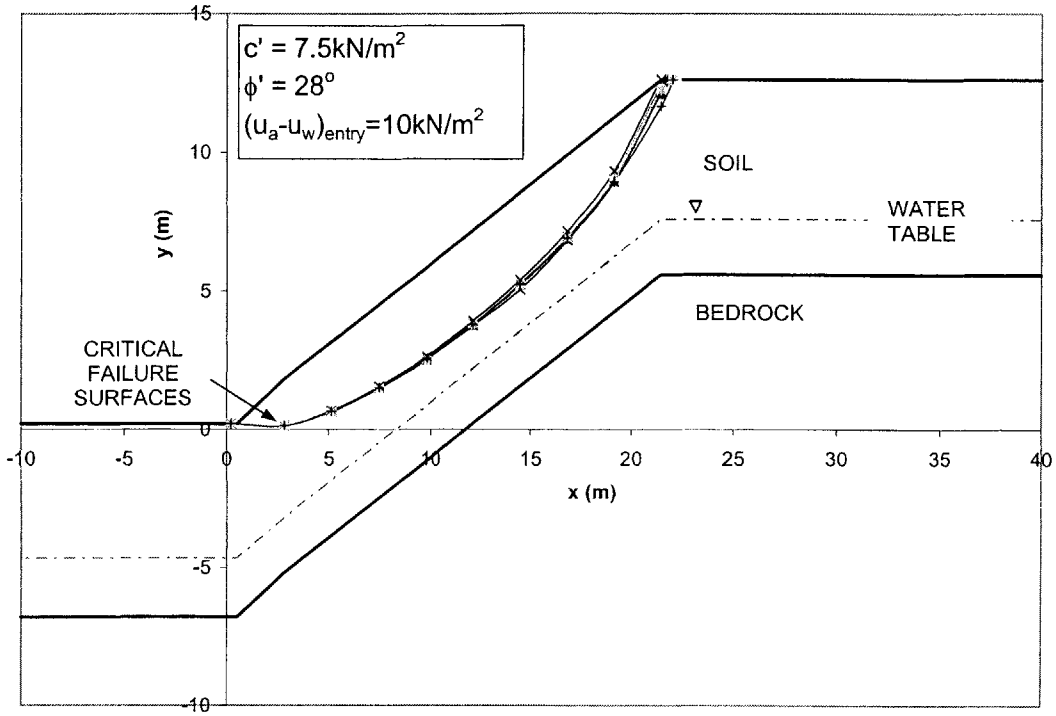

Figure 2.66. Illustration of Critical Failure Surfaces with Time Starting from a Shallow Initial Trial Surface

Figure 2.66 is intended to illustrate the different critical surfaces obtained during the search procedure that forms part of the part of the process to determine the minimum Factor of Safety in the slope. The critical failure surface at a time of 5 hours, along which failure will occur is shown in Figure 2.67.

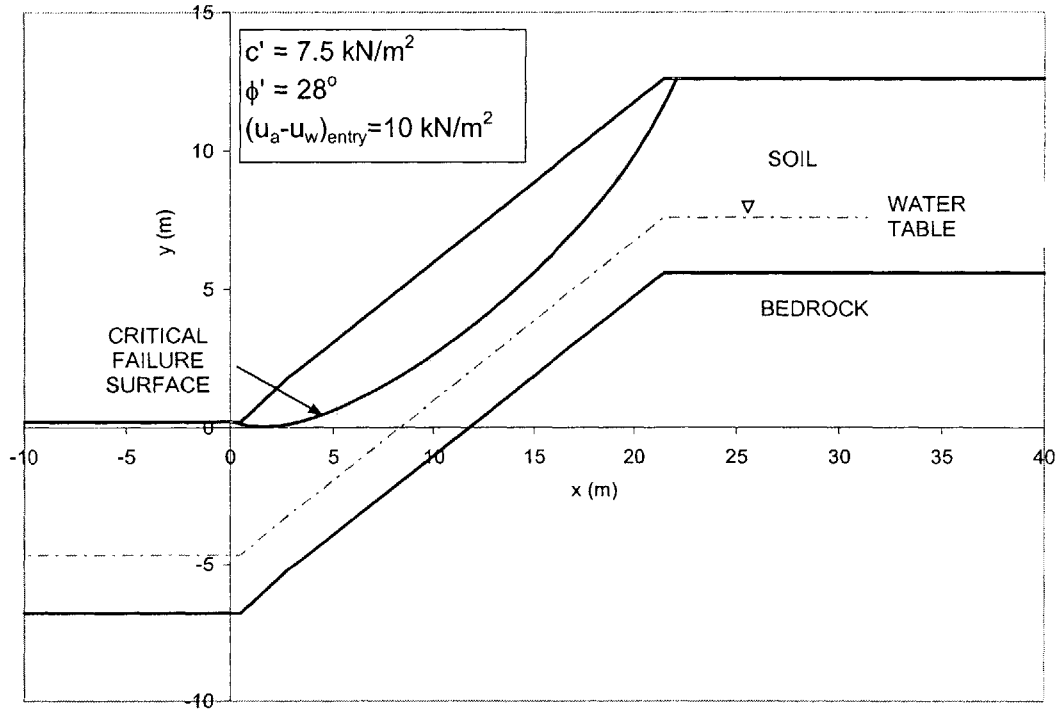

Figure 2.67. Critical Failure Surface in Slope

Figure 2.67 shows that the slope will fail along a shallow failure surface. Failure takes place as a result of the decrease in unsaturated strength caused by infiltrating rain.

A comparison of Figures 2.62 and 2.65 shows that a search for the critical failure surface is necessary for a comprehensive stability study. Based on a specified failure surface (Figure 2.62) one would conclude that the slope would survive the rainfall event, whereas if a search was performed for the critical surface (Figure 2.65) one would conclude that the slope would fail.

2-3.4. DISCUSSION

The combined hydrology stability model developed in this chapter allows one to evaluate the stability of a slope for a single rainfall event as a function of time. It can be appreciated that different rainfall characteristics, and antecedent moisture conditions, will result in different pore pressures profiles, and hence different Factors of Safety with time. This is the spatial hazard of landsliding. In a specific slope, failure can occur as a result of a wide range of rainfall characteristics (intensity and duration) for given antecedent conditions. The combined model developed in this chapter allows one to determine the combinations of rainfall intensities and durations that can lead to slope failure. This, in turn, allows for the definition of a landslide initiation threshold in terms of the intensity and duration of the triggering event. Combinations of intensity and duration lying above the threshold are capable of initiating landsliding in the slope, and those that lie below are not. Figure 2.68 shows a schematic of such an initiation threshold derived for a hypothetical slope.

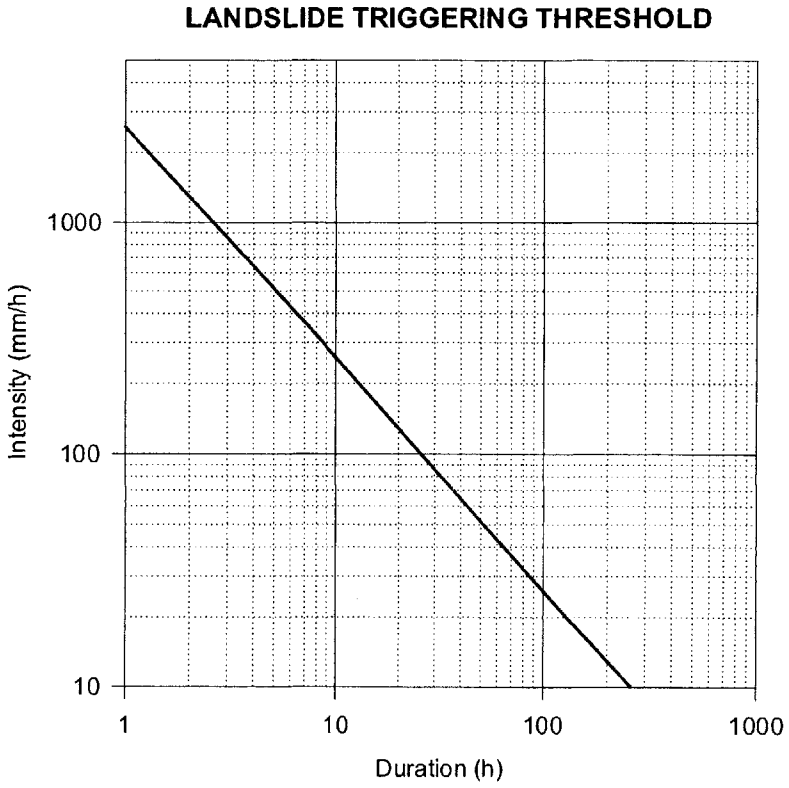

Figure 2.68. Schematic of Landslide Initiation Threshold

Caine (1980) performed a review of previously published worldwide data on rainfall-induced landslides and plotted intensity-duration combinations known to have caused landslides. This is shown in Figure 2.69.

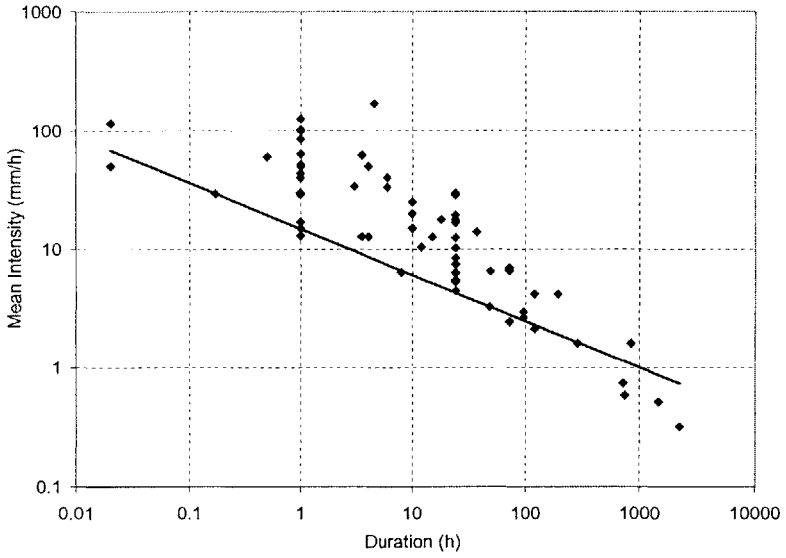

Figure 2.69. Worldwide Landslide Initiation Threshold (after Caine, 1980)

The probability that a triggering rainfall will occur can then be determined from the intensity distribution of the local rainfall records. This probability represents temporal hazard of landsliding, which can now be assigned a quantitative value.

In addition, such initiation thresholds can and have been used in real-time landslide warning systems such as in California (Keefer et al., 1987).

2-3.5. CONCLUSIONS

In this chapter, a combined hydrologic stability model was developed based on the Infiltration model developed in Part 2-1, and the stability model in Part 2-3. This model is more advanced, and better suited for landslide analyses than other models proposed in the literature, because it has been specifically designed for this purpose. It includes:

(a) An infiltration model that solves the pressure (as opposed to moisture content) based form of the flow equation, and therefore considers both saturated and unsaturated flow.
(b) The incorporation of suction and unsaturated strength into stability analyses.
(c) A search for the critical failure surface, and hence minimum Factor of Safety in the slope.

These factors are essential for the study of landslides, particularly shallow landslides. The model allows one to asses the state of stability of a slope prior, during and after rainfall as a function of time. This is done for a specified failure surface. A method was outlined whereby the critical failure surface, and hence minimum Factor of Safety in the slope, can be determined as a function of time, thereby estimating the spatial hazard of landsliding. Landslide initiation thresholds for a specific slope can be established using the combined model. This, coupled with the local rainfall records allows one to estimate temporal landslide hazards. Therefore, landslide hazards can be assessed deterministically.

CHAPTER 3

FAILURE MECHANISMS

3.1 INTRODUCTION

Landslides occur in various parts of the world under different geological and climatic settings. Over the years, a significant amount of research has been devoted to identify the mechanisms of rainfall induced landslides, but these remain poorly understood. The reasons for this include the inherent complexity of the phenomena, the limited field data available and the fact that current models used to study landslides are too simplistic. In general, rainfall induced landslides occur because rainwater increases subsurface pore pressures, which cause a reduction in soil strength that may ultimately lead to failure. This chapter, after describing some of the previous work by others, presents a comprehensive study on landside failure mechanisms. The latter is made possible by the development of more advanced hydrologic and stability models that were discussed in Chapter 2. Landslide failure mechanisms are classified into two categories related to the manner in which a slope is saturated during a rainfall event, namely saturation from below by a rising water table, and saturation from above by rainfall infiltration. For each category, conceptual failure mechanism(s) are first proposed, and then illustrated with a series of hypothetical slopes.

3.2 PREVIOUS WORK

One of the earliest studies on landslides was that conducted by Campbell (1975), who proposed that during rainfall a saturated zone develops at the hydraulic conductivity discontinuity between the soil and the underlying bedrock. This zone progresses upwards with continued rainfall causing a rise in the water table, and the generation of excess pore pressures. In certain slopes, this increase in pore pressures could be sufficient to trigger a landslide at the strength interface between the soil and bedrock. This mechanism, although widely accepted to this day, failed to explain why many landslides observed in the field were shallow, with failure surfaces within the first couple of meters of soil. Several studies attempting to explain these shallow landslides followed.

These studies showed that the infiltration of rainwater has an adverse effect on its stability by increasing pore pressures in the unsaturated zone of the slope.
However, the magnitude of increase in pressures necessary to trigger a landslide, remains a matter of debate. Based on this, landslide studies can be separated into three categories according to the effects the rainwater has on suction (since the pore pressures are initially negative in unsaturated soil) as:

(a) Suction is eliminated during rainfall: One of the first studies on shallow landslides was conducted by Lumb (1975) who proposed that rainwater infiltrates into a slope in the form of a downward traveling saturated wetting front that eliminates the suction above it. This leads to a reduction in unsaturated soil strength and ultimately failure. This mechanism was also suggested in subsequent studies e.g. Morgenstern and Matos (1975), Brand et al. (1984), Pradel and Raad (1995). Figure 3.1 shows a schematic of this mechanism.

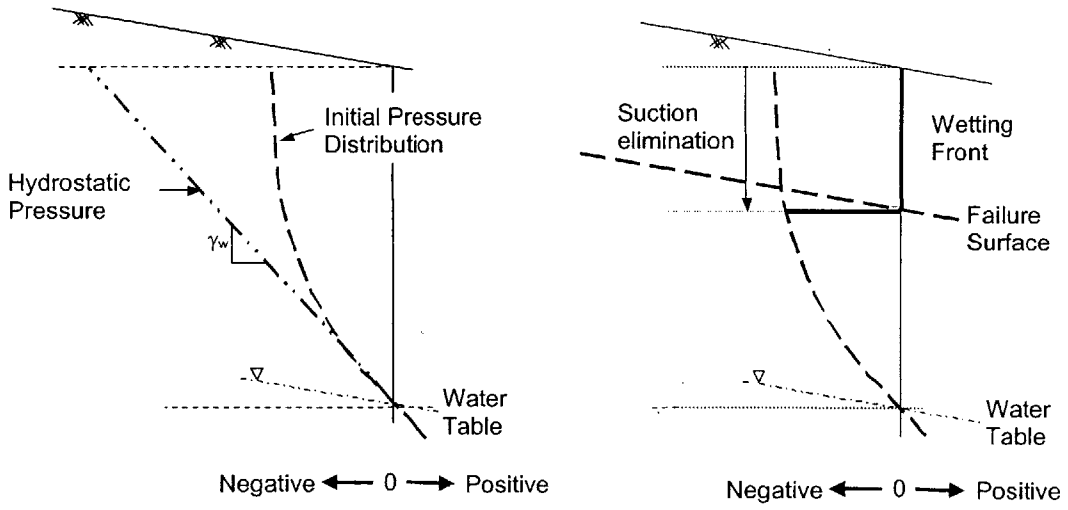

Figure 3.1. Schematic of Failure Mechanism by Elimination of Suction (Negative, 0, Positive Indicate sign of pore pressures)

The problem with these studies is that they are largely conceptual, in that they provide limited support by analyses, and/or field measurements. This initiated further research and ensuing studies can be separated as follows:

(b) Positive pore pressures during rainfall: These studies support the notion that positive pore pressures need to develop during a rainfall event to cause failure, and the elimination of suction does not reduce strength sufficiently to cause landsliding e.g. Johnson and Sitar (1990), Reid (1992), Angeli (1995). These studies provide a strong analytical basis in the form of combined hydrologic and stability modeling e.g. Costa (1998). Figure 3.2 shows a schematic of this mechanism.

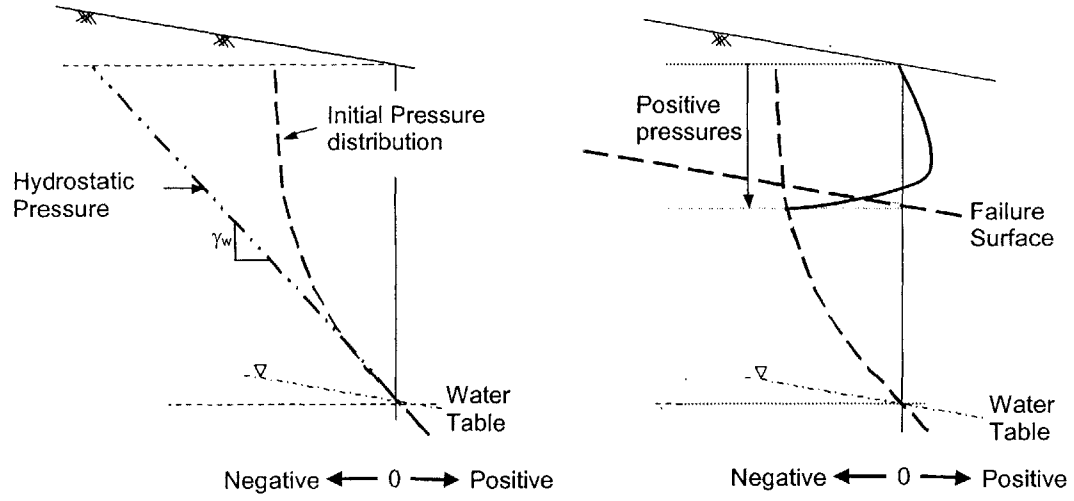

Figure 3.2. Schematic of Failure Mechanism by Development of Positive Pressures (Negative, 0, Positive Indicate sign of pore pressures)

Field observations of failed slopes, though limited, have also shown that positive pressures develop during rainfall e.g. Johnson and Sitar (1995). Because of the strong theoretical and practical support, this mechanism is generally accepted amongst investigators.

(c) Suction is reduced during rainfall: These studies are based on the notion that even the reduction of suction during rainfall can be sufficient to initiate a landslide. e.g. Ho and Fredlund (1982), Rahardjo et al., (1995). These studies incorporate unsaturated soil mechanics, since failure is assumed to take place in soil that remains unsaturated. Figure 3.3 shows a schematic of this mechanism.

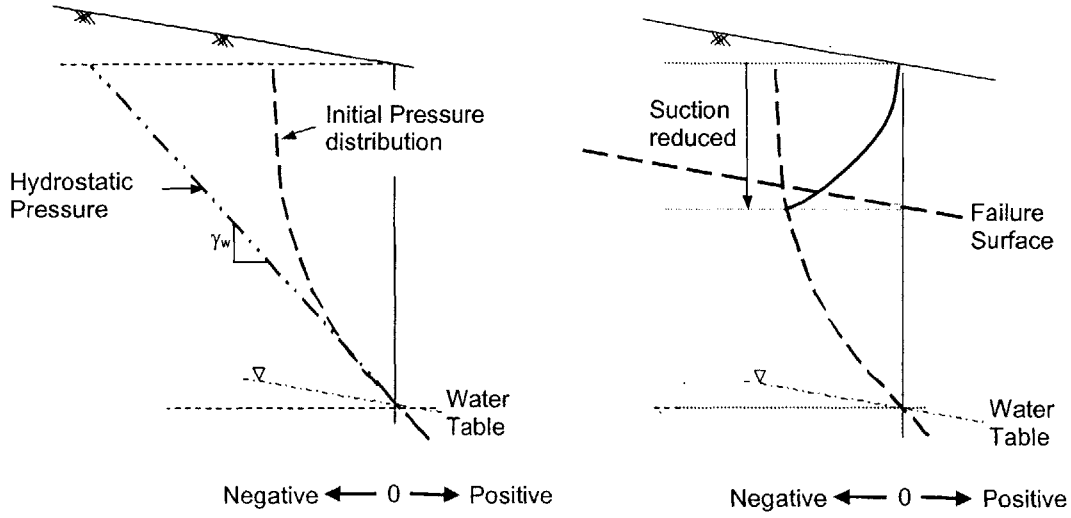

Figure 3.3. Schematic of Failure Mechanism by Reduction of Suction (Negative, 0, Positive Indicate sign of pore pressures)

These mechanisms remain conceptual and studies provide little or no theoretical support, a problem that is compounded by the limited understanding of unsaturated soil behavior. Furthermore, there have been very limited and unreliable field observations where changes in suction have been recorded during rainfall, which is understandable since these changes in suction are often very rapid, and difficult to measure.

There is, therefore, no general agreement on the mechanisms that lead to shallow landslides and these remain poorly understood. To better understand these mechanisms, a combined hydrologic stability model was developed in Chapter 2, and is used to conduct an extensive study of rainfall-induced slope failure. A summary of the results, and the conclusions that can be drawn from them are provided in the following sections.

3.3 FAILURE MECHANISMS

Landslides are complex phenomena and their initiation is affected by a great number of factors. These factors can be classified into three major categories: geometric factors, geologic factors, and hydrologic factors, while recognizing that other factors also play a role. Table 3.1 attempts to list some of these factors.

Geometry	Geology		Hydrology		Others
	Soil	Rock	Site	Trigger	
Slope Inclination	Thickness	Location of Bedrock	Location of Water Table	Rainfall Intensity	Surface Conditions such as Vegetation, Cracks and Micro-Pores
	Stratigraphic Setting (Homogenous/ Heterogeneous)	Fracture Geometry	Subsurface Flow Regime	Rainfall Duration	
	Strength Properties (Saturated and Unsaturated)	Strength	Antecedent Moisture Content		
	Unit Weight (Saturated and Unsaturated)	Conductivity			
	Hydraulic Conductivity				
	Characteristic Curves				
	Grain and Pore Size Distribution				
	Porosity				
	Conductivity				

Table 3.1. Some Factors that Affect Landslide Initiation

Figure 3.4 shows in schematic form, some of the factors listed in Table 3.1.

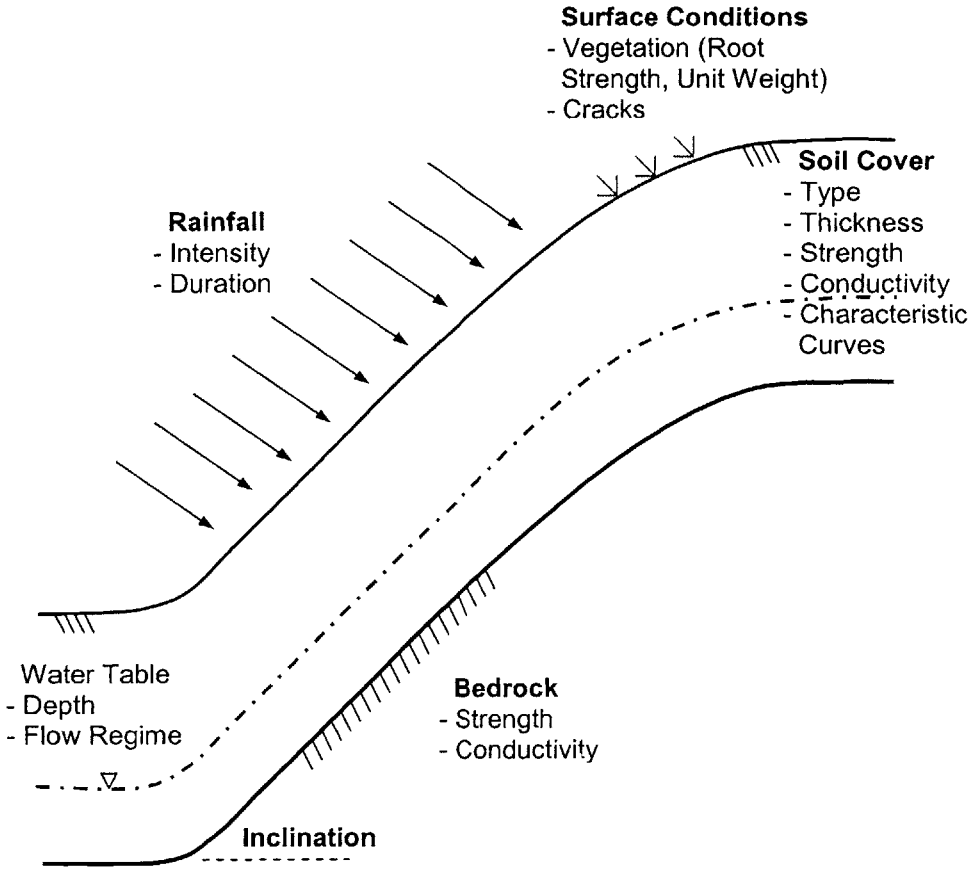

Figure 3.4. Schematic of Some Factors that Affect Landslide Initiation

A critical combination of these factors, and the interaction between them is required for landslide initiation. In this section, landslides are classified into two categories related to the manner in which a slope is saturated during a rainfall event, namely saturation from below by a rising water table, and saturation from above by rainfall infiltration. For each category, conceptual failure mechanisms are first proposed, and then illustrated with a series of hypothetical slopes using the combined hydrologic stability model developed in Chapter 2.

Prior to performing numerical analyses, it is necessary to specify realistic values (ranges of values) for each of the parameters that enter the landslide analyses. For this purpose, a compilation of the values of various parameters was obtained through an extensive

study of published work (e.g. Lacasse and Nadim, 1998; Kulhawy, 1997, 1998; Duncan, 2000) where landsliding was documented. These are presented in Table 3.2, and illustrated in Figure 3.5.

PARAMETER		VALUE OR RANGE
SYMBOL	DEFINITION	
z	Depth of the soil layer below the ground surface	
z_w	Depth to the water table below the ground surface	0 - z (m)
h_w	Depth of the water table above the bedrock	0 - z (m)
ϕ'	Angle of shearing resistance	$15-35^{\circ}$ (0°)
c'	Cohesion	0 –100 kN/m^2
β	Slope angle	$25-45^{\circ}$
γ_s	Saturated unit weight of soil	18 – 22 kN/m^2
γ_w	Unit weight of water	9.81 kN/m^2
K_s	Hydraulic Conductivity (m/s)	$1\times10^{-7}-1\times10^{-4}$
$(u_a - u_w)_{entry}$	Air Entry Pressure	0 – 100 kN/m^2
D	Rainfall Duration (h)	2 – 16 h
I	Rainfall Intensity (mm/hr)	10 – 300 mm/hr
θ_s	Saturated Moisture Content	
θ_i	Antecedent Moisture Content	$\theta_r < \theta_i < \theta_s$
θ_r	Residual Moisture Content	$0 < \theta_r < \theta_s$
n	van Genuchten Parameter	0.5 - 3.5
δ	van Genuchten Parameter	0.001 - 0.03

Table 3.2. Symbols and Typical Range of Values of Parameters used in Landslide Analyses

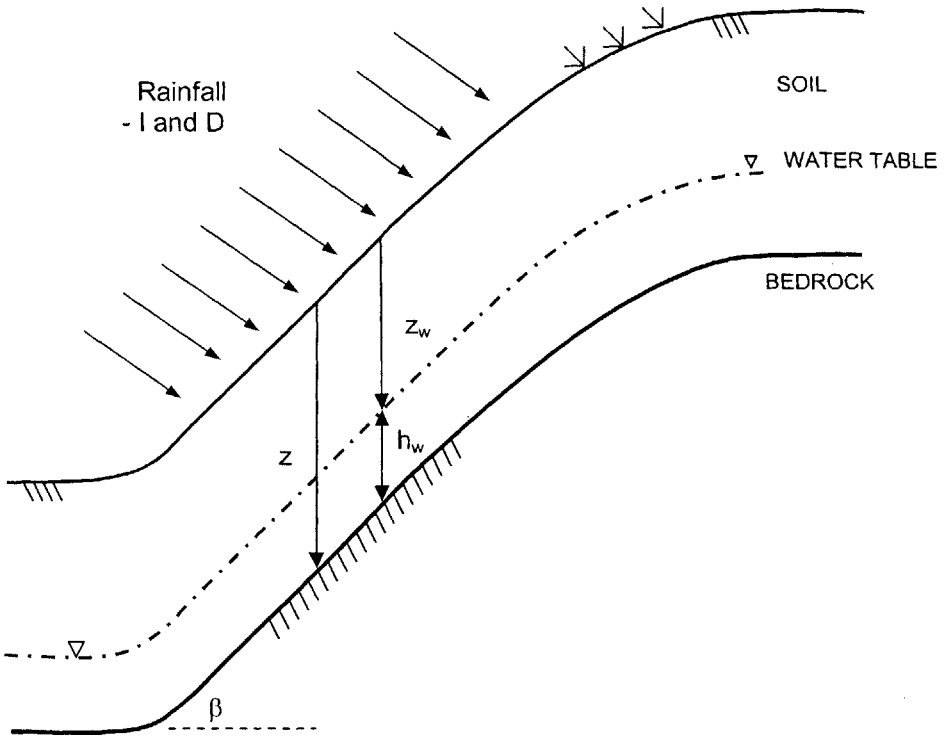

Figure 3.5. Schematic of Parameters in Landslide Analyses

In the following sections, the Coulomb Model is used to describe saturated soil strength, and the Bishop (1959) Model is used for unsaturated strength. As stated in Chapter 2, Part 5-2, this model is considered to be a more intuitive model than the Independent State Variable Model (Fredlund et al., 1978) and so is used.

3.3.1 FAILURE BY SATURATION FROM BELOW

In order to model the effects of infiltration on subsurface pore pressures and stability of a slope, it has been traditionally assumed that a saturated zone develops at the hydraulic conductivity interface between the soil and the underlying bedrock. This occurs both due to the effects of infiltrating rainwater, and recharge from higher slope sectors. This zone progresses upwards with continued rainfall causing a rise in the main water table, and the generation of excess pore pressures. Given favorable site conditions, this increase in pore pressures could be sufficient to trigger a landslide at the strength interface between the soil and bedrock. This is illustrated in Figure 3.6.

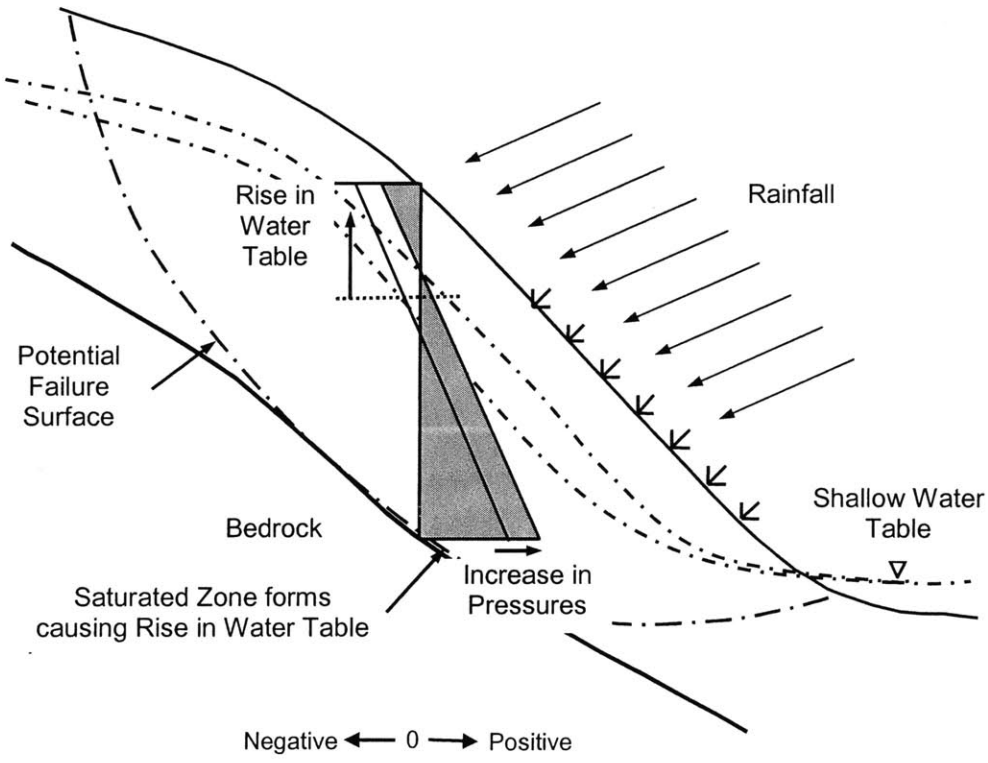

Figure 3.6. Schematic of Failure Mechanism caused by Saturation from Below (Negative, 0, Positive Indicate sign of pore pressures)

This mechanism was first suggested by Campbell (1975), and remains to this day, a widely accepted mechanism for deep seated slides. To demonstrate this mechanism, consider the hypothetical slope shown in Figure 3.7.

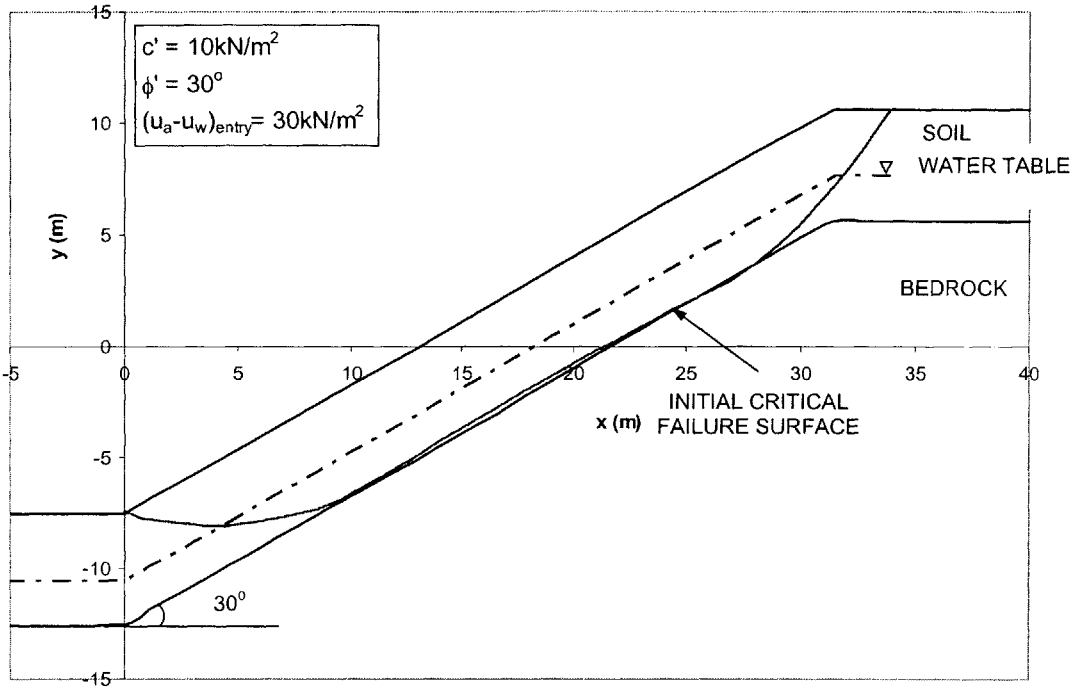

Figure 3.7. Slope Geometry and Strength Parameters

The saturated soil strength parameters are shown in Figure 3.7, and the Effective Strength Model (Bishop, 1959) (see Chapter 2 Part 2-2) is used to describe unsaturated strength, with an air entry pressure of $(u_a - u_w)_{entry} = 30kN/m^2$. The water table is assumed to be at a depth of 3m below the ground surface. A search for the critical failure surface is performed, as detailed in Chapter 2, Part 2-2, and the results are shown in Figure 3.7.

The critical failure surface is located at the strength discontinuity between the soil and bedrock (see Figure 3.7). A Factor of Safety of 1.2 is computed on this surface, and hence the slope is stable.

We now assume a rainfall event takes place that causes a 1m rise in the water table. The subsurface pore pressures are altered as shown in Figure 3.8.

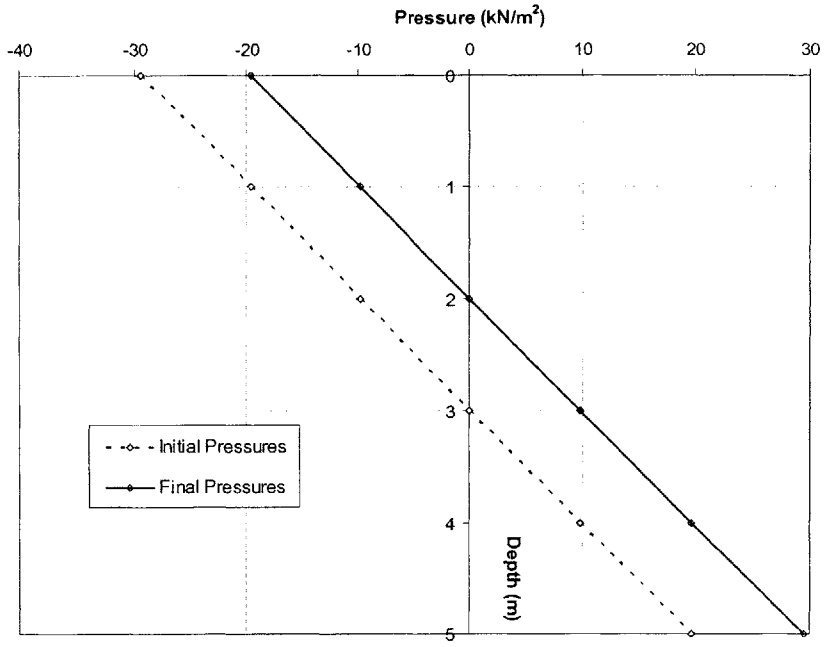

Figure 3.8. Initial and Final Pressure Distributions

The new critical failure surface is located with the new hydraulic conditions and is shown in Figure 3.9.

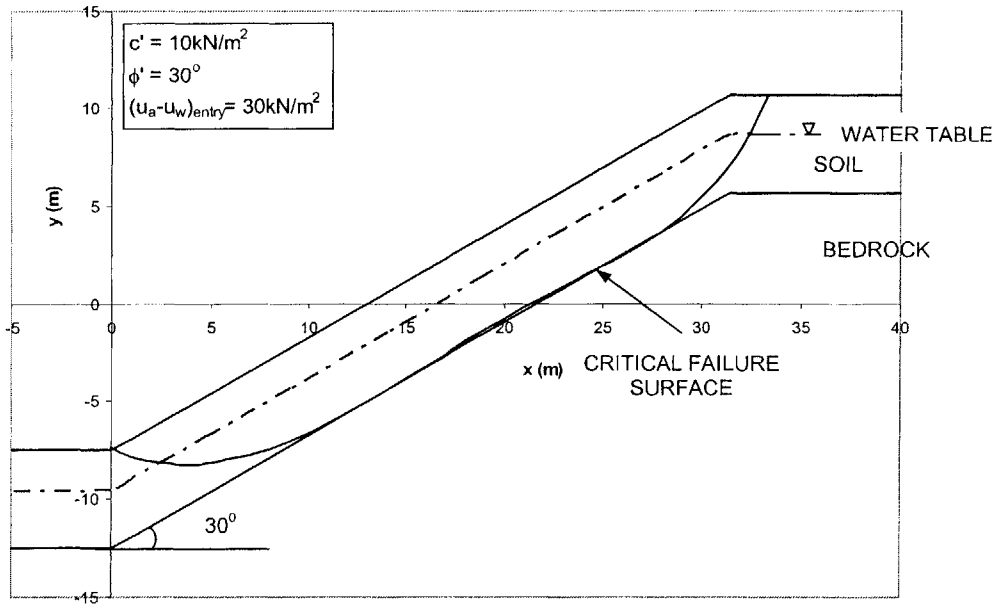

Figure 3.9. Critical Failure Surface for a Rise in Water Table

The Factor of Safety on the surface in Figure 3.9 is computed to be 0.90, indicating a landslide. The failure surface lies at the soil bedrock interface resulting in a deep seated landslide.

This example illustrates that a rise in the water table can lead to a reduction in soil strength that can be sufficient to trigger a landslide. This demonstrates the failure mechanism caused by saturation from below. Since this mechanism is the most widely accepted and commonly adopted mechanism for deep seated landslides, no further discussion is provided in this section.

3.3.2 FAILURE BY SATURATION FROM ABOVE

As mentioned in the introduction to this Chapter, the mechanisms of landslides caused by infiltrating rainwater from the surface of the slope downwards are poorly understood. While there is common agreement between investigators that infiltrating rainwater has an adverse effect on slope stability, there is no general agreement on the processes by which landsliding occurs. These processes, and the mechanisms of the resulting landslides are therefore studied in more detail in this section.

Prior to rainfall, the initial moisture content distribution in the slope is defined by the location of the water table and antecedent rain. A subsurface pore pressure distribution is associated with this moisture content distribution through the soil characteristic curves, and the subsurface flow regime. As it rains and rainwater infiltrates into the soil, the moisture content increases. This causes an increase in the pore pressures, which may ultimately lead to instability. In this study, a distinction is made between failure mechanisms depending on whether infiltrating rainwater reduces suction, eliminates suction, or causes positive pressures to develop. The specific hydrologic response of the soil will depend on the rainfall intensity in relation to the saturated conductivity of the soil at the slope surface, as well as on the soil intrinsic hydraulic properties. In general, if the intensity is less than the saturated conductivity, the rainwater cannot fully saturate the soil and all the rainwater infiltrates into slope causing a reduction of suction. If the intensity has similar magnitude to the saturated conductivity, a wetting front develops and infiltrates into the slope eliminating suction, and if the intensity is greater than the saturated conductivity positive pressures develop.

To illustrate these mechanisms, the combined hydrology-stability model that was developed in Chapter 2 will be used to assess the state of stability of hypothetical slopes, prior and during/after a rainfall event.

Recall, from Chapter 2, that this model combined a variably saturated flow model, with a slope stability model. Both variably saturated flow, and slope stability through soil strength, depend on unsaturated soil properties. Unsaturated soil properties can be described using the soil characteristic curves, namely the soil moisture retention curve, and the hydraulic conductivity curve. These were described in Part 2-1 of Chapter 2.

Figure 3.10 shows a schematic of the soil moisture retention curve, along with the definition of some of the parameters that were introduced in Part 2-1 of Chapter 2.

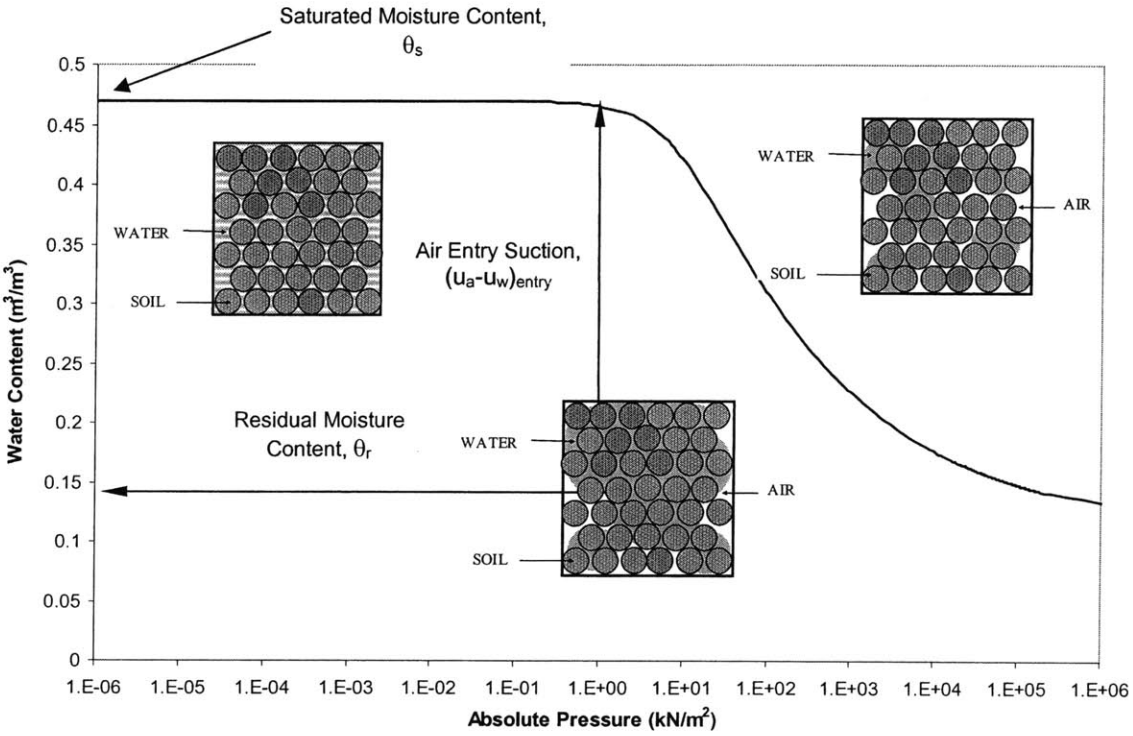

Figure 3.10. Schematic of Soil Moisture Retention Curve

In particular, Figure 3.10 illustrates the definition of the air entry pressure, $(u_a - u_w)_{entry}$, which is the pressure below which changes in pressure do not produce significant changes in moisture content (see Figure 3.10). There is some ambiguity in the definition of the air entry pressure, and as a result various methods have been developed to determine the air entry pressure. Depending on the method adopted, different air entry pressure may be evaluated. The air entry pressure will be determined for different soils, and compared throughout this Chapter. However, in light of what has been just stated above, these comparisons are made for qualitative value rather than rigorous quantitative value.

Several models have been developed to describe the soil characteristic curves. The models developed by van Genuchten (1980) will be used in this Chapter. These were described in Chapter 2, Part 2-1.

It is worth mentioning here that the air entry suction, also affects unsaturated strength, if the Effective Stress Model (Bishop, 1959) is used, as was described in Part 2-2 of Chapter 2. Figure 3.11 shows a schematic of the influence of the air entry suction on unsaturated strength.

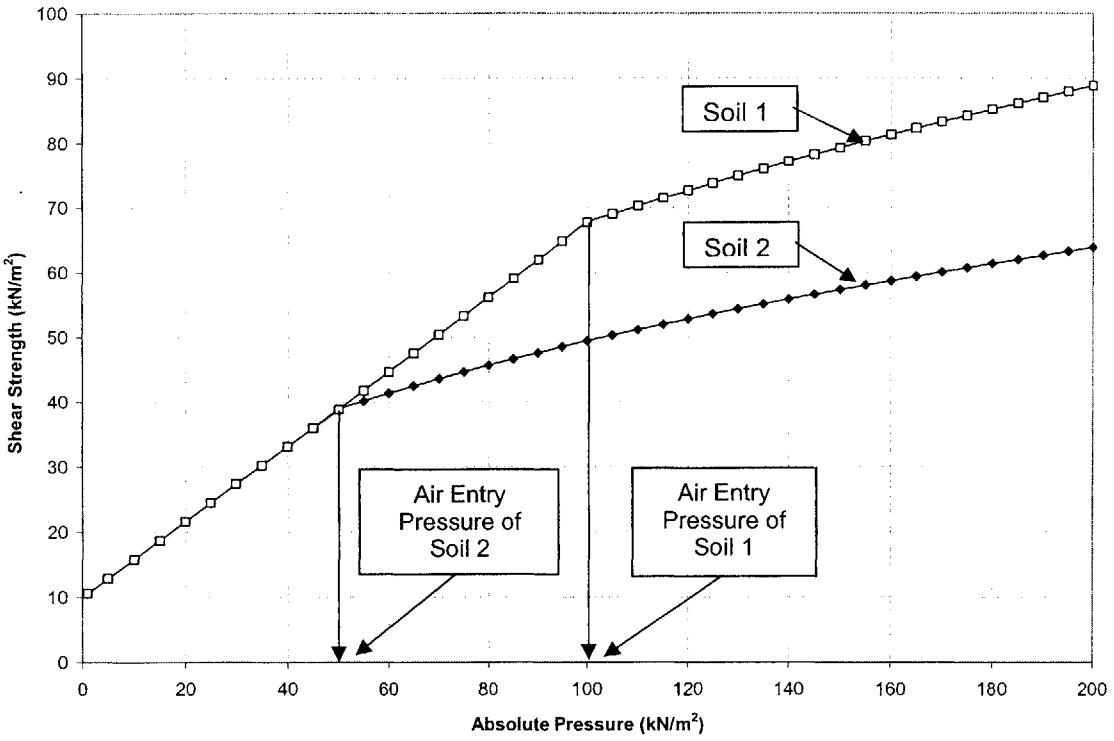

Figure 3.11. Schematic of Influence of Air Entry Suction on Unsaturated Strength

The air entry pressure will therefore affect both hydrologic and stability analyses. Again, because of the ambiguous definition of the air entry suction, no strong, rigorous quantitative conclusions will be made regarding it in this Chapter, and instead conclusions are made for qualitative value.

3.3.2.1 REDUCTION OF SUCTION

When the intensity of a rainfall event is less than the saturated conductivity of the soil at the surface, all the rainwater infiltrates into the slope and suction in the wetted zone is reduced. This is to say that the pore pressures increase, but remain negative, as is shown in Figure 3.12.

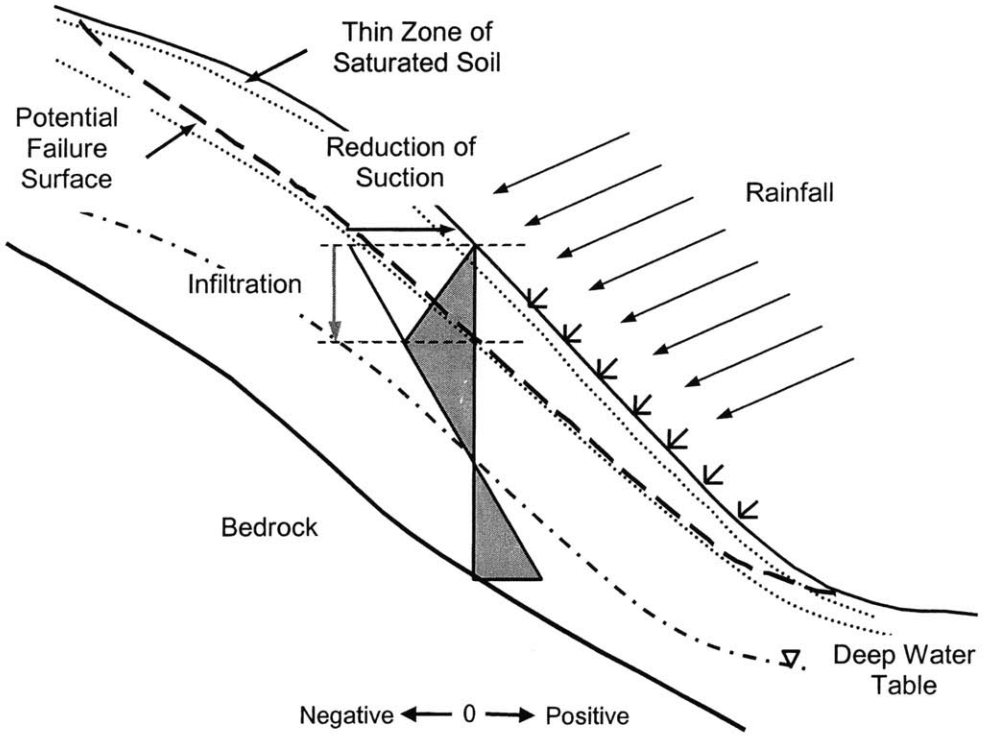

Figure 3.12. Schematic of Failure Mechanism (Reduction of Suction) (Negative, 0, Positive Indicate sign of pore pressures)

This reduction of suction causes a corresponding reduction in soil strength. In this section, we show that in certain slopes a reduction in unsaturated strength can be sufficient to initiate a landslide.

Consider the slope shown in Figure 3.13.

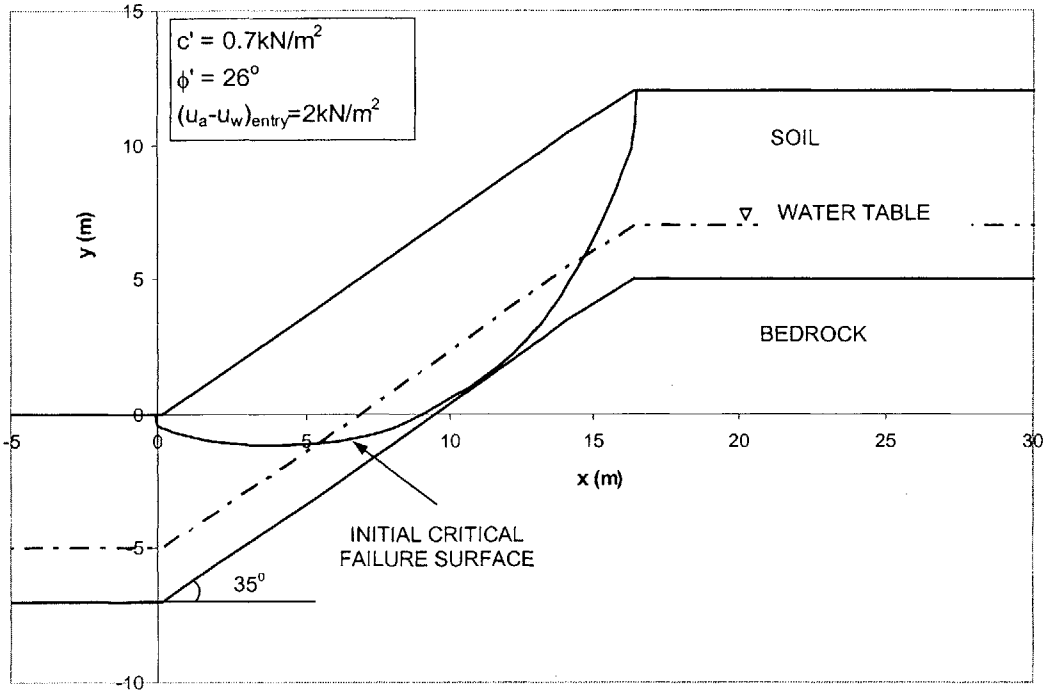

Figure 3.13. Slope Properties and Initial Critical Failure Surface

The slope geometric and soil strength parameters are shown in Figure 3.13. The soil hydraulic parameters are taken to be:

Saturated moisture content of soil $\theta_s = 0.47$

Residual moisture content of soil $\theta_r = 0.11$ (see Chapter 2 Part 2-1)

Saturated conductivity $K_s = 250\text{cm/day} = 2.89 \times 10^{-5}\text{m/s}$

Specific storage coefficient $S_S = 0.005$ (see Chapter 2 Part 2-1)

It is necessary to adopt models to describe unsaturated soil properties through the characteristic curves. For this purpose, the models developed by van Genuchten (1980) are used (see Chapter 2 Part 2-1). The parameters of these models are chosen to be $n = 3$ and $\delta = 0.007$, and the resulting soil characteristic curves are as shown in Figures 3.14 and 3.15.

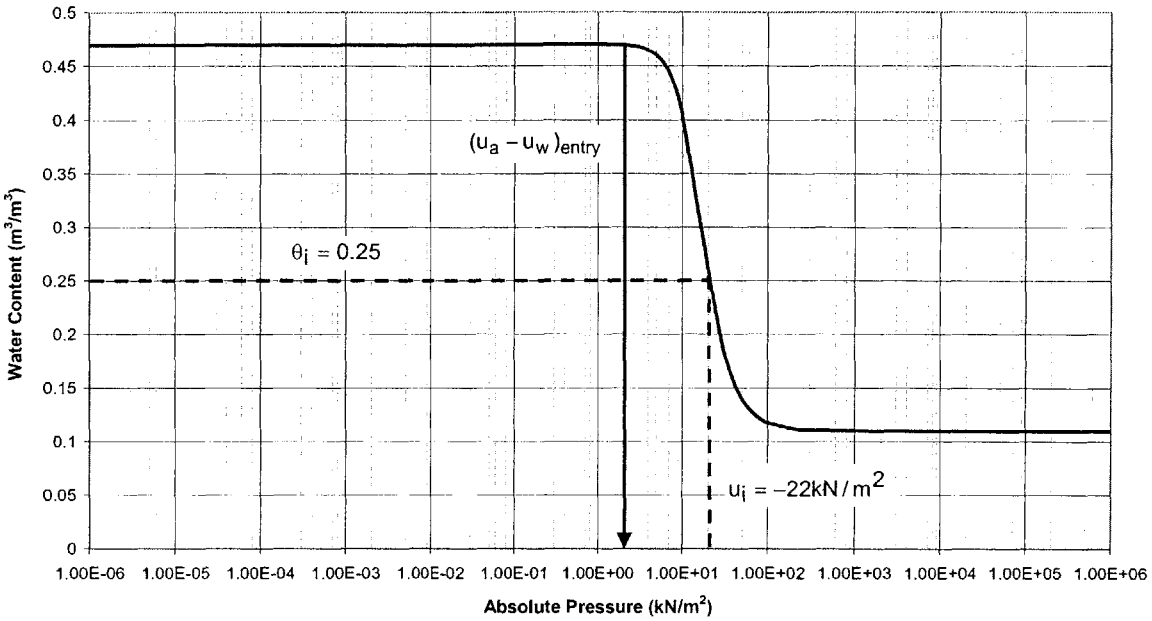

Figure 3.14. Moisture Retention Characteristic Curve

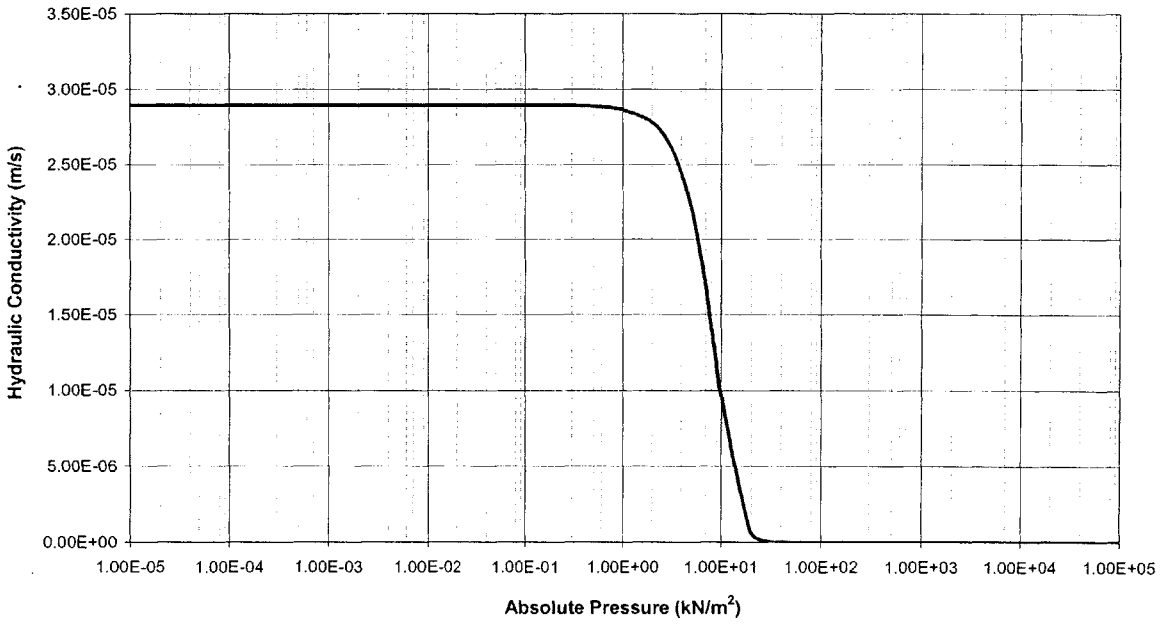

Figure 3.15. Hydraulic Conductivity Characteristic Curve

Note that the air entry pressure in Figure 3.14 is about $(u_a - u_w)_{entry} = 2kN/m^2$. This is used in the Effective Stress Model (Bishop, 1959) Model for unsaturated soil strength (see Chapter 2 Part 2-1).

INITIAL CONDITIONS

Let the water table in a slope be located at a depth of z_w m below the ground surface. Assuming an infinite slope and full capillarity, so that hydrostatic conditions prevail, steady state conditions dictate that flow occurs parallel to the slope surface in both the saturated and unsaturated zones. The corresponding pore pressures vary linearly with depth as:

$$u_w = (z - z_w)\gamma_w \cos^2 \beta \qquad [3.1]$$

where:

- u_w is the mean pore water pressures at a depth z below the ground surface
- z_w is the depth of the water table below the ground surface
- γ_w is the unit weight of water
- β is the inclination of the slope to the horizontal

A problem arises when adopting Equation [3.1] for the pressure distribution throughout the unsaturated soil, namely that very high, sometimes unrealistic pressures result away from the water table. Furthermore, the initial pressure distribution will also be governed by the initial moisture content distribution, which in turn depends on antecedent rainfall. So, instead of using Equation [3.1] throughout the unsaturated zone, it is only used at depths close to the water table, and an initial and constant pressure is assumed at shallow depths below the ground surface. This initial pressure will depend on the initial moisture content as stated previously. This is shown schematically in Figure 3.16.

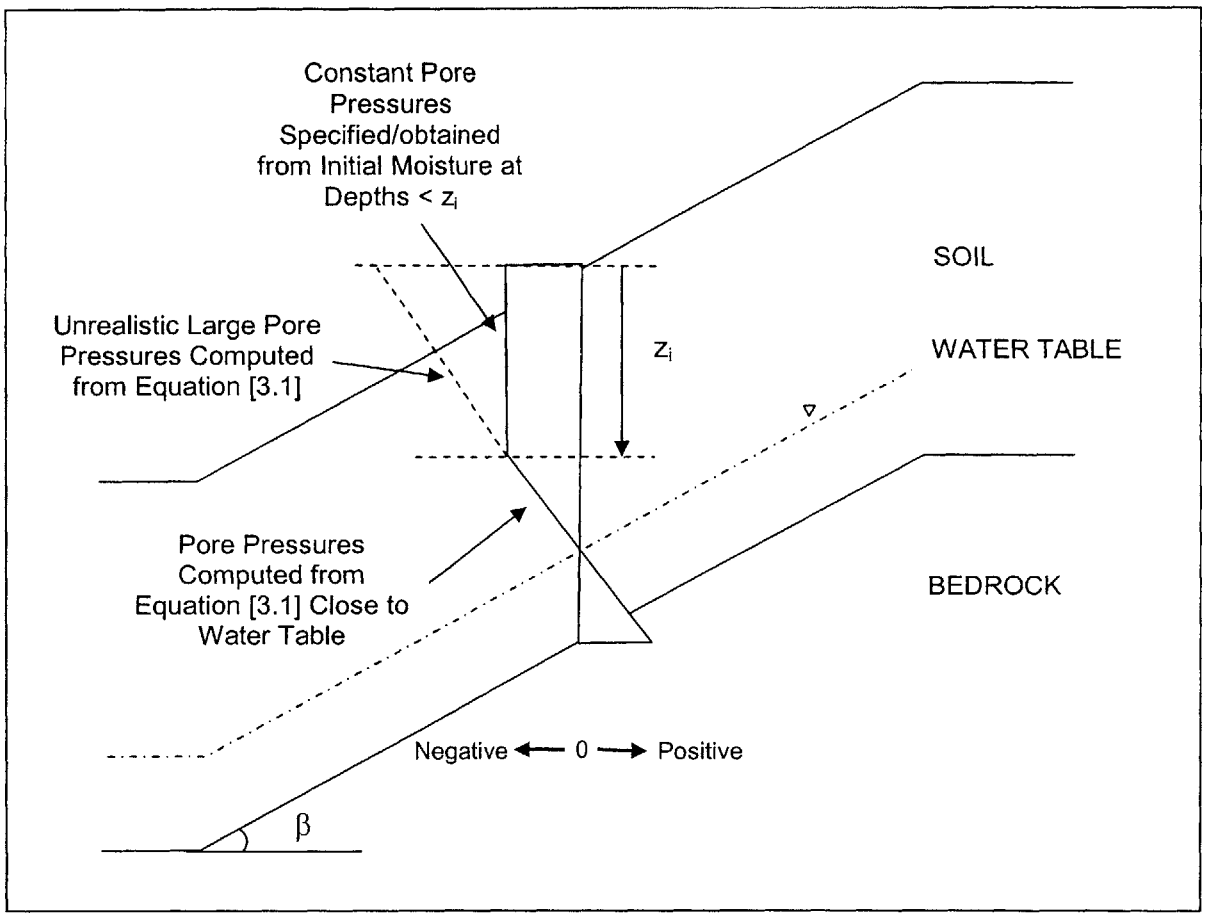

Figure 3.16. Illustration of Initial Pore Pressure Distribution Selection (Negative, 0, Positive Indicate sign of pore pressures)

In this particular example, an initial moisture content of $\theta_i = 0.25$ is assumed. This results in an initial pressure of about $u_i = -22 kN/m^2$, which is obtained from the characteristic curves (see Figure 3.14). Note that this initial moisture content indicates relatively dry conditions, since it is slightly greater than the residual moisture content of the soil. The soil characteristic functions are also used to determine the depth below the ground surface, z_i at which this moisture content is reached under the assumption of full capillarity (see Figure 3.14). The initial pressure distribution is then obtained by specifying the value $u_i = -22 kN/m^2$ at depths smaller than z_i, and computing the pore pressures at depths greater than z_i from Equation [3.1] (see Figure 3.16).

The Coulomb model is used to describe saturated strength, and the Bishop (1959) model is used to describe unsaturated strength. A search for the critical failure surface in the slope is performed, and the results are shown in Figure 3.13. A Factor of Safety of 1.23 is obtained as the minimum Factor of Safety in the slope, and hence the slope is initially stable.

STABILITY DURING/AFTER RAINFALL

We assume a rainfall event with constant intensity, $I = 75mm/hr$ occurs for duration of 8 hours. Note that this intensity is less than the saturated conductivity of the soil at the surface. Figure 3.17 shows the water content distribution at selected times, prior to, during and after rain, and Figure 3.18 shows the corresponding pore pressure profiles.

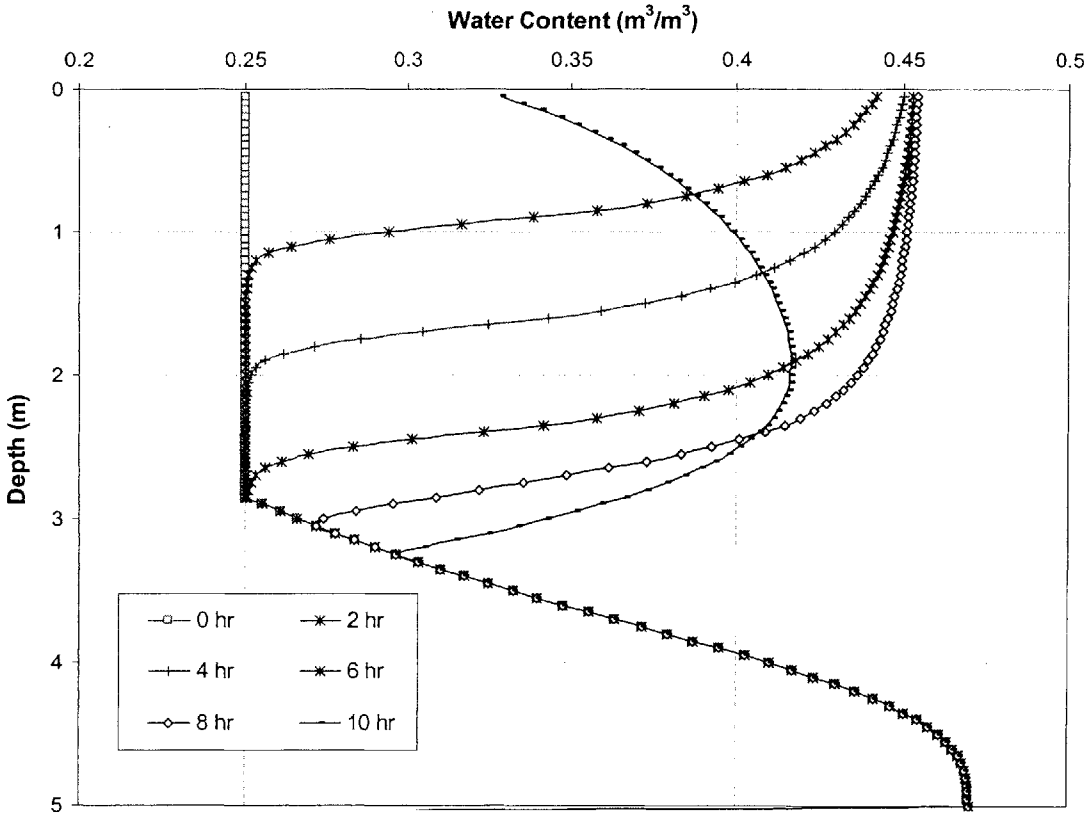

Figure 3.17. Moisture Content Profiles at Selected Times

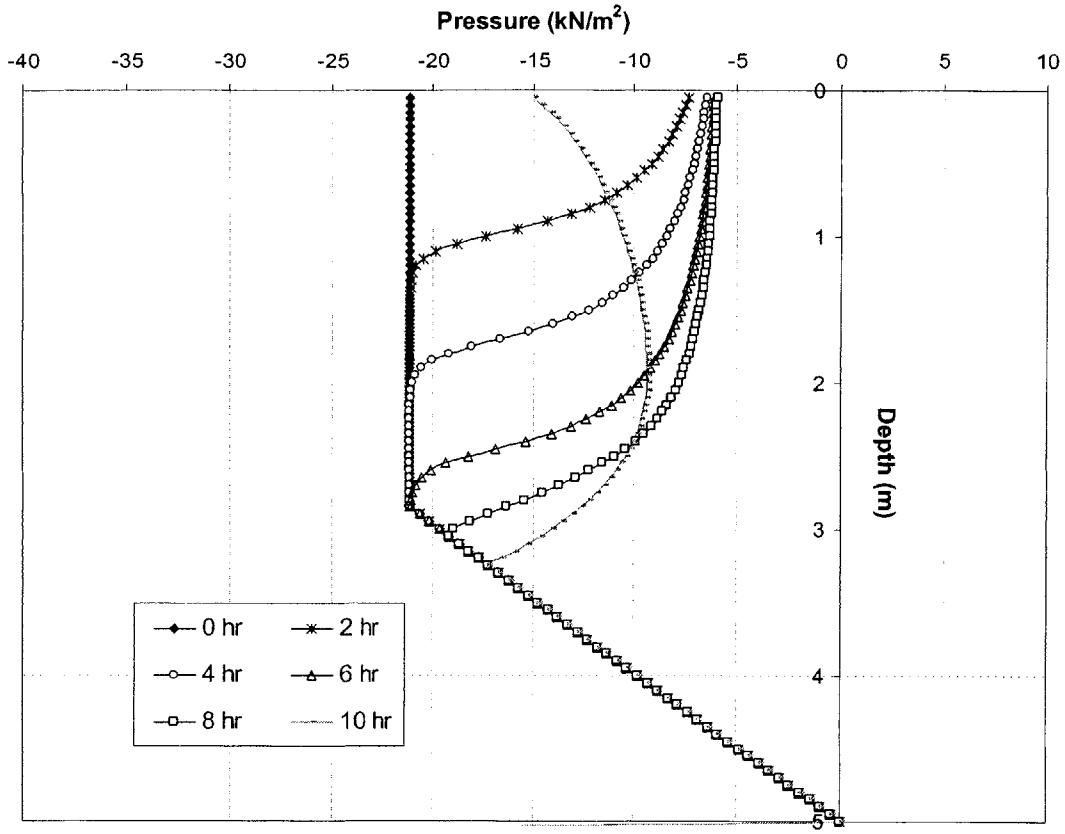

Figure 3.18. Pore Pressure Profiles at Selected Times

Note that the moisture and pressure profiles at time t=0 hr in Figures 3.17 and 3.18 describe initial conditions.

Figure 3.17 shows that the rainwater increases the moisture content in the soil, as infiltration takes place. The intensity of the rain is insufficient to fully saturate the soil, and so the soil does not reach full saturation as shown in Figure 3.17. The initial suction in the soil is reduced, and the pore pressures remain negative, because the intensity of the rain is less than the saturated conductivity of the soil. This is shown in Figure 3.18.

Figure 3.18 shows that the maximum pore pressures occur at the end of the 8 hour rainfall event. Moisture and pressure redistribution takes place immediately after the

cessation of rain e.g. t=10 hr. Given the pressure profiles in Figure 3.18, the procedure described in Chapter 2, Part 5-2, is then used to asses the stability of the slope.

It is worth making a couple of comments prior to this:

Stability models require the specification of a pore pressure distribution. The majority of current landslide studies adopt or assume a single pressure distribution (at a particular time) in stability analyses. This is frequently taken to be the maximum pressures during rainfall, as it is assumed that these would result in lowest stability conditions.

However, as will be shown in this Chapter, deciding on which pressure distribution (time) to use in stability analyses is not a simple problem. It is a critical combination of factors that lead to instability, and this critical combination need not necessarily imply maximum pore pressures. For a comprehensive landslide study, one needs to determine the variation of Factor of Safety with time, both during and after the end of rain. From this, the critical failure surface, on which the Factor of Safety in the slope is minimum can be obtained.

Another problem that arises is that of specifying a potential failure surface. Many of the current landslide studies rely on stability models that require the assumption of a failure surface on which Factors of Safety are computed. Fewer, more comprehensive studies, employ a search for the critical failure surface, as described in Chapter 2, Part 2-2. But such analyses, require the selection of an initial trial failure surface from which the critical surface is located. Different critical failure surfaces may be obtained depending on the chosen initial failure surface. This is because the stability problem is indeterminate, and so, Factors of Safety on these critical surfaces may be local minima but not global minima. This problem was discussed in Chapter 2, Part 2-2. Hence, it is necessary to select several initial surfaces from which the critical failure surface, along which the Factor of Safety is a global minimum can be located.

In this study, two initial surfaces are selected, a deep surface and a shallow one. A deep failure surface is defined as being located below the water table, along the soil bedrock interface. A shallow failure surface is one located above the water table, in the unsaturated zone of the slope. Figure 3.19 shows the initial shallow failure surface, and

Figure 3.20 shows the initial deep failure surface. Figure 3.21 shows an arbitrary failure surface which is also used in the analyses.

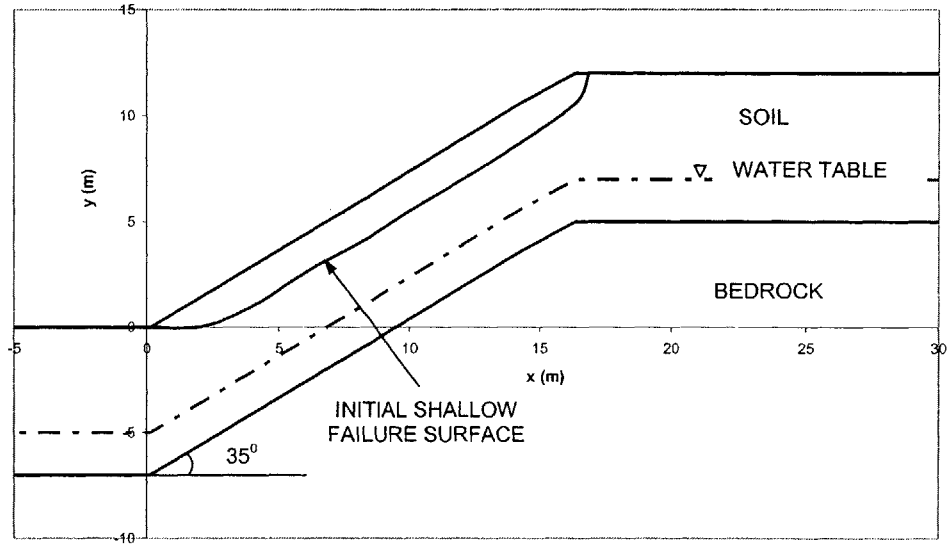

Figure 3.19. Initial Shallow Failure Surface

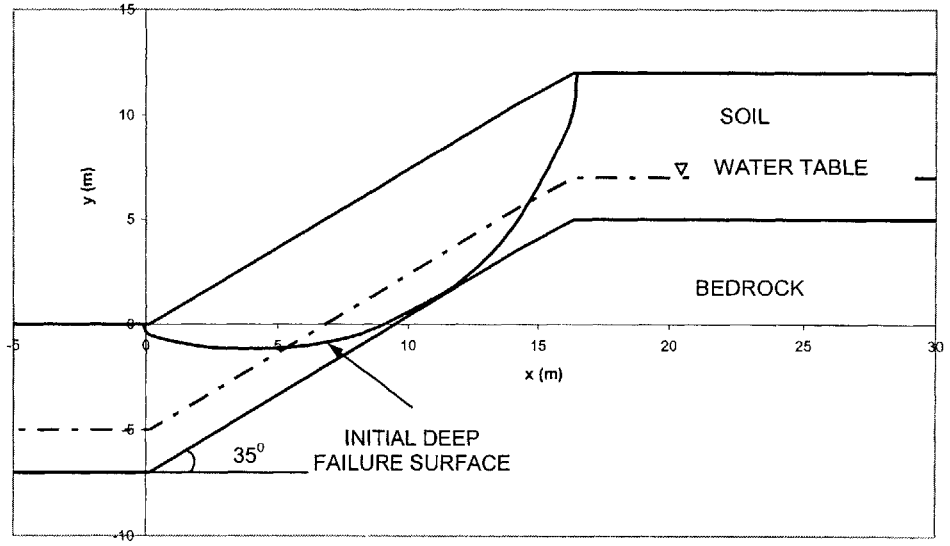

Figure 3.20. Deep Failure Surface

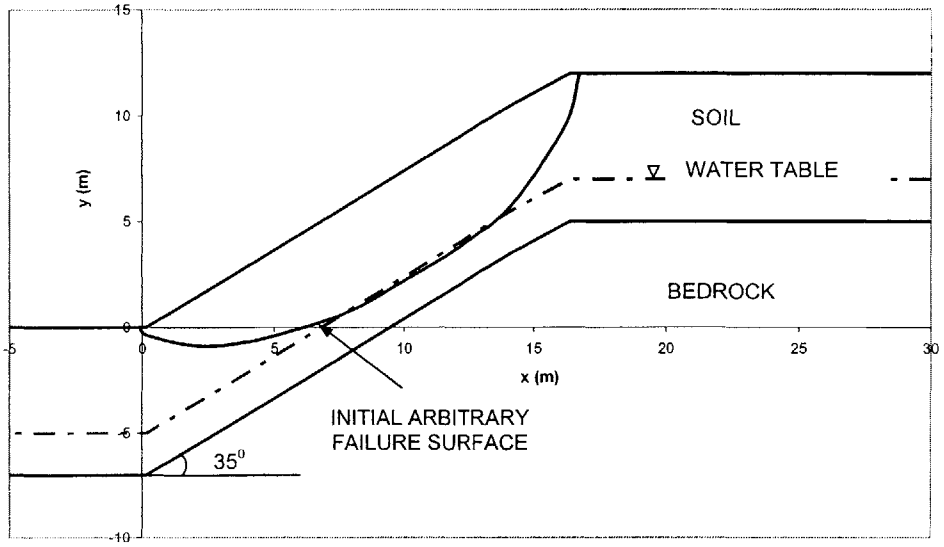

Figure 3.21. Arbitrary Failure Surface

The resulting critical failure surfaces obtained from each case, and the variation of Factor of Safety with time is computed. This is shown in Figure 3.22. Figure 3.22 also shows the variation of Factor of Safety with time on an arbitrarily chosen failure surface, without a search for the critical failure surface.

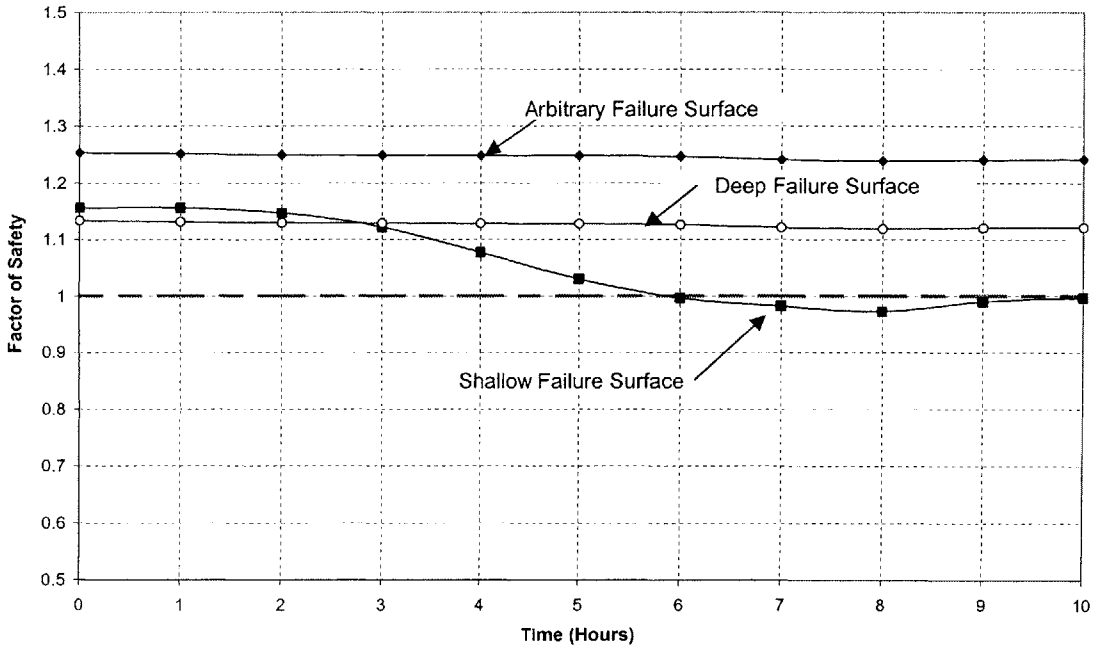

Figure 3.22. Variation of Factor of Safety with Time Starting with Several Initial Failure Surfaces

The shallow failure surface line in Figure 3.22 shows the variation of Factor of Safety on critical failure surfaces that are obtained from the initially shallow trial failure surface in Figure 3.19. Similarly, the deep failure surface line shows the variation of Factor of Safety on critical failure surfaces that are obtained from the initially deep trial failure surface in Figure 3.20. Figure 3.22 shows that starting with an initial shallow failure surface results in the critical failure surface in the slope for which the Factor of Safety is a global minimum. Failure occurs along a shallow failure surface at time of about 6 hours, when the Factor of Safety falls below a value of one.

As an illustration of the search for the critical failure surface process, Figure 3.23 shows the different critical failure surfaces at different times that are obtained starting from the initially shallow failure surface in Figure 3.19.

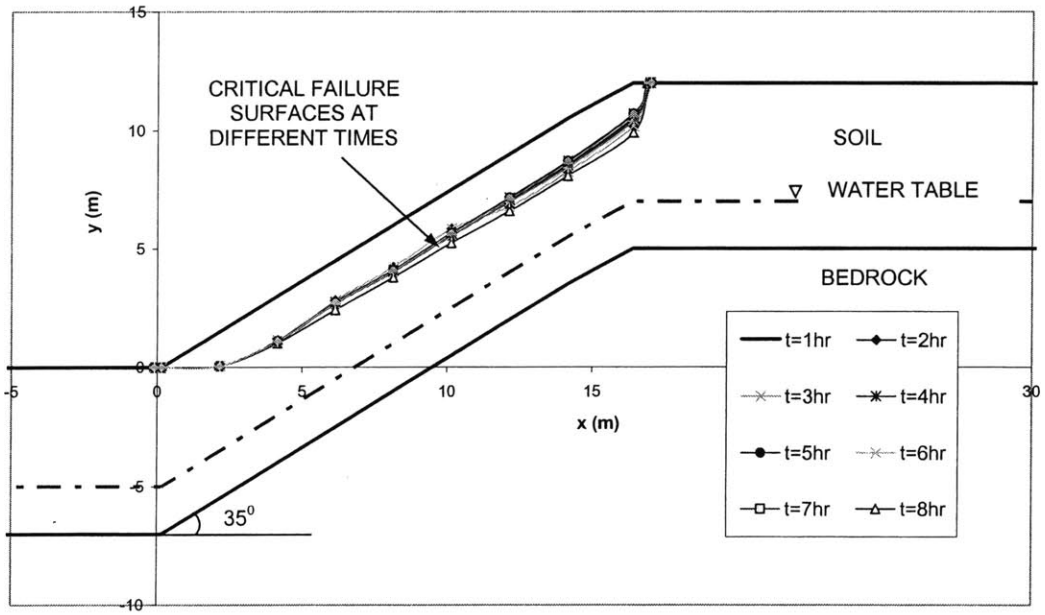

Figure 3.23. Critical Failure Surfaces with Time Starting with Shallow Initial Failure Surface

Figure 3.22 also shows the variation of Factor of Safety with time along an arbitrarily specified failure surface. This surface is kept constant with time (no search is performed) and hence changes in Factors of Safety occur only as a result of changes in pressures.

Several comments can be made with regard to Figure 3.22:

(a) It is evident that landslide analyses that do not employ a procedure to search for the critical failure surface are incomplete. This is because if the variation of Factor of Safety with time were computed on a specified failure surface, even if it is the initial critical failure surface, Factors of Safety are not the minimum in the slope, and hence are overestimated leading to unconservative conclusions.

(b) Figure 3.22 shows that starting with different initial failure surfaces may result in different critical failure surfaces, and hence different Factors of Safety with time (see shallow and deep initial failure surface lines in Figure 3.22). As stated previously, these result in local minimum Factors of Safety that may not be global. It is therefore necessary to start with different initial failure surfaces to locate the critical one on which the Factor of Safety is a global minimum.

In this example, the location of critical failure surface changes with time. Initially and in the early stages of rainfall, the critical surface is located deep and this is shown by the lower Factor of Safety for the deep slope in Figure 3.24. With time, and continued rain, the critical surface becomes located shallower as infiltrating rain increases the pressures near the soil surface. The final critical surface on which failure occurs is shallow. This is also shown in Figure 3.24.

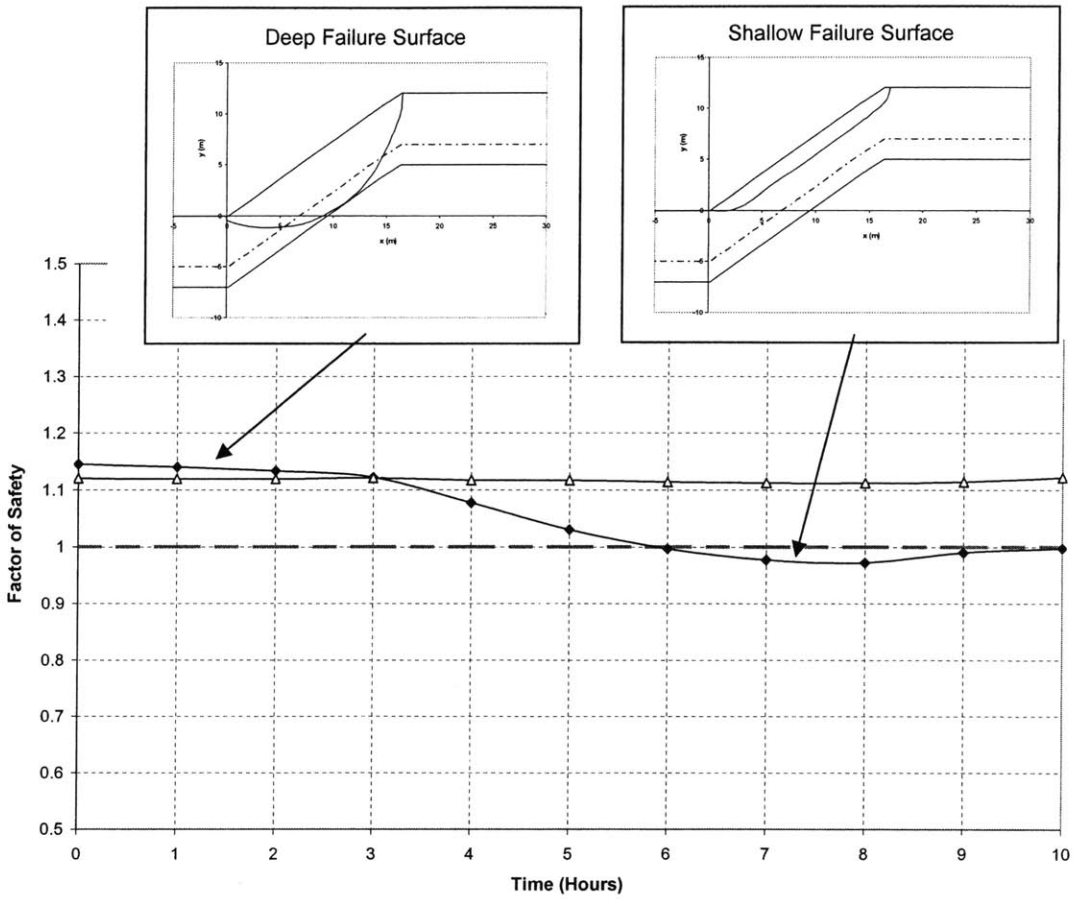

Figure 3.24. Variation of Factors of Safety and Critical Failure Surfaces with Time

The final critical surface on which the Factor of Safety is a global minimum is shown in Figure 3.25.

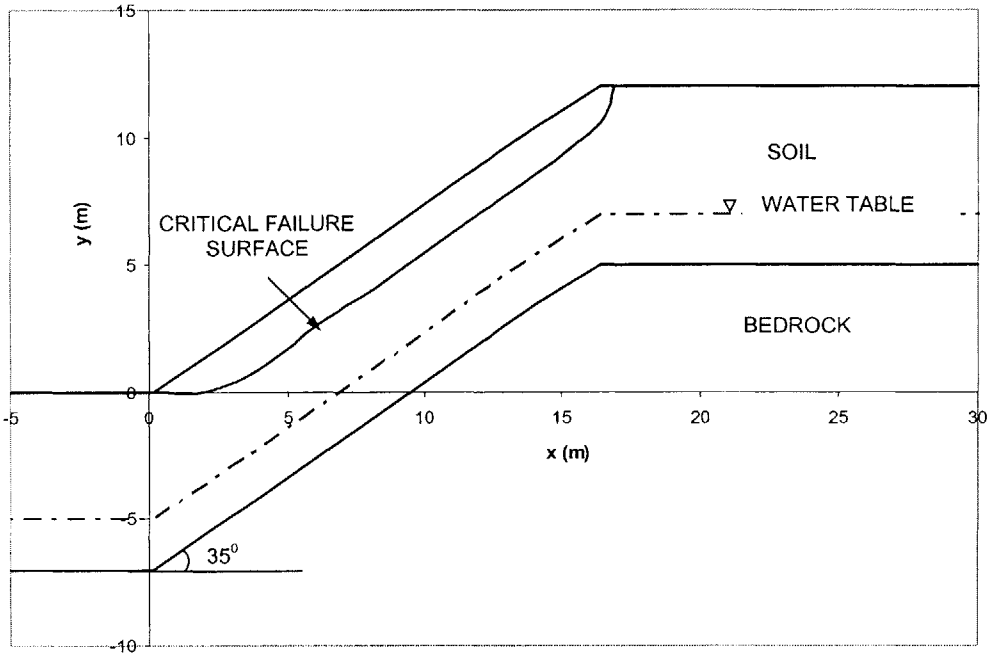

Figure 3.25. Critical Failure Surface

It is worth noting that the critical failure surface lies in the unsaturated zone of the slope, where the soil strength has been reduced by the infiltrating rainwater, and the resulting landslide is shallow, and translational as can be seen from the shape of the failure surface. Failure occurs at a time of about 6 hours (see Figure 3.24), and therefore occurs during the rainfall event, at a time when the generated pressures are close to maximum (see Figure 3.18).

This example shows that when in some slopes, and when the infiltrating rainwater reduces suction, it can cause sufficient loss of strength to generate a landslide. This is an important result since it remains a matter of debate amongst investigators whether a reduction of suction is sufficient to cause slope failure or whether positive pressures necessarily have to develop.

3.3.2.2 ELIMINATION OF SUCTION

When the rainfall intensity is close in magnitude to the saturated conductivity of the surface soil, all the rainwater infiltrates into the slope at a rate equal to the saturated conductivity. An infiltrating wetting front develops and migrates into the slope eliminating the suction in the wetted soil above it, as is shown in Figure 3.26.

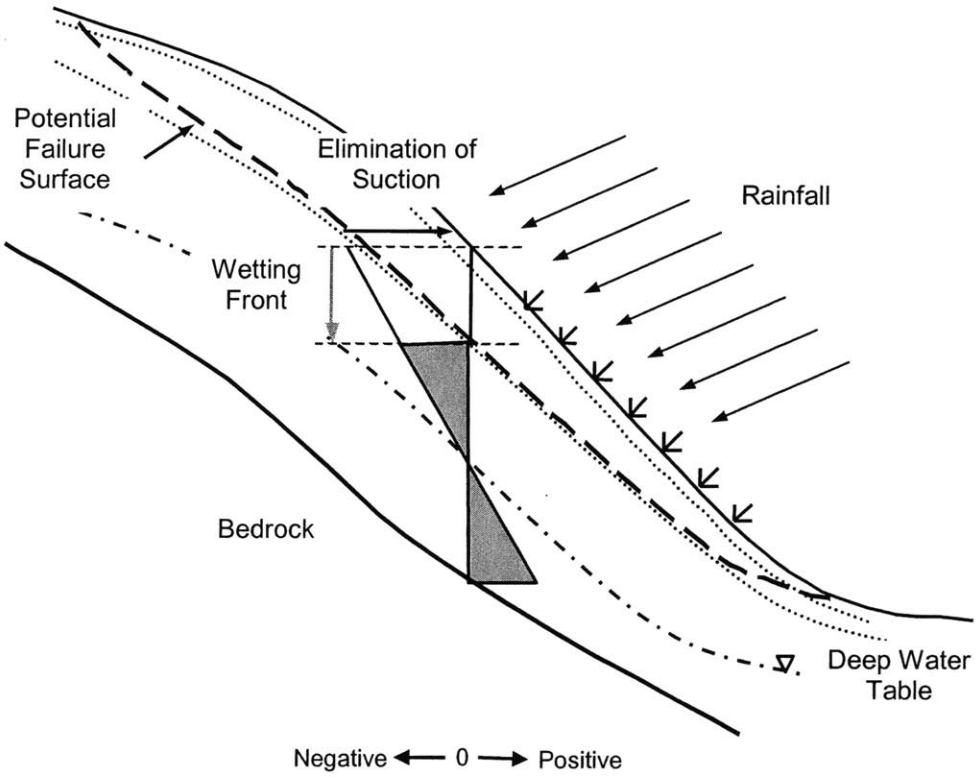

Figure 3.26. Schematic of Failure Mechanism (Elimination of Suction) (Negative, 0, Positive Indicate sign of pore pressures)

The infiltrating rainwater causes a reduction in strength, which given certain site conditions, can be sufficient to initiate a landslide.

To illustrate the mechanism of failure by elimination of suction, we reconsider the slope analyzed in Section 3.3.2.1, which is shown again in Figure 3.27.

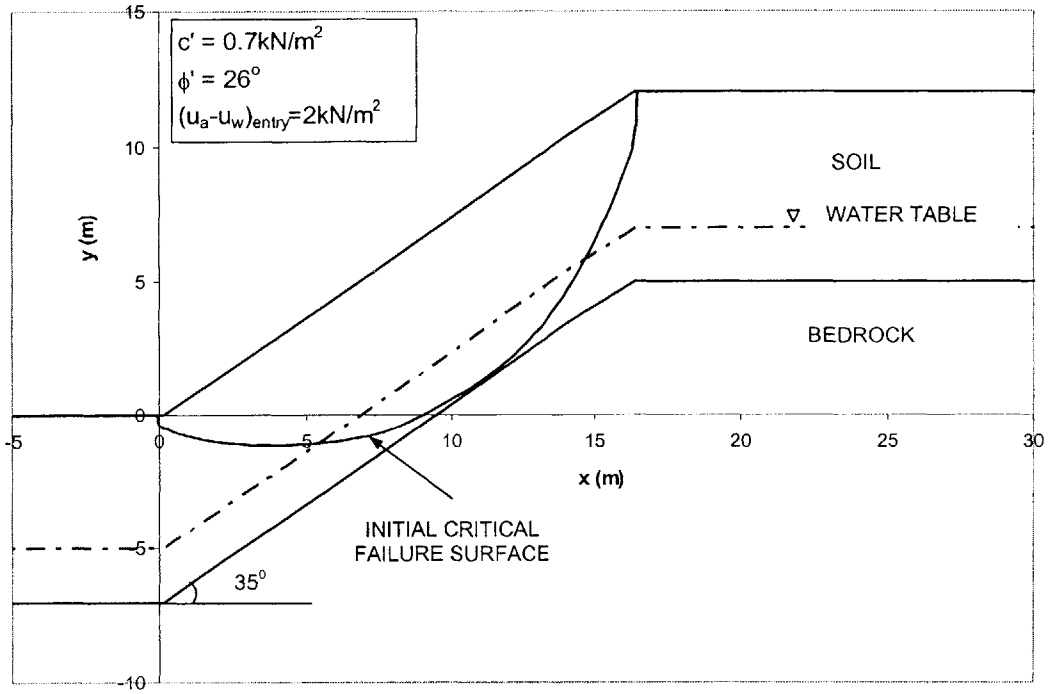

Figure 3.27. Slope Properties and Initial Critical Failure Surface

Note that this is the same slope, with the same properties that was considered in Section 3.3.2.1. Specifically, the slope geometric properties (slope angle, and length), soil strength parameters, and characteristic curves (Figures 3.14 and 3.15) are the same as those considered previously.

Initially, a Factor of Safety of 1.23 is computed on the critical failure surface shown in Figure 3.25, and so the slope is initially stable.

We now assume that a rainfall event with constant intensity, $I = 125\text{cm}/\text{hr}$ occurs for duration of 8 hours. Note that this intensity is close in magnitude to the saturated conductivity of the soil. Figure 3.28 shows the water content distribution at selected times, prior to, during and after rain, and Figure 3.29 shows the corresponding pore pressure profiles.

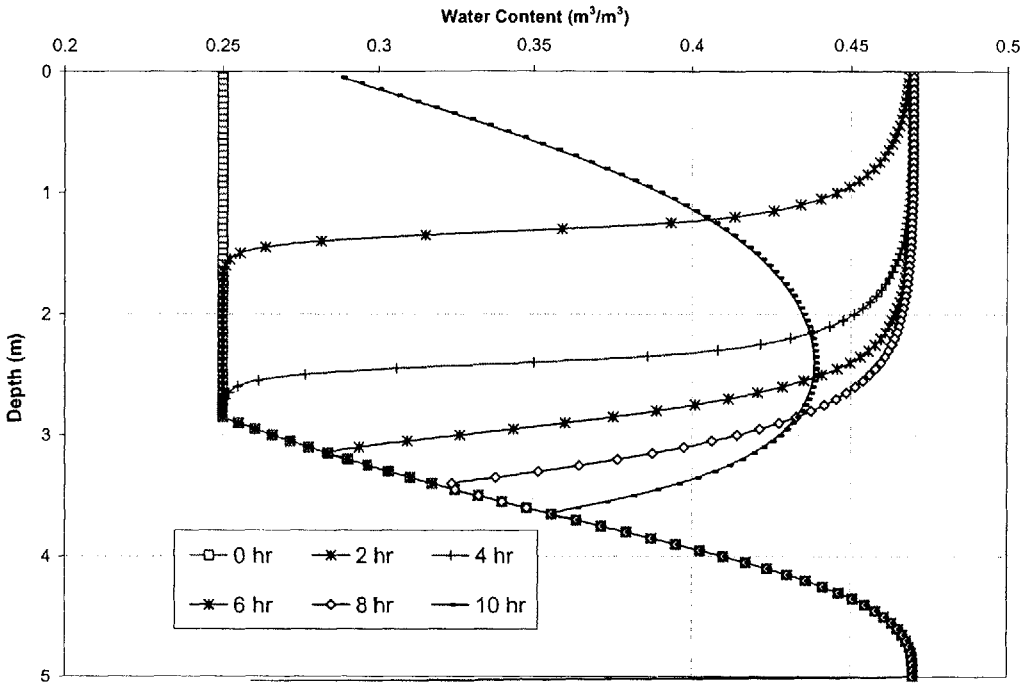

Figure 3.28. Moisture Content Distributions at Selected Times

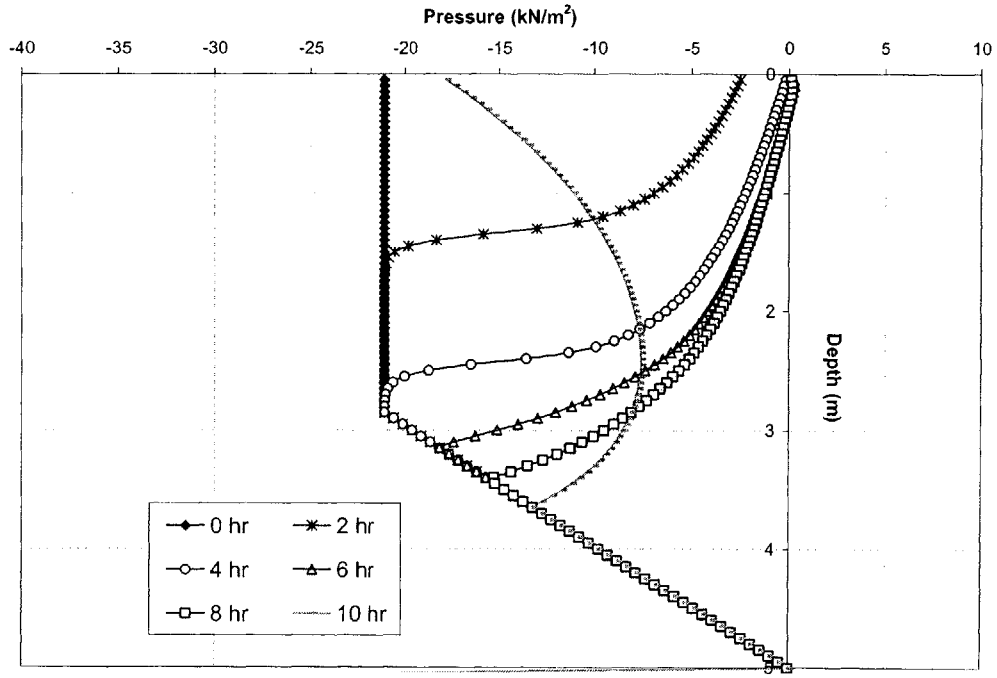

Figure 3.29. Pore Pressure Profiles at Selected Times

Figure 3.28 shows that a wetting front develops with the soil fully saturated, and migrates down the slope with time. This is shown as a zone of saturated soil forming at early times into the rainfall event (e.g. see Figure 3.28 at 2 hours), which travels into the soil, as a saturated zone with time. As this happens, the suction is eliminated above the wetting front as shown in Figure 3.29.

To assess the stability of the slope during and after rain, a search for the critical failure surface is performed at each time using the pore pressure distributions shown in Figure 3.29. Figure 3.30 shows the variation of Factor of Safety with time.

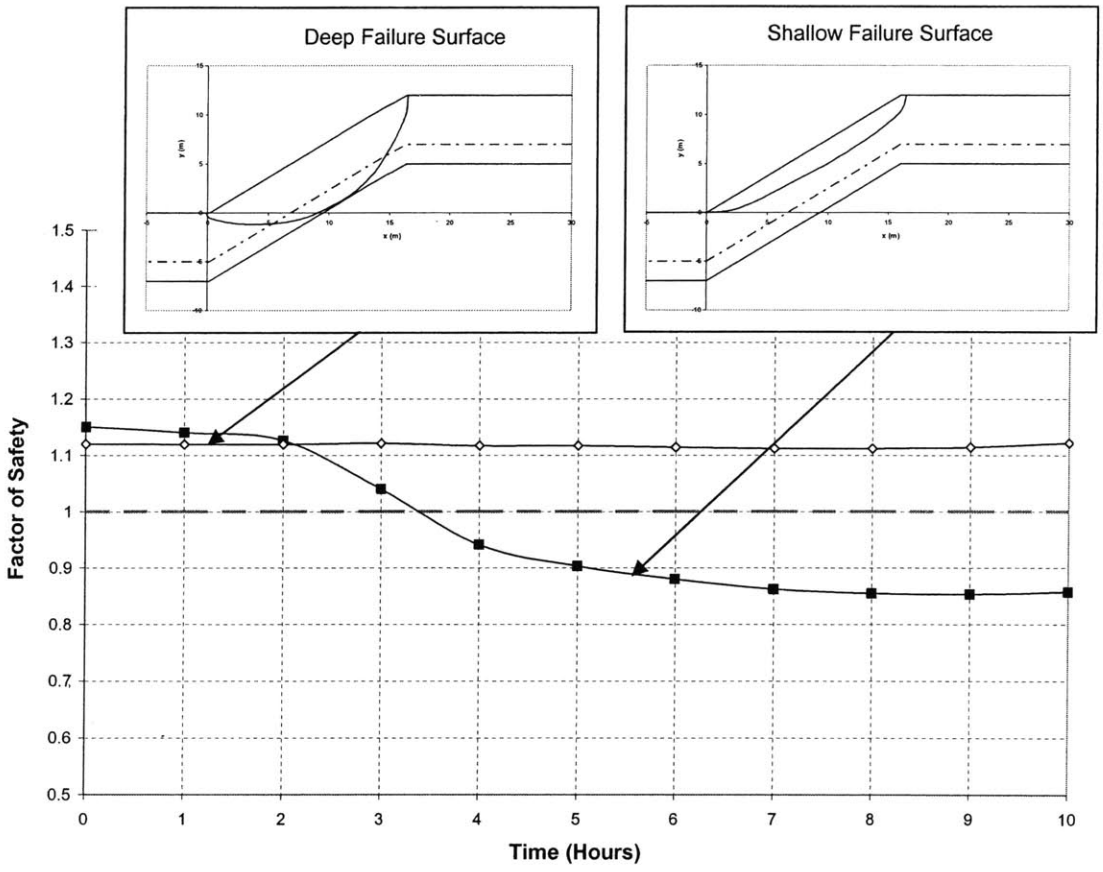

Figure 3.30. Variation of Factors of Safety and Critical Failure Surfaces with Time

Figure 3.30 shows that initially, the critical failure surface is located deep into the slope at the soil bedrock interface, and the slope is stable. With time, and as the rainwater

eliminates suction (see Figure 3.29), the Factor of Safety decreases. The location of the critical failure surface changes, at a time of about 2 hours, when it becomes shallow, and is located in the unsaturated zone of the soil above the water table. The Factor of Safety continues to decrease with time, and failure occurs at a time of about 3 ½ hours. The failure surface is shallow and translational. The critical failure surface is shown in Figure 3.31.

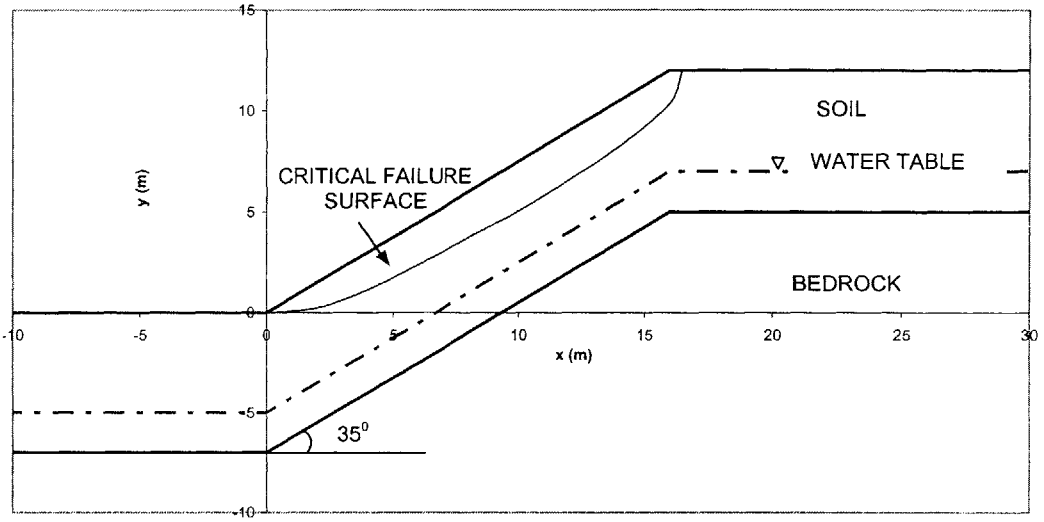

Figure 3.31. Critical Failure Surface

Figure 3.32 compares the variation of Factor of Safety with time for both cases of reduction of suction, and elimination of suction.

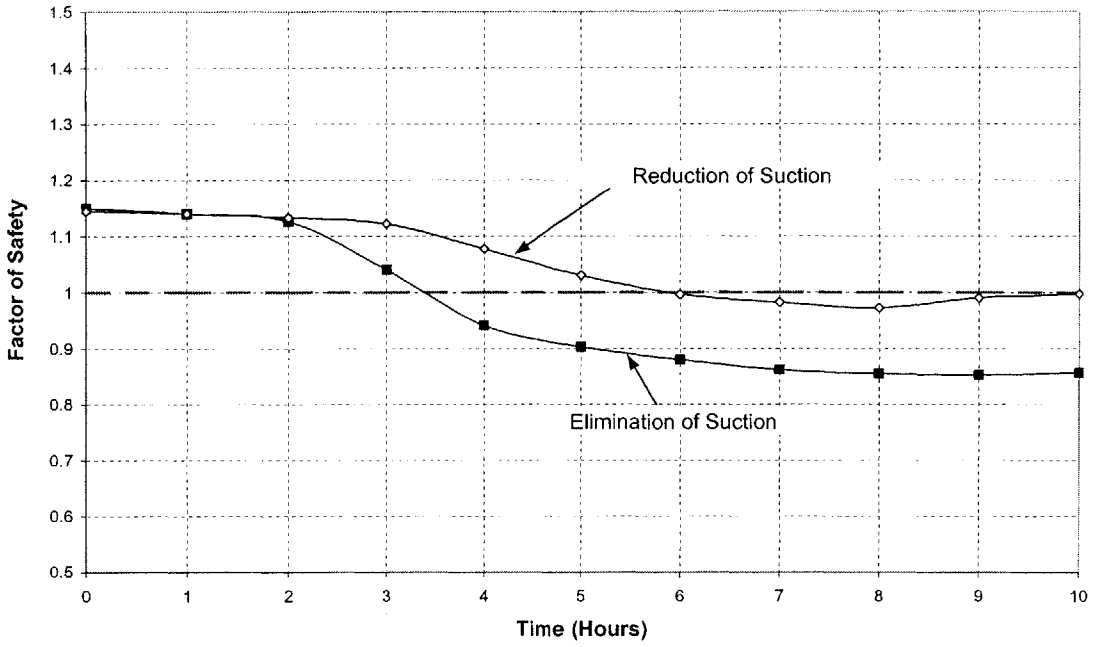

Figure 3.32. Comparison of Variations of Factors of Safety for Reduction and Elimination of Suction

Figure 3.32 shows that initially, the Factor of Safety is the same in both cases of reduction and elimination of suction. This is to be expected, since the initial conditions have been chosen to be the same. However, with time, and as the rainwater infiltrates the slope, the Factor of Safety at any time is smaller in the case of elimination of suction than in the case of reduction of suction. This is because the higher rainfall intensity leads to larger pore pressures (compare Figures 3.18 and 3.29) on the potential failure surface. Failure occurs in the case of reduction of suction at a time of about 6 hours, which is close to the end of rainfall (at 8 hours). Failure in the case of elimination of suction occurs at an earlier time of about 3 ½ hours.

3.3.2.3 DEVELOPMENT OF POSITIVE PRESSURES

When the intensity of rainfall is greater in magnitude than the saturated conductivity of the soil at the surface, the soil is unable to transmit the infiltrating rainwater at that rate, and excess water ponds on or, more likely because of inclination, runs off the slope surface. Infiltration takes place at the potential infiltration rate (see Chapter 2, Part 2-1) of the soil and positive pressures are generated behind an infiltrating front, as is illustrated in Figure 3.33.

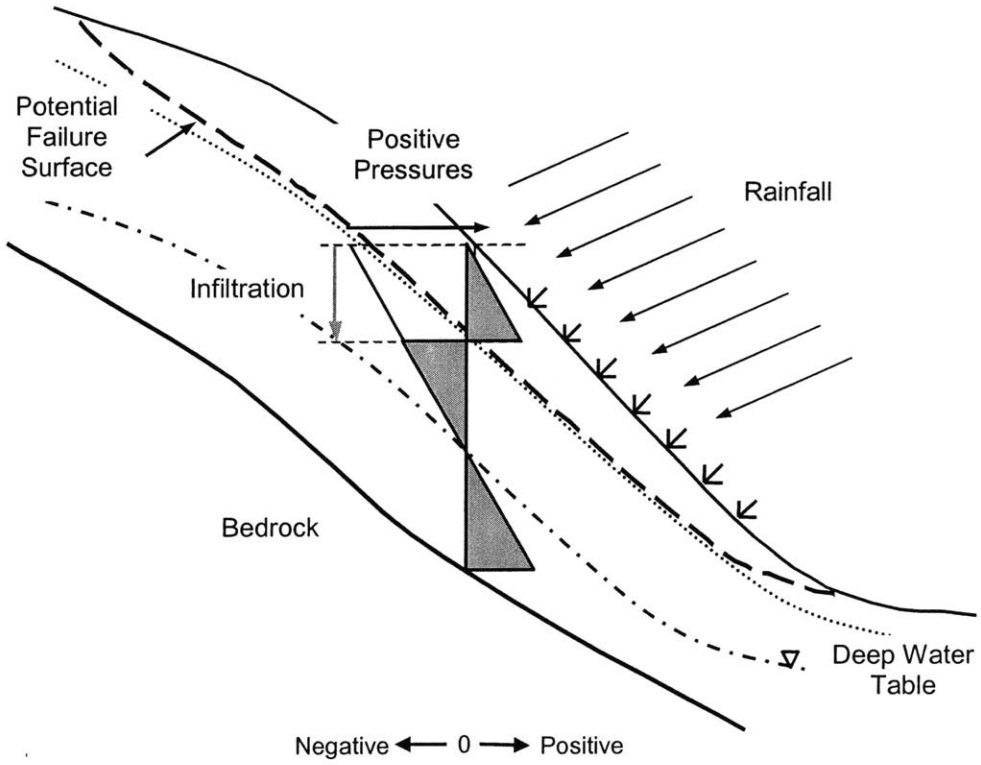

Figure 3.33. Schematic of Failure Mechanism (Development of Positive Pressures) (Negative, 0, Positive Indicate sign of pore pressures)

The infiltrating rainwater causes the development of positive pressures, which given certain site conditions, can reduce soil strength sufficiently to initiate a landslide.

To illustrate the mechanism of failure by positive pressure development, we reconsider the slope analyzed in the previous two sections, which is shown again in Figure 3.34.

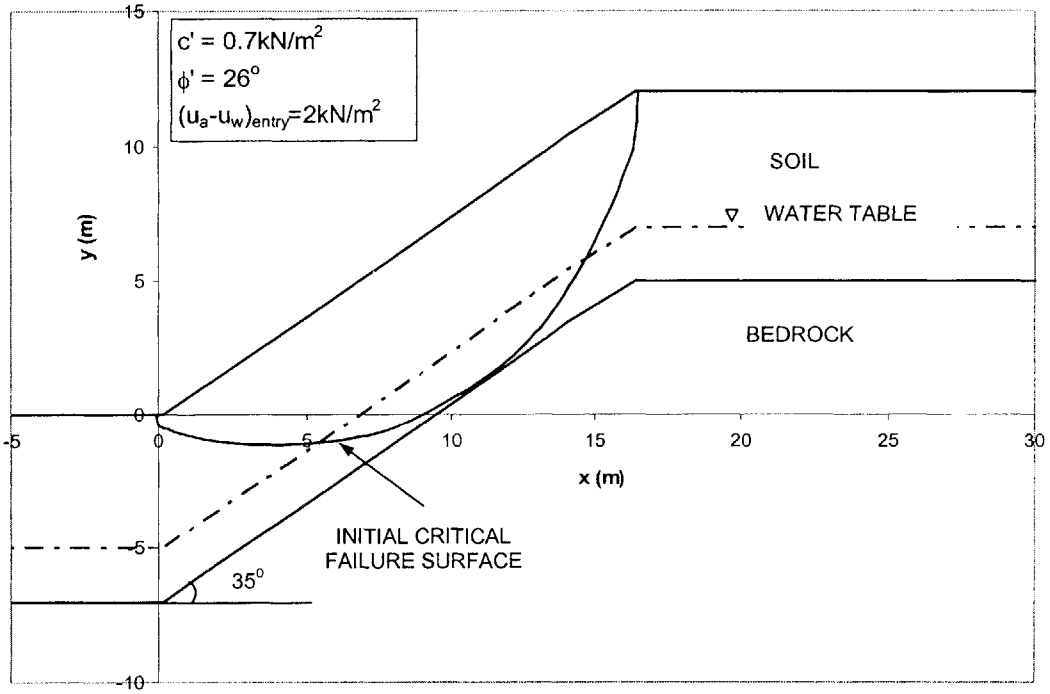

Figure 3.34. Slope Properties and Initial Critical Failure Surface

The soil strength parameters are shown in Figure 3.34, and the soil characteristic curves are the same as those that were shown in Figures 3.26 and 3.27.

Initially, a Factor of Safety of 1.23 is computed on the critical failure surface shown in Figure 3.34, and so the slope is initially stable.

We now assume that a rainfall event with constant intensity, $I = 250\text{mm}/\text{hr}$ occurs for duration of 8 hours. Note that this intensity is greater in magnitude than the saturated conductivity of the soil. Figure 3.35 shows the water content distribution at selected times, prior to, during and after rain, and Figure 3.36 shows the corresponding pore pressure profiles.

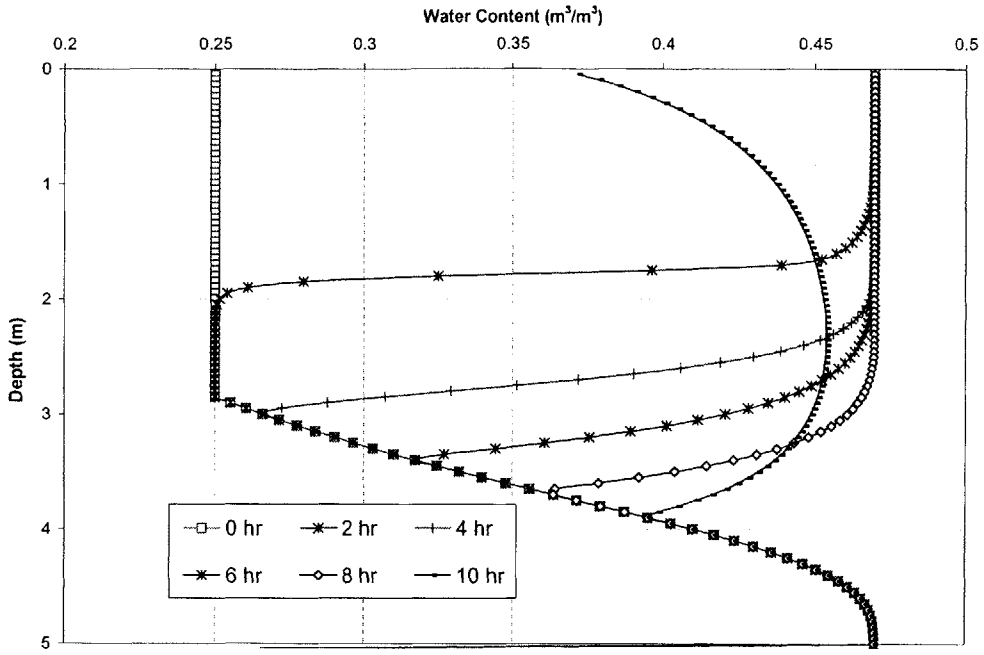

Figure 3.35. Moisture Content Distributions at Selected Times

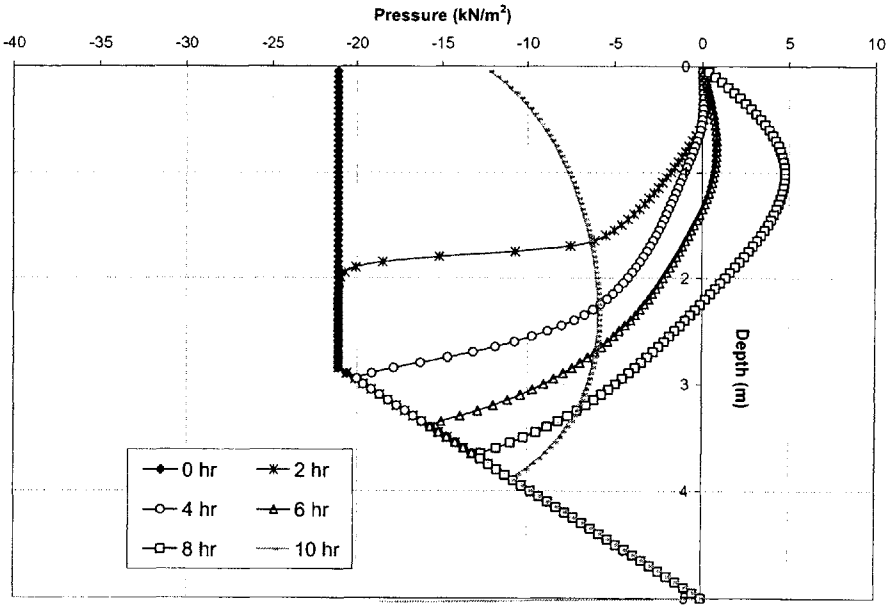

Figure 3.36. Pore Pressure Profiles at Selected Times

Figure 3.35 shows that rainfall causes the full saturation of the soil, and the saturated zone migrates into the soil with continuing time, and rainfall.

As this happens, and since the rainfall intensity is greater than the saturated conductivity of the soil, positive pore pressures develop in the saturated zone as shown in Figure 3.36. Figure 3.37 shows the variation of Factor of Safety with time.

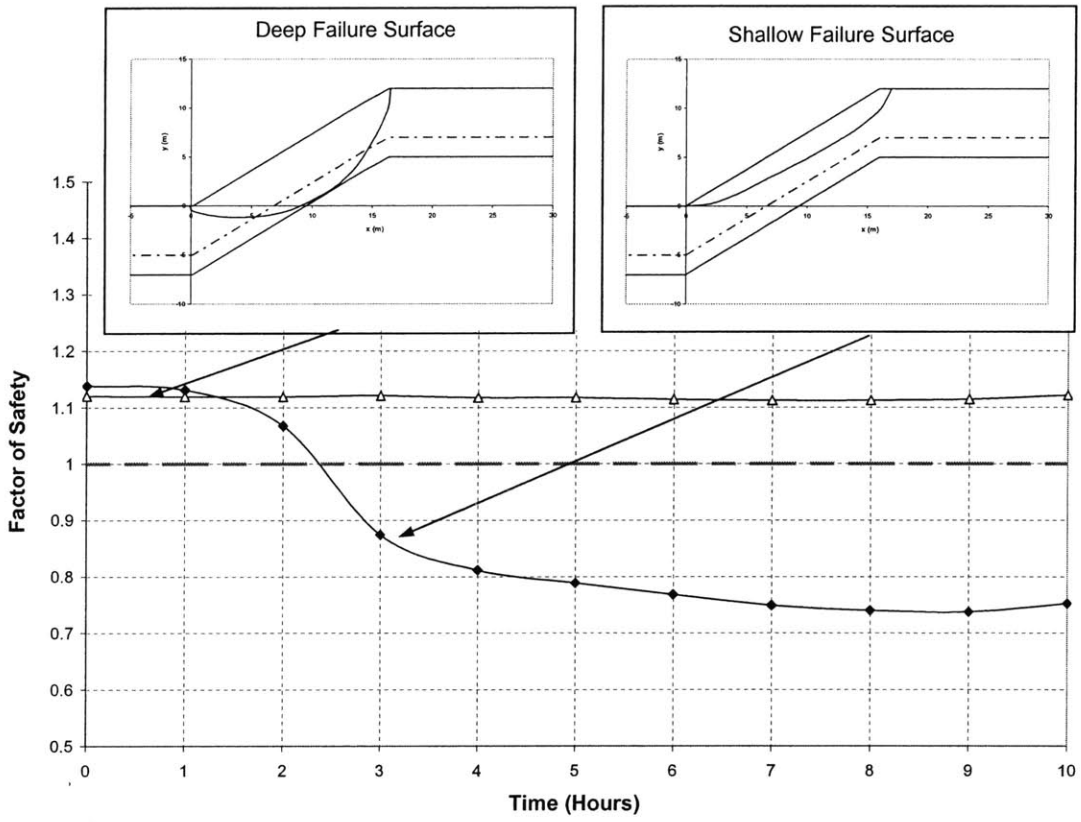

Figure 3.37. Variation of Factors of Safety and Critical Failure Surfaces with Time

Figure 3.37 shows that at early times, the critical failure surface is located deep in the slope, along the soil bedrock interface. As it rains, and positive pressures develop near the surface of the soil, the critical failure surface becomes shallow as shown in Figure 3.37. Failure occurs at a time of about 2 ½ hours after the start of rain, along a shallow translational failure surface. This failure surface is shown in Figure 3.38.

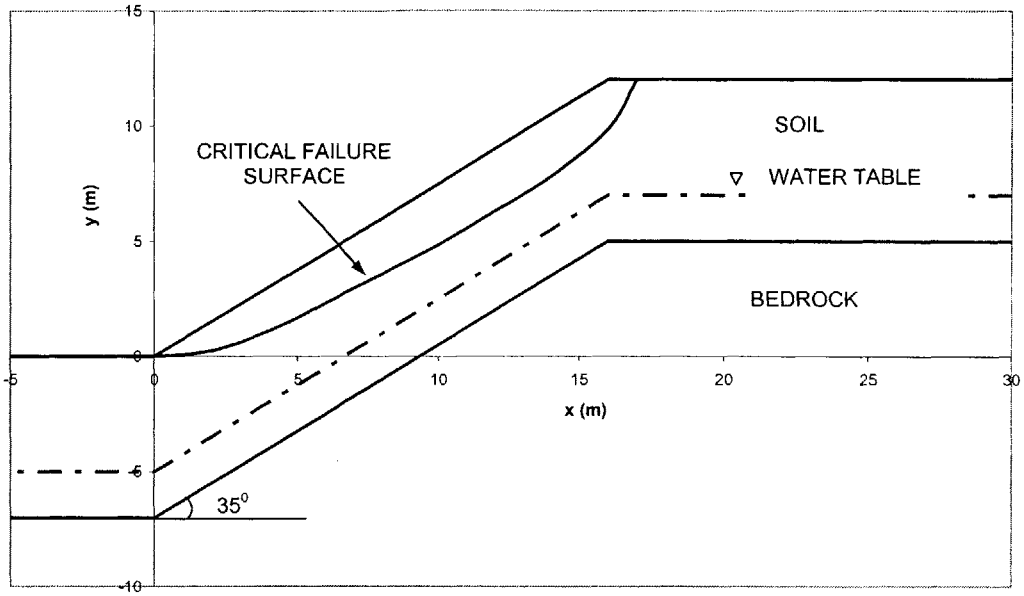

Figure 3.38. Critical Failure Surface

Figure 3.39 compares the variation of Factor of Safety with time for the cases of reduction of suction, elimination of suction and development of positive pressures.

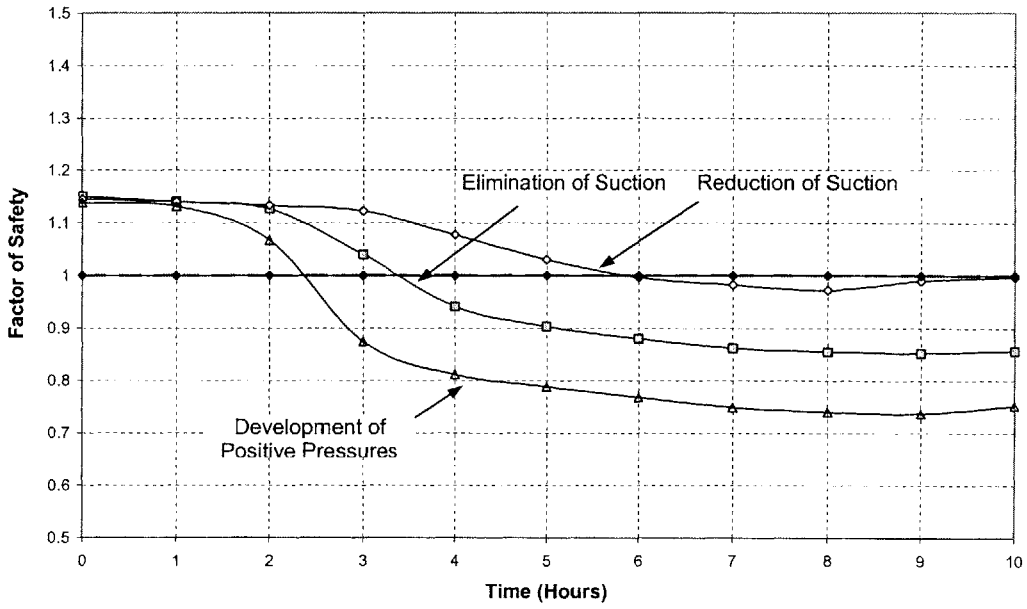

Figure 3.39. Comparison of Variation of Factors of Safety for Reduction of Suction, Elimination of Suction, and Development of Positive Pressures

Figure 3.39 shows that initially, the Factor of Safety is the same for all three cases considered, because the initial conditions are taken to be the same for each. With time, and as the rainwater infiltrates into the slope, the Factor of Safety decreases in all three cases. The decrease is greatest in the case when positive pressures develop because this is the case where the largest pressures develop in the unsaturated zone of the slope. These larger pressures cause a greater reduction in strength, and therefore lower Factors of Safety. Failure occurs in all three cases during the rainfall event. The failure surface in all cases is shallow and translational located above the water table, where infiltrating rainwater has altered pressures (reduced or eliminated suction, or developed positive pressures). The time to failure is smaller in the case of the development of positive pressures than in the case of elimination of suction which is lower than in the case of reduction of suction. This is because the larger generation of pressures causes a quicker reduction in strength sufficient to cause failure. Failure, in all three cases, occurs during the rainfall event, at times less than 8 hours.

FURTHER EXAMPLES

Based on the previous discussion, and examples, it is evident that that slopes that fail by the reduction of suction, will also fail by the elimination of suction, and development of positive pressures. This is because greater rainfall intensities cause larger build ups of pressures (elimination of suction, and development of positive pressures) on a potential failure surface, and greater reductions of strength to cause failure.

Alternatively stated, there are slopes that fail by the elimination of suction, that would otherwise remain stable when suction is simply reduced. Similarly, there are slopes that fail by the development of positive pressures, that would otherwise remain stable when suction is reduced or eliminated.

To illustrate this, consider the slope shown in Figure 3.40.

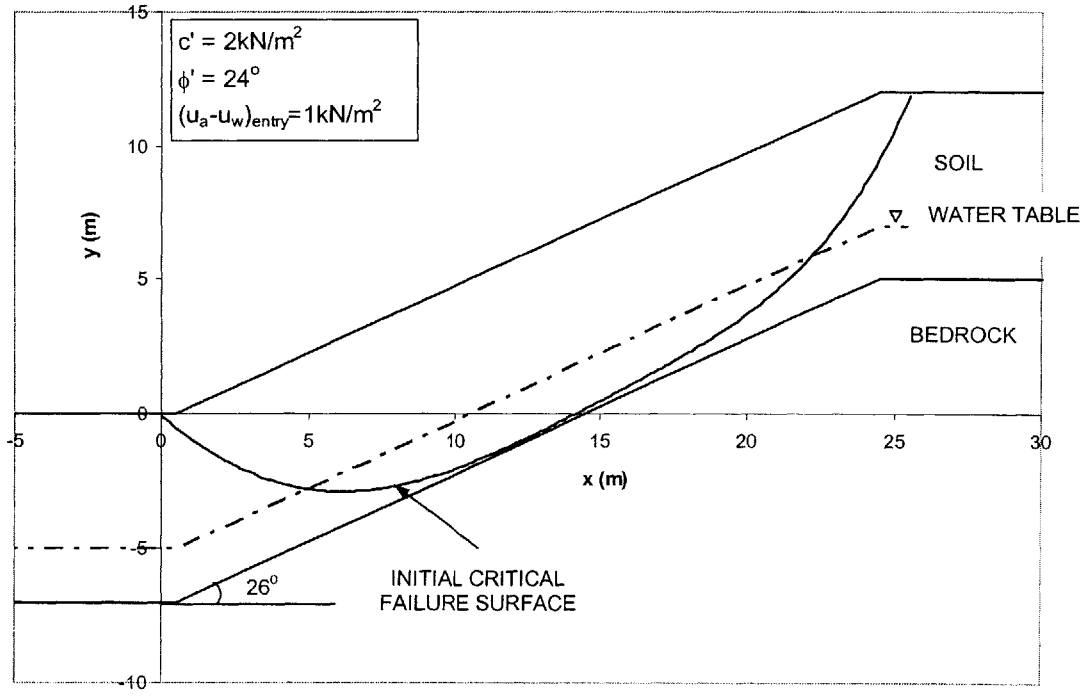

Figure 3.40. Slope Properties and Initial Critical Failure Surface

Note that this slope is less steep than the slope considered previously, and that the soil strength is larger than the example in Section 3.3.2.1.

The hydraulic parameters are assumed to be:

Saturated moisture content of soil $\theta_S = 0.47$. This is the same θ_S as in the example in Section 3.3.2.1.

Residual moisture content of soil $\theta_r = 0.11$ (See Figure 3.10). This is the same θ_r as in the example in Section 3.3.2.1.

Saturated conductivity $K_S = 2.3 \times 10^{-5} m/s$. This K_S is different from the K_S in the example in Section 3.3.2.1, it is smaller.

Specific storage coefficient $S_S = 0.0025$ (see Chapter 2, Part 2-1). This S_S is different from the S_S in the example in Section 3.3.2.1, it is smaller.

The van Genuchten (1980) model is used to describe the soil characteristic curves with the parameters $n = 1.24$ and $\delta = 0.011$. The resulting characteristic curves are shown in Figures 3.41 and 3.42. The van Genuchten (1980) parameters considered in this example are different from the ones considered in the example in Section 3.3.2.1, and so the characteristic curves are also different. They are different in such a way that the characteristic curves in this example, particularly the moisture retention curve, has a steeper slope than in the example in Section 3.3.2.1 (compare Figures 3.41 and 3.42 to 3.14 and 3.15). The air entry pressure, is smaller in this example, than in the example considered in Section 3.3.2.1 (compare Figure 3.41 to 3.12).

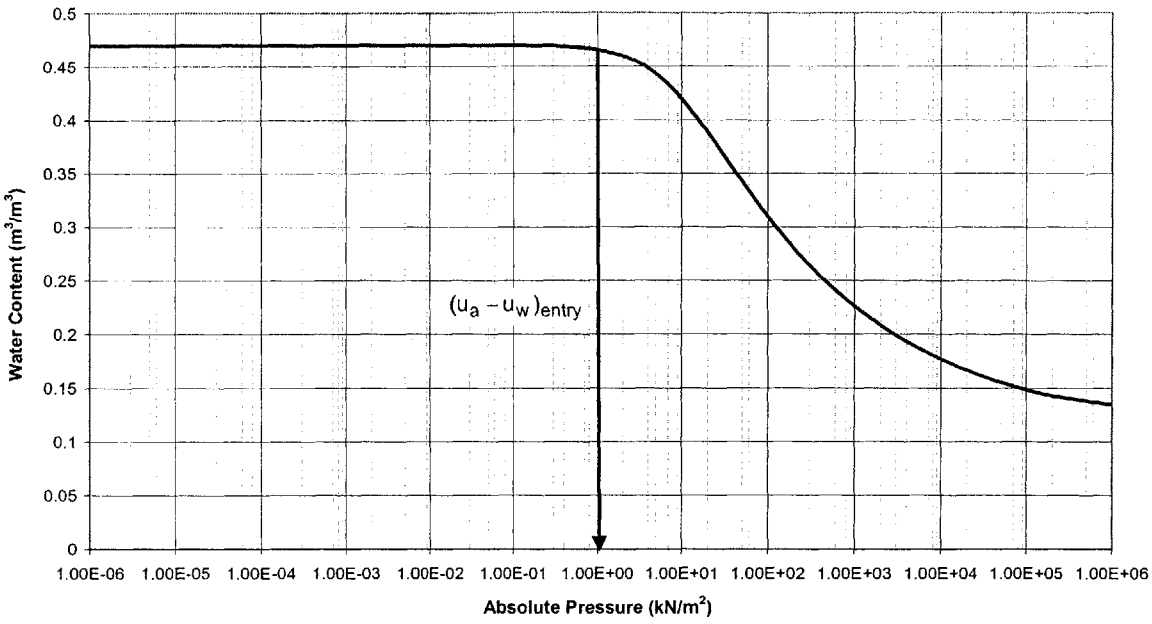

Figure 3.41. Moisture Retention Characteristic Curve

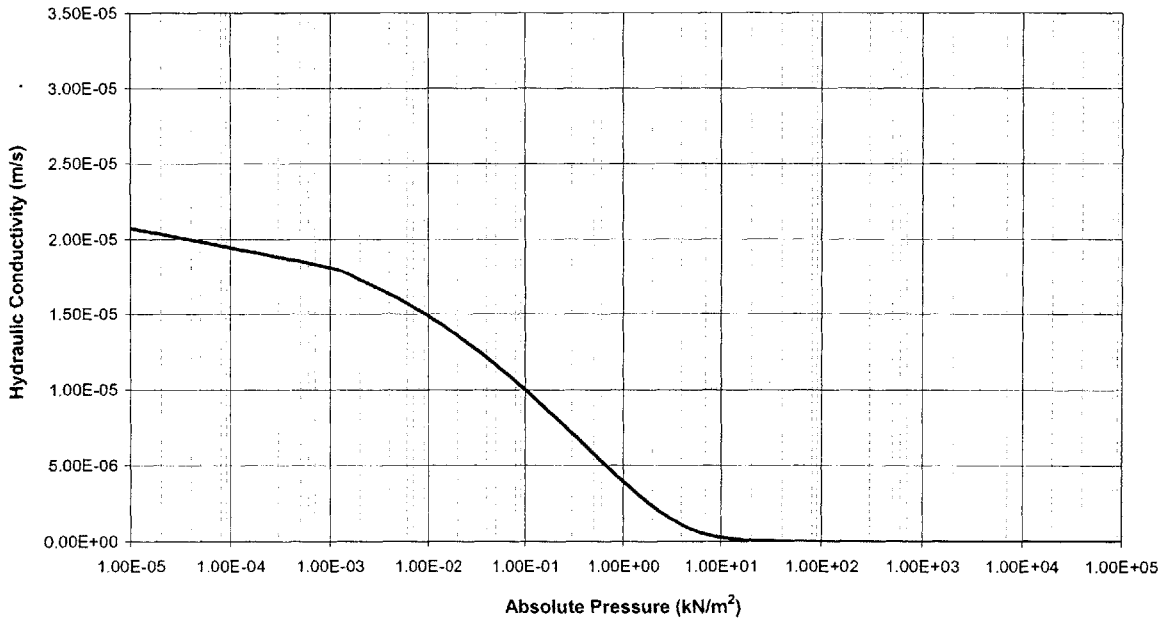

Figure 3.42. Hydraulic Conductivity Characteristic Curve

INITIAL CONDITIONS AND STATE OF STABILITY

We assume that the initial moisture content in the unsaturated zone of the slope is $\theta_i = 0.4$, indicating wet antecedent conditions. The initial moisture content and pore pressure distributions in the slope are as shown in Figures 3.43 and 3.44 respectively at time $t = 0$.

The initial pore pressure distribution is used in the stability model to locate the critical failure surface in the slope, which is shown in Figure 3.40. A Factor of Safety of 1.55 is computed along this surface and hence the slope is initially stable.

STABILITY DURING/AFTER RAINFALL

We assume a rainfall event of constant intensity $I = 150mm/hr$ takes place for a duration of 6 hours. This intensity is greater in magnitude than the saturated conductivity of the soil. The moisture content distribution and pore pressures profiles are shown at selected times in Figures 3.43 and 3.44 respectively.

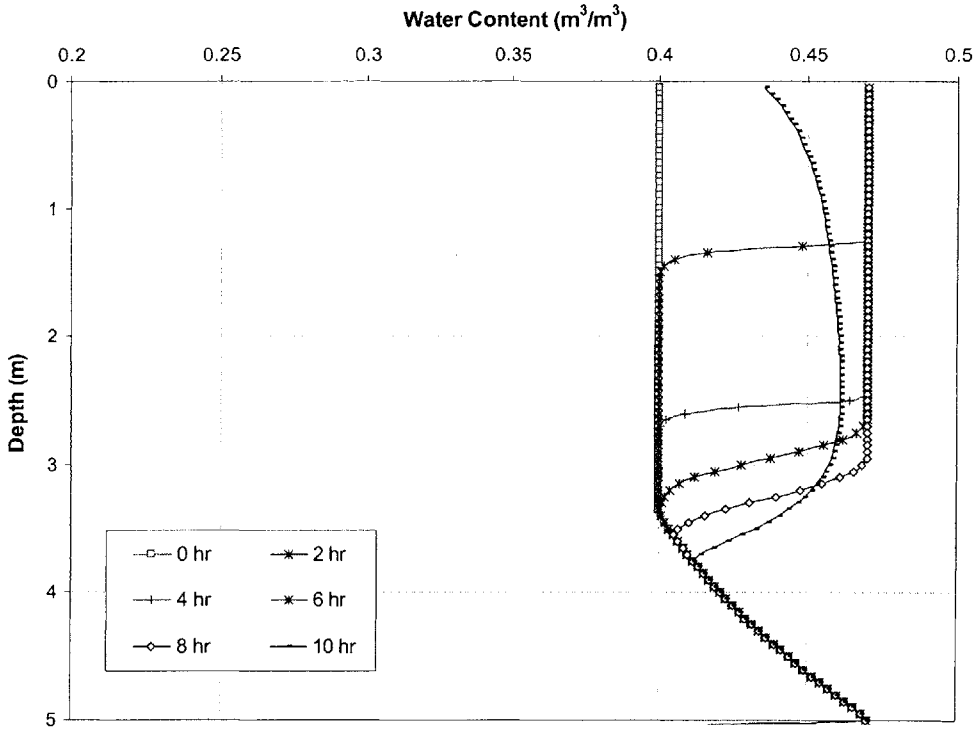

Figure 3.43. Moisture Content Profiles at Selected Times

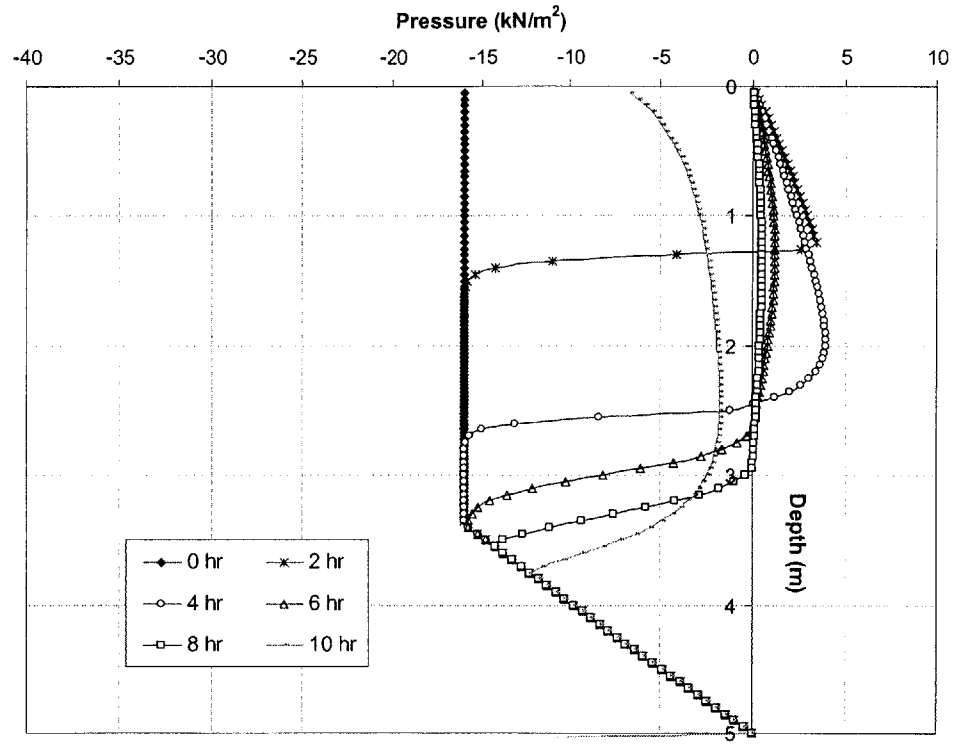

Figure 3.44. Pore Pressure Profiles at Selected Times

Figure 3.43 shows that the rain is sufficiently intense to fully saturate the soil. Because of this, the soil becomes fully saturated, and this saturated zone travels into the slope with continued time and rainfall. The soil, therefore, gets saturated from the surface downwards with increasing time and rainfall. Figure 3.44 shows that at any time t during rainfall, positive pressures develop above the infiltration depth, again because the intensity of the rainfall is greater than the saturated conductivity of the soil. Two interesting observations can be made with regard to the generation of positive pressures during rainfall, and in reference to Figure 3.44. First, the maximum pore pressures do not occur at the end of rainfall, but rather at an earlier time, e.g. the maximum pressures at time $t = 4hr$ are greater than those at $t = 6hr$. This is a result of the hydrologic assumption that no ponding takes place on the surface and any excess rainwater runs off. Consequently, the positive pressures that develop are dissipated. Second, as redistribution takes places, for times greater than $t = 6hr$ in Figure 3.44, positive pressures are observed throughout a greater depth of soil. The combined effect of these two observations again emphasizes the need for stability analyses to be performed in

relation to time to obtain the correct critical failure surface and minimum Factor of Safety in the slope.

The variation of Factor of Safety with time, and the critical failure surfaces are shown in Figure 3.45.

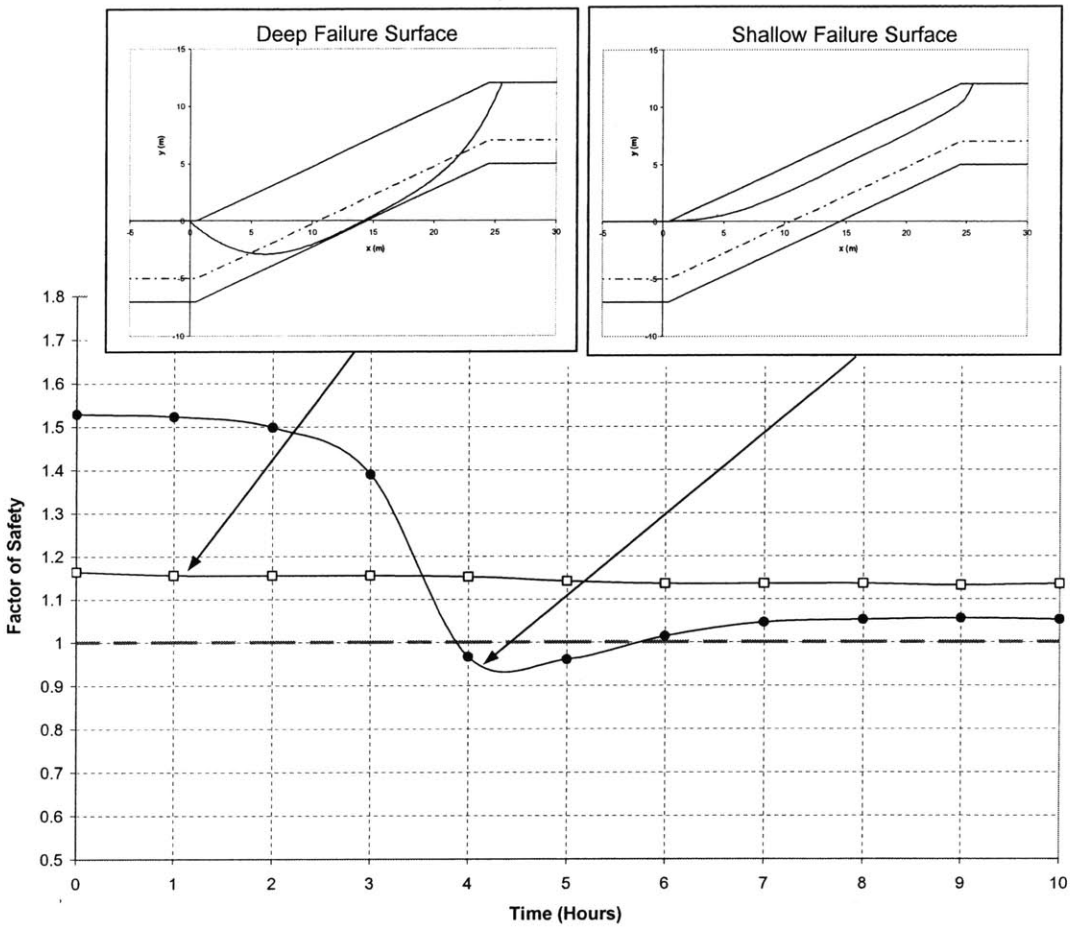

Figure 3.45. Variation of Factor of Safety and Critical Failure Surfaces with Time

Figure 3.45 shows that initially, the critical failure surface lies deep at the soil bedrock interface. As the rainfall increases the pressures in the otherwise unsaturated zone of the slope, the critical surface becomes shallower. Failure occurs at a time of about 3 ½ hours, along a shallow translational failure surface as shown in Figure 3.45.

This example illustrates that when the intensity of the incident rainfall is greater than the saturated conductivity of the surface soil, the rainwater infiltrates into the slope generating positive pressures, which consequently result in loss of strength, and ultimately landsliding.

We now analyze the stability of the slope during two other rainfall events. Both events are for a duration of 6 hours, but in the first event, the rainfall intensity is less than the saturated conductivity of the soil, leading to a reduction of suction, and in the second event the rainfall intensity is similar in magnitude to the saturated conductivity, leading to the elimination of suction.

Figure 3.46 shows the moisture distributions, and Figure 3.47 shows the pressure distributions when the rainfall intensity is less than the saturated conductivity of the soil. Similarly, Figure 3.48 shows the moisture distributions, and Figure 3.49 shows the pressure distributions when the rainfall intensity is close in magnitude to the saturated conductivity of the soil.

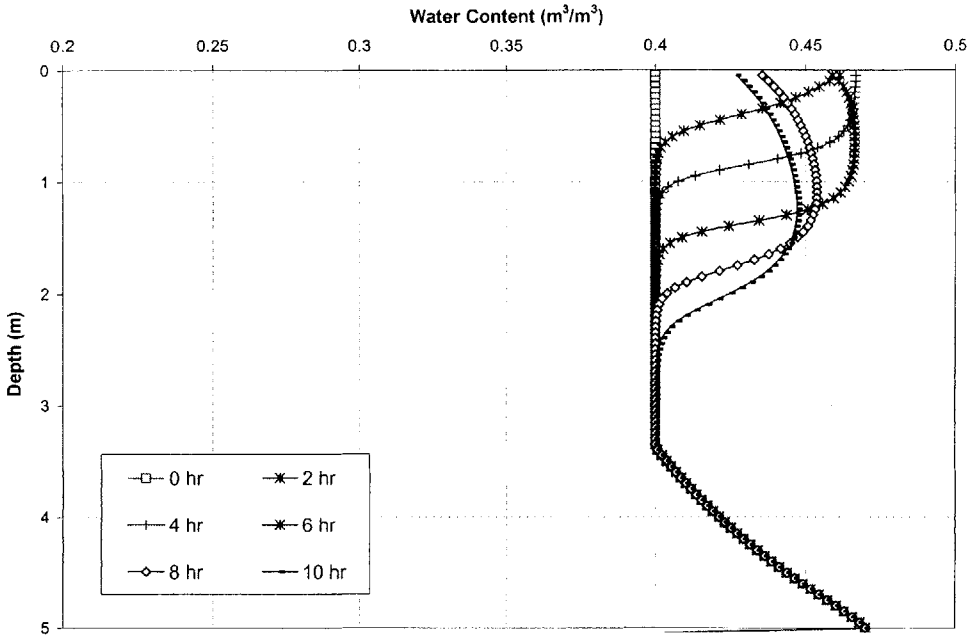

Figure 3.46. Moisture Content Profiles at Selected Times (Reduction of Suction)

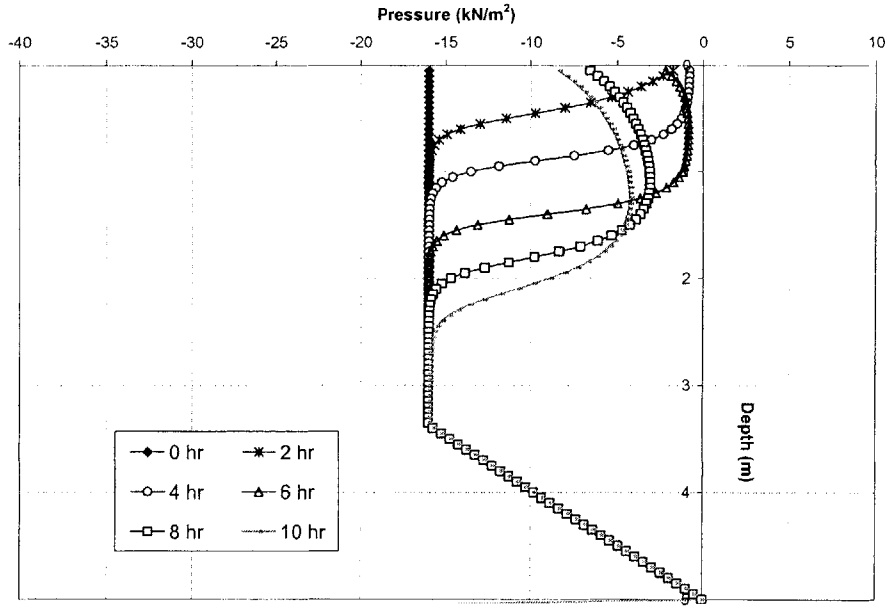

Figure 3.47. Pore Pressure Profiles at Selected Times (Reduction of Suction)

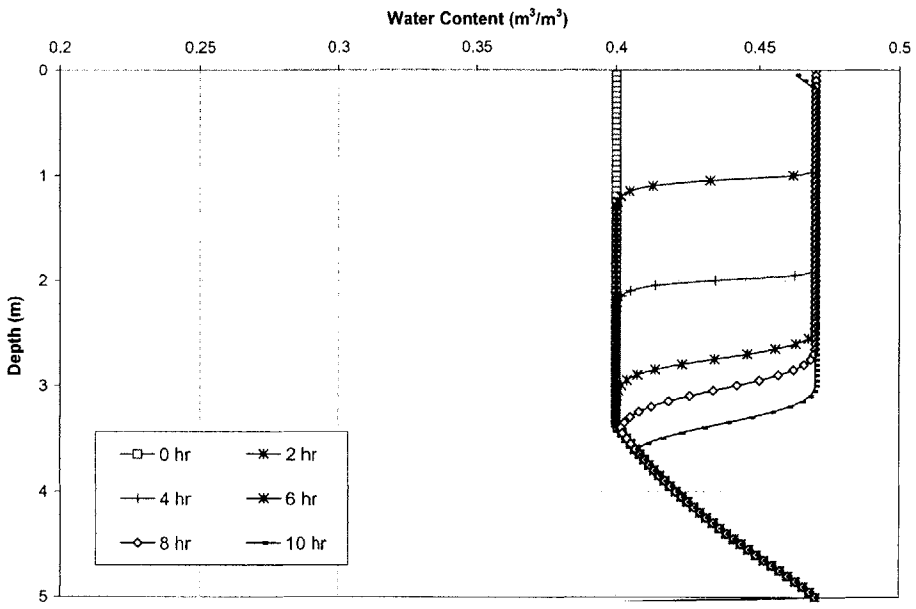

Figure 3.48. Moisture Content Profiles at Selected Times (Elimination of Suction)

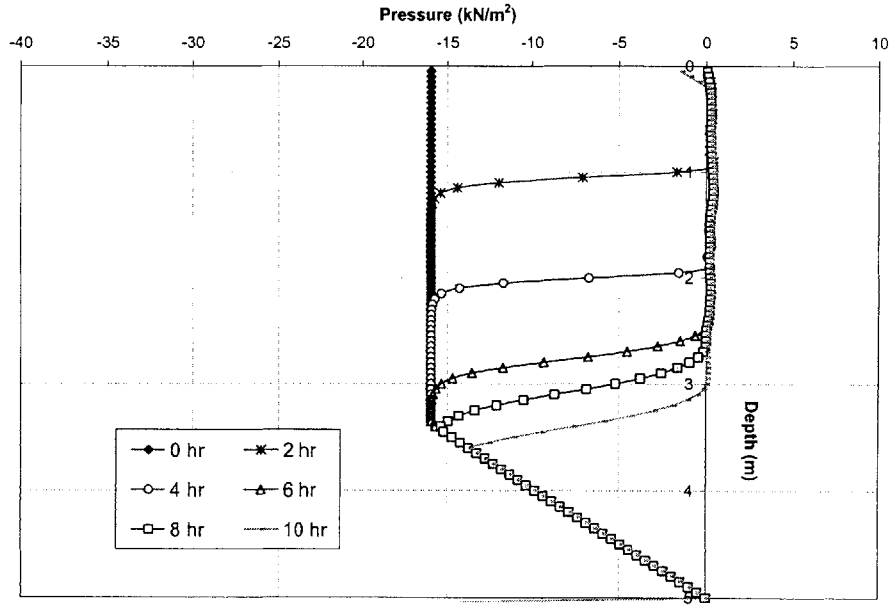

Figure 3.49. Pore Pressure Profiles at Selected Times (Elimination of Suction)

Figure 3.50 shows the variation of Factor of Safety with time for the three cases of:

(a) Development of positive pressures, when the rainfall intensity is greater in magnitude than the saturated conductivity of the soil
(b) Reduction of suction, when the rainfall intensity is smaller in magnitude than the saturated conductivity of the soil
(c) Elimination of suction, when the rainfall intensity is similar in magnitude to the saturated conductivity of the soil

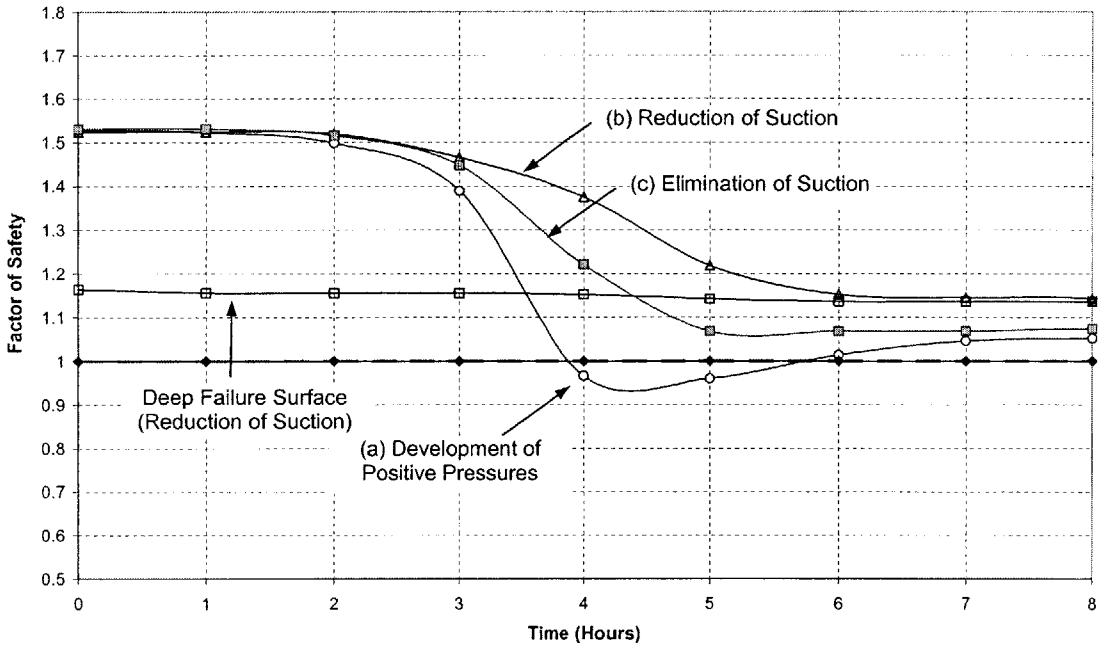

Figure 3.50. Comparison of Variation of Factors of Safety for Development of Positive Pressures, Reduction of Suction, and Elimination of Suction

Figure 3.50 also shows the variation of Factor of Safety on a deep failure surface, located at the soil bedrock interface, for the case of reduction of suction.

Several observations are made with regard to Figure 3.50:

(a) The Factor of Safety drops below a value of one only in the case when the rainfall intensity is greater than the saturated conductivity of the soil, and positive pressures

develop. In both cases of reduction, and elimination of suction, the Factor of Safety remains above one during and after rainfall, indicating that the slope remains stable.

(b) If one compares the results in Figure 3.50 to those in Figure 3.39, and one considers one case for a shallow failure surface, e.g. the case of elimination of suction, then the decrease in Factor of Safety from the initial value is greater in this example (in Figure 3.50), than in the previously considered example (Figure 3.39). The reason for this is the particular shape of the characteristic curves. In this example, the characteristic curves of the soil, particularly the moisture retention curve (Figure 3.41) are less steep than the ones in the example in Section 3.3.2.1 (Figure 3.26). As a result, the same change in moisture content causes a larger change in pressures. We can therefore conclude that soils with shallower characteristic curves, particularly moisture retention curves tend to develop larger pressures during a rainfall event, and so are less stable than soils with steeper characteristic curves.

(c) For the case of reduction of suction, i.e. in the case when the rainfall intensity was small, the critical failure surface in the slope remains located deep, at the soil bedrock interface. As rainwater infiltrates into the slope, it reduces the suction near the soil surface, and causes a reduction in strength, and hence a drop in Factor of Safety on a shallow failure surface. However, at no time during the rainfall event is this drop large enough so that the shallow failure surface is the critical one (see Figure 3.50). The critical surface on which the Factor of Safety is minimum remains located at the soil bedrock interface.

(d) The dissipation of positive pressures takes place at a faster rate than when suction is eliminated or reduced. This is because of the larger difference in head, which is the driving force for flow and redistribution.

(e) Following on what has been said in point 4, redistribution can take place at a slow rate after rainfall has ended. This can have significant consequences, specifically that the state of stability of a slope may decrease even after the end of rainfall. This is demonstrated in the following example.

Consider the slope shown in Figure 3.51.

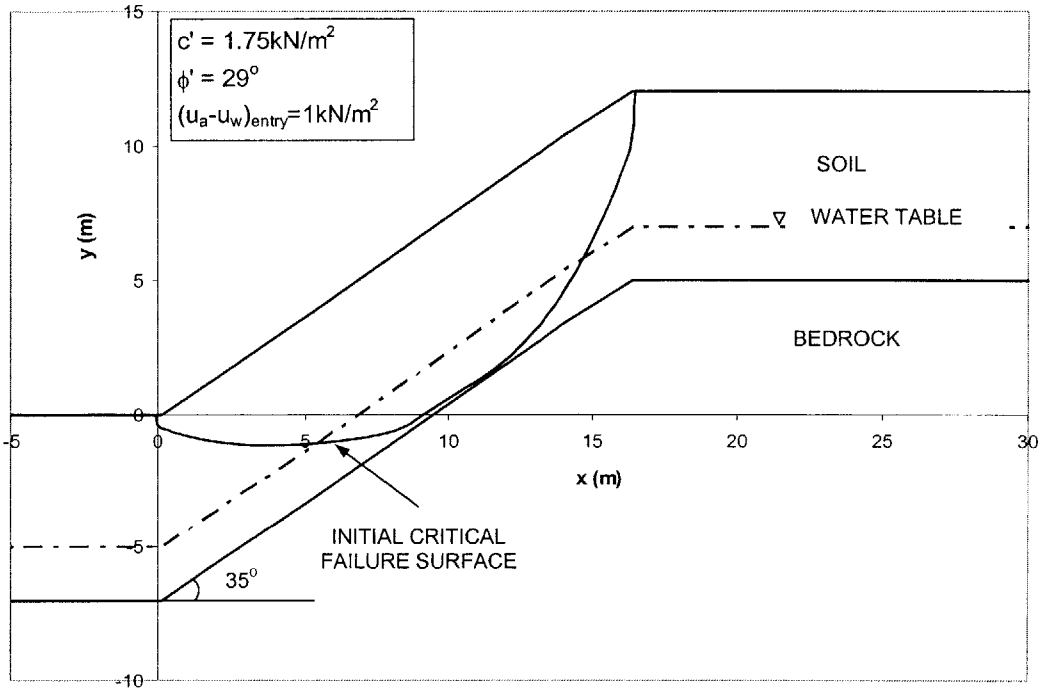

Figure 3.51. Slope Properties and Initial Critical Failure Surface

The soil strength parameters are shown in Figure 3.51. These strength parameters are greater than the ones of the soil considered in the example in Section 3.3.2.1, and shown in Figure 3.11.

The hydraulic parameters are assumed to be:

Saturated moisture content of soil $\theta_s = 0.47$. This is the same θ_s as in the example in Section 3.3.2.1.

Residual moisture content of soil $\theta_r = 0.11$ (See Figure 3.10). This is the same θ_r as in the example in Section 3.3.2.1.

Saturated conductivity $K_s = 2.89 \times 10^{-5} m/s$. This K_s is the same K_s as in the example in Section 3.3.2.1.

Specific storage coefficient $S_S = 0.002$ (see Chapter 2, Part 2-1). This S_S is different from the S_S in the example in Section 3.3.2.1, it is smaller.

The van Genuchten (1980) model is used to describe the soil characteristic curves with the parameters $n = 2.8$ and $\delta = 0.015$. The resulting characteristic curves are shown in Figures 3.52 and 3.53. The van Genuchten (1980) parameters considered in this example are different from the ones considered in the example in Section 3.3.2.1, and so the characteristic curves are also different. They are different in such a way that the characteristic curves in this example, particularly the moisture retention curve, has a slightly steeper slope than in example in Section 3.3.2.1 (compare Figures 3.52 and 3.53 to 3.14 and 3.15). The air entry pressure is smaller in this example than in the example in Section 3.3.2.1 (compare Figure 3.52 to 3.12).

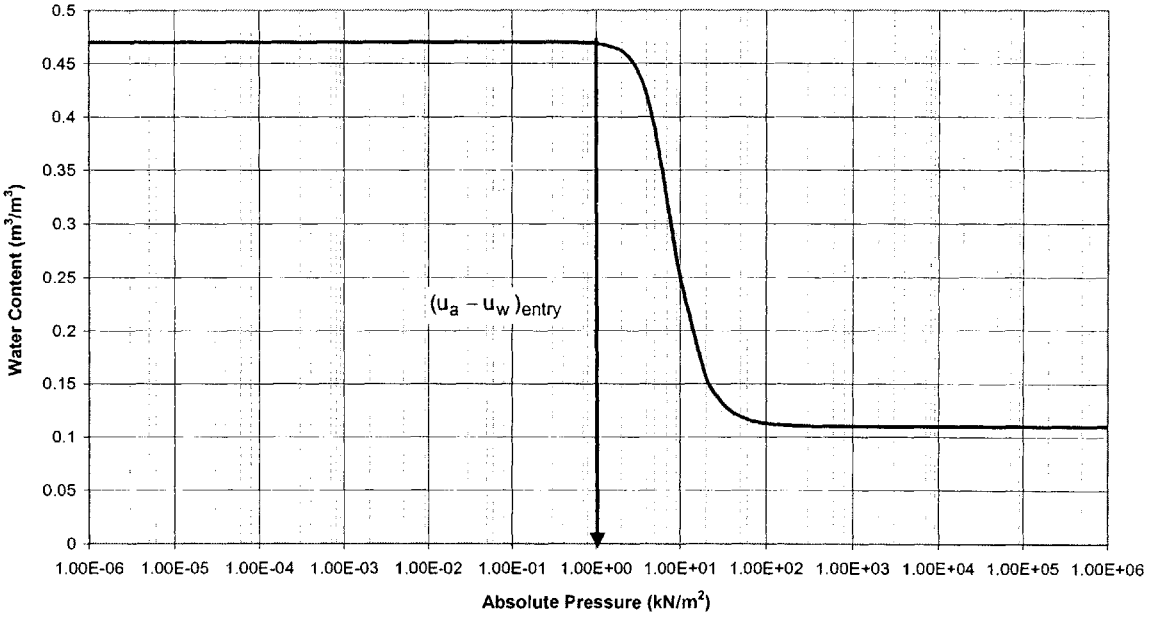

Figure 3.52. Moisture Retention Characteristic Curve

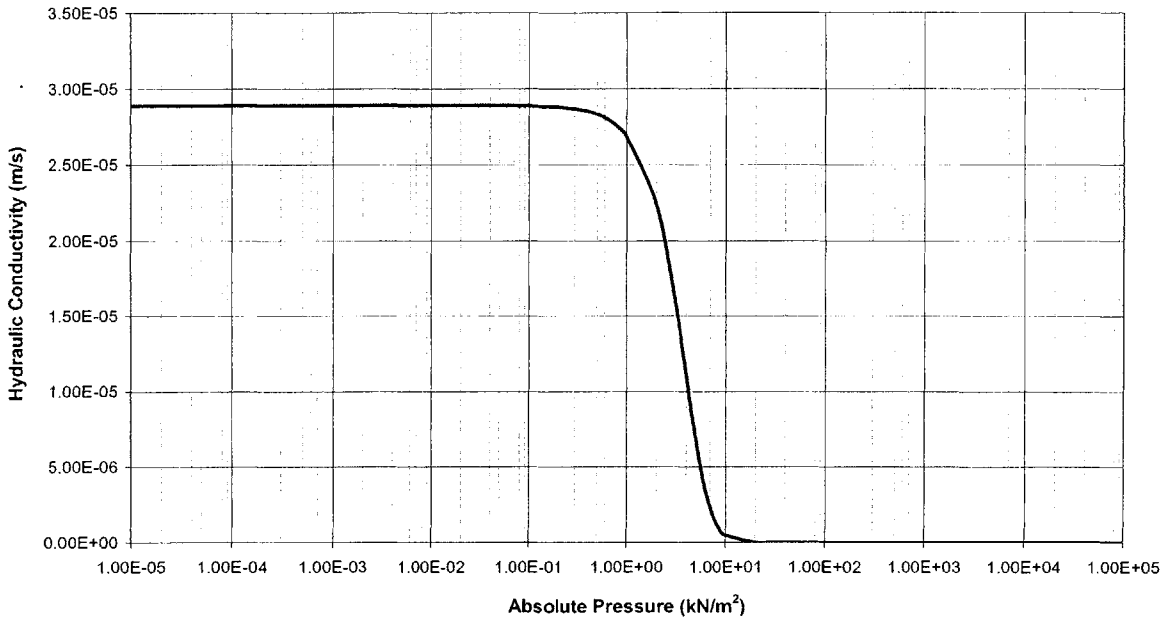

Figure 3.53. Hydraulic Conductivity Characteristic Curve

The initial state of stability of the slope is assessed, and a Factor of Safety of 1.2 is computed on the critical failure surface shown in Figure 3.51.

We now assume a rainfall of intensity $I = 105mm/hr$ takes place for duration of 4 hours. Note that this intensity is close in magnitude to the saturated conductivity of the soil. The resulting moisture content and pore pressures are shown in Figures 3.54 and 3.55.

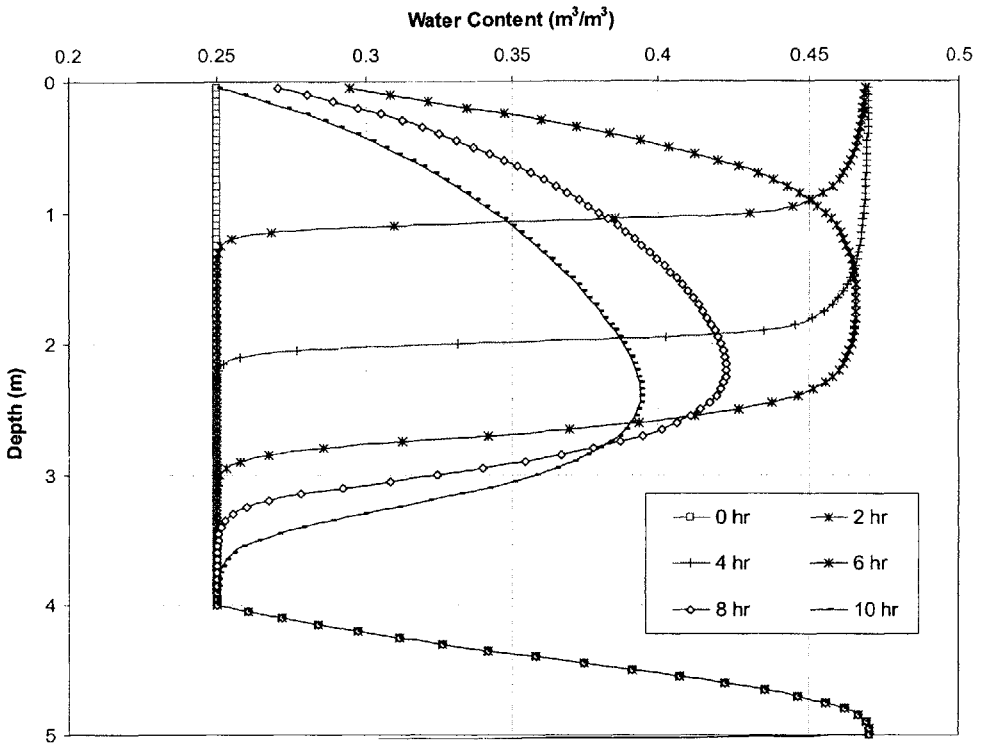

Figure 3.54. Moisture Content Profiles at Selected Times

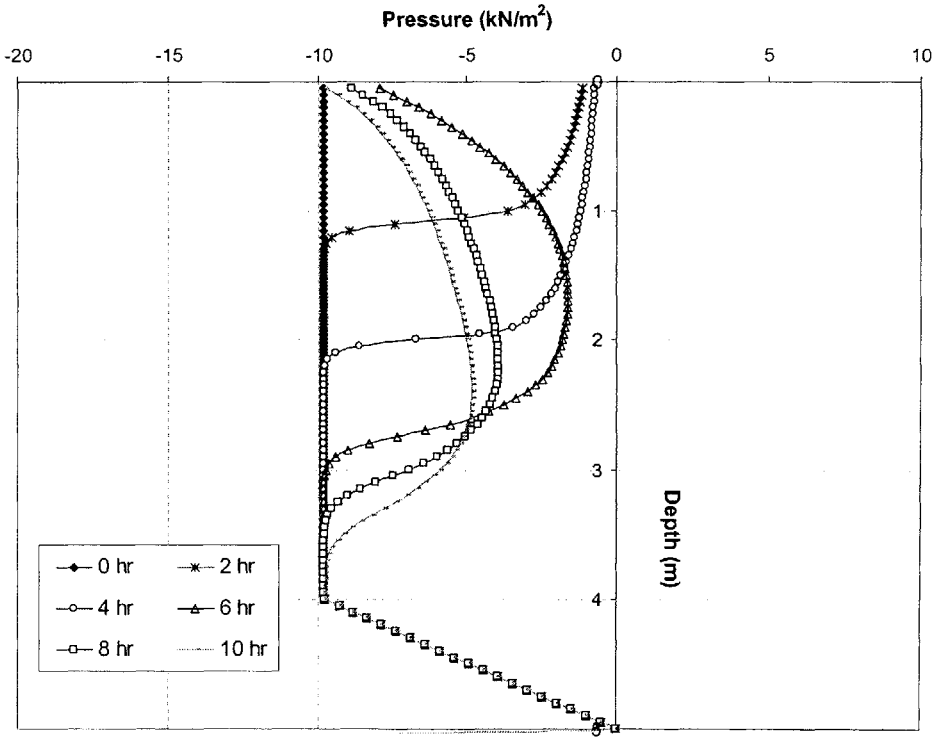

Figure 3.55. Pressure Head Profiles at Selected Times

Figures 3.54 shows that at early stages in the rainfall event, the soil near the surface is near saturation, since the moisture content is close to the saturated moisture content of the soil. Figure 3.55 shows that the initial negative pressures are eliminated during rain. An important observation is made with regard to Figures 3.54 and 3.55. After the cessation of rain at 4 hours, moisture (and pressure) redistribution takes place, e.g. at t = 6 and 8 hr. Because of the specific hydraulic properties of the soil, redistribution takes place at a slow rate, allowing pressures to continue to increase at significant depths below the ground surface. This allows large pressures to be maintained for a significant time after the end of rain.

The stability of the slope is assessed and the results are shown in Figure 3.56.

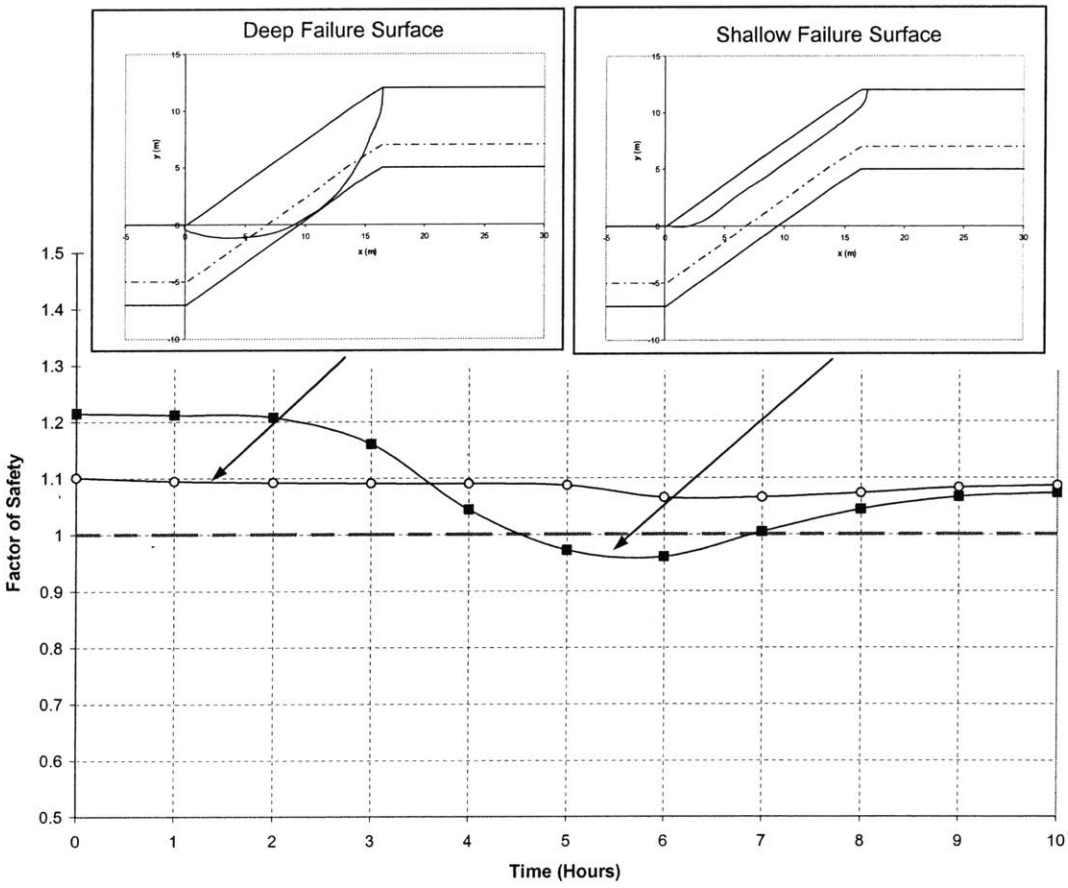

Figure 3.56. Variation of Factor of Safety with and Critical Failure Surfaces

Figure 3.56 shows that failure occurs, after the rain stops, at a time of about 4½ hours. Failure occurs as a result of the slow redistribution of moisture caused by the specific hydraulic properties of the soil. This is an important observation since the majority of current landslide studies tend to only asses the stability of a slope during rainfall, by using the maximum generated pressures in stability analyses. This is based on the assumption that failure will occur during the rainfall event, which is not necessarily the case as shown in this example. As a matter of fact, if one were to perform such analyses in this example, the slope would have been deemed stable. Hence, a complete landslide study should include stability analyses both during and after rainfall.

This mechanism can also explain field observations of failed slopes and landslides that have occurred after the cessation of rain, such as in the La Conchita, California Landslide that occurred in January 2005.

This example also reinforces what had been stated in the introduction of this chapter, namely that a critical combination of factors need not imply maximum pressures that develop during rain.

There are other mechanisms than those which were described in this section, by which positive pressures can be generated by infiltrating rainwater. These can occur in both homogenous and heterogeneous soils, and are described in the following sections. Note that these mechanisms are still classified as failures caused by the generation of positive pressures.

3.3.2.3.1. GRADUAL DEVELOPMENT OF LARGE PRESSURES (PERCHED WATER TABLE)

It is widely accepted that large (hydrostatic) positive pressures can develop when a lower conductivity soil layer, such as a clay layer, retards an infiltrating front. This leads to the development of a so-called perched water table above the lower conductivity layer. This mechanism is illustrated in this section. In addition, we also show that the

gradual development of positive pressures can occur in homogenous soils, a mechanism that has, for the most part, been overlooked in the literature.

3.3.2.3.1a. HETEROGENEOUS SOILS

When a low conductivity heterogeneity exists in the subsurface of an otherwise homogenous soil layer, infiltrating rainwater may be sufficiently retarded to allow for large (hydrostatic) positive pressures to develop. This positive pressure accumulation is known as a so called perched water table. This is shown schematically in Figure 3.57.

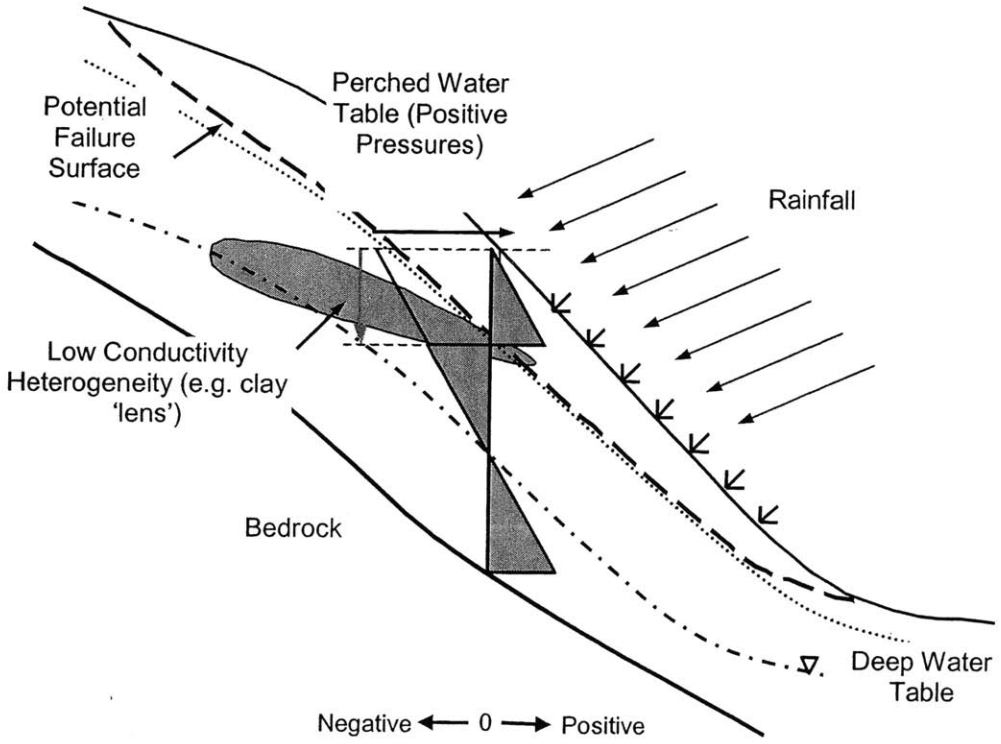

Figure 3.57. Illustration of Failure Mechanism (Perched Water Table in Heterogeneous Soil) (Negative, 0, Positive Indicate sign of pore pressures)

To illustrate the development of a perched water table, we consider the slope with geometric properties shown in Figure 3.58.

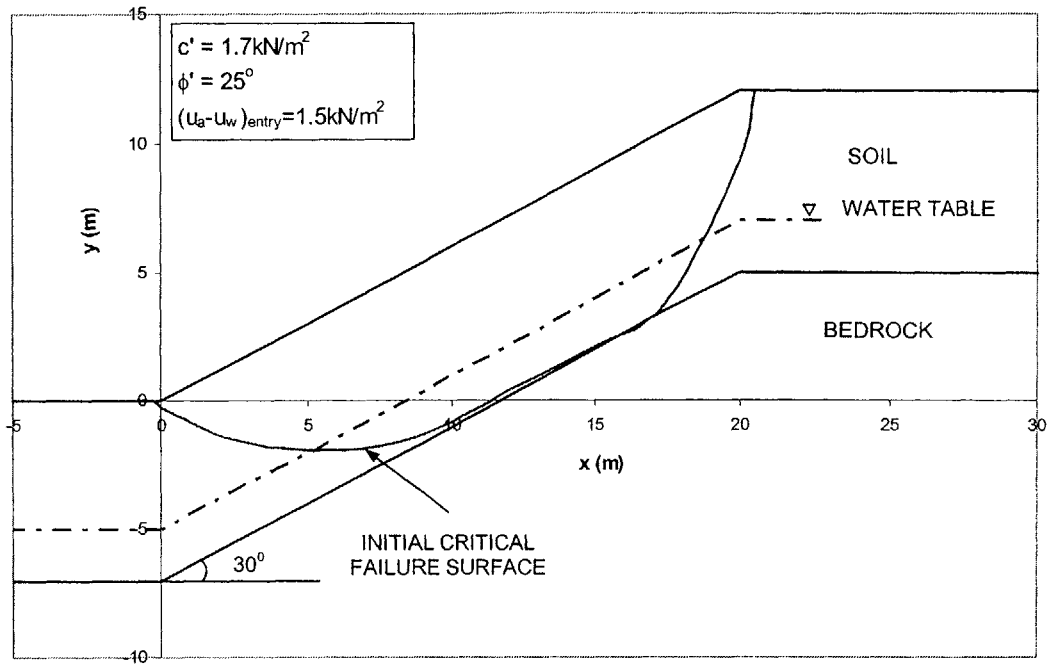

Figure 3.58. Slope Properties and Initial Critical Failure Surface

The soil strength parameters are shown in Figure 3.58, and while the angle of shear resistance is almost the same as the one in the example in Section 3.3.2.1, the cohesion is greater.

The hydraulic parameters are assumed to be:

Saturated moisture content of soil $\theta_s = 0.47$. This is the same θ_s as in the example in Section 3.3.2.1.

Residual moisture content of soil $\theta_r = 0.11$ (See Figure 3.10). This is the same θ_r as in the example in Section 3.3.2.1.

Saturated conductivity $K_s = 2.89 \times 10^{-5} m/s$. This K_s is the same K_s as in the example in Section 3.3.2.1.

Specific storage coefficient $S_s = 0.002$ (see Chapter 2, Part 2-1). This S_s is different from the S_s in the example in Section 3.3.2.1, it is smaller.

The van Genuchten (1980) model is used to describe the soil characteristic curves with the parameters $n = 1.5$ and $\delta = 0.01$. The resulting characteristic curves are shown in Figures 3.59 and 3.60. The van Genuchten (1980) parameters considered in this example are different from the ones considered in the example in Section 3.3.2.1, and so the characteristic curves are also different. They are different in such a way that the characteristic curves in this example, particularly the moisture retention curve, has a shallower (smaller) slope than in example in Section 3.3.2.1 (compare Figures 3.59 and 3.60 to 3.14 and 3.15). When this is the case, large changes in pressures take place for small changes in moisture content. The air entry pressure is smaller in this example than in the example in Section 3.3.2.1 (compare Figure 3.59 to 3.12).

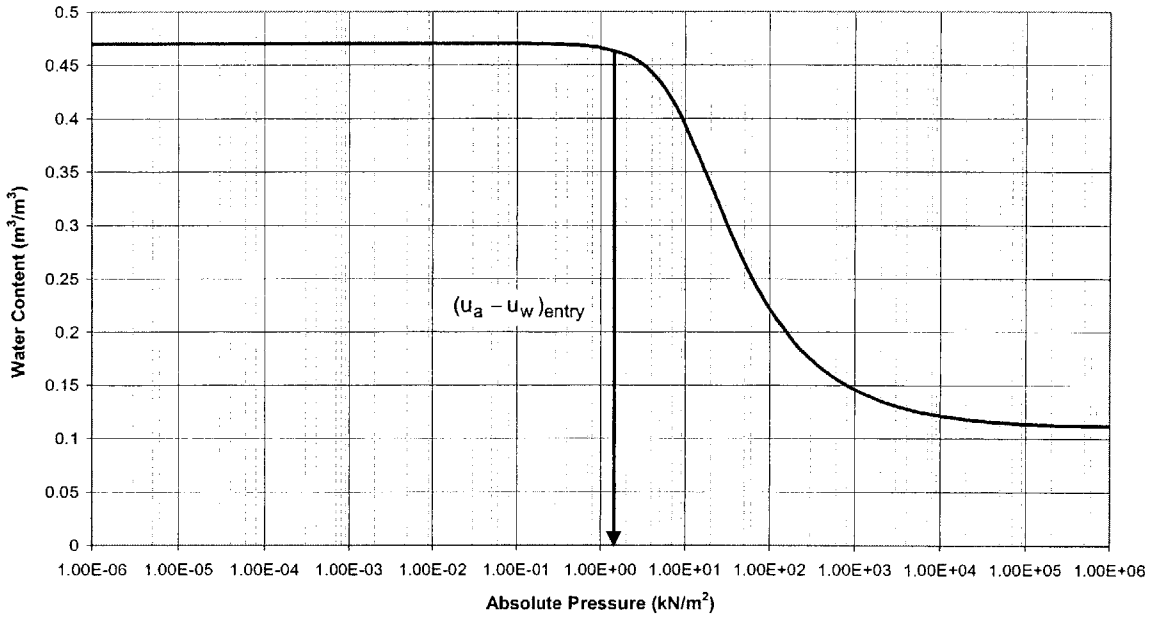

Figure 3.59. Moisture Retention Characteristic Curve

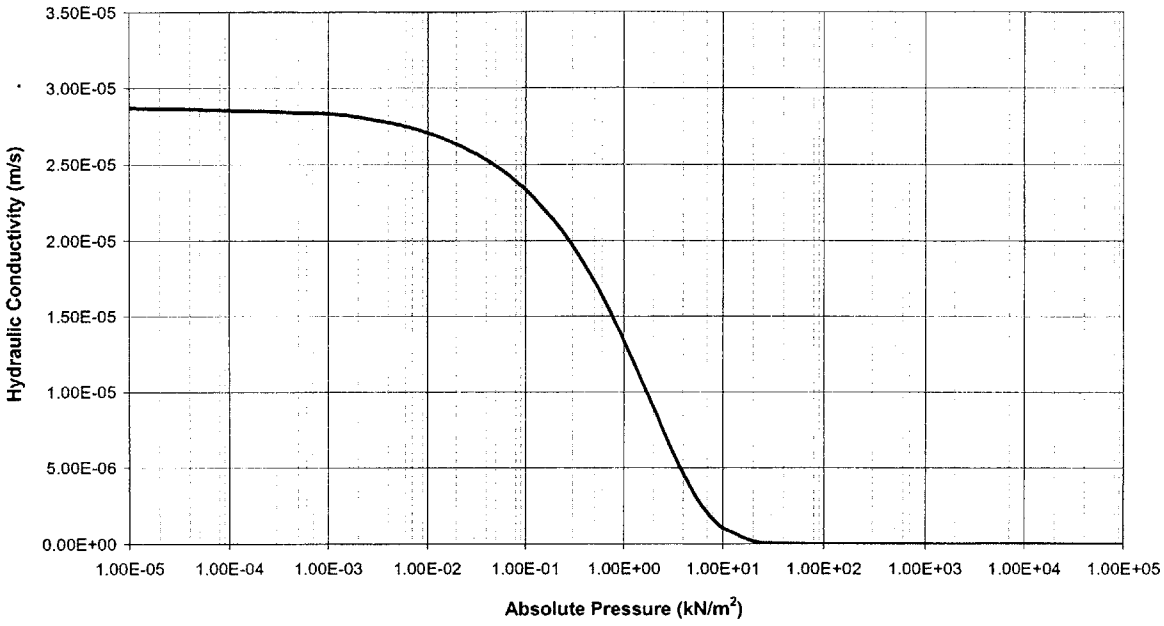

Figure 3.60. Hydraulic Conductivity Characteristic Curve

To investigate the effects of a low conductivity heterogeneity in the subsurface, we first consider a slope made up of a homogenous soil, with the strength parameters shown in Figure 3.58, and hydraulic parameters in Figures 3.59 and 3.60. We then compare the results of this case to the case when a low conductivity heterogeneity is present in the subsurface.

HOMOGENOUS SOIL LAYER

We assume an initial moisture content of $\theta_i = 0.37$, and assess the initial stability of the slope. A Factor of Safety of 1.17 is computed on the critical failure surface shown in Figure 3.58. The failure surface is located deep at the soil bedrock interface.

We now assume a rainfall event of intensity $I = 60\text{mm}/\text{hr}$ takes place for duration of 8 hours. This intensity is almost of the same magnitude as the saturated conductivity of the soil. The subsurface moisture content profiles and corresponding pore pressure distributions at various times are shown in Figures 3.61 and 3.62 respectively.

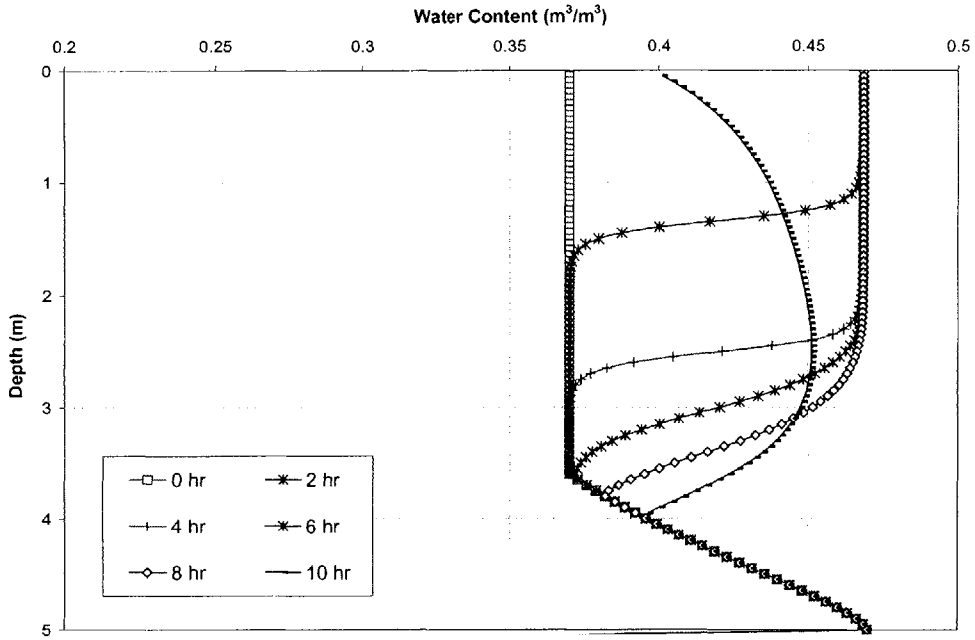

Figure 3.61. Moisture Content Profiles at Selected Times

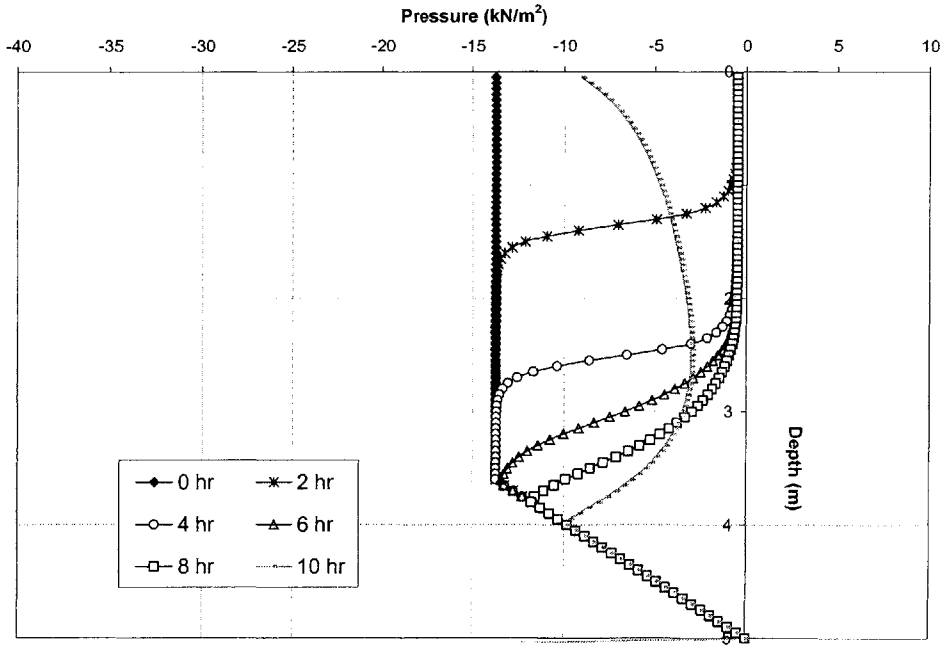

Figure 3.62. Pore Pressure Profiles at Selected Times

Figure 3.61 shows that a wetting front forms at early times during the rainfall event, with the soil at saturation. The wetting front migrates into the slope with time, eliminating the suction above the infiltrated zone. This is shown in Figure 3.62.

Figure 3.63 shows the variation of the Factor of Safety with time.

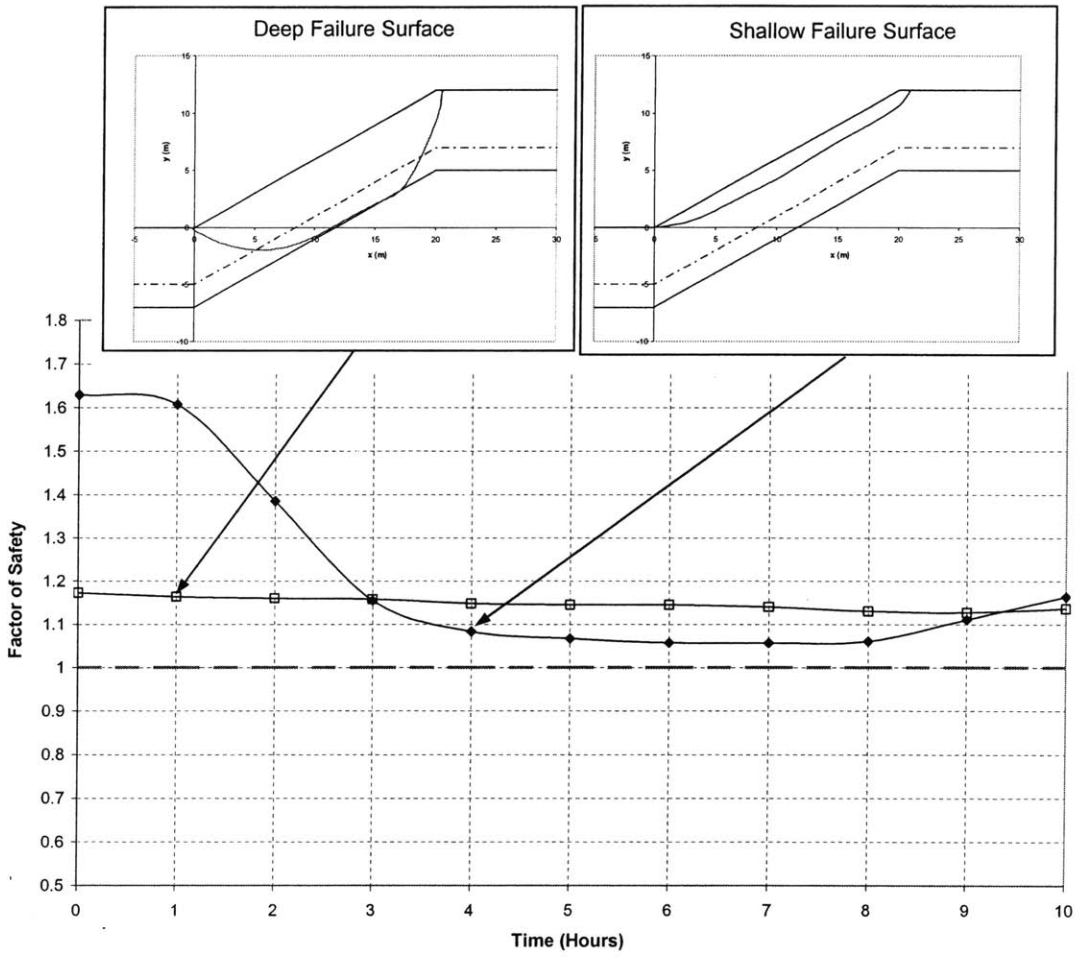

Figure 3.63. Variation of Factor of Safety with and Critical Failure Surfaces

Figure 3.63 shows that the Factor of Safety decreases with time as the rainwater eliminates suction in the infiltration zone. At a time of about 3 hours, the critical failure surface in the slope is shallow and translational located above the water table as shown in Figure 3.63. The Factor of Safety does however, remain above the value of one, and hence the slope remains stable throughout the rainfall event.

HETEROGENEOUS SOIL LAYER

We assume that a low conductivity heterogeneity of 0.5 m thickness is located at a depth of 1.5 m below the ground surface. We assume that the saturated conductivity of this heterogeneity is $K_S = 4 \times 10^{-6} m/s$. The variation of conductivity with depth is thus as shown in Figure 3.64.

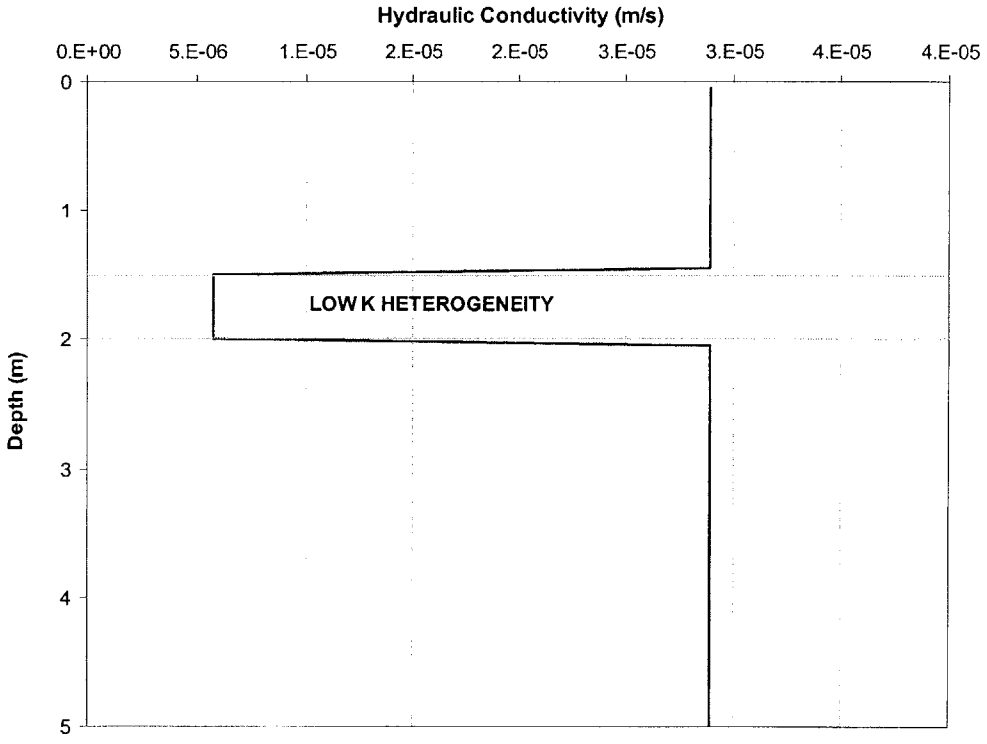

Figure 3.64. Saturated Conductivity Distribution in Soil

Because of the lower hydraulic conductivity in the heterogeneity, the hydraulic properties of the soil will be different to those in the surrounding soil. The characteristic curves of the heterogeneity are shown in Figures 3.65 and 3.66.

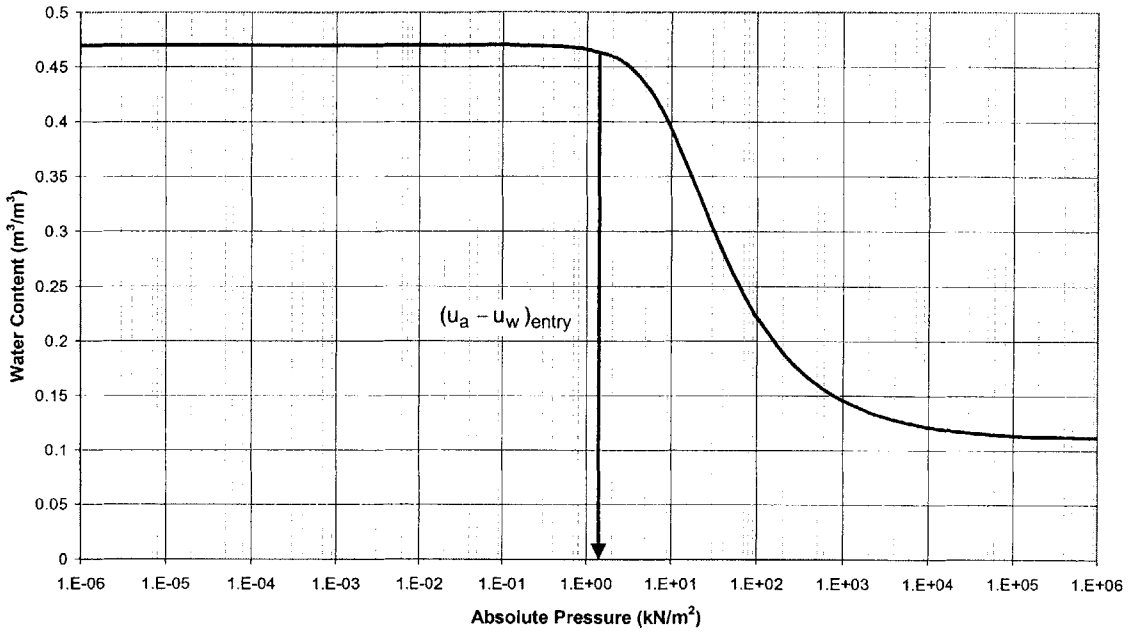

Figure 3.65. Moisture Retention Characteristic Curve

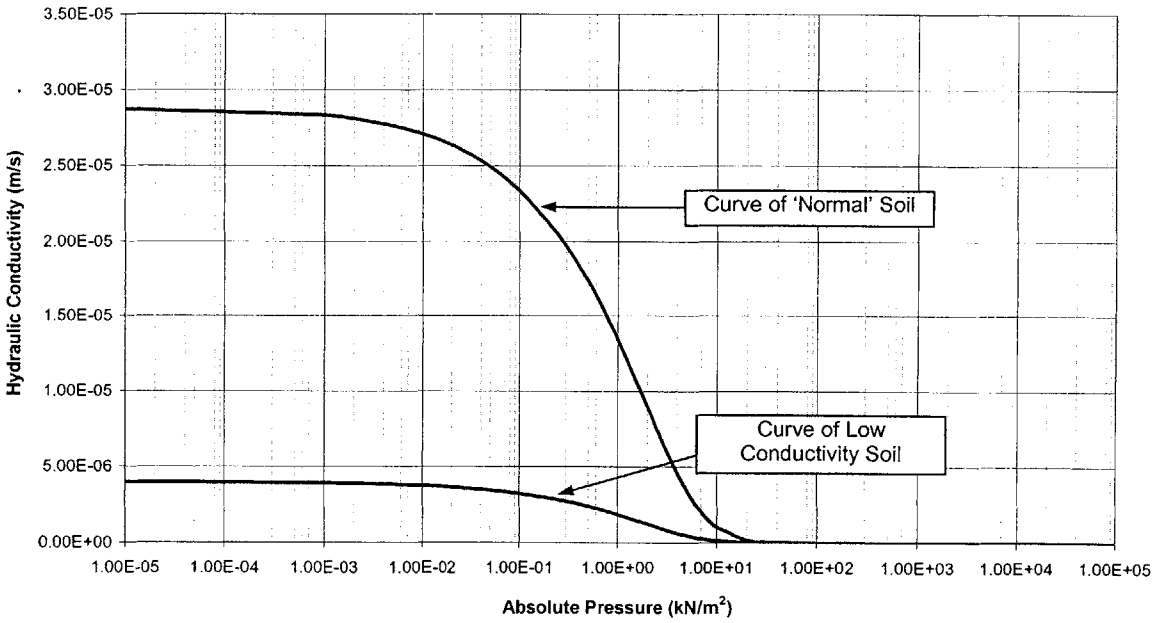

Figure 3.66. Hydraulic Conductivity Characteristic Curve

The moisture retention curve is the same in both soils because we have retained the van Genuchten (1980) parameters. The hydraulic conductivity curve is however different

because of the different saturated conductivity of the heterogeneity. This is show in Figure 3.66.

For clarity of discussion, the saturated strength properties of the heterogeneity are assumed to be the same as those of the surrounding soil. This, of course, need not be the case, and Chapter 2 illustrated how heterogeneous strength properties can be incorporated into the analyses.

We now assume a rainfall event of intensity $I = 60mm/hr$ takes place for duration of 8 hours. The subsurface moisture content profiles and corresponding pore pressure distributions at various times are shown in Figures 3.67 and 3.68 respectively.

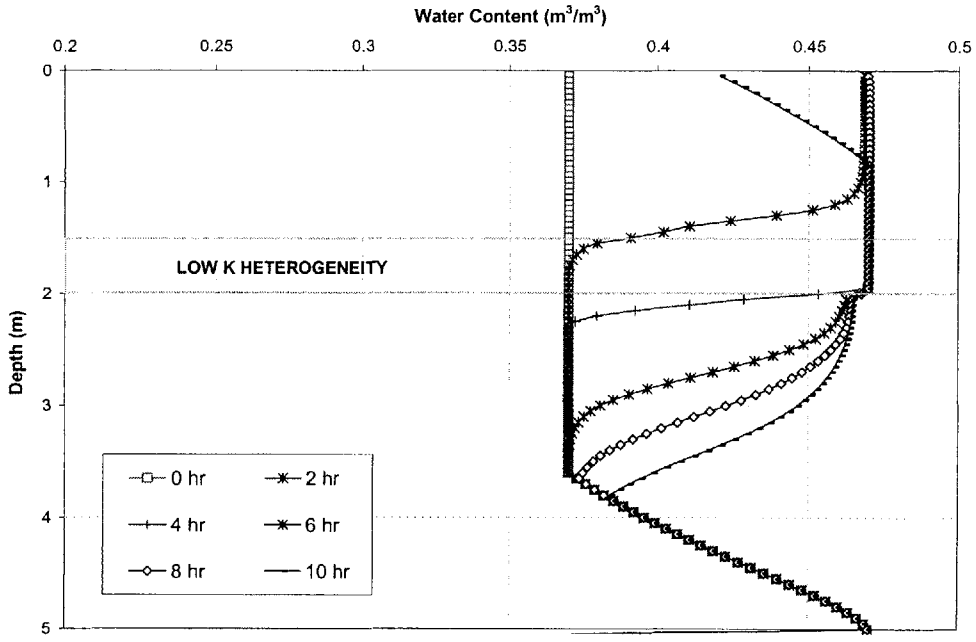

Figure 3.67. Moisture Content Profiles at Selected Times

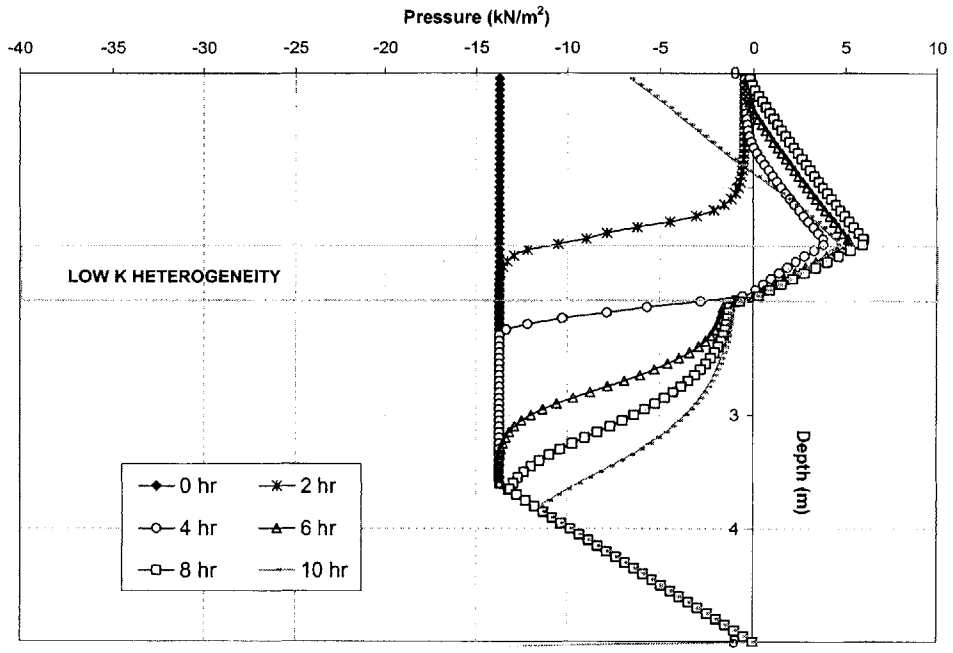

Figure 3.68. Pore Pressure Profiles at Selected Times

Figure 3.67 shows that in the presence of the heterogeneity, a wetting front develops and infiltrates into the slope. When the front reaches the heterogeneity, it is retarded by the lower conductivity heterogeneity. As this happens, the soil above the heterogeneity is at full saturation. Figure 3.68 shows that there is a pore pressure build up above the heterogeneity. As the wetting front is retarded by the heterogeneity, positive pressures develop above it, and these pressures increase with time. This is in contrast to the case when no heterogeneity was present, shown in Figure 3.62, where no positive pressures develop and suction is simply eliminated.

When the positive pressures become large in magnitude, and close to hydrostatic, a so-called perched water table is said to have developed. A temporal analysis is performed and the resulting variation of the Factor of Safety with time is shown in Figure 3.69.

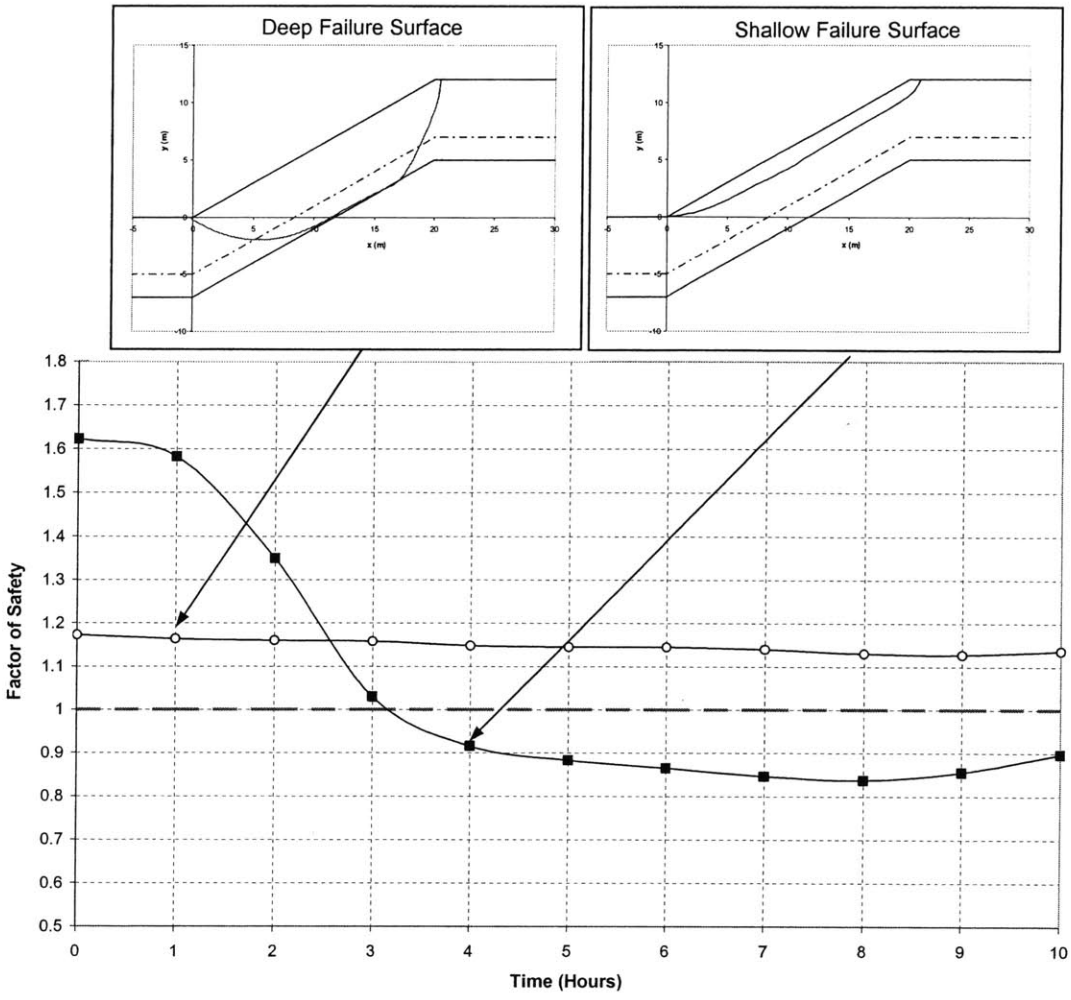

Figure 3.69. Variation of Factor of Safety and Critical Failure Surfaces with Time

Figure 3.69 shows that in the presence of the heterogeneity, the decrease in Factor of Safety is sufficient to cause failure, since it drops below a value of one. This occurs at a time of about 3 hours into the rainfall event. The critical failure surface is shallow, and located at a depth close to the hydraulic discontinuity (because of build up of pressures). The gradual development of positive pressures above a low conductivity heterogeneity causes sufficient loss of strength to generate a landslide.

3.3.2.3.1b. HOMOGENEOUS SOILS

It has been traditionally assumed that large positive pressures could only develop behind an infiltrating front if the front is retarded by a low conductivity heterogeneity as shown in Section 3.3.2.1. More recent studies however, have shown that large positive pressures may also develop in homogenous soil layers, where the saturated conductivity of the soil decreases with depth below the ground surface (e.g. Bevan, 1982; Bras, 1988). This decrease in conductivity is not infrequent, and can be attributed to a variety of factors which include the depositional processes involved in soil formation, desiccation and cracking of the soil surface, vegetation, etc. In this section, we show that the rate of decrease of conductivity can have important implications on the stability of a slope during a rainfall event. In particular, we show that in certain slopes, large positive pressures can develop resulting in a landslide. Various attempts have been made in the literature, to mathematically describe the variation of conductivity with depth (e.g. Bevan, 1982). Bevan (1982) relates the decrease of conductivity with depth using an exponential function, such that:

$$K_S(z) = K_S(z=0)\exp(-\lambda z) \qquad [3.2]$$

where:

λ is a constant

$K_S(z=0)$ is the saturated conductivity of the soil at the surface

Consider the slope shown in Figure 3.70.

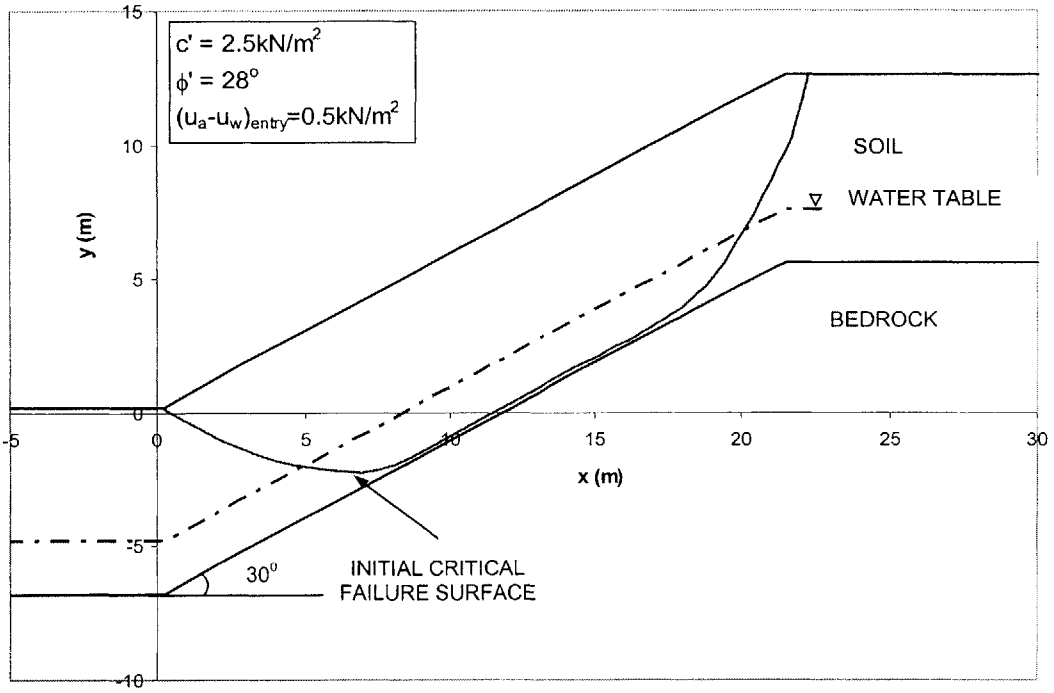

Figure 3.70. Slope Properties and Initial Critical Failure Surface

The soil strength parameters are shown in Figure 3.70. In this example, the cohesion is greater than that of the soil in Section 3.3.2.1.

The hydraulic parameters are assumed to be:

Saturated moisture content of soil $\theta_S = 0.47$. This is the same θ_S as in the example in Section 3.3.2.1.

Residual moisture content of soil $\theta_r = 0.11$ (see Figure 3.10). This is the same θ_r as in the example in Section 3.3.2.1.

Saturated conductivity $K_S = 2.89 \times 10^{-5} m/s$. This K_S is the same K_S as in the example in Section 3.3.2.1.

Specific storage coefficient $S_S = 0.001$ (see Chapter 2, Part 2-1). This S_S is different from the S_S in the example in Section 3.3.2.1, it is smaller.

The van Genuchten (1980) model is used to describe the soil characteristic curves with the parameters $n = 1.9$ and $\delta = 0.017$. The resulting characteristic curves are shown in Figures 3.71 and 3.72. The van Genuchten (1980) parameters considered in this example are different from the ones considered in the example in Section 3.3.2.1, and so the characteristic curves are also different. They are different in such a way that the characteristic curves in this example, particularly the moisture retention curve, has a shallower (smaller) slope than in example in Section 3.3.2.1 (compare Figures 3.71 and 3.72 to 3.14 and 3.15). When this is the case, large changes in pressures take place for small changes in moisture content. The air entry pressure is smaller in this example than in the example in Section 3.3.2.1 (compare Figure 3.71 to 3.12).

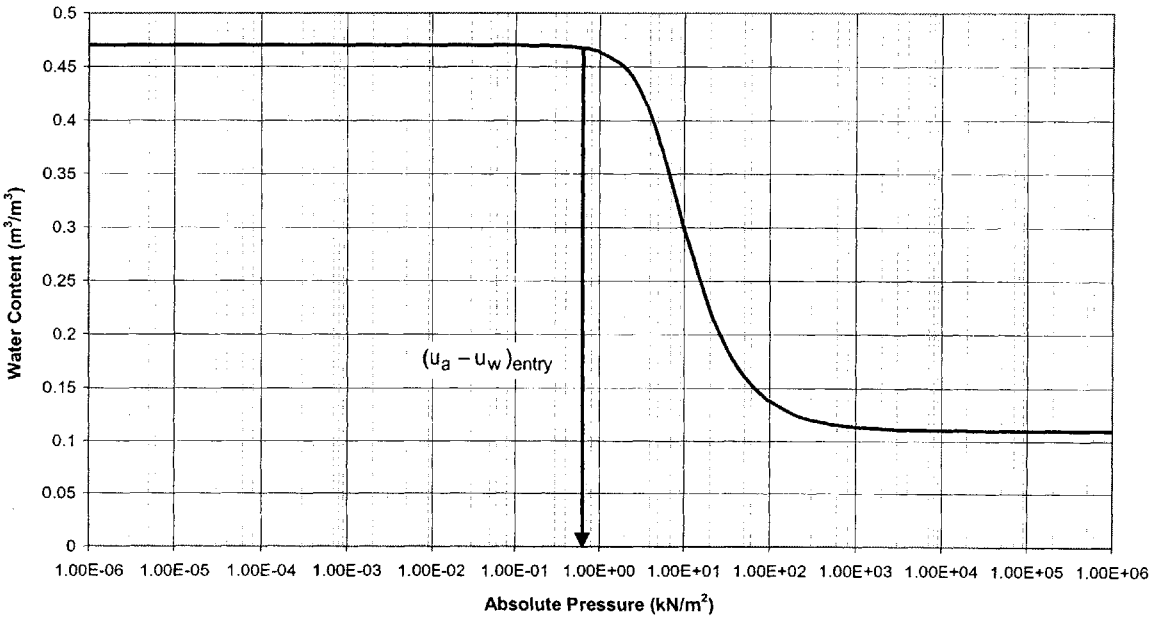

Figure 3.71. Moisture Retention Characteristic Curve

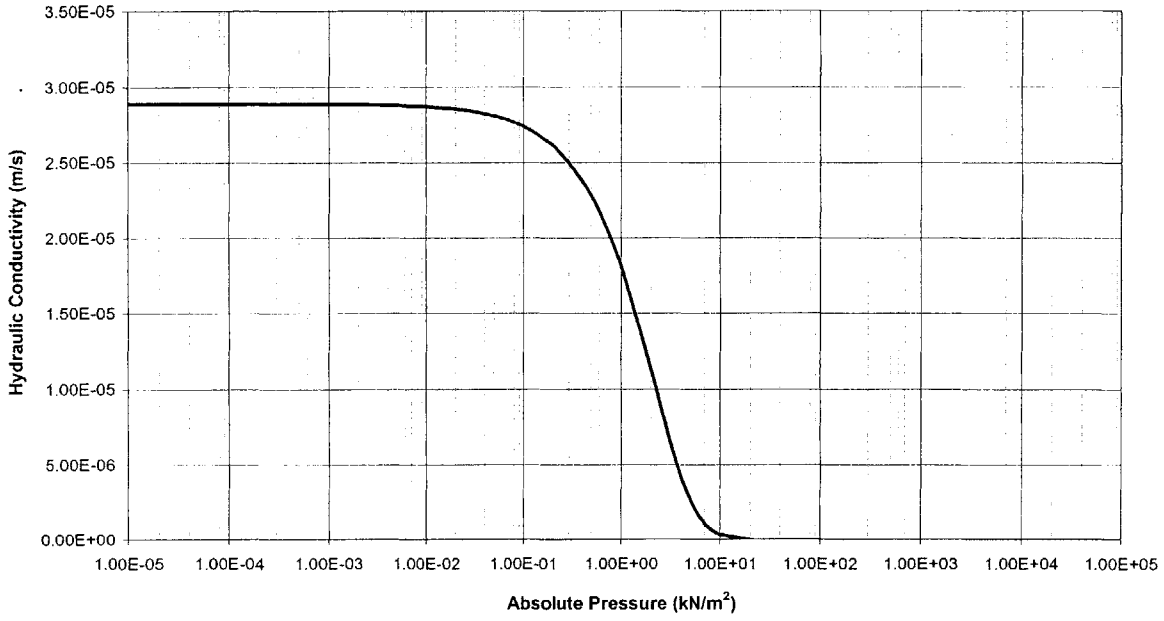

Figure 3.72. Hydraulic Conductivity Characteristic Curve

To investigate the effects of decreasing saturated conductivity of the soil with depth below the ground surface, we first consider a slope made up of a soil with constant saturated conductivity with depth. We then compare the results of this case to the case when the saturated conductivity decreases with depth below the ground surface.

CONSTANT SATURATED CONDUCTIVITY SOIL

We assume an initial moisture content of $\theta_i = 0.38$ and asses the initial state of stability of the slope. The critical surface is shown in Figure 3.70, and a Factor of Safety of 1.21 is computed.

We now assume a rainfall event of intensity $I = 40mm/hr$ for a duration 8 hours. The moisture content and pore pressure profiles at selected times are shown in Figures 3.73 and 3.74 respectively.

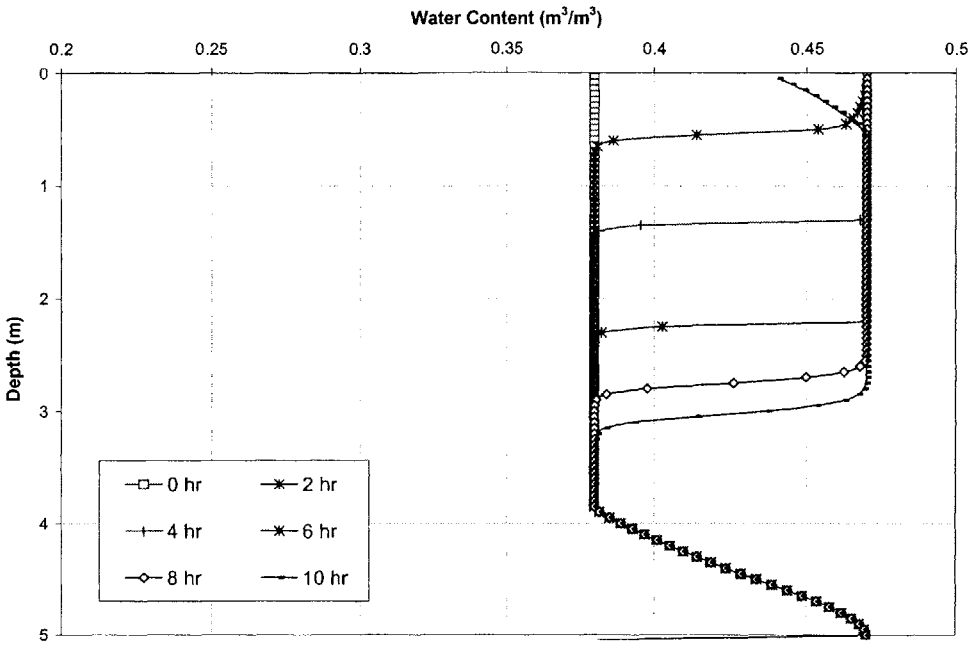

Figure 3.73. Moisture Content Profiles at Selected Times

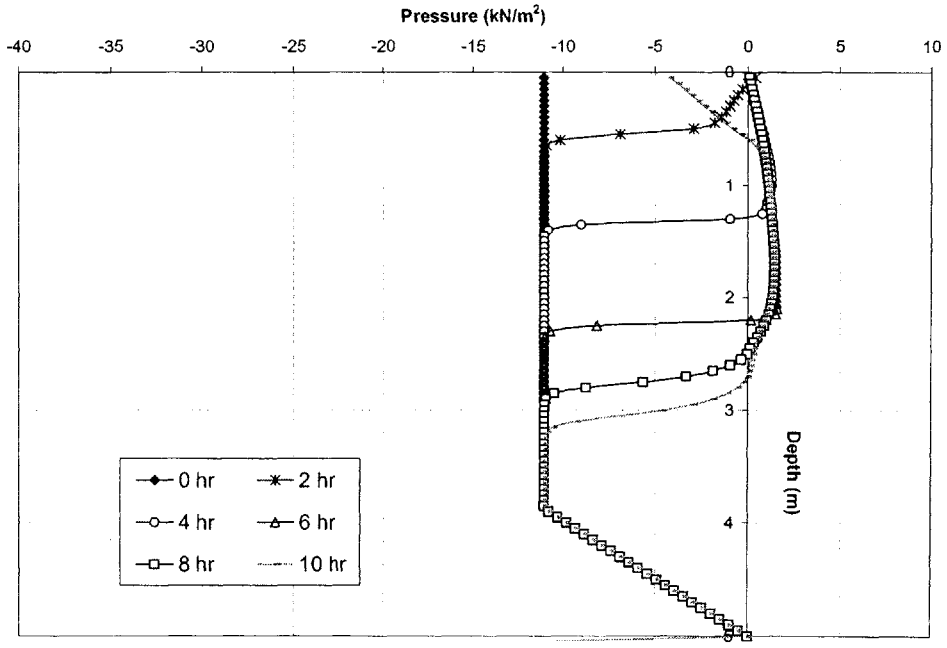

Figure 3.74. Pore Pressure Profiles at Selected Times

Figure 3.73 shows that the rainfall event causes the saturation of the slope at the surface. A wetting front forms, and travels downwards with time and rainfall. Small positive pressures develop behind the infiltrating front as is shown in Figure 3.74. The stability of the slope during the rainfall event is assessed, and the variation of Factor of Safety with time is shown in Figure 3.75.

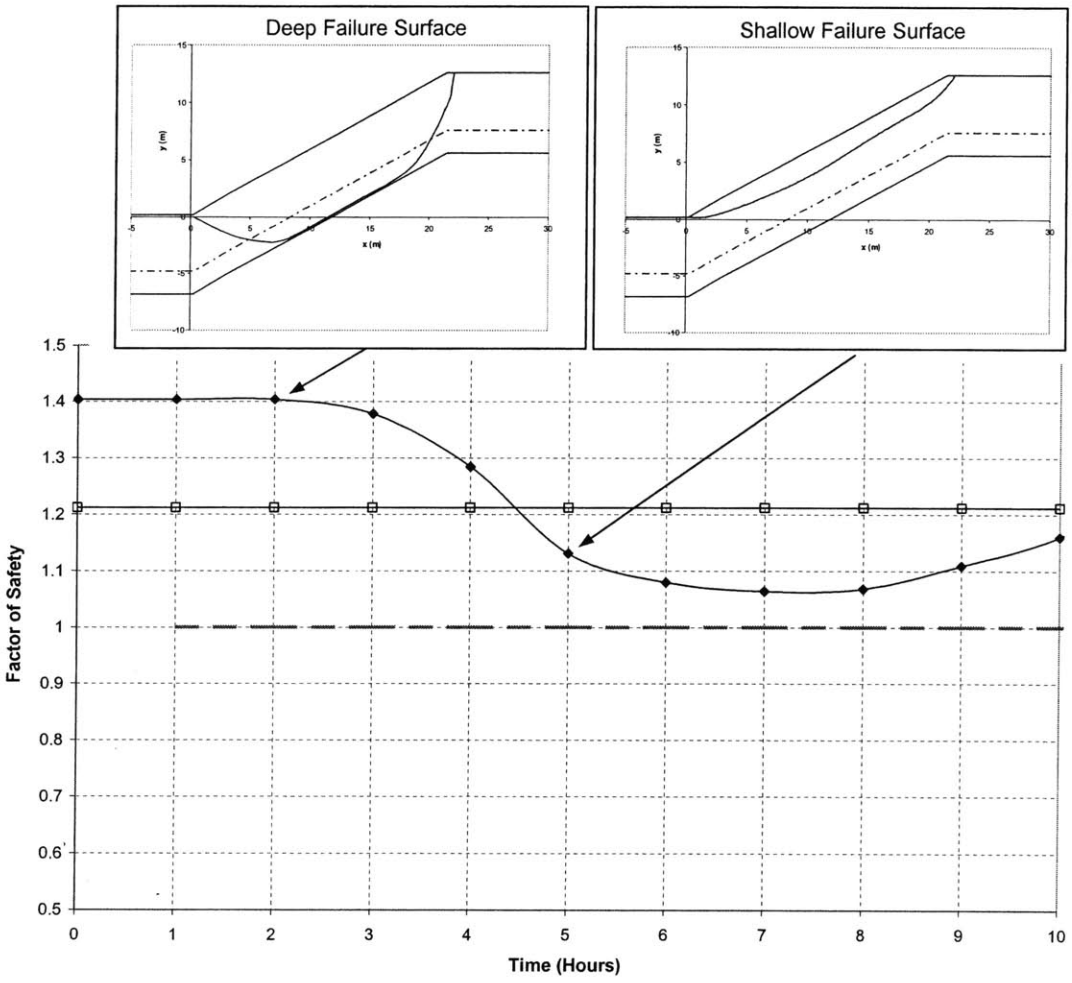

Figure 3.75. Variation of Factor of Safety with Time and Critical Failure Surfaces

Figure 3.75 shows that initially the critical failure surface is located at the soil bedrock interface, and the slope is stable. As it rains, there is a decrease in the Factor of Safety, and at a time of about 4 ½ hours, the critical failure surface in the slope becomes

shallow, and located above the water table. The Factor of Safety continues to decrease with time, but remains above the value of one, and so the slope remains stable during the rainfall event.

DECREASING SATURATED CONDUCTIVITY SOIL

We now assume that the saturated conductivity of the soil decreases with depth. We adopt the relationship proposed by Bevan (1982) for saturated conductivity, and assume that $K_S(z=0) = 2.9 \times 10^{-5} m/s$ and the constant $\lambda = 1.15 \times 10^{-5}\ m^{-1}$ so that $K_S(z)$ is assumed to decrease exponentially with depth as shown in Figure 3.76.

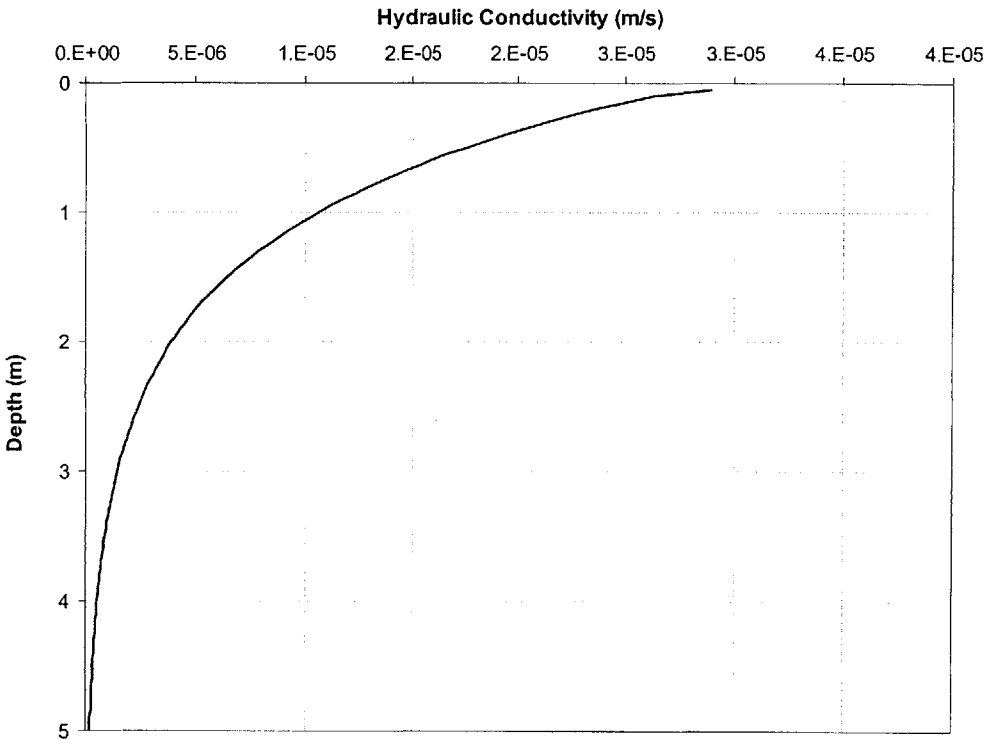

Figure 3.76. Assumed Variation of Saturated Conductivity with Depth Below Ground Surface

Furthermore, we assume that all other soil properties remain constant with depth below the ground surface, and the only variable is the saturated conductivity of the soil. The moisture retention curve will, therefore remain the same as the original soil moisture retention curve and is shown in Figure 3.77. The soil hydraulic conductivity characteristic

curve will, on the other hand, vary with depth depending on the saturated conductivity. This is shown in Figure 3.78.

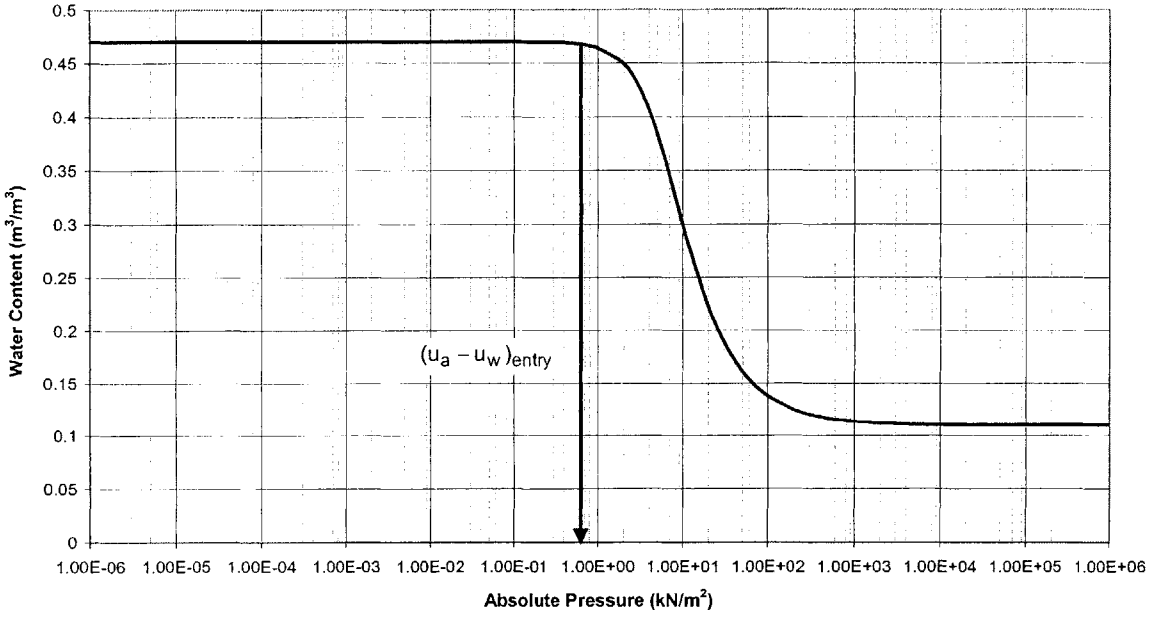

Figure 3.77. Moisture Retention Characteristic Curve

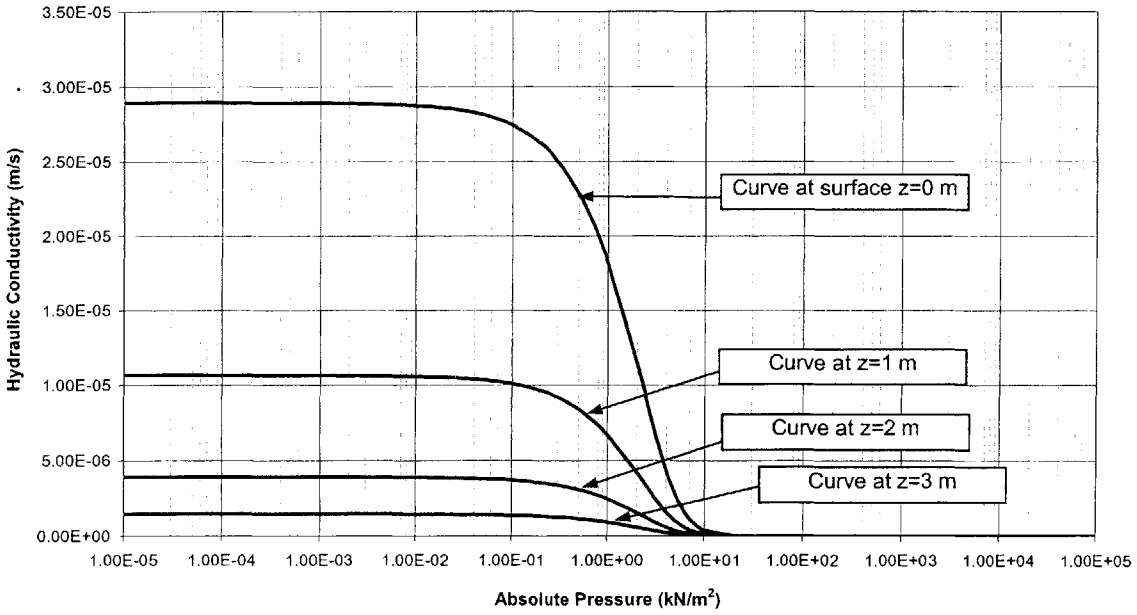

Figure 3.78. Hydraulic Conductivity Characteristic Curve

We now assume the same rainfall event of intensity $I = 40mm/hr$ for a duration 8 hours. The moisture content and pore pressure profiles at selected times are shown in Figures 3.79 and 3.80 respectively.

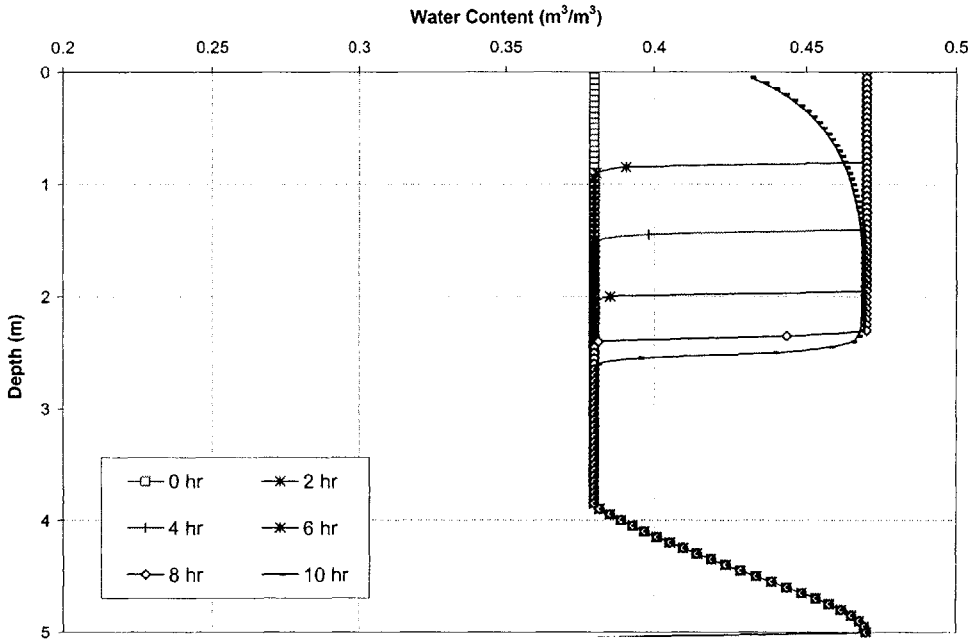

Figure 3.79. Moisture Content Profiles at Selected Times

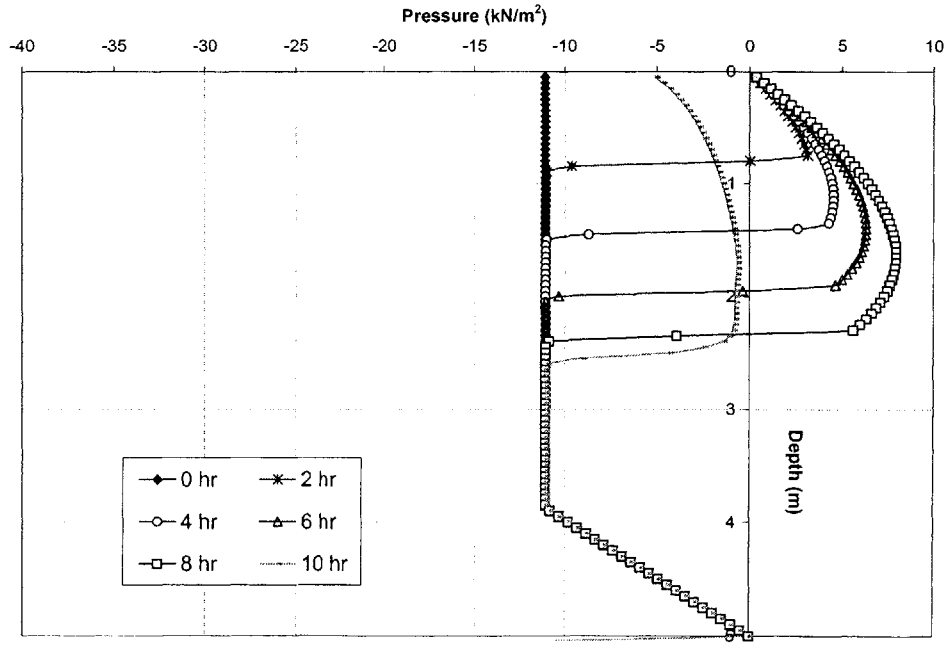

Figure 3.80. Pore Pressure Profiles at Selected Times

Figure 3.79 shows that a wetting front develops, and migrates down the slope with time. Figure 3.80 shows that large positive pressures develop behind the infiltrating front. These pressures develop gradually, and slowly increase with time. The rate and magnitude of this increase is dependent on the rate of decrease of conductivity with depth. This illustrates that large positive pressures (limiting to a perched water table) can develop without the necessity of the presence of a low conductivity layer, as has been commonly assumed in many landslide studies.

The stability of the slope is assessed, and the variation of Factor of Safety with time is shown in Figure 3.81.

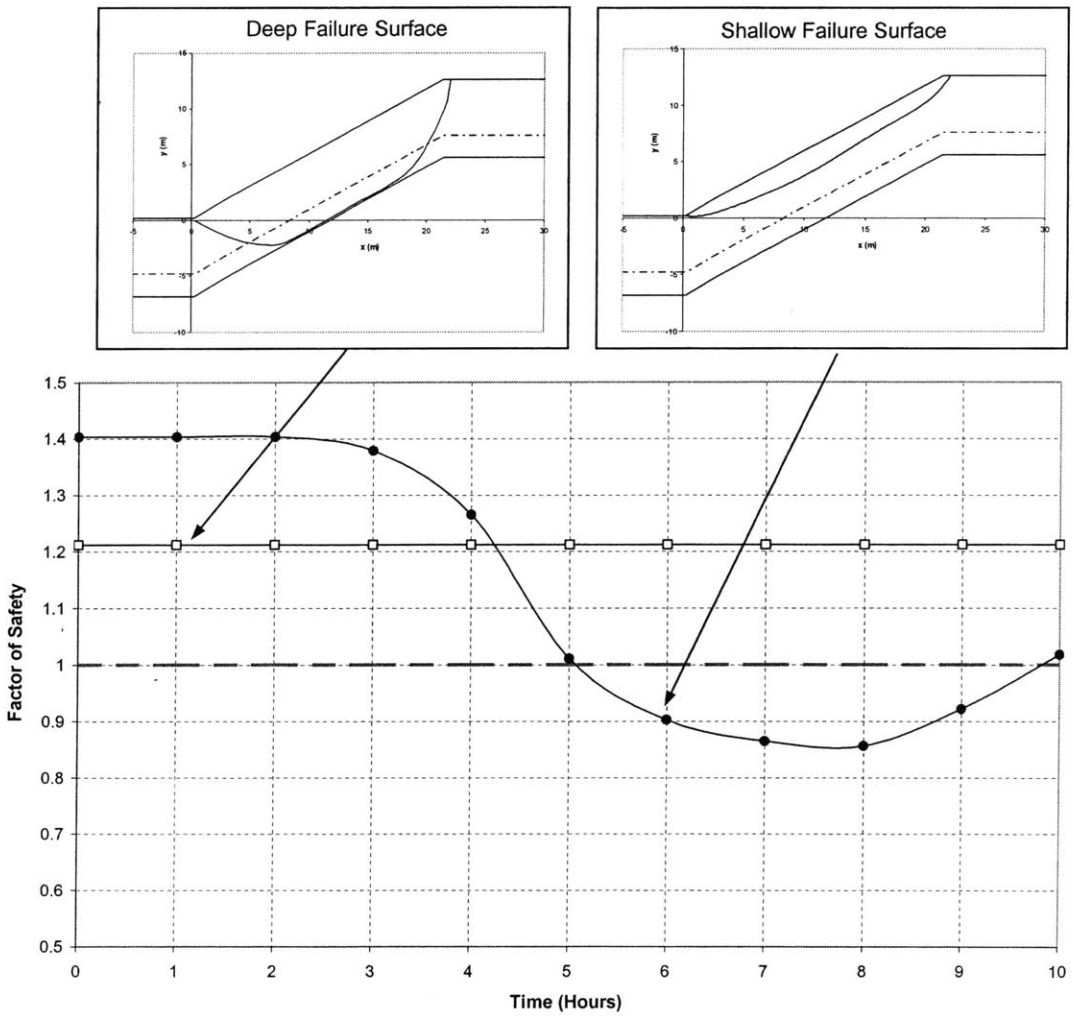

Figure 3.81. Variation of Factor of Safety and Critical Failure Surfaces with Time

Figure 3.81 shows that initially the critical failure surface is located at the soil bedrock interface. The Factor of Safety then decreases with time, and failure takes place at a time of about 5 hours. Failure occurs along a shallow failure surface that is located above the water table. This is shown in Figure 3.81.

Figure 3.82 compares the variation of Factor of Safety with time in both cases when the hydraulic conductivity is constant with depth and when it decreases.

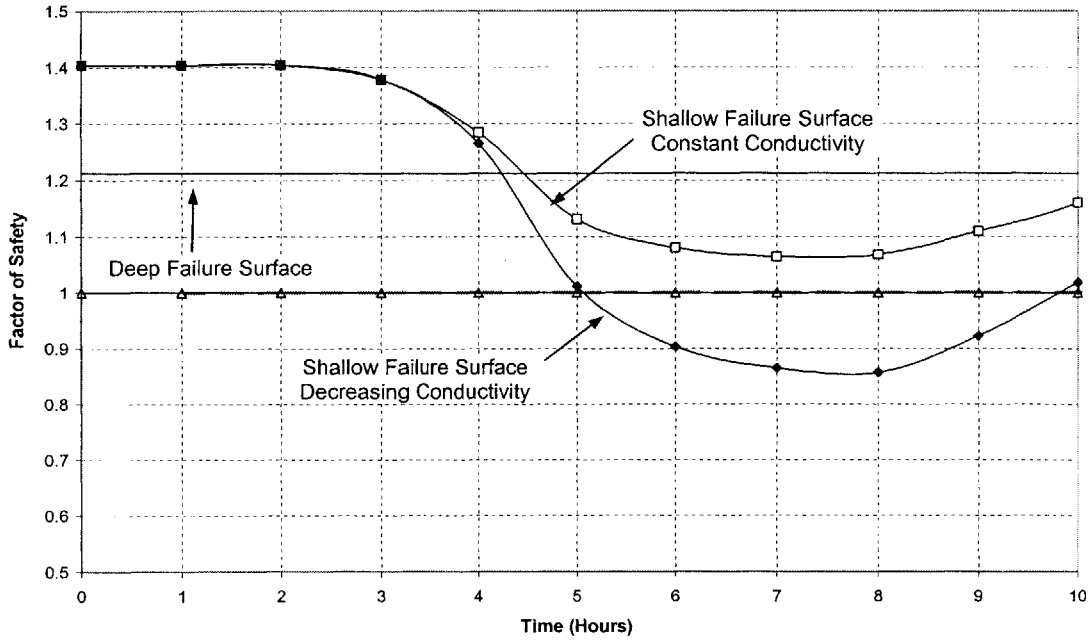

Figure 3.82. Comparison of Variation of Factor of Safety with Time for Constant and Decreasing Conductivity with Depth

Figure 3.82 clearly shows that failure occurs in the case when the hydraulic conductivity decreases with depth. This is because of the large positive pressures that are generated behind the infiltrating front. These pressures reduce the soil strength sufficiently to generate a shallow landslide.

3.3.2.3.2. SUDDEN DEVELOPMENT OF LARGE PRESSURES

The landslide mechanisms described thus far have been based on the gradual increase of pressures caused by infiltrating rainwater. There have, however, been several field observations and reports of the sudden occurrence of landslides documented in the literature, e.g. Lambe (1980), Torres et al. (1998). The mechanisms of such landslides are not understood. In this section, we propose a possible mechanism to explain the sudden occurrence of such slides.

Figure 3.83a shows an initial pressure distribution in a slope. If during a short, intense rainfall, the rate of infiltration is equal to the potential infiltration rate (saturated hydraulic conductivity), suction is eliminated down to a certain depth (Figure 3.83b). Suppose that the rainfall intensity suddenly exceeds the infiltration rate, whether due to a rapid increase in intensity (not uncommon given the high natural temporal variability of rainfall events), or a rapid decrease in conductivity (for the possible reasons explained Section 3.3.2.1) or a combination of both.

Large positive pressures (approaching hydrostatic) rapidly develop behind the wetting front as illustrated in Figure 3.83c, and may cause an associated sudden failure. This phenomenon which was observed by Lambe (1980), and Torres et al. (1998) cannot be explained by the usual gradual change from negative to hydrostatic pressure conditions. Moreover, this phenomenon can occur in homogenous soils without the requirement of a low permeability layer to retard the front, as will be illustrated in this section.

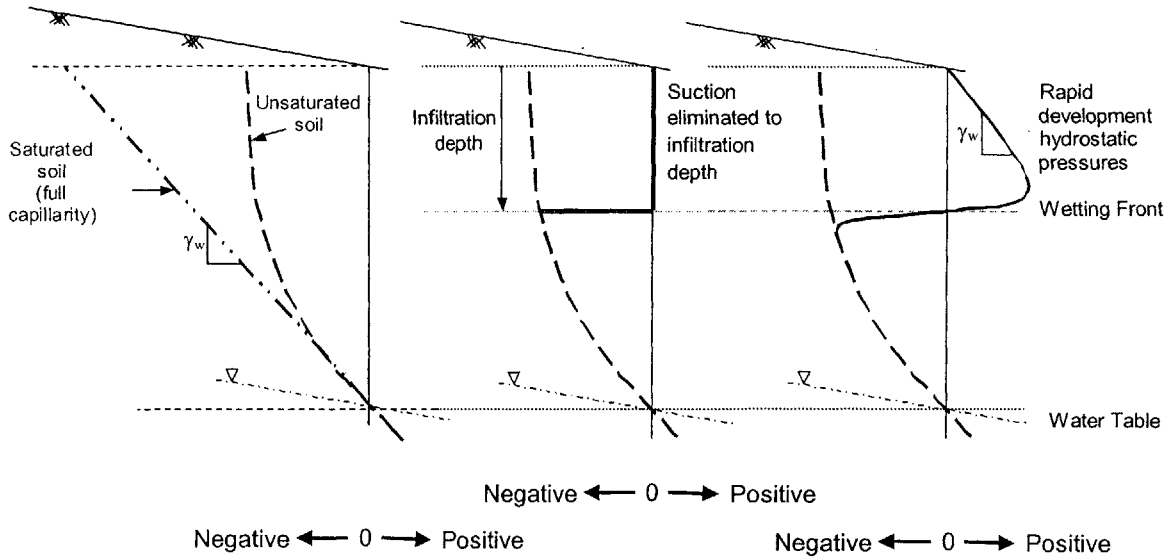

Figure 3.83a. Initial Pore Pressure Distribution

Figure 3.83b. Pore Pressure Distribution if Infiltration Rate Equal to Rainfall Intensity

Figure 3.83c. Rapid Development of Hydrostatic Pressures as Rainfall Intensity Exceeds Infiltration Rate

Figure 3.83. Sudden Generation of Hydrostatic Pressures (Negative, 0, Positive Indicate sign of pore pressures)

To numerically illustrate this mechanism, consider the slope with geometric and strength properties shown in Figure 3.84.

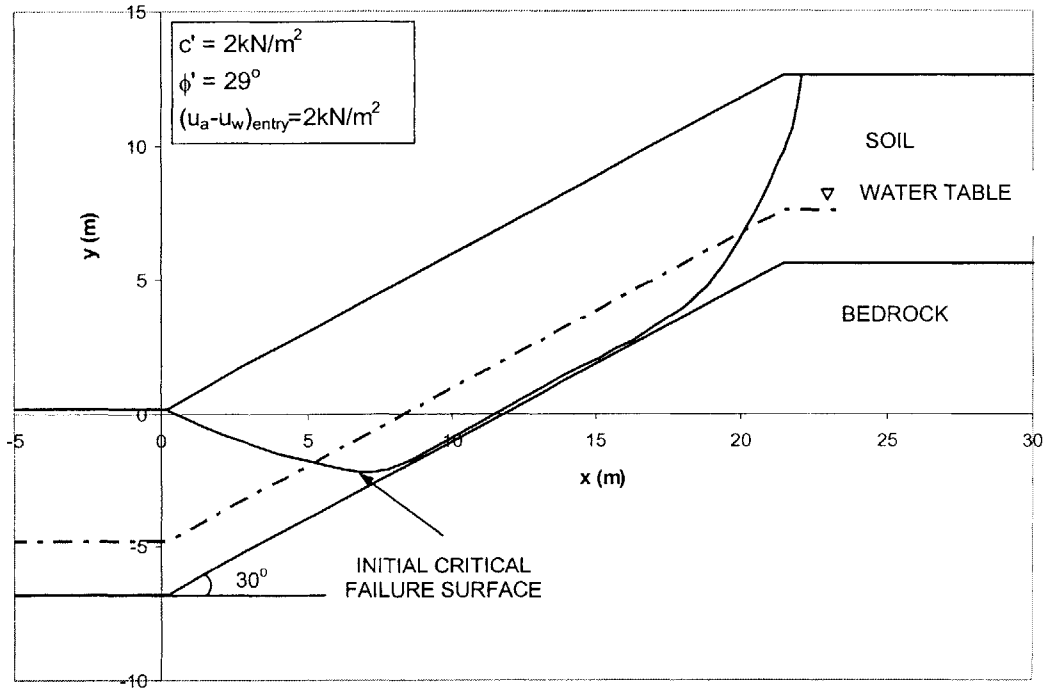

Figure 3.84. Slope Properties and Initial Critical Failure Surface

The soil strength parameters are shown in Figure 3.84. In this example, the cohesion and the angle of shearing resistance of the soil are greater than that of the soil in Section 3.3.2.1.

The hydraulic parameters are assumed to be:

Saturated moisture content of soil $\theta_s = 0.47$. This is the same θ_s as in the example in Section 3.3.2.1.

Residual moisture content of soil $\theta_r = 0.11$ (see Figure 3.10). This is the same θ_r as in the example in Section 3.3.2.1.

Saturated conductivity $K_s = 2.3 \times 10^{-5} m/s$. This K_s is smaller than the K_s of the soil in the example in Section 3.3.2.1.

Specific storage coefficient $S_s = 0.0025$ (see Chapter 2, Part 2-1). This S_s is different from the S_s in the example in Section 3.3.2.1, it is smaller.

The van Genuchten (1980) model is used to describe the soil characteristic curves with the parameters $n = 1.05$ and $\delta = 0.017$. The resulting characteristic curves are shown in Figures 3.85 and 3.86. The van Genuchten (1980) parameters considered in this example are different from the ones considered in the example in Section 3.3.2.1, and so the characteristic curves are also different. They are different in such a way that the characteristic curves in this example, particularly the moisture retention curve, has a significantly shallower (smaller) slope than in example in Section 3.3.2.1 (compare Figures 3.85 and 3.86 to 3.14 and 3.15). Because of this, small changes in soil moisture can cause very large changes in pressures. The hydraulic conductivity curve is also significantly shallower, and this is shown in Figure 3.86, which is to the same scale as Figure 3.13. The air entry pressure is the same in this example than in the example in Section 3.3.2.1 (compare Figure 3.85 to 3.12).

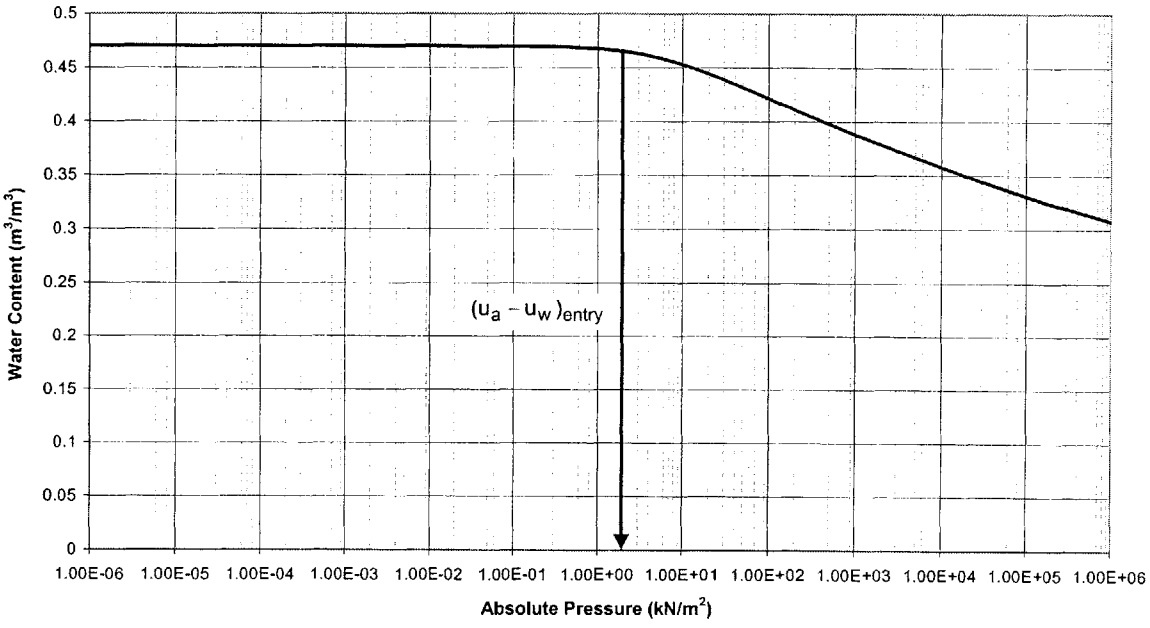

Figure 3.85. Moisture Retention Characteristic Curve

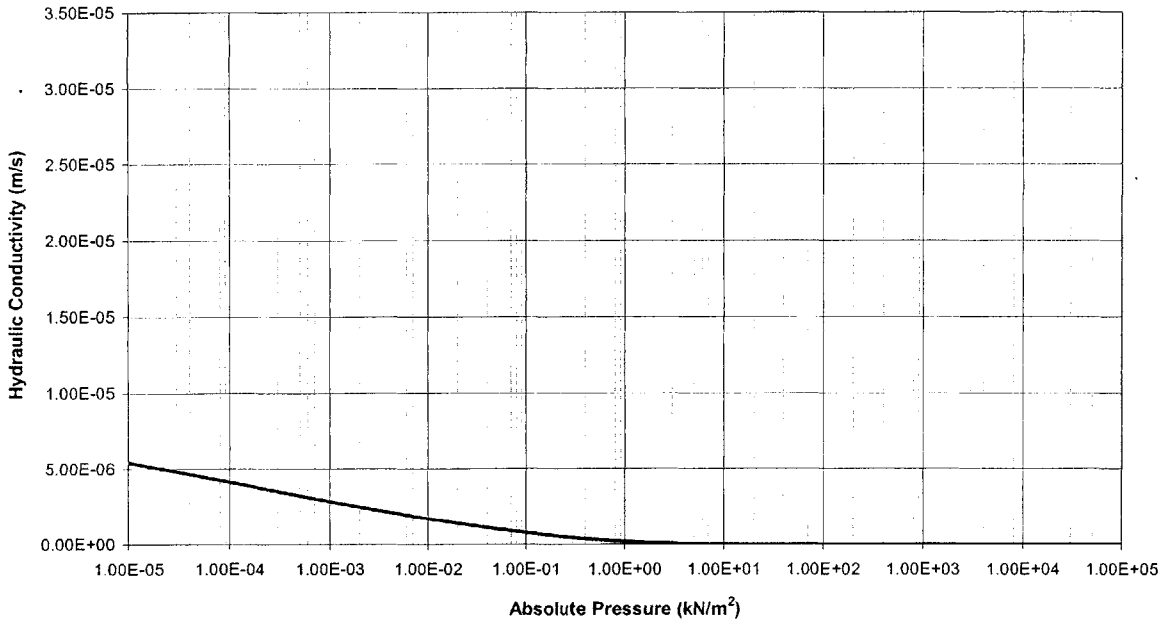

Figure 3.86. Hydraulic Conductivity Characteristic Curve

To investigate the effects of a sudden increase in rainfall intensity on the stability of slopes, we first consider a rainfall event with constant intensity. We then compare the results of this case, to the case where the rainfall intensity suddenly increases.

CONSTANT RAINFALL INTENSITY

We assume an initial moisture content of $\theta_i = 0.4$, and the initial state of stability of the slope is assessed. The critical failure surface is shown in Figure 3.84, and a Factor of Safety of 1.22 is computed indicating a stable slope.

We assume a rainfall event with intensity $I = 10mm/h$ takes place for a duration of 8 hours. Figure 3.87 shows the moisture distributions, and Figure 3.88 shows the pore pressure distributions at selected times.

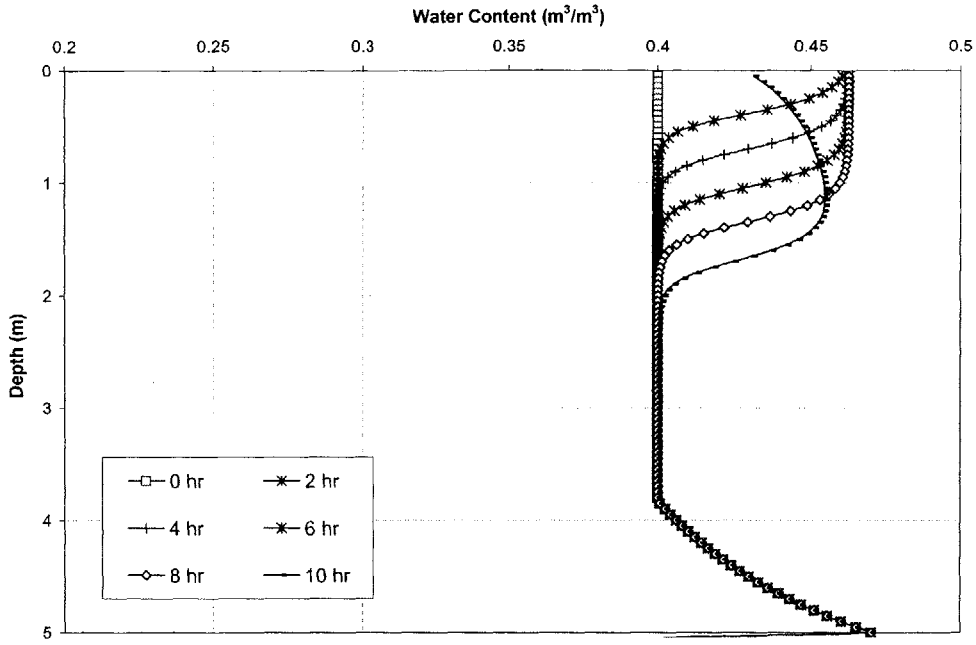

Figure 3.87. Moisture Content Profiles at Selected Times

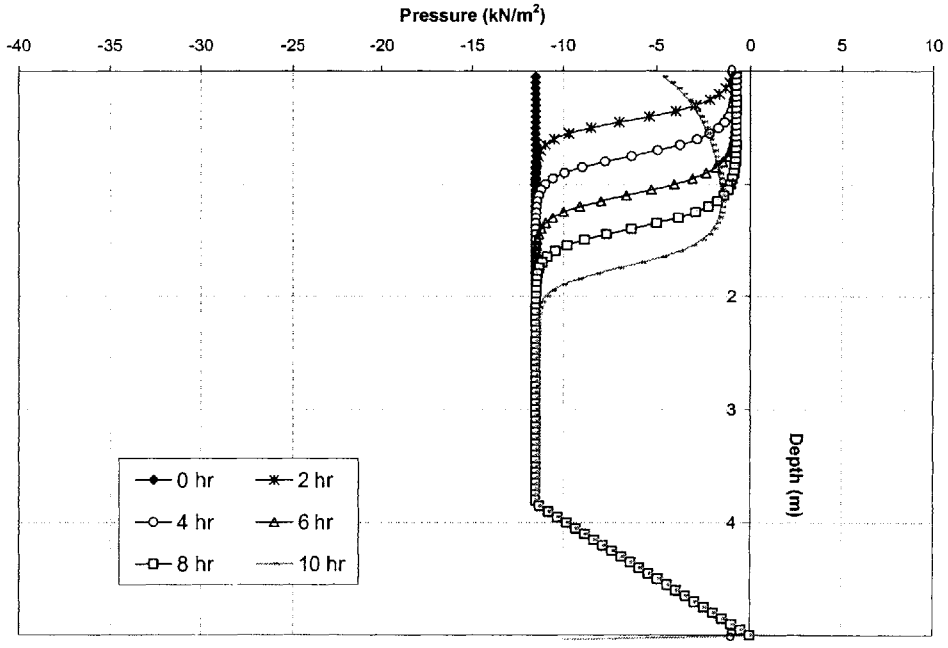

Figure 3.88. Pore Pressure Profiles at Selected Times

Figure 3.87 shows that the initial moisture content in the soil is increased as a result of infiltration, and that the initial suction is reduced, and almost eliminated as shown in Figure 3.88. Figure 3.89 show the variation of Factor of Safety with time.

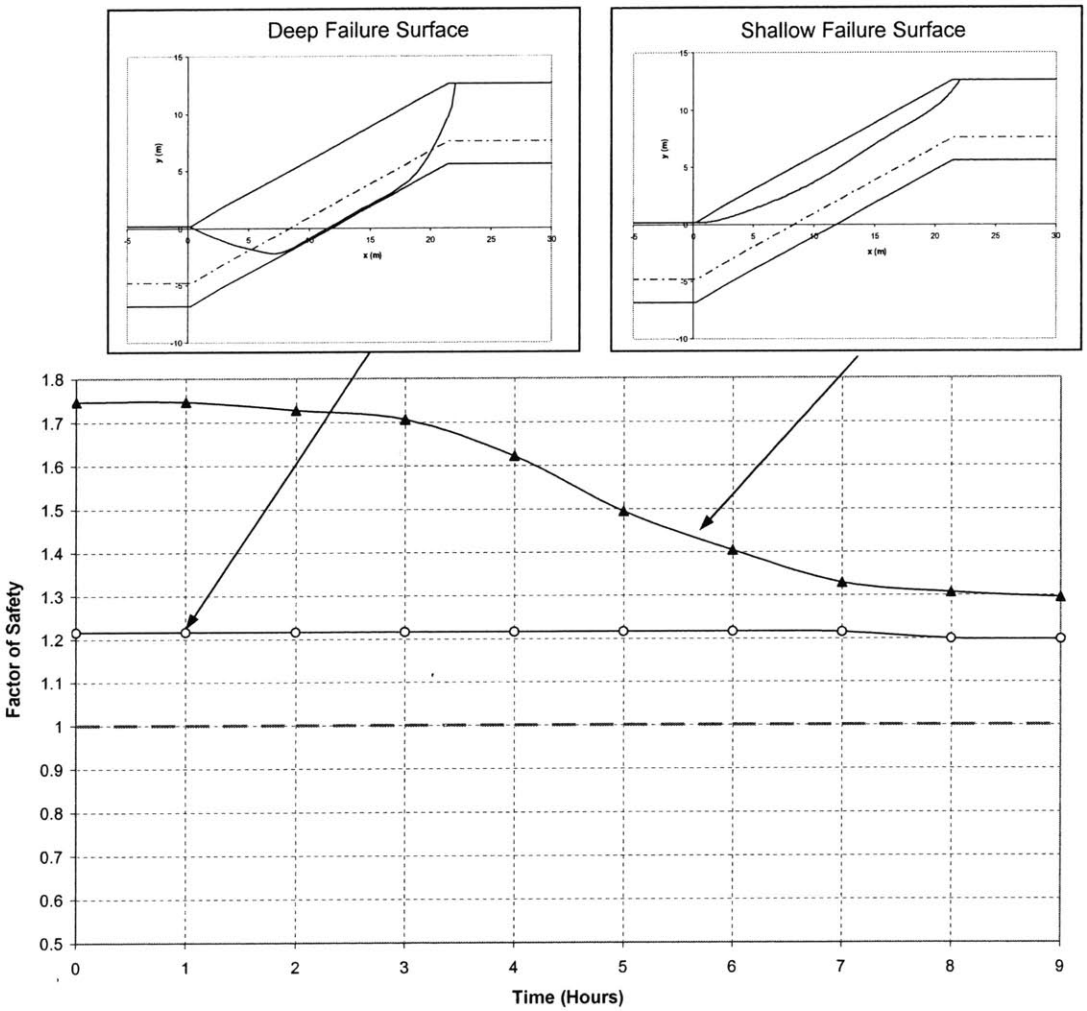

Figure 3.89. Variation of Factors of Safety and Critical Failure Surfaces with Time

Figure 3.89 shows that the Factor of Safety decreases with time as a result of rainfall. The critical failure surface, however is located deep into the slope at the soil bedrock interface, as shown in Figure 3.89. At no time does the Factor of Safety on a shallow failure surface drop below the one on the deep failure surface. Since the Factor of Safety remains above a value of one, the slope remains stable as a result of the rain.

SUDDEN INCREASE IN RAINFALL INTENSITY

We now assume a rainfall event takes place for a duration of 8 hours, where for the first 4 hours, the rainfall intensity is $I = 10mm/h$, and then there is a sudden increase in intensity from $I = 10mm/h$ to $I = 150mm/h$ for the following 4 hours. The hydrologic response of the slope to this type of event in terms of moisture content and pore pressure profiles is shown in Figures 3.90 and 3.91 respectively.

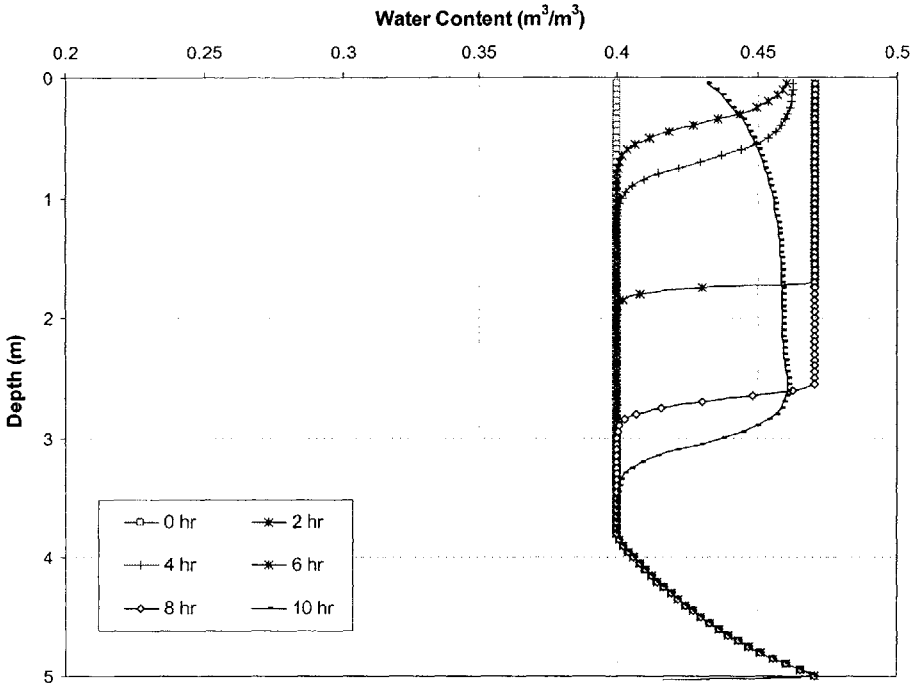

Figure 3.90. Moisture Content Profiles at Selected Times

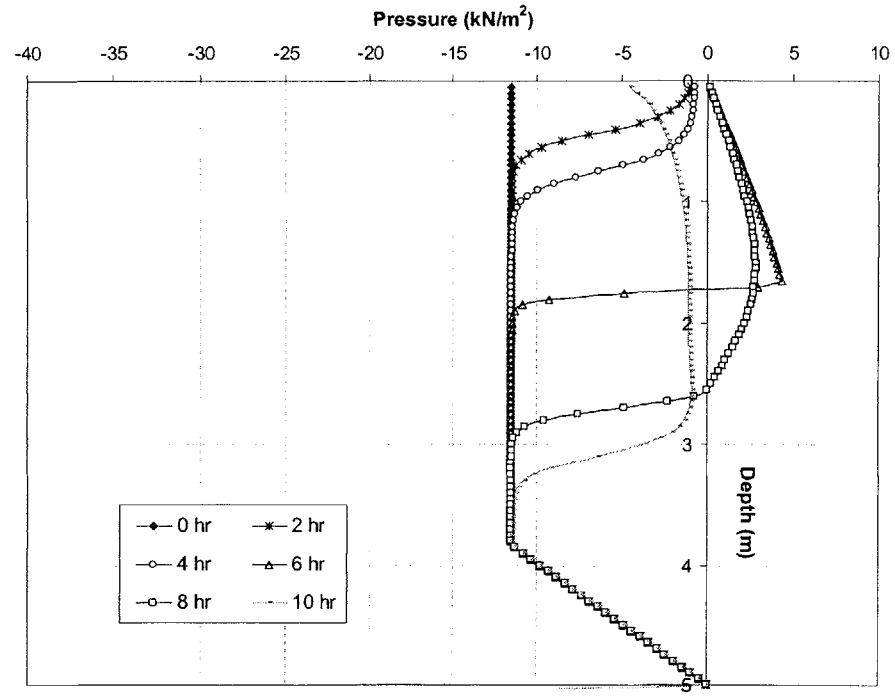

Figure 3.91. Pore Pressure Profiles at Selected Times

Figure 3.90 shows that during the first 4 hours of rain, the intensity is insufficient to fully saturate the soil since it is less than the saturated conductivity of the soil at the surface. The moisture content increases as a result of rain but complete saturation is not reached as is shown in Figure 3.90. This is also reflected in the pore pressures (see Figure 3.91), where suction is reduced but not completely eliminated by the infiltrating rainwater. These results, for times $t < 4$ hours, are the same as those obtained in Figures 3.87 and 3.88.

When the sudden increase in intensity occurs at a time of 4 hours, saturation is reached and an immediate response is observed in the subsurface pore pressures (see Figure 3.91). Positive pressures are rapidly generated behind the infiltrating water as is shown in Figure 3.91.

The immediate development of positive pressures is attributed to the sudden increase in rainfall intensity only. Had the soil conductivity been assumed to decrease with depth as for example in Section, a more dramatic response in terms of pore pressures would have been observed. The only requirement for a sudden increase in pressures to occur

is for the rain intensity to suddenly exceed the potential infiltration rate of the soil at any depth. It is interesting to show this phenomenon through the rainwater infiltration rate into the soil. This is done in Figure 3.92.

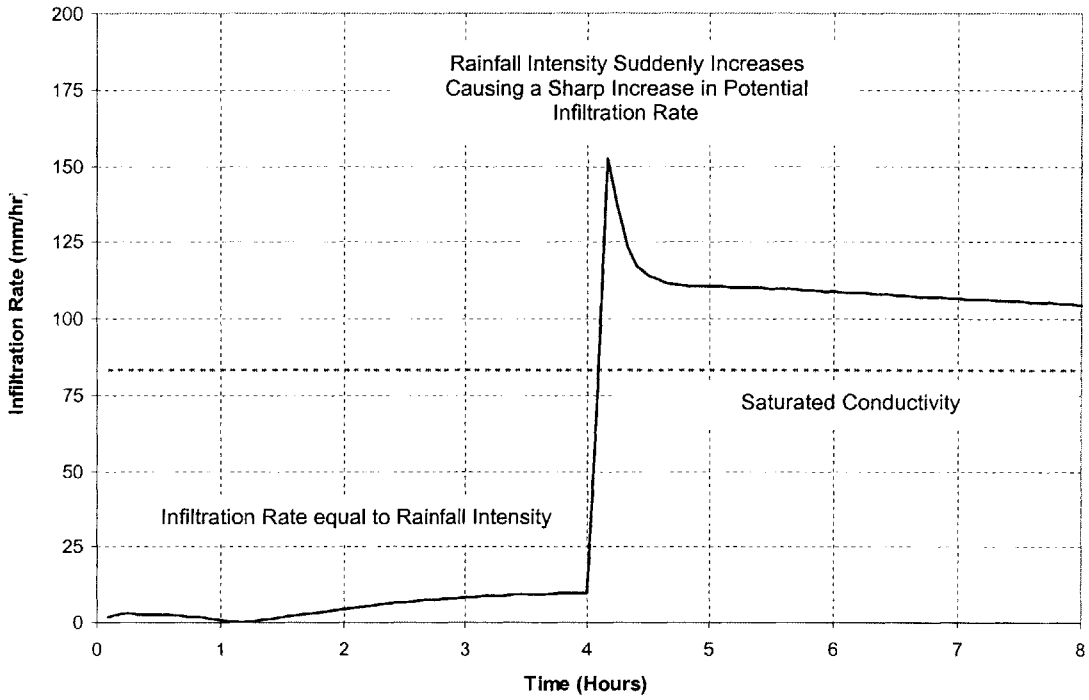

Figure 3.92. Variation of Infiltration Rate with Time (Sudden Development of Positive Pressures)

Figure 3.92 shows that during the early stages of rain, all the rainwater infiltrates into the soil, at a rate equal to the rainfall intensity. When the sudden increase in intensity occurs, it exceeds the potential infiltration rate, and there is a sharp increase in the infiltration rate into the soil. This causes the sudden generation of large positive pressures.

The positive pressures continue to increase with continued rainfall, though gradually and pressure redistribution takes places at the end of rain (see Figure 3.91).

The stability of the slope is assessed, and the variation of Factor of Safety with time is shown in Figure 3.93.

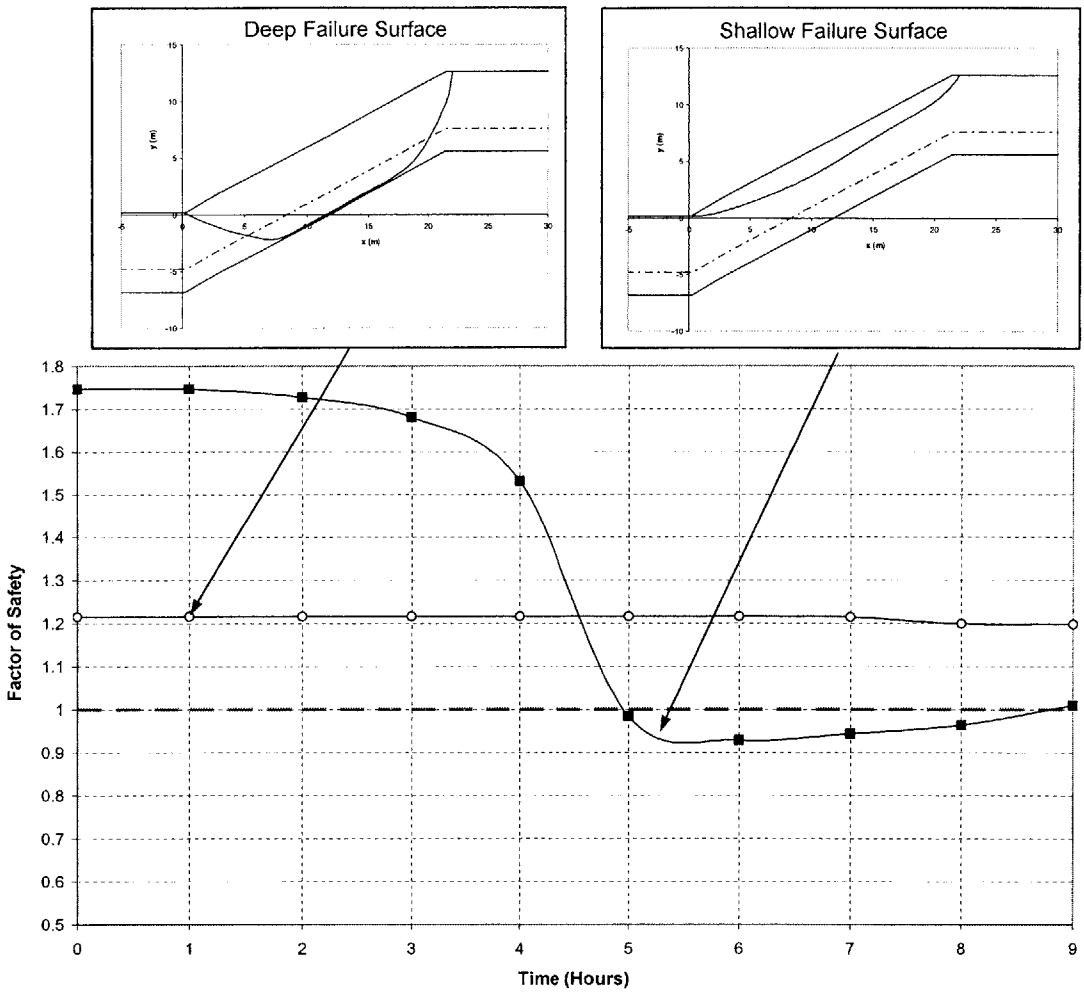

Figure 3.93. Variation of Factors of Safety and Critical Failure Surfaces with Time

Figure 3.93 shows that there is a decrease in the Factor of Safety with time, and as a result of infiltration. Importantly, Figure 3.93 shows that there is a sharp drop in the Factor of Safety on a shallow failure surface at a time of about 4 hours. This is the time when the sudden increase in rainfall intensity was assumed to occur (see Figure 3.92). Failure occurs at a time shortly after the sudden increase in intensity, and occurs on a shallow failure surface located above the water table, as shown in Figure 3.93.

This is in contrast to what was observed when the intensity of the rainfall was assumed constant and not to increase with time, in which case no failure was observed (see Figure 3.89). Figure 3.94 compares the variation of Factor of Safety in the case of constant rainfall intensity, and the case where a sudden increase in intensity is assumed.

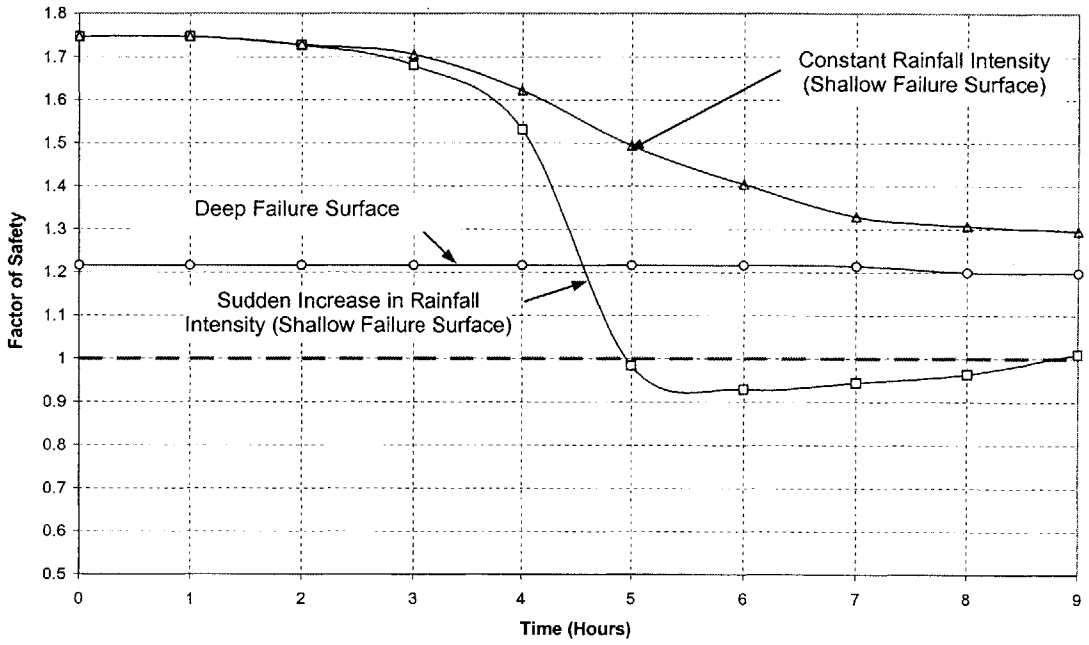

Figure 3.94. Comparison of Variation of Factor of Safety with Time for Sudden Increase and Constant in Rain Intensity

We therefore conclude that the sudden increase in intensity is responsible for the sudden generation of pore pressures, that lead to a sudden loss of strength, and a sudden landslide.

In summary, this example illustrates that under certain conditions, large positive pressures may suddenly develop behind an infiltrating front that ultimately result in a sudden landslide. This occurs when the rainwater penetration rate suddenly exceeds the potential infiltration rate of the soil, and this can be as a result of a sudden increase in rainfall intensity and/or a rapid decrease in soil conductivity with depth. This mechanism may be responsible for the many sudden landslides observed and reported in the literature, which have remained inadequately explained.

3.3.2.4. INTERMEDIATE FAILURES

It is interesting to note that landslides associated with the saturation of the soil from the surface downwards have failure surfaces that are shallow but are not necessarily entirely within the zone wetted by infiltrating rain. In fact, extensive numerical examples (not presented here) show that in many slopes, a portion of the failure surface is frequently located below the wetted zone. In such instances, landsliding occurs because of the increase of pressures along only a section of the failure surface that has been saturated by infiltrating rain. The portion along the failure surface on which pressures are increased may be large or small depending on the properties of the slope and the rainfall event. Figure 3.95 shows a schematic of this failure mechanism.

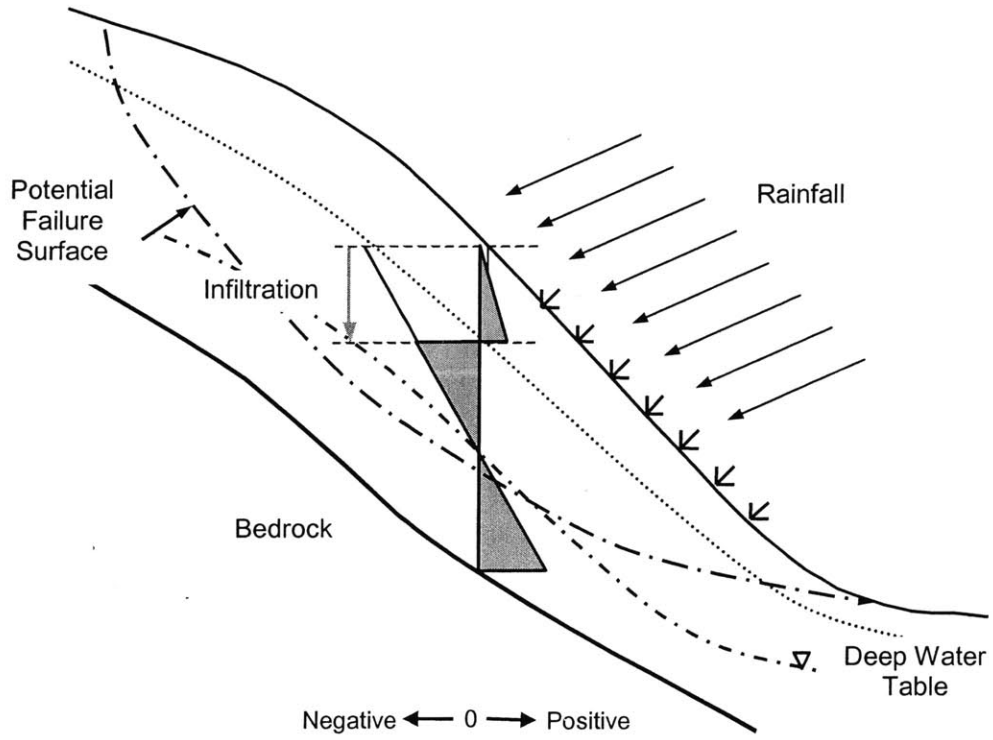

Figure 3.95. Illustration of Failure Mechanism (Intermediate Failure) (Negative, 0, Positive Indicate sign of pore pressures)

In this section, we study the effects of an increase in pore pressures along a section of a potential failure surface, and show that this can have important consequences with regard to location of the failure surface, and hence type (and mass volume) of a landslide. In particular, we show that it is possible for failure to occur along a deeper failure surface than was encountered in the examples discussed in Section 3.3.2.1s. This results in deeper seated landslides with more circular failure surfaces than were previously encountered. The mechanism that leads to landsliding is therefore an increase in pore pressures along a section of the failure surface, which results in a corresponding decrease in strength along the same portion that may be sufficient to initiate a landslide. This increase in pore pressures may be in the form of a reduction of suction, elimination of suction, or the development of positive pressures. This mechanism is not entirely different to the ones proposed in previous sections, since failure still occurs as a result of saturation of the soil from the surface of the soil downwards, and in fact should still be classified as such.

It is nonetheless important to study such mechanisms because they have not been previously proposed, and provide an explanation for field observations that have documented relatively deep seated slides that occurred without a significant rise in the main water table.

We illustrate this mechanism numerically using the slope shown in Figure 3.96.

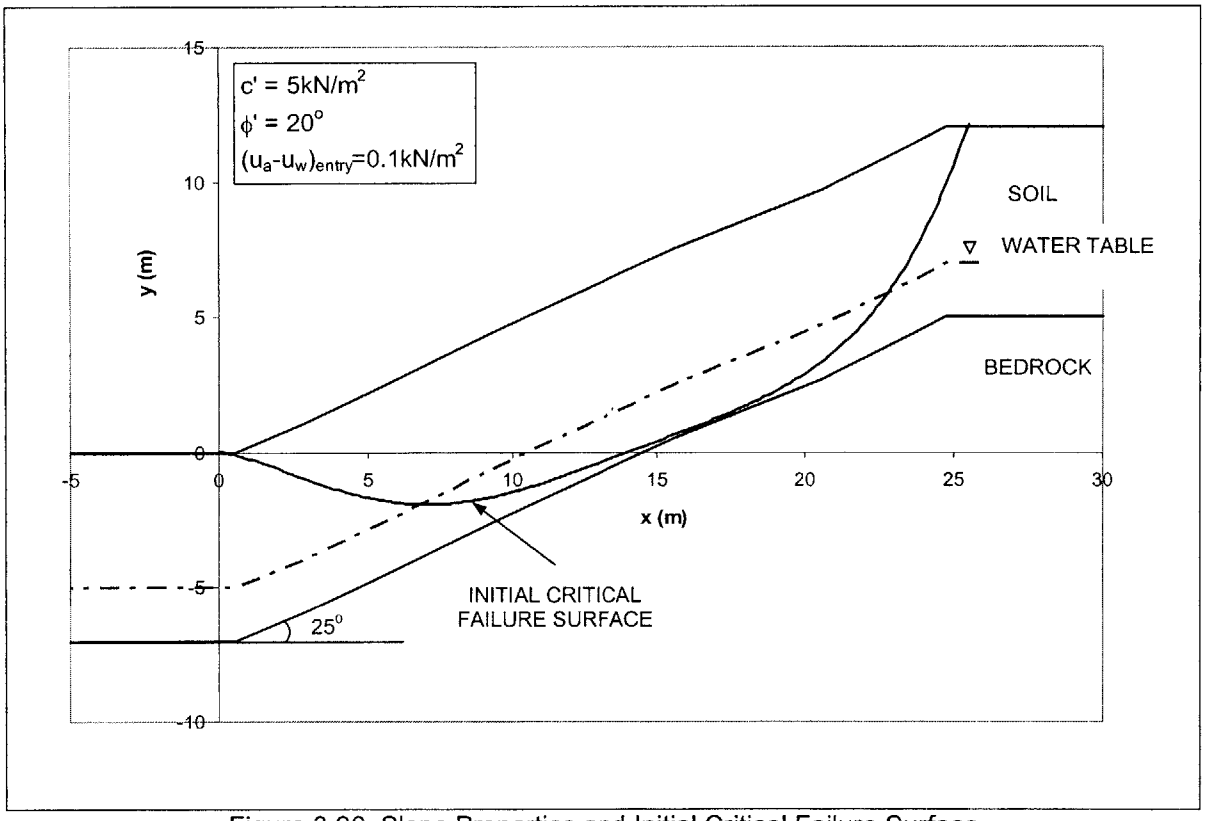

Figure 3.96. Slope Properties and Initial Critical Failure Surface

The soil strength parameters are shown in Figure 3.84. Note that in this example, the cohesion of the soil is significantly greater than the cohesion of the soil considered in the example in Section 3.3.2.1, and that the angle of shearing resistance of the soil is smaller in this example.

The hydraulic parameters are assumed to be:

Saturated moisture content of soil $\theta_S = 0.47$. This is the same θ_S as in the example in Section 3.3.2.1.

Residual moisture content of soil $\theta_r = 0.11$ (see Figure 3.10). This is the same θ_r as in the example in Section 3.3.2.1.

Saturated conductivity $K_S = 3.5 \times 10^{-5} m/s$. This K_S is larger than the K_S of the soil in the example in Section 3.3.2.1.

Specific storage coefficient $S_S = 0.0025$ (see Chapter 2, Part 2-1). This S_S is different from the S_S in the example in Section 3.3.2.1, it is smaller.

The van Genuchten (1980) model is used to describe the soil characteristic curves with the parameters $n = 0.75$ and $\delta = 0.025$. The resulting characteristic curves are shown in Figures 3.97 and 3.98. The van Genuchten (1980) parameters considered in this example are different from the ones considered in the example in Section 3.3.2.1, and so the characteristic curves are also different. They are different in such a way that the characteristic curves in this example, particularly the moisture retention curve, has a significantly shallower (smaller) slope than in example in Section 3.3.2.1 (compare Figures 3.97 and 3.98 to 3.14 and 3.15). Because of this, small changes in soil moisture can cause very large changes in pressures. Furthermore, the air entry pressure is smaller in this example, than in the example of Section 3.3.2.1 (compare Figure 3.97 to 3.12).

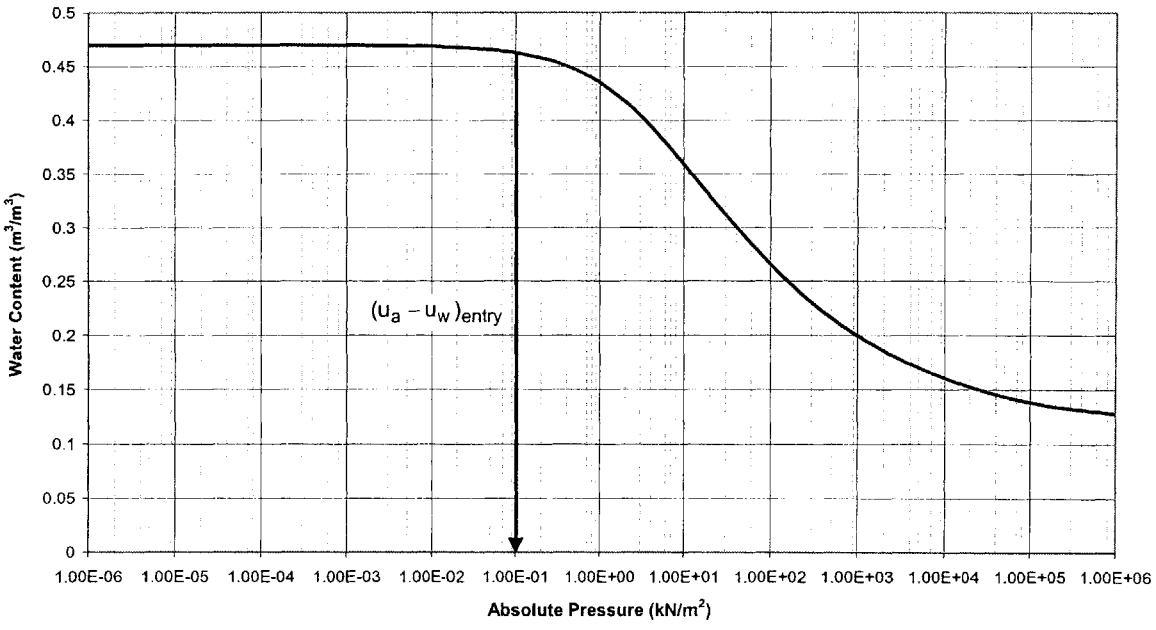

Figure 3.97. Moisture Retention Characteristic Curve

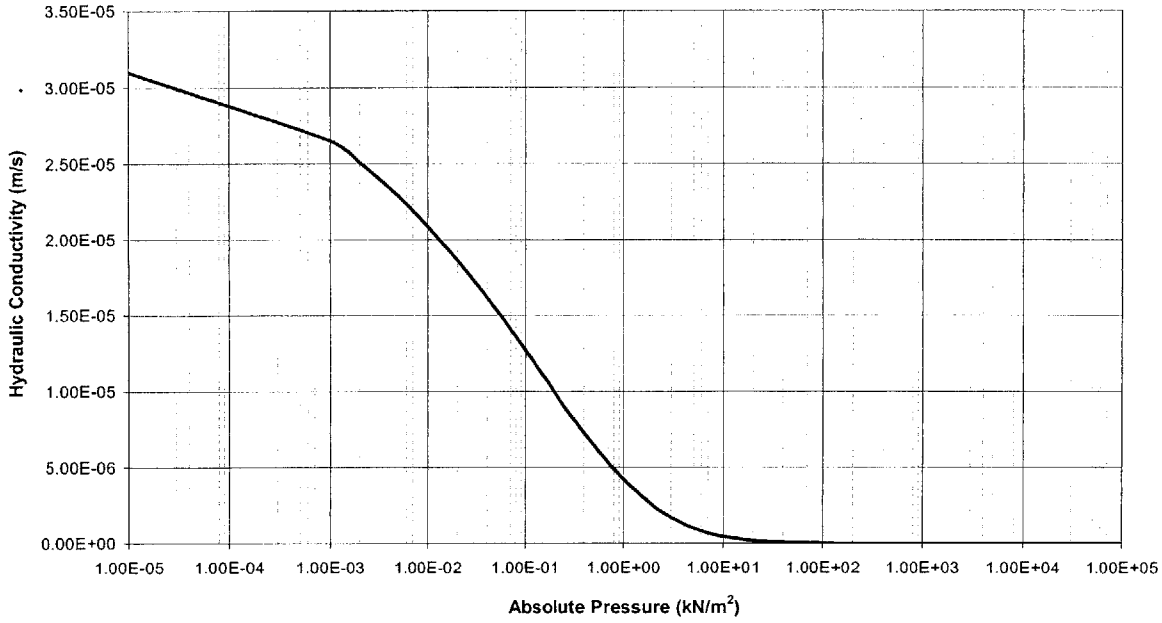

Figure 3.98. Hydraulic Conductivity Characteristic Curve

An initial moisture content of $\theta_i = 0.4$ is assumed, and the initial stability of the slope is assessed and the resulting critical surface is shown in Figure 3.96. A Factor of Safety of 1.18 is computed and the slope is stable.

We assume a rainfall event of constant intensity $I = 100mm/h$ occurs for a duration of 8 hours. This intensity is greater than the saturated conductivity of the soil at the surface, and hence one would expect saturation to be reached (see Figure 3.99) and positive pressures to develop (see Figure 3.100).

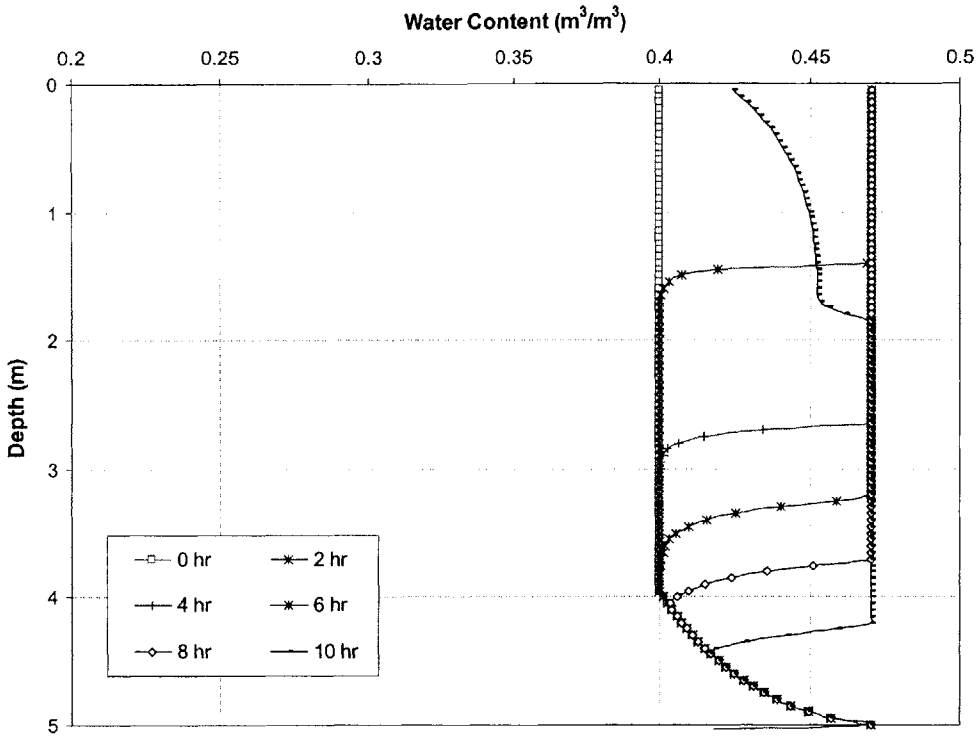

Figure 3.99. Moisture Content Profiles at Selected Times

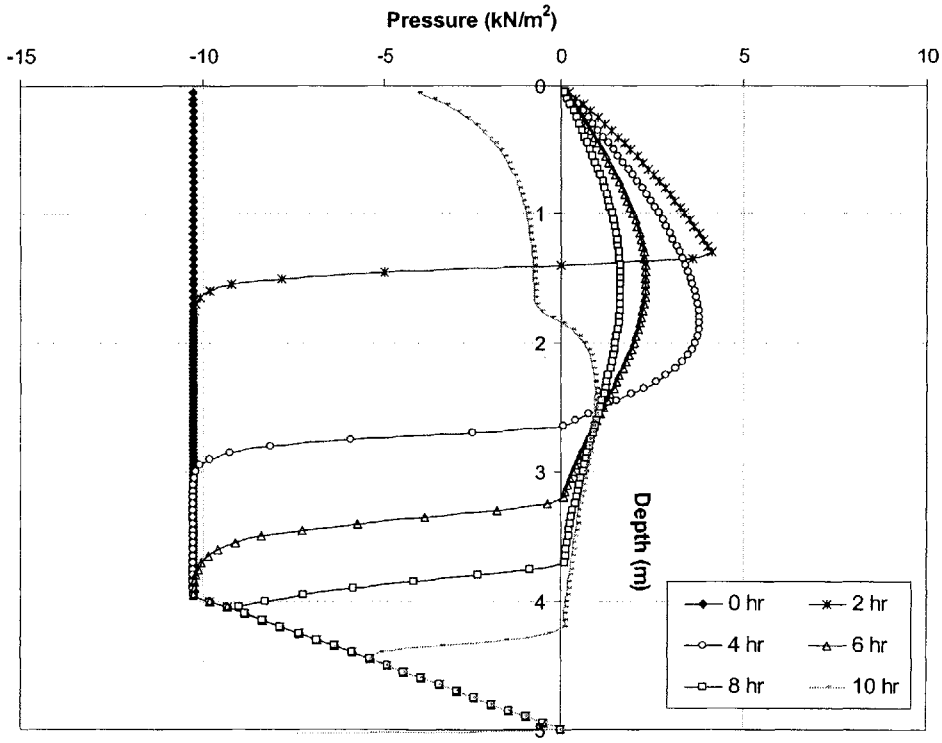

Figure 3.100. Pore Pressure Profiles at Selected Times

Figure 3.100 shows that positive pressures develop throughout the infiltration depth, behind the wetting front.

The stability of the slope is assessed using three initial trial failure surfaces; a shallow surface, a deep surface, and an intermediate surface with a depth in between the first two. These are shown in Figures 3.101, 3.102 and 3.103 respectively.

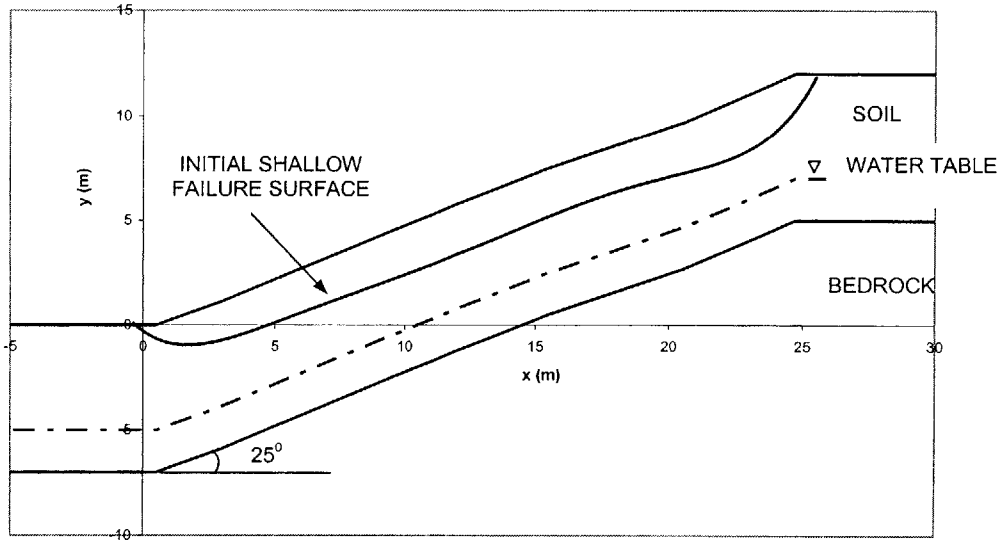

Figure 3.101. Shallow Failure Surface

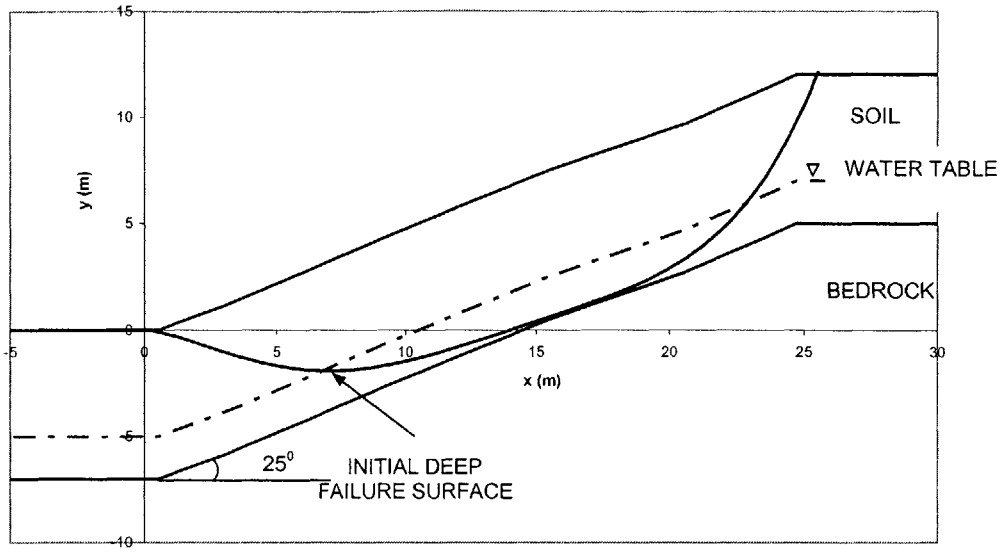

Figure 3.102. Deep Failure Surface

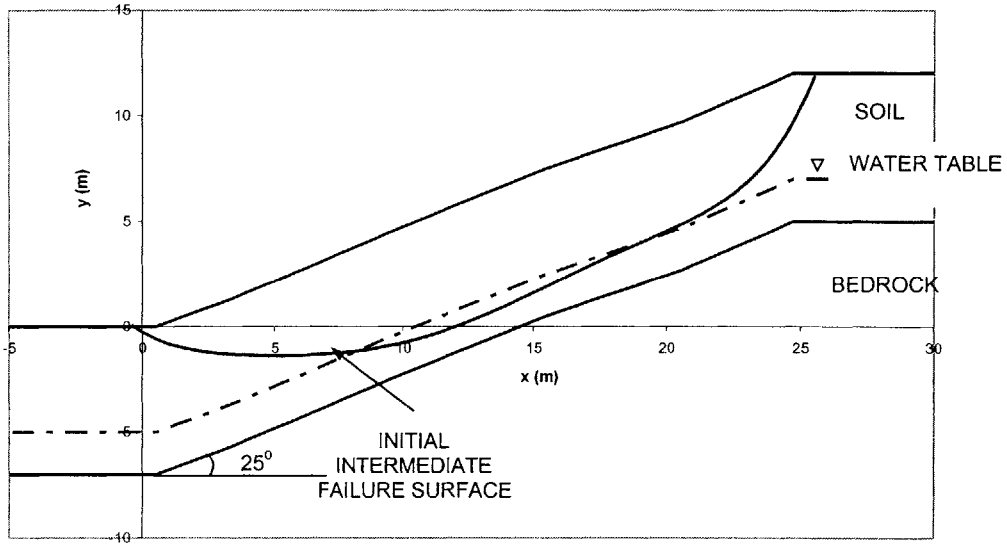

Figure 3.103. Intermediate Failure Surface

The variation of Factor of Safety with time starting from each of the failure surfaces is shown in Figure 3.104.

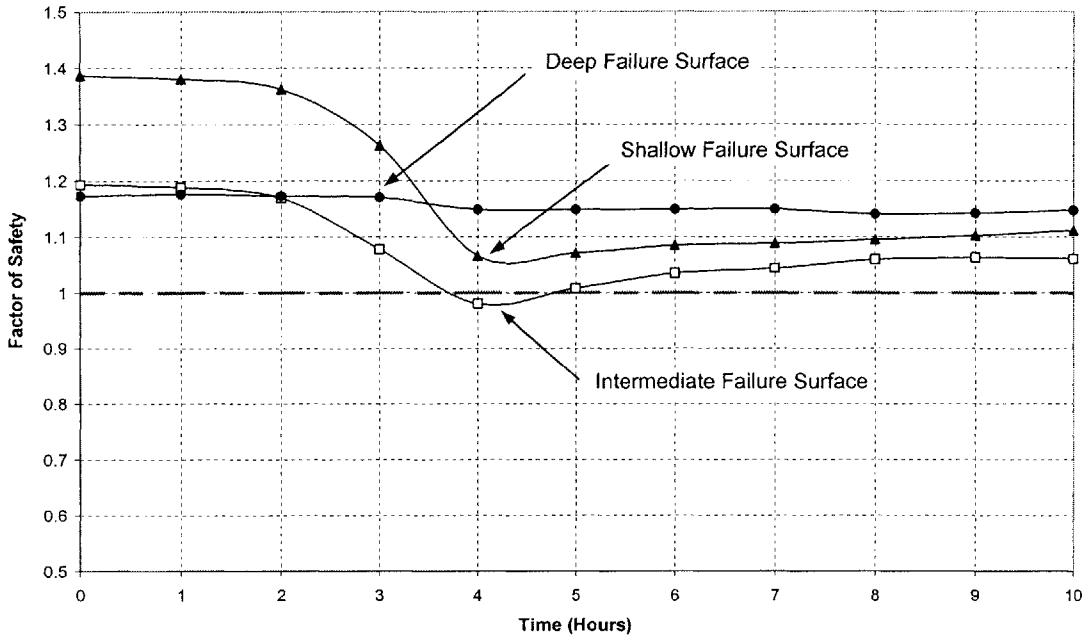

Figure 3.104. Variation of Factor of Safety with Time Starting with Various Initial Failure Surfaces

Figure 3.104 shows that the critical failure surface in the slope is initially located deep along the soil bedrock interface. However, with rainwater infiltration, this critical surface moves upwards towards the slope surface. At a time of about 4 hours into the event, failure occurs along an intermediate failure surface.

The critical surfaces with time are shown in Figure 3.105.

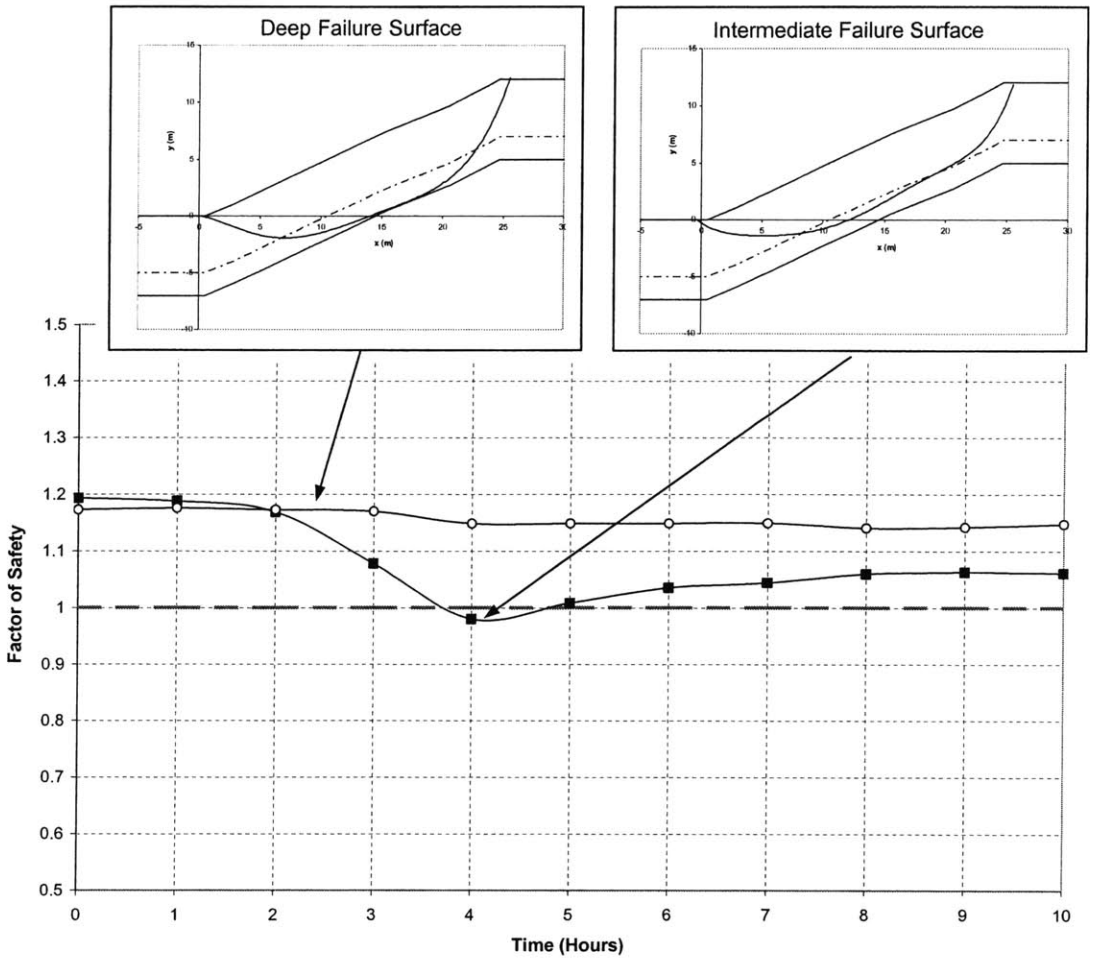

Figure 3.105. Variation of Factor of Safety and Critical Failure Surfaces with Time

Figure 3.105 shows that initially, the critical failure surface in the slope is located deep in the slope. With time, and rainfall, failure occurs along an intermediate failure surface. Part of the failure surface is above, and part is below the water table. The landslide is large, and rotational in shape. The landslide is therefore classified as having an intermediate failure surface. The rainfall alters the pore pressures on only a portion of the failure surface, and this is sufficient to cause failure. This is because suction plays an important role in the initial stability of the slope, and changes in suction, though only on a portion of the failure surface, can have significant effects.

3.4 RESULTS AND DISCUSSION

The series of examples presented in this chapter illustrate various landslide failure mechanisms. These, along with extensive further studies on different slopes not shown here, allow one to draw some general conclusions as to the type of landslide a particular slope is most susceptible to. The conclusions are made with respect to the slope geometric, geologic and hydrologic properties, as well as the properties of the triggering event. A distinction is made between those slopes susceptible to failure by saturation from below, and those susceptible to failure by saturation from above. Prior to doing so, it is worth mentioning a few factors that decrease the state of stability of a slope, and promote slope failure, whether it be by saturation from below, or from above. These factors include:

(a) Slope Angle: The greater the slope angle the less stable a slope is, and so, slopes with steep inclinations tend to be less stable than slopes with shallow inclinations

(b) Depth to Bedrock (Thickness of soil layer): The greater the depth to the bedrock from the ground surface, or, the thicker the soil layer, the greater the weight of soil that may potentially fail. As a result, slopes with thick soil layers tend to be less stable than slopes where the thickness of the soil layer is small.

3.4.1 FAILURE BY SATURATION FROM BELOW

Slopes susceptible to failure by saturation from below are typically slopes where the depth to the water table is shallow. An example with a shallow water table was used to illustrate the mechanism of failure by saturation from below in Section 3.2. When the depth to the water table is shallow, the extent of the unsaturated zone of the slope is small, and the moisture content in the unsaturated zone is typically large, and suction is typically small. As a result, suction does not play a very important role in increasing the stability of the slope. The critical failure surface in the slope, initially, typically lies along the soil bedrock interface, where the pore pressures are maximum. This was shown in Section 3.2.

During a rainfall event, infiltrating rainwater percolates directly to the water table since the depth is shallow, and because of the high moisture content and therefore high conductivity of the soil. The rainwater causes a rise in the water table, promoting failure

along the strength discontinuity between soil and rock, where the pore pressures are maximum. A rise in the main water table usually takes place slowly, during long duration rainfall events. It also occurs during low intensity rainfall, such that all the incident rainfall infiltrates into the slope, reaching the water table directly. During high intensity rainfall, a small, saturated zone of soil may develop near the slope surface, and any additional rainfall is observed as surface runoff. The rainfall characteristic that promote failure by saturation from below are therefore, small intensity, and long duration. Table 3.3 attempts to list, in relative terms, the factors that contribute to failure by saturation from below.

Geometry	**Geology**		**Hydrology**	
	Soil	**Rock**	**Site**	**Trigger**
Slope Inclination: Steep	Thickness: Thick	Location of Bedrock: Deep	Location of Water Table: Shallow	Rainfall Intensity: Low
	Stratigraphic Setting (Homogenous/ Heterogeneous): Homogenous	Fracture Network: None/Intact Rock	Subsurface Flow Regime: Hydrostatic/Steady State Flow	Rainfall Duration: Long
	Strength Properties (Saturated and Unsaturated): Low Saturated	Strength: Very High	Antecedent Moisture Content: High	
	Unit Weight (Saturated and Unsaturated): High	Conductivity: Very Low		
	Conductivity: High			
	Pore Size Distribution: Uniform			
	Grain Size Distribution: Uniform			
	Porosity: High			
	Conductivity: Very high			
	Characteristic Curves: Not very important			

Table 3.3. Factors Contributing to Failure by Saturation from Below

The factors in Table 3.3 are shown graphically in Figure 3.106.

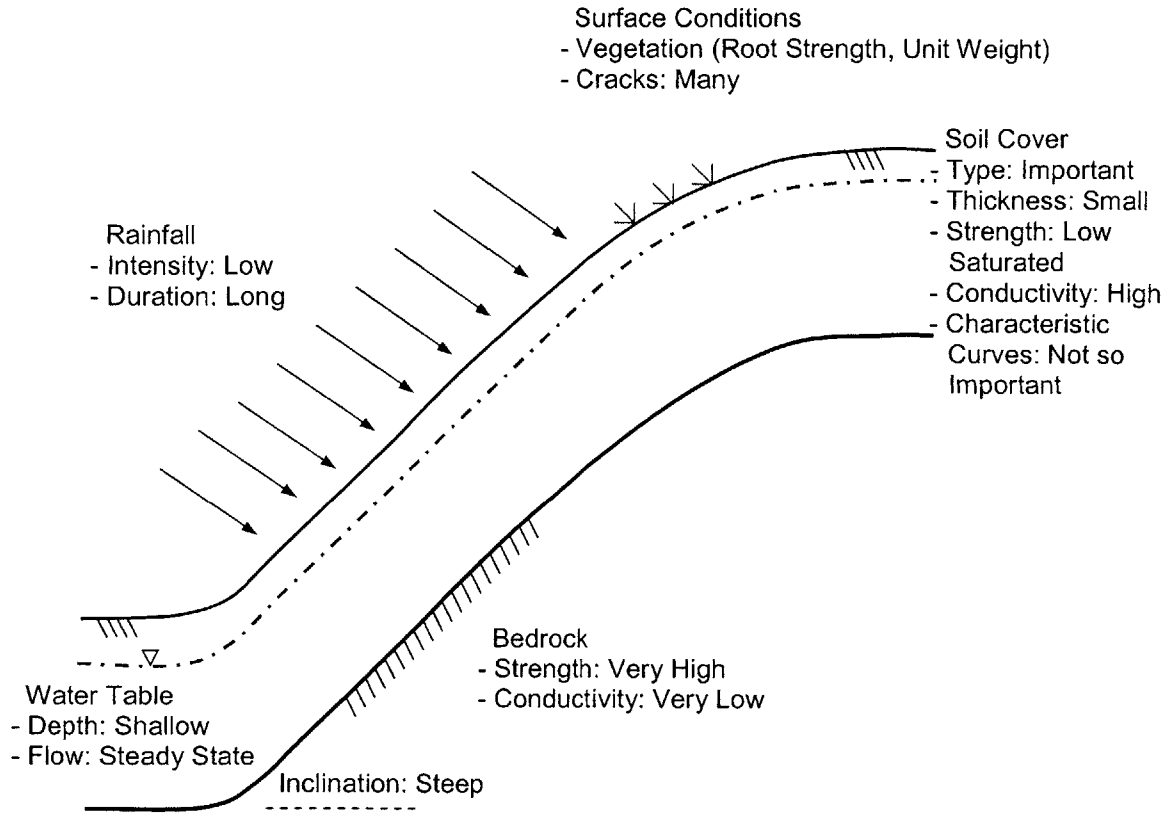

Figure 3.106. Illustration of Factors Contributing to Failure by Saturation from Below

The factors in Table 3.3, and shown in Figure 3.106 contribute to failure by saturation from below. The hydrologic factors, e.g. shallow water table, high conductivity of soil, and low conductivity of bedrock, cause the infiltrating rainwater to percolate directly to the water table, causing it to rise. As this happens, the pore pressures along the soil bedrock hydraulic conductivity interface increases. The stability factors, e.g. low saturated strength of soil, high strength of rock, promote failure along the soil bedrock interface because of the strength discontinuity. The combined effect of these factors is to promote landsliding by saturation from below.

3.4.2 FAILURE BY SATURATION FROM ABOVE

Slopes susceptible to failure by saturation from above are typically slopes where the depth to the water table is relatively large.

When this is the case, the extent of the unsaturated zone of the slope is large, and the moisture content in the unsaturated zone can typically become small leading to high values of suction. The high suction plays an important role in increasing the stability of the slope.

During a rainfall event, a wetting front forms near the soil surface, and migrates downwards into the slope with increasing time and rainfall. This typically occurs during high intensity, short duration rainfall. The infiltrating rainwater increases the pore pressures (decreases the suction) in the unsaturated zone of the slope, causing the loss of strength, which ultimately leads to failure. Failure occurs along a shallow failure surface, close to where the pore pressures (suction) have been altered by rain.

Section 3.3 demonstrated this using several example slopes, where the depth to the water table was large, and the effects of changes in suction were significant.

Table 3.4 attempts to list, in relative terms, the factors that contribute to failure by saturation from above.

Geometry	Geology		Hydrology	
	Soil	Rock	Site	Trigger
Slope Inclination: Steep	Thickness: Thick	Location of Bedrock: Deep	Location of Water Table: Deep	Rainfall Intensity: High (Higher than Conductivity of Soil)
	Stratigraphic Setting (Homogenous/ Heterogeneous): Homogenous or Heterogeneous	Fracture Network: None/Intact	Subsurface Flow Regime: Transient flow in unsaturated soil	Rainfall Duration: Short
	Strength Properties (Saturated and Unsaturated): Low Unsaturated	Strength: High	Antecedent Moisture Content: Low (High initial suction)	
	Unit Weight (Saturated and Unsaturated): High	Conductivity: Low		
	Conductivity: Low			
	Pore Size Distribution: Non-Uniform			
	Grain Size Distribution: Non-Uniform			
	Porosity: Low			
	Conductivity: Low			
	Characteristic Curves: Very Important. Shallow moisture retention curve with Low air entry pressure			

Table 3.4. Factors Contributing to Failure by Saturation from Above

The factors in Table 3.4 are shown graphically in Figure 3.107.

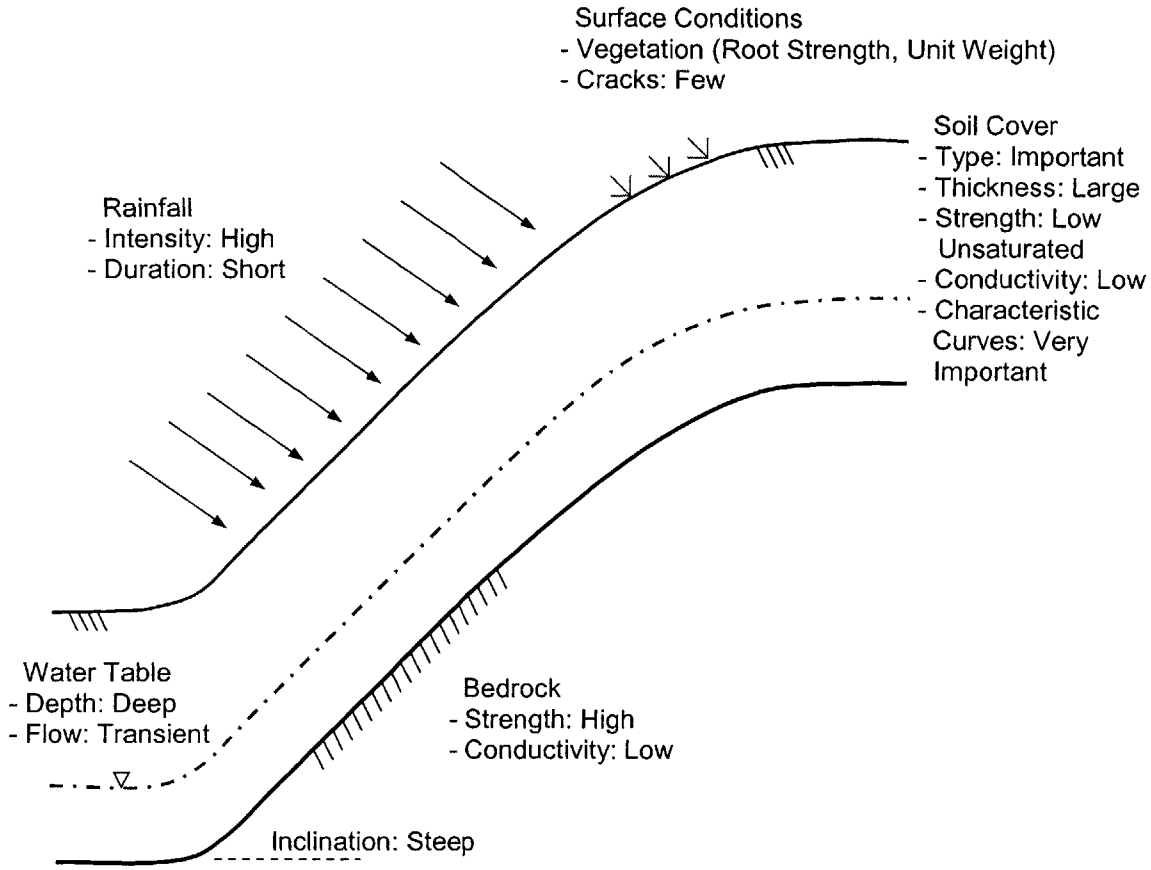

Figure 3.107. Illustration of Factors Contributing to Failure by Saturation from Above

The factors in Table 3.4, and shown in Figure 3.107 contribute to failure by saturation from above. The hydrologic factors, e.g. deep water table, and low conductivity of soil, promote the slow infiltration of rainwater in the unsaturated zone, causing an increase in the pore pressures in the unsaturated zone of the slope. The stability factors, e.g. low unsaturated saturated strength of soil, promote failure in the unsaturated zone of the slope. The combined effect of these factors is to promote landsliding by saturation from above.

Since the failure surface in shallow landslides is in unsaturated soil, unsaturated soil properties (through characteristic curves) are of particular significance. Suction plays a key role in such failures, and it influences both the strength, and the hydraulic properties of the soil.

STRENGTH

As stated previously, slopes that fail by saturation from above are slopes which are initially held stable by the high initial suction in the unsaturated zone of the slope. Failure takes place when this initially high suction is reduced, or eliminated by infiltrating rainwater.

The strength of such slopes is such that it sensitive to changes in moisture content, i.e. small changes in moisture content by infiltrating rainwater cause large changes in unsaturated strength.

This can be translated in terms of the soil moisture characteristic curve. Soils that experience large changes in pressure from small changes in moisture, have soil moisture retention curves that are shallow, with a small air entry pressure. This is illustrated in Figure 3.108.

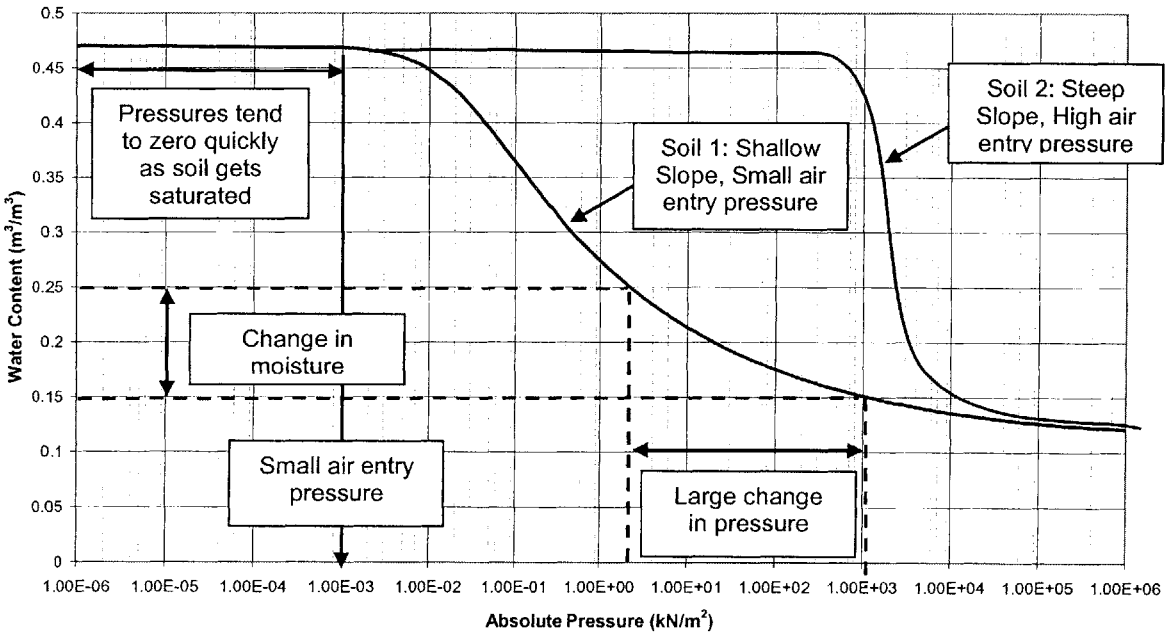

Figure 3.108. Properties of Moisture Retention Curve that Promote Failure by Saturation from Above for Two Soils with Different Air Entry Pressures

In Figure 3.108, for Soil 1:

(a) Small changes in moisture content cause large changes in pressures (see Figure 3.108). For example, a rainfall event that increases the initial moisture content from $0.15m^3/m^3$ to $0.25m^3/m^3$ increases the pressures by more than two orders of magnitude (see Figure 3.108). When this is the case, even low intensity rainfall events are capable of reducing the initial suction in the soil significantly, or eliminating it.

(b) The small air entry value causes the pressures (suction) to quickly tend to zero as the soil gets saturated during rain. This way, as the soil is saturated, the suction is eliminated, and with continued rain, positive pressures begin to build up.

Both points (a) and (b) above, cause the initial suction to be reduced and eliminated during a rainfall event, as the moisture content in the soil increases.

If, now, one considers two soils with the same air entry pressure, as shown in Figure 3.109, then:

(a) What has been stated in regard to Figure 3.108 is true, namely that Soil 1, with the shallow characteristic curve will experience a larger change in pressures for a given change in moisture content
(b) But the strength of this soil, Soil 1, remains greater than that of Soil 2. This is because the suction in the soil, after the increase in moisture content is greater in Soil 1 than it is in Soil 2.

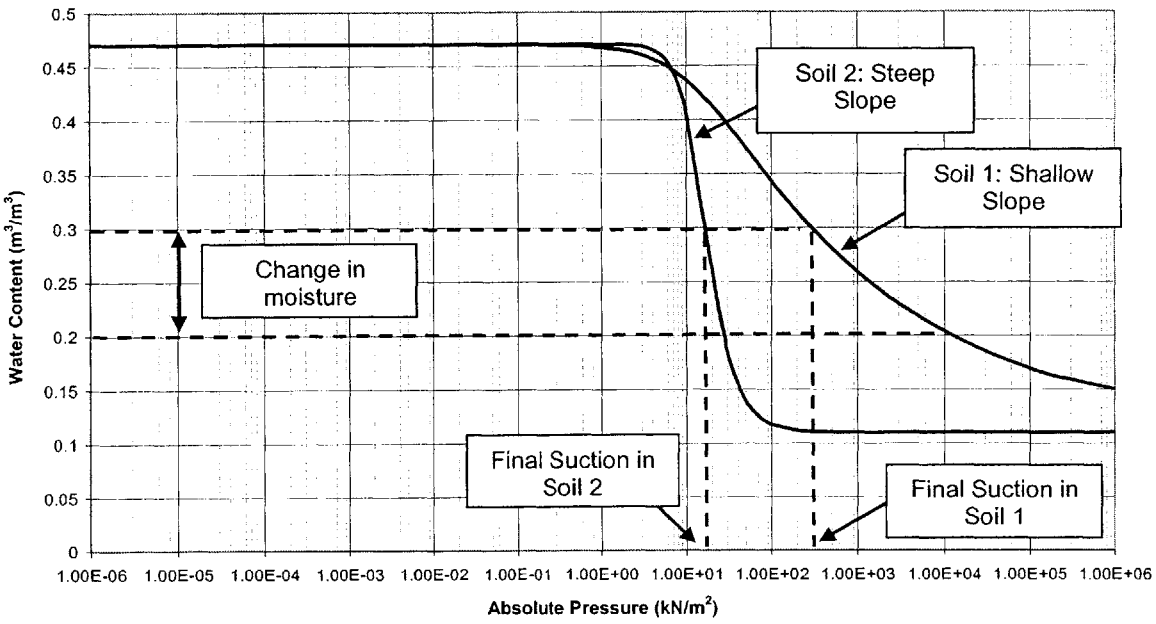

Figure 3.109. Properties of Moisture Retention Curve that Promote Failure by Saturation from Above for Two Soils with Same Air Entry Pressure

From Figure 3.109, we can therefore conclude that the strength of Soil 1, the soil with the shallower characteristic curve is greater than that of Soil 2.

Various attempts have been made to formally relate the strength of unsaturated soils to the soil characteristic curve. This is discussed in more detail in Chapter 5. Nonetheless, the strength of unsaturated soils, and how it is related to the soil characteristic curves remains a matter of debate amongst investigators, and research continues in this field, e.g. at the laboratories at MIT. The simple illustrations above do, to a certain degree show the effects of the soil characteristic curve on strength.

The effect of the shape of the soil moisture retention curve on unsaturated strength can also be examined by considering the Effective Stress Model (Bishop, 1959) for unsaturated soil strength. The arguments that follow have not been previously presented in the literature, and the idea of attempting to relate the Effective Stress Model to the shape of the characteristic curve is new. According to the Effective Stress Model, unsaturated strength can be described as:

$$\tau = c' + [(\sigma - u_a) + \chi(u_a - u_w)]\tan\phi' \qquad [3.3]$$

where:

σ is the total normal stress

$(u_a - u_w)$ is the soil suction

c' is the effective cohesion

ϕ' is the angle of internal friction of the soil

τ is the shear strength of the soil

χ is the effective stress parameter, and:

$$\chi = \left[\frac{(u_a - u_w)}{(u_a - u_w)_{entry}}\right]^{-0.55} \qquad [3.4]$$

where:

$\left[\frac{(u_a - u_w)}{(u_a - u_w)_{entry}}\right]$ is the suction ratio

$(u_a - u_w)_{enrty}$ is the air entry suction

We note that the suction ratio $\left[\frac{(u_a - u_w)}{(u_a - u_w)_{entry}}\right]$ is representative of the slope of the soil characteristic curve. Hence, the effective stress parameter χ in Equation [3.4] is also a function of the slope of the characteristic curve. For a fixed air entry pressure, $(u_a - u_w)_{entry}$, and a constant (specified) moisture content, the steeper the slope of the characteristic curve, the smaller the value of the soil suction $(u_a - u_w)$. This is illustrated in Figure 3.109. For example, at a moisture content 0.3 m^3/m^3, the suction in Soil 1 (steep characteristic curve) is greater than the suction in Soil 2 (shallower characteristic curve) at that same moisture content.

As shown in Figure 3.109, the steeper the characteristic curve the smaller the value of the soil suction. Since the effective stress parameter χ in Equation [3.4] is inversely proportional to the soil suction, the smaller the value of the suction, the larger the value of the effective stress parameter. The unsaturated strength of a soil in Equation [3.3] is directly proportional to the effective stress parameter, and so the larger the value of χ, the greater the unsaturated strength.

Unsaturated strength, according to the Effective Stress Model, is however, directly proportional to the soil suction. Since the soil suction decreases with increasing steepness of the characteristic curve, there is a decrease in the soil strength. These are two opposing effects, and their combined effect can be examined by re-writing the strength equation in [3.3] as:

$$\tau = c' + \left[(\sigma - u_a) + \left[\frac{(u_a - u_w)}{(u_a - u_w)_{entry}} \right]^{-0.55} (u_a - u_w) \right] \tan\phi' \qquad [3.5]$$

Simplifying Equation [3.5] gives:

$$\tau = c' + \left[(\sigma - u_a) + \left[\frac{1}{(u_a - u_w)_{entry}} \right]^{-0.55} (u_a - u_w)^{0.45} \right] \tan\phi' \qquad [3.6]$$

And:

$$\tau = c' + \left[(\sigma - u_a) + \left[(u_a - u_w)_{entry} \right]^{0.55} (u_a - u_w)^{0.45} \right] \tan\phi' \qquad [3.7]$$

If one assumes that the exponents of the soil suction, and the air entry are both 0.5, then Equation [3.7] can be expressed as:

$$\tau = c' + \left[(\sigma - u_a) + \sqrt{(u_a - u_w)_{entry}} \sqrt{(u_a - u_w)} \right] \tan\phi' \qquad [3.8]$$

Equation [3.8] shows that the unsaturated strength is approximately proportional to the square root of the air entry pressure, and the square root of the soil suction.

Therefore:

(a) Soils with smaller air entry pressures tend to exhibit lower unsaturated strength, and
(b) The greater the suction, the greater the soil strength

Therefore, soils with steeper characteristic curves tend to have lower unsaturated strength than soils with shallow characteristic curves for the same air entry pressure, and at the same moisture content.

The air entry pressure, and the shape of the soil characteristic curve can be related to physical properties of soils as:

(a) The value of the air entry suction can be attributed, amongst other factors, to the soil pore size distribution. In general, soils with large pore sizes tend to have small values of the air entry suction, whereas soils with small pore sizes tend to have high values of air entry suction.

(b) The shape of the soil moisture retention curve can be attributed, amongst other factors, to the soil grain size distribution. In general, soils with a uniform grain size distribution tend to exhibit steep characteristic curves, whereas soils that are well graded exhibit shallow characteristic curves. .

With this in mind, and with what has been stated above, we can conclude that uniform soils, tend to be more susceptible to failure by saturation from above than well graded soils. This is because well graded soils tend to show greater unsaturated strength, since the soil suction is greater at the same moisture content.

These observations are, however, general guidelines, and the problem is more complex. This is because strength will also depend on the saturated strength parameters, c' and ϕ' as shown in Equation [3.8]. These parameters will, in general, be different for soils with different characteristic curves, and this has to be taken into consideration.

CONDUCTIVITY

Slopes that fail by saturation from above are slopes that are composed of soils with low unsaturated hydraulic conductivity. This allows for large pressures to develop behind an infiltrating front, because the front is retarded by the low conductivity.

In terms of the conductivity characteristic curve, this would imply a curve with a shallow slope that is located near the origin, where the absolute pressure is zero.

When the slope of the conductivity curve is shallow, large changes in suction, will cause small changes in conductivity and the conductivity remains low. When the conductivity curve is located close to the origin, i.e. when the air entry pressure is small, the conductivity of the soil remains at a low unsaturated value for large changes in suction. At high values of suction, the conductivity of the soil is very small, since the curve is located near the origin. This is illustrated in Figure 3.111.

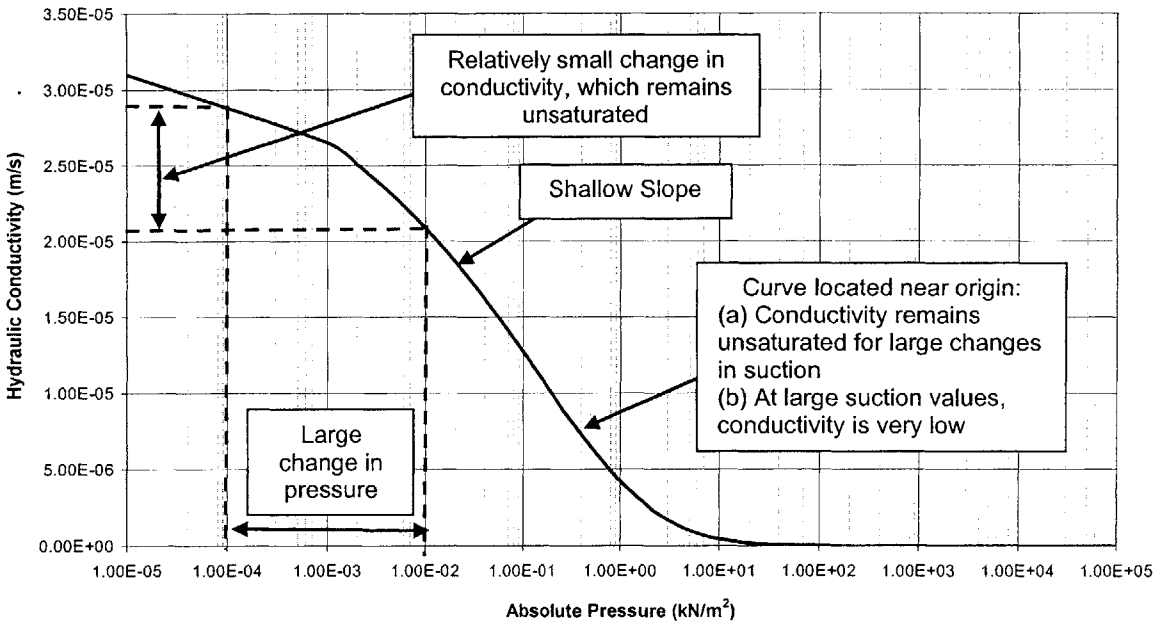

Figure 3.111. Properties of Hydraulic Conductivity Curve that Promote Failure by Saturation from Above

In general, soils with a uniform grain size distribution tend to exhibit steep conductivity curves, whereas soils that are well graded exhibit shallow conductivity curves. We therefore conclude that uniform soils, tend to be more susceptible to failure by saturation from above than well graded soils. This conclusion is consistent with the one made in previously with regard to strength.

3.5 CONCLUSIONS

Landslides can occur in a wide variety of different geological and hydrogeological settings, and many factors add to the complexity of the phenomena. This chapter presented some of the most important factors, both hydrological and geological, that play an important role in landslide initiation. A distinction was made between landslide mechanisms depending on the manner is which a slope gets saturated during rain. In particular, mechanisms were classified depending on whether the slope gets saturated from the bottom upwards, by a rising water table, or from the surface downwards, by infiltrating rainwater. Examples on different slopes presented in this chapter, and the following discussions show that, in general:

(a) Slopes with great depths to bedrock and shallow water tables, tend to fail by saturation from below, with failure surfaces typically along the soil bedrock interface resulting in a deep seated landslide

(b) Slopes with deep water tables tend to fail by saturation from above, with shallow failure surfaces that are located above the water table.

A comprehensive study of the mechanisms of shallow landslides was performed since these are poorly understood. These landslides occur because of changes in the initial suction in the unsaturated zone of the slope that plays a key role in stabilizing slopes. We showed that decreases in suction by infiltrating rainwater can reduce soil strength sufficiently to initiate a landslide. In particular, we showed that reduction of suction can generate a landslide. This is an important result since it remains a matter of debate amongst investigators in the field. Suction can also be eliminated during a rainfall event, or positive pressures may develop, and failures can occur in both cases.

It has been traditionally assumed that a low conductivity heterogeneity must be present in the subsurface to retard an infiltrating front sufficiently for positive pressures, in the form of a perched water table to develop. While we showed that this is true, we also showed that the presence of a low conductivity heterogeneity is not necessary for positive pressures to develop. We described two methods, previously unaddressed in the literature, in which positive pressures may develop behind an infiltrating front in a homogenous soil, ultimately causing failure. The first is when the saturated conductivity of the soil decreases with depth below the ground surface, and the second is when rate of infiltration suddenly exceeds the water transmission rate of the soil. In the first case, positive pressures develop gradually behind an infiltrating front. This causes the gradual loss of strength that leads to a landslide. In the second case, positive pressures develop rapidly behind an infiltrating front causing the sudden of strength, that generates an immediate landslide. This mechanism explains many field observations of sudden landsliding, e.g. Lambe (1959), and Torres et al. (1998).

A mechanism by which larger landslides with deep failure surfaces was also proposed. This mechanism is based on the saturation of the slope from above by infiltrating rainwater which increases the pressures along a section of a potential failure surface. As this happens, there is a decrease in the unsaturated soil strength along that section of the failure surface, and this decrease can be sufficient to generate a landslide. This mechanism may explain why such slides with deep failure surface have been observed in the field, without a rise in the main water table.

Several other important observations were made with regard to landslide modeling including:

a. Landslide studies should investigate all possible failure mechanisms so as not to overlook the critical mechanism, and avoid unconservative results.
b. Landslide studies should include a search for the critical failure surface, as opposed to postulating and specifying one particular surface, even if it is the initial critical surface.
c. This search should start from several initial trial surfaces.

d. A time dependent analysis of the state of stability of a slope is essential since it was shown that failure may take place both during a rainfall event, and after the end of rain, because of pressure redistribution.

This landslide study has enabled a much better understanding of landslide failure mechanisms, though it has also been shown that these mechanisms can be very complex, and depend on a large number of factors.

CHAPTER 4

UNCERTAINTIES

In this chapter, the uncertainties that enter the different stages of the landslide hazards assessment procedure, and their effects are described. The chapter is divided into two parts. Part 4-1 describes the sources of uncertainties and how they enter landslide analyses. Part 4-2 provides practical solutions to the uncertainty problem. Influence diagrams are used to simplify the hazards assessment procedure (decision analyses), and sensitivity analyses are performed to evaluate the relative influence of parameters on the landslide analyses. This allows one to formally retain parameters with the greatest influence for probabilistic analyses in Chapter 5, and eliminate parameters with the least influence.

4.1. SOURCES OF UNCERTAINTIES

Given that uncertainties are so important in geology and geotechnical engineering, attempts have been made to categorize them, e.g. Baecher (1978, 1972) Christian et al. (1994), Lacasse and Nadim (1996). In this study, we use the categories formulated in Einstein and Baecher (1982) and reviewed in Einstein (1995) namely:

- Innate spatial (and temporal) variability of geological factors or of nature in general
- Errors introduced by measuring and estimating engineering properties, including statistical fluctuation
- Model uncertainties
- Load uncertainty
- Omissions

In this chapter, emphasis is placed on the first three sources of uncertainties, particularly the first two. Chapter 6 is devoted to model uncertainty. This is done because the "load" in landslide problems is related to nature. Omissions, to quite an extent are related to

the care and completeness of work, hence, beyond keeping in mind that they represent a potential problem, they will not be considered.

It should also be noted that when formally assessing uncertainties, this can be done both by the relative frequency or the subjective approach. These approaches and their applicability have been discussed by Baecher (1972), Einstein and Baecher (1982), and Einstein (1995).

SOURCES OF UNCERTAINTIES IN THE STAGES OF THE LANDSLIDE DECISION ANALYSIS

Figure 4.1 shows the decision analysis cycle. Applying this decision making process to the landslide problem can take the form shown in Figure 4.2. This particular diagram was introduced by Einstein (1988) to duplicate the standard landslide mapping procedure which is done in steps similar to the sequence of boxes on the left side of Figure 4.2. The updating cycle (Updating in Figure 4.1) can, amongst other things, represent the observational method in geotechnical engineering (Terzaghi, 1961; Peck, 1969; Einstein, 1988).

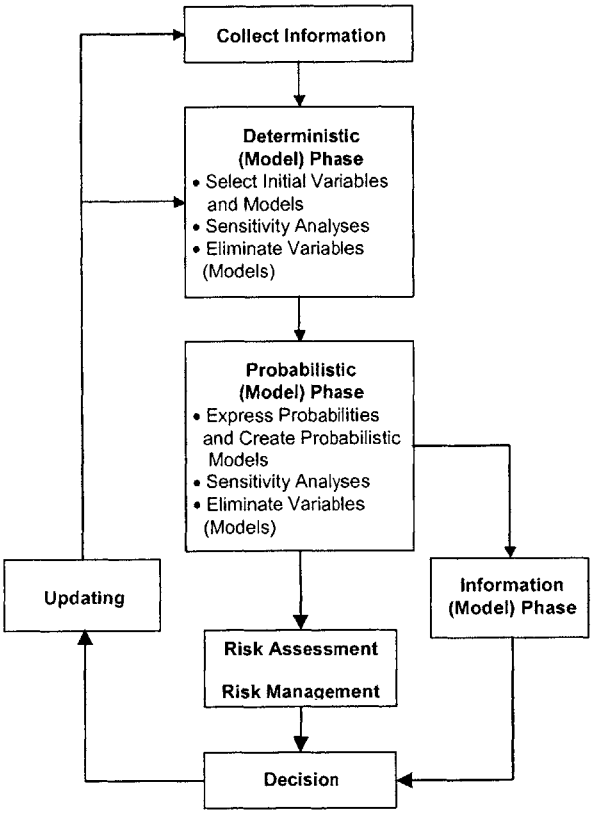

Figure 4.1. The Decision Analysis Cycle

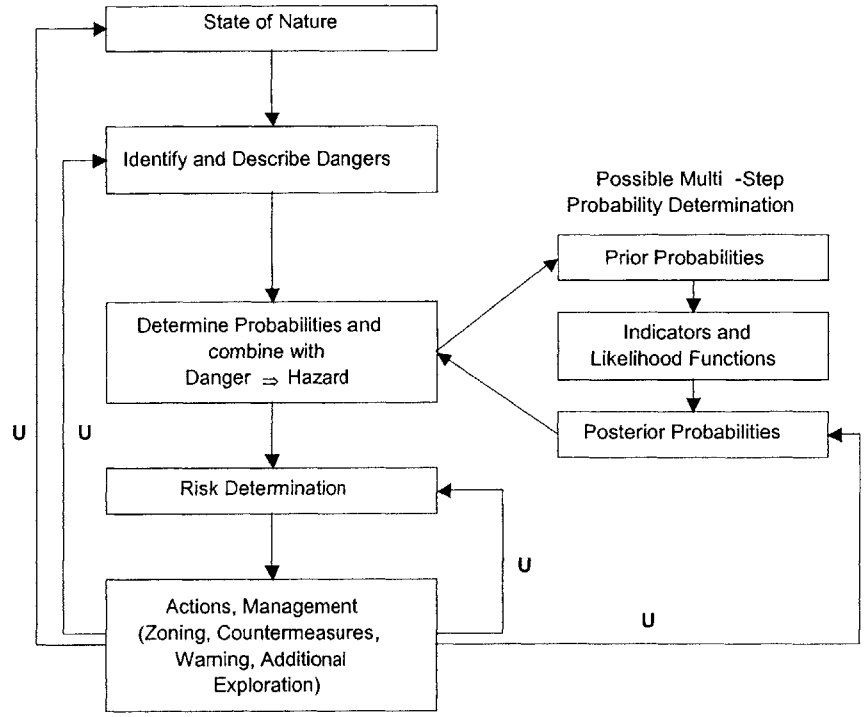

Figure 4.2. Decision Analytical Approach to Landslide Risk Assessment and Management (U=Updating)

While the structures in Figures 4.1 and 4.2 imply that the uncertainties, expressed in the form of probabilities, enter only in particular steps, uncertainties actually enter everywhere. Nevertheless, Figures 4.1 and 4.2 have the advantage of structuring the decision making process, and they will therefore, be used as a basis for the uncertainty discussions in this study.

4.1.1. STATE OF NATURE

Here most of the uncertainties are caused by innate spatial and temporal variability. However, if the state of nature is explored and tested, i.e. observed, measured and documented, it also involves measurement, estimation and statistical fluctuation errors. Also, if as they usually do, interpretation of exploration and testing rely on a model, model uncertainty enters. Figure 4.3 schematically shows examples for the sources of uncertainty in determining the state of nature, while Table 4.1 attempts to list parameters describing the state of nature and to what extent they are affected by each of the sources of uncertainty.

SPATIAL VARIABILITY

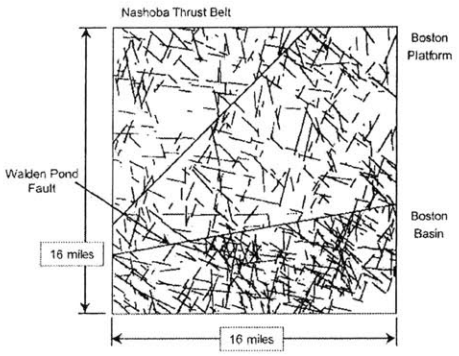

Example: Spatial Variability in Rock Joint Orientation in the Boston Area

RANDOM MEASUREMENT ERRORS

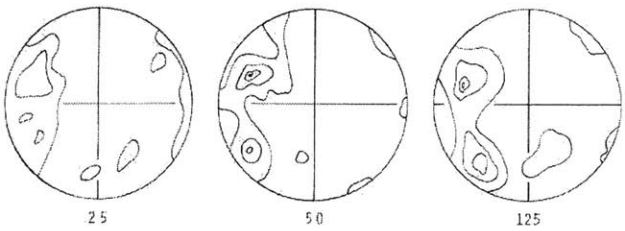

Example: Typical Changes in Pole Diagrams as the Number of Poles Sampled Increases. Poles Randomly Sampled from Population of Size 725

BIAS

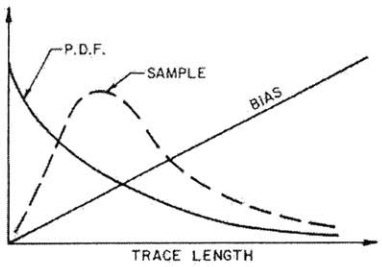

Example: Simple Length Bias in Sampling Trace Lengths

STATISTICAL FLUCTUATION

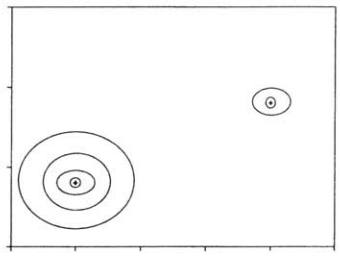

Example: Different Joint Orientation Contour Diagrams as Produced by Statistical Fluctuation

MODEL UNCERTAINTY

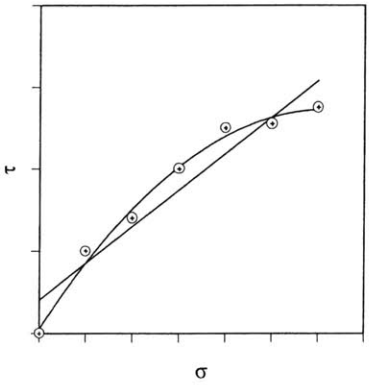

Example: Curved $\tau - \sigma$ Envelope better represents Data than the Straight Coulomb Model

Figure 4.3. Sources of Uncertainties when Determiniing the State of Nature

STATE OF NATURE	SOURCES OF UNCERTAINTY			
	Spatial/Temporal Variability	Measurement Uncertainty		Model Uncertainty (model = interpretation of exploration or test results)
		Error	Bias	
TRIGGER ZONE				
GEOLOGY				
SOIL				
Thickness	H	M	L	L
Stratigraphic Setting (homogenous/heterogeneous)	L	M	M	L
Strength Properties	M	M	M	L
Unit Weight	L	L	L	L
Pore Size Distribution	M	M	M	M
Grain Size Distribution	M	M	M	M
Porosity	M	M	M	M
Conductivity	M	M	L	M
BEDROCK				
Fracture Geometry	M	M	H	M
Strength	L	M	M	H
Conductivity	M	M	M	M
SURFACE CONDITIONS				
Vegetation	M	L	L	L
Cracks and Micro-Pores	M	M	M	M
HYDROLOGY				
Depth to Water Table	M	M	L	L
Subsurface Flow Regime	M	M	H	M
Antecedent Moisture Content	M	M	M	M
RAINFALL				
Intensity	H	H	M	H
Duration	M	M	L	L
SLOPE GEOMETRY				
Inclination	M	L	L	L
Depth to Bedrock	M	M	L	L

LEGEND:	
H	In most cases
M	In some cases
L	Rarely

Table 4.1. State of Nature with Sources of Uncertainty (example landslide trigger zone)

4.1.2. IDENTIFY AND DESCRIBE DANGER/THREAT

This process involves combining the state of nature observations into an entity, namely, the physical description of the soil/rock mass that might move, how it might be triggered

and how it might move, the latter possibly subdivided into main movement and runout or more components. Generic, qualitative or quantitative descriptions (Varnes, 1984; UNESCO, 1991; IUGS, 1997; TRB, 1994) of the possible landslide phenomena exist and can be applied to the particular location of the danger. Uncertainties can range from not knowing which phenomena will occur to extent and timing. Table 4.2 is an attempt at associating uncertainties with phenomena. (Not surprisingly these uncertainties will be mostly subjectively expressed.)

DANGER IDENTIFICATION	SOURCES OF UNCERTAINTY			
	Spatial/Temporal Variability	Measurement Uncertainty		Model Uncertainty (model = interpretation of exploration or test results)
		Error	Bias	
Type of Phenomenon	×		×	×
Size of Phenomenon	×	×	×	×
Exact Location	×	×	×	
Time	×		×	(×)

Table 4.2. Sources of Uncertainty Affecting Danger Identification. (x) Applies when Model includes Temporal Components

A step further or in parallel with the identification and description of the danger will be a description of the mechanism which in turn can be in form of empirical relationships, e.g. between rainfall intensity/duration and landslide incidence, all the way to mechanistic models at a variety of levels of detail, e.g. see Chapter 3.

Uncertainties associated with the description of the state of nature (see above) will propagate into the identification and description of dangers. In addition, model uncertainty will be another major source of uncertainty. This is discussed in more detail in Chapter 6.

4.1.3. DETERMINE PROBABILITIES

In this step one associates the previously mentioned uncertainties with probabilities and obtains a probability of the danger materializing, i.e. hazards. This process can, on the one hand, be in form of a subjective, intuitive assessment of the state of nature and the resulting landslide with a direct subjective association of probabilities to the landslide. This was done e.g. in the often described case of creeping slopes in the area of Villars,

where Noverraz (1988) directly predicted acceleration, stationarity or deceleration. Clearly this can be only done by experts. At the other extreme of determining probabilities is the propagation of uncertainties through an analytical model of the mechanism where each parameter is associated with a probability be that in form of distributions or moments. Such probabilistic modeling can be done with tools ranging from First Order Second Moment (FOSM) Analyses (Cornell, 1972; Ang and Tang, 1978) to Point Estimate Methods (Rosenblueth, 1977), to Monte Carlo simulations (Ang and Tang ,1984). Chapter 5 discusses probabilistic modeling using such tools, based on the mechanistic models developed in Chapter 2. In this step, another important uncertainty enters, namely the dependence or independence of parameters. This is considered a type of model uncertainty and is discussed in more detail in Chapter 6. Having said this, the dependence/independence of parameters is also affected by measurement uncertainties in that the measurements may reveal dependency where there is none in reality or vice versa.

4.1.4. RISK DETERMINATION AND ACTIONS OR RISK MANAGEMENT

Since this study is concerned with hazards determination, no further discussions are made here with regard to the risk determination and risk management stages. Reference is made to Einstein (1997) and Einstein and Karam (2001) for a more detailed discussion.

In summary, different types of uncertainties enter all the phases of the hazards assessment procedure (decision analysis cycle), rendering the problem of uncertainty capturing complex. The problem is made even more complex when one considers the uncertainties in the decision cycle (Figure 4.1) itself that come about from the simplifications made. Possible solutions to these problems are presented in the next section. Section 4.2.1 deals with simplifications to the decision analyses through the use of influence diagrams, and Section 4.2.2. deals with the simplifications to the parameter uncertainty problem through the formal elimination of variables using sensitivity analyses. There remains the problem of model uncertainty, and this is dealt with in detail in Chapter 6.

4.2. SOLUTIONS TO THE UNCERTAINTY PROBLEM

With what has been stated in Section 4.1, it is clear that describing uncertainties poses significant problems. Since it is necessary to be able to do something about landslide assessments in spite of these complexities, a possible approach, which makes use of influence diagrams to simplify the decision analyses procedure is outlined in this section.

4.2.1. SIMPLIFICATION WITH THE DECISION MAKING PROCESS

4.2.1.1. INFLUENCE DIAGRAMS

Figures 4.1 and 4.2 already gave an indication of how to simplify the decision making process namely through elimination of variables and simplification of models. This simplification can be systematically structured using influence diagrams, and it can be implemented based on sensitivity analyses.

Influence diagrams are classic tools of decision analysis which represent all state- and decision variables, and connect them amongst themselves and with the results, to show dependencies. They are very helpful in structuring a problem but require substructuring if a problem is complex, see e.g. Ashley et al. (1979). Figures 4.4 and 4.5 are attempts at structuring the "state of nature", and "describe danger" parts of the landslide decision making processes. Clearly, state of nature involves mostly state variables except for the decisions regarding observation/exploration. The next step, danger description, involves decisions on models/mechanisms. Once the general structure has been set out (Figure 4.5), danger description can be substructured using more detailed influence diagrams such as those for hydrologic modeling (Figure 4.6) and stability modeling (Figure 4.7).

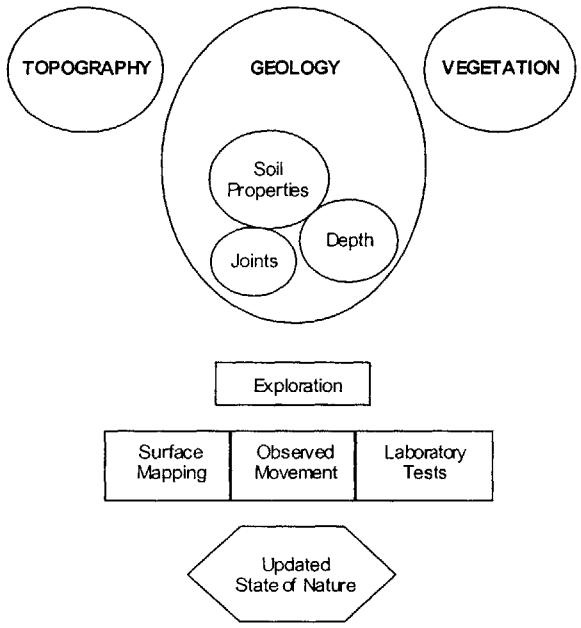

Figure 4.4. Possible Influence Diagram for State of Nature Assessment

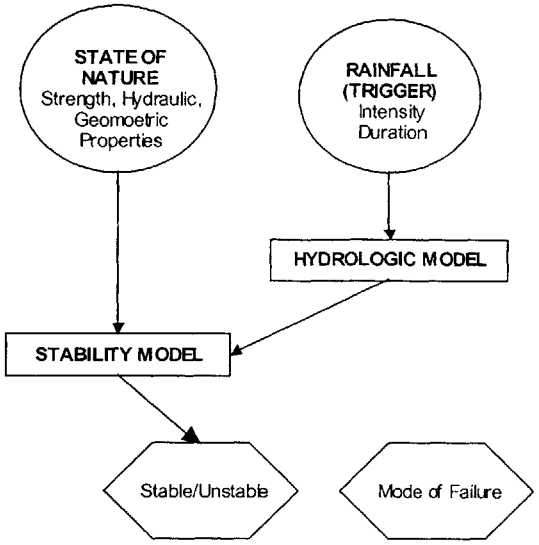

Figure 4.5. Possible Influence Diagram for Danger Assessment

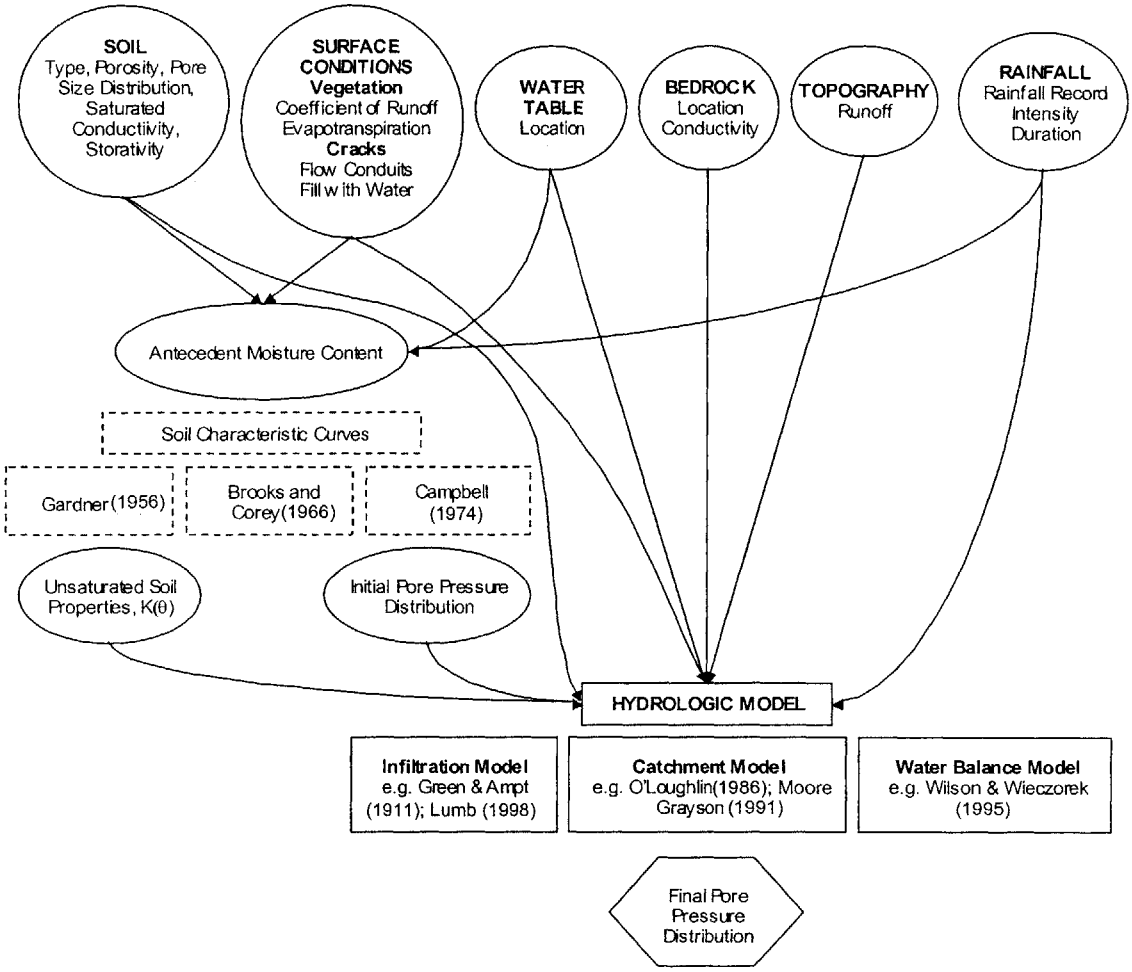

Figure 4.6. Possible Influence Diagram for Hydrologic Modeling

The unsaturated soil properties, $K(\psi)$, and initial pressure distribution can be directly measured, either in the field or in the lab. Alternatively, these can be related to the antecedent moisture content indirectly through the soil characteristic curves. Models exist for these curves. These are, therefore, shown in Figure 4.6 with boxes that have dashed lines indicating that these models can and are often used, but this is not necessary.

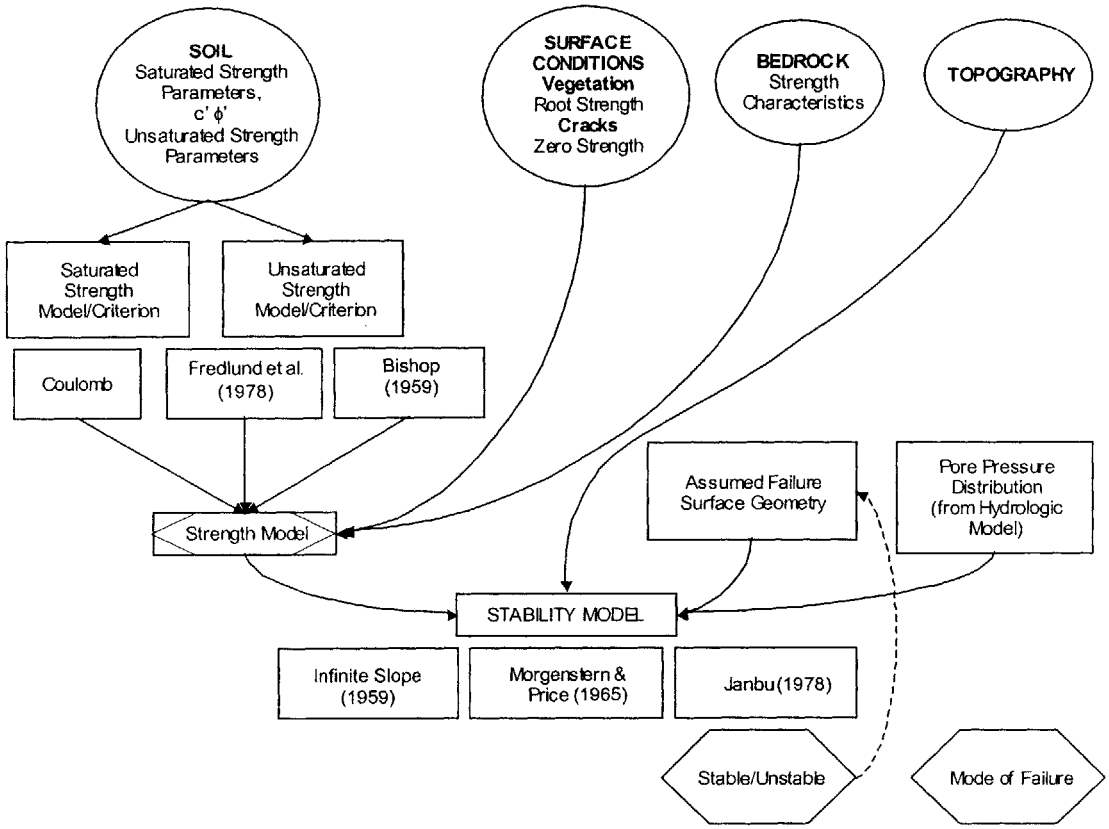

Figure 4.7 Possible Influence Diagram for Stability Modeling

where:

the ovals represent state variables (models) which are uncertain (random) quantities that are relevant to the decision problem. These are usually not in the control of the decision maker, e.g. state of nature.

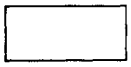

the rectangles represent decision variables (models) that are usually in the control of the decision maker, e.g. choice of stability model

the diamonds are values or output in the decision process.

dashed symbols imply temporary/intermediate steps

The influence diagrams can be expanded by comments on the connecting lines. Such comments would be largely based on judgment. For instance, one can mention the degree of uncertainty and the importance of a particular variable on the connecting line. This can then be used to eliminate some of the variables.

4.2.2. SENSITIVITY ANALYSES

A formal elimination of variables has to be done with sensitivity analyses. This includes both state and decision variables. Models have to be selected to perform sensitivity analyses, and these, by themselves are subject to model uncertainty, which is discussed in Chapter 6.

4.2.2.1. HYDROLOGIC SENSITIVITY ANALYSES

It has been extensively documented in the literature (e.g. Freeze, 1980) that the most uncertain parameter in hydrologic analyses is the saturated conductivity of the soil. The saturated conductivity typically exhibits very large spatial and temporal variability, and this is evident in the typical values that have been documented for the coefficient of variation of hydraulic conductivity which ranges from 50% – 500% (Freeze, 1980; Harr 1984; Benson et al., 1999). This will also become evident through the sensitivity analyses that are performed in this section. The effects of different parameters on hydrologic analyses are first performed using the widely used Green - Ampt (1911) hydrologic model, and then using the finite difference model developed in Chapter 2.

4.2.2.1.1. GREEN - AMPT (1911) MODEL

The Green – Ampt (1911) is a simple one-dimensional infiltration model that assumes infiltration occurs vertically downwards from a slope surface in the form of a migrating wetting front according to Darcy's Law. Because of its simplicity, it the model remains one of the most widely used ones, particularly in landslide analyses. The input parameters of the model are the saturated hydraulic conductivity of the soil, the soil wettable porosity (which is the difference between the saturated and residual moisture

contents), and ψ, a constant soil suction head assumed to act in front of the wetting front. The model's output is in the form of the depth to which complete soil saturation occurs. The model is described in more detail in Section 6-1.2 of Chapter 6.

Figures 4.8 to 4.11 show the effects of the different input parameters on moisture content profiles in a layer of soil at a time of 2 hours after the start of infiltration. Similarly, Figures 4.12 to 4.15 show the moisture profiles at time 4 hours.

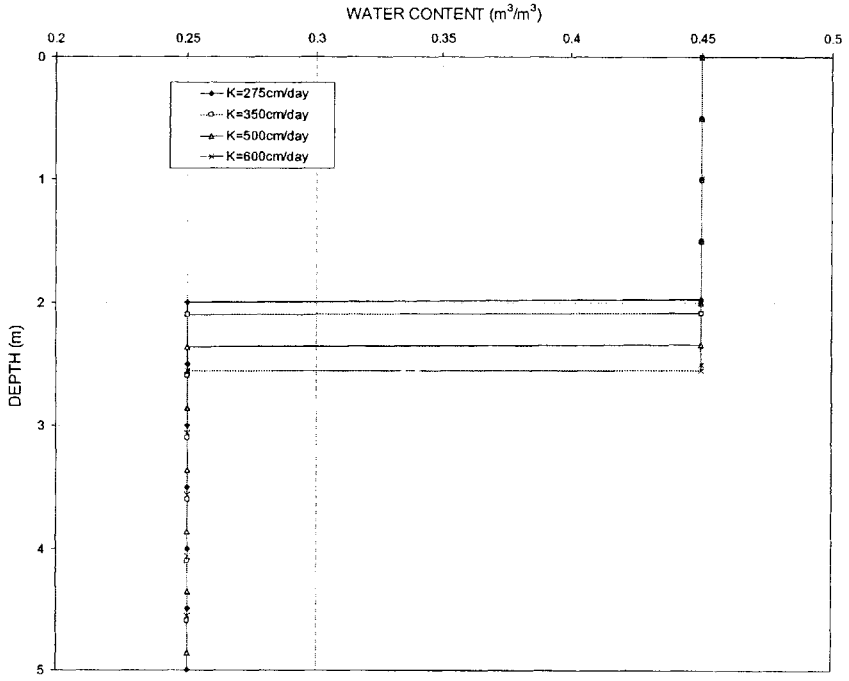

Figure 4.8. Sensitivity of Hydrologic Analyses to Hydraulic Conducitivity at 2 Hours (Green – Ampt Model)

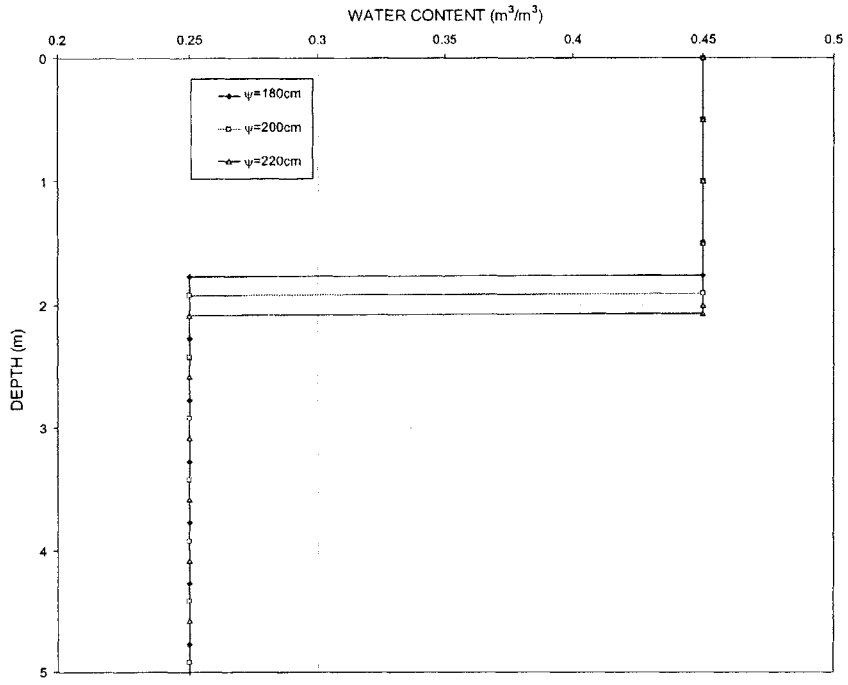

Figure 4.9. Sensitivity of Hydrologic Analyses to Constant Suction Head at 2 Hours (Green – Ampt Model)

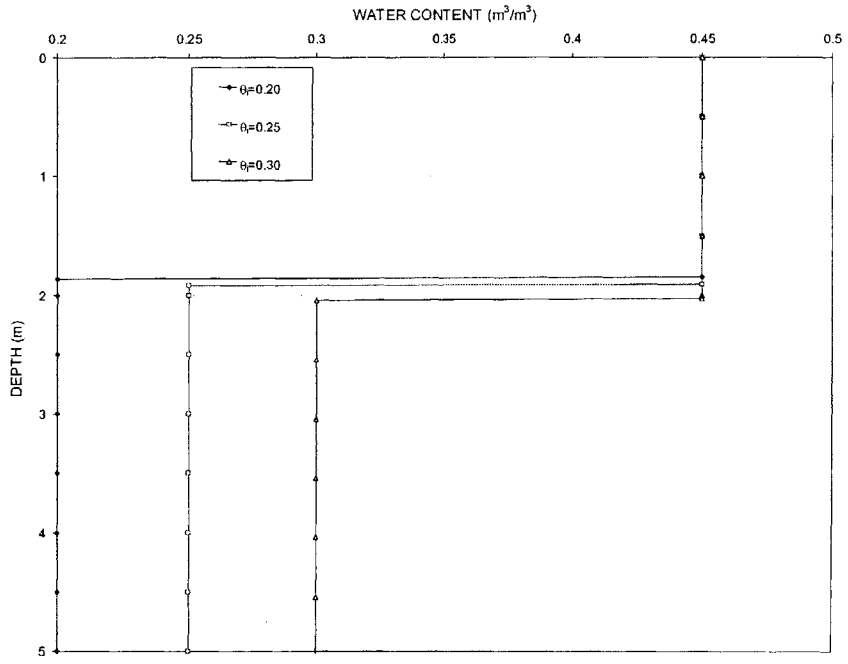

Figure 4.10. Sensitivity of Hydrologic Analyses to Initial (Antecedent) Moisture Content at 2 Hours (Green – Ampt Model)

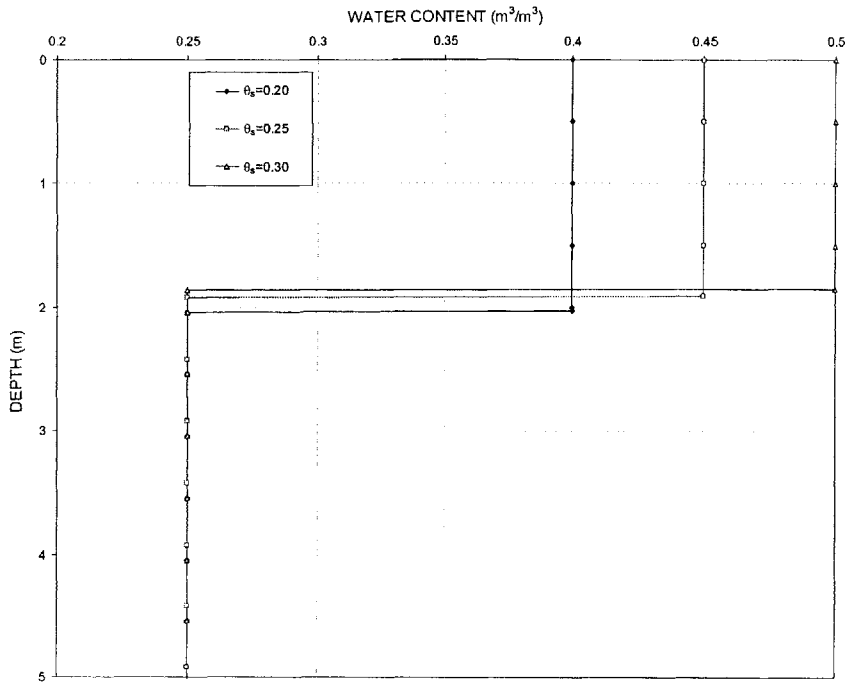

Figure 4.11. Sensitivity of Hydrologic Analyses to Saturated Moisture Content at 2 Hours (Green – Ampt Model)

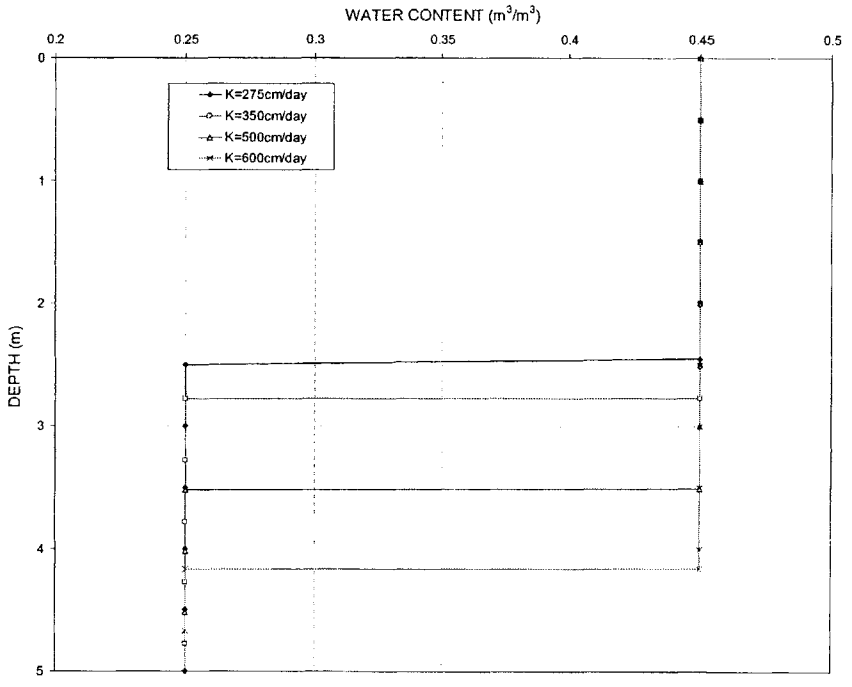

Figure 4.12. Sensitivity of Hydrologic Analyses to Hydraulic Conducitivity at 4 Hours (Green – Ampt Model)

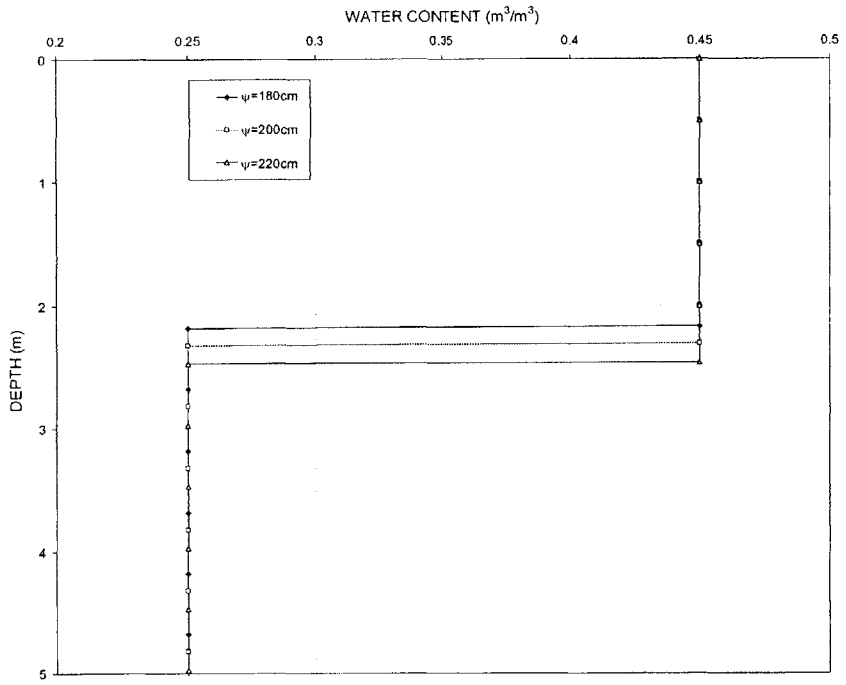

Figure 4.13. Sensitivity of Hydrologic Analyses to Constant Suction Head at 4 Hours (Green – Ampt Model)

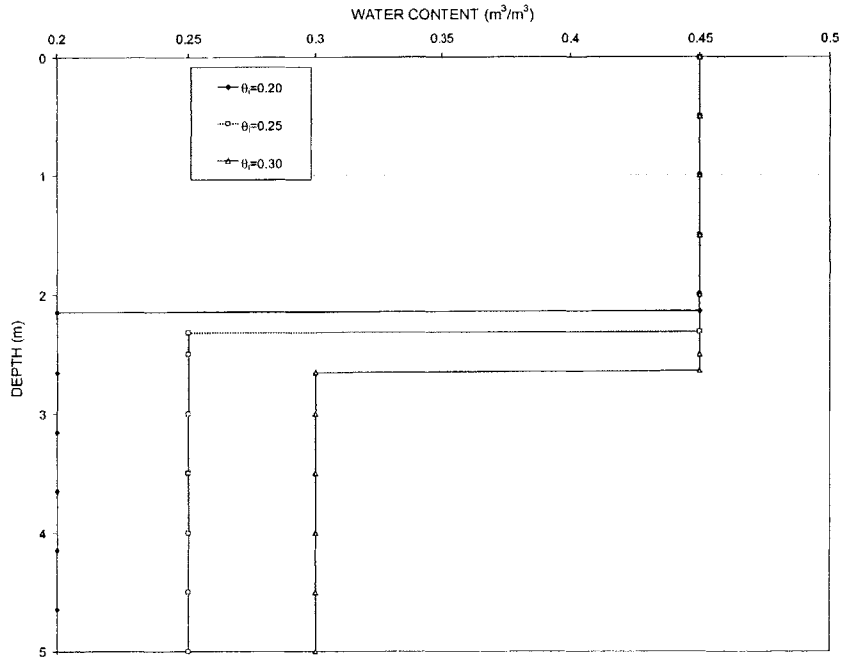

Figure 4.14. Sensitivity of Hydrologic Analyses to Initial (Antecedent) Moisture Content at 4 Hours (Green – Ampt Model)

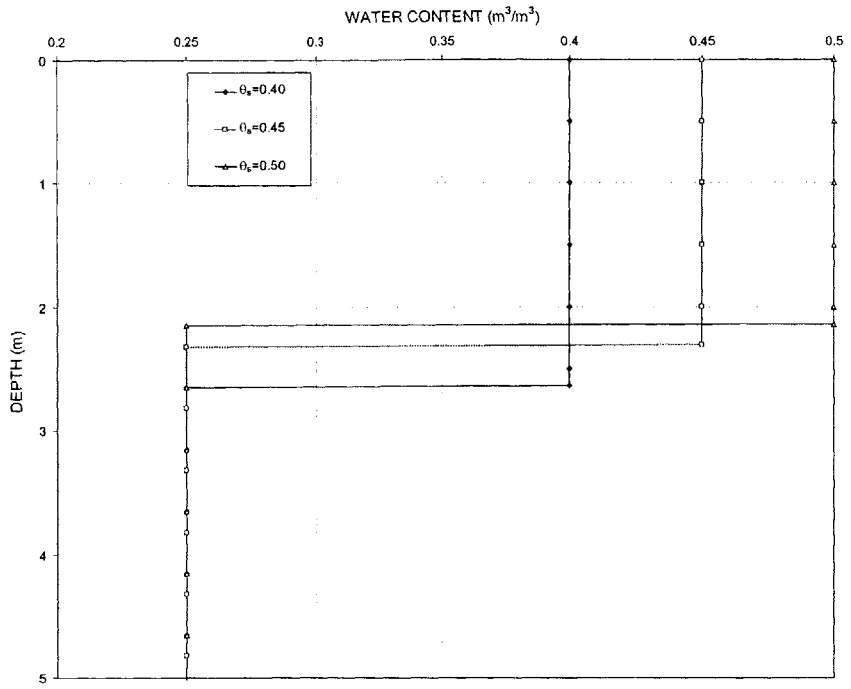

Figure 4.15. Sensitivity of Hydrologic Analyses to Saturated Moisture Content at 4 Hours (Green – Ampt Model)

Figures 4.8 to 4.11 and 4.12 to 4.15 show that the most influential parameter in hydrologic analyses is the hydraulic conductivity of the soil. The conductivity has the greatest effect on the depth to which saturation occurs (depth of penetration of wetting front), and hence the pore pressures above this depth. Appendix C-1 shows the sensitivity of other hydrologic parameters to the various input parameters of the Green – Ampt (1911) model, and the results presented there again show that the hydraulic conductivity of the soil is the most influential parameter.

It is, however, worth making a few more comments regarding Figures 4.8 to 4.15 in the context of landslide analyses:

a. The Green – Ampt (1911) model can only be used to predict moisture profiles with time. This is a significant drawback since it is the pore pressures (and not the moisture contents) that are needed for stability, and hence landslide analyses. The effects of different parameters on hydrologic analyses can

therefore not be thoroughly examined using the model. Nonetheless, some general results can be drawn.

b. The initial or antecedent moisture content distribution of the soil depends on the distribution of rainfall over a certain period of time, say through a season. The initial moisture distribution governs the initial pressure (suction) distribution through the soil characteristic curves. Therefore, the initial moisture distribution influences the initial state of stability of a slope. The influence becomes less important as the soil is saturated (see Figures 4.10 and 4.14). This was discussed in more detail in Chapter 3.
c. The saturated moisture content of the soil has an influence on the analyses as well, which is not very evident in Figures 4.11 and 4.15 because of the simplicity of the Green – Ampt Model. Specifically, the saturated moisture content will determine the amount of water required to cause saturation to a particular depth. This, in turn, is what affects the rate of advancement of a wetting front, and the pore pressures that develop.

Given what has been stated above, it is necessary to conduct more in-depth sensitivity analyses, and this can only be done using a more advanced model, such as the one developed in Chapter 2. These analyses are presented next.

4.2.2.1.2. ADVANCED HYDROLOGIC MODEL

A better understanding of the effects of different parameters on hydrologic analyses is gained by performing sensitivity analyses using the infiltration model developed in Chapter 2. The input parameters for the infiltration model include the soil properties, i.e. saturated conductivity, saturated and residual moisture contents, specific storage coefficient and the characteristic curves (see Chapter 2), as well as the initial (antecedent) moisture content distribution in the soil. To investigate the effects of the input parameters, we assume a soil layer consisting of a uniform soil with, saturated moisture content $\theta_s = 0.47 cm^3/cm^3$, residual moisture content $\theta_r = 0.11 cm^3/cm^3$, and saturated conductivity $K_s = 250 cm/day$. The van Genuchten (1980) model is used to describe the soil characteristic curves, and this model has two parameters, n and ∂ (see Chapter 2). The parameters are taken to be n = 3, and ∂ = 0.0068, and the characteristic curves are shown in Figures 4.16 and 4.16. We assume an initial and constant moisture content $\theta_i = 0.23 cm^3/cm^3$, which results in an initial and constant pressure distribution shown in Figure 4.18 at time t = 0 hours.

We then assume a constant infiltration flux at the soil surface equal to 175 cm/day for duration of 8 hours. Figure 4.18 shows the resulting distributions at times of 4 and 8 hours. These two cases are used as base cases for sensitivity analyses. The influence of the different parameters on hydrologic analyses are then investigated at these two times of 4 and 8 hours. Figures 4.19 to 4.25 show the effects of the various parameters on the pore pressure profiles at a time of 4 hours, and Figures 4.26 to 4.32 show the effects of the various parameters on the pore pressure profiles at a time of 8 hours, at the end of infiltration.

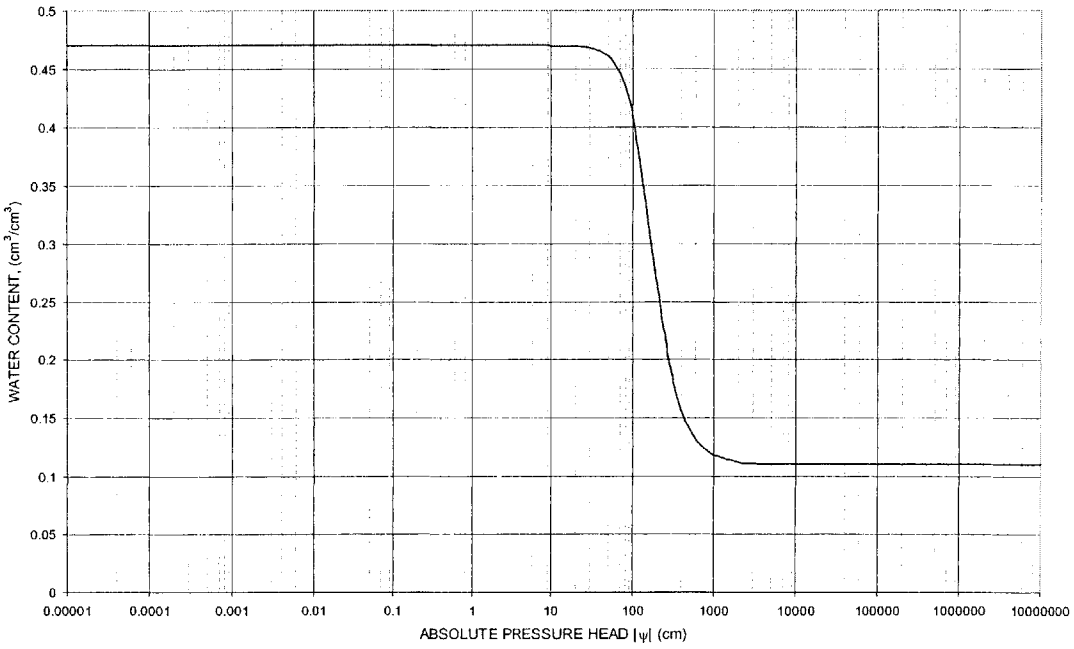

Figure 4.16. Soil Moisture Content Charcateristic Curve

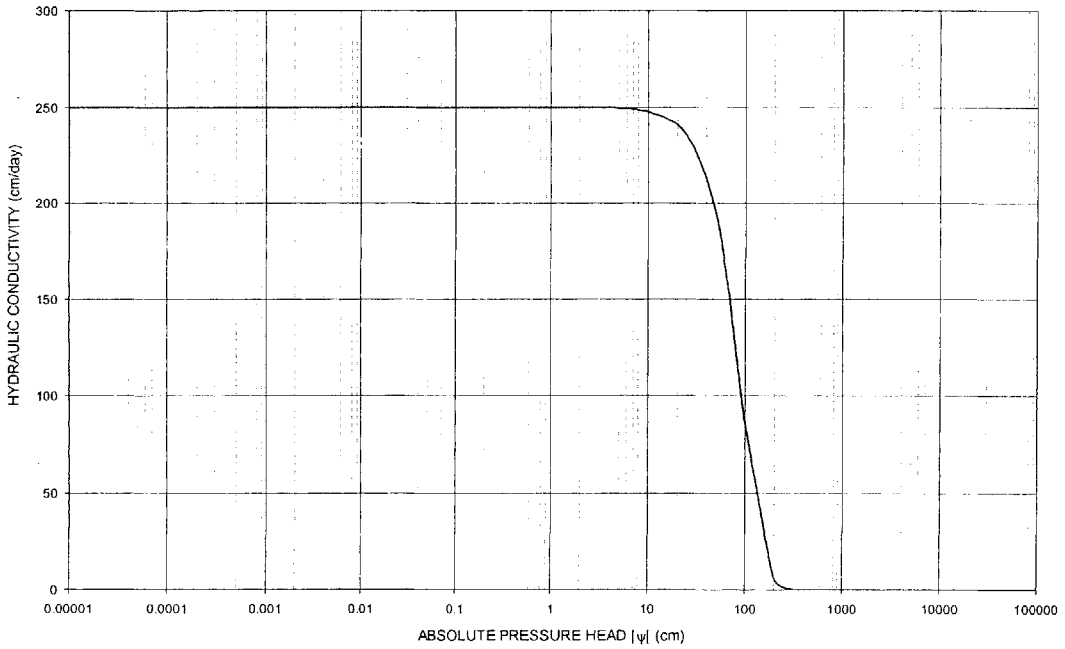

Figure 4.17. Soil Hydraluic Conducitivity Charcateristic Curve

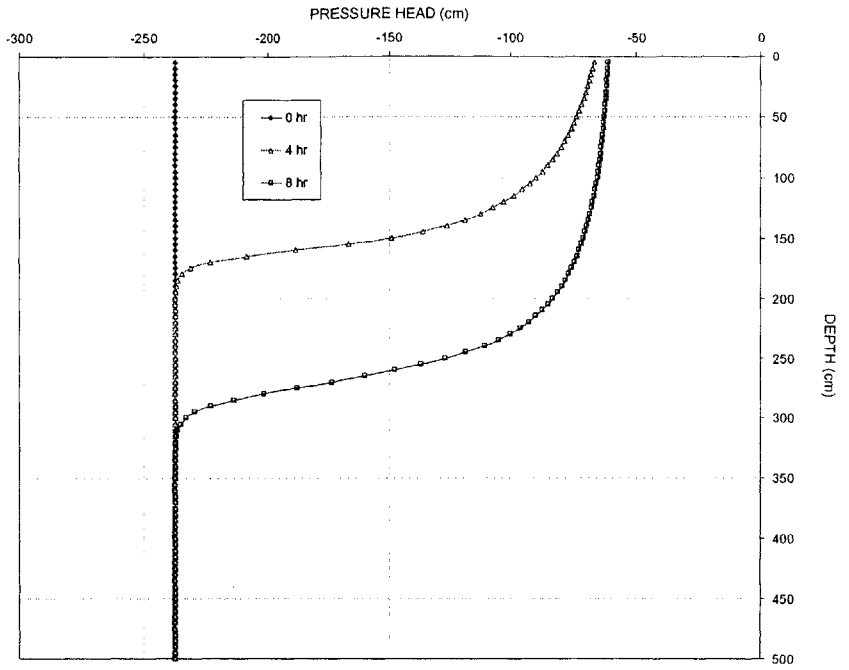

Figure 4.18. Initial Pressure Distribution, and Distributions at Times 4 and 8 Hours

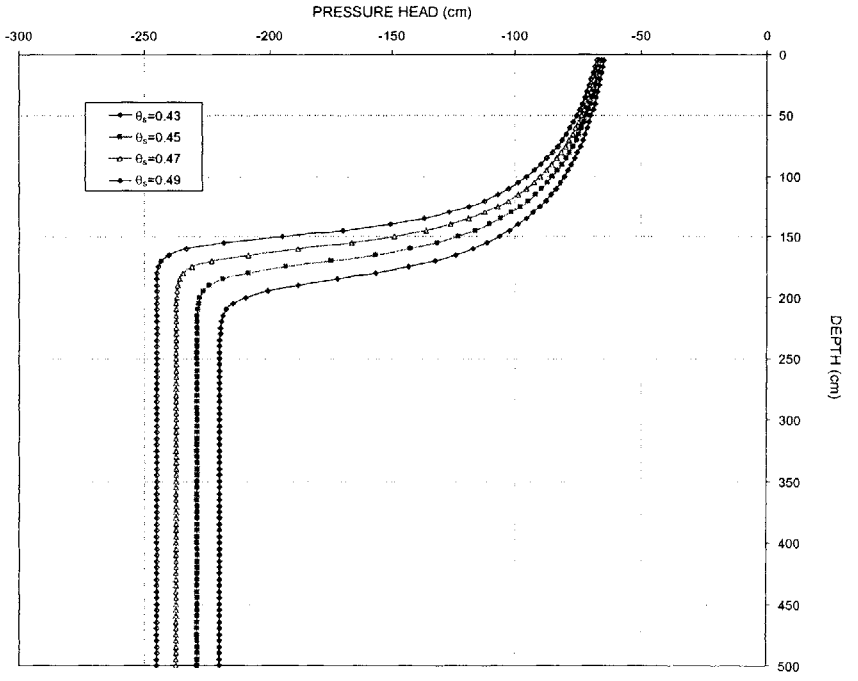

Figure 4.19. Sensitivity of Hydrologic Analyses to Saturated Moisture Content at 4 Hours (Advanced Finite Difference Model)

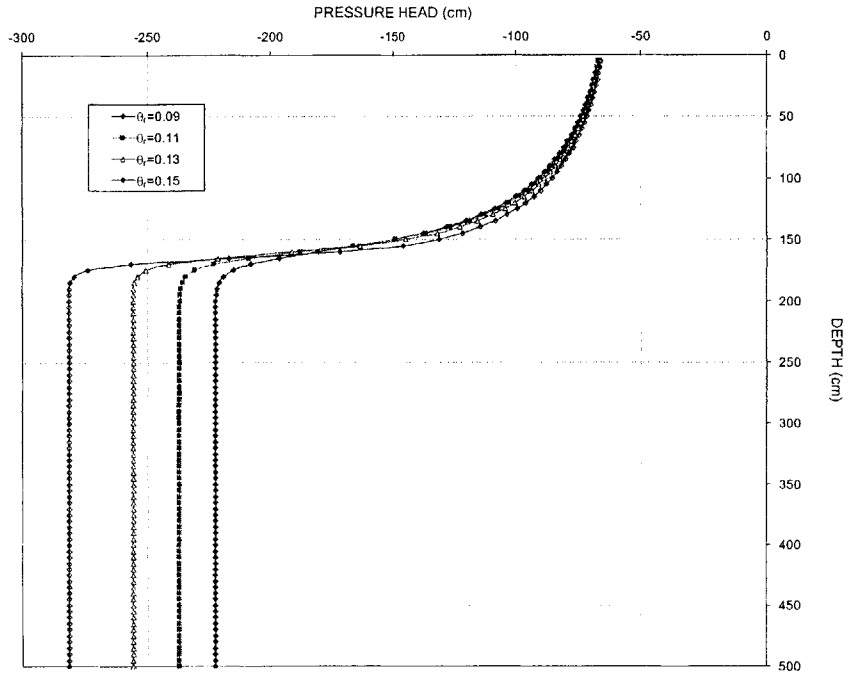

Figure 4.20. Sensitivity of Hydrologic Analyses to Residual Moisture Content at 4 Hours (Advanced Finite Difference Model)

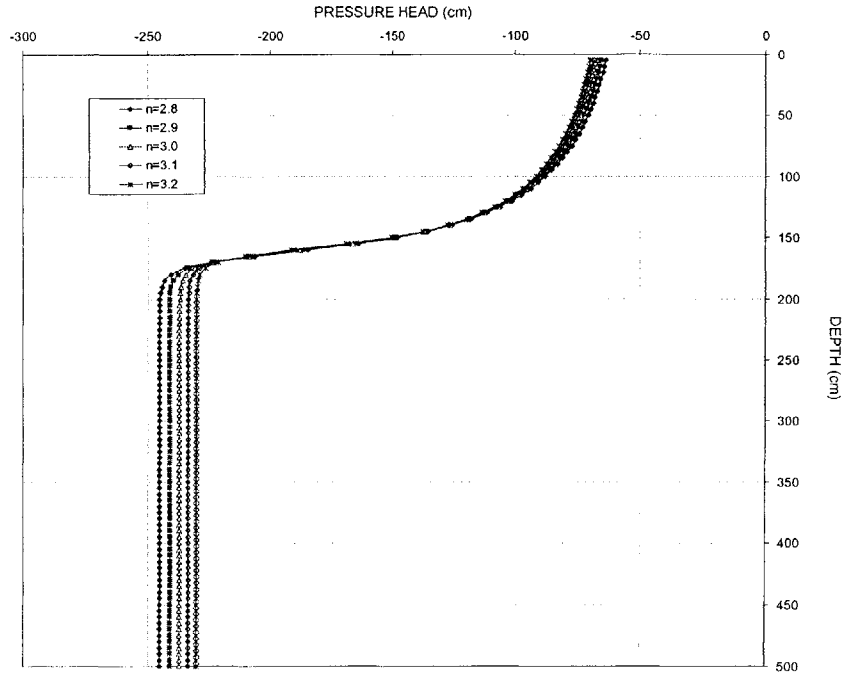

Figure 4.21. Sensitivity of Hydrologic Analyses to Parameter n of the van Genuchten (1980) Model at 4 Hours (Advanced Finite Difference Model)

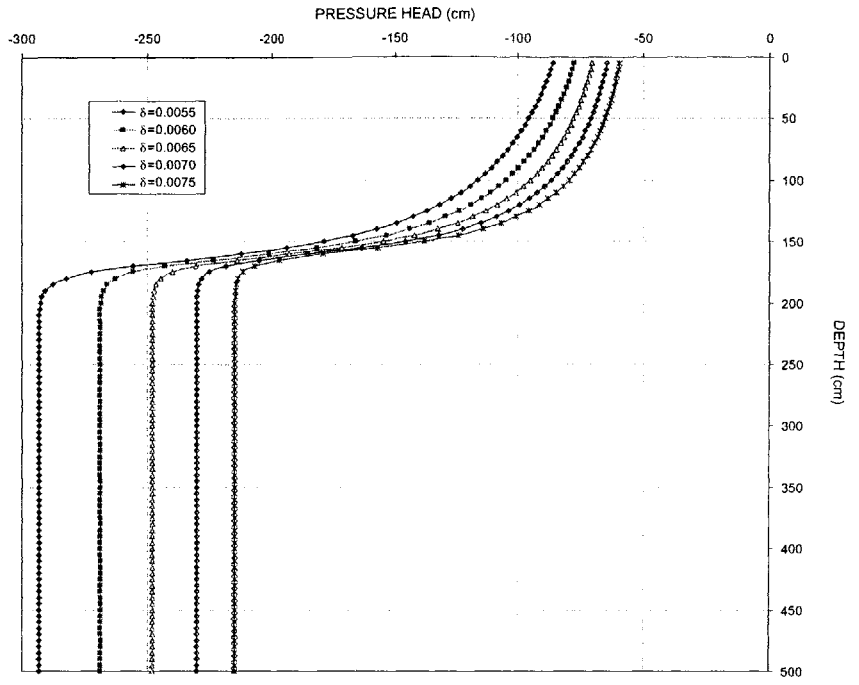

Figure 4.22. Sensitivity of Hydrologic Analyses to Parameter ∂ of the van Genuchten (1980) Model at 4 Hours (Advanced Finite Difference Model)

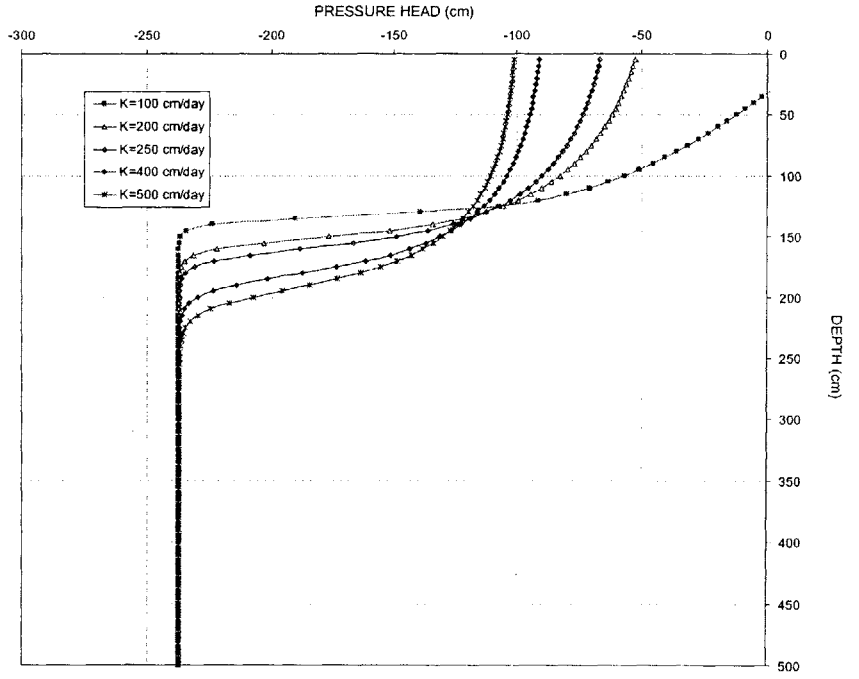

Figure 4.23. Sensitivity of Hydrologic Analyses to Hydraulic Conductivity at 4 Hours (Advanced Finite Difference Model)

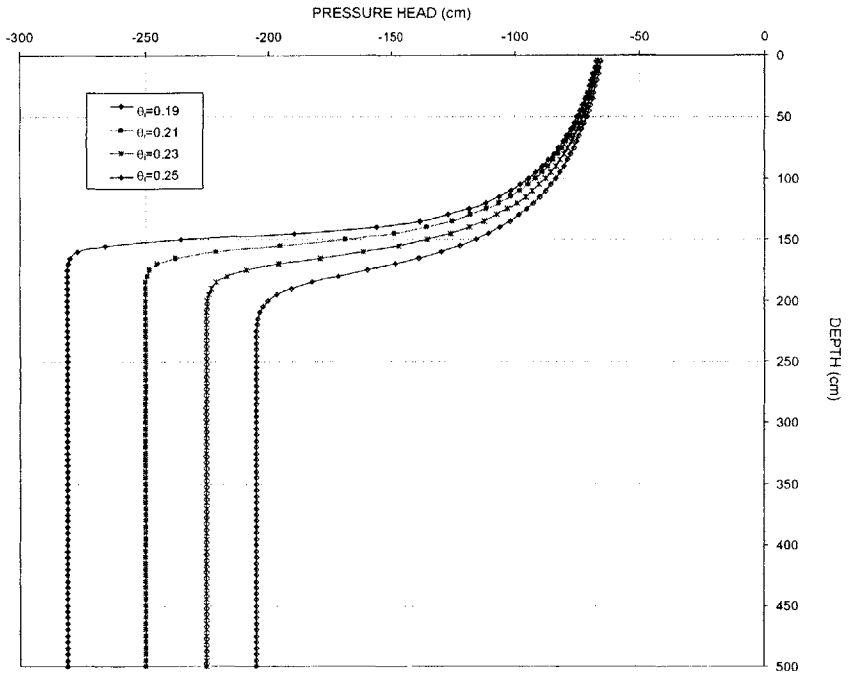

Figure 4.24. Sensitivity of Hydrologic Analyses to Initial (Antecedent) Moisture Content at 4 Hours (Advanced Finite Difference Model)

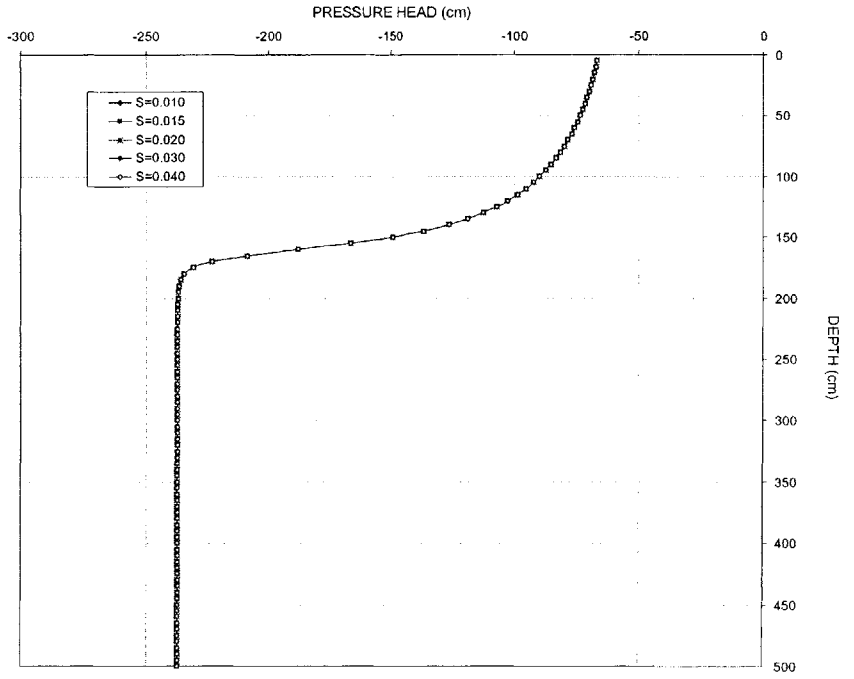

Figure 4.25. Sensitivity of Hydrologic Analyses Storage Coefficient at 4 Hours (Advanced Finite Difference Model)

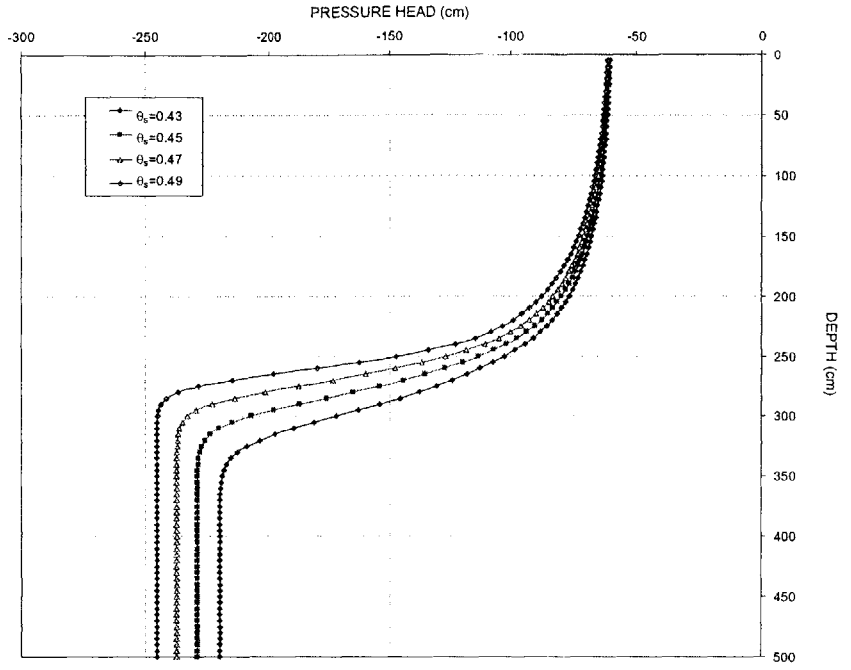

Figure 4.26. Sensitivity of Hydrologic Analyses to Saturated Moisture Content at 8 Hours (Advanced Finite Difference Model)

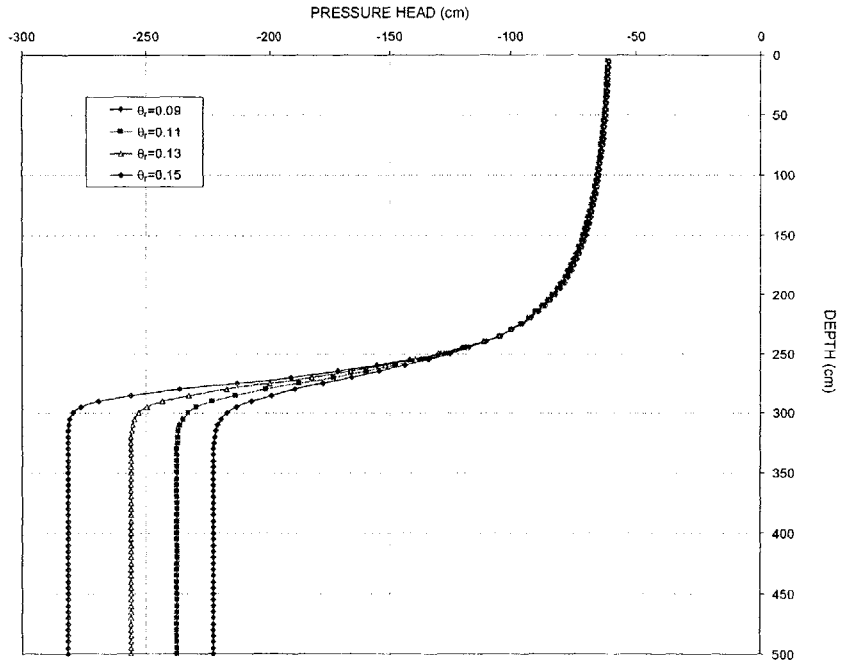

Figure 4.27. Sensitivity of Hydrologic Analyses to Residual Moisture Content at 8 Hours (Advanced Finite Difference Model)

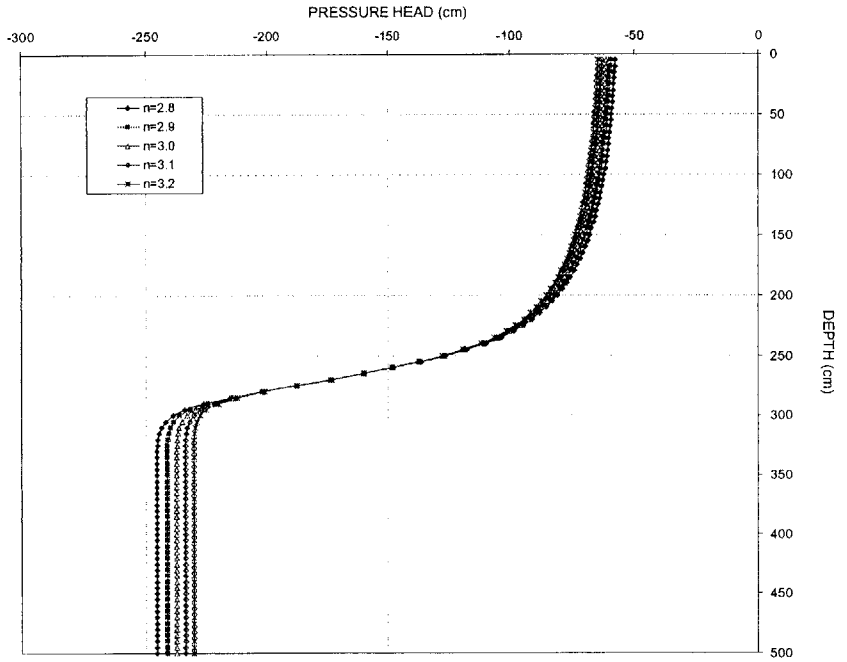

Figure 4.28. Sensitivity of Hydrologic Analyses to Parameter n of the van Genuchten (1980) Model at 8 Hours (Advanced Finite Difference Model)

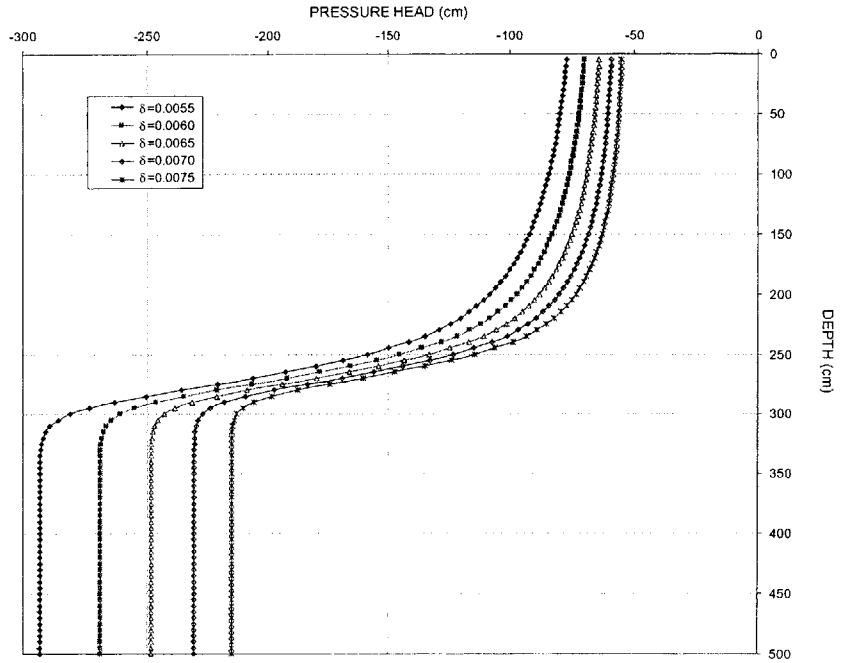

Figure 4.29. Sensitivity of Hydrologic Analyses to Parameter ∂ of the van Genuchten (1980) Model at 8 Hours (Advanced Finite Difference Model)

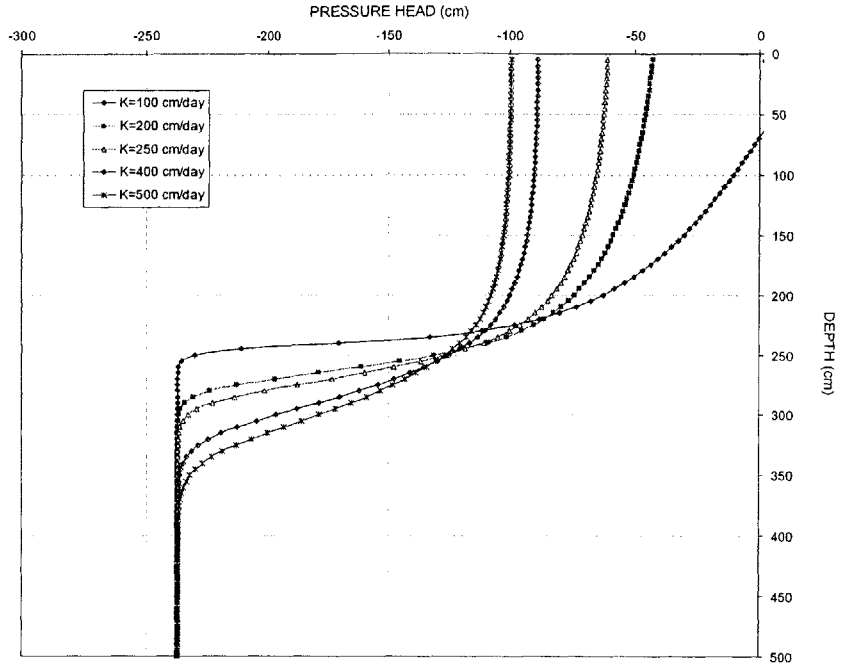

Figure 4.30. Sensitivity of Hydrologic Analyses to Hydraulic Conductivity at 8 Hours (Advanced Finite Difference Model)

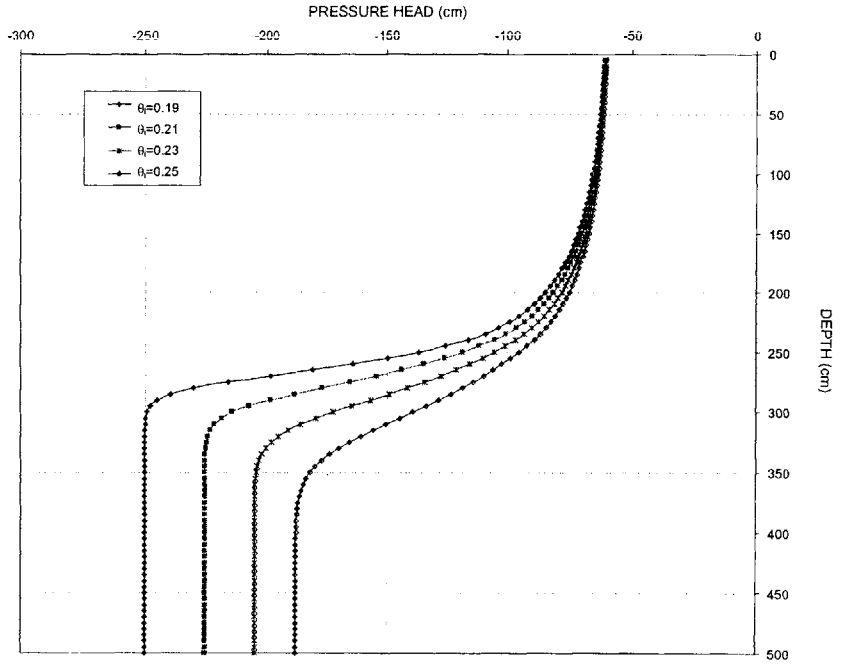

Figure 4.31. Sensitivity of Hydrologic Analyses to Initial (Antecedent) Moisture Content at 8 Hours (Advanced Finite Difference Model)

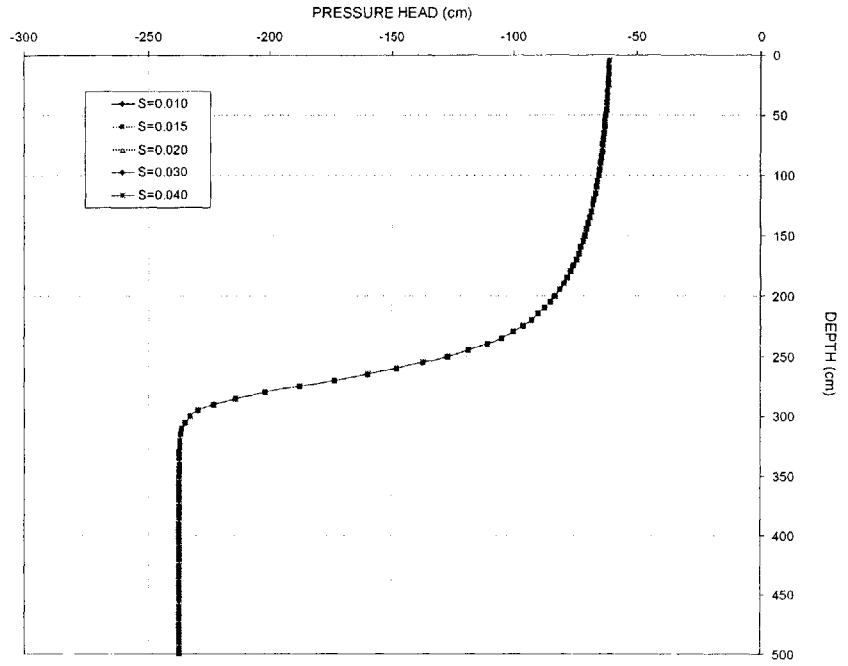

Figure 4.32. Sensitivity of Hydrologic Analyses Storage Coefficient at 8 Hours (Advanced Finite Difference Model)

Several comments can be made with regard to Figures 4.19 to 4.32:

a. The hydraulic conductivity of the soil has the greatest influence on the pore pressures that are generated during the infiltration process. This confirms the many observations, both theoretical and experimental that have been documented in the literature, e.g. Freeze (1977), Brass and Protopapas (1998).

b. The Storage Coefficient (see Chapter 2 for definition) has the least effect. In fact, Figure shows that the Storage Coefficient has no effect on the resulting pressure distributions. This is because the infiltration rate is lower than the saturated conductivity of the soil, allowing for all the water to penetrate through. The soil remains unsaturated, and so the Storage Coefficient has no effect. To better understand the effects of Storage Coefficient, the infiltration rate is increased to 325 cm/day, such that it exceeds the conductivity of the soil, allowing for positive pressures to be generated. Figure 4.33 shows the effects of Storage Coefficient on the pressure profiles at a time of 4 hours.

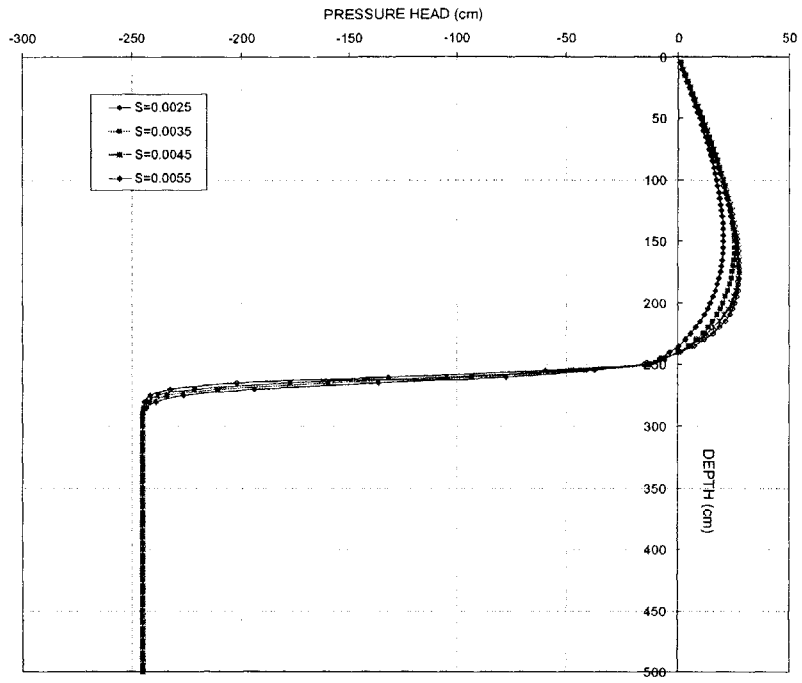

Figure 4.33. Sensitivity of Hydrologic Analyses Storage Coefficient at 8 Hours High Infiltration Rate (Advanced Finite Difference Model)

Figure 4.33 shows that although the Storage Coefficient has an effect on the results in this example, it remains the least influential parameter in the analyses.

c. The initial (antecedent) moisture content governs the initial pressures in the soil, and in the context of landslide analyses, therefore, the initial state of stability of the soil. Furthermore, the antecedent moisture content also governs the hydraulic conductivity of the soil, in such a way that higher moisture contents imply lower initial suction, and hence larger hydraulic conductivity. This is evident through the soil characteristic curves, e.g. Figures 4.16 and 4.17. The rate of water transmission during rainfall is, however, dependent on both the hydraulic conductivity as well as the suction (driving) head through Darcy's Law. The opposing effects of increased conductivity and smaller suction head have complex effects on water transmission through the soil during rainfall. Therefore, the role of antecedent moisture content is important in landslide analyses, though complex. This was discussed in more detail in Chapter 3.

d. The soil characteristic curves also play an important role in determining the initial pressure distribution in the soil (see Figures 4.21, 4.22 and 4.27, 4.28), and this was

also discussed in Chapter 3. The effects on the pressures that develop during infiltration are less evident.

In conclusion, given the results presented in this section, and those in Appendix C-1, the hydraulic conductivity of the soil is retained for probabilistic analyses in Chapter 5, whereas other parameters are eliminated.

4.2.2.2. STABILITY SENSITIVITY ANALYSES

In this section, sensitivity analyses to investigate the influence of different parameters on stability analyses are performed. This is done first using the Infinite Slope Model (Skempton & DeLory, 1959), and then using the more advanced stability model developed in Chapter 2.

4.2.2.2.1. INFINITE SLOPE MODEL (SKEMPTON & DELORY, 1959)

The Infinite Slope Model (Skempton & DeLory, 1957) is a Limit Equilibrium stability model that is based on the assumption that the depth to length ratio is a slope is very small. In such cases, the stability of a slope can be modeled in one dimension, z, the depth below the ground surface (see Figure 4.34). The Factor of Safety in an Infinite Slope can be expressed as (Skempton & DeLory, 1957):

$$F = \frac{c'}{\gamma_s z \sin\beta\cos\beta} + \frac{\tan\phi'}{\tan\beta} + \left[\frac{z_w - z}{z}\right]\left(\frac{\gamma_w \tan\phi'}{\gamma_s \tan\beta}\right) \qquad [4.1]$$

where the parameters in Equation [4.1] are defined in Table 4.3, and Figure 4.34.

Equation [4.1] can also be written as:

$$F = \frac{c'}{\gamma_s z \sin\beta\cos\beta} + \frac{\tan\phi'}{\tan\beta} - m\left(\frac{\gamma_w \tan\phi'}{\gamma_s \tan\beta}\right) \qquad [4.2]$$

where m is the degree of saturation in the slope defined as $m = \frac{h_w}{H}$, and h_w and H are defined in Figure 4.34.

The model has been chosen for sensitivity analyses because it remains to this day, the most widely used model in landslide analyses, and it is relatively easy to vary parameters in the model. This is because the model assumes that the failure surface is always along the soil bedrock interface, and hence one can simply vary parameters and investigate the effects on the results of stability analyses.

PARAMETER	SYMBOL	VALUE OR RANGE
Depth to soil-bedrock interface/failure surface (m)	H	
Depth below ground surface (m)	z	0 - H (m)
Cohesion (kN/m^2)	c'	10 –100 kN/m^2 (0 kN/m^2)
Angle of shearing resistance	ϕ'	$10 - 40^o$ (0^o)
Saturated unit weight of soil (kN/m^2)	γ_s	18 – 22 kN/m^2
Slope angle	β	$10 - 60^o$
Unit weight of water (kN/m^2)	γ_w	9.81 kN/m^2
Depth of water table from ground surface (m)	z_w	0 - H (m)

Table 4.3. Definition of Parameters and Range used in Sensitivity Study

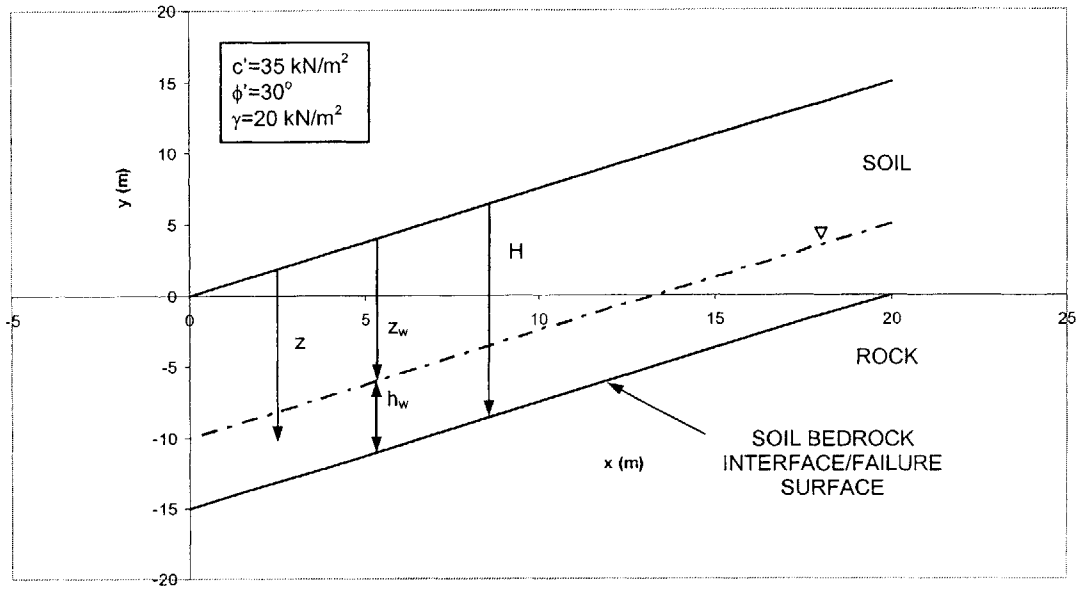

Figure 4.34. Slope Geometry and Definition of Parameters

Figures 4.35 to 4.38 show the influence of different parameters on stability analyses for the range of values given in Table 4.3.

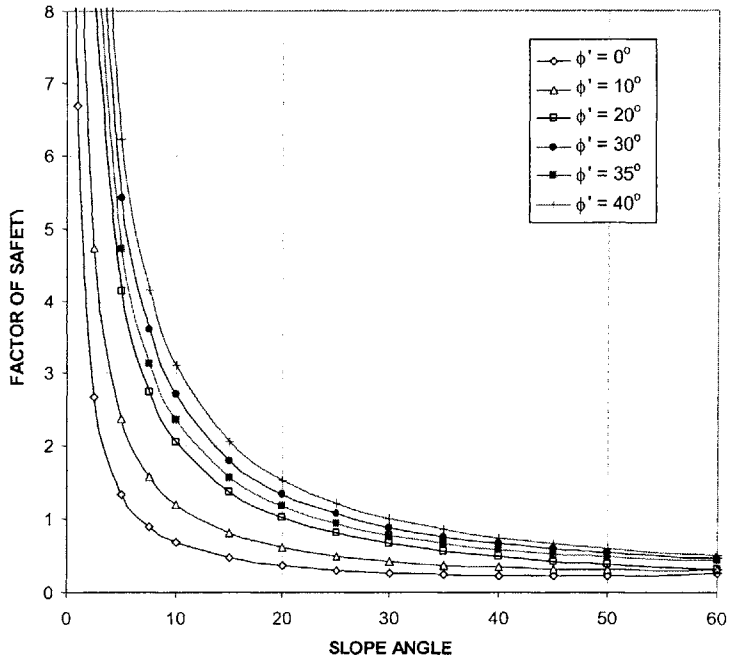

Figure 4.35. Effect Angle of Shearing Resistance and Slope Angle on Factor of Safety

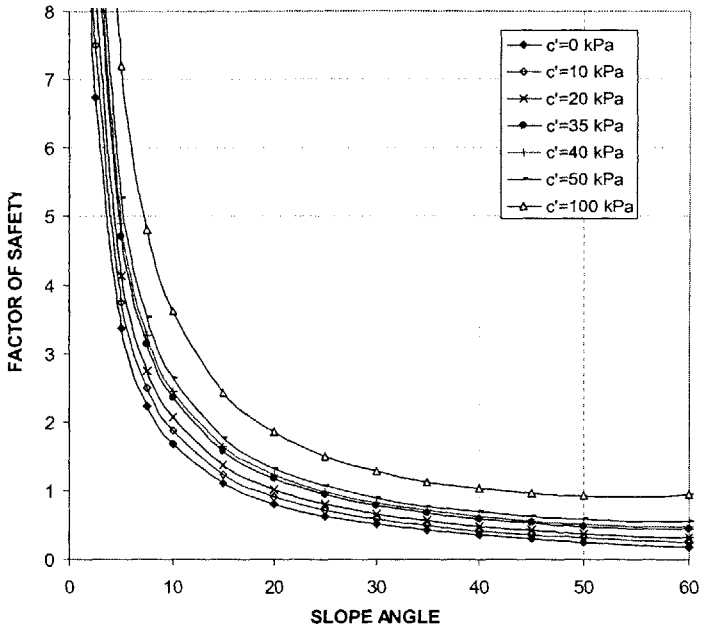

Figure 4.36. Effect of Cohesion and Slope Angle on Factor of Safety

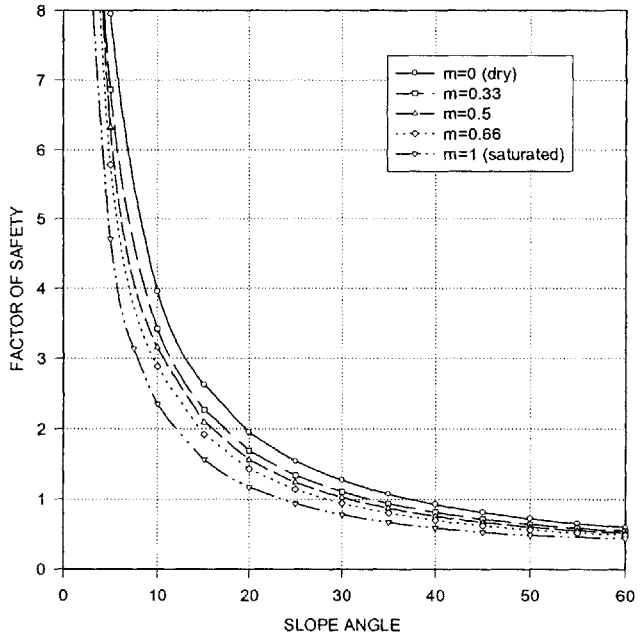

Figure 4.37. Effect of Degree of Saturation and Slope Angle on Factor of Safety

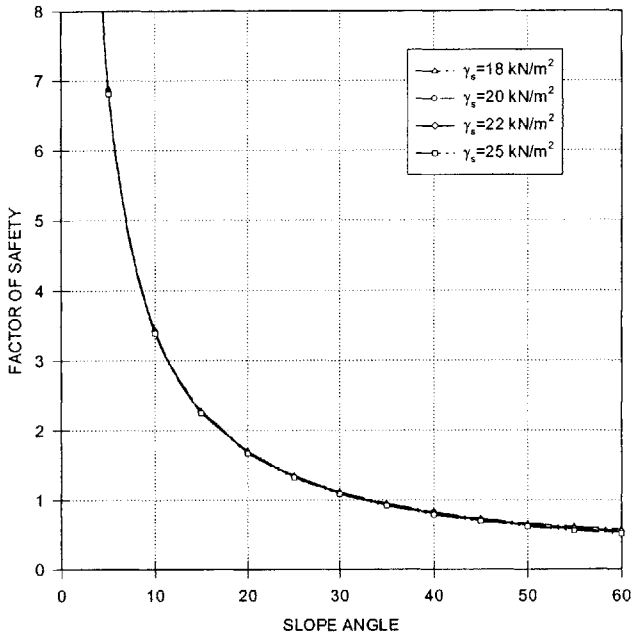

Figure 4.38. Effect of Unit Weight and Slope Angle on Factor of Safety

Based on the results in Figures 4.35 to 4.38, it is for instance, obvious that unit weight can be eliminated as a variable. The soil strength parameters c' and ϕ' are the most influential parameters, and these are retained for probabilistic analyses in Chapter 5. Prior to performing probabilistic analyses, one can take the sensitivity analyses a step further, and vary two parameters simultaneously, while including correlation. Figures 4.39, and 4.40 show this for positive and negative correlation of the parameters c' and ϕ', although this may practically not be a very meaningful example since one can be reasonably certain that c' and ϕ' are negatively correlated. These types of sensitivity analyses do however serve to show where correlation can be important and where not.

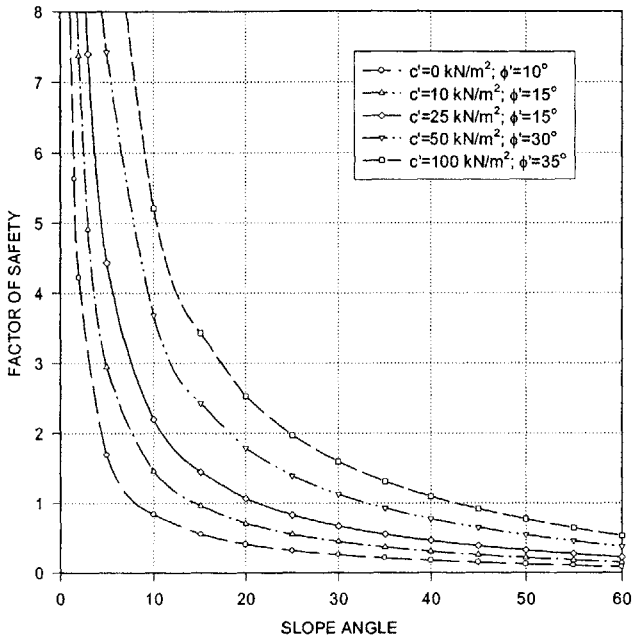

Figure 4.39. Effect of Positive Positive Correlation between c' and ϕ' and Slope Angle on Factor of Safety

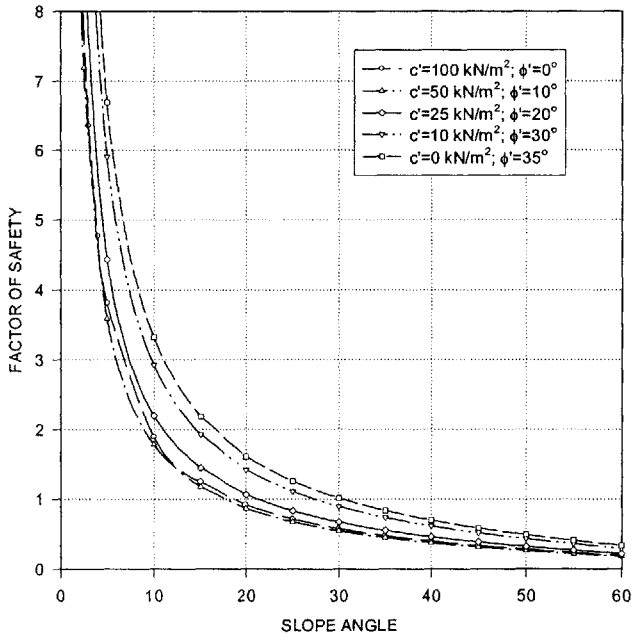

Figure 4.40. Effect of Negative Correlation between c' and ϕ' and Slope Angle on Factor of Safety

More extensive sensitivity analyses involving one, and two parameters using the Infinite Slope Model are given in Appendix C-2.

4.2.2.2.2. ADVANCED STABILITY MODEL

In this section, the sensitivity of stability analyses to various parameters is investigated using the advanced stability model that was developed in Chapter 2. In order to perform meaningful sensitivity analyses, so that the results can be directly compared, it is necessary to show the results on plots of, say, Factor of Safety against slope angle, as was done in the previous section. This was simple using the Infinite Slope Model since the assumption that the critical failure surface is at the soil bedrock interface is (almost) inherent. This is not the case with the advanced model that was developed in Chapter 2. Recall that the model includes a search for the critical failure surface in a slope along which the Factor of Safety is minimum. Therefore, prior to any analyses, it is necessary to select various slopes, with differing inclinations to the horizontal, which will be used in the sensitivity study. It is also necessary to locate the critical failure surface in each of these slopes. Figures 4.41 to 4.46 show six slopes that have been chosen for this purpose, along with the soil and geometric properties, and critical failure surfaces. The slopes are inclined at angles 10^o to 60^o to the horizontal in increments of 10^o. In each slope, the depth to the bedrock from the ground surface is taken to be 5 m, and the depth of the water table is 3 m, thus keeping the ratio m (see previous section for definition) constant at $m = \frac{2}{5}$. The length of the slope is also kept the same at 35 m.

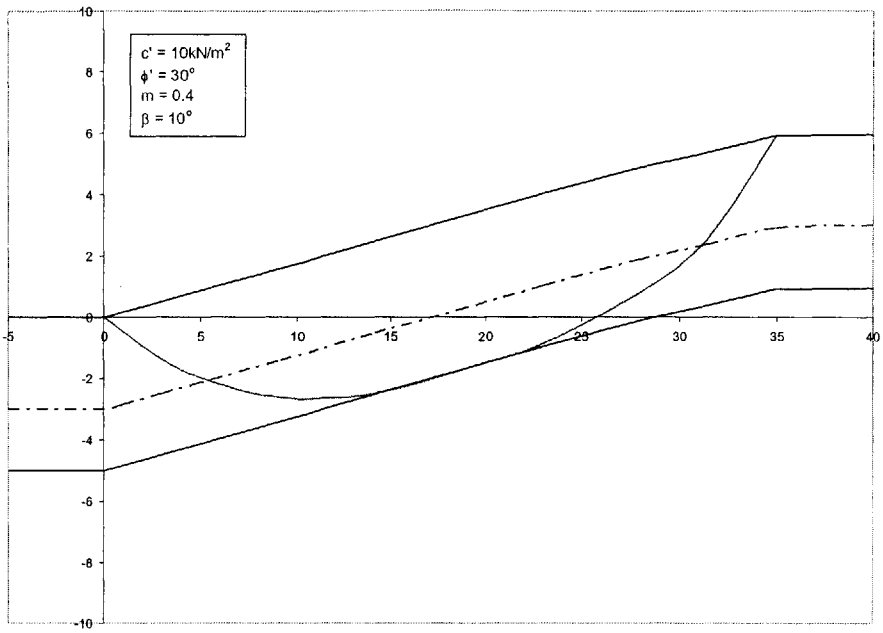

Figure 4.41. Slope 1 Parameters Used in Sensitivity Analyses

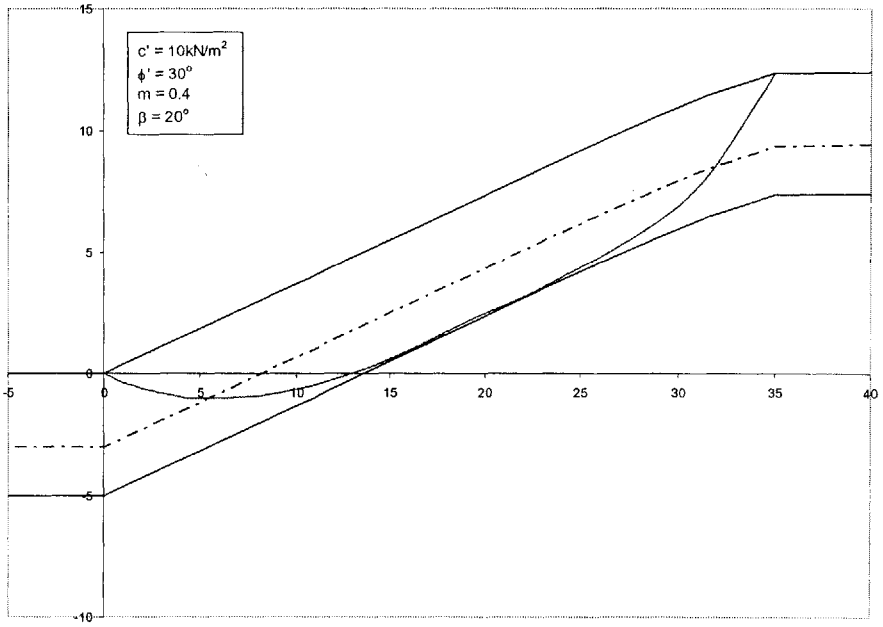

Figure 4.42. Slope 2 Parameters Used in Sensitivity Analyses

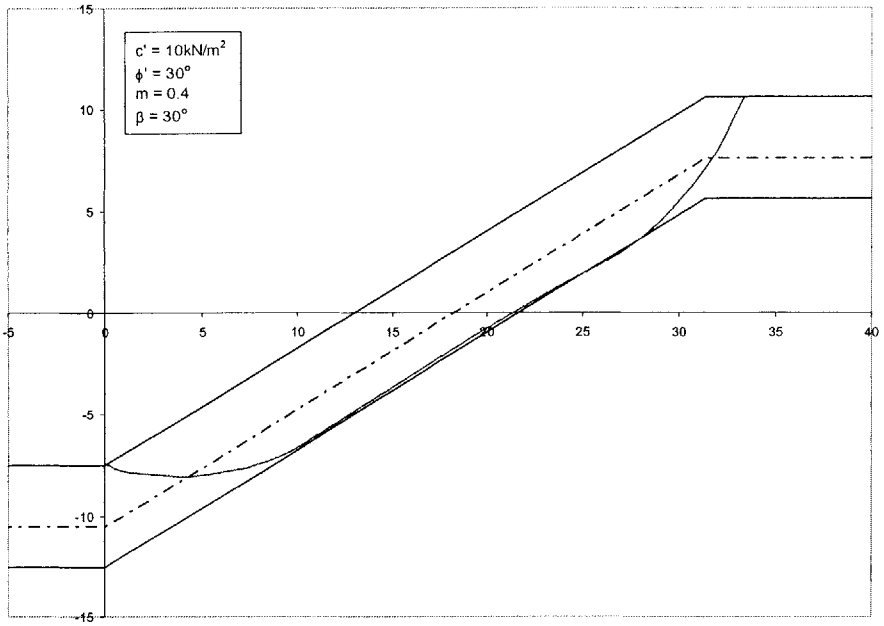

Figure 4.43. Slope 3 Parameters Used in Sensitivity Analyses

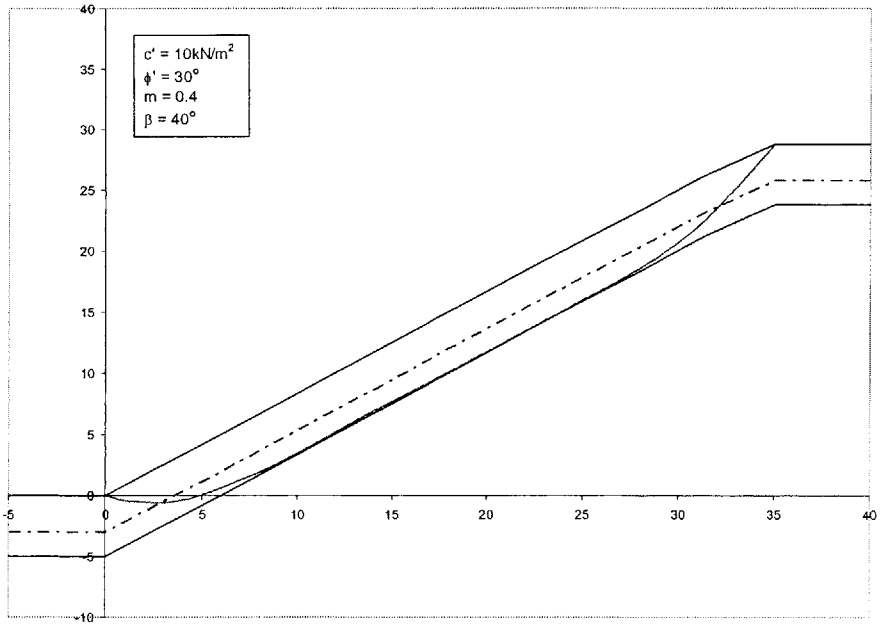

Figure 4.44. Slope 4 Parameters Used in Sensitivity Analyses

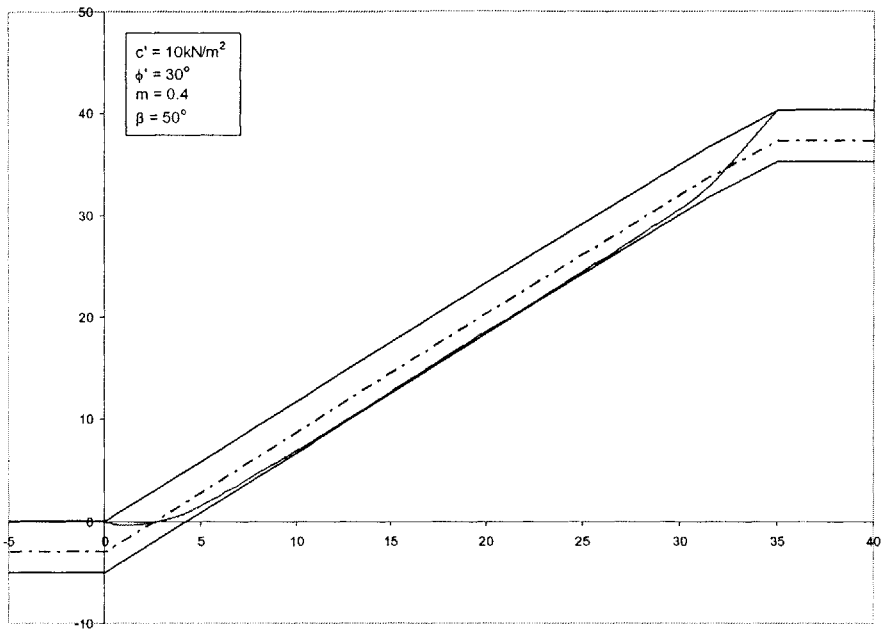

Figure 4.45. Slope 5 Parameters Used in Sensitivity Analyses

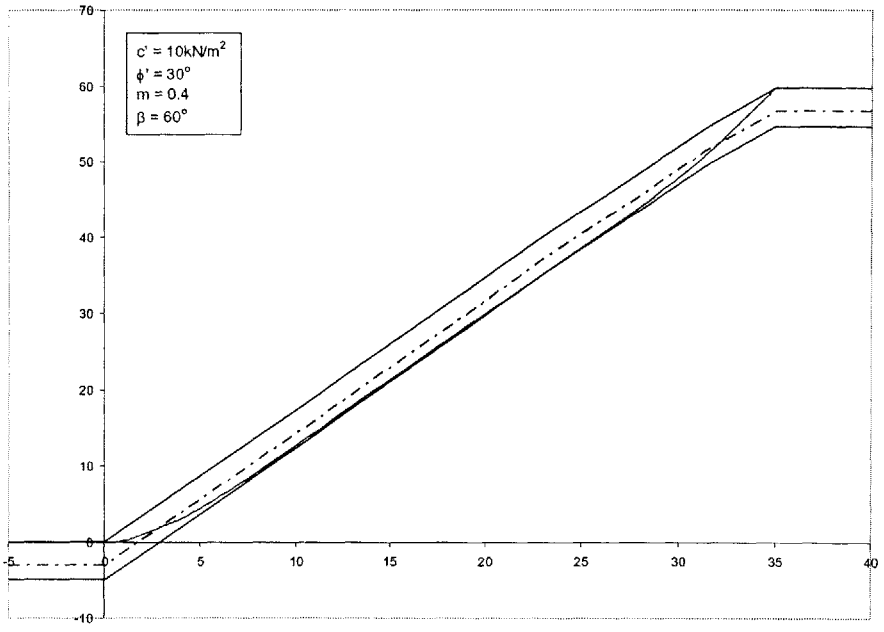

Figure 4.46. Slope 6 Parameters Used in Sensitivity Analyses

Figures 4.47 to 4.51 show one parameter sensitivity analyses, based on the slopes shown in Figures 4.41 to 4.46.

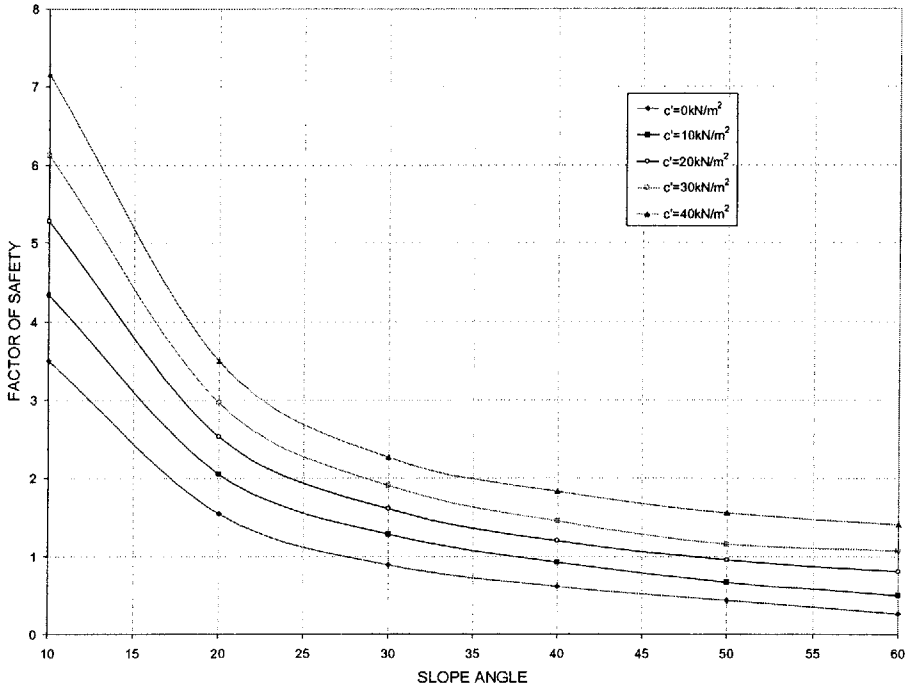

Figure 4.47. Effect of Cohesion and Slope Angle on Factor of Safety (Advanced Model)

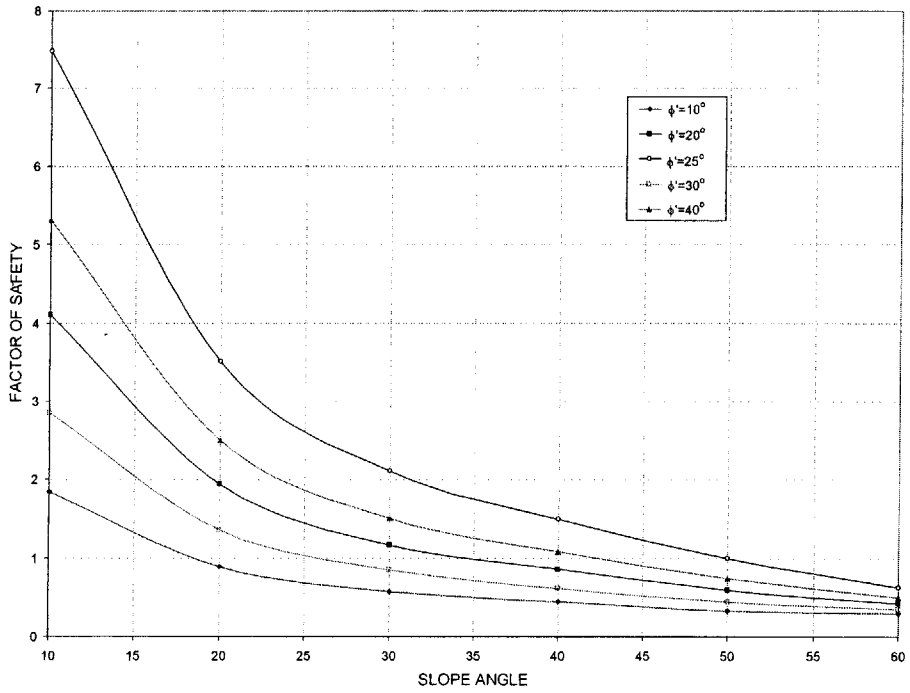

Figure 4.48. Effect of Angle of Shear Resistance and Slope Angle on Factor of Safety (Advanced Model)

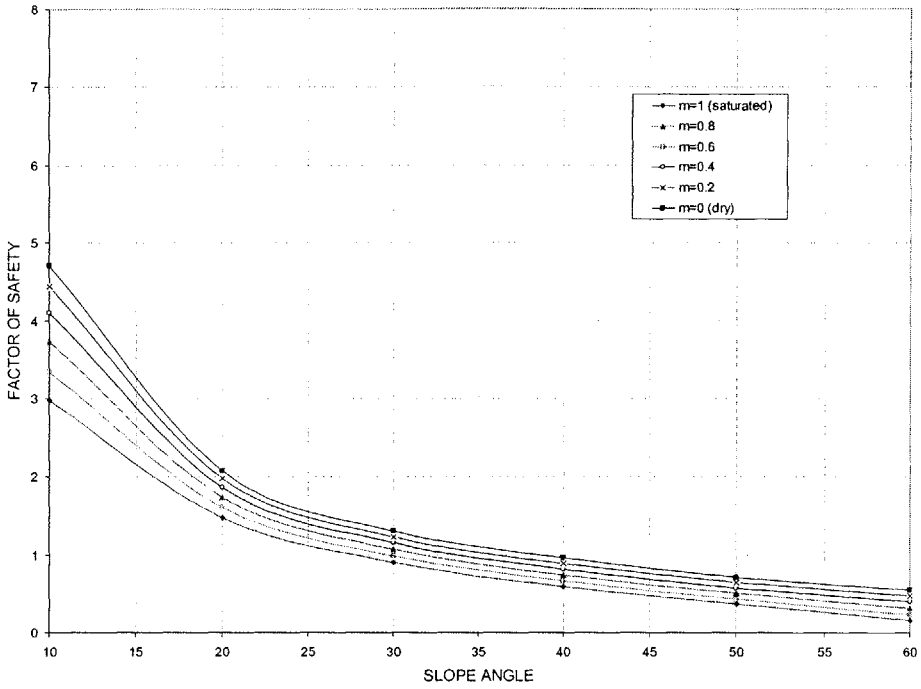

Figure 4.49. Effect of Water Table Depth and Slope Angle on Factor of Safety (Advanced Model)

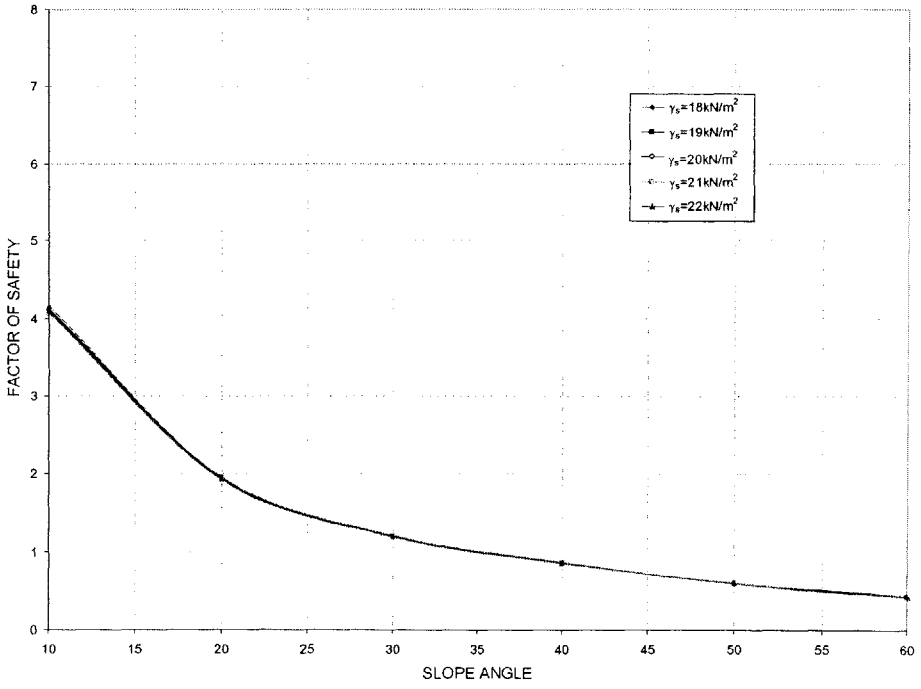

Figure 4.50. Effect of Saturated Unit Weight of Soil and Slope Angle on Factor of Safety (Advanced Model)

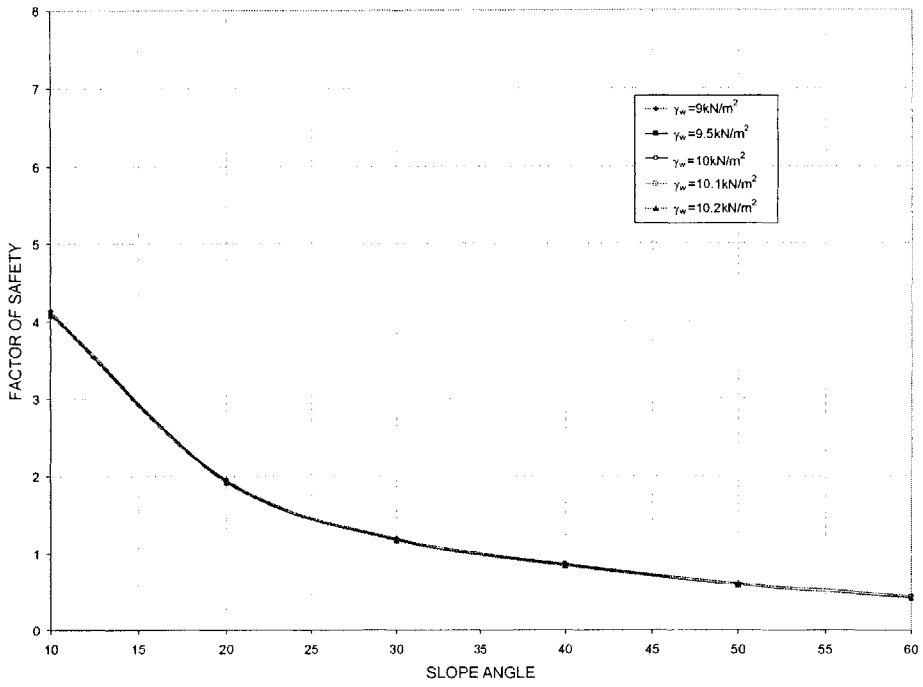

Figure 4.51. Effect of Unit Weight of Water and Slope Angle on Factor of Safety (Advanced Model)

Figures 4.47 to 4.51 are consistent with the results obtained using the Infinite Slope Model that are shown in Figures 4.35 to 4.38. They also show that most influential parameters are the soil strength parameters c' and ϕ'.

Figures 4.52 and 4.53 show two parameter sensitivity analyses for the soil strength parameters including correlation, and again the results are consistent with those shown in Figures 4.39 and 4.40.

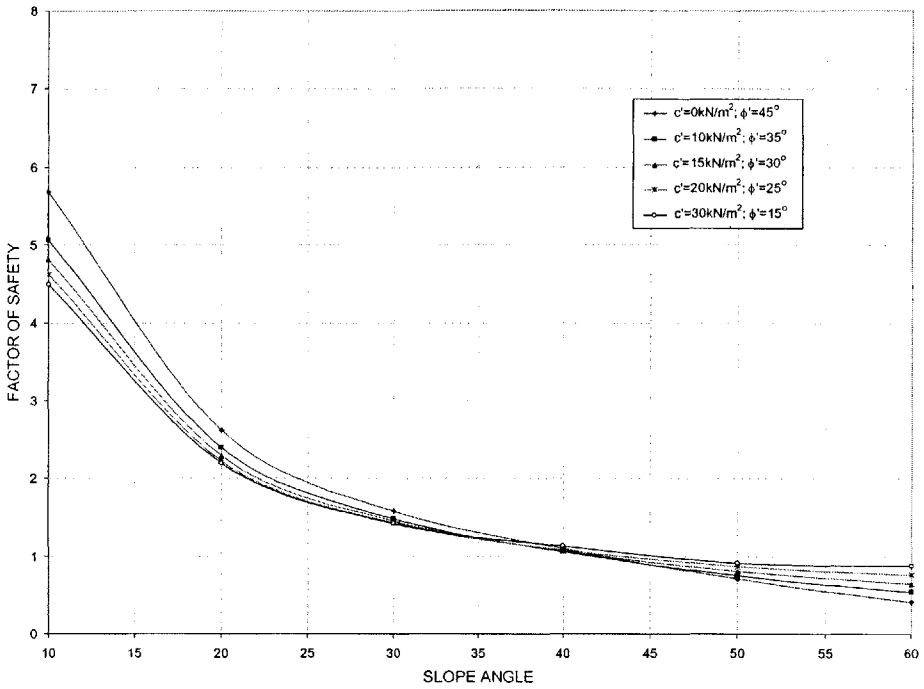

Figure 4.52. Effect of Negative Correlation between c' and ϕ' and Slope Angle on Factor of Safety (Advanced Model)

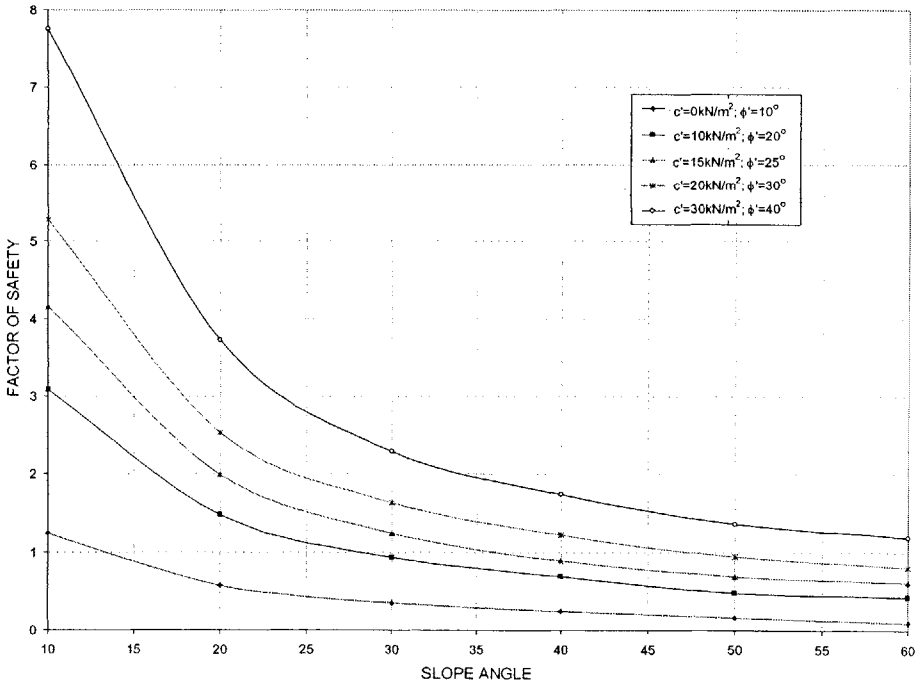

Figure 4.53. Effect of Positive Correlation between c' and ϕ' and Slope Angle on Factor of Safety

The results of the sensitivity of stability analyses presented in this section, as well as those in Appendix C-2, show that the most influential parameters are the soil strength parameters and these are retained for probabilistic analyses in Chapter 5. The results of two parameter sensitivity analyses show that correlation between the strength parameters is important. This is considered as a type of model uncertainty, and this is studied in more detail in Chapter 6.

4.3. CONCLUSIONS

In this chapter, the sources of uncertainty were classified, and how they enter the different stages of the landslide decision analysis procedure were described. Solutions to the uncertainty problem were presented through simplifications to the decision making procedure. This involves the use of influence diagrams and sensitivity analyses. Sensitivity of hydrologic and stability analyses were performed. The results show that the saturated conductivity of the soil is the major contributor to uncertainties in hydrologic analyses, and the soil strength parameters are the major contributors to uncertainties in stability analyses. These parameters are retained for probabilistic analyses in Chapter 5. Other parameters have little influence, and are left out of probabilistic analyses.

Sensitivity analyses also serve an important purpose in decision making by simplifying the relationships and pointing out where it is necessary and worthwhile to get detailed information on uncertainties. For example, it was shown that correlation between the soil strength parameters is important. The issue of model uncertainty was brought up and is dealt with in more detail in Chapter 6.

CHAPTER 5

PROBABILISTIC LANDSLIDE HAZARDS ASSESSMENT

In this chapter, landslide hazards are assessed within a probabilistic framework. This represents the second phase of the decision analysis cycle.

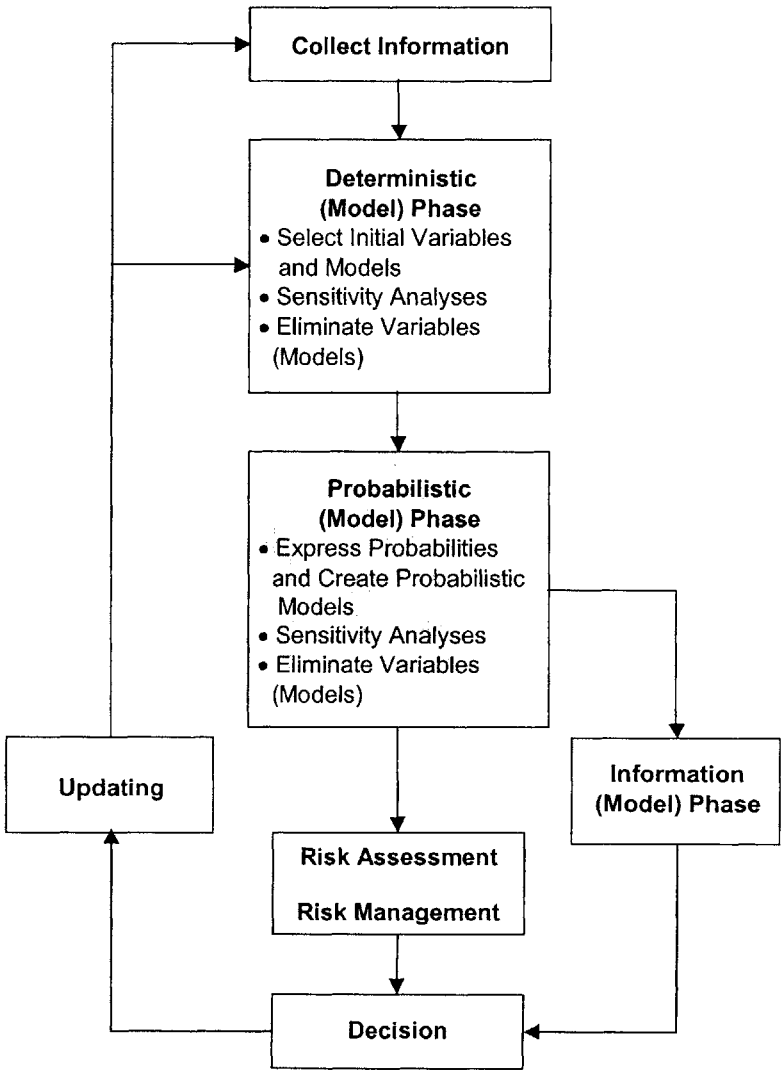

Figure 5.1. The Decision Analysis Cycle

Techniques are developed whereby uncertainties are systematically incorporated into the hazard assessment procedure by introducing uncertainties in the hydrologic and stability models developed in Chapter 2.

In Part 5-1, Monte Carlo methods are used to propagate uncertainties through the infiltration model that was developed in Chapter 2, based on uncertain hydraulic conductivity. The results are in the form of mean values and standard deviations of pore pressure profiles that are generated during a rainfall event.

In Part 5-2, the basic principles of slope reliability analyses are introduced. The reliability of slopes is assessed using second moment reliability methods and based on the Hasofer and Lind (1974) reliability index. From an assumed distribution of the Factor of Safety in a slope, probabilities of failure are estimated.

In Part 5-3, Monte Carlo methods are used to propagate uncertainties through the slope stability model developed in Chapter 2. The results are in the form of generated relative frequency density plots for the Factor of Safety, which are used to estimate probability distributions. From these distributions, probabilities of slope failure are computed. The results are compared with the second moment results in Part 5-2.

In Part 5-4, reliability methods are used to asses slope reliability during rainfall. This combines the analyses performed in Parts 5-1 and 5-2. The results are in the form of the variation of the Hasofer and Lind (1974) reliability index with time during and after a rainfall event. From this, and an assumed distribution of the Factor of Safety, a plot of the variation of slope reliability with time is derived. When this is coupled with probabilities of rainfall occurrence, landslide hazards (spatial and temporal) are estimated in a second moment context.

In Part 5-5, Monte Carlo Methods are used to asses slope reliability during rainfall in a full probability distribution context. This combines the analyses performed in Parts 5-1 and 5-3. The results are in the form of the variation of probability of slope failure (or reliability) with time during and after rain. Landslide hazards (spatial and temporal) are computed based on these results and probabilities of rainfall occurrence. The results of the Monte Carlo Methods are compared to those of second moment analyses.

In this Chapter, no correlation is assumed between uncertain parameters, e.g. soil strength parameters c' and ϕ'. Correlation is studied in detail in Chapter 6.

PART 5-1:
UNCERTAINTY PROPAGATION IN VARIABLY SATURATED FLOW

Flow in variably saturated soils with uncertain hydraulic properties is studied. Chapter 2 dealt with basic flow principles and derived the equation for variably saturated flow as:

$$\left(S_s S(\psi) + C(\psi)\right)\frac{\partial \psi}{\partial t} = \frac{\partial}{\partial z}\left[K(\psi)\left(\frac{\partial \psi}{\partial z} + 1\right)\right] \qquad [5.1]$$

where:

S_s is the specific storage

$S(\psi)$ is the degree of saturation

$C(\psi) = \frac{d\theta}{d\psi}$ is the specific moisture capacity

$K(\psi)$ is the conductivity characteristic function

The solution to Equation [5.1] requires specification of the soil characteristic curves, $\theta(\psi)$ and $K(\psi)$. Several models have been developed to describe the soil characteristic curves. One such model is the van Genuchten (1980) model which was discussed in Chapter 2 and is given by:

$$S(\psi) = 1 \text{ and } \theta(\psi) = \theta_s \qquad \psi \geq 0 \qquad [5.2]$$

$$S(\psi) = \frac{\theta(\psi) - \theta_r}{\theta_s - \theta_r} = \frac{1}{\left(1 + \left(\delta|\psi|\right)^n\right)^m} \qquad \psi < 0 \qquad [5.3]$$

$$K(\psi) = K_s \qquad \psi \geq 0 \qquad [5.4]$$

$$K(\psi) = K_s S(\psi)^{0.5}\left(1 - \left(1 - S(\psi)^{\frac{1}{m}}\right)^m\right)^2 \qquad \psi < 0 \qquad [5.5]$$

where:

θ_r is the residual moisture content

θ_s is the saturated moisture content

δ and n are empirical coefficients, and $m = 1 - 1/n$, and all other parameters are defined above.

Uncertainty in hydraulic parameters will lead to uncertainty in the soil characteristic curves, and hence uncertainty in flow modeling Equation [5.1]. Because of the high non-linearity and complexities involved, it is not practical to perform a complete probabilistic characterization of the model's output in terms of pore pressures. Consequently, a probabilistic sensitivity analysis using Monte Carlo techniques is used to predict the second moment characteristics of the model's output. Using the Monte Carlo technique, one or more of the hydraulic parameters are randomized from known or assumed probability distributions. Based on their probability distribution functions, N values of each hydraulic parameter are randomly selected. For each sample set, the soil characteristic curves, $K(\psi)$ in Equations [5.4] and [5.5], and $\theta(\psi)$ in Equations [5.2] and [5.3], are computed and the flow model is solved to generate N outcomes of the pressure head $\psi(t)$ and moisture content $\theta(t)$ profiles at any given time, t. At time t, the first and second moments (mean and variance) of the N outcomes are determined at each node in the profile. The number of simulations, N is made large enough so that the mean and variance of $\psi(t)$ and $\theta(t)$ are insensitive to the value N.

In this study, the soil saturated hydraulic conductivity K_S is assumed uncertain. It has been extensively documented in the literature (e.g. Philips, 1978; Cherry, 1979; Bear, 1988; Freeze and Cherry, 1990) that the soil hydraulic conductivity is the most uncertain soil hydraulic parameter and is the main contributor to uncertainty in hydrologic analyses. Uncertainty in K_s will result in uncertainty in the $K(\psi)$ characteristic curve of Equations [5.4] and [5.5].

The hydraulic conductivity is assumed to follow a Lognormal distribution (Freeze, 1980) with known/specified mean value and standard deviation. N values of K_S are randomly

generated. For each value of K_S, the soil characteristic curves are computed using the van Genuchten (1980) model in Equations [5.2] through [5.5]. The flow Equation [5.1] is then solved for each value of K_s to result in a sample of N pressure head $\psi(t)$ and moisture content $\theta(t)$ profiles at any given time, t. The mean value and standard deviation of these profiles is computed, thus characterizing uncertainty, in a second moment context. The Monte Carlo technique is implemented in a spreadsheet, and details are given in the following section.

5-1.1. SPREADSHEET IMPLEMENTATION

Chapter 2 described a spreadsheet based finite difference method by which the flow equation in variably saturated media can be solved deterministically. In this section, this method is extended to account for uncertainties in the soil hydraulic conductivity.

5-1.1.a. RANDOM NUMBER GENERATION

A cell in the spreadsheet is designated as a cell for random number generation. Microsoft Excel's random number generator is used to randomly generate numbers from the uniform distribution between 0 and 1 in this cell. This can be done by either using Excel's Random Number Generator Add-In or by typing the function "=RAND()" in the cell. Note that every time the F9 key is pressed, a different number is returned in the cell. Let U denote this variable. The probability density function $f_U(u)$, and cumulative distribution function $F_U(u)$ are given by:

$$f_U(u) = \begin{cases} 1, & 0 \le u \le 1 \\ 0, & \text{otherwise} \end{cases} \qquad [5.6]$$

$$F_U(u) = \begin{cases} u, & 0 \le u \le 1 \\ 0, & \text{otherwise} \end{cases} \qquad [5.7]$$

5-1.1.b. TRANSFORMATION OF VARIABLES

Using a transformation of variables, the random numbers generated from the uniform distribution are transformed into random numbers generated from any desired distribution. The transformation is as follows:

Suppose that one wants to generate numbers for a variable X, with cumulative distribution function $F_X(x)$, i.e. $X \sim F_X(x)$.

Let $U = F_X(x)$. $x(u) = F_X^{-1}(u)$. Since $F_X(x)$ is a monotonically increasing function of x, $F_U(u)$ is expressed as $F_U(u) = F_X\left(F_X^{-1}(u)\right) = u$. Therefore, using the transformation $x(u) = F_X^{-1}(u)$ one can generate variables X with the desired distribution $X \sim F_X(x)$. A graphical representation of this transformation is shown in Figure 5.2. Figure 5.2a shoes the probability density function of the uniformly distributed variable that is generated using the random number generator. This is transformed through $x(u) = F_X^{-1}(u)$ which is shown in Figure 5.2b, to result in a variable X with the desired distribution as shown in Figure 5.2c.

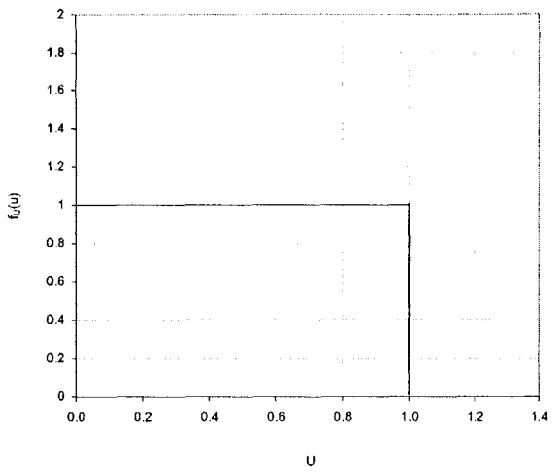

Figure 5.2a. PDF of Uniform Variable

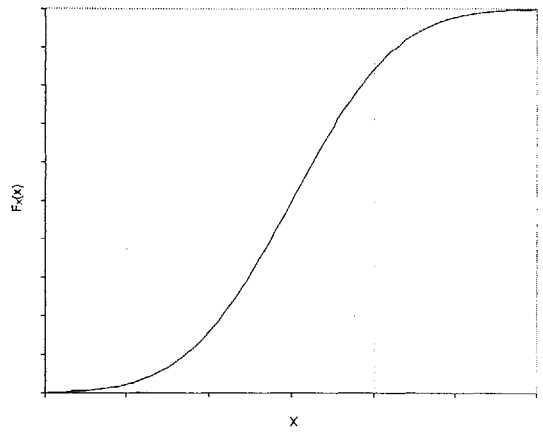

Figure 5.2b. Transformation of Variables

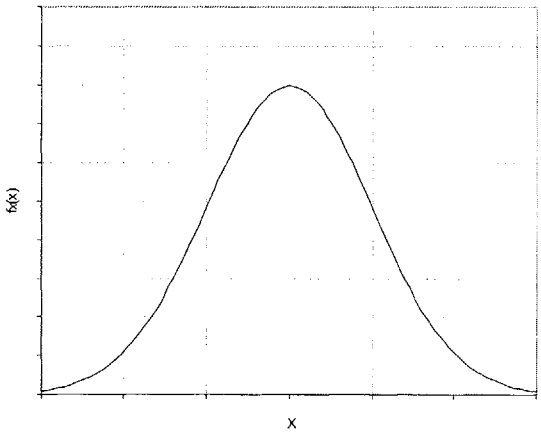

Figure 5.2c. PDF of Transformed Variable

Figure 5.2. Graphical Illustration of Transformation of Variables

In this study, the hydraulic conductivity of the soil is assumed uncertain and to follow a lognormal distribution, i.e. $K_s \sim LN(m_{\ln K_s}, \sigma^2_{\ln K_s})$, where $m_{\ln K_s}$ and $\sigma^2_{\ln K_s}$ are parameters of the distribution. The theoretical probability density function of the hydraulic conductivity is given by:

$$f_{K_S}(K_S) = \frac{1}{K_S \sigma_{\ln K_S} \sqrt{2\pi}} \exp\left(-\frac{1}{2}\left[\frac{\ln K_S - m_{\ln K_S}}{\sigma_{\ln K_S}} \right]^2 \right) \qquad [5.8]$$

The cumulative distribution function of K_s, $F_{K_s}(K_s)$ is obtained by integrating $f_{K_s}(K_s)$. This is done numerically. The value of $F_{K_s}(K_s)$ for any given K_s, and parameters of the distribution can also be obtained, in this case of a lognormal variable, using the '=LOGDIST()' function in Microsoft Excel.

So, to generate random values of K_s from a lognormal distribution with known parameters, random numbers are first generated using the '=RAND()' function. This results in variables u with density function as shown in Figure 5.2a. These are then transformed to random numbers of a lognormal distribution using the '=LOGINV()' function in Microsoft Excel. This corresponds to the $x(u) = F_X^{-1}(u)$ transformation in Figure 5.2b. The '=LOGINV()' function is inserted into the K_s cell, and every time the F9 key is pressed, a new value for K_s is generated based on the lognormal distribution with the specified parameters (Figure 5.3c).

5-1.1.c. MONTE CARLO SIMULATIONS

Each time the F9 key is pressed, a random K_s is generated and the soil characteristic curves, $K(\psi)$ and $\theta(\psi)$ are computed based on a lognormal K_s. The flow model developed in Chapter 2 is automatically solved to result in pore pressure $\psi(t)$ and moisture content $\theta(t)$ profiles at all times, t. A Visual Basic Subroutine is recorded in Microsoft Excel to automate the process of Monte Carlo simulations, and results in tables of values of pressure head and moisture content at all desired times.

5-1.2. NUMERICAL EXPERIMENTS

In this section, numerical infiltration experiments are performed on a soil, and the Monte Carlo Method is used to investigate the effects of uncertain hydraulic conductivity on predicted pore pressure $\psi(t)$ and moisture content $\theta(t)$ profiles. The van Genuchten (1980) Model is used to describe the characteristic curves of the soil. The saturated water content of the soil is taken to be $\theta_s = 0.47 m^3/m^3$ and the residual water content is $\theta_r = 0.11 m^3/m^3$. The parameters of the model are taken to be n = 1.24 and δ =

0.011 (see Equations [5.2] to [5.5]). The resulting characteristic curves are shown in Figures 5.3 and 5.4.

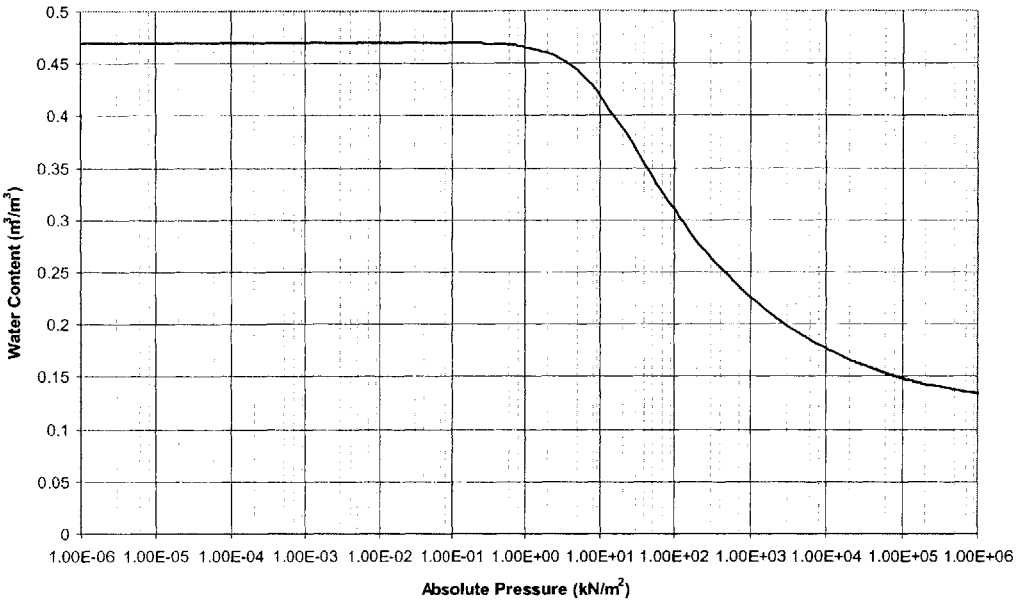

Figure 5.3. Soil Moisture Retention Curve

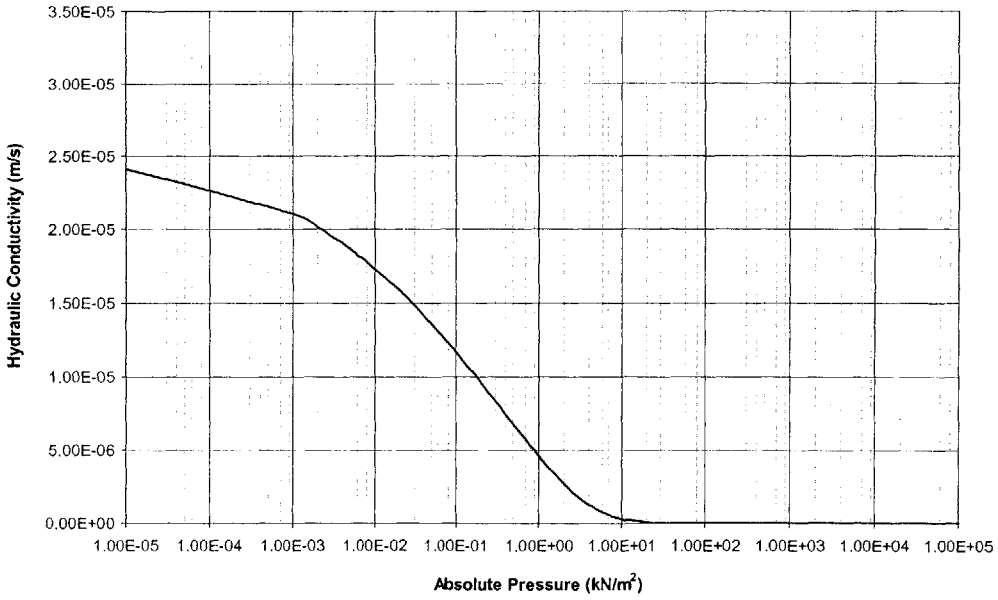

Figure 5.4. Hydraulic Conductivity Curve

Two numerical infiltration experiments are performed on the soil with different $\left(\frac{q}{K_s}\right)$ ratio, where q is the water application rate. The initial conditions are uniform initial moisture $\theta_i = 0.4\ m^3/m^3$ (and hence initial pressure which is computed from the soil moisture characteristic curve in Figure 5.2).

EXAMPLE 1: $\left(\frac{q}{K_s}\right) < 1$

In the first example, water is introduced at the top of a layer of soil at a rate of $q = 25cm/day$ for the first eight hours, followed by a zero application rate. The ratio $\left(\frac{q}{K_s}\right)$ is therefore taken to be $\left(\frac{q}{K_s}\right) = \frac{25}{250} < 1$ for the first eight hours, followed by $\left(\frac{q}{K_s}\right) = 0$. Since the $\left(\frac{q}{K_s}\right)$ ratio is less than 1, the water supply rate is insufficient to fully saturate the soil. The initial suction in the soil would be reduced during water application. The hydraulic conductivity of the soil is assumed deterministic. The flow equation is solved, and the moisture content at selected times are shown in Figure 5.5.

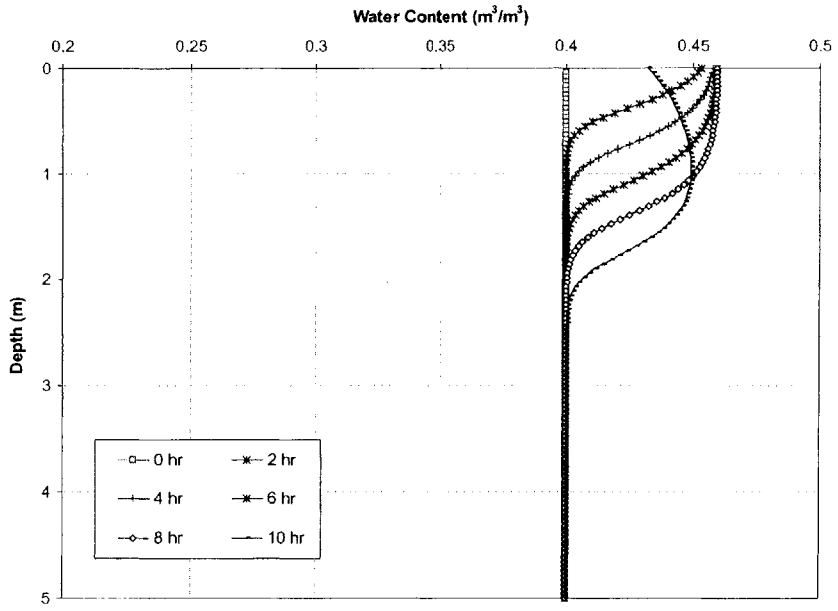

Figure 5.5. Moisture Content Profiles for Deterministic K_s and $\left(\frac{q}{K_s}\right) < 1$

The pore pressure profiles are shown in Figure 5.6.

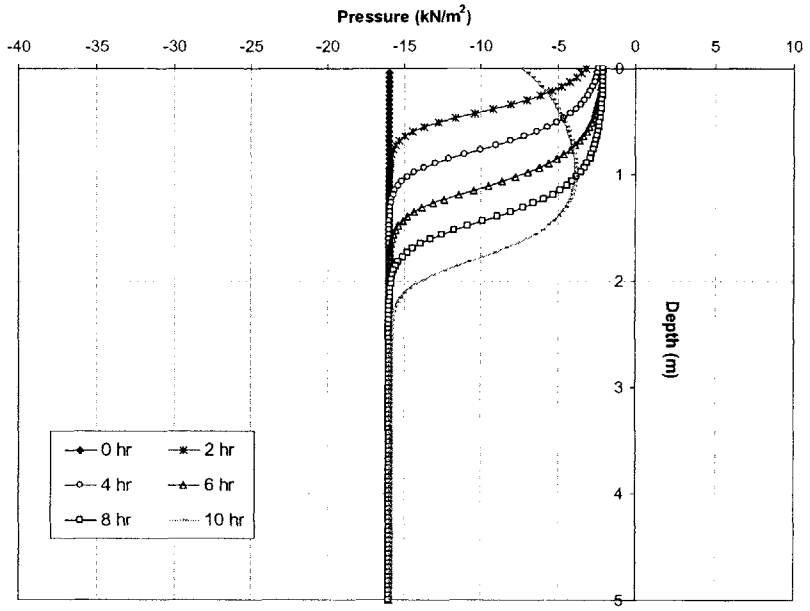

Figure 5.6. Pressure Head Profiles for Deterministic K_s and $\left(\frac{q}{K_s}\right)<1$

Figure 5.6 shows that the initial suction is reduced as a result of water application but remain negative as $\left(\frac{q}{K_s}\right)<1$. Moisture and pressure redistribution takes places at times t > 8 hours, as shown in Figures 5.5 and 5.6 respectively.

The hydraulic conductivity is randomized as described in Section 5-2.1. The mean value and standard deviation of the moisture profiles are shown in Figures 5.7 and 5.8, and the mean value and standard deviation of the pressure profiles are shown in Figures 5.9 and 5.10.

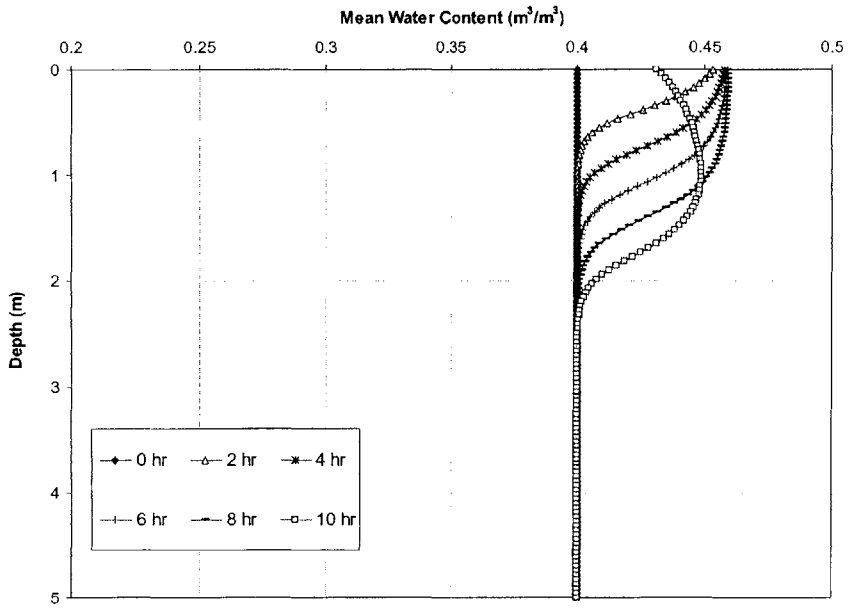

Figure 5.7. Mean of Moisture Content Profiles for Lognormal K_s and $\left(\frac{q}{K_s}\right)<1$

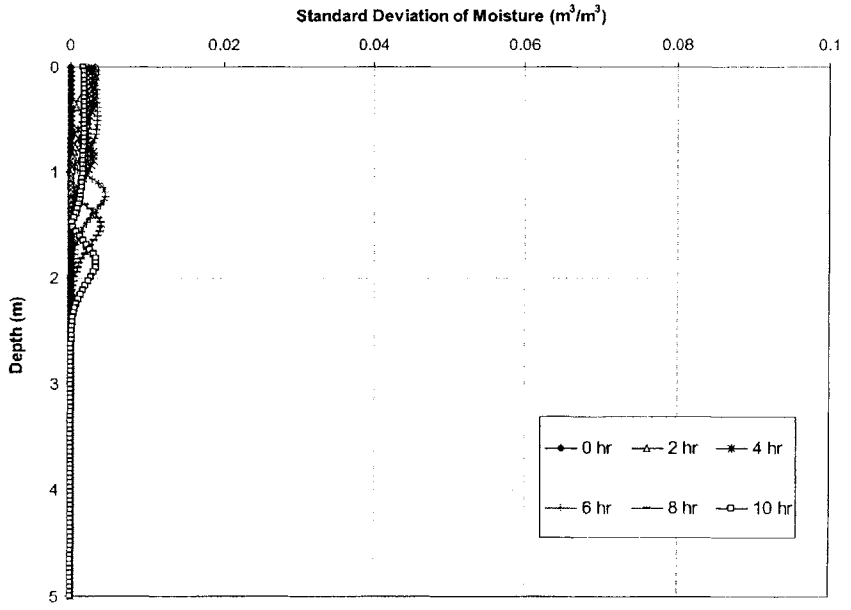

Figure 5.8. Standard Deviation of Moisture Profiles for Lognormal K_s and $\left(\frac{q}{K_s}\right)<1$

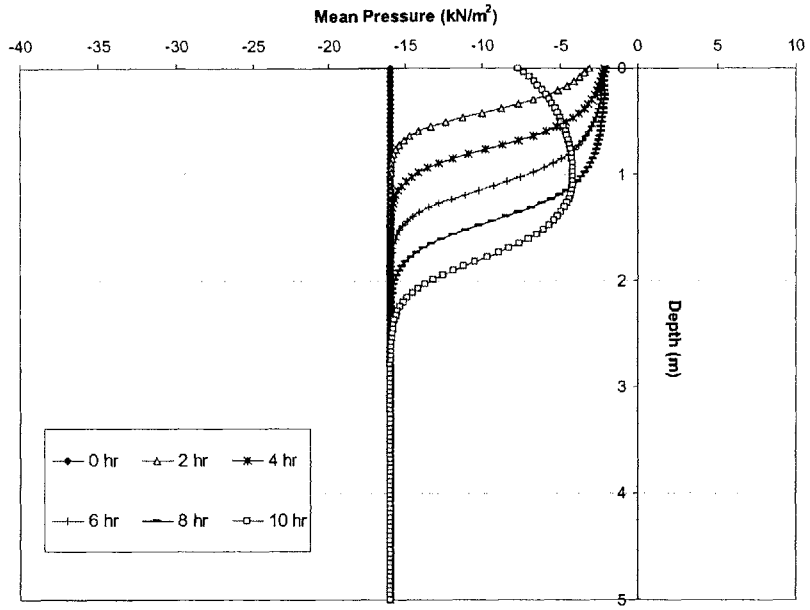

Figure 5.9. Mean of Pressure Profiles for Lognormal K_s and $\left(\frac{q}{K_s}\right)<1$

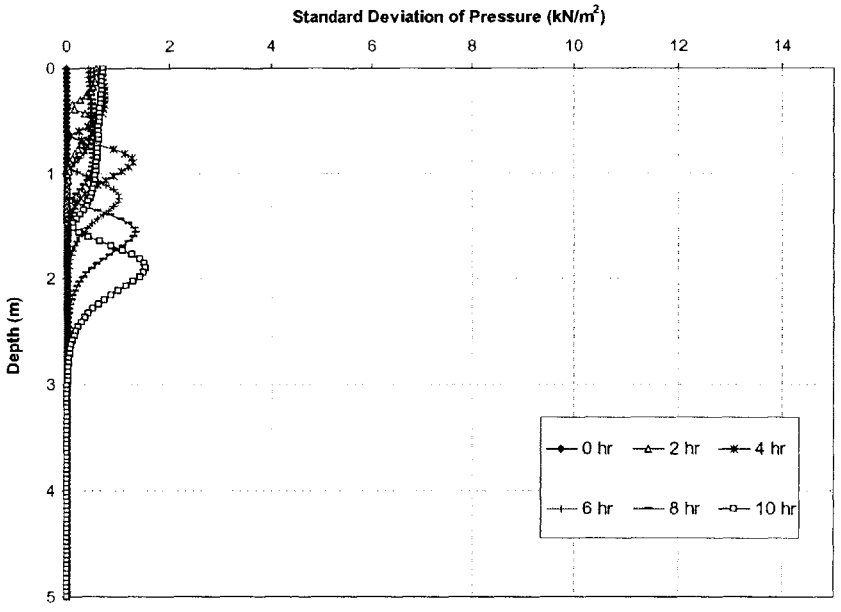

Figure 5.10. Standard Deviation of Pressure Profiles for Lognormal K_s and $\left(\frac{q}{K_s}\right)<1$

EXAMPLE 2: $\left(\frac{q}{K_s}\right) > 1$

In the second example, the water application rate is $375 cm/day$ for the first eight hours, followed by a zero application rate. $\left(\frac{q}{K_s}\right) = \frac{375}{250} > 1$ for the first eight hours, followed by $\left(\frac{q}{K_s}\right) = 0$. Since $\left(\frac{q}{K_s}\right)$ is greater than 1, the water supply rate is large enough to fully saturate the soil. As the soil reaches saturation, the initial suction is eliminated and positive pressures develop within the saturated zone. The moisture content and pressure head profiles for deterministic K_s are shown in Figures 5.11 and 5.12 respectively.

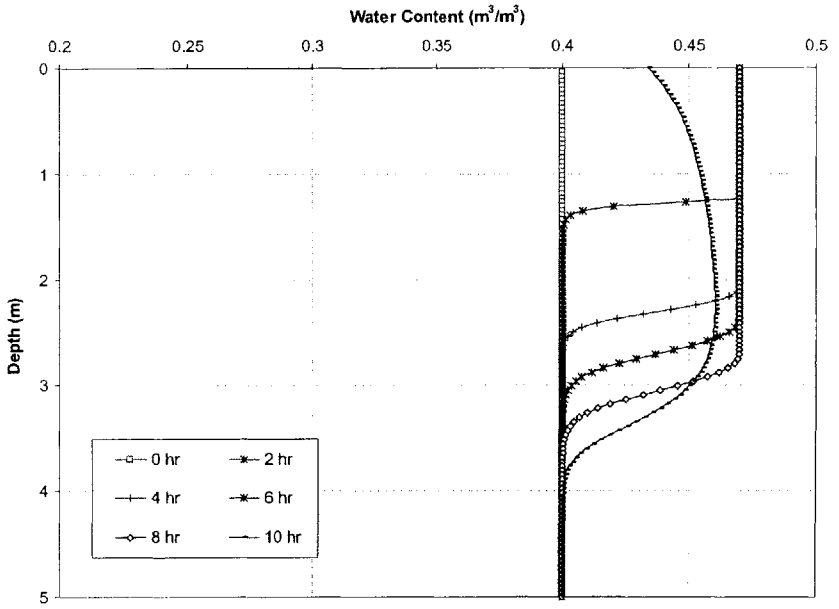

Figure 5.11. Moisture Content Profiles for Deterministic K_s and $\left(\frac{q}{K_s}\right) > 1$

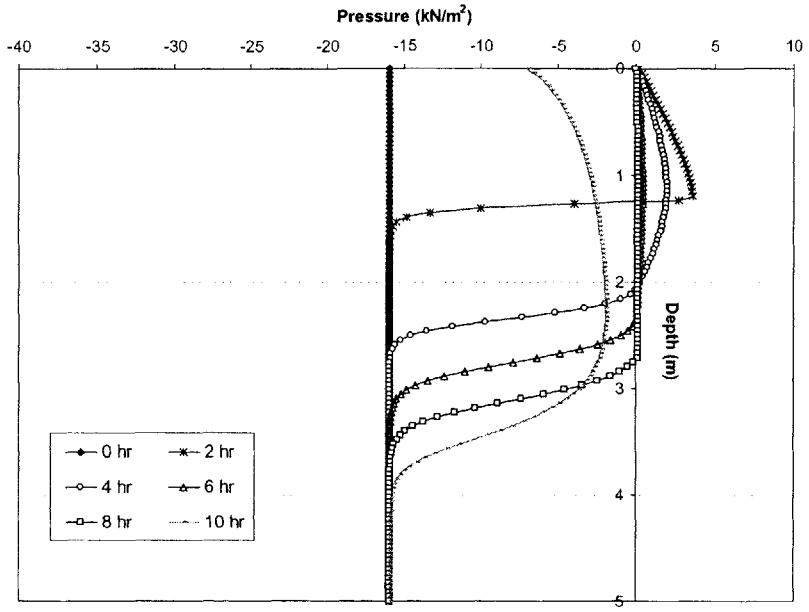

Figure 5.12. Pressure Head Profiles for Deterministic K_s and $\left(\frac{q}{K_s}\right) > 1$

K_s is randomized and assumed Lognormal. The mean value and standard deviation of the moisture content profiles are shown in Figures 5.13 and 5.14, and the mean value and standard deviation of pressure head profiles are shown in Figures 5.15 and 5.16.

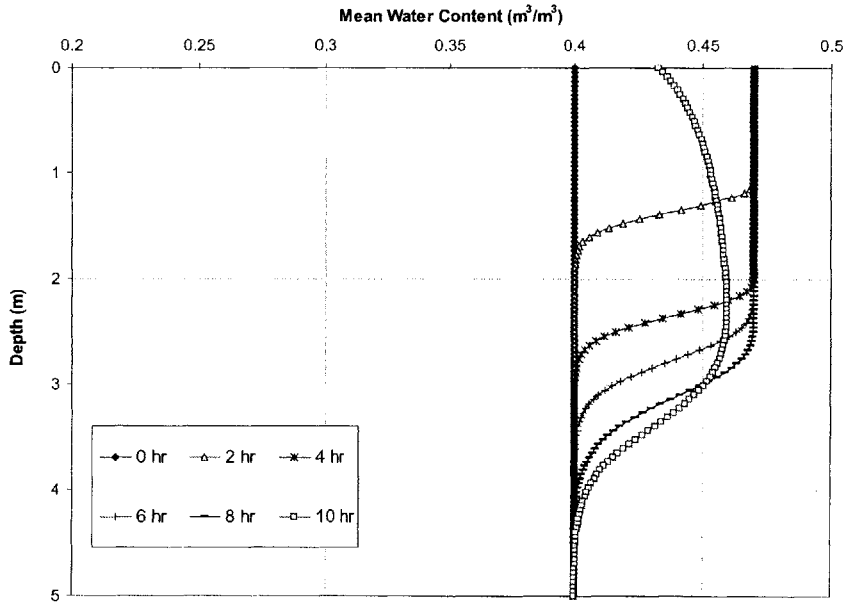

Figure 5.13. Mean of Moisture Content Profiles for Lognormal K_s and $\left(\frac{q}{K_s}\right) > 1$

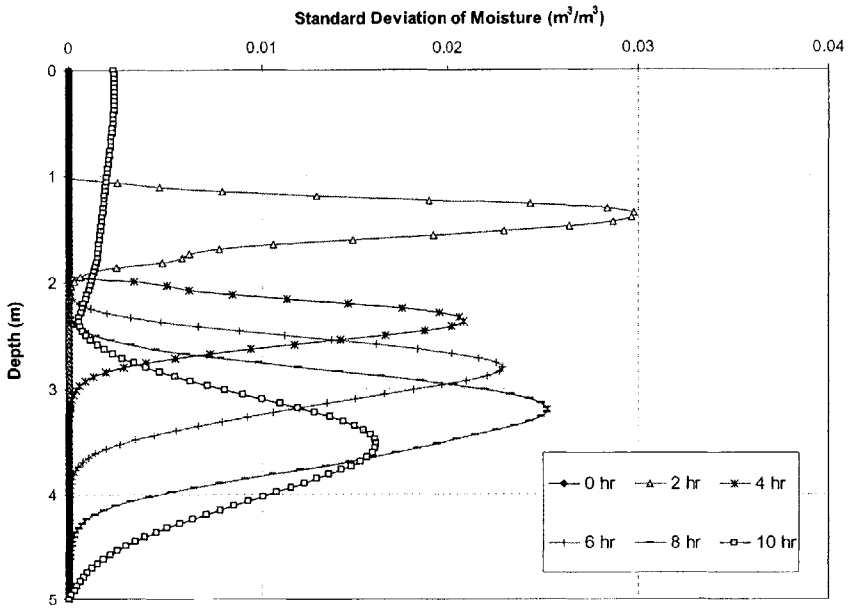

Figure 5.14. Standard Deviation of Moisture Profiles for Lognormal K_s and $\left(\frac{q}{K_s}\right) > 1$

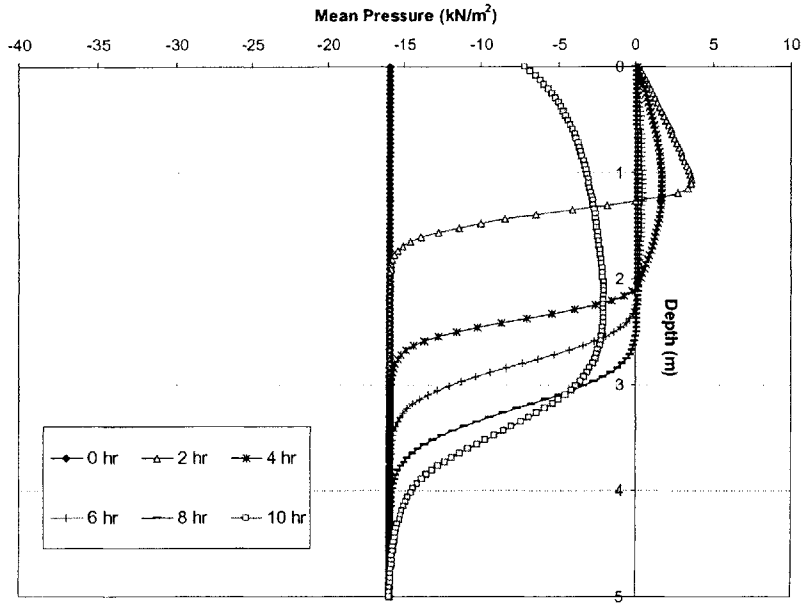

Figure 5.15. Mean of Pressure Profiles for Lognormal K_s and $\left(\frac{q}{K_s}\right) > 1$

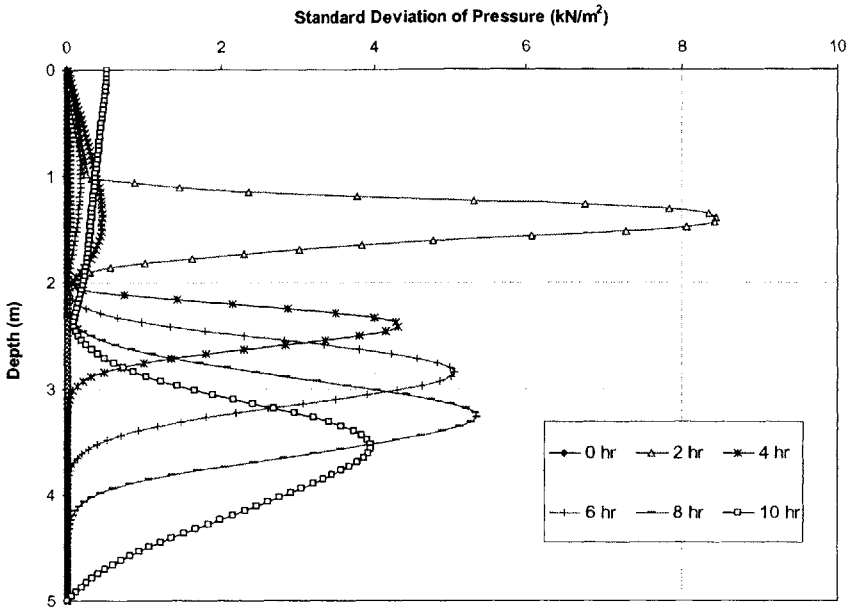

Figure 5.16. Standard Deviation of Pressure Profiles for Lognormal K_s and $\left(\frac{q}{K_s}\right) > 1$

5-1.3. RESULTS AND DISCUSSION

The results of the two numerical examples show that expected (mean) values of the moisture and pressure profiles when the saturated conductivity of the soil, K_s, is uncertain are (almost) the same as the profiles for deterministic K_s. This is true in both examples, and is shown in Figures 5.5 and 5.7 for moisture content, and 5.6 and 5.9 for pressure when $\left(\frac{q}{K_s}\right) < 1$, and in Figures 5.11 and 5.13 for moisture, and 5.12 and 5.15 for pressure when $\left(\frac{q}{K_s}\right) > 1$. These figures show that the profiles are the same whether K_s is deterministic or uncertain. Uncertainty in K_s does, however, propagate through the flow equation to result in uncertainty in the moisture content and pressure head profiles. This uncertainty is expressed by the standard deviations in the moisture (Figures 5.8 and 5.14) and pressure (Figures 5.10 and 5.16) profiles.

Several observations can be made with regard to the uncertainty in water content profiles in Figures 5.8 and 5.14.

a. The peaks in the standard deviations at any time t occur at the wetting front where the slope of the moisture content profile is greatest. Consider Figure 5.13 for example. At a time of 2 hours, the wetting front has infiltrated the soil to a depth of about 1.5 m. The standard deviation in the water content profile is greatest at that depth of about 1.5 m as shown in Figure 5.14. Similarly, at a time of 4 hours, both the wetting front and the maximum standard deviation occur at a depth of about 2.5 m.

b. The peaks in standard deviations (maxima) travel downwards with time as the wetting front penetrates the soil deeper. With time and continued water application, the wetting front infiltrates deeper into the soil, and since the maximum standard deviations occur at the wetting front, these also travel downwards with the front, e.g. the peak is at depth 1.5 m at t = 2 hours, 2.5 m at 4 hours, and so on. This is true both during and after water application, as can be seen at time 10 hours. When water is no longer applied, moisture redistribution takes place at a rate governed by the hydraulic conductivity function. Flow of water (moisture) therefore continues, and there is uncertainty in this flow, because of the uncertainty in K_s, and this is reflected in the standard deviation at time 10 hours.

c. The standard deviations (uncertainty) cover a greater range with increasing infiltration depth (and time). In Figure 5.14, at a time of 2 hours, the uncertainty in water content is localized near the wetting front at depths of about 1 m to 2 m, and there is virtually no uncertainty in the profiles at other depths. With time, say at 8 hours, the uncertainty in the profiles covers a larger range of depths from about 2.5 m to 4.5 m.

d. The standard deviations in moisture profiles depends on the water application rate, and more specifically on the $\left(\frac{q}{K_s}\right)$ ratio in such a way that as the $\left(\frac{q}{K_s}\right)$ ratio increases, so do the standard deviations. This is illustrated in Figures 5.8 and 5.14, which show greater uncertainty with increasing $\left(\frac{q}{K_s}\right)$ ratio. Therefore, for a soil with a given K_s, as the water application rate increases, uncertainty in the results also increases.

Very similar observations can be made with regard to the uncertainty in pressure head profiles, expressed as standard deviations shown in Figures 5.10 and 5.16. Specifically that:

a. Peaks in the standard deviations at any time t occur at the wetting front where the slope of the pressure head is greatest (see Figures 5.15 and 5.16 for example).

b. These peaks travel downwards with time as the wetting front penetrates the soil deeper. In Figure 5.16 for example, at a time of 2 hours, the peak is at about 1.5 m, and at 8 hours is at about 3.5 m.

c. The standard deviations (uncertainty) in the results cover a larger range with increasing infiltration depth (time). In Figure 5.16, the uncertainty covers depths 1 m – 2 m at time 2 hours, and 2.5 m – 4 m at time 8 hours.

d. The uncertainty increases with increasing $\left(\frac{q}{K_s}\right)$ ratio as shown in Figures 5.10 and 5.16.

These results can be explained by considering the soil characteristic curves shown in Figures 5.3 and 5.4. Uncertainty in K_s leads to uncertainty in the soil hydraulic conductivity characteristic curve, since it is a function of K_s as expressed in Equations [5.4] and [5.5]. This uncertainty results in uncertainty in the soil moisture characteristic curve, since these two curves are related.

The largest uncertainties in the computed moisture profiles occur near the wetting front where the change in moisture content is greatest. This is the location where the change in hydraulic conductivity of the soil is greatest (as dictated by $K(\psi)$), and so uncertainties in K_s will result in the largest uncertainties near the wetting front. Moreover, the sharper the wetting front, the larger the uncertainties.

As a consequence, the largest uncertainties in pressures will also occur near the wetting front (as dictated by $\theta(\psi)$), and will be larger for sharper fronts. This explains the peaks in standard deviations of the pressure profiles that are observed near the wetting fronts.

The effects of the $\left(\frac{q}{K_s}\right)$ ratio, also become evident by examining the soil characteristic curves. As the $\left(\frac{q}{K_s}\right)$ ratio increases, the change in moisture content (and pressure heads), and hence uncertainties in K_s will propagate to larger uncertainties in the computed moisture profiles (and pressure heads).

From the results and discussions presented above, it is evident, though not surprising that the sharpness of a wetting front, and the uncertainties associated with the moisture (and pressure) profiles depends on the characteristic curves.

To demonstrate this further, consider the infiltration experiment in Example 1 performed on a different soil, with the characteristic functions shown in Figures 5.17 and 5.18.

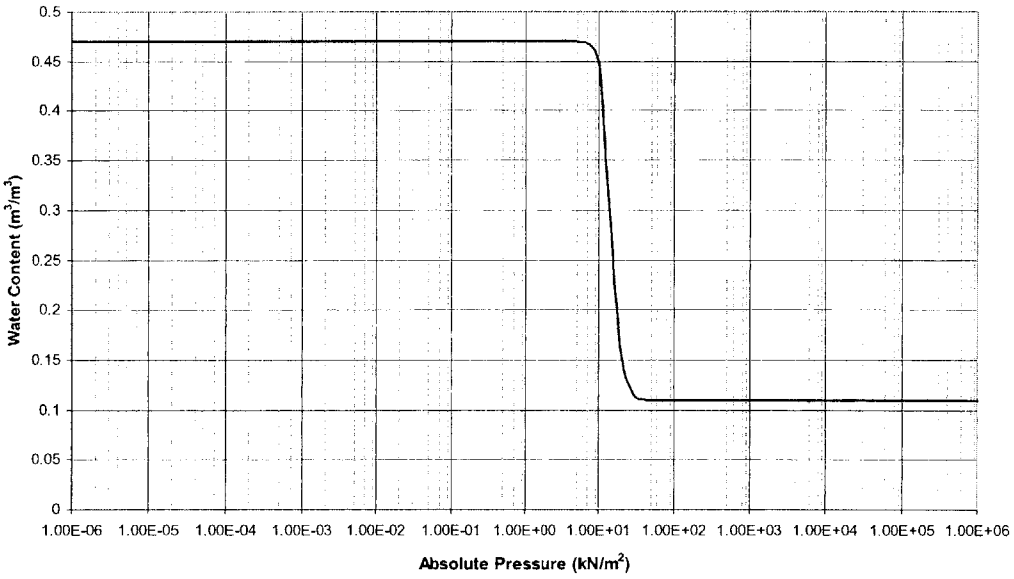

Figure 5.17. Soil Moisture Retention Curve (Soil 2)

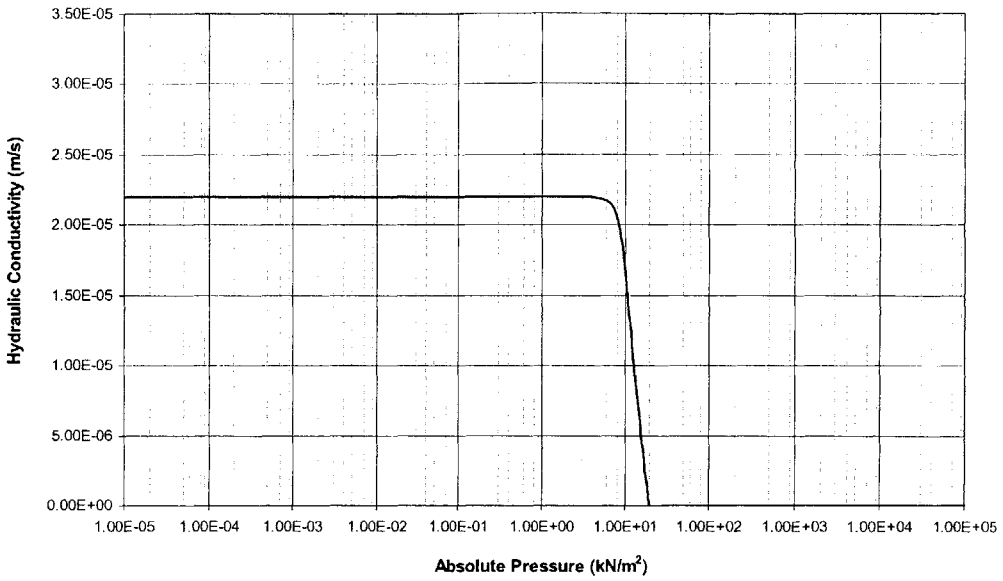

Figure 5.18. Hydraulic Conductivity Curve (Soil 2)

The van Genuchten (1980) model is used to describe the soil characteristic curves. The model parameters n and δ are purposely chosen so that the characteristic curves are steeper than those of the soil considered previously and shown in Figures 5.3 and 5.4. Furthermore, they have been fitted in such a way that the soil moisture curves of both soils intersect at a water content equal to the initial water content $\theta_i = 0.4\ m^3/m^3$. By doing so, the initial water content $\theta_i = 0.4\ m^3/m^3$ that was used in Example 1, can also be used in this example, allowing one to directly compare the results of both cases.

Monte Carlo techniques are used to propagate uncertainty through the flow model using the properties of the second soil, using the same $\left(\frac{q}{K_s}\right)$ ratio the one in Example 1. The mean water content profiles are shown in Figure 5.19.

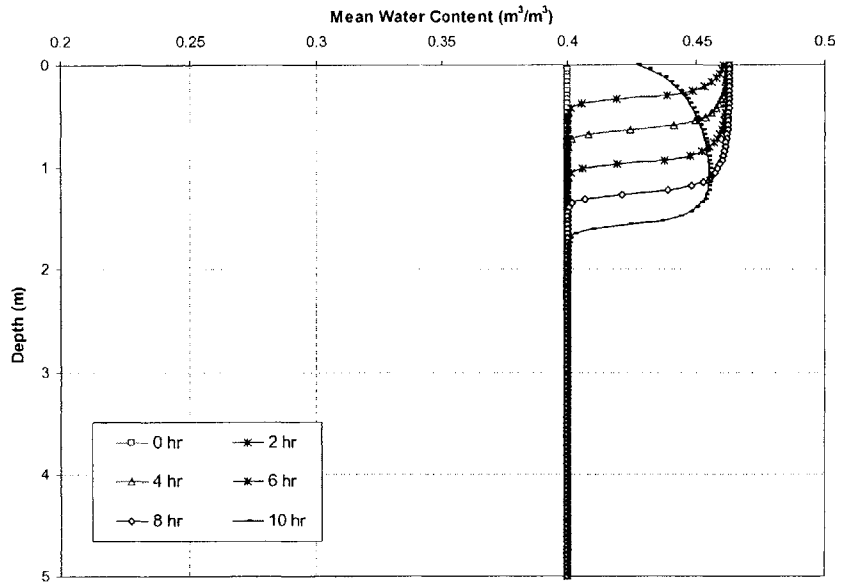

Figure 5.19. Mean of Moisture Content Profiles for Lognormal K_s and $\left(\frac{q}{K_s}\right) < 1$ (Soil 2)

Figures 5.19 shows that a sharp wetting front forms in the soil with the steep characteristic curves, and infiltrates into the slope with time. Figure 5.20 shows the uncertainty in the moisture profiles.

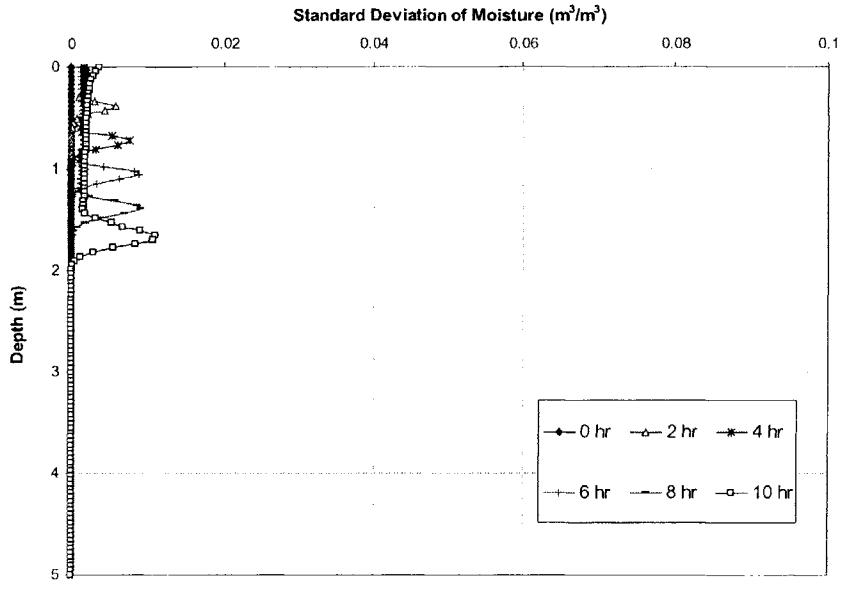

Figure 5.20. Standard Deviation of Moisture Content Profiles for Lognormal K_s and $\left(\frac{q}{K_s}\right) < 1$ (Soil 2)

Figure 5.21a compares the moisture profiles in both soils, and Figure 5.21b compares the standard deviations in the profiles.

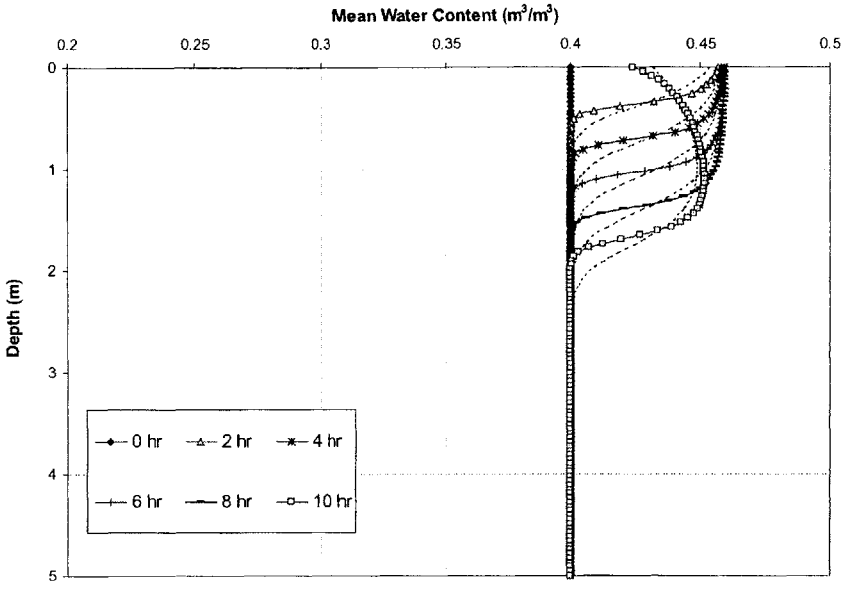

Figure 5.21a. Comparison of Mean Moisture Profiles in both Soils (Symbols are for soil with steep curves, dashed lines for soil with mild curves)

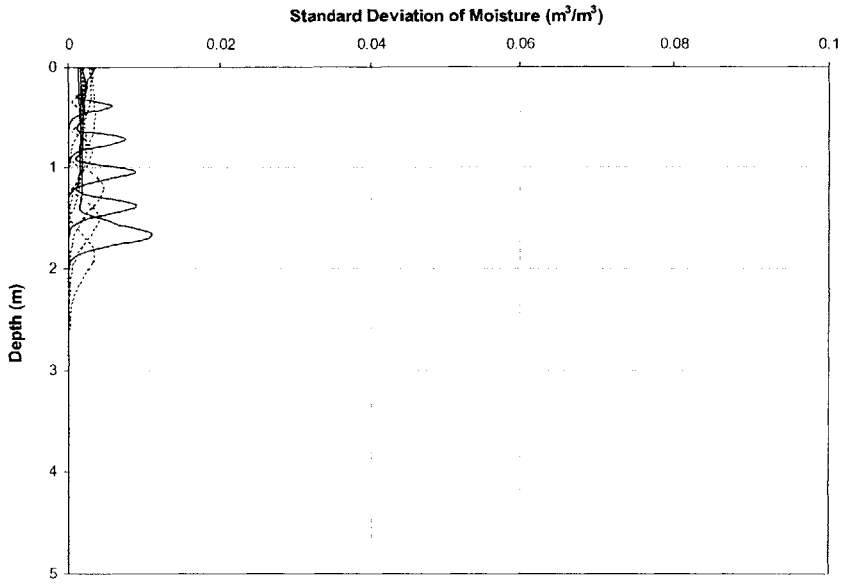

Figure 5.21b. Comparison of Standard Deviations in Moisture Profiles in both Soils (Solid lines are for soil with steep curves, dashed lines for soil with mild curves)

Figure 5.21a shows that the wetting front that develops in the soil with steeper characteristic curves is significantly sharper than the one that develops in the soil Example 1 with the milder characteristic curves. As a consequence, the uncertainty in the profiles is also larger as demonstrated in Figure 5.21b. The uncertainty is however, more localized, when compared to the uncertainty in the profiles with the soil with the milder curves that exhibit smaller uncertainty that is spread over a larger range.

In conclusion, soils with steeper soil characteristic curves tend to develop sharp wetting fronts, and as a consequence tend to show large uncertainties that are localized near the wetting front. Soils with milder characteristic curves tend not to develop distinct wetting fronts, and as a result, show smaller uncertainties that are spread over a large range.

The shape of soil characteristic curves is governed by grain size distribution, pore size distribution (soil structure), as well as percentage fines, amongst other factors.

(a) Uniform soils tend to show characteristic curves that have steep slopes, whereas well graded soils tend to show characteristic curves with less steep (milder) slopes. This is because in a uniform soil, water drains out of most of the pores at the same (similar) value of suction. This is illustrated in Figure 5.22.
(b) Regarding the influence of fines, the greater the clay content, in general, the greater the water retention at any particular suction, and the less steep (or milder) the slope of the characteristic curve. In a sandy soil, most of the pores are relatively large, and once the large pores are emptied at a given suction, only a small amount of water remains. As a result, the slope of the characteristic curve is steep.
(c) In a clayey soil, most of the pores are relatively small. When this is the case, more of the water is adsorbed, so that decreasing the suction causes a more gradual decrease in water content, and hence the slope of the characteristic curve is less. This is illustrated in Figure 5.22.

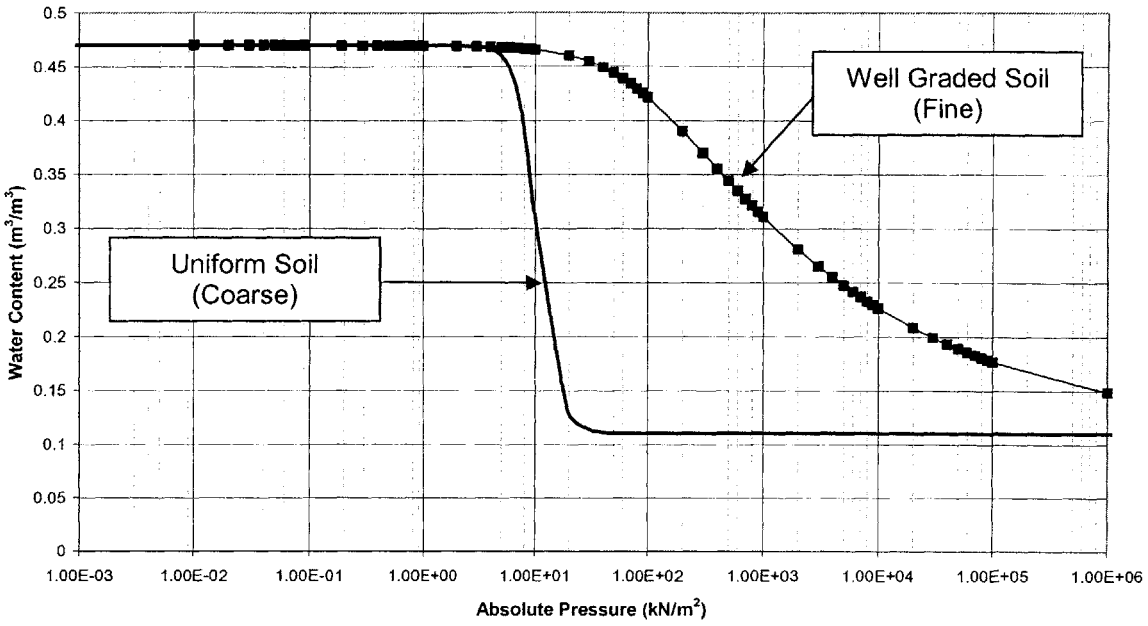

Figure 5.22. Comparison of Characteristic Curves for Uniform and Well Graded Soils

The results in this section, therefore show that uniform soils tend to develop sharper wetting fronts than well graded soils. As a consequence, the uncertainty in the profiles at the front is large. Well graded soils do not develop distinct wetting fronts and the uncertainty in the pressure (and moisture) profiles is spread over a large area.

In all the analyses in this study the uncertainty in K_s is held constant, although it is obvious that larger uncertainties in K_s will lead to larger uncertainties in moisture content and pressure head computations. Furthermore, K_s has been assumed to be the only uncertain hydraulic parameter. The analyses could be extended to include uncertainties in other parameters.

5-1.4. CONCLUSIONS

Monte Carlo techniques were used to propagate uncertainty through the finite difference variably saturated flow model developed in Chapter 2. The hydraulic conductivity of the soil was assumed uncertain and to follow a lognormal distribution with known parameters. These parameters can be, for example, estimated from field or laboratory data obtained at random locations. Based on these moments and the assumed lognormal probability distribution, this study used Monte Carlo techniques to solve the one dimensional flow equation and estimate the mean value and variance of the moisture content and pressure head profiles for a specified water application rate and duration.

The results of numerical experiments show that uncertain soil hydraulic conductivity does not affect the mean value of the moisture content and pressure head profiles, but results in uncertainty in these profiles. The uncertainty in both profiles increases with increasing $\left(\frac{q}{K_s}\right)$ ratio, and water application duration. Peaks in standard deviation of the moisture and pressure profiles occur at the wetting front where the slope of these profiles is maximum. The values of standard deviation at these peaks are directly related to the soil moisture content and hydraulic conductivity characteristic curves. Characteristic curves are related to grain size and pore size distribution. Uniform soils tend to develop sharp wetting fronts with a high degree of localized uncertainty, whereas well graded soils do not develop distinct fronts, and as a result uncertainty is widespread.

If it is assumed that horizontal flow components are negligible compared to the vertical, an assumption extensively used and theoretically backed, the results in this section can be considered as good representations of those in a three dimensional field.

PART 5-2:
BASIC PRINCIPLES OF RELIABILITY ANALYSES

In this part of the chapter, the basic principles of reliability analyses are introduced. Spreadsheet based techniques are developed with which one can systematically incorporate the inherent uncertainties in parameters into stability analyses. Methods are developed whereby the so called Hasofer and Lind (1974) reliability index can be computed within the spreadsheet environment. This is first done for a specified failure surface, and then extended to include a search for the critical reliability based failure surface in the slope, on which the Hasofer and Lind (1974) reliability index is minimum. This corresponds to the surface along which failure is most probable. Basic reliability charts are developed in two and three dimensions. Through a series of examples, the effects of uncertainties in parameters defined by their standard deviations, on the Hasofer and Lind (1974) reliability index (and slope reliability) are investigated.

5-2.1.a. FAILURE PROBABILITY

The probability of failure of a slope can be formulated in terms of a general performance function $G(\underline{X})$, where $\underline{X}$ is a vector of random variables, and $G(\underline{X})$ is a function relating to the state of stability of the slope. $G(\underline{X})$ is a function of the Factor of Safety commonly taken to be:

$$G(\underline{X}) = F(\underline{X}) - 1 \qquad [5.9]$$

where $F(\underline{X})$ is the Factor of Safety.

The probability of failure is the probability that the vector of random variables $\underline{X}$ belongs to the failure region, D_F. This is expressed as:

$$P[\text{failure}] = P_F = P[\underline{X} \in D_F] \qquad [5.10]$$

The probability of failure in can be expressed in terms of the performance function as:

$$P_F = P[G(\underline{X}) < 0] \quad [5.11]$$

Let $f_{\underline{X}}(\underline{X})$ denote the joint probability density function of the vector of random variables $\underline{X}$. The probability of failure of a slope is given by the integral of $f_{\underline{X}}(\underline{X})$ over the failure domain defined by $G(\underline{X}) < 0$. Hence,

$$P_F = \int \ldots \int_{\underline{X} \in D_F} f_{\underline{X}}(\underline{X}) dx_1 \ldots dx_n \quad [5.12]$$

Consequently, the probability of safe performance, or the reliability of the slope is given by:

$$P[\text{safety}] = P_S = \text{Reliability} = P[\underline{X} \in D_S] \quad [5.13]$$

where D_S is the safe domain.

And, the reliability of the slope is given by:

$$\text{Reliability} = \int \ldots \int_{\underline{X} \in D_S} f_{\underline{X}}(\underline{X}) dx_1 \ldots dx_n \quad [5.14]$$

In terms of the performance function:

$$\text{Reliability} = P[G(\underline{X}) > 0] \quad [5.15]$$

Since the events 'failure' and 'safety' are mutually exclusive and collectively exhaustive, one can relate the reliability of a slope to the probability of failure as:

$$\text{Reliability} = 1 - P_F \quad [5.16]$$

With the performance function as defined in Equation [5.9], the probability of failure in terms of Factor of Safety in the case of one variable is given by:

$$P_f = P[F < 1] = \int_{-\infty}^{1} f_{FS}(F)dF \qquad [5.17]$$

This is illustrated in Figure 5.23.

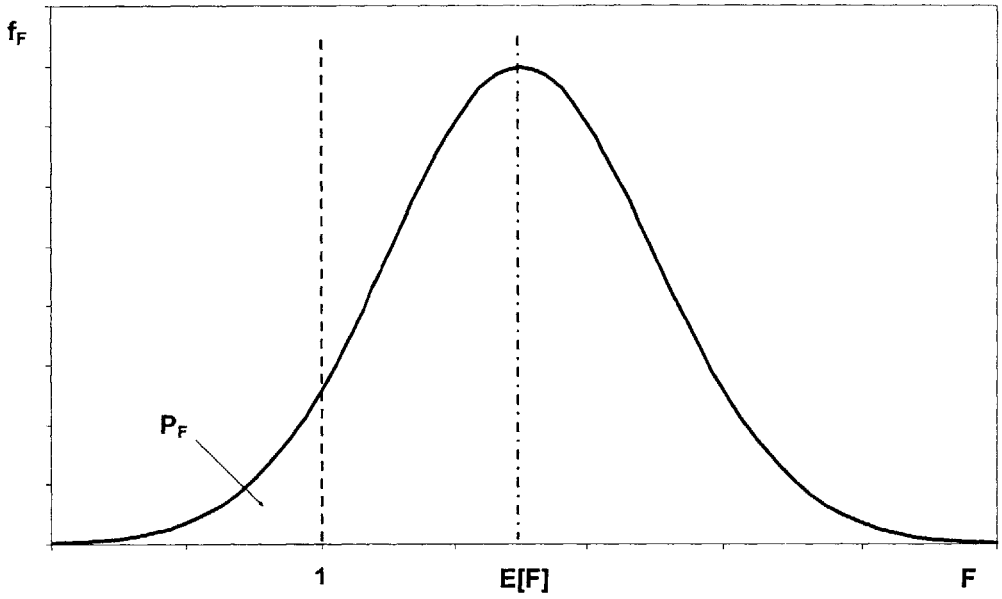

Figure 5.23. Failure Probability for G(X)=F-1

5-2.1.b. THE RELIABILITY INDEX

The performance function, as defined by Equation [5.9], is a function of several random variables. To determine the reliability (or probability of failure) in Equations [5.12] and [5.14], the probability density function of the performance function must be evaluated. This requires multiple integration of the joint probability density function of the random variables over the entire safe (or failure) domain. The joint probability density function of the random variables is generally not well defined and the performance function is very often implicit. Hence, evaluating the probability density function of the performance function is often not possible. In addition, even if the joint probability density function of

the random variables is known, the multi-dimensional integrals in [5.12] and [5.13] present mathematical difficulties.

To overcome these difficulties, the method of moments is used to estimate the expected value and variance of the performance function from the expected value and variance of the random variables on which the performance function depends. The results are expressed in terms of the reliability index, β. The reliability index β provides more information and is a better indication of the stability of a slope than the performance function (e.g. Factor of Safety) alone because it incorporates information on the uncertainty in the values of the performance function. It also provides a good comparative measure of safety; slopes with higher β are considered safer than slopes with lower β. The reliability index also provides a means by which the probability of failure can be estimated by assuming the shape of the probability distribution of the performance function.

Several definitions of the reliability index exist. These depend on the form of the performance function, and different reliability indices are obtained from different performance functions formats. The most commonly used definition of reliability index in slope stability analyses is the Mean-Value First-Order Second-Moment (MFOSM) reliability index (Ang and Tang, 1975). In MFOSM, the performance function is expanded about the mean values of the parameters $E[X_i]$ and only the first order terms are kept. The reliability index, β, for uncorrelated variables is then given by:

$$\beta = \frac{E[G(\underline{X})]}{\sigma[G(\underline{X})]} = \frac{E[G(\underline{X})]}{\sqrt{\sum_{i=1}^{n}\left(\frac{\partial G(\underline{X})}{\partial X_i}\right)\Big|_m^2 \mathrm{Var}[X_i]}} \qquad [5.18]$$

where:

$\left(\frac{\partial G(X)}{\partial X_i}\right)\Big|_m$ indicate that the partial derivatives are evaluated at the mean point $E[\underline{X}]$.

For correlated variables, the reliability index is expressed as:

$$\beta = \frac{E[G(\underline{X})]}{\sigma[G(\underline{X})]} = \frac{E[G(\underline{X})]}{\sqrt{\sum_{i=1}^{n}\left(\frac{\partial G(\underline{X})}{\partial X_i}\right)\Big|_m^2 Var[X_i] + 2\sum_{i=1}^{n}\left(\frac{\partial G(\underline{X})}{\partial X_i}\right)\left(\frac{\partial G(\underline{X})}{\partial X_j}\right)\Big|_m Cov[X_i, X_j]}} \quad [5.19]$$

Taking the performance function and limit state as $G(\underline{X}) = F - 1 = 0$, the reliability index in [5.19] can be expressed as:

$$\beta = \frac{E[F]-1}{\sigma[F]} = \frac{E[F]-1}{\sqrt{\sum_{i=1}^{n}\left(\frac{\partial F}{\partial X_i}\right)\Big|_m^2 Var[X_i] + 2\sum_{i=1}^{n}\left(\frac{\partial F}{\partial X_i}\right)\left(\frac{\partial F}{\partial X_j}\right)\Big|_m Cov[X_i, X_j]}} \quad [5.20]$$

where:

n	is the number of random variables (parameters)
E[F]	is the expected value of the factor of safety
σ[F]	is the standard deviation of the factor of safety

Because the performance function is usually implicit in slope stability analysis, the partial derivatives in Equations [5.19] and [5.20] are frequently approximated numerically (Li, 1991; Wolff, 1994; Christian et al., 1994).

5-2.1.c. THE HASOFER AND LIND (1974) INVARIANT RELIABILITY INDEX

To overcome the problem of dependence of reliability index on performance function, Hasofer and Lind (1974) proposed an invariant definition of the reliability index. In this format, all the random variables $\underline{X}$ are transformed into a standardized parameter space $\underline{Z}$ by an orthogonal transformation such that:

$$Z_i = \frac{X_i - E[X_i]}{\sigma_{X_i}} \quad [5.21]$$

and $E[Z_i] = 0$, $Var[Z_i] = 1$, and $Cov[Z_i, Z_j] = 0$.

Hasofer and Lind (1974) defined the reliability index as the minimum distance between the origin and the limit state surface in the transformed parameter space $\underline{Z}$.

Expanding the performance function, G($\underline{Z}$) in a Taylor series at the most probable failure point $\underline{Z}^*$ and retaining only the first order terms gives the so-called Hasofer and Lind (1974) reliability index β as:

$$\beta = \frac{E[G(\underline{Z})]}{\sigma[G(\underline{Z})]} = \frac{-\sum_{i=1}^{n} Z_i \left(\frac{\partial G(\underline{Z})}{\partial Z_i} \right)_*}{\sqrt{\sum_{i=1}^{n} \left(\frac{\partial G(\underline{Z})}{\partial Z_i} \right)_*^2}} \qquad [5.22]$$

where $\left(\frac{\partial G(\underline{Z})}{\partial Z_i} \right)_*$ indicate that the partial derivatives are evaluated at the most probable failure point ($\underline{Z}^*$).

Geometrically, β is the shortest distance from the origin (mean value vector of $\underline{Z}$) to the failure boundary in transformed space. This is shown schematically in Figure 5.24 for the two dimensional case.

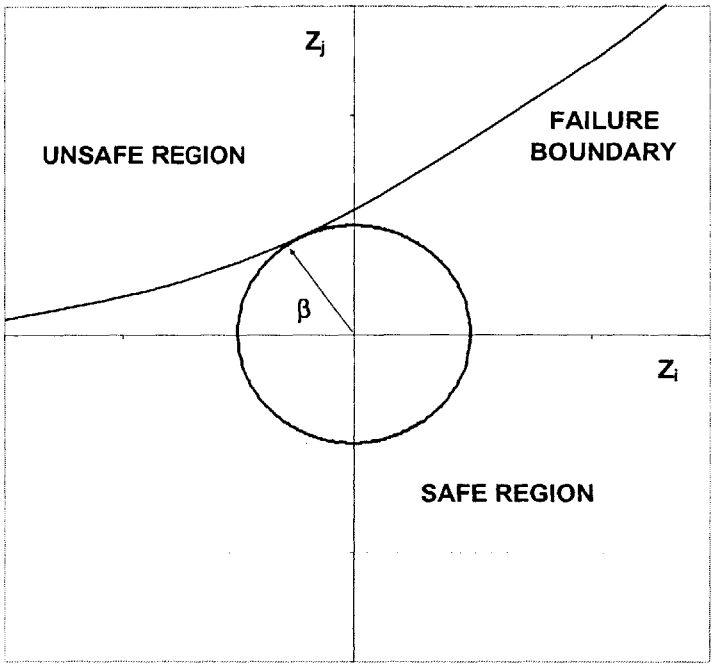

Figure 5.24. Hasofer and Lind (1974) Reliability Index in Transformed Variable Space

An iterative procedure is usually required to locate the most probable failure point and β (Hasofer and Lind, 1974; Parkinson, 1978; Ditlevsen 1981; Ang and Tang; 1984). A number of iterative algorithms for the calculation of β are available in the literature, but Li and Lumb (1987) and Li and White (1987) observed that the algorithm proposed by Parkinson (1978) is the most convenient for probabilistic slope stability analyses. Li and Lumb (1987) presented an exact procedure for computing β for a performance function formulated using Morgenstern and Price's (1988) Method. Chowdhury and Xu (1992) have also presented an algorithm similar to that proposed by Parkinson (1978).

In the space of the original variables, the Hasofer and Lind (1974) reliability index can be expressed in matrix form as (Veneziano, 1974):

$$\beta = \min_{\underline{X} \in D_F} \sqrt{(\underline{X} - E[\underline{X}])^T \underline{\Sigma}_X^{-1} (\underline{X} - E[\underline{X}])} \qquad [5.23]$$

where:

$\underline{X}$ is a vector representing the set of random variables

$E[\underline{X}]$ is the vector of expected or mean values of $\underline{X}$

$\underline{\Sigma}_X$ is the covariance matrix of the vector $\underline{X}$

D_F is the failure region

In the space of the original variables, the quadratic form in Equation [5.23] corresponds to ellipsoids centered about the mean value vector $E[\underline{X}]$. The general equation of the ellipsoids is given by:

$$(\underline{X} - E[\underline{X}])^T \underline{\Sigma}_X^{-1} (\underline{X} - E[\underline{X}]) = \beta^2 \qquad [5.24]$$

Each axis of an ellipsoid is parallel to a corresponding coordinate axis if the variables are uncorrelated. In the case of correlated variables, the axes of the ellipsoid are tilted. One can define a one standard deviation $(1-\sigma)$ dispersion ellipsoid, with $\beta = 1$ in Equation [5.24]. Equation [5.24] is plotted in Figure 5.25 for a generic two dimensional case of two variables X_1 and X_2, with mean values m_1 and m_2, and standard deviations σ_1 and σ_2 respectively. This is done for different values of the correlation coefficient ρ. When X_1 and X_2 are uncorrelated, the axes of the ellipse are parallel to the coordinate axes. This is shown and labeled $\rho = 0$ in Figure 5.25. When X_1 and X_2 are correlated, the ellipse rotates and changes its aspect ratio.

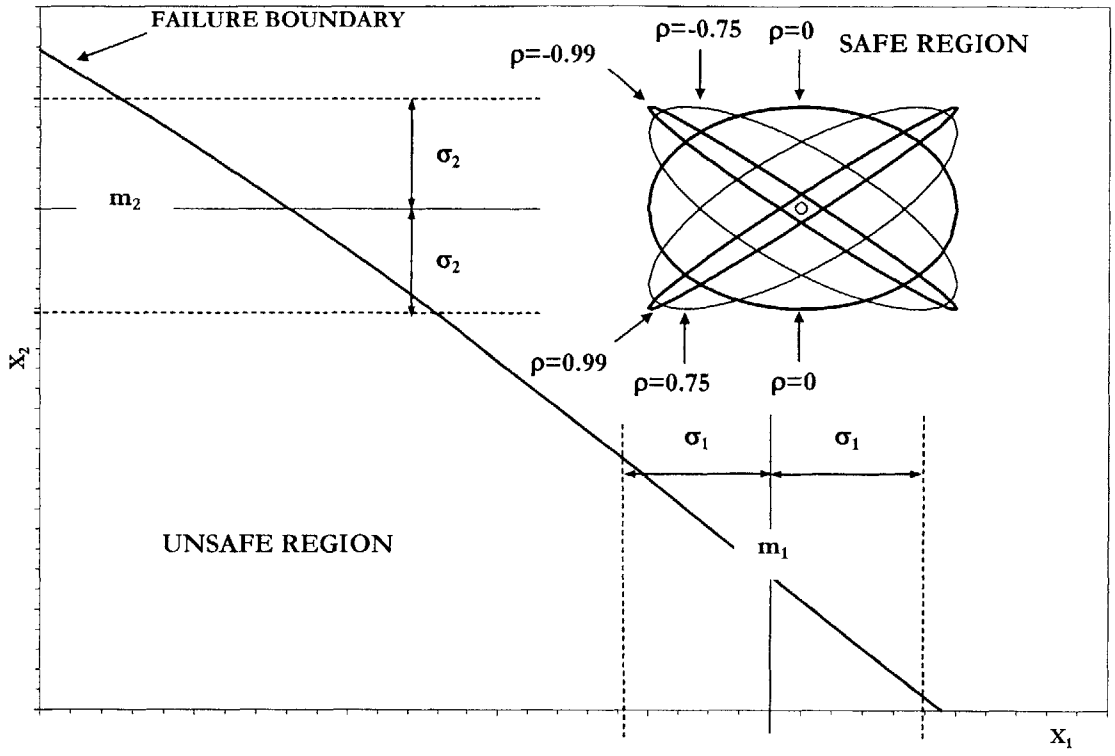

Figure 5.25. $1-\sigma$ Dispersion Ellipsoid in Two Dimensions for Different ρ

In order to illustrate the meaning of reliability index in the present context of slope stability, consider a two dimensional problem, where the soil strength parameters c' and ϕ' are considered random variables, with all other parameters deterministic. A basic reliability chart is shown in Figure 5.26.

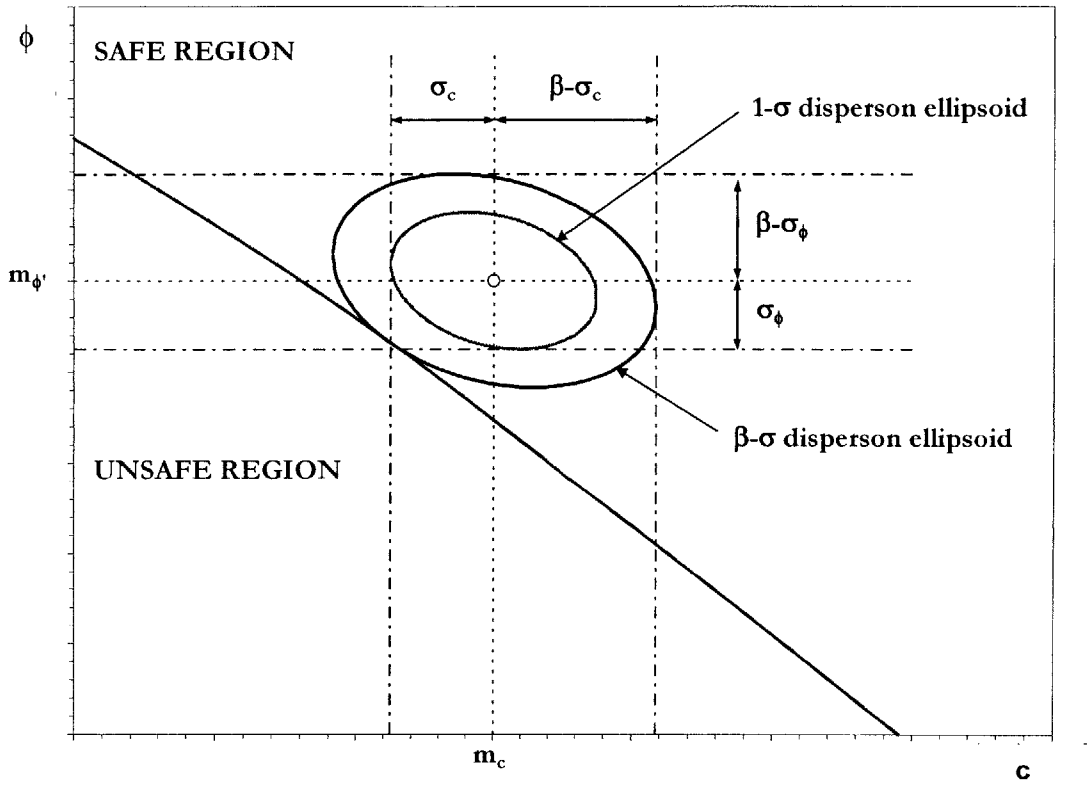

Figure 5.26. Illustration of Basic Reliability Chart for Two Dimensional Problem

The mean values and standard deviations of c and ϕ are denoted by m_c, σ_c and m_ϕ, σ_ϕ respectively. The failure surface in Figure 5.26 is defined by $F(c,\phi)=1$, or equivalently by the performance function $G(c,\phi)=F(c,\phi)-1=0$, where F is the factor of safety which is a function of c and ϕ. This failure surface separates the c - ϕ random space into two regions; a safe region and a failure region. Assuming that c and ϕ are negatively correlated, the $1-\sigma$ dispersion ellipsoid is tilted as shown in Figure 5.26. The Hasofer and Lind (1974) reliability index is interpreted as the distance from the mean point to the largest $\beta-\sigma$ dispersion ellipsoid, centered at the mean vector E[X] that lies within the safe region. This $\beta-\sigma$ dispersion ellipsoid is tangential to the failure surface boundary as shown in Figure 5.26. The point at which the $\beta-\sigma$ dispersion ellipsoid is tangential to the failure surface is the critical failure point. This corresponds to the most probable failure point if c and ϕ are have Joint Normal Distribution. (Shinozuka, 1978).

Probabilities of failure can be related to the reliability index if the distribution of the Factor of Safety or performance function is known or assumed. In the case of a normally distributed Factor of Safety, the probability of failure is given by:

$$P_F = P[F(\underline{X}) < 1] = \Phi(-\beta_{HL}) \qquad [5.25]$$

where Φ is the standard normal cumulative distribution function.

If the input variables are not normally distributed, Equation [5.31] provides an approximation to the probability of failure.

5-2.2. SLOPE RELIABILITY ANALYSES

5-2.2.1. MEAN VALUE FIRST ORDER RELIABILITY INDEX

In this section, the Mean-Value First Order Reliability Index formulation is applied to the Infinite Slope Model (Skempton and DeLory, 1957). An advantage of doing so, is that an explicit expression for the reliability index can be derived. The Factor of Safety in an infinite slope can be expressed as (Skempton & DeLory, 1957):

$$F = \frac{c' + [(\gamma_s - \gamma_w)z + z_w\gamma_w]\cos^2\beta\tan\phi'}{\gamma_s z\sin\beta\cos\beta} \qquad [5.26]$$

The Factor of Safety is expressed as a function of a random vector $\underline{X}$ of all the uncertain parameters in Equation [5.26], and:

$$F = G(\underline{X}) \qquad [5.27]$$

Since Equation [5.26] is a non-linear function of $\underline{X}$, It is necessary to linearize $F = G(\underline{X})$ to propagate uncertainty in a first-order second moment context. This is done by a Taylor's series expansion about the mean values of the parameters. The partial derivatives of the factor of safety with respect to each parameter have to be determined, and $F = G(\underline{X})$ is approximated to the first order as:

$$F = G(\underline{X}) \overset{1}{=} G'(\underline{X}) = G(\underline{m}_X) + \sum_{i=1}^{n} \left.\frac{\partial G(\underline{X})}{\partial X_i}\right|_{m_{X_i}} \left(X_i - m_{X_i}\right) \qquad [5.28]$$

where $G(\underline{X}) \overset{1}{=}$ indicates a first order approximation to $G(\underline{X})$, and n is the number of uncertain parameters in $\underline{X}$.

The partial derivatives in Equation [5.28] for the Infinite Slope Model assuming γ_w is deterministic are shown in Equations [5.29] to [5.34].

$$\frac{\partial G}{\partial c'} = \frac{1}{\gamma_s z \sin\beta\cos\beta} \qquad [5.29]$$

$$\frac{\partial G}{\partial \phi'} = \left[\frac{z\gamma_s + (z_w - z)\gamma_w}{z\gamma_s \tan\beta}\right]\sec^2\phi' \qquad [5.30]$$

$$\frac{\partial G}{\partial z_w} = \left(\frac{\gamma_w \tan\phi'}{z\gamma_s \tan\beta}\right) \qquad [5.31]$$

$$\frac{\partial G}{\partial \gamma_s} = -\left(\frac{1}{\gamma_s}\right)^2\left\{\frac{c'}{z\sin\beta\cos\beta} + \left(\frac{z_w}{z} - 1\right)\left(\frac{\gamma_w \tan\phi'}{\tan\beta}\right)\right\} \qquad [5.32]$$

$$\frac{\partial G}{\partial z} = -\left(\frac{1}{z}\right)^2\left\{\frac{c'}{\gamma_s \sin\beta\cos\beta} + \left(\frac{z_w \gamma_w \tan\phi}{\gamma_s \tan\beta}\right)\right\} \qquad [5.33]$$

$$\frac{\partial G}{\partial \beta} = \left\{\left(\frac{1}{\tan^2\beta}\right)\left\{\left(\frac{c'}{z\gamma_s}\right)\tan^2\beta\left(1+\tan^2\beta\right) - \left\{\tan\phi\left(1 - m\frac{\gamma_w}{\gamma_s}\right) + \left(\frac{c'}{z\gamma_s}\right)\right\}\left(1+\tan^2\beta\right)\right\}\right\}\left(\beta - m_\beta\right) \qquad [5.34]$$

The Mean-Value First Order Reliability Index is then given by:

$$\beta = \frac{E[G(\underline{X})]}{\sigma[G(\underline{X})]} = \frac{E[G(\underline{X})]}{\sqrt{\sum_{i=1}^{n}\left(\frac{\partial G(\underline{X})}{\partial X_i}\right)\Big|_m^2 \mathrm{Var}[X_i] + 2\sum_{i=1}^{n}\left(\frac{\partial G(\underline{X})}{\partial X_i}\right)\left(\frac{\partial G(\underline{X})}{\partial X_j}\right)\Big|_m \mathrm{Cov}[X_i, X_j]}} \qquad [5.35]$$

where $E[G(\underline{X})] = G(E[\underline{X}])$

A vector $\underline{B}$ of the partial derivatives can be expressed as:

$$\underline{B} = \left[\frac{\partial G}{\partial c'} \quad \frac{\partial G}{\partial \phi'} \quad \frac{\partial G}{\partial \gamma_s} \quad \frac{\partial G}{\partial \beta} \quad \frac{\partial G}{\partial z} \quad \frac{\partial G}{\partial z_w} \right]^T \qquad [5.36]$$

The vector $\underline{B}$ can be considered as an influence coefficient vector i.e. the coefficients that translate changes in each parameter from its mean, to corresponding changes in the Factor of Safety. This is explored in more detail in the following example.

Consider the slope shown in Figure 5.27.

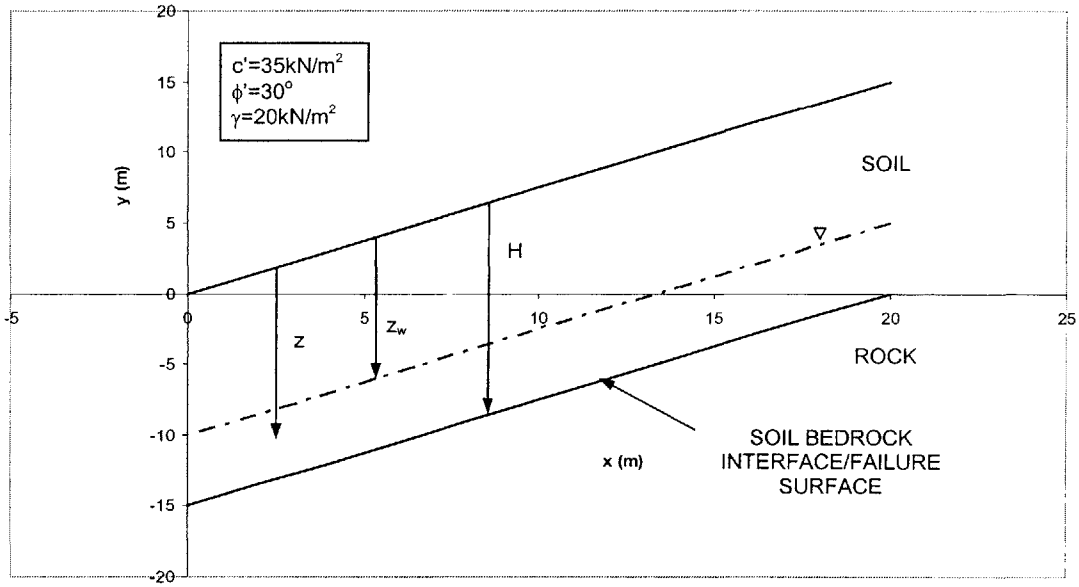

Figure 5.27. Slope Geometry and Definition of Parameters

The expected values (E[X]) and coefficients of variation (V[X]), defined as

$V[X] = \frac{\sqrt{Var[X]}}{E[X]}$ of the parameters are taken to be those in Table 5.1.

Parameter, X	Symbol	E[X]	V[X]
Cohesion (kN/m^2)	c'	35	0.1
Angle of shearing resistance	ϕ'	30	0.05
Saturated unit weight of soil (kN/m^2)	γ_s	20	0.01
Slope angle	β	35	0.05
Depth to failure surface (m)	z	15	0.05
Unit weight of water (kN/m^2)	γ_w	9.81	0
Depth of water table from ground surface (m)	z_w	10	0.05

Table 5.1. Expected Values, E[X], and Coefficients of Variation, V[X], of Parameters

The expected value of the Factor of Safety is computed to be E[F] = 0.938. Assuming uncorrelated parameters, the contribution of each parameter to the variance of the Factor of Safety is shown in Table 5.2.

PARAMETER, X	$\left.\frac{\partial F}{\partial X_i}\right\|_m$	VARIANCE, Var[X_i]	$\left(\left.\frac{\partial F}{\partial X_i}\right\|_m\right)^2 .V[X_i]$	% CONTRIBUTION
c'	0.007094518	12.25	0.000616569	9.34
ϕ'	0.02780067	2.25	0.001738974	26.36
γ_s	-0.003429478	0.04	4.70453E-07	0.0071
β	-0.033256698	3.0625	0.003387149	51.35
z	-0.034528884	0.5625	0.000670637	10.16
z_w	0.026962512	0.25	0.000181744	2.75
Var[F] =			**0.006595544**	**100 %**

Table 5.2. Contribution of Each Parameter to Var[F]

The results in Table 5.2 are shown graphically in Figure 5.28.

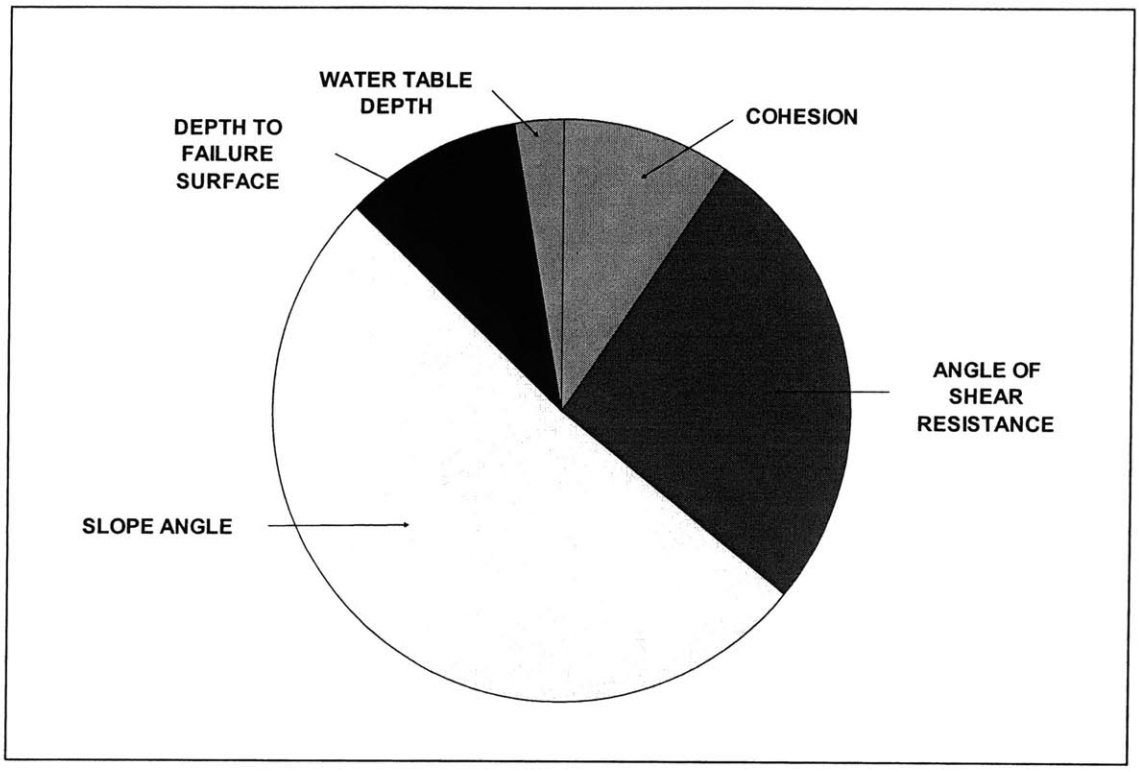

Figure 5.28. Percentage Contribution of Each Parameter to Var[F]

Figure 5.28 provides some insights into the contributors to the uncertainty in the Factor of Safety, and shows that the greatest contributions come from uncertainties in slope angle, the soil strength parameters, c' and ϕ' and uncertainties in location of failure surface (expressed as depth in this example). The Mean Value First Order Second Moment reliability index is computed to be $\beta = 0.762$. If the Factor of Safety is assumed to be normally distributed, the probability of failure is given by $P_f = \Phi(\beta) = 0.777258$.

5-2.2.2. RELIABILITY ANALYSES AND THE HASOFER AND LIND (1974) RELIABILITY INDEX

5-2.2.2.a. RELIABILITY ANALYSES FOR A SPECIFIED FAILURE SURFACE

In this section, a spreadsheet based approach is described by which the Hasofer and Lind (1974) reliability index can be computed for a specified failure surface using Janbu's Generalized Procedure of Slices (1973). This approach was first introduced by Low (1996), and later used by Low and Tang (1997). In this approach, one literally sets up a dispersion ellipsoid in the spreadsheet and minimizes its size subject to the constraint that it be tangent to the failure surface. In doing so, one works in the space of

the original variables, thereby bypassing the steps of transformed space and rotated frame of reference (see Section 5-2.3).

It is convenient to write the reliability index as:

$$\beta = \min_{x \in \underline{\Omega}} \sqrt{\left[\frac{X_i - m_i}{\sigma_i}\right]^T \underline{\Gamma}^{-1} \left[\frac{X_i - m_i}{\sigma_i}\right]} \qquad [5.37]$$

where:

$\underline{\Gamma}^{-1}$ is the inverse of the correlation matrix

The spreadsheet approach is best illustrated by an example. For this purpose, consider the slope in Figure 5.29.

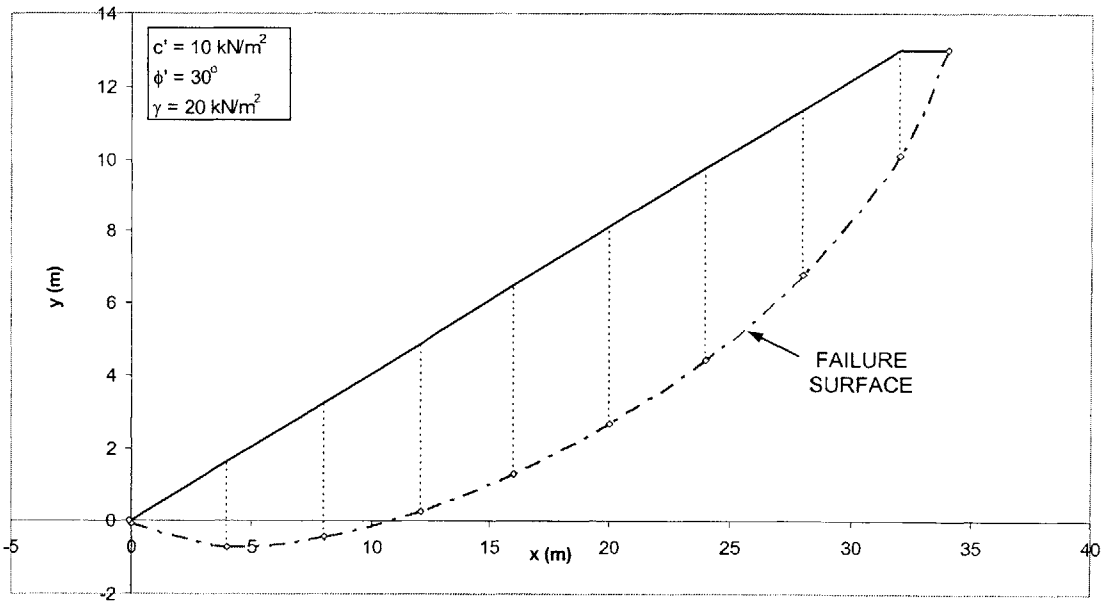

Figure 5.29. Slope Geometry and Soil Properties

Figure 5.29 shows the slope geometric, and soil strength parameters, as well as a specified failure surface. In Chapter 2, a method to locate the critical deterministic failure

surface in a slope was described. This method is implemented for the slope in Figure 5.29 starting using the failure surface shown in that figure as an initial failure surface. The resulting critical failure surface is shown in Figure 5.30.

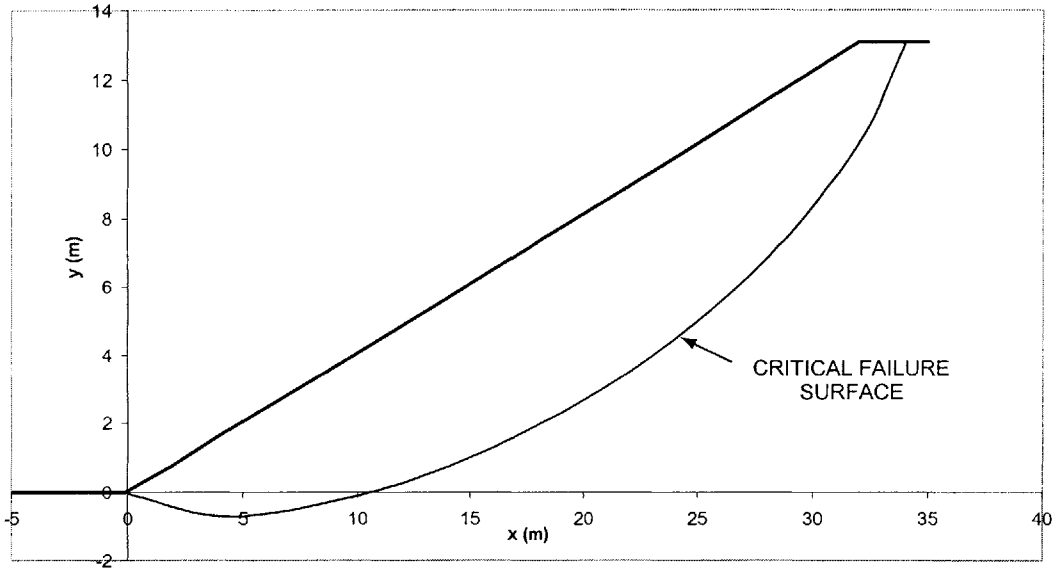

Figure 5.30. Critical Deterministic Failure Surface in Slope

A Factor of Safety of F =1.47 is obtained on this surface.

For reliability analyses, one needs to specify the mean values and covariance matrix between the uncertain qualities. For simplicity, we assume that the soil strength parameters c' and ϕ', and the pore pressure ratio r_u are the only uncertain quantities. These are the main contributors to the uncertainty in Factor of Safety if the slope angle is deterministic (see Chapter 4). Having said this, the same procedure applies still applies if other parameters are considered uncertain. The procedure is described in Figure 5.31.

Step 1. A spreadsheet is set up as in the deterministic case, which was discussed in detail in Part 2 of Chapter 2.

Step 2. The mean values $E[X_i]$, standard deviations $\sigma[X_i]$, and correlation matrix $\underline{\Gamma}$ of the uncertain quantities are specified (see Figure 5.32).

Step 3. A check is performed to ensure that the specified covariance matrix is positive definite. This is done by computing the determinant of the covariance matrix, labeled $\det[\underline{\Gamma}]$ and ensuring it is strictly greater than zero. This is done using the '=DET[]' function is Microsoft Excel. Since this involves a matrix manipulation, one needs to hold the Shift and Ctrl Keys while pressing Enter.

Step 4. All formulae that involve the uncertain quantities (c', ϕ', and r_u in this case) are computed based on the "X values", which are originally taken to be equal to the mean values. These are highlighted in Figure 5.32. So, for example, the c' values in the c' column are set to be equal to the cell which contains the "X value" of c' (see Figure 5.32).

Step 5. Intermediate computations:

The transpose of $\left(\frac{X_i - m_i}{\sigma_i}\right)$ is computed using the '=TRANSPOSE()' function in Microsoft Excel. The inverse of the correlation matrix is computed using the '=MINVERSE()' function, and the product $\left[\frac{X_i - m_i}{\sigma_i}\right]^T \underline{\Gamma}^{-1} \left[\frac{X_i - m_i}{\sigma_i}\right]$ is computed using the '=MMULT()' function.

Step 6. β is then computed as $\beta = \sqrt{\left[\frac{X_i - m_i}{\sigma_i}\right]^T \underline{\Gamma}^{-1} \left[\frac{X_i - m_i}{\sigma_i}\right]}$, using the '=SQRT()' function.

Step 7. Solver is invoked from the Toolbars Menu to minimize β, by changing the "X values", subject to the constraints $F(\underline{X}) = 1$, $\underline{X} \geq 0$ and $\sigma' \geq 0$. The result is $\beta = \min_{x \in \underline{\Omega}} \sqrt{\left[\frac{X_i - m_i}{\sigma_i}\right]^T \underline{\Gamma}^{-1} \left[\frac{X_i - m_i}{\sigma_i}\right]}$.

Figure 5.31. Spreadsheet Procedure for Computing β on a Specified Failure Surface

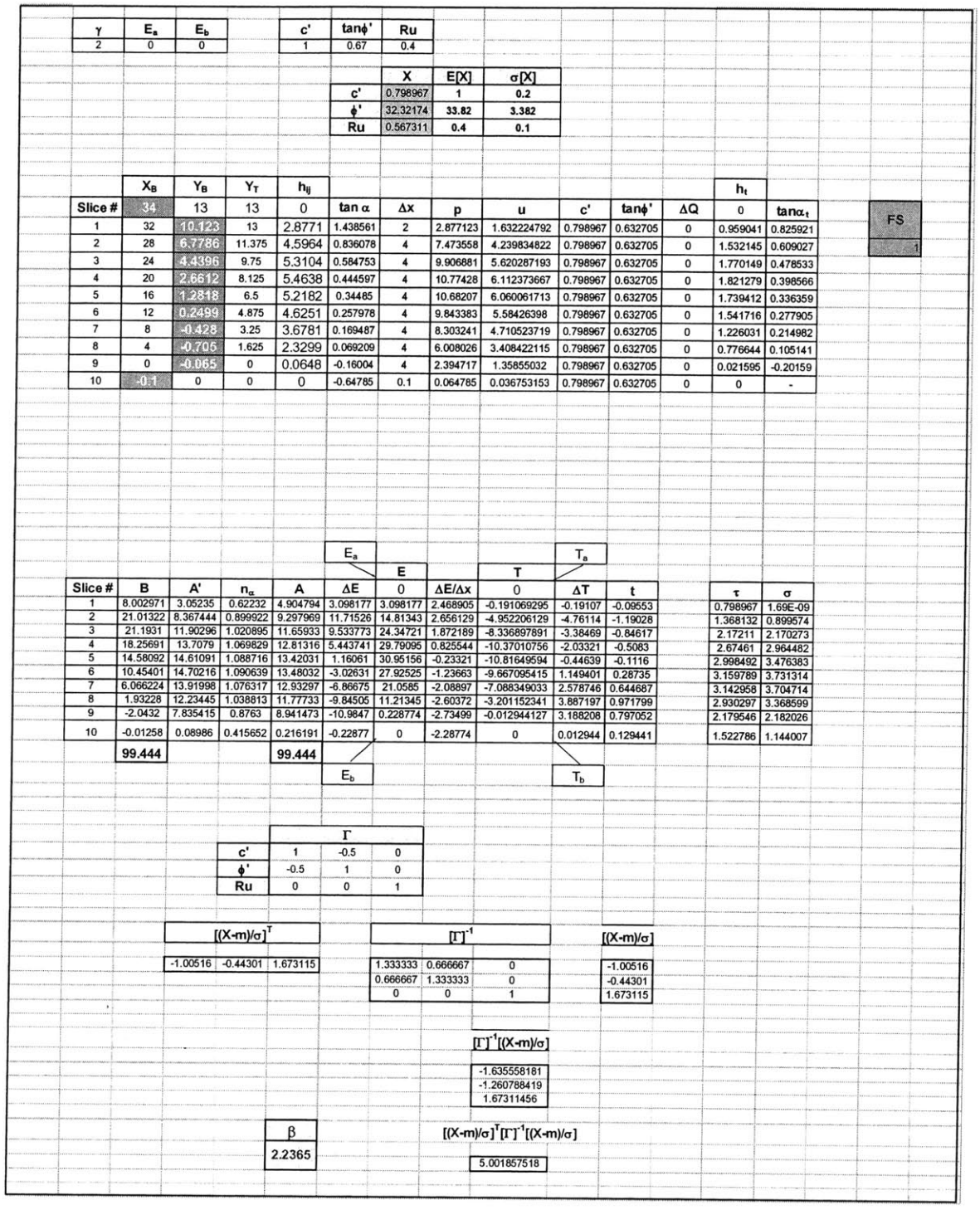

γ	E_a	E_b		c'	tanϕ'	Ru
2	0	0		1	0.67	0.4

	X	E[X]	σ[X]
c'	0.798967	1	0.2
ϕ'	32.32174	33.82	3.382
Ru	0.567311	0.4	0.1

Slice #	X_B = 34	Y_B	Y_T	h_{ij}	tan α	Δx	p	u	c'	tanϕ'	ΔQ	h_t = 0	$\tan\alpha_t$
1	32	10.123	13	2.8771	1.438561	2	2.877123	1.632224792	0.798967	0.632705	0	0.959041	0.825921
2	28	6.7786	11.375	4.5964	0.836078	4	7.473558	4.239834822	0.798967	0.632705	0	1.532145	0.609027
3	24	4.4396	9.75	5.3104	0.584753	4	9.906881	5.620287193	0.798967	0.632705	0	1.770149	0.478533
4	20	2.6612	8.125	5.4638	0.444597	4	10.77428	6.112373667	0.798967	0.632705	0	1.821279	0.398566
5	16	1.2818	6.5	5.2182	0.34485	4	10.68207	6.060061713	0.798967	0.632705	0	1.739412	0.336359
6	12	0.2499	4.875	4.6251	0.257978	4	9.843383	5.58426398	0.798967	0.632705	0	1.541716	0.277905
7	8	-0.428	3.25	3.6781	0.169487	4	8.303241	4.710523719	0.798967	0.632705	0	1.226031	0.214982
8	4	-0.705	1.625	2.3299	0.069209	4	6.008026	3.408422115	0.798967	0.632705	0	0.776644	0.105141
9	0	-0.065	0	0.0648	-0.16004	4	2.394717	1.35855032	0.798967	0.632705	0	0.021595	-0.20159
10	-0.1	0	0	0	-0.64785	0.1	0.064785	0.036753153	0.798967	0.632705	0	0	-

FS
1

Slice #	B	A'	n_α	A	ΔE	E: E_a = 0	ΔE/Δx	T: T_a = 0	ΔT	t	τ	σ
1	8.002971	3.05235	0.62232	4.904794	3.098177	3.098177	2.468905	-0.191069295	-0.19107	-0.09553	0.798967	1.69E-09
2	21.01322	8.367444	0.899922	9.297969	11.71526	14.81343	2.656129	-4.952206129	-4.76114	-1.19028	1.368132	0.899574
3	21.1931	11.90296	1.020895	11.65933	9.533773	24.34721	1.872189	-8.336897891	-3.38469	-0.84617	2.17211	2.170273
4	18.25691	13.7079	1.069829	12.81316	5.443741	29.79095	0.825544	-10.37010756	-2.03321	-0.5083	2.67461	2.964482
5	14.58092	14.61091	1.088716	13.42031	1.16061	30.95156	-0.23321	-10.81649594	-0.44639	-0.1116	2.998492	3.476383
6	10.45401	14.70216	1.090639	13.48032	-3.02631	27.92525	-1.23663	-9.667095415	1.149401	0.28735	3.159789	3.731314
7	6.066224	13.91998	1.076317	12.93297	-6.86675	21.0585	-2.08897	-7.088349033	2.578746	0.644687	3.142958	3.704714
8	1.93228	12.23445	1.038813	11.77733	-9.84505	11.21345	-2.60372	-3.201152341	3.887197	0.971799	2.930297	3.368599
9	-2.0432	7.835415	0.8763	8.941473	-10.9847	0.228774	-2.73499	-0.012944127	3.188208	0.797052	2.179546	2.182026
10	-0.01258	0.08986	0.415652	0.216191	-0.22877	0	-2.28774	0	0.012944	0.129441	1.522786	1.144007
	99.444			99.444	E_b =				T_b =			

Γ			
c'	1	-0.5	0
ϕ'	-0.5	1	0
Ru	0	0	1

$[(X-m)/\sigma]^T$		
-1.00516	-0.44301	1.673115

$[\Gamma]^{-1}$		
1.333333	0.666667	0
0.666667	1.333333	0
0	0	1

$[(X-m)/\sigma]$
-1.00516
-0.44301
1.673115

$[\Gamma]^{-1}[(X-m)/\sigma]$

-1.635558181
-1.260788419
1.67311456

β
2.2365

$[(X-m)/\sigma]^T[\Gamma]^{-1}[(X-m)/\sigma]$

5.001857518

Figure 5.32. Spreadsheet Solution for Computing β for Specified Failure Surface

The spreadsheet procedure in Figure 5.31 is implemented to obtain the Hasofer and Lind (1974) reliability index on the critical deterministic failure surface shown in Figure 5.30. The solution obtained by the spreadsheet is shown in Figure 5.32. The reliability

index is computed to be $\beta = 2.23$. This is the shortest distance, in units of standard deviation, from the mean value vector (m_c, m_ϕ, m_{r_u}) to the failure surface. The final "X values" are (0.799, 32.32, 0.567), shown as shaded cells in Figure 5.32, and represent the point at which the expanding dispersion ellipsoid is tangential to the failure surface, defined by F =1.

5-2.2.2.b. RELIABILITY ANALYSES WITH SEARCH FOR CRITICAL FAILURE SURFACE

In this section, a method is described by which the critical probabilistic (reliability based) failure surface in the slope is located using spreadsheet techniques. This is to an extent, very similar to the spreadsheet procedure described in Figure 5.31, with the exception of allowing some of the coordinates of the failure surface to change during the iterations involved in computing β. The steps of the procedure are shown in Figure 5.33.

Step 1. The mean values, standard deviations, and correlation matrix of the uncertain quantities are specified. A check for positive definite covariance matrix is performed.

Step 2. All formulae that involve the uncertain quantities are computed based on the "X values", which are originally taken to be equal to the mean values.

Step 3. The column vector $\left(\frac{X_i - m_i}{\sigma_i}\right)$ for each variable is set up for computing β.

Step 4. β is computed as in Step 6 of Figure 5.31.

Step 5. Solver is then invoked to minimize β, by changing the "X values" and the shaded cells of the coordinates of the failure surface (see Figure 5.34), subject to the constraints $F(\underline{X}) = 1$, $\underline{X} \geq 0$ and $\sigma' \geq 0$. Additional constraints are imposed on the first and last coordinates of the failure surface to avoid unreasonable results. The constraints on these coordinates were discussed in detail in Part 2 of Chapter 2.

Figure 5.33. Spreadsheet Procedure for Reliability Analyses with Search for Critical Probabilistic Failure Surface

The spreadsheet solution is shown in Figure 5.34.

γ	E_a	E_b		c'	tanϕ'	Ru
2	0	0		1	0.67	0.4

	X	E[X]	σ[X]
c'	0.925809	1	0.2
ϕ'	32.3323	33.82	3.382
Ru	0.593013	0.4	0.1

Slice #	X_B	Y_B	Y_T	h_{ij}	tan α	Δx	p	u	c'	tanϕ'	ΔQ	h_t	$\tan\alpha_t$
1	32	9.6857	13	3.3143	1.340108	2.473135	3.314267	1.965404842	0.925809	0.632963	0	1.104756	0.798068
2	28	6.2819	11.375	5.0931	0.85097	4	8.407415	4.985709694	0.925809	0.632963	0	1.697716	0.608901
3	24	4.0039	9.75	5.7461	0.569482	4	10.83922	6.427804123	0.925809	0.632963	0	1.915358	0.46538
4	20	2.3223	8.125	5.8027	0.420408	4	11.54878	6.84858174	0.925809	0.632963	0	1.934235	0.38146
5	16	1.0514	6.5	5.4486	0.317723	4	11.2513	6.672174555	0.925809	0.632963	0	1.8162	0.318305
6	12	0.1276	4.875	4.7474	0.230942	4	10.19597	6.046344882	0.925809	0.632963	0	1.582456	0.260549
7	8	-0.45	3.25	3.7002	0.144453	4	8.447549	5.00951022	0.925809	0.632963	0	1.233394	0.199707
8	4	-0.644	1.625	2.2689	0.048418	4	5.969035	3.539717668	0.925809	0.632963	0	0.756284	0.101967
9	0	-0.049	0	0.0488	-0.14877	4	2.317643	1.374393179	0.925809	0.632963	0	0.016263	-0.14451
10	-0.1	0	0	0	-0.4879	0.1	0.04879	0.028932935	0.925809	0.632963	0	0	-

FS
1

Slice #	B	A'	n_α	A	ΔE	E_a / E	ΔE/Δx	T	T_a / ΔT	t	τ	σ
						0		0				
1	10.62583	4.231822	0.661056	6.40161	4.224225	4.224225	2.80938	-0.267539083	-0.26754	-0.10818	0.925809	-1.3E-09
2	23.81903	8.797073	0.892401	9.857762	13.96127	18.18549	3.04315	-5.906754729	-5.63922	-1.4098	1.429365	0.795554
3	22.61536	12.56533	1.027298	12.23143	10.38393	28.56942	1.954817	-9.551459397	-3.6447	-0.91118	2.309021	2.185296
4	18.57941	14.33667	1.075938	13.32481	5.254605	33.82403	0.697809	-11.55279812	-2.00134	-0.50033	2.830867	3.009745
5	14.23868	15.17636	1.090975	13.91082	0.327866	34.15189	-0.48042	-11.74326651	-0.19047	-0.04762	3.158827	3.52788
6	9.768677	15.16862	1.088143	13.93992	-4.17125	29.98065	-1.52706	-10.22792148	1.515345	0.378836	3.308523	3.76438
7	5.307367	14.2756	1.069125	13.35261	-8.04524	21.93541	-2.34836	-7.277111661	2.95081	0.737702	3.269919	3.70339
8	1.353604	12.43678	1.028236	12.09526	-10.7417	11.19375	-2.71737	-3.196502521	4.080609	1.020152	3.016743	3.303405
9	-1.85229	8.104537	0.886223	9.145026	-10.9973	0.196433	-2.73018	-0.016014525	3.180488	0.795122	2.236754	2.071124
10	-0.01019	0.103974	0.558284	0.186239	-0.19643	0	-1.96433	0	0.016015	0.160145	1.504304	0.913947
	104.45			104.45	E_b				T_b			

Γ			
c'	1	-0.5	0
ϕ'	-0.5	1	0
Ru	0	0	1

$[(X-m)/\sigma]^T$

-0.37095	-0.43989	1.930134

$[\Gamma]^{-1}$

1.333333	0.666667	0
0.666667	1.333333	0
0	0	1

$[(X-m)/\sigma]$

-0.37095
-0.43989
1.930134

$[\Gamma]^{-1}[(X-m)/\sigma]$

-0.787862972
-0.833818904
1.930134245

β
2.0939

$[(X-m)/\sigma]^T[\Gamma]^{-1}[(X-m)/\sigma]$

4.38446519

Figure 5.34. Spreadsheet Solution for Reliability Analyses with Search of Critical Probabilistic Failure Surface

The Hasofer and Lind (1974) reliability index is computed to be $\beta = 2.09$. The X_B and Y_B columns define the critical reliability based failure surface in the slope which takes into account the uncertainties in the input parameters. Figure 5.35 shows the deterministic and reliability based failure surfaces.

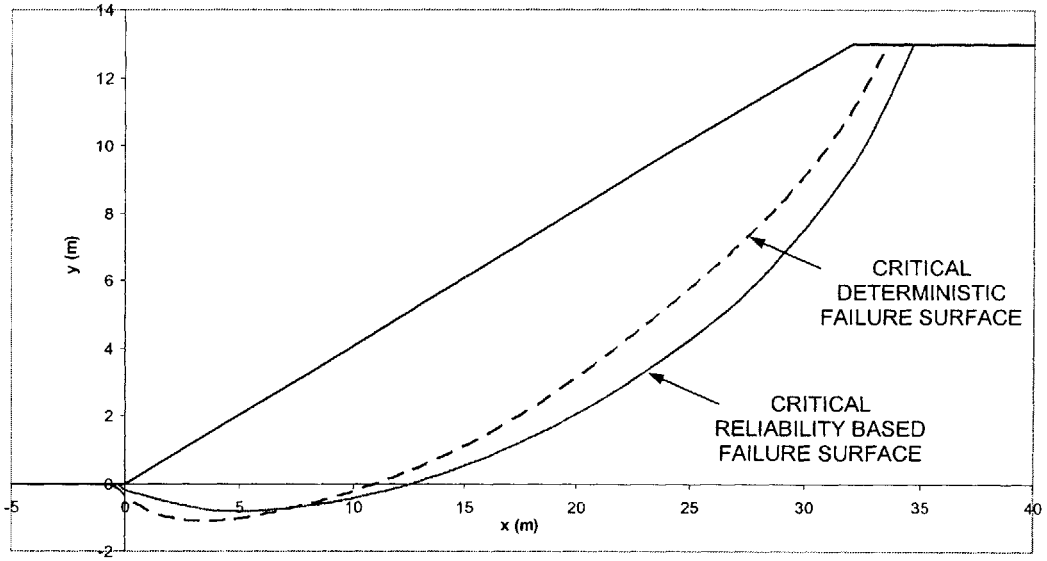

Figure 5.35. Critical Deterministic and Probabilistic Failure Surfaces in Slope

The critical failure surfaces obtained from deterministic and reliability based analyses are different (Figures 5.32 and 5.34). As a consequence, the reliability indices on both surfaces are different (Figures 5.32 and 5.34). This is investigated in more detail in the next section.

5-2.2.3. APPLICATION OF SPREADSHEET TECHNIQUES TO GENERAL SLOPES

In this section, techniques are described whereby the reliability analyses performed in the previous section can be used for more general problems involving slopes with defined geometry, unsaturated soil strength, depth to water tables and seepage conditions, depth to bedrock, and other site conditions. The spreadsheet based approach is used to analyze the reliability of different slopes in various scenarios. The soil strength parameters c' and ϕ' are assumed uncertain, although other parameters can be included as variables. The effects of the degree of uncertainty in c' and ϕ' is investigated. Prior to doing so, it is necessary to define a range of typical values which

are taken to be $V_{c'} = 10 - 25\%$, and $V_{\phi'} = 10 - 33\%$ (Harr, 1984; Kulhawy, 1992; Lacasse and Nadim, 1994; Duncan, 2000), where $V = \frac{\sigma}{m}$, the coefficient of variation.

EXAMPLE 1: Deep Failure Surface (Very Deep Bedrock)

Consider the slope shown in Figure 5.36.

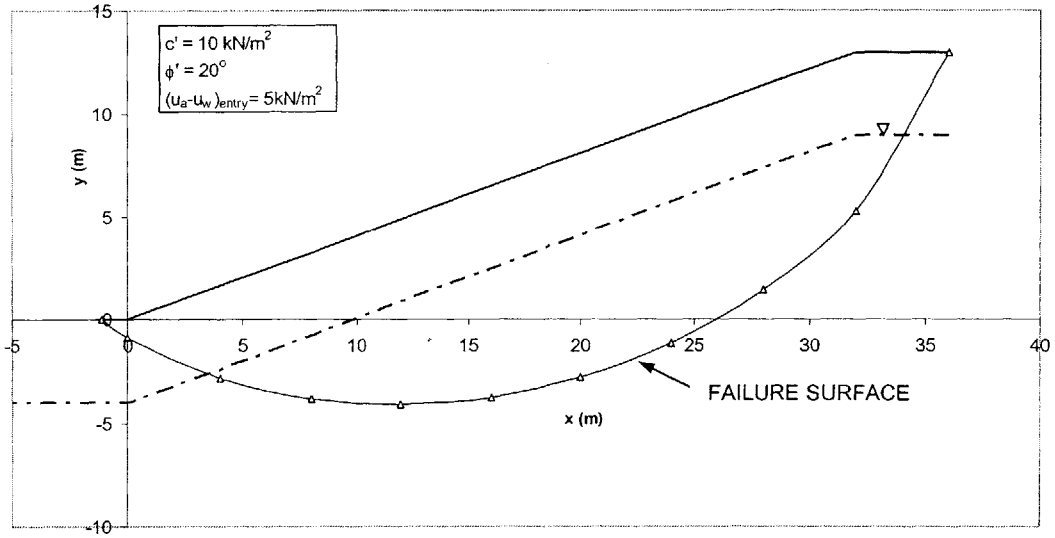

Figure 5.36. Slope Geometry and Strength Parameters

The slope geometry is shown in Figure 5.36, and the water table is taken to be at a depth of 4 m below the ground surface with seepage parallel to the slope surface. The soil strength parameters are taken to be those shown in Figure 5.36, and the Effective Stress Model (Bishop, 1959) is used for unsaturated soil strength with an air entry suction of $(u_a - u_w) = 5\text{kN/m}^2$ (see Part 2 of Chapter 2). All parameters are assumed deterministic initially.

In Chapter 2, a method was described by which the critical deterministic failure surface can be located in a slope with known parameters. This method is applied and the resulting critical failure surface is shown in Figure 5.36. A Factor of Safety of 1.15 is computed on this surface.

We now assume that the soil strength parameters c' and ϕ' are uncertain, while all other parameters remain deterministic. The mean values and standard deviations of c' and ϕ' are taken to be:

$c' \sim (m_{c'} = 10 kN/m^2,\ \sigma_{c'} = 2 kN/m^2)$ and $\phi' \sim (m_{\phi'} = 20^o,\ \sigma_{\phi'} = 2.5^o)$

c' and ϕ' are assumed uncorrelated, and the correlation matrix is $\underline{\Gamma} = \begin{bmatrix} 1 & 0 \\ 0 & 1 \end{bmatrix}$

The spreadsheet procedure described in Figure 5.31 is implemented to obtain the reliability index along the deterministic failure surface in Figure 5.36. A value of $\beta = 1.66$ is obtained. The critical combination of c' and ϕ' is $c'^* = 8.5 kN/m^2$ and $\phi'^* = 16.3^o$.

A reliability chart for this slope can be derived by determining all the combinations of c' and ϕ' that would cause failure along the deterministic failure surface, and is shown in Figure 5.37.

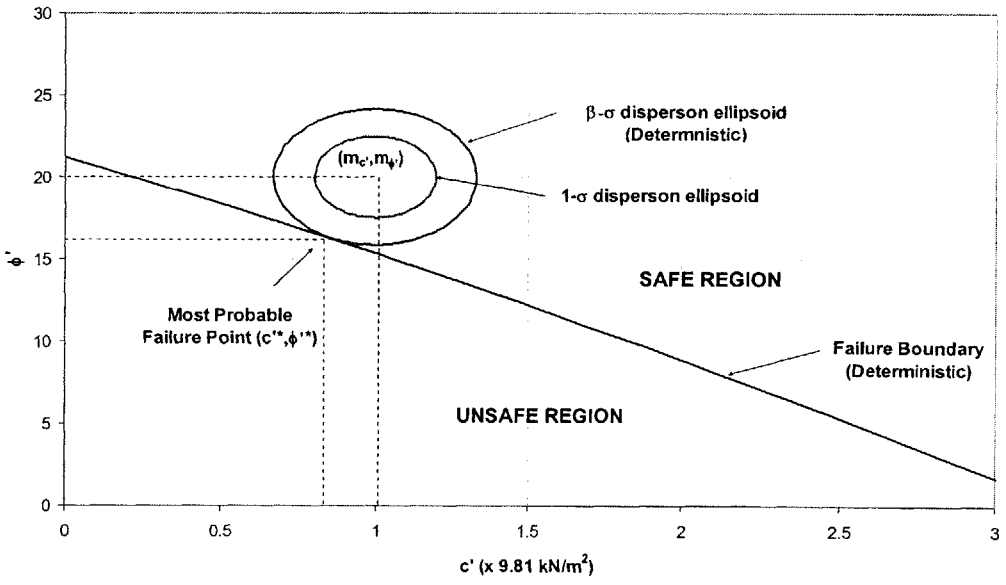

Figure 5.37. Reliability Chart on Critical Deterministic Failure Surface, and $1-\sigma$ and $\beta-\sigma$ Dispersion Ellipsoids

Figure 5.37 shows the $1-\sigma$ and $\beta-\sigma$ dispersion ellipsoids. Note that both these ellipsoids are centered around the mean value vector of c' and ϕ', and their axes are parallel to the corresponding coordinate axes. This is because no correlation is assumed between the variables. Figure 5.37 also shows the $\beta-\sigma$ dispersion ellipsoid is tangential to failure surface at the critical failure point (c'^*,ϕ'^*). If c' and ϕ' are jointly normally distributed, then (c'^*,ϕ'^*) corresponds to the most probable failure point.

The reliability analyses have been based on a critical failure surface found from a deterministic search. The spreadsheet procedure in Figure 5.33 can be implemented to determine the critical reliability based failure surface and obtain the Hasofer and Lind (1974) reliability index on that surface. Recall that this is not the same as the critical deterministic based surface, because during the optimization procedure in the search for the reliability index, not only are the values of the random variables (c' and ϕ' in this case) allowed to vary, but also the coordinates of the failure surface. The results are shown in Figure 5.38.

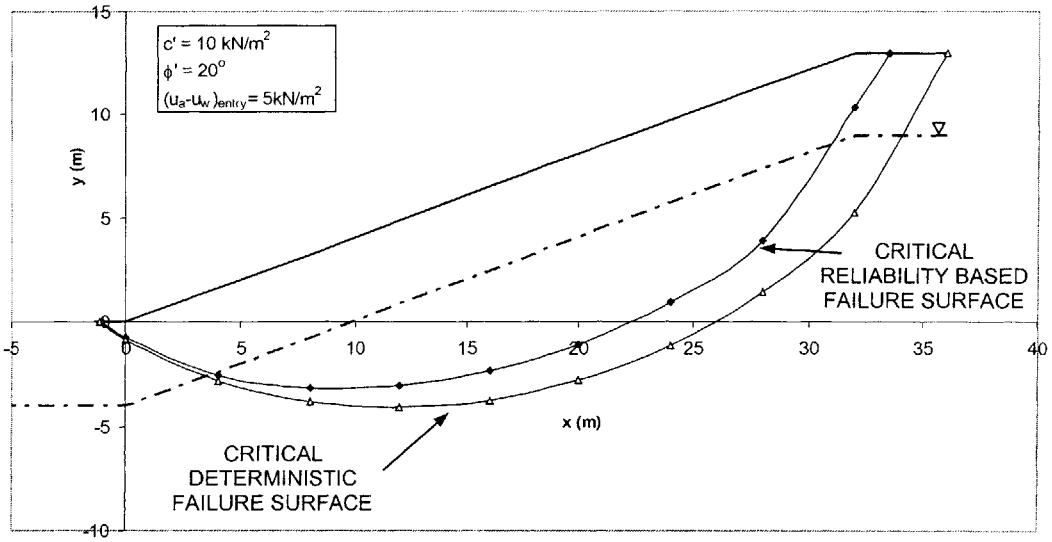

Figure 5.38. Critical Deterministic and Reliability Based Failure Surfaces

Figure 5.38 also shows the critical deterministic failure surface, and shows that the critical reliability failure surface is different from the deterministic one. This is due to

uncertainties in c' and ϕ', which are taken in account when searching for the critical reliability based failure surface.

The Hasofer and Lind (1974) reliability index along this surface is computed to be $\beta = 1.31$, and the critical failure combination of c' and ϕ' is $c' = 8.9$ kN/m^2 and $\phi' = 17^o$. A reliability chart is derived in this case, after defining the failure surface boundary from combinations of c' and ϕ' that cause failure on the reliability based failure surface .This is shown in Figure 5.39.

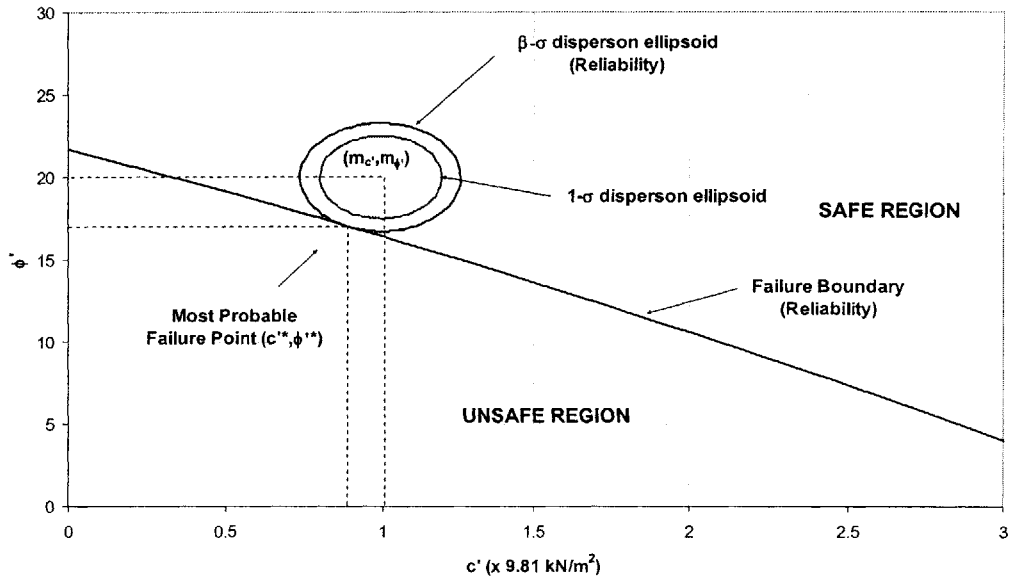

Figure 5.39. Basic Reliability Chart Based on Probabilistic Critical Failure Surface

Figure 5.39 shows the $1-\sigma$ and $\beta-\sigma$ dispersion ellipsoids, as well as the critical failure point, which is the most probable failure point in the case of normally distributed variables. There is a difference in the values of β when the deterministic failure surface is used to evaluate β, and when the reliability based surface is used. This is because of the different failure surfaces in each case (see Figure 5.38) and is shown in Figure 5.40.

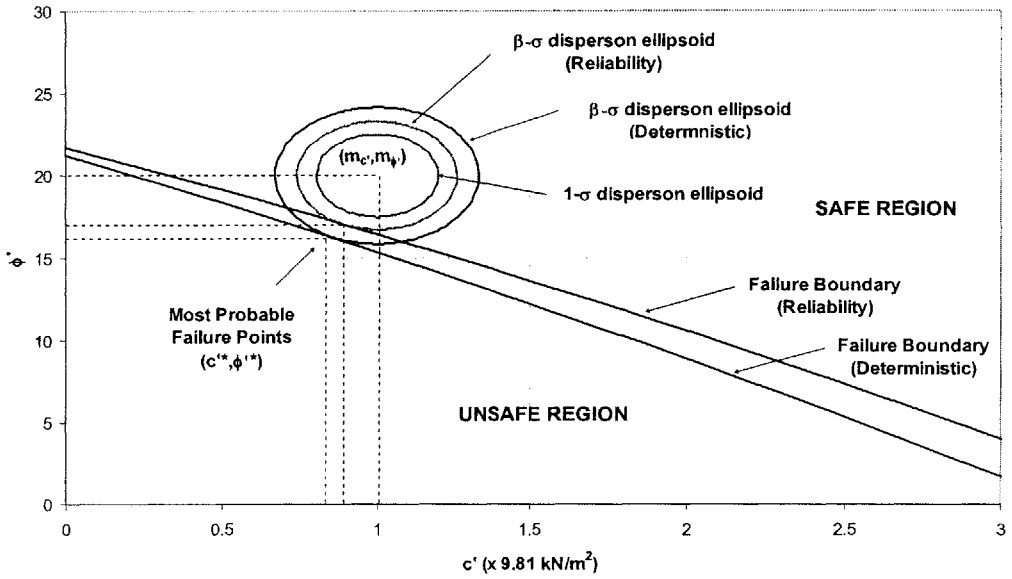

Figure 5.40. Reliability Chart for Deterministic and Reliability Based Analyses

The reliability index computed from the deterministic failure surface is larger than the one determined from the critical reliability based failure surface. This implies a smaller probability of failure, and hence using the deterministic failure surface to evaluate β will lead to unconservative results. If the Factor of Safety is assumed Normal $P_f = \Phi(-\beta) = 0.05$ (deterministic) and $P_f = \Phi(-\beta) = 0.095$ (reliability). The difference can therefore be significant. This is important since the majority of the analyses in the literature rely on the deterministic surface for the evaluation of β, and as shown in this example, results are unconservative because of the overestimation of β.

EXAMPLE 2: SHALLOW BEDROCK

Consider the slope shown in Figure 5.41.

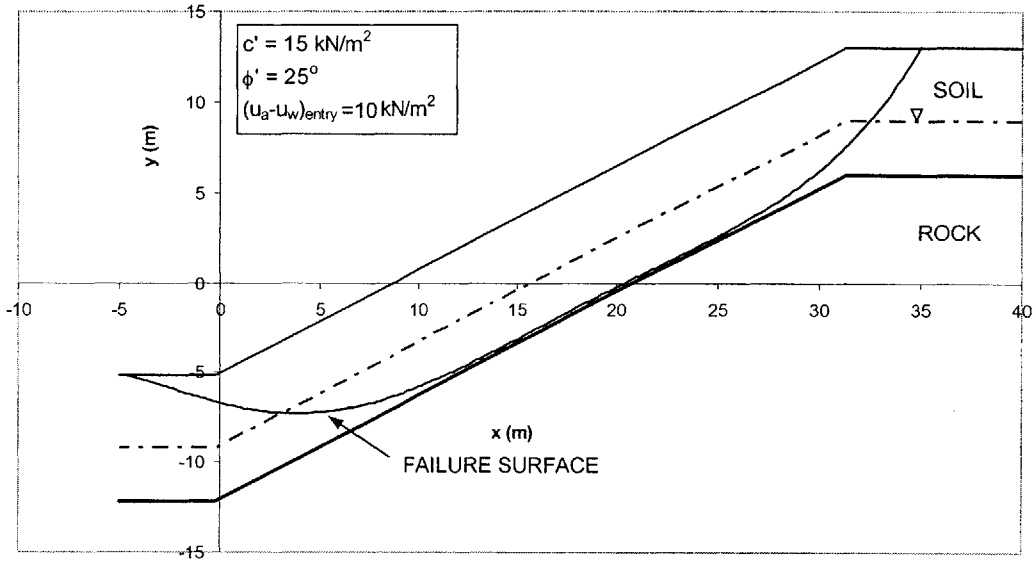

Figure 5.41. Slope Geometry and Strength Parameters

The saturated soil strength parameters are shown in Figure 5.41. The air entry pressure is taken to be $(u_a - u_w)_{entry} = 10 kN/m^2$. Recall that this is obtained from the soil moisture characteristic curve (as explained in Chapter 2), and is used in the Effective Stress Model for unsaturated strength (see Chapter 2). The water table is assumed at depth 4 m below the ground surface, and the depth to bedrock is 7 m. Based on these parameters, the deterministic failure surface is located and shown in Figure 5.41. A Factor of Safety of 1.18 is computed.

We now assume that the saturated soil strength parameters are uncertain, with mean values and standard deviations of c' and ϕ' as:

$c' \sim (m_{c'} = 15 kN/m^2, \sigma_{c'} = 5 kN/m^2)$ and $\phi' \sim (m_{\phi'} = 25^o, \sigma_{\phi'} = 5^o)$ and c' and ϕ' are assumed uncorrelated.

The reliability index on the critical deterministic shown in Figure 5.41 is computed and a value of $\beta = 0.93$ is obtained. A reliability chart is derived and is shown in Figure 5.42.

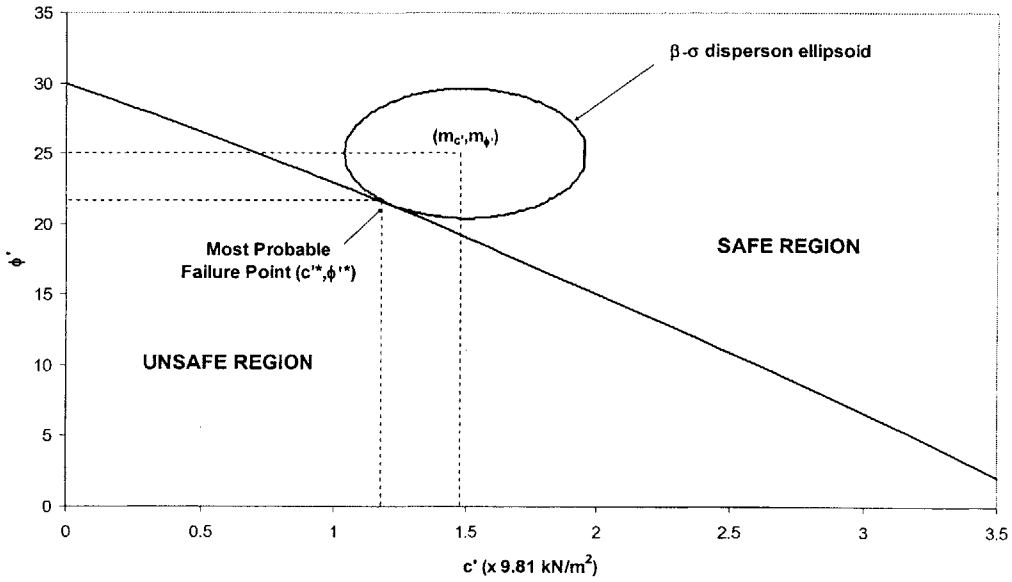

Figure 5.42. Reliability Chart Derived From Deterministic Analyses

The $\beta - \sigma$ dispersion ellipsoid is shown in Figure 5.42, and is tangential to the failure boundary at the critical failure point $c'^* = 12$ kN/m^2 and $\phi'^* = 21.4^o$.

The critical reliability based failure surface is located given the uncertainty in strength parameters, and is shown in Figure 5.43.

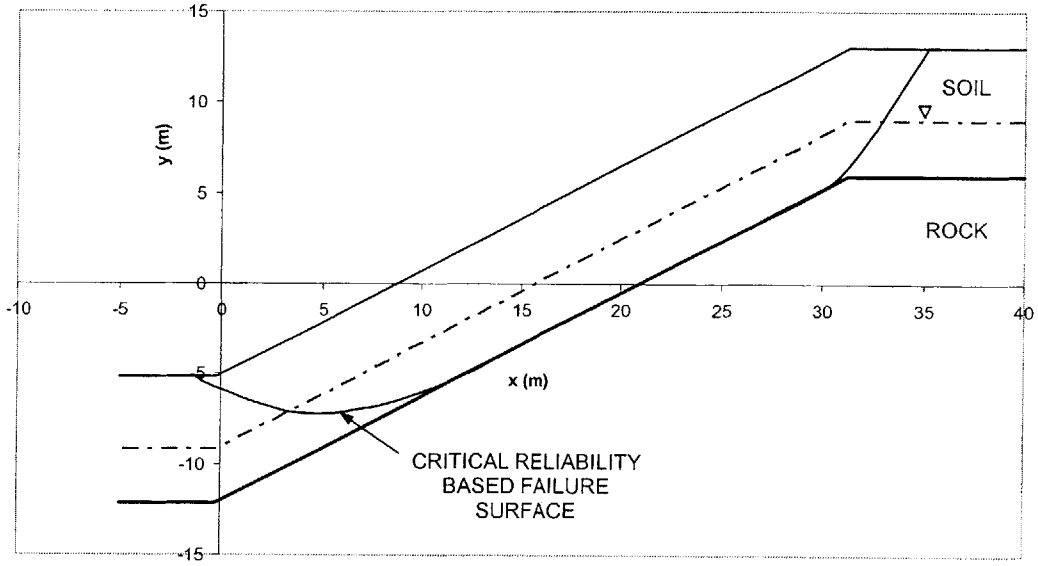

Figure 5.43. Critical Reliability Based Failure Surface

The critical reliability based failure surface is different than the deterministic one. A value of $\beta = 0.72$ is computed, and the critical failure point is $c'^* = 13$ kN/m^2 and $\phi'^* = 22^o$. The reliability chart based on the reliability surface is shown in Figure 5.44.

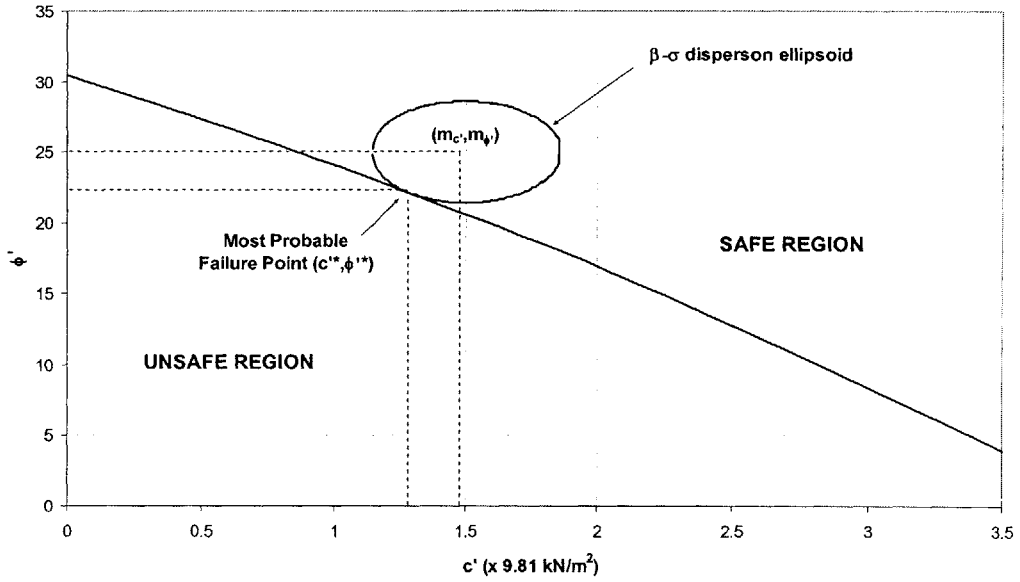

Figure 5.44. Reliability Chart Based on Probabilistic Critical Failure Surface

The smaller value of β based on reliability analyses highlights the importance of performing reliability analyses to determine β, as in the case of Example 1. If the Factor of Safety is assumed Normal $P_f = \Phi(-\beta) = 0.129$ (deterministic) and $P_f = \Phi(-\beta) = 0.232$ (reliability). Using the deterministic surface will lead to unconservative results.

A comparison of the results in Examples 1 and 2 shows the importance of incorporating uncertainties into stability analyses. In Example 1, the Factor of Safety was computed to be 1.15, and F = 1.18 in Example 2. Based on these results alone, one would conclude that the slope in Example 2 is safer. When uncertainties are included, the probability of failure of the slope in Example 1 is 0.095, and 0.232 in Example 2. The slope in Example 1 is therefore more reliable.

EXAMPLE 3: Effects of Parameter Uncertainty

We reconsider the slope shown in Figure 5.41, and assume that the soil strength parameters are:

$$c' \sim (m_{c'} = 15 kN/m^2,\ \sigma_{c'} = 2.5 kN/m^2)$$

$$\phi' \sim (m_{\phi'} = 25^o,\ \sigma_{\phi'} = 5^o)$$

c' and ϕ' are assumed uncorrelated, and the correlation matrix is:

$$\underline{\Gamma} = \begin{bmatrix} 1 & 0 \\ 0 & 1 \end{bmatrix}$$

Note that the standard deviation of c' is taken to be smaller than the one is Example 2. also note that the Factor of Safety in the slope is the same as that obtained in Example 2, since uncertainties are not taken into account in Factor of Safety computations. The reliability index on the critical deterministic failure surface is computed to be $\beta = 1.07$, and the reliability chart is shown in Figure 5.45.

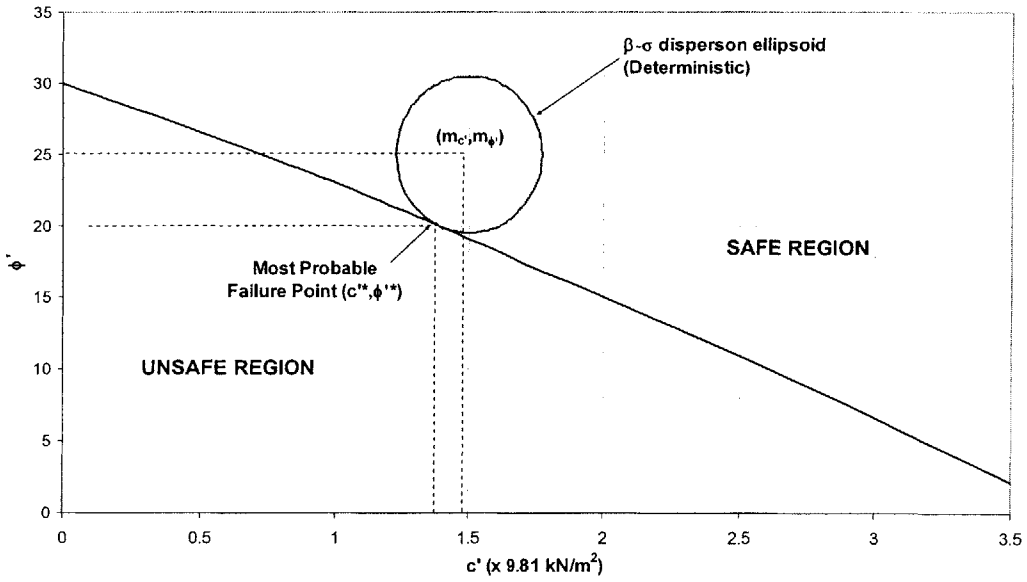

Figure 5.45. Reliability Chart Derived From Deterministic Analyses

The reliability based critical surface is located and shown in Figure 5.46.

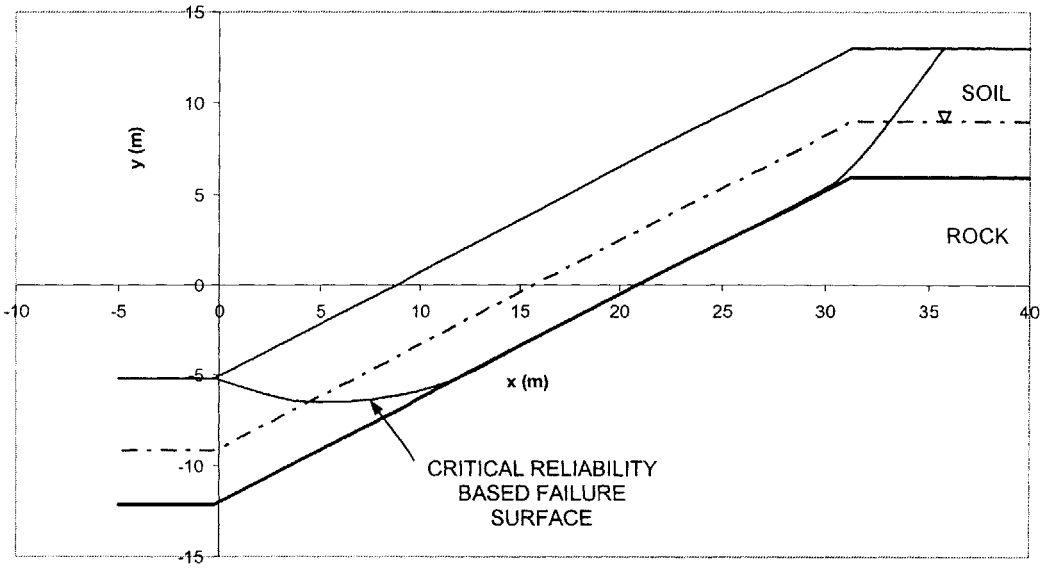

Figure 5.46. Critical Reliability Based Failure Surface

A reliability chart is derived, and shown in Figure 5.47, along with the $\beta - \sigma$ dispersion ellipsoid.

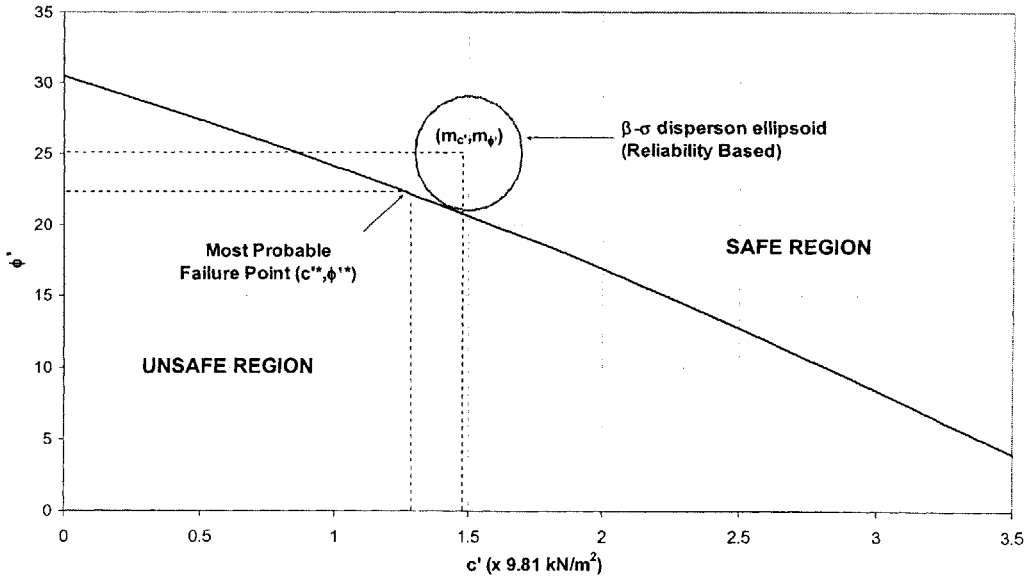

Figure 5.47. Reliability Chart Based on Probabilistic Critical Failure Surface

The reliability index is computed to be $\beta = 0.85$. Figure 5.48 compares the reliability charts.

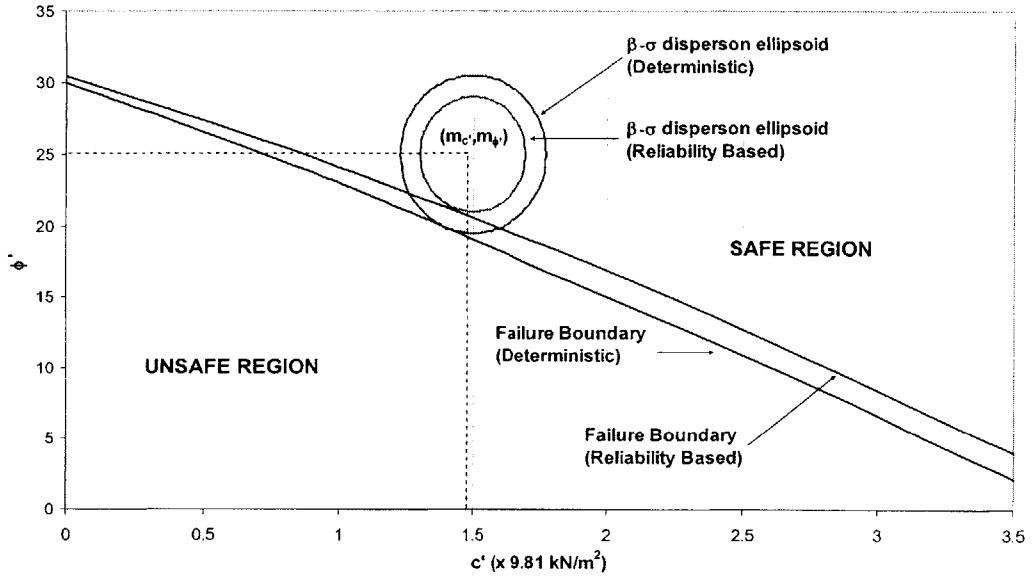

Figure 5.48. Reliability Chart for Deterministic and Reliability Based Analyses

Figure 5.48 shows that different failure boundaries are obtained whether the deterministic or reliability based critical surfaces are used, and this leads to the difference in the values of β which is reflected in the different $\beta - \sigma$ dispersion ellipsoids.

The values of β computed in this example is greater than the β computed in the Example 2. This implies a safer slope, and is a result of the smaller uncertainty in c' that is assumed in this example. Smaller parameter uncertainty, would result in smaller uncertainty in Factor of Safety, and hence larger values of β (or smaller probability of failure).

Graphically, the $1 - \sigma$ dispersion ellipsoid is smaller when the uncertainty in the parameter(s) is smaller, and so it can grow larger in size before touching the failure boundary. This implies larger values of β, as shown in Figure 5.48.

It is interesting to note that the ratio $\frac{\beta_{deterministic}}{\beta_{reliability}}$ increases with increasing parameter uncertainty. This ratio is greater in Example 2 than in this example, as $\frac{\beta_{deterministic}}{\beta_{reliability}} = \frac{0.93}{0.72} > \frac{\beta_{deterministic}}{\beta_{reliability}} = \frac{1.07}{0.85}$. What this indicates is that the deviation between computing β from the deterministic surface from computing β from the reliability based surface increases as parameter uncertainty increases. Deterministic based reliability indices therefore become more and more unconservative as parameter uncertainty increases.

5-2.3. CONCLUSIONS

This part of the chapter introduced basic concepts of reliability analyses, and described techniques by which uncertainties in parameters can be systematically incorporated into the analyses. The Hasofer and Lind (1974) reliability index was formulated as an optimization problem that was solved using spreadsheet techniques in the space of the original variables. This includes a search for the critical reliability failure surface in a slope. The reliability index corresponds to the dispersion ellipsoid that is tangential to the failure boundary defined in the case of slope stability by F = 1. A method to derive reliability charts was also introduced.

Numerical examples were used to illustrate the effects of parameter uncertainty, on slope reliability.

Several important conclusions were made.

1. Larger (Compare Examples 1 and 2) or same (compare Examples 2 and 3) Factors of Safety do not necessarily imply more reliable slopes. A more rational approach to assessing the state of stability of slope is through the reliability index which incorporates uncertainties in parameters.
2. Larger uncertainties in parameters lead to lower values of the Hasofer and Lind (1974) reliability index, and hence larger probabilities of slope failure.
3. Reliability analyses performed on the critical deterministic failure surface results in larger values of β and are therefore unconservative. This is important since many of

current analyses are based on using this surface for reliability analyses. As parameter uncertainty increases, the deviation between the reliability based β and the deterministic based β increases and deterministic analyses become more and more unconservative.

PART 5-3:
PROBABILISTIC SLOPE STABILITY ANALYSES

In this Part of the chapter, probabilistic slope stability analyses are performed. Monte Carlo techniques are used to derive a probability distribution for the Factor of Safety, based on assumed probability distributions for the soil strength parameters. The simulated Factor of Safety distribution is compared to the theoretical Normal and Lognormal probability distributions. The probability of slope failure is obtained from the simulated distribution. This is compared to the results of the second moment reliability analyses performed in Part 5-2.

5-3.1. THE MONTE CARLO TECHNIQUE

The Monte Carlo Method and its application within a spreadsheet were described in Part 5-1. This involves generating random numbers from the uniform distribution between 0 and 1, and transforming these numbers to random variables from an assumed distribution. In this section, the soil strength parameters c' and ϕ' are assumed random variables that follow the Normal distribution with known parameters (mean values and standard deviations). The same procedure applies if other parameters are assumed uncertain. A similar procedure also applies if the strength parameters are assumed to follow different distributions. The case of uncorrelated c' and ϕ' is considered. Such is the case if, for example, c' and ϕ' are assumed to be independent.

To generate random values of c' and ϕ' from a Normal distribution with known parameters, if c' and ϕ' are assumed uncorrelated, random numbers are first generated using the '=RAND()' function. These are transformed to random numbers of a Normal distribution using the '=NORMINV()' function in Microsoft Excel. The '=NORMINV()' function is inserted into the c' and ϕ' cells, and every time the F9 key is pressed, new values of c' and ϕ' are generated based on the Normal distribution with the specified parameters, $m_{c'}$ and $\sigma_{c'}$ for c', and $m_{\phi'}$ and $\sigma_{\phi'}$ for ϕ'.

This procedure is used to generate random values of c' and ϕ'. The Factor of Safety is computed for each combination of c' and ϕ'. A random sample of the Factor of Safety is therefore obtained, and its probability distribution can be estimated for a large sample. The probability of failure can then be approximated from the generated distribution of Factor of Safety as;

$$P_F = \int_{-\infty}^{1} f_{F(c',\phi')} dF \qquad [5.38]$$

where $f_{F(c',\phi')}$ is the generated probability distribution of the Factor of Safety, F.

5-3.2. STATISTICAL ANALYSES OF GENERATED DISTRIBUTIONS OF FACTOR OF SAFETY

In this chapter and in Chapter 6, statistical analyses are performed on the distributions of Factor of Safety that are generated using Monte Carlo techniques. This is done to gain a better understanding of the shape of these distributions. Attempts are also made to fit theoretical probability distributions to the generated distributions of the Factor of Safety. In this section, we briefly describe some of these statistics, the techniques used to fit probability distributions, and their implementation within a spreadsheet. In particular, we develop a simple and elegant method in which the Method of Maximum Likelihood is used to estimate the distribution parameters of the theoretical distribution which is fitted to the generated distribution of the Factor of Safety.

5-3.2.1. DISTRIBUTION STATISTICS

As an initial attempt to better understand the shape of the distribution of the Factor of Safety, two statistical indicators are used that describe the deviation of the distribution from the Normal distribution.

5-3.2.1.1. COEFFICIENT OF SKEWNESS

The coefficient of Skewness characterizes the degree of asymmetry of a distribution around its mean. Positive skewness indicates a distribution with an asymmetric tail extending toward more positive values. Negative skewness indicates a distribution with

an asymmetric tail extending toward more negative values. The coefficient of skewness is computed as:

$$\gamma_1 = \frac{E\left[(X - E[X])^3\right]}{\sqrt{\left\{E\left[(X - E[X])^2\right]\right\}^3}} \qquad [5.39]$$

where E[] is expectation

γ_1 is computed using the function "=SKEW()" in Excel.

5-3.2.1.2. COEFFICIENT OF KURTOSIS

Kurtosis characterizes the relative peakedness or flatness of a distribution compared with the normal distribution. Positive kurtosis indicates a relatively peaked distribution. Negative kurtosis indicates a relatively flat distribution.
The coefficient of kurtosis is computed as:

$$\gamma_2 = \frac{E\left[(X - E[X])^4\right]}{\left\{E\left[\left(X - (E[X])^2\right)\right]\right\}^2} \qquad [5.40]$$

γ_2 is computed using the function "=KURT()" in Excel.

5-3.2.2. DISTRIBUTION FITTING

Theoretical probability distributions are fitted to the generated distributions of the Factor of Safety. Three distributions in particular are considered, namely the Normal, Lognormal and Gamma distributions.

5-3.2.2.a. NORMAL DISTRIBUTION

$$f_X(x) = \frac{1}{\sqrt{2\pi}\sigma} e^{-\left(\frac{x-m}{\sigma}\right)^2} \quad [5.41]$$

where:

m = E[X] is the mean or expected value of X

σ^2 = Var[X] is the variance of X

5-3.2.2.b. LOGNORMAL DISTRIBUTION

$$f_X(x) = \frac{1}{x\sqrt{2\pi}\sigma} e^{-\left(\frac{\ln x - m_{\ln x}}{\sigma_{\ln x}}\right)^2} \quad [5.42]$$

where:

$$m_{\ln X} = 2\ln(m) - \frac{1}{2}\ln(\sigma^2 + m^2) \quad [5.43]$$

$$\sigma^2_{\ln X} = -2\ln(m) + \ln(\sigma^2 + m^2) \quad [5.44]$$

with m and σ as defined previously.

5-3.2.2.c. GAMMA DISTRIBUTION

$$f_X(x) = \frac{\lambda^r}{\Gamma(r)} e^{-\lambda x} x^{r-1} \quad [5.45]$$

where:

$$m = E[X] = \frac{r}{\lambda} \quad [5.46]$$

$$\sigma^2 = Var[X] = \frac{r}{\lambda^2} \quad [5.47]$$

with m and σ as defined previously.

The three distributions considered are characterized by two parameters. In order to fit these distributions to the generated distributions of the Factor of Safety, the parameters of the distributions have to be estimated. Parameter estimation can be done using classical analyses, or using Bayesian techniques. In the classical analyses, the parameters of the distributions can be estimated using interval estimation, or point estimation. In this study, we consider point estimation using classical analyses.

The two most commonly used methods for point estimation of distribution parameters are the Method of Moments and the Method of Maximum Likelihood.

5-3.2.2.1. METHOD OF MOMENTS

The Method of Moments is a long established procedure for finding point estimators. In the Method of Moments, the sample moments are equated to those of the fitted distribution in order to estimate the parameters.

Therefore,

$$m = E[X] = \overline{X} = \frac{1}{n}\sum_{i=1}^{n} X_i \qquad [5.48]$$

$$\sigma^2 = Var[X] = \overline{\sigma}^2 = \frac{1}{n}\sum_{i=1}^{n} \left(X_i - \overline{X}\right)^2 \qquad [5.49]$$

where:

$\overline{X} = \frac{1}{n}\sum_{i=1}^{n} X_i$ is the sample average, that is computed using the "=AVERAGE()" function

$\overline{\sigma}^2 = \frac{1}{n}\sum_{i=1}^{n} \left(X_i - \overline{X}\right)^2$ is the sample variance, that is computed using the "=VAR()" function

Using these estimates for the expected value and variance of X, and the relations of the parameter distribution to these, one estimates the parameters using the Method of Moments.

NORMAL DISTRIBUTION

The distribution parameters are m = E[X] and σ^2 = Var[X], and the estimates in [5.48] and [5.49] are used directly.

LOGNORMAL DISTRIBUTION

The distribution parameters are $m_{\ln X}$ and $\sigma^2_{\ln X}$, and these are estimated as by substituting for m and σ^2 in Equations [5.48] and [5.49], into Equations [5.43] and [5.44].

GAMMA DISTRIBUTION

The distribution parameters are r and λ, and these are estimated as by substituting for m and σ^2 in Equations [5.48] and [5.49], into Equations [5.46] and [5.47].

5-3.2.2.2. METHOD OF MAXIMUM LIKELIHOOD

The Method of Maximum likelihood is preferred to the Method of Moments to estimate distribution parameters because it makes more use of information contained in a sample, and the estimators are asymptotically unbiased, with minimum mean squared error.

For a random variable X with known or assumed probability distribution, $f_X(x)$, and a sample $\{x_1,...,x_n\}$, the likelihood function of $\underline{\theta}$, where $\underline{\theta}$ represents the set of unknown parameters is defined as:

$$\ell(\underline{\theta}) = \prod_{i=1}^{n} f_X(x_i \mid \underline{\theta}) \qquad [5.50]$$

The Maximum Likelihood estimates of the distribution parameters are those that maximize the likelihood function in Equation [5.50]. For many distributions, it is convenient to express a log-likelihood function $L(\underline{\theta})$, as:

$$L(\underline{\theta}) = \ln\{\ell(\underline{\theta})\} \qquad [5.51]$$

$$L(\underline{\theta}) = \sum_{i=1}^{n} f_X(x_i \mid \underline{\theta}) \qquad [5.52]$$

Maximizing log-likelihood to obtain the Maximum Likelihood estimators to distributions parameters is the same as maximizing likelihood since the logarithm function is monotonic.

Maximizing likelihood (or log-likelihood) can be done by imposing stationary conditions on the likelihood (or log-likelihood) function and solving for the parameters $\underline{\theta}$. This, however, is not always possible since no analytical form of the partial derivatives exists e.g. for the Gamma distribution, and one has to resort to numerical methods.

SPREADSHEET IMPLEMENTATION OF THE METHOD OF MAXIMUM LIKELIHOOD

Numerical methods may be required to maximize the likelihood (or log-likelihood) function. One method for doing this is to write a computer code, such as in VBA in Excel, for this purpose. This, however, may be time consuming both to write and implement. This is particularly true is high accuracy is desired. A simpler and more elegant approach is to set up the problem as an optimization problem, and make use of a spreadsheet's optimization tool, such as Solver in Excel. The method is described in the following steps.

Step 1. Arrange the sample values of the variable X in a column, and compute the sample mean and variance. This is done using the "=AVERAGE()" and "=VAR()" functions in Excel.

Step 2. Compute the Method of Moments estimators for the parameters of the distribution using the sample mean and variance in Step 1, as described in Section 5-3.2.2.1.

Step 3. Compute the likelihood (Equation [5.50]) and log-likelihood (Equation [5.51]) functions at each sample point x_i. The probability density at each sample point x_i is computed using the following functions in Excel: "=NORMDIST()" for the Normal distribution, "=LOGNORMDIST()" for the Lognormal distribution and "=GAMMADIST()" for the Gamma distribution.

Step 4. Compute the log-likelihood function of the sample by summing the log-likelihood at each sample point x_i. Note that in the majority of spreadsheets one has to work with the log-likelihood function instead of the likelihood function, particularly when the number of sample points is very large. This is because the log-likelihood function involves a summation of the log-likelihoods at each of the sample points (as opposed to a product for the likelihood function). The spreadsheet is capable is dealing with sums of large numbers, but there may be difficulties in obtaining the product as this becomes very large for large samples.

Step 5. Specify initial estimates of the distribution parameters. Good initial estimates to these parameters are the Method of Moment estimators, which are determined from the sample average and variance, as described in Step 2.

Step 6. Set up the problem as an optimization problem in Excel. This is done using the optimization tool Solver. The objective function is to maximize the log-likelihood function of the sample by varying the parameter estimators.

Step 7. Invoke Solver to maximize log-likelihood and obtain the Method of Maximum Likelihood estimators to the distribution parameters. Convergence criteria can be specified to ensure the desired accuracy.

By performing Steps 1 to 7, the Method of Maximum Likelihood estimators are obtained very rapidly. The procedure is slightly slower for larger samples, but remains much quicker than running other numerical methods based on varying the values of the estimators to determine those that maximize log-likelihood.

5-3.2.3. STANDARD ERROR TERM

As a simple goodness of fit test of the fitted distribution to the generated distribution of Factor of Safety, we compute an error term as:

$$e = \sqrt{\sum_i (x_i - x')^2} \qquad [5.53]$$

where:

- e error term
- x_i the relative frequency of the generated distribution
- x' the theoretical probability density of the distribution

One can use better measures of goodness of fit, such as the Kolmogorov-Smirnov test for Normality, and/or fit different distributions to the generated distribution, but that is not the intention in this study. The relative values of e are used as simple quantitative measures to compare the fit of the generated distribution to the Normal, Lognormal and Gamma distributions.

5-3.3. NUMERICAL EXAMPLES

We illustrate the Monte Carlo procedure using the slope shown in Figure 5.49.

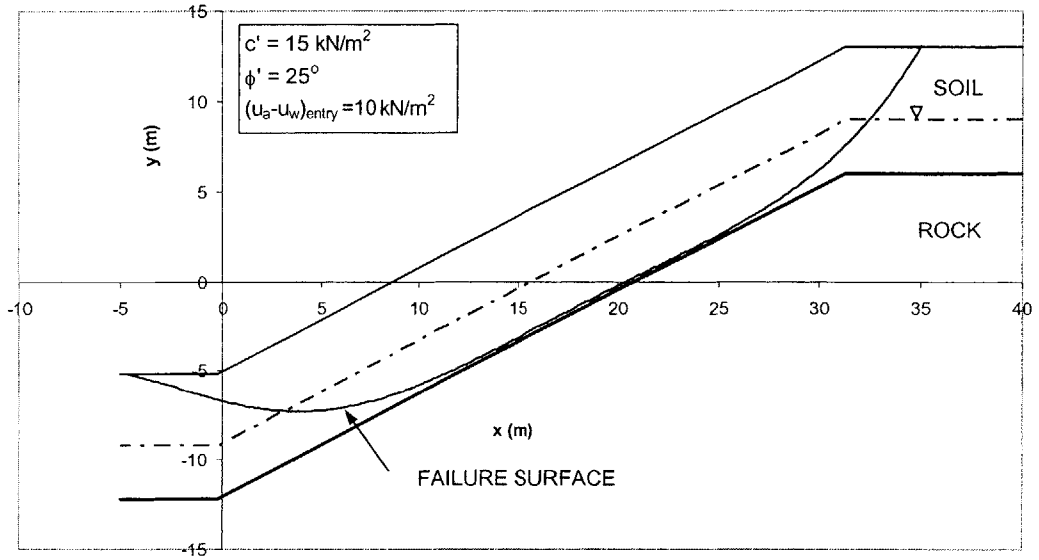

Figure 5.49. Slope Geometry and Strength Parameters

We assume that the saturated strength parameters are uncertain and uncorrelated, with parameters:

$$c' \sim (m_{c'} = 15 kN/m^2,\ \sigma_{c'} = 5 kN/m^2);\ \phi' \sim (m_{\phi'} = 25^o,\ \sigma_{\phi'} = 5^o);\ \underline{\Gamma} = \begin{bmatrix} 1 & 0 \\ 0 & 1 \end{bmatrix}$$

This slope was analyzed in a second moment reliability context in Example 2 of Section 5-2.2.2.3, and a reliability index was computed to be $\beta = 0.72$ on the critical reliability based failure surface. The probability of slope failure was computed from the reliability index by assuming a distribution for the Factor of Safety. When the Factor of Safety was assumed to be Normally distributed, $P_F = \Phi(-\beta)$, and in this example, $P_F = \Phi(-\beta) = 0.234$.

We analyze the reliability of the slope using Monte Carlo techniques. We assume that c' and ϕ' follow a Normal distribution, and by doing so the probability density functions of each parameter becomes known, since the parameters of the distribution are known

(specified). A random sample is generated for c' and ϕ', and from this, a random sample of the Factor of Safety can be generated on the failure surface.

Figure 5.50 shows the probability density function of the Factor of Safety that is obtained from the Monte Carlo analyses, and Figure 5.51 shows the cumulative distribution function.

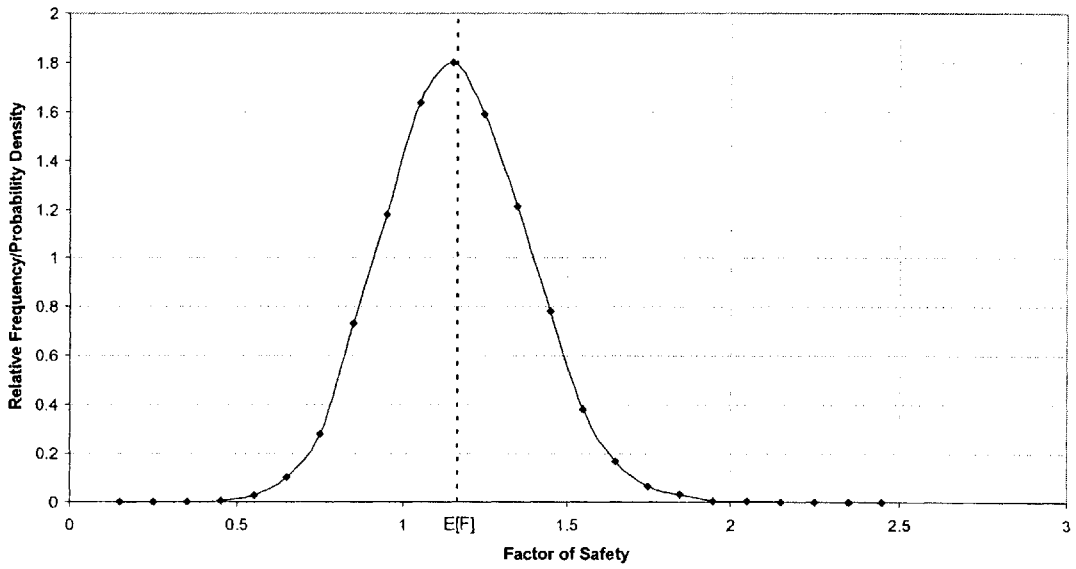

Figure 5.50. Simulated Probability Density Function of Factor of Safety for Normally Distributed and Uncorrelated c' and ϕ'

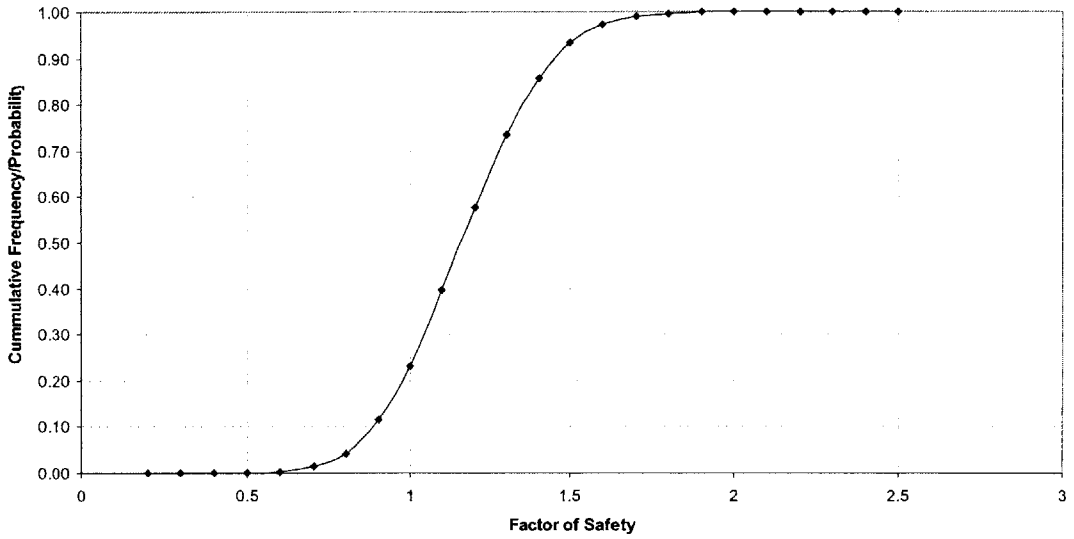

Figure 5.51. Simulated Probability Distribution Function of Factor of Safety for Normally Distributed and Uncorrelated c' and ϕ'

To gain a better understanding of the distribution of Factor of Safety, we compute the statistics described in Section 5-3.2. These are shown in Table 5.3.

	Simulated Distribution
Expected Value, E[F]	1.163
Standard Deviation, σ[F]	0.220
Skewness	0.1734
Kurtosis	0.1384
Probability of Failure	0.230

Table 5.3. Summary Statistics of Simulated Distribution

Table 5.3 shows that the value coefficient of Skewness of the distribution is small indicating a symmetric distribution about the expected value. Table 5.3 also shows that the value of the coefficient of Kurtosis is small indicating no significant peakedness of the distribution when compared to the Normal distribution.

We use the Method of Maximum likelihood in Section 3-2.2.2. to estimate the parameters of the Normal, Lognormal and Gamma distributions that best fit the generated data. These are shown in Table 5.4.

Fitted Distribution	Maximum Likelihood Parameters		Error Term, e	Probability of Failure
	E[F]/ E[ln(F)]/ r	σ[F]/σ[ln(F)]/ λ		
Normal	1.163	0.220	0.158	0.229
Lognormal	0.133	0.196	0.350	0.249
Gamma	27.865	23.950	0.195	0.241

Table 5.4. Fitted Distributions to Simulated Distribution

Table 5.4 shows that the error term for the Normal distribution is the smallest amongst those distributions considered, indicating that Normal distribution fits the distribution of the Factor of Safety in Figure 5.50 better than the Lognormal and Gamma distributions.

We compare the simulated distribution with the fitted Normal distribution for probability density in Figure 5.52, and cumulative distribution in Figure 5.53.

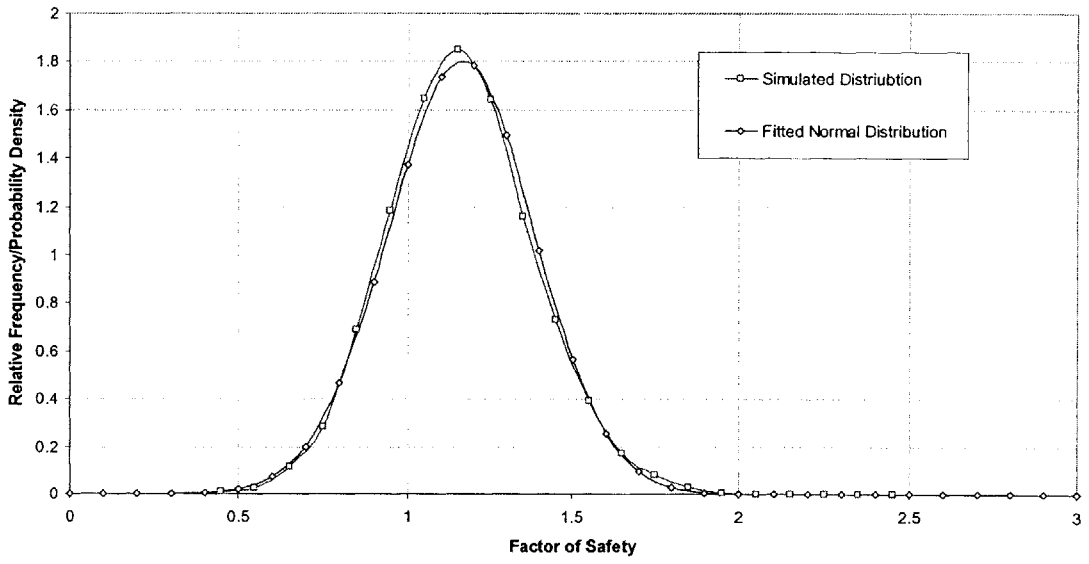

Figure 5.52. Comparison of Simulated Probability Density of Factor of Safety with Fitted Normal Distribution for Normally Distributed and Uncorrelated c' and ϕ'

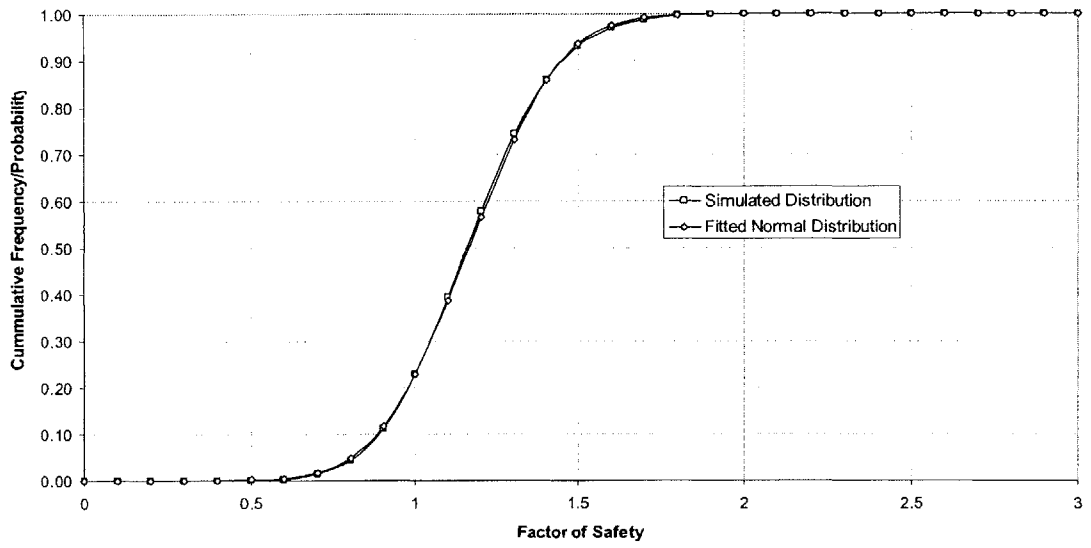

Figure 5.53. Comparison of Simulated Cumulative Distribution of Factor of Safety with Fitted Normal Distribution for Normally Distributed and Uncorrelated c' and ϕ'

The distribution of the Factor of Safety can be approximated by the Normal distribution when c' and ϕ' follow a Normal distribution, as shown in Figures 5.52 and 5.53. The actual simulated distribution, however, is not exactly Normal, but is well approximated by the Normal distribution. No attempt has been made to fit an exact distribution to the Factor of Safety, or test, rigorously, the goodness of fit to the Normal.

The simulated cumulative distribution function of F is used to approximate the probability of slope failure, and in this example, $P_F = 0.233$.

The probability of failure computed from reliability analyses ($P_F = \Phi(-\beta) = 0.234$) is almost the same as that computed from Monte Carlo analyses ($P_F = 0.233$). This is because the distribution of the Factor of Safety is well approximated by the Normal distribution (see Figure 5.52). Since this is the case, the assumption of Normality in computing $P_F = \Phi(-\beta)$ is valid.

In this example, Example 2 Section 5-2.2.2.3 was analyzed. There is no particular reason for this, and the results would have been the same if Example 1 was analyzed instead. Tables 5.5 and 5.6 summarize the statistics of the distribution, and the Maximum Likelihood parameters of the fitted distributions.

	Simulated Distribution
Expected Value, E[F]	1.178
Standard Deviation, σ[F]	0.134
Skewness	0.0613
Kurtosis	0.0042
Probability of Failure	0.091

Table 5.5. Summary Statistics of Simulated Distribution

Fitted Distribution	Maximum Likelihood Parameters		Error Term, e	Probability of Failure
	E[F]/ E[ln(F)]/ r	σ[F]/σ [ln(F)]/ λ		
Normal	1.178	0.134	0.140	0.093
Lognormal	0.157	0.116	0.330	0.087
Gamma	76.926	65.330	0.239	0.087

Table 5.6. Fitted Distributions to Simulated Distribution

Table 5.6 again shows that the simulated distribution is well approximated by the Normal distribution, and this is shown in Figure 5.54.

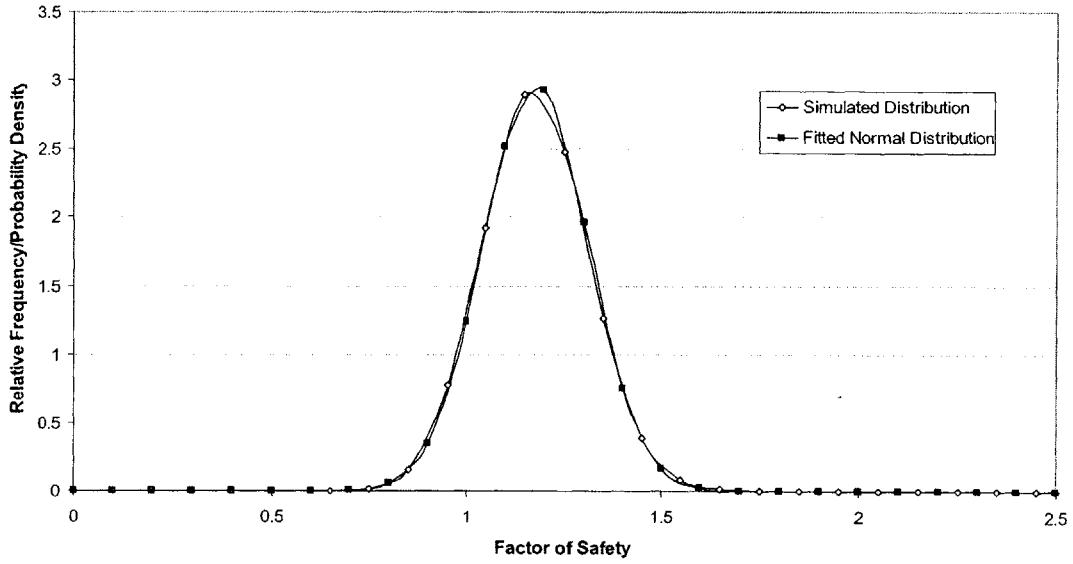

Figure 5.54. Comparison of Simulated Probability Density of Factor of Safety with Fitted Normal Distribution for Normally Distributed and Uncorrelated c' and ϕ'

The probability of failure is computed to be $P_F = 0.091$, which compares well with that obtained from second moment analyses, $P_F = \Phi(-\beta) = 0.095$.

5-3.4. CONCLUSIONS

In this section, the Monte Carlo Method was used to asses slope reliability. This was done using spreadsheet techniques. A numerical example illustrated the method. The results were compared to those obtained by second moment reliability analyses based on the Hasofer and Lind (1974) reliability index, and are in good agreement. This is because the probability distribution of the Factor of Safety for Normally distributed strength parameters, though not exactly Normal, is well approximated by the Normal distribution.

PART 5-4:
RELIABILITY BASED LANDSLIDE HAZARDS ASSESSMENT

In this part of the chapter, the reliability of slopes during and after rainfall events is assessed in a second moment context, producing the second moment assessment of landslide hazards. This combines the uncertainty analyses performed on the infiltration model in Part 5-1, with the slope reliability analyses performed in Part 5-2. The results are in the form of the variation of the Hasofer and Lind (1974) reliability index with time during and after a rainfall event. From this, and an assumed distribution of the Factor of Safety, the variation of the probability of slope failure with time can be approximated.

Uncertainty in assessing landslide hazards arises from uncertainty in the rainfall characteristics, soil hydraulic parameters, as well as strength parameters, and slope geometry. These were discussed in more detail in Chapter 4. In this part of Chapter 5, the major contributors to uncertainty are assumed to be the soil hydraulic conductivity, and soil strength parameters. Other parameters can be included in the analyses, in a very similar way as to what is done in this part.

The Factor of Safety in a slope is not a direct function of the hydraulic conductivity of the soil, but is a function of the pore pressures that are generated during rain. Therefore, assessing the effects of uncertainties in hydraulic conductivity on uncertainties in computed Factors of Safety in a second moment reliability context requires an estimation of the mean values and standard deviations of the generated pore pressures.

One way to do this is to deterministically model flow, and use the computed pressures as estimates to the mean values. The standard deviations (variances) of the pressures need to be specified by assuming (or specifying values of) coefficients of variation for the pore pressures. This has to be done judgmentally, and typical coefficients of variation can be obtained from published literature or specified subjectively. These can be in the form of specified numbers that are assumed constant with time, or time dependent functions.

Alternatively, as an initial step, uncertainties in hydraulic conductivity can be propagated through the flow model into uncertainties in pore pressures using the Monte Carlo method (see Part 5-1). The second moment characteristics (mean values and standard deviations) of the pore pressure profiles can be estimated based on the results. These second moment characteristics can then be used in the slope reliability analyses.

If we assume that the soil strength parameters are uncertain, the vector of uncertain quantities that the Factor of Safety is a function of is:

$$\underline{X} = \begin{bmatrix} c' \\ \phi' \\ u_1 \\ . \\ . \\ . \\ u_n \end{bmatrix} \sim (E[\underline{X}], \underline{\sum}) \qquad [5.54]$$

where:

$u_1,...,u_n$ are the mean pore pressures acting on the base of slices 1, ..., n.

$E[\underline{X}]$ is the mean value vector of $\underline{X}$

$\underline{\sum}$ is the covariance matrix of $\underline{X}$

$E[\underline{X}]$ contains the mean values of the pore pressures $u_1,...,u_n$. These are obtained from deterministic or Monte Carlo analyses of the flow model as explained previously. Similarly, $\underline{\sum}$ contains the standard deviations (variances) of the pore pressures $u_1,...,u_n$, which are set judgmentally, or obtained from Monte Carlo analyses.

5-4.1. PROCEDURE

Since the Factor of Safety in [5.39] is a function of $\underline{X}$, second moment reliability analyses can be performed as described in Figure 5.55.

Step 1. Perform Monte Carlo analyses on the flow model, and obtain the second moments of the pore pressure profiles with time. This was described in Part 5-1. The results are in the form of variation of mean values and standard deviations of the pore pressures with depth below ground surface, and with time (see Part 5-1).

Step 2. Divide the total time t_r desired to perform the analyses into discrete time steps t_i. The total time is the duration of rain plus some specified time after cessation of rain.

Step 3. Set up a spreadsheet as was described in Part 5-2, and specify an initial trail failure surface.

Step 4. Specify the mean value vector, $E[\underline{X}]$, and covariance matrix, $\underline{\Sigma}$, of the vector $\underline{X}$, where $\underline{X}$ is the vector of uncertain quantities acting along the base of a slice of the failure surface.

Some parameters, such as the soil strength parameters, are assumed to have second moments (mean values and variances) that are depth and time independent. Their mean values and variances are, therefore, constant and their respective numerical values are specified as numbers in $E[\underline{X}]$ and $\underline{\Sigma}$.

The mean values and standard deviations of the pore pressures on the other hand are functions of both depth below the ground surface, and time. So, formulae are inserted into the cells containing these values. These formulae instruct the spreadsheet to extract the mean values and standard deviations of the pore pressures at the base of each slice of the failure surface from the results of the Monte Carlo analyses at any time step t_i. The '=LOOKUP()' function in Excel is used for this.

Step 5. Compute β from $\beta = \sqrt{\left[\frac{X_i - m_i}{\sigma_i}\right]^T \underline{\Gamma}^{-1} \left[\frac{X_i - m_i}{\sigma_i}\right]}$, where $\underline{\Gamma}^{-1}$ is the inverse of the correlation matrix of $\underline{X}$.

Step 6. Solver in Excel is invoked to minimize β, by changing the 'X values', and allowing the coordinates of the initially specified to be varied. By doing so, the Hasofer and Lind (1974) reliability index is computed at time t_i.

Step 7. Repeat Steps 4 to 6 for all times t_i, $t_i = 0, \ldots, t_r$.

Figure 5.55. Spreadsheet Procedure for Slope Reliability Analyses During Rainfall

Note that the procedure in Figure 5.55 assumes that the second moments of the pore pressures are obtained from Monte Carlo analyses. This is shown in Step 4. If, on the other hand, one assumes that the second moments are time independent, then one simply specifies the values in $E[\underline{X}]$ and $\underline{\sum}$, and no formulae are required.

At time t_i, the spreadsheet varies the coordinates of the failure surface in search for the critical surface (see Step 6 in Figure 5.55). As this is done, the mean values and standard deviations of the pore pressures change since they are a function of depth below the ground surface. These are automatically extracted by the spreadsheet from the Monte Carlo results at t_i during each iteration of failure surface using the functions in Step 4.

The procedure described in Figure 5.55 assumes that the pore pressures at different depths are uncorrelated. Correlation can be included into the analyses by specifying the correlation coefficients between the $u_1,...,u_n$ in the covariance matrix $\underline{\sum}$. This again can be either specified judgmentally, or estimated from the results of the Monte Carlo analyses. In the latter case, the correlation coefficients between $u_1,...,u_n$ can be estimated using the '=CORREL()' function in Excel at each time step. This function is inserted into the off-diagonal terms (covariances) of the covariances matrix $\underline{\sum}$. More generally, one can attempt to estimate a correlation function between $u_1,...,u_n$. This function would be a function of the lag in depths between any two variables u_i, and u_j, i.e. $|(i-j)|$, and time.

Initially, at time t = 0 hours, if one assumes hydrostatic conditions, and the location of the water table is known, then the subsurface pore pressures can be defined. This is to say that there is perfect correlation between the pore pressures $u_1,...,u_n$, since $u = 0$ at the water table by definition.

When it rains, and rainwater infiltrates into the slope, the pore pressures above the maximum infiltration depth are altered. While there still may be a certain degree of correlation between the pore pressures above the infiltration depth, correlation is reduced. Correlation between the pore pressures below the water table is, however, unaffected by rain, and remains high.

While the variables $u_1,...,u_n$ are probably correlated, particularly at depths greater than the maximum infiltration depth since hydrostatic conditions prevail, $u_1,...,u_n$ are assumed uncorrelated in this study. The justification for this assumption is in the fact that the main contributors to the uncertainties in the Factor of Safety will be the strength parameters (variance and covariance terms) followed by the uncertainties in pressures (variance terms). Hence, the covariance terms between pressures will have smaller values, and are less significant than the variance and covariances terms of the strength parameters and of the variance terms of the pressures.

The procedure in Figure 5.55 can be extended to include strength parameters that are either functions of depth or of time or both. In such cases, formulae are entered into the strength parameter cells that instruct the spreadsheet to compute the mean values and standard deviations of the parameters at each depth, and time step. Correlation can also be included in a similar manner. This is similar to what is done in Step 4 of Figure 5.55 for the pore pressures.

The procedure is automated using a VBA code in Excel. The results are in the form of a plot of the Hasofer and Lind (1974) reliability index with time during and after rain. From an assumed distribution of Factor of Safety, this can be transformed into a plot of probability of failure (reliability) with time.

The procedure is best illustrated by examples. For this, we consider two examples where in the first, the rainfall intensity is less than the saturated conductivity of the soil, and in the second, the intensity is greater than the conductivity.

5-4.2. NUMERICAL EXAMPLES

EXAMPLE 1: LANDSLIDE HAZARDS WITH RAINFALL INTENSITY LESS THAN SATURATED CONDUCTIVITY

Consider the slope shown in Figure 5.56.

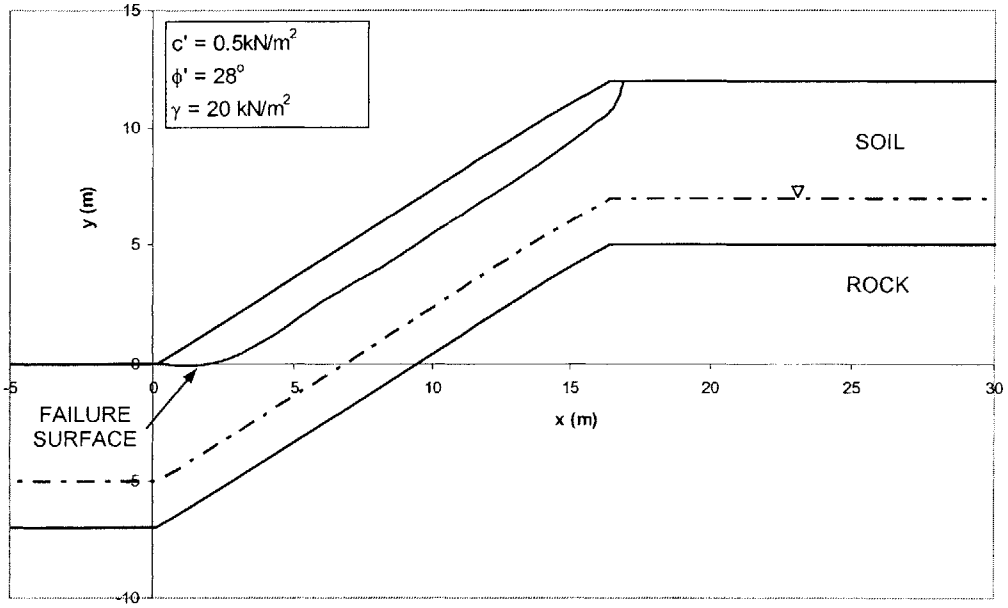

Figure 5.56. Slope Geometric and Strength Parameters

The slope geometric and soil strength parameters are shown in Figure 5.56. The soil hydraulic parameters are taken to be:

Saturated moisture content of soil $\theta_s = 0.47$

Residual moisture content of soil $\theta_r = 0.11$ (see Chapter 2)

Saturated conductivity $K_s = 250\text{cm/day} = 2.89 \times 10^{-5}\text{m/s}$

Specific storage coefficient $S_s = 0.005$ (see Chapter 2)

The van Genuchten (1980) Models are used to describe the soil characteristic curves, with parameters $n = 3$ and $\delta = 0.007$ (see Chapter 2). The soil characteristic curves are as shown in Figures 5.57 and 5.58.

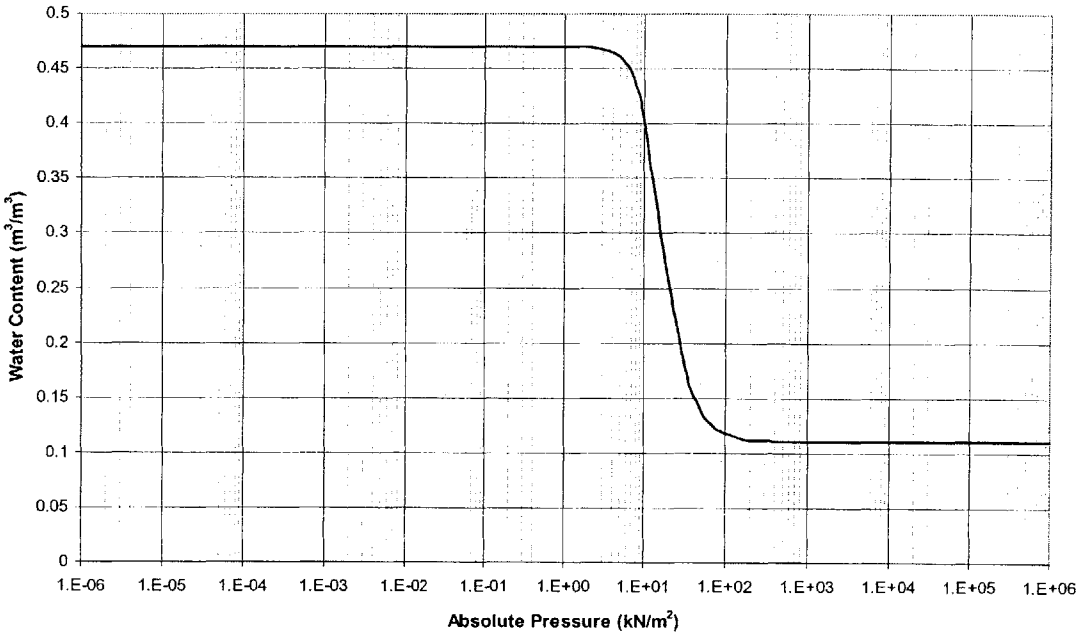

Figure 5.57. Moisture Retention Characteristic Curve

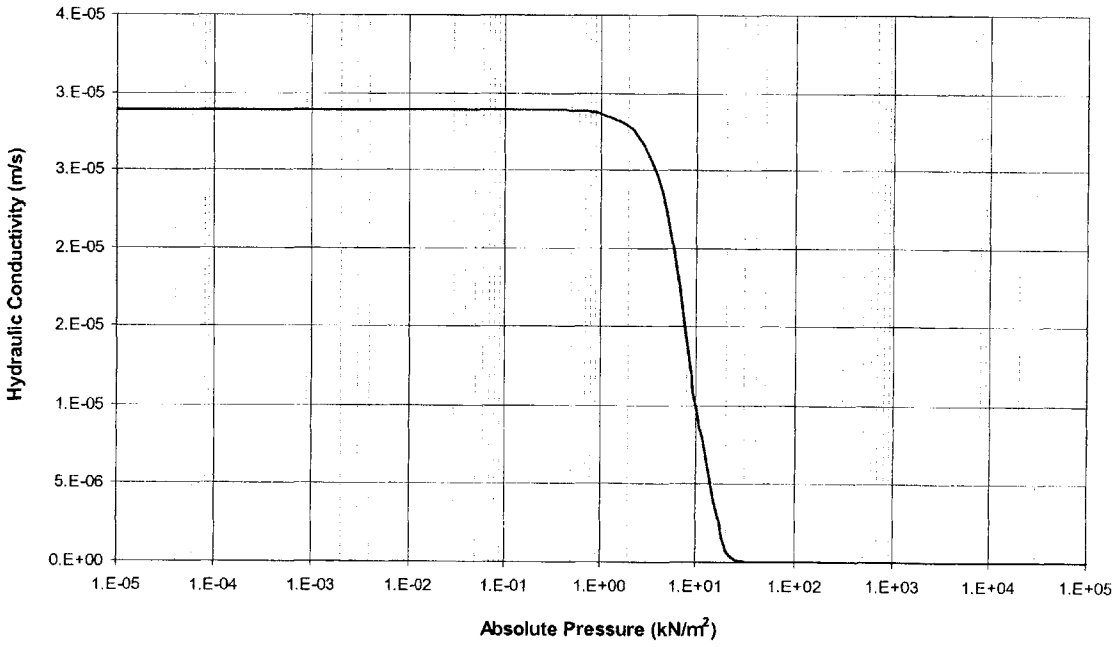

Figure 5.58. Hydraulic Conductivity Characteristic Curve

The moisture content in the soil is initially assumed to be constant $\theta_i = 0.25$.

We assume a rainfall event with constant intensity, $I = 75mm/hr$ takes place for duration of 8 hours. When all parameters are deterministic, Chapter 2 described a procedure whereby the variation of Factor of Safety in slope with time can be computed as a function of time. The results of the deterministic analyses are shown in Figure 5.59.

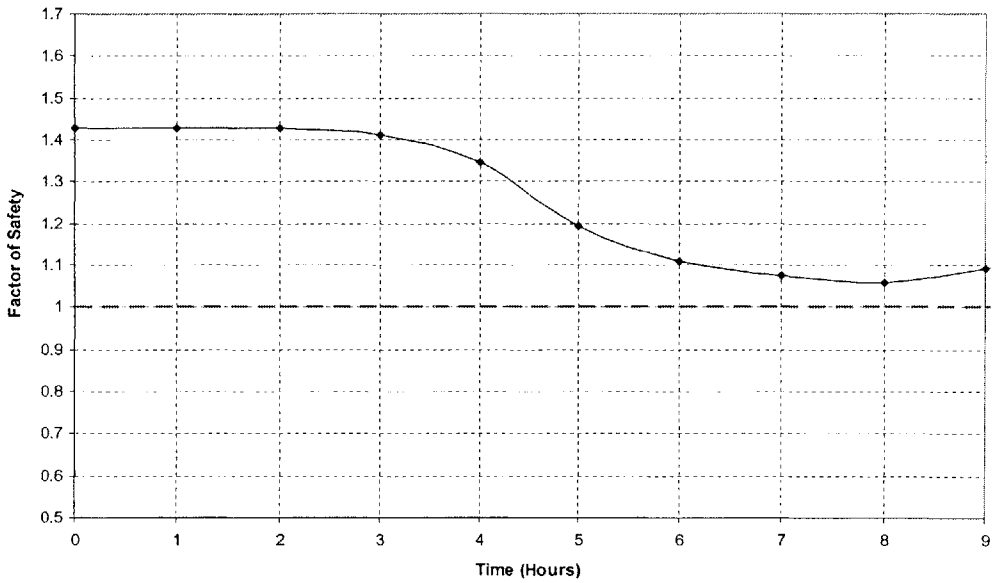

Figure 5.59. Variation of Factor of Safety with Time from Deterministic Analyses

Figure 5.59 shows that the Factor of Safety decreases with time as rainwater infiltrates into the slope. The minimum Factor of Safety occurs at time 8 hours, which corresponds to the end of rain. Since the Factor of Safety is greater than 1 at all times, the slope remains stable. The Factor of Safety increases after this time as pressure redistribution takes place.

Figure 5.56 shows the critical deterministic failure surface at time t = 8 hours. This is the surface on which the Factor of Safety is minimum.

We now assume that the soil hydraulic conductivity is uncertain, and follows a Lognormal distribution as $K_S \sim LN(\ m_{K_S} = 250cm/day, \sigma^2_{K_S} = (125cm/day)^2)$. The Monte Carlo techniques described in Part 5-1 are used to compute the mean values and

standard deviations of the pore pressure profiles with time. These are shown in Figures 5.60 and 5.61.

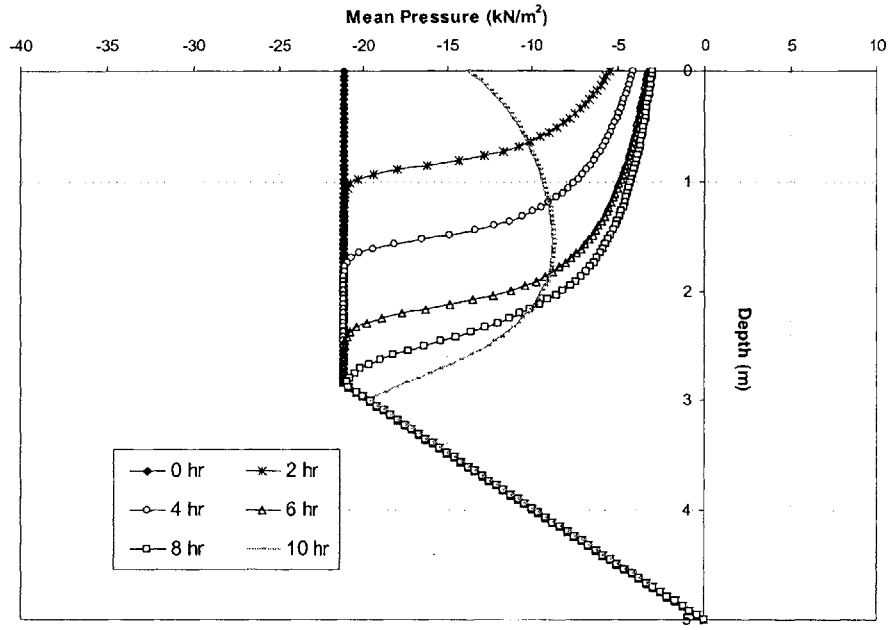

Figure 5.60. Variation of Mean Values of Pore Pressure Profiles with Time

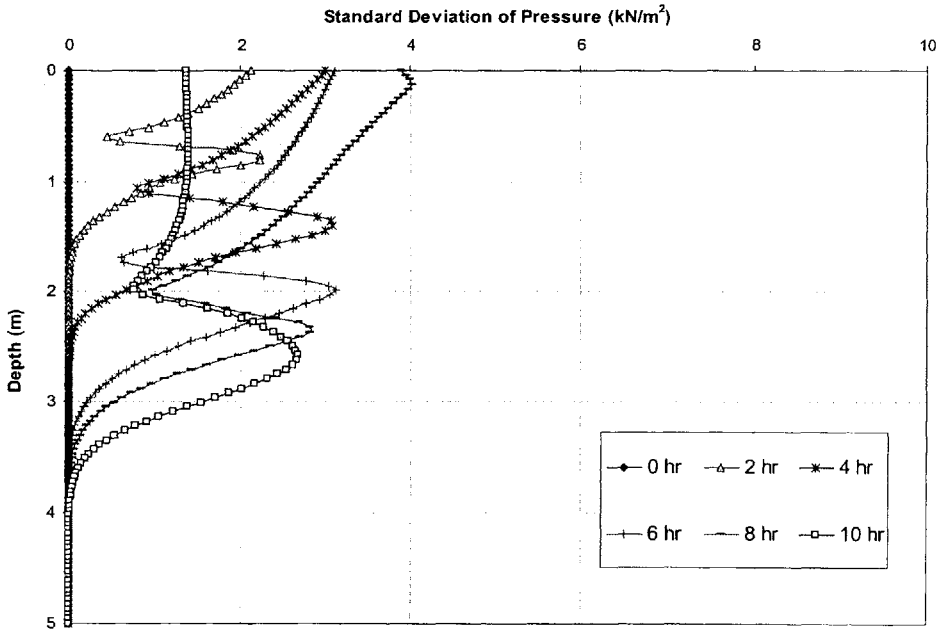

Figure 5.61. Variation of Standard Deviation of Pore Pressure Profiles with Time

The results of the Monte Carlo analyses in Figures 5.60 and 5.61 are used to compute the mean values and standard deviations of the pore pressures acting on a failure

surface at any time t_i. These are used in Step 4 in the procedure for reliability computations described in Figure 5.55. So, for example, consider time t = 4 hours. If the depth to the base of slice j from the ground surface is 1.5 m, then the mean value of u_j in vector $E[\underline{X}]$ would be about $E[u_j] = -12 kN/m^2$ (see Figure 5.60 at t=4 hr), and the standard deviation of u_j in vector $\underline{\sum}$ would be about $\sigma[u_j] = 3 kN/m^2$ (see Figure 5.61 at t=4 hr). These are automatically obtained using the '=LOOKUP()' function in Excel. The expected values and standard deviations of the pore pressures acting on the bases of other slices are obtained in a similar way.

We assume that the soil strength parameters are uncertain, with parameters:

$$c' \sim (m_{c'} = 0.5 kN/m^2,\ \sigma_{c'} = 0.125 kN/m^2);\ \phi' \sim (m_{\phi'} = 28^o,\ \sigma_{\phi'} = 7^o);\ \underline{\Gamma} = \begin{bmatrix} 1 & 0 \\ 0 & 1 \end{bmatrix}$$

Having specified these parameters, we now have set up the problem for second reliability analyses, since $E[\underline{X}]$ and $\underline{\sum}$ are entirely specified. β is computed as in Step 5 of Figure 5.55.

β is then minimized in Step 6, and during each iteration, the appropriate values of $E[u_j]$, and $\sigma[u_j]$ are used. This results in the Hasofer and Lind (1974) reliability index at time t_i.

The critical values of the parameters in $\underline{X}$, ($\underline{X}^*$) are obtained. These correspond to the most probable failure point (see Part 5-2) if $\underline{X}$ has Joint Normal distribution. The problem has dimensions of $(2+n)$, where n is the number of slices, and the 2 comes from the 2 soil strength parameters. The Hasofer and Lind (1974) reliability index corresponds to the hyper ellipsoid in $(2+n)$ space that is tangential to the failure surface, defined by $F(\underline{X}) = 1$ in $(2+n)$ space.

The process is then repeated for all times i.

Figure 5.62 shows the variation of the Hasofer and Lind (1974) reliability index with time.

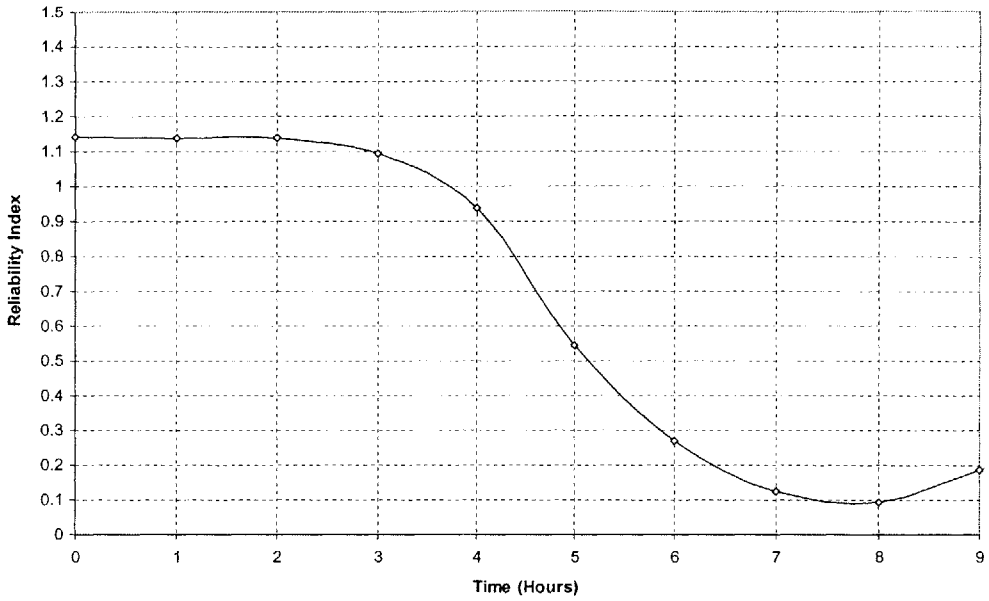

Figure 5.62. Hasofer and Lind (1974) Reliability Index with Time

The shape of variation of reliability index with time in Figure 5.62, follows that of the Factor of Safety with time in Figure 5.59. That is to say that the reduction in Factor of Safety with time is reflected in the reliability index, while incorporating uncertainty in parameters. The reliability index decreases with time during rain, and with pressure build up. As rain stops at t=8 hours, pressure redistribution takes place causing an increase in reliability index. The critical reliability based failure surface at time t = 8 hours is shown in Figure 5.63.

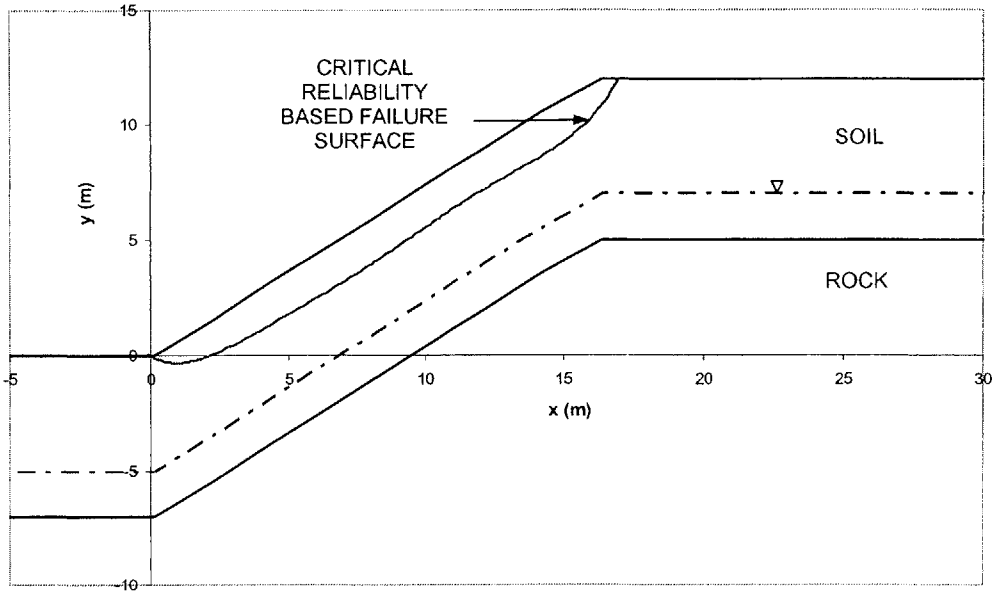

Figure 5.63. Critical Reliability Based Failure Surface at t = 8 hours

This is the surface along which failure is most probable, while taking into account the uncertainties in the vector $\underline{X}$.

If we assume that the Factor of Safety is Normally distributed, then a plot of probability of slope failure can be computed as shown in Figure 5.64.

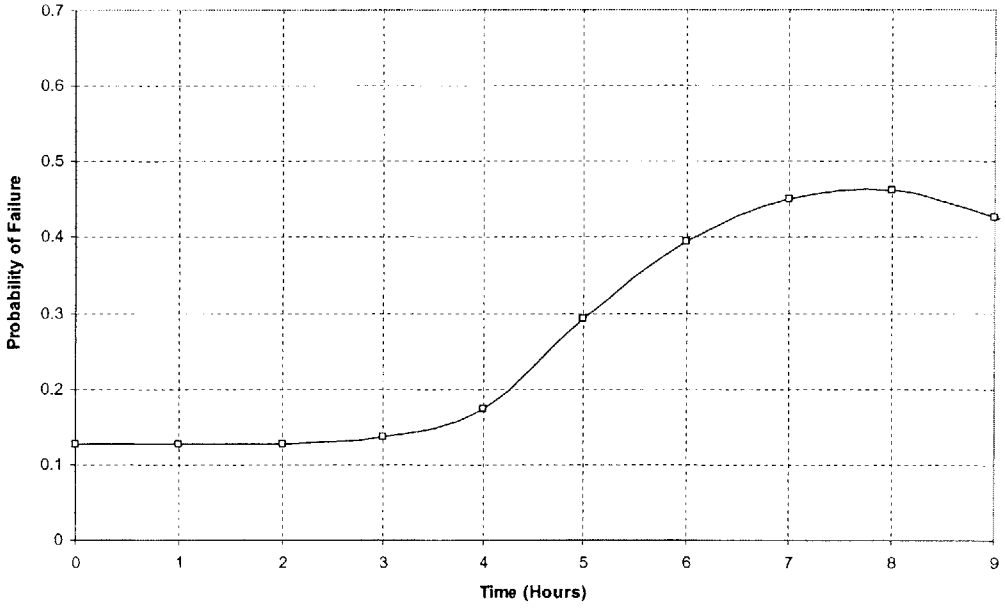

Figure 5.64. Probability of Slope Failure with Time

EXAMPLE 2: LANDSLIDE HAZARDS WITH RAINFALL INTENSITY GREATER THAN SATURATED CONDUCTIVITY

Consider the slope shown in Figure 5.65.

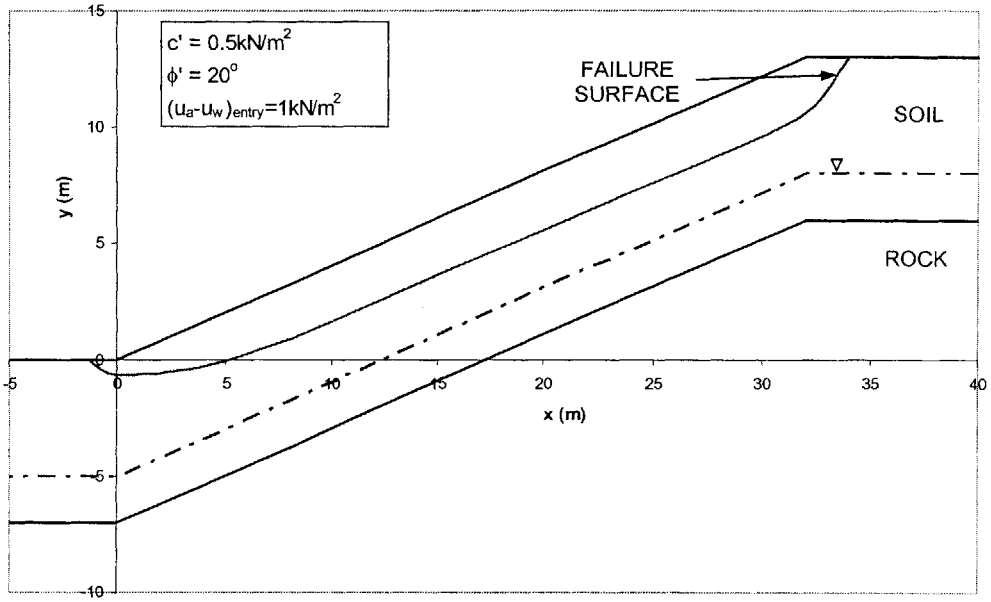

Figure 5.65. Slope Properties and Failure Surface

The slope geometric and soil strength parameters are shown in Figure 5.65, and the hydraulic parameters are:

Saturated moisture content of soil $\theta_s = 0.47$

Residual moisture content of soil $\theta_r = 0.11$

Saturated conductivity $K_s = 200\text{cm/day} = 2.31\times10^{-5}\text{m/s}$

Specific storage coefficient $S_s = 0.0025$

The van Genuchten (1980) model is used to describe the unsaturated soil curves with the parameters $n = 1.24$ and $\delta = 0.011$. The resulting curves are shown in Figures 5.66 and 5.67.

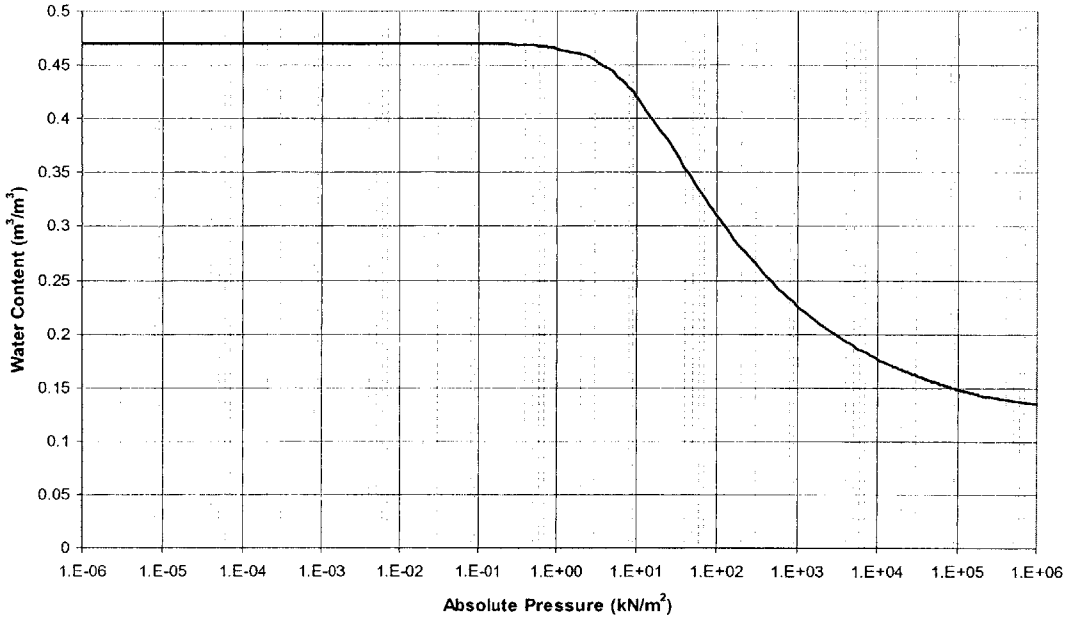

Figure 5.66. Moisture Retention Characteristic Curve

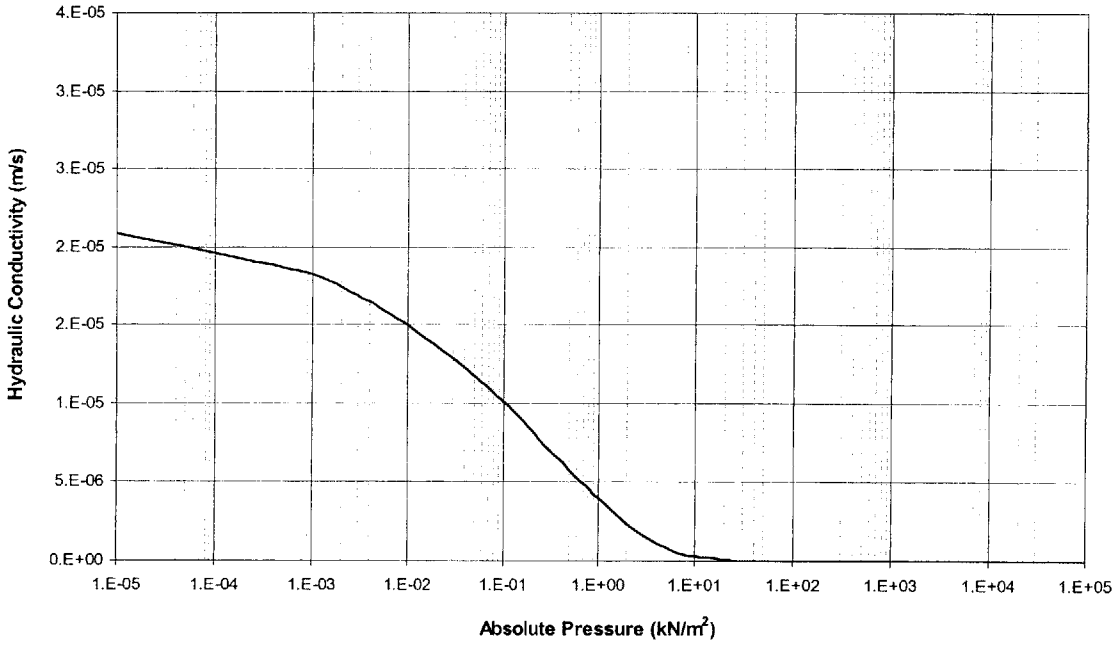

Figure 5.67. Hydraulic Conductivity Characteristic Curve

The soil is initially assumed to be at constant moisture content $\theta_i = 0.40$. A rainfall event of constant intensity $I = 375cm/day = 155mm/hr$ takes place for duration of 8 hours.

We assume that the soil hydraulic conductivity is Lognormally distributed as,

$K_s \sim LN(\ m_{K_s} = 200cm/day, \sigma^2_{K_s} = (100cm/day)^2)$.

The mean values and standard deviations of the pore pressure profiles with time are shown in Figures 5.68 and 5.69.

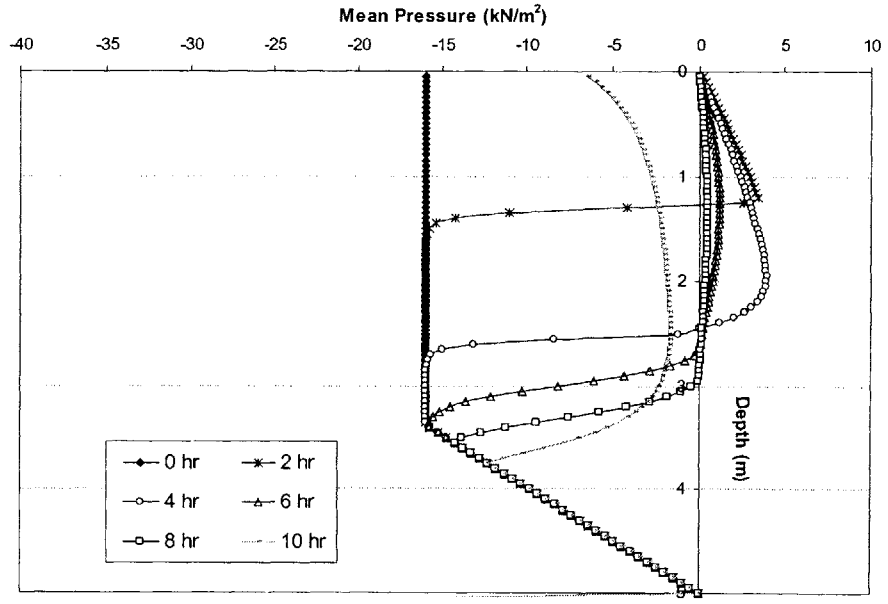

Figure 5.68. Variation of Mean Values of Pore Pressure Profiles with Time

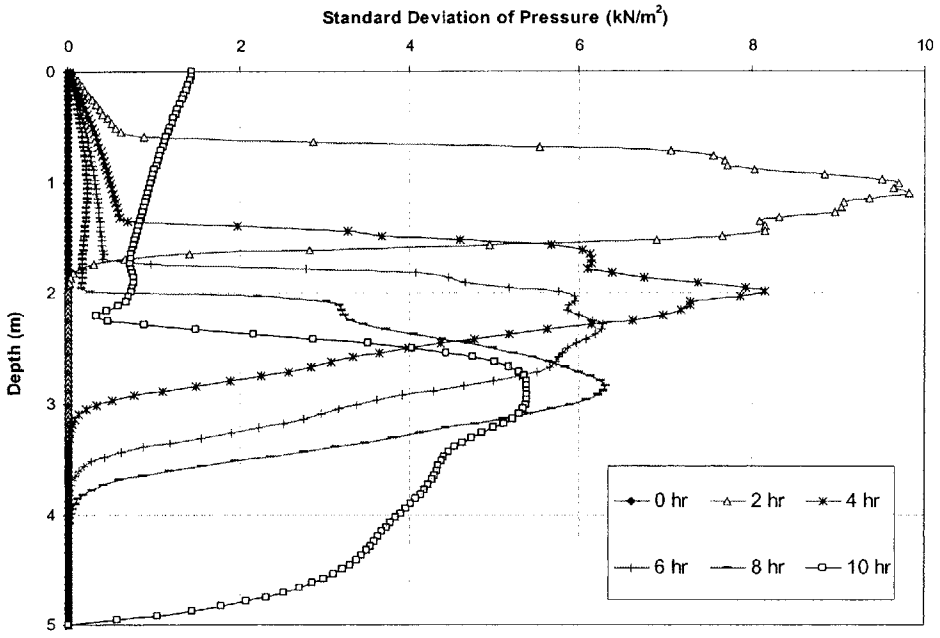

Figure 5.69. Variation of Standard Deviation of Pore Pressure Profiles with Time

We assume that the soil strength parameters are uncertain, with parameters; $c' \sim (m_{c'} = 0.5 kN/m^2,\ \sigma_{c'} = 0.017 kN/m^2)$, $\phi' \sim (m_{\phi'} = 20^o,\ \sigma_{\phi'} = 6.67^o)$, and c' and ϕ' are assumed uncorrelated. The variation of the reliability index with time is shown in Figure 5.70.

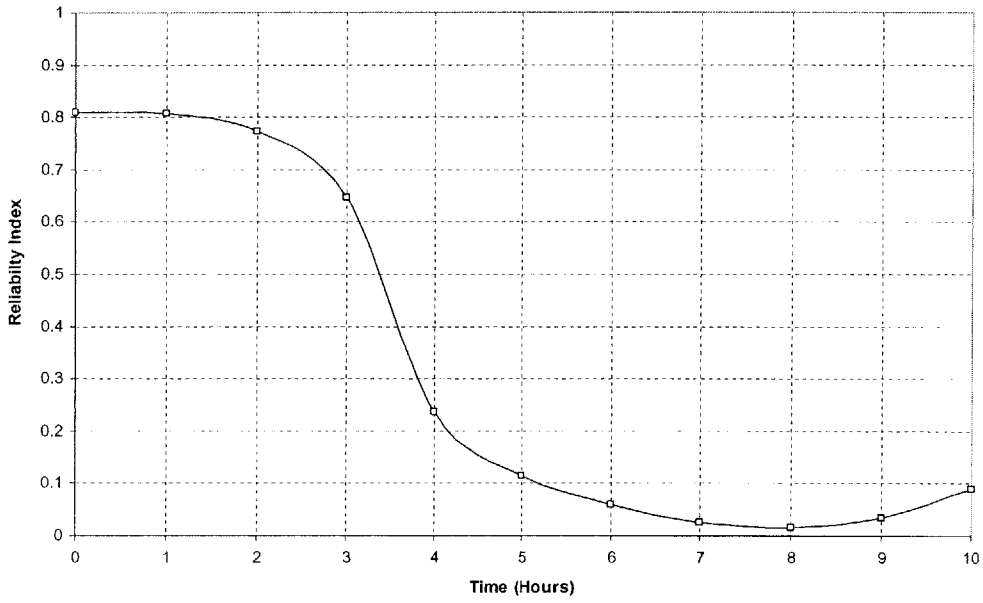

Figure 5.70. Hasofer and Lind (1974) Reliability Index with Time

Assuming a Normal distribution for the Factor of Safety, probabilities of failure with time can be computed and are as shown in Figure 5.71.

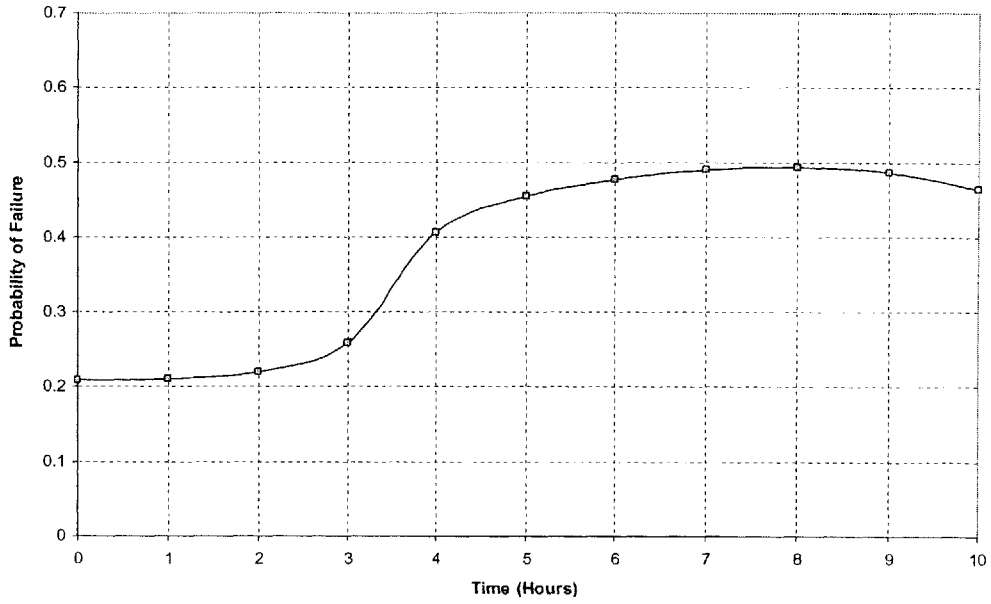

Figure 5.71. Probability of Slope Failure with Time

Figures 5.62 and 5.70 provide plots of the variation of reliability index with time. These functions are continuous functions with time, although they are computed at discrete time intervals, as discussed in Figure 5.55. The time interval is taken to be 1 hours when obtaining Figures 5.62 and 5.70 (and hence 5.63 and 5.71). Clearly, the smaller the time interval, the more accurate the results, and the accuracy of Figures 5.62 and 5.70 can be improved this way. This would lead to smoother curves that show the decrease of reliability index with time, as the rainwater infiltrates the slope deeper, and causes an increase in pressures on the failure surface. Another way to increase accuracy is in the convergence criteria when obtaining β. Since $\beta = \sqrt{\left[\frac{X_i - m_i}{\sigma_i}\right]^T \underline{\Gamma}^{-1} \left[\frac{X_i - m_i}{\sigma_i}\right]}$, the criteria for convergence in Excel during the optimization procedure can be made more stringent. This would also lead to increased accuracy.

5-4.3. CONCLUSIONS

In this part of the chapter, techniques were described whereby the reliability of slopes during and after a rainfall event could be assessed in a second moment context. The procedure involves specifying the second moment characteristics of uncertain quantities and computing the Hasofer and Lind (1974) reliability index based on these as a function of time. The reliability based critical failure surface is also obtained by the iterative procedure. By assuming a probability distribution for the Factor of Safety, the probability of slope failure (or reliability) can be computed as a function of time. If the Factor of safety is assumed to be Normal, the probability of failure is given by $P_F = \Phi(-\beta)$. This can be used as an estimate to the failure probability when the Factor of Safety is non Normal. The procedure was demonstrated in two example slopes, where in the first the rainfall intensity is less than the saturated conductivity, and rainwater reduces the initial suction in the soil. In the second, the rainfall intensity is greater than the saturated conductivity, and positive pressures develop.

PART 5-5:
PROBABILISTIC LANDSLIDE HAZARDS ASSESSMENT

In this section, Monte Carlo techniques are used to assess slope reliability, and hence landslide hazards during and after rainfall events. Uncertain parameters are assumed to follow specified probability distributions. Random numbers of each parameter are generated from the appropriate distribution, and the variation of Factor of Safety with time is computed for each generated set. This results in a random sample of Factors of Safety at each time, t_i. From this, the probability distribution of the Factor of Safety at each time t_i can be approximated. The probability of failure at each time t_i is then estimated from the probability distribution of F.

5-5.1. PROCEDURE

The uncertain parameters are assumed to be the soil hydraulic conductivity, and strength parameters. Other parameters can be included in a similar way as is described in this section. The procedure is as described in Figure 5.72.

Step 1. Divide the total time t_r desired to perform the analyses into discrete time steps t_i. This total time is the duration of rain plus some specified time after cessation of rain.

Step 2. At time t_i, generate a random set (K_s, c', ϕ') of the uncertain parameters from the assumed distributions. Normal and Lognormal distributions are assumed, although other distributions can be included in a similar fashion.

Step 3. For the generated value of K_s at time t_i, the flow model is solved, and the pore pressure variation with depth below ground surface is computed.

Step 4. The pore pressures are used along with the generated values of c' and ϕ' to compute the Factor of Safety at time t_i.

Step 5. Repeat the process for all times t_i, $t_i = 0, \ldots, t_r$. This results in one sample of the variation of Factor of safety with time.

Step 6. Repeat Steps 2 to 5 *k* times. This results in a sample of size *k* for the variation of Factor of Safety with time. Obviously, *k* has to be large for accuracy of results.

Step 7. Derive the probability distribution of Factor of Safety at each time t_i.

Step 8. Estimate the probability of slope failure (or reliability) from the derived distribution of F at each t_i.

Step 9. Repeat Steps 7 and 8 for all times t_i, $t_i = 0, \ldots, t_r$. This results in the variation of probability of failure with time.

Figure 5.72. Procedure for Probabilistic Slope Stability Analyses During Rainfall Using Monte Carlo Methods

5-5.2. NUMERICAL EXAMPLES

To illustrate the procedure, we reconsider the two examples analyzed in Part 5-4.2.

EXAMPLE 1: LANDSLIDE HAZARDS WITH RAINFALL INTENSITY LESS THAN SATURATED CONDUCTIVITY

Reconsider Example 1 in Part 5-4.2, with the slope shown in Figure 5.56. We assume that the soil hydraulic conductivity is Lognormally distributed, as:

$$K_s \sim LN(\, m_{K_s} = 250 cm/day\,,\, \sigma^2_{K_s} = (50 cm/day)^2\,)$$

The soil strength parameters are assumed Normally distributed and uncorrelated, with parameters:

$$c' \sim N(m_{c'} = 0.5 kN/m^2,\ \sigma_{c'} = 0.125 kN/m^2)$$

$$\phi' \sim N(m_{\phi'} = 28^o,\ \sigma_{\phi'} = 7^o)$$

and $\underline{\Gamma} = \begin{bmatrix} 1 & 0 \\ 0 & 1 \end{bmatrix}$. c' and ϕ' are also assumed to be independent of K_s.

Assuming these distributions, the procedure described in Figure 5.72 is implemented. Figure 5.73 shows a plot of the Coefficient of Variation, V, of the Factor of Safety with time, where the Coefficient of Variation, V is defined as:

$$V[F] = \frac{\sqrt{Var[F]}}{E[F]} \qquad [5.55]$$

where E[F] is the expected value of the Factor of Safety, and Var[F] is the variance.

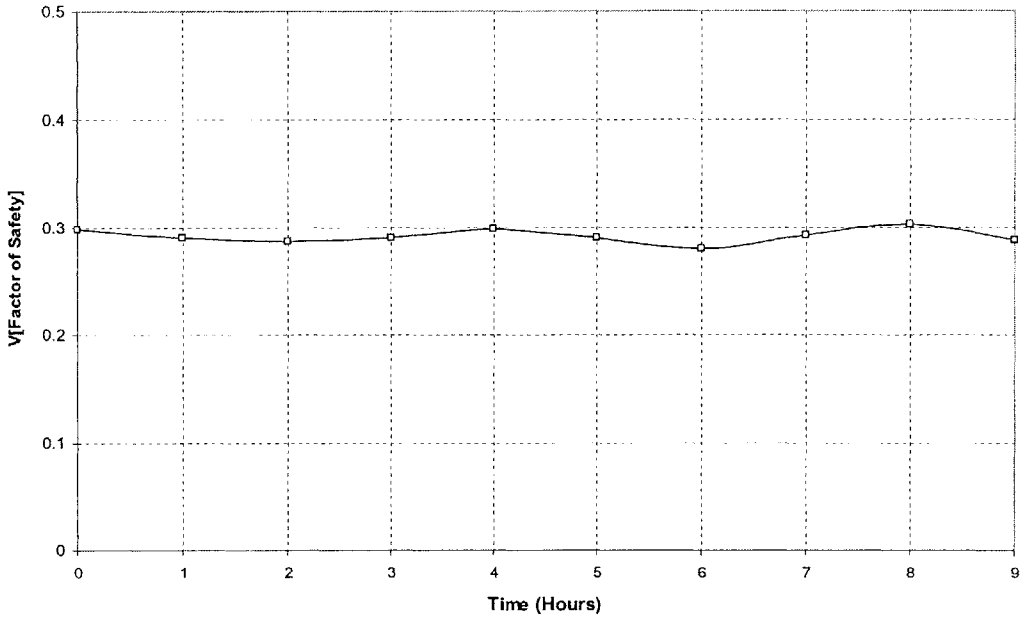

Figure 5.73. Coefficient of Variation of Factor of Safety with Time

Figure 5.73 shows that the coefficient of variation of the Factor of Safety remains more or less constant with time. This is because of the assumption that the uncertainty in the parameters (strength and conductivity) is independent of time.

Therefore, with time, and as the expected value of the Factor of Safety decreases, so does the standard deviation (see also Figures 5.74 to 5.77).

Since a large sample of Factor of Safety values is obtained at any time t_i during the Monte Carlo procedure, one can show such distributions as relative frequency density plots. Figures 5.74 to 5.77 do this for various times. These are used as estimates to the true probability density of the Factor of Safety.

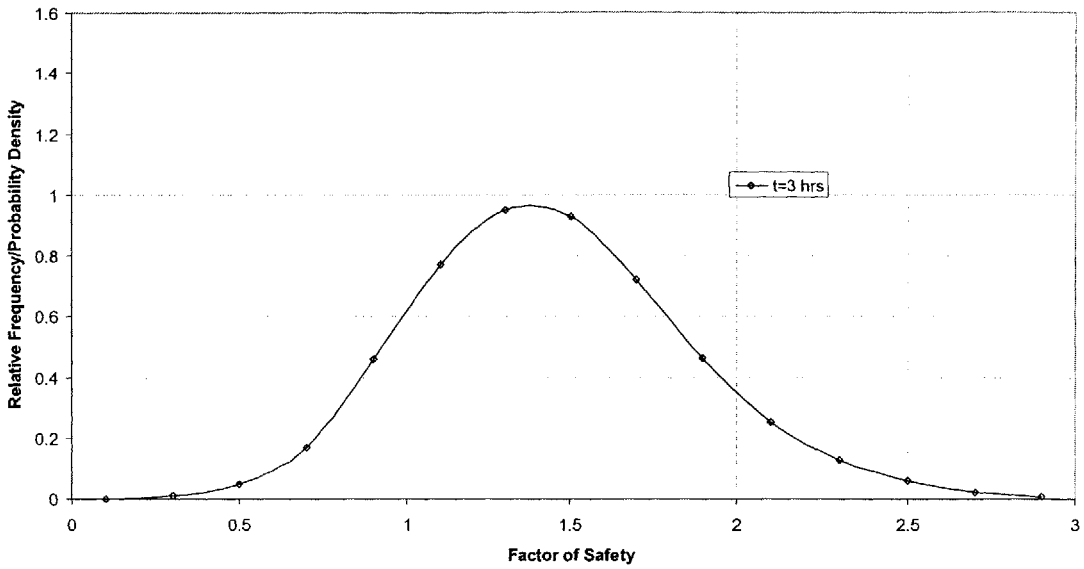

Figure 5.74. Relative Frequency Density of Factor of Safety at Time, t = 3 hours

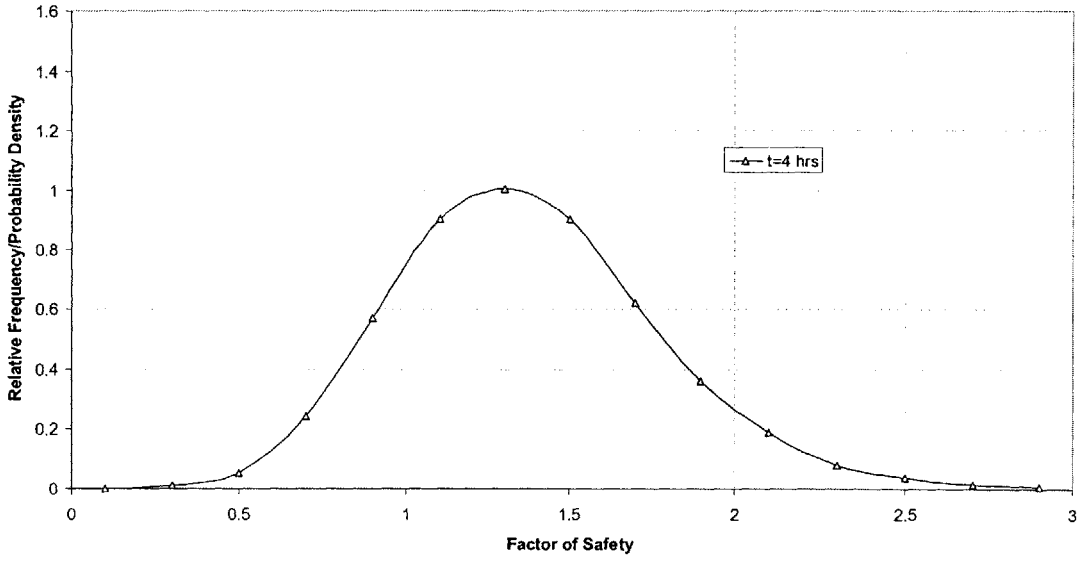

Figure 5.75. Relative Frequency Density of Factor of Safety at Time, t = 4 hours

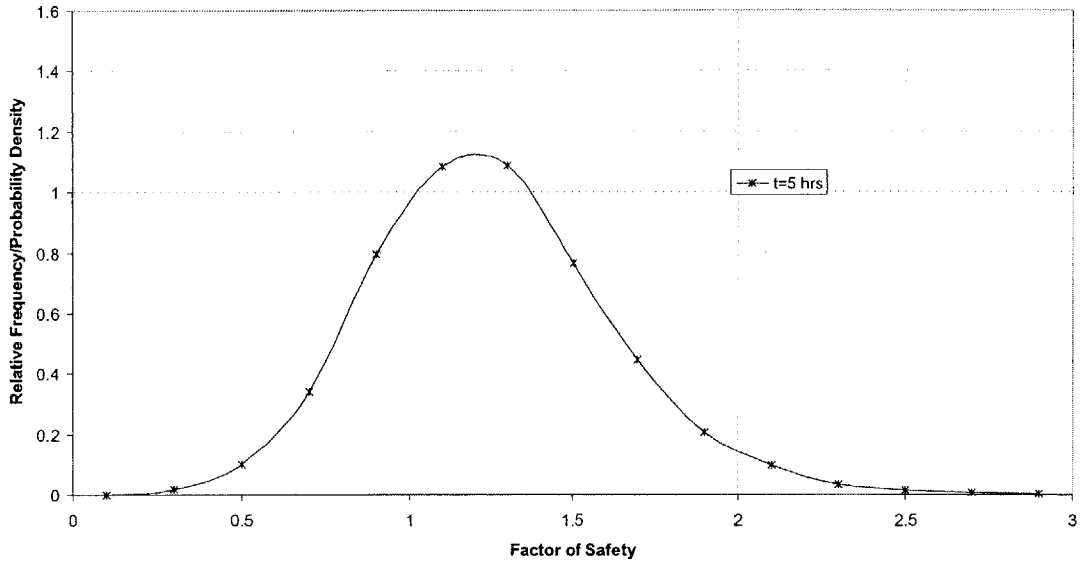

Figure 5.76. Relative Frequency Density of Factor of Safety at Time, t = 5 hours

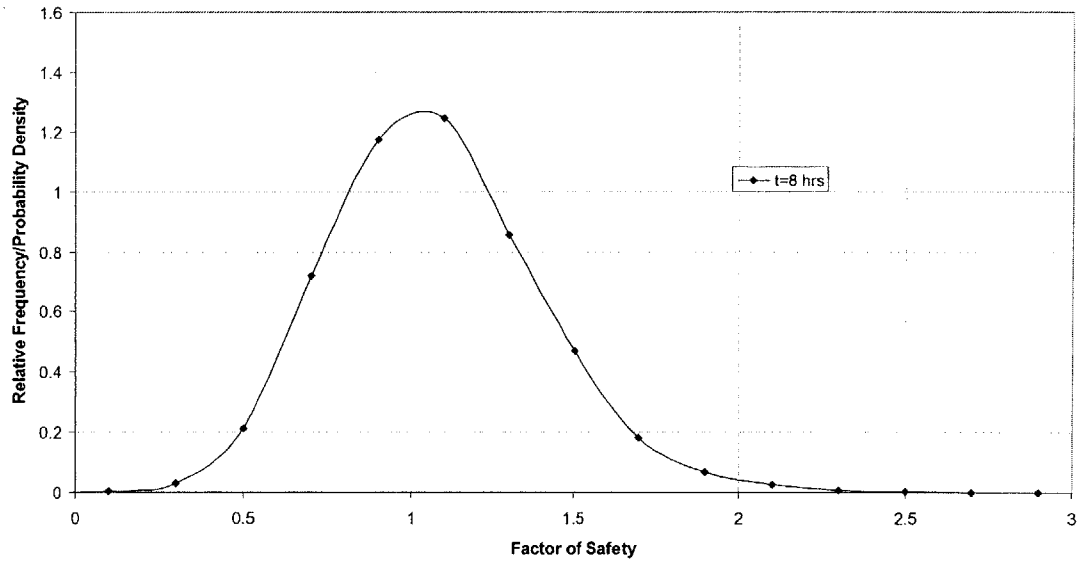

Figure 5.77. Relative Frequency Density of Factor of Safety at Time, t = 8 hours

Figure 5.78 shows these distributions on the same plot.

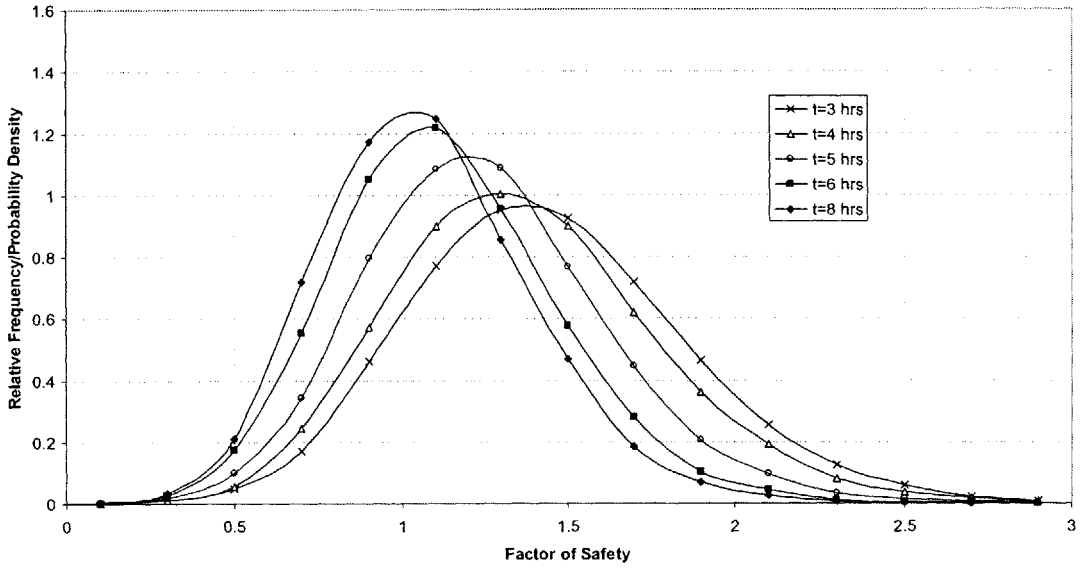

Figure 5.78. Distribution of Factor of Safety at Selected Times

Figure 5.78 shows that the distribution of Factor of Safety moves leftwards, towards the origin with time. As this happens, the probability of slope failure increases, since the area under the density plots where $F < 1$, or $P_F = \int_{-\infty}^{1} f_{F(c',\phi')} dF$ increases. Since the coefficient of variation of the Factor of Safety remains more or less unchanged with time (see Figure 5.73), as the expected value of the Factor of Safety decreases so does the standard deviation. As this happens, the distribution of F becomes more centered about the expected value causing an even greater increase in probability of failure with time.

One can also plot the distribution of the Factor of Safety for times after the end of rain, in which case the distribution would move rightwards away from the origin. This would happen as the excess pressures developed during rain dissipate. As this takes place, the probability of failure decreases. This continues to take place until all the excess pressures have dissipated, and the steady state conditions in the slope prior to rain are restored. The distribution of Factor of Safety returns to its original distribution at t = 0 hours. Figure 5.79 shows a plot of the distribution of Factor of Safety as redistribution takes place, at times t = 9 hours, and t = 10 hours.

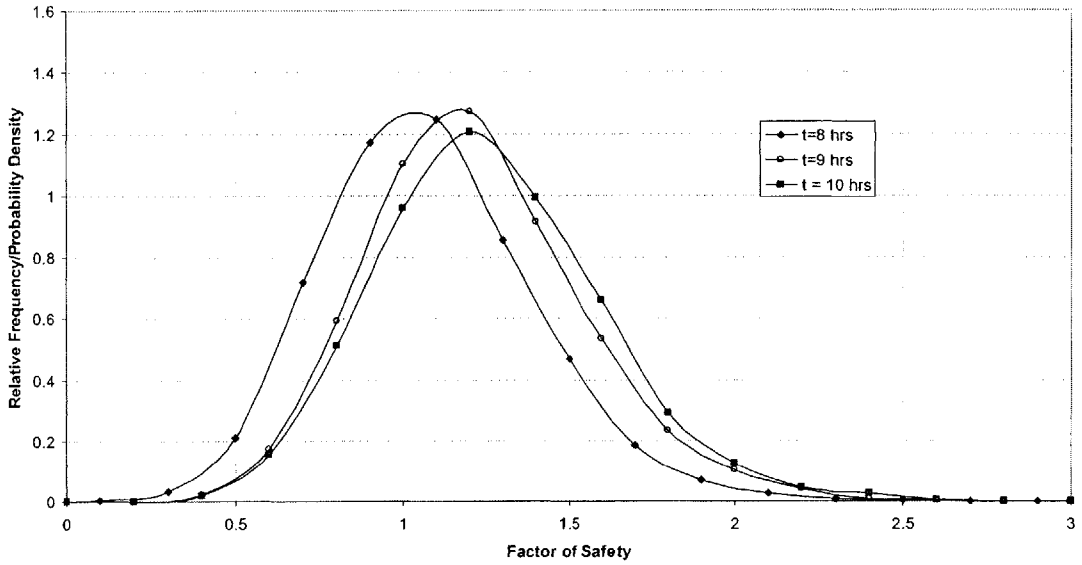

Figure 5.79. Distribution of Factor of Safety at Selected Times after Rain Showing Redistribution

Figure 5.80 shows the probability of failure with time.

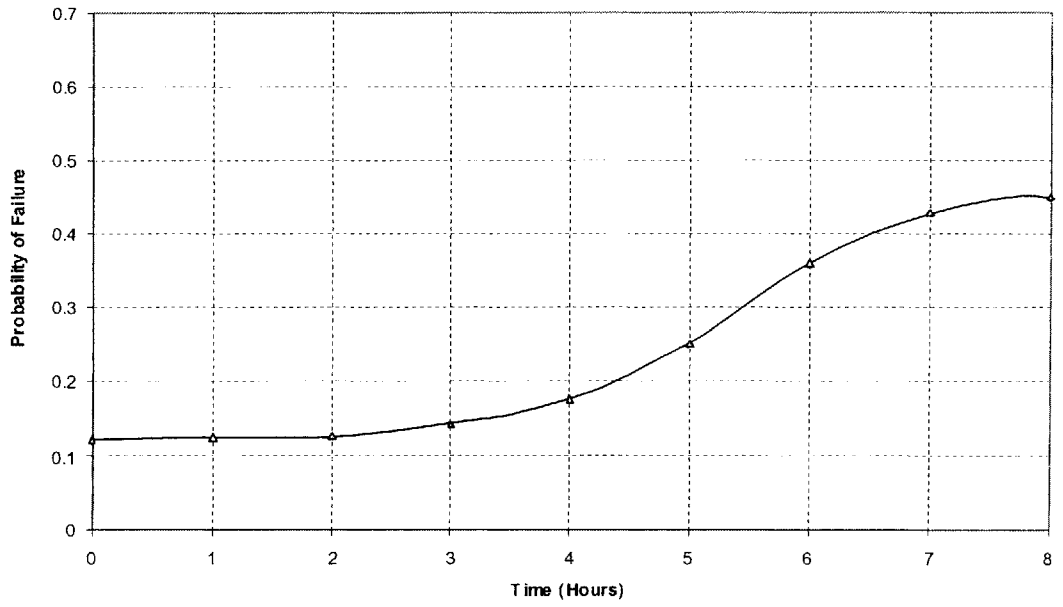

Figure 5.80. Variation of Probability of Failure with Time from Monte Carlo Analyses

Figure 5.80 shows that as it rains, and rainwater infiltrates into the slope, the probability of failure increases. This takes place until the end of rain (t = 8 hours), when the pressures redistribute causing a reduction in the failure probability.

In order to gain a better understanding of the effects of pore pressures, and uncertainty in pore pressures (through uncertainty in hydraulic conductivity) on the uncertainty in the Factor of Safety we examine the distributions in Figures 5.74 to 5.77 in more detail. We compute the statistics and Maximum Likelihood distribution parameters presented in Section 5-3.2 at various times, and these are shown in Tables 5.7 to 5.16.

	Simulated Distribution
Expected Value, E[F]	1.445
Standard Deviation, σ[F]	0.419
Skewness	0.4238
Kurtosis	0.6415
Probability of Failure	0.138

Table 5.7. Summary Statistics of Simulated Distribution at time 3 hours

Fitted Distribution	Maximum Likelihood Parameters		Error Term, e	Probability of Failure
	E[F]/ E[ln(F)]/ r	σ[F]/σ[ln(F)]/ λ		
Normal	1.445	0.419	0.246	0.144
Lognormal	0.323	0.309	0.330	0.148
Gamma	11.882	8.224	0.158	0.143

Table 5.8. Fitted Distributions to Simulated Distribution at time 3 hours

	Simulated Distribution
Expected Value, E[F]	1.370
Standard Deviation, σ[F]	0.400
Skewness	0.4895
Kurtosis	0.6629
Probability of Failure	0.138

Table 5.9. Summary Statistics of Simulated Distribution at time 4 hours

Fitted Distribution	Maximum Likelihood Parameters		Error Term, e	Probability of Failure
	E[F]/ E[ln(F)]/ r	σ[F]/σ[ln(F)]/ λ		
Normal	1.445	0.419	0.246	0.144
Lognormal	0.323	0.309	0.330	0.148
Gamma	11.336	7.846	0.158	0.143

Table 5.10. Fitted Distributions to Simulated Distribution at time 4 hours

	Simulated Distribution
Expected Value, E[F]	1.253
Standard Deviation, σ[F]	0.365
Skewness	0.4942
Kurtosis	0.6682
Probability of Failure	0.251

Table 5.11. Summary Statistics of Simulated Distribution at time 5 hours

Fitted Distribution	Maximum Likelihood Parameters		Error Term, e	Probability of Failure
	E[F]/ E[ln(F)]/ r	σ[F] / σ [ln(F)]/ λ		
Normal	1.253	0.365	0.295	0.244
Lognormal	0.181	0.308	0.344	0.279
Gamma	11.362	9.071	0.167	0.264

Table 5.12. Fitted Distributions to Simulated Distribution at time 5 hours

	Simulated Distribution
Expected Value, E[F]	1.137
Standard Deviation, σ[F]	0.336
Skewness	0.4911
Kurtosis	0.6903
Probability of Failure	0.360

Table 5.13. Summary Statistics of Simulated Distribution at time 6 hours

Fitted Distribution	Maximum Likelihood Parameters		Error Term, e	Probability of Failure
	E[F]/ E[ln(F)]/ r	σ[F] / σ [ln(F)]/ λ		
Normal	1.137	0.336	0.302	0.342
Lognormal	0.082	0.313	0.376	0.396
Gamma	10.999	9.673	0.187	0.376

Table 5.14. Fitted Distributions to Simulated Distribution at time 6 hours

	Simulated Distribution
Expected Value, E[F]	1.078
Standard Deviation, σ[F]	0.319
Skewness	0.4986
Kurtosis	0.6812
Probability of Failure	0.428

Table 5.15. Summary Statistics of Simulated Distribution at time 8 hours

Fitted Distribution	Maximum Likelihood Parameters		Error Term, e	Probability of Failure
	E[F]/ E[ln(F)]/ r	σ[F]/σ[ln(F)]/ λ		
Normal	1.078	0.319	0.317	0.403
Lognormal	0.029	0.313	0.361	0.463
Gamma	10.992	10.195	0.167	0.442

Table 5.16. Fitted Distributions to Simulated Distribution at time 8 hours

Several observations can be made with regard to Tables 5.7 to 5.16:

- With increasing time, the expected value of the Factor of Safety decreases, and there is a corresponding increase in the probability of failure.
- At any time, t, the value of the coefficient of Skewness is small, indicating small asymmetry in the distribution around the mean. This is shown in Figure 5.78.
- The value of the coefficient of Skewness increases with time. This shows that the distribution of Factor of Safety becomes more asymmetric with time, as is also shown in Figure 5.78.
- The value of the coefficient of Kurtosis remains more or less the same with time. This indicates that the relative peakedness of the distribution of Factor of Safety compared to the Normal distribution remains the same. This is also illustrated in Figures 5.78.
- The fit of the Normal distribution to the simulated distribution of Factor of Safety is better at early times, and becomes less and less accurate with time. This is shown by the error e terms that increase with time in Tables 5.7 to 5.16.
- At any time t, the best fit distribution to the simulated distribution of Factor of Safety is the Gamma distribution.

Tables 5.7 to 5.16 show that at early times during rain the distribution of Factor of Safety can be approximated by the Normal distribution. With increasing time, the distribution of the Factor of Safety tends further away from the Normal distribution. This happens because as time increases, so do the pore pressures on the failure surface. As the pore pressures increase, so do the uncertainties in the pore pressures caused by uncertainties in the hydraulic conductivity. This was discussed in more detail in Section 5-1.3. Therefore, with increasing time, the impact of the uncertainties in pore pressures on the uncertainty in the Factor of Safety increases. As a consequence, the influence of

the pore pressures on the shape of the distribution of the Factor of Safety also increases. With time, the Factor of Safety is better approximated by the Gamma distribution than by the Normal (or Lognormal) distributions. This is shown in Figure 5.81 which shows the simulated distributions of Factors of Safety (shown in symbols) at various times, and the fitted Gamma distributions (shown by dashed lines).

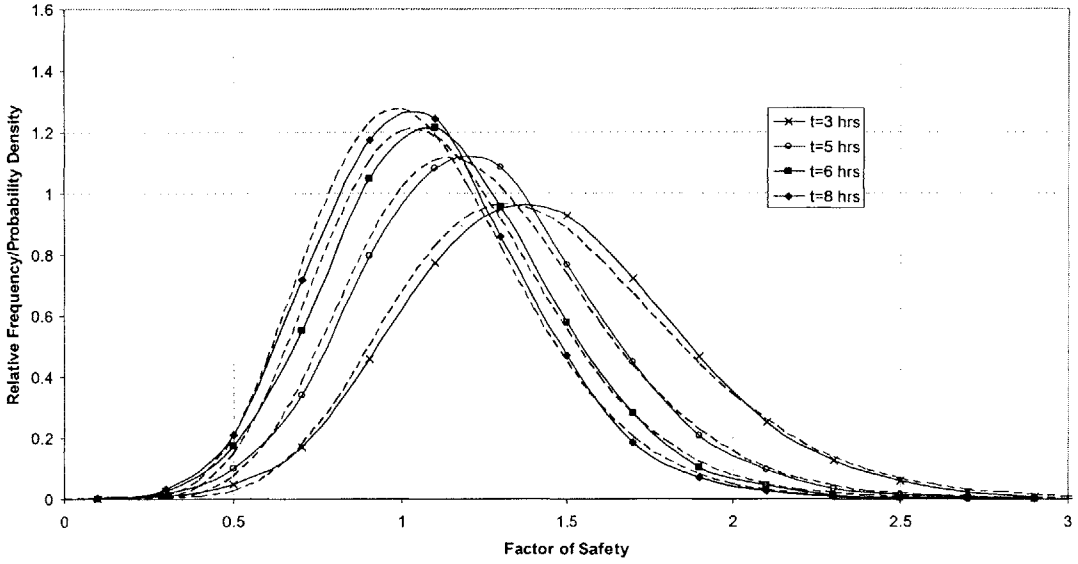

Figure 5.81. Comparison of Simulated (Symbols) Distribution of Factor of Safety with Fitted Gamma Distributions (Dashed Lines)

Figure 5.82 compares the distribution of the Factor of Safety at time t = 3 hours with the Normal and Lognormal distributions, and Figure 5.83 does so for time t = 8 hours.

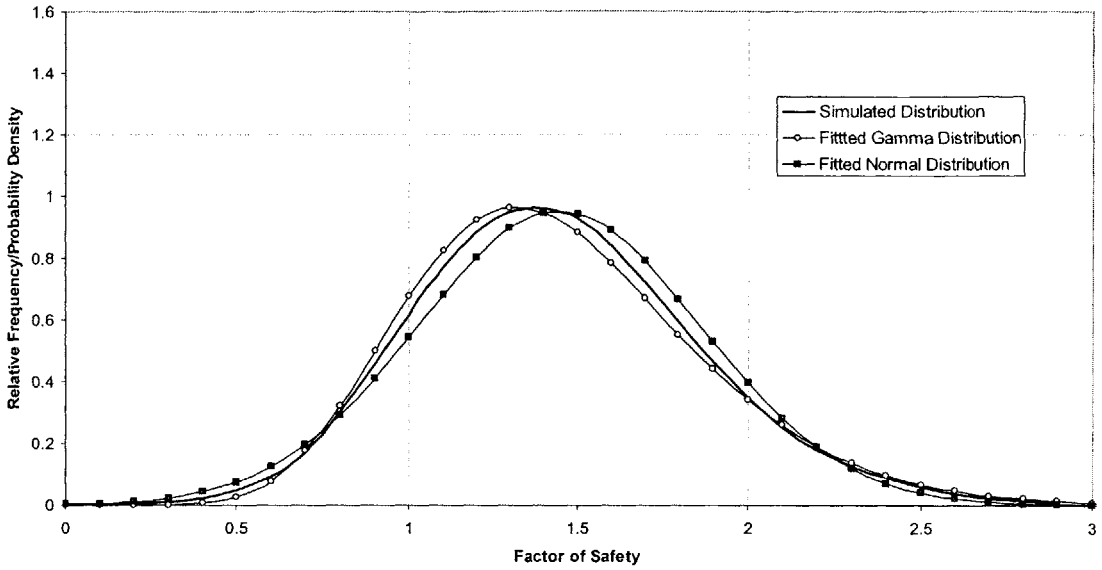

Figure 5.82. Comparison of Distribution of Factor of Safety with Fitted Normal and Gamma Distributions at t = 3 hours

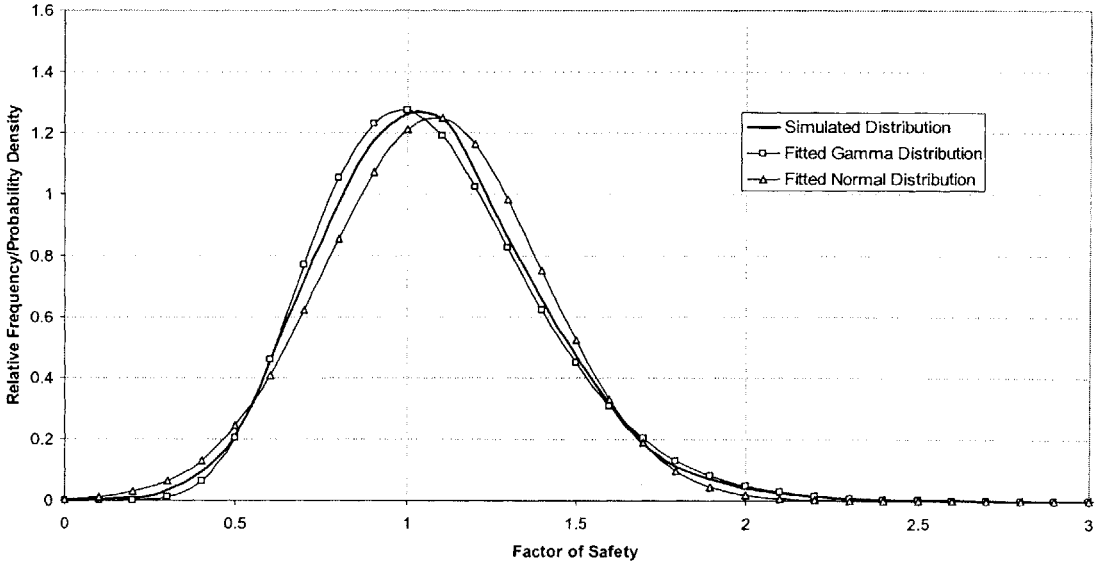

Figure 5.83. Comparison of Distribution of Factor of Safety with Fitted Normal and Gamma Distributions at t = 8 hours

Figures 5.82 and 5.83 show the increase in the deviation of the distribution of Factor of Safety from the Normal distribution with time. This deviation is in the form of a change from a symmetric distribution to a more asymmetric distribution. This is also evident in Figures 5.74 to 5.77. The distributions of Factors of Safety are better approximated by the Gamma distribution than by the Normal distribution. As this takes place, and since

the since the coefficient of variation of Factor of Safety remains more or less unchanged with time (see Figure 5.73), the probability of failure increases further. This is also shown in Tables 5.7 to 5.16 which show the greater failure probability for the Gamma distributions than for the Normal distributions.

Recall from Part 5-3.2 that when the strength parameters c' and ϕ' are the only uncertain parameters, then the distribution of Factor of Safety could be well approximated by the Normal distribution. This means that at any time during rain, the distribution of F would be well approximated by the Normal distribution if c' and ϕ' are the only uncertain parameters. We assume that the saturated conductivity is deterministic. Figure 5.84 compares the coefficient of variation (see Equation [5.55]) of the Factor of Safety when only the strength parameters are assumed uncertain, with when both strength and hydraulic parameters are uncertain.

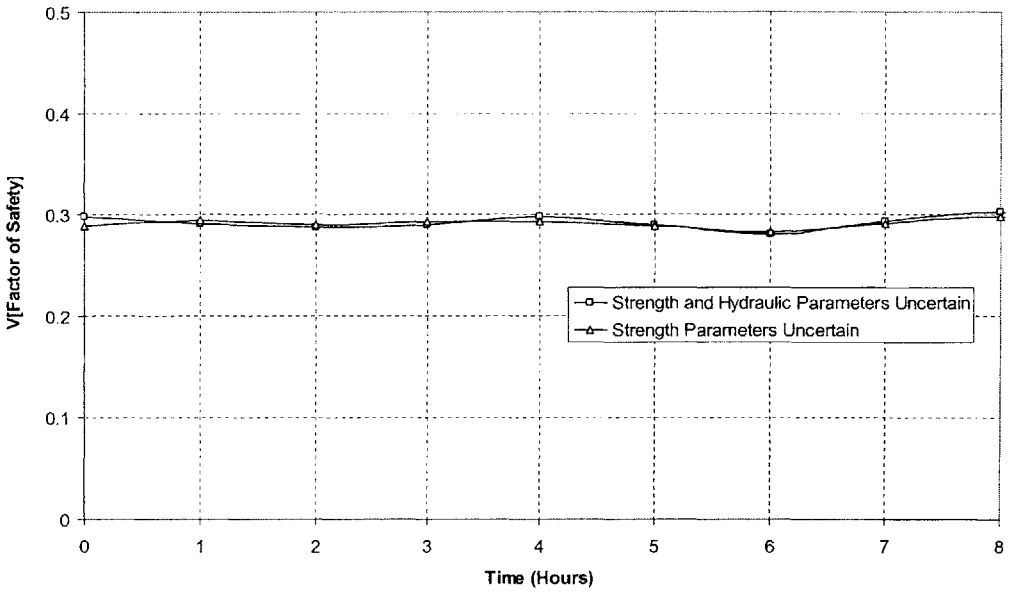

Figure 5.84. Comparison of the Coefficient of Variation of Factor of Safety with Time when Strength Parameters are Uncertain and when Strength and Hydraulic Parameters are Uncertain

Figure 5.84 shows that the coefficient of variation of Factor of Safety is slightly greater when both strength and hydraulic parameters are uncertain, because the increased uncertainty causes an increase in the variance (and standard deviation) of the Factor of Safety. Figure 5.84 therefore shows that with the parameters assumed in this example,

uncertainty in the strength parameters is the largest contributor to the uncertainty in the Factor of Safety, while the uncertainty in pore pressures does not have a very significant impact. However, the uncertainty in pore pressures has an effect on the shape of the distribution of Factor of Safety. Figure 5.85 shows the distribution of the Factor of Safety at times, t= 3 hours, t = 5 hours and t = 8 hours.

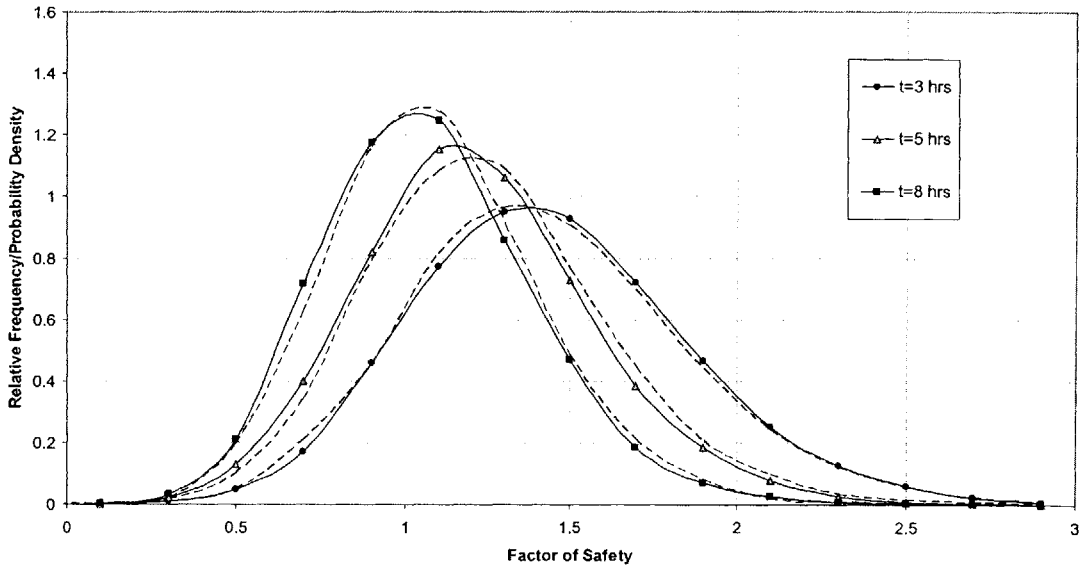

Figure 5.85. Comparison of the Distributions of Factor of Safety with Time when Strength Parameters are Uncertain (Dashed Lines) and when Strength and Hydraulic Parameters are Uncertain (Solid Lines and Symbols)

The solid line distributions with symbols in Figure 5.85 are those for the case when both the strength and hydraulic parameters are uncertain, and the dashed lines are those for the case when only the strength parameters are uncertain. Figure 5.85 shows that when only the strength parameters are uncertain, the distribution of the Factor of Safety remains symmetric with time. It can be shown that these distributions are well represented by the Normal distribution. When uncertainty in the hydraulic conductivity (and hence pressures) is introduced, it causes a change in the shape of the distribution of Factor of Safety, and the shape becomes asymmetrical. The distributions are better approximated by the Gamma distribution than by the Normal distribution.

In conclusion, when the rainfall intensity is less than the saturated conductivity of the soil, the uncertainties in the strength parameters are larger contributors to uncertainty in the Factor of Safety than uncertainties in conductivity (and hence pressures). The

uncertainty in conductivity, does however, affect the shape of the distribution of the Factor of Safety. The distributions deviate from the Normal distribution, and this deviation increases with increasing time (and pressures). The distributions, particularly at larger times, are better approximated by the Gamma distribution than by the Normal distribution.

The intent here is to gain a better understanding of the distribution of Factor of Safety and the changes it goes through with time. The intent, however, is not for a rigorous assessment of these distributions, and/or to fit probability distribution models to the simulated distributions. The assessment is simple and comparative, considering only the Normal, Lognormal and Gamma distributions, and the true distributions of Factor of Safety are neither exactly.

We now compare the results of the Monte Carlo analyses, with those from the second moment reliability analyses performed in the Section 5-4.2. This is done in Figure 5.86.

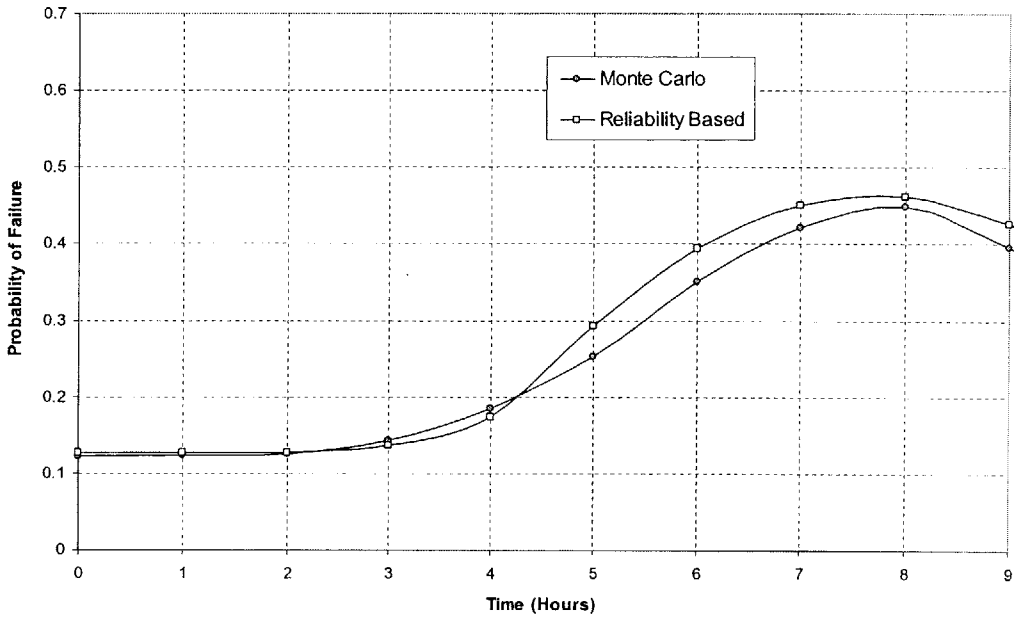

Figure 5.86. Comparison of Probabilities of Failure from Second Moment and Monte Carlo Analyses

Figure 5.86 shows that there is, in general, good agreement between the results of both methods to assess slope reliability. This is particularly the case at early times during the

rainfall event, when the distribution of the Factor of Safety more closely follows a Normal distribution.
With time, and as the distribution of Factor of Safety deviates from Normality the discrepancies between the results increases.

Nevertheless, second moment reliability analyses, and computed probabilities of failure based on β, provide a good means by which slope reliability can be assessed, and the results are comparable to those obtained from probabilistic analyses.

EXAMPLE 2: LANDSLIDE HAZARDS WITH RAINFALL INTENSITY GREATER THAN SATURATED CONDUCTIVITY

In a second example, we consider Example 2 presented in Section 5-4.2, where the rainfall intensity is greater than the saturated conductivity of the soil, allowing for positive pressures to develop. Figure 5.87 shows a plot of the coefficient of variation (see Equation [5.55]) of Factor of Safety with time.

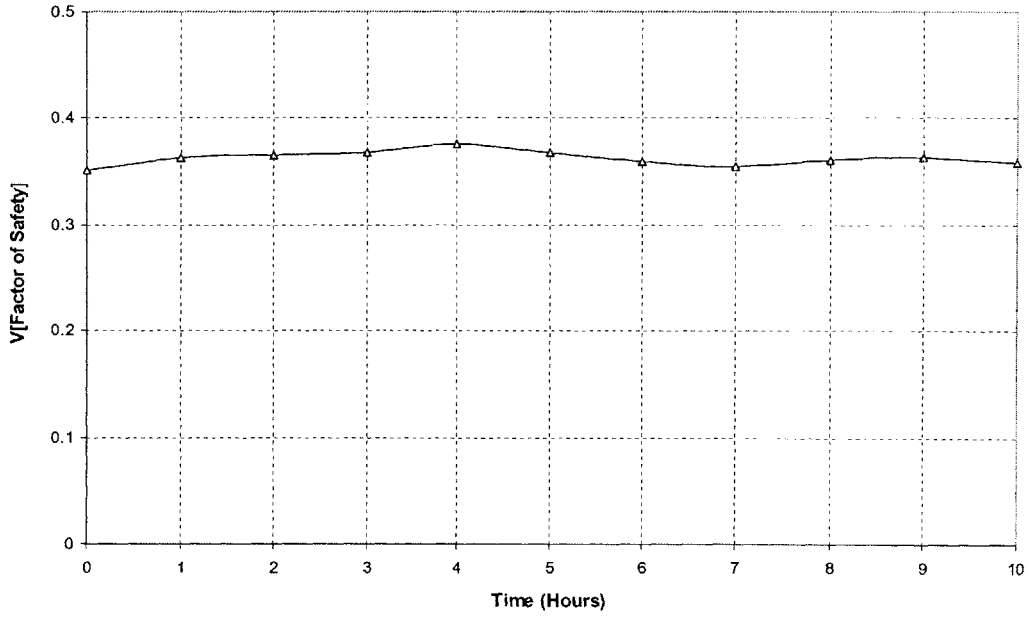

Figure 5.87. Coefficient of Variation of Factor of Safety with Time

Figure 5.87 shows that the coefficient of variation of Factor of Safety remains more or less the same during the rain event. The coefficient of variation is greater in this

example, than in Example 1 (see Figure 5.73), because the coefficient of variation of the strength parameters is greater in this example, while the coefficient of variation of the conductivity is the same. Larger uncertainties in c' and ϕ' translate to larger uncertainties in the Factor of Safety, and hence larger coefficients of variation for the same expected value of Factor of Safety.

Figure 5.88 shows the distribution of Factor of Safety at selected times, and shows the leftwards shift towards the origin with time, causing a decrease in the expected value of the Factor of Safety.

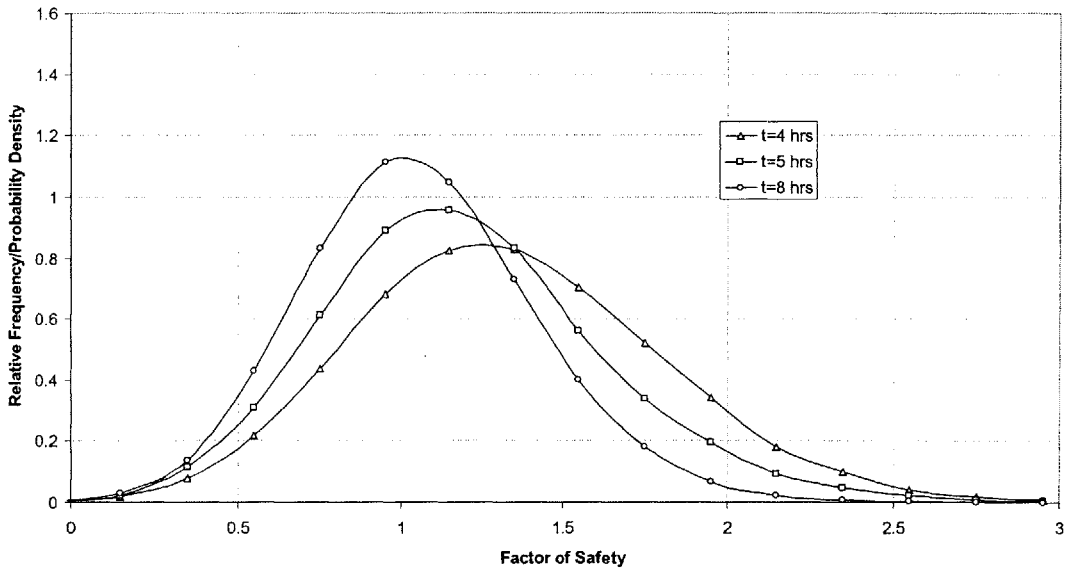

Figure 5.88. Distribution of Factor of Safety at Selected Times

We compute the statistics and Maximum Likelihood distribution parameters presented in Section 5-3.2 at different times, and these are shown in Tables 5.17 to 5.22.

	Simulated Distribution
Expected Value, E[F]	1.283
Standard Deviation, σ[F]	0.471
Skewness	0.2761
Kurtosis	0.0995
Probability of Failure	0.288

Table 5.17. Summary Statistics of Simulated Distribution at time 4 hours

Fitted Distribution	Maximum Likelihood Parameters		Error Term, e	Probability of Failure
	E[F]/ E[ln(F)]/ r	σ[F]/σ[ln(F)]/ λ		
Normal	1.284	0.471	0.133	0.273
Lognormal	0.173	0.426	0.213	0.343
Gamma	6.231	4.851	0.364	0.322

Table 5.18. Fitted Distributions to Simulated Distribution at time 4 hours

	Simulated Distribution
Expected Value, E[F]	1.144
Standard Deviation, σ[F]	0.430
Skewness	0.4538
Kurtosis	0.4633
Probability of Failure	0.390

Table 5.19. Summary Statistics of Simulated Distribution at time 5 hours

Fitted Distribution	Maximum Likelihood Parameters		Error Term, e	Probability of Failure
	E[F]/ E[ln(F)]/ r	σ[F]/σ[ln(F)]/ λ		
Normal	1.147	0.428	0.188	0.366
Lognormal	0.079	0.375	0.290	0.416
Gamma	6.187	5.394	0.211	0.422

Table 5.20. Fitted Distributions to Simulated Distribution at time 5 hours

	Simulated Distribution
Expected Value, E[F]	1.009
Standard Deviation, σ[F]	0.358
Skewness	0.3152
Kurtosis	0.3838
Probability of Failure	0.509

Table 5.21. Summary Statistics of Simulated Distribution at time 8 hours

Fitted Distribution	Maximum Likelihood Parameters		Error Term, e	Probability of Failure
	E[F]/ E[ln(F)]/ r	σ[F]/σ[ln(F)]/ λ		
Normal	1.010	0.358	0.194	0.489
Lognormal	-0.035	0.347	0.476	0.540
Gamma	6.491	6.427	0.417	0.542

Table 5.22. Fitted Distributions to Simulated Distribution at time 8 hours

Similar comments can be made with regard to Tables 5.17 to 5.22 as were made with regard to Tables 5.6 to 5.17 in Example 1. Particularly that the distributions of Factor of Safety deviate from the Normal distribution with time and increasing pressures. This is

shown by the increase in the error e term with time. The increase in e is not as significant in this example as it was in Example 1. In addition, the distributions of Factor of Safety are best approximated by the Normal distribution at all times. Figure 5.89 compares the generated distributions (symbols) with the fitted Normal distributions (dashed lines) at times t = 3, 5 and 8 hours.

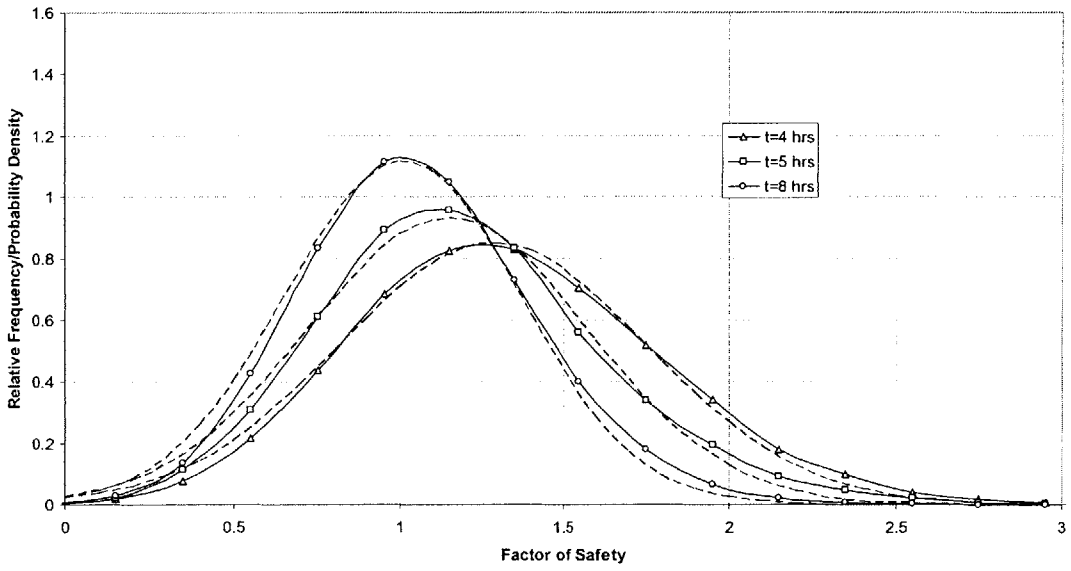

Figure 5.89. Comparison of Simulated (Symbols) Distribution of Factor of Safety with Fitted Normal Distributions (Dashed Lines)

The $\left(\frac{q}{K_s}\right)$ ratio is greater in this example than in Example 1, and therefore uncertainty in the pressures is greater than in the first example (compare Figures 5.61 and 5.69). The effect of larger $\left(\frac{q}{K_s}\right)$ ratio is an increase in the coefficient of variation of the Factor of Safety when compared to the case of deterministic conductivity, and this is shown in Figure 5.90.

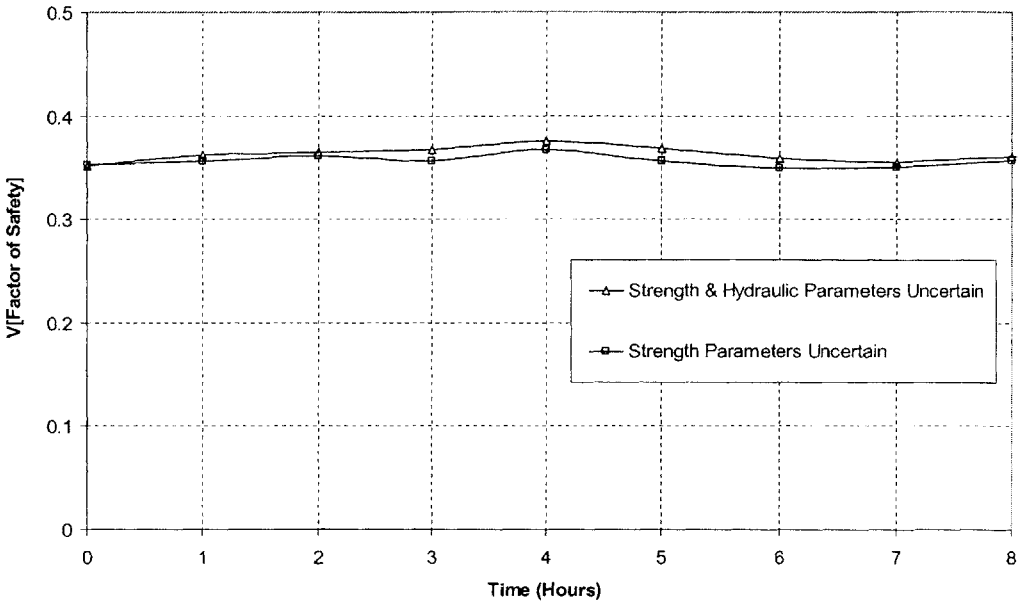

Figure 5.90. Comparison of the Coefficient of Variation of Factor of Safety with Time when Strength Parameters are Uncertain and when Strength and Hydraulic Parameters are Uncertain

Figure 5.90 shows that in this example, the difference in coefficients of variation of Factor of Safety when the conductivity is deterministic and uncertain is greater than in Example 1, which is shown in Figure 5.84.

However, although the $\left(\frac{q}{K_s}\right)$ ratio is greater, the coefficient of variation of the strength parameters is also greater. In Example 1, the coefficient of variation of the strength parameters $V_{c'} = \frac{\sqrt{Var[c']}}{E[c']} = V_{\phi'} = \frac{\sqrt{Var[\phi']}}{E[\phi']} = \frac{1}{4}$ and in this example $V_{c'} = \frac{\sqrt{Var[c']}}{E[c']} = V_{\phi'} = \frac{\sqrt{Var[\phi']}}{E[\phi']} = \frac{1}{3}$. Consequently, the distributions of c' and ϕ' have a greater influence on the distribution of the Factor of Safety. Since the strength parameters are greater contributors to the uncertainty in Factor of Safety than the conductivity (and this is shown by the slight difference in coefficients of variation of the Factor of Safety when the conductivity is deterministic and when it is uncertain in Figures 5.84 and 5.90), the shape of the distribution of Factor of Safety tends towards the one where only the strength parameters are uncertain. Section 5-3.2 showed that when c' and ϕ' are

Normally distributed, the Factor of Safety is well approximated by the Normal distribution. Therefore, in this example, and because of the larger coefficients of variation of the strength parameters, the distribution of Factor of Safety at any time is better approximated by the Normal distribution than by the Lognormal distribution, or the Gamma distribution as in Example 1.

Figure 5.91 compares the distributions of the Factor of Safety at t = 4 hours and t = 8 hours, when only the strength parameters are uncertain, and when the strength and hydraulic parameters are uncertain.

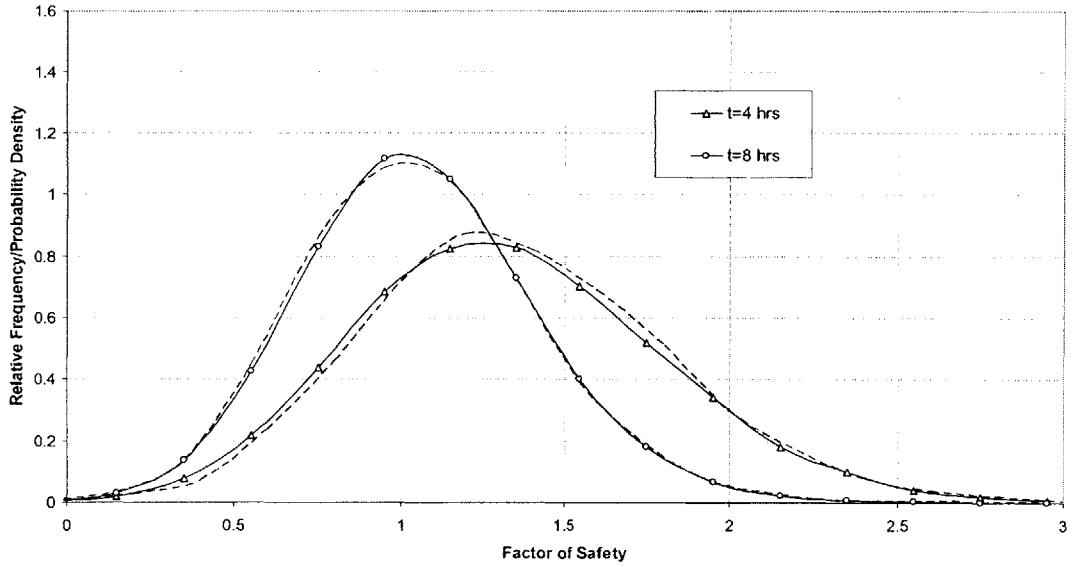

Figure 5.91. Comparison of the Distributions of Factor of Safety with Time when Strength Parameters are Uncertain (Dashed Lines) and when Strength and Hydraulic Parameters are Uncertain (Solid Lines)

The solid line distributions with symbols in Figure 5.91 are those for the case when both the strength and hydraulic parameters are uncertain, and the dashed lines are those for the case when only the strength parameters are uncertain. Figure 5.91 shows that the shape of the distribution of Factor of Safety is almost the same when the conductivity is deterministic and when it is uncertain.

Figure 5.92 shows the probability of failure with time.

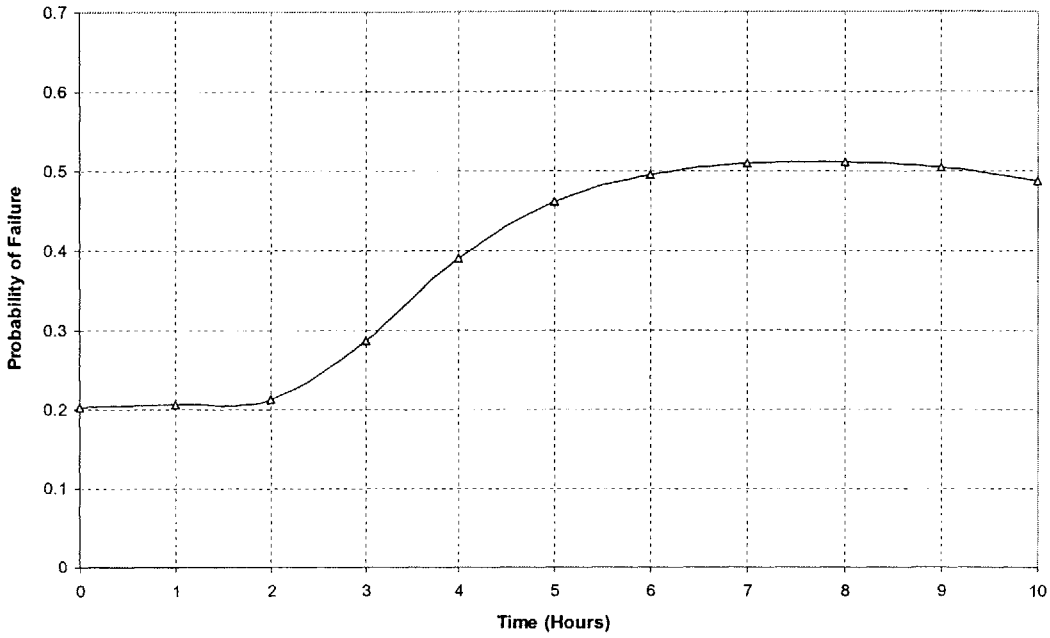

Figure 5.92. Variation of Probability of Failure with Time from Monte Carlo Analyses

The results are compared with those obtained from second moment reliability analyses in Figure 5.93.

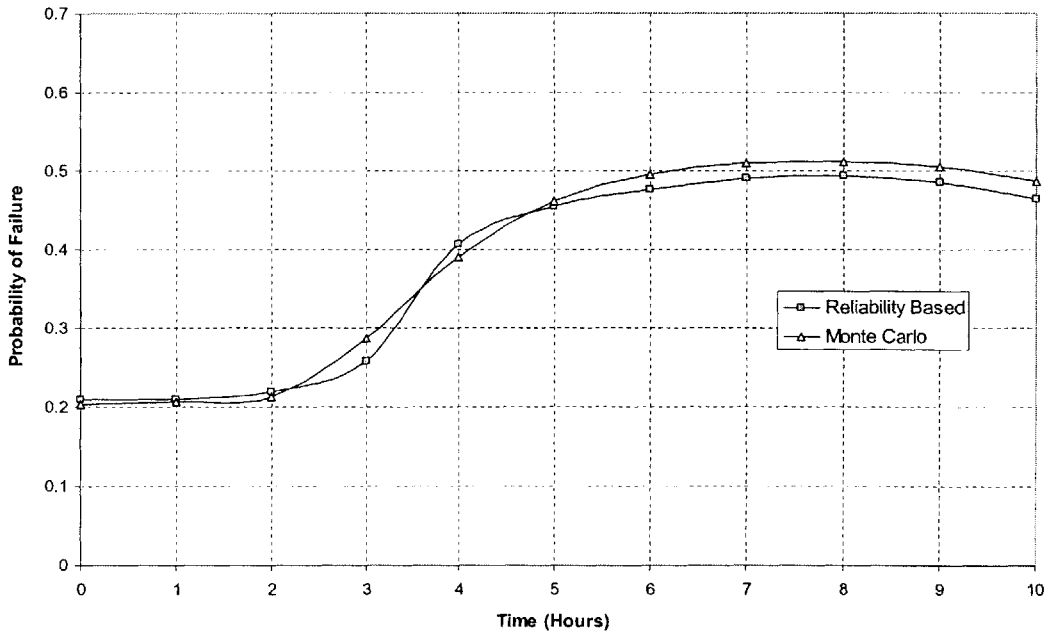

Figure 5.93. Comparison of Probabilities of Failure from Second Moment and Monte Carlo Analyses

The agreement between the results of second moment and Monte Carlo analyses is very good. The results compare better in this example than in Example 1, because the shape of the distributions of Factor of Safety remain well approximated by the Normal distribution with time.

5-5.3. TEMPORAL LANDSLIDE HAZARDS

The analyses performed in this (and the previous) part of Chapter 5 are inherently spatial in nature, because they are on the single slope scale. The probabilities of failure that are computed from the analyses are in the strict sense conditional probabilities of failure. These are probabilities of failure conditioned on the rainfall characteristics that are assumed in the analyses. The results are therefore in the form of $P[\text{failure} \mid \text{rainfall i}]$. This rainfall can be, for example, the n^{th} year storm. The temporal probability of occurrence of such a rainfall i, e.g. annual, can be obtained from the local rainfall records. The unconditional (annual or other) probability of slope is then, from the definition of conditional probability:

$$P[\text{failure}] = P[\text{failure} \mid \text{rainfall i}] \times P[\text{rainfall i}] \qquad [5.41]$$

This represents the temporal hazard of landsliding. Performing such an analyses, therefore, allows one to compute landslide hazards, which by definition include spatial and temporal components. The analyses could be extended to include several storms, and the total probability theorem, in one form or other, can be used to estimate landslide hazards.

5-5.4. COMMENTS ON PROBABILITIES OF FAILURE

Reliability indices and probabilities of failure provide a rational means in which uncertainties in parameters are systematically incorporated into the analyses. Probabilities of failure, whether computed from reliability analyses, or form Monte Carlo methods, do not have the meaning of true frequentist probability. These probabilities, therefore, have to be treated in a relative sense rather than absolute probabilities. This is because of the assumptions, and simplifications made in the models that are used to compute the probabilities. The probabilities are also, lower bounds on the probability of

failure because of factors neglected in the analyses (Christian et al., 1994). Though the attempt has been made to keep these omissions to a minimum, they still exist, and therefore, the results are conservative in the sense that these are not considered.

5.5-4. UPDATING

Once landslide hazards have been assessed, decisions are made. This is shown in Figure 5.1. Decisions can be in the form of countermeasures, which are either active, such as tiebacks, or passive such as a protective gallery. Decisions can alternatively be in the form of obtaining more information, on the parameters, for example, through laboratory studies, or in the field. This is represented by the information phase in Figure 5.1. Decisions can also be to do nothing. In either case, new information is acquired, and landslide hazards can, and should be updated. This is represented in the updating cycle shown in Figure 5.1.

The updating cycle is the essence of the observational approach (Terzaghi, 1961; Peck, 1969; Einstein, 1978), and is modeled via Bayes' theorem:

$$f''(\theta_i \mid Z) = k\ell(Z \mid \theta_i)f'(\theta_i) \qquad [5.42]$$

where:

$f'(\theta_i)$	is the *a priori* probability distribution of the state θ_i
$f''(\theta_i \mid Z)$	is the *a posteriori* probability distribution of that state θ_i given the observed information Z.
$\ell(Z \mid \theta_i)$	is the likelihood of observing Z given θ_i
k	is a normalization constant

Engineering judgment, professional opinion, and expert knowledge can be expressed as subjective probabilities, and Bayes' theorem provides a means by which this information can be combined with observations.

5-5.5. CONCLUSIONS

Techniques were developed whereby uncertainties are systematically incorporated into the landslide hazard procedure, allowing one to probabilistically assess these hazards. This was done by developing techniques based on second moment analyses, and Monte Carlo Methods that allow one to propagate uncertainties through the combined hydrology stability model that was developed in Chapter 2. The result is a more advanced probabilistic model that is better capable of representing reality than current models used in landslide analyses.

Results from hydrologic analyses showed that pore pressure distributions, and uncertainties in these distributions depend on the shape of the soil characteristic curves. Uniform soils tend to develop sharper wetting fronts than well graded soils. As a consequence, the uncertainty in the pressure (and moisture) profiles at the sharper front is large. This uncertainty is localized in a small area of soil near the wetting front. On the other hand, well graded soils do not develop distinct wetting fronts and as a result, the uncertainty in the pressure (and moisture) profiles is small. This uncertainty is spread over a large area of soil near the wetting front.

Results from stability analyses showed that reliability indices and probabilities of failure are a better measure of stability than the Factor of Safety since uncertainties in parameters are taken into account. Larger Factors of Safety do not necessarily imply more stable slopes. Results from second moment reliability analyses are in good agreement with probabilistic analyses based on the Monte Carlo method. This is because the probability distribution of the Factor of Safety can be well approximated by the Normal distribution.

Results from combined hydrologic and stability analyses showed that uncertainties in the soil strength parameters have a greater influence on probabilities of slope failure, and landslide hazards, than uncertainties in the hydraulic conductivity of the soil. As a consequence, the probability distribution of the Factor of Safety depends, to a large extent, on the probability distributions of the soil strength parameters. The influence of uncertainties in hydraulic conductivity becomes more apparent at greater times during a rainfall event, as the pore pressures along a potential failure surface increase.

Nonetheless, in general, if the soil strength parameters are Normally distributed, the distribution of Factor of Safety at any time is also Normal.

The analyses are spatial in nature because they are performed on the single slope scale. When coupled with the local rainfall records the temporal component of landslide hazards can be estimated. This presents probabilistic phase of the decision analysis procedure for landslides. Decisions are made based on the results of the probabilistic hazards assessment. These can be in the form of obtaining new information, or taking action. In either case, landslide hazards can, and should be updated, which is typically done using Bayesian analysis.

CHAPTER 6

MODEL UNCERTAINTY

Landslide hazards assessment relies heavily on modeling. Models include those for hydrologic and stability analyses, as well as others. Figure 6.1 shows possible models used in hydrologic analyses, and Figure 6.2 shows those used in stability analyses. These models vary in scale, dimensionality and complexity. They are all, however, analytical models resulting from the theories assumed to apply to physical processes, and are therefore subject to uncertainties as they attempt to represent reality. The issue of model uncertainty has been given little attention in the literature, and this is the case in both fields of hydrologic and stability analyses. It is therefore not surprising that very few studies have dealt with the issue in combined hydrology and stability analyses, particularly in the context of landslide analyses. This is because model uncertainty is the most difficult source of uncertainty to represent and capture. It is however, an issue that is gaining that has recently been gaining some attention e.g. Einstein (1995); Einstein and Karam (2001); Lacasse (2003).

This chapter attempts to raise awareness of the problem of model uncertainty, and highlight some of the effects it may have on landslide hazards assessment through the effects on hydrologic, stability and combined modeling. The chapter is divided into three parts. Part 6-1 deals with hydrologic model uncertainty, and Part 6-2 deals with stability model uncertainty. Emphasis is placed on Part 6-2. Parts 6-1 and 6-2 are in turn subdivided into two parts. The first deals with model uncertainty that arises from idealizations and simplifications made in each model, and this includes models that are used within the same models, e.g. different soil characteristic models can be used within the same hydrologic model, and different soil strength models can be used within the same stability model. The second part deals with model uncertainty that arises from the models themselves, and assesses the effects of using different models (hydrologic and stability) on landslide hazards. Part 6-3 compares the effects of hydrologic and stability model uncertainty, and some general conclusions are drawn with regard to the relative effect of each on landslide hazards. Figure 6.3 shows a schematic outline of the chapter.

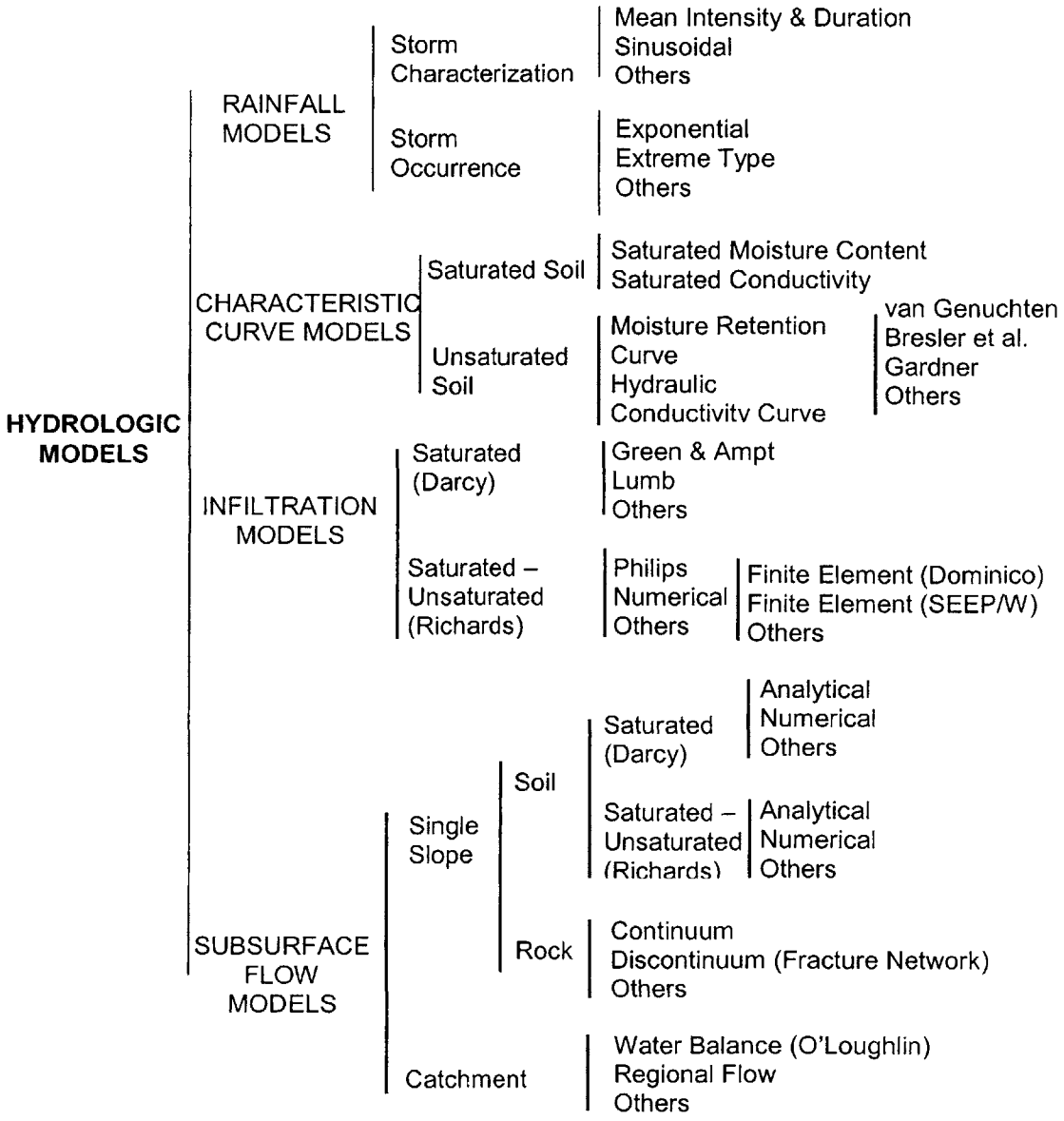

Figure 6.1. Possible Models used for Hydrologic Analyses

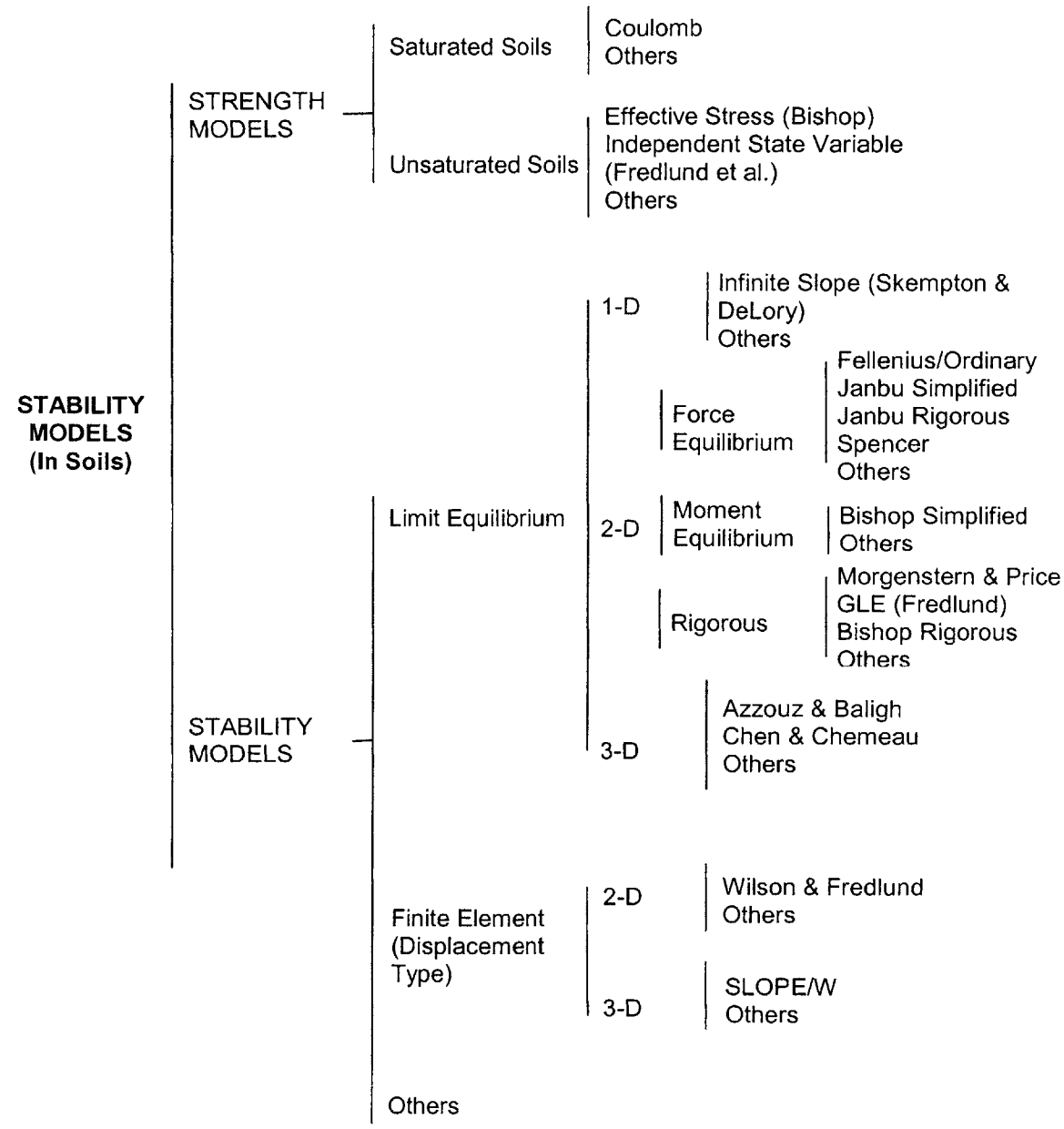

Figure 6.2. Possible Models used for Stability Analyses

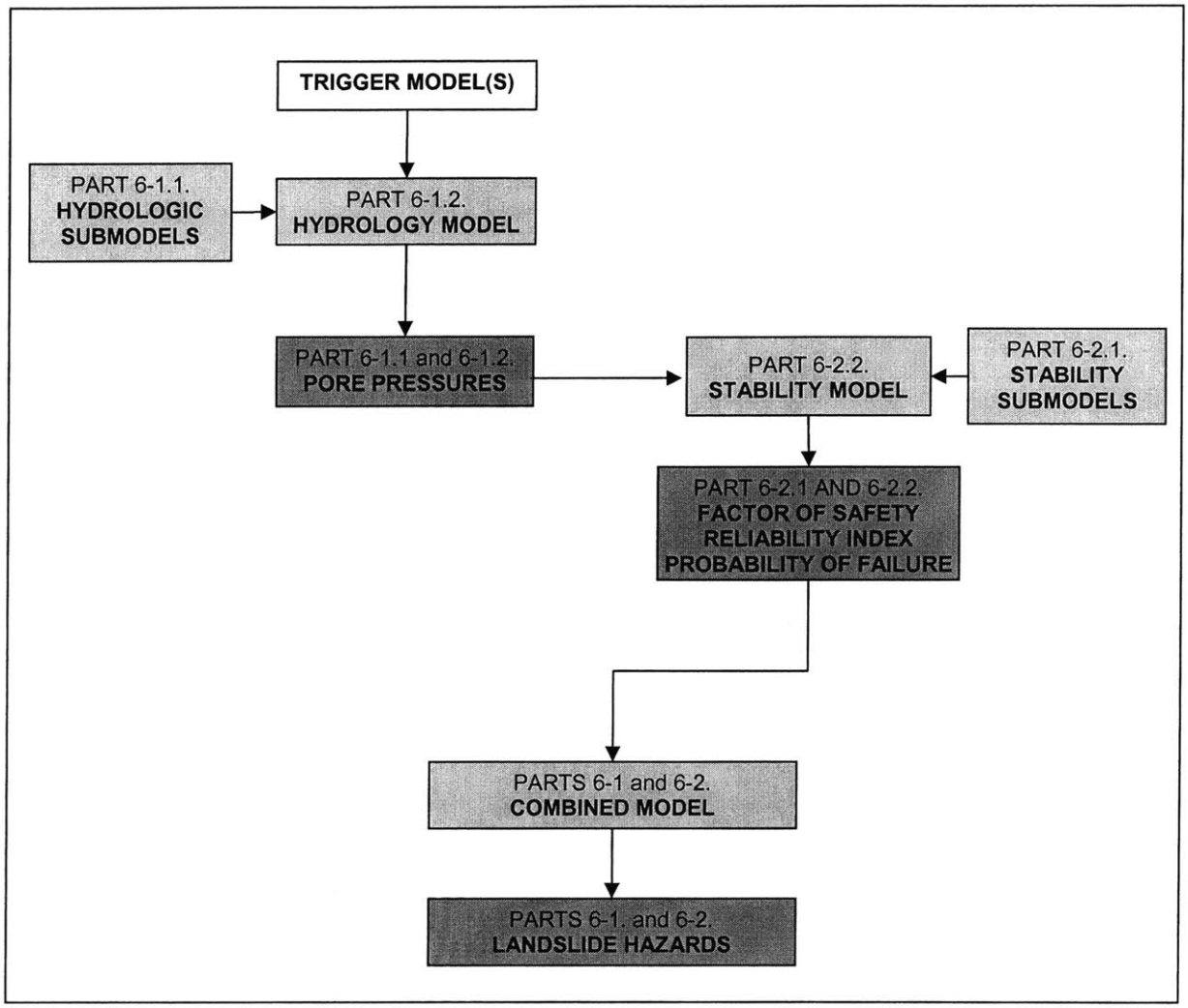

Figure 6.3. Schematic Outline of Chapter 6. The Effects of Different Submodels and Models (shown in lightly shaded boxes) on Hydrologic, Stability, Combined Modeling and Landslide Hazards (shown in dark boxes) are Investigated

The arrows in Figure 6.3 indicate the sequence with which landslide hazards are assessed. One starts off with a trigger model, and evaluates the hydrologic response of a slope to the triggering event. This output, in the form of pore pressure distributions with time, is then used in a stability model to evaluate the state of stability of a slope, using indicators such as Factors of Safety in the deterministic case, and reliability indices and probabilities in the probabilistic case. The combined hydrologic – stability model is then used to evaluate landslide hazards.

From Figure 6.3, and the sequence that has just been mentioned, it is evident that model uncertainty from hydrologic models (and submodels) has an effect on the results of

hydrologic modeling (pore pressures) as well as on landslide hazards. This is investigated in Part 6-1 of this Chapter, and hence the reason for the Part 6-1 indicated in the combined model and landslide hazards boxes in Figure 6.3. Similarly, model uncertainty from stability models (and submodels) has an effect on the results of hydrologic modeling (pore pressures) as well as on landslide hazards. This is investigated in Part 6-2 of this Chapter, and hence the reason for the Part 6-2 indicated in the combined model and landslide hazards boxes in Figure 6.3. Doing this allows one to compare the relative influence of model uncertainty from hydrologic models, and stability models on landslide hazards, and this is done at the end of the Chapter.

Various example slopes will be used to investigate the effects of different models and submodels shown in Figure 6.3 on hydrologic, stability and landslide hazards. Unless otherwise stated the following models and submodels are used:

For hydrologic analyses:

(a) The infiltration model developed in Chapter 2, Part 2-1 is used, with the van Genuchten (1981) model (see Chapter 2, Part 2-1) as a submodel for the soil characteristic curves.
(b) For probabilistic analyses, the hydraulic conductivity of the soil is assumed to follow a Lognormal Distribution.

For stability analyses:

(a) The stability model developed in Chapter 2, Part 2-2 that is based on the Janbu Simplified Model is used, with the Effective Stress Model (see Chapter 2, Part 2-2) as a submodel for unsaturated soil strength.
(b) For probabilistic analyses, the soil strength parameters c' and ϕ':
    i. Are assumed to follow Normal Distributions.
    ii. Are assumed to be uncorrelated. While one can be reasonably certain that c' and ϕ' are (negatively) correlated, particularly in soils, we assume that they are uncorrelated in order to evaluate the effects of a particular model (submodel) at any one time, rather than the combined effects of the model (submodel) and correlation. Correlation is investigated in detail in Section 6-2.1.3.1 of the Chapter.

PART 6 -1
MODEL UNCERTAINTY IN HYDROLOGIC ANALYSES

Figure 6.1 showed possible models for hydrologic analyses. These are typically models for the trigger (rainfall), as well as models to describe what happens when rainwater enters the soil.

Rainfall models include models for characterizing a particular rainstorm (characterization models), and models for predicting the occurrence of storms (occurrence models). Characterization models enter hydrologic analyses as input parameters or boundary conditions, e.g. see Chapter 2. Occurrence models attempt to predict, probabilistically, the occurrence of rainstorms. They enter landslide analyses to estimate the temporal component of landslide hazards (see Chapter 5). These models are subject to model uncertainty, but a detailed investigation is beyond the scope of this study.

Models to represent what happens to the rainwater as it enters the soil range from infiltration models on the single slope case, to subsurface flow models on the catchment or regional scale. In this chapter, emphasis is placed on infiltration models. Infiltration modeling is affected by two sources of model uncertainty:

(a) From models used within the infiltration model, such as the soil characteristic curve models (see Chapter 2), and
(b) From the infiltration model itself.

Note that different soil characteristic models can be used within the same infiltration model, and the same soil characteristic models can be used in different infiltration models.

Figure 6.4 shows a schematic of what will be studied in more detail in Part 6-1 of this chapter.

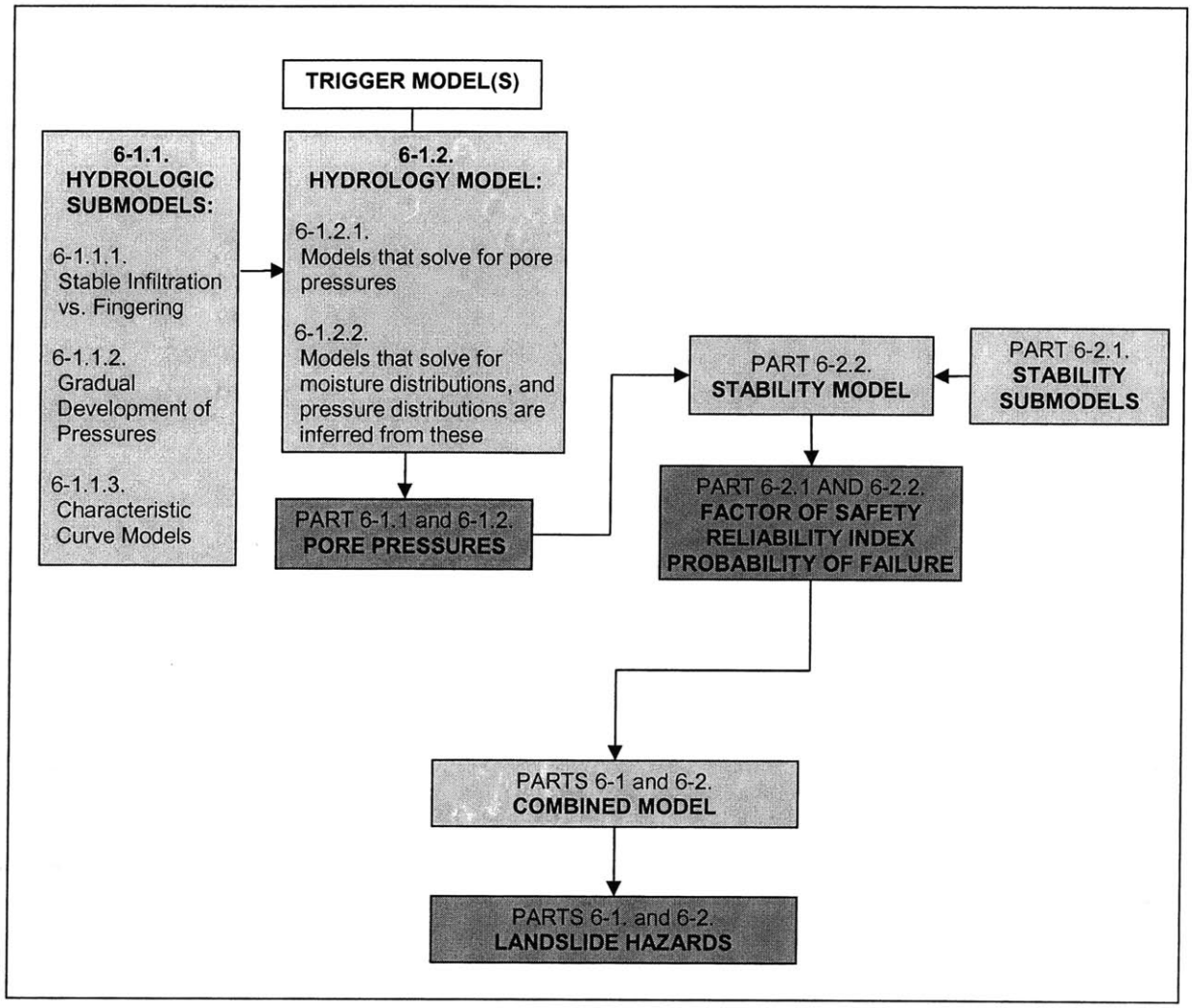

Figure **6.4.** Schematic showing Hydrologic Modeling.
The effects of the different submodels (shown in the lightly shaded box) and the different types of hydrologic models (shown in lightly shaded box) on the results of hydrologic analyses (pore pressures in the dark shaded box) and on landslide hazards (dark box) are investigated

6-1.1. MODEL UNCERTAINTY FROM SUBMODELS IN INFILTRATION MODELS

Different simplifications and assumptions/submodels are made in different infiltration models, leading to the different complexity (and dimensionality) of such models. In this Section we study the effects of different submodels on the results of hydrologic analyses and landslide hazards. For example, the infiltration model developed in Chapter 2, assumes one dimensional vertical infiltration, whereas the process of infiltration is much more complex. There is however, one overriding assumption that is inherent to the vast majority of infiltration models, namely that of stable infiltration.

6-1.1.1. STABLE INFILTRATION

In this Section, we asses, qualitatively, the assumption of stable infiltration in hydrologic modeling. This is shown in bold in Figure 6.5.

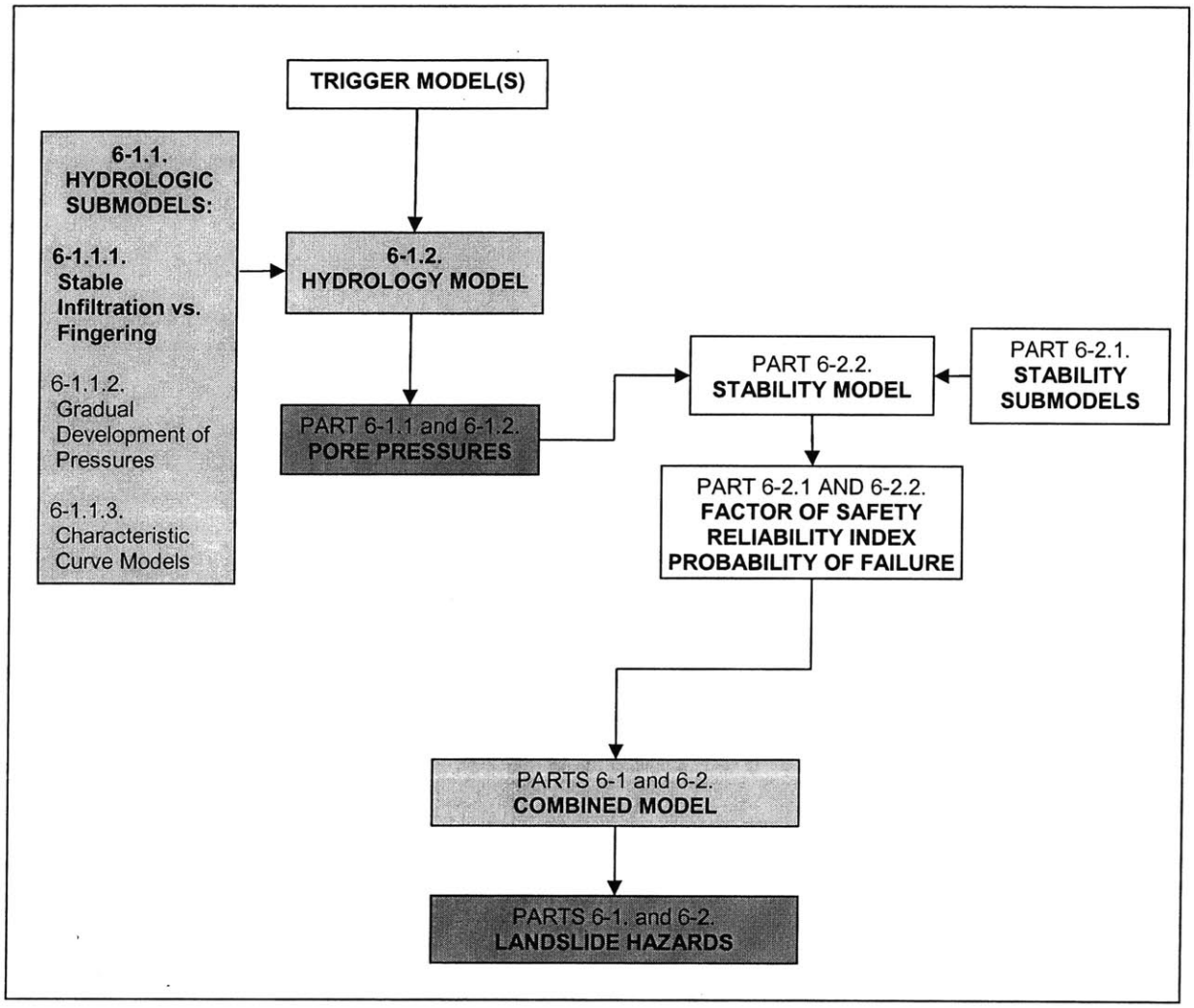

Figure 6.5. The effects of stable infiltration (shown in bold in the lightly shaded submodels box) on the results of hydrologic analyses (pore pressures in the dark shaded box) and on landslide hazards (dark box) are investigated

When the rate of water application e.g. rainfall is less than the saturated conductivity of the soil, the intensity is not sufficient to fully saturate the soil. The vast majority of infiltration models, including the one developed in Chapter 2, assumes that water infiltrates the soil in the form of a stable and planar wetting front. Numerous laboratory

infiltration experiments have, however, shown that in many cases, preferential flow paths develop through which water flows (Hill, 1952). Traditionally, it had been believed that this phenomenon only occurs in heterogeneous soils, but more recent studies e.g. Hill and Parlange (1972), Liu et al. (1994) have shown that this can occur in homogenous soils as well.

In heterogeneous soils, the phenomenon can be attributed to funneling, which is flow directed by heterogeneous structures (Kung, 1998), and/or channeling, which is flow thorough cracks and micro-pores (Tindall and Kunkel, 1997). In homogenous soils, the phenomenon, also known as fingering, is caused by gravity driven wetting front instability when the infiltrating flux is insufficient to fully saturate the soil (Hill, 1952). This condition can occur with a uniform application rate, or when there is an increase in hydraulic conductivity of the soil with depth, e.g. when a fine-textured soil overlies a coarser layer (Culligan et al., 1997). During infiltration, the wetting front will encounter inherent microscopic heterogeneities that cause small perturbations in the front. If the pressures acting to destabilize flow exceed those to stabilize it, then a finger will develop from this perturbation (Kueper and Frind, 1994).

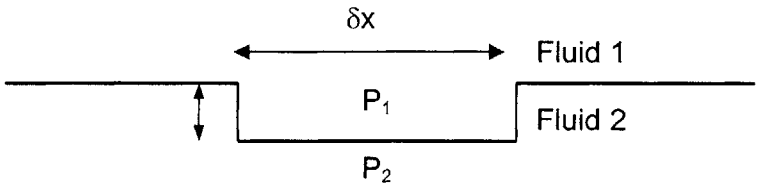

$$P_1 = \gamma_1 \delta x - \frac{q \upsilon_1 \delta x}{k}$$

$$P_2 = \gamma_2 \delta x - \frac{q \upsilon_2 \delta x}{k}$$

where:
q is the water application rate
γ is unit weight
υ is viscosity
k is permeability

$$P_1 - P_2 = (\gamma_1 - \gamma_2)\delta x - (\upsilon_1 - \upsilon_2)\frac{q \delta x}{k}$$

Condition for instability, and finger formation is:

$$P_1 > P_2$$

Since in the case of water infiltration, Fluid 1 is water, and Fluid 2 is air:
$\gamma_1 = \gamma_w$, $\upsilon_1 = \upsilon_w$ and $\gamma_2 = 0$, $\upsilon_2 = 0$,

the condition for instability is expressed as:

$$q < \frac{\gamma_w k}{\upsilon_w} \equiv K_s$$

where:

K_s is the hydraulic conductivity

Figure 6.6. Wetting Front Instability

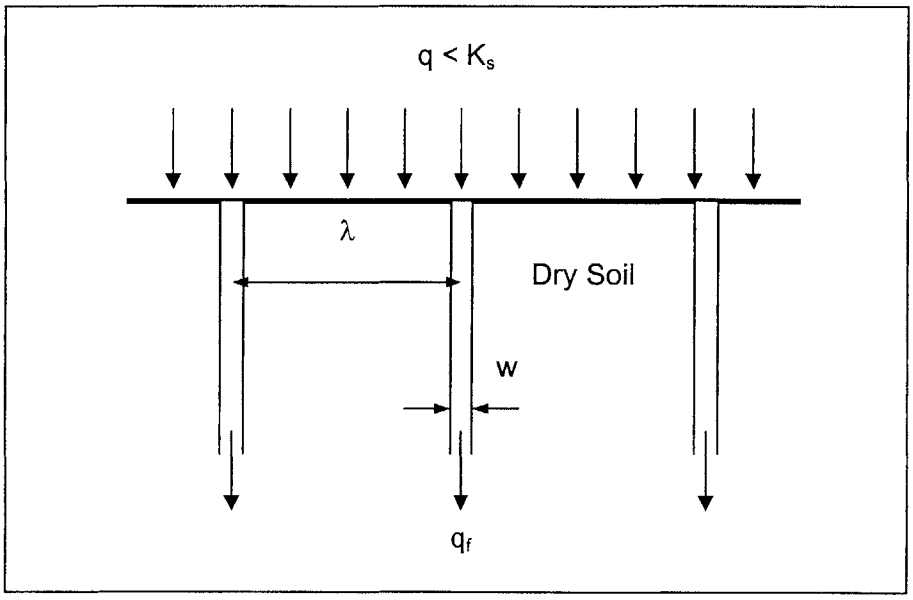

Figure 6.7. Finger Development and Characteristics

Attempts have been made to describe finger properties (Glass et al., 1975; Hill, 1952), characterized by width λ and spacing w (see Figure 6.7) and several numerical infiltration models have been developed to model the process of fingering (e.g. Hendrickx and Yao, 1996; Glass et al., 1991; Dekker and Ritsema, 1994). These models remain crude at best, because of the complexities involved in the process. These models are, therefore, themselves subject to model uncertainty.

The effect of finger development and preferential flow is that infiltration takes place at a greater rate than that described by a stable infiltration model, such as the one in Chapter 2. The rate of infiltration is equal to the velocity of flow through the fingers. This velocity $u_f = \frac{q_f}{\theta}$ where q_f is the water flux through the fingers, and θ is the moisture content (see Figure 6.7). It has been observed experimentally that $q_f \approx K_s$ the saturated conductivity of the soil, and hence $u_f \approx \frac{K_s}{\eta}$ where η is the soil porosity.

The implications of finger development with regard to landslide analyses can be significant. The infiltrating rainwater can percolate directly, and much quicker than described by stable models, to the water table causing it to rise. If such is the case, the failure mechanism by which landsliding would take place would be different than that predicted by a stable model. Failure would take place by saturation from below (see Chapter 3) as opposed to failure by saturation from above (see Chapter 3) which is what is predicted by the stable model.

6-1.1.2. GRADUAL DEVELOPMENT OF PRESSURES

Another assumption frequently used in hydrologic analyses is that of the gradual development of pressures during rainfall. If, however, during a short intense rainfall the rate of infiltration is equal to the rainfall intensity, suction is eliminated down to a certain depth. Once the rainfall intensity exceeds the infiltration rate, whether due to a decrease in the infiltration rate with time, or due to an increase in rainfall intensity large pressures rapidly develop behind the wetting front, and may cause an associated sudden failure. This phenomenon which was observed by Lambe (1980), cannot be explained by the assumption of a gradual change of pressures from negative to hydrostatic conditions. Moreover, this phenomenon can occur in homogenous soils without the requirement of a low permeability layer to retard the front. This mechanism for the sudden generation of large pressures was discussed in Chapter 3. Hydrologic models that make the assumption of gradual change of pressures are incapable of capturing this phenomenon. This is particularly true for models that are based on the solution to the moisture based form of the variably saturated (or unsaturated) flow Equation (see Part 2-1 of Chapter 2).

6-1.1.3. CHARACTERISTIC CURVE SUBMODEL UNCERTAINTY

More advanced infiltration models that solve for the unsaturated and/or variably saturated flow Equation require the specification of unsaturated soil properties through models for the characteristic functions of the soil. This was discussed in Part 2-1 of Chapter 2. Various characteristic curve models have been proposed in the literature e.g. Gardner (1956), Brooks and Corey (1966), Bresler et al. (1978), van Genuchten (1981). These are subject to model uncertainty as they attempt to represent the true behavior of unsaturated soils.

In this Section, we try to illustrate model uncertainty that from the characteristic curve models. We investigate the effects of assuming different characteristic curve models on the pressure profiles that results from hydrologic analyses, and the implications these have on estimated landslide hazards. This is shown in bold in Figure 6.8.

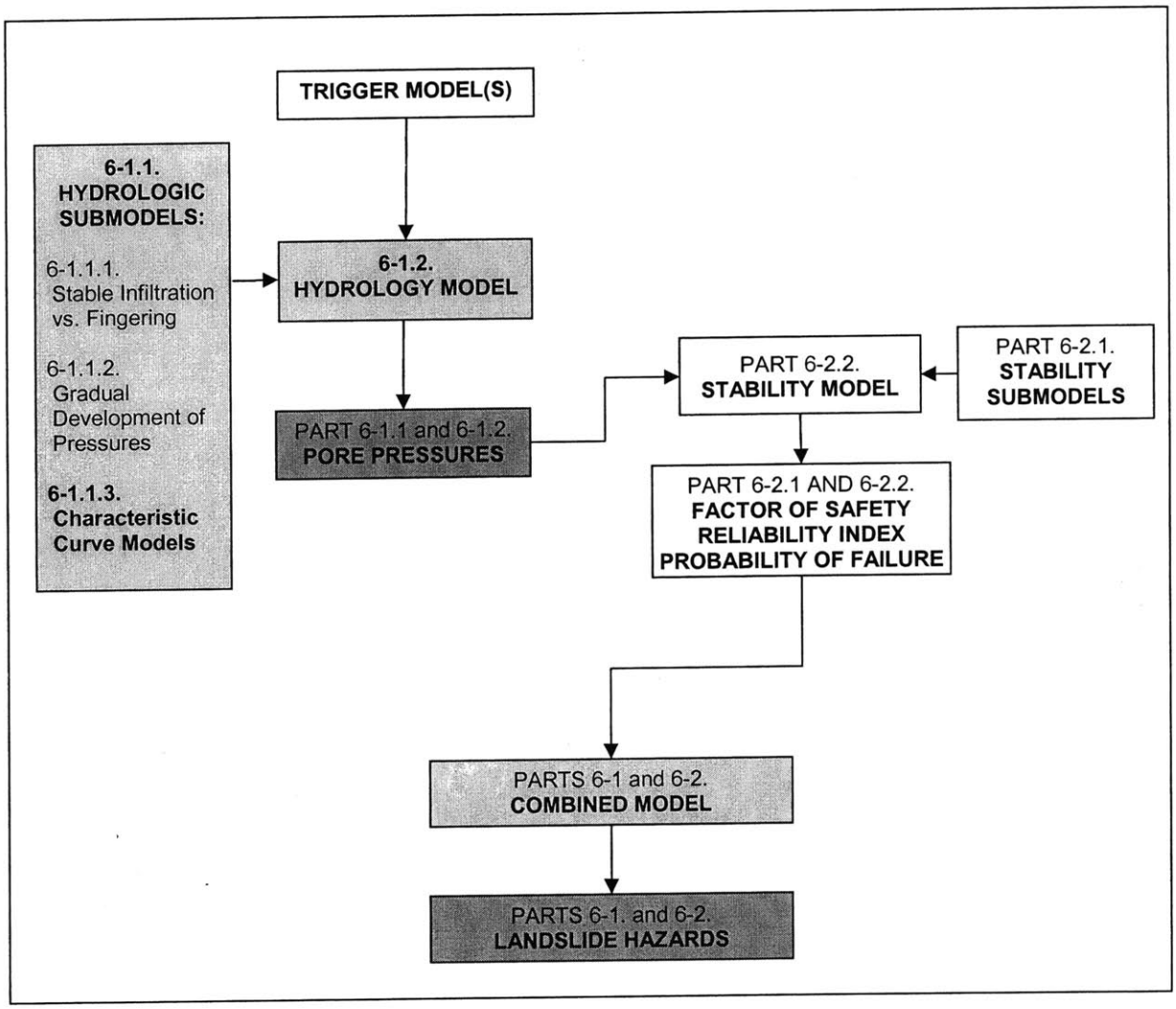

Figure **6.8.** The effects of characteristic curve models (shown in bold in the lightly shaded submodels box) on the results of hydrologic analyses (pore pressures in the dark shaded box) and on landslide hazards (dark box) are investigated

For this purpose we consider the models developed by van Genuchten (1981) and those by Bresler et al., (1978). The van Genuchten (1981) models were described in Chapter

2, Part 2-1 (see Equations [2.1] to [2.4]), and have been used in the analyses in this study thus far. The Bresler et al., (1978) model is given by:

$$S_e = 1 \qquad \psi \geq \psi_{entry} \qquad [6.1]$$

$$S_e = \left(\frac{\psi_{entry}}{\psi} \right)^{\beta} \qquad \psi < \psi_{entry} \qquad [6.2]$$

$$K = K_s \qquad \psi \geq \psi_{entry} \qquad [6.3]$$

$$K = K_s \left(\frac{\psi_{entry}}{\psi} \right)^{\alpha} \qquad \psi < \psi_{entry} \qquad [6.4]$$

where:

α and β are empirical coefficients

ψ_{entry} is the air entry pressure head value

K_s is the saturated conductivity

$S_e = \frac{\theta - \theta_r}{\theta_s - \theta_r}$ where θ_s is the saturated moisture content, and θ_r is the residual moisture content, defined in Chapter 2, Part 2-1.

As with the van Genuchten (1980) model, the Bresler et al., (1978) model has two parameters, α and β. These need to be specified/assumed, and are subject to parameter uncertainty.

To investigate the effects of characteristic curve model uncertainty on hydrologic analyses, and landslide hazards, we consider the slope shown in Figure 6.9.

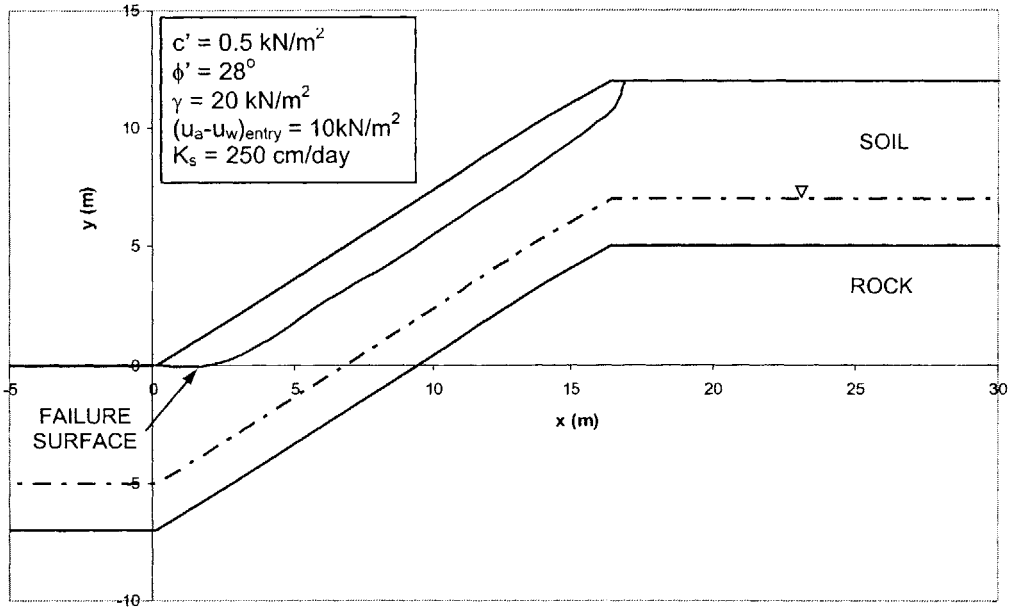

Figure 6.9. Slope Geometric and Strength Parameters

The slope geometric and soil strength parameters are shown in Figure 6.9.

6-1.1.3.a. VAN GENUCHTEN (1980) SUBMODEL

The van Genuchten (1980) Model (see Chapter 2) is used to describe the soil characteristic curves which are shown in Figures 6.10 and 6.11.

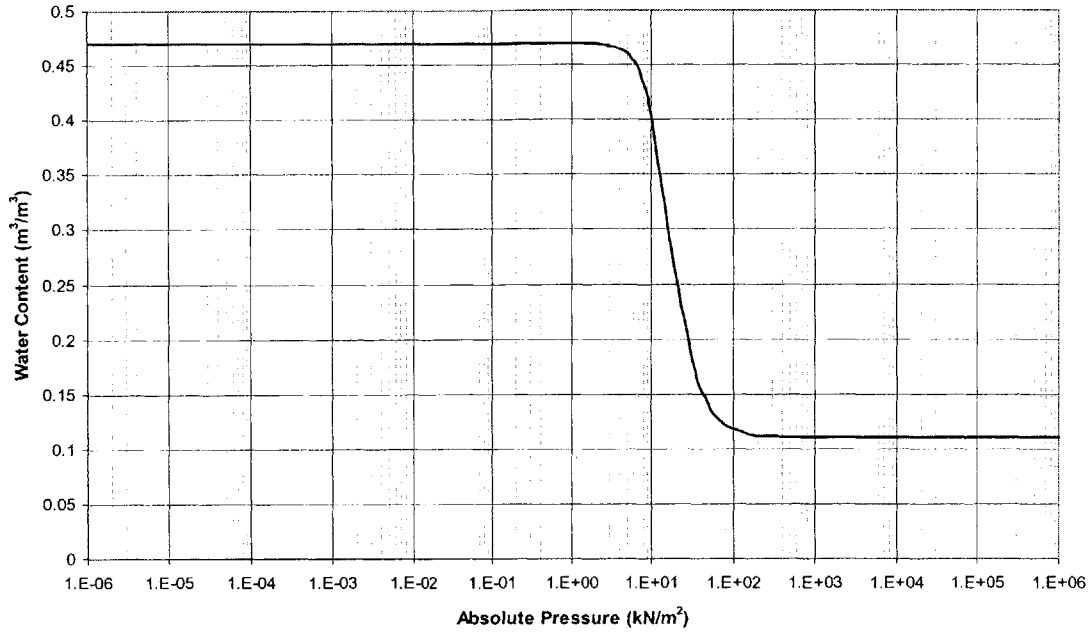

Figure 6.10. Moisture Retention Characteristic Curve

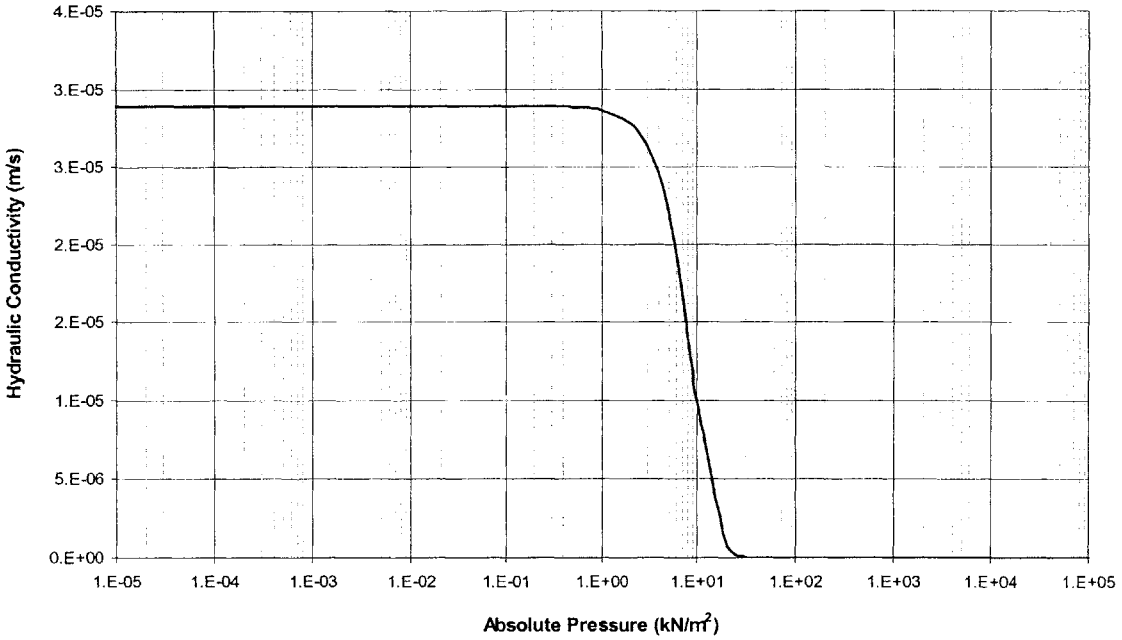

Figure 6.11. Hydraulic Conductivity Characteristic Curve

A rainfall event with intensity, $I = 75mm/hr$ is assumed to occur for a duration of 8 hours. The moisture content and pressure profiles at different times are as shown in Figures 6.12 and 6.13 respectively.

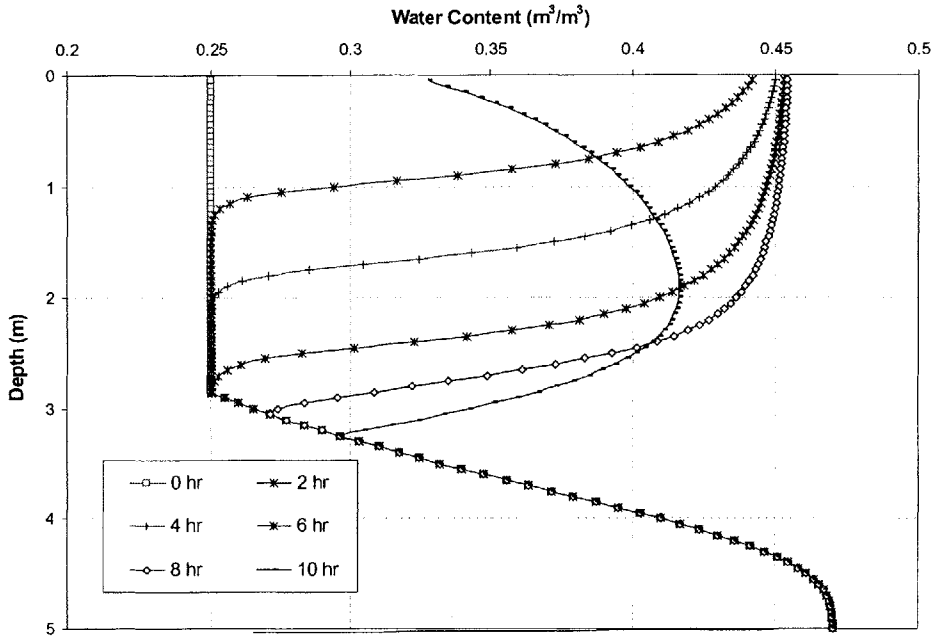

Figure 6.12. Moisture Content Profiles with Time using the van Genuchten (1980) Model

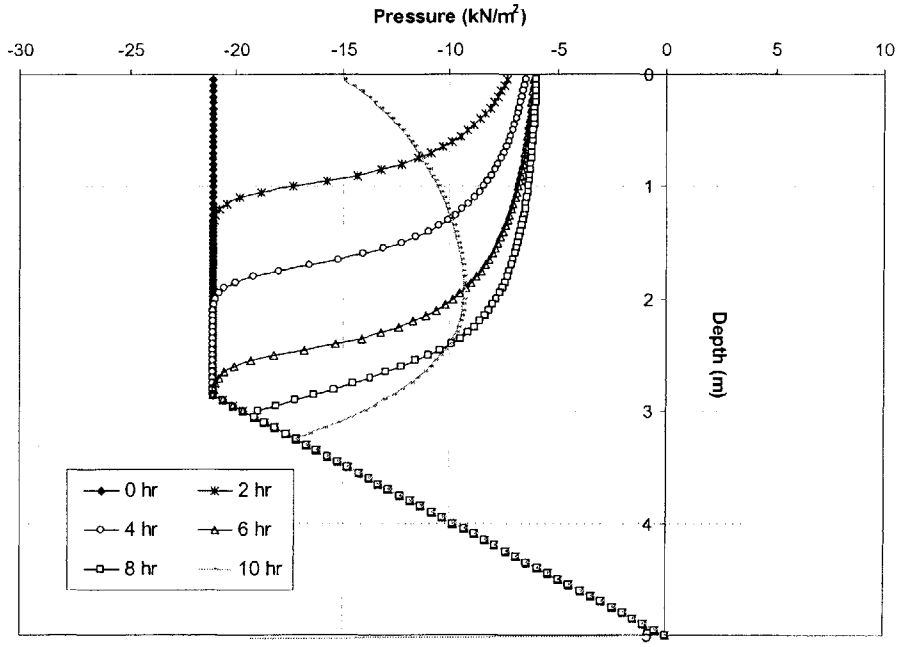

Figure 6.13. Pressure Profiles with Time using the van Genuchten (1980) Model

6-1.1.3.b. BRESLER ET AL. (1978) SUBMODEL

In order to perform a meaningful comparison of both characteristic curve models, the parameters α and β of the Bresler et al., (1978) model (see Equations [6.1] to [6.4]) are chosen in such a way so that the initial suction in the soil corresponding to the initial moisture content of $\theta_i = 0.25$ (see Figure 6.12) is the same for both models. This is shown in Figure 6.14.

Figures 6.14 and 6.15 show the moisture content and hydraulic conductivity characteristic curves using both models.

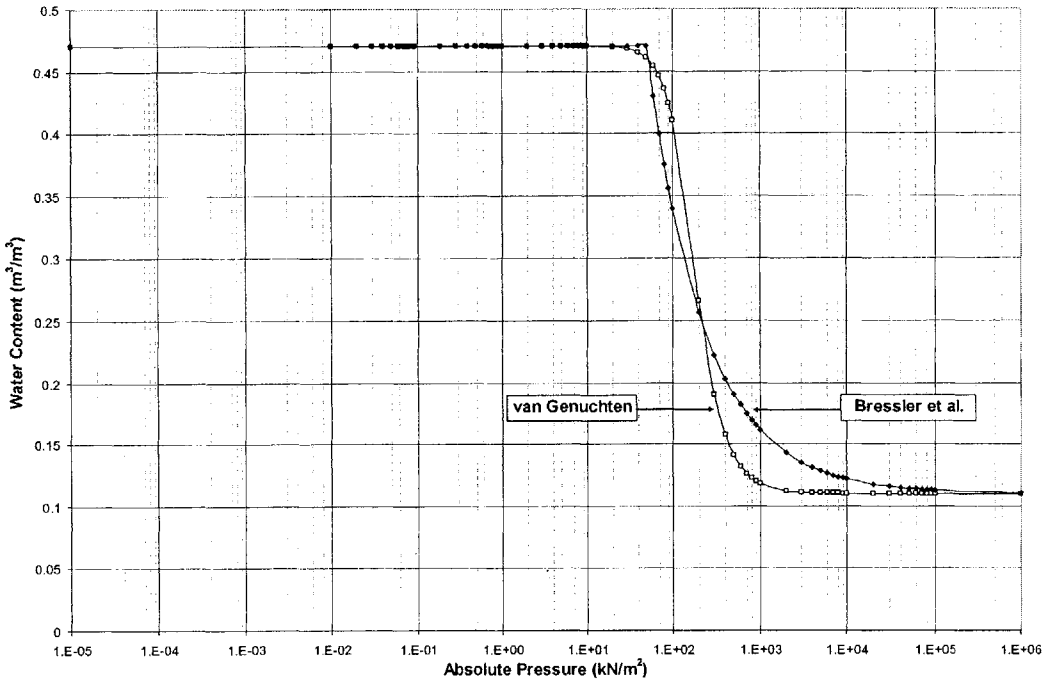

Figure **6.14.** Comparison of Moisture Characteristic Curve Using Two Characteristic Models

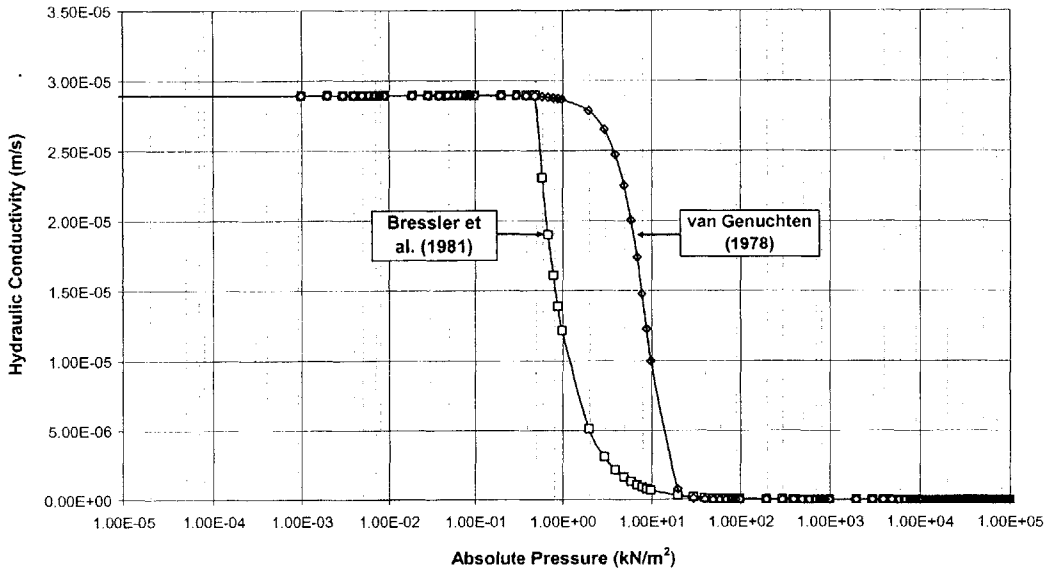

Figure 6.15. Comparison of Conductivity Characteristic Curve Using Two Characteristic Models

The difference in the curves of Figures 6.14 and 6.15 already illustrates characteristic curve model uncertainty for the specified parameters of each model, even when these have been chosen to best match each other.

Figure 6.16 shows moisture content profiles during the rain event using the van Genuchten (1980) model, and Figure 6.17 shows these using the Bresler et al., (1978) model.

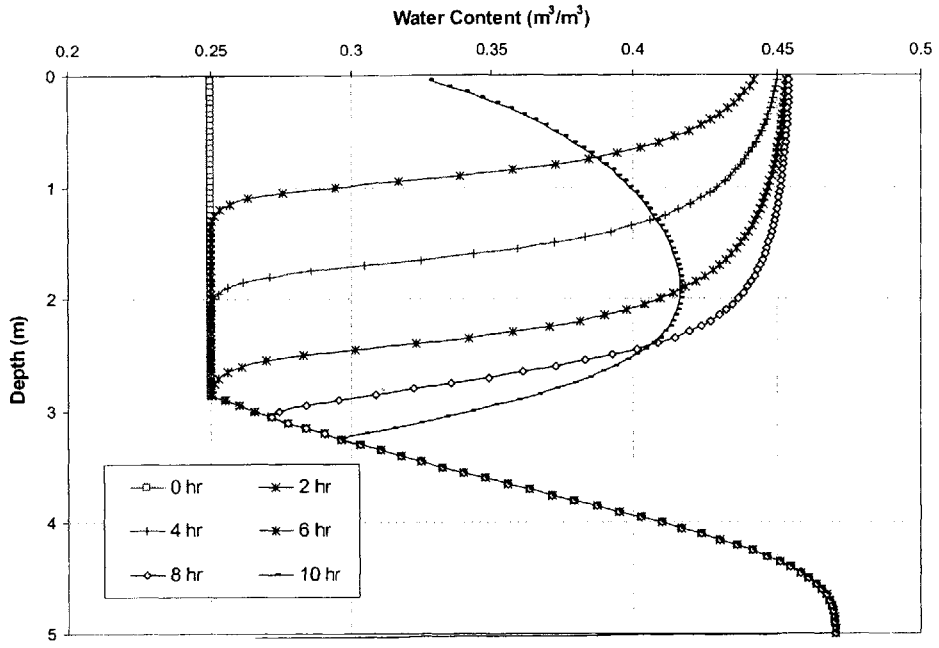

Figure **6.16.** Moisture Content Profiles with Time using the van Genuchten (1980) Model

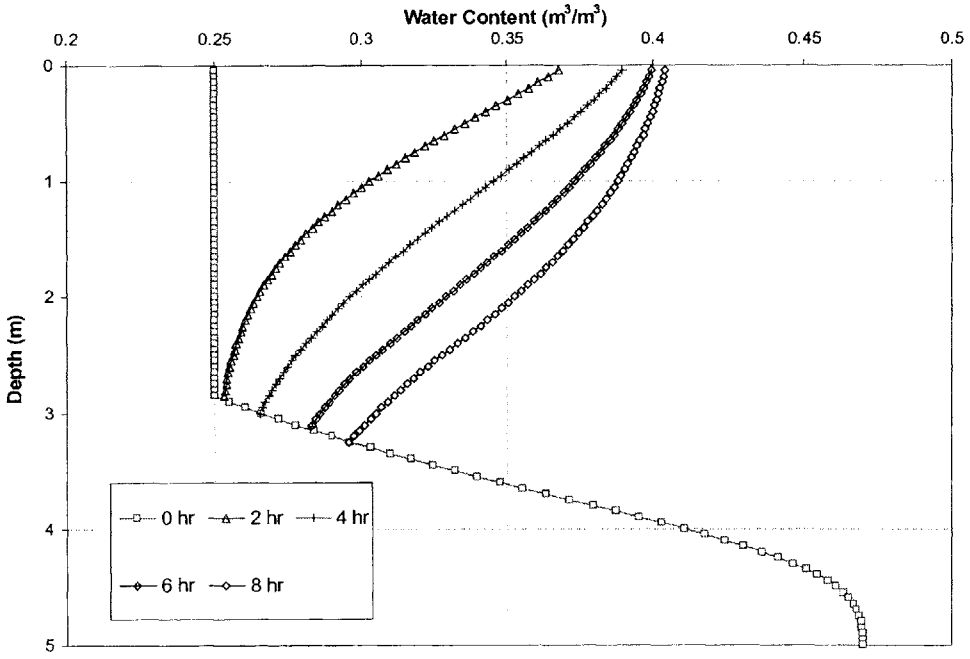

Figure **6.17.** Moisture Content Profiles with Time using the Bresler et al., (1978) Model

Figure 6.18 shows pressure profiles using the van Genuchten (1980) model, and Figure 6.19 shows these using the Bresler et al., (1978) model.

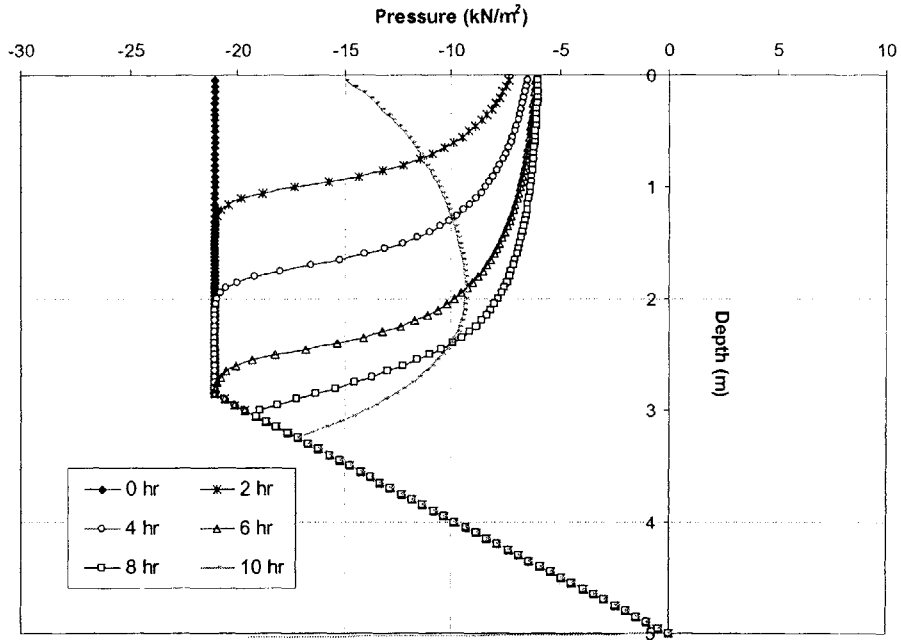

Figure **6.18.** Pressure Profiles with Time using the van Genuchten (1980) Model

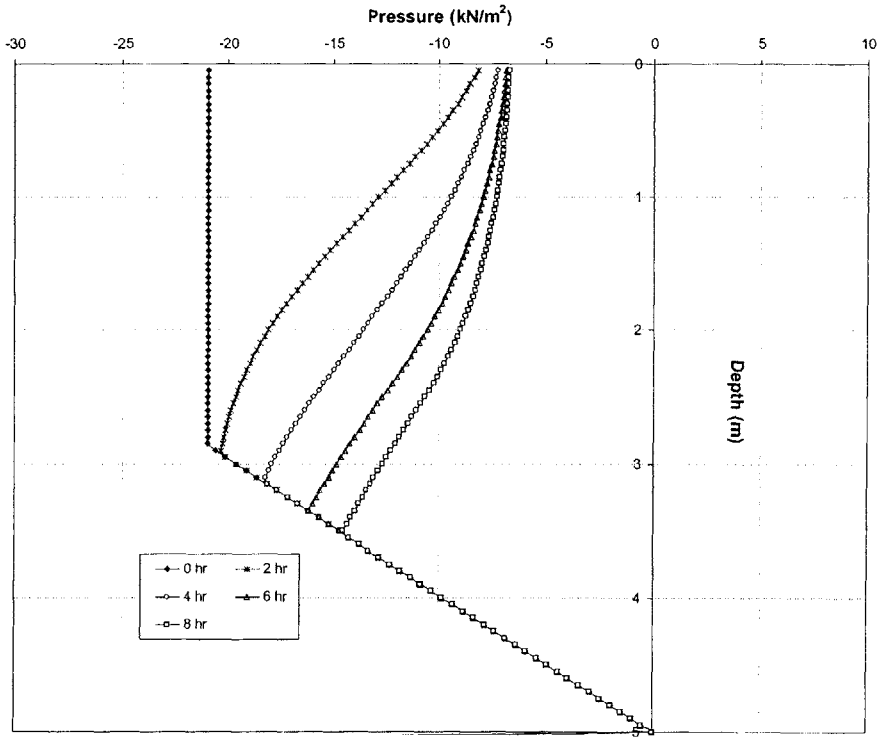

Figure **6.19.** Pressure Profiles with Time using the Bresler et al., (1978) Model

Figures 6.16 and 6.17, and 6.18 and 6.19 illustrate the effects of characteristic curve model uncertainty on the results of hydrologic analyses. Comparing Figures 6.18 and 6.19 shows that the moisture profiles are sharper when the van Gentchen (1978) model is used. This is because the moisture retention curve using the van Genuchten (1980) model is steeper, and the results in Figures 6.18 and 6.19 are consistent with what has been described in more detail in Part 5-1 of Chapter 5.

Figure 6.20 compares the pressure profiles, which will be used in stability analyses later, using both models.

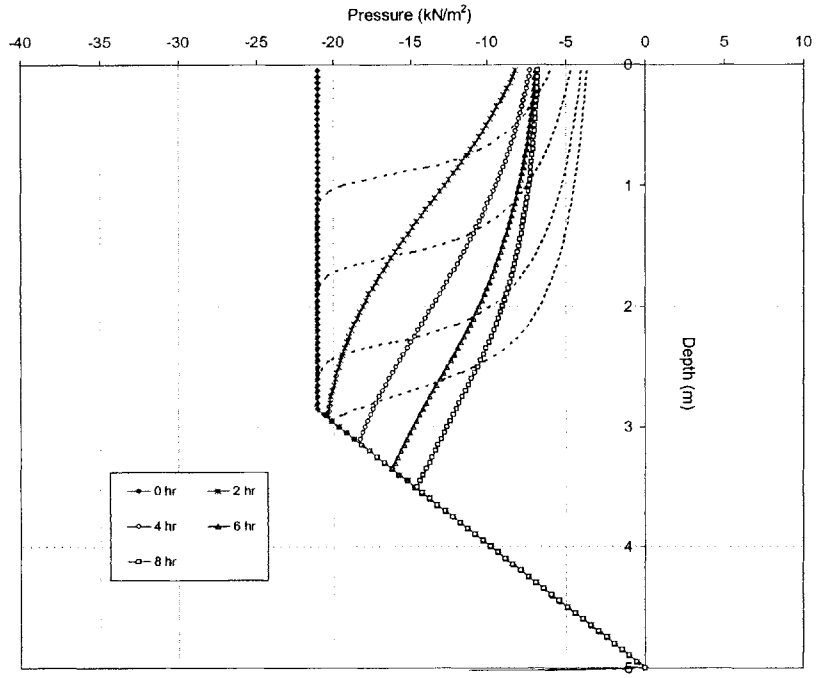

Figure **6.20.** Comparison of Pressure Profiles from van Genuchten (1980) Model (Dashed Lines) and Bressler et al. (1980) Model (Solid Lines and Symbols)

The difference in the results in Figure 6.20 illustrates the effects of characteristic curve model uncertainty on the results of hydrologic analyses, through the different pressure profiles.

Figure 6.21 shows the variation of Factor of Safety with time using both models, and illustrates the effects of characteristic model uncertainty on deterministic landslide hazards assessment.

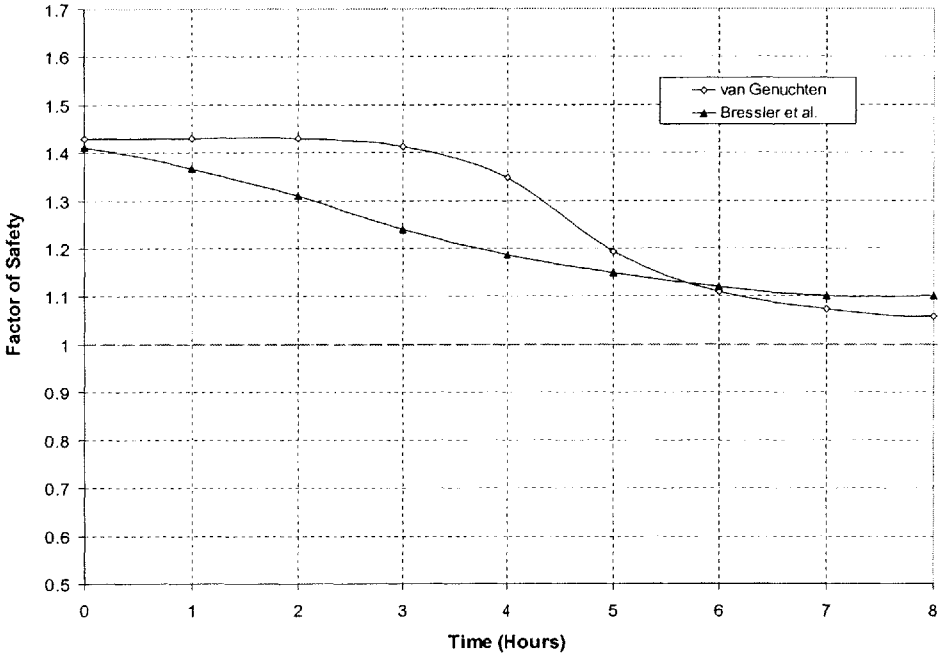

Figure **6.21.** Comparison of Deterministic Results using the van Genuchten (1980) and Bresler et al., (1978) Models

Figure 6.21 shows that even though the parameters have been chosen to give the same initial conditions (and the same initial Factor of Safety at t = 0 hrs in Figure 6.21), the Factor of Safety can be significantly different depending on the model chosen. This is particularly the case at earlier times during the rain event, as different models predict different degrees of saturation (see Figures 6.16 and 6.17), and hence different pore pressures (see Figures 6.18, 6.19 and 6.20) on the failure surface, which as shown in Figure 6.9 is at depth of about 2 m below the ground surface. The results from both models converge with time, as both models predict the complete saturation of the soil at the failure surface, and the pore pressures become similar in magnitude. So, for a shorter duration rain event, say 3 hours, each model would predict significantly different results, and the effects of characteristic model uncertainty would be more substantial. For longer duration rain, both models predict saturation and the results from both models are similar.

We now investigate the effects of characteristic model uncertainty on probabilistic landslide hazards assessment. We assume that c', ϕ' and K_s are uncertain with the following distributions:

$c' \sim N(m_{c'} = 0.5kN/m^2, \sigma_{c'} = 0.0125kN/m^2)$; $\phi' \sim N(m_{\phi'} = 28^o, \sigma_{\phi'} = 7^o)$;

$K_s \sim LN(m_{K_s} = 250cm/day, \sigma^2_{K_s} = (125cm/day)^2)$; and these parameters are uncorrelated.

The uncertainty in the saturated conductivity will lead to uncertainty in the soil characteristic curves using each of the van Genuchten (1980) and Bressler et al. (1978) models. Since these models predict different characteristic curves, the uncertainty in these curves will also be different, and in this example we investigate the effects of the different uncertainty on probabilistic landslide hazards.

Figure 6.22 shows the variation of probability of slope failure with time using both characteristic curve models.

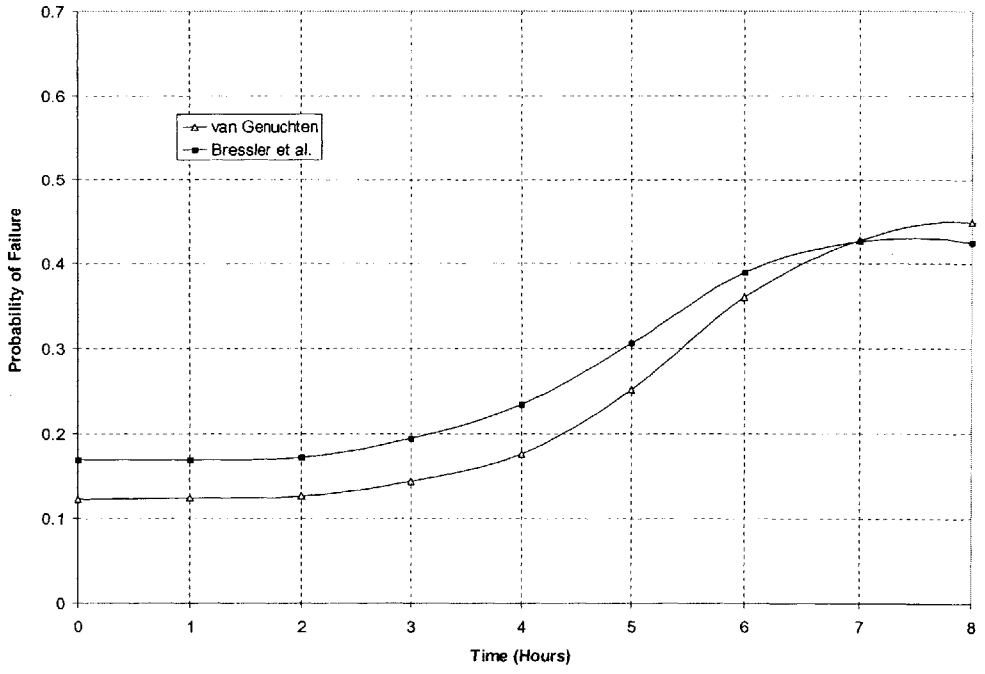

Figure 6.22. Comparison of Probabilistic Results using the van Genuchten (1980) and Bresler et al., (1978) Models

Figure 6.21 shows that the effects of characteristic model uncertainty on probabilistic analyses can be significant. The difference in the probabilities of failure in Figure 6.23 is solely due to the different characteristic models. This difference is greatest at early times, when the pore pressures on the failure surface are most different (see Figure 6.21). The results become more similar when the pressures on the failure surface become similar (see Figure 6.21) with increasing time.

6-1.2. MODEL UNCERTAINTY FROM HYDROLOGIC MODELS

Various hydrologic models have been proposed over the years, some of which are shown in Figure 6.1. Infiltration models are hydrologic models that predict pore pressures in the subsurface given certain hydrologic boundary conditions, e.g. rainfall. These models are used in landslide analyses. Infiltration models differ in two major ways; in whether they solve for the moisture based or pressure based form of the flow Equation (see Chapter 2), and in dimensionality. In this Section, only one dimensional models are considered. In this Section we study the effects of model uncertainty from different hydrologic models on the results of hydrologic analyses and landslide hazards. This is shown schematically in Figure 6.23.

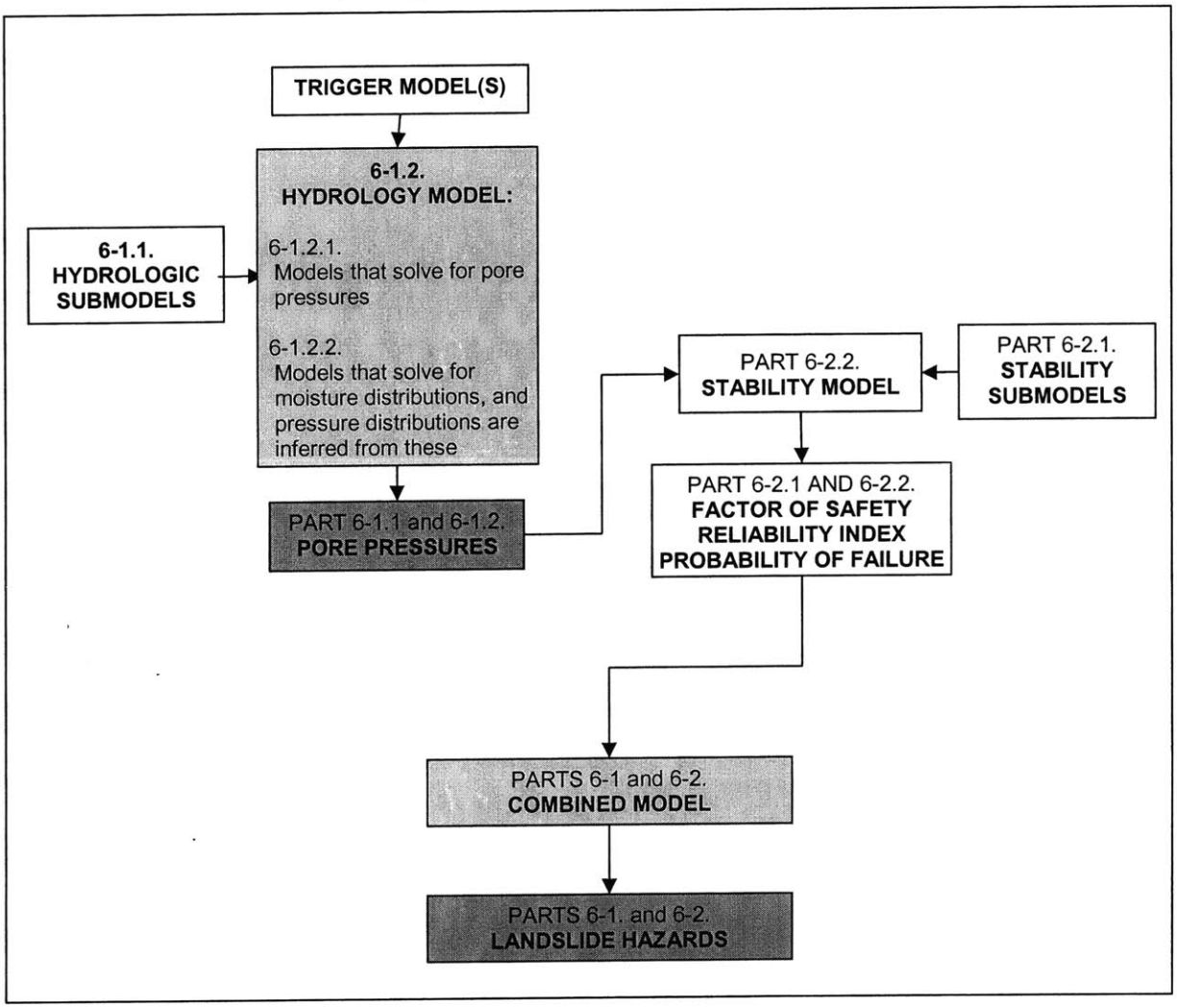

Figure **6.23.** The effects of different hydrologic models (shown in bold in the lightly shaded hydrologic models box) on the results of hydrologic analyses (pore pressures in the dark shaded box) and on landslide hazards (dark box) are investigated

Section 6-1.2.1 deals with models that solve for the pressure based form of the flow Equation, and 6-1.2.2. deals with models that solve for the moisture based form of the flow Equation.

6-1.2.1. MODELS THAT SOLVE FOR PRESSURE BASED FORM OF FLOW EQUATION

Models that solve the pressure based form of the flow Equation result in pressure profiles with time. These are used directly in stability models when assessing landslide hazards. One such infiltration model was developed in Chapter 2, where the model output is in the form of pore pressures for a set of initial and boundary conditions. The model is a finite difference solution to the one dimensional variably saturated flow Equation. Further details of the model are given in Part 2-1 of Chapter 2. To illustrate model uncertainty from hydrologic models, we compare the results from this model with those from HYDRUS (Vogel et al., 1996). Water is applied on top of an initially uniformly moist ($\theta_i = 0.08\,m^3/m^3$) homogenous soil. The soil characteristic curves are shown in Figures 6.24 and 6.25.

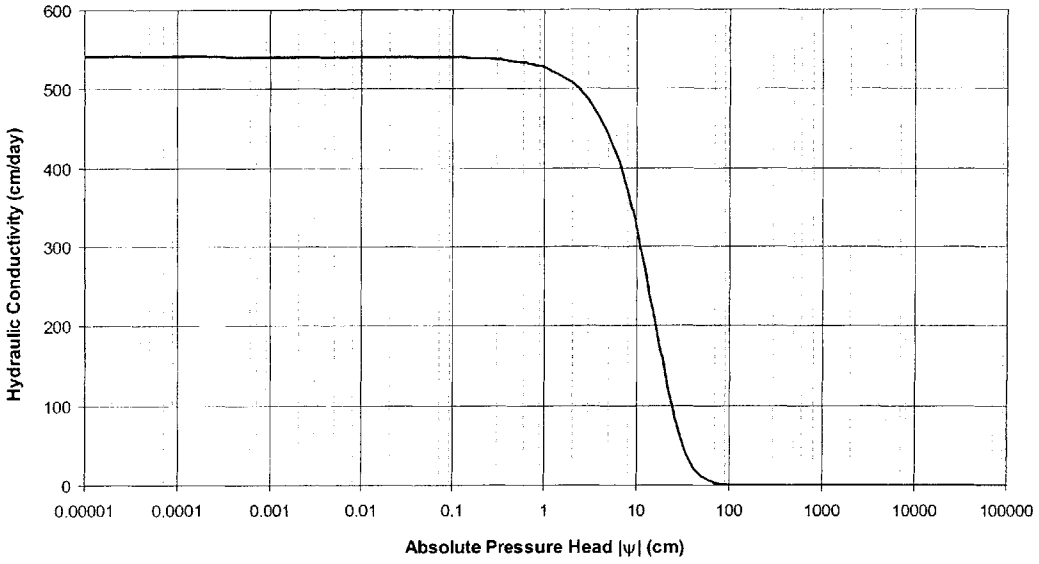

Figure **6.24.** Moisture Retention Curve

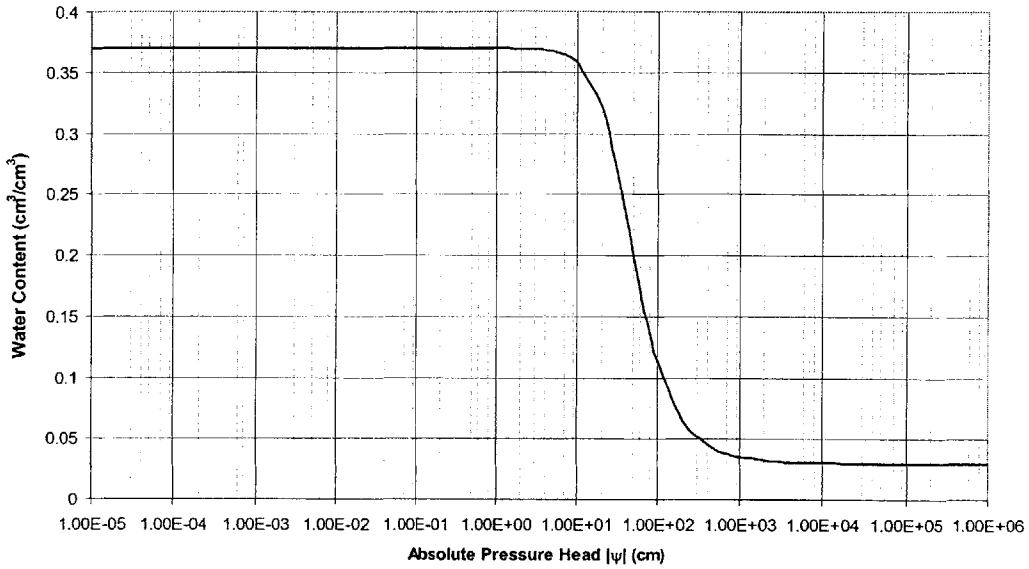

Figure **6.25.** Hydraulic Conductivity Curve

Water is applied at a constant rate of 2.5 cm/h for the first 4 hours, followed by a zero application rate. Figures 6.26 and 6.27 compare the results obtained by the spreadsheet model with those from Vogel et al. (1996).

The results from the spreadsheet model are shown in symbols and those from Vogel et al. (1996) are shown as solid lines.

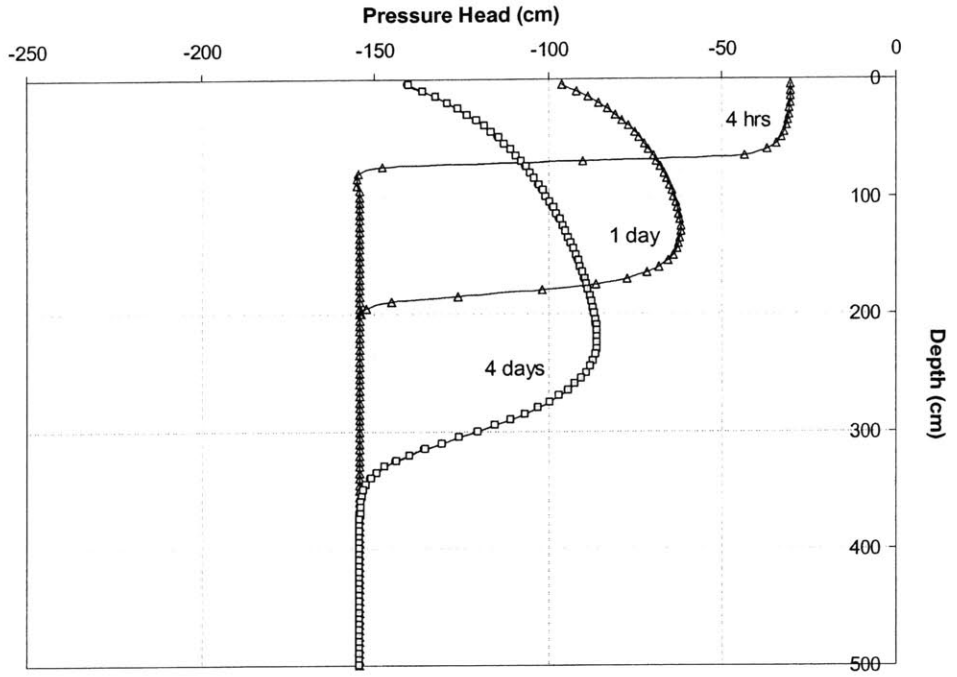

Figure 6.26. Pressure Head Profiles Generated by HYDRUS (solid lines) and the Spreadsheet Based Numerical Scheme (symbols)

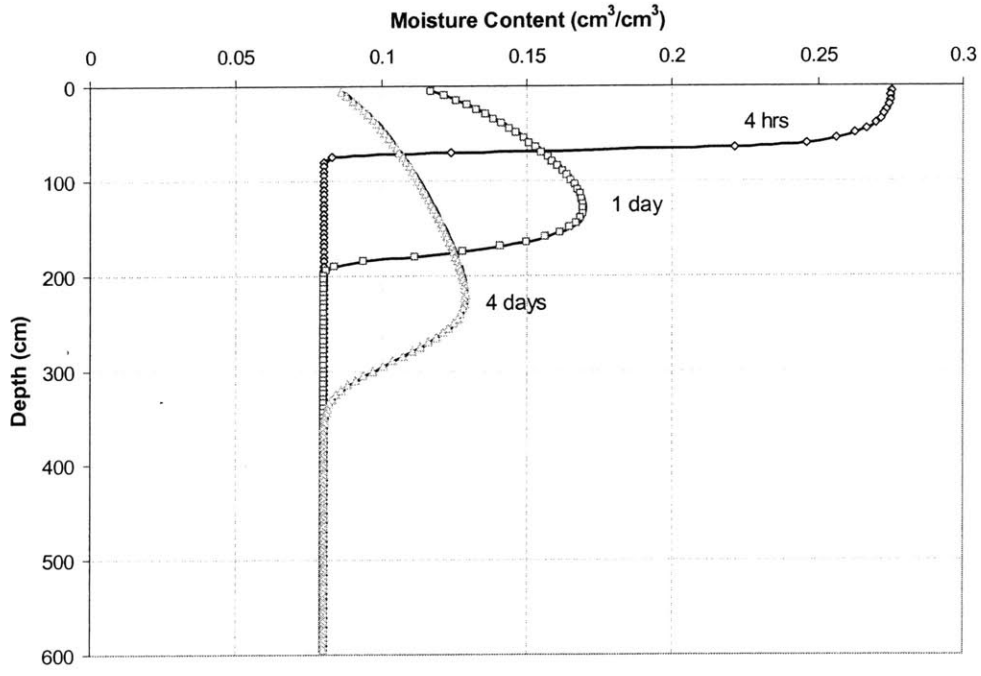

Figure 6.27. Moisture Content Profiles Generated by HYDRUS (solid lines) and the Spreadsheet Based Numerical Scheme (symbols)

The results in Figures 6.26 and 6.27 show that there is not a significant difference between the results using the two models. Both models solve for the one dimensional pressure based form of the variably flow Equation (and hence the same mathematical Equation) with the same initial boundary conditions. The results are almost the same, differences may occur in the efficiency of solutions.

6-1.2.2. MODELS THAT SOLVE FOR MOISTURE BASED FORM OF FLOW EQUATION

Models that solve the moisture based form of the flow Equation result in moisture profiles with time. Pressures and pressure profiles are then inferred from these moisture distributions, through the soil characteristic curves, and used in stability models when assessing landslide hazards. In general, this is not a problem if the soil remains unsaturated, i.e. the water application rate (rainfall intensity) is less than the saturated conductivity of the soil, because there is a unique relationship between moisture and pressure described by the moisture retention curve. However, if the soil becomes saturated, then problems arise, because no unique solution exists for pressure. In other words, pressures can be greater or equal to zero at saturated moisture content. The pressures have to be inferred from the moisture distribution. It is therefore, desirable to use models that solve the pressure based form of the flow Equation in the context of landslide hazards assessment, and this is one of the reasons behind the development of the infiltration model in Chapter 2. Nonetheless, the majority of infiltration models that have been developed in the literature solve the moisture based form, because they have been developed in different fields of study, e.g. agriculture, and used as such. It is therefore, still necessary to study model uncertainty that arises from such infiltration models. More so, because some of these models are indeed still being used in landslide analyses, and in particular, one of the most widely used infiltration models is the Green and Ampt (1911) model.

GREEN - AMPT (1911) MODEL

The Green – Ampt (1911) Model is a simple one-dimensional physically based infiltration model that relates the rate of infiltration to measurable soil properties such as its porosity, hydraulic conductivity, and the moisture content. The model has been shown to

give reasonable predictions when compared to more rigorous approaches based on unsaturated flow (Wallace, 1975). Because of this, and its simplicity, it is an extensively used model.

The model is based on the following assumptions, which are illustrated in Figure 6.28:

a. The soil surface is maintained constantly wet by ponded water of negligible depth
b. There is a distinct, sharp wetting front that separates a wetted zone from an unsaturated zone in the soil with an initial constant moisture content θ_i
c. The saturated hydraulic conductivity in the wetted zone, K_s is constant throughout the soil, and does not change with time
d. There is a constant soil suction just in front of the wetting front
e. The effects of runoff and evapotranspiration are negligible

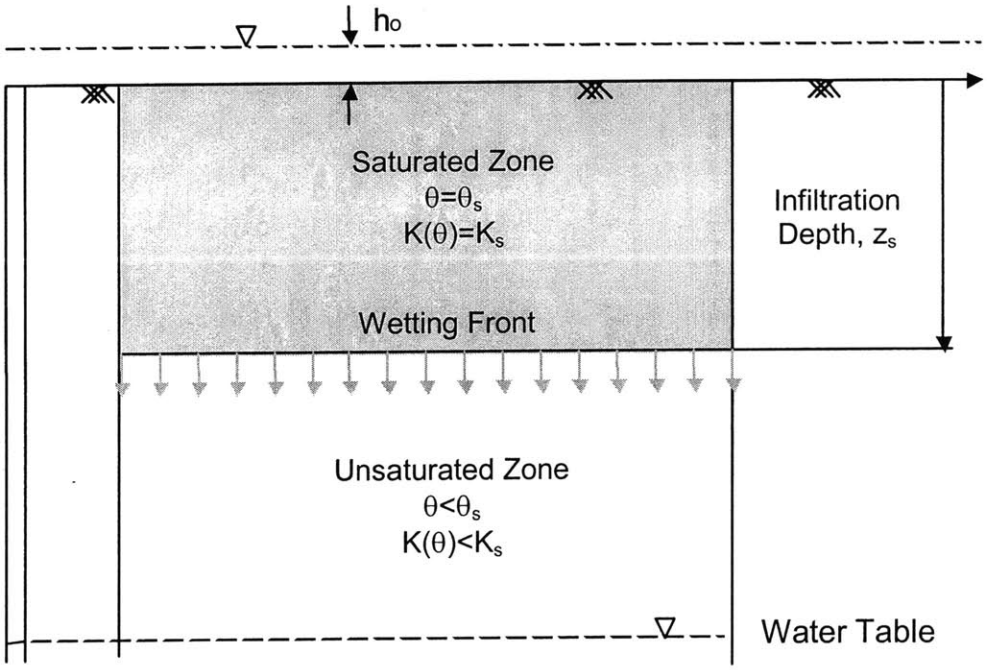

Figure 6.28 Schematic of an advancing wetting front

The Green & Ampt (1911) model assumes that infiltration occurs vertically downwards from a slope surface that is ponded to a depth, h_0 into the soil in the form of a migrating wetting front according to Darcy's Law (see Figure 6.28).

The rate of infiltration, f(t) is defined as the rate at which the rainwater enters the soil surface. The cumulative infiltration, F(t) is the accumulated depth of water infiltrated into the soil during a given period of time and is equal to the integral of the infiltration rate over that period:

$$F(t) = \int_0^t f(\tau)d\tau \qquad [6.5]$$

where:

τ is a dummy variable of time in the integration.

Conversely, the infiltration rate is the time derivative of the cumulative infiltration:

$$f(t) = \frac{dF(t)}{dt} \qquad [6.6]$$

The infiltration rate in [6.2] according to the Green & Ampt (1911) model is given by:

$$f(t) = K_s\left[\frac{\psi\Delta\theta + F(t)}{F(t)}\right] \qquad [6.7]$$

where:

K_s is the saturated hydraulic conductivity of the soil

ψ is the constant soil suction head in front of the wetting front, $\psi = \frac{(u_a - u_w)}{\gamma_w}$

$\Delta\theta$ is the change in moisture content

F(t) is the cumulative infiltration in [6.1]

Since the infiltration rate is the time derivative of the cumulative infiltration, a differential Equation is obtained as:

$$\frac{dF(t)}{dt} = K_s\left[\frac{\psi\Delta\theta + F(t)}{F(t)}\right] \qquad [6.8]$$

And:

$$F(t) - \psi\Delta\theta \ln\left(1 + \frac{F(t)}{\psi\Delta\theta}\right) = K_s t \qquad [6.9]$$

Equation [6.9] is the Green & Ampt (1911) Equation for cumulative infiltration, $F(t)$. The time required to saturate the soil to a depth, z_s, is given by:

$$T_s = \frac{\Delta\theta}{K_s}\left[z_s - \psi \ln\left(\frac{\psi + z_s}{\psi}\right)\right] \qquad [6.10]$$

There are two requirements for a particular rainfall event to saturate the soil to z_s:

a. Rainfall intensity must exceed the infiltration rate into the soil, i.e. $I \geq f(t)$
b. Rainfall duration must be long enough to saturate soil to z_s i.e. the rainfall duration, $D \geq T_s$.

From these requirements, it is possible to relate the minimum intensity I_{min} and the minimum duration D_{min} to saturate soil to z_s as:

$$I_{min} = \frac{\Delta\theta}{D_{min}}\left[z_s - \psi \ln\left(\frac{\psi + z_s}{\psi}\right)\right]\left(\frac{z_s + \psi}{z_s}\right) \qquad [6.11]$$

Application of the Green & Ampt (1911) model requires an estimate of the assumed constant suction head ψ ahead of the wetting front. The American Society of

Agricultural Engineers (1983) has published typical values to be used as Green & Ampt (1911) parameters for various soils classes.

To illustrate the effects of infiltration model uncertainty, consider the slope shown in Figure 6.29, with the characteristic curves in Figures 6.30 and 6.31.

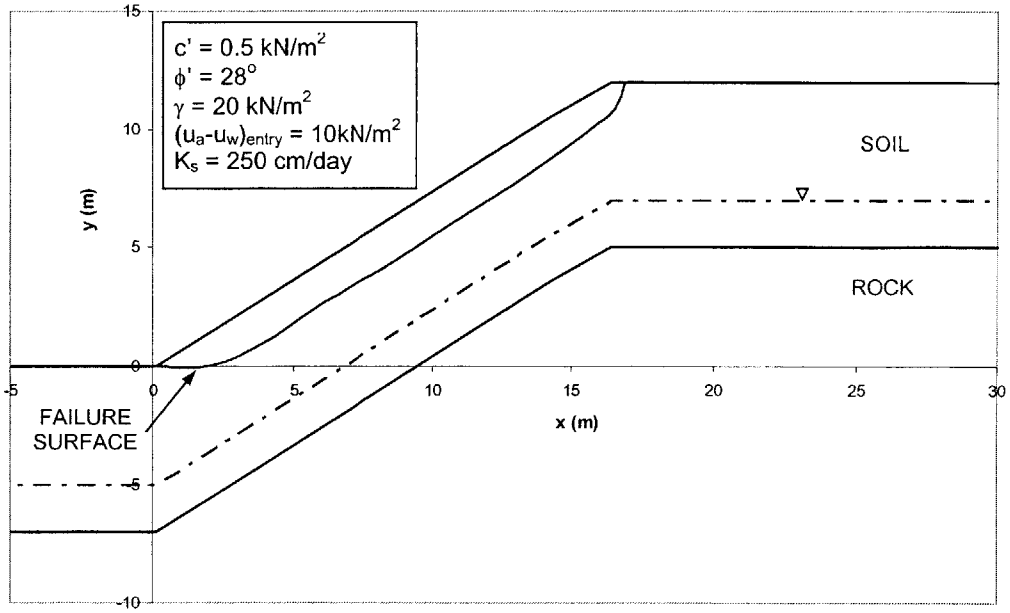

Figure 6.29. Slope Geometric and Strength Parameters

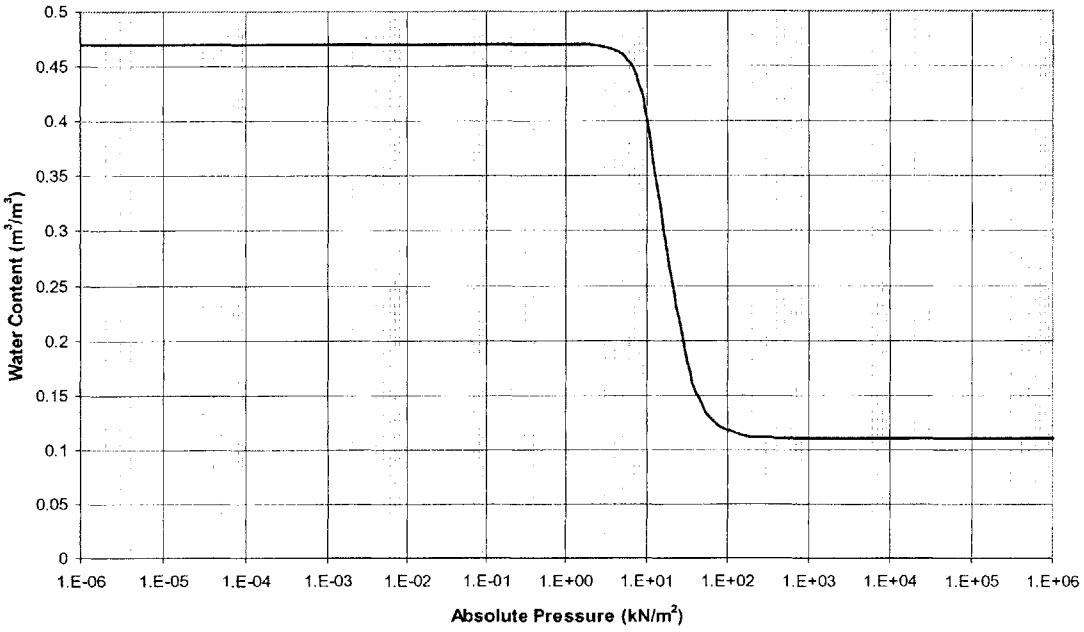

Figure 6.30. Moisture Retention Characteristic Curve

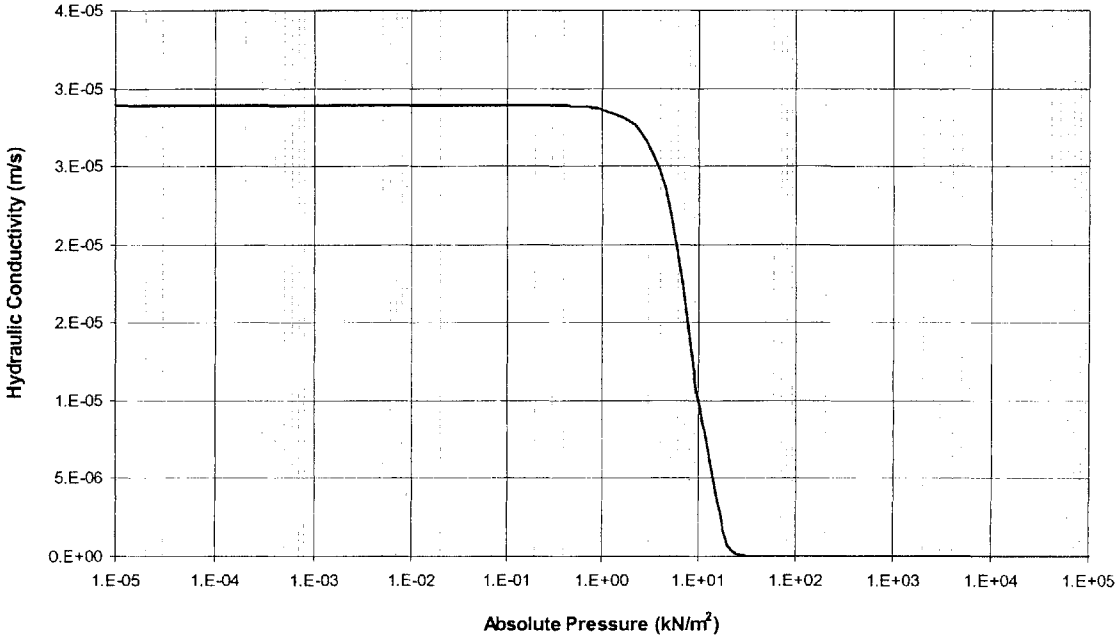

Figure 6.31. Hydraulic Conductivity Characteristic Curve

A rainfall event with intensity, $I = 75mm/hr$ is assumed to occur for a duration of 8 hours. The moisture content and pressure profiles at different times obtained using the finite difference model developed in Chapter 2 are shown in Figures 6.32 and 6.33 respectively.

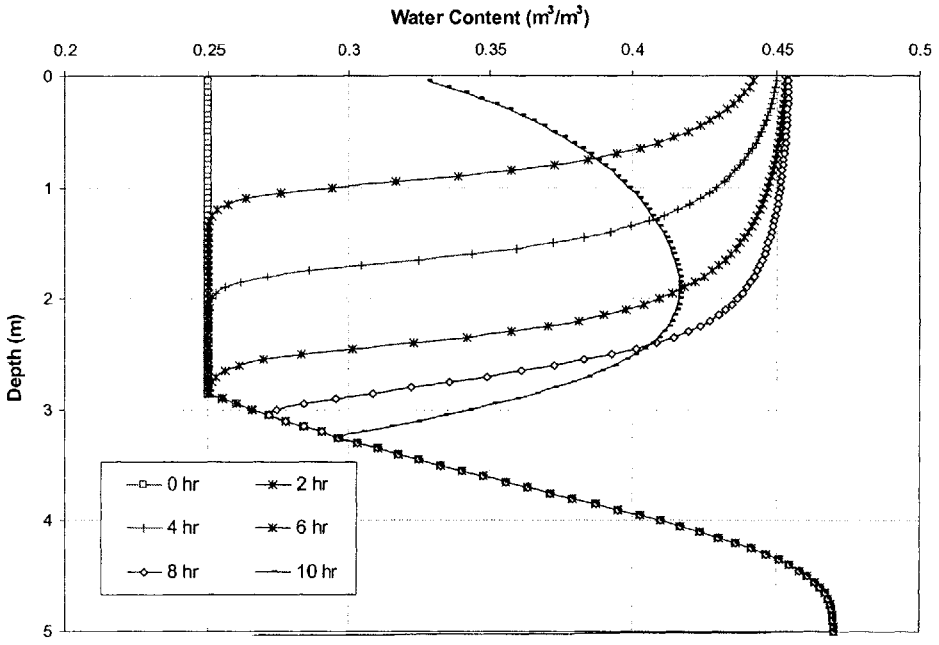

Figure 6.32. Moisture Content Profiles with Time using the van Genuchten (1980) Model

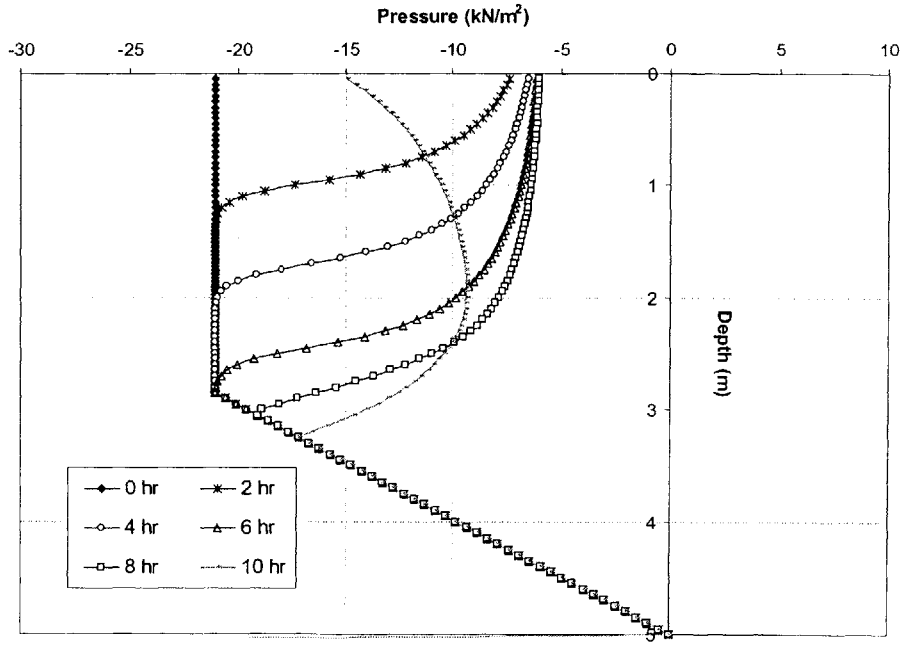

Figure 6.33. Pressure Profiles with Time using the van Genuchten (1980) Model

We now analyze the response of the slope to rainfall using the Green – Ampt (1911) Model. We assume the value of $\psi = 2\text{m}$. This value of ψ is chosen because it is close to the value of the initial pressure head in the soil that corresponds to an initial moisture content of $\theta_i = 0.25$. This is illustrated in Figure 6.34. Choosing this value of ψ will allow for a better comparison of the results of the Green – Ampt (1911) Model with those obtained from the finite difference infiltration model developed in Chapter 2.

We use the Green – Ampt (1911) Model to derive moisture content profiles with time, and these are shown at various times in Figure 6.34.

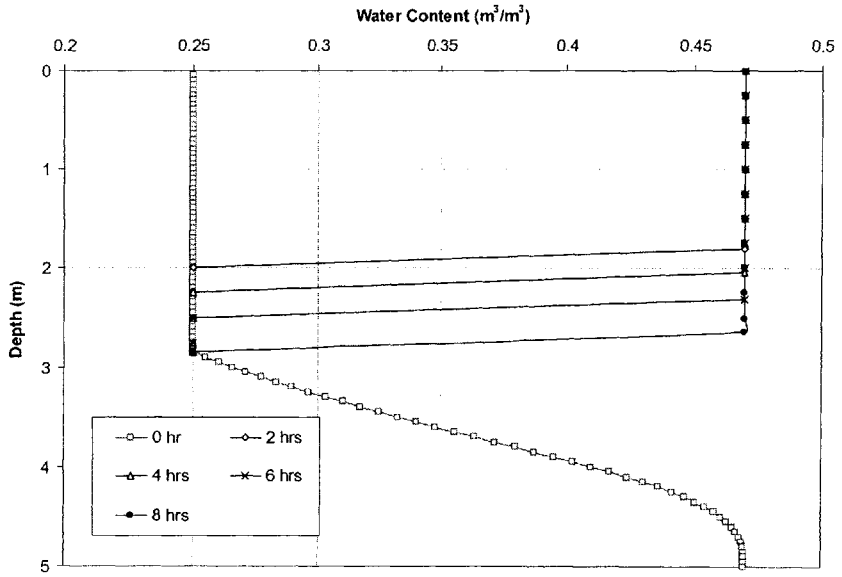

Figure. 6.34. Moisture Content Profiles with Time for Green – Ampt (1911) Model with $\psi = 2\text{m}$.

Figure 6.35 compares the moisture profiles obtained by the Green – Ampt (1911) Model with those obtained by the infiltration model developed in Chapter 2.

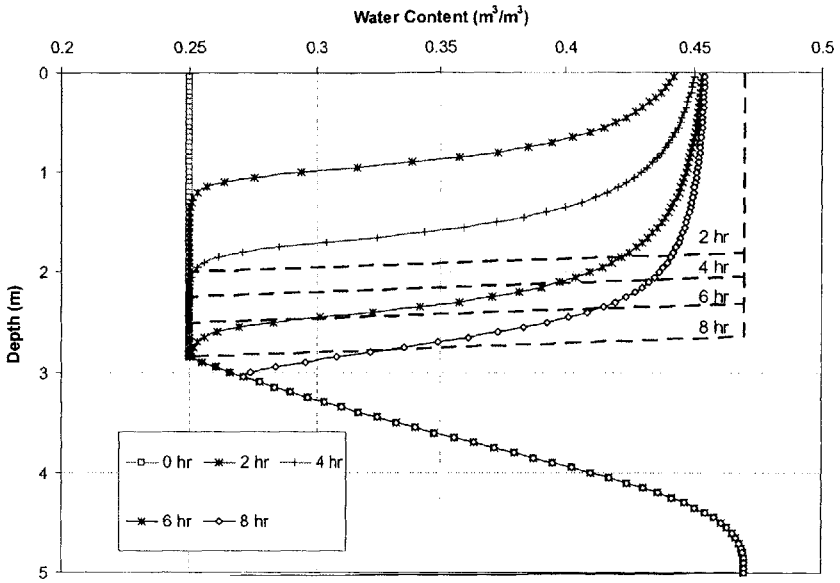

Figure 6.35. Comparison of Moisture Content Profiles with Time for Green – Ampt (1911) Model (Dashed Lines) and Infiltration Model (Solid lines with Symbols)

The solid lines with symbols in Figure 6.35 are the results of the infiltration model, and the dashed lines are the results using the Green – Ampt (1911) Model. Since the Green – Ampt (1911) model is a model for saturated infiltration, it is only capable of predicting depths to full saturation. This reflected in Figure 6.35, where the soil is either fully saturated ($\theta=\theta_s=0.47$) or at initial moisture content, ($\theta=\theta_i=0.25$). This also explains the sharp change in moisture content for the Green – Ampt (1911) model in Figure 6.35. Figure 6.35, therefore, illustrates the effects of infiltration model uncertainty on the results of hydrologic analyses.

The problem mentioned at the beginning of this Section arises when using the Green – Ampt (1911) model for landslide analyses, namely that the model is incapable of predicting the generated pressures during rain, and these have to be inferred. We consider two boundary (extreme) cases of possible generated pressures:

a. The case where the initial suction is eliminated in a thin layer of soil at the surface. In this case, the pressures would be reduced throughout the infiltration depth as shown in Figure 6.36, which is idealized.

b. The case where the initial suction is eliminated throughout the infiltration depth. This is shown in Figure 6.37, which again is idealized.

There is a third boundary (extreme) case for the pressures, namely the development of full hydrostatic pressures within the infiltration depth. This is not considered in this example because the rainfall intensity is less than the saturated conductivity of the soil.

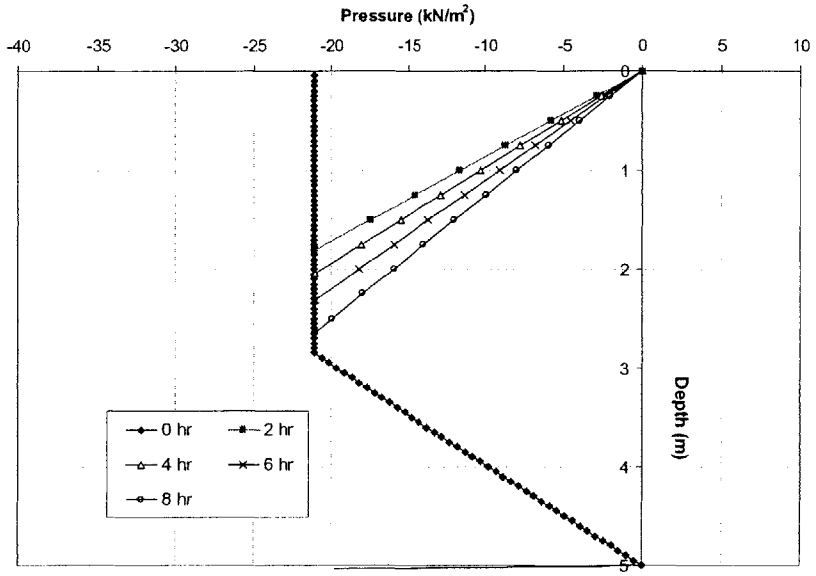

Figure 6.36. Pressure Profiles with Time for Green – Ampt (1911) Model Assuming Infiltration Reduces Suction

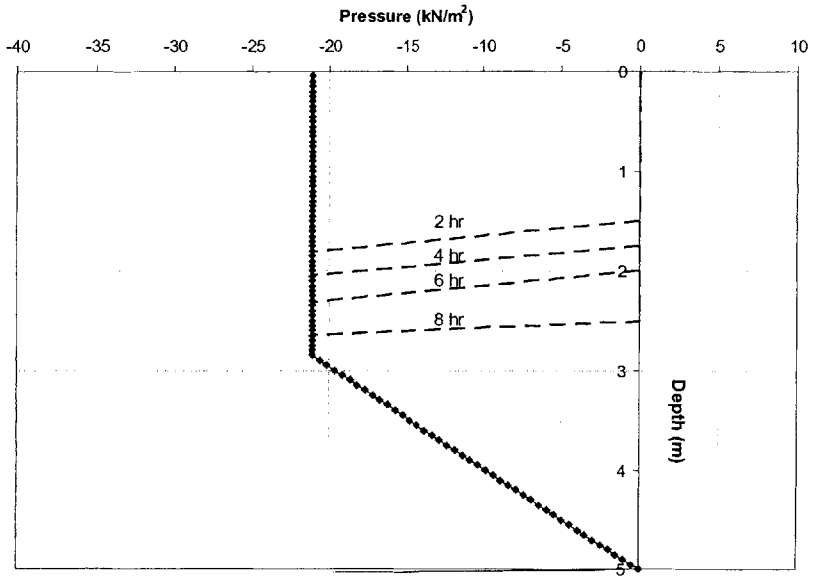

Figure 6.37. Pressure Profiles with Time for Green – Ampt (1911) Model Assuming Infiltration Eliminates Suction

Figures 6.38 and 6.39 compare these two boundary cases to the results from the infiltration model of Chapter 2, and illustrate model uncertainty on the results of hydrologic analyses based on pressures.

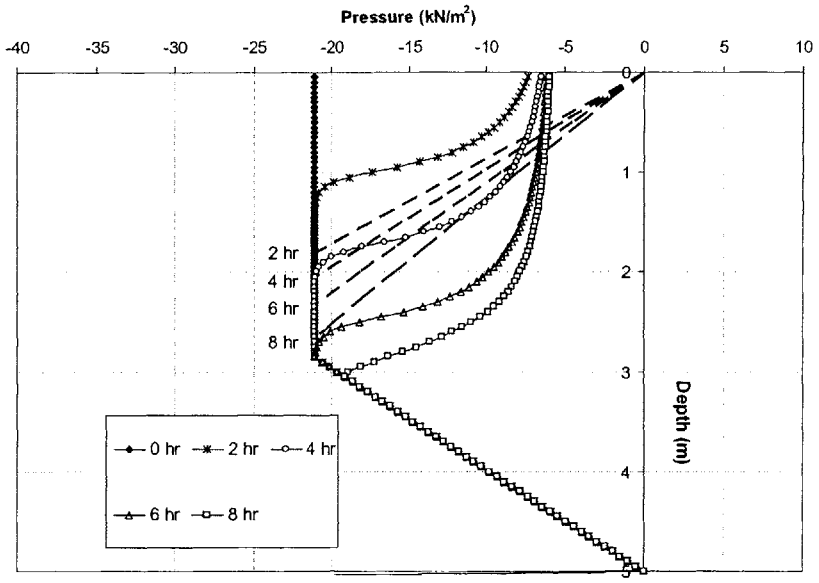

Figure 6.38. Comparison of Pressure Profiles with Time for Green – Ampt (1911) Model (shown as dashed lines) and Infiltration Model (shown as solid lines and symbols) for Case where Suction is Reduced

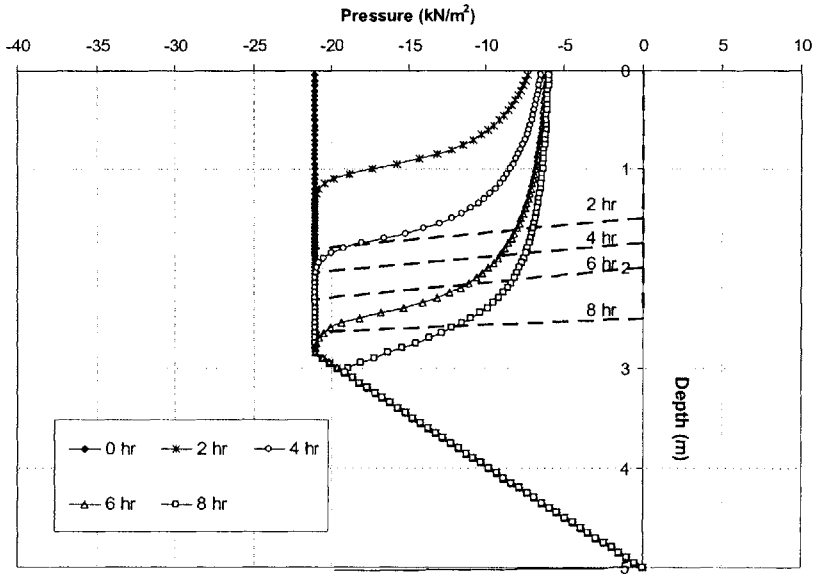

Figure 6.39. Comparison of Pressure Profiles with Time for Green – Ampt (1911) Model (shown as dashed lines) and Infiltration Model (shown as solid lines and symbols) for Case where Suction is Eliminated

The dashed lines in Figures 6.38 and 6.39 are results obtained by the Green – Ampt (1911) Model, and the solid lines with symbols those obtained by the infiltration model developed in Chapter 2.

The Green – Ampt (1911) results in Figures 6.38 and 6.39 can be used as a basis to asses the stability of the slope shown in Figure 6.29 as a result of rain. The variation of Factor of Safety with time is shown in Figure 6.40.

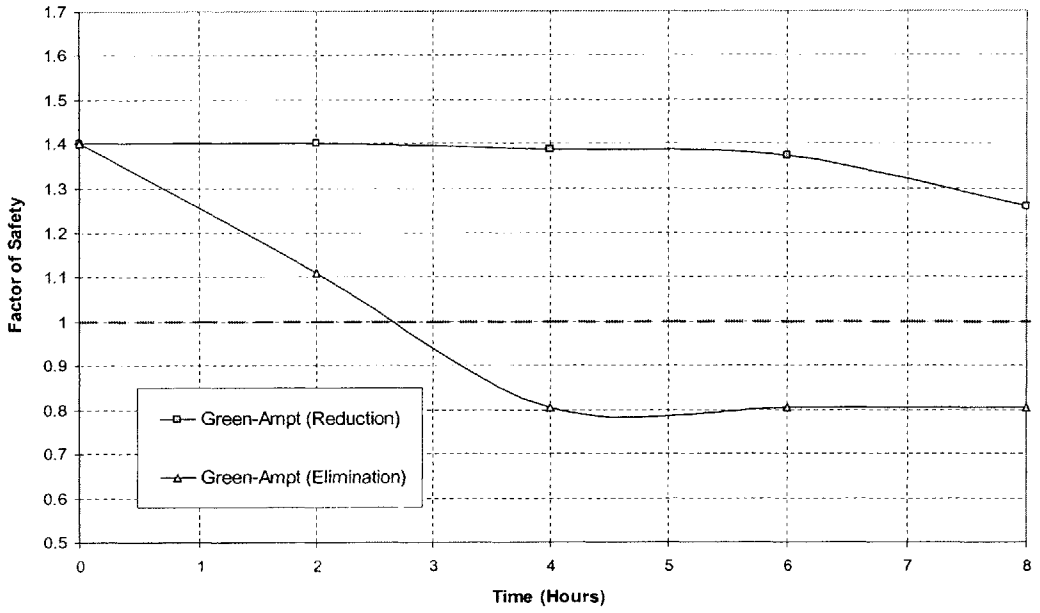

Figure 6.40. Variation of Factor of Safety with Time During Rain Using Green – Ampt (1911) Model

The results are compared with those obtained by the infiltration model in Figure 6.41.

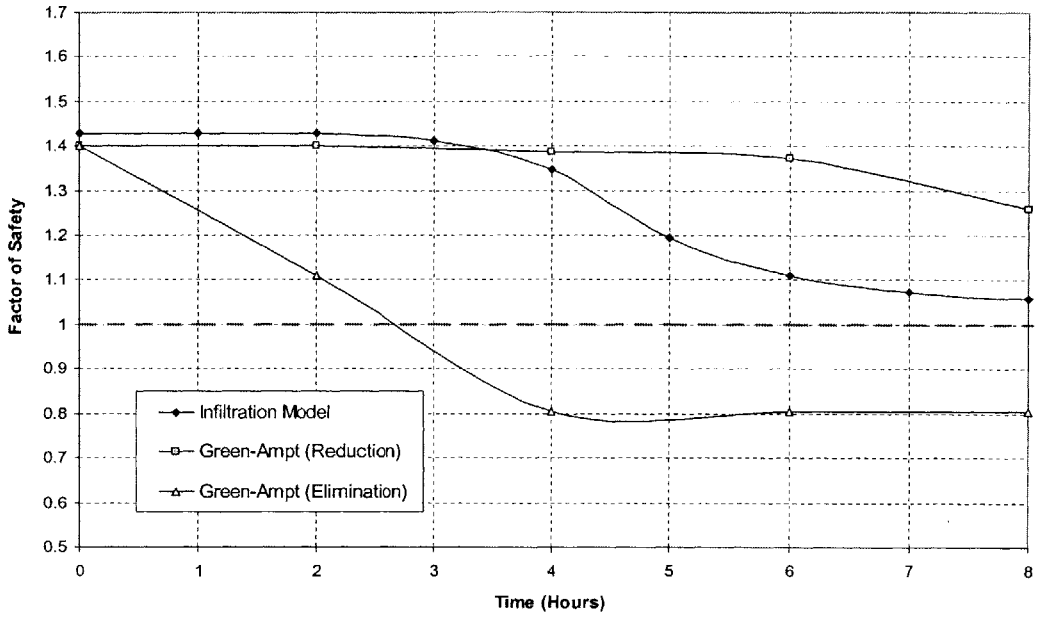

Figure 6.41. Comparison of Variation of Factor of Safety with Time During Rain Using Green – Ampt (1911) and Infiltration Models

Figure 6.41 clearly shows that there is a significant difference in the results of the infiltration model developed in Chapter 2, and those obtained for the two boundary cases using the Green – Ampt (1911) Model. The results of the infiltration model lie in between those predicted by the Green – Ampt Model. Both the infiltration model and the Green – Ampt when suction is assumed to be reduced, predict a decrease in Factor of Safety, but that the slope remains stable throughout rain. The Green – Ampt with the assumption that suction is eliminated throughout the infiltration depth predicts slope failure. Figure 6.41 therefore clearly shows the significance of hydrologic model uncertainty on landslide analyses, as different conclusions on stability are arrived at using the different hydrologic models.

To conclude, there are two types of hydrologic models, those that solve the pressure based form of the flow Equation, and those that solve the moisture based form, and assume pressures. Model uncertainty from the former is not very significant, because the models solve the same mathematical Equation, with the same initial and boundary conditions. Model uncertainty is significant in the latter and different assumptions regarding pressure distributions can result in very different results and conclusions on stability.

PART 6 -2
MODEL UNCERTAINTY IN STABILITY ANALYSES

Figure 6.2 shows possible models used in stability analyses. These include models to describe soil strength, and models to asses slope stability. Both types of models are subject to model uncertainty. It is worth mentioning here that different strength models can be used in the same stability model, and the same strength model can be used in different stability models.

In this Section, we investigate the effects of model uncertainty on stability analyses, and landslide hazards. Since stability models are idealized, submodels/assumptions are made to simplify the problem of stability. The effects of these submodels on stability analyses, and landslide hazards are first evaluated using the same stability model, the Janbu Generalized Method of Slices (1978). These submodels include failure models, models for soil strength, and the parameters used in the strength models, as well as others. We then investigate the effects of using different stability models to asses the landslide hazards of the same slope.

Figure 6.42 shows a schematic of what will be studied in more detail in Part 6-1 of this chapter.

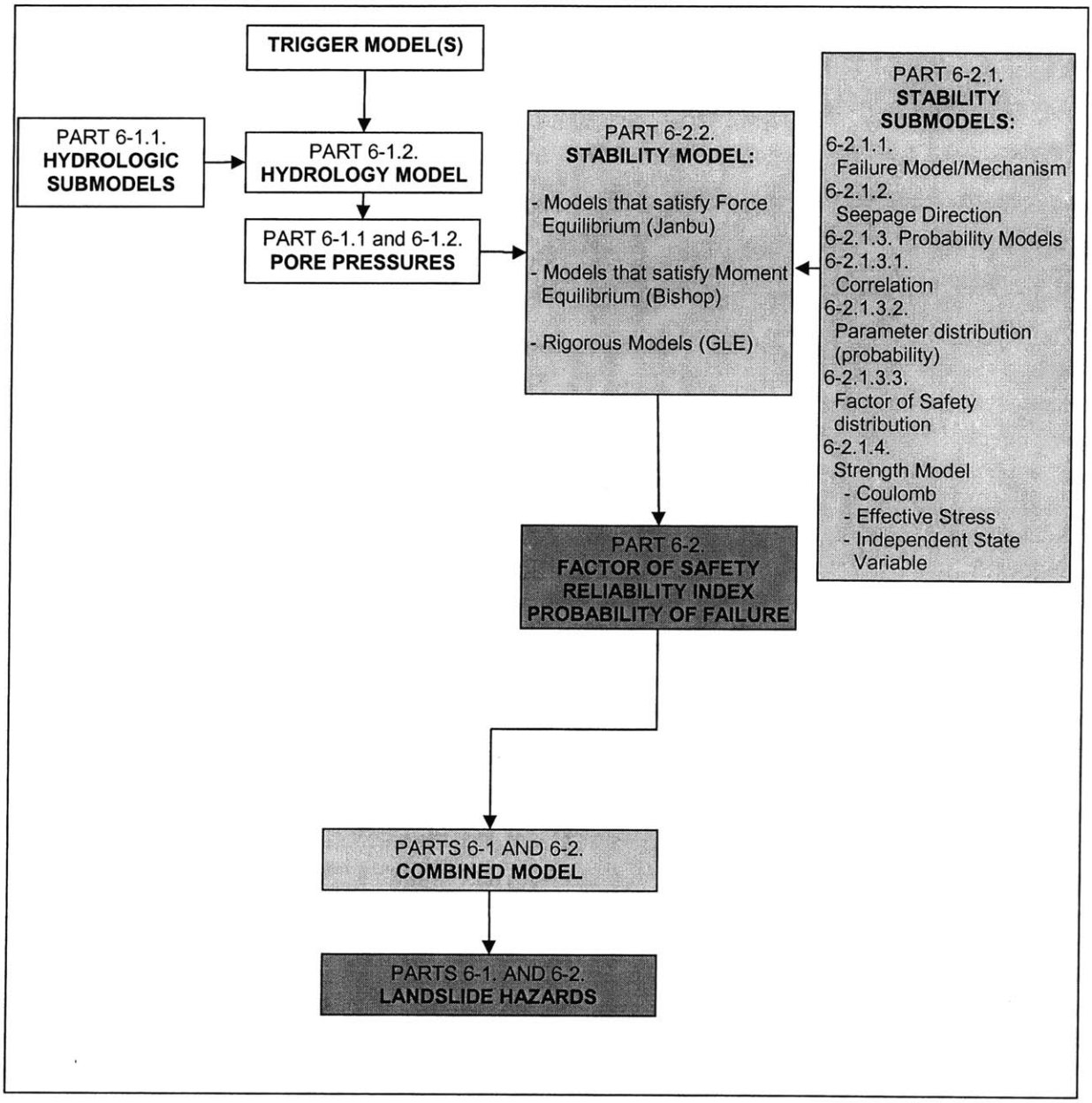

Figure **6.42.** Schematic showing Stability Modeling.
The effects of the different submodels (shown in the lightly shaded box) and the different types of stability models (shown in lightly shaded box) on the results of stability analyses (Factors of safety, reliability indices and probabilities of failure in the dark shaded box) and on landslide hazards (dark box) are investigated

6-2.1. MODEL UNCERTAINTY FROM SUBMODELS IN STABILITY MODELS

In this Section, we study the effects of model uncertainty form submodels in stability models on stability modeling and landslide hazards assessments. This is shown schematically in Figure 6.43.

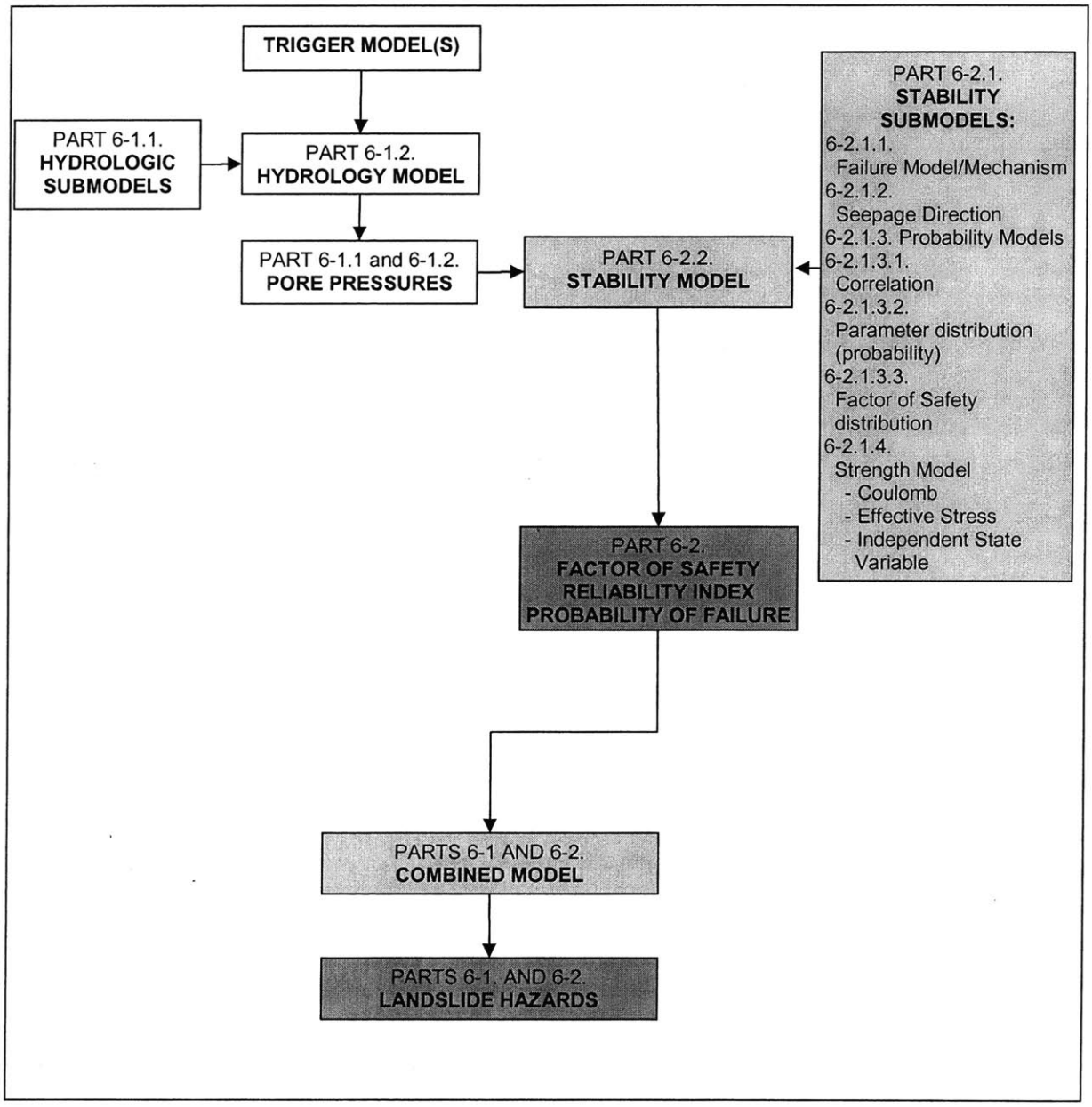

Figure **6.43.** Schematic showing Stability Modeling.
The effects of the different submodels (shown in the lightly shaded box) on the results of stability analyses (Factors of safety, reliability indices and probabilities of failure in the dark shaded box) and on landslide hazards (dark box) are investigated

6-2.1.1. FAILURE SUBMODEL/MECHANISM UNCERTAINTY

A failure model (mechanism) must be postulated in order to perform stability analyses using Limit Equilibrium Stability Models. These types of stability models are discussed in more detail in Section 6-2.2. In this Section, we briefly discuss the importance of postulating the critical failure mechanism. Figure 6.44 shows in bold what is studied in this Section.

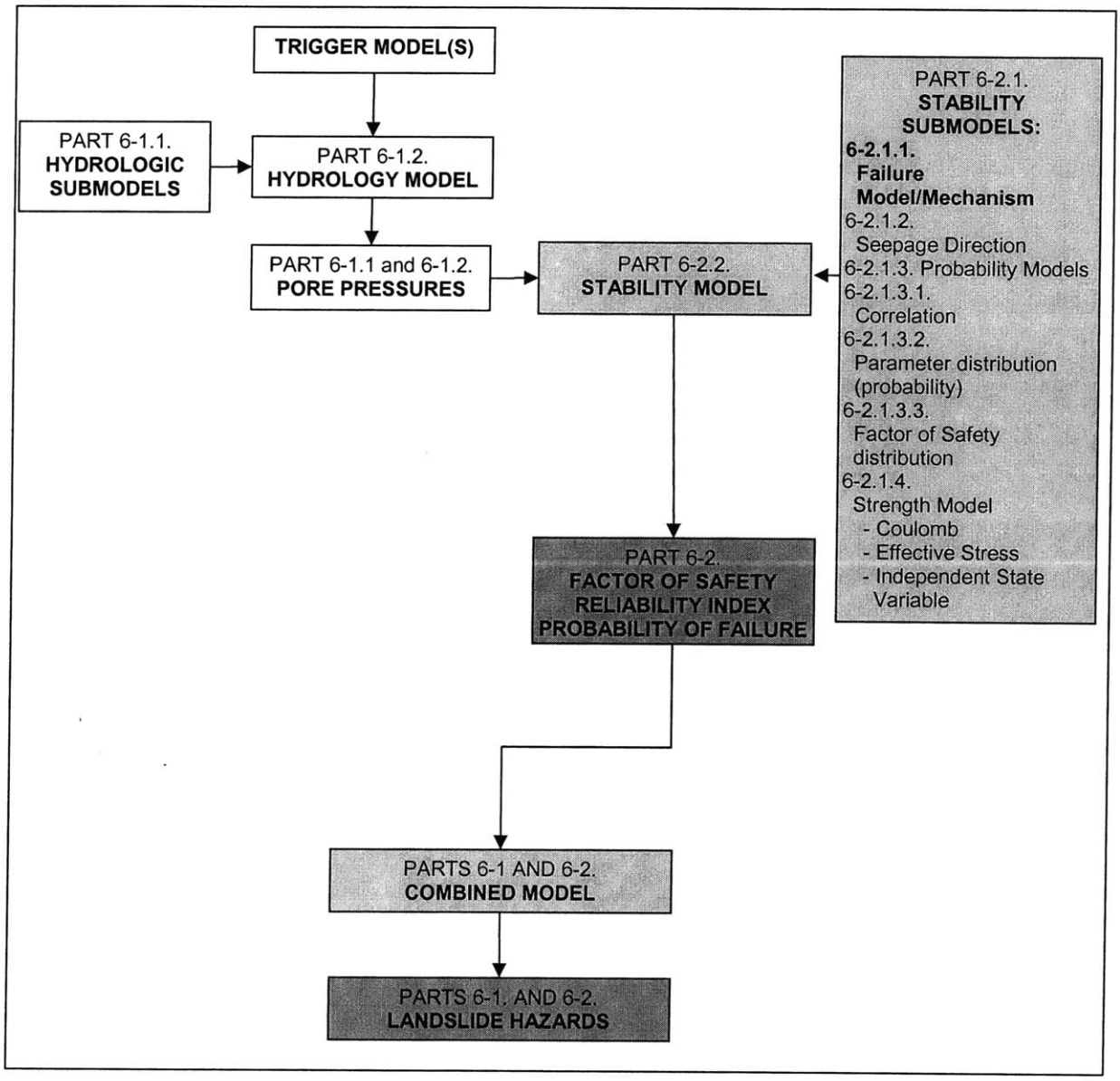

Figure **6.44.** The effects of failure model/mechanism (shown in bold in the lightly shaded stability submodels box) on the results of landslide hazards (dark box) are investigated

Uncertainty arises from the chosen failure model, and this type of uncertainty can be the most significant source of uncertainty in stability analyses. Uncertainty in failure mechanisms arises because of the representation of these mechanisms with models or, even more fundamentally, in the knowledge about the mechanisms. This is particularly true in the study of landslides, since these mechanisms are poorly understood. Chapter 3 provided a study on landslide failure mechanisms in an attempt to increase understanding, which will, in turn, reduce this type of uncertainty. However, the study is by no means complete and failure model uncertainty presents a significant source of uncertainty in stability analyses.

The problem is somewhat dealt with by using stability models that include a search for the critical failure surface in a slope (see Part 2-2 of Chapter 2). But even these types of analyses are subject to failure model uncertainty since an initial trial failure surface has to be chosen, and the results can vary significantly depending on this initial surface. This problem was discussed in more detail in Part 2-2 of Chapter 2, and in Chapter 3.

To illustrate the effects of failure model uncertainty on landslide analyses, we consider the slope shown in Figure 6.45.

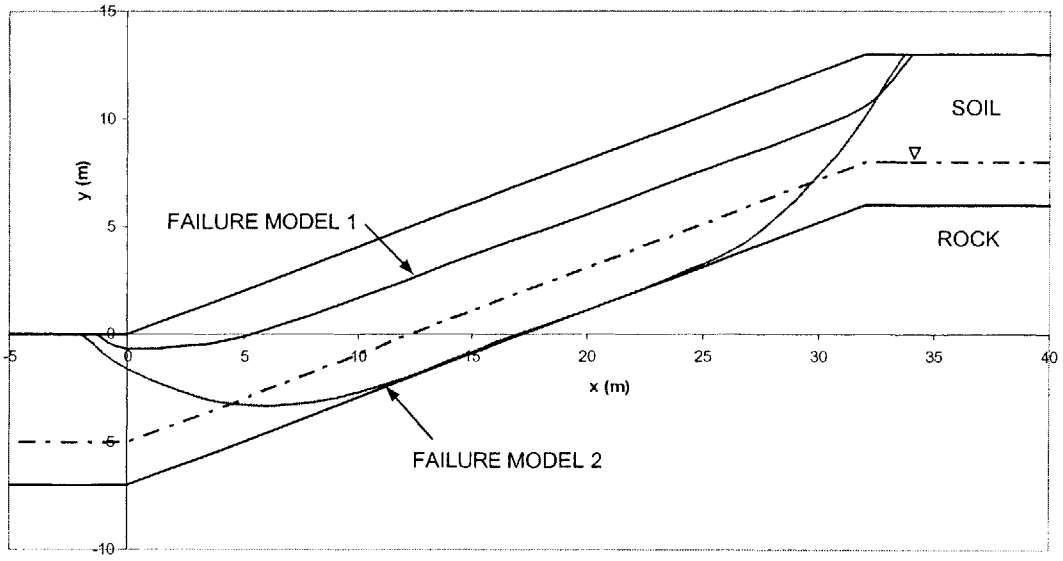

Figure 6.45. Slope Geometry and Two Failure Models

Two failure models are assumed, the first is a shallow translational landslide, and the second is a deeper, more rotational failure surface located at the interface between soil and rock.

A rainfall event of intensity $I = 375cm/day = 155mm/hr$ is assumed to take place for a duration of 8 hours. The stability of the slope is assessed for both failure mechanisms, and the results are shown in Figure 6.46.

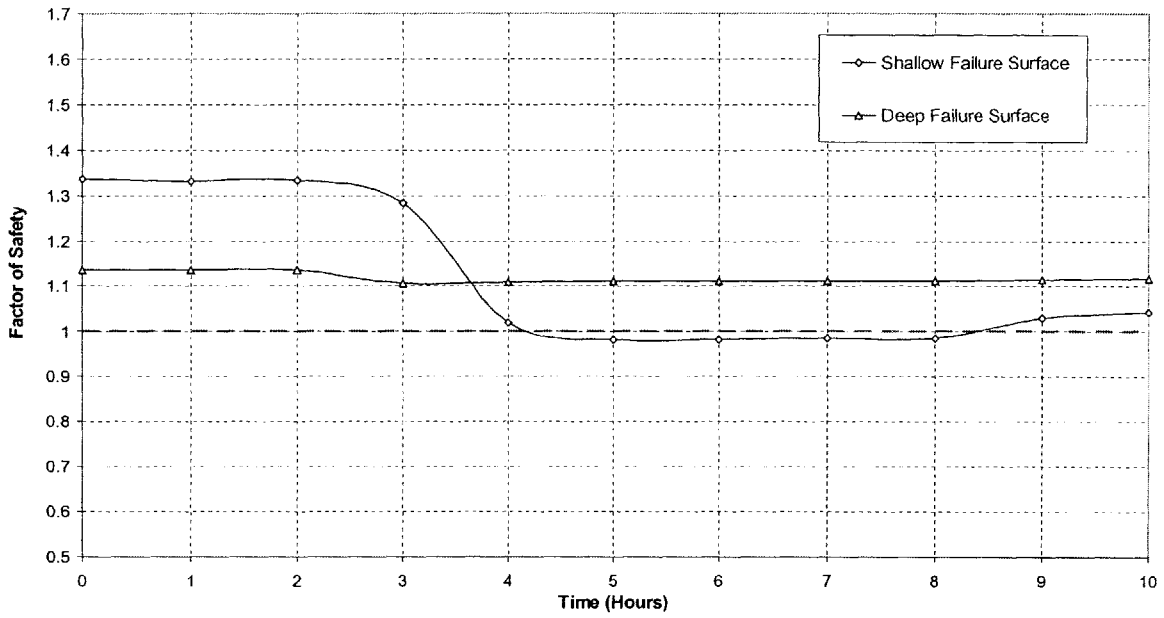

Figure 6.46. Variation of Factor of Safety with Time for Two Failure Models

Figure 6.46 shows that if the mechanism of shallow landsliding is adopted, then one would conclude that failure would occur as a result of rain. If, however, the mechanism of a deep slide is adopted, then the slope would remain stable. These are evidently significantly different conclusions regarding stability that come about from the different assumed failure mechanisms. The effects of failure model uncertainty can therefore be very important.

Moreover, Figure 6.46 shows that the failure model a slope most likely will fail in may vary with time. At early times, the more critical failure surface is the deeper surface, since the Factor of Safety on that surface is smaller than on the shallow surface. However, as it rains, and rainwater infiltrates into the slope, the shallow failure model

becomes more critical, since the effects of rain are greater than at depths. This is shown in Figure 6.46.

Therefore, in stability modeling that assumes a specific failure surface, this must be done by selecting different locations, and shapes of the failure surface. In modeling that includes a search for the critical failure surface, several initial trial failure surfaces must be chosen to ensure the final surface is the correct critical failure surface. This was discussed in more detail in Chapter 3.

6-2.1.2. SEEPAGE DIRECTION SUBMODEL UNCERTAINTY

In this Section, we investigate the effects of seepage direction on stability analyses, and deterministic and probabilistic landslide hazards assessment. . Figure 6.47 shows in bold what is studied in this Section.

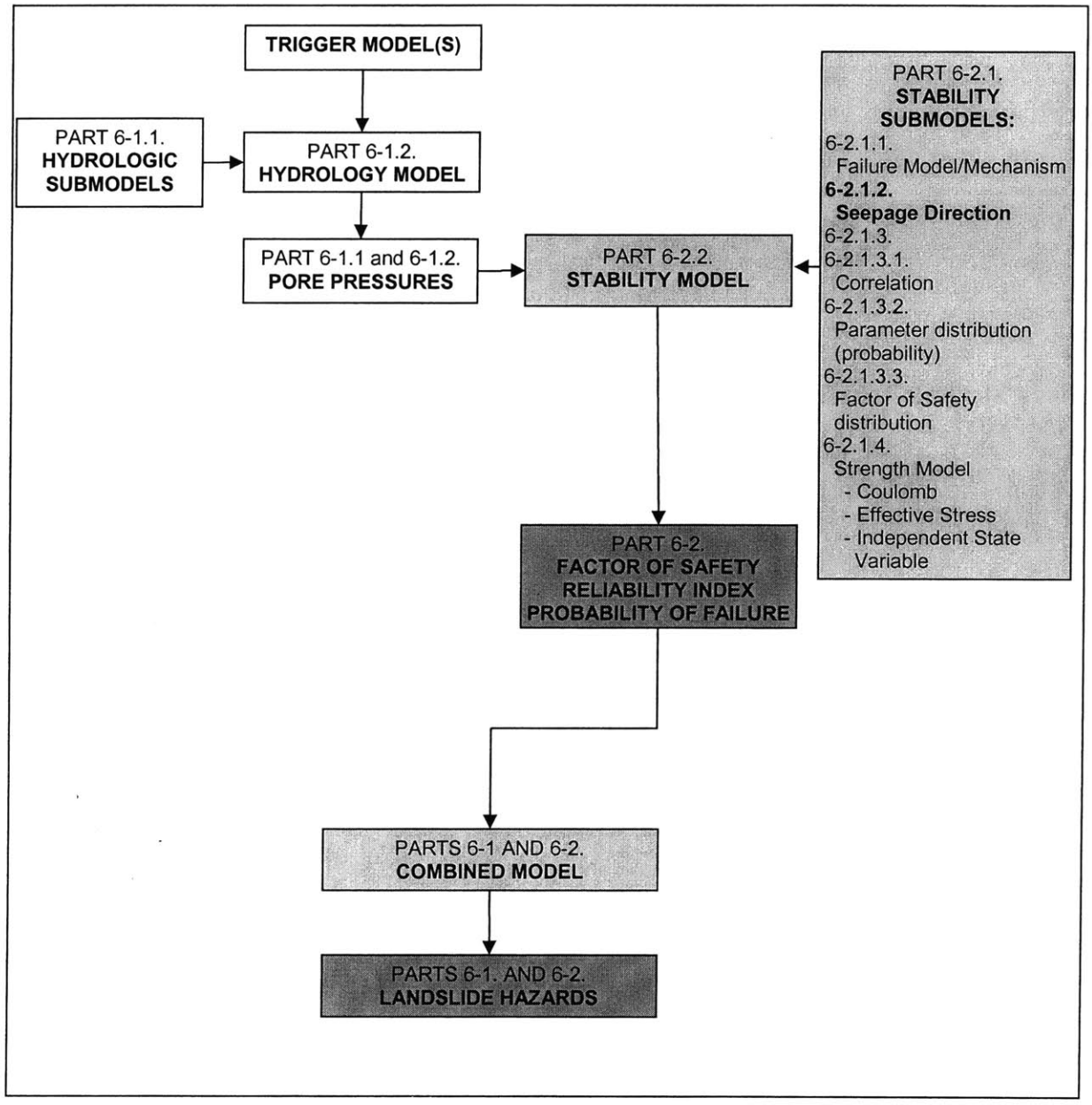

Figure **6.47.** Effects of seepage direction (shown in the lightly shaded submodels box) on the results of stability analyses (Factors of safety, reliability indices and probabilities of failure in the dark shaded box) and on landslide hazards (dark box) are investigated

6-2.1.2.1. BACKGROUND

It is commonly assumed that seepage in an infinite slope is parallel to the slope. The geometry of infinite slopes constrains the direction of the pore pressure gradient to be normal to the ground surface, but it does not constrain the gradient magnitude. Iverson (1991) showed that the infinite slope geometry constraints on the pore pressure gradient are considerably less stringent than the assumption of parallel to slope seepage. In the X' direction parallel to the slope (see Figure 6.48), because the water table in an infinite slope is parallel to the ground surface, the pore pressure gradient $\frac{\partial u_w}{\partial X'}$ is equal to zero. The gradient of pore water pressures in the Y' direction (see Figure 6.48) perpendicular to the slope, on the other hand is not constrained by the infinite slope geometry as strictly as $\frac{\partial u_w}{\partial X'}$.

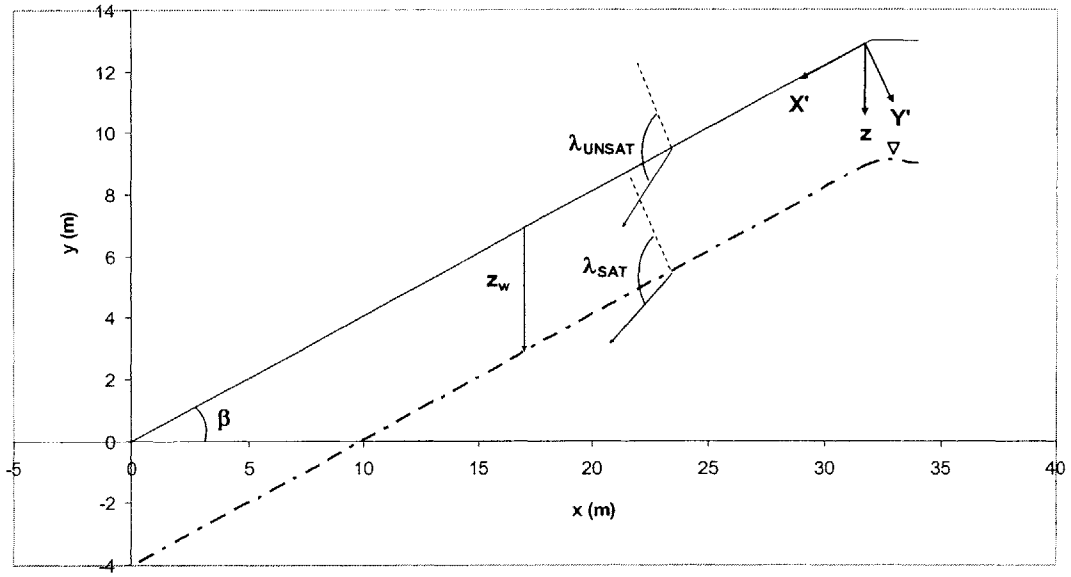

Figure **6.48.** Notations and axes used for seepage direction

Iverson (1991) showed that:

$$\frac{\partial u_w}{\partial Y'} = \gamma_w \left(\frac{\sin\beta}{\tan\lambda} + \cos\beta \right) \qquad [6.12]$$

where:

β is the slope angle

λ is the seepage direction from the normal to the slope (see Figure 6.48)

$\lambda = 90^{o}$ corresponds to parallel to slope seepage. Seepage directions $\lambda > 90^{o}$ correspond to in-slope seepage, whereas directions $\lambda < 90^{o}$ correspond to out of slope seepage.

While the assumption of parallel to slope seepage may be justified below the water Table where the soil is saturated, and moisture content is constant and equal to the saturated moisture content of the soil, it is not as justified in the unsaturated zone of the slope. Moisture content typically increases with depth below the ground surface in the unsaturated zone, producing a component of flow perpendicular to the slope.

The saturated analyses by Iverson (1991) can be extended to include the effects of seepage direction on the pore pressures in both the saturated and unsaturated zones of the soil. A more general expression for the pore pressure variation accounting for the effects of non-parallel seepage throughout the subsurface is:

$$u(z) = u_w(z)\left(\frac{\partial u_w}{\partial Y'}\right)\cos\beta \qquad [6.13]$$

where:

$u_w(z)$ is the pore pressure distribution in the vertical direction z (see Figure 6.48)

$\left(\frac{\partial u_w}{\partial Y'}\right)$ is the pore pressure gradient in the direction perpendicular to the slope surface, and expressed in Equation [6.12].

Note that when $\lambda = 90^{o}$ (parallel to slope seepage) Equation [6.13] reduces to [6.12].

The derivation of Equation [6.13] and its application, as discussed in the following Section have also been presented in Einstein and Karam (2001).

In saturated soil, because of constant moisture content, $\left(\frac{\partial u_w}{\partial Y'}\right)$ is as expressed in Equation [6.12]. In unsaturated soil, $\left(\frac{\partial u_w}{\partial Y'}\right)$ depends on the variation of moisture content in both the horizontal and vertical directions in the slope, as well as the soil moisture retention curve. $\left(\frac{\partial u_w}{\partial Y'}\right)$ can still be expressed in the form show in Equation [6.12] with an appropriate λ value. Note that the seepage direction in saturated ($\lambda_{saturated}$) and unsaturated soil ($\lambda_{unsaturated}$) need not be the same.

6-2.1.2.2. SEEPAGE DIRECTION SUBMODEL UNCERTAINTY IN STABILITY ANALYSES

A good example to illustrate the effects of seepage on slope stability is shown in Figure 6.49.

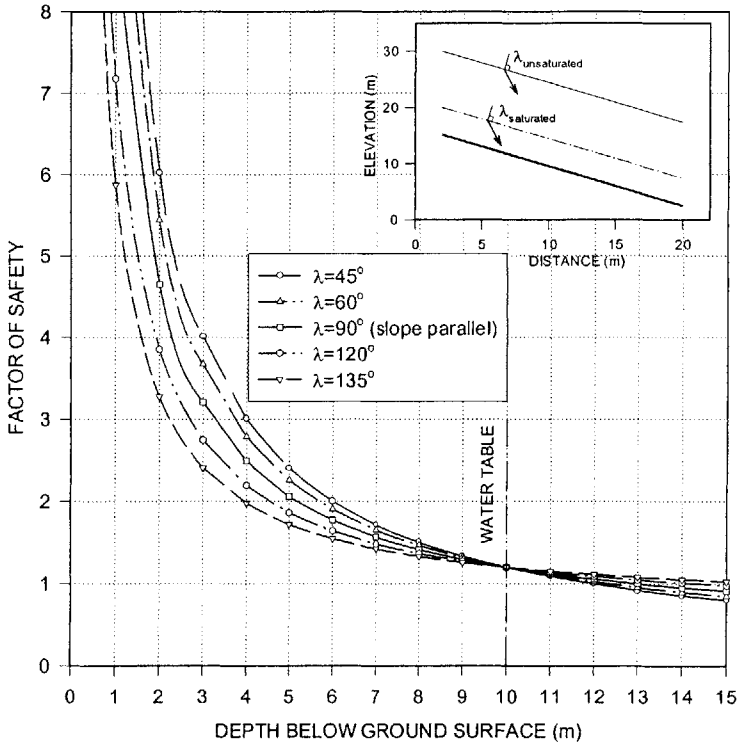

Figure 6.49. Effect of Groundwater Flow Direction on Factor of Safety in the Infinite Slope Model

The Infinite Slope Stability Model (Skempton and DeLory, 1950) is used to asses the stability of the slope in Figure 6.49, with different seepage directions. Figure 6.49 shows the effects of seepage on stability analyses. While the effects are not very significant numerically in saturated soil below the water table, they are important above the water where the soil is unsaturated. Figure 6.49 is not intended to provide a rigorous assessment of the effects of groundwater flow direction on stability, since the direction of flow is assumed to be the same above and below the water table and constant over the entire depth (both are unnecessary restrictions), but to provide a comparison of different assumptions using the same stability model. A more rigorous assessment of the effects of seepage on stability is shown in Figure 6.50.

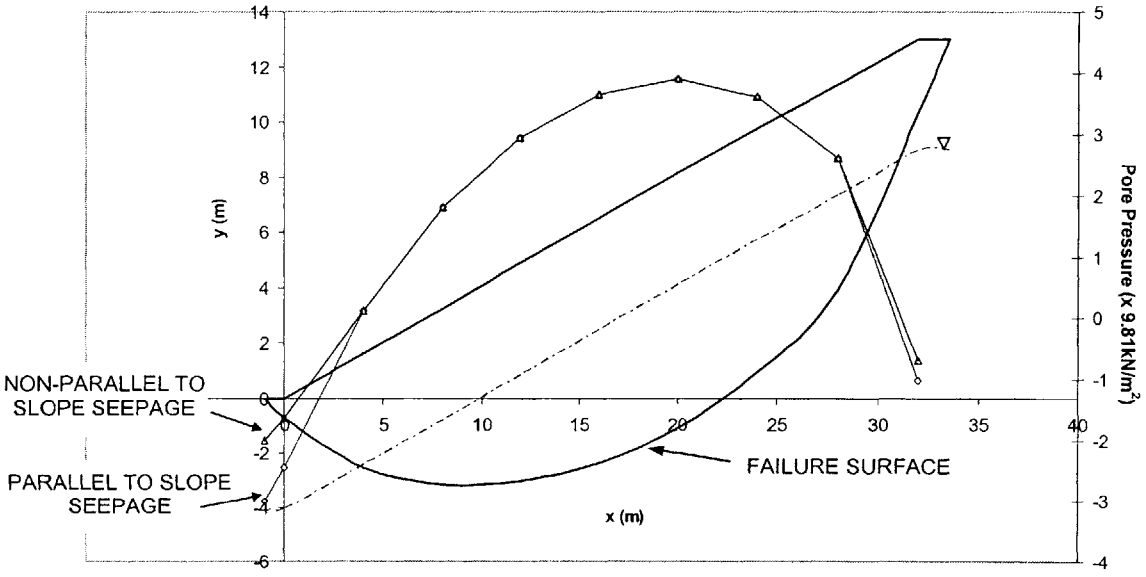

Figure 6.50. Pore Pressure Distributions on Failure Surface for Seepage Parallel and Non-Parallel to Slope in the Unsaturated Zone of the Slope

Figure 6.50 compares the pore pressure distribution along the failure surface in a slope for the cases of seepage parallel and non parallel to slope. For the non parallel seepage case, flow is assumed to occur parallel to the slope below the water table, but at an angle $\lambda_{unsaturated} = 120^{o}$ above the water table. The pressures are greater (less negative) in the unsaturated soil when $\lambda_{unsaturated} = 120^{o}$, compared to when seepage is parallel to the slope and $\lambda_{unsaturated} = 90^{o}$. This causes a reduction in effective stress, which causes a corresponding reduction in strength in the unsaturated soil. This

is reflected in stability analyses performed on the slope, where a Factor of Safety of 1.13 is computed when in slope seepage ($\lambda_{unsaturated} = 120^o$) is assumed, compared to a Factor of Safety of 1.15 in the case of parallel to slope seepage ($\lambda_{unsaturated} = 90^o$).

Different seepage directions will also have an effect on the location of the critical failure surface (minimum Factor of Safety) in a slope. Figure 6.51 compares the critical failure surfaces that are obtained when seepage is assumed to take place parallel to the slope in both saturated and unsaturated soil ($\lambda_{unsaturated} = 90^o$), and when $\lambda_{unsaturated} = 120^o$ in the unsaturated soil, with parallel to slope seepage in saturated soil.

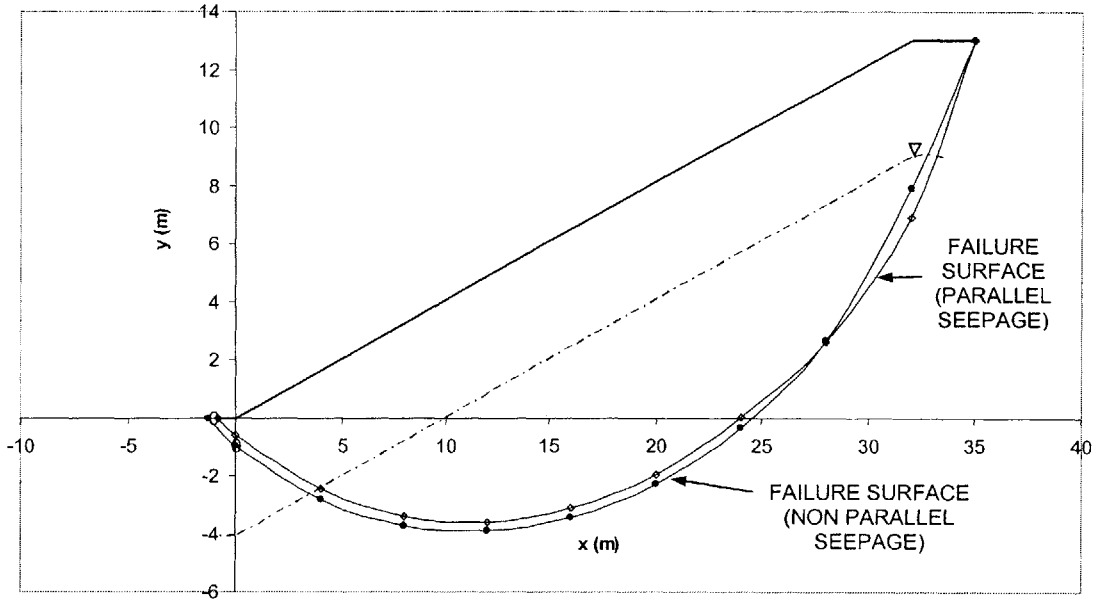

Figure 6.51. Critical Failure Surfaces in Slope for Parallel and Non-Parallel to Slope Seepage in the Unsaturated Zone of the Slope

A Factor of Safety of 1.15 is computed on the critical failure surface with seepage parallel to the slope in both the saturated and unsaturated zones of the slope. A Factor of Safety of 1.11 is obtained on the critical failure surface with $\lambda_{unsaturated} = 120^o$. Figure 6.51 shows that seepage direction has an effect on the location of the critical failure surface. The difference in Factors of Safety in this example is not very significant

numerically, because of the particular hydraulic conditions in the slope, and the failure surface lying in mostly saturated soil. But as will be illustrated in the next Section, seepage direction can have significant influence on landslide hazards, and is particularly relevant to shallow landslides, where failure can take place in unsaturated soil.

6-2.1.2.3. SEEPAGE DIRECTION SUBMODEL UNCERTAINTY IN LANDSLIDE HAZARDS ASSESSMENT

In this Section, the effects of seepage direction on landslide hazards are analyzed. For this purpose, we consider the two following examples.

LANDSLIDE HAZARDS WITH RAINFALL INTENSITY LESS THAN SATURATED CONDUCTIVITY

In this example, the rainfall intensity is less than the saturated conductivity of the soil at the surface, and so all the rainwater infiltrates into the slope, and causes an increase in moisture content, but saturation is not reached. Consider the slope shown in Figure 6.52.

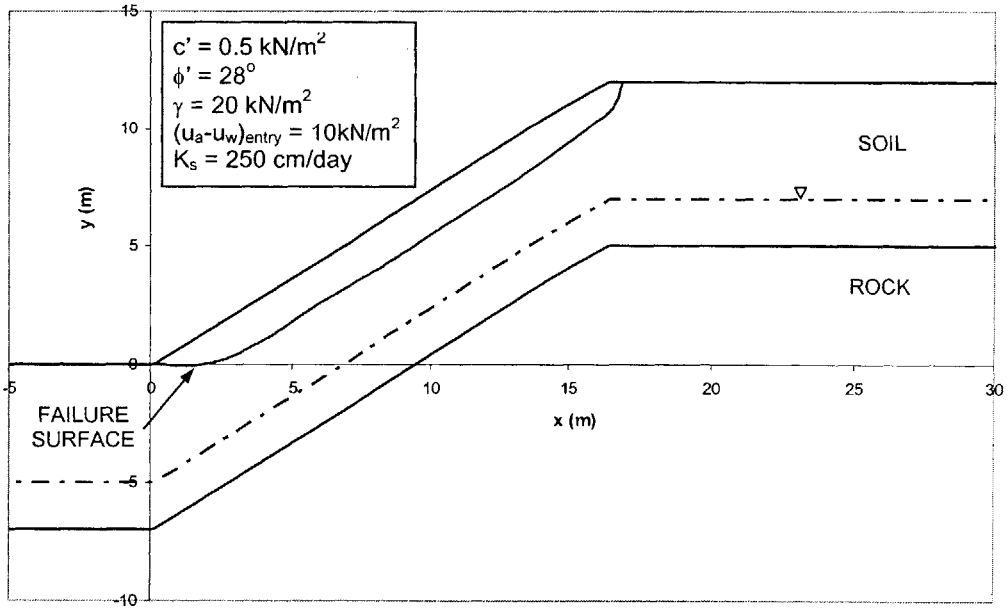

Figure 6.52. Slope Geometric and Strength Parameters

The slope geometric and soil strength and hydrologic parameters are shown in Figure 6.52 and the soil characteristic curves are shown in Figures 6.53 and 6.54.

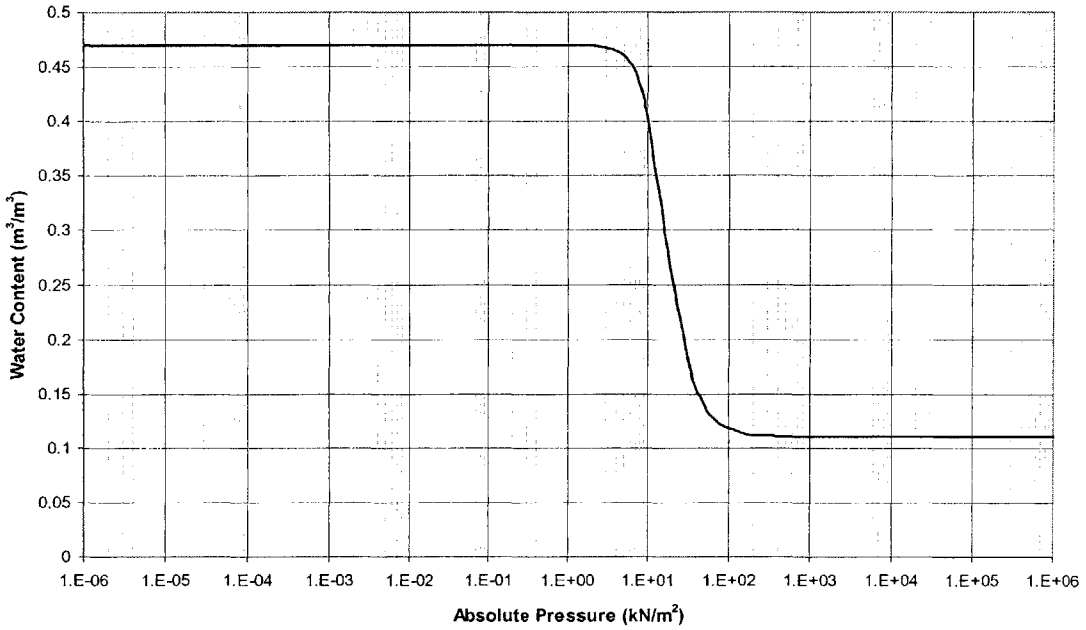

Figure 6.53. Moisture Retention Characteristic Curve

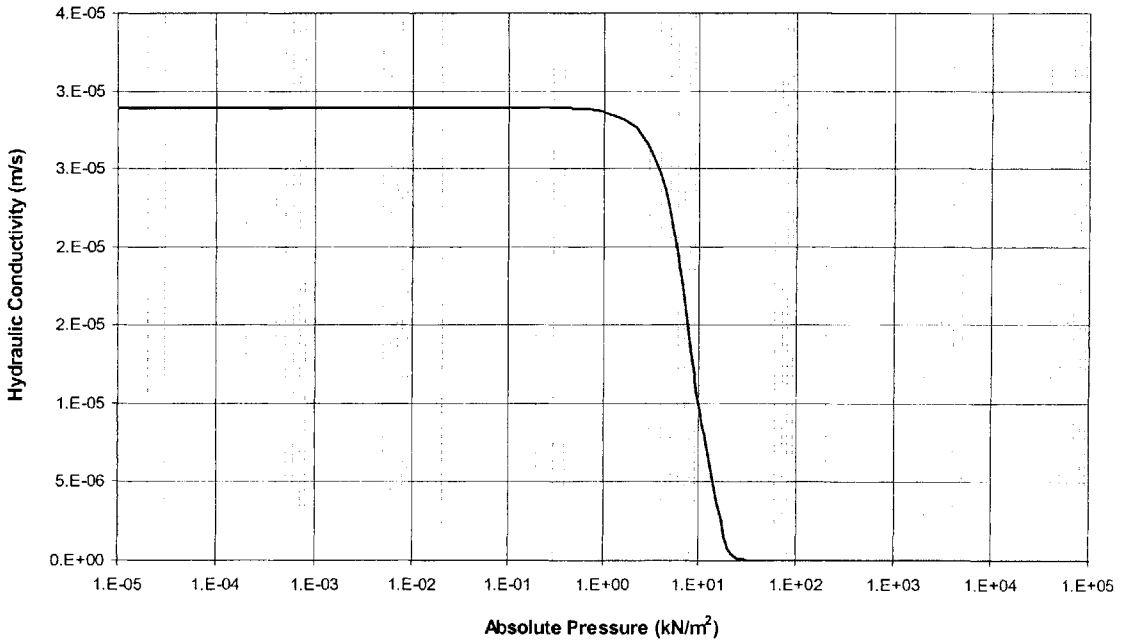

Figure 6.54. Hydraulic Conductivity Characteristic Curve

A rainfall event with intensity, $I = 75mm/hr$ is assumed to occur for a duration of 8 hours. Figure 6.55 shows moisture profiles, and Figure 6.56 shows pressure profiles at selected times.

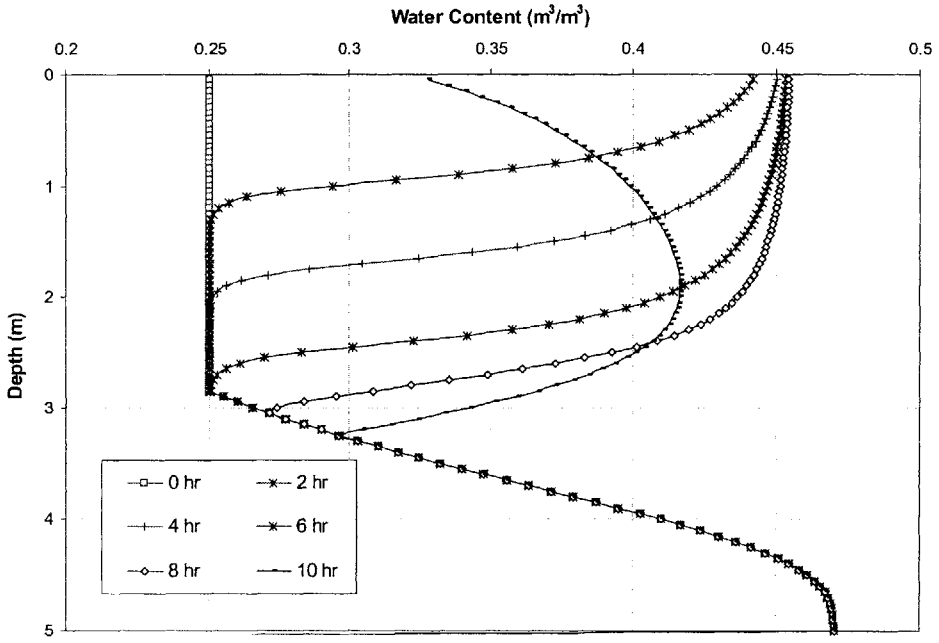

Figure 6.55. Moisture Content Profiles with Time using the van Genuchten (1980) Model

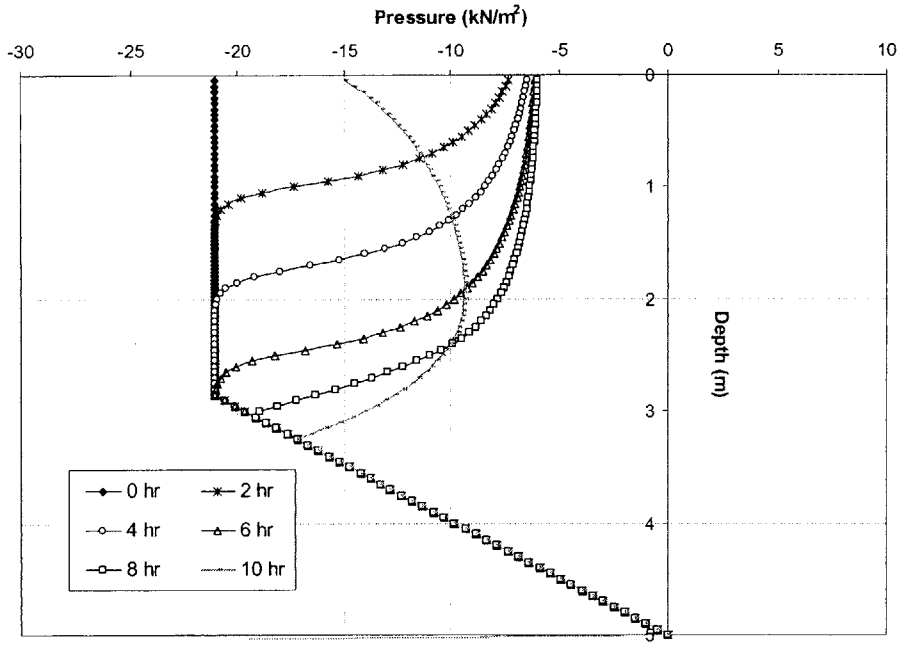

Figure 6.56. Pressure Profiles with Time using the van Genuchten (1980) Model

The stability of the slope is assessed for different values of $\lambda_{unsaturated}$ in the unsaturated soil, while assuming parallel to slope seepage in the saturated soil. The results are shown in Figure 6.57.

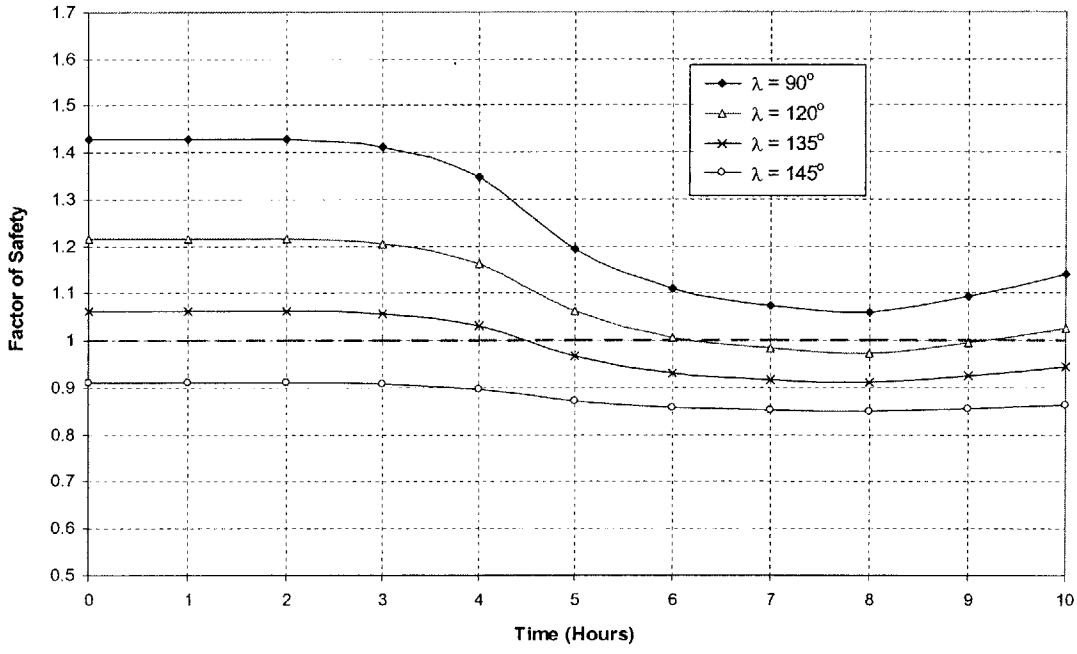

Figure 6.57. Variation of Factors of Safety with Time for different λ and $I < K_s$

Note that the value of $\lambda = 90^o$ in Figure 6.57 corresponds to parallel to slope seepage.

Figure 6.57 shows that there is a significant difference in the Factors of Safety for the different values of λ. The difference is greatest at early times during the rainfall event, when the soil on the failure surface is still unsaturated. With time and continued rain, moisture content in the soil on the failure surface increases (see Figure 6.56), and the effects of different values of λ decrease. They do, nonetheless, have significant effects on the results, and lead to different conclusions regarding stability.

We now assume that the soil strength parameters and hydraulic conductivity are uncertain with the following distributions:

$c' \sim N(m_{c'} = 0.5kN/m^2,\ \sigma_{c'} = 0.0125kN/m^2)$; $\phi' \sim N(m_{\phi'} = 28^o,\ \sigma_{\phi'} = 7^o)$;

$K_S \sim LN(m_{K_S} = 250cm/day, \sigma^2_{K_S} = (125cm/day)^2)$; and these parameters are uncorrelated.

Figure 6.58 shows the variation of the probability of failure with time for the case of parallel to slope seepage, $\lambda = 90^o$, and for the case when $\lambda = 120^o$.

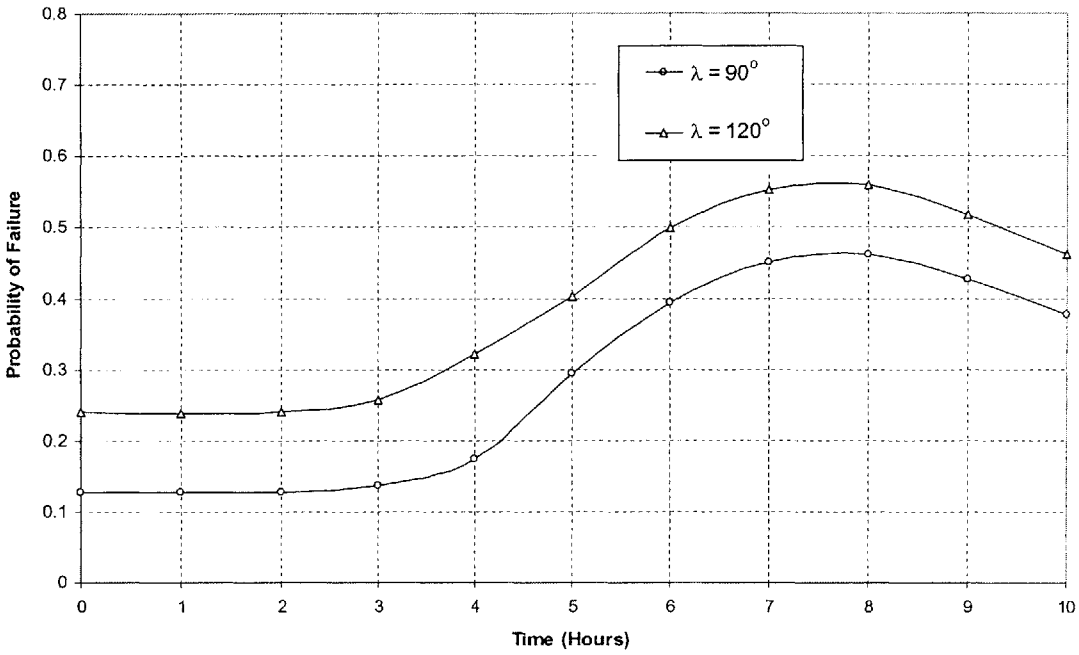

Figure 6.58. Variation of Probability of Failure with Time for different λ and $I < K_s$

Figure 6.58 clearly shows that different values of λ can lead to different probabilities of slope failure, and illustrates the effects of seepage direction on landslide hazards.

LANDSLIDE HAZARDS WITH RAINFALL INTENSITY GREATER THAN SATURATED CONDUCTIVITY

In this example, we consider the slope shown in Figure 6.59.

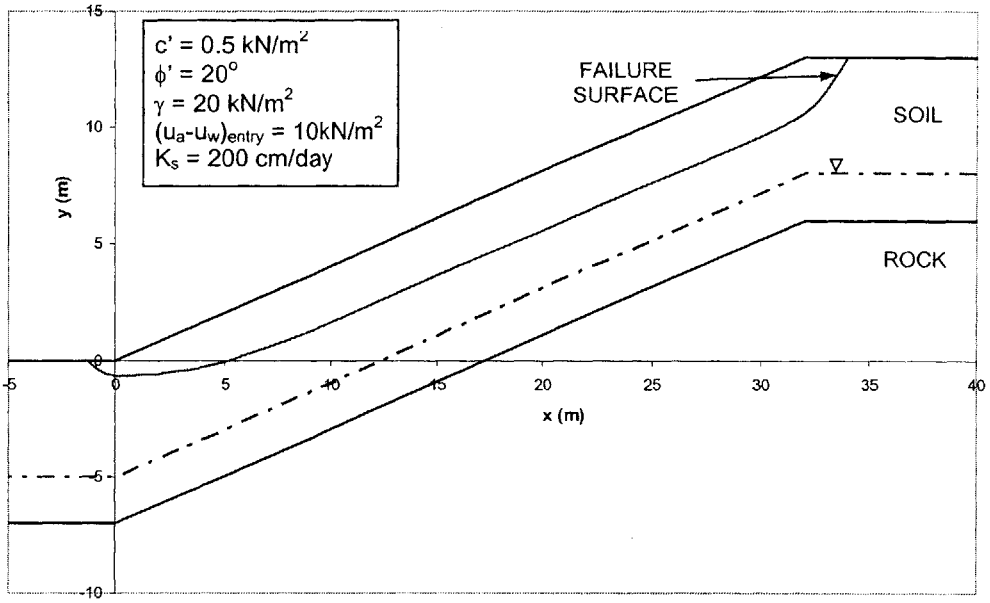

Figure 6.59. Slope Properties and Failure Surface

The soil characteristic curves are shown in Figures 6.60 and 6.61.

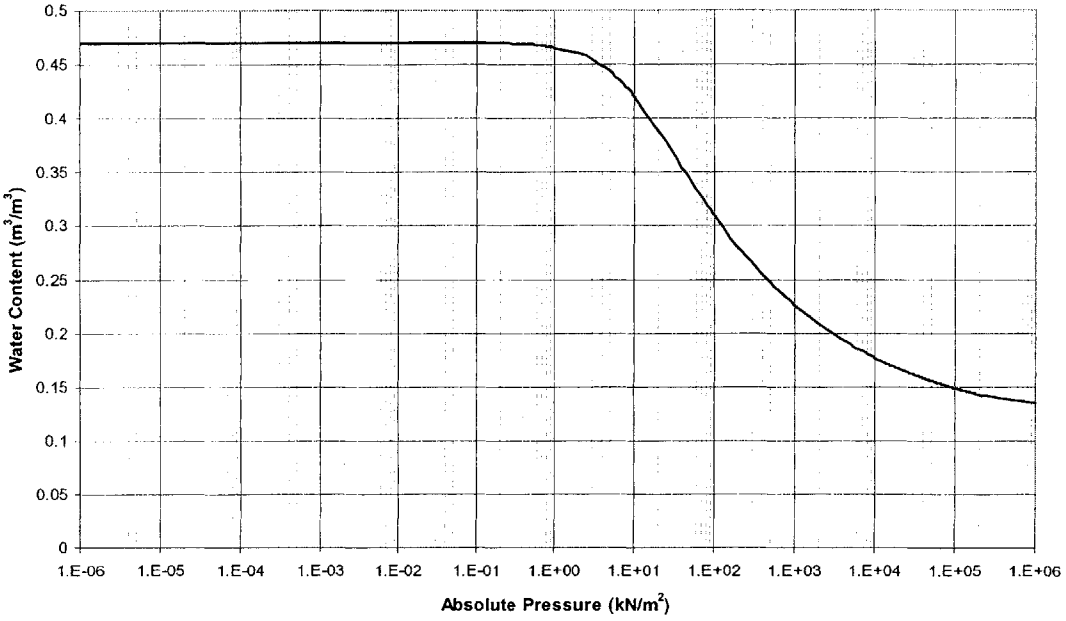

Figure 6.60. Moisture Retention Characteristic Curve

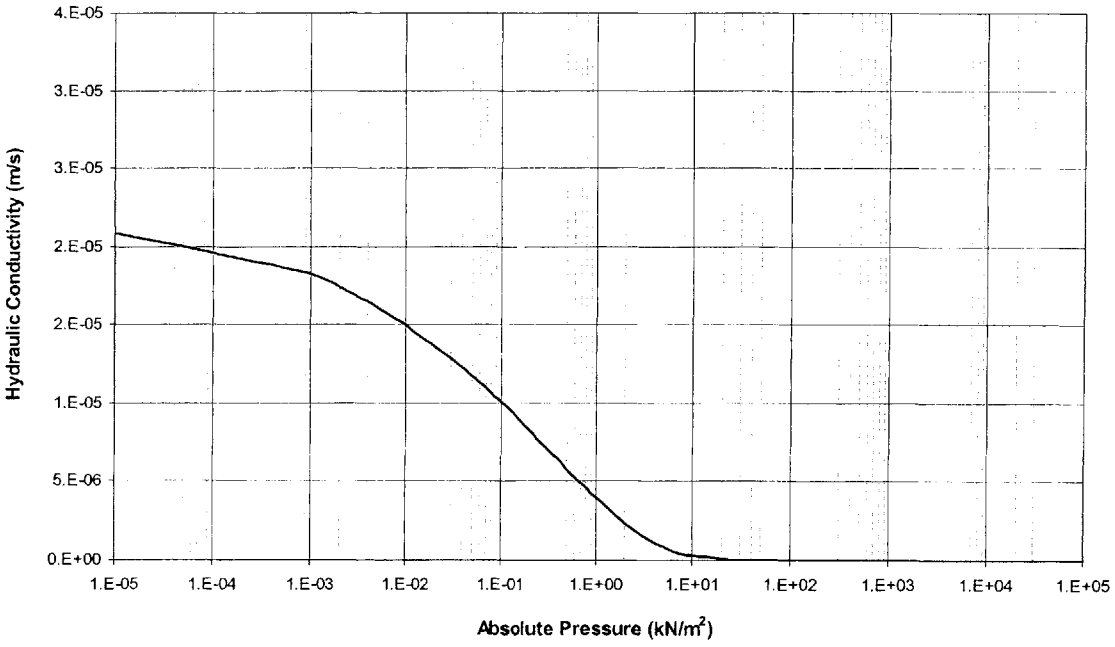

Figure 6.61. Hydraulic Conductivity Characteristic Curve

A rainfall event of intensity $I = 375cm/day = 155mm/hr$ (greater than the saturated conductivity of the soil at the surface) is assumed to take place for a duration of 8 hours. Figure 6.62 shows moisture profiles, and Figure 6.63 shows pressure profiles at selected times.

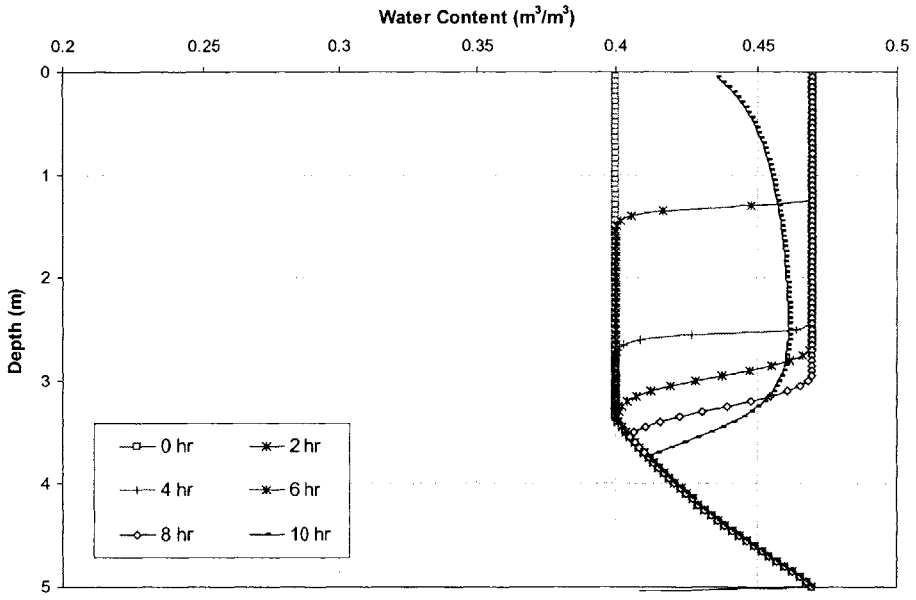

Figure 6.62. Moisture Content Profiles with Time using the van Genuchten (1980) Model

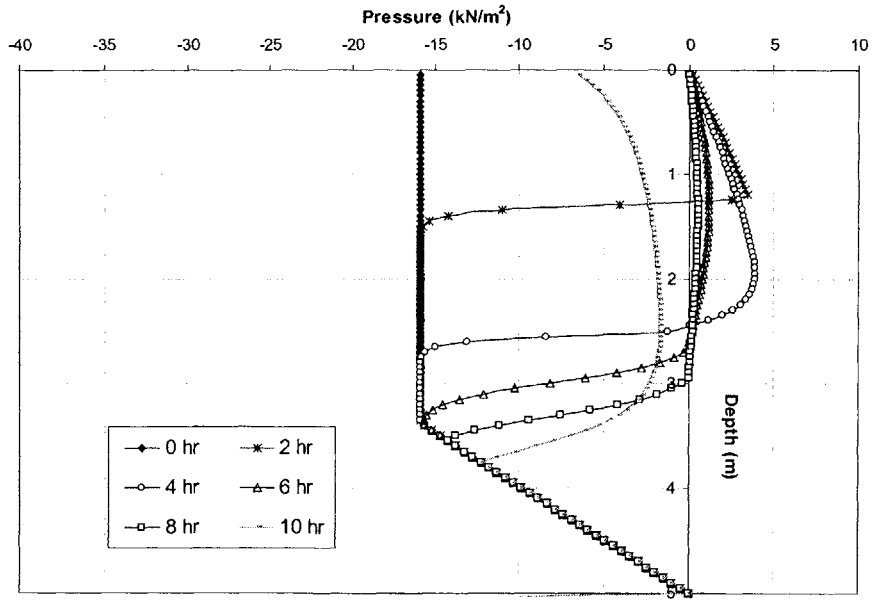

Figure 6.63. Pressure Profiles with Time using the van Genuchten (1980) Model

The stability of the slope is assessed for different values of λ in the unsaturated soil, while assuming parallel to slope seepage in the saturated soil, and the results are shown in Figure 6.64.

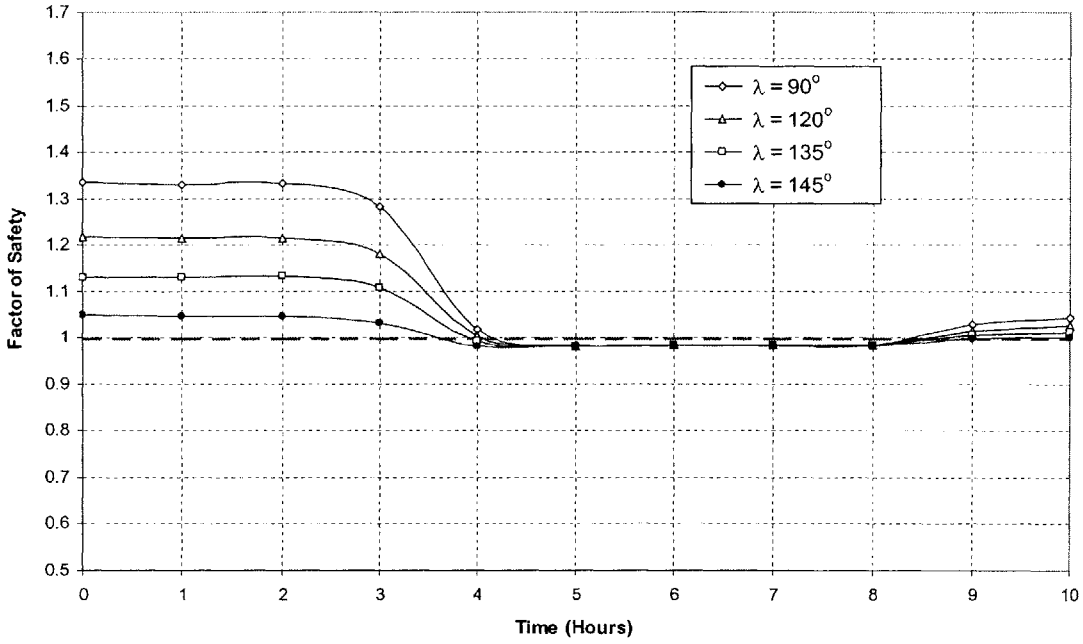

Figure 6.64. Variation of Factors of Safety with Time for different λ and $I > K_s$

Figure 6.64 illustrates the effects of different values of λ on stability. The difference in the results is greatest at early times during the rainfall event, since the rainwater has not yet penetrated the soil deep enough to saturate the entire failure surface (see Figure 6.63). With time and increasing infiltration depth, the rainwater saturates the soil on the failure surface completely. As a consequence, the effects of λ on stability decrease. At a time of about 4 hours, the soil on the entire failure surface is saturated, and λ has little effects on stability, since it is assumed that parallel to slope seepage takes places in saturated soil.

We now assume that the soil strength parameters, and hydraulic conductivity are uncertain and follow the distributions:

$$c' \sim N(m_{c'} = 0.5 kN/m^2,\ \sigma_{c'} = 0.017 kN/m^2);\ \phi' \sim N\phi' \sim (m_{\phi'} = 20^o,\ \sigma_{\phi'} = 6.67^o)$$

$K_s \sim LN(m_{K_s} = 200cm/day, \sigma^2_{K_s} = (100cm/day)^2)$; and these parameters are uncorrelated.

Figure 6.65 shows the variation of the probability of failure with time for the case of parallel to slope seepage when $\lambda = 90^o$, and for the case when $\lambda = 120^o$.

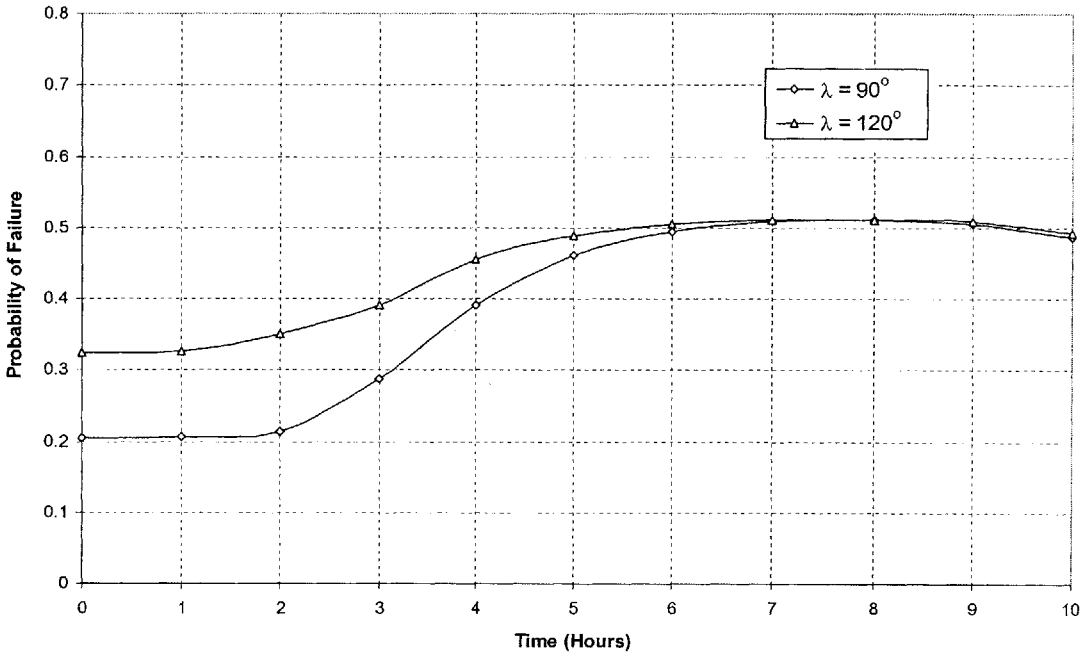

Figure 6.65. Variation of Probabilities of Failure with Time for different λ and $I > K_s$

Figure 6.65 shows that the effects of λ on the probability of slope failure, and hence landslide hazards, is again most significant at early times. The effects become less significant with time and rainwater infiltration as soil on the failure surface gets saturated.

6-2.1.2.4. DISCUSSION ON SEEPAGE DIRECTION SUBMODEL UNCERTAINTY

The two examples presented in the preceding Sections illustrate the effects of different values of λ on stability analyses, and landslide hazards. The results show that λ can have significant influence on both deterministic and probabilistic results, and therefore on landslide hazards. The effects are more significant in the first example, where the

rainfall intensity is less than the saturated conductivity, and the soil remains unsaturated. $\lambda = 90^{o}$ in Figures 6.57, 6.58, 6.64 and 6.65 corresponds to parallel to slope seepage. Figures 6.57 and 6.64 show that seepage directions $\lambda > 90^{o}$, which are more likely in unsaturated soil, result in lower Factors of Safety. This is also shown in Figures 6.58 and 6.65 by higher probabilities of failure. Thus, the assumption of parallel to slope seepage, which is commonly adopted in stability analyses, can be unconservative. This result is particularly relevant to the study of shallow landslides, where failure may occur in unsaturated soil.

6-2.1.2.5. CONCLUSIONS ON SEEPAGE SUBMODEL UNCERTAINTY

The effects of seepage direction on slope stability analyses, and landslide hazard assessments were investigated. This is a type of model uncertainty that comes about because of different assumptions in the same stability model. We showed that different seepage directions can significantly affect stability analyses and landslide hazards assessments.

Seepage directions $\lambda > 90^{o}$ cause an increase in pore pressures and hence a decrease in strength if the soil is unsaturated. Conversely, seepage directions $\lambda > 90^{o}$ cause a reduction in pore pressures, and hence an increase in shear strength if the soil is saturated. Correspondingly, seepage directions $\lambda < 90^{o}$ tend to decrease the strength of saturated soil, and increase the strength of unsaturated soil. This is particularly relevant to the study of shallow rainfall induced landslides where failure can occur in unsaturated soil as a result of changes in suction. For such failures, we showed that the assumption of parallel to slope seepage can lead to unconservative results, by overestimating Factors of Safety and underestimating probabilities of failure.

6-2.1.3. PARAMETER DISTRIBUTION SUBMODEL UNCERTAINTY

Second moment reliability and probabilistic analyses such as those performed in Chapter 5 require the assumption of models for the distribution of uncertain parameters.

These models include models for:

(a) Correlation between parameters, and
(b) The probability distribution of parameters

In this Section, we investigate the effects of different parameter models on slope reliability and probabilistic analyses, and on landslide hazards. Emphasis is placed on the soil strength parameters as uncertain parameters.

6-2.1.3.1. CORRELATION SUBMODEL UNCERTAINTY

The issue of model uncertainty from correlation between strength parameters was alluded to in Chapter 4, where the Infinite Slope Stability Model (Skempton and DeLory, 1950) was used to perform sensitivity analyses by varying c' and ϕ' assuming positive and negative correlation. The analyses showed that different correlation can have significant effects on stability analyses. In this Section, we investigate the effects of correlation between c' and ϕ' more rigorously through the effects on slope reliability and probabilities of failure, as well as on landslide hazards assessments. Figure 6.66 shows in bold what is studied in this Section.

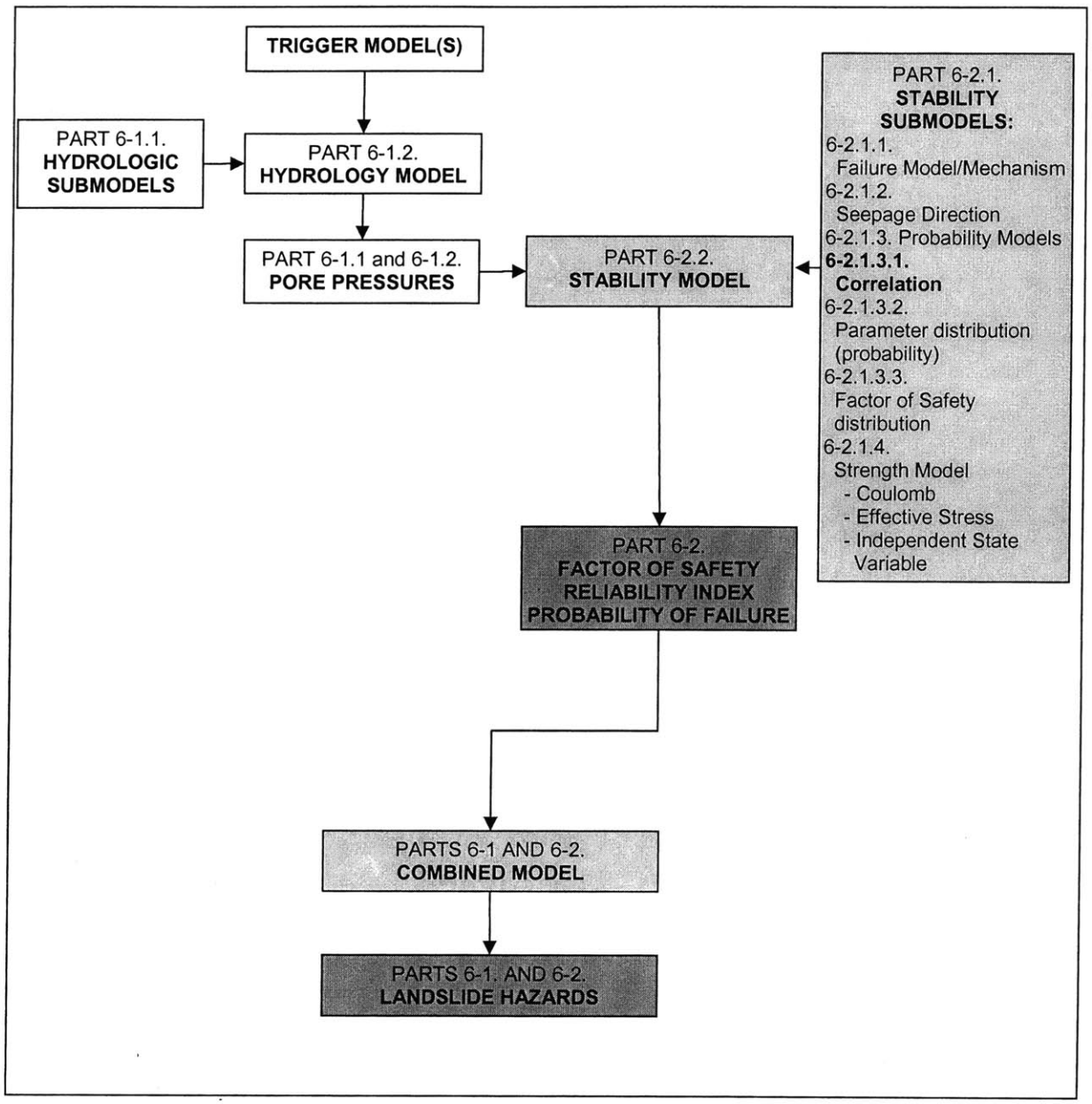

Figure **6.66.** Effects of correlation (shown in the lightly shaded submodels box) on the results of stability analyses (Factors of safety, reliability indices and probabilities of failure in the dark shaded box) and on landslide hazards (dark box) are investigated

6-2.1.3.1.1. CORRELATION SUBMODEL UNCERTAINTY IN MEAN VALUE FIRST ORDER SECOND MOMENT (MFOSM) RELIABILITY ANALYSES

Consider the slope shown in Figure 6.67.

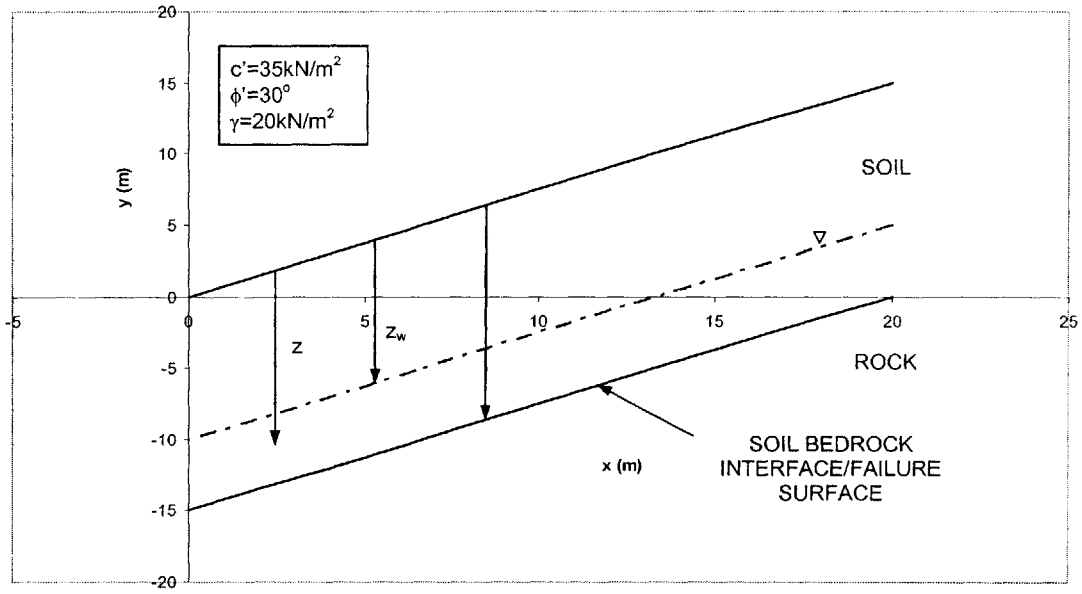

Figure **6.67.** Slope Geometry and Definition of Parameters

The reliability of the slope in Figure 6.67 was assessed in Chapter 5, Part 5-2.2.1 by computing the mean value first order second moment reliabilty index based on the parameters and their uncertainty shown in Table 6.1.

Parameter, X	Symbol	E[X]	V[X]
Cohesion (kN/m^2)	c'	35	0.1
Angle of shearing resistance	ϕ'	30	0.05
Saturated unit weight of soil (kN/m^2)	γ_s	20	0.01
Slope angle	β	35	0.05
Depth to failure surface (m)	z	15	0.05
Unit weight of water (kN/m^2)	γ_w	9.81	0
Depth of water Table from ground surface (m)	z_w	10	0.05

Table 6.1. Expected Values, E[X], and Coefficients of Variation, V[X], of Parameters

The Mean Value First Order Second Moment reliability index was computed to be $\beta = 0.762$, resulting in a probability of failure $P_f = \Phi(\beta) = 0.78$, when the Factor of Safety was assumed to be normally distributed.

An advantage of the Mean Value First Order Second Moment reliability index applied to the Infinite Slope Model is that analytical expressions for the partial derivatives that are required to compute β can be derived. In particular, the derivatives of the Factor of Safety with respect to c' and ϕ' were given as:

$$\frac{\partial F}{\partial c'} = \frac{1}{\gamma_s z \sin\beta \cos\beta} \qquad [6.14]$$

$$\frac{\partial F}{\partial \phi'} = \left[\frac{z\gamma_s + (z_w - z)\gamma_w}{z\gamma_s \tan\beta}\right] \sec^2 \phi' \qquad [6.15]$$

The first order second moment approximation to the variance of the Factor of Safety is given by:

$$\text{Var}[F] = \sum_{i=1}^{n} \left(\frac{\partial F}{\partial X_i}\right)\Big|_m^2 \text{Var}[X_i] + 2\sum_{i=1}^{n} \left(\frac{\partial F}{\partial X_i}\right)\left(\frac{\partial F}{\partial X_j}\right)\Big|_m \text{Cov}[X_i, X_j] \qquad [6.16]$$

where:

X_i and X_j are the uncertain parameters of the vector $\underline{X} = [c' \;\; \phi' \;\; \gamma_s \;\; \beta \;\; z \;\; z_w]^T$.

The contribution to the variance of the Factor of Safety from the covariance terms between c' and ϕ' is given by:

$$2\left(\frac{\partial F}{\partial c'}\right)\left(\frac{\partial F}{\partial \phi'}\right)\Big|_m \text{Cov}[c', \phi'] \qquad [6.17]$$

where and $\left(\frac{\partial F}{\partial c'}\right)\left(\frac{\partial F}{\partial \phi'}\right)\Big|_m$ are the partial derivatives given in Equations [6.14] and [6.15], evaluated at the mean values of c' and ϕ'.

Since the mean values of all parameters are positive (or zero), the sign of the product in Equation [6.17] will depend on the sign of $Cov[c',\phi']$, since $\left(\frac{\partial F}{\partial c'}\right)\left(\frac{\partial F}{\partial \phi'}\right)\Big|_m$ is positive. For the slope shown in Figure 6.67 and parameters in Table 6.1, the product in Equation [6.17] becomes:

$$2\left(\frac{\partial F}{\partial c'}\right)\left(\frac{\partial F}{\partial \phi'}\right)\Big|_m Cov[c',\phi'] = 0.002\rho \qquad [6.18]$$

where ρ is the correlation coefficient.

Equation [6.18] is a linear function of ρ, and the contribution to the variance of the Factor of Safety depends on the sign of ρ.

No correlation between the strength parameters, c' and ϕ' implies if the value of one of the parameters is known, no conclusion can be made on the value of the other. The term in Equation [6.18] is zero, and there is no contribution to the variance of the Factor of Safety.

Positive correlation between c' and ϕ', implies that when c' increases (or is above its mean value) ϕ' increases also (or is above its mean value). The term in Equation [6.18] is positive, increasing the variance of the Factor of Safety. As the uncertainty in the Factor of Safety increases, β decreases, leading to higher reliability.

Alternatively, negative correlation between the strength parameters, c' and ϕ', implies that when c' increases (or is above its mean value) ϕ' decreases (or is lower than its mean value). The term in Equation [6.18] is negative, reducing the variance of the Factor of Safety. As the uncertainty in the Factor of Safety decreases, β increases, leading to lower reliability.

In practice, one can be reasonably sure that the strength parameters are negatively correlated and this correlation leads to an increase in slope reliability compared to when the parameters are uncorrelated. The relative contribution of correlation to the variance of the Factor of Safety is shown in Figures 6.68, 6.69 and 6.70 for different correlation.

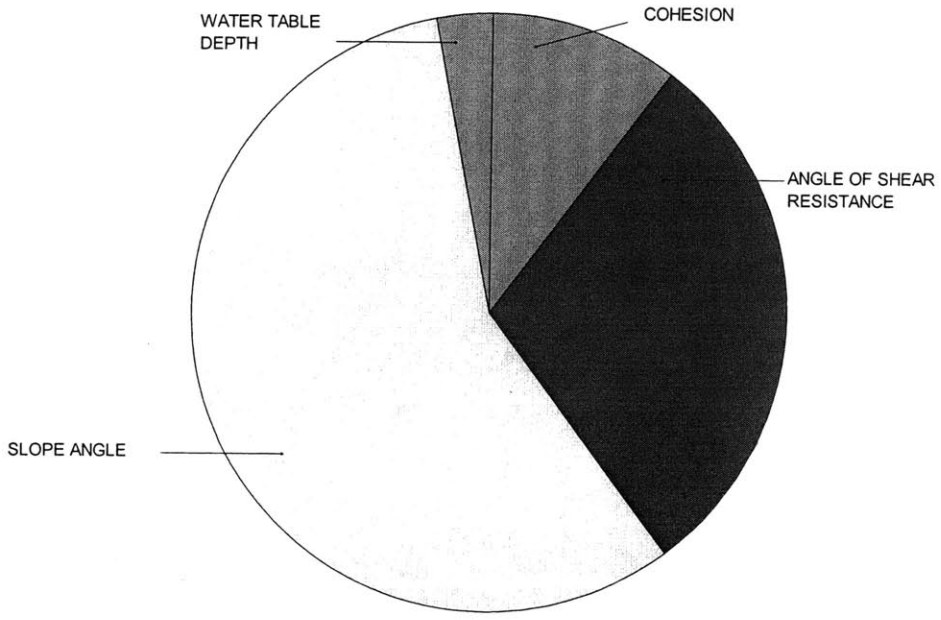

Figure 6.68. Relative Contribution of Uncertainty in Parameters to Uncertainty of Factor of Safety (Uncorrelated Strength Parameters $\rho = 0$)

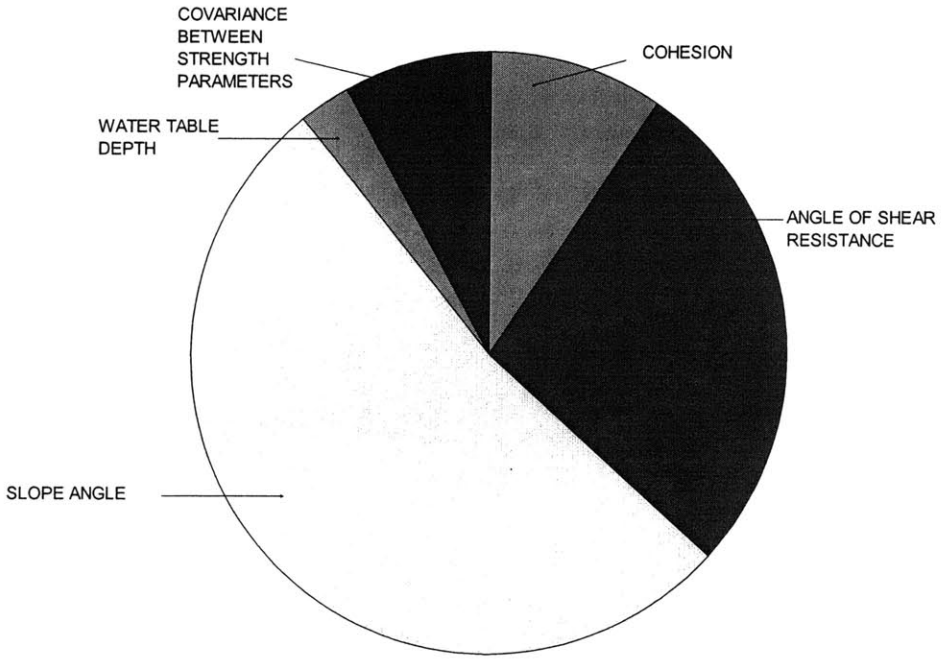

Figure 6.69. Relative Contribution of Uncertainty in Parameters to Uncertainty of Factor of Safety (Strength Parameters Correlated $\rho = -0.25$)

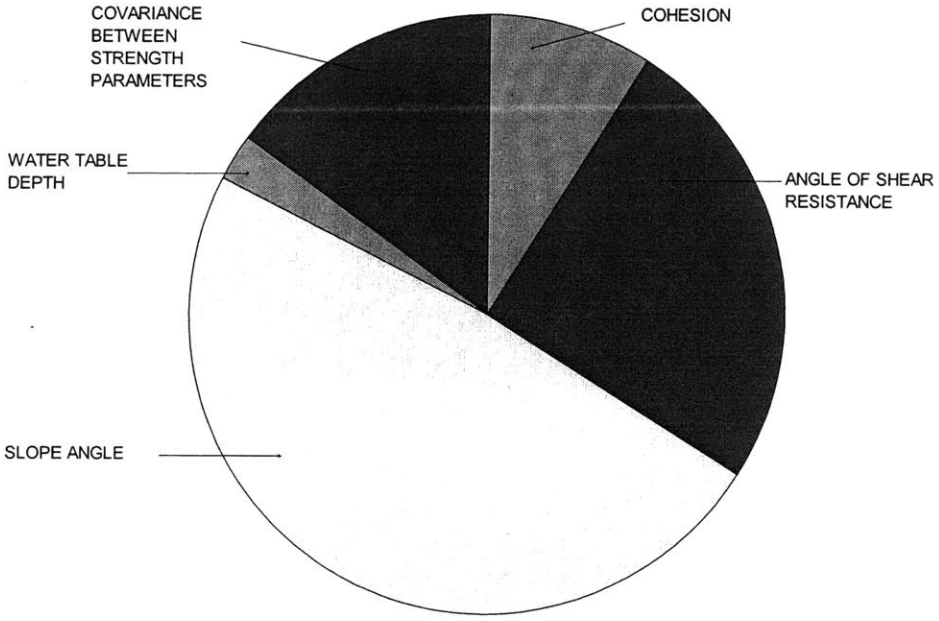

Figure 6.70. Relative Contribution of Uncertainty in Parameters to Uncertainty of Factor of Safety (Strength Parameters Correlated $\rho = -0.5$)

Figures 6.68 to 6.70 show that the contribution of correlation between strength parameters to the variance of the Factor of Safety can be significant. In fact, in this example, it is greater than the contribution from other parameters, such as the location of the water table (degree of saturation in the slope) and cohesion.

6-2.1.3.1.2. CORRELATION SUBMODEL UNCERTAINTY IN HASOFER AND LIND (1974) RELIABILITY ANALYSES

To illustrate the effects of correlation model uncertainty on the Hasofer and Lind (1974) reliability index, and reliability analyses we consider the slope presented in Figure 6.71.

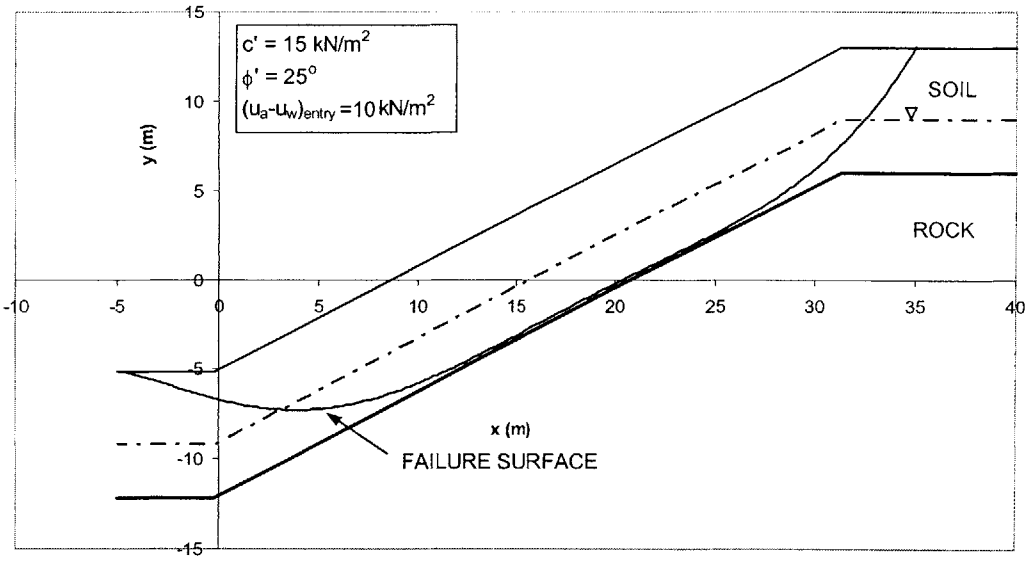

Figure 6.71. Slope Geometry and Strength Parameters

The reliability of this particular slope was analyzed in Example 2 of Part 5-2 in Chapter 5 where c' and ϕ' were assumed uncorrelated. Figure 6.72 shows the reliability chart that was obtained on the critical deterministic failure surface shown in Figure 6.71, and the reliability index was computed to be $\beta = 0.93$.

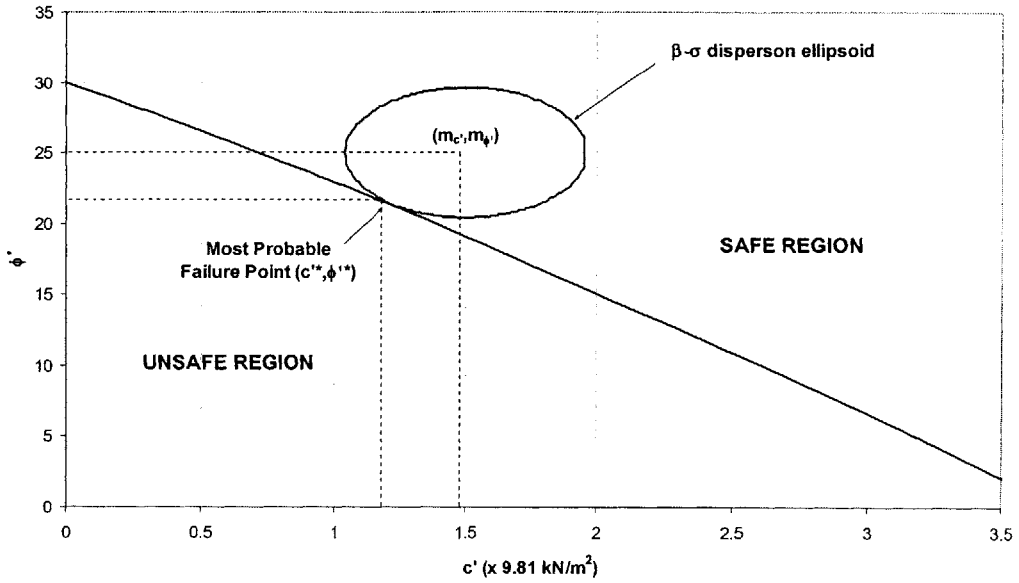

Figure **6.72.** Reliability Chart Derived From Deterministic Analyses for Uncorrelated Variables

We now assume that c' and ϕ' are negatively correlated, with correlation coefficient $\rho = -0.25$. The reliability index on the deterministic surface in Figure 6.71 is computed to be $\beta = 1.11$, when (negative) correlation is introduced. A reliability chart is derived and is shown in Figure 6.73.

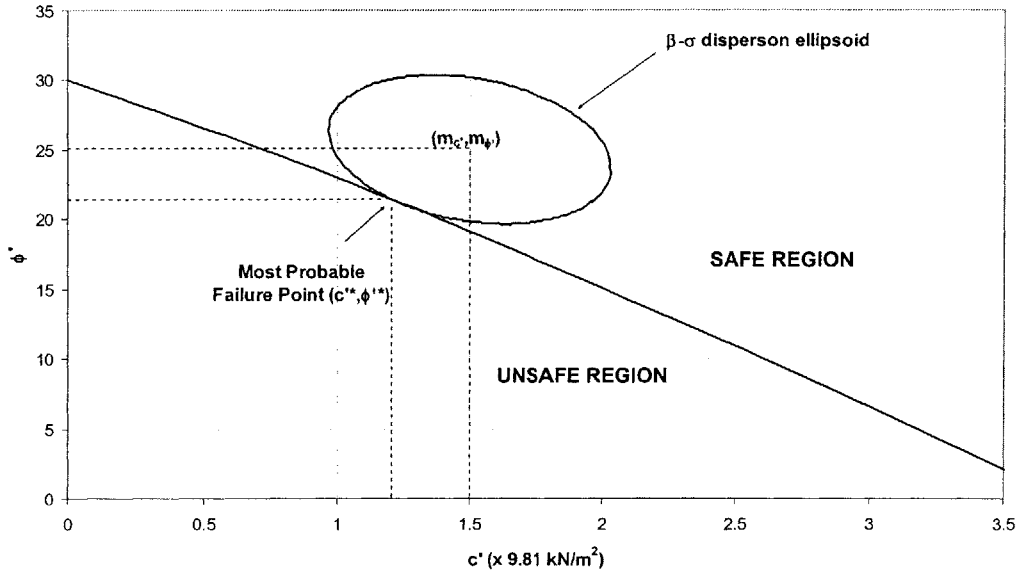

Figure 6.73. Reliability Chart Derived From Deterministic Analyses Assuming Negatively Correlated Soil Strength Parameters

Figure 6.73 also shows the $\beta - \sigma$ dispersion ellipsoid, which is tangential to the failure boundary at the critical failure point $c'^* = 11.8$ kN/m^2 and $\phi'^* = 21.6^o$. The $\beta - \sigma$ dispersion ellipsoid in Figure 6.73 is tilted because of the assumed correlation between c' and ϕ'. The direction of the tilt is in the direction of the major axis of the ellipsoid (which is also in the direction of the failure boundary), when negative correlation is assumed.

Figure 6.73 compares the $\beta - \sigma$ dispersion ellipsoids in the case of no correlation, and when correlation is assumed.

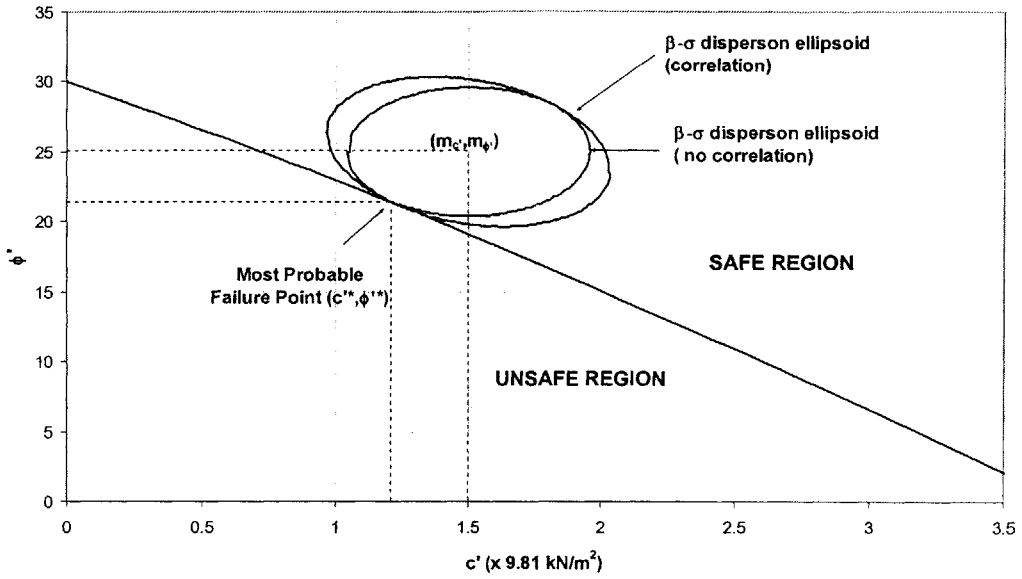

Figure 6.74. Comparison of Reliability Charts Assuming Uncorrelated and Negatively Correlated Soil Strength Parameters (Deterministic Case)

The size of the $\beta-\sigma$ dispersion ellipsoid when correlation is included is larger than the one when no correlation is included. The tilt in the dispersion ellipsoid allows it to increase in size more than when the ellipsoid is not tilted before hitting the failure boundary. As a result β is larger in the case of correlated variables (β=1.11) compared to the case of uncorrelated variables (β=0.93). Because of this, the reliability of the slope is also greater in the case of correlated variables than in the case of uncorrelated variables.

The analyses performed above are based on the critical deterministic failure surface. When the parameters are uncertain, the uncertainty affects the location of the critical failure surface. This was discussed in Part 5-4 of Chapter 5. There exists, therefore, a critical reliability based failure surface that is obtained after including the uncertainty in parameters. The procedure to locate this failure surface was shown in Figure 5.34 in Chapter 5.

We locate the critical reliability based failure surface in the slope in this example, which is shown in Figure 6.75.

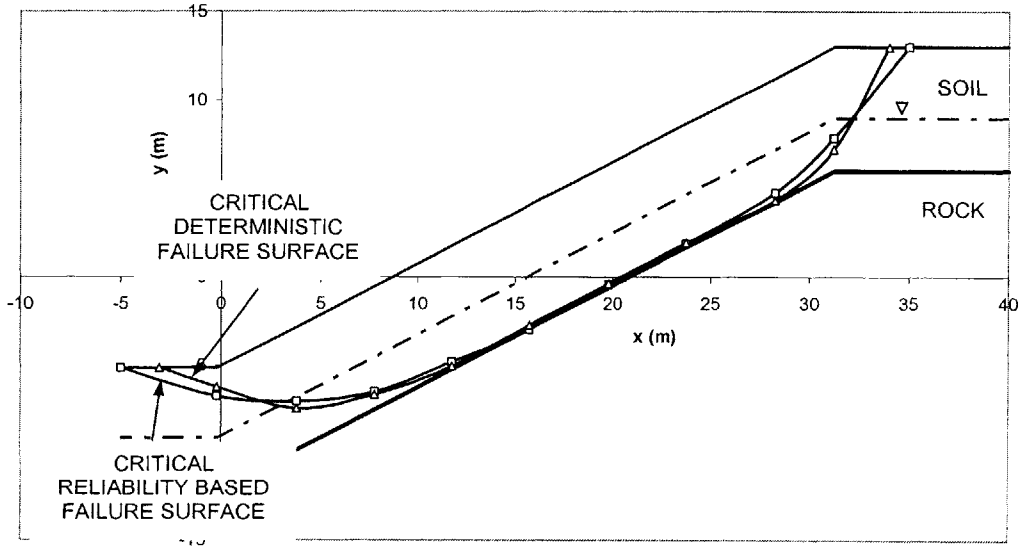

Figure 6.75. Critical Reliability Based Failure Surfaces Assuming Negatively Correlated Soil Strength Parameters (square symbols) and Critical Deterministic Failure Surface (triangle symbols)

Note that although the critical deterministic failure surface in the slope is the same whether or not correlation is assumed between uncertain parameters (this is reflected in the same failure boundary in both cases in Figure 6.74), the critical reliability surface is different. This is shown in Figure 6.75. This is because the reliability index depends on both the uncertainty in parameters, as well as the correlation between them.

A value of $\beta = 1.01$ is computed and the critical failure point is $c'^* = 11.9$ kN/m^2 and $\phi'^* = 21.9^o$. The reliability chart is shown in Figure 6.76.

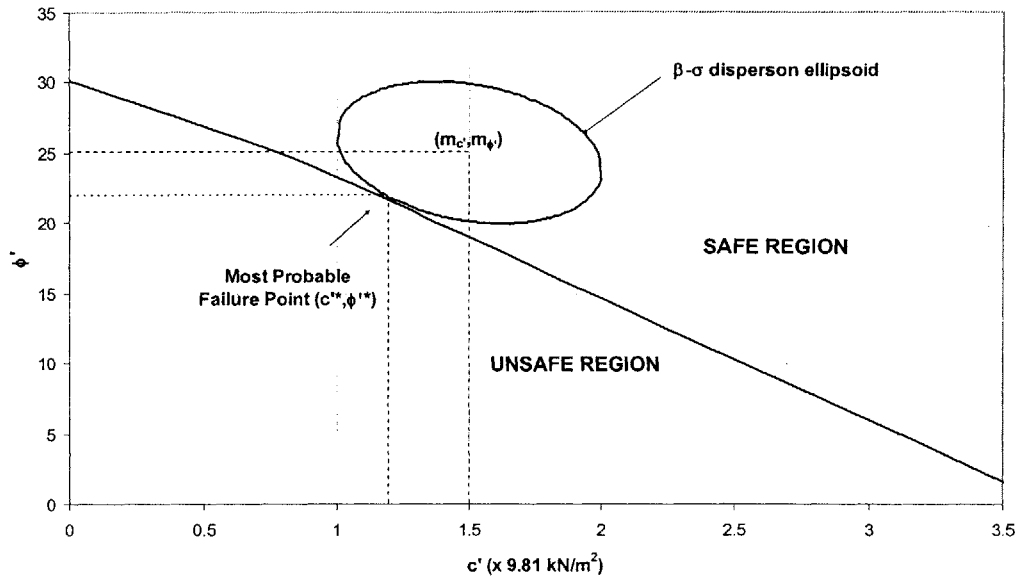

Figure **6.76.** Reliability Chart Assuming Negatively Correlated Soil Strength Parameters

Figure 6.77 compares the reliability charts for the cases of correlation and no correlation, and shows the difference in the failure boundary that result from the different critical reliability failure surfaces.

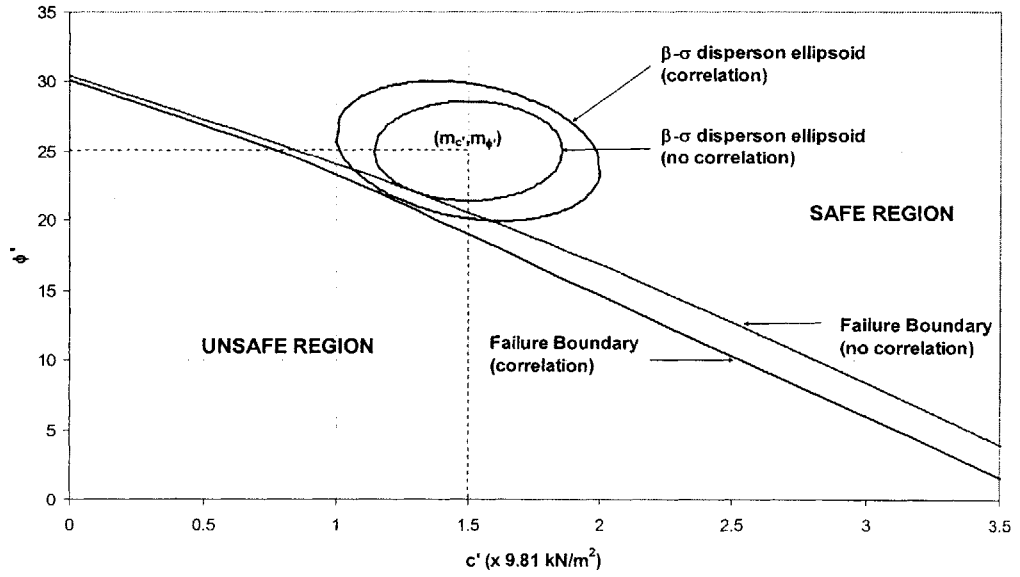

Figure **6.77.** Comparison of Reliability Charts Assuming Uncorrelated and Negatively Correlated Soil Strength Parameters (Reliability Case)

The reliability index was computed to be $\beta = 0.72$ in the case when no correlation is assumed (see Example 2 in Part 5-2 of Chapter 5).

The effect of correlation on reliability analyses is evident by comparing the reliability indices for the cases of correlation and no correlation. This is true whether reliability analyses are based on the critical deterministic failure surface ($\beta = 0.93$ for no correlation vs. $\beta = 1.11$ for correlation) or the critical reliability based failure surface ($\beta = 0.72$ for no correlation vs. $\beta = 1.01$ for correlation).

This is illustrated graphically in the reliability charts shown in Figures 6.74 and 6.77. The reliability index in the case where negative correlation is assumed between the soil strength parameters is larger than when no (negative) correlation is assumed in both Figures 6.74 and 6.77. Because of the tilt in the ellipsoid when correlation is introduced, the ellipsoid can grow larger in size before becoming tangential to the failure boundary (see Figure 6.77 for example). This implies a larger value of β than in the case when no correlation is assumed.

The effects of correlation can also be demonstrated by comparing probabilities of failure that are computed from β, as $P_F = \Phi(-\beta)$ assuming that the Factor of Safety is Normally distributed. In this case, on the critical deterministic failure surface ($P_F = 0.176$ for no correlation vs. $P_F = 0.133$ for correlation) and on the critical reliability based failure surface ($P_F = 0.235$ for no correlation vs. $P_F = 0.157$ for correlation).

Reliability analyses, therefore, that assume uncorrelated strength parameters lead to lower probabilities of failure (through larger β) and are therefore conservative. This is important, and may have significant practical implications when designing or managing slopes.

6-2.1.3.1.3. CORRELATION SUBMODEL UNCERTAINTY IN PROBABILISTIC SLOPE STABILITY ANALYSES

In this Section, we use the Monte Carlo techniques developed in Chapter 5, Part 5-3 to asses the effects of correlation between strength parameters on probabilistic slope stability analyses. In Part 5-3 of Chapter 5, the Monte Carlo Method and its application within the spreadsheet environment to generate random numbers from the Normal distribution was described. This involves generating random numbers from the uniform distribution between 0 and 1, and transforming these numbers to random variables from the Normal distribution. This was demonstrated for the case of uncorrelated c' and ϕ', where each parameter was generated from its appropriate distribution. In the case when correlation between c' and ϕ' is introduced, c' and ϕ' become dependent. Random numbers of the vector $\begin{bmatrix} c' \\ \phi' \end{bmatrix}$ need to be generated from the specified/known distribution of the vector. In this study, we assume that c' and ϕ' are joint normally distributed, in which case, the vector $\begin{bmatrix} c' \\ \phi' \end{bmatrix}$ is jointly Normal, and values of c' and ϕ' need to be generated from the Multivariate (Bivariate in this case) Normal distribution.

To do so, one needs to first specify the distribution parameters of the vector $\begin{bmatrix} c' \\ \phi' \end{bmatrix}$, i.e. the mean values and standard deviations of c' and ϕ', as well as the covariance (or the correlation coefficient ρ) between them.

The covariance matrix, $\underline{\Sigma}$, of $\begin{bmatrix} c' \\ \phi' \end{bmatrix}$ can be expressed as:

$$\underline{\Sigma} = \begin{bmatrix} Var[c'] & Cov[c',\phi'] \\ Cov[c',\phi'] & Var[\phi'] \end{bmatrix} \qquad [6.19]$$

$$\underline{\Sigma} = \begin{bmatrix} \sigma_{c'}^2 & \rho\sigma_{c'}\sigma_{\phi'} \\ \rho\sigma_{c'}\sigma_{\phi'} & \sigma_{\phi'}^2 \end{bmatrix} \qquad [6.20]$$

The covariance matrix in [6.20] is a square, symmetric and positive definite matrix.

Because of this, using a Choleski decomposition, $\underline{\Sigma}$ can be expressed as:

$$\underline{\Sigma} = \underline{C}\underline{C}^T \qquad [6.21]$$

where:

$\underline{C}$ is a lower triangular matrix, the Choleski Matrix.

$\underline{C}^T$ is the transpose of $\underline{C}$, an upper triangular matrix.

With $\underline{\Sigma}$ as expressed in [6.21], the Choleski Matrix $\underline{C}$ is given by:

$$\underline{C} = \begin{bmatrix} \sigma_{c'} & 0 \\ \rho\sigma_{\phi'} & \sigma_{\phi'}\sqrt{1-\rho^2} \end{bmatrix} \qquad [6.22]$$

Now, suppose we have a vector $\underline{Z} = \begin{bmatrix} Z_1 \\ Z_2 \end{bmatrix}$, where Z_1 and Z_2 are standard Normal variates with Z ~ N (0, 1).

If we express $\begin{bmatrix} c' \\ \phi' \end{bmatrix} = \underline{m} + \underline{C}\underline{Z}$, then the vector $\begin{bmatrix} c' \\ \phi' \end{bmatrix}$ is joint Normally distributed with mean value vector $\underline{m} = \begin{bmatrix} m_{c'} \\ m_{\phi'} \end{bmatrix}$, and covariance matrix $\underline{\Sigma}$ in Equation [6.20], since the covariance matrix of $\underline{Z}$ is $\underline{I}$, where $\underline{I}$ is the identity matrix.

Using this, to generate random variables from the Bivariate Normal distribution, two (independent) random numbers X_1 and X_2 are generated from the U[0,1] distribution. This is done using the '=RAND()' function in Excel. These are transformed into two standard Normal variables Z_1 and Z_2 from the Standard Normal distribution. This is done using the '=NORMSDIST()' function. Values of c' and ϕ' are then obtained by the operation:

$$\begin{bmatrix} c' \\ \phi' \end{bmatrix} = \underline{m} + \underline{\underline{C}}\underline{Z} \qquad [6.23]$$

Or:

$$\begin{bmatrix} c' \\ \phi' \end{bmatrix} = \begin{bmatrix} m_{c'} \\ m_{\phi'} \end{bmatrix} + \begin{bmatrix} \sigma_{c'} & 0 \\ \rho\sigma_{\phi'} & \sigma_{\phi'}\sqrt{1-\rho^2} \end{bmatrix} \begin{bmatrix} Z_1 \\ Z_2 \end{bmatrix} \qquad [6.24]$$

The '=MMULT()' function is used for the operation in [6.24] in Excel, and so the process can be automated within the spreadsheet.

A function in Visual Basic Editor is developed to return the Cholesky Matrix, and is used as one would use matrix manipulations in Microsoft Excel, i.e. holding down the Shift and Ctrl Keys while pressing the Enter Key. This is shown in Figure 6.78.

```
Function Cholesky(Mat As Range)

Dim A, L() As Double, s As Double
A = Mat
n = Mat.Rows.Count
m = Mat.Columns.Count

If n <> m Then
    Cholesky = "Not Symmetric!"
    Exit Function
End If

ReDim L(1 To n, 1 To n)
For j = 1 To n
    s = 0
    For k = 1 To j - 1
    s = s + L(j, k) ^ 2
    Next k
    L(j, j) = A(j, j) - s
    If L(j, j) <= 0 Then Exit

For L(j, j) = Sqr(L(j, j))
    For i = j + 1 To n
     s = 0
     For k = 1 To j - 1
     s = s+L(i, k)*L(j, k)
     Next k
     L(i,j)=(A(i,j)-s)/L(j,j)
    Next i

Next j
Cholesky = L
End Function
```

Figure 6.78. Cholesky Function

This process is used to generate random values of c' and ϕ', and the Factor of Safety is computed for each combination of c' and ϕ'. A random sample of the Factor of Safety is therefore obtained, and its probability distribution can be estimated for a large sample.

The probability of failure can then be approximated from the generated distribution of Factor of Safety as:

$$P_F = \int_{-\infty}^{1} f_{F(c',\phi')} dF \qquad [6.25]$$

where $f_{F(c',\phi')}$ is the generated probability distribution of the Factor of Safety, F. The probability in Equation [6.25] is the probability that the Factor of Safety lies below the critical value 1.

EXAMPLE 1: SHALLOW BEDROCK

In the first example, we asses the stability of the slope shown in Figure 6.79.

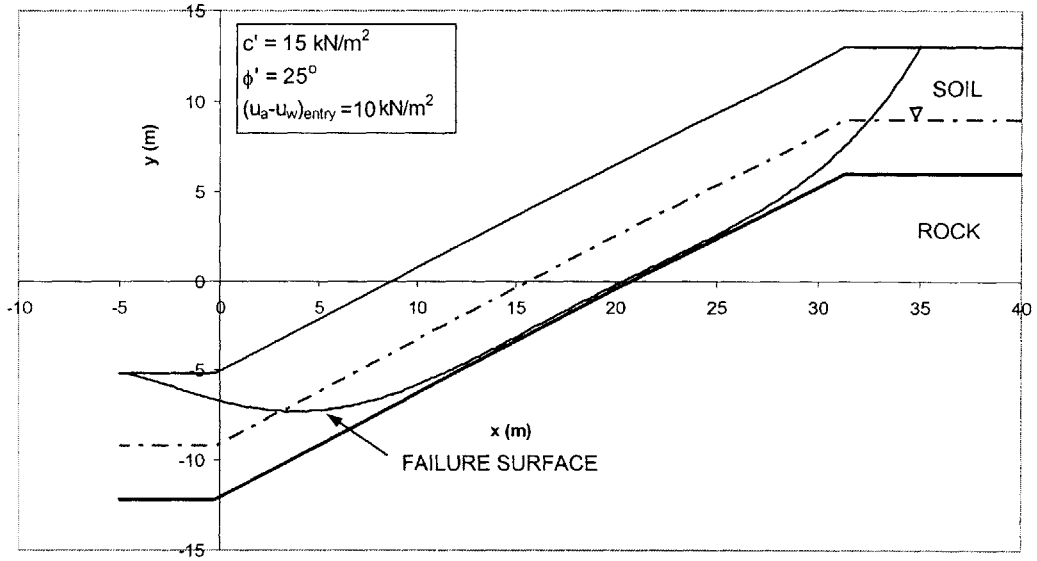

Figure 6.79. Slope Geometry and Strength Parameters

We assume that the vector $\begin{bmatrix} c' \\ \phi' \end{bmatrix}$ is assumed Joint Normal and distributed as:

$$\begin{bmatrix} c' \\ \phi' \end{bmatrix} \sim N\left(\begin{bmatrix} 1.5 \\ 25 \end{bmatrix}, \begin{bmatrix} 5^2 & (\rho)(5)(5) \\ (\rho)(5)(5) & 5^2 \end{bmatrix} \right)$$

where ρ is the correlation coefficient between c' and ϕ'.

The case when c' and ϕ' are assumed uncorrelated was analyzed in Part 5-3 of Chapter 5, and the relative frequency/probability distribution of the Factor of Safety is shown again in Figure 6.80.

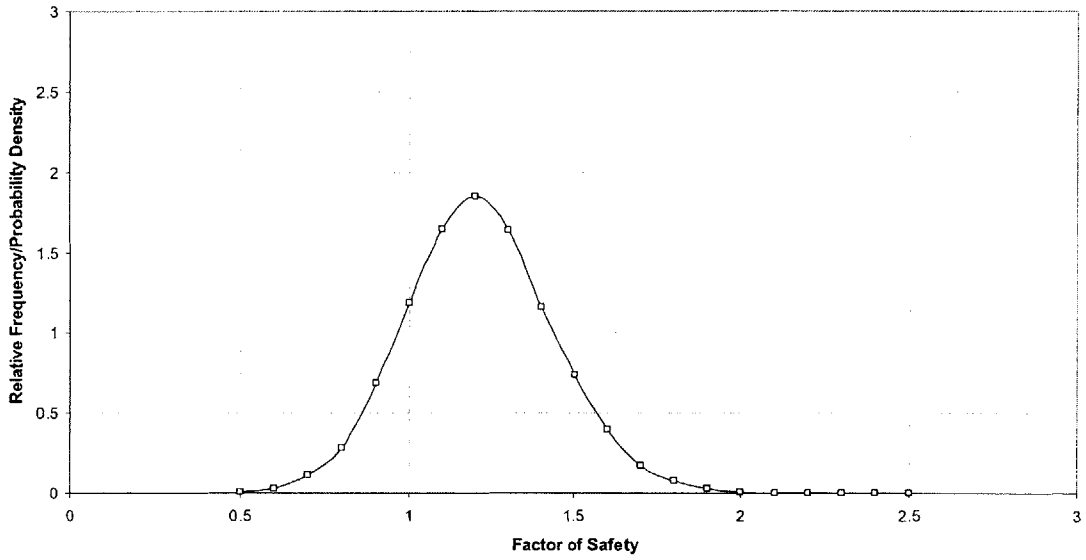

Figure 6.80. Simulated Distribution of Factor of Safety for Uncorrelated Variables

The expected value of the Factor of Safety is E[F] = 1.18, and the standard deviation is $\sigma[F] = 0.22$. The probability of failure is computed according to Equation [6.25], and is $P_F = 0.233$.

We now assume that c' and ϕ' are negatively correlated, with $\rho = -0.25$. The simulated distribution of Factor of Safety is shown in Figure 6.81.

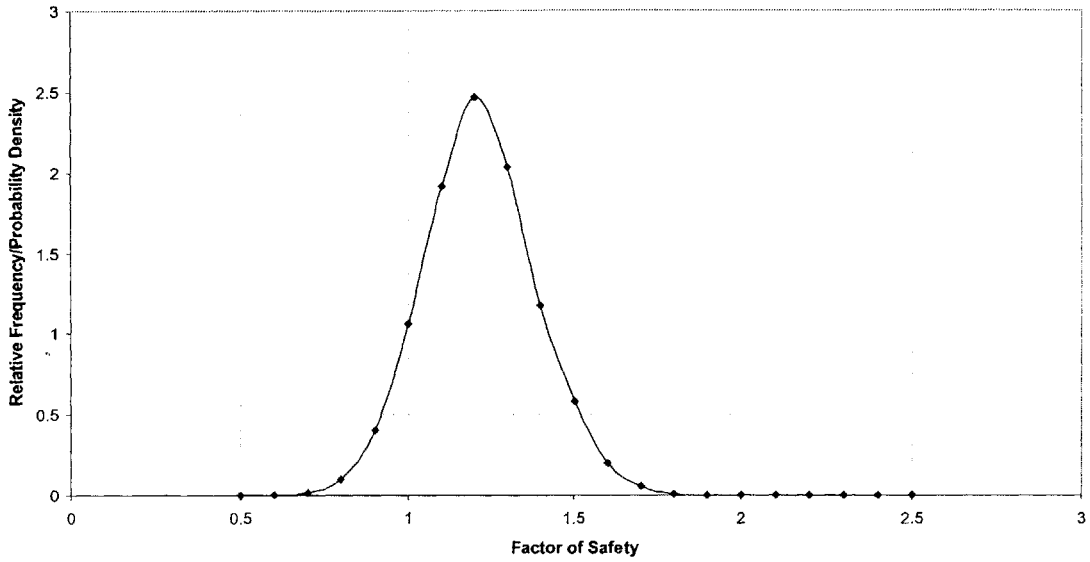

Figure 6.81. Simulated Distribution of Factor of Safety for Correlated Variables

The expected value of the Factor of Safety is E[F] = 1.18, and the standard deviation is $\sigma[F] = 0.17$. The probability of failure is computed to be $P_F = 0.158$.

Figure 6.82 compares the simulated distributions in Figures 6.80 and 6.81.

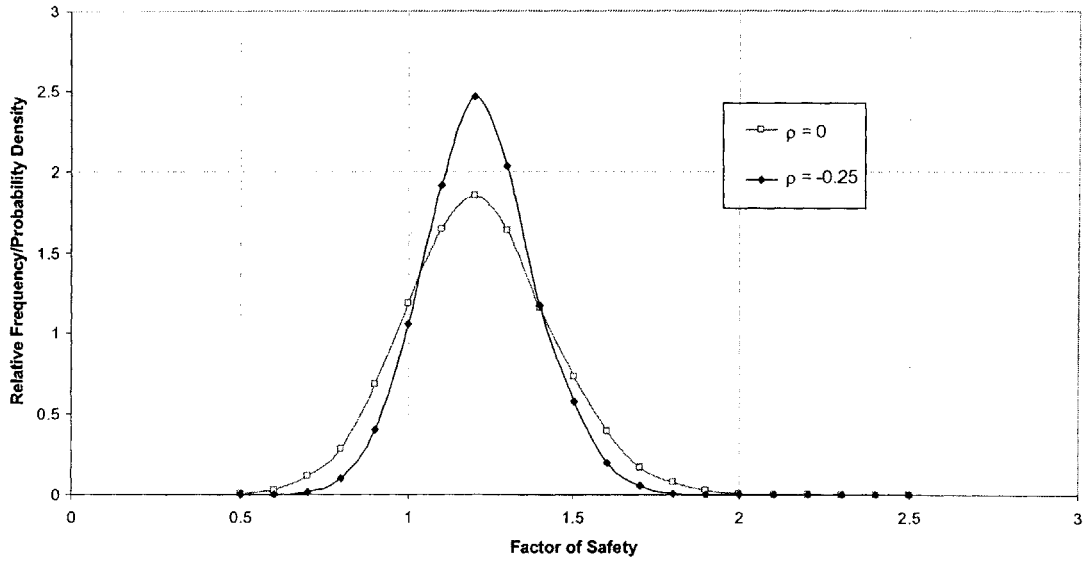

Figure 6.82. Comparison of Simulated Distributions of Factor of Safety for Correlated and Uncorrelated Variables

Figure 6.82 illustrates the effects of correlation on the distribution of the Factor of Safety. Correlation (negative) between c' and ϕ' seems to have little effect on the expected value of the Factor of Safety, but the standard deviation is significantly reduced. As a result, the probability of failure is reduced when c' and ϕ' are correlated.

Figure 6.83 shows the effects of different degrees of correlation between c' and ϕ' on the distribution of the Factor of Safety.

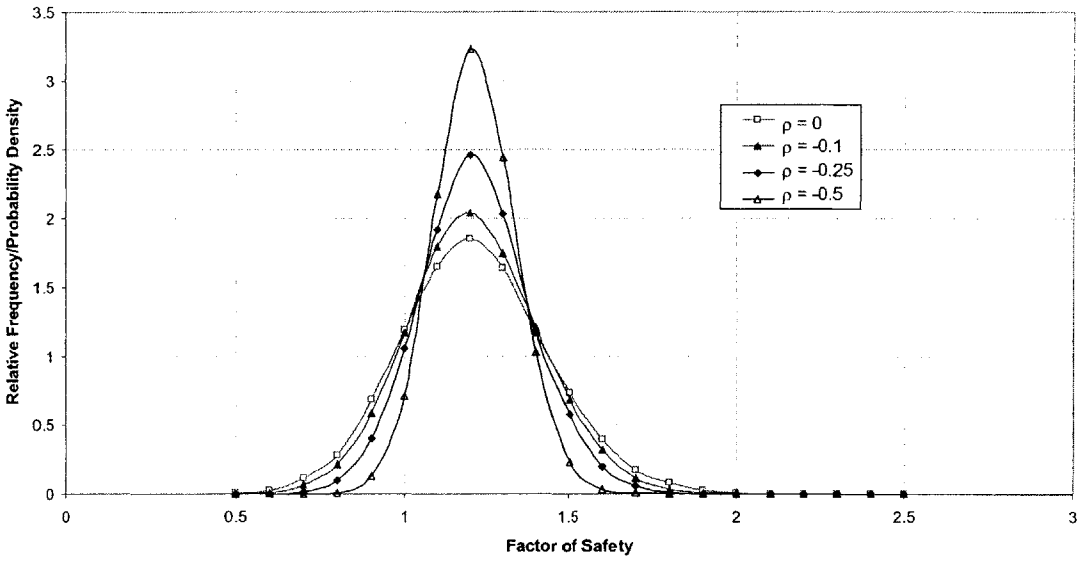

Figure 6.83. Simulated Distributions of Factor of Safety for Different Degrees of Correlation

Figure 6.83 shows that the stronger the (negative) correlation between c' and ϕ' the smaller the variance (standard deviation) of the Factor of Safety. The expected value of Factor of Safety on the other hand remains the same (almost). So does the shape of the distribution. Therefore, the stronger the (negative) correlation, the smaller the probability of failure.

In order to gain a better understanding of the effects of correlation on the distribution of Factor of Safety, we compute the statistics and the distribution fitting parameters that

were presented in Part 5-2 of Chapter 5. This is done for the case when $\rho = 0$ in Tables 6.2 and 6.3. These are the same results as were obtained in Part 5-2 of Chapter 5.

	Simulated Distribution
Expected Value, E[F]	1.178
Standard Deviation, σ[F]	0.134
Skewness	0.0613
Kurtosis	0.0042
Probability of Failure	0.091

Table 6.2. Summary Statistics of Simulated Distribution for $\rho = 0$

Fitted Distribution	Maximum Likelihood Parameters		Error Term, e	Probability of Failure
	E[F]/ E[ln(F)]/ r	σ[F] / σ [ln(F)]/ λ		
Normal	1.178	0.134	0.140	0.092
Lognormal	0.157	0.116	0.330	0.087
Gamma	76.926	65.330	0.239	0.087

Table 6.3. Fitted Distributions to Simulated Distribution for $\rho = 0$

The results for the case when $\rho = -0.1$ are shown in Tables 6.4 and 6.5, and the summary statistics for when $\rho = -0.25$ are shown in Table 6.6.

	Simulated Distribution
Expected Value, E[F]	1.176
Standard Deviation, σ[F]	0.110
Skewness	-0.0484
Kurtosis	1.1055
Probability of Failure	0.054

Table 6.4. Summary Statistics of Simulated Distribution for $\rho = -0.1$

Fitted Distribution	Maximum Likelihood Parameters		Error Term, e	Probability of Failure
	E[F]/ E[ln(F)]/ r	σ[F] / σ [ln(F)]/ λ		
Normal	1.176	0.109	0.165	0.054
Lognormal	0.158	0.094	0.301	0.046
Gamma	115.390	98.118	0.227	0.048

Table 6.5. Fitted Distributions to Simulated Distribution for $\rho = -0.1$

	Simulated Distribution
Expected Value, E[F]	1.176
Standard Deviation, σ[F]	0.072
Skewness	-0.04187
Kurtosis	10.0606
Probability of Failure	0.005

Table 6.6. Summary Statistics of Simulated Distribution for $\rho = -0.25$

A comparison of Tables 6.2, 6.4 and 6.6 shows the effects of correlation on the distribution of the Factor of Safety. In particular, that correlation does not affect the expected value of the Factor of Safety, but significantly reduces variance (standard deviation). This causes a significant reduction in the probability of failure. The Skewness as correlation is increased remains very close to zero as in the case of uncorrelated variables. This implies that the distribution is symmetric about the mean, and can be well approximated by the Normal distribution in the case of correlated variables, as was the case where the variables were uncorrelated (see Part 5-4 of Chapter 5). This is also reflected in Tables 6.3 and 6.5 that show that the best fit distribution (with minimum error term) is the Normal distribution, which gives similar results to the ones computed from the simulated distribution. The Kurtosis on the other hand increases significantly with correlation. This shows that as correlation between c' and ϕ' increases, the distribution of Factor of Safety becomes more and more peaked. This was shown in Figure 6.83.

EXAMPLE 2: DEEP FAILURE SURFACE (VERY DEEP BEDROCK)

We also investigate the effects of correlation on the slope shown in Figure 6.84.

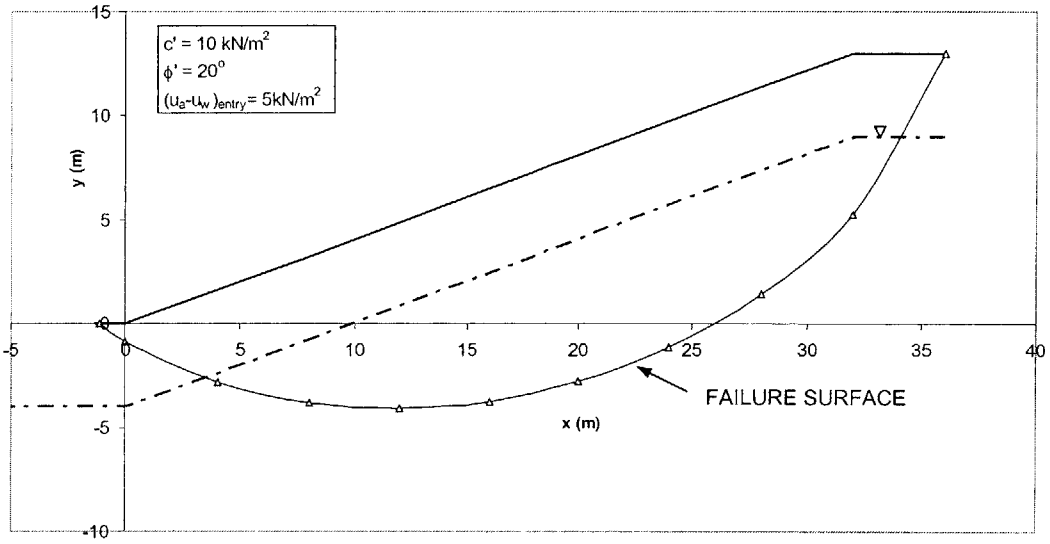

Figure 6.84. Slope Geometry and Strength Parameters

We assume that the c' and ϕ' are distributed as:

$$c' \sim N(m_{c'} = 10kN/m^2,\ \sigma_{c'} = 2kN/m^2);\ \phi' \sim N(m_{\phi'} = 20^o,\ \sigma_{\phi'} = 2.5^o)$$

The distributions of Factor of Safety for various degrees of correlation are shown in Figure 6.85.

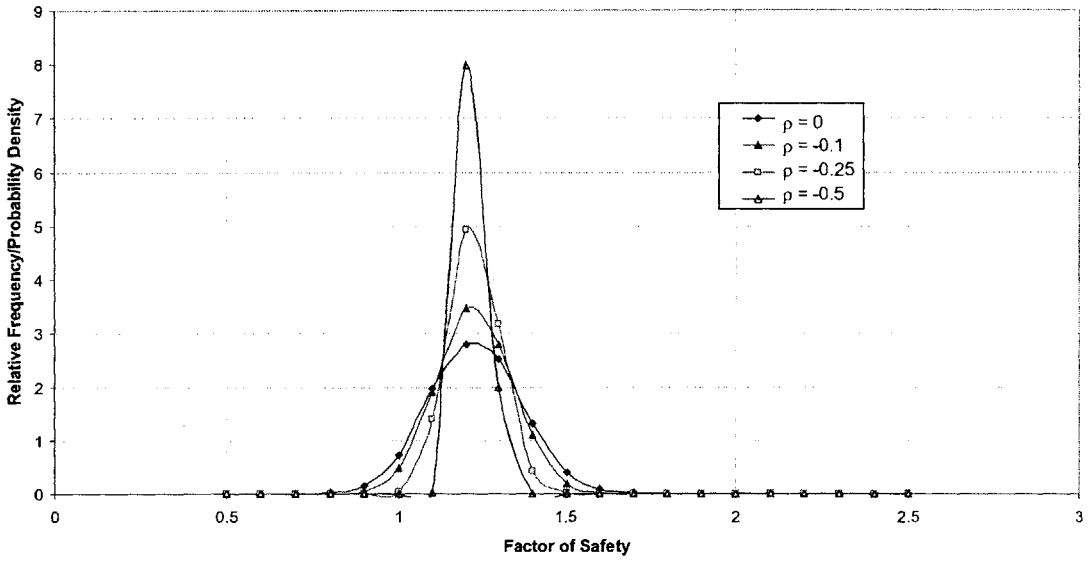

Figure 6.85. Simulated Distributions of Factor of Safety for Different Degrees of Correlation

Similar comments can be made with regard to effects of correlation on the distribution of Factor of Safety in Figure 6.85 as was done in Figure 6.83.

The results in Figures 6.83 and 6.85, which show that correlation seems to have little effect on the expected value (and shape of the distribution of the Factor of Safety), but reduces the variance are interesting. This is because the results are what one would expect to get using First Order Second Moment (FOSM) approximations.

Using FOSM, the Factor of Safety is linearized about the mean values of the parameters c' and ϕ', and:

a. The expected value of the Factor of Safety is the Factor of Safety evaluated at the expected values of c' and ϕ'.

b. The variance of the Factor of Safety decreases (as a linear function) with increasing negative ρ.

c. The distribution of Factor of Safety is Normal when c' and ϕ' are Normal.

The results in Figures 6.83 and 6.85 are consistent with points a. to c. above, and seem to suggest that the Factor of Safety Equation can be approximated by a linear function of c' and ϕ', particularly around the mean values of c' and ϕ'.

To explore this further, we plot the Factor of Safety against c' (with ϕ' at its expected value) in Figure 6.86 and against ϕ' (with c' at its expected value) in Figure 6.87.

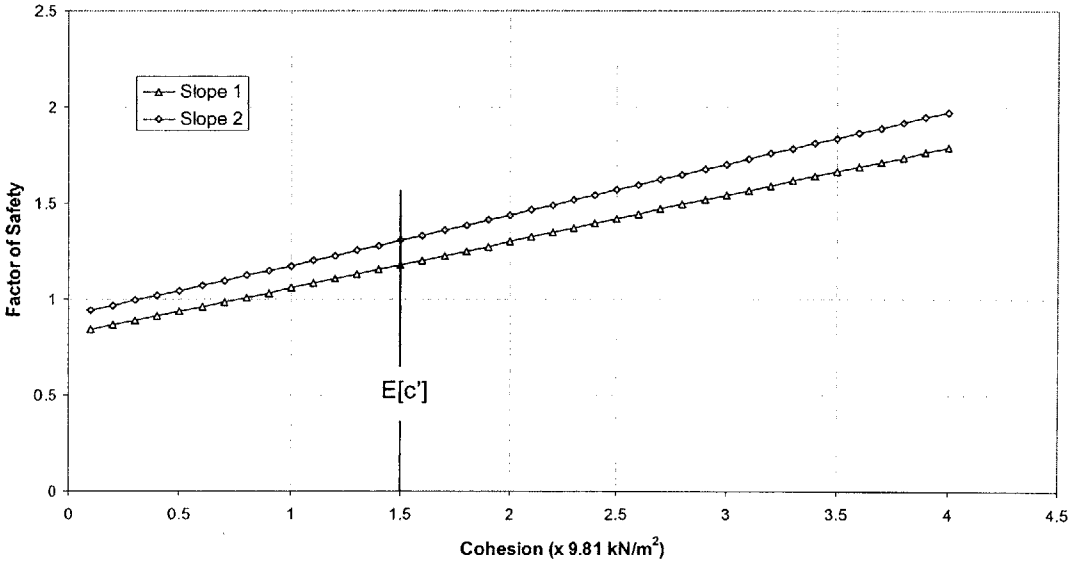

Figure 6.86. Factor of Safety against Cohesion (with ϕ' at its expected value)

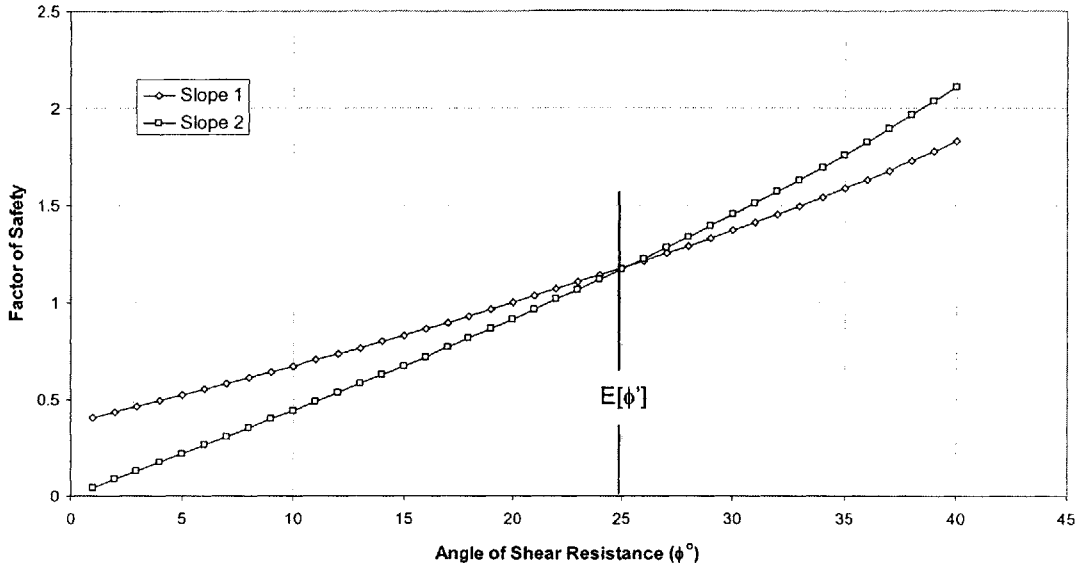

Figure 6.87. Factor of Safety against Angle of Shear Resistance (with c' at its expected value)

Slope 1 in Figures 6.86 and 6.87 refers to the slope in Example 1, and Slope 2 to the one in Example 2.

Figures 6.86 and 6.87 show that the Factor of Safety can indeed be approximated by a linear function in c' and ϕ', particularly around the mean values of these parameters. This explains why the expected values of the Factors of Safety remain almost the same in Figures 6.83 and 6.85. Since the Factors of Safety in Figures 6.86 and 6.87 are approximately linear, one would expect the variance of the Factor of Safety to decrease linearly with increasing (negative) correlation. This is, in fact, the FOSM approximation as well. We plot the variance of Factor of Safety for different values of ρ in Figure 6.88 for both slopes.

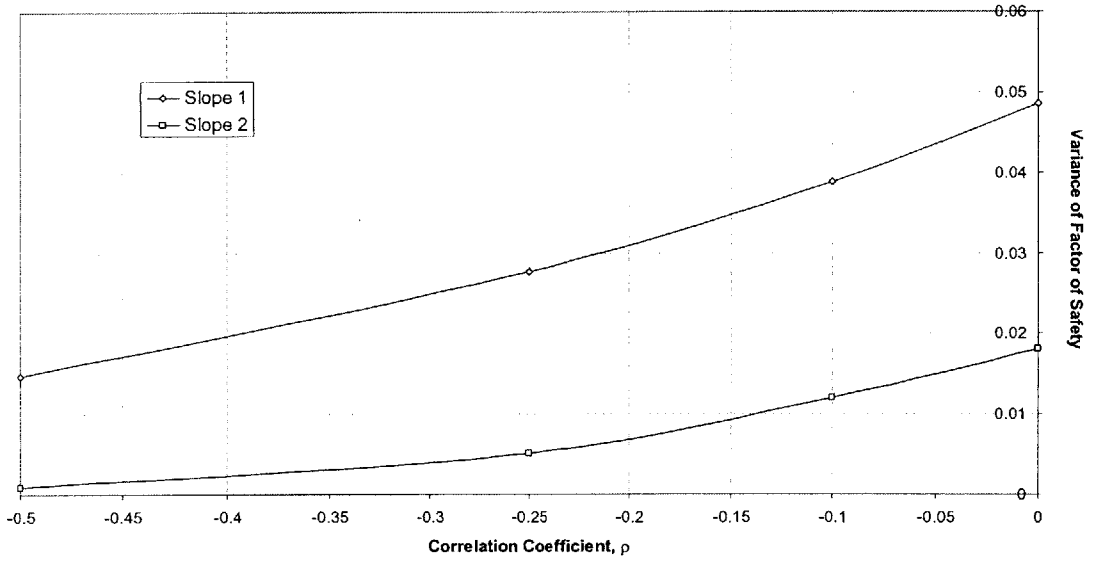

Figure 6.88. Variance of Factor of Safety against Correlation

Figure 6.88 shows the decrease of variance of Factor of Safety with correlation coefficient. Though the decrease is not exactly linear, it can be approximated by a straight line (the R^2 value for the best fit line for Slope 1 is $R^2 = 0.98$, and that for Slope 2 is $R^2 = 0.92$). The linearity of Factor of Safety with c' and ϕ' also explains why the distribution of Factor of Safety can be approximated by the Normal distribution when c' and ϕ' are Normal, whether or not correlation is assumed between c' and ϕ'.

We compare the results of the probabilistic analyses in Slope 1 with those from the second moment reliability analyses.

	Second Moment Reliability Analyses		**Probabilistic Analyses**		
	β	$P_F = \Phi(-\beta)$	E[F]	σ_F	P_F
c' and ϕ' Normal and uncorrelated	0.72	0.235	1.18	0.22	0.233
c' and ϕ' Jointly Normal with $\rho = -0.25$	1.01	0.157	1.18	0.17	0.158

Table 6.7. Comparison of Results from Second Moment Reliability and Probabilistic Analyses

Table 6.7 shows that the results from second moment analyses are in very good agreement with those from probabilistic analyses, based on the Monte Carlo method. This is because, and as shown in Figure 6.83, the distribution of Factor of Safety is well approximated by the Normal distribution, in which case computing probabilities of failure from $P_F = \Phi(-\beta)$ leads to accurate results. A more detailed discussion on the linearity of Factor of Safety, and a comparison of the results of FOSM, reliability and probabilistic analyses is provided in Appendix D.

6-2.1.3.1.4. CORRELATION SUBMODEL UNCERTAINTY IN LANDSLIDE HAZARDS ASSESSMENTS

In order to investigate the effects of correlation on landslide hazards, we consider the slope shown in Figure 6.89.

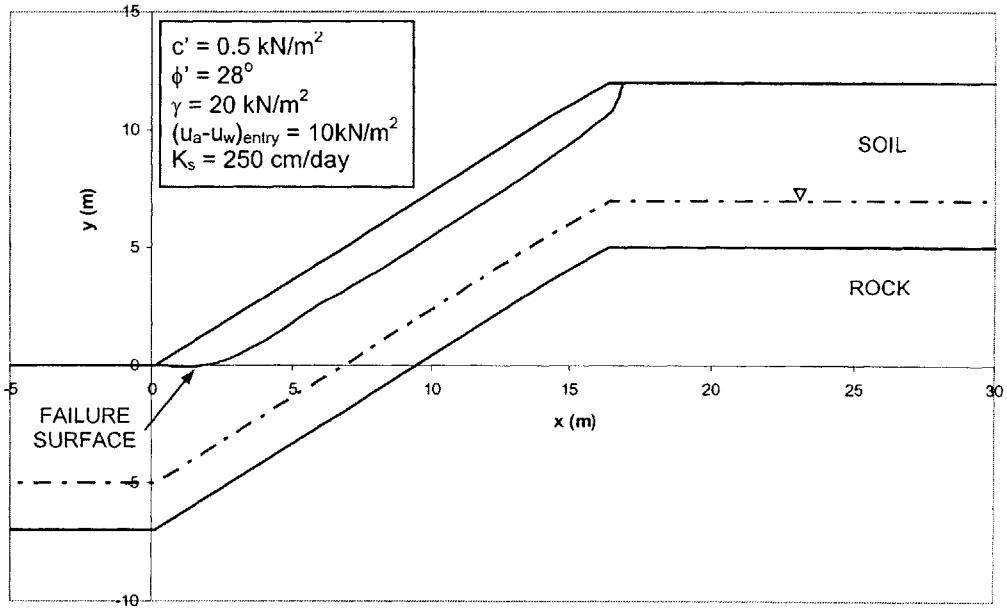

Figure 6.89. Slope Geometric and Strength Parameters

We assume that c' and ϕ' are Joint Normally distributed with parameters:

$$\begin{bmatrix} c' \\ \phi' \end{bmatrix} \sim N\left(\begin{bmatrix} 0.5 \\ 28 \end{bmatrix}, \begin{bmatrix} 0.0125^2 & (-0.25)(0.0125)(7) \\ (-0.25)(0.0125)(7) & 7^2 \end{bmatrix} \right), \text{ i.e. } \rho = -0.25 \text{ and}$$

$$K_S \sim LN(m_{K_S} = 250cm/day, \sigma^2_{K_S} = (125cm/day)^2)$$

and c' , ϕ' and K_S are uncorrelated.

We assume a rainfall event with intensity, $I = 75mm/hr$ occurs for a duration of 8 hours. Figure 6.90 shows moisture profiles, and Figure 6.91 shows pressure profiles at selected times.

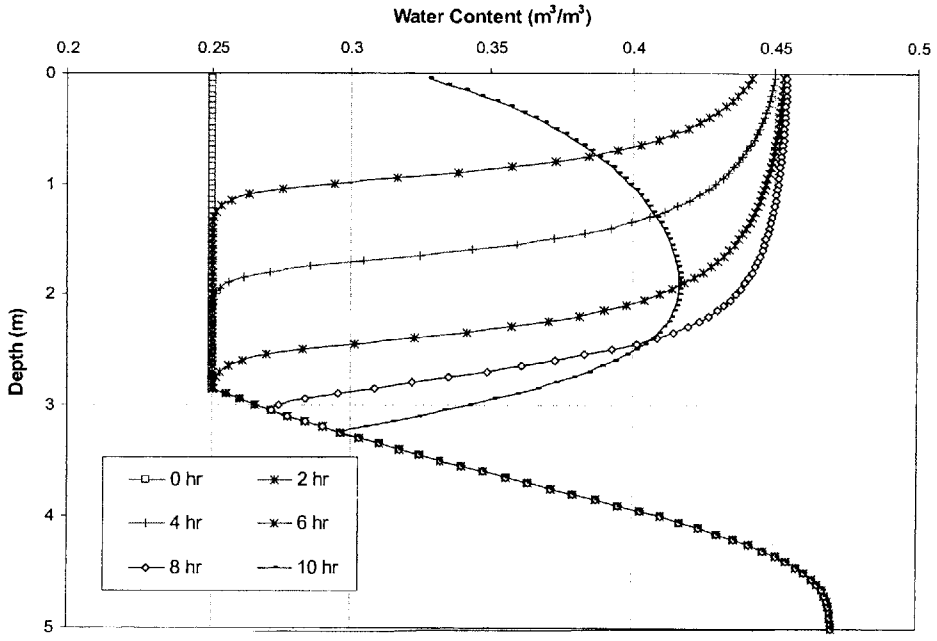

Figure 6.90. Moisture Content Profiles with Time using the van Genuchten (1980) Model

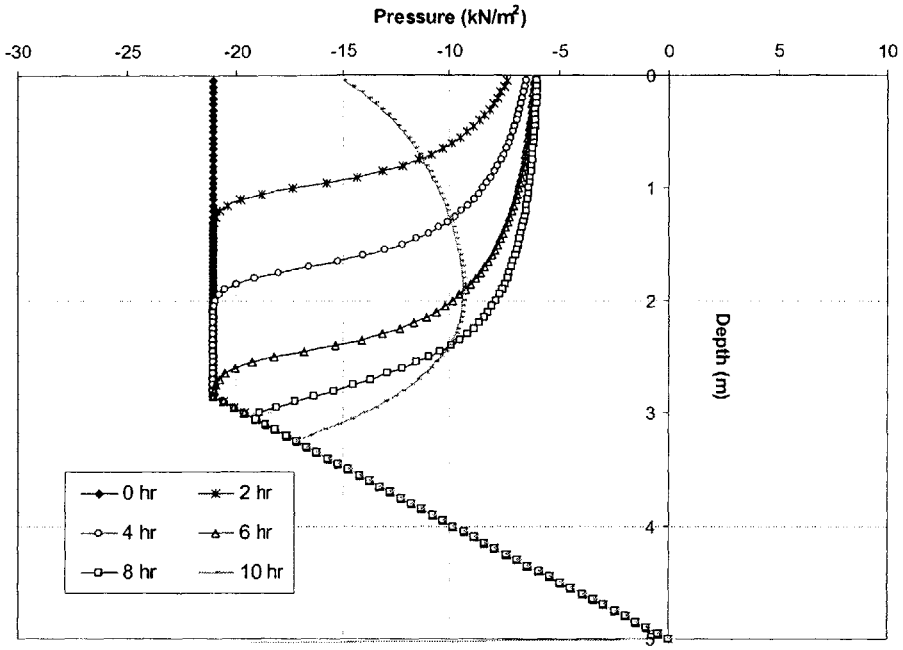

Figure 6.91. Pore Pressure Profiles with Time using the van Genuchten (1980) Model

Figure 6.92 compares the distribution of Factor of Safety at selected times when c' and ϕ' are correlated with those when c' and ϕ' are uncorrelated.

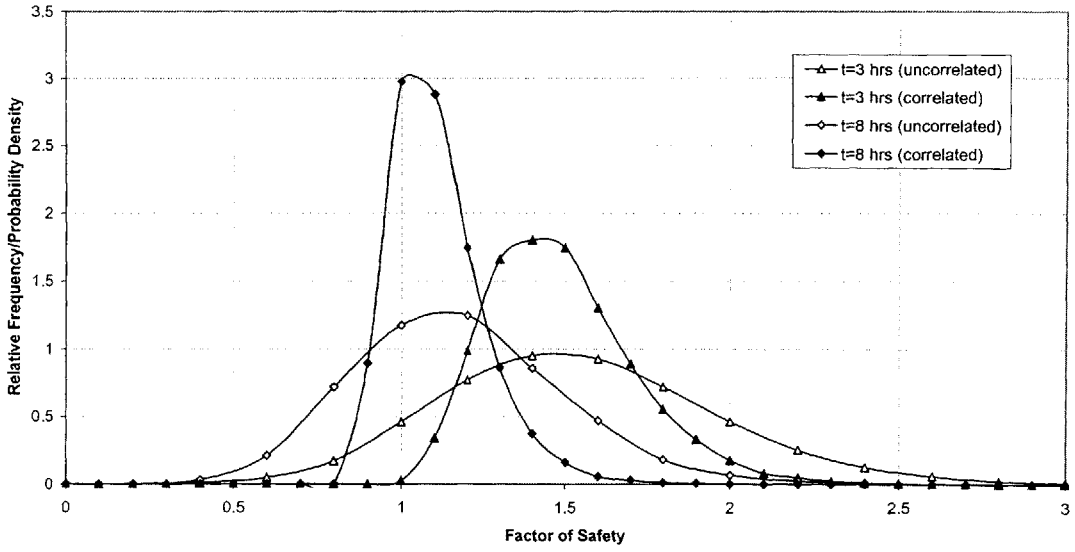

Figure 6.92. Comparison of Simulated Distributions of Factor of Safety at Selected Times for Correlated and Uncorrelated Variables

Figure 6.92 shows the effects of (negative) correlation between c' and ϕ' on the distribution of Factor of Safety. Specifically that correlation causes a significant reduction in the variance of the Factor of Safety at any time, t. Because of this, the distribution is more peaked when correlation is included between the strength parameters. Tables 6.8 and 6.9 show summary statistics for the case of uncorrelated strength parameters, and Tables 6.10 and 6.11 show the statistics when the strength parameters are negatively correlated.

	Simulated Distribution
Expected Value, E[F]	1.44
Standard Deviation, σ[F]	0.418
Skewness	0.433
Kurtosis	0.449

Table 6.8. Summary Statistics of Distribution for Uncorrelated Strength Parameters (t=3 hours)

	Simulated Distribution
Expected Value, E[F]	1.08
Standard Deviation, σ[F]	0.32
Skewness	0.489
Kurtosis	0.65

Table 6.9. Summary Statistics of Distribution for Uncorrelated Strength Parameters (t=8 hours)

	Simulated Distribution
Expected Value, E[F]	1.44
Standard Deviation, σ[F]	0.228
Skewness	0.851
Kurtosis	1.2996

Table 6.10. Summary Statistics of Distribution for Correlated Strength Parameters (t=3 hours)

	Simulated Distribution
Expected Value, E[F]	1.06
Standard Deviation, σ[F]	0.144
Skewness	1.280
Kurtosis	2.856

Table 6.11. Summary Statistics of Distribution for Correlated Strength Parameters (t=8 hours)

Tables 6.8 and 6.9, and 6.10 and 6.11 show that the expected values of the Factor of Safety are more or less the same when correlation is introduced than when the strength parameters are uncorrelated. They also show the decrease in the standard deviation when correlation is included. The distributions for correlated strength parameters are much more peaked, and this is reflected in the higher values of the coefficient of

Kurtosis. The peakedness of the distribution decreases with time as shown in Tables 6.9 and 6.11. This is because as time passes, pore pressures are greater and hence the uncertainty in the pressures is also greater. Having said this, it is evident that the effects of correlation are significant at any time, t, despite the fact that the hydraulic conductivity of the soil is also uncertain. This is because the uncertainties in c' and ϕ', and hence correlation between them, have a much greater effect on the uncertainty in the Factor of Safety, and hence distribution of Factor of Safety at any t, than the hydraulic conductivity. This was discussed in more detail in Part 5-5, of Chapter 5.

The probability of failure at any time t can be computed using Equation [6.25], and this is done for the correlated and uncorrelated cases in Figure 6.93.

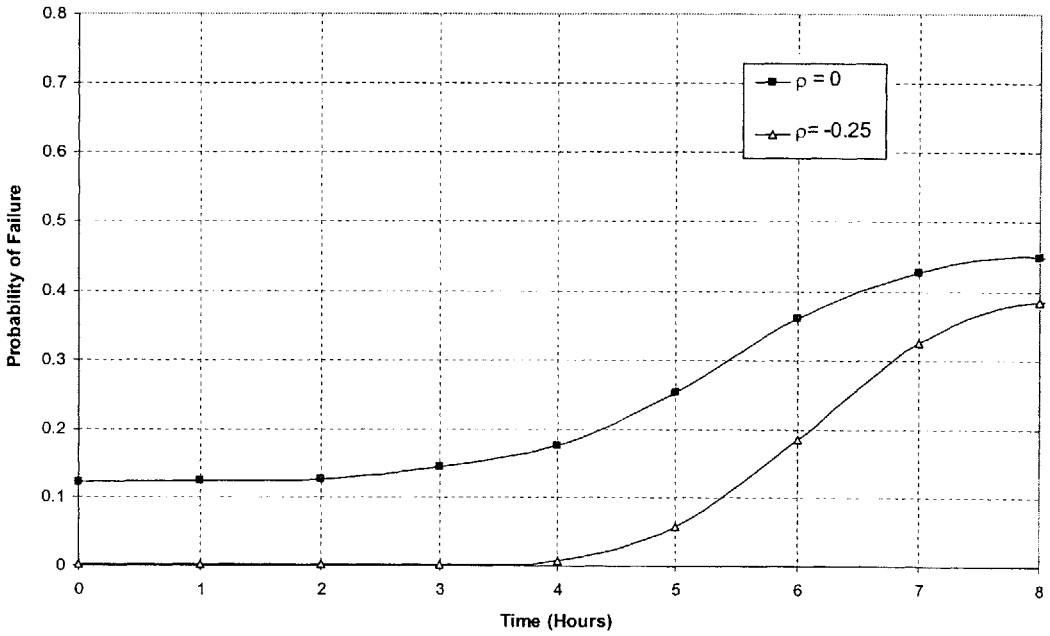

Figure 6.93. Comparison of Probability of Failure for Correlated and Uncorrelated Variables

The effects of correlation between c' and ϕ' on probabilities of failure and hence landslide hazards are evident in Figure 6.93. Figure 6.93 shows that landslide hazards assessments are significantly affected by the correlation model assumed between the strength parameters.

6-2.1.3.2. PARAMETER PROBABILITY DISTRIBUTION SUBMODEL UNCERTAINTY

A problem arises when the soil strength parameters c' and ϕ' are assumed to be Normally distributed, namely that negative values of these parameters can occur. This is true whether c' and ϕ' are assumed correlated or not. Negative values of c' and ϕ' are impossible, and this causes problems with the assumption of Normality, whether in a theoretical context, or simulation context (as with the Monte Carlo Method for example).

To overcome this problem, different probability distributions of c' and ϕ' can be assumed that ensure strictly positive values. These can take the form of bounded distributions, and one such distribution is the truncated Normal distribution. Another, more commonly adopted distribution is the Lognormal distribution. The assumption of Lognormal strength parameters has also been suggested in recent experimental studies, e.g. Griffiths et al., (2002).

In this Section, we investigate the effects of assuming Lognormal strength parameters on probabilistic slope stability analyses, and landslide hazards. Figure 6.94 shows in bold what is studied in this Section.

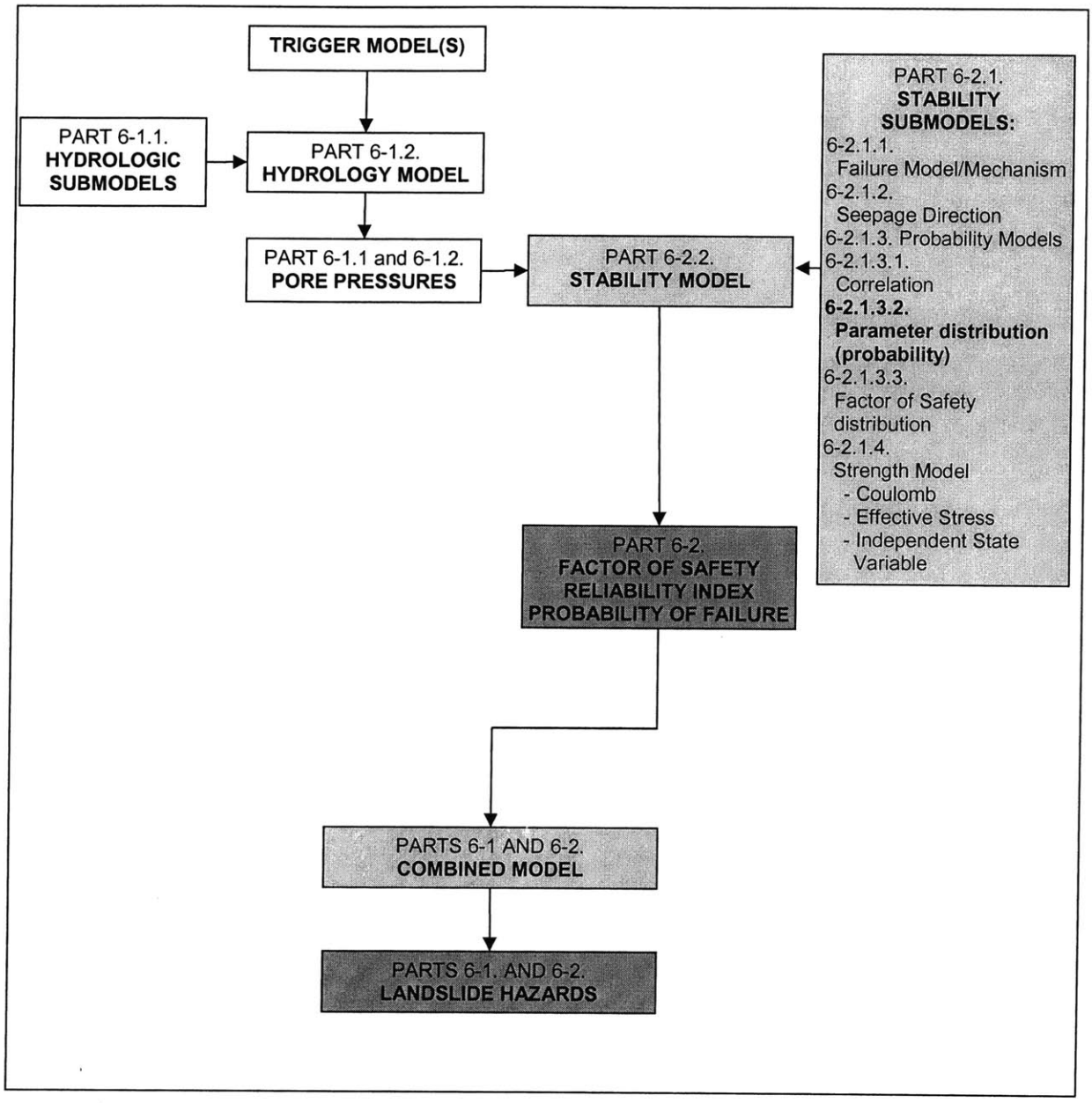

Figure **6.94.** Effects of parameter distribution models (shown in the lightly shaded submodels box) on the results of stability analyses (Factors of safety, reliability indices and probabilities of failure in the dark shaded box) and on landslide hazards (dark box) are investigated

6-2.1.3.2.1. PROBABILITY DISTRIBUTION SUBMODEL UNCERTAINTY IN SLOPE RELIABILITY ANALYSES

In this Section, we investigate the effects of Lognormal soil strength parameters on slope reliability analyses. When the soil strength parameters have Lognormal distribution, the problem has to be transformed into Normal space in order to perform reliability analyses.

The variables $c' \sim LN(m_{\ln c'}, \sigma^2_{\ln c'})$ and $\phi' \sim LN(m_{\ln \phi'}, \sigma^2_{\ln \phi'})$, need to be transformed to Normally distributed variables, and this is done through the logarithm transformation. Since, $c' \sim LN(m_{\ln c'}, \sigma^2_{\ln c'})$ and $\phi' \sim LN(m_{\ln \phi'}, \sigma^2_{\ln \phi'})$, then $\ln c' \sim N(m_{c'}, \sigma^2_{c'})$ and $\ln \phi' \sim N(m_{\phi'}, \sigma^2_{\phi'})$, where:

$$m_{c'} = 2\ln(m_{\ln c'}) - \frac{1}{2}\ln(\sigma^2_{\ln c'} + m^2_{\ln c'}) \tag{6.23}$$

$$\sigma^2_{c'} = -2\ln(m_{\ln c'}) + \ln(\sigma^2_{\ln c'} + m^2_{c'}) \tag{6.24}$$

$$m_{\phi'} = 2\ln(m_{\ln \phi'}) - \frac{1}{2}\ln(\sigma^2_{\ln \phi'} + m^2_{\ln \phi'}) \tag{6.25}$$

$$\sigma^2_{\phi'} = -2\ln(m_{\ln \phi'}) + \ln(\sigma^2_{\ln \phi'} + m^2_{\phi'}) \tag{6.26}$$

The failure boundary, defined by combinations of c' and ϕ' that result in Factors of Safety equal to 1, also needs to be transformed into Normal space. This is done by replacing c' and ϕ', in the Factor of Safety Equation with $e^{\ln c'}$ and $e^{\ln \phi'}$, therefore defining the failure boundary in ln c' and ln ϕ' space. Once the problem is transformed into Normal space, the procedures described in Chapter 5, Part 5-4 can be employed, and the Hasofer and Lind (1974) reliability index can be computed as shown in Figure 5.38.

The problem can be transformed further into standard Normal space, by defining two new variables c'* and ϕ'^* as:

$$c'^* = \frac{(\ln c' - m_{c'})}{\sigma_{c'}} \qquad [6.27]$$

$$\phi'^* = \frac{(\ln \phi' - m_{\phi'})}{\sigma_{\phi'}} \qquad [6.28]$$

c'^* and ϕ'^* are both standard Normal variables such that they have zero mean values, and unit variances. The problem can then be solved as described in Figure 5.38 of Chapter 5 in the standard Normal space.

To illustrate this, consider the following examples:

EXAMPLE 1: SHALLOW BEDROCK

Consider the slope shown in Figure 6.95.

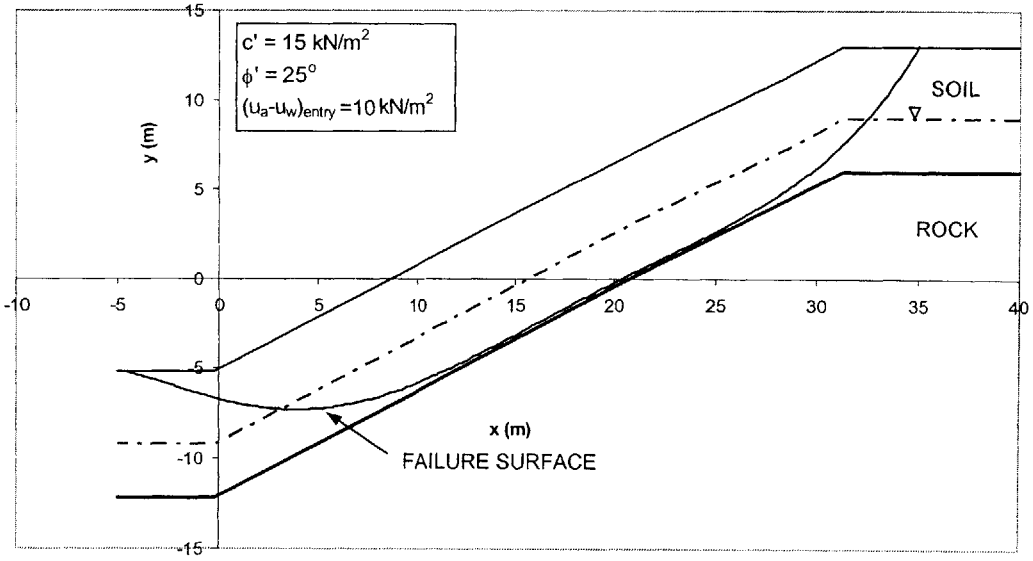

Figure 6.95. Slope Geometry and Strength Parameters

We assume that the soil strength parameters c' and ϕ' follow Lognormal distributions as: $c' \sim LN(m_{c'} = 15kN/m^2,\ \sigma_{c'} = 5kN/m^2)$; $\phi' \sim LN(m_{\phi'} = 25^o,\ \sigma_{\phi'} = 5^o)$; and c' and ϕ' are uncorrelated. Note that the parameters of these models are the same as those for the Normal distributions models that were used in Part 5-3 of Chapter 5.

Figure 6.96 shows the failure boundary, and $\beta - \sigma$ dispersion ellipsoid in the transformed Normal space, ln c' and ln ϕ'.

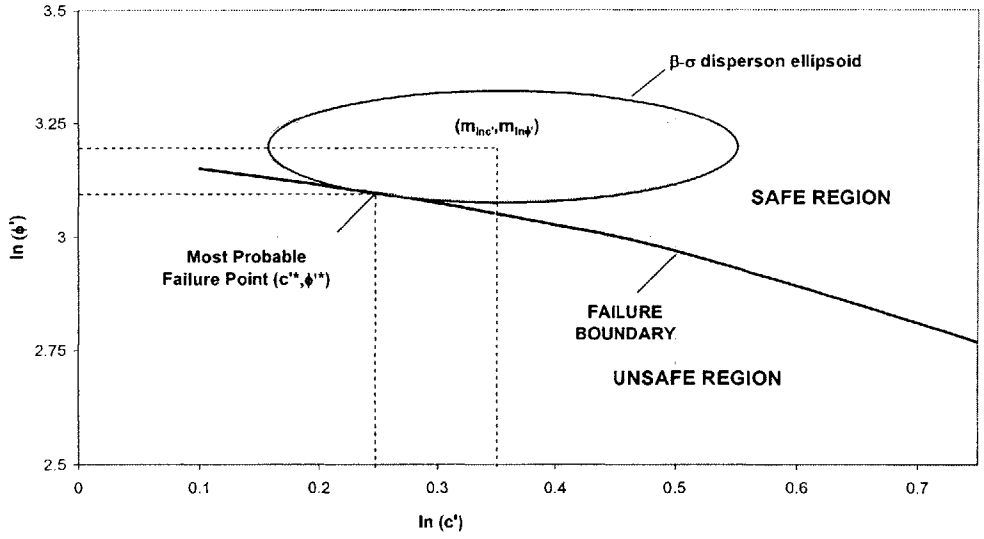

Figure 6.96. Failure Boundary, and $\beta - \sigma$ Dispersion Ellipsoid in Transformed Normal Space

Figure 6.97 shows the failure boundary, and $\beta - \sigma$ dispersion ellipsoid in the transformed standard Normal space, c'^* and ϕ'^*, where c'^* and ϕ'^*, are as given in Equations [6.27] and [6.28] respectively, and are Normal variables with zero mean and unit variance (hence standard Normal variables).

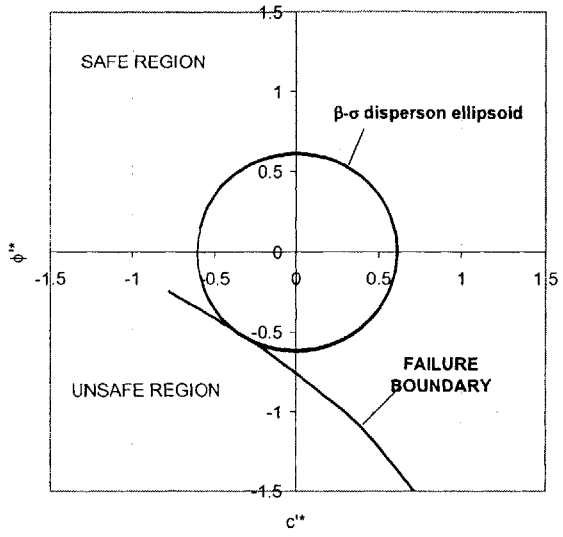

Figure 6.97. Failure Boundary, and $\beta - \sigma$ Dispersion Ellipsoid in Standard Normal Space

The Hasofer and Lind (1974) reliability index is computed to be $\beta = 0.66$, and assuming a Normal distribution for the Factor of Safety, this corresponds to a probability of failure of $P_f = \Phi(-\beta) = 0.256$. Comments on this probability of failure are provided in Table 6.15.

EXAMPLE 2: DEEP FAILURE SURFACE (VERY DEEP BEDROCK)

Consider the slope shown in Figure 6.98.

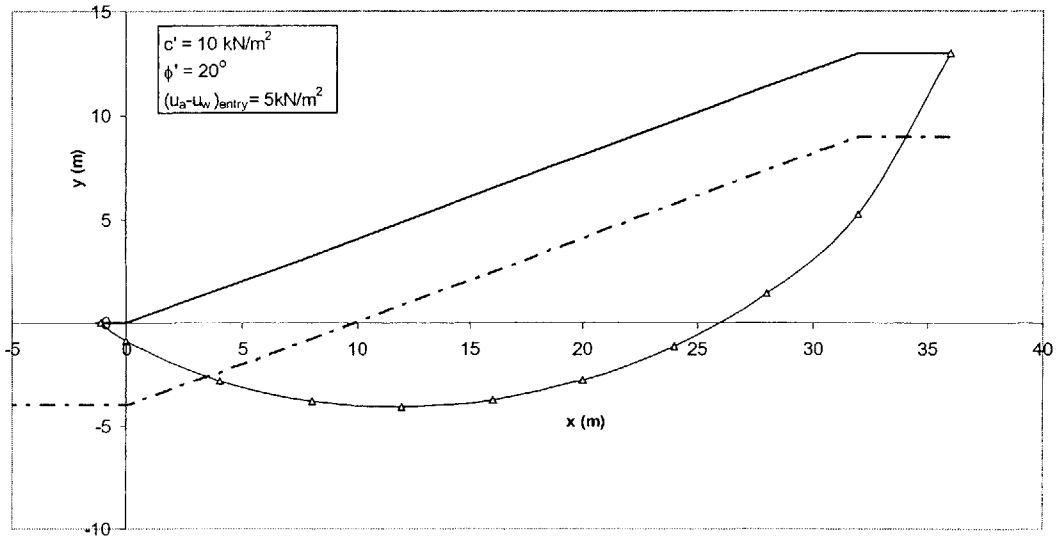

Figure 6.98. Slope Geometry and Strength Parameters

We assume that: $c' \sim LN(m_{c'} = 10kN/m^2,\ \sigma_{c'} = 2kN/m^2)$; $\phi' \sim LN\ (m_{\phi'} = 20^o,\ \sigma_{\phi'} = 2.5^o)$, and c' and ϕ' are uncorrelated.

We transform the problem to Normal space, and Figure 6.99 shows the failure boundary, and $\beta - \sigma$ dispersion ellipsoid in the transformed Normal space, ln c' and ln ϕ'.

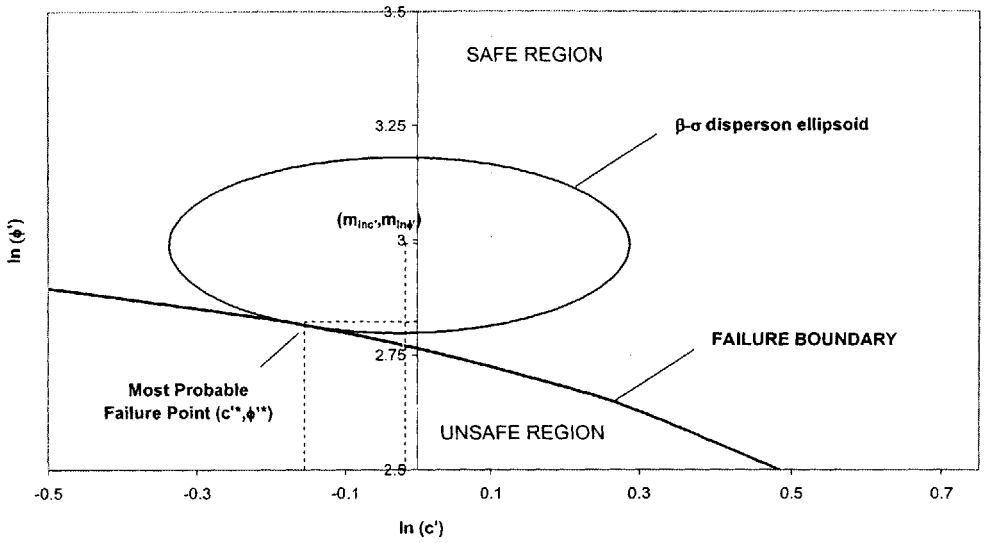

Figure 6.99. Failure Boundary, and β – σ Dispersion Ellipsoid in Transformed Normal Space

Figure 6.100 shows the failure boundary, and β – σ dispersion ellipsoid in the transformed standard Normal space, c'* and ϕ'*.

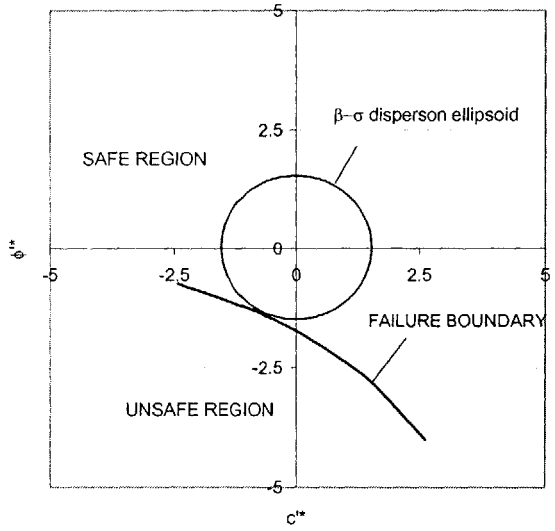

Figure 6.100. Failure Boundary, and β – σ Dispersion Ellipsoid in Standard Normal Space

The Hasofer and Lind (1974) reliability index is computed to be $\beta = 1.54$, and assuming a Normal distribution for the Factor of Safety, this corresponds to a probability of failure of $P_f = \Phi(-\beta) = 0.06$. Comments on this probability of failure are provided in Table 6.15.

6-2.1.3.2.2. DISTRIBUTION SUBMODEL UNCERTAINTY IN PROBABILISTIC SLOPE STABILITY ANALYSES

We investigate the effects of Lognormal strength parameters on probabilistic slope stability analyses by considering the following examples:

EXAMPLE 1: SHALLOW BEDROCK

Consider the slope shown in Figure 6.101.

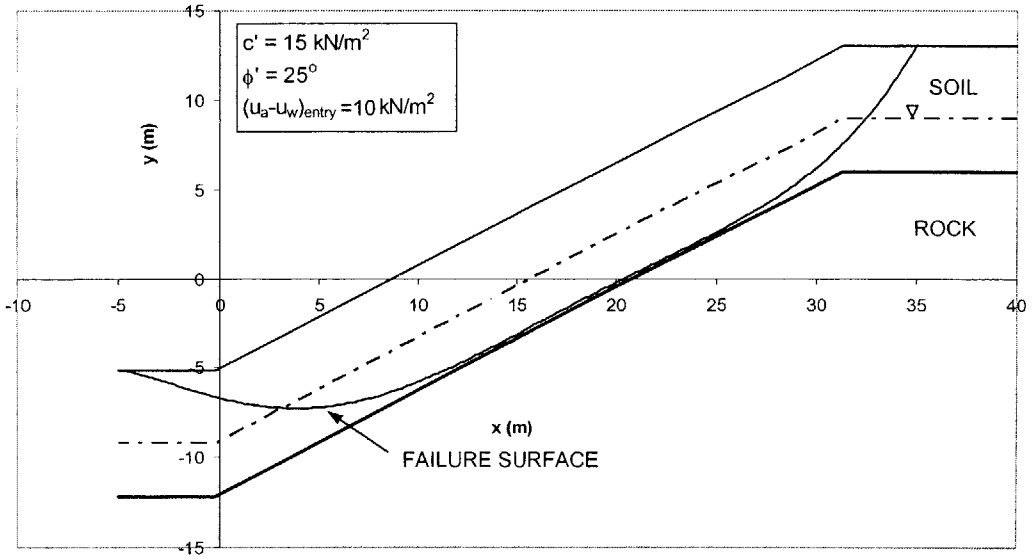

Figure 6.101. Slope Geometry and Strength Parameters

We assume that the soil strength parameters c' and ϕ' follow Lognormal distributions as: $c' \sim LN(m_{c'} = 15kN/m^2, \sigma_{c'} = 5kN/m^2)$; $\phi' \sim LN(m_{\phi'} = 25^o, \sigma_{\phi'} = 5^o)$; and c' and ϕ' are uncorrelated.

Monte Carlo techniques are used to generate random samples of c' and ϕ' from their respective distributions. The technique for generating random variables from a Lognormal distribution was discussed in Part 5-1 of Chapter 5. A random sample of

Factor of Safety is therefore computed. Figure 6.102 shows the relative frequency/probability distribution of the Factor of Safety.

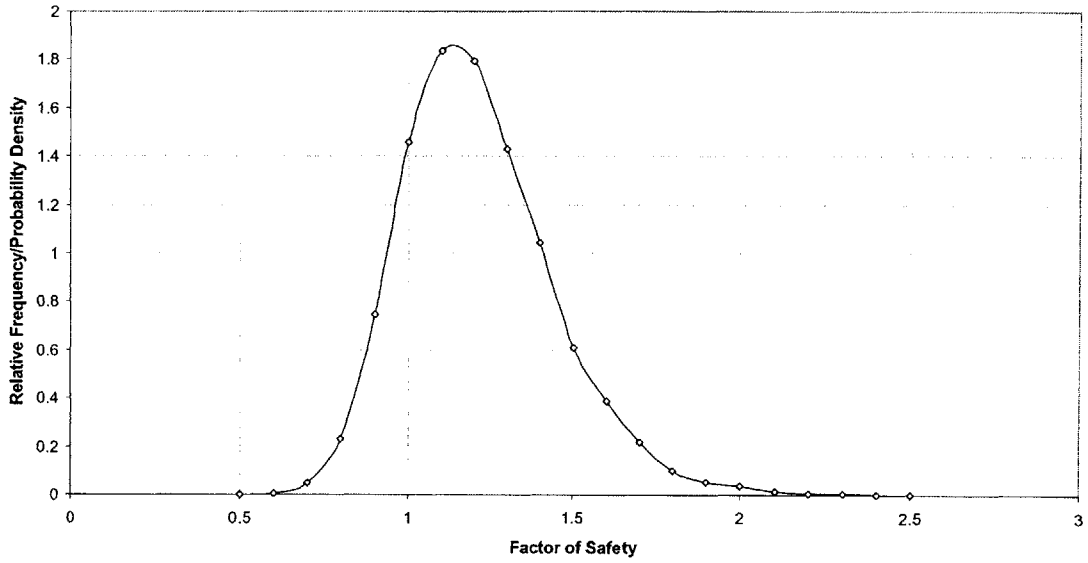

Figure 6.102. Simulated Distribution of Factor of Safety for Lognormal Soil Strength Parameters

The expected value of the Factor of Safety is computed to be E[F] = 1.16, and the standard deviation is $\sigma[F] = 0.23$. The probability of failure is computed according to Figure 6.102 as $P_F = 0.248$.

The shape of the distribution of the Factor of Safety is different from that obtained in Section 6.3.3.1.3, when c' and ϕ' are Normal. To gain a better understanding on the shape of the distribution of the Factor of Safety, we compute the summary statistics that are shown in Table 6.12.

	Simulated Distribution
Expected Value, E[F]	1.163
Standard Deviation, σ[F]	0.227
Skewness	0.7404
Kurtosis	1.1846
Probability of Failure	0.248

Table 6.12. Summary Statistics of Simulated Distribution for Lognormal c' and ϕ'

Comparing Tables 6.2 and 6.12 shows the difference in the distributions of Factor of Safety when c' and ϕ' are Normal compared to when they are Lognormal. The Kurtosis in both cases is more or less the same, indicating no change in the peakedness of the distribution. The Skewness is different however. While when c' and ϕ' are Normally distributed the Skewness is almost zero, Table 6.12 shows that the Skewness is significant when c' and ϕ' are Lognormal. This implies an asymmetry in the distribution of Factor of Safety, and this is reflected in Figure 6.102.

Table 6.13 shows a summary of fitted theoretical distributions to the generated distribution of Factor of Safety.

Fitted Distribution	Maximum Likelihood Parameters		Error Term, e	Probability of Failure
	E[F]/ E[ln(F)]/ r	σ[F]/σ[ln(F)]/ λ		
Normal	1.163	0.227	0.582	0.237
Lognormal	0.132	0.192	0.120	0.245
Gamma	26.134	22.473	0.267	0.241

Table 6.13. Fitted Distributions to Simulated Distribution for Lognormal c' and ϕ'

Table 6.13 shows that the lognormal distribution leads to the smallest error term, and hence is the best fit distribution. These results show that the distribution of the Factor of Safety in Figure 6.102, follows the Lognormal distribution more closely than it does the Normal distribution. Figure 6.103 shows this, by comparing the simulated distribution with the fitted Normal and Lognormal distributions.

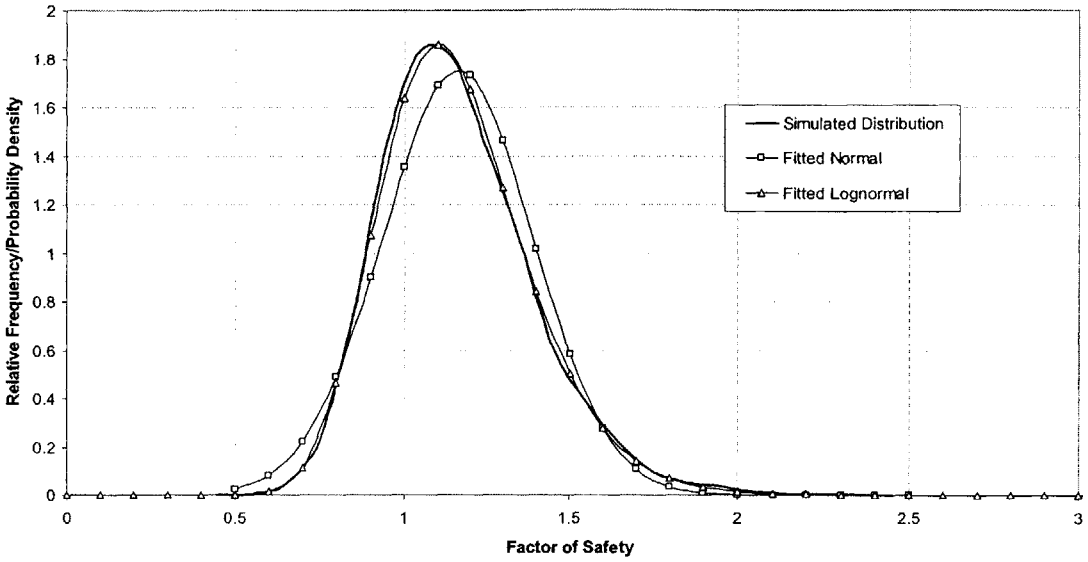

Figure 6.103. Comparison of Simulated Distribution of Factor of Safety with the Fitted Normal and Lognormal Distributions

The chosen/assumed probability distribution model for the uncertain strength parameters therefore has an effect on the shape of the probability distribution of the Factor of Safety. This illustrates distribution model uncertainty. Since the distribution of Factor of Safety is different, so is the probability of failure.

In the case of Lognormally distributed c' and ϕ', the distribution of the Factor of Safety is well approximated by the Lognormal distribution. In this example, the probability of failure is greater when c' and ϕ' are Lognormal compared to when they are Normal. Figure 6.104 compares the distribution of Factor of Safety when c' and ϕ' are Normal and when they are Lognormal.

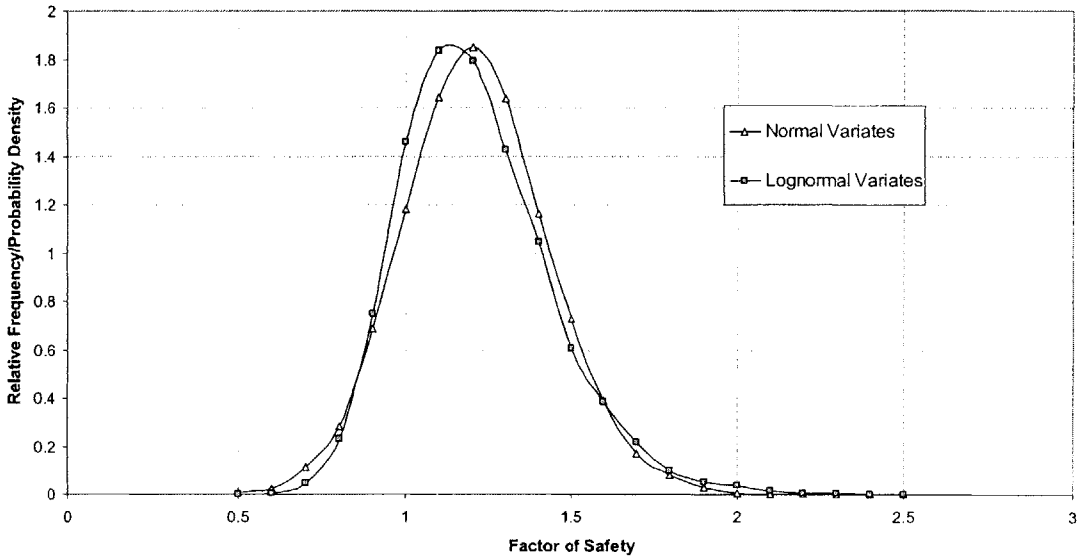

Figure 6.104. Comparison of Simulated Distributions of Factor of Safety with for Normal and Lognormal Strength Parameters

Figure 6.104 shows that this is the case, since the area under the distribution when c' and ϕ' are Lognormal where F < 1 (i.e. probability of failure), is greater than that under the distribution when c' and ϕ' are Normal.

EXAMPLE 2: DEEP FAILURE SURFACE (VERY DEEP BEDROCK)

Consider the slope shown in Figure 6.105.

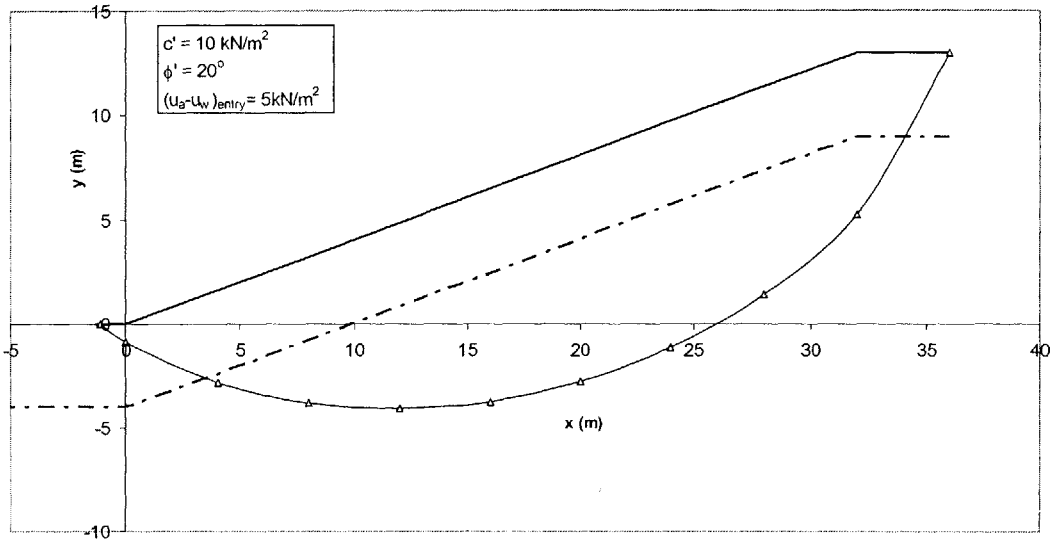

Figure 6.105. Slope Geometry and Strength Parameters

We assume that: $c' \sim LN(m_{c'} = 10kN/m^2,\ \sigma_{c'} = 2kN/m^2)$; $\phi' \sim LN\ (m_{\phi'} = 20^o,\ \sigma_{\phi'} = 2.5^o)$, and c' and ϕ' are uncorrelated.

Figure 6.106 shows the simulated distribution of Factor of Safety, and Figure 6.107 compares the simulated distribution with the fitted Normal and Lognormal distributions.

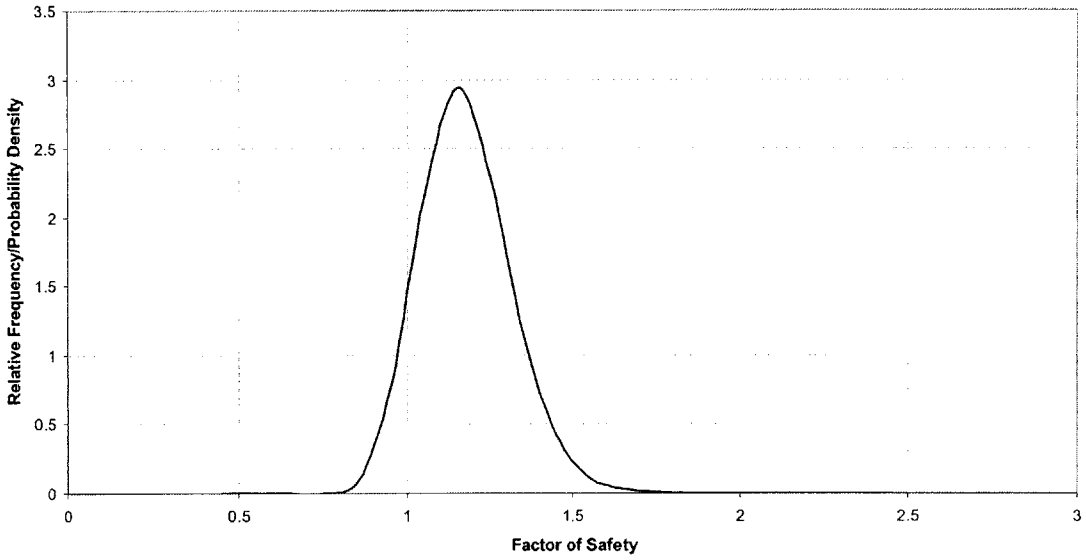

Figure 6.106. Simulated Distribution of Factor of Safety for Lognormal Soil Strength Parameters

The expected value of the Factor of Safety is E[F] = 1.18, and $\sigma[F] = 0.14$.

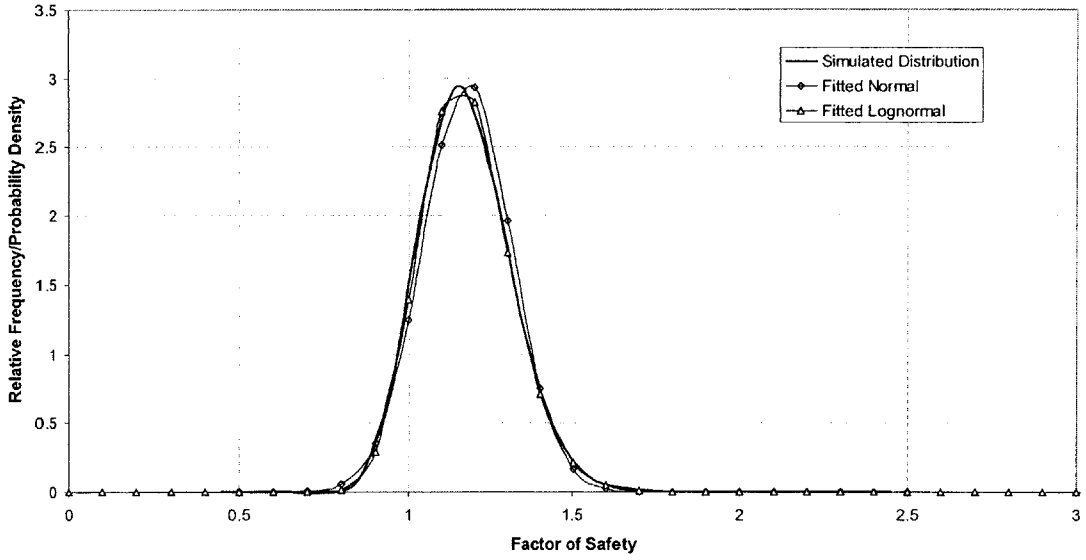

Figure 6.107. Comparison of Simulated Distribution of Factor of Safety with the Fitted Normal and Lognormal Distributions

Table 6.14 shows a summary of the parameters of the fitted distributions in this example, and shows that the distribution of Factor of Safety is better approximated by the Lognormal distribution than by the Normal distribution, when c' and ϕ' are Lognormal.

Fitted Distribution	Maximum Likelihood Parameters		Error Term, e	Probability of Failure
	E[F]/ E[ln(F)]/ r	σ[F]/σ[ln(F)]/ λ		
Normal	1.176	0.136	0.390	0.098
Lognormal	0.155	0.115	0.107	0.088
Gamma	74.995	63.790	0.158	0.092

Table 6.14. Fitted Distributions to Simulated Distribution for Lognormal c' and ϕ'

Figure 6.108 compares the distributions of Factor of Safety when c' and ϕ' are Normal, and when c' and ϕ' are Lognormal.

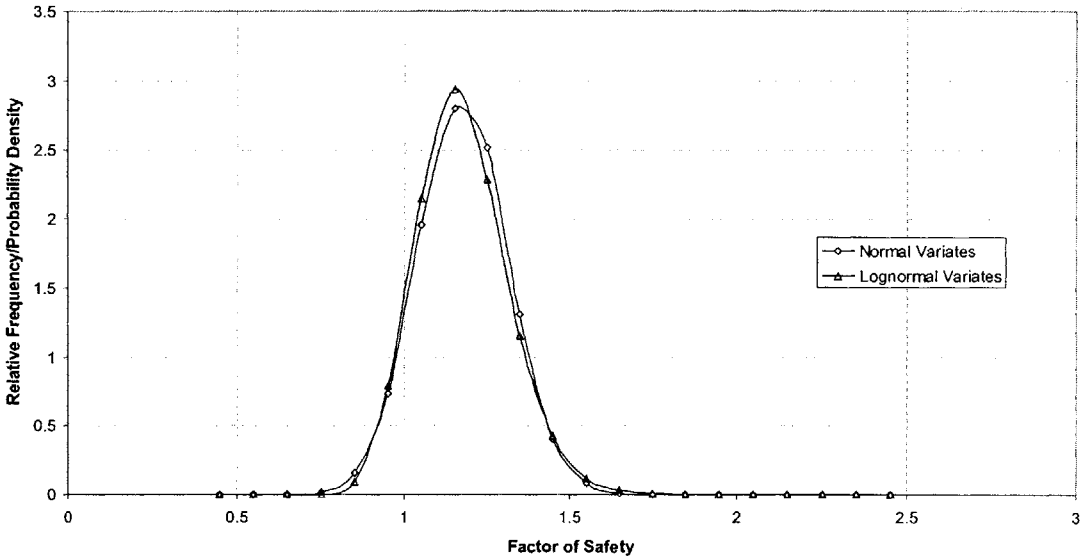

Figure 6.108. Comparison of Simulated Distributions of for Normal and Lognormal Strength Parameters

The probability of failure when c' and ϕ' are Normal is $P_F = 0.091$, and $P_F = 0.08$ when c' and ϕ' are Lognormal. This is illustrated in Figure 6.108, which shows the larger failure probability when c' and ϕ' are Normal. This result is different to the one obtained in the first, where the probability of failure was greater when c' and ϕ' are Lognormal.

Therefore, no general conclusion can be made regarding the value of the probability of failure when c' and ϕ' are Normal compared to when they are Lognormal. The probability of failure will depend on the expected value and variance of the Factor of Safety in the particular slope. Although these may be similar in magnitude for both cases of Normal and Lognormal c' and ϕ', the particular values of expected value and variance of Factor of Safety are important. These, in turn, will depend on the expected

values and variances of the uncertain parameters c' and ϕ'. If the Factor of Safety has expected value much greater than the critical value of one, and a small variance, then the probability of failure for Lognormal c' and ϕ' would be smaller than that when c' and ϕ' are Normal. If, on the other hand, the expected value of Factor of Safety is close to the value of one, and it has a large variance, then probability of failure for Lognormal c' and ϕ' would be greater than that when c' and ϕ' are Normal.

In summary, we conclude that the distribution of Factor of Safety in a slope will depend on the distribution model for c' and ϕ'. When c' and ϕ' are Normal, the distribution of Factor of Safety is well approximated be the Normal distribution, and when c' and ϕ' Lognormal, the distribution of Factor of Safety is well approximated be the Lognormal distribution. No general conclusion can be made regarding the magnitude of the probability of failure which will depend on the particular case under consideration. These results illustrate the effects of parameter model distribution on the results of probabilistic slope stability analyses.

Table 6.15 summarizes the results of reliability and probabilistic analyses performed on the slopes in Examples 1 and 2.

	Second Moment Reliability Analyses		**Probabilistic Analyses**		
	β	$P_F = \Phi(-\beta)$	E[F]	σ_F	P_F
SLOPE 1					
c' and ϕ' Normal	0.72	0.235	1.18	0.22	0.233
c' and ϕ' Lognormal	0.66	0.256	1.18	0.23	0.249
SLOPE 2					
c' and ϕ' Normal	1.31	0.095	1.17	0.13	0.091
c' and ϕ' Lognormal	1.54	0.060	1.18	0.14	0.080

Table 6.15. Comparison of Results from Second Moment Reliability and Probabilistic Analyses

Table 6.15 shows that the results of reliability analyses are in good agreement with probabilistic analyses when c' and ϕ' are Normal, because the distribution of Factor of Safety can be approximated by the Normal distribution. The agreement between the results is however, not as good when c' and ϕ' are Lognormal. There are two reasons for this: The first is because the failure boundary in the transformed space of ln c' and ln ϕ' is non linear leading to inaccuracies in reliability analyses. The second is because the distribution of Factor of Safety is better approximated by the Lognormal distribution, when c' and ϕ' are Lognormal. In Example 1, the probability of failure is overestimated, and in Example 2 it is underestimated. A more thorough discussion on this is provided in Appendix D.

6-2.1.3.2.3. DISTRIBUTION SUBMODEL UNCERTAINTY IN LANDSLIDE HAZARDS

In order to investigate the effects of parameter distribution model on landslide hazards, we reconsider the following two examples.

LANDSLIDE HAZARDS WITH RAINFALL INTENSITY LESS THAN SATURATED CONDUCTIVITY

In this example, we consider the slope shown in Figure 6.109.

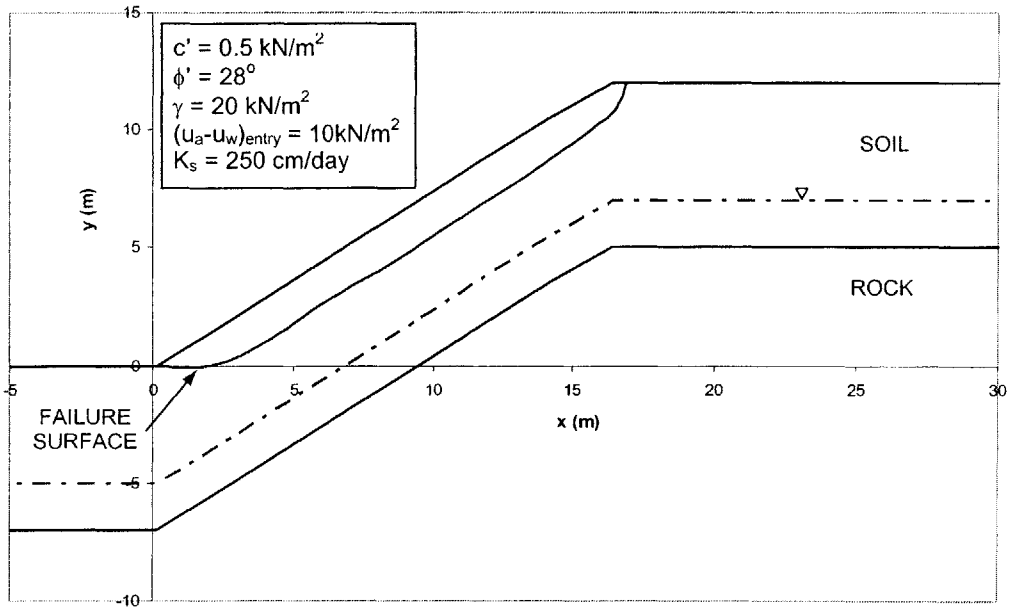

Figure 6.109. Slope Geometric and Strength Parameters

We assume a rainfall event with intensity, $I = 75mm/hr$ occurs for a duration of 8 hours.

Figure 6.110 shows moisture profiles, and Figure 6.111 shows pressure profiles at selected times.

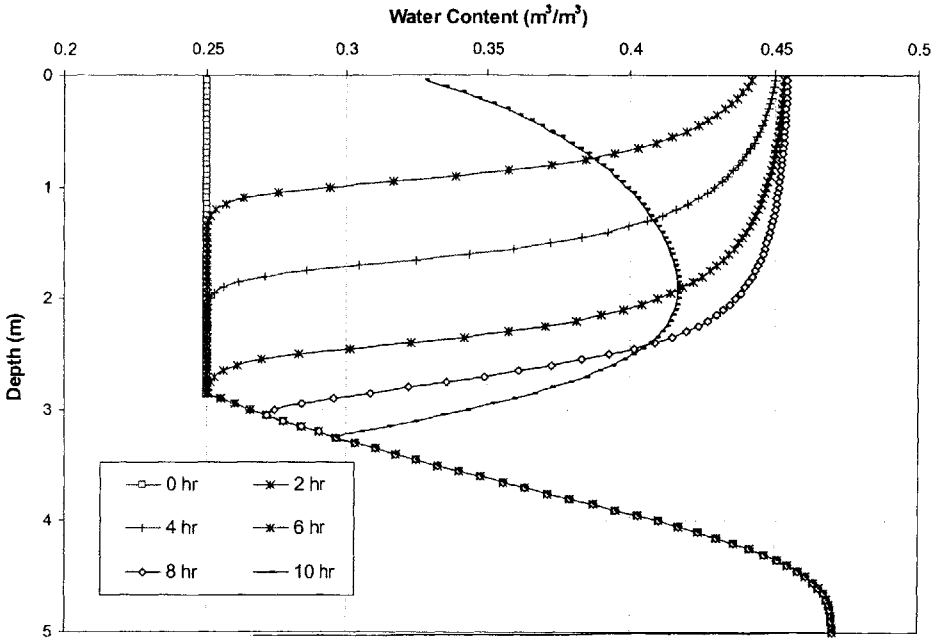

Figure 6.110. Moisture Content Profiles with Time using the van Genuchten (1980) Model

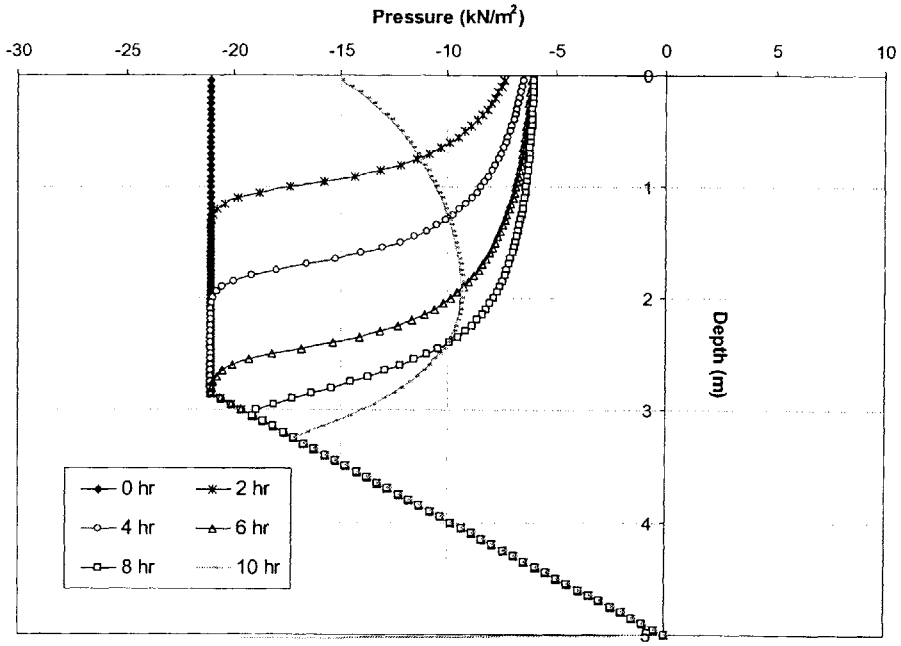

Figure 6.111. Pressure Profiles with Time using the van Genuchten (1980) Model

Figure 6.112 shows the expected value of the Factor of Safety with time into the rainfall event.

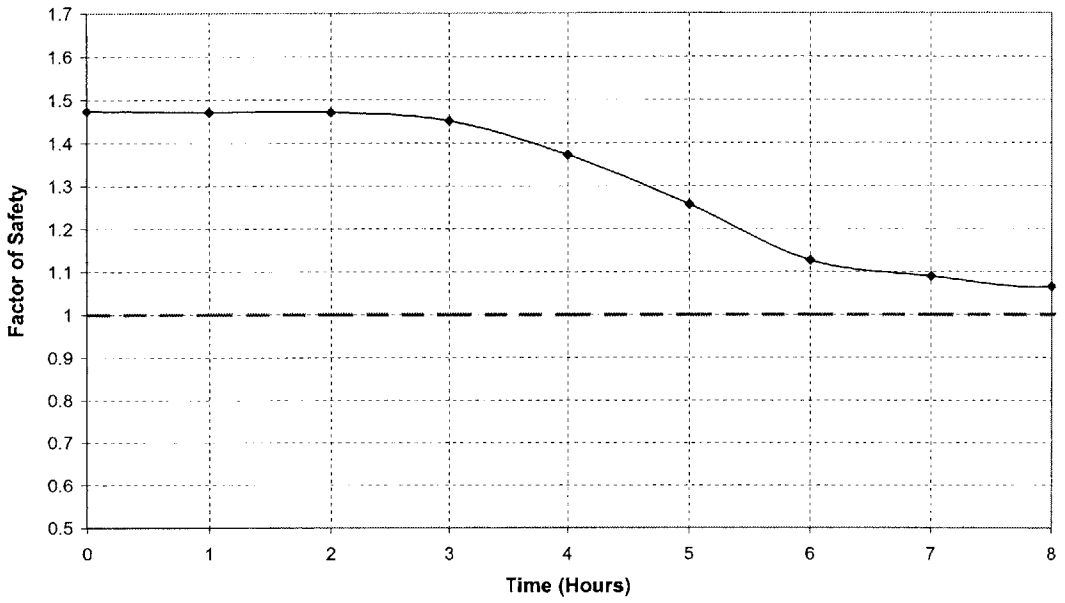

Figure **6.112.** Expected Value of Factor of Safety with Time for Lognormal Strength Parameters

We now assume that the strength parameters are hydraulic conductivity are uncertain and distributed as:

$c' \sim LN(m_{c'} = 0.5kN/m^2, \quad \sigma_{c'} = 0.125kN/m^2), \quad \phi' \sim \quad LN(m_{\phi'} = 28^o, \quad \sigma_{\phi'} = 7^o) \quad ,$

$K_s \sim LN(m_{K_s} = 250cm/day, \sigma^2_{K_s} = (125cm/day)^2);$

and c', ϕ' , and K_s are uncorrelated.

Figure 6.113 shows the probability distribution of the Factor of Safety at selected times.

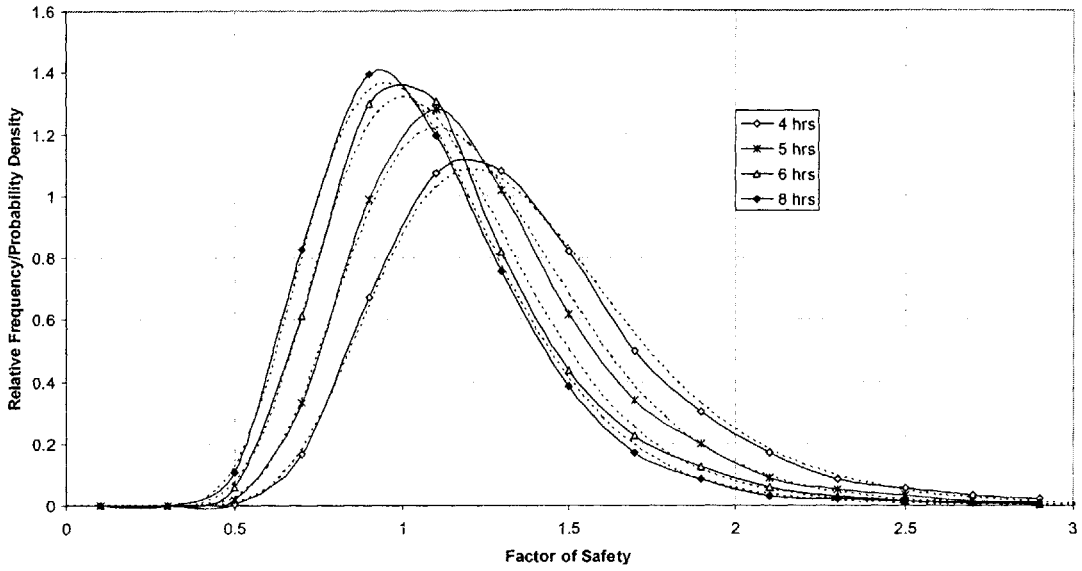

Figure **6.113.** Distributions of Factor of Safety at Selected Times (Continuous Lines are Simulated Distributions and Dashed Lines are Fitted Lognormal Distribution)

Figure 6.113 shows how the distribution of Factor of Safety moves towards the origin with increasing time into the rain event. This causes a decrease in the expected value of the Factor of Safety which is reflected in Figure 6.112.

To gain a better understanding of the shape of the distributions of Factor of Safety we examine the statistics shown in Tables 6.16 through 6.23. Tables 6.16 and 6.17 present the statistics for time t = 4 hours, Tables 6.18 and 6.19 for time 5 hours , Tables 6.20 and 6.21 for time 6 hours, and Tables 6.22 and 6.23 for time 8 hours.

	Simulated Distribution
Expected Value, E[F]	1.378
Standard Deviation, σ[F]	0.432
Skewness	1.5795
Kurtosis	5.5139
Probability of Failure	0.168

Table 6.16. Summary Statistics of Simulated Distribution at time 4 hours

Fitted Distribution	Maximum Likelihood Parameters		Error Term, e	Probability of Failure
	E[F]/ E[ln(F)]/ r	σ[F]/σ[ln(F)]/ λ		
Normal	1.377	0.432	0.755	0.191
Lognormal	0.277	0.291	0.168	0.170
Gamma	11.656	8.462	0.356	0.174

Table 6.17. Fitted Distributions to Simulated Distribution at time 4 hours

	Simulated Distribution
Expected Value, E[F]	1.247
Standard Deviation, σ[F]	0.381
Skewness	1.5500
Kurtosis	6.2325
Probability of Failure	0.268

Table 6.18. Summary Statistics of Simulated Distribution at time 5 hours

Fitted Distribution	Maximum Likelihood Parameters		Error Term, e	Probability of Failure
	E[F]/ E[ln(F)]/ r	σ[F]/σ[ln(F)]/ λ		
Normal	1.246	0.381	0.803	0.259
Lognormal	0.179	0.285	0.197	0.265
Gamma	12.162	9.757	0.393	0.260

Table 6.19. Fitted Distributions to Simulated Distribution at time 5 hours

	Simulated Distribution
Expected Value, E[F]	1.139
Standard Deviation, σ[F]	0.354
Skewness	1.4633
Kurtosis	4.0728
Probability of Failure	0.393

Table 6.20. Summary Statistics of Simulated Distribution at time 6 hours

Fitted Distribution	Maximum Likelihood Parameters		Error Term, e	Probability of Failure
	E[F]/ E[ln(F)]/ r	σ[F]/σ[ln(F)]/ λ		
Normal	1.139	0.354	0.866	0.348
Lognormal	0.087	0.289	0.230	0.382
Gamma	11.794	10.359	0.434	0.368

Table 6.21. Fitted Distributions to Simulated Distribution at time 6 hours

	Simulated Distribution
Expected Value, E[F]	1.084
Standard Deviation, σ[F]	0.345
Skewness	1.8008
Kurtosis	9.0610
Probability of Failure	0.466

Table 6.22. Summary Statistics of Simulated Distribution at time 8 hours

Fitted Distribution	Maximum Likelihood Parameters		Error Term, e	Probability of Failure
	E[F]/ E[ln(F)]/ r	σ[F]/σ[ln(F)]/ λ		
Normal	1.084	0.345	0.827	0.404
Lognormal	0.036	0.294	0.157	0.451
Gamma	11.393	10.512	0.371	0.433

Table 6.23. Fitted Distributions to Simulated Distribution at time 8 hours

Several conclusions can be made with regard to Tables 6.16 through 6.23:

a. The expected value of the Factor of Safety decreases with time, which leads to an increase in the probability of failure.
b. The coefficient of Kurtosis is greater than one at all times, indicating a more peaked distribution relative to the Normal distribution.
c. The coefficient of Skewness remains more or less the same with time, and is greater than zero. The distribution is therefore not symmetric about the mean value of Factor of Safety as it would be if the distribution were Normal.
d. The best fitted distribution seems to be the Lognormal distribution, as it is the distribution that has the lowest error term e. This indicates that the distribution of Factor of Safety is better approximated by the Lognormal distribution than by the Normal or Gamma distributions.

The results in this Section are different than what was obtained in Part 5-5 of Chapter 5, when c' and ϕ' were assumed to be Normally distributed:

In Part 5-5 of Chapter 5, we first concluded that the distributions of c' and ϕ' have a larger effect on the distribution of the Factor of Safety than the distribution of the saturated conductivity of the soil. We also concluded that when c' and ϕ' are Normal, the distribution of Factor of Safety could be well approximated by the Normal (at early times after the start of rain) and Gamma distributions (at later times after the start of rain), because of the non-Normality of the saturated conductivity. In this example, when c' and ϕ' are Lognormal, they have a sufficient effect on the distribution of Factor of Safety that it is better approximated by the Lognormal distribution than by the Normal and/or Gamma distributions.

In Section 6.3.3.2.1 we showed that when c' and ϕ' are uncertain and Lognormally distributed, then the Factor of Safety is well approximated by the Lognormal distribution. So, if the hydraulic conductivity were deterministic in this example, then at any time t, i.e. for a given pressure distribution, the only uncertain parameters are c' and ϕ' and these are Lognormally distributed, so we would expect the Factor of Safety to be Lognormally distributed as well. This indicates that the uncertainty in c' and ϕ', and hence the

distributions of c' and ϕ' have a larger effect on the resulting distribution of the Factor of Safety than the distribution of the hydraulic conductivity, confirming the results obtained in Section 6.3.3.2.1.

The probability of failure at any time t is computed from the distributions in Figure 6.113 as $P_F = \int_{-\infty}^{1} f_{F(c',\phi')} dF$, and this is shown in Figure 6.114.

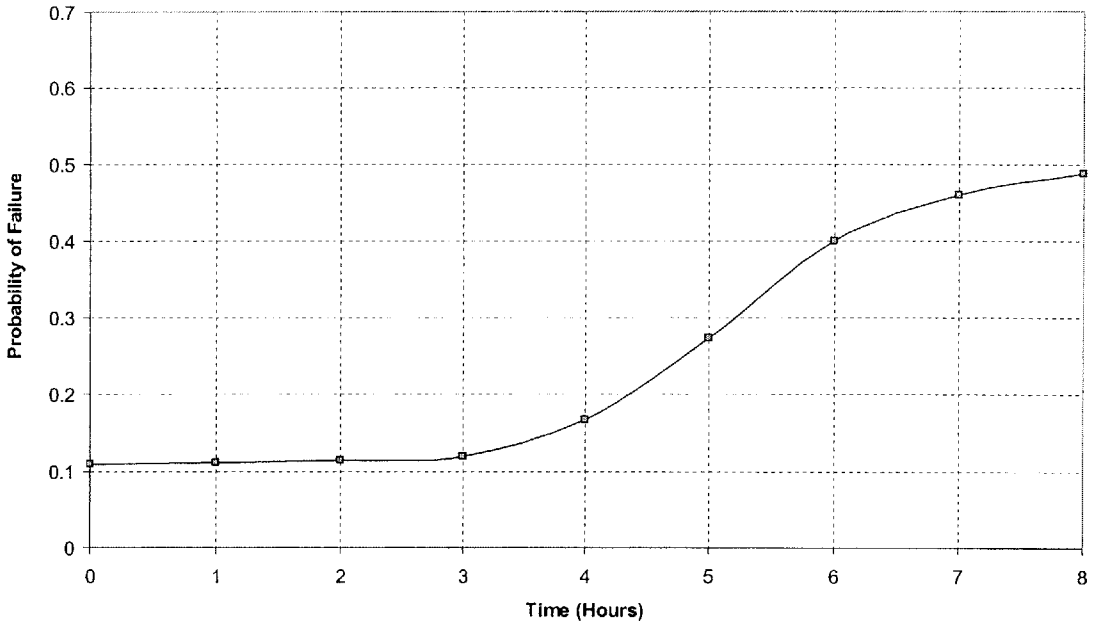

Figure **6.114.** Probability of Failure with Time for Lognormal Strength Parameters

Figure 6.114 shows the increase in failure probability with time. Figure 6.115 compares the probability of failure when c' and ϕ' are Lognormal with those when c' and ϕ' are Normal (which were obtained in Part 5-5 of Chapter 5).

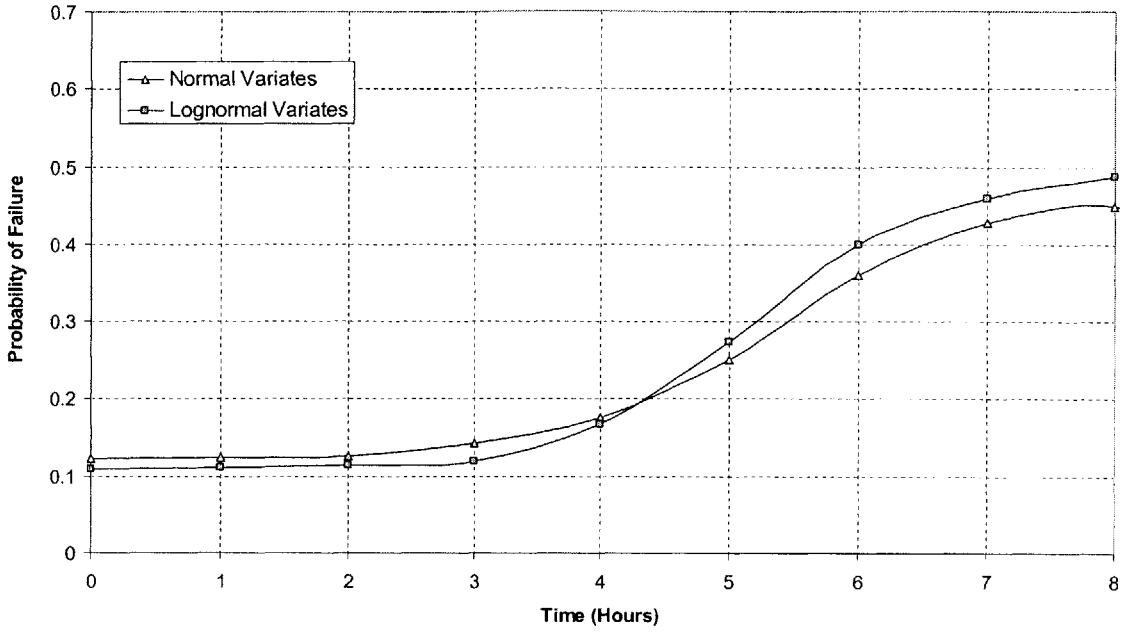

Figure **6.115.** Comparison of Probability of Failure for Normal and Lognormal Strength Parameters

Figure 6.115 shows that at early times into the rain event, the failure probability is slightly greater when c' and ϕ' are Normal, but at later times it is greater when c' and ϕ' are Lognormal. The reason for this is explained in Figure 6.116, which compares the distribution of Factor of Safety at selected times when c' and ϕ' are Lognormal with those when c' and ϕ' are Normal.

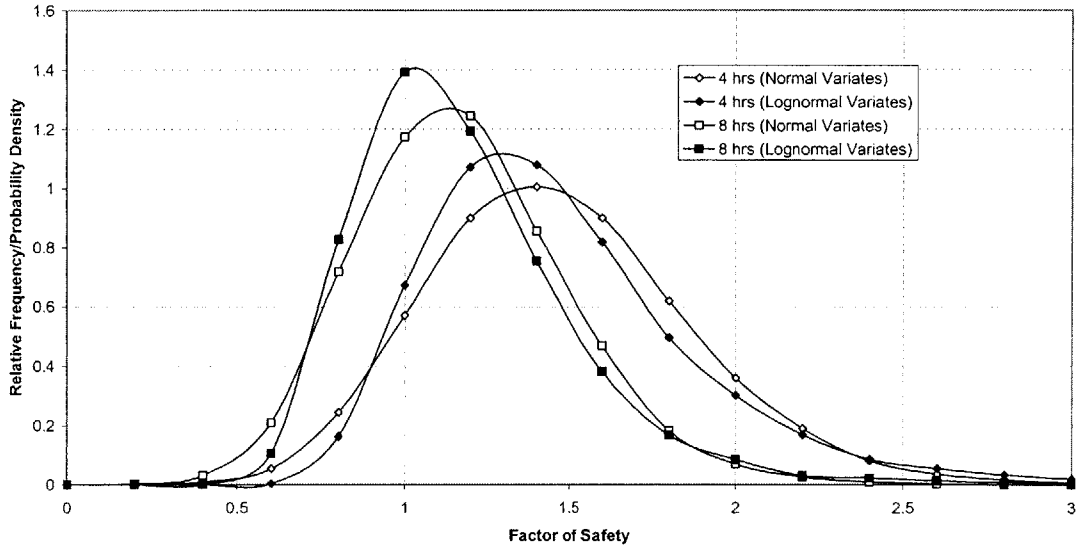

Figure **6.116.** Comparison of Probability Distribution of Factor of Safety at Selected Times for Normal and Lognormal Strength Parameters

The distributions in Figure 6.116 show that at early times, the failure probability is slightly greater when c' and ϕ' are Normal, but at later times it is greater when c' and ϕ' are Lognormal. These results confirm what had been stated in Section 6-2.1.3.2.1, namely that one cannot generalize whether the probability of failure when c' and ϕ' are Lognormal will be greater or less than the probability of failure when c' and ϕ' are Normal.

Figures 6.115 and 6.116 both illustrate the effects of parameter distribution model uncertainty on landslide hazards.

LANDSLIDE HAZARDS WITH RAINFALL INTENSITY GREATER THAN SATURATED CONDUCTIVITY

In this example, we consider the slope shown in Figure 6.117.

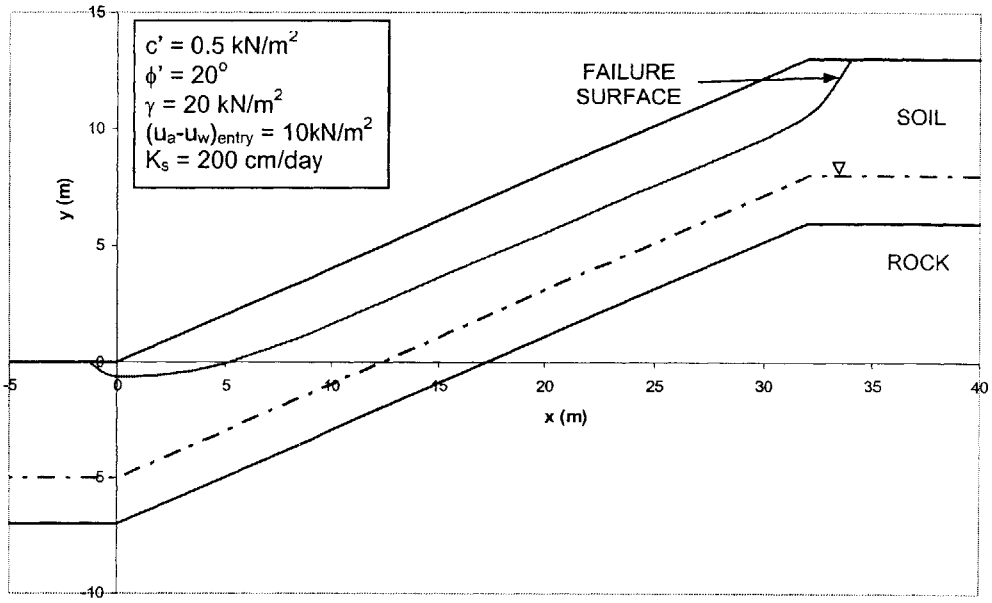

Figure 6.117. Slope Properties and Failure Surface

We assume a rainfall event of intensity $I = 375cm/day = 155mm/hr$ occurs for a duration of 8 hours. Figure 6.118 shows moisture profiles, and Figure 6.119 shows pressure profiles at selected times.

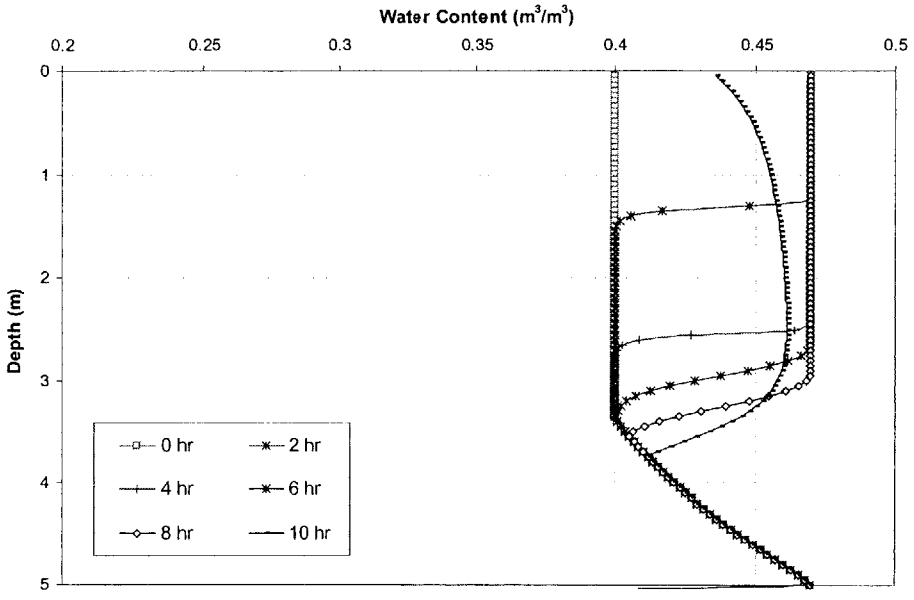

Figure 6.118. Moisture Content Profiles with Time using the van Genuchten (1980) Model

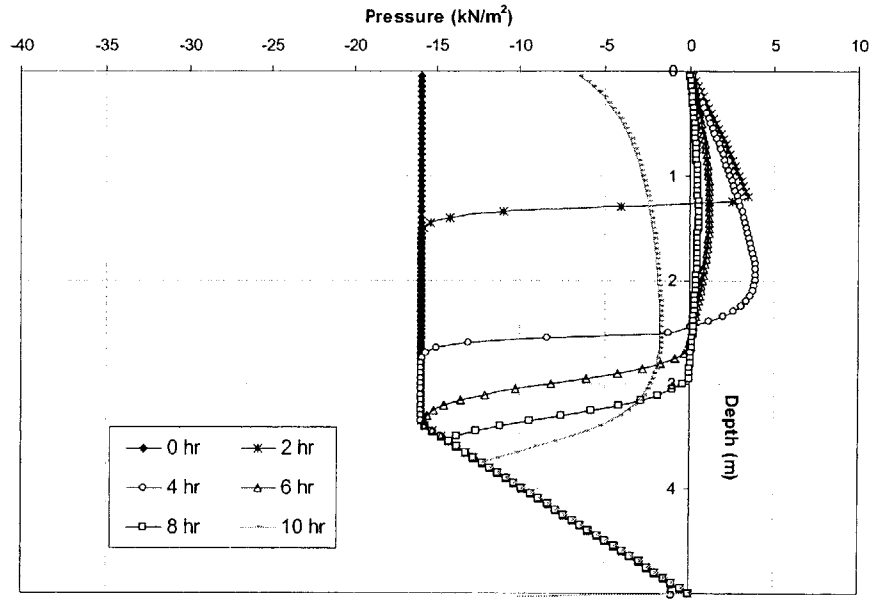

Figure 6.119. Pressure Profiles with Time using the van Genuchten (1980) Model

Figure 6.120 shows the expected value of Factor of Safety with time.

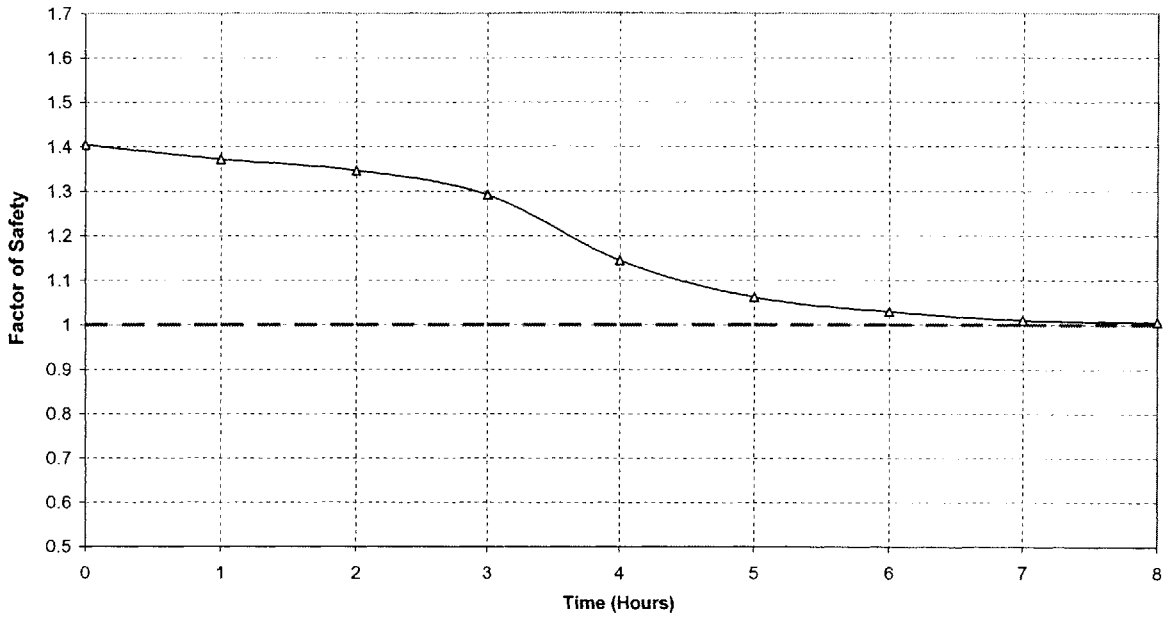

Figure **6.120.** Expected Value of Factor of Safety with Time for Lognormal Strength Parameters

We now assume that the soil hydraulic conductivity and strength parameters are distributed as:

$K_S \sim LN(m_{K_S} = 200cm/day, \sigma^2_{K_S} = (100cm/day)^2)$;

$c' \sim LN(m_{c'} = 0.5kN/m^2,\ \sigma_{c'} = 0.017kN/m^2)$, $\phi' \sim LN(m_{\phi'} = 20^o,\ \sigma_{\phi'} = 6.67^o)$, and c', ϕ' and K_S are uncorrelated.

The probability distributions of the Factor of Safety at different times are shown in Figure 6.121, and show a shift towards the origin with increasing time into the rainfall event.

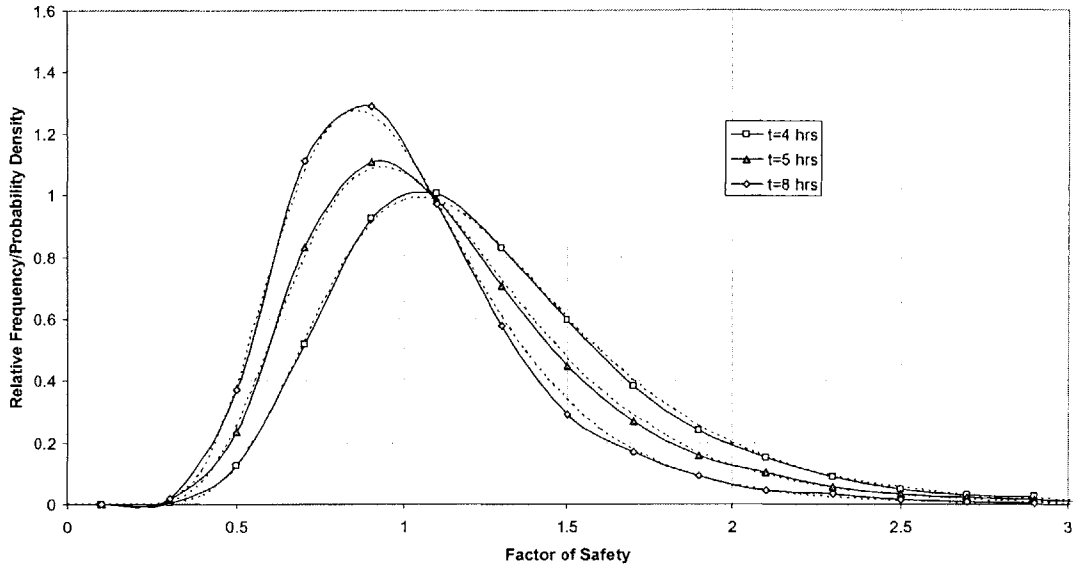

Figure **6.121.** Distributions of Factor of Safety at Selected Times (Continuous Lines are Simulated Distributions and Dashed Lines are Fitted Lognormal Distribution)

Tables 6.24 through 6.29 summarize the statistics and properties of the fitted distributions for this example.

	Simulated Distribution
Expected Value, E[F]	1.274
Standard Deviation, σ[F]	0.490
Skewness	1.5702
Kurtosis	5.3409
Probability of Failure	0.315

Table 6.24. Summary Statistics of Simulated Distribution at time 4 hours

Fitted Distribution	Maximum Likelihood Parameters		Error Term, e	Probability of Failure
	E[F]/ E[ln(F)]/ r	σ[F] / σ [ln(F)]/ λ		
Normal	1.274	0.490	0.749	0.288
Lognormal	0.176	0.360	0.086	0.312
Gamma	7.741	6.077	0.292	0.300

Table 6.25. Fitted Distributions to Simulated Distribution at time 4 hours

	Simulated Distribution
Expected Value, E[F]	1.144
Standard Deviation, σ[F]	0.450
Skewness	1.5428
Kurtosis	4.7662
Probability of Failure	0.438

Table 6.26. Summary Statistics of Simulated Distribution at time 5 hours

Fitted Distribution	Maximum Likelihood Parameters		Error Term, e	Probability of Failure
	E[F]/ E[ln(F)]/ r	σ[F]/σ[ln(F)]/ λ		
Normal	1.144	0.450	0.828	0.374
Lognormal	0.066	0.366	0.122	0.428
Gamma	7.456	6.516	0.347	0.407

Table 6.27. Fitted Distributions to Simulated Distribution at time 5 hours

	Simulated Distribution
Expected Value, E[F]	1.023
Standard Deviation, σ[F]	0.387
Skewness	1.8782
Kurtosis	8.9039
Probability of Failure	0.558

Table 6.28. Summary Statistics of Simulated Distribution at time 8 hours

Fitted Distribution	Maximum Likelihood Parameters		Error Term, e	Probability of Failure
	E[F]/ E[ln(F)]/ r	σ[F]/σ[ln(F)]/ λ		
Normal	1.023	0.387	0.889	0.476
Lognormal	-0.038	0.345	0.139	0.544
Gamma	8.289	8.100	0.376	0.520

Table 6.29. Fitted Distributions to Simulated Distribution at time 8 hours

Similar comments can be made with regard to Tables 6.24 through 6.29 as were made with regard to Tables 6.16 through 6.23. The distribution of the Factor of Safety is Skewed and better approximated by the Lognormal distribution than by the Gamma or Normal distributions. This is shown in Figure 6.121. We also note that the fit to the Lognormal distribution is better in this example than in the previous example, because of the smaller error term. This is because of the greater uncertainty in the strength parameters, expressed by the larger coefficients of variation $V_{c'} = \frac{\sqrt{Var[c']}}{E[c']} = V_{\phi'} = \frac{\sqrt{Var[\phi']}}{E[\phi']} = \frac{1}{3}$ in this example, compared to $V_{c'} = \frac{\sqrt{Var[c']}}{E[c']} = V_{\phi'} = \frac{\sqrt{Var[\phi']}}{E[\phi']} = \frac{1}{4}$ in the previous example. Consequently, the effects the distributions of c' and ϕ' have a greater effect on the distribution of the Factor of Safety, and since these are Lognormal, the distribution of the Factor of Safety tends towards the distribution when

only c' and ϕ' are uncertain (and the conductivity is deterministic) which is a Lognormal distribution as was shown in Section 6.3.3.2.1.

Figure 6.122 compares the probability of failure when c' and ϕ' are Lognormal with those when c' and ϕ' are Normal (which were obtained in Part 5-5 of Chapter 5).

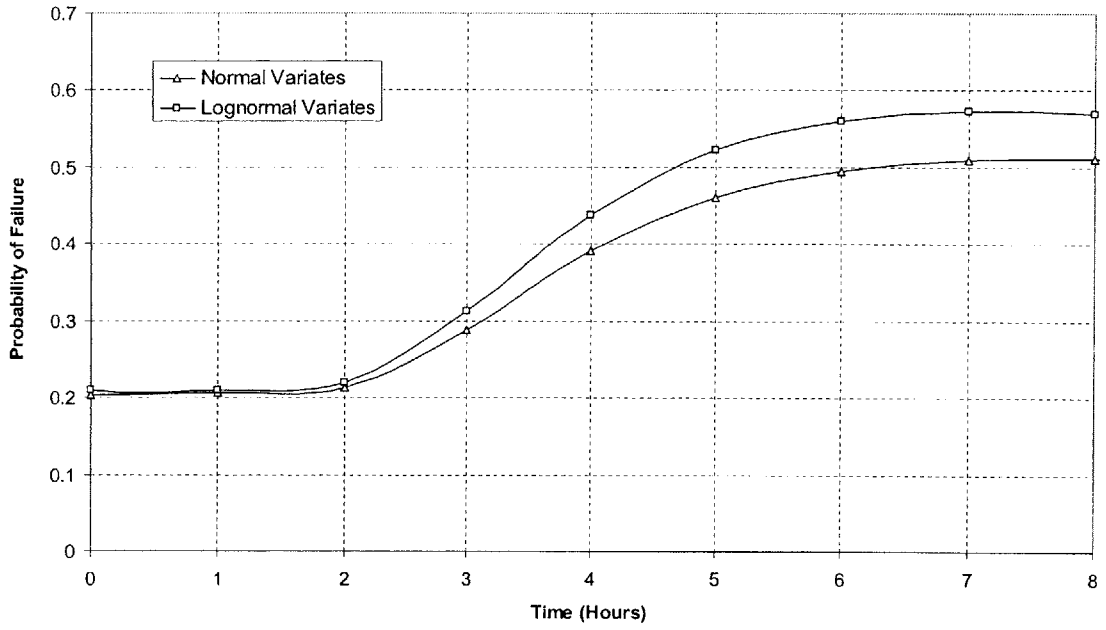

Figure **6.122.** Comparison of Probability of Failure for Normal and Lognormal Strength Parameters

Figure 6.122 shows that in this example, the probability of failure when c' and ϕ' are Lognormal is greater at all times than the failure probability when c' and ϕ' are Normal. Figure 6.123 compares the distributions of Factor of Safety at different times when c' and ϕ' are Lognormal with those when c' and ϕ' are Normal (which were obtained in Part 5-5 of Chapter 5).

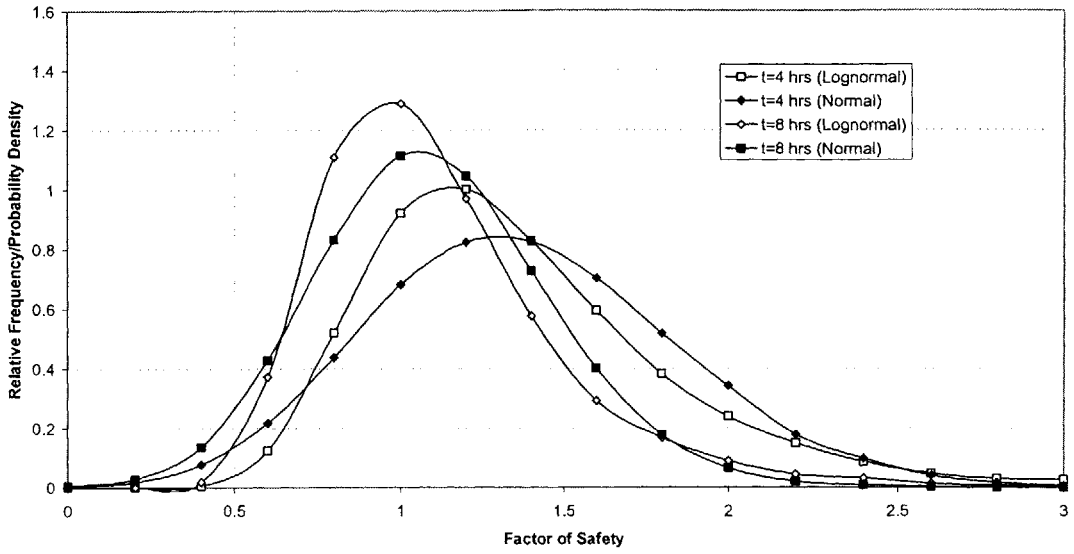

Figure 6.123. Comparison of Probability Distribution of Factor of Safety at Selected Times for Normal and Lognormal Strength Parameters

Figures 6.120 and 6.121 again illustrate the effects of parameter distribution model uncertainty on landslide hazards, and that these effects can be significant.

6-2.1.3.2.4. SUMMARY ON PARAMETER DISTRIBUTION SUBMODEL UNCERTAINTY

Chapter 5, Part 5-5, investigated the effects of parameter uncertainties on landslide hazards, and we showed that uncertainties in c' and ϕ' have a greater effect on uncertainties in the Factor of Safety than the saturated conductivity of the soil. In this Section, we showed that the distributions of c' and ϕ' have a greater effect on the distribution of the Factor of Safety than the distribution of the conductivity of the soil. The results are summarized in Tables 6.30 to 6.34:

Parameter	Distribution	Coefficient of Variation (Uncertainty)	Distribution of Factor of Safety	Comments
c'	Normal	Small or Large	Normal	Factor of Safety approximately linear function of c' and ϕ' and distribution of Factor of Safety is Normal
ϕ'	Normal	Small or Large		
K_s	Deterministic	Zero		

Table 6.30. Distribution of Factor of Safety for Normal Strength Parameters and Deterministic Conductivity

Parameter	Distribution	Coefficient of Variation (Uncertainty)	Distribution of Factor of Safety	Comments
c'	Lognormal	Small or Large	Lognormal	Distribution of Factor of Safety is also Lognormal
ϕ'	Lognormal	Small or Large		
K_s	Deterministic	Zero		

Table 6.31. Distribution of Factor of Safety for Lognormal Strength Parameters and Deterministic Conductivity

Parameter	Distribution	Coefficient of Variation (Uncertainty)	Distribution of Factor of Safety	Comments
c'	Normal	Large	Normal	Uncertainties in c' and ϕ' more important than in K_s and govern distribution of Factor of Safety which is Normal
ϕ'	Normal	Large		
K_s	Lognormal	Typical		

Table 6.32. Distribution of Factor of Safety for Normal Strength Parameters (Large Uncertainty) and Lognormal Conductivity

Parameter	Distribution	Coefficient of Variation (Uncertainty)	Distribution of Factor of Safety	Comments
c'	Normal	Small	Gamma/ Normal	Uncertainties in K_S become important but not as important as c' and ϕ' and distribution of Factor of Safety is Gamma/ Normal
ϕ'	Normal	Small		
K_S	Lognormal	Typical		

Table 6.33. Distribution of Factor of Safety for Normal Strength Parameters (Small Uncertainty) and Lognormal Conductivity

Parameter	Distribution	Coefficient of Variation (Uncertainty)	Distribution of Factor of Safety	Comments
c'	Lognormal	Small or Large	Lognormal	Uncertainties in c' and ϕ' more important than in K_S and govern distribution of Factor of Safety which is Lognormal
ϕ'	Lognormal	Small or Large		
K_S	Lognormal	Typical		

Table 6.34. Distribution of Factor of Safety for Lognormal Strength Parameters and Lognormal Conductivity

We therefore conclude that the distribution of the Factor of Safety, in terms of both shape and parameters (expected value and variance) is dependent on the distributions of c', ϕ' and K_S as well as the parameters (uncertainties) of these distributions. c' and ϕ' are the main contributors to the uncertainty in Factors of Safety, and hence their distributions affect the distributions of Factor of Safety more than the distribution of K_S.

No general conclusion can be made as to whether probabilities of failure (hazards) are greater or less based solely on the distribution of c' and ϕ' e.g. when c' and ϕ' are Normal compared to when they are Lognormal. Probabilities of failure will depend on the particular case under study.

6-2.1.3.3. FACTOR OF SAFETY PROBABILITY DISTRIBUTION SUBMODEL UNCERTAINTY

In this Chapter, and in Chapter 5, attempts were made to fit theoretical probability distributions to the Factor of Safety in a slope. This was done for stability analyses, and coupled hydrologic and stability analyses. Suppose that these derived distributions are used to assess landslide hazards. One assumes the Factor of Safety in a slope (or series of slopes in a certain region) to follow a theoretically derived distribution, and assesses hazards based on these distributions. There are uncertainties associated with doing this, because uncertainties arise when fitting theoretical probability distributions to simulated distributions of the Factor of Safety. There are two types of uncertainties that enter:

(a) Model uncertainty when assuming that the true distribution of the Factor of Safety follows a theoretical probability distribution such as the Normal, Lognormal or Gamma distribution.
(b) Parameter uncertainty when estimating the parameters of these probability models. The Method of Maximum Likelihood was used for this purpose in this study, and estimating the parameters of the distribution depend on the sample of Factor of Safety obtained using Monte Carlo analyses. These parameters will therefore be different for every sample of Factor of Safety, and are so subject to parameter uncertainty.

Uncertainties in the distribution of the Factor of Safety translate to uncertainties in estimating probabilities from these distributions, e.g. the probability of failure $P[F] < 1$, and hence uncertainties in estimating landslide hazards.

6-2.1.4. CONCLUSIONS ON DISTRIBUTION SUBMODEL UNCERTAINTY

The effects of parameter distribution model uncertainty on probabilistic slope stability analyses, and landslide hazards were assessed. We showed that these effects can be significant, and can lead to different conclusions regarding stability and landslide hazards. In particular, we showed that including (negative) correlation between the strength parameters reduces the uncertainty (variance) in Factors of Safety and therefore reduces probabilities of failure. We showed that assuming Lognormal

distributions for the strength parameters (as opposed to Normal distributions) changes the shape of the distribution of the Factor of Safety, and this affects probabilities of slope failure and landslide hazards. No general conclusion can be drawn with regard to whether probabilities of failure are greater (or less) in the case of Lognormal parameters compared to Normal parameters, and these have to be determined on a case by case basis. Furthermore, when assessing landslide hazards, for a specific case, which probability of failure is greater (when the strength parameters are Normal and when they are Lognormal) can change with time as shown in Figure 6.115. In Figure 6.115 at early times, the probability of failure when the parameters are Normal is greater, but at later times, when they are Lognormal it is greater.

Fitting probability distributions to the Factor of Safety is also uncertain, as uncertainties enter in estimating the parameters of these distributions, e.g. mean value and variance, and the distributions themselves, e.g. normal, lognormal, gamma or other. This is another source of uncertainty that can affect landslide hazards assessments.

6-2.1.4. STRENGTH SUBMODEL UNCERTAINTY

Stability analyses require submodels of models to represent soil strength. While the strength of saturated soils is well represented by the Coulomb Model, the strength of unsaturated soils is not well represented. This is mainly because of the lack of understanding of the mechanisms that generate unsaturated strength. In this Section, after providing some theoretical background, we investigate the effects of unsaturated strength model uncertainty on slope reliability and probabilistic analyses, and on landslide hazards. Figure 6.123 shows in bold what is studied in this Section.

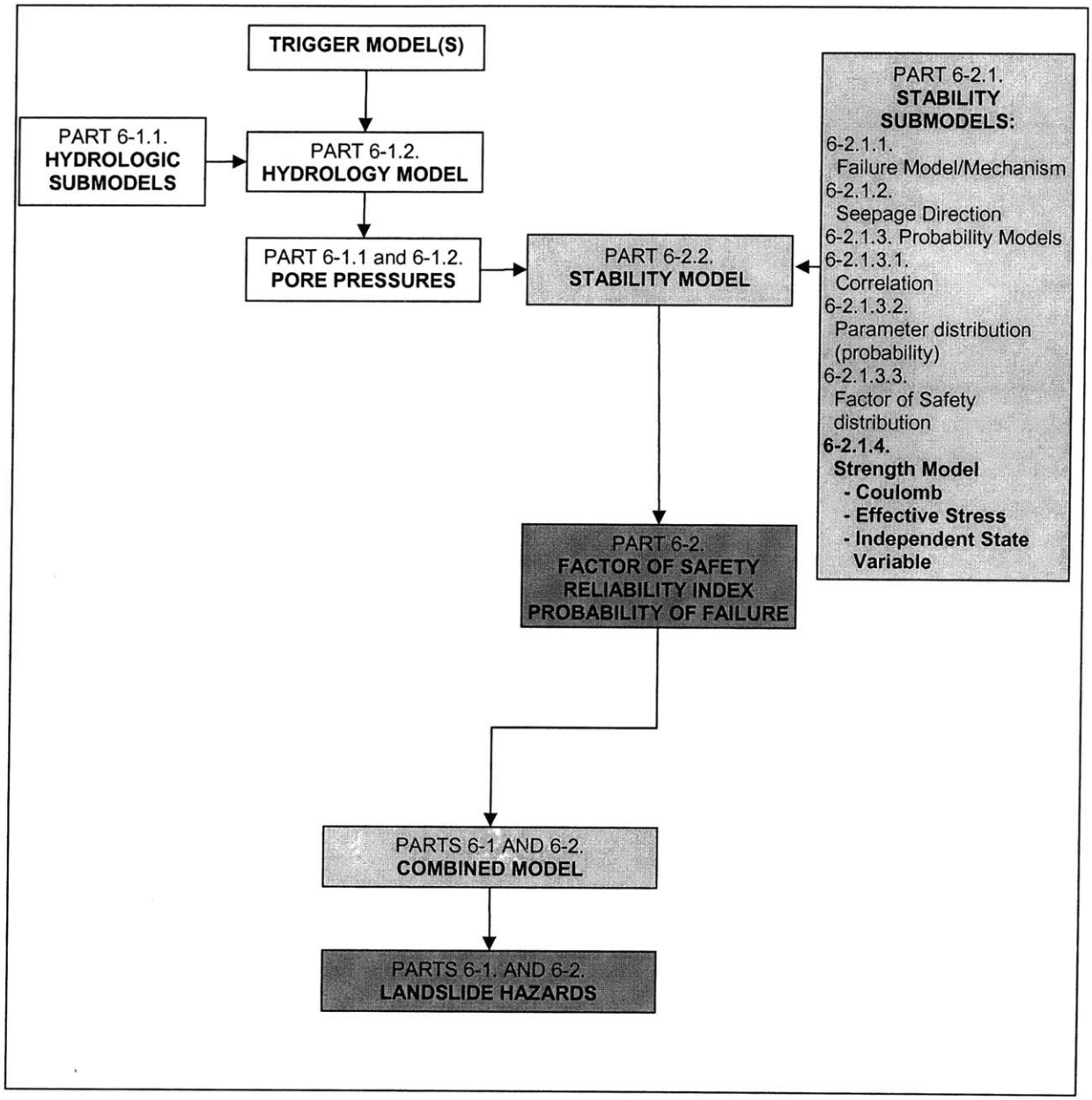

Figure **6.123.** Effects of unsaturated strength models (shown in the lightly shaded submodels box) on the results of stability analyses (Factors of safety, reliability indices and probabilities of failure in the dark shaded box) and on landslide hazards (dark box) are investigated

6-2.1.4.1. BACKGROUND

Models to represent the strength of soils need to be adopted to perform stability analyses. The shear strength of saturated soils is described using the Coulomb Model and the effective stress concept (Terzaghi, 1936):

$$\tau = c' + (\sigma - u_w)\tan\phi' \qquad [6.26]$$

Or:

$$\tau = c' + \sigma' \tan\phi' \qquad [6.27]$$

where:

σ is the total normal stress

u_w is the pore water pressure

σ' is the effective normal stress $\sigma' = (\sigma - u_w)$

c' is the effective cohesion or shear stress when the net or effective normal stress is equal to zero

ϕ' is the angle of internal friction of the soil

τ is the shear strength of the soil

The shear strength of unsaturated soils is, however, much less understood. Over the years, several models have been proposed to predict the unsaturated shear strength. The philosophy behind these models is different with regard to the contribution of suction towards unsaturated strength.

Bishop (1959) originally proposed a shear strength Equation for unsaturated soils by extending the effective stress principle (Terzaghi, 1936) for saturated soils. The model can be expressed as:

$$\tau = c' + [(\sigma - u_a) + \chi(u_a - u_w)]\tan\phi' \qquad [6.28]$$

where χ is a so called effective stress parameter, and represents the proportion of suction, $(u_a - u_w)$ that contributes to strength.

Significant difficulties were encountered in the interpretation and experimental determination of the parameter χ, and interest in the model was lost for some years.

Fredlund et al. (1978) proposed a relationship to explain the shear strength of unsaturated soils in terms of two independent stress state variables as:

$$\tau = c' + (\sigma - u_a)\tan\phi' + (u_a - u_w)\tan\phi^b \qquad [6.29]$$

This model assumes a linear variation of unsaturated strength with suction, $(u_a - u_w)$, and the parameter ϕ^b, is constant, and can be empirically set. Although it is widely recognized that the relationship between unsaturated strength and suction is non linear, the model has, and continues to be widely used as a model for unsaturated strength, because of its simplicity. This is particularly the case in slope stability studies.

In recent years, however, there has been growing interest in the originally proposed effective stress approach by Bishop (1959). This is partly because of the need for a better model for unsaturated strength, and partly because advancements in experimental procedures have allowed for the better determination of χ.

In the next Section, the two models for unsaturated soil strength, namely the Effective Stress Model (Bishop, 1959), Independent State Variable Model (Fredlund et al., 1978) are described in more detail. These two models, along with the Coulomb Model for saturated strength, are then used to investigate the effect of strength model uncertainty on stability analyses.

6-2.1.4.1.a. INDEPENDENT STATE VARIABLE SUBMODEL (Fredlund et al., 1978)

In the Independent State Variable Model, the net normal stress, $(\sigma - u_a)$ and suction, $(u_a - u_w)$ are considered independent stress state variables. In doing so, an extended

Coulomb criterion for unsaturated soils can be formulated (Fredlund et al., 1978). Assuming a planar failure envelope, the unsaturated shear strength can be written as:

$$\tau = c' + (\sigma - u_a)\tan\phi' + (u_a - u_w)\tan\phi^b \qquad [6.30]$$

where:

σ is the total normal stress

u_a is the pore air pressure

$(u_a - u_w)$ is the soil suction

σ' is the effective normal stress $\sigma' = (\sigma - u_w)$

c' is the effective cohesion or shear stress when the net or effective normal stress is equal to zero

ϕ' is the angle of internal friction of the soil

ϕ^b is the angle indicating the rate of change in shear strength relative to changes in suction, $(u_a - u_w)$

τ is the shear strength of the soil

Figure 6.124 shows a three-dimensional schematic of the proposed unsaturated failure envelope in τ - $(\sigma - u_a)$ - $(u_a - u_w)$ space.

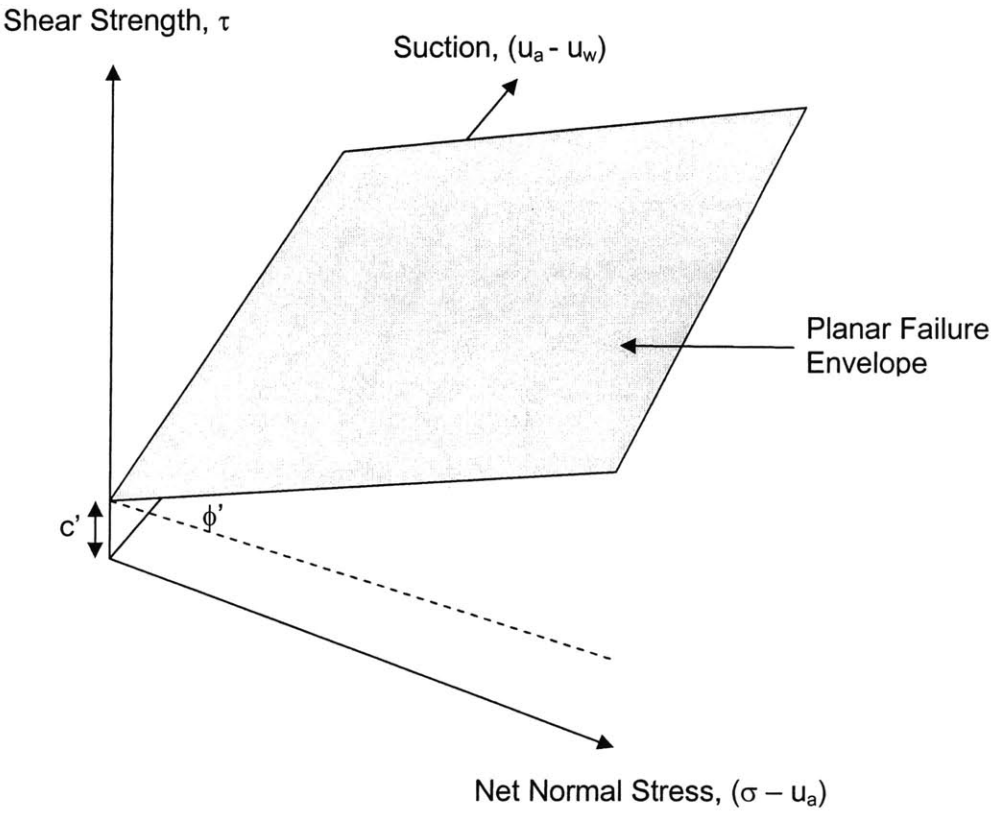

Figure **6.124.** Schematic of Independent State Variable Model Failure Envelope for Constant ϕ^b

The envelope in Figure 6.124 is planar for constant parameter ϕ^b. In such cases, ϕ^b is the slope of shear strength against suction plot when the net normal stress is held constant. This is illustrated in Figure 6.125.

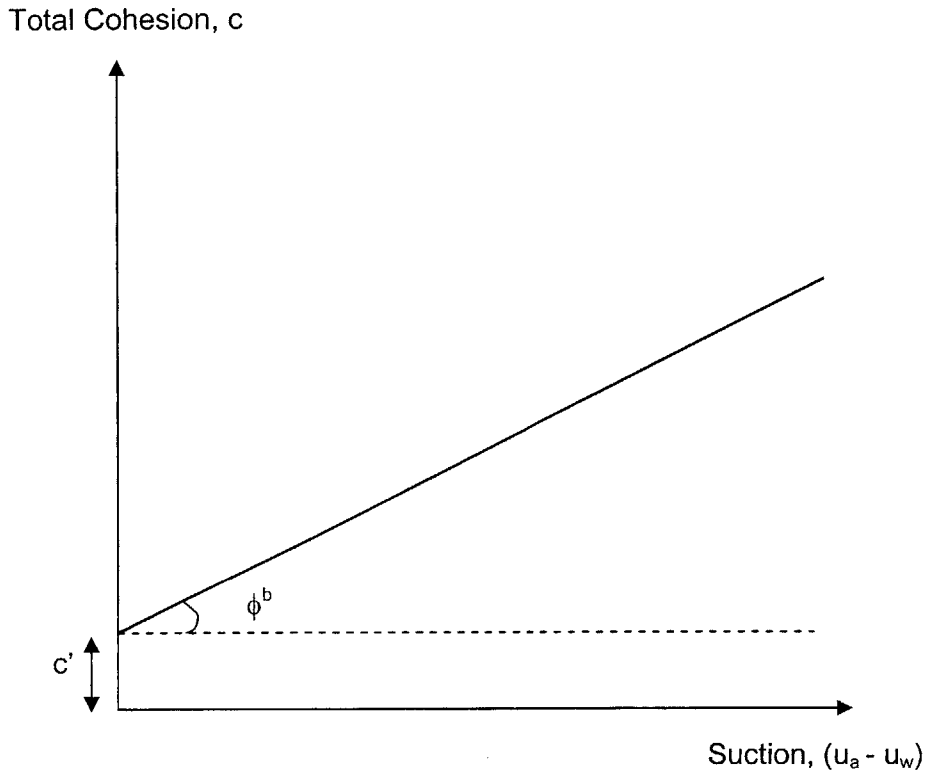

Figure **6.125.** Schematic of Increase in Total Cohesion with Suction

The angle ϕ^b provides an additional component of soil cohesion caused by suction. The total cohesion of the soil, c therefore, has two components, and can be expressed as:

$$c = c' + (u_a - u_w)\tan\phi^b \qquad [6.31]$$

The shear strength Equation for unsaturated soils can then be reduced to the same format as that used for saturated soils:

$$\tau = c + (\sigma - u_a)\tan\phi' \qquad [6.32]$$

where c is the total cohesion in Equation [6.31].

As saturation is approached, the pore air pressure u_a becomes equal to the pore water pressure, u_w. When $u_a = u_w$, $c = c'$, and Equation [6.32] reverts to the Coulomb Model for a saturated soil.

$$\tau = c' + (\sigma - u_w)\tan\phi' \qquad [6.33]$$

This model for unsaturated strength has been extensively used in the literature, because of the assumption of linearity of unsaturated strength with suction. This is particularly true since the parameter ϕ^b has been empirically set in many of these studies.

However, it has long been recognized that the parameter ϕ^b is highly non-linear with suction (Satija, 1978; Ho and Fredlund, 1982; Gan et al., 1988, Gan and Fredlund, 1988; Rahardjo et al., 1995).

Rahardjo et al. (1995) describe experimental procedures by which ϕ^b can be determined, and showed that ϕ^b is equal to ϕ' for a saturated soil, decreases with decreasing degree of saturation and stabilizes to a constant value at relatively large suctions, the values of which depend on the type of soil. These laboratory procedures have proven to be demanding and time-consuming, particularly for fine-grained materials, in which the coefficient of permeability of the material is very low. The equipment used for this purpose is generally expensive and sophisticated, and the level of expertise required for the determination of ϕ^b is often beyond that of many geotechnical engineering laboratories. In addition, due to the strong non-linearity of ϕ^b with suction, the predictive capacity of the approach is limited to situations where the suction range used in the laboratory to establish ϕ^b is the same as that expected in the field (Khalili & Khabbaz, 1998). Hence, for good predications of strength, the testing suction range must cover what is expected to be encountered in the field.

Given these limitations, and the recent advancements in experimental procedures, there has been growing interest in the originally proposed Effective Stress Model (Bishop, 1959).

6-2.1.4.1.b. EFFECTIVE STRESS SUBMODEL (Bishop, 1959)

In the originally proposed Bishop (1959) Model, the shear strength is determined on the basis of the effective strength parameters c' and ϕ' and a single stress variable defined as:

$$\sigma' = (\sigma - u_a) + \chi(u_a - u_w) \qquad [6.34]$$

where:

σ' is the effective stress

χ is the effective stress parameter

Unsaturated shear strength is expressed as:

$$\tau = c' + [(\sigma - u_a) + \chi(u_a - u_w)]\tan\phi' \qquad [6.35]$$

The pore air pressure u_w is frequently assumed to be zero, in which case Equation [6.35] reduces to:

$$\tau = c' + [(\sigma) + \chi(-u_w)]\tan\phi' \qquad [6.36]$$

The effective stress parameter χ has a value of 1 for saturated soils and 0 for dry soils. When $\chi = 1$, unsaturated strength in Equation [6.35] becomes:

$$\tau = c' + \sigma'\tan\phi' \qquad [6.36]$$

which is identical to the saturated Coulomb Model where c' and ϕ' are the saturated strength parameters.

The advantage of the effective stress model is that the change in the shear strength with changes in total stress, pore water pressure and pore air pressure is related to a single stress variable, $\sigma' = (\sigma - u_a) + \chi(u_a - u_w)$. As a result, a complete characterization of the

soil strength requires matching of a single stress history rather than two or three independent stress variables, as in the Independent State Variable Model where the state variables are $\sigma' = (\sigma - u_a)$, and suction $(u_a - u_w)$. Furthermore, the approach requires very limited testing of soils in an unsaturated state.

However, a major difficulty of the effective stress approach has been in the determination of the parameter χ. χ in Equation [6.35] is an empirical parameter representing the proportion of soil suction that contributes to the effective stress. Considerable attempts have been made to quantify χ both theoretically and experimentally. Most attempts have focused on finding a relationship between χ and the degree of saturation S_r (Vanapalli et al., 1996; Oberg and Sallfors, 1997; Bao et al., 1998). Vanapalli et al. (1996), for example, propose:

$$\chi = \left(\frac{\theta - \theta_r}{\theta_r - \theta_s} \right) \qquad [6.37]$$

where:

θ is the moisture content in the soil

θ_s is the saturated moisture content of soil (see Chapter 2)

θ_r is the residual moisture content of soil (see Chapter 2)

Other attempts have also been made to quantify χ using simple capillary models, but with little or no success. More recent approaches (Kogho et al., 1993; Modaressi and Abou-Bekr, 1994; Khalili and Khabbaz, 1998) consider χ as a function of the suction, and have attempted to relate χ to the soil water characteristic curve (see Chapter 2).

Khalili and Khabbaz (1998) propose a unique relationship between the effective stress parameter χ and the ratio of the suction over the air entry value, based on the shear strength data of 14 soils reported in the literature. χ is expressed as:

$$\chi = \left[\frac{(u_a - u_w)}{(u_a - u_w)_{entry}} \right]^{-0.55} \qquad [6.38]$$

where:

$\left[\frac{(u_a - u_w)}{(u_a - u_w)_{entry}} \right]$ is the suction ratio

$(u_a - u_w)_{enrty}$ is the air entry suction (as defined in Chapter 2).

The fit to the data has a correlation coefficient of 0.94.

Geiser (2000) tested the applicability of the single effective stress relationship proposed by Khalili and Khabbaz (1998), based on an extensive experimental program on various silts at the Swiss Federal Institute of Technology at Lausanne, and confirmed the relationship.

In this study, the Independent State Variable Model (Fredlund et al, 1978) with constant parameter ϕ^b and the Effective Stress Model (Bishop, 1959), with the parameter χ as proposed by Khalili and Khabbaz (1998) are used. Strength model uncertainty is assessed using these models in both deterministic and probabilistic slope stability analyses. The effects of strength model uncertainty on landslide hazards are then investigated.

6-2.1.4.2. STRENGTH SUBMODEL UNCERTAINTY FOR PLANAR FAILURE SURFACE

The strength of unsaturated soil is described using the Independent State Variable Model, and the Effective Stress Model for different parameter values. The variation of strength using the different models in relation to suction $(u_a - u_w)$ is shown in Figure 6.126.

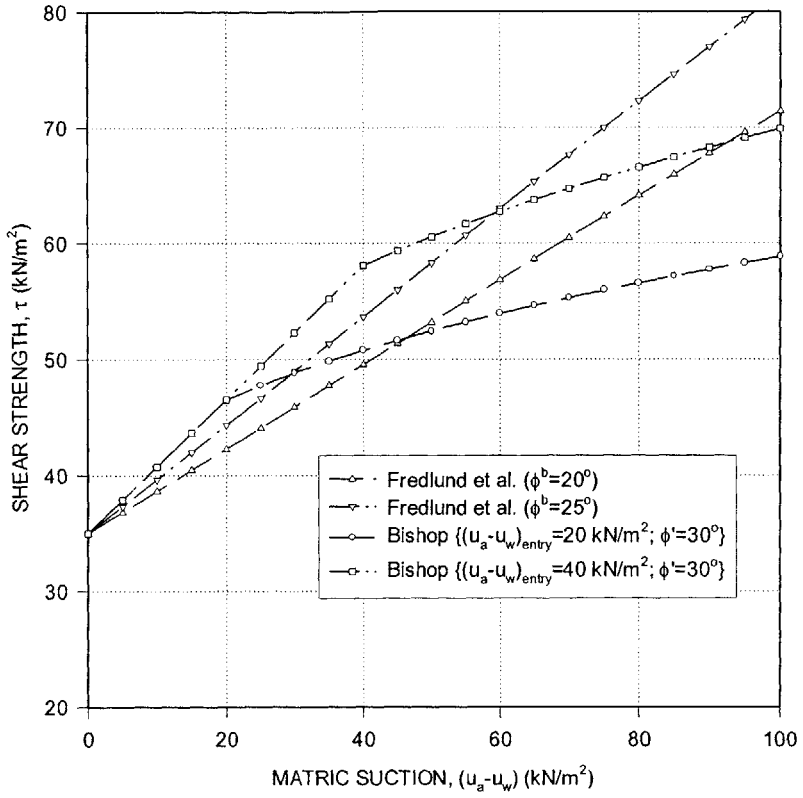

Figure **6.126.** Illustration of Strength Model Uncertainty

Figure 6.126 illustrates the effects of parameter uncertainty (different values of the parameters in the same strength model) and strength model uncertainty.

A simple and good example to illustrate the effects of model uncertainty on stability analyses considers the stability of the slope in Figure 6.127. Figure 6.127 shows the results of Infinite Slope Stability analyses on the slope using the different strength models, and therefore illustrates the effects of strength model uncertainty on stability analyses.

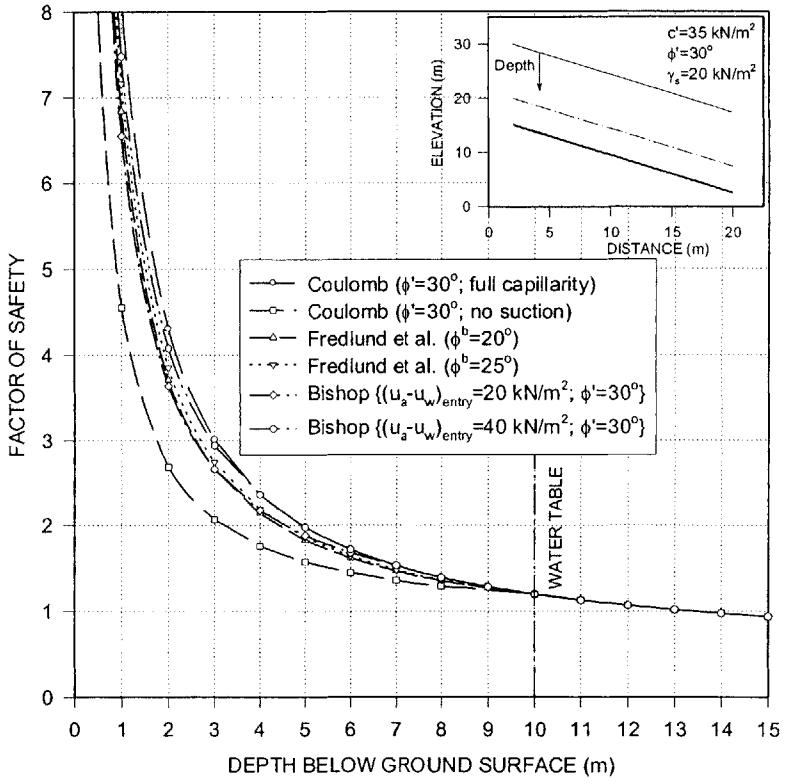

Figure **6.127.** Effect of Strength Model Uncertainty (Figure 6.126) on Stability

Two boundary cases are used in the Coulomb Model, that of full capillarity, and that of no contribution from suction towards stability. The case of full capillarity corresponds to hydrostatic pressures in both the saturated (positive pressures) and unsaturated (negative pressures) zones of the slope. The case of no suction corresponds to hydrostatic pressures in the saturated (positive pressures) and zero pressures in the unsaturated zone of the slope. These are boundary cases because they consider the maximum and minimum possible contributions of suction towards strength.

Figure 6.127 shows that different strength models result in different values of the Factor of Safety, and different conclusions on stability. The Coulomb model with full contribution from suction, and no contribution from suction are upper and lower bounds to the Factor of Safety. Neither case accurately represents reality, but provide an envelope within which and the actual Factor of Safety (from the actual unsaturated soil strength) lies.

6-2.1.4.3. STRENGTH SUBMODEL UNCERTAINTY IN SLOPE DETERMINISTIC AND RELIABILITY ANALYSES

To illustrate the effects of strength model uncertainty on slope stability analyses, we analyze the stability of a slope using three models for unsaturated strength, namely the Effective Stress Model, the Independent State Variable Model, and the Coulomb Model.

EFFECTIVE STRESS MODEL

Consider the slope shown in Figure 6.128. We assume the saturated strength parameters shown in Figure 6.128, and an air entry pressure of $(u_a - u_w)_{entry} = 10 kN/m^2$. This air entry pressure is used in the Effective Stress Model for unsaturated strength (see Equations [6.35] and [6.38]).

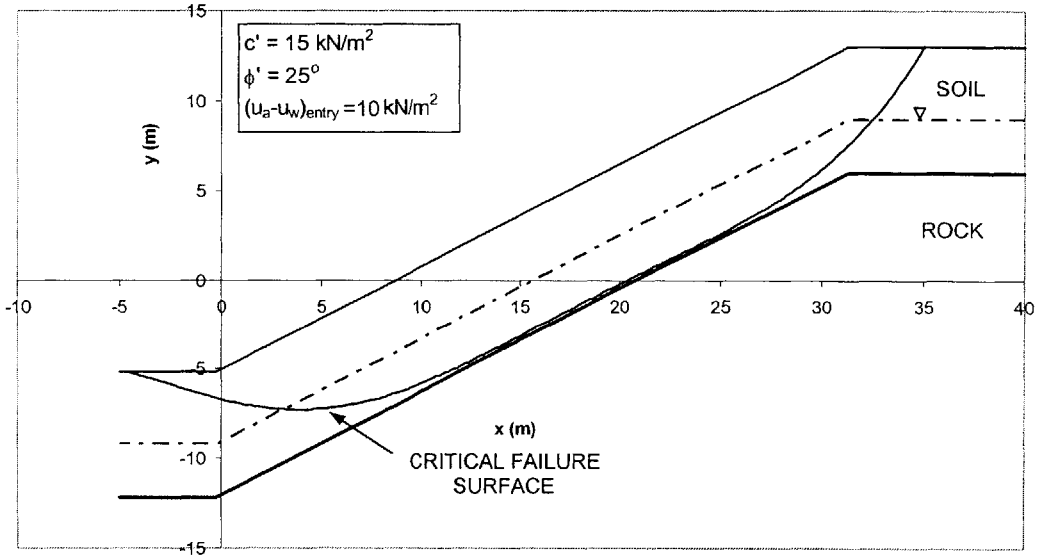

Figure 6.128. Slope Geometry and Strength Parameters

This slope was analyzed in Chapter 5, Part 5-3, and the Factor of Safety in the slope was computed to be 1.18 on the critical deterministic failure surface.

We now assume that the soil strength parameters are uncertain and that, $c' \sim (m_{c'} = 15kN/m^2,\ \sigma_{c'} = 5kN/m^2)$; $\phi' \sim (m_{\phi'} = 25^o,\ \sigma_{\phi'} = 5^o)$; and that c' and ϕ' are uncorrelated.

The critical reliability based failure surface is located as shown in Figure 6.128, and the Hasofer and Lind (1974) reliability index is computed to be 0.72. A simple reliability chart is shown in Figure 6.129.

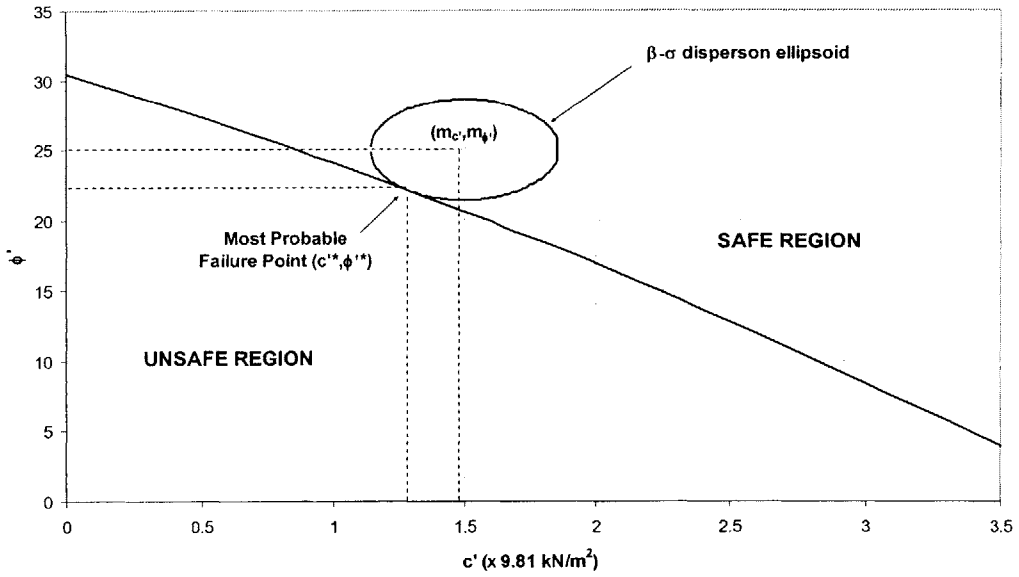

Figure 6.129. Reliability Chart Based on Critical Reliability Based Failure Surface

INDEPENDENT STATE VARIABLE MODEL

We adopt the Independent State Variable Model (Fredlund et al., 1978) for unsaturated soil strength. In addition to the saturated soil strength parameters, the angle of shearing resistance with respect to suction is taken to be $\phi^b = 15^o$. The critical deterministic failure surface is located and shown in Figure 6.130.

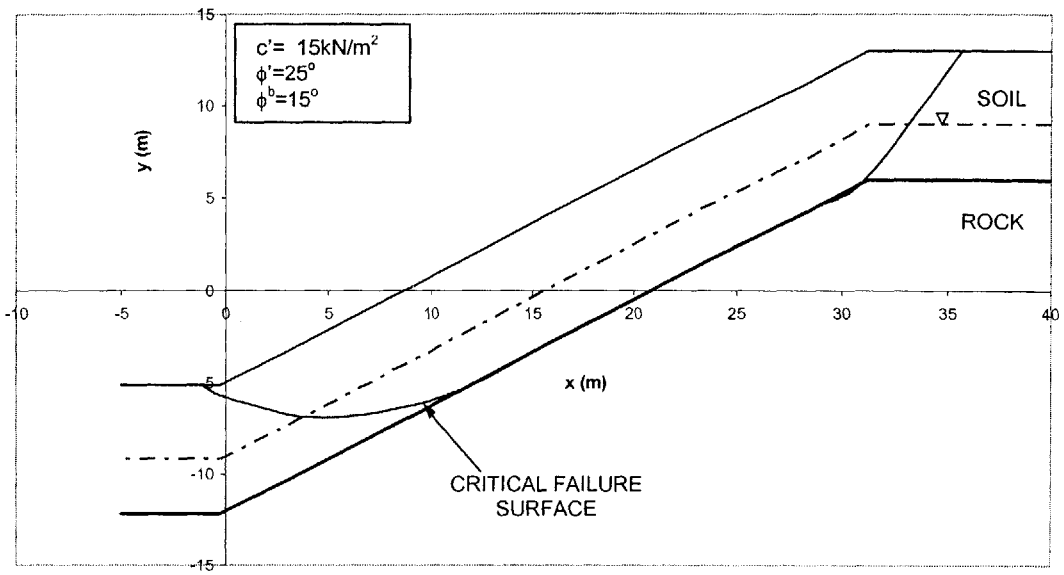

Figure 6.130. Critical Deterministic Failure Surface with Independent State Variable Model

A Factor of Safety of 1.15 is obtained on this surface, and this is the minimum Factor of Safety in the slope.

We now assume that the saturated soil strength parameters c' and ϕ' are uncertain, with mean values and standard deviations given by:

$c' \sim (m_{c'} = 15kN/m^2,\ \sigma_{c'} = 0.5kN/m^2)$; $\phi' \sim (m_{\phi'} = 25^o,\ \sigma_{\phi'} = 5^o)$; c' and ϕ' are assumed uncorrelated, and we assume the unsaturated soil parameter ϕ^b is deterministic.

The reliability index based on the deterministic surface shown in Figure 6.130 is computed to be 0.78.

A search for the critical reliability failure surface is performed, and the results are shown in Figure 6.131.

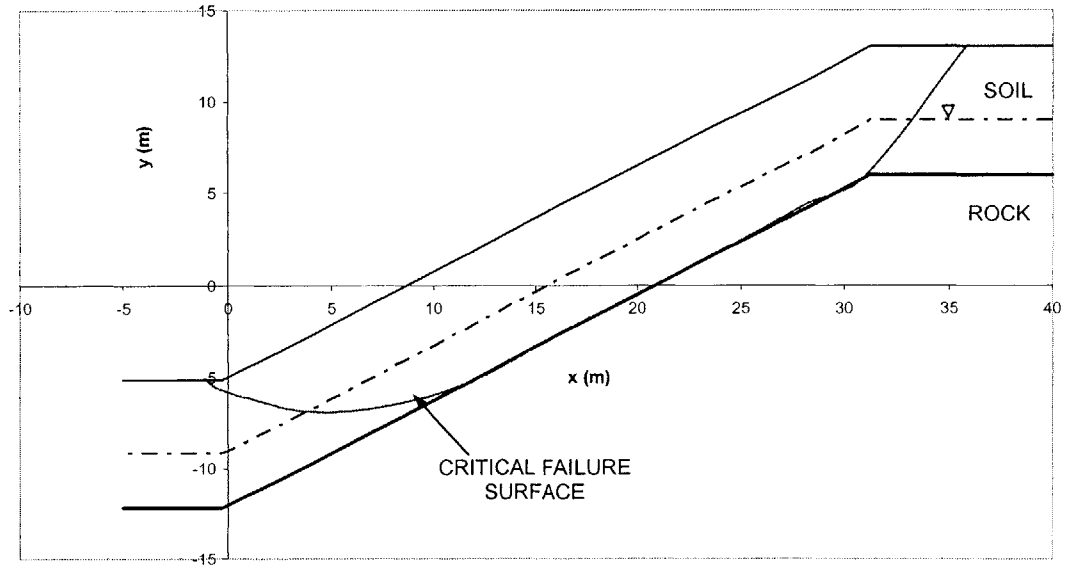

Figure 6.131. Critical Reliability Based Failure Surface with Independent State Variable Model

The Hasofer and Lind (1974) reliability index is computed to be $\beta = 0.74$ and the critical failure point is $c'^* = 12.8$ kN/m^2 and $\phi'^* = 22^o$. The reliability chart is shown in Figure 6.132.

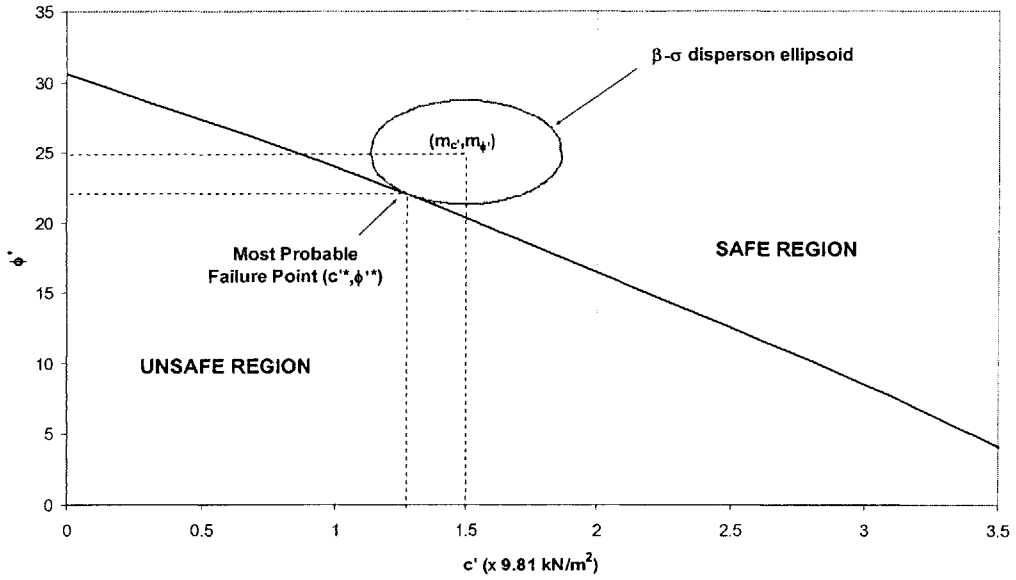

Figure 6.132. Reliability Chart Using Independent State Variable

$\beta = 0.74$ using the Independent State Variable Model is close in magnitude to the $\beta = 0.72$ when the Effective Stress Model was assumed. The greater value of β with the Independent State Variable Model than the Effective Stress Model suggests a more stable slope. This is in contradiction to the conclusion made based on the Factor of Safety alone, where in the case of the Effective Stress Model F = 1.18, and the slope is more stable than in the case when the Independent State Variable Model was used, and F = 1.15. This can be explained by examining parameter uncertainty, and the unsaturated soil strength models in both cases. In the Effective Stress Model, unsaturated strength is computed based on the effective stress parameters c' and ϕ', as:

$$\tau = c' + (\sigma - \chi u_w) \tan \phi' \qquad [6.39]$$

where:

χ is the effective stress parameter

In the Independent State Variable Model, unsaturated strength is computed based on the effective stress parameter c' and the parameter ϕ^b as:

$$\tau = c' + (\sigma - u_w) \tan \phi^b \qquad [6.40]$$

When the effective stress parameters c' and ϕ' are assumed uncertain, while all other parameters (particularly χ and ϕ^b) are deterministic, uncertainty in the shear strength, and hence in the Factor of Safety is greater in the Effective Stress Model (Equation [6.39]), compared to the Independent State Variable Model (Equation [6.40]). This results in a larger value of β when the Independent State Variable Model is adopted, because of the smaller uncertainty in the Factor of Safety (assuming the uncertainty in c' and ϕ' is the same in both models). In this example, the difference in the computed reliability indices is not very significant numerically ($\beta = 0.74$ using the Independent State Variable Model and $\beta = 0.72$ using the Effective Stress Model), but different nonetheless.

COULOMB MODEL

Reconsider the slope shown in Figure 6.133. We assume the Coulomb Model for soil strength in both saturated and unsaturated soil. We therefore assume the saturated or effective strength parameters of the soil in both the saturated and unsaturated zones of the soil. A Factor of Safety F=1.24 is computed in the slope.

We assume that the strength parameters are uncertain parameters c' and ϕ', with mean values and standard deviations:

$c' \sim (m_{c'} = 15 kN/m^2,\ \sigma_{c'} = 5 kN/m^2)$; $\phi' \sim (m_{\phi'} = 25^o,\ \sigma_{\phi'} = 5^o)$; and that c' and ϕ' are uncorrelated.

The critical reliability based failure surface in the slope is located and shown in Figure 6.133.

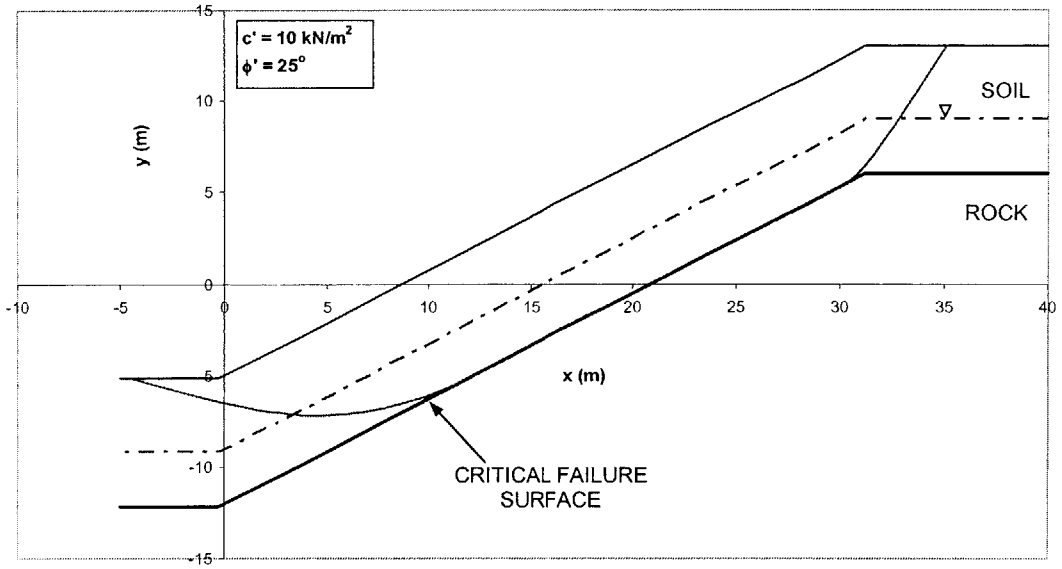

Figure 6.133. Critical Reliability Based Failure Surface with Coulomb Model

The reliability index $\beta = 1.03$ is computed and the critical failure point is $c'^* = 12\ kN/m^2$ and $\phi'^* = 20.7^o$. The reliability chart is shown in Figure 6.134.

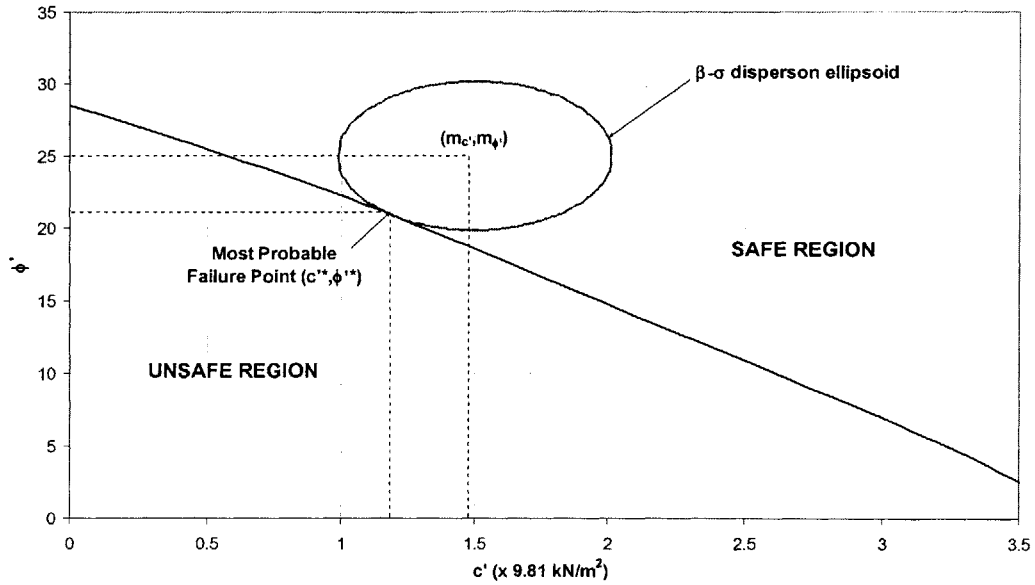

Figure 6.134. Reliability Chart Derived using Coulomb Model

The critical reliability failure surface, computed Hasofer and Lind (1974) reliability index, and the failure boundary are different in the case when the Coulomb Model is adopted for unsaturated strength, compared to when the Effective Stress, and Independent State Variables Models were used.

Adopting the Coulomb Model neglects the difference between saturated and unsaturated strength, leading to larger unsaturated strength, and hence a safer slope. This is reflected in the greater value of Factor of Safety (F=1.24 using the Coulomb Model compared to F=1.18 using the Effective Stress Model, and F=1.15 using the Independent State Variable Model) in deterministic analyses, and β in the reliability analyses ($\beta = 1.03$ using the Coulomb Model, compared to $\beta = 0.72$ using the Effective Stress Model and $\beta = 0.74$ using the Independent State Variable Model).

We therefore can conclude that the unsaturated strength model has an effect on both slope deterministic and reliability analyses. Table 6.35 summarizes the results of the analyses performed in this Section.

MODEL TO DESCRIBE UNSATURATED STRENGTH	DETERMINISTIC ANALYSES (FACTOR OF SAFETY)	RELIABILITY ANALYSES	
		β	$P_F = \Phi(-\beta)$
Coulomb Model	1.24	1.03	0.151
Effective Stress Model (Bishop, 1959)	1.18	0.72	0.236
Independent State Variable Model (Fredlund et al., 1978)	1.15	0.74	0.229

Table 6.35. Comparison of Results of Deterministic and Reliability Analyses Using Different Strength Models

Table 6.35 shows that the results of deterministic (Factor of Safety) and reliability (β and $P_F = \Phi(-\beta)$) analyses are affected by the model used to describe unsaturated strength.

In deterministic analyses, in addition to describing unsaturated strength differently, different unsaturated strength models lead to different critical deterministic failure surfaces, and different Factors of Safety.

In reliability analyses, in addition to describing unsaturated strength differently, different unsaturated strength models lead to different critical reliability based failure surfaces, and hence different failure boundaries and different reliability indices. This is reflected in Figure 6.135 which shows the effects of strength model uncertainty on the failure boundary, and reliability index.

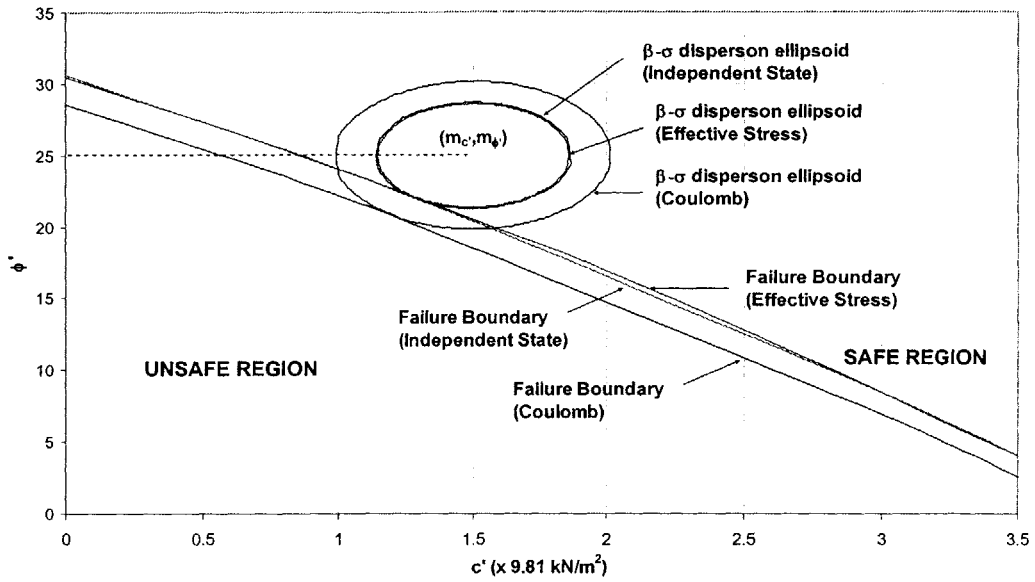

Figure 6.135. Comparison of Reliability Charts Derived Using Different Strength Models

Table 6.35 and Figure 6.135 show that there is a significant numerical difference in the results between the Effective Stress and Independent State Variable Models, and the Coulomb Model. Adopting either unsaturated strength model results in a less stable slope, with a smaller Factor of Safety, and larger probability of failure compared to the Coulomb Model.

The difference in the deterministic and reliability analyses (see Table 6.35, and Figure 6.135) using the Effective Stress Model, and the Independent State Variable Model is not very significant numerically in this example. There are two reasons for this:

(a) The slope geometry in this example (see Figure 6.133) is such that the critical failure surface lies, for the most part, below the water table in saturated soil, and hence unsaturated strength does not play a very significant role. This is not always the case as will be shown in a later Section (6-2.1.4.7).

(b) The specific value of the parameters that are assumed in both strength models (χ in the Effective Stress Model and ϕ^b in the Independent State Variable Model) are such that both models result in unsaturated strengths that are close in

magnitude at any given suction value. This again is not always the case as will be shown a later Section (6-2.1.4.7).

ADDITIONAL EXAMPLES

Since in the Independent State Variable Model, the net normal stress, $(\sigma - u_a)$ and suction, $(u_a - u_w)$ are considered independent stress state variables (see Figure 6.124), it is worth investigating the effects of uncertain ϕ^b on slope reliability analyses. For this purpose, we consider two additional examples that concern the slope shown in Figure 6.136.

In the first example the soil strength parameters, c', ϕ' and ϕ^b are assumed uncertain and uncorrelated. Specifically, we assume c', ϕ' and ϕ^b have mean values and standard deviations as:

$c' \sim (m_{c'} = 1.5 kN/m^2,\ \sigma_{c'} = 0.5 kN/m^2)$; $\phi' \sim (m_{\phi'} = 25^o,\ \sigma_{\phi'} = 5^o)$;

$\phi^b \sim (m_{\phi^b} = 15^o,\ \sigma_{\phi^b} = 5^o)$.

The critical reliability based failure surface is located, and shown in Figure 6.136.

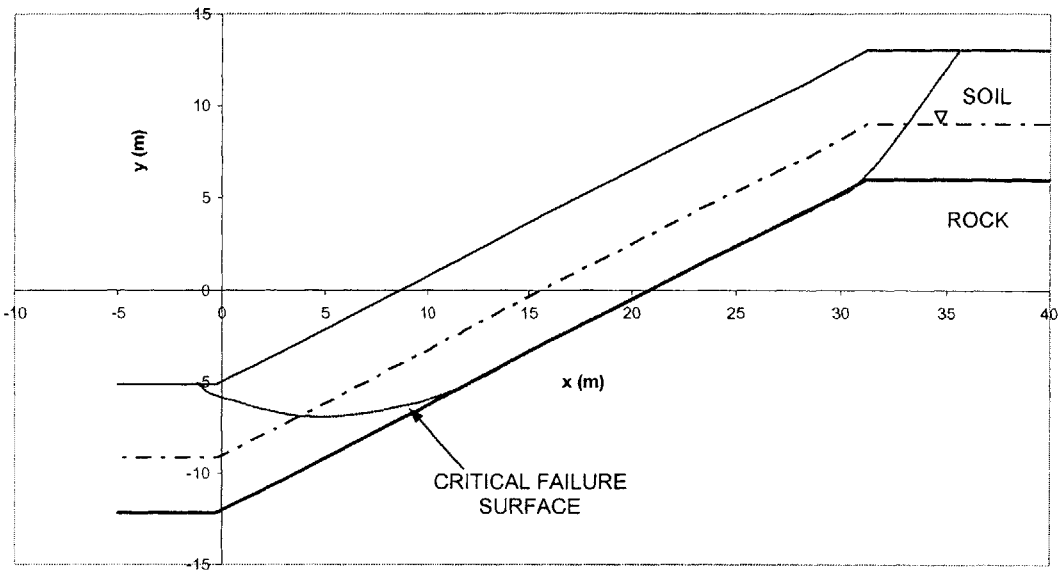

Figure **6.136.** Critical Reliability Based Failure Surface Using Independent State Variable Model with Uncertain Strength Parameters

The Hasofer and Lind (1974) reliability index is computed to be $\beta = 0.735$. The critical failure point is $c'^{*} = 12.8$ kN/m^2, $\phi'^{*} = 22^o$, and $\phi^{b*} = 14.8^o$. The reliability index when the parameter ϕ^b is assumed uncertain ($\beta = 0.735$), is slightly lower than in the case when ϕ^b is deterministic ($\beta = 0.74$). The lower value of β is because of the added uncertainty to the Factor of Safety when ϕ^b is assumed uncertain. The critical value of $\phi^{b*} = 14.8^o$ is close in magnitude to the mean value, and so it doesn't affect the value of β significantly. This is because of the particular site conditions in this example, where the critical failure surface lies, for the most part, in saturated soil as is shown in Figure 6.136.

Had the critical surface been in unsaturated soil, the effects of uncertain ϕ^b on β would have been greater.

We now introduce correlation between the strength parameters. Clayey soils, typically exhibit high values of cohesion c' and low values of angle of shear resistance ϕ'. These types of soil also typically exhibit high unsaturated strengths because of the ability to

sustain high values of suction given their pore size (grain size) distribution. Sandy soils, on the other hand, typically exhibit high values of angle of shear resistance and lower values of cohesion. These types of soil, usually exhibit low unsaturated strength because they sustain large suction values because if the larger pore (and grain) size distribution. With this in mind, c' and ϕ^b are assumed to be slightly positively correlated, and ϕ' and ϕ^b are assumed to be negatively correlated.

With the vector of strength parameters as $\begin{bmatrix} c' \\ \phi' \\ \phi^b \end{bmatrix}$, the correlation matrix is taken to be:

$$\underline{\Gamma} = \begin{bmatrix} 1 & -0.25 & 0.1 \\ -0.25 & 1 & -0.1 \\ 0.1 & -0.1 & 1 \end{bmatrix}$$

The chosen values of correlation coefficient in $\underline{\Gamma}$ assume negative correlation is assumed between c' and ϕ^b, and positive correlation is assumed between ϕ' and ϕ^b.

The Hasofer and Lind (1974) reliability index is computed to be $\beta = 0.84$. This value of $\beta = 0.84$ is greater than the value of $\beta = 0.735$. We therefore conclude that the inclusion of (realistic) correlation between the soil strength parameters, saturated and unsaturated, has the effect of increasing β, and hence slope reliability compared to when no correlation is assumed.

6-2.1.4.4. STRENGTH SUBMODEL UNCERTAINTY IN PROBABILISTIC SLOPE STABILITY ANALYSES

In this Section, we briefly investigate the effects of strength model uncertainty on probabilistic slope stability analyses. We consider the slope shown in Figure 6.137.

This slope was used in the reliability analyses performed in the previous Section 6-2.1.4.5. The Effective Stress Model is first used for unsaturated strength, and the results

are compared to those obtained using the Independent State Variable Model for two cases, where in the first, the parameter ϕ^b is assumed deterministic, and in the second ϕ^b is assumed uncertain.

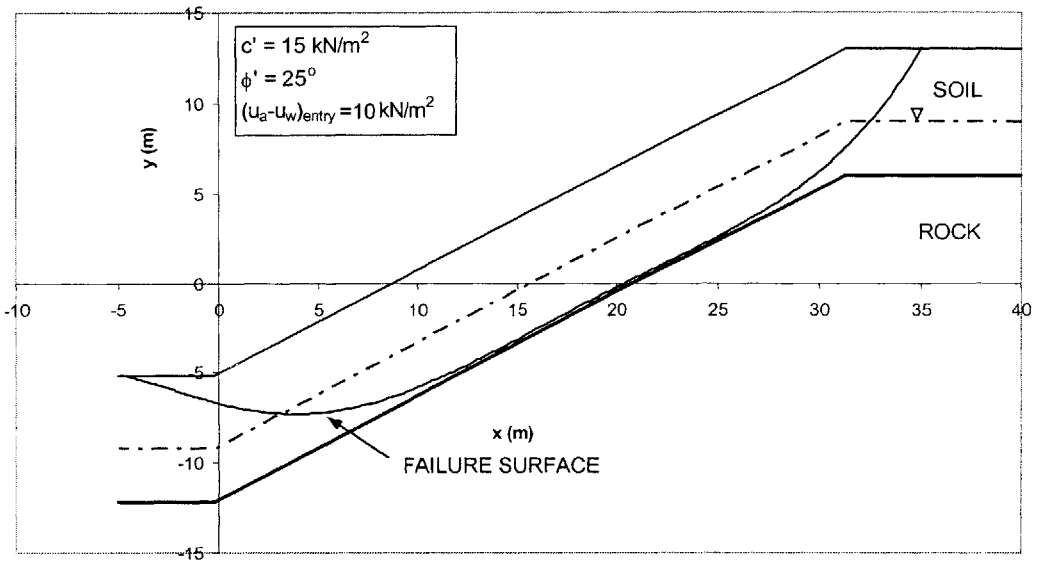

Figure 6.137. Slope Geometry and Strength Parameters

Figure 6.138 compares the distribution of Factor of Safety when the Independent State Variable Model with deterministic $\phi^b = 15^o$ is used with that when the Effective Stress Model with $(u_a - u_w)_{entry} = 10kPa$ is used. In both cases the uncertain parameters are the effective strength parameters c' and ϕ'. The parameters of both models have been purposely chosen to give similar results so that the effects of model uncertainty (as opposed to parameter uncertainty) can be better investigated.

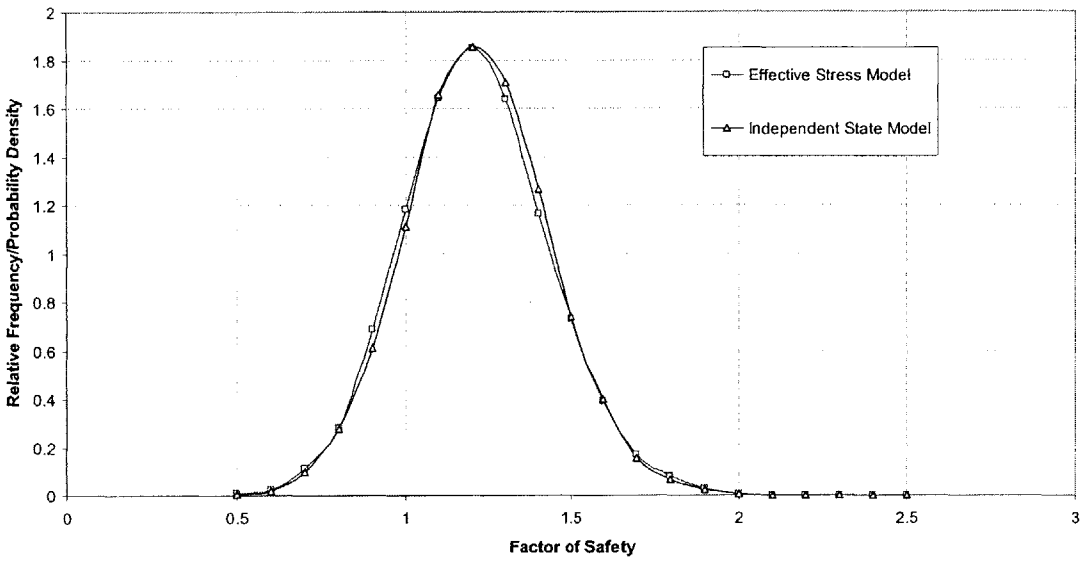

Figure 6.138. Comparison of Distribution of Factor of Safety Using the Effective Stress and Independent State Variable Models (Effective Strength Parameters Uncertain)

The expected value of the Factor of Safety when the Independent State Variable Model is used is E[F] = 1.17 compared to E[F] = 1.18 when the Effective Stress Model is used, and the standard deviation is $\sigma_F = 0.21$ compared to $\sigma_F = 0.22$. The probability of failure is $P_F = 0.212$ compared to $P_F = 0.233$. Figure 6.138 shows that the shape of the distribution of the Factor of Safety is not affected by the strength model used. The expected value and standard deviation, however, are. When the Independent State Variable Model with constant $\phi^b = 15^o$ is used, there is a slight reduction in the standard deviation. The reason for this was explained in Section 6-2.1.4.5. This, coupled with the lower expected value leads to a smaller probability of failure when the Independent State Variable Model is used compared to the Effective Stress Model. The difference in the results between both models is not very significant numerically. The reasons for this were particular to this example, and discussed in Section 6-2.1.4.5, and are mainly due to the geometry of the slope, and the particular values of χ and ϕ^b.

Figure 6.139 compares the results of probabilistic analyses when the Independent State Variable Model with uncertain ϕ^b is used. ϕ^b is assumed to be Normally distributed as $\phi^b \sim N(m_{\phi^b} = 15^o, \sigma_{\phi^b} = 5^o)$.

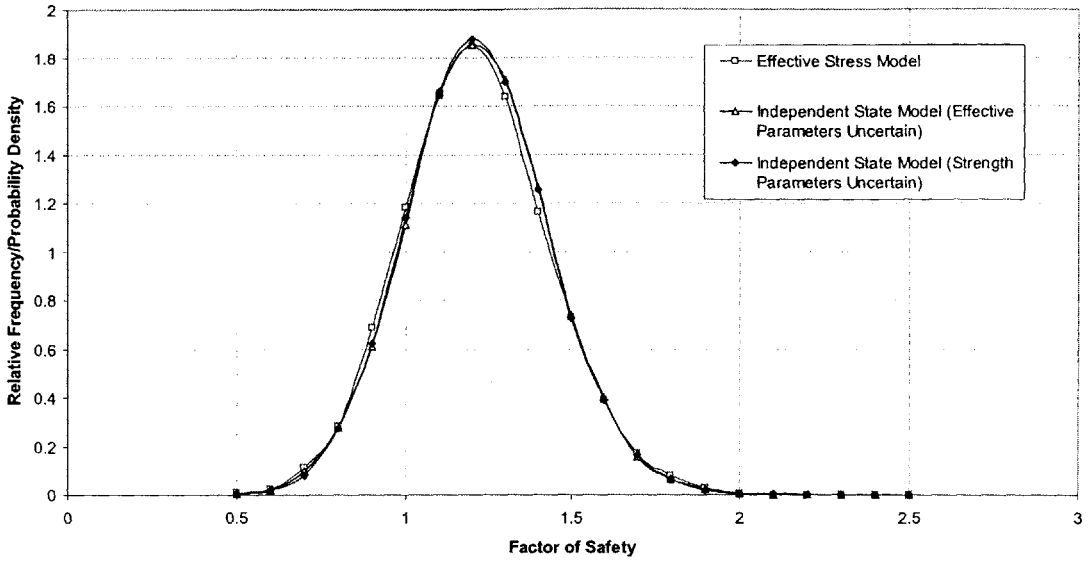

Figure **6.139.** Comparison of Distribution of Factor of Safety Using the Effective Stress and Independent State Variable Models (Effective Strength and ϕ^b Parameters Uncertain)

The expected value of the Factor of Safety is E[F] = 1.17, and the standard deviation is $\sigma_F = 0.215$. The probability of failure is $P_F = 0.215$. Including uncertainty in ϕ^b has the effect of increasing the uncertainty in the Factor of Safety ($\sigma_F = 0.215$ compared to $\sigma_F = 0.21$) and hence increasing the probability of failure ($P_F = 0.215$ compared to $P_F = 0.212$). This was also discussed in Section 6-2.1.4.5.

The results of the probabilistic analyses are in good agreement with those from reliability analyses in Section 6-2.1.4.5. This is because of the shape of the distribution of Factor of Safety in Figures 6.138 and 6.139, which can be well approximated by the Normal distribution. Therefore the estimation of the probability of failure using $P_F = \Phi(-\beta)$ in reliability analyses is accurate.

The results in this Section show that although strength model uncertainty affects the results of probabilistic analyses, the effects are not very significant numerically. This is because of the location of the failure surface in the slope in Figure 6.137, specifically that it lies mostly in saturated soil, where strength is described by the Coulomb Model. These effects would have been much more prominent if the failure surface was in unsaturated soil, as we will show in the following Section.

6-2.1.4.5. STRENGTH SUBMODEL UNCERTAINTY IN LANDSLIDE HAZARDS ASSESSMENTS

The effects of strength model uncertainty on landslide hazards are assessed. Two numerical examples are considered. In the first, the rainfall intensity is lower than the saturated conductivity of the soil, and the initial suction is reduced by infiltrating rain. In the second, the rainfall intensity is greater than the saturated conductivity of the soil, allowing for positive pressures to develop. The Effective Stress and Independent State Variable Models are used for unsaturated strength with different parameters in each model.

LANDSLIDE HAZARDS WITH RAINFALL INTENSITY LESS THAN SATURATED CONDUCTIVITY

This example considers the slope shown in Figure 6.140.

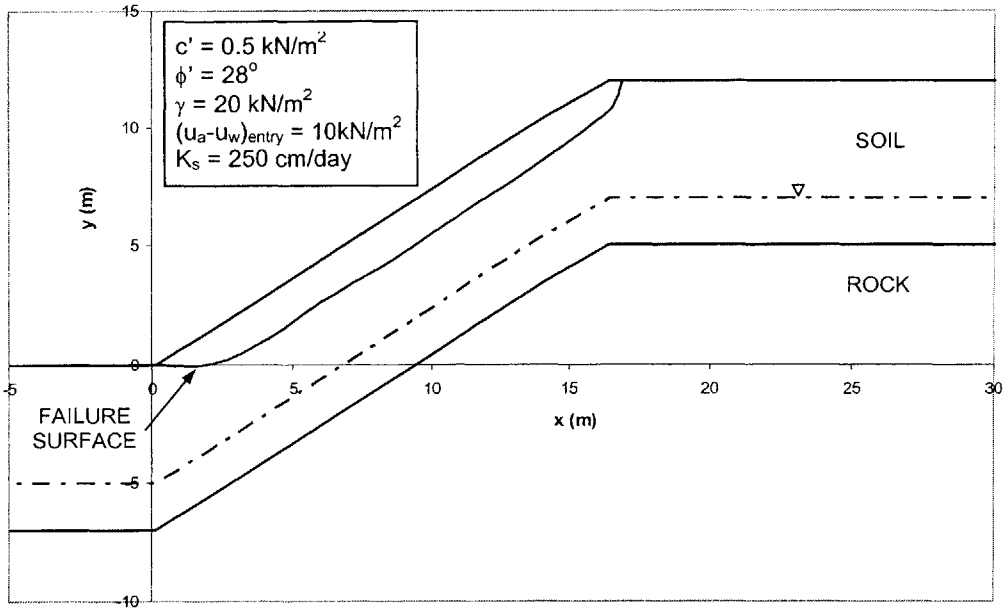

Figure 6.140. Slope Geometric and Strength Parameters

We assume a rainfall event with intensity, $I = 75mm/hr$ occurs for a duration of 8 hours. Figure 6.141 shows moisture profiles, and Figure 6.142 shows pressure profiles at selected times.

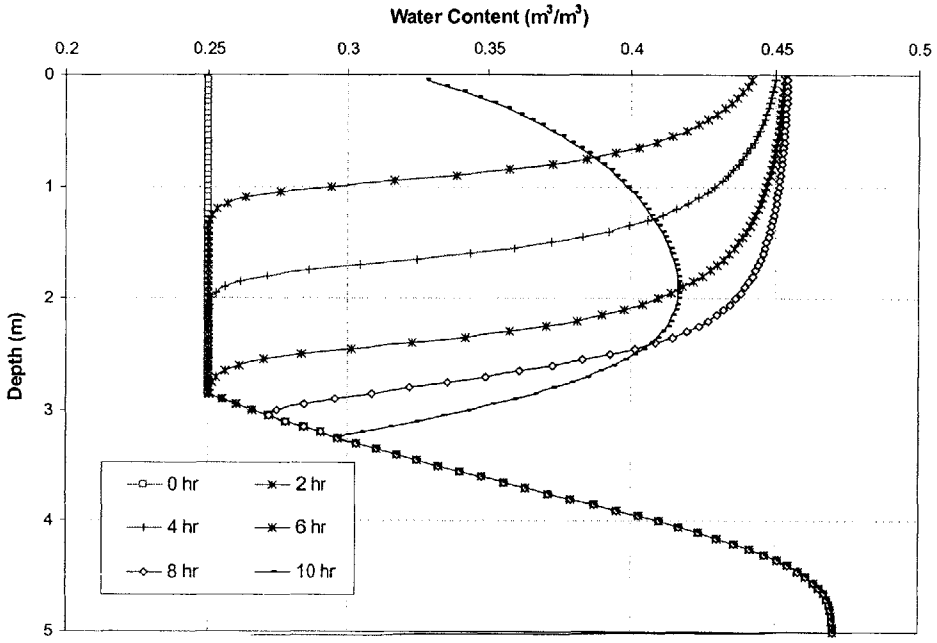

Figure 6.141. Moisture Content Profiles with Time using the van Genuchten (1980) Model

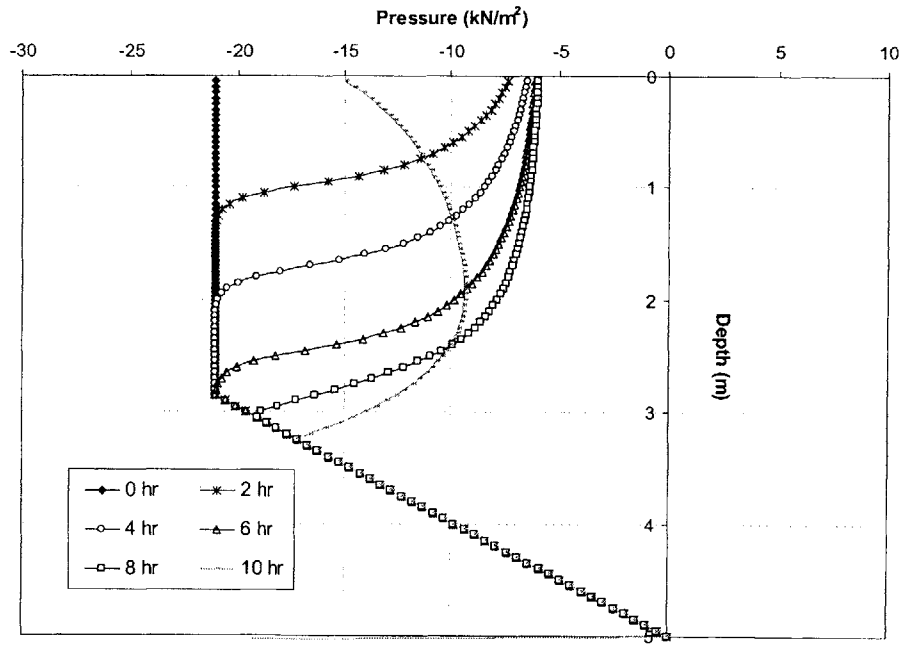

Figure 6.142. Pressure Profiles with Time using the van Genuchten (1980) Model

The variation of Factor of Safety with time is computed using the Effective Stress Model for unsaturated strength, with different values of the air entry pressure $(u_a - u_w)_{entry}$. The results are shown in Figure 6.143.

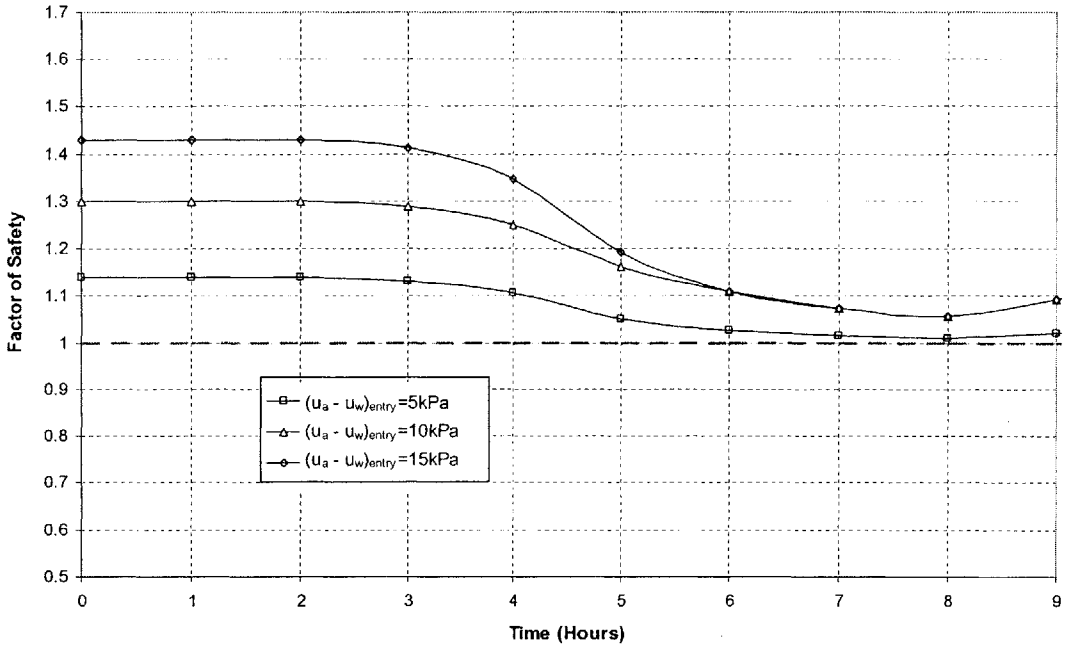

Figure **6.143.** Variation of Factor of Safety with Time Using the Effective Stress Model with Different Parameters

Figure 6.143 shows the effects of assuming different values of the air entry pressure $(u_a - u_w)_{entry}$ on the Factors of Safety. There is a significant difference in the results at early times during the rain event, because the soil on the failure surface is unsaturated, with high values of suction. As a result, the parameter $\chi = \left[\frac{(u_a - u_w)}{(u_a - u_w)_{entry}}\right]^{-0.55}$ is significantly different for different values of $(u_a - u_w)_{entry}$. This leads to a large difference in unsaturated strength, and Factors of Safety.

With time, and increasing depth of rainwater infiltration, the moisture content increases in the soil along the failure surface, leading to a reduction in suction (see Figure 6.142).

As this takes place, the parameter $\chi = \left[\frac{(u_a - u_w)}{(u_a - u_w)_{entry}}\right]^{-0.55}$ increases and tends towards the saturated value of $\chi = 1$, causing a reduction in strength and Factor of Safety. The relationship between strength and suction is non-linear, as presented in Equation [6.35]. At times t > 6 hours, the rainwater has increased the moisture content on the failure surface sufficiently so that the suction is less than the air entry value $(u_a - u_w)_{entry}$ for both cases when $(u_a - u_w)_{entry} = 10kPa$ and $(u_a - u_w)_{entry} = 15kPa$. Because of this, the parameter χ takes on a value of $\chi = 1$ in both these cases, and as a result strength is defined by the saturated strength Coulomb Model. This is the reason for the two Factor of Safety curves in Figure 6.143 leading to identical results in both cases for times t > 6 hours. This is not the case, however, when $(u_a - u_w)_{entry} = 5kPa$, since the soil remains at moisture content less than the saturated value (see Figure 6.141). As a result the Factor of Safety is lower in this case for times t > 6 hours, as shown in Figure 6.143. Figure 6.143 also illustrates parameter model uncertainty since different values of the air entry pressure are used in the Effective Stress Model. The effects of parameter uncertainty are highlighted in Figure 6.143, which shows significantly different results depending on the chosen value of air entry suction.

The variation of Factor of Safety with time is then determined using the Independent State Variable Model for unsaturated strength for different and constant values of ϕ^b. The results are shown in Figure 6.144.

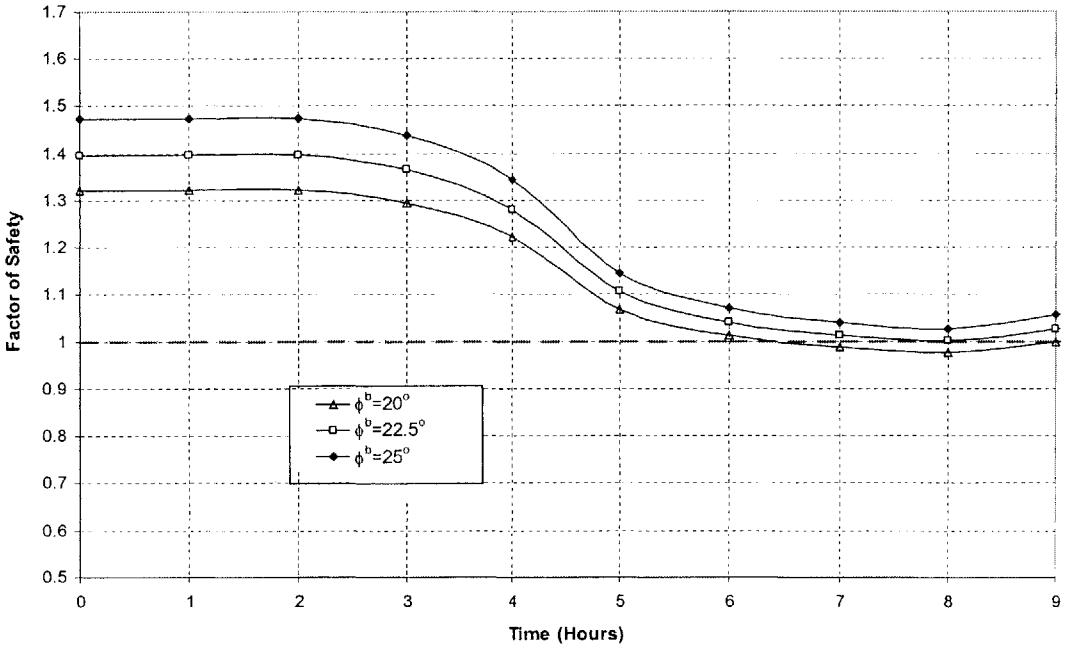

Figure **6.144.** Variation of Factor of Safety with Time Using the Independent State Variable Model with Different Parameters

Figure 6. 441 shows that different results are obtained for the different values of ϕ^b. The difference is greatest at early times during the rain event, when the soil is unsaturated, and its strength is defined by the unsaturated strength model in Equation [6.30]. As time passes and the moisture content (and pressures) in the soil on the failure surface increases (see Figures 6.141 and 6.142), unsaturated strength is reduced, and this is observed in the reduction of Factor of Safety with time. Figure 6.144 shows that the Factor of Safety for lower values of ϕ^b is smaller than for larger values of ϕ^b at any time during rain. This is because in the Independent State Variable Model unsaturated strength is proportional to the parameter ϕ^b. Figure 6.144 also illustrates parameter uncertainty since different values of ϕ^b are used in the unsaturated strength model. Figure 6.144 shows the importance of parameter uncertainty since different conclusions on stability are reached depending on the chosen value of ϕ^b.

In the Independent State Variable Model, unsaturated strength is a linear function of the parameter ϕ^b if ϕ^b is constant, and this is reflected in Figure 6.144. Figure 6.144 shows that the difference in Factor of Safety at any time is the same between when $\phi^b = 20^o$ and $\phi^b = 22.5^o$ and when $\phi^b = 22.5^o$ and $\phi^b = 25^o$. This is to say that the difference in Factor of Safety at any time between any two values of ϕ^b, is a linear function of the difference in the values of ϕ^b. This is not the case for the Effective Stress Model, and as shown in Figure 6.143. The strength relationship is non-linear and this is evident in Figure 6.143.

Figure 6.145 compares the variation of the Factor of Safety with time for both strength models with different parameters. The intent here is to show the wide range of results, and not for showing specific values.

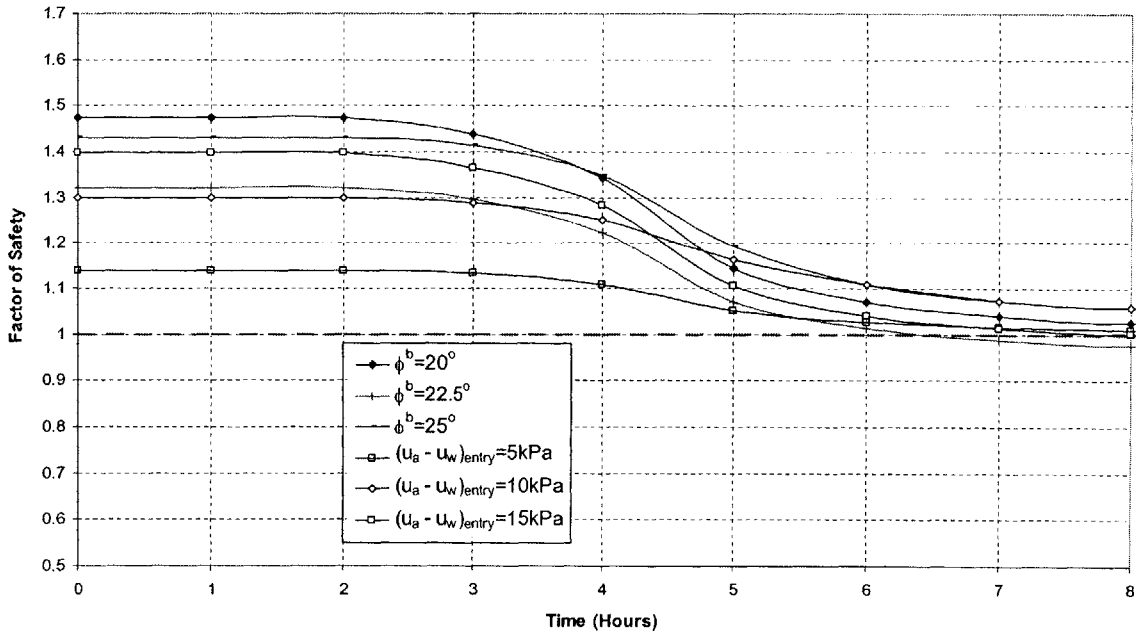

Figure **6.145.** Comparison of Variation of Factor of Safety with Time Using Different Strength Models with Different Parameters

Figure 6.145 illustrates the effects of strength model uncertainty on stability analyses, and deterministic landslide hazard assessments. These effects can be very significant, and lead to different conclusions with regard to stability of the slope during the rain event (failure vs. no failure).

We now assume that the soil strength parameters and saturated conductivity are uncertain, and follow the distributions:

$c' \sim N(m_{c'} = 0.5kN/m^2,\ \sigma_{c'} = 0.125N/m^2)$; $\phi' \sim N\phi' \sim (m_{\phi'} = 28^o,\ \sigma_{\phi'} = 7^o)$;

$K_s \sim LN(\ m_{K_s} = 250cm/day, \sigma^2_{K_s} = (125cm/day)^2)$; and these parameters are uncorrelated.

Monte Carlo techniques are used to estimate the probability of slope failure from generated distributions of the Factor of Safety at different times. This is done using both unsaturated strength models, with different parameters. Figure 6.146 shows the probability of failure with time when the Effective Stress Model is used for strength.

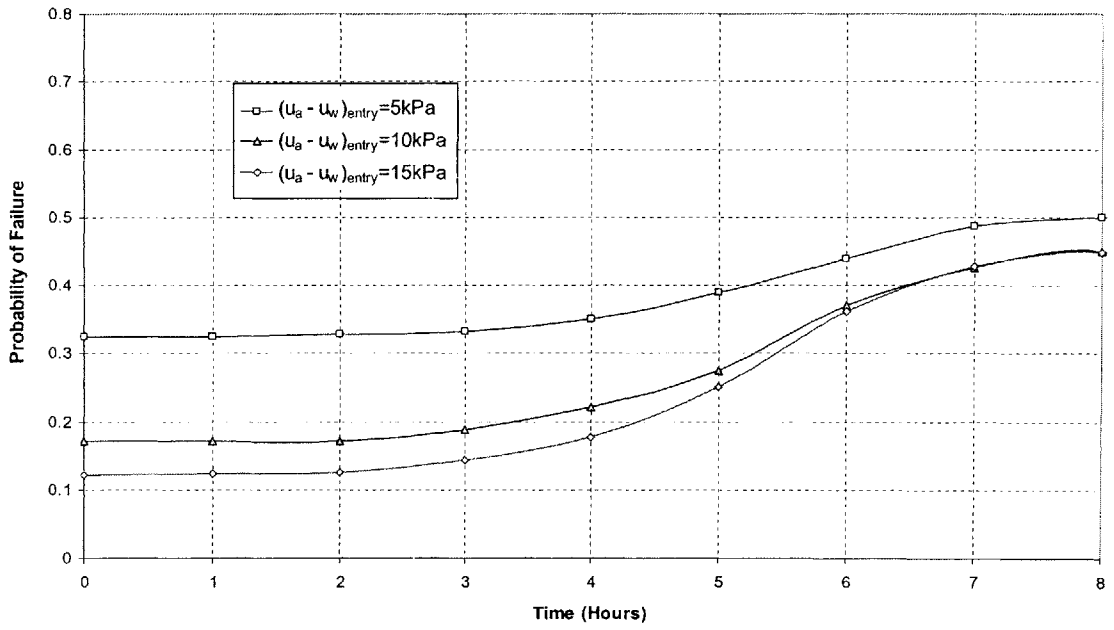

Figure **6.146.** Variation of Failure Probability with Time Using the Effective Stress Model with Different Parameters

Figure 6.146 clearly shows the effects of assuming different parameter values for $(u_a - u_w)_{entry}$ on landslide hazards, and hence illustrates parameter uncertainty using the Effective Stress Model. As in the deterministic case, the difference in the results is greatest at early times, when the suction in the soil on the failure surface is large.

The variation of probability of failure with time is then estimated using the Independent State Variable Model for unsaturated strength, and the results are shown in Figure 6.147.

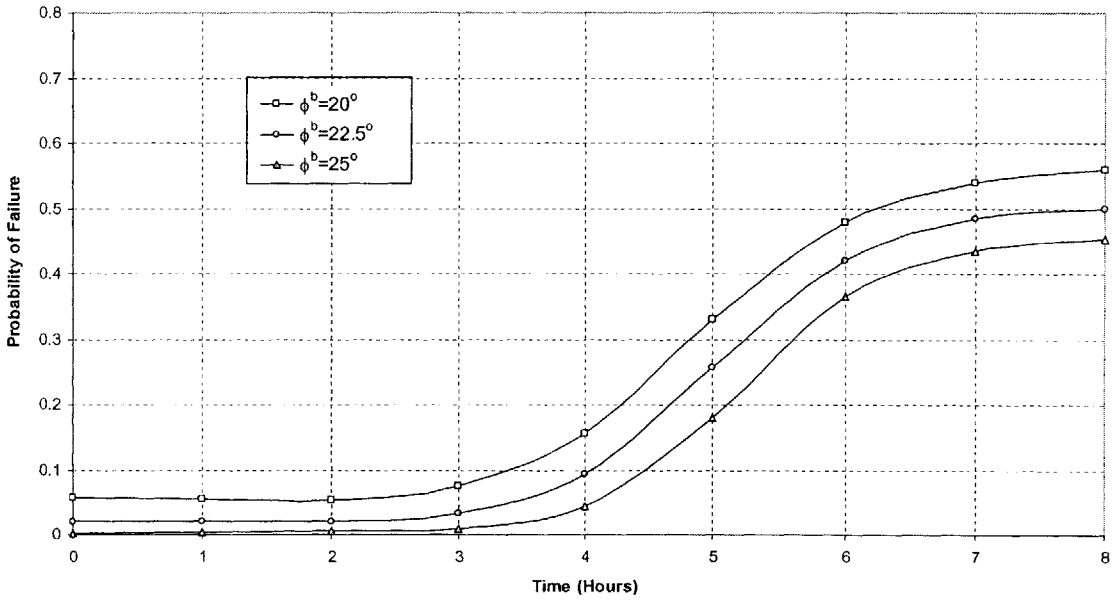

Figure **6.147.** Variation of Failure Probability with Time Using the Independent State Variable Model with Different Parameters

Figure 6.147 shows the influence of parameters uncertainty on landslide hazards, and illustrates parameter uncertainty using the Independent State Variable Model for strength.

Figure 6.148 shows the variation of probability of failure with time for the different strength models, with the different parameters. Again, the intent in Figure 6.148 is to show the large difference in the results rather than specific values.

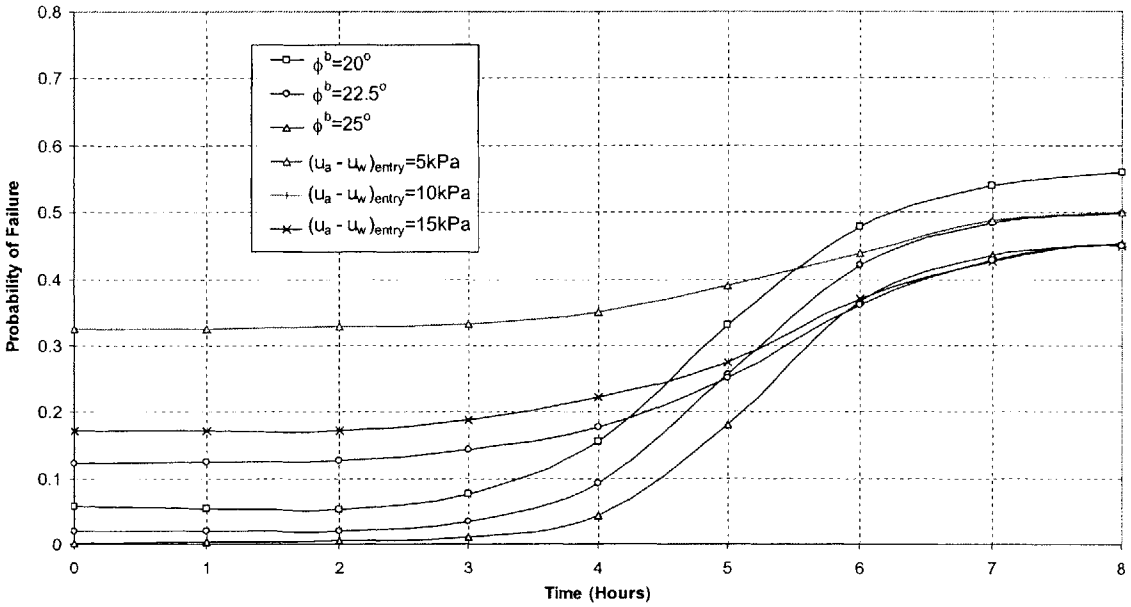

Figure **6.148.** Comparison of Variation of Failure Probability with Time Using Different Strength Models with Different Parameters

Figure 6.148 shows that significantly different results are obtained by using the different strength models. It highlights the effects of strength model uncertainty on landslide hazards, which clearly can be very important.

LANDSLIDE HAZARDS WITH RAINFALL INTENSITY GREATER THAN SATURATED CONDUCTIVITY

In this example, we consider the slope shown in Figure 6.149.

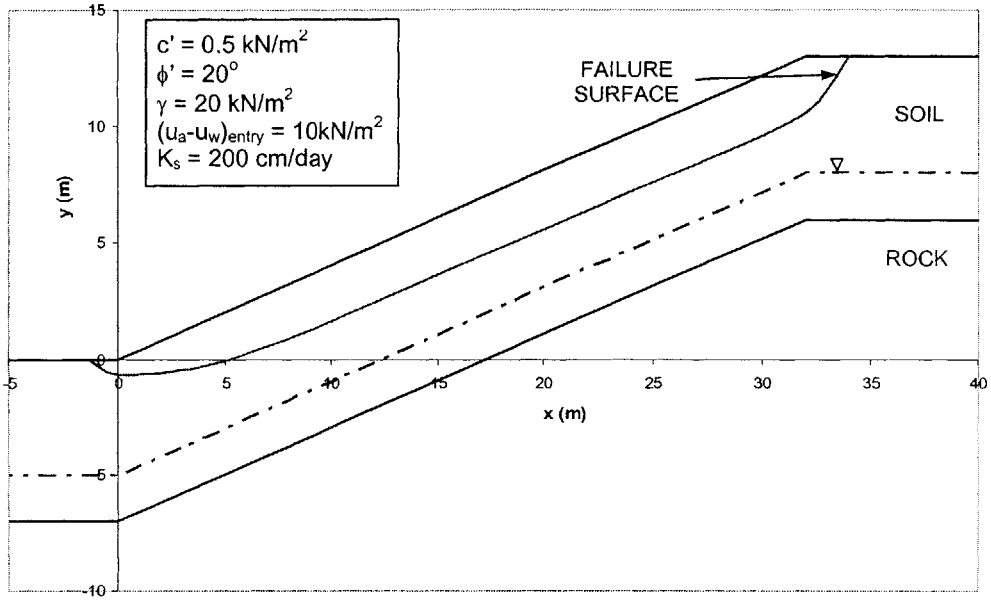

Figure 6.149. Slope Properties and Failure Surface

We assume a rainfall event of intensity $I = 375\text{cm/day} = 155\text{mm/hr}$ to occur for a duration of 8 hours. Since the intensity of the rain is greater than the saturated conductivity of the soil, the rain fully saturates the soil, and allows for pore pressures to develop. Figure 6.150 shows moisture profiles, and Figure 6.151 shows pressure profiles at selected times.

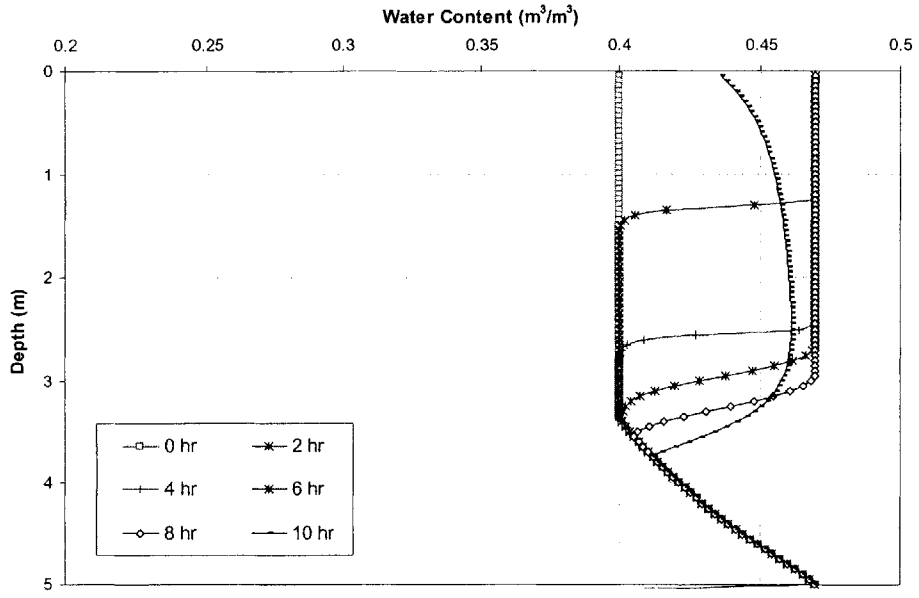

Figure 6.150. Moisture Content Profiles with Time using the van Genuchten (1980) Model

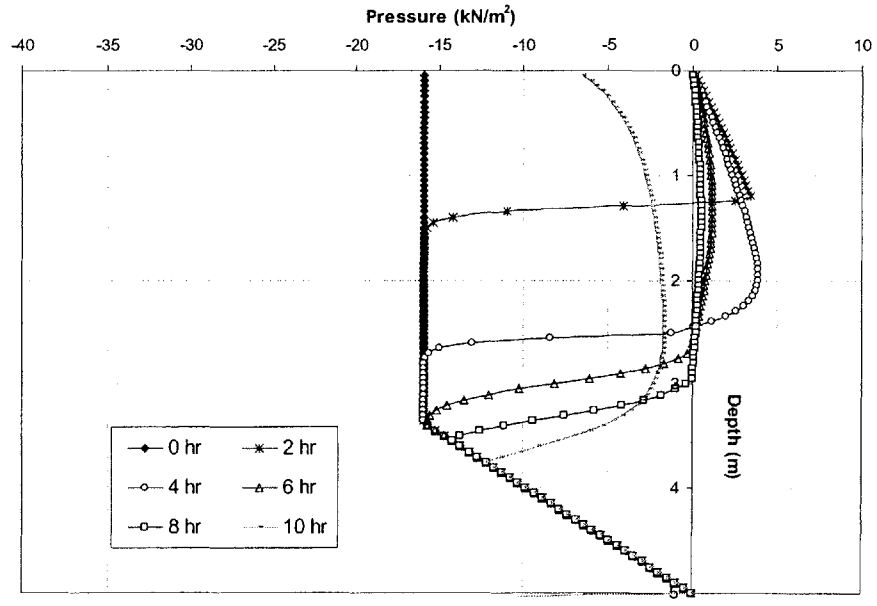

Figure 6.151. Pressure Profiles with Time using the van Genuchten (1980) Model

We asses the stability of the slope deterministically using the Effective Stress Model with different values of the air entry suction $(u_a - u_w)_{entry}$ and the results are shown in Figure 6.152.

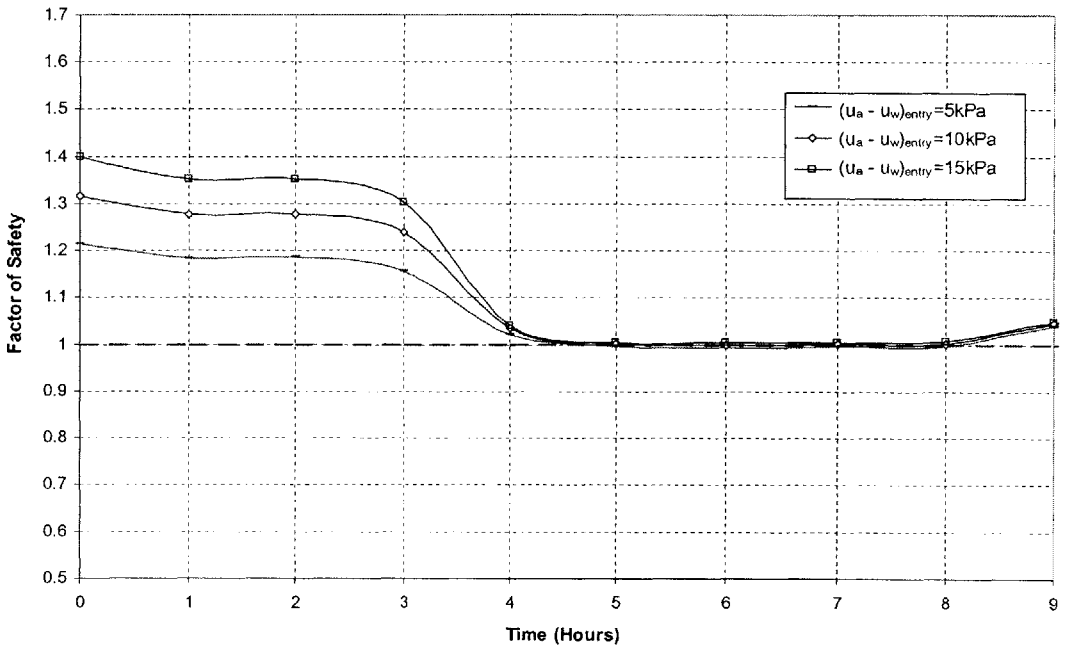

Figure **6.152.** Variation of Factor of Safety with Time Using Effective Stress Model with Different Parameters

Figure 6.152 shows the effects of different $(u_a - u_w)_{entry}$ values, on the results and so illustrates parameter model uncertainty using the Effective Stress Model. The difference is greatest at early times during rain. This is when the soil at the failure surface is unsaturated, and strength is descried by the Effective Stress Model. At times t > 4 hours, the rainwater has penetrated deep enough to fully saturate the soil on the failure surface (see Figures 6.150 and 6.151). $\chi = 1$ and the soil strength is described by the Coulomb Model. As a consequence, the results are the same for all values of $(u_a - u_w)_{entry}$ considered as shown in Figure 6.152.

Figure 6.153 shows the results of deterministic analyses when the Independent State Variable Model is used for unsaturated strength.

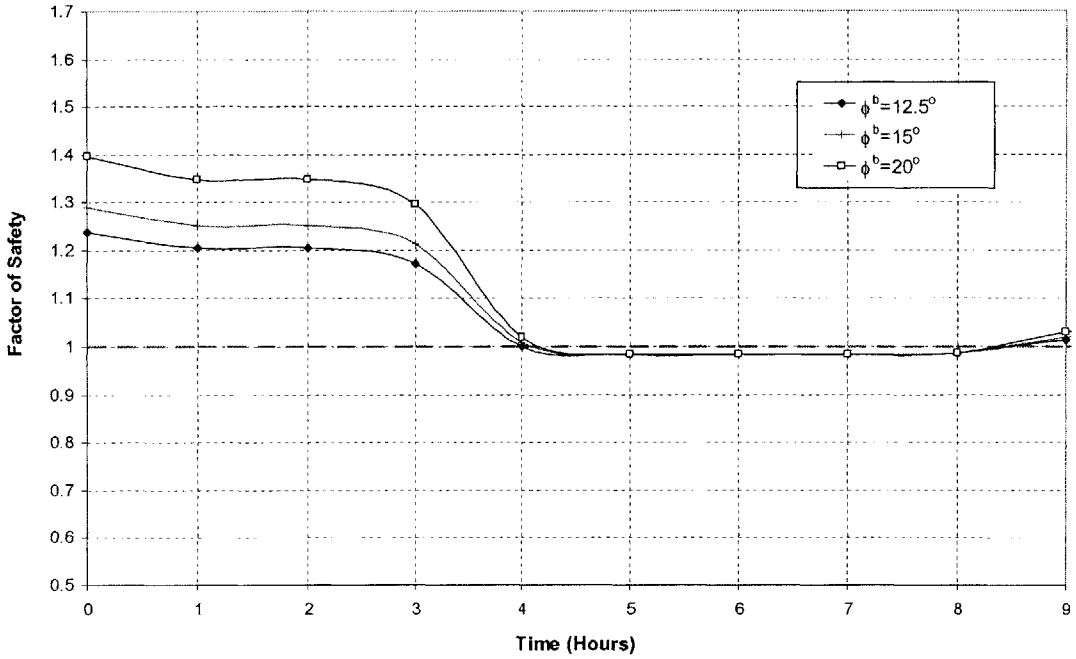

Figure **6.153.** Variation of Factor of Safety with Time Using Independent State Variable Model with Different Parameters

Figure 6.153 illustrates parameter model uncertainty by showing that the variation of Factor of Safety depends on the value of ϕ^b, and different values can lead to different results. The effects of different ϕ^b are greatest at early times. As it continues to rain, and the rainwater saturates the soil, the results converge as shown in Figure 6.153, since soils strength is described by the Coulomb Model.

Figure 6.154 compares the results from using both unsaturated strength models with the different parameters.

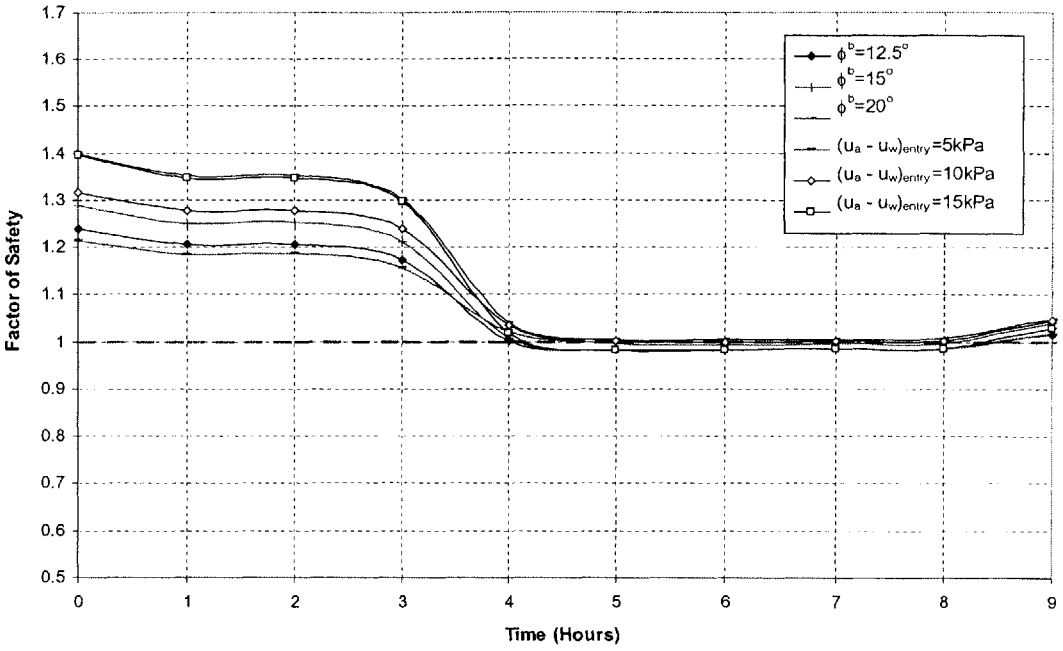

Figure **6.154.** Comparison of Variation of Factor of Safety with Time Using Different Strength Models with Different Parameters

Figure 6.154 shows that different results are obtained using the different strength models, and shows the effects of strength model uncertainty on deterministic landslide hazard assessments. There is a clear difference in the results, particularly at early times during rain, when the soil is still unsaturated. With time, and as the soil gets saturated, the difference in the results becomes not very significant numerically. Having said this, the difference is important because it leads to different conclusions regarding stability.

We now assume that the soil strength and hydraulic parameters are uncertain with the following distributions:

$c' \sim N(m_{c'} = 0.5kN/m^2,\ \sigma_{c'} = 0.017kN/m^2);\ \phi' \sim N\phi' \sim (m_{\phi'} = 20^o,\ \sigma_{\phi'} = 6.67^o);$

$K_s \sim LN(m_{K_s} = 200cm/day, \sigma^2_{K_s} = (100cm/day)^2)$; and these parameters are uncorrelated.

Figure 6.155 shows the probability of failure with time using the Independent State Variable Model with different parameter values, and Figure 6.156 shows the probability of failure with time using the Effective Stress Model with different parameters.

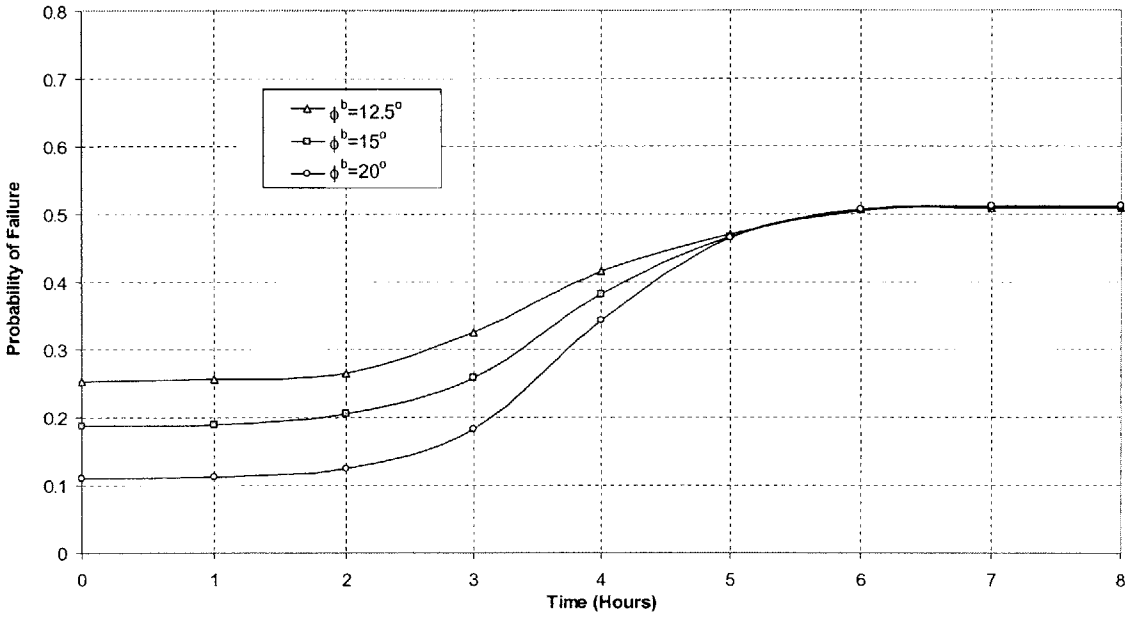

Figure **6.155.** Variation of Failure Probability with Time Using the Independent State Variable Model with Different Parameters

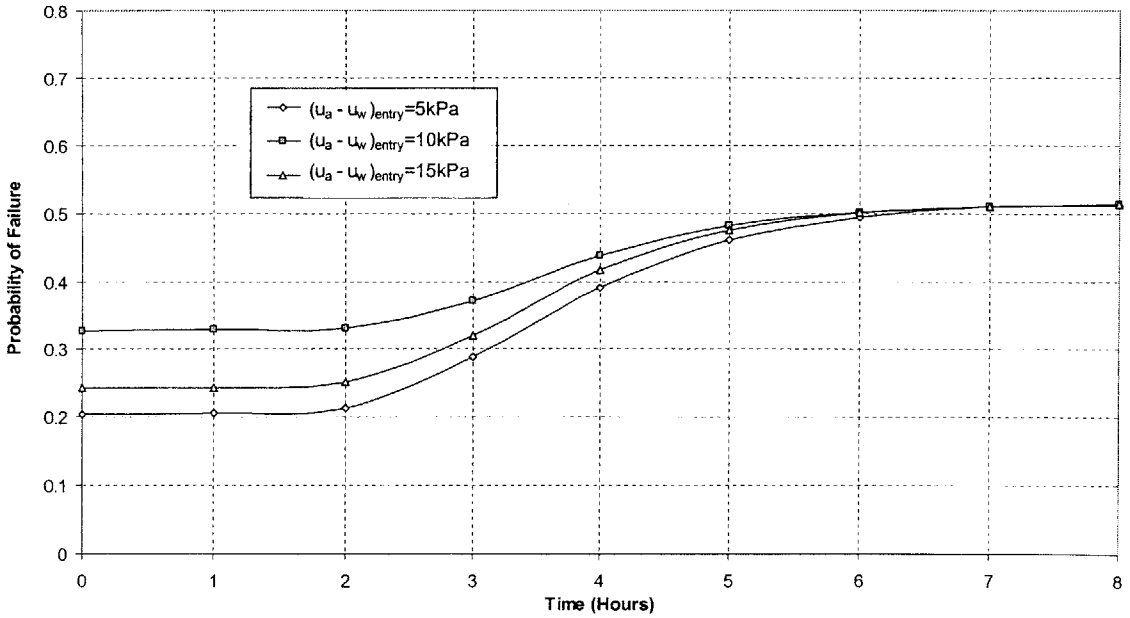

Figure **6.156.** Variation of Failure Probability with Time Using Effective Stress Model with Different Parameters

Figure 6.157 compares the variation of probability of failure with time when the Effective Stress and Independent State Models are used for unsaturated strength for select parameter values.

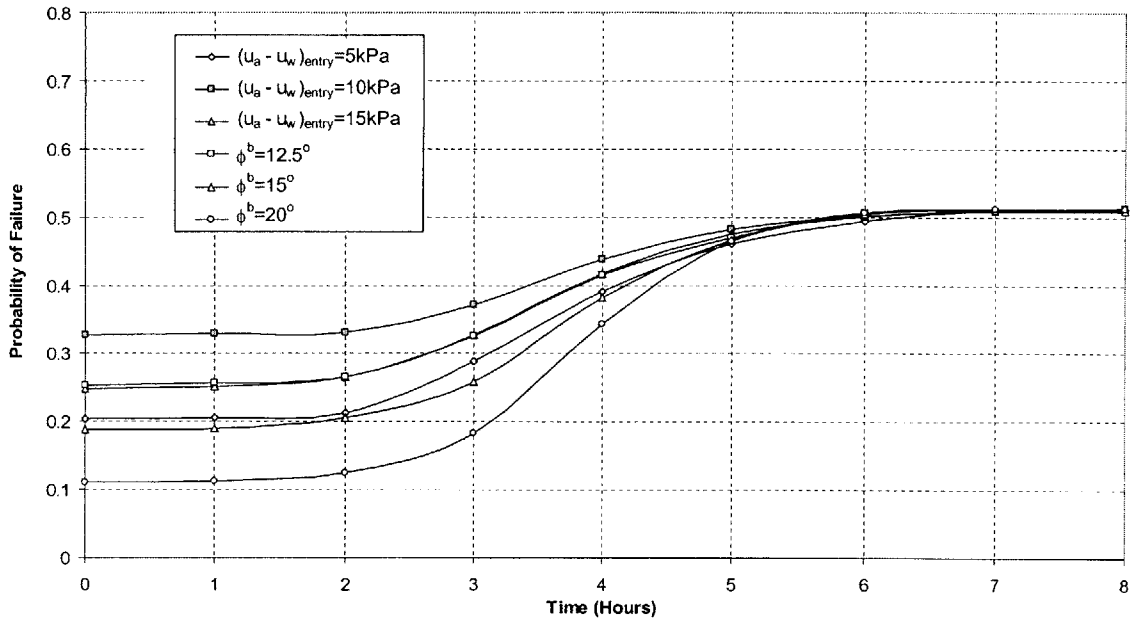

Figure **6.157.** Comparison of Variation of Failure Probability with Time Using Different Strength Models with Different Parameters

Figure 6.157 illustrates the effects of strength model uncertainty on landslide hazards. The effects of are greatest at early times during the rain event, and become less significant with time, as the rainwater fully saturates the soil on the failure surface. As this happens soil strength is described by the Coulomb Model in all cases.

6-2.1.4.6. CONCLUSIONS ON STRENGTH SUBMODEL UNCERTAINTY

In this Section, (unsaturated) strength model uncertainty was investigated in the context of deterministic and reliability based slope stability analyses, as well as the effects on landslide hazards, both deterministically and probabilistically.

We showed that the extent to which (unsaturated) strength model uncertainty affects the results depends, not surprisingly, on the location of the failure surface relative to the

water table. When the failure surface lies in saturated soil, the effects are not very significant, but when the failure surface lies in unsaturated soil, the effects are considerable.

Since shallow landslides have failure surfaces that typically lie in unsaturated soil, where changes in moisture (and suction) are important (see Chapter 3), unsaturated strength model uncertainty is particularly relevant, and significantly affects the results of landslide hazards assessments, whether these are deterministic or probabilistic.

6-2.2. MODEL UNCERTAINTY FROM STABILITY MODELS

In this Section, the effects of using different stability models for slope stability and reliability are investigated. The aim is to provide insights into stability model uncertainty that arises from the stability model itself.

The Equations for the Factors of Safety against force and moment equilibrium are derived using the General Limit Equilibrium (GLE) Model (Fredlund et al., 1981). The GLE provides a general theory wherein other methods of Limit Equilibrium can be viewed as special cases. Fredlund et al. (1981) developed the GLE Model adopting the Independent State Variable (Fredlund et al., 1978) Model for unsaturated strength. In this Section, the GLE Model is developed using the Effective Stress Model (Bishop, 1959) for unsaturated strength, since this is the model for strength used throughout this study. Techniques are developed to solve the Equations for the Factor of Safety using the GLE Model in a spreadsheet. These are simpler and quicker to implement than current numerical analyses, which require specialized computer software, e.g. SLOPE/W (Geo-Slope International Inc., 1998). The GLE Model is then used to investigate stability model uncertainty for deterministic and probabilistic slope stability analyses, and the effects on landslide hazards assessments.

Figure 6.158 shows a schematic of what will be studied in more detail in this Section.

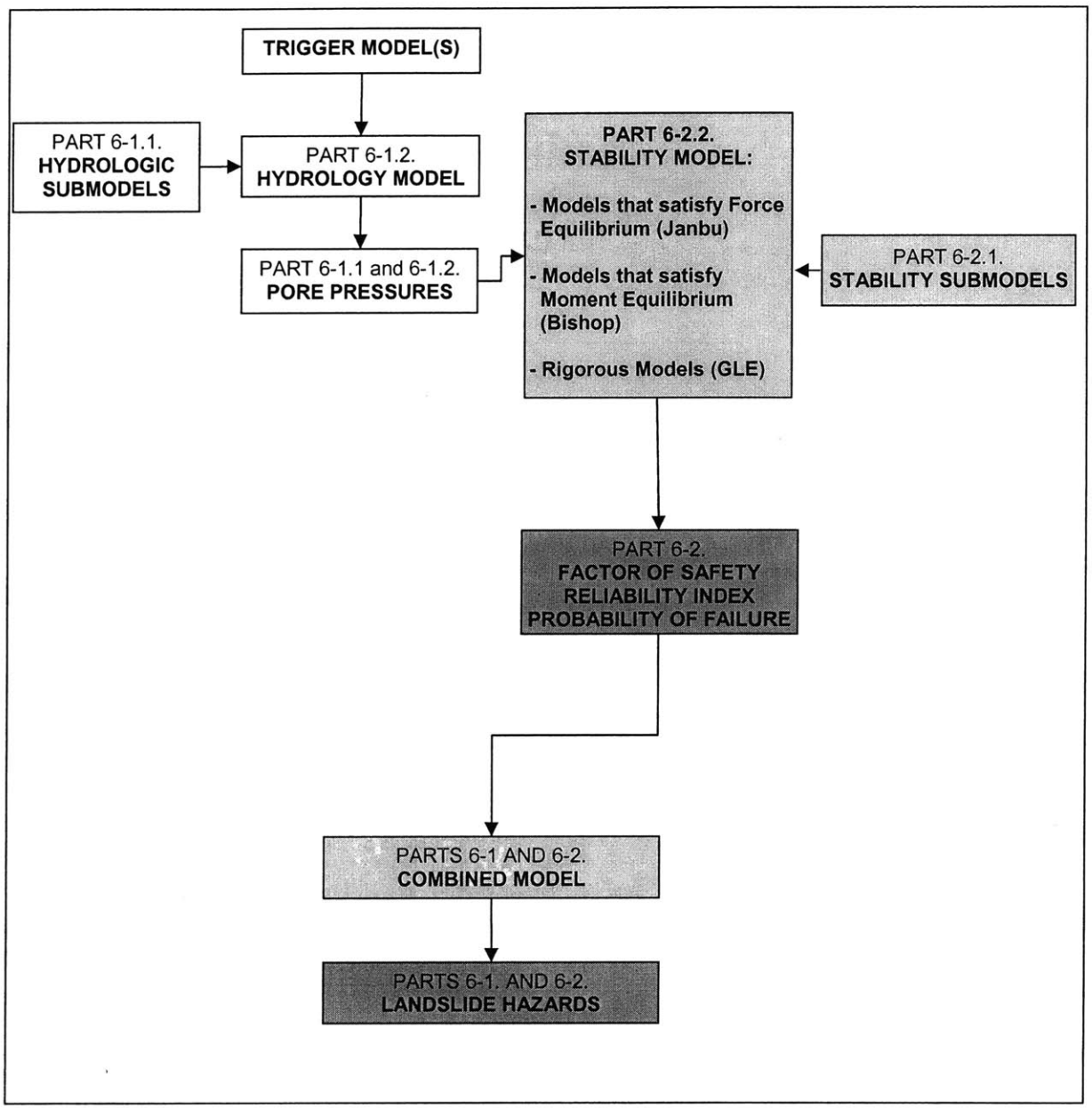

Figure 6.158. Effects of different stability model (shown in the lightly shaded stability models box) on the results of stability analyses (Factors of safety, reliability indices and probabilities of failure in the dark shaded box) and on landslide hazards (dark box) are investigated

6-2.2.1. LIMIT EQUILIBRIUM STABILITY MODELS

The Limit Equilibrium Method is a well-established method that is extensively used for stability analyses. The main assumptions of the Limit Equilibrium Method include:

a. A failure mechanism must be postulated, involving slip surfaces which may be planar or curved.
b. A failure model, in terms of soil strength parameters, must be adopted.
c. The static equilibrium of both the overall mechanism and of each element or slice (see Figures 6.159 and 6.160) must be satisfied by resolving forces in two orthogonal directions and by taking moments of boundary forces. However, all Limit Equilibrium Methods do not satisfy the three criteria of force and moment equilibrium.
d. Internal stresses in the soil 'blocks' are not considered.
e. The factor of safety is uniform along the slope surface such that the same proportion of strength is mobilized on all the slip surface.

All Limit Equilibrium Models for slope stability analysis divide a slide mass into n smaller slices. Each slice is affected by a general system of forces as shown in Figures 6.159 and 6.160.

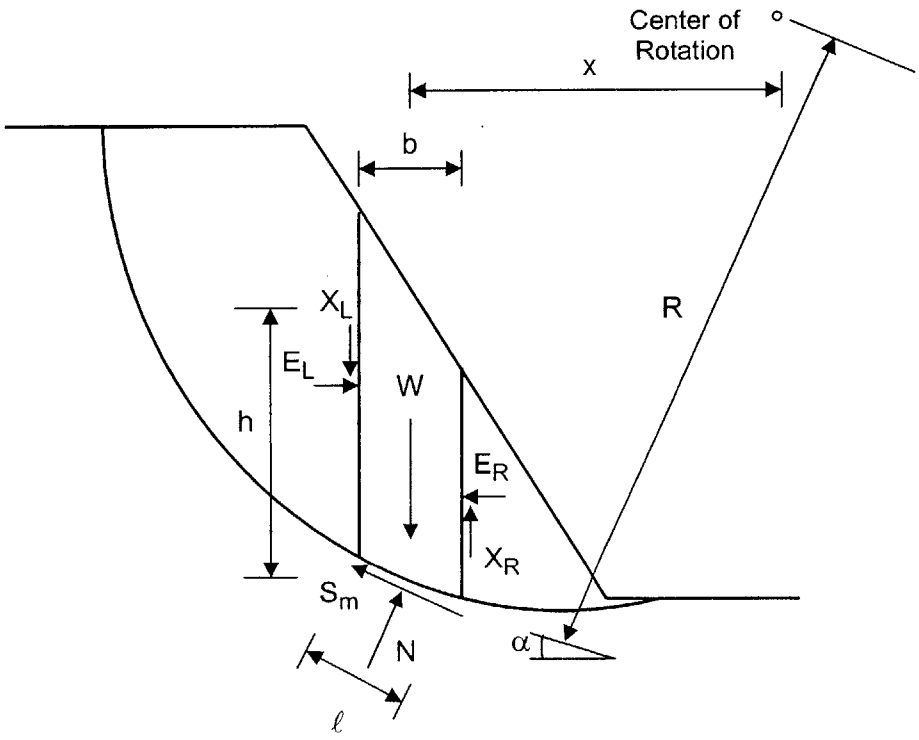

Figure 6.159. Definition of Parameters for Circular Failure Surface

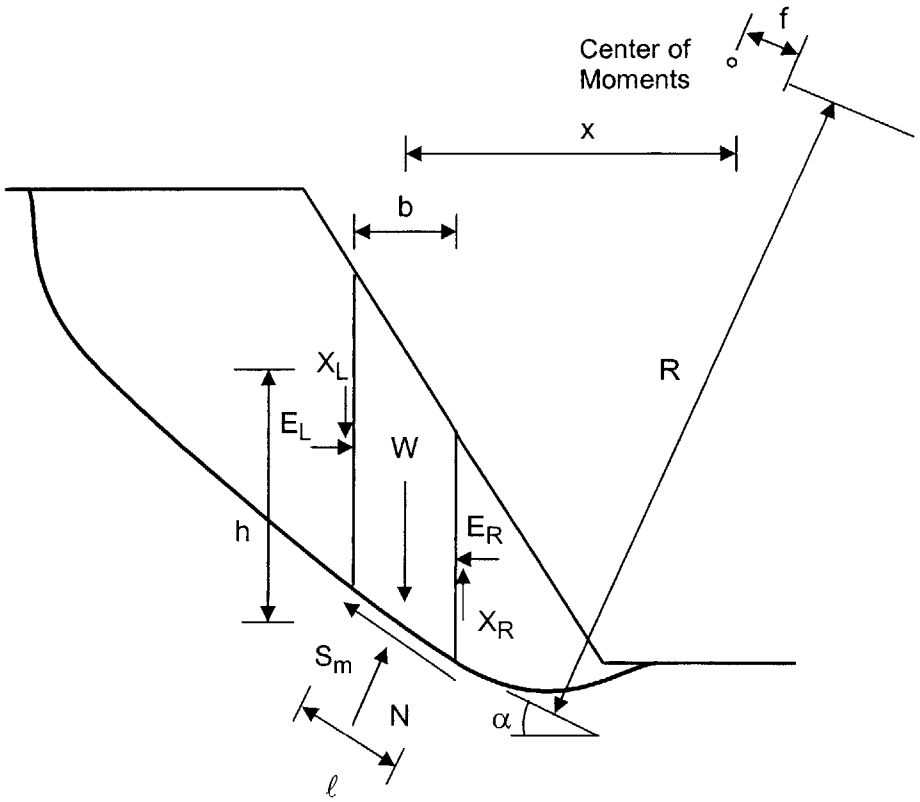

Figure 6.160. Definition of Parameters for Non-Circular Failure Surface

The variables are defined as:

W the total weight of the slice of width b and height h

N the total normal force acting on the base of the slice

S_m the shear force mobilized on the base of the slice

E the horizontal interslice normal force (the L and R subscripts designate the left and right sides of the slice)

X the vertical interslice shear force (the L and R subscripts designate the left and right sides of the slice)

R the radius for a circular failure surface or the moment arm associated with the mobilized shear force S_m for arbitrary failure surface

f the perpendicular offset of the normal force, N from the center of rotation or from the center of moments

x the horizontal distance from the centerline of each slice to the center of rotation or to the center of moments

h the vertical distance from the center of the base of a slice to the ground surface

α the angle the base of a slice makes to the horizontal

ℓ the length of the base of a slice

For a system with n slices, there are (6n – 2) unknowns. Since only 4n Equations of static equilibrium (3n from static equilibrium, n from a model relating shear strength to normal stress e.g. Coulomb) can be written, the solution is statically indeterminate. Assumptions are therefore necessary to make the problem solvable. Stability Models differ in the assumptions they make to solve the problem. Common stability models and the assumptions each make are:

Bishop's Simplified Method assumes that all the interslice shear forces are zero, reducing the number of unknowns by (n – 1). This leaves (4n – 1) unknowns and horizontal equilibrium is not satisfied for one slice.

Janbu's Simplified Method also assumes all the interslice shear forces are zero, leaving (4n – 1) unknowns. Moment equilibrium is not satisfied.

Janbu's Generalized Method assumes a location of the thrust line, reducing the number of unknowns to (4n – 1). Moment equilibrium, though satisfied with this assumption, is not rigorously satisfied. It will be if the correct location of the thrust line is assumed.

Morgenstern – Price Method rigorously satisfies static equilibrium by assuming that the interslice resulting force inclination varies according to a 'portion' of an arbitrary function. This leaves 4n unknowns and 4n Equations.

Table 6.36 lists the common models and the conditions of static equilibrium that are satisfied by each.

Stability Model	Assumption	Force Equilibrium		Moment Equilibrium
		Horizontal	Vertical	
Janbu Simplified	X = 0	Yes	Yes	No
Janbu Generalized	Arbitrary location of X	Yes	Yes	Not Rigorously
Bishop Simplified	X = 0	Yes	No	Yes
Morgenstern - Price	Location of X functional relationship	Yes	Yes	Yes

Table 6.36. Methods of Stability Analysis and Conditions of Static Equilibrium

A General Limit Equilibrium (GLE) Model (Fredlund et al., 1981) can be developed to encompass most of the assumptions used by various models and may be used to analyze circular and noncircular failure surfaces. As a result, various Limit Equilibrium stability models are special cases of the GLE Model.

Fredlund et al. (1981) derive the GLE Equations for force and moment equilibrium based on the Independent State Variable Model for unsaturated strength (see Section 6-2.1.4.2). In this study, the GLE formulation is derived using the Effective Stress Model

for unsaturated strength (see Section 6-2.1.4.3). Prior to doing so, it is worth noting that as with the Infinite Slope Model, all Limit Equilibrium models suffer from the drawback that they can only be used upto a certain angle of inclination of any particular slice. This angle was derived for the Infinite Slope Model in Appendix B.

6-2.2.1.a. GENERAL LIMIT EQUILIBRIUM (GLE) MODEL

The mobilized shear force at the base of a slice can be written using the shear strength Equation for an unsaturated soil with the Effective Stress Model as:

$$S_m = \frac{\ell}{F}\{c' + (\sigma - u_a) + \chi(u_a - u_w)\tan\phi'\} \qquad [6.41]$$

where:

χ is the effective stress parameter

ℓ is the length of the base of the slice

F is the Factor of Safety, defined as the factor by which the shear strength parameters must be reduced in order to bring the soil mass into a state of limiting equilibrium along the failure surface

The normal force at the base of a slice, N, is derived by summing forces in the vertical direction:

$$W - (X_R - X_L) - S_m \sin\alpha - N\cos\alpha = 0 \qquad [6.42]$$

Substituting Equation [6.42] into [6.41] and replacing the $(\sigma\ell)$ term with N gives:

$$W - (X_R - X_L) - \left\{\frac{c'\ell}{F} + \frac{N\tan\phi'}{F} - \frac{u_w\chi\ell\tan\phi'}{F}\right\}\sin\alpha - N\cos\alpha = 0 \qquad [6.43]$$

If the pore air pressure $u_a = 0$.

Rearranging results in:

$$N = \frac{W - (X_R - X_L) - \left\{\frac{c'\ell}{F} - \frac{u_w \chi \ell \tan\phi'}{F}\right\}\sin\alpha}{\left(\cos\alpha + \frac{\tan\phi' \sin\alpha}{F}\right)} \qquad [6.44]$$

The Factor of Safety, F, in Equation [6.44] is equal to the moment equilibrium Factor of Safety F_m, when solving for moment equilibrium, and is equal to the force equilibrium Factor of Safety, F_f, when solving for force equilibrium.

The vertical interslice shear forces X_R and X_L, in the normal force Equation [6.44] can be computed using an interslice force function, as described later.

Two independent Factor of Safety Equations can be derived, one with respect to moment equilibrium, and the other with respect to horizontal force equilibrium.

FACTOR OF SAFETY WITH RESPECT TO MOMENT EQUILIBRIUM

Moment equilibrium can be satisfied with respect to an arbitrary point above the central portion of the failure surface. Consider moment equilibrium for the surface shown in Figure .

$$\sum Wx - \sum Nf - \sum S_m R = 0 \qquad [6.45]$$

Substituting Equation [6.41] into [6.45], and replacing the $(\sigma\ell)$ term with N gives:

$$\sum Wx - \sum Nf = \frac{1}{F_m} \sum \{c'\ell + (N - u_w \chi \ell)\tan\phi'\} R \qquad [6.46]$$

where:

F_m is the Factor of Safety with respect to moment equilibrium

Rearranging yields:

$$F_m = \frac{\sum \{c' \ell + (N - u_w \chi \ell) \tan \phi'\} R}{\sum Wx - \sum Nf} \qquad [6.47]$$

FACTOR OF SAFETY WITH RESPECT TO FORCE EQUILIBRIUM

The Factor of Safety with respect to Force Equilibrium is derived by summing forces in the horizontal direction for all slices:

$$\sum S_m \cos \alpha - \sum N \sin \alpha = 0 \qquad [6.48]$$

Substituting Equation [6.41] into [6.48] replacing the $(\sigma \ell)$ term with N gives:

$$\frac{1}{F_f} \sum \{c' \ell + (N - u_w \chi \ell) \tan \phi'\} \cos \alpha = \sum N \sin \alpha \qquad [6.49]$$

where:

F_f is the Factor of Safety with respect to force equilibrium

Rearranging yields:

$$F_f = \frac{\sum \{c' \ell + (N - u_w \chi \ell) \tan \phi'\} \cos \alpha}{\sum N \sin \alpha} \qquad [6.50]$$

The interslice normal forces, E_R and E_L are computed by summing horizontal forces on each slice (see Figures 6.159 and 6.160):

$$E_R - E_L = N \cos \alpha \tan \alpha - S_m \cos \alpha \qquad [6.51]$$

Substituting for $N\cos\alpha$ from Equation [6.42] into Equation [6.51], and rearranging gives:

$$E_R - E_L = \{W - (X_R - X_L) - S_m \sin\alpha\}\tan\alpha - S_m \cos\alpha \qquad [6.52]$$

And simplifying:

$$E_R = E_L + \{W - (X_R - X_L)\}\tan\alpha - \frac{S_m}{\cos\alpha} \qquad [6.53]$$

The interslice normal forces are calculated from Equation [6.53] by integrating from left to right across the slope. The assumption is made that the interslice shear forces, X, can be related to the interslice normal forces, E, by a mathematical function (Morgenstern and Price, 1969):

$$X = \lambda f(x) E \qquad [6.54]$$

where:

f(x) is a functional relationship which describes the manner in which the magnitude of X/E varies across the slip surface

λ is a scaling constant which represents the proportion of the function, f(x), used for solving the factor of safety Equation.

Having defined this functional relationship, the interslice shear forces, X, can be related to the interslice normal forces, E, and the Factor of Safety equations can be solved.

Several functional relationships f(x) have been proposed in the literature for slope stability analyses. Examples include: a constant function, half-sine, trapezoidal, etc.

The Bishop Simplified Model satisfies moment equilibrium, while assuming that the interslice shear forces $X = 0$. Factors of Safety from the Bishop Model, therefore, correspond to the moment Factors of Safety in the GLE Model (Equation [6.47), with $\lambda = 0$ in Equation [6.54].

The Janbu Simplified Model satisfies force equilibrium, while assuming that the interslice shear forces $X = 0$. Factors of Safety from the Janbu Simplified Model, therefore, correspond to the force Factors of Safety in the GLE Model (Equation [6.50]) with $\lambda = 0$ in Equation [6.54].

6-2.2.1.b. SPREADSHEET IMPLEMENTATION OF THE GLE MODEL

The Factor of Safety Equations with respect to moment and force equilibrium (Equations [6.47] and [6.50]) are non linear. The Factors of Safety F_m and F_f appear on both sides of the Equations, since they appear in Equation [6.44] for the normal force. So, iterative techniques are required to solve for these. Several of these techniques have been proposed in the literature, e.g. Fredlund (1985). A much simpler and quicker technique is described in Figure 6.161, which makes use of a spreadsheet's iterative circular function.

Step 1. Specify appropriate cells for the interslice normal, E_R and E_L and shear forces X_R and X_L (see Figure 6.162). Insert the Equation for E_R (Equation [6.53]) and E_L (E_L =-E_R) into the cells. Set X_R = X_L = 0 for the first iteration.

Step 2. Specify a cell as the initial estimate of the Factor of Safety and set this cell to 1 for the first iteration as in Figure 6.162.

Step 3. Insert the Equations for the shear force (Equation [6.41]) and normal force (Equation [6.44]) as in Figure 6.162. Use the estimate of the Factor of Safety (Step 2) in these Equations.

Step 4. Select the Tools - Options – Iteration – Calculation tab in Excel. Set the Calculations to Manual and set the Iterations to 10,000.

Step 5. Compute the Factor of Safety according to Equation [6.47] for moment equilibrium and [6.50] for force equilibrium.

Step 6. Compute X_R and X_L and E_R and E_L from the computed value of F in Step 5.

Step 7. Set the cell for the Factor of Safety to be equal to the estimate of F cell designated in Step 2. Once this is done, the spreadsheet automatically iterates through the values of F and convergence is reached very quickly.

Figure 6.161. Spreadsheet Procedure for Iterative Procedure in GLE Model

	X_B	Y_B	Y_T	h_{ij}								h_t		
Slice #	36	13	13	0	tan α	Δx	p	u	c'	tanϕ'	ΔQ	0	$\tan\alpha_t$	FS
1	31.22	7.87	13	5.13	1.0732218	4.78	5.13	0.8475	1.5	0.4663077	0	1.71	0.822147	
2	28.27	4.76	11	6.24	1.0542373	2.95	11.37	1.68	1.5	0.4663077	0	2.08	0.762533	1.484708
3	23.77	1.89	8.6906	6.800599	0.6377778	4.5	13.041	2.1004	1.5	0.4663077	0	2.266866308	0.587684	
4	19.77	-0.43	6.3812	6.811198	0.58	4	13.612	2.1084	1.5	0.4663077	0	2.270399282	0.59995	
5	15.77	-3	4.0718	7.071797	0.6425	4	13.883	2.3038	1.5	0.4663077	0	2.35726559	0.558283	
6	11.77	-4.82	1.7624	6.582396	0.455	4	13.654	1.9368	1.5	0.4663077	0	2.194131898	0.485783	
7	7.77	-6.52	-0.547	5.972995	0.425	4	12.555	1.4797	1.5	0.4663077	0	1.990998205	0.37995	
8	3.77	-7.07	-2.856	4.213594	0.1375	4	10.187	0.1602	1.5	0.4663077	0	1.40453118	0.213283	
9	-0.23	-6.77	-5.166	1.604192	-0.075	4	5.8178	-1.797	1.5	0.4663077	0	0.534730821	-0.04149	
10	-5	-5.16	-5.16	0	-0.337526	4.77	1.6042	-3	1.5	0.4663077	0	0	-	

MOMENT FACTOR OF SAFETY

Slice Number	Width, b (m)	Height, H (m)	α	h (m)	l (m)	x (m)	f (m)	R (m)	u	γ	W (kN)	c'	f'	X_R	X_L	Initial Estimate of F	m = {cos + (tan ϕ' sin α)/F)}	Normal Force, N
10.00	4.78	2.57	47.02	0.00	7.01	0.00	0.00	0.00	0.85	2.00	24.52	1.50	0.47	21.60	0.00	1.48	0.77	-2.93
9.00	2.95	5.69	46.51	0.00	4.29	0.00	0.00	0.00	1.68	2.00	33.54	1.50	0.47	17.03	-21.60	1.48	0.90	-9.16
8.00	4.50	6.52	32.53	0.00	5.34	0.00	0.00	0.00	2.10	2.00	58.68	1.50	0.47	-11.95	-17.03	1.48	0.67	75.93
7.00	4.00	6.81	30.11	0.00	4.62	0.00	0.00	0.00	2.11	2.00	54.45	1.50	0.47	24.24	11.95	1.48	1.18	33.80
6.00	4.00	6.94	32.72	0.00	4.75	0.00	0.00	0.00	2.30	2.00	55.53	1.50	0.47	-22.12	-24.24	1.48	0.61	83.52
5.00	4.00	6.83	24.47	0.00	4.39	0.00	0.00	0.00	1.94	2.00	54.62	1.50	0.47	19.97	22.12	1.48	0.72	76.00
4.00	4.00	6.28	23.03	0.00	4.35	0.00	0.00	0.00	1.48	2.00	50.22	1.50	0.47	-15.94	-19.97	1.48	1.22	36.38
3.00	4.00	5.09	7.83	0.00	4.04	0.00	0.00	0.00	0.16	2.00	40.75	1.50	0.47	5.89	15.94	1.48	0.78	64.40
2.00	4.00	2.91	-4.29	0.00	4.01	0.00	0.00	0.00	-0.25	2.00	23.27	1.50	0.47	-13.88	-5.89	1.48	0.95	33.22
1.00	4.77	0.80	-18.65	0.00	5.03	0.00	0.00	0.00	-0.32	2.00	7.65	1.50	0.47	8.34	13.88	1.48	1.10	13.49

FORCE FACTOR OF SAFETY

c'l cos α	(N-ul)tanϕ'cosα	c'lcos α + (N-ul)tanϕ'cosα	Nsin α	Sm	X_R	X_L	W-(X_R-X_L) tan α	W-(X_R-X_L) tan α - Sm/cos α	E_L 0.00	E_R 0.00
7.17	-2.82	4.35	-2.15	4.30	21.60	0.00	49.49	43.19	0.00	43.19
4.43	-5.25	-0.83	-6.65	-0.81	17.03	-21.60	76.09	77.26	-43.19	34.07
6.75	25.45	32.20	40.83	25.72	-11.95	-17.03	40.67	10.16	-34.07	-23.91
6.00	9.70	15.70	16.96	12.23	24.24	11.95	38.70	24.57	23.91	48.48
6.00	28.47	34.47	45.15	27.60	-22.12	-24.24	37.04	4.24	-48.48	-44.24
6.00	28.64	34.64	31.47	25.64	19.97	22.12	23.87	-4.29	44.24	39.95
6.00	12.85	18.85	14.23	13.80	-15.94	-19.97	23.06	8.07	-39.95	-31.88
6.00	29.45	35.45	8.77	24.10	5.89	15.94	4.22	-20.11	31.88	11.77
6.00	15.91	21.91	-2.48	14.80	-13.88	-5.89	-1.15	-15.99	-11.77	-27.76
7.16	6.66	13.82	-4.31	9.82	8.34	13.88	-0.71	-11.08	27.76	16.68

Figure 6.162. Spreadsheet Implementation of GLE Model

6-2.2.2. STABILITY MODEL UNCERTAINTY ON CIRCULAR FAILURE SURFACE

A simple and good example to compare different Limit Equilibrium Stability Methods has been presented in Fredlund and Krahn (1977). The slope with the circular failure surface shown in Figure 6.163 was analyzed, and the results are presented in the same Figure 6.163, as a function of λ.

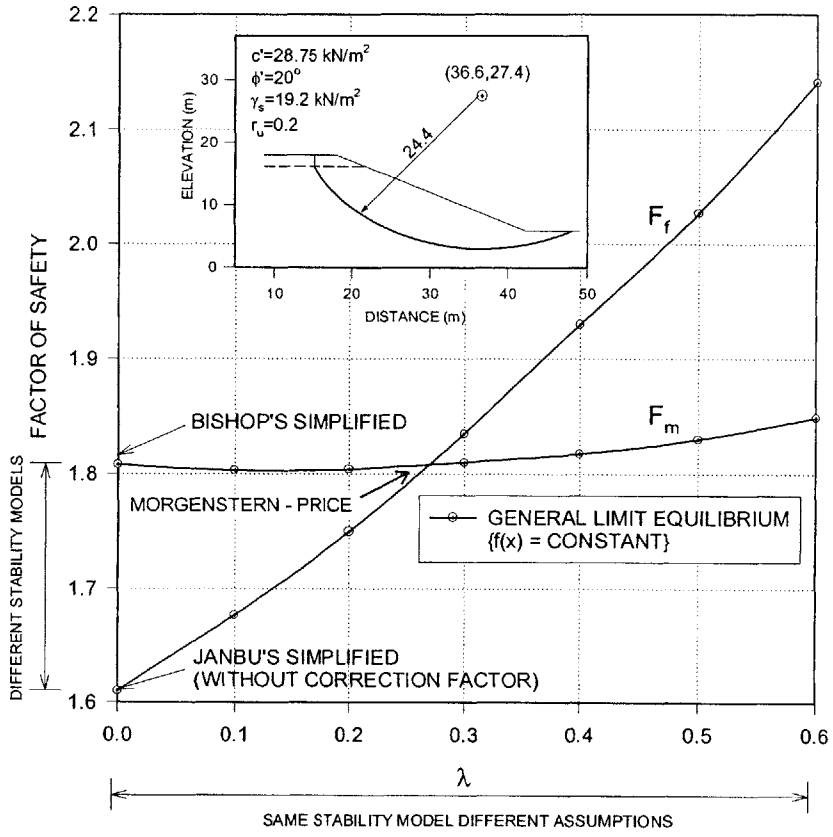

Figure 6.163. Comparison of Factors of Safety for a Simple Circular Slip Surface (modified after: Fredlund and Krahn (1977). r_u is the pore pressure ratio (see Chapter 2)

In Figure 6.163, F_f is the Factor of Safety with respect to force equilibrium and F_m is the Factor of Safety with respect to moment equilibrium using the General Limit Equilibrium Model (Fredlund and Krahn, 1977).

The Bishop Simplified Method is a special case of the moment equilibrium factor of safety when the interslice shear forces are set to zero i.e. $\lambda = 0$. Similarly, the Janbu Simplified Method is a special case of the force equilibrium factor of safety when the interslice shear forces are set to zero i.e. $\lambda = 0$. For the Morgenstern and Price Method, both force and moment equilibrium are satisfied for a specified function f(x), and hence corresponds to where $F_f = F_m$ in Figure 6.

Figure 6.163 illustrates the significance of model uncertainty in two ways. First, it shows the different Factors of Safety obtained from different stability models for the case where the interslice shear forces are set to zero ($\lambda = 0$). Second, it shows the effects of different assumptions using the same stability model with different values of λ.

The effects of model uncertainty (for values of λ less than the Morgenstern – Price) are greatest when $\lambda = 0$, which corresponds to the Simplified stability models. Since these are the most widely adopted models for stability analyses, stability model uncertainty can have significant effects on the results.

Figure 6.163 shows the sensitivity to the force Factor of Safety with respect to λ. Clearly adopting different values of λ can result in significant differences in force Factors of Safety, and hence conclusions on stability. The moment Factor of Safety, on the other hand, is not as sensitive to different values of λ.

6-2.2.3. STABILITY MODEL UNCERTAINTY ON NON CIRCULAR FAILURE SURFACE

We investigate stability model uncertainty for non circular failure surfaces for two slopes. In the first slope, the failure surface is shallow, and translational because of the assumed presence of shallow bedrock. In the second slope the failure surface is deep and rotational (but non circular). The terms deep and shallow are used in a relative sense.

In both examples, stability model uncertainty is investigated in a deterministic context (Factors of Safety), a second moment reliability context (reliability index and reliability charts) and probabilistic context (Monte Carlo Methods). Different coefficients of

variation, and correlation are assumed for the uncertain strength parameters in each example. Specifically, we investigate stability model uncertainty by:

a. Comparing the Factors of Safety obtained using different stability models

b. Comparing the Reliability Indices from second moment analyses, and Reliability Charts using different stability models.

c. Comparing the Probabilities of Failure from second moment reliability and Monte Carlo analyses.

EXAMPLE 1: SHALLOW FAILURE SURFACE (SHALLOW BEDROCK)

Consider the slope shown in Figure 6.164.

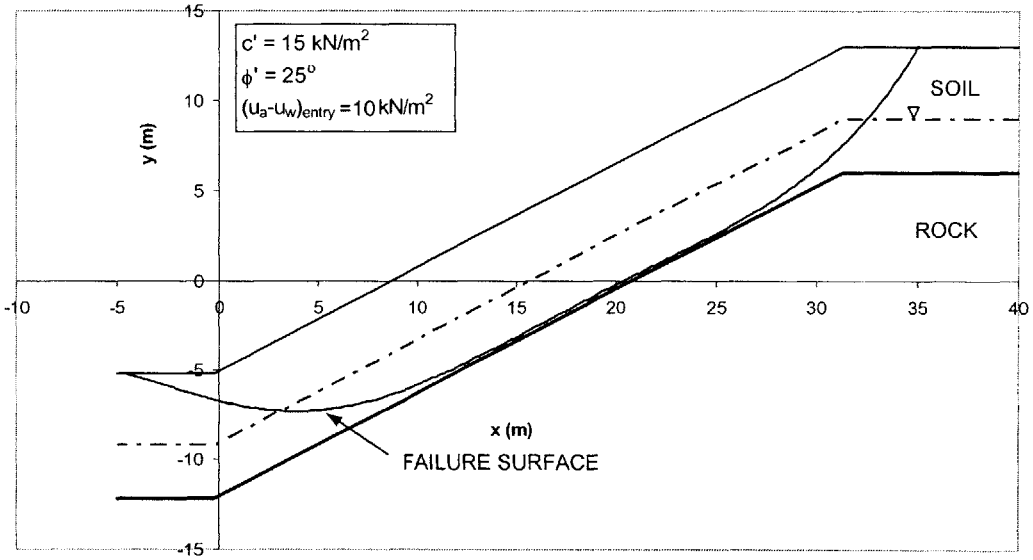

Figure 6.164. Slope Geometry and Strength Parameters

DETERMINISTIC ANALYSES (FACTORS OF SAFETY)

The soil strength parameters shown in Figure 6.164 are used for deterministic analyses. We compute the Factor of Safety on the failure surface shown in Figure 6.164 for different stability models, namely the Janbu Simplified and Generalized Models, and the Bishop Simplified Model. The GLE Model is used to assess stability against force and

moment equilibrium using different but constant values of λ. The results are shown in Figure 6.165.

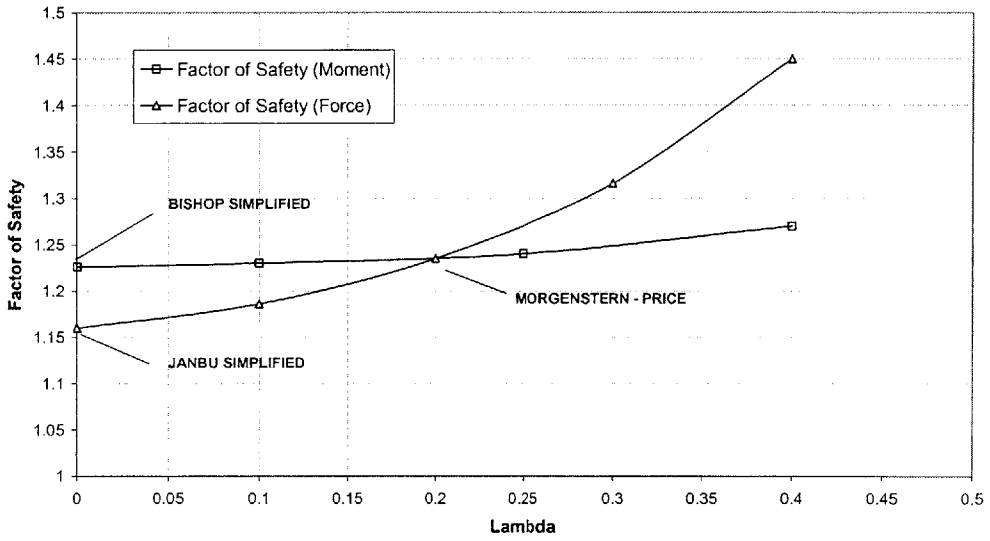

Figure 6.165. Variation of Force and Moment Factors of Safety with λ

When $\lambda = 0$, the force Factor of Safety corresponds to the Janbu Simplified Model, and the moment Factor of Safety corresponds to the Bishop Simplified Model. The point of interSection of the two Factor of Safety curves gives the value of λ at which both force and moment equilibrium is satisfied. This corresponds to the Morgenstern – Price Model. The Janbu Generalized Model cannot be shown on such a plot because the value of λ is not known, only the direction of the thrust is assumed.

The results are presented in Table 6.37.

Stability Model	Factor of Safety
Janbu Simplified	1.16
Janbu Generalized	1.23
Bishop Simplified	1.23
Morgenstern - Price	1.22

Table 6.37. Comparison of Factors of Safety from Different Stability Models on a Specified Non Circular Failure Surface

Table 6.37 shows that assessing stability using different models results in different Factors of Safety, though slightly different, can affect conclusions on stability. The Factor of Safety using the Janbu Generalized Model is the same as that obtained using the Morgenstern – Price Model. This is because of the shape of the failure surface is translational, and force equilibrium governs. The Bishop Model results in a slightly smaller Factor of Safety.

Figure 6.165 shows the sensitivity of the force Factor of Safety to λ, and shows the sharp rise in F_f with increasing λ. The moment Factor of Safety, on the other hand, is less sensitive to λ. This demonstrates model uncertainty from different assumptions in the same stability model, in addition to showing the effects of different models on stability analyses.

RELIABILITY ANALYSES (RELIABILITY INDICES)

We now assume that the soil strength parameters are uncertain with the following second moment parameters:

$c' \sim (m_{c'} = 15 kN/m^2,\ \sigma_{c'} = 5 kN/m^2)$; $\phi' \sim (m_{\phi'} = 25^o,\ \sigma_{\phi'} = 5^o)$, and we assume that c' and ϕ' are uncorrelated.

JANBU SIMPLIFIED MODEL

The reliability index computed using the Janbu Simplified Model is $\beta = 0.92$. A Reliability Chart is derived and shown in Figure 6.166, which also shows the $\beta - \sigma$ dispersion ellipsoid.

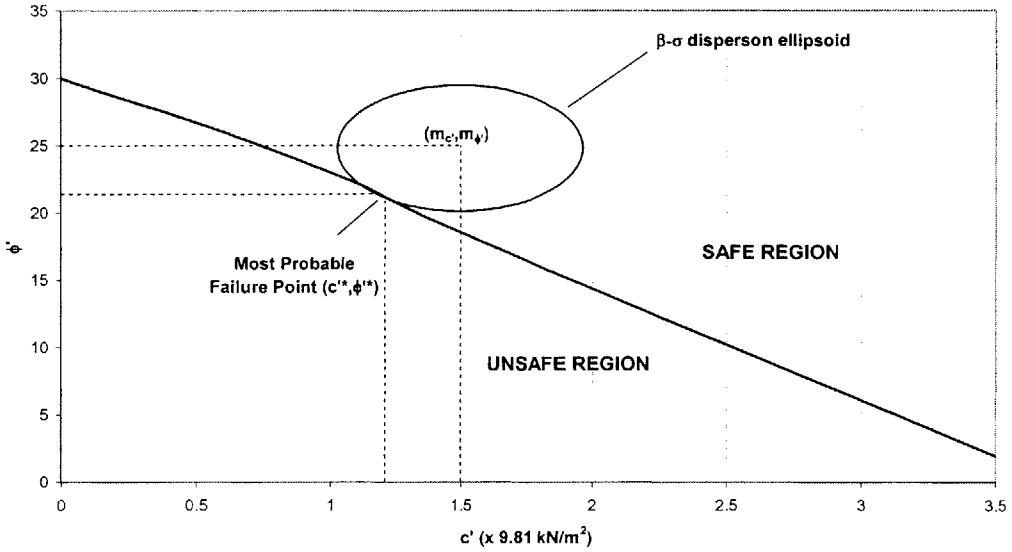

Figure 6.166. Stability Chart and $\beta-\sigma$ Dispersion Ellipsoid using the Janbu Simplified Model

JANBU GENERALIZED MODEL

The reliability index computed using the Janbu Simplified Model is $\beta = 1.0.5$. The Reliability Chart and the $\beta-\sigma$ dispersion ellipsoid are shown in Figure 6.167.

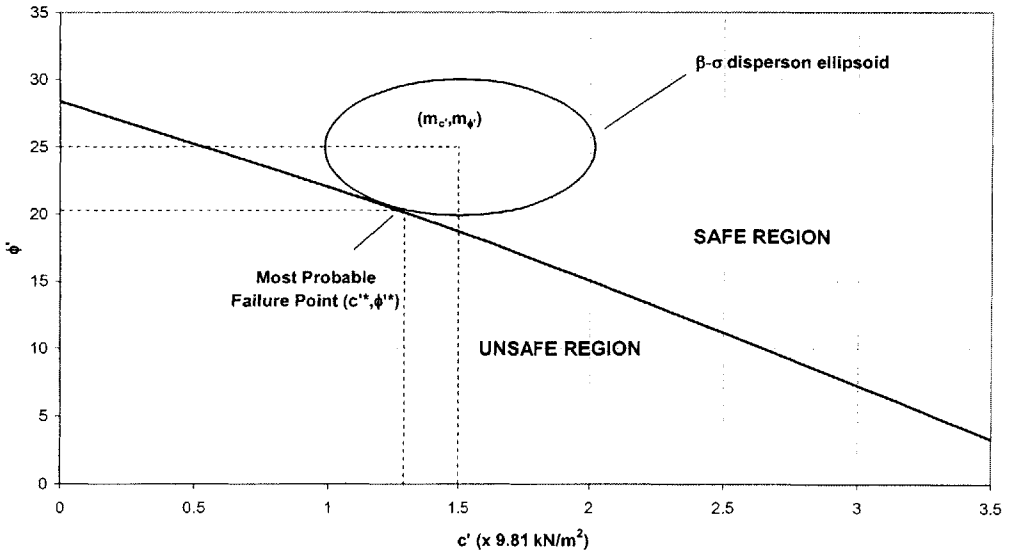

Figure 6.167. Stability Chart and $\beta-\sigma$ Dispersion Ellipsoid using the Janbu Generalized Model

BISHOP SIMPLIFIED MODEL

The reliability index computed using the Bishop Simplified Model is $\beta = 1.08$. The Reliability Chart and the $\beta - \sigma$ dispersion ellipsoid are shown in Figure 6.168.

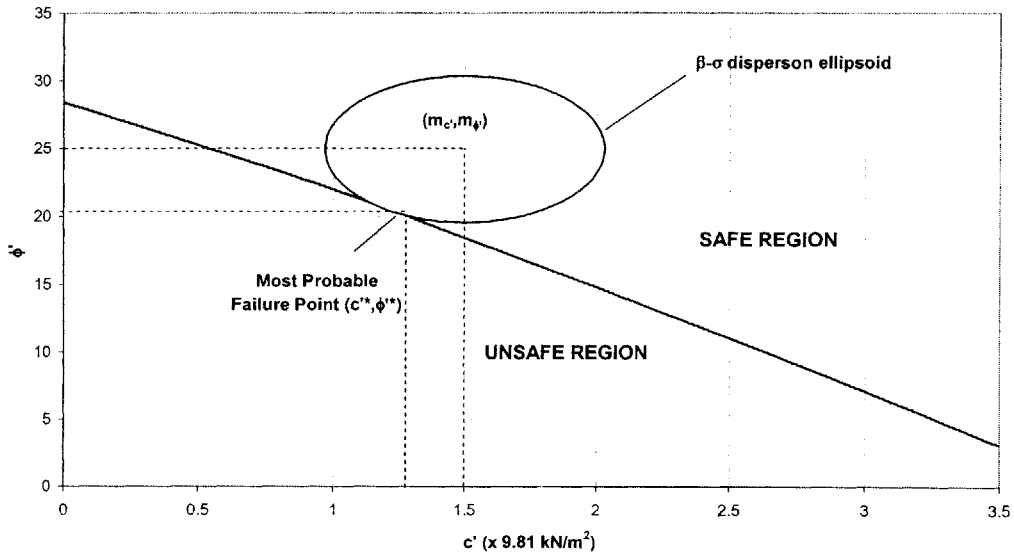

Figure 6.168. Stability Chart and $\beta - \sigma$ Dispersion Ellipsoid using the Bishop Simplified Model

MORGENSTERN – PRICE MODEL

The GLE Model is used to determine the value of λ at which force and moment equilibrium are both satisfied (see Figure 6.165), and this value is used in the GLE Model to result in the Morgenstern – Price Model. The reliability index computed is computed to be $\beta = 1.06$, and the Reliability Chart and $\beta - \sigma$ dispersion ellipsoid are shown in Figure 6.169.

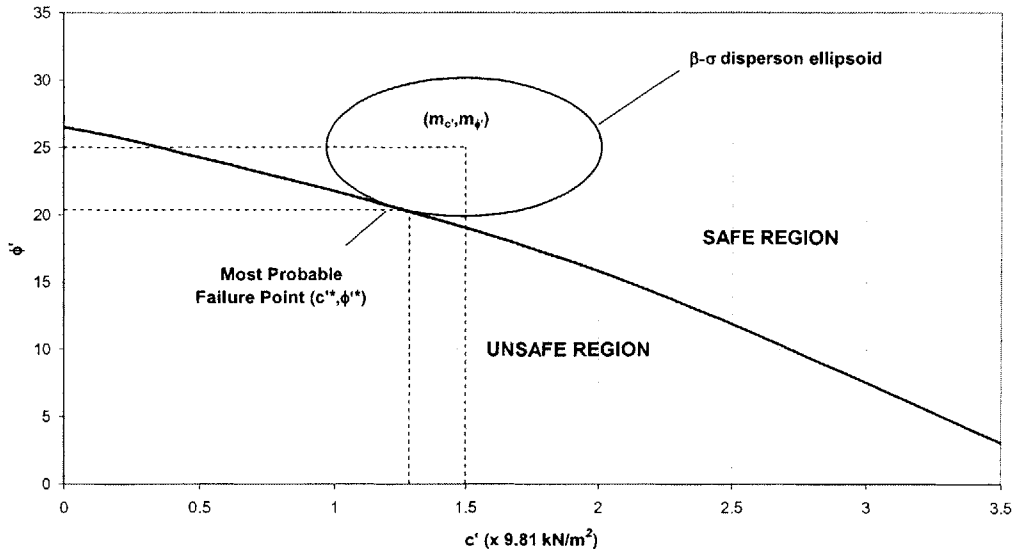

Figure 6.169. Reliability Chart and $\beta - \sigma$ Dispersion Ellipsoid using the Morgenstern - Price Model

The Reliability Charts shown in Figures 6.166 through 6.169, are different in that not only are the $\beta - \sigma$ ellipsoids different, but they also do not have the same failure boundary. This is because different stability models require different combinations of c' and ϕ' to bring the Factor of Safety to its critical value of one. Stability model uncertainty is therefore also illustrated in its effect on Reliability (and Stability) Charts. Figure 6.170 shows the derived Reliability Charts, with the failure boundaries, and $\beta - \sigma$ ellipsoids for the stability models considered.

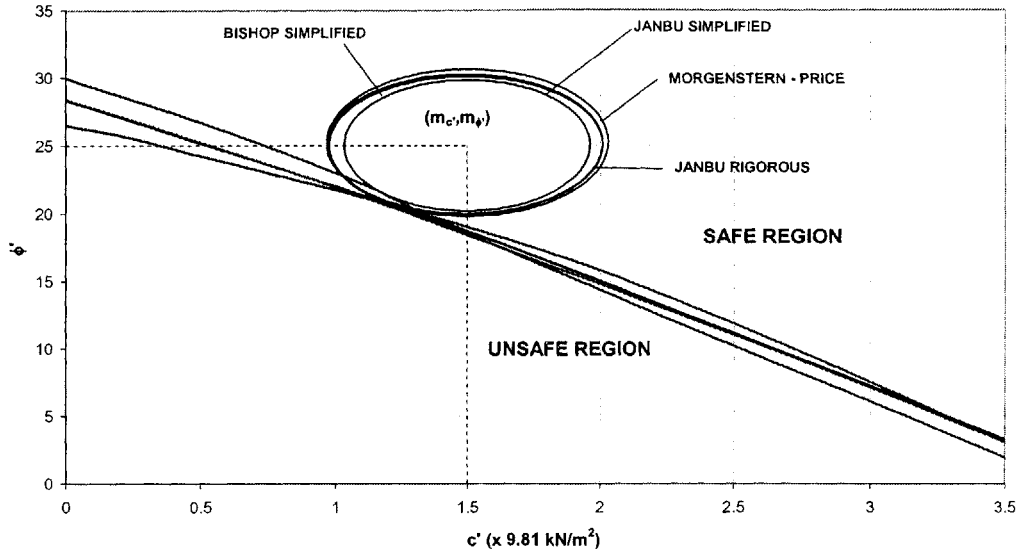

Figure 6.170. Illustration of Different Reliability Charts Obtained by Different Stability Models for Same Slope

The intent of Figure 6.170 is to compare, graphically, the effects of model uncertainty on Reliability Charts, and computed Reliability Indices.

Table 6.38 summarizes the Reliability Indices obtained from each stability method.

Stability Model	Reliability Index, β
Janbu Simplified	0.92
Janbu Generalized	1.05
Bishop Simplified	1.08
Morgenstern - Price	1.06

Table 6.38. Comparison of Reliability Indices obtained by Different Stability Models on a Specified Non Circular Failure Surface

By assuming a probability distribution for the Factor of Safety, probabilities of slope failure can be computed using the reliability indices in Table 6.38. If we assume that the Factor of Safety is Normally distributed, then probabilities of failure can be computed as $P_F = \Phi(-\beta)$.

Table 6.39 shows probabilities of failure from different stability models.

Stability Model	Reliability Index, β	Probability of Failure
Janbu Simplified	0.92	0.179
Janbu Generalized	1.05	0.147
Bishop Simplified	1.08	0.140
Morgenstern - Price	1.06	0.145

Table 6.39. Comparison of Reliability Indices and Probabilities of Failure obtained by Different Stability Models on a Specified Non Circular Failure Surface

Using the GLE formulation, we show the variation of the Reliability Index with λ in Figure 6.171. This is done for both the force and moment Equations of Factor of Safety.

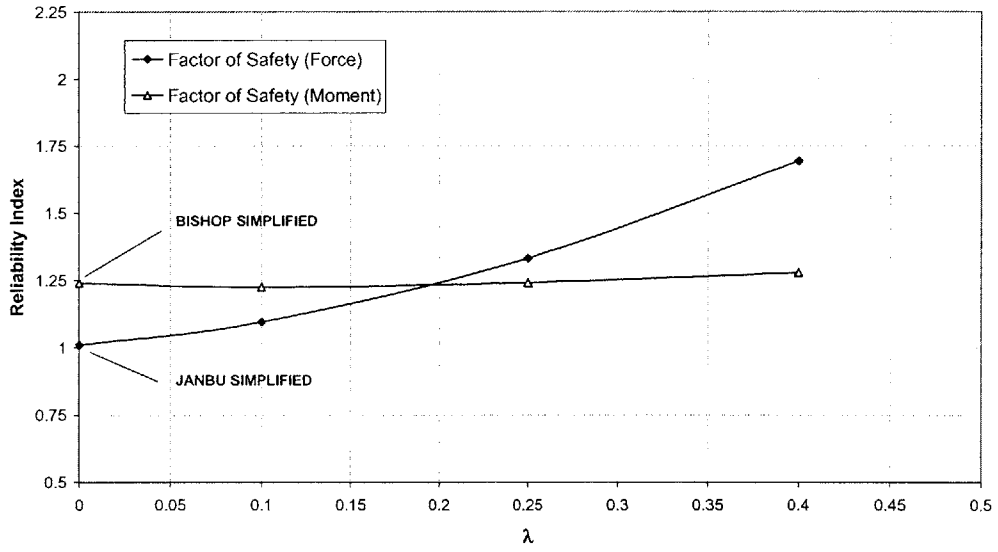

Figure **6.171.** Variation of Reliability Index with λ

Assuming that the Factor of Safety is Normally distributed, the Reliability Index plot in Figure 6.171, is transformed into a probability of failure plot, as is shown in Figure 6.172.

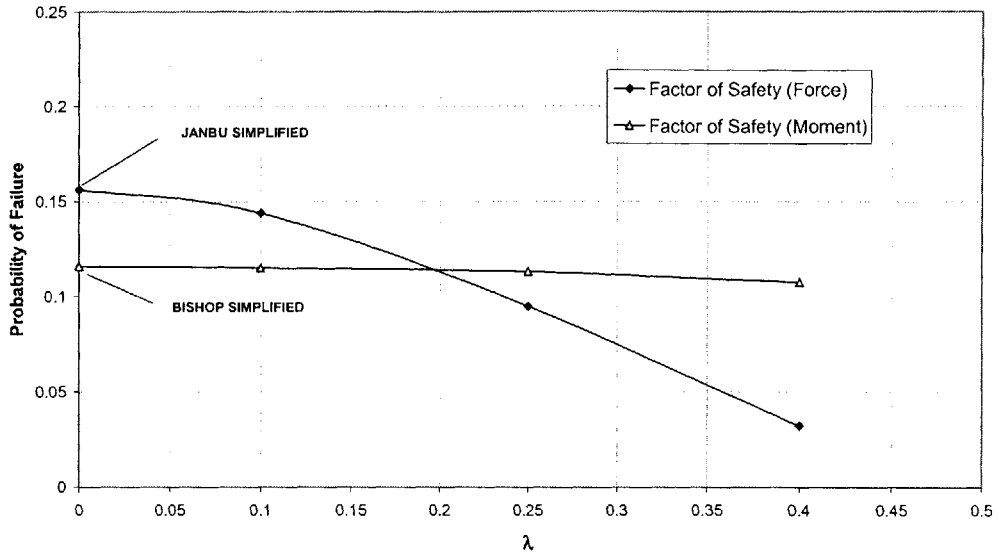

Figure 6.172. Variation of Failure Probability with λ Assuming Normal Factor of Safety

Figures 6.171 and 6.172 clearly show the effects of stability model uncertainty on computed Reliability Indices and probabilities of failure. They also show the effects of different assumptions using the same stability model. This is illustrated for different values of λ.

PROBABILISTIC ANALYSES (MONTE CARLO TECHNIQUES)

The Monte Carlo Method is used to estimate the probability of slope failure from an assumed distribution of the uncertain strength parameters. By doing so, the effects of stability model uncertainty on probabilistic analyses are examined. This is done by generating a distribution of the Factor of Safety from which probabilities of failure are directly computed. Monte Carlo analyses will also allow one to examine the effects of stability model uncertainty on the distribution of the Factor of Safety.

We assume the strength parameters are Joint Normally distributed with parameters:

$$c' \sim N(m_{c'} = 15kN/m^2,\ \sigma_{c'} = 5kN/m^2);\ \phi' \sim N(m_{\phi'} = 25^o,\ \sigma_{\phi'} = 5^o);\ \rho = 0$$

The Monte Carlo Method for generating correlated random variables from the Bivariate Normal distribution for correlated variables was discussed in Section 6-2.1.3.1.3.

Figure 6.173 compares the distribution of the Factor of Safety obtained using the different stability models.

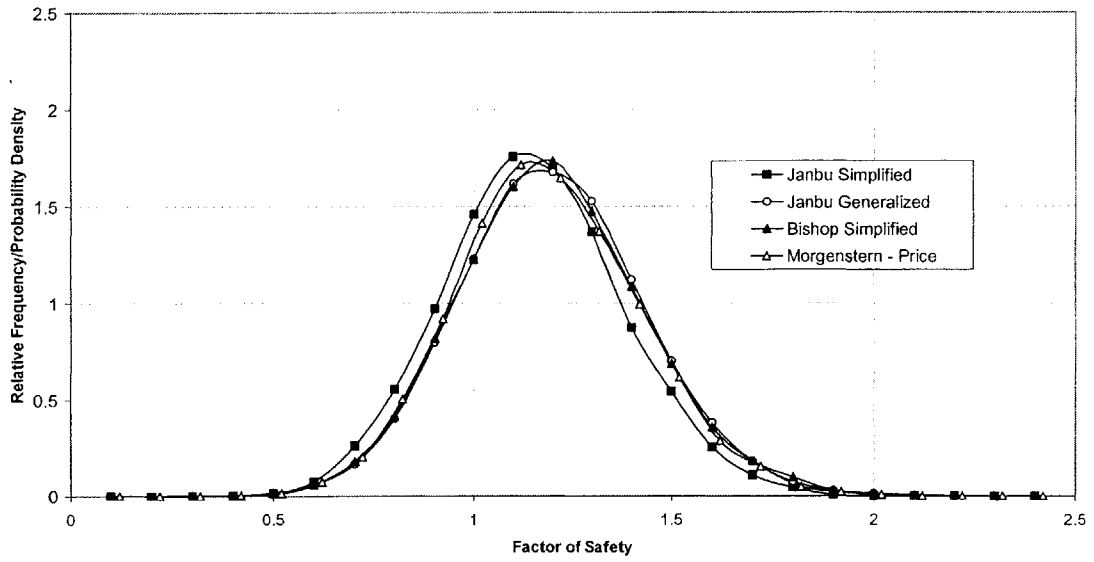

Figure 6.173. Comparison of Generated Distributions of Factor of Safety Suing Different Stability Models

Table 6.40 summarizes the expected values and standard deviations, as well as computed probabilities of failure using the different stability models.

We also attempt to investigate the effects of stability model uncertainty on the shape of the distribution of the Factor of Safety. In order to do this quantitatively, we compute an error term, e, as:

$$e = \sqrt{\sum_i (x_i - x')^2} \qquad [6.53]$$

where:

- e error term
- x_i the relative frequency of the generated distribution
- x' the theoretical probability density of the distribution

Where the theoretical distribution is taken to be the Normal distribution, since in Chapter 5 Part 5-3, we showed that the Factor of Safety closely follows a Normal distribution for Normally distributed strength parameters.

Stability Model	**Deterministic Analyses**	**Reliability Analyses**		**Probabilistic Analyses**			
	Factor of Safety	β	$P_F = \Phi(-\beta)$	**E[F]**	σ_F	P_F	Error Term, e
Janbu Simplified	1.16	0.92	0.179	1.19	0.23	0.183	0.095
Janbu Generalized	1.23	1.05	0.147	1.24	0.21	0.144	0.212
Bishop Simplified	1.23	1.08	0.140	1.25	0.22	0.147	0.159
Morgenstern - Price	1.22	1.06	0.145	1.24	0.24	0.149	0.249

Table 6.40. Comparison of Deterministic, Reliability and Probabilistic Results from Different Stability Models

Table 6.40 shows that different Factors of Safety, reliability indices and probabilities of failure are obtained using the different stability models. The difference is more significant in the probabilities of failure than in the Factors of Safety. The Janbu Simplified Model underestimates the reliability index and overestimates the probability of failure when compared to the rigorous Morgenstern – Price Model, because of the assumption that $\lambda = 0$. This is a conservative assumption since interslice forces are assumed to be zero. The Bishop Model overestimates the reliability index and underestimates the probability of failure because of the assumption that $\lambda = 0$, and because of the regular shape of the failure surface. The Bishop Model satisfies moment equilibrium, but fails to satisfy force equilibrium. When the failure surface is regular and translational, forces are important, and this leads to an underestimation of the failure probability using the Bishop Simplified Model.

For each stability model, the results of second moment reliability analyses, and probabilistic analyses using Monte Carlo techniques are in good agreement, e.g. For the Janbu Simplified Model, $P_F = \Phi(-\beta) = 0.179$ using reliability analyses, and $P_F = 0.183$ using Monte Carlo techniques.

The agreement is good, because, as shown in Figure 6.173, the distribution of the Factor of Safety is well approximated by the Normal distribution. This is also shown through the small value of the error term, e, in Table 6.40.

The error term, e, remains more or less the same for the different stability models. This implies that the derived distributions of the Factors of Safety using different models, shown in Figure 6.173, all closely follow the Normal distribution.

We therefore conclude that the different stability models, do not have a significant effect on the shape of the distribution of Factor of Safety. This is to be somewhat expected since they are based on the same GLE Model, and hence same basic mathematical form. The distribution is well approximated by the Normal distribution for all the stability models considered.

EXAMPLE 2: DEEP ROTATIONAL FAILURE SURFACE

In this example, we consider the slope shown in Figure 6.174.

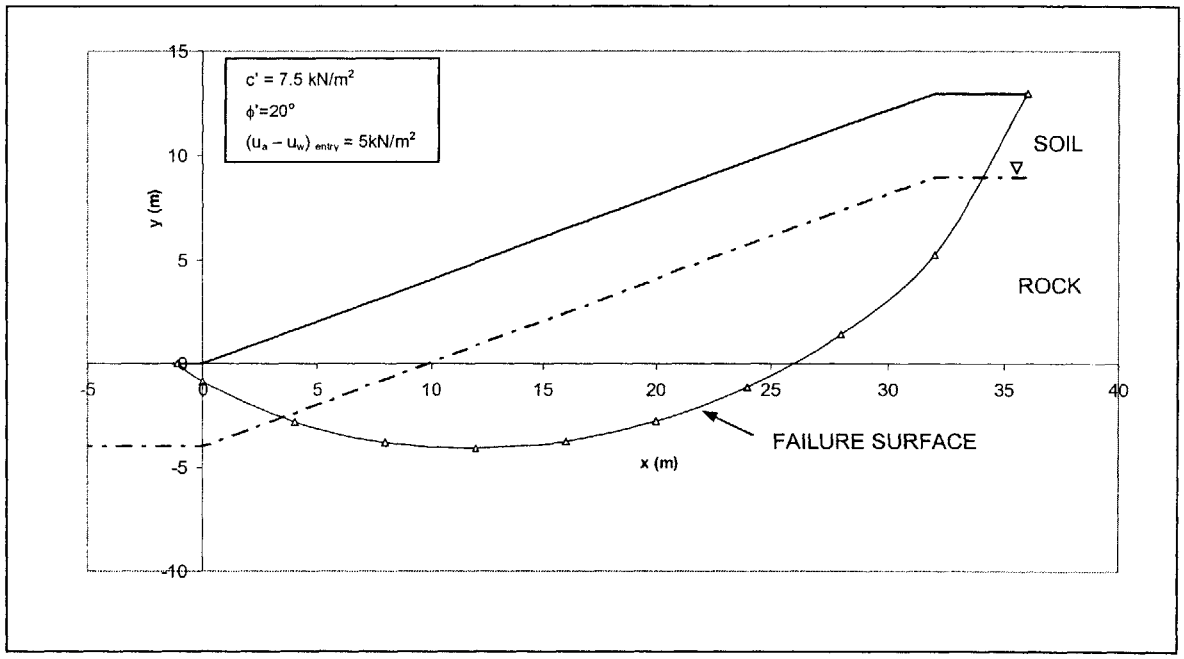

Figure 6.174. Slope Geometry and Strength Parameters

DETERMINISTIC ANALYSES

The soil strength parameters shown in Figure 6.174 are used for deterministic analyses. Deterministic stability analyses are performed using the GLE Model, and the variation of Factor of Safety with λ is shown in Figure 6.175.

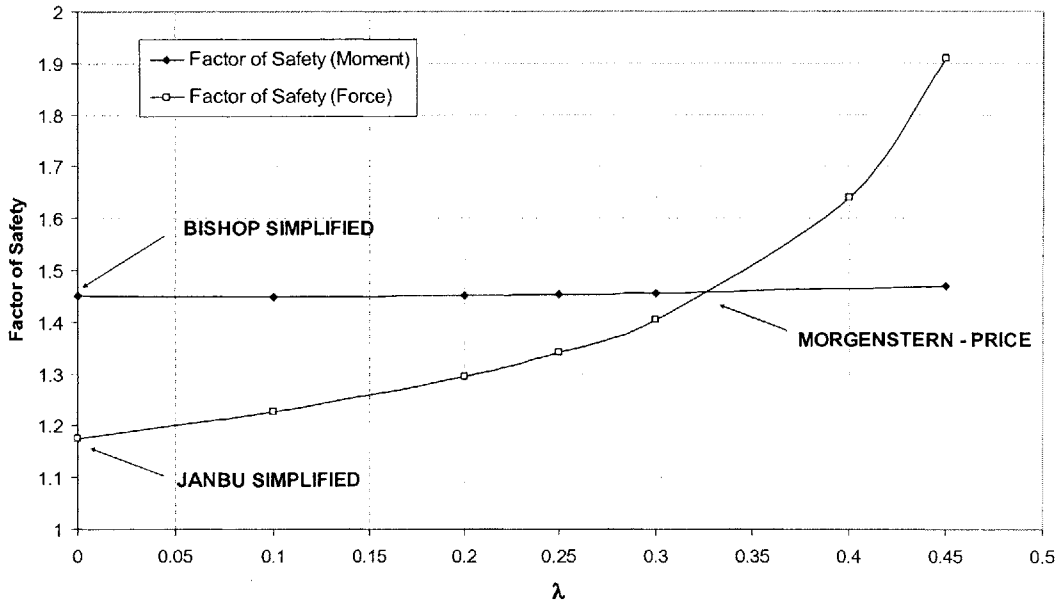

Figure 6.175. Variation of Force and Moment Factors of Safety with λ

The value of λ where both force and moment equilibrium are satisfied is $\lambda = 0.33$, and this is used in the GLE Model to result in the Morgenstern – Price Model. The Factors of Safety from the different stability models are shown in Table 6.41.

Stability Model	Factor of Safety
Janbu Simplified	1.18
Janbu Generalized	1.40
Bishop Simplified	1.47
Morgenstern - Price	1.46

Table 6.41. Factors of Safety Using Different Stability Models

Table 6.41 shows that different stability models result in different Factors of Safety, and conclusions on stability. The Bishop Simplified Model gives a value of Factor of Safety that is close to that obtained by the Morgenstern – Price Model. This is because of the rotational shape of the failure surface, where moment equilibrium governs. Both the Janbu Simplified and Rigorous Models, particularly the Simplified Model, underestimate the Factor of Safety compared to the Morgenstern – Price because these models satisfy force equilibrium, and not moment equilibrium.

RELIABILITY AND PROBABILISTIC ANALYSES

Stability model uncertainty on slope reliability is investigated in second moment reliability, and probabilistic contexts. We assume that the soil strength parameters are uncertain with the following second moment parameters:

$$c' \sim (m_{c'} = 7.5 kN/m^2,\ \sigma_{c'} = 1.875 kN/m^2) \text{ and } \phi' \sim (m_{\phi'} = 22^o,\ \sigma_{\phi'} = 7.3^o)$$

We assume that c' and ϕ' are uncorrelated. The Reliability Index is computed using the different stability models. Figure 6.176 compares the reliability charts obtained using the different models.

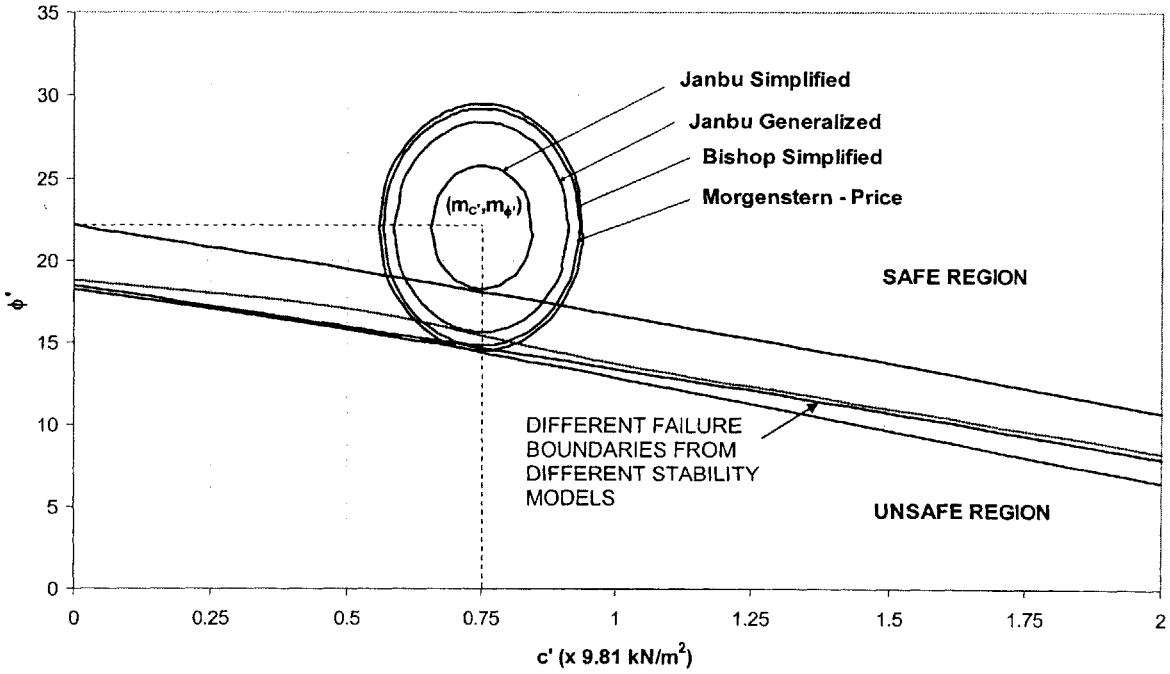

Figure 6.176. Illustration of Different Reliability Charts Obtained by Different Stability Models on Same Slope

Figure 6.176 also shows the different failure boundaries, and the different $\beta - \sigma$ dispersion ellipsoids that are obtained by the different stability models. Probabilities of failure are estimated from $P_F = \Phi(-\beta)$ assuming that the Factor of Safety is Normal, and the results are presented in Table 6.42.

Monte Carlo techniques are used to generate probability distributions of the Factor of Safety for the different stability models, from which probabilities of failure are computed directly. The results of the analyses, which are not presented here, show that using different stability models affect the expected value and standard deviation (variance) of the Factor of Safety, but have little effect on the shape of the distribution. These are the same observations as those made in Example 1 and shown in Figure 6.173, and Table 6.40.

The results of deterministic, reliability and probabilistic analyses are summarized in Table 6.42.

Stability Model	**Deterministic Analyses**	**Reliability Analyses**		**Probabilistic Analyses**		
	F	β	$P_F = \Phi(-\beta)$	**E[F]**	σ_F	P_F
Janbu Simplified	1.18	0.51	0.305	1.21	0.38	0.300
Janbu Generalized	1.40	0.87	0.192	1.42	0.45	0.188
Bishop Simplified	1.47	1.02	0.154	1.47	0.46	0.153
Morgenstern - Price	1.46	0.98	0.163	1.45	0.46	0.160

Table 6.42. Comparison of Deterministic, Reliability and Probabilistic Results from Different Stability Models

Tables 6.40 and 6.42 demonstrate the effects of stability model uncertainty on computed Factors of Safety, reliability indices and probabilities of failure. Figures 6.170 and 6.176 show these effects on reliability charts.

In the first example, where the failure surface is shallow and translational, Factors of Safety that are similar in magnitude are obtained using different stability models. Janbu's Generalized Model gives results that are in good agreement with the rigorous

Morgenstern – Price Model. The discrepancies in the results are greater in reliability analyses and failure probabilities. This difference is, however, not very significant numerically.

In Example 2, the failure surface is deep and rotational. There is a more significant difference in Factors of Safety from different stability models in this example than in Example 1. This is much more evident in the computed probabilities of failure, and can lead to different conclusions on slope stability (reliability). The results from Bishop's Model are in good agreement with the rigorous Morgenstern – Price Model, whereas Janbu's Simplified Model underestimates Factors of Safety, and hence overestimates failure probabilities significantly.

The shape of the failure surface, therefore, is an important factor in determining the degree to which stability model uncertainty affects stability analyses, both deterministic and probabilistic.

Generally, for shallow translational failure surfaces, Janbu's Models compare well with the Morgenstern – Price Model, and although Bishop's Model underestimates Factors of Safety and failure probabilities, the results are comparable. Model uncertainty from stability models, is therefore not very important when the failure surface is translational. For deep rotational failure surfaces, Bishop's Model compares well with the Morgenstern – Price Model. Janbu's Models, particularly the Janbu Simplified Model can significantly underestimate Factors of Safety and failure probabilities. Model uncertainty from stability models, is therefore important when the failure surface is rotational.

For each stability model, Tables 6.40 and 6.42 show that probabilities of failure estimated from reliability analyses are in good agreement with those from the Monte Carlo analyses. This is because the distribution of Factor of Safety is well approximated by the Normal distribution when the uncertain parameters are the soil strength parameters, and these are Normally distributed, whether correlated or uncorrelated (see Figure 6.173). The stability models considered in this study follow the same general mathematical form of the Factors of Safety Equations in [6.47] and [6.50]. The difference lies in the value of λ, the interslice force function, which is assumed constant for each stability model, i.e. $\lambda = 0$ for Janbu's Simplified and Bishop's Models, and $\lambda = \lambda^*$ a

constant corresponding to the value of λ when both force and moment equilibrium are satisfied in the Morgenstern – Price Model. Hence the assumption of Normality of the Factor of Safety in computing probabilities of failure from $P_F = \Phi(-\beta)$ holds. This is true for different coefficients of variation of the uncertain parameters, and correlation.

6-2.2.4. STABILITY MODEL UNCERTAINTY IN BACK ANALYSIS OF SLOPES

In Chapter 2, we presented the case of a failed slope in Walton's Wood, England (Early and Skempton, 1959). The site conditions are shown in Figure 6.177.

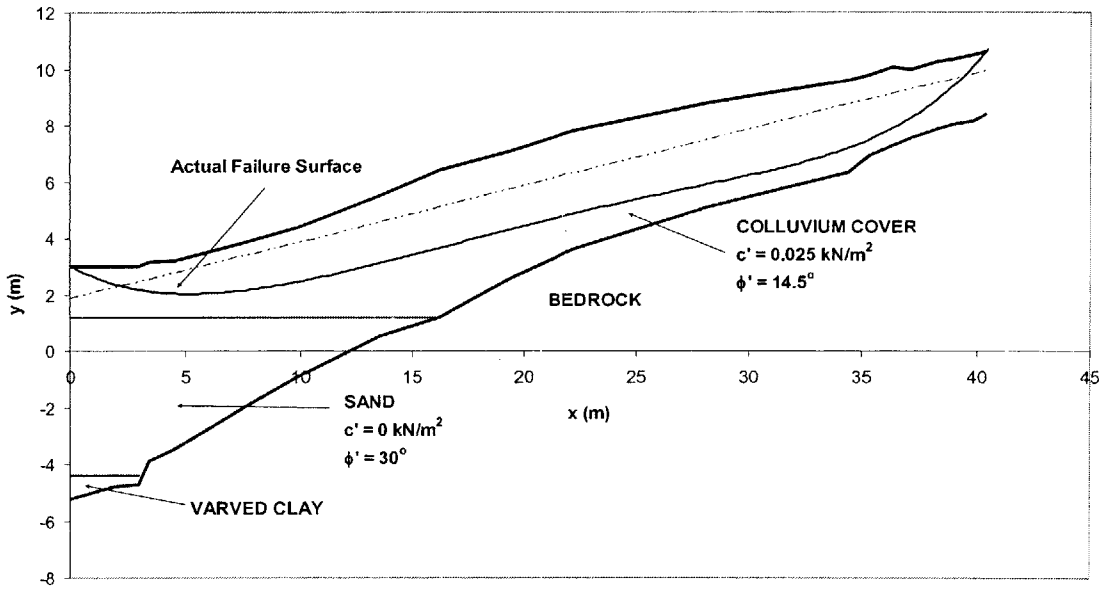

Figure **6.177.** Site Conditions and Actual Failure Surface of Landslide

We performed some back analyses of the failed slope, using c'=0 and ϕ'=14.8 as measured properties. Figure 6.178 shows a simple stability chart in terms of the effective stress parameters c' and ϕ' for that particular slope. A single set of laboratory tests were conducted and the results are shown as the encircled cross in Figure 6.178. We indicate with contour lines around this point how possible spatial variability and measurement uncertainties would show up. Figure 6.178 also illustrates model uncertainty from different stability models. It shows the results from stability models previously considered as well as those from the Ordinary Method of Slices (Fellenius, 1950). The region (band) of model uncertainty is not very significant numerically (with

the exception of the conservative infinite slope model) because of the regular nature of the failure surface. However, these differences can be critical in assessing the stability of slopes as in the Walton's Wood case where different models lead to different conclusions regarding stability (failure or no failure). The Infinite Slope Model suggests slope failure as the measure data lie in the unstable zone, whereas the other stability models suggest a stable slope. So, different conclusions on stability are reached depending on the stability model used.

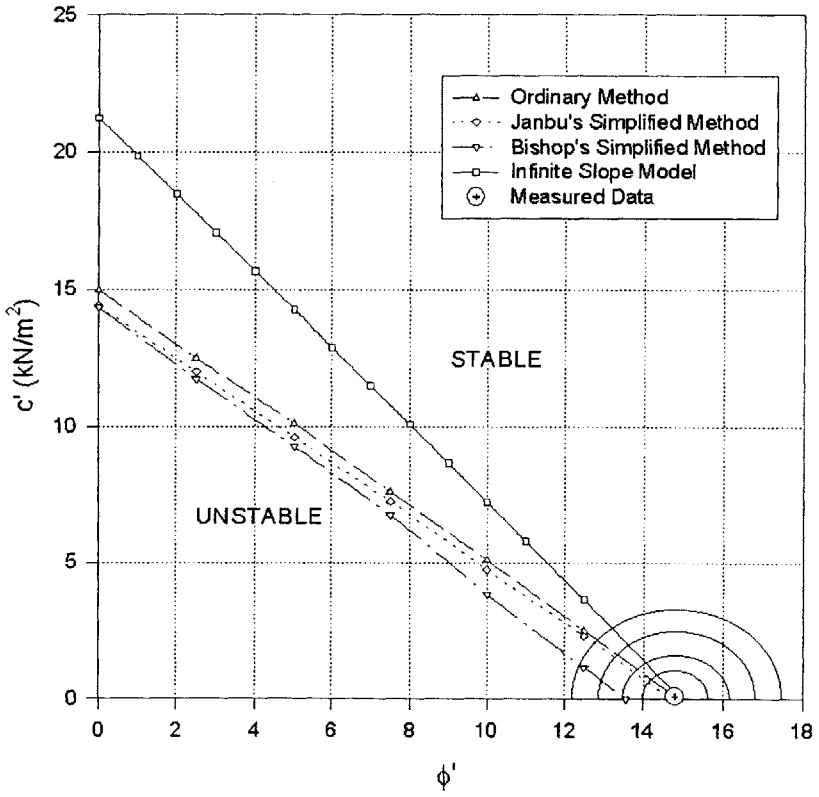

Figure **6.178.** Measurement and Model Uncertainty in a Simple Stability Chart for the Walton's Wood Landslide (Model Uncertainty Calculated, Measurement Uncertainty Estimated – see text)

6-2.2.4.5. STABILITY MODEL UNCERTAINTY IN LANDSLIDE HAZARDS ASSESSMENTS

In this Section, the effects of stability model uncertainty on landslide hazards are investigated. This is done in both deterministic and probabilistic contexts on two example slopes.

EXAMPLE 1: SHALLOW LANDSLIDE WITH TRANSLATION FAILURE SURFACE

Consider the slope shown in Figure 6.179.

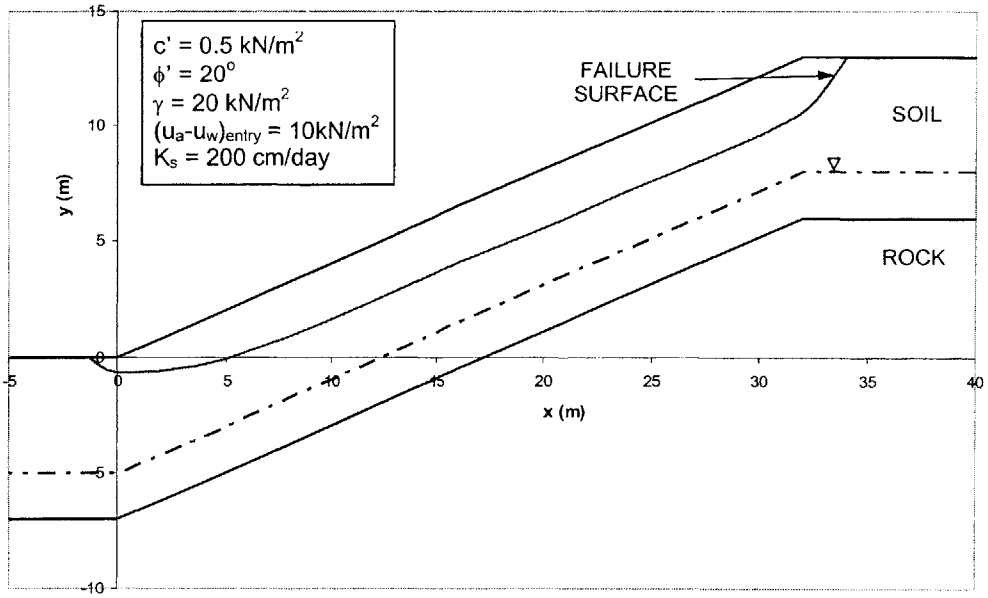

Figure 6.179. Slope Properties and Failure Surface

A rainfall event of intensity $I = 375cm/day = 155mm/hr$ is assumed to take place for a duration of 8 hours. Figure 6.180 shows moisture profiles, and Figure 6.181 shows pressure profiles at selected times.

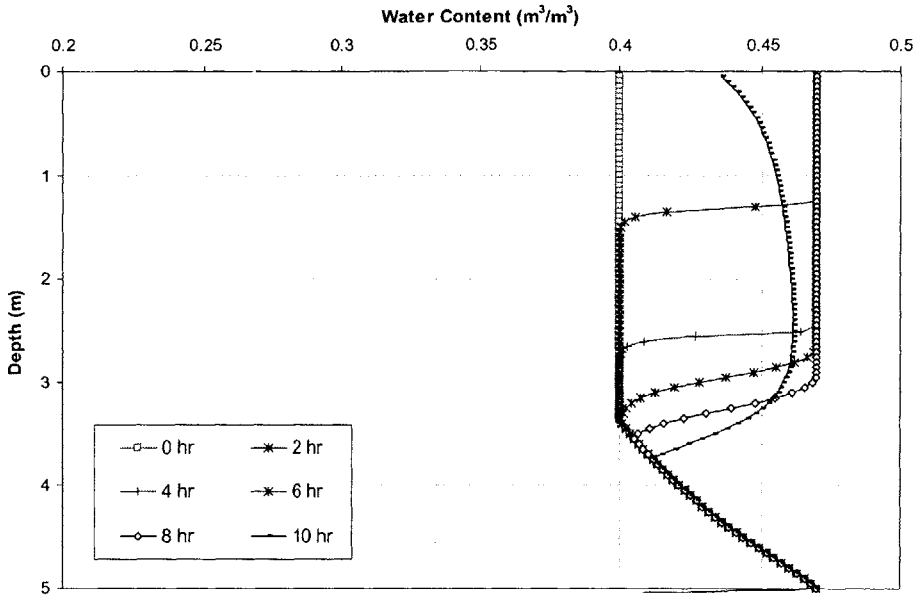

Figure 6.180. Moisture Content Profiles with Time using the van Genuchten (1980) Model

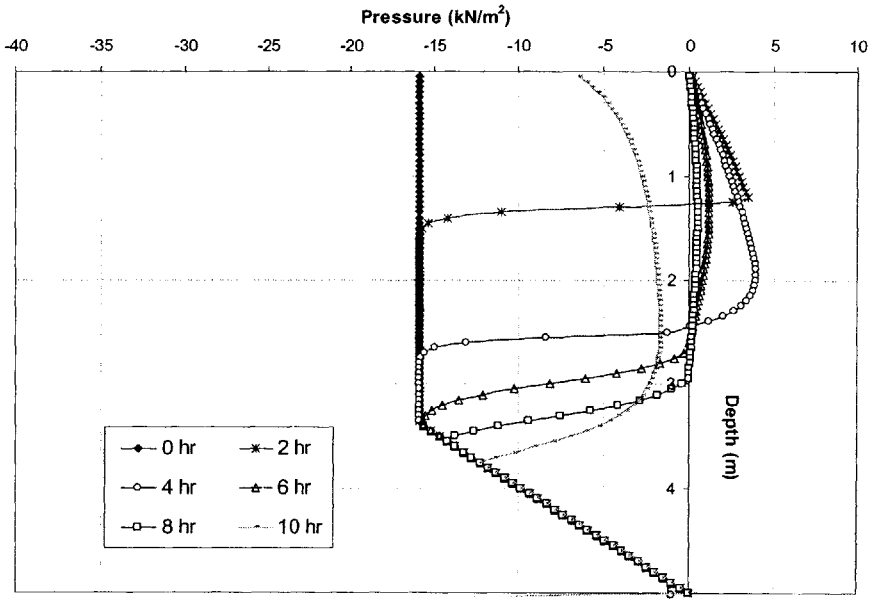

Figure 6.181. Pressure Profiles with Time using the van Genuchten (1980) Model

The stability of the slope is assessed using different stability models, and the results are shown in Figure 6.182.

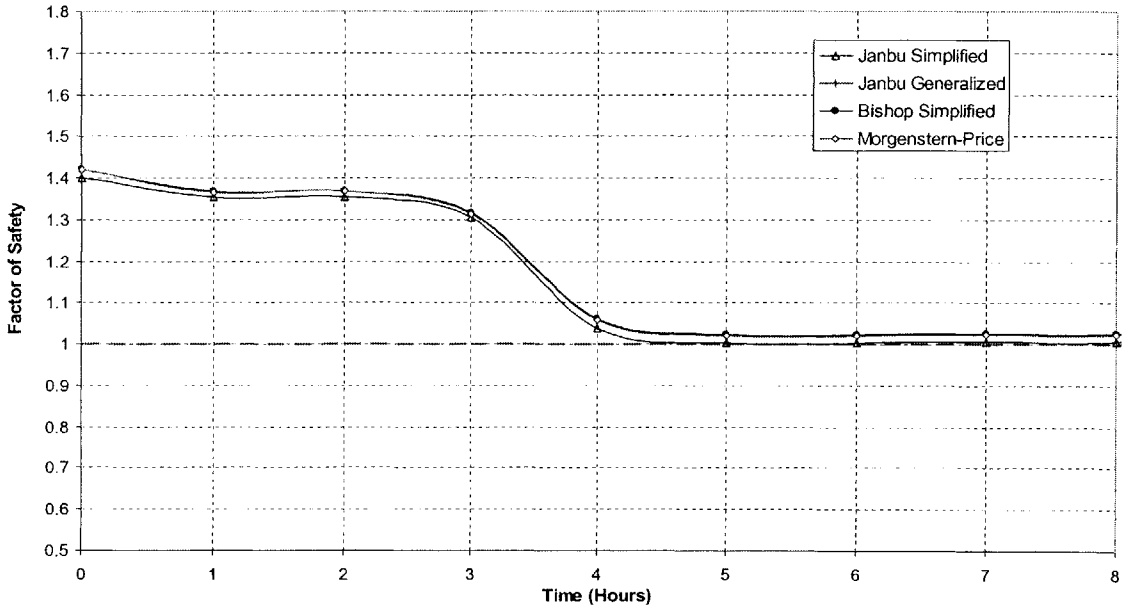

Figure **6.182.** Variation of Factor of Safety with Time Using Different Stability Models

Figure 6.182 illustrates stability model uncertainty in deterministic landslide hazards assessment. The effects in this particular example are not very significant numerically.

We now assume that the soil hydraulic and strength parameters are uncertain and follow the distributions:

$c' \sim N(m_{c'} = 0.5kN/m^2,\ \sigma_{c'} = 0.017kN/m^2)$; $\phi' \sim N(m_{\phi'} = 20^o,\ \sigma_{\phi'} = 6.67^o)$ and

$K_S \sim LN(\ m_{K_S} = 200cm/day, \sigma^2_{K_S} = (100cm/day)^2)$.

c', ϕ' and K_S are assumed uncorrelated.

Figure 6.183 shows the effects of stability model uncertainty on probabilistic landslide hazards assessment.

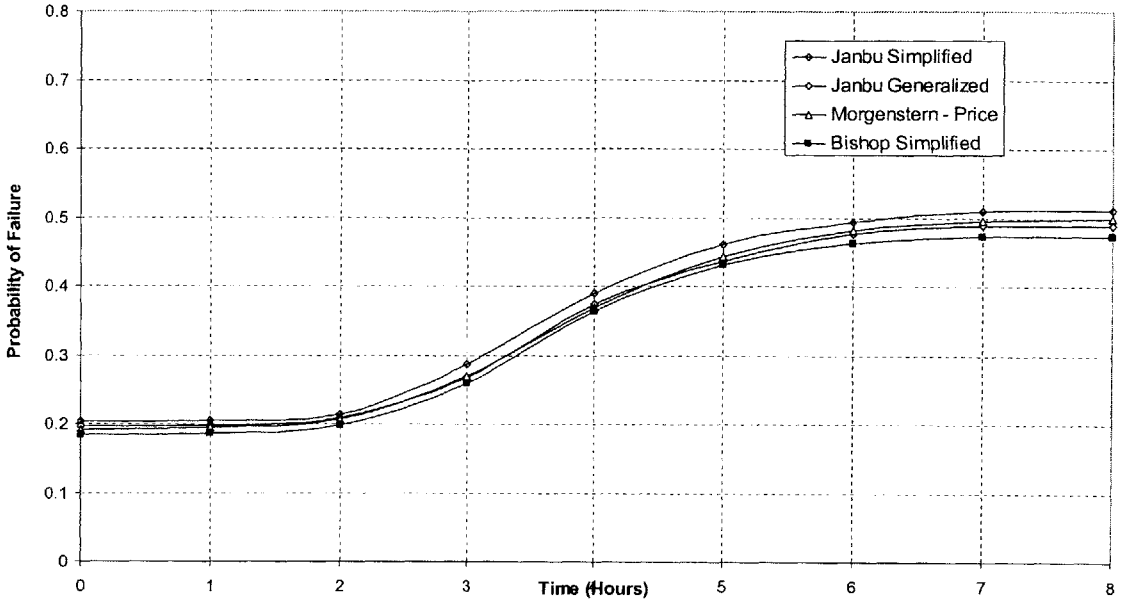

Figure 6.183. Variation of Failure Probability with Time Using Different Stability Models

Figure 6.183 again shows that the results are not very significant numerically in this particular example. This is because of the translational, and regular shape of the failure surface (see Figure 6.179). The fact that the hydraulic conductivity of the soil is randomized does not have a significant effect on the differences in the computed Factors of Safety in Figure 6.183. This makes sense, since randomizing the hydraulic conductivity will have the same effects in each of the stability models, and hence the stability analyses considered. The results in Figure 6.183 and conclusions made there from, are the same as those made in Section 6-2.2.4, namely that stability model uncertainty does not have a significant influence on slope stability analyses, and landslide hazards assessment when the failure surface is regular. This is discussed further in the next Section.

6-2.2.6. DISCUSSION ON STABILITY MODEL UNCERTAINTY

The results in Sections 6-2.2.4 and 6-2.2.6 show that the effects of stability model uncertainty on deterministic and probabilistic landslide hazards assessment depend on the shape of the failure surface. The effects are not very significant numerically for regular translational surfaces, and become more significant as the surface becomes more irregular and rotational. In such instances different stability models can lead to different conclusions regarding slope stability and reliability, and hence different estimates of hazard.

Comparing the results from different simplified models (Janbu's and Bishop's) with those obtained from the rigorous Morgenstern – Price Model, we conclude that the shape of the failure surface, in general, will also dictate the best method for analyzing the state of stability (or reliability) of a slope.

1. For shallow, long planar failure surfaces that are parallel to the ground surface, models that satisfy force equilibrium, such as the Janbu Simplified and Rigorous Models can be used with reliable accuracy.
2. For failure surfaces that can be approximated by arcs or circles, models that satisfy moment equilibrium, such as the Bishop Simplified Model can be used with reliable accuracy.
3. For better accuracy, and whenever possible, the Morgenstern – Price Model should be used.
4. For important landslide hazard assessments, the GLE model should be used to assess stability (and reliability) for different values (functions) of λ, since it encompasses other stability models.

6-2.2.7. CONCLUSIONS ON STABILITY MODEL UNCERTAINTY

Stability model uncertainty and its effects on slope stability and reliability analyses were investigated. This was illustrated for circular and non circular failure surfaces. Two examples slopes were used to study the effects of stability model uncertainty in slopes with non circular failure surfaces. The first assumes a shallow translational failure surface, and the second assumes a deep rotational surface. We showed that the extent of stability model uncertainty is dependent on the shape of the failure surface. The results can vary significantly when the failure surface is rotational, leading to different conclusions regarding stability.

The effects of stability model uncertainty are more significant in probabilistic analyses than they are in deterministic analyses.

The shape of the distribution of Factor of Safety from Monte Carlo analyses is unaffected by the model used to asses stability, since they have the same mathematical form given by the GLE Model. The Factor of Safety is well approximated by the Normal distribution, when the uncertain parameters are the soil strength parameters, and these are Normally distributed. As a consequence, estimating probabilities from second moment reliability analyses give results that are in good agreement with those from Monte Carlo analyses, irrespective of the stability model used.

The effects of stability model uncertainty on landslide hazards were also investigated. Landslides caused by the saturation from the surface downwards by infiltrating rainwater (see Chapter 3) typically have failure surfaces that are shallow and translational. Stability model uncertainty does not have a significant effect on hazard assessments of such slides because of the regular nature of the failure surface. However, and as was discussed in Chapter 3, there are other landslide mechanisms that lead to different shapes of the failure surface. When the failure surface is located deep along the soil bedrock interface, for example, for landslides caused by saturation from below, then stability model uncertainty will have a more significant impact on the results of hazards assessments. This was shown in Example 2 of Section 6-2.2.4. We can therefore conclude that stability model uncertainty has to be investigated on a case by case basis when assessing landslide hazards, and its importance should be determined from such analyses.

6-3. CONCLUSIONS ON MODEL UNCERTAINTY

In this Chapter, model uncertainty and its effects on hydrologic and stability modeling, and landslide hazards assessments was studied. .

Model uncertainty in hydrologic models comes from the hydrologic models themselves, and from models (submodels) used within the hydrologic models, particularly the soil characteristic curve models.

There are two types of hydrologic models:

(a) Models that solve the pressure based form of the flow Equation, and
(b) Models that solve the moisture based form, from which pressures are inferred.

Model uncertainty from the type (a) models is not very significant, because the models basically solve the same mathematical Equation, with the same initial and boundary conditions. For such models, model uncertainty from the models themselves in not very significant, but model uncertainty from the submodels (particularly the soil characteristic curves) is a significant source.

Model uncertainty from type (b) models is very significant. Moisture distributions are inferred from pressure distributions, and assumptions are required to do so. Different assumptions can result in very different results and conclusions on stability. Model uncertainty from submodels (characteristic curves) plays a less important role in contributing to model uncertainty in the results.

Model uncertainty in stability models comes from the stability models themselves, and from models (submodels) used within the stability models. These submodels are models such as for unsaturated soil strength, parameter probability distributions, and correlation. Stability analyses require one to postulate a failure mechanisms, even, to a certain extent those models that search for the critical failure surface. It is essential that the postulated mechanism be the appropriate/critical one, and several trial failure surfaces need to be assessed prior to determining the critical failure mechanism.

There are two types of (Limit Equilibrium) stability models, simplified models, such as Janbu's and Bishop's, and rigorous, such as the Morgenstern – Price Model. Model uncertainty from the stability models themselves is not very significant because this depends on the shape of the failure surface, and in general, shallow landslides exhibit regular translational failure surface. Model uncertainty from the submodels can however, be very significant. The results on different slopes show that:

(a) Correlation between strength parameters has a significant effect on slope landslide hazards, more so than the actual probability distribution of the parameters (Normal and Lognormal)

Since shallow landslides frequently have failure surfaces in unsaturated soil:

(b) The unsaturated strength model has a significant effect on landslide hazards
(c) Seepage direction, particularly in unsaturated soil, also has a significant effect on landslide hazards

In general, if appropriate hydrologic models (those that solve for pressures) and stability models (with the critical postulated failure mechanism) are used in landslide hazards assessment, then model uncertainty from the submodels used in stability analyses are the most significant source.

The results show where models need to be developed and used. Model uncertainty from correlation models can be, to a certain extent, approximated through extensive laboratory experiments and field measurements. Seepage direction, can also, to a certain extent, be measured in the field.

There is however a need to develop more adequate, and reliable unsaturated strength models, and means to estimate the parameters of such models. These models will, undoubtedly, depend on the soil characteristic curves, and so, as an initial step, there is a need to develop more adequate models to represent unsaturated soil properties, and methods to determine the parameters of such models. This will, in turn, reduce model uncertainty in hydrologic analyses that arises from the characteristic curve models used in the analyses.

This Chapter aimed at bringing to attention the importance of model uncertainty in landslide analyses, which rely heavily on models, rather than to provide specific solutions to the problem. It is by no means a rigorous assessment of model uncertainty and its effects on landslide analyses, but showed how complex the issue is. Only the effects of a particular source of model uncertainty were studied at one time, e.g. from strength models in the same stability model, and this was complex enough. The issue becomes much more complex and difficult to study if model uncertainty from two or more sources is considered at the same time. For example, assessing the effects on stability of different strength models used in different stability models, or on landslide hazards of different strength models in the stability model, with different characteristic curve models in the hydrologic model. Another example involves investigating the effects of the (negative) correlation between the soil strength parameters, at the same time as another source of model uncertainty on stability analyses, and landslide hazards.

In order to do this, one would essentially need to consider two sources of model uncertainty, and evaluate their effects on stability, hydrologic, and/or combined modeling (landslide hazards) simultaneously. As an example, consider models for strength, and stability. These are two sources of model uncertainty that affect stability analyses, and landslide hazards. If one were to investigate the effects of model uncertainty from both sources, then what one needs to do is consider the effects of using different strength models in different stability models. If one considers only two models for strength, the Effective Stress Model (Bishop, 1959), and the Independent State Variable Model (Fredlund et al., 1978), and only two models for stability, Janbu's Generalized Model (Janbu, 1979), and Bishop's Simplified Model (Bishop, 1959), then one would need to evaluate the effects of using the following combinations of models on stability analyses and landslide hazards:

(a) The Effective Stress Model (Bishop, 1959) in Janbu's Generalized Model (Janbu, 1979), and the Independent State Variable Model (Fredlund et al., 1978) in Bishop's Simplified Model (Bishop, 1959).
(b) The Effective Stress Model (Bishop, 1959) in Bishop's Simplified Model (Bishop, 1959), and the Independent State Variable Model (Fredlund et al., 1978) in Janbu's Generalized Model (Janbu, 1979).

In addition to:

(c) The Effective Stress Model (Bishop, 1959) and the Independent State Variable Model (Fredlund et al., 1978) in Janbu's Generalized Model (Janbu, 1979).
(d) The Effective Stress Model (Bishop, 1959) and the Independent State Variable Model (Fredlund et al., 1978), in Bishop's Simplified Model (Bishop, 1959).

While points (c) and (d) involve investigating the effects of model uncertainty from one source (strength), and have been discussed in this Chapter, points (a) and (b) involve investigating the effects of model uncertainty from two sources. This has not been done in this Chapter, although it can be done in a similar way to what has been done in this Chapter. The results of the model uncertainty investigations are not immediately obvious, in that it is not clear whether model uncertainty from two sources leads to greater/smaller uncertainty in stability analyses, and landslide hazards assessments. Detailed investigations of this type eventually need to be done to address this. It is also quite evident that the number of combinations of models that this needs to be done for quickly increases as the number of models considered increases, and hence will require extensive further studies.

The issue of model uncertainty becomes even more complex, and almost impossible to study if parameter uncertainty in the models is considered as well, since these are related, i.e. more refined models are better at representing reality, and reduce the effects of model uncertainty, but also may require specification of a greater number of parameters than simpler models, and these are subject to parameter uncertainty.

While this is not considered in this Chapter, the Chapter did, nonetheless, shed some light into the effects of model uncertainty on landslide hazards assessments, and showed that these effects can be very significant. In particular, it highlighted the relative significance of the different types of model uncertainty. This helps in determining where it is worthwhile to refine and/or use better models. It also presented ways in which model uncertainty can be assessed, and given their significance these should be accounted for, one way or another, in landslide hazards and risk assessments.

CHAPTER 7

CONCLUSIONS AND RECOMMENDATIONS

7.1. CONCLUSIONS

Landslides are natural phenomena which often have detrimental consequences. Landslide hazards can be systematically assessed by using the principle of decision making under uncertainty (Figure 7.1). This was done in this study.

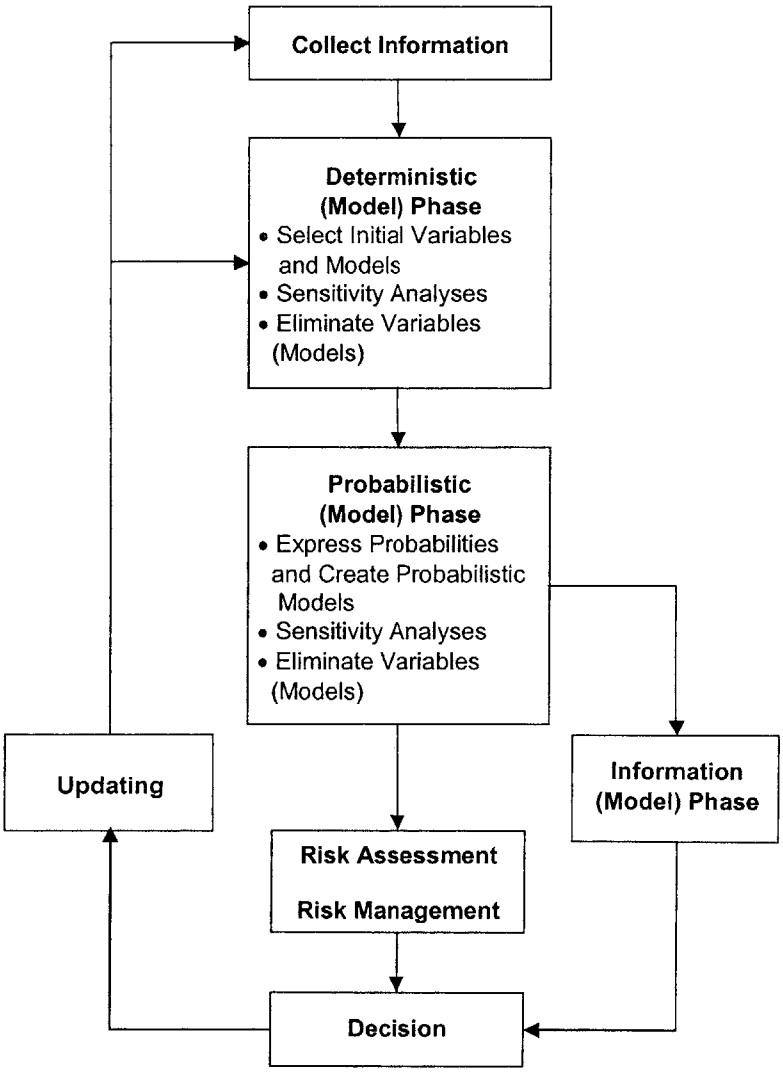

Figure 7.1. The Decision Analysis Cycle

Specifically, this study attempted to evaluate landslide hazards, and is therefore mainly concerned with the deterministic, and probabilistic phases of the decision making process shown in Figure 7.1.

In the deterministic phase, one selects the initial variables, and develops deterministic models. In Chapter 2, a model to assess landslide hazards in a deterministic context was developed. The model is based on combined hydrologic and stability analyses, for which advanced hydrologic and stability models had to be first developed:

(a) **Hydrologic Model:**

The hydrologic model is a one dimensional finite difference infiltration model. It is more advanced than other infiltration models being currently used in landslide analyses because:

i. It solves the variably saturated flow equation, and is thus capable of accounting for both saturated and unsaturated flow processes.
ii. It involves a variable top boundary condition which automatically changes from being flux driven, when the layer of soil near the slope surface is not fully saturated and rainwater enters the soil, to being head driven, when the layer of soil near the slope surface is fully saturated, and the soil cannot accept additional rainfall, which is observed as surface runoff.

(b) **Stability Model:**

The stability model is a two dimensional limit equilibrium model that is based on the Janbu Generalized procedure of Slices (1978). It is more advanced than other stability models being currently used in landslide analyses because:

i. It includes a search for the critical failure surface in a slope, along which the Factor of Safety is minimum
ii. It incorporates unsaturated soil strength, which is critical in landslide analyses, particularly in shallow landslides. Specifically, the Effective Stress Model (Bishop, 1959) is used for unsaturated strength, a model which is re-gaining popularity amongst investigators in the field, and has, thus far, not been widely used in landslide analyses.

(c) **Combined Model:**

When combined, the hydrologic – stability model is more advanced than current combined models being used in landslide analyses, because it includes a time dependent state of stability analysis. This combined model allows one to assess landslide hazards deterministically.

The combined model was then used to study the mechanisms of landslides in Chapter 3. We showed that there are two distinct ways in which landslides can occur, which are related to the manner in which a slope gets saturated during rainfall, namely saturation from below by a rising water table, and saturation from above by infiltrating rainwater. It was shown that in general:

(i) Slopes with great depths to bedrock and shallow depths to the water table, tend to fail by saturation from below, with failure surfaces typically along the soil bedrock interface resulting in a deep seated landslide. Such landslides occur because the rise in the water table causes an increase in the pore pressures at the soil bedrock interface.

(ii) Slopes with deep water tables tend to fail by saturation from above, with shallow failure surfaces that are located above the water table. Such landslides occur because the infiltrating rainwater increases the pore pressures (reduces or eliminates the initial suction, or causes positive pressures to develop) in the otherwise unsaturated zone of the slope. Since the mechanisms of these shallow landslides are not well understood, they were studied in detail in Chapter 3. We showed that when the infiltrating rainwater reduces the initial suction, this may be sufficient to generate a landslide. This is an important result since it remains a matter of debate amongst investigators in the field. While it is well known that positive pressures can develop when a low conductivity heterogeneity, e.g. a clay lens, exists in the subsurface, we showed that there are several other mechanisms by which this can happen. Positive pressures can develop:

    (ii)-1. Gradually, for example when there is a decrease in the hydraulic conductivity of the soil with depth, or

(ii)-2. Suddenly, when rate of infiltration suddenly exceeds the water transmission rate of the soil, for example, when there is a sudden increase in rainfall intensity.

This can occur in both homogenous and heterogeneous soils, and these positive pressures can ultimately generate a landslide.

We also showed that failure can take place during a rainfall event as a result of the increase in pore pressures, or after the end of rain, because of pressure redistribution. For the same strength parameters, and initial conditions, we showed that uniform soils tend to be more susceptible to failure than well graded soils, because of the lower contribution of suction to unsaturated strength.

Landslide hazards include, by definition, the expression of uncertainties in probabilistic form, and these uncertainties enter all the different stages of the landslide hazard procedure. Chapter 4 described the sources of uncertainties as they relate to landslide analyses. Deterministic sensitivity analyses were performed to investigate the relative effects of different parameters on hydrologic and stability analyses. We showed that the most influential variable in hydrologic modeling is the hydraulic conductivity of the soil, and the most influential variables in stability modeling are the soil strength parameters. These results allow one to formally eliminate the other variables that have a less significant influence on the results.

In Chapter 5, techniques were described by which parameter uncertainties can be formally incorporated into the hazard assessment procedure. These techniques are efficient, spreadsheet-based and simple to implement and allow one to evaluate the reliability of a system, e.g. slope, using second moment reliability methods, based on the Hasofer and Lind (1974) reliability index, and probabilistically based on the Monte Carlo method. Specifically, this showed the following effects of parameter uncertainties:

(a) **Hydrologic Modeling:**

Hydrologic modeling showed that sharp wetting fronts tend to develop in uniform soils, and that, consequently, uncertainties in the moisture profiles are large and localized near the wetting front. Well graded soils do not develop sharp wetting fronts and uncertainties in the moisture profiles are small and spread over a large depth.

(b) **Stability Modeling:**

Stability modeling showed that the distribution of the Factor of Safety in a slope is closely related to the probability distribution of the strength parameters. When the soil strength parameters are Normally distributed, the distribution of the Factor of Safety can be well approximated by the Normal distribution. Because of this, and because a linear approximation of the Factor of Safety Equation with respect to the strength parameters is a good one, the results of First-Order Second Moment and Second Moment reliability analyses, and probabilistic analyses based on Monte Carlo methods are in good agreement.

(c) **Combined Modeling:**

Combined modeling showed that the soil strength parameters have a greater effect on landslide hazards than the soil hydraulic conductivity. As a result, the distributions of the Factors of Safety with time during and after a rainfall event, are highly dependent on the distributions of the strength parameters. We therefore conclude that with regard to parameter uncertainty, for more accurate landslide hazards evaluations, better information on the distributions of the strength parameters is required.

Chapter 6 studied model uncertainty and its effects on landslide hazards assessments. This is the least understood and most difficult source of uncertainty to capture. Model uncertainty arises because of the simplifications and assumptions in the models (and submodels) used in hydrologic, stability and combined modeling. Chapter 6 showed the following sources and effects of model uncertainties:

(a) **Hydrologic Modeling:**

Model uncertainty in hydrologic models comes from the hydrologic models themselves, and from models and submodels used within the hydrologic models.

i. Hydrologic models can be classified into models that solve the flow Equation for pore pressures, and models that solve the flow Equation for moisture distributions from which pressure distributions are inferred. Model uncertainty from the former is not significant, but it is from the latter because assumptions need to be made to infer pressure distributions from moisture distributions, and different assumptions can lead to significantly different pressure distributions.
ii. Submodels typically used in hydrologic models include those for the soil characteristic curves such as the van Genutchen (1978) and Bresler et al. (1981) models, as well as models for stable infiltration, amongst others. It was shown that the characteristic curve submodels are the most significant source of model uncertainty from submodels, and in fact, these are a more significant source of model uncertainty than the hydrologic models themselves.

(b) **Stability Modeling:**

Model uncertainty in stability models comes from the stability models themselves, and from models and submodels used within the stability models.

i. Stability models (Limit Equilibrium) can be classified into models that satisfy force equilibrium, models that satisfy moment equilibrium, and models that satisfy both force and moment equilibrium, known as rigorous models. Model uncertainty from stability models depends on the shape (geometry) of the failure surface. In the case of shallow landslides with regular, translational failure surfaces, model uncertainty from stability models is not a very significant source.
ii. Submodels typically used in stability models include those for unsaturated soil strength, such as the Effective Stress Model (Bishop, 1959), and the Independent State Variable Model (Fredlund et al., 1978), parameter probability distribution, seepage direction, amongst others. It was shown that the submodels for unsaturated soil strength, and correlation between strength parameters are the most significant

source of model uncertainty from submodels. These are a more significant source of model uncertainty than the stability models themselves.

(c) **Combined Modeling:**

Model uncertainty in combined models comes from the model uncertainty in hydrologic and stability models. We showed that model uncertainty from stability models, are more significant sources of model uncertainty in combined models, and hence landslide hazards assessments, than model uncertainty from hydrologic models.

Although Chapter 6 does not provide specific solutions to the model uncertainty problem, it does shed some light into the effects of model uncertainty on landslide hazards assessment, and where better models need to be developed. This is discussed in the following section.

7.2. Recommendations and Future Work

Despite recent efforts and advances in the field of landslides, a comprehensive hazard assessment still remains a challenge. This is due to the complexity of the phenomena, the many factors that affect it, and the associated incomplete understanding of the mechanisms involved. There are several ways in which current landslide analyses can be improved which include:

(a) More accurate information on parameters
(b) Better understanding of landslide mechanisms
(c) Developing better hydrologic, stability and combined models and submodels
(d) Formal incorporation of uncertainties

Obtaining more accurate information on parameters (point (a) above) decreases parameter uncertainty, and leads to improved landslide analyses. Chapters 4 and 5 studied parameter uncertainty, and in light of the results recommendations are made in the following section.

There exists an interrelationship between understanding the mechanisms of landslides (point (a) above) and developing the models required to do so (point (b) above). In order to better understand the mechanisms, models that are better suited for landslide analyses need to be developed. These models, in turn, require a better understanding of the mechanisms. A cyclic process of modeling landslides, and understanding their mechanisms needs to be applied. Because of this, recommendations are made to develop better models (point (b) above) in the following section. Based on this, landslide mechanisms can be better understood.

Chapters 5 and 6 studied uncertainties, and presented techniques in which uncertainties can be formally incorporated into the assessment procedure (point (d) above). Recommendations based on the results of these Chapters are made in the following section.

(a) More accurate information on parameters

The results of the deterministic sensitivity analyses in Chapter 4, and the probabilistic analyses in Chapter 5 have shown which parameters are most important in landslide analyses. Based on the results of these Chapters, the following recommendations are made:

(i) Hydrologic Models

We showed that the most important parameter in hydrologic modeling is the hydraulic conductivity of the soil. A better knowledge of the hydraulic conductivity through extensive field and laboratory tests is therefore recommended for more accurate landslide hazards estimations.

(ii) Stability Models

We showed that the most important parameters in stability modeling are the soil strength parameters. A better knowledge of these parameters through extensive field and laboratory tests is recommended for more accurate landslide hazards estimations. We, in particular, showed that the correlation between strength parameters has a significant

influence on stability modeling, and so better techniques to estimate correlation is recommended for more accurate landslide hazards evaluations.

(iii) Combined Models

We showed that the soil strength parameters have a greater effect on landslide hazards than the soil hydraulic conductivity. We therefore conclude that for more accurate landslide hazards evaluations, better information on the distributions of the strength parameters is required.

The recommendations in this section relate to obtaining more accurate information on parameters. Issues relating to obtaining more accurate information must thus, be taken into account. These are issues which include representative sampling whether in the field or in the laboratory, sample disturbance, testing methods and procedures, etc. Ideally, an optimal sampling/testing/exploration plan can be devised and used.

(b) Developing Better Models and Submodels

Improvements to the models and submodels used in landslide analysis include:

(i) Trigger Models

The trigger in rainfall induced landslides, is rainfall, and rainfall models need to be developed and used in landslide analyses. Rainfall models used in current landslide studies, including this one, simply assume that a rainfall event can be represented by a mean rainfall intensity, and a duration of the rainfall. Better models that model the variation of these characteristics with time are needed to more accurately represent these events.

(ii) Hydrologic Models and Submodels

Chapter 6 studied the effects of hydrologic model uncertainty on hydrologic analyses, and landslide hazards, both quantitatively and qualitatively. It showed that the most significantly source of uncertainty comes from submodels used for the soil characteristic

curves. So better models for these are needed for more accurate landslide hazards assessments. This is described in the following. Also described are some of the most important improvements that need to be made in hydrologic models.

(ii)-1. Submodels

Characteristic Curve Submodels: In Chapter 6, we showed that the submodels for the soil characteristic curves can have a very significant influence on hydrologic analyses, and landslide hazards. There is, therefore, a need to develop better models to represent the characteristics of unsaturated soils. To be able to do this, better laboratory equipment, and techniques to measure unsaturated properties, particularly the soil suction need to be developed. Research is currently being undertaken at the laboratories at MIT to do this (e.g. Sjoblom, 2000; Toker, 2002, 2004). Developing better models to represent the soil characteristic curves will, most probably, require the introduction of additional parameters. Difficulties may be encountered in measuring these parameters, and the added parameter uncertainty because of the introduction of additional parameters need to be taken into consideration when developing better models. There is an added complication regarding the soil characteristic curves, specifically that they exhibit hysteresis. This is important since wetting of the soil occurs during rainfall, and infiltration, and drying occurs at the end of rain, during moisture redistribution.

Unstable Infiltration Submodels: One of the fundamental assumptions of the infiltration model developed in Chapter 2, and the vast majority of commonly used infiltration models is that of stable infiltration. During stable infiltration, rainwater is assumed to infiltrate the slope in the form of a stable wetting front. While this is the case when the rainfall intensity (application rate) is greater than the saturated conductivity of the soil at the surface, experimental evidence has shown that this is frequently not the case when the rainfall intensity (application rate) is less than the saturated conductivity of the soil, e.g. Hills (1969), Parlange (1982), Culligan and Parlange (1998). When the rainfall intensity (application rate) is less than the saturated conductivity of the soil, preferential flow or fingering takes place in both heterogeneous and homogenous soils. Several models have been developed to predict finger development and propagation e.g. Dekker, 1998, but these remain crude at best. This is because the mechanisms of

finger development are poorly understood. With the better understanding of these mechanisms, and the development of more representative models, these should be incorporated into infiltration models, such as the one developed in Chapter 2, thereby accounting for finger phenomena.

(ii)-2. Models

Multi - Dimensionality: The majority of hydrologic models used in current landslide analyses are one-dimensional, and although the processes of infiltration are predominantly vertical, two and three dimensional effects can be included to refine the model. While during the infiltration process, when it is raining on a slope, water travels downwards into a slope, this is not necessarily the case during the redistribution process, after the end of rain. Under some circumstances, moisture (and pressure) redistribution in the horizontal direction can be significant. This is the case, for example, when the hydraulic conductivity of the soil in the horizontal direction is of similar magnitude as the hydraulic conductivity in the vertical direction.

Coupled Infiltration and Subsurface Flow Models: Hydrologic models that have been used in landslide analyses have been either infiltration models, or subsurface flow models. Infiltration models, such as the model developed in Chapter 2, model the effects of rainwater infiltration on the single slope scale. These models predict the changes in moisture (and pressure) distributions as the rainwater enters the slope from the surface. Subsurface flow models, on the other hand, are models for groundwater flow usually on the regional, e.g. catchment basin scale. These models predict changes in moisture (and pressure) distributions, or in effect groundwater levels, and subsurface flow regimes. They include regional scale effects such as recharge from higher altitude slope sectors, convergent or divergent flow with changes in topography, exfiltration from bedrock, amongst other factors. In order to better model the effects of rainfall on the hydrologic response of a slope, it is necessary to develop a model that includes both an infiltration model, as well as a groundwater recharge model. This model would, in essence, be a combination of an infiltration model such as the one developed in Chapter 2, and a subsurface flow model. In doing so, the complete hydrologic response of slopes to rainfall can be determined, and this would include simultaneously assessing the effects of infiltrating water, and subsurface flow regimes, such as groundwater recharge, etc.

(iii) Stability Models and Submodels

Chapter 6 studied the effects of stability model uncertainty on stability analyses, and landslide hazards, mostly quantitatively but also qualitatively. It showed that the most significantly source of uncertainty comes from submodels used for unsaturated soil strength, correlation between strength parameters, and seepage direction. So better submodels for these need to be developed for more accurate landslide hazards assessments. This is described in the following. Also discussed are improvements and refinements that need to be made to the majority of stability models used in current landslide analyses. There naturally is a long list of such improvements, but selected are a few that are most important.

(iii)-1. Submodels

Unsaturated Strength Submodels: The results of this study have shown that the submodels used in stability analyses can have a very significant influence on hydrologic analyses, and landslide hazards. Submodels for unsaturated soil strength, parameter probability distribution and correlation, and seepage direction are particularly important. While the probability distributions and correlation between parameters, can be estimated by extensive laboratory studies, and seepage direction can be estimated by field measurements and observations, there is a need to develop better models to represent unsaturated soil strength. Developing better models for unsaturated strength will, as an initial step, require the development of better models for the soil characteristic curves, since unsaturated strength is dependent on these. This was described in (a) of the preceding section. As was also stated in point (a) developing better models, typically requires the introduction of additional parameters, and the added parameter uncertainty associated with these parameters needs to be accounted for.

(iii)-2. Models

Limit Analysis Stability Models: The majority of stability models used in current landslide analyses, as well as the stability model developed in Chapter 2, rely on Limit Equilibrium Methods. These are relatively simple and easy to implement with common tools such as a spreadsheet as described in Chapter 2. Upper and Lower Bound

Solutions to the statically indeterminate stability problem have been developed and have found occasional use. These are based on Limit analysis, which takes advantage of the lower and upper bound theorems of plasticity theory to provide rigorous bounds on the true solution of a stability problem. Statically admissible stress fields are constructed for lower bound analysis and kinematically admissible velocity fields are constructed for upper-bound analysis of soil slopes. Models to solve these are more computationally intensive and often require finite element analyses. For a better landslide hazards assessment, such finite element models can be used in conjunction with Limit Equilibrium Methods to determine the state of stability of a slope more accurately. Having said this, and because of the complexity of Upper and Lower Bound Solutions, as well as the finite element method itself, care has to be taken to ensure that any model developed as such must remain easy to understand and simple to implement.

Model Dimensionality: The majority of stability models being used in current landslide analyses are one (e.g. Infinite Slope Model, Skempton and DeLory, 1959), or two dimensional (e.g. Janbu's, 1959, 1978, and Bishop's 1959, Models) models. These models assume that the geometry of landslides, particularly shallow landslides is such that the depth to length ratio is small, and that the width of landslides is great. In such geometries, three dimensional effects are not very significant. Having said this, three dimensional effects become important when the landslide geometry is not as what has just been described. Different models exist to include three dimensional effects, and these should be accounted for in more accurate stability models.

Displacements: The majority of stability models are 'static' models in the sense that they do not include the effects of movements in slopes on stability. These movements or displacements can be important particularly in the case of slow moving (active) landslides, and creeping slopes. While displacements have been somewhat accounted for in various landslide hazards studies, this has been, for the most part, done subjectively. A better knowledge of the creep phenomena is needed before better models to represent it can be developed, and later included in stability analyses. Alternatively, these displacements can be accounted for through an updating process (the updating cycle in Figure 7.1), where the prior state of stability of a slope is updated given the observations of slope movements (displacements) through a Bayesian type analysis, to result in the posterior state of stability. While this is a possibility, there has, as of yet, not been any attempt to account for displacements this way.

Progressive Failure: The majority of stability models used in current landslide analyses, do not include progressive failure. The mechanisms by which progressive failure takes place are not yet well understood, and this is reflected through the lack of models to represent progressive failure. Nevertheless, it is important to include progressive failure particularly since landslide tend to occur in mountainous regions.

Following on what has been said above specifically that landslides tend to occur in mountainous regions, it is also important to include regional effects in stability modeling. These are large scale effects, such as the effects of failing higher altitude slopes on the stability of lower altitude slopes. This, in general, will require models to predict landslide velocity, and runout distance (and volume). These processes are also not well understood making it difficult to include them in current stability models.

Vegetation: The majority of stability models used in landslide analyses do not include the effects of vegetation on stability. Vegetation is general influences the stability of a slope in two opposing ways:

i. The vegetation root strength increases the stability of a slope by literally holding together the soil at the slope surface. Attempts have been made to include root strength in stability analyses as a component of the cohesion of a soil, but this has not gained wide acceptance. Better models are needed to include the effects of root strength on stability.

ii. The weight of vegetation on a slope surface (particularly large trees) adds a destabilizing component to slopes, and hence decreases stability. While this has been recently acknowledged, it is not widely accounted for in stability analyses.

(iv) Combined Models

Combined models couple hydrologic models with stability models. Developing better hydrologic and stability models, therefore, will lead to the development of better combined models. There is another issue, however that arises, namely that of model validation.

The infiltration model developed in Chapter 2 was validated by comparing the results of numerical analyses to the results from infiltration experiments. The stability model developed in Chapter 2 was validated by assessing the stability of a failed slope and comparing the location of the predicted critical failure surface with the one obtained from field observations. The combined hydrologic – stability model developed in Chapter 2, was, however, not validated. To do so requires the simultaneous validation of the hydrologic and stability models. This, in turn, requires simultaneous information on rainfall characteristics, and site conditions (hydrologic and stability) from failed slopes. There are only limited data making such a validation very difficult. What is, in essence, lacking are quality data collection and storage of historic landslide events in the form of reliable landslide inventories. For this, it is necessary to combine all possible efforts for the development of comprehensive landslide databases. Maximum use should also be made of modern communication tools for the exchange of such information. A properly organized data collection, storage and exchange is thus required for the purpose of building such inventories and evaluating landslide hazards.

(c) Formal incorporation of uncertainties

This study, Chapters 5 and 6 in particular, investigated uncertainties from parameters, and from models.

i. **Parameter Uncertainty:** Chapter 5 studied parameter uncertainty, and described simple, easy to implement techniques with which these uncertainties can be systematically incorporated into the hazards assessment procedure. These techniques were applied to the case when the hydraulic conductivity of the soil, as well as the strength parameters were uncertain. They can be extended to include more variables in a similar way to what was described in Chapter 5. In particular, there is a need to assess uncertainties in the parameters of the trigger, namely the rainfall intensity and duration. While the techniques in Chapter 5 can be used to do this, this has not been done in this study.
ii. **Model Uncertainty:** Chapter 6 studied model uncertainty, and showed this source of uncertainty can have significant effects on landslide hazards. While the Chapter demonstrated which sources of model uncertainty are most important, it did not provide ways in which uncertainty from models can be rationally included in landslide

analyses. This needs to be done. Furthermore, model uncertainty from only one source was studied in Chapter 6, and further extensive studies that investigate the effects of model uncertainty from two or more sources need to be performed.

The Earth's surface is a dynamic system, constantly evolving through the actions of geological, geomorphological and meteorological processes. Landslides form one aspect of this evolution that occurs in a wide variety of geological, hydrogeological and climatic conditions. Given the complexities involved, the task of assessing landslide hazards is formidable. Nevertheless, given the very considerable losses, human and economic, there is a clear responsibility to do all that can be done to anticipate and mitigate these hazards. Landslide hazards assessment is of fundamental importance to policy makers and government agencies, and serves as an aid to rational land use planning and sustainable development. Finally, most importantly the ultimate aim of landslide hazards assessments is to save lives, and this requires bringing all the relevant disciplines together in a fully integrated manner.

APPENDIX A

SOLUTION OF A TRIDIAGONAL LINEAR SYSTEM OF EQUATIONS

In this appendix an algorithm for solving a tridiagonal linear system of n equations with n unknowns is presented. The method is based on the factorization of the original matrix as the product of a lower and an upper triangular matrix. Let the original system be:

$$\begin{bmatrix} b_1 & c_1 & 0 & \cdots & 0 \\ a_2 & b_2 & c_2 & & \\ 0 & a_3 & b_3 & c_3 & \\ \vdots & & & & \\ & & a_{n-1} & b_{n-1} & c_{n-1} \\ 0 & \cdots & 0 & b_n & c_n \end{bmatrix} \begin{bmatrix} x_1 \\ x_2 \\ \vdots \\ x_{n-1} \\ x_n \end{bmatrix} = \begin{bmatrix} f_1 \\ f_2 \\ \vdots \\ f_{n-1} \\ f_n \end{bmatrix}$$

or

$$\underline{A}\underline{x} = \underline{f} \qquad [A1]$$

Let:

$$\begin{bmatrix} w_1 & 0 & 0 & & 0 \\ a_2 & w_2 & 0 & & \\ 0 & a_3 & w_3 & & \\ & & & & \\ . & & & & \\ . & & & & \\ . & & & & \\ & & & & \\ & 0 & a_{n-1} & & w_{n-1} \\ 0 & 0 & a_n & & w_n \end{bmatrix} \begin{bmatrix} 1 & \beta_1 & 0 & & 0 \\ 0 & 1 & \beta_2 & & \\ 0 & 0 & 1 & \beta_3 & \\ & & & & \\ . & & & & \\ . & & & & \\ . & & & & \\ & & & & \\ & & & 1 & \beta_{n-1} \\ 0 & & & 0 & 1 \end{bmatrix} = \begin{bmatrix} w_1 & w_1\beta_1 & 0 & & 0 \\ a_2 & a_2\beta_1 + w_2 & w_2\beta_2 & & \\ 0 & a_3 & a_3\beta_2 + w_3 & & \\ . & & & & \\ . & & & & \\ . & & & & \\ & & & & \\ & & & & w_{n-1}\beta_{n-1} \\ 0 & & & a_n & a_n\beta_{n-1} + w_n \end{bmatrix}$$

or

$$\underline{L}\underline{U} = \underline{A} \qquad [A2]$$

with obvious definitions of **L** and **U**.

Thus, the factorization is realized with:

$$w_1 = b_1 \qquad [A3]$$

$$\beta_i = \frac{c_i}{w_i} \quad i = 1,2,...,n-1 \qquad [A4]$$

$$w_i = b_i - a_i\beta_{i-1} \; i = 2,...,n \qquad [A5]$$

or

$$\beta_1 = \frac{c_1}{b_1} \qquad [A6]$$

$$\beta_i = \frac{c_i}{b_i - a_i\beta_{i-1}} \; i = 2,...,n \qquad [A7]$$

From [A1] and [A2]:

$$\underline{L}\underline{U}\underline{x} = \underline{f} \qquad [A8]$$

or

$$\underline{U}\underline{x} = \underline{L}^{-1}\underline{f} \qquad [A9]$$

Writing:

$$\underline{L}^{-1}\underline{f} = \underline{y} \qquad [A10]$$

or

$$\underline{L}\underline{y} = \underline{f} \qquad [A11]$$

The solution of the original system is reduced to the solution of the two triangular systems:

$$\underline{L}\underline{y} = \underline{f} \qquad [A12]$$

And

$$\underline{U}\underline{x} = \underline{y} \qquad [A13]$$

In order to link this with the development of the finite difference scheme in Chapter, we notice $b_i = B_i$; $c_i = A_i$; $a_i = -D_i$; and $f_i = E_i$, where B_i, A_i, D_i and E_i are defined in Chapter 2.

The solution of $\underline{L}\underline{y} = \underline{f}$ is:

$$y_1 = \frac{f_1}{w_1} = \frac{f_1}{b_1} \qquad [A14]$$

$$y_i = \frac{f_i - a_i y_{i-1}}{w_i} = \frac{f_i - a_i y_{i-1}}{b_i - a_i \beta_{i-1}} \qquad i = 2,...,n \qquad \text{[A15]}$$

Then, the solution to $\underline{U}\underline{x} = \underline{y}$ is:

$$x_n = y_n = \frac{f_n - a_n y_{n-1}}{b_n - a_n \beta_{n-1}} \qquad \text{[A16]}$$

$$x_i = y_i - \beta_i x_{i+1} = -\beta_i \left(x_{i+1} - \frac{y_i}{\beta_i} \right) \qquad i = n-1,...,1 \qquad \text{[A17]}$$

Let $\omega_1(i)$ and $\omega_2(i)$ be two intermediate variables defined as:

$$\omega_1(i) = -\beta_i \qquad i = 1,2,...,n-1 \qquad \text{[A18]}$$

$$\omega_2(i) = \frac{y_i}{\beta_i} \qquad i = 1,2,...,n-1 \qquad \text{[A19]}$$

Then,

$$\omega_1(1) = -\beta_1 = -\frac{c_1}{b_1} = \frac{A_1}{B_1} \qquad \text{[A20]}$$

$$\omega_2(1) = \frac{y_1}{\beta_1} = \frac{f_1}{b_1 \beta_1} = -\frac{f_1}{b_1 \omega_1(1)} = -\frac{E_1}{A_1} \qquad \text{[A21]}$$

And,

$$\omega_1(i) = -\beta_i = -\frac{c_i}{b_i - a_i \beta_{i-1}} = \frac{A_i}{B_i - D_i \omega_i(i-1)}$$

$$\omega_1(i) = \frac{A_i}{B_i - D_i \omega_i(i-1)} \qquad i = 2,...,n-1 \qquad \text{[A22]}$$

$$\omega_2(i) = \frac{y_i}{\beta_i} = \frac{1}{\beta_i} \left(\frac{f_i - a_i y_{i-1}}{b_i - a_i \beta_{i-1}} \right)$$

$$= \frac{f_i - a_i\beta_{i-1}\omega_2(i-1)}{\beta_i(b_i - a_i\beta_{i-1})} = \frac{f_i - a_i\beta_{i-1}\omega_2(i-1)}{c_i}$$

$$= \frac{E_i - D_i\varpi_1(i-1)\omega_2(i-1)}{-A_i} = \frac{D_i\varpi_1(i-1)\omega_2(i-1) - E_i}{A_i}$$

Hence,

$$\omega_2(i) = \frac{D_i\varpi_1(i-1)\omega_2(i-1) - E_i}{A_i} \qquad i = 2,...,n-1 \qquad \text{[A23]}$$

$\omega_1(i)$ and $\omega_2(i)$ for $i = 1,...,n-1$ are computable using only the knowledge of system matrix and the constant terms.

Once, $\omega_1(1)$ and $\omega_2(1)$ have been computed from [A20] and [A21], the $\omega_1(i)$ and $\omega_2(i)$ can be computed from [A22] and [A23]. Then we have:

$$x_n = \frac{f_n - a_n y_{n-1}}{b_n - a_n\beta_{n-1}} = \frac{f_n - a_n\beta_{n-1}\varpi_2(n-1)}{b_n - a_n\beta_{n-1}}$$

$$x_n = \frac{f_n - D_n\varpi_1(n-1)\varpi_2(n-1)}{B_n - D_n\omega_1(n-1)} \qquad \text{[A24]}$$

and

$$x_i = -\beta_i\left(x_{i+1} - \frac{y_i}{\beta_i}\right)$$

$$x_i = \omega_1(i)(x_{i+1} - \omega_2(i)) \qquad i = n-1,...,1 \qquad \text{[A25]}$$

APPENDIX B

THEORETICAL MAXIMUM SLOPE ANGLE FOR USE IN THE INFINITE SLOPE STABILITY MODEL

The Factor of Safety for an infinite slope (see Figure B1) can be expressed as (Skempton & DeLory, 1957):

$$F = \frac{c'}{\gamma_s z \sin\beta\cos\beta} + \frac{\tan\phi'}{\tan\beta} + \left[\frac{z_w - z}{z}\right]\left(\frac{\gamma_w \tan\phi'}{\gamma_s \tan\beta}\right) \qquad [B1]$$

which is re-written as:

$$F = \frac{c'}{\gamma z \sin\alpha\cos\alpha} + \frac{\tan\phi'}{\tan\alpha} - m\left(\frac{\gamma_w \tan\phi'}{\gamma \tan\alpha}\right) \qquad [B2]$$

where

c' is the cohesion of the soil

ϕ' is the angle of internal friction of the soil

γ is the unit weight of the soil

γ_w is the unit weight of water

α is the inclination of the slope to the horizontal

z is the depth below the ground surface

z_w is the depth of the water table below the ground surface

m is the degree of saturation of the soil, $m = \left[\frac{z_w - z}{z}\right]$

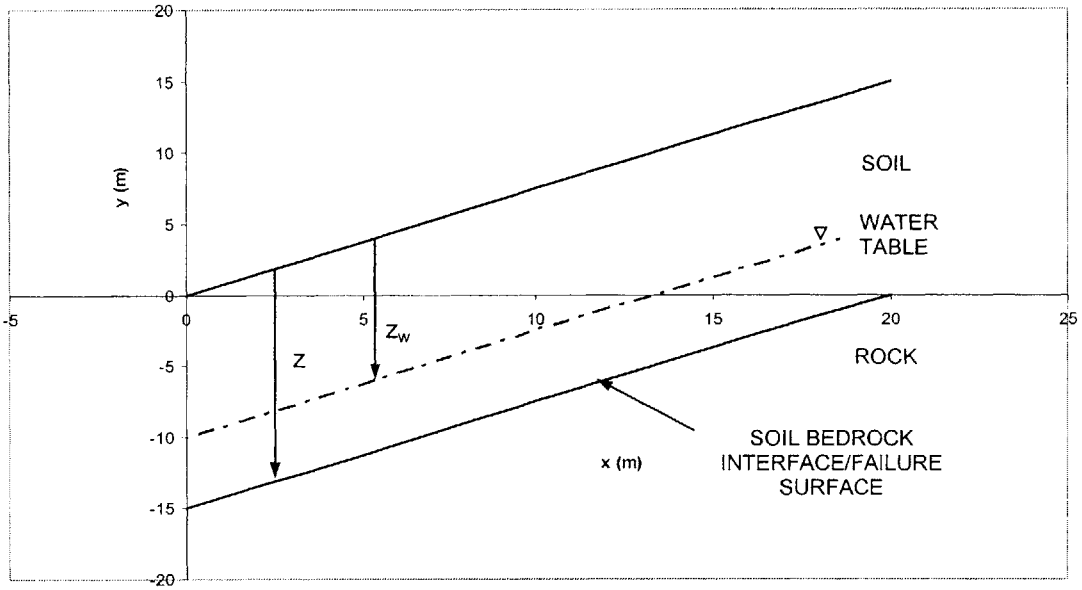

Figure B1. Infinite Slope Geometry and Definition of Parameters

Rearranging Equation [B2] yields:

$$F = \frac{c'}{\gamma_s z \sin\beta\cos\beta} + \left(1 - m\frac{\gamma_w}{\gamma_s}\right)\left(\frac{\tan\phi'}{\tan\beta}\right) \qquad [B3]$$

For a slope with given soil and hydraulic properties, one would expect the factor of safety to be a monotonically decreasing function of the slope angle. However, this is not be the case for an infinite slope, with the Factor of Safety in Equations [B1]. There exists an upper bound to the slope angle above which the Infinite Slope Model breaks down.

B2. DETERMINATION OF MAXIMUM SLOPE ANGLE

B2.1 ANALYTICAL SOLUTION

If the Factor of Safety in Equation [B3] is not a monotonically decreasing function of the slope angle within the range $0 \le \beta \le 90$, then there exists at least one local minimum

within this range. To obtain these minima, we differentiate Equation [B3] with respect to the slope angle.

$$\frac{\partial F}{\partial \beta} =$$

$$-\frac{c'}{z\gamma_s}(\sin\beta\cos\beta)^{-2}[(\sin\beta)(-\sin\beta)+(\cos\beta)(\cos\beta)]-\tan\phi'\left(1-m\frac{\gamma_w}{\gamma_s}\right)(\tan\beta)^{-2}\sec^2\beta \qquad [B4]$$

$$\frac{\partial F}{\partial \beta} = -\frac{c'}{z\gamma_s}(\sin\beta\cos\beta)^{-2}\left[\cos^2\beta-\sin^2\beta\right]-\tan\phi'\left(1-m\frac{\gamma_w}{\gamma_s}\right)\left(\frac{\sec^2\beta}{\tan^2\beta}\right) \qquad [B5]$$

Simplifying Equation [B5] and substituting for $\sec^2\beta = 1+\tan^2\beta$:

$$\frac{\partial F}{\partial \beta} = -\frac{c'}{z\gamma_s\sin^2\beta}+\frac{c'}{z\gamma_s\cos^2\beta}-\tan\phi'\left(1-m\frac{\gamma_w}{\gamma_s}\right)\left(\frac{1+\tan^2\beta}{\tan^2\beta}\right) \qquad [B6]$$

Since $\frac{1}{\sin^2\beta} = \cos ec^2\beta = \left(1+\frac{1}{\tan^2\beta}\right)$ and $\frac{1}{\cos^2\beta} = \sec^2\beta = \left(1+\tan^2\beta\right)$, Equation [B6] becomes:

$$\frac{\partial F}{\partial \beta} = -\left(\frac{c'}{z\gamma_s}\right)\left(1+\frac{1}{\tan^2\beta}\right)+\left(\frac{c'}{z\gamma_s}\right)\left(1+\tan^2\beta\right)-\tan\phi'\left(1-m\frac{\gamma_w}{\gamma_s}\right)\left(1+\frac{1}{\tan^2\beta}\right) \qquad [B7]$$

$$\frac{\partial F}{\partial \beta} = \left(\frac{c'}{z\gamma_s}\right)\left(1+\tan^2\beta\right)-\left\{\tan\phi'\left(1-m\frac{\gamma_w}{\gamma_s}\right)+\left(\frac{c'}{z\gamma_s}\right)\right\}\left(1+\frac{1}{\tan^2\beta}\right) \qquad [B8]$$

Factorizing $\frac{1}{\tan^2\beta}$ out of Equation [B8]:

$$\frac{\partial F}{\partial \beta} = \left(\frac{1}{\tan^2 \beta}\right)\left\{\left(\frac{c'}{z\gamma_s}\right)\tan^2 \beta\left(1+\tan^2 \beta\right) - \left\{\tan\phi\left(1 - m\frac{\gamma_w}{\gamma_s}\right) + \left(\frac{c'}{z\gamma_s}\right)\right\}\left(1+\tan^2 \beta\right)\right\} \quad \text{[B9]}$$

Setting $\frac{\partial F}{\partial \beta} = 0$ in Equation [B9] to obtain the critical value of the slope angle:

$$\frac{\partial F}{\partial \beta} = \left(\frac{1}{\tan^2 \beta}\right)\left\{\left(\frac{c'}{z\gamma_s}\right)\tan^2 \beta\left(1+\tan^2 \beta\right) - \left\{\tan\phi'\left(1 - m\frac{\gamma_w}{\gamma_s}\right) + \left(\frac{c'}{z\gamma_s}\right)\right\}\left(1+\tan^2 \beta\right)\right\} = 0$$

[B10]

The solutions to Equation [10] are:

1. Trivial solution: $\tan^2 \beta = \infty$ and $\beta = 90$
2. $$\left\{\left(\frac{c'}{z\gamma_s}\right)\tan^2 \beta\left(1+\tan^2 \beta\right) - \left\{\tan\phi'\left(1 - m\frac{\gamma_w}{\gamma_s}\right) + \left(\frac{c'}{z\gamma_s}\right)\right\}\left(1+\tan^2 \beta\right)\right\} = 0 \quad \text{[B11]}$$

Expanding Equation [B11]:

$$\left(\frac{c'}{z\gamma_s}\right)\tan^2 \beta + \left(\frac{c'}{z\gamma_s}\right)\tan^4 \beta - \left\{\tan\phi'\left(1 - m\frac{\gamma_w}{\gamma_s}\right) + \left(\frac{c'}{z\gamma_s}\right)\right\} - \left\{\tan\phi'\left(1 - m\frac{\gamma_w}{\gamma_s}\right) + \left(\frac{c'}{z\gamma_s}\right)\right\}\tan^2 \beta = 0$$

[B12]

$$\left(\frac{c'}{z\gamma_s}\right)\tan^4 \beta - \left\{\tan\phi'\left(1 - m\frac{\gamma_w}{\gamma_s}\right)\right\}\tan^2 \beta - \left(\tan\phi'\left(1 - m\frac{\gamma_w}{\gamma_s}\right) + \left(\frac{c'}{z\gamma_s}\right)\right) = 0 \quad \text{[B13]}$$

We now define two dimensionless parameters:

(a) A dimensionless stability number, $A = \left(\frac{c'}{z\gamma_s}\right)$

(b) A dimensionless pore pressure parameter $B = \left(1 - m\frac{\gamma_w}{\gamma_s}\right)$

Equation [B13] can be expressed in terms of the parameters A and B as:

$$A\tan^4\beta - B\tan\phi'\tan^2\beta - \{A + B\tan\phi'\} = 0 \qquad [B14]$$

Solving Equation [B14] for $\tan^2\beta$:

$$\tan^2\beta = \frac{B\tan\phi' \pm \sqrt{(B\tan\phi')^2 + 4A(A + B\tan\phi')}}{2A} \qquad [B15]$$

$\tan\beta$ is found from Equation [B15] as:

$$\tan\beta = \left(\frac{B\tan\phi' \pm \sqrt{B^2\tan^2\phi + 4A(A + B\tan\phi')}}{2A}\right)^{\frac{1}{2}} \qquad [B16]$$

Hence, the slope angle can be expressed as:

$$\beta = \tan^{-1}\left\{\left(\frac{B\tan\phi' \pm \sqrt{B^2\tan^2\phi' + 4A(A + B\tan\phi')}}{2A}\right)^{\frac{1}{2}}\right\} \qquad [B17]$$

Equations [B15] to [B17] can be written out in full in terms of the soil properties, as is done in Equations [B18] through to [B20]:

$$\tan^2\beta = \frac{\left(1 - m\frac{\gamma_w}{\gamma_s}\right)\tan\phi' \pm \sqrt{\left(\left(1 - m\frac{\gamma_w}{\gamma_s}\right)\tan\phi'\right)^2 + 4\left(\frac{c'}{z\gamma_s}\right)\left(\left(\frac{c'}{z\gamma_s}\right) + \left(1 - m\frac{\gamma_w}{\gamma_s}\right)\tan\phi'\right)}}{2\left(\frac{c'}{z\gamma_s}\right)}$$

[B18]

$$\tan\beta = \left\{ \frac{\left(1 - m\frac{\gamma_w}{\gamma_s}\right)\tan\phi' \pm \sqrt{\left(\left(1 - m\frac{\gamma_w}{\gamma_s}\right)\tan\phi'\right)^2 + 4\left(\frac{c'}{z\gamma_s}\right)\left(\left(\frac{c'}{z\gamma_s}\right) + \left(1 - m\frac{\gamma_w}{\gamma_s}\right)\tan\phi'\right)}}{2\left(\frac{c'}{z\gamma_s}\right)} \right\}^{\frac{1}{2}}$$

[B19]

$$\beta = \tan^{-1}\left\{ \left\{ \frac{\left(1 - m\frac{\gamma_w}{\gamma_s}\right)\tan\phi' \pm \sqrt{\left(\left(1 - m\frac{\gamma_w}{\gamma_s}\right)\tan\phi'\right)^2 + 4\left(\frac{c'}{z\gamma_s}\right)\left(\left(\frac{c'}{z\gamma_s}\right) + \left(1 - m\frac{\gamma_w}{\gamma_s}\right)\tan\phi'\right)}}{2\left(\frac{c'}{z\gamma_s}\right)} \right\}^{\frac{1}{2}} \right\}$$

[B20]

From Equation [B20] slope angles can be found at which the factor of safety is at a local minimum in terms of the soil and slope hydraulic properties. These slope angles are interpreted as the maximum slope angles that can theoretically be used in the infinite slope stability model.

B-2.2. SPECIAL CASES:

A. COHESION, $c' = 0$

When the cohesion of the soil $c' = 0$, the dimensionless stability number $A = \left(\frac{c'}{z\gamma_s}\right) = 0$ and there is no solution to Equation [B20]. The factor of safety at any particular depth is obtained by substituting $c' = 0$ into Equation [B1] to get:

$$F = \frac{\tan\phi'}{\tan\beta} + \left[\frac{z_w - z}{z}\right]\left(\frac{\gamma_w \tan\phi'}{\gamma_s \tan\beta}\right) \qquad [B21]$$

Rearranging Equation [B21] yields:

$$F = \left(1 - m\frac{\gamma_w}{\gamma_s}\right)\left(\frac{\tan\phi'}{\tan\beta}\right) \qquad [B22]$$

Differentiating Equation [B22], and setting to zero to obtain maximum slope angles:

$$\frac{\partial F}{\partial \beta} = \left(\frac{1}{\tan^2\beta}\right)\left\{\tan\phi'\left(1 - m\frac{\gamma_w}{\gamma_s}\right)\left(1 + \tan^2\beta\right)\right\} = 0 \qquad [B23]$$

The solutions to Equation [B23] are:

1. Trivial solution: $\tan^2\beta = \infty$ and $\beta = 90$
2. $\tan\phi'\left(1 - m\frac{\gamma_w}{\gamma_s}\right)\left(1 + \tan^2\beta\right) = 0$ [B24]

Assuming that $\phi' > 0$ and since $\tan\phi'\left(1 - m\frac{\gamma_w}{\gamma_s}\right) > 0$, the solution to Equation [B24] is:

$$\tan^2\beta = -1 \qquad [B25]$$

The roots of Equation [B25] are imaginary, complex conjugates i.e. $\tan\beta = \pm i$ and no real solution for β is obtained. Hence, if the cohesion of the soil $c' = 0$ the infinite slope stability model can be used for all slope angles within the range $0 \le \beta \le 90$.

B. ANGLE OF SHEARING RESISTANCE, $\phi' = 0$

When the angle of shearing resistance of the soil $\phi' = 0$, there are two solutions to the differential Equation [B10]:

1. Trivial solution: $\tan^2\beta = \infty$ and $\beta = 90$

2. Substituting for $\tan\phi' = 0$ in Equation [B19], we obtain $\tan\beta = 1$ and $\beta = 45$.

This result is independent of the value of the stability number $A = \left(\frac{c'}{z\gamma_s}\right)$. Hence, if the angle of shearing resistance of the soil $\phi' = 0$, the infinite slope stability model can only be used upto a slope angle of $\beta = 45$, independently of the cohesion of the soil.

B-2.4. NUMERICAL SOLUTION

We develop a simple computer program (attached at the end of this Appendix) to verify the analytical results obtained in Equations [B18] through to [B20]. The program has a user interface, where several parameters can be input, namely:

a. The cohesion c' and the angle of shearing resistance ϕ' of the soil
b. The depth to the soil-bedrock interface z, from the ground surface
c. The depth to the water table z_w, from the ground surface.

The computer program computes the factor of safety at a depth z according to Equation [B1], for various slope angles and determines the slope angle for which the factor of safety is minimum. The procedure followed is as follows:

1. The program starts off by computing the factor of safety for $\beta_0 = 0$, which is infinite irrespective of the soil properties.
2. The slope angle is then increased by an increment $\Delta\beta$, where any desired $\Delta\beta$ is specified by the user.
3. The factor of safety is then computed for slope angles $\beta_1 = \beta_0 + \Delta\beta$, $\beta_2 = \beta_1 + \Delta\beta = \beta_0 + 2\Delta\beta$, and so on.
4. This process is continued until the computed factor of safety reaches a minimum value when $\beta = \beta_{max}$, after which it starts to increase for slope angles greater than β_{max}. The program stops the iterations and displays the slope angle β_{max}.

B-2.5. COMPARISON OF ANALYTICAL AND NUMERICAL RESULTS

To compare the analytical result in Equation [B20] with the numerical result from the computer program, we compute the maximum slope angle for a specific case where $A = \left(\frac{c'}{z\gamma_s}\right) = 0.1$ and $B = \left(1 - m\frac{\gamma_w}{\gamma_s}\right) = 0.77$ (corresponding to a value of $m = 0.5$ for $\gamma_s = 21.3\,kN/m^2$) as a function of the angle of shearing resistance ϕ' of the soil. The results are shown in Figure B2.

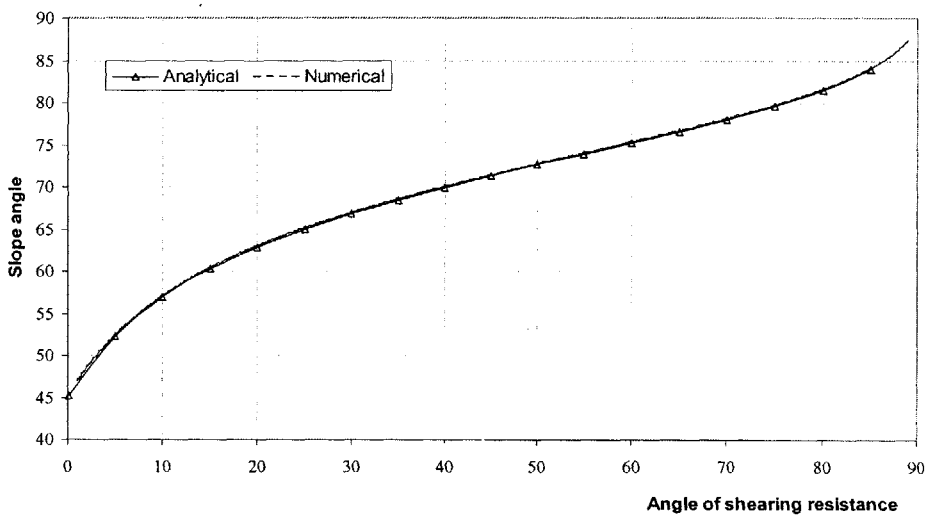

Figure B2. Comparison of Analytical and Numerical Maximum Slope Angles

The results shown in Figure B2 are almost identical. Minor deviations are attributed to the granularity of the iterations, $\Delta\beta$ and inherent calculation errors in the written code.

The problem of maximum angle has been recognized in the literature, and it has been suggested that the Rankine Active $\alpha = \left(45 + \frac{\phi'}{2}\right)$ angle be used as maximum base angle (Bishop, 1959; Abramson, 1998). Figure B3 shows a plot of the results of this Appendix with the Rankine Active angle.

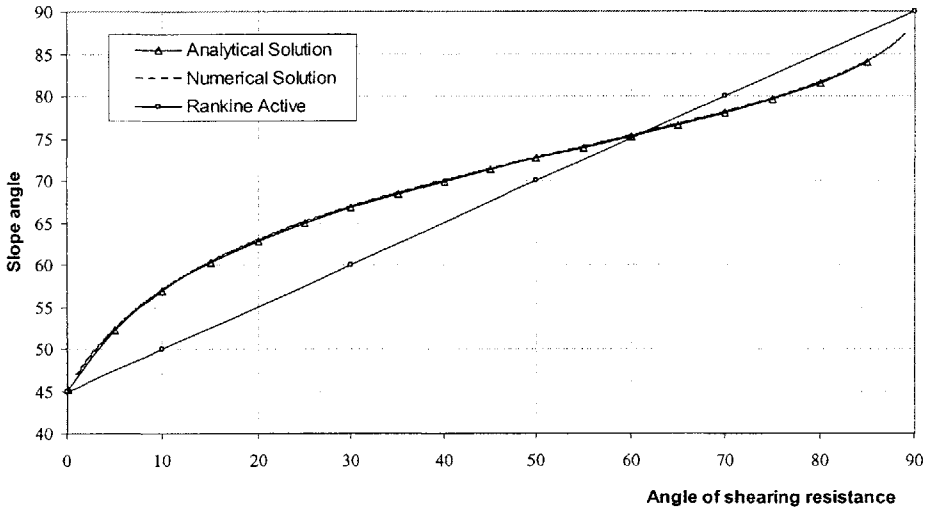

Figure B3. Comparison of Results in Appendix and Rankine Active

Figure B3 shows that under certain conditions, depending on the A and B parameters, the Rankine Active condition can be lead to errors (e.g. $\phi' > 60^{o}$ in Figure B3), and lead to unconservative results since the Factor of Safety is overestimated.

B-3. COMPUTER CODE

```
#include <stdio.h>
#include <math.h>

#define PI 3.14159

int main(int argc, char *argv[])
{
   float gw = 9.81;
   float c, gs, zw, z, phi, beta;
   float F, prev_F, cutoff_beta;
   float beta_step, phi_step;
   float beta_start, phi_start;
   float beta_end, phi_end;
   int answer;
   FILE *fptr = stdout;

   FILE *fptr2 = stdout;
   float rad_phi, rad_beta;

   printf("C = ");
   scanf("%f",&c);
   printf("\nGs =");
   scanf("%f",&gs);
   printf("\nZ =");
   scanf("%f",&z);
   printf("\nZw =");
   scanf("%f",&zw);

   printf("\n\n");
   printf("Beta <start> <end> <delta> =");
   scanf("%f %f %f",&beta_start, &beta_end, &beta_step);

   printf("\n\n");
   printf("phi <start> <end> <delta> =");
   scanf("%f %f %f",&phi_start, &phi_end, &phi_step);

   printf("\n\n");
   printf("Output to a file ? (1=yes) (0=no)");
   scanf("%d",&answer);

   if ( (answer == 1) )
   {
      fptr = fopen("mechanics.txt","w");

        fptr2 = fopen("mechanics2.txt","w");
   }

   phi = phi_start;
   beta = beta_start;

   while (phi <= phi_end)
   {
```

```
      fprintf(fptr,"Phi = %f\n",phi);
      fprintf(fptr,"Beta   F\n");
      rad_phi = phi*PI/180.0;

        beta = beta_start;

        prev_F = 99999.999;
      while (beta <= beta_end)
      {
         rad_beta = beta*PI/180.0;
         F = (c/(gs * z * sin(rad_beta)*cos(rad_beta))) +
             (tan(rad_phi)/tan(rad_beta)) +
             ( ((zw/z)-1) * ( (gw * tan(rad_phi)) /
(gs*tan(rad_beta))));
         fprintf(fptr,"%f   %f\n",beta, F);

             if ( (F < prev_F) && (prev_F != 0) )

             {

                   prev_F = F;

             }

             else if ( (F > prev_F) && (prev_F != 0) )

             {

                   cutoff_beta = beta;

                   prev_F = 0;

             }

             beta = beta + beta_step;
      }

        printf("cutoff beta = %f\n",cutoff_beta);

        fprintf(fptr2,"%f  %f\n",phi, cutoff_beta);
      phi = phi + phi_step;
   }
}
```

APPENDIX C

SENSITIVITY ANALYSES

PART C-1. HYDROLOGIC SENSITIVITY ANALYSES

In this Appendix, results of sensitivity analyses on the Green – Ampt (1911) hydrologic model are presented. The rate of infiltration according to the Green - Ampt (1911) Model is given by:

$$f(t) = K_s\left[\frac{\psi + z_s}{z_s}\right] \qquad \text{[C-1.1]}$$

where:

K_s is the saturated hydraulic conductivity of the soil

ψ is the constant soil suction head in front of the wetting front,

$$\psi = \frac{(u_a - u_w)}{\gamma_w}$$

z_s is the depth of saturation (advancement of wetting front)

$f(t)$ is the cumulative infiltration rate in [C-1.1]

The time required to saturate the soil to z_s is:

$$T_s = \frac{\Delta\theta}{K_s}\left[z_s - \psi \ln\left(\frac{\psi + z_s}{\psi}\right)\right] \qquad \text{[C-1.2]}$$

where:

$\Delta\theta$ is the change in moisture content $\Delta\theta = \theta_s - \theta_i$

θ_i is the initial (antecedent) moisture content

θ_s is the saturated moisture content (porosity)

It is possible to relate the minimum intensity, I_{min}, to the minimum duration, T_{min} that will cause saturation to z_s by:

$$I_{min} = \frac{\Delta\theta}{T_{min}}\left[z_s - \psi \ln\left(\frac{\psi + z_s}{\psi}\right)\right]\left(\frac{z_s + \psi}{z_s}\right) \qquad \text{[C-1.3]}$$

Further details of the model are given in Chapter 6. In this Appendix, sensitivity analyses are performed to investigate the effects of the input parameters which are shown in Table C-1.1 on:

(a) The infiltration rate in [C-1.1]
(b) The minimum time required to saturate the soil to a particular depth
(c) Rainfall characteristics (intensity and duration) required to saturate the soil to a particular depth

PARAMETER		VALUE OR RANGE
SYMBOL	DEFINITION	
z_s	Depth of saturation	0 - z_w (depth to water table)
ψ	Constant matric suction head	0.25 – 2.0 (m)
θ_s	Saturated moisture content (Porosity)	0.2 – 0.5
θ_i	Initial (antecedent) moisture content	0.05 – 0.39
K_s	Saturated conductivity of soil	0.036 – 1800 (mm/h)

Table C-1.1 Definition of parameters and range used in sensitivity study

Table C-1.2 shows the parameters chosen for the base case scenario.

PARAMETER		VALUE OR RANGE
SYMBOL	DEFINITION	
z_s	Depth of saturation	6 m
ψ	Constant matric suction head	0.75 m
θ_s	Saturated moisture content/Porosity	0.4
θ_i	Antecedent moisture content	0.1
K_s	Saturated conductivity of soil	18 mm/h

Table C-1.2 Parameters used for Base Case

C-1.1. Sensitivity of Infiltration Rate

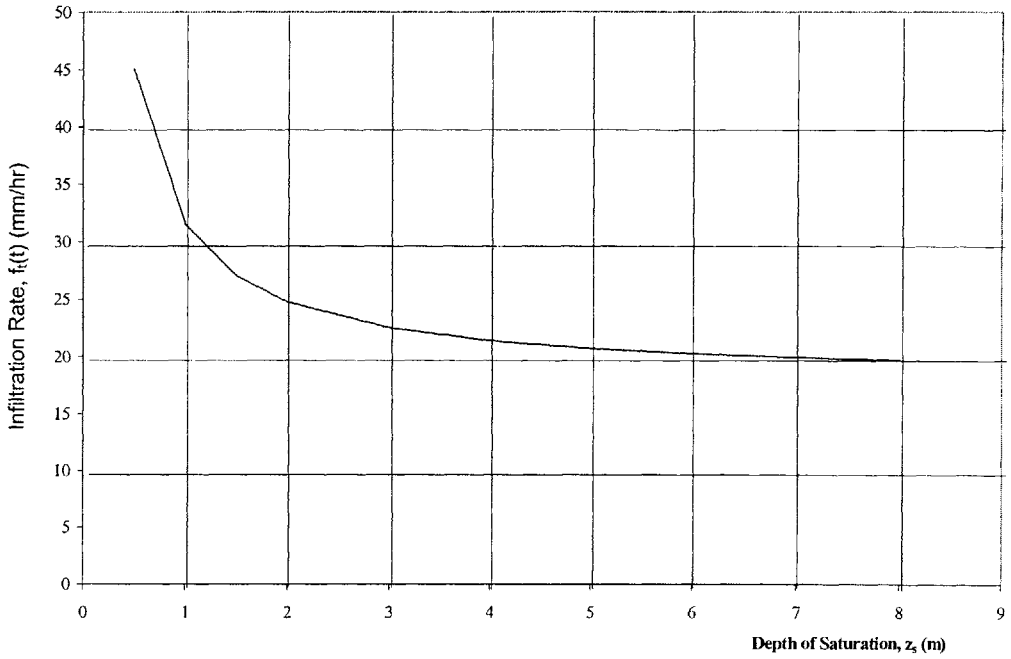

Figure C-1.1. Sensitivity of Infiltration Rate to Depth of Saturation

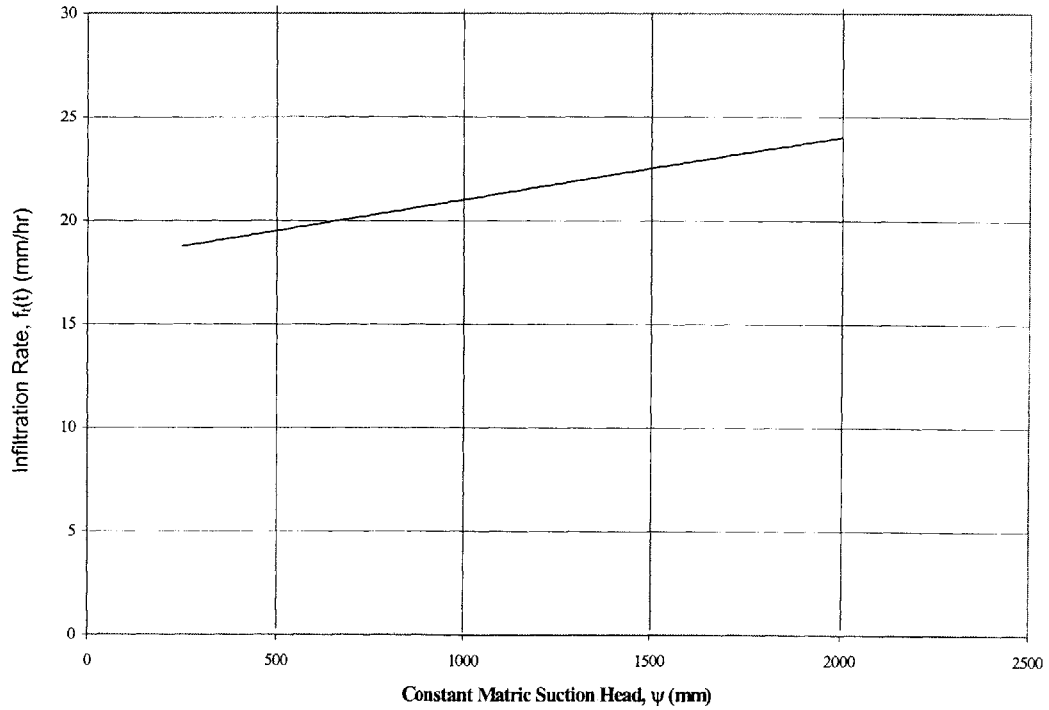

Figure C-1.2. Sensitivity of Infiltration Rate to Constant Matric Suction

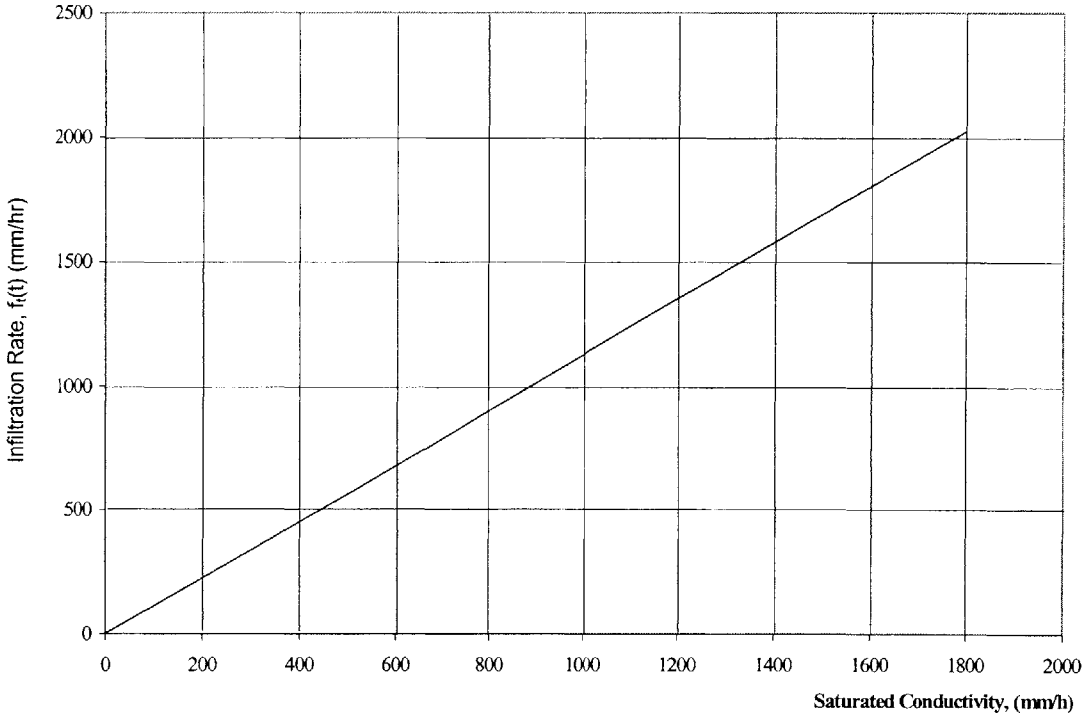

Figure C-1.3. Sensitivity of Infiltration Rate to Saturated Conductivity

C-1.2. Sensitivity of Minimum Time Required to Saturate Soil

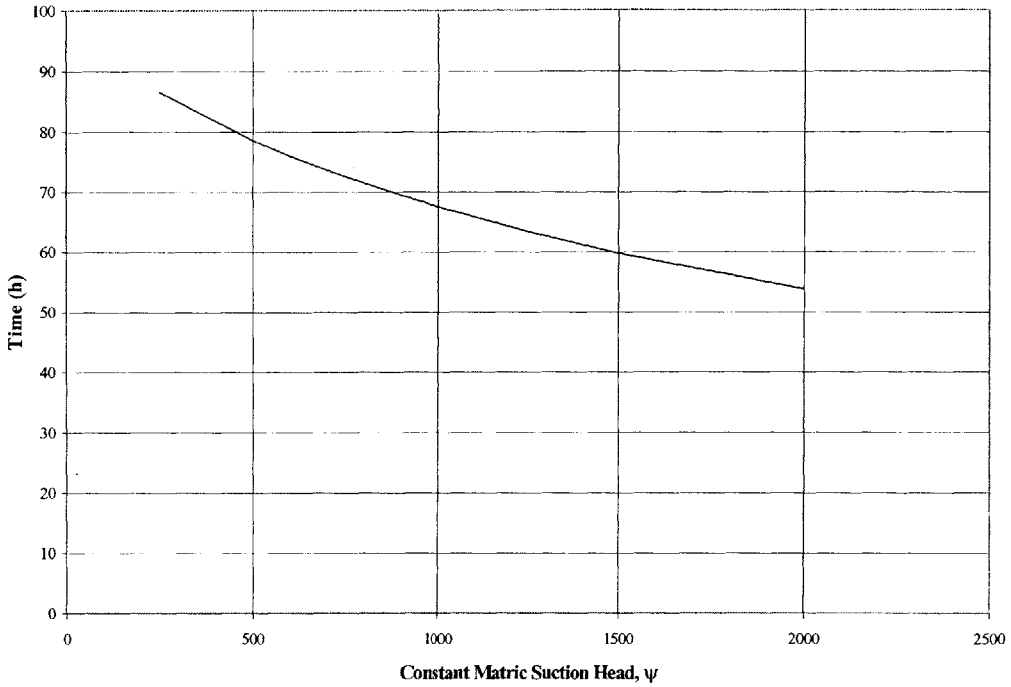

Figure C-1.4. Sensitivity of Time Required to Saturate Soil to Matric Suction Head

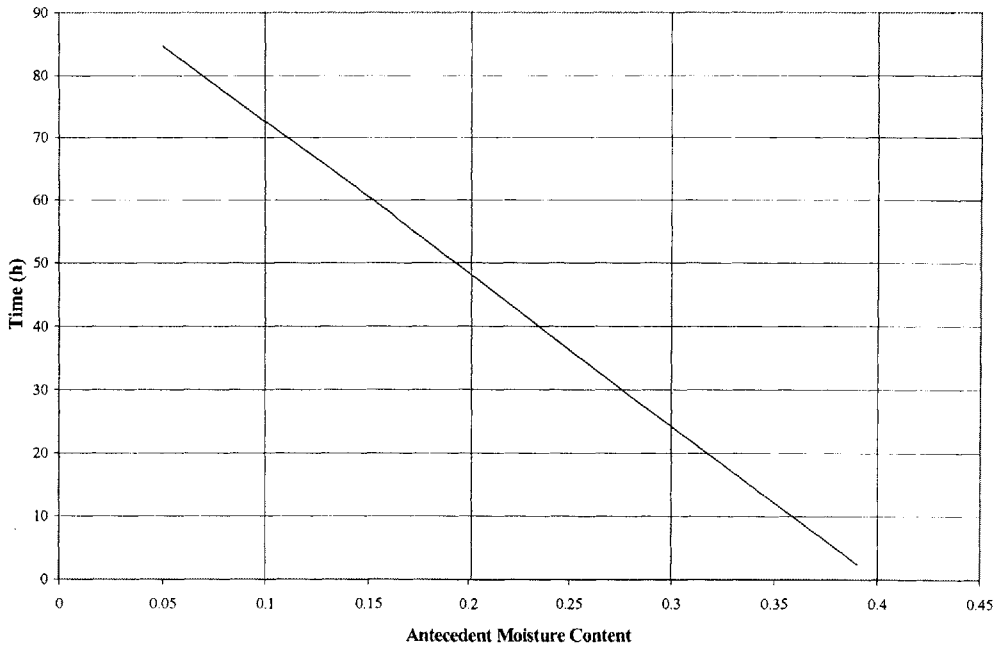

Figure C-1.5. Sensitivity of Time Required to (Initial) Antecedent Moisture Content

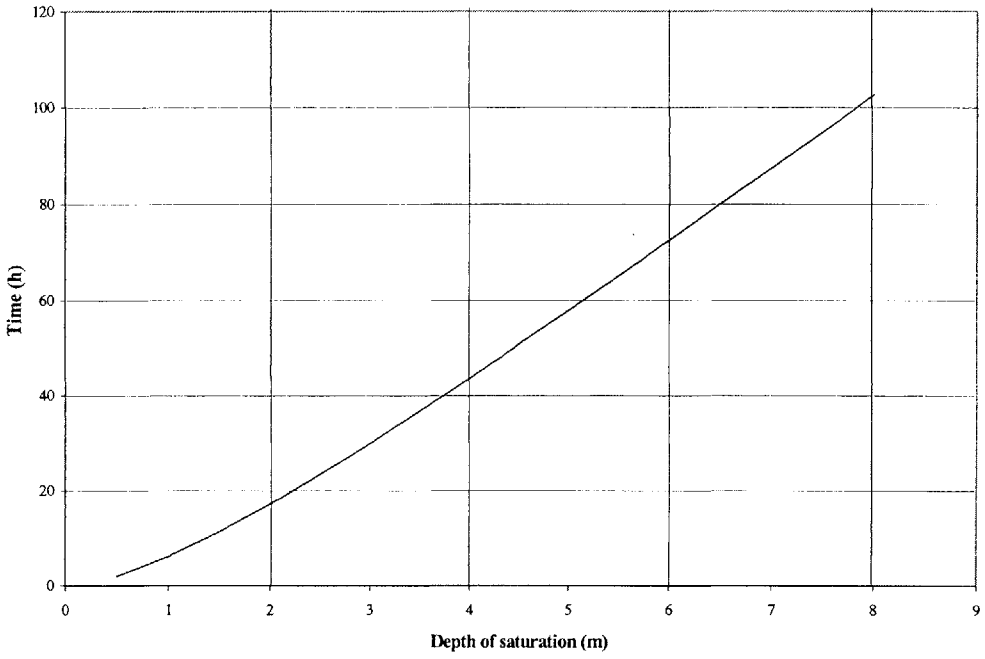

Figure C-1.6. Sensitivity of Time Required to Saturate Soil to Particular Depth

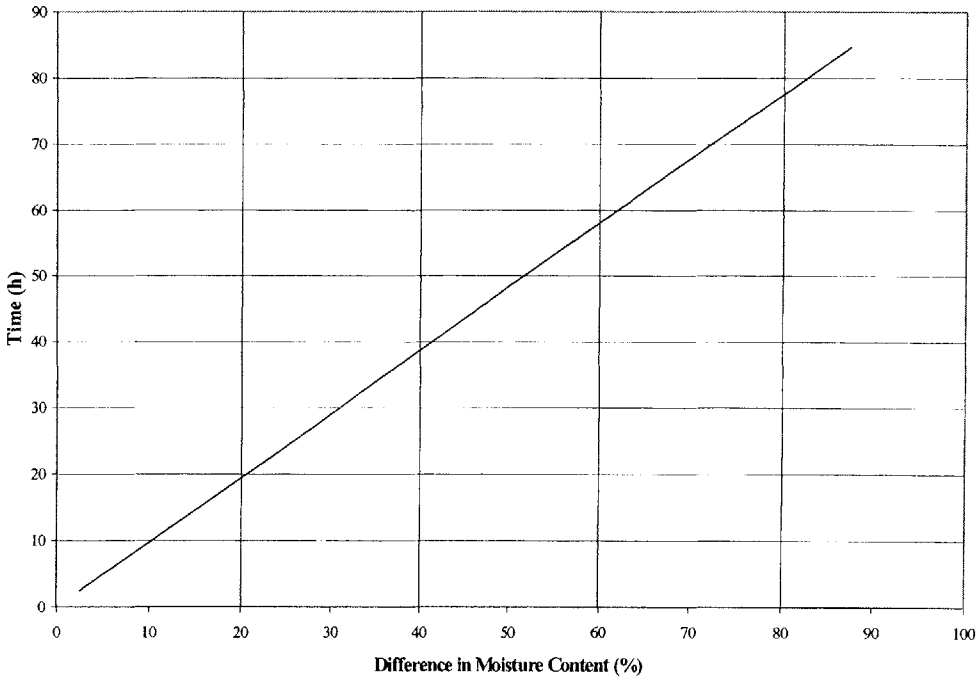

Figure C-1.7. Sensitivity of Time Required to Difference in Initial and Final Moisture Contents

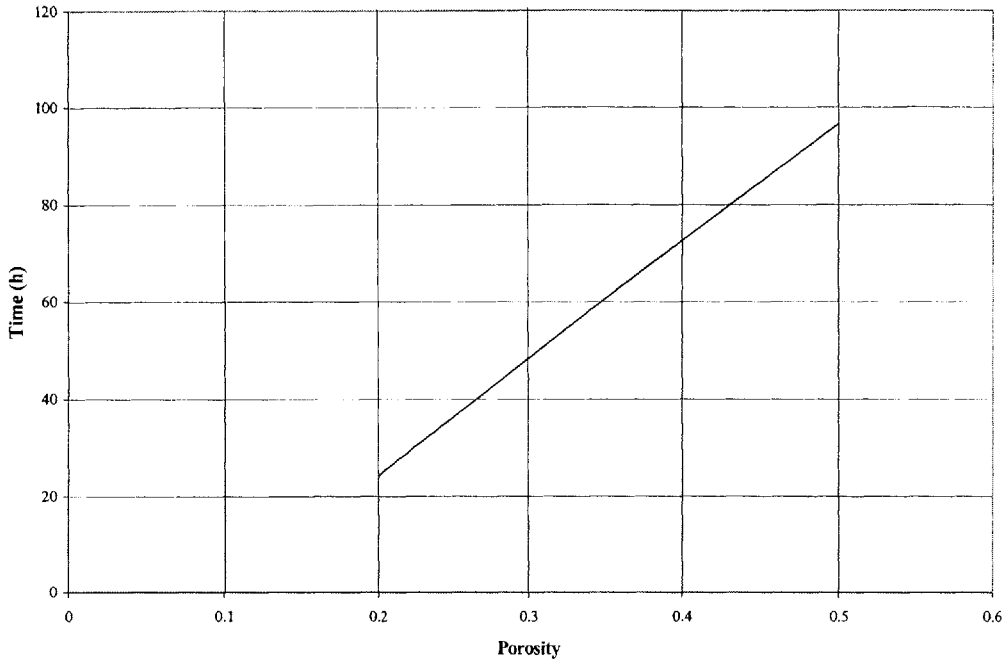

Figure C-1.8. Sensitivity of Time Required to Saturate Soil to Saturated Moisture Content (Porosity)

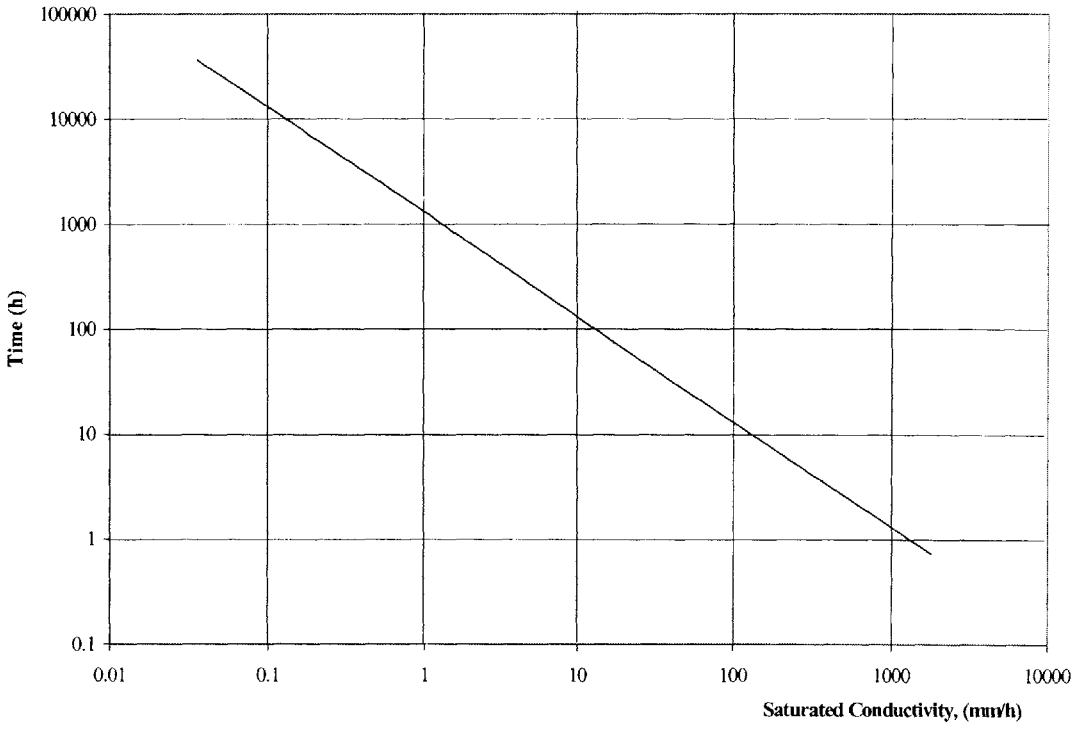

Figure C-1.9. Sensitivity of Time Required to Saturate Soil to Saturated Moisture Content (Saturated Conductivity)

C-1.3. Sensitivity of Rainfall Characteristics Required to Saturate Soil

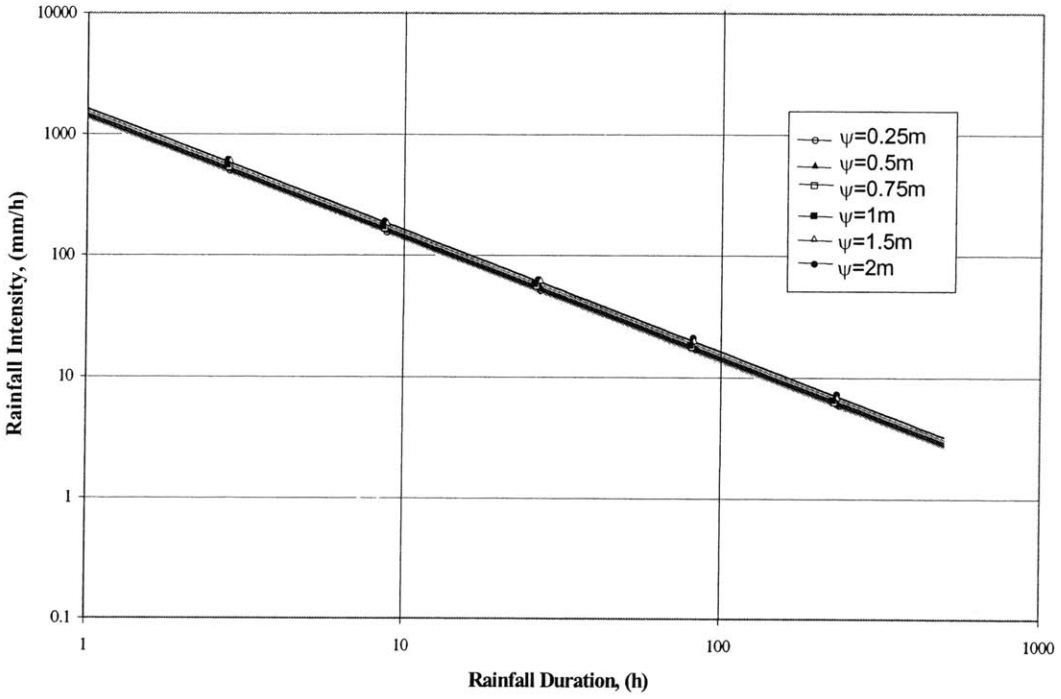

Figure C-1.10. Sensitivity of Rainfall Characteristics to Matric Suction Head

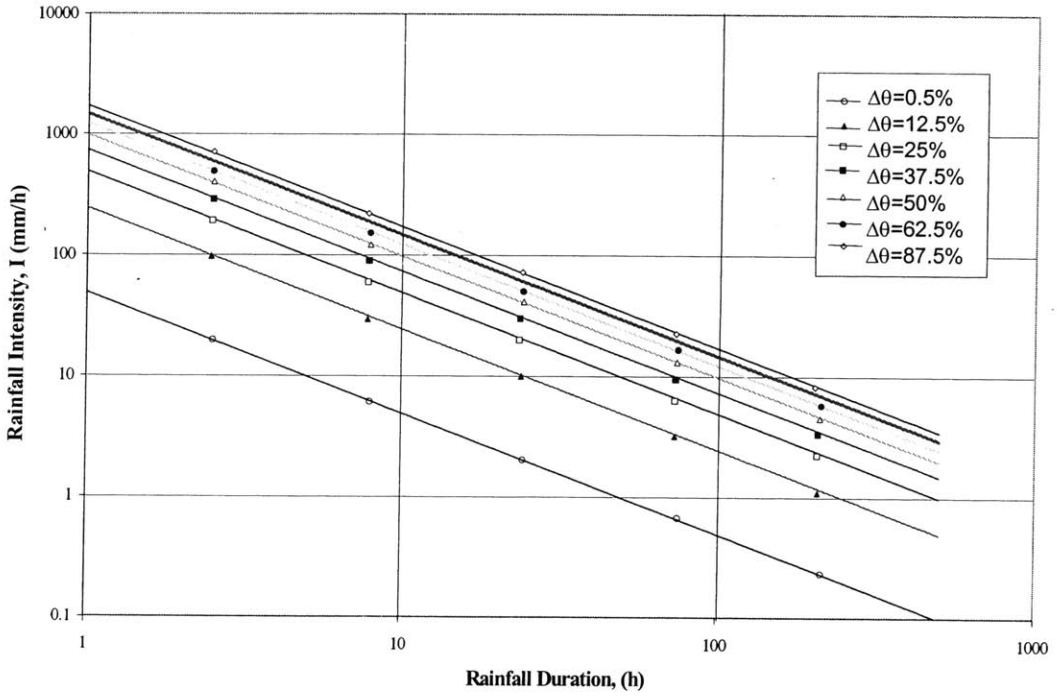

Figure C-1.11. Sensitivity of Rainfall Characteristics to Moisture Content

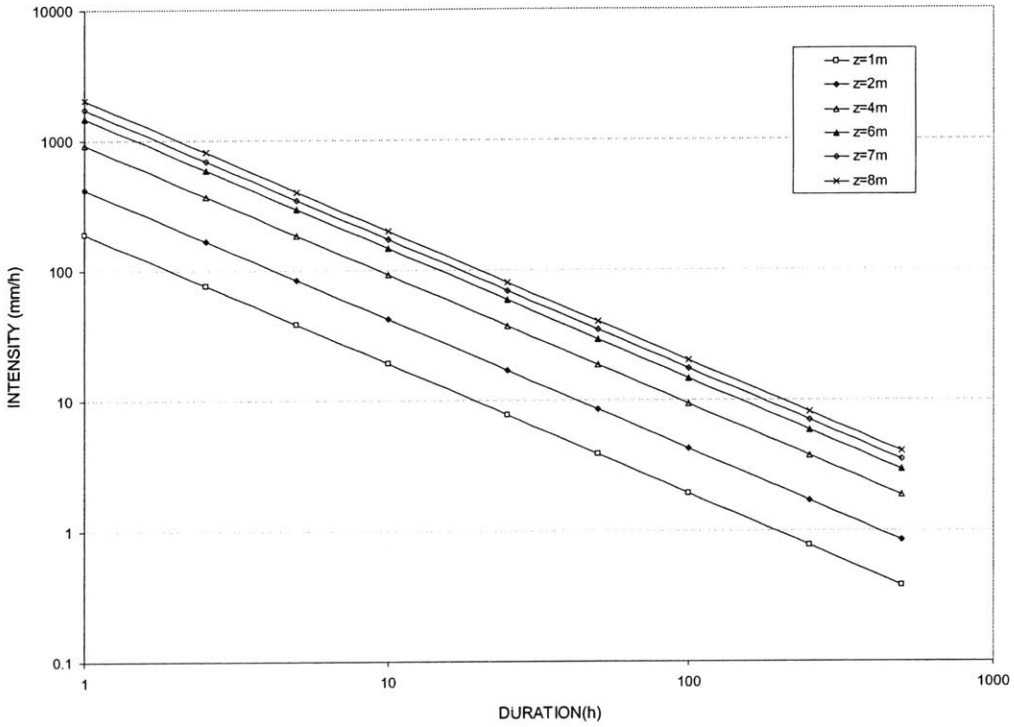

Figure C-1.12. Sensitivity of Rainfall Characteristics to Saturation Depth

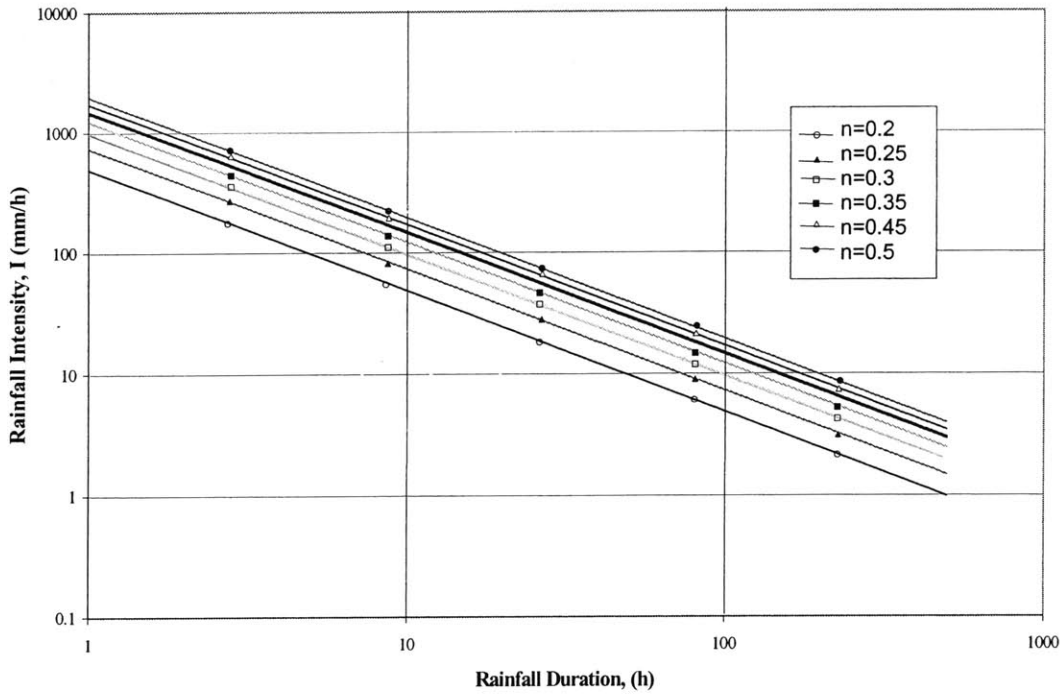

Figure C-1.13. Sensitivity of Rainfall Characteristics to Saturated Moisture Content (Porosity)

PART C-2. STABILITY SENSITIVITY ANALYSES

In this Appendix, the influence of different parameters on stability analyses is presented using the Infinite Slope Model. Part C-2.1 deals with one parameter sensitivity analyses, and Part C-2.2 deals with two parameter sensitivity analyses that include correlation. Parts C-2.3, and C-2.4 deal with sensitivity analyses performed as a function of the depth of the failure surface below the ground surface. This will give an indication to the relative importance of different parameters in relation to the location of the failure surface. 2-

The slope in consideration is shown in Figure C-2.1, and the variation of Factor of Safety is shown in Figure C-2.2. This will be used as the base case for the sensitivity analyses, which will allow one to better investigate the effects of each parameter on the stability analyses by comparing the results to this case.

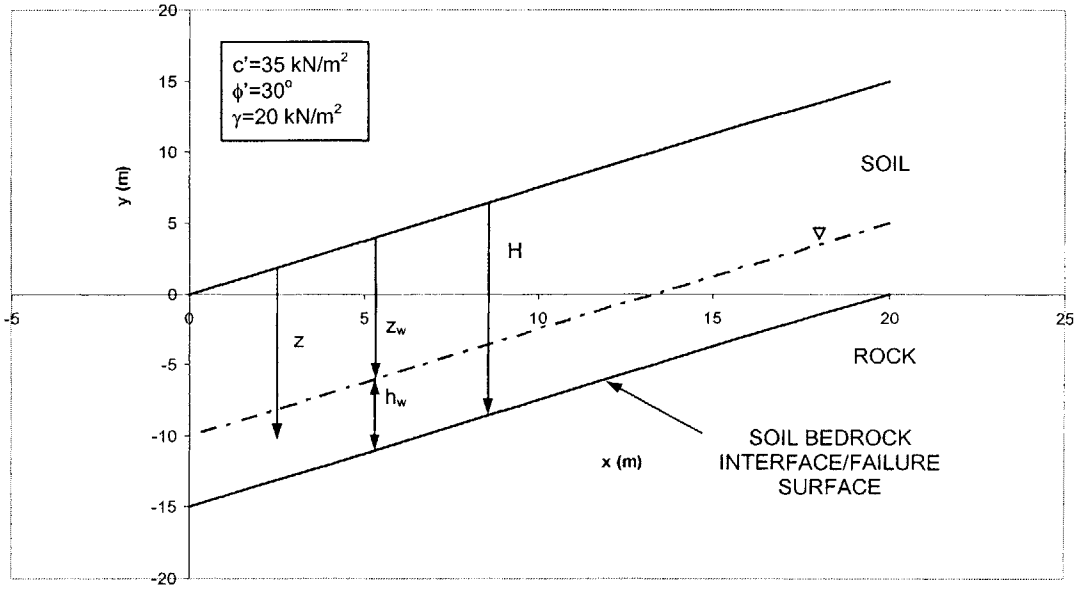

Figure C-2.1. Slope Geometry and Parameters for Base Case

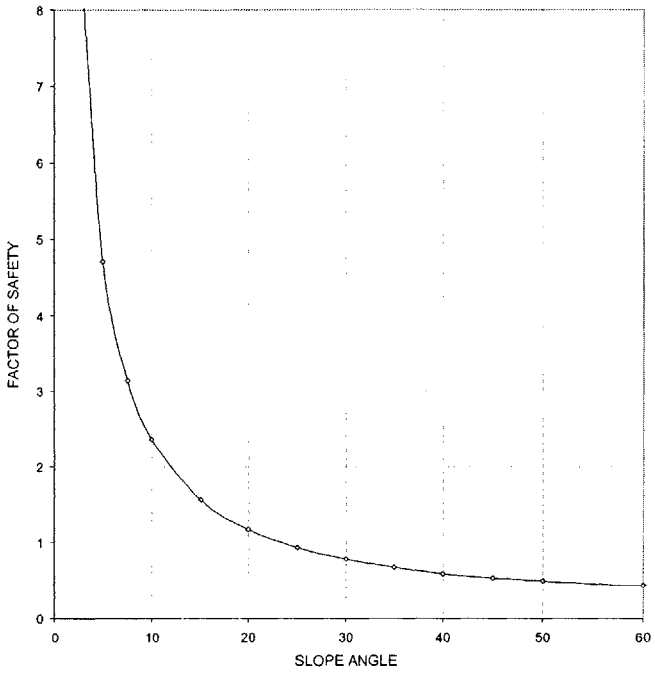

Figure C-2.2. Factor of Safety against Slope Angle for Base Case

C-2.1: ONE PARAMETER SENSITIVITY ANALYSES

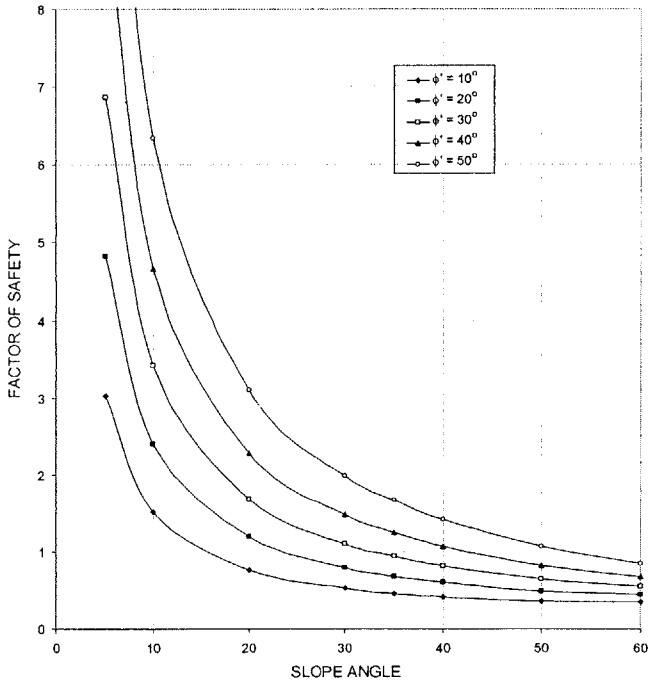

Figure C-2.3. Effect of Angle of Shear Resistance and Slope Angle on Factor of Safety

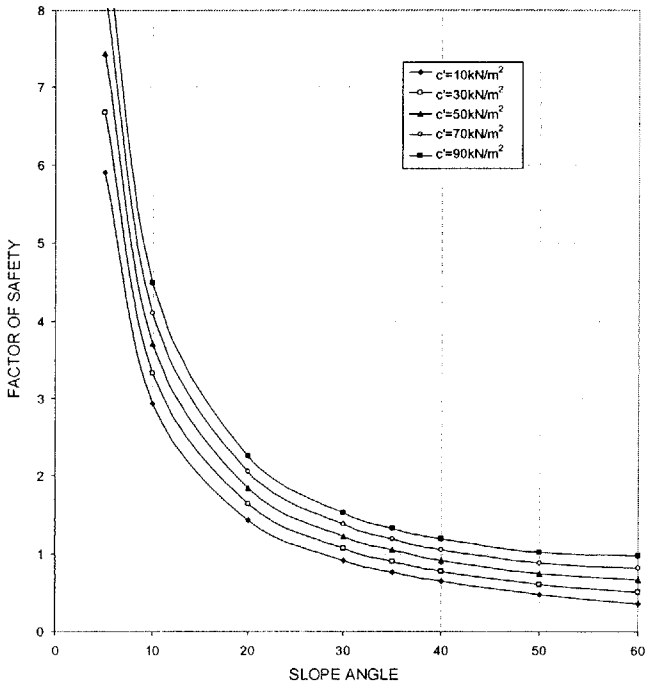

Figure C-2.4. Effect of Cohesion and Slope Angle on Factor of Safety

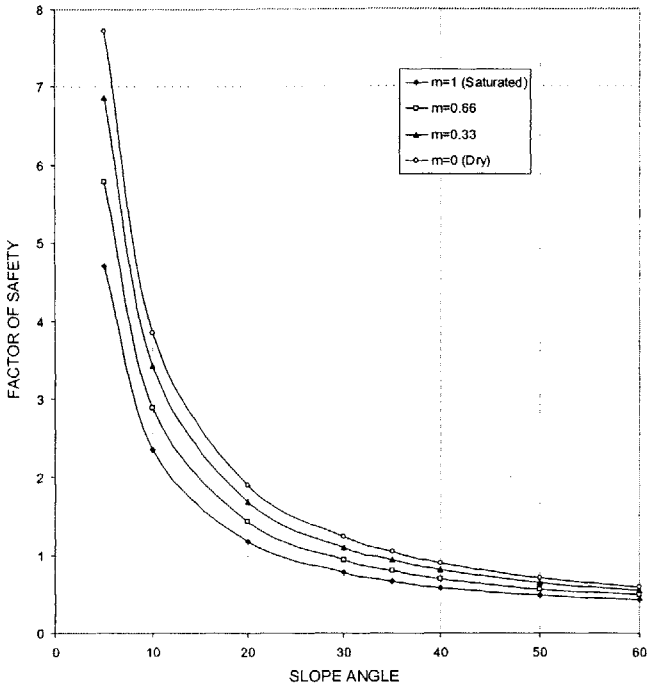

Figure C-2.5. Effect of Degree of Saturation and Slope Angle on Factor of Safety

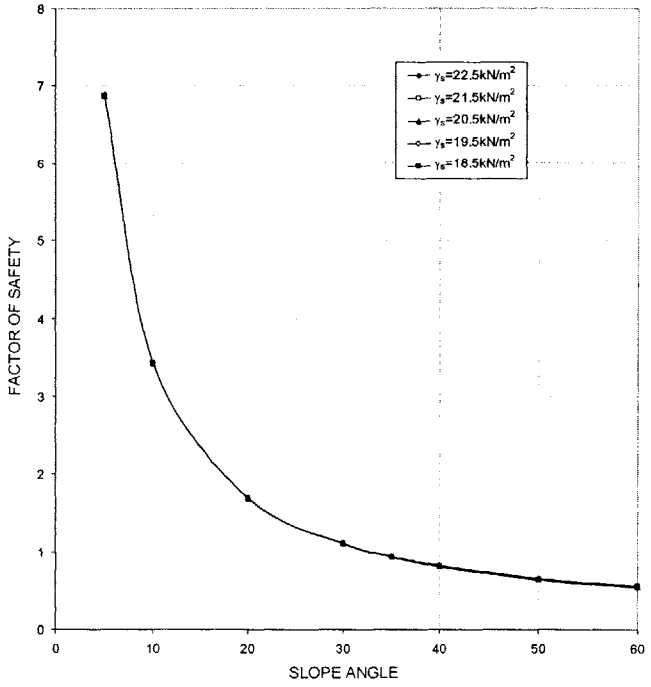

Figure C-2.6. Effect of Saturated Unit Weight of Soil and Slope Angle on Factor of Safety

C-2.2: TWO PARAMETER SENSITIVITY ANALYSES

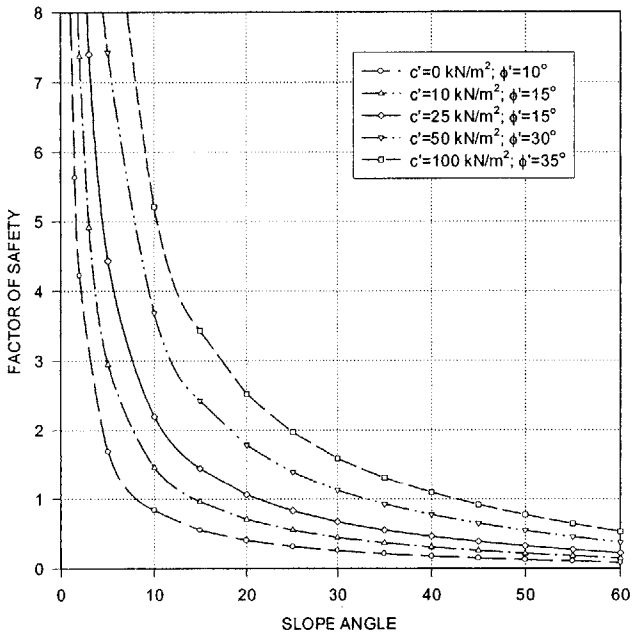

Figure C-2.7. Effect of Positive Correlation between c' and ϕ', and Slope Angle on Factor of Safety

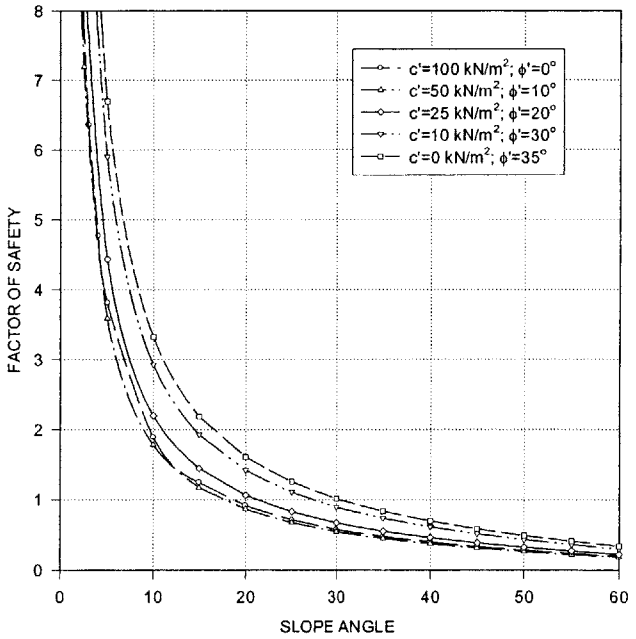

Figure C-2.8. Effect of Negative Correlation between c' and ϕ', and Slope Angle on Factor of Safety

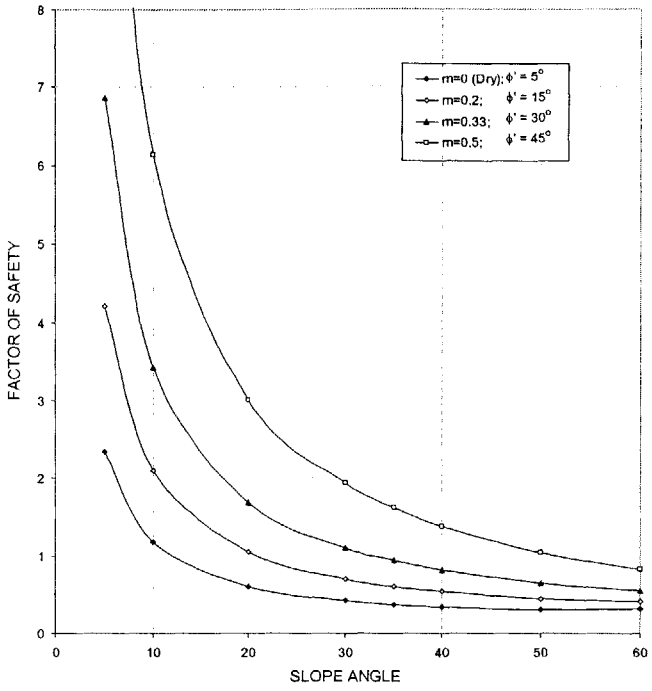

Figure C-2.9. Effect of Positive Correlation between ϕ' and Degree of Saturation, and Slope Angle on Factor of Safety

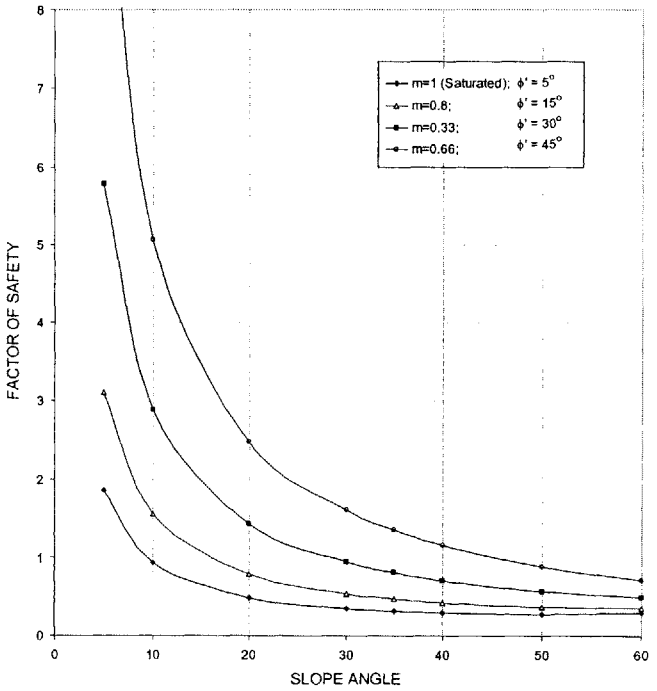

Figure C-2.10. Effect of Negative Correlation between ϕ' and Degree of Saturation, and Slope Angle on Factor of Safety

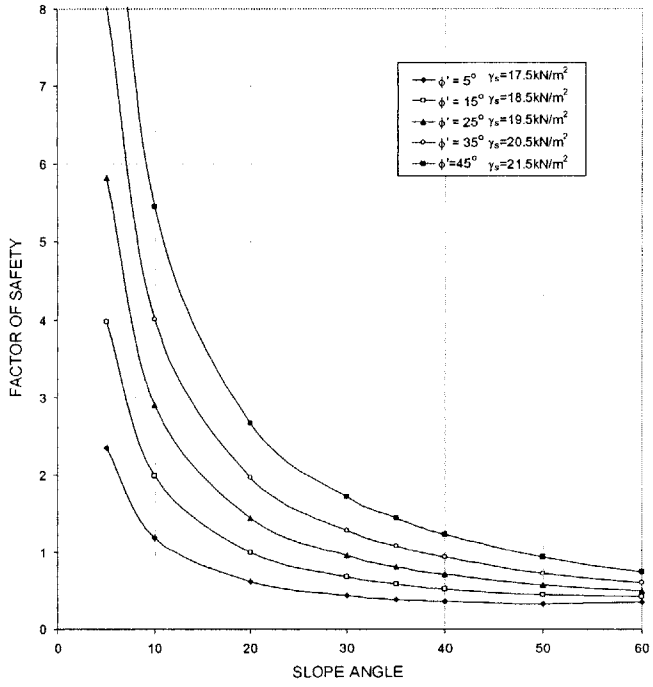

Figure C-2.11. Effect of Positive Correlation between ϕ' and Unit Weight of Soil, and Slope Angle on Factor of Safety

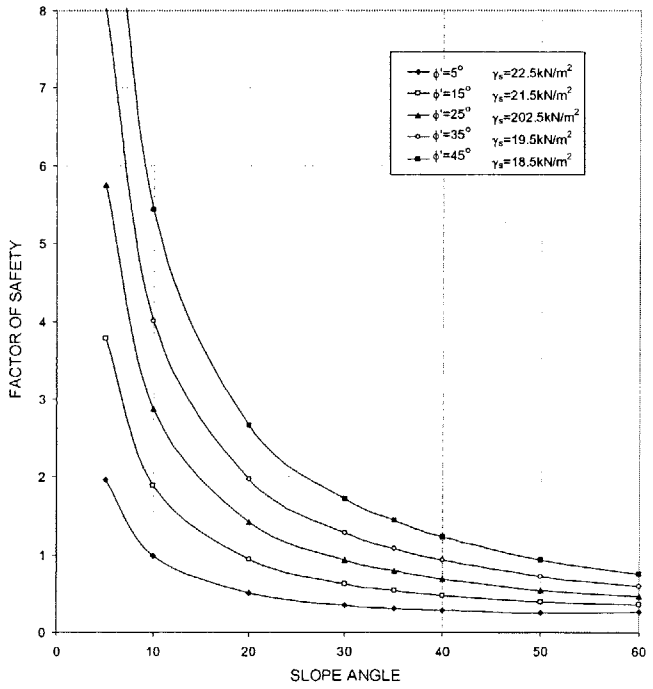

Figure C-2.12. Effect of Negative Correlation between ϕ' and Unit Weight of Soil, and Slope Angle on Factor of Safety

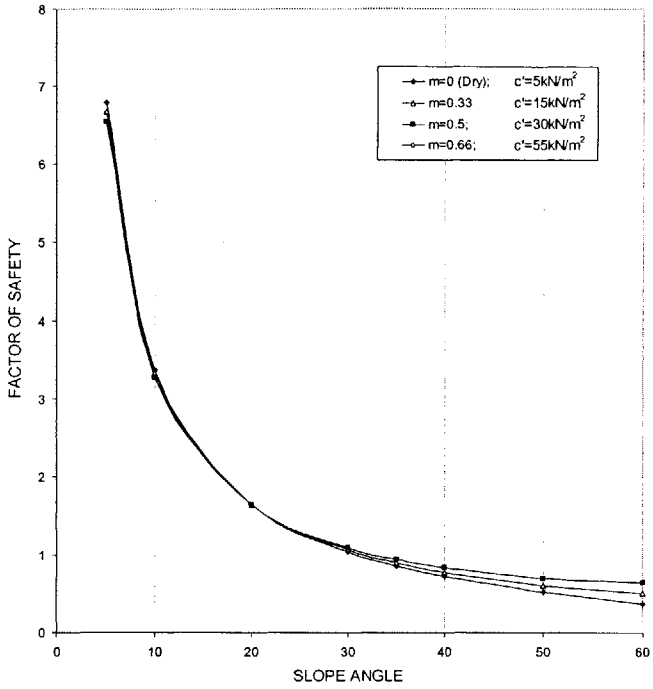

Figure C-2.13. Effect of Positive Correlation between c' and Degree of Saturation, and Slope Angle on Factor of Safety

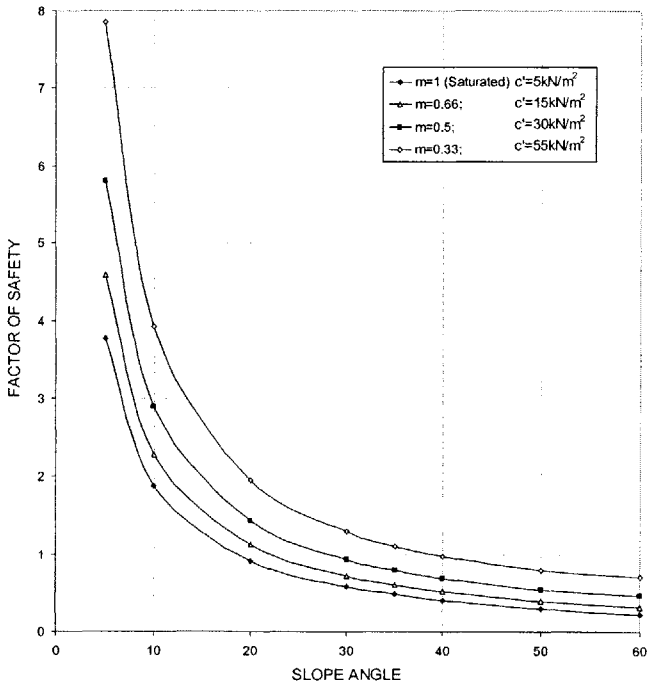

Figure C-2.14. Effect of Negative Correlation between c' and Degree of Saturation, and Slope Angle on Factor of Safety

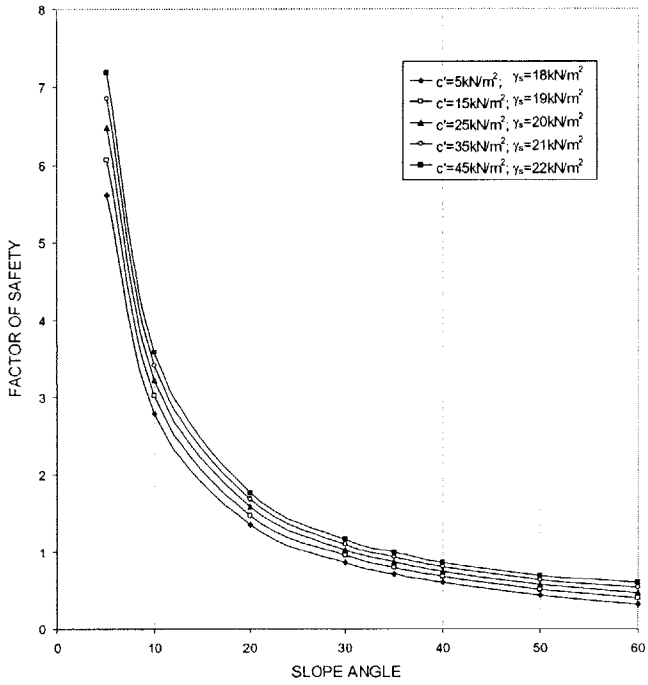

Figure C-2.15. Effect of Positive Correlation between c' and Saturated Unit Weight of Soil, and Slope Angle on Factor of Safety

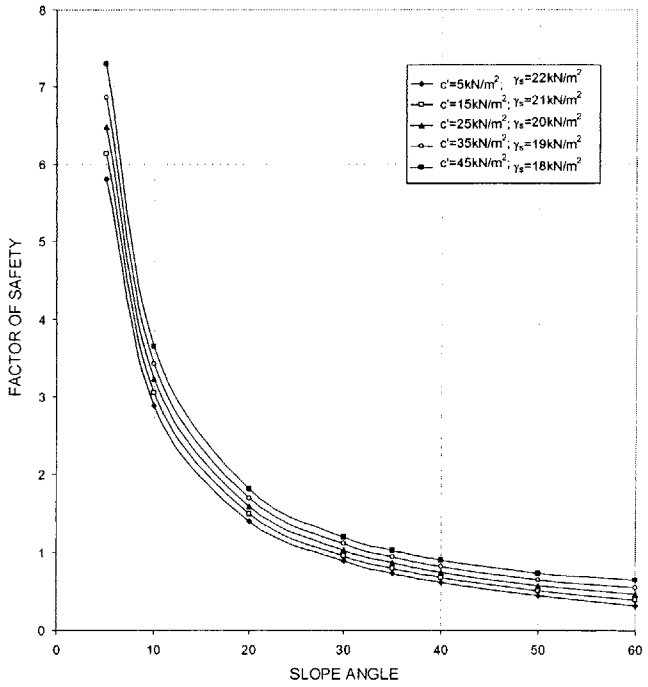

Figure C-2.16. Effect of Negative Correlation between Degree c' and and Saturated Unit Weight of Soil, and Slope Angle on Factor of Safety

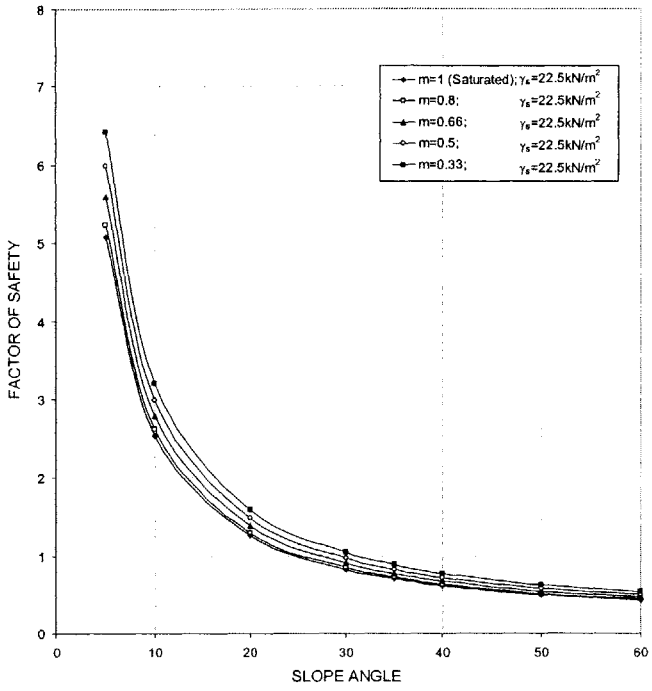

Figure C-2.17. Effect of Positive Correlation between Degree of Saturation and Saturated Unit Weight of Soil, and Slope Angle on Factor of Safety

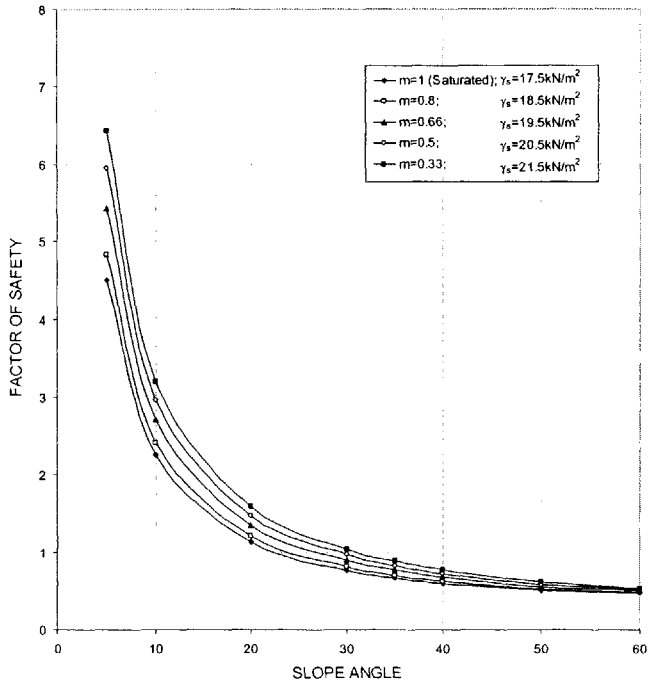

Figure C-2.18. Effect of Negative Correlation between Degree of Saturation and Saturated Unit Weight of Soil, and Slope Angle on Factor of Safety

In the above analyses, the failure surface has been assumed to be at the strength discontinuity at the soil bedrock interface, while lying in the soil. This is done since the Infinite Slope Model requires an assumption of the location of the potential failure surface.

This is, however, not necessarily the case, particularly in the context of rainfall induced landslides, where the failure surface may be shallow. This was discussed in detail in Chapter 3. It is therefore, also interesting to plot the variation of Factor of Safety with depth below the ground surface. This depth can be thought of as being representative of the depth of the potential failure surface below the ground surface.

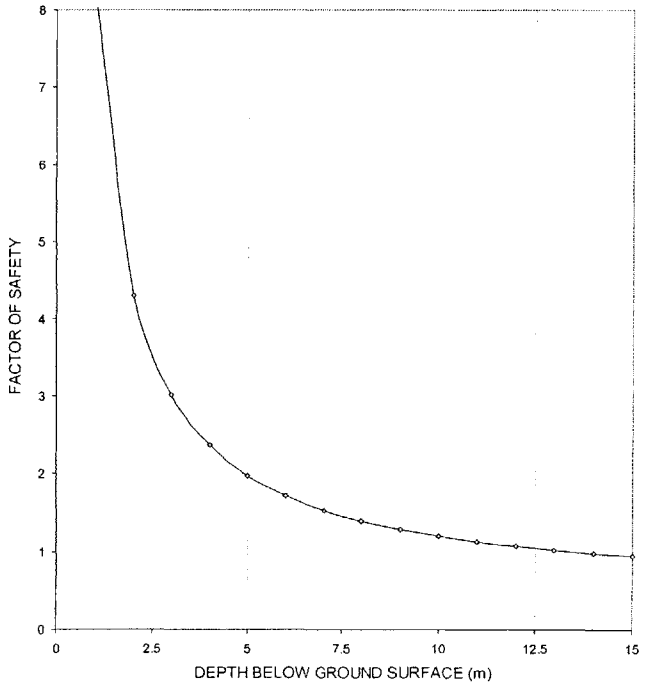

Figure C-2.19. Factor of Safety against Depth for Base Case

C-2.3: ONE PARAMETER SENSITIVITY ANALYSES

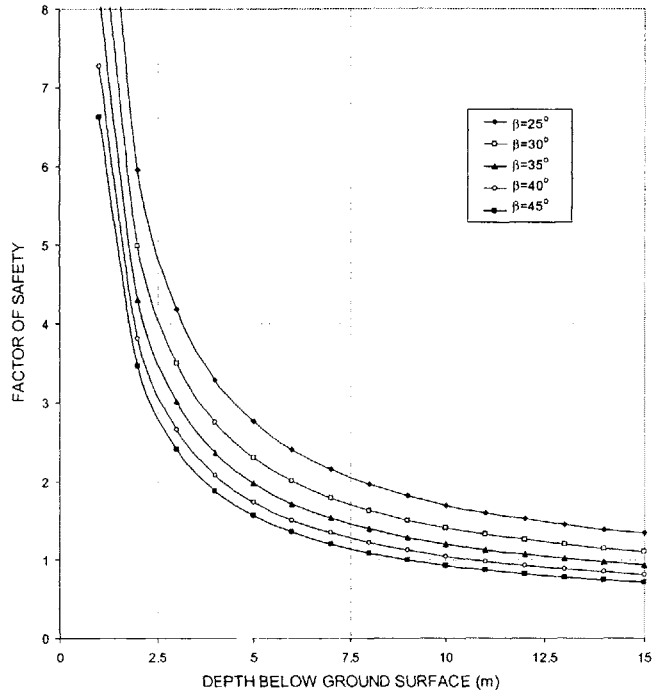

Figure C-2.20. Effect of Slope Angle and Depth on Factor of Safety

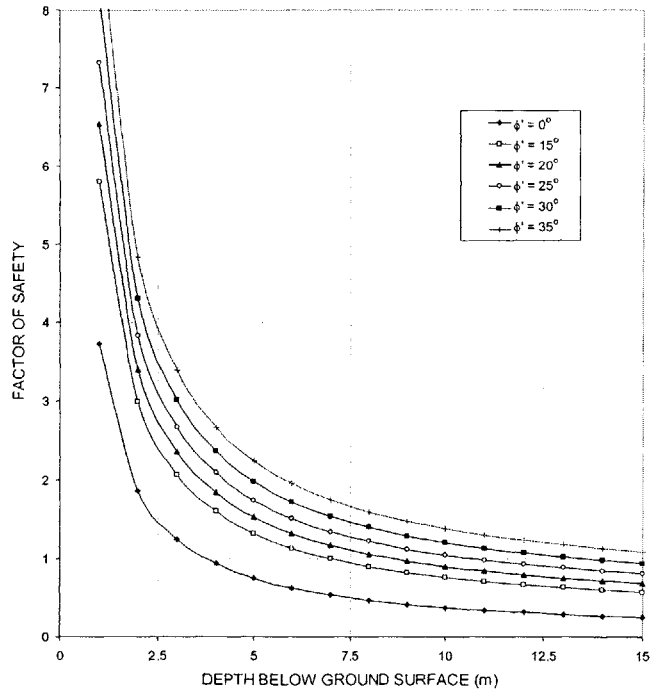

Figure C-2.21. Effect of Angle of Shear Resistance and Depth on Factor of Safety

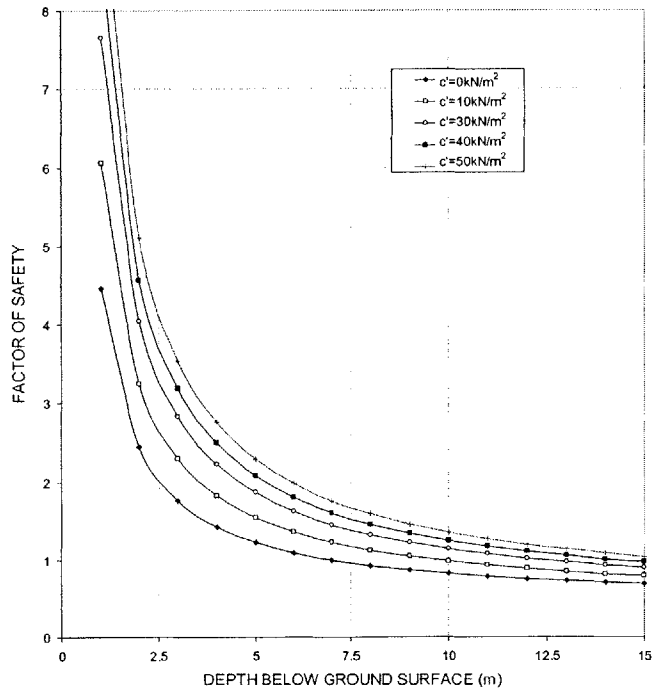

Figure C-2.22. Effect of Cohesion and Depth on Factor of Safety

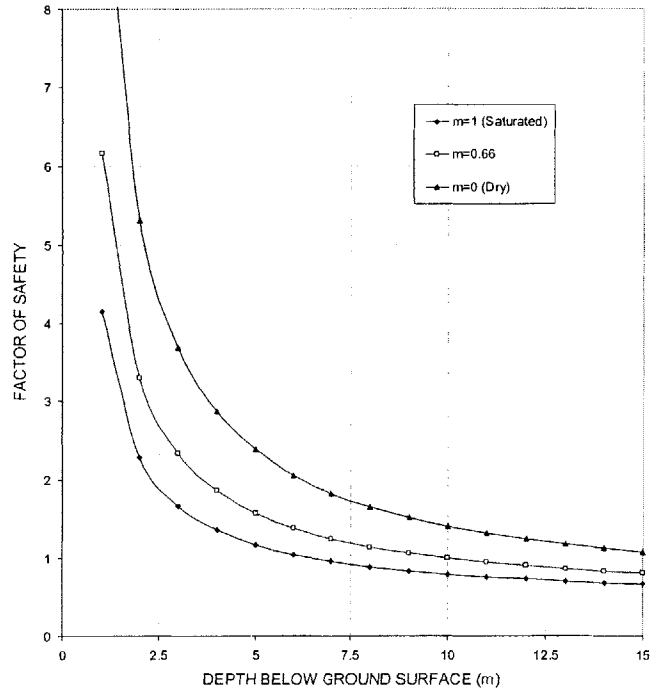

Figure C-2.23. Effect of Angle of Degree of Saturation and Depth on Factor of Safety

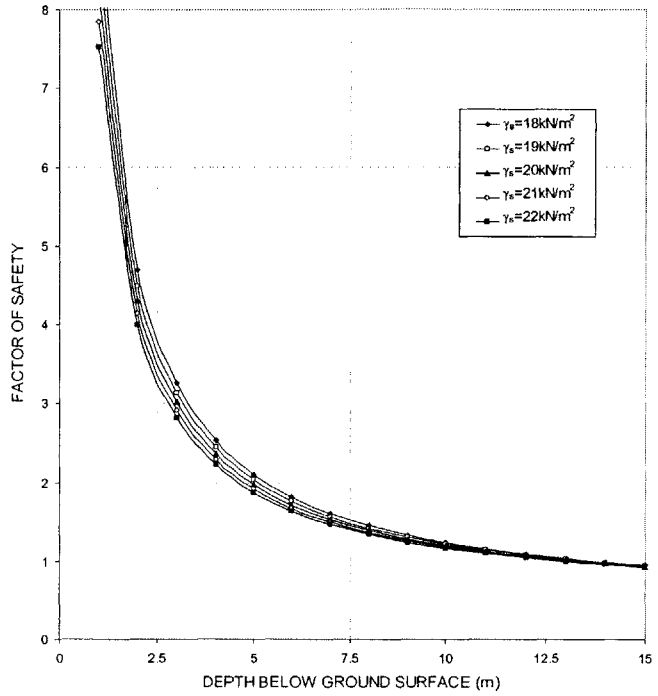

Figure C-2.24. Effect of Unit Weight and Depth on Factor of Safety

PART C-2.4: TWO PARAMETER SENSITIVITY ANALYSES

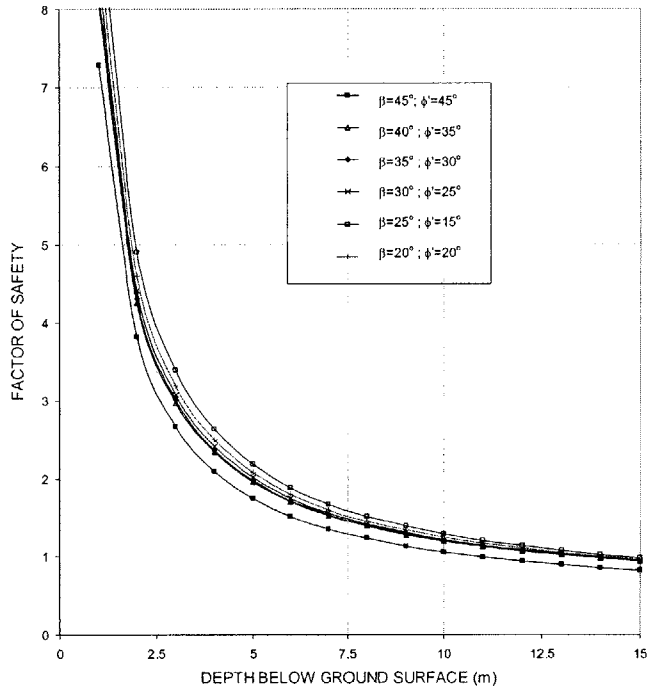

Figure C-2.25. Effect of Positive Correlation between ϕ' and Slope Angle, and Depth on Factor of Safety

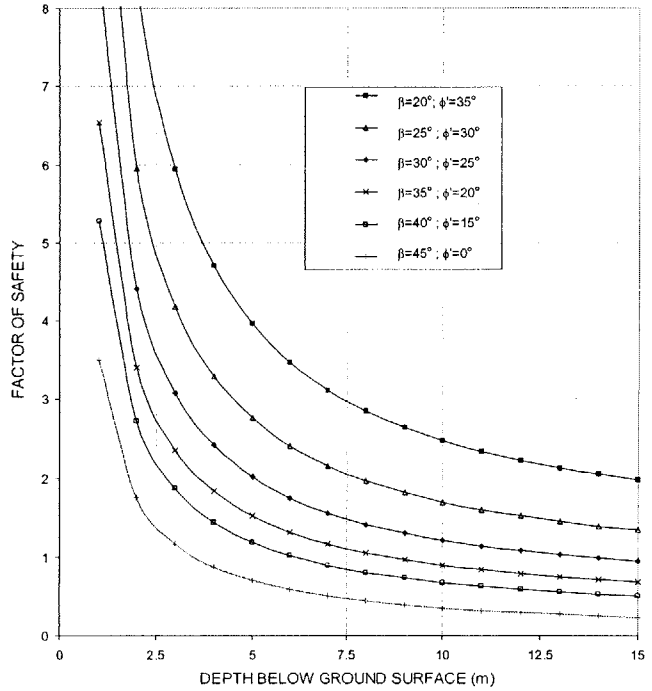

Figure C-2.26. Effect of Negative Correlation between ϕ' and Slope Angle, and Depth on Factor of Safety

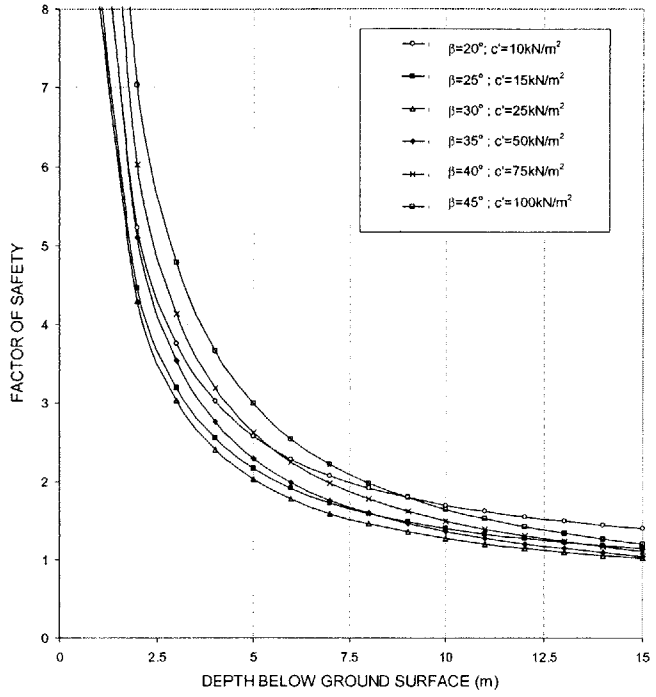

Figure C-2.27. Effect of Positive Correlation between c' and Slope Angle, and Depth on Factor of Safety

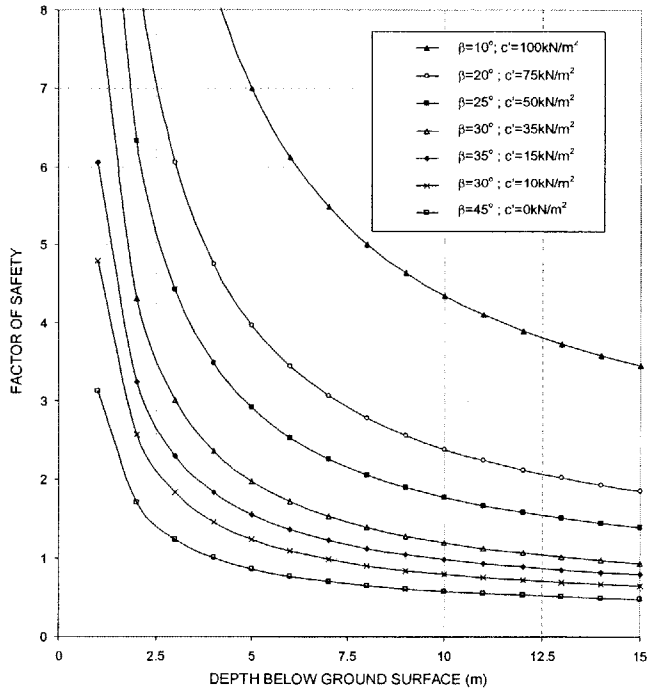

Figure C-2.28. Effect of Negative Correlation between c' and Slope Angle and Degree of Saturation, and Depth on Factor of Safety

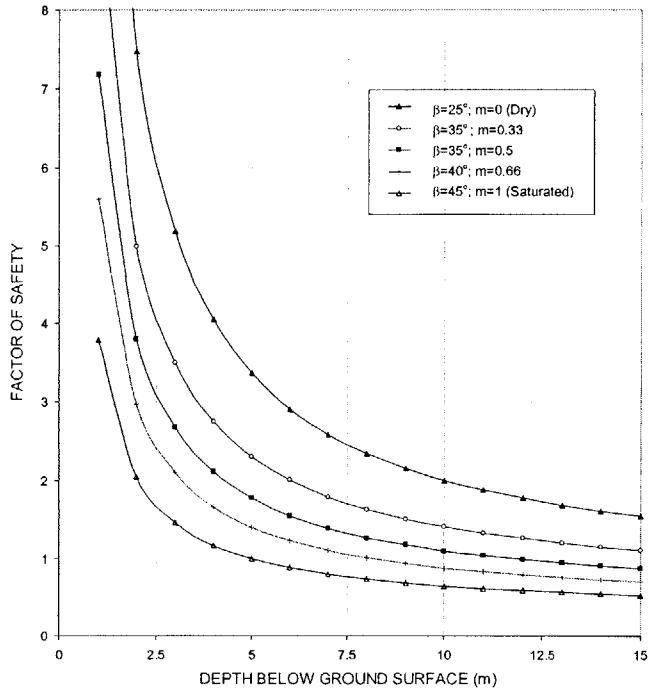

Figure C-2.29. Effect of Positive Correlation between Slope Angle and Degree of Saturation, and Depth on Factor of Safety

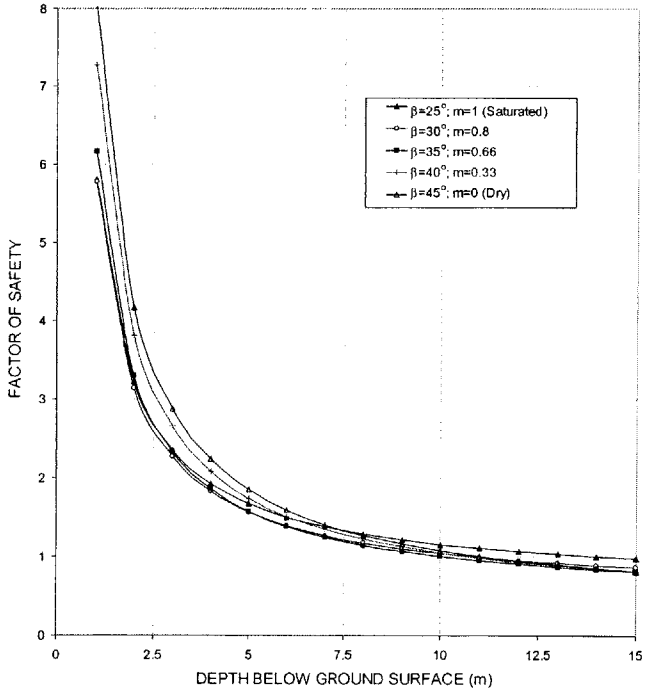

Figure C-2.30. Effect of Negative Correlation between Slope Angle and Degree of Saturation, and Depth on Factor of Safety

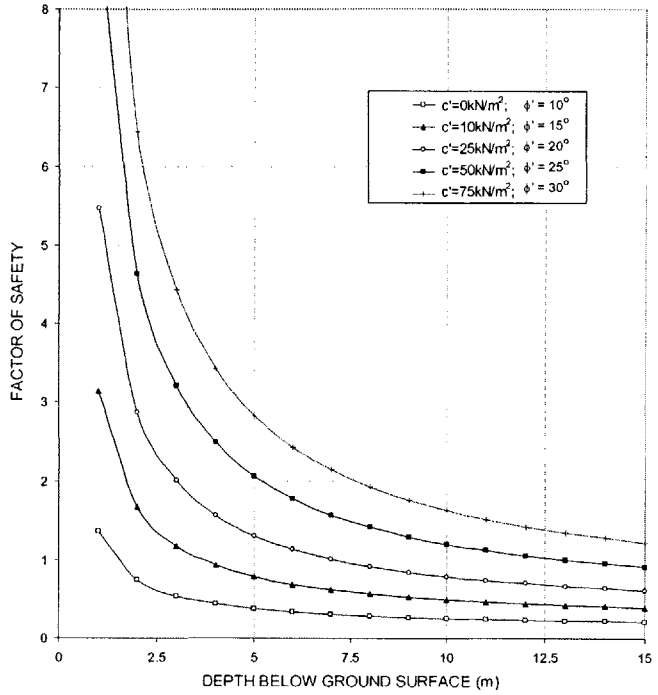

Figure C-2.31. Effect of Positive Correlation between c' and ϕ', and Depth on Factor of Safety

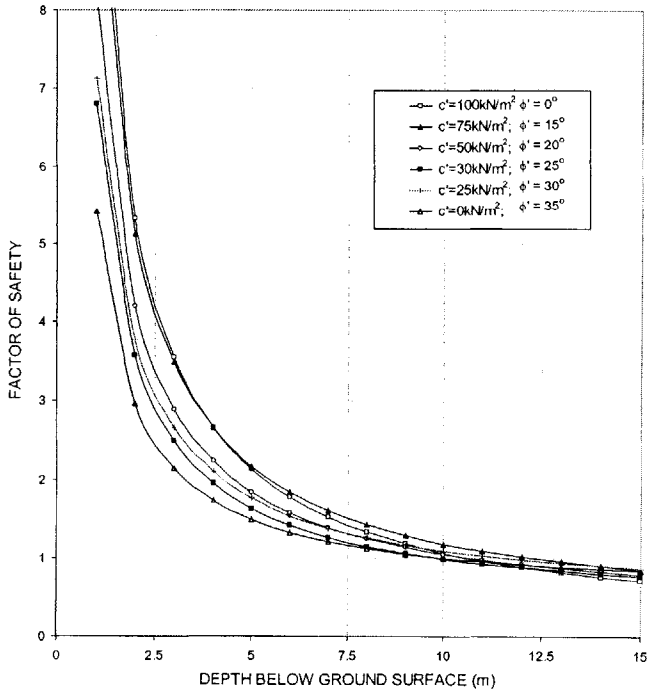

Figure C-2.32. Effect of Negative Correlation between c' and ϕ', and Depth on Factor of Safety

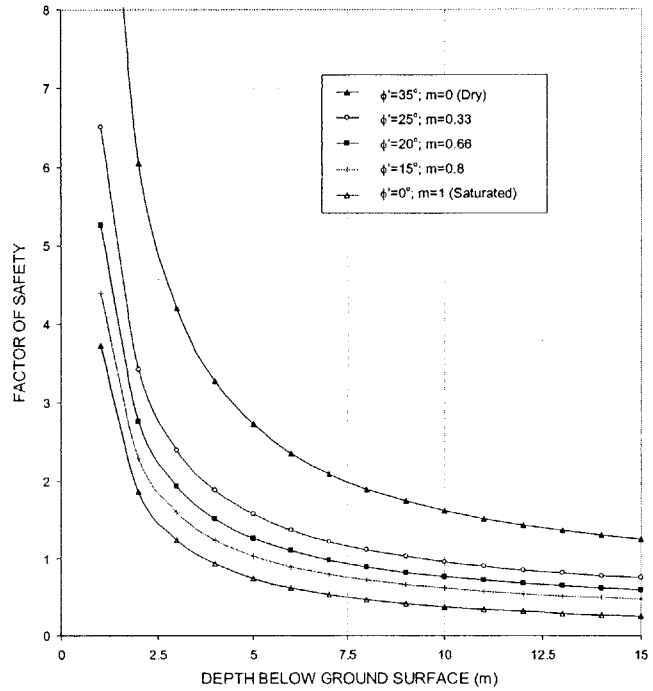

Figure C-2.33. Effect of Positive Correlation between ϕ' and Degree of Saturation, and Depth on Factor of Safety

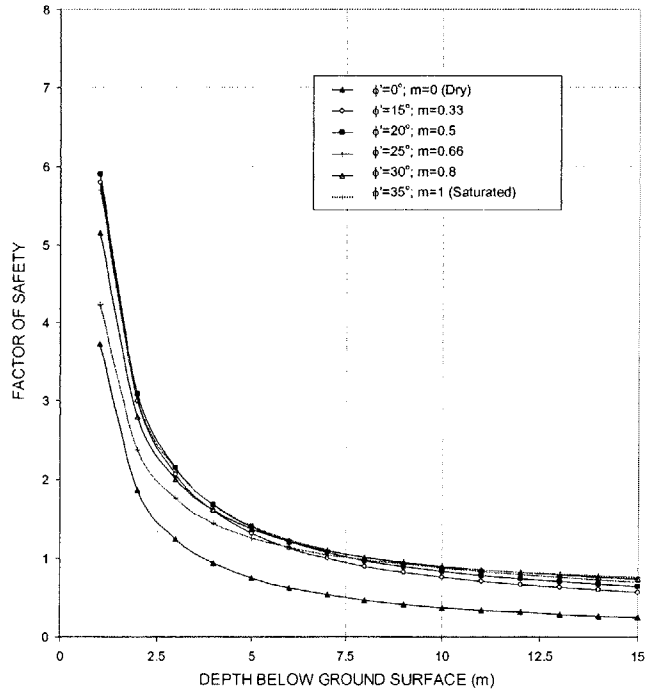

Figure C-2.34. Effect of Negative Correlation between ϕ' and Degree of Saturation, and Depth on Factor of Safety

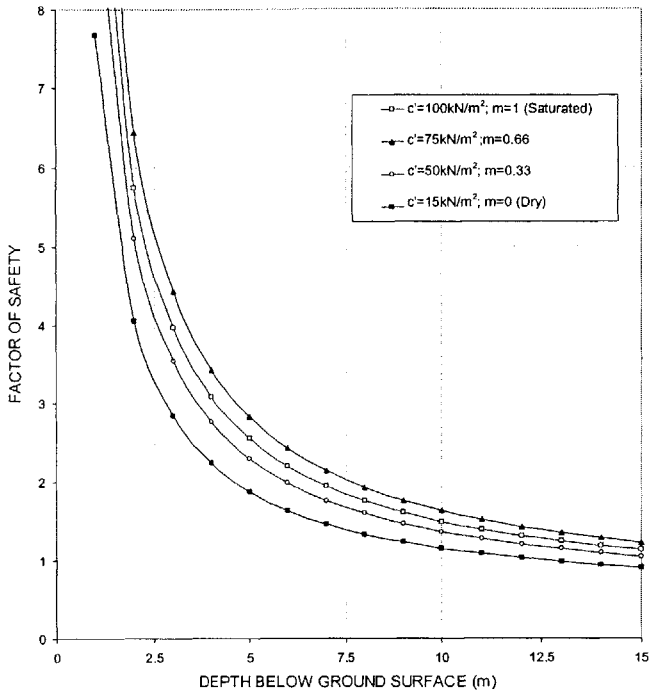

Figure C-2.35. Effect of Positive Correlation between c' and Degree of Saturation, and Depth on Factor of Safety

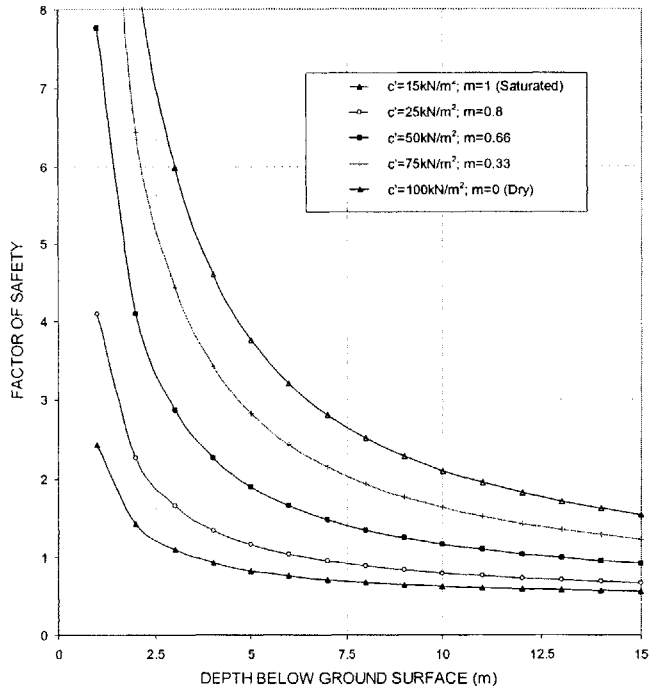

Figure C-2.36. Effect of Negative Correlation between c' and Degree of Saturation, and Depth on Factor of Safety

APPENDIX D
A COMPARISON OF SLOPE STABILITY METHODS

The instability of natural slopes is a major geologic hazard in many regions of the world. The degree of stability of a slope may be expressed through the factor of safety F, which is the ratio between a soil resistance measure and the associated applied load. Hence values of F larger than 1 are associated with stability and values smaller than one indicate unstable conditions. For natural slopes that exhibit low depth to length ratios (so-called infinite slopes) the factor of safety is given by (Skempton and DeLory, 1957):

$$F = \frac{c'}{\gamma z \sin\alpha\cos\alpha} + \frac{\tan\phi'}{\tan\alpha} - m\left(\frac{\gamma_w \tan\phi'}{\gamma\tan\alpha}\right) \qquad \text{(D-1)}$$

where

c' is the cohesion of the soil

ϕ' is the angle of internal friction of the soil

γ is the unit weight of the soil

γ_w is the unit weight of water

α is the inclination of the slope to the horizontal

m is the degree of saturation of the soil

As indicated above, the failure criterion is $F < 1$. For example, a slope with the parameters in Table 1 has F= 1.15 and is stable.

z (m)	5
z_w (m)	2.5
m	0.5
c' (kN/m^2)	25
ϕ'	30
α	35
γ (kN/m^2)	20
γ_w (kN/m^2)	9.81

Table D-1. Slope Parameters

However, if the parameters are uncertain, there may be a nonzero probability of slope failure. Of the variables in Table D-1, the most uncertain ones are the strength parameters c' and ϕ', with typical coefficients of variation $V_{c'} = 0.20$ and $V_{\phi'} = 0.25$. Experience has shown that they follow a Normal distribution.

In the following, we investigate how uncertainty on c' and ϕ' affects the reliability of infinite slopes. We start by using a first-order second-moment (FOSM) approach and then compare results with a second-moment (SM) analysis and Monte Carlo simulation.

D-1. FIRST-ORDER SECOND-MOMENT (FOSM) RELIABILITY INDEX

A first approximation to the reliability of slopes is obtained by linearizing the function in Eq. D-1 around the mean value of the strength parameters. This gives

$$F(c',\phi') = F(m_{c'},m_{\phi'}) + \frac{\partial F(c',\phi')}{\partial c'}(c'-m_{c'}) + \frac{\partial F(c',\phi')}{\partial \phi'}(\phi'-m_{\phi'}) \qquad \text{(D-2)}$$

where

$$\frac{\partial F(c',\phi')}{\partial c'} = \frac{1}{\gamma z \sin\beta\cos\beta}, \qquad \frac{\partial F(c',\phi')}{\partial \phi'} = \left[\frac{\gamma - m\gamma_w}{\gamma \tan\beta \cos^2\phi'}\right]$$

The Mean-Value First Order Reliability Index is then given by:

$$\beta_{FOSM} = \frac{E[F(c',\phi')] - 1}{\sqrt{Var[F(c',\phi')]}} \qquad \text{(D-3)}$$

Assuming that the parameters in Table D-1 are mean values and that c' and ϕ' are the only random quantities, are independent, and have coefficients of variation $V_{c'} = 0.20$ and $V_{\phi'} = 0.25$, one finds $E[F(c',\phi')] = 1.15$, $Var[F(c',\phi')] = 0.0467$, and $\beta_{FOSM} = 0.714$. Under the assumption of normality, the probability of slope failure is

$P_f = \Phi(-0.714) = 0.237$, where Φ is the standard normal cumulative distribution function.

D-2. SECOND-MOMENT (SM) RELIABILITY INDEX

A more accurate evaluation of slope reliability is obtained by using the actual nonlinear expression of F in Eq. D-1 and calculating the second moment reliability index. Figure D-1a shows the failure boundary (obtained by setting F = 1) in the space of the original variables c' and ϕ', and the largest dispersion ellipse contained in the safe region. Figure D-1b shows the same geometrical objects in the space of the variables $c^* = \frac{(c'-m_{c'})}{\sigma_{c'}}$ and $\phi^* = \frac{(\phi'-m_{\phi'})}{\sigma_{\phi'}}$, linearly transformed to have zero mean and unit variance. The second moment reliability index β corresponds to the radius of the tangent circle in Figure 1b. The reliability index can be obtained using an iterative procedure as shown in Figure 1c, or using the optimization procedures discussed in Chapter 5, Part 5-2.

In this example, β = 0.739 and the associated probability of failure is $P_f = \Phi(-\beta) = 0.230$. Due to the small nonlinearity of the function $F(c',\phi')$, these results are close to those from FOSM analysis.

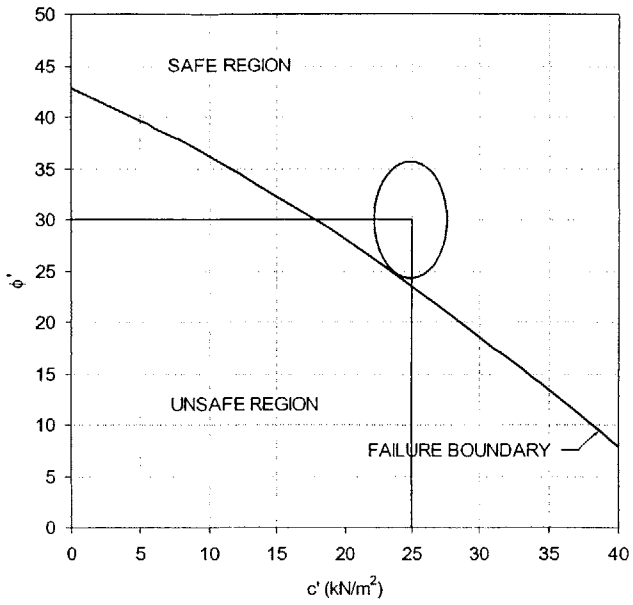

Figure D-1a. Failure boundary and critical dispersion ellipse in the space of the original variables

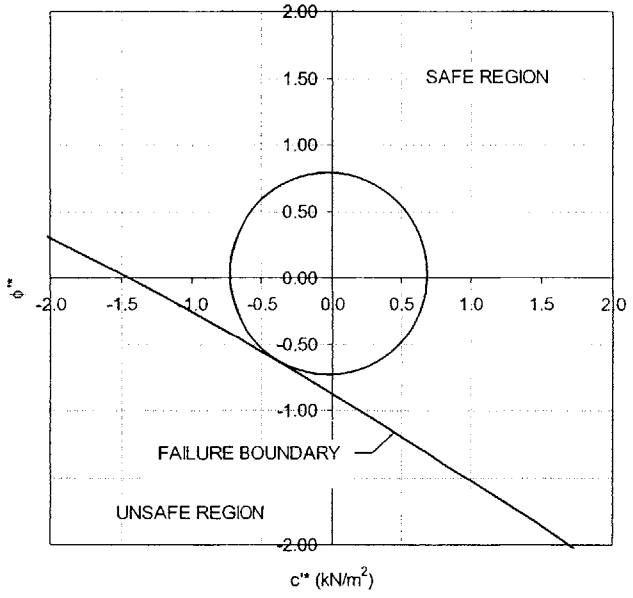

Figure D-1b. Failure boundary and critical dispersion disc in the space of the transformed variables

Transformed Space $\underline{Z} \sim (\underline{0}, \underline{I})$

Original Space $\underline{X} \sim (\underline{m}, \underline{\Sigma})$

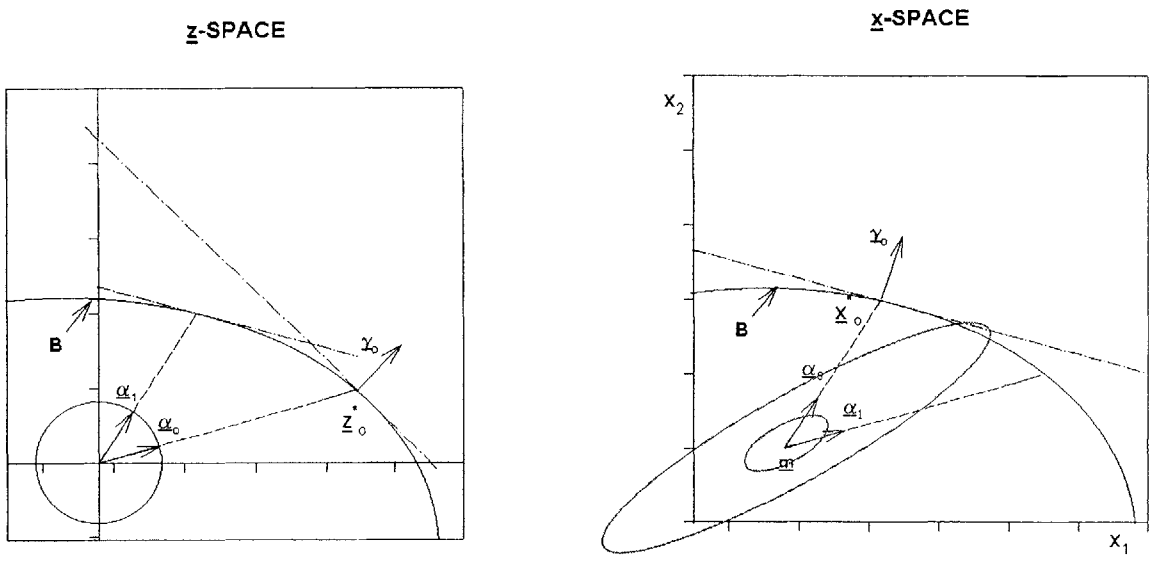

1. Select initial unit vector, $\underline{\alpha}_o$

2. Find $\underline{z}^*_o = \beta_o \underline{\alpha}_o$
   where $\beta_o = \min\{\beta : \beta\underline{\alpha}_o \in D_F\}$

3. Linearize B around $\underline{z}^*_o$

   Let $\underline{\gamma}_o$ be the unit external vector:

$$\underline{\gamma}_o = \left.\frac{\text{grad } g(\underline{z})}{|\text{grad } g(\underline{z})|}\right|_{\underline{z}^*_o}$$

$$\propto \left[\left.\begin{matrix} \frac{\partial g(\underline{z})}{\partial z_i} \\ \vdots \end{matrix}\right|_{\underline{z}^*_o}\right]$$

4. Go back to step 2 with $\underline{\alpha}_o$ replaced with $\underline{\alpha}_1 = \underline{\gamma}_o$.

   Iterate until convergence in β and $\underline{z}^*$.

1. Select initial unit vector, $\underline{\alpha}_o$

2. Find $\underline{x}^*_o = \underline{m} + \delta\underline{\alpha}_o \in B$ and calculate β_o as:

$$\beta_o = \delta\left(\underline{\alpha}_o^T \underline{\Sigma}^{-1} \underline{\alpha}_o\right)^{\frac{1}{2}}$$

3. Linearize B at $\underline{x}^*_o$. (Calculate $\underline{\gamma}_o$ as in $\underline{z}$ space).

4. The next search direction $\underline{\alpha}_1$ is that of the β point according to the linearized boundary.
   From analytical geometry,
   $\underline{\alpha}_1 \propto \underline{\Sigma}\underline{\gamma}_o$.

5. Go back to Step 2 until convergence.

Figure D-1c. Iterative Technique to Compute Reliability Index

D-3. MONTE CARLO SIMULATION

The exact probability of failure can be obtained by either numerical integration of the joint density of c' and ϕ' over the unsafe region in Figure D-1a, or alternatively through Monte Carlo simulation. Using the latter approach, we have simulated 20,000 (c', ϕ') pairs and for each pair we have calculated the value of F using Eq. D-1. The empirical probability density function of F is shown in Figure D-2. The empirical probability of failure is $P_f = P[F < 1] = 0.223$. Again due to near-linearity of the function $F(c',\phi')$, this probability is close to those obtained through FOSM and SM analysis.

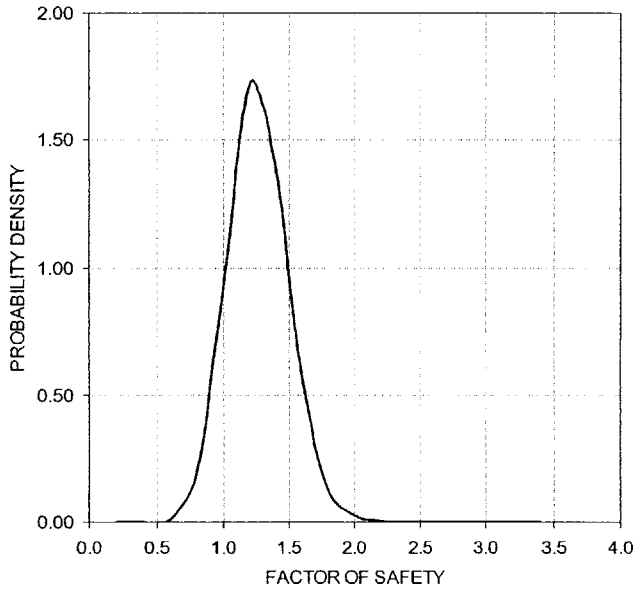

Figure D-2. Empirical probability density function of the factor of safety

D-4. DISCUSSION

Suppose that, in a given geological setting, the slope parameters (including c' and ϕ') are similar, but that the slope angle a may vary. It is then of interest to determine how the probability of failure varies as a function of α. By repeating the Monte Carlo simulations for different slope angles α, one obtains the results in Figure D-3.

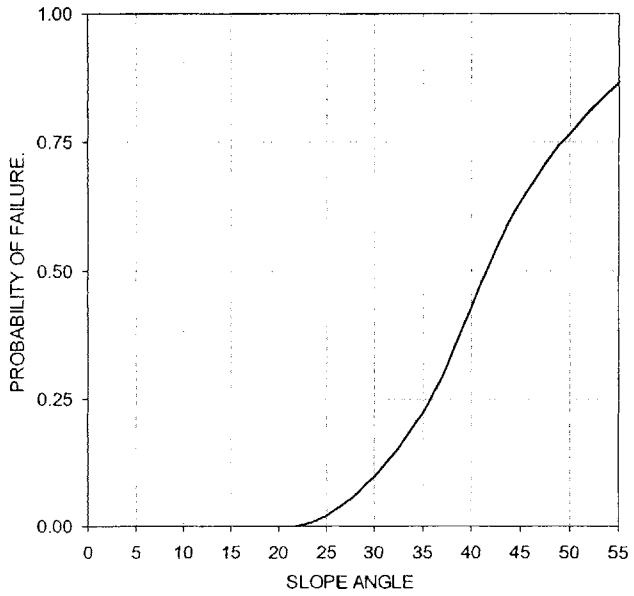

Figure D-3. Probability of slope failure as a function of slope angle

Figure D-4 compares the results of FOSM, SM, and Monte Carlo simulations, and confirms the good agreement between the different types of analyses.

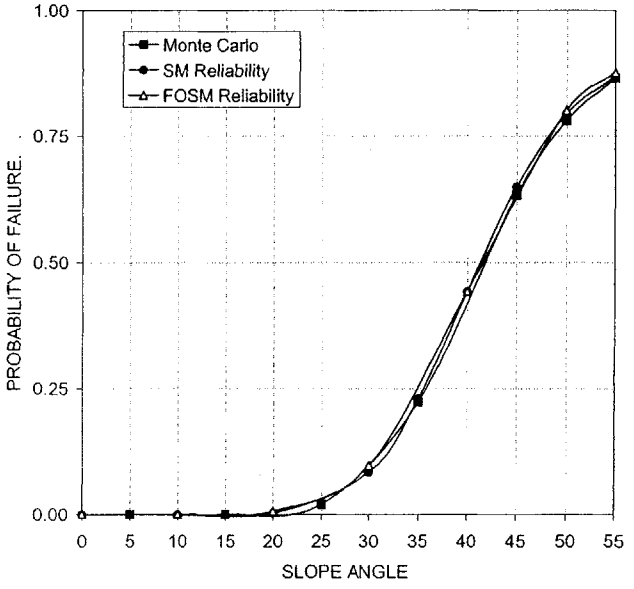

Figure D-4. Comparison of Failure Probability for Different Types of Analyses

Based on Figure D-3 (and/or D-4), agencies can prioritize where action needs to be taken. For example, one may decide to intervene on slopes with a probability of failure

greater than a given value. These actions can be active, such as providing drainage or tie-backs, or passive, such as building protective galleries. Drainage has the effect of reducing the degree of saturation in the slope, hence reducing the weight of water and increasing stability.

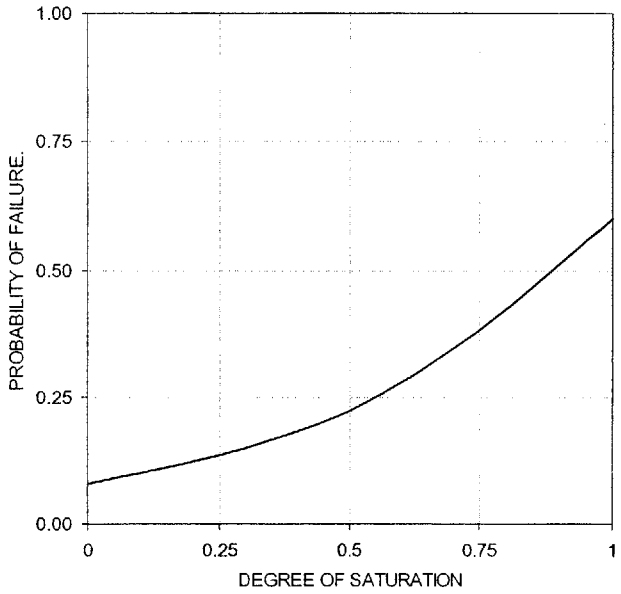

Figure D-5. Probability of slope failure against degree of saturation

Figure D-5 shows the probability of failure as a function of degree of saturation, all other parameters having the mean values in Table D-1. Plots of this type allow decision makers to determine optimal intervention levels.

D-5. CORRELATION

In the following, we investigate the effects of correlation between the strength parameters c' and ϕ' on slope reliability.

D-5.1. FIRST-ORDER SECOND-MOMENT (FOSM) RELIABILITY INDEX

The First Order Second Moment Analysis that resulted in $\beta_{FOSM} = 0.714$, and under the assumption of normality, $P_f = \Phi(-0.714) = 0.237$, assumed that the strength parameters

c' and ϕ' are independent. Now suppose that c' and ϕ' are correlated with correlation coefficient ρ.

$$\text{Var}[F(c',\phi')] = \left(\frac{\partial F(c',\phi')}{\partial c'}\right)^2 \sigma_{c'}^2 + \left(\frac{\partial F(c',\phi')}{\partial \phi'}\right)^2 \sigma_{\phi'}^2 + 2\rho \left(\frac{\partial F(c',\phi')}{\partial c'}\right)\left(\frac{\partial F(c',\phi')}{\partial \phi'}\right) \sigma_{c'}\, \sigma_{\phi'} \quad \text{(D-4)}$$

$\left(\frac{\partial F(c',\phi')}{\partial c'}\right)$ and $\left(\frac{\partial F(c',\phi')}{\partial \phi'}\right)$ (since $(\gamma - m\gamma_w) > 1$) are both positive quantities and so $\beta_{FOSM} = \frac{E[F(c',\phi')] - 1}{\sqrt{\text{Var}[F(c',\phi')]}}$ is inversely proportional to the correlation coefficient ρ, and the relationship in Eq. D-4 is shown in Figure D-6.

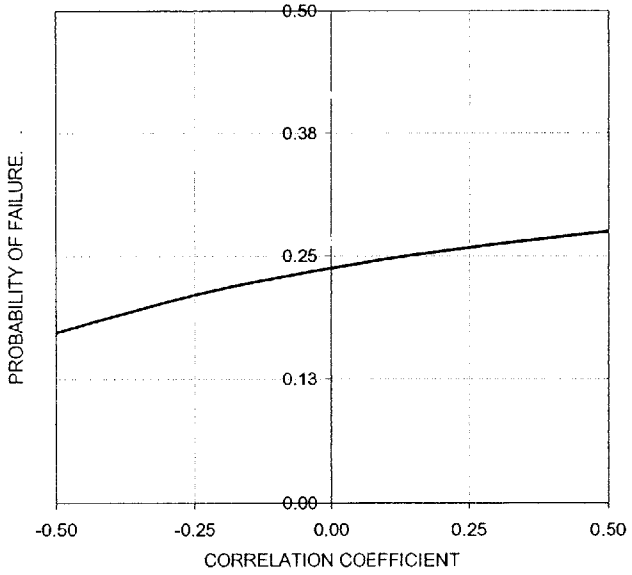

Figure D-6. Failure Probability for Different Correlation using FOSM

D-5.2. SECOND-MOMENT (SM) RELIABILITY INDEX

Correlation causes the dispersion ellipse in Figure D-1a to tilt. The direction of tilt is such that the ellipse can grow larger in size for negative correlation before hitting the failure boundary, and is smaller for positively correlation. Figure D-7a shows the dispersion ellipse for ρ = 0.5, and Figure D-7b shows it for ρ= -0.5.

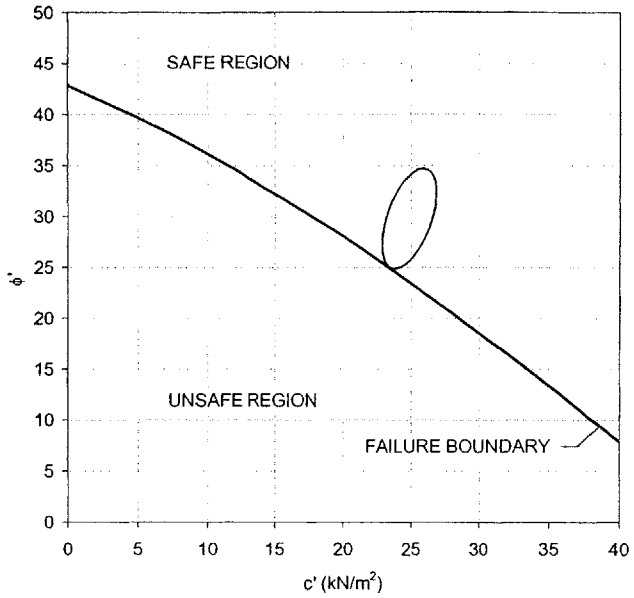

Figure D-7a. Dispersion Ellipse for ρ= 0.5

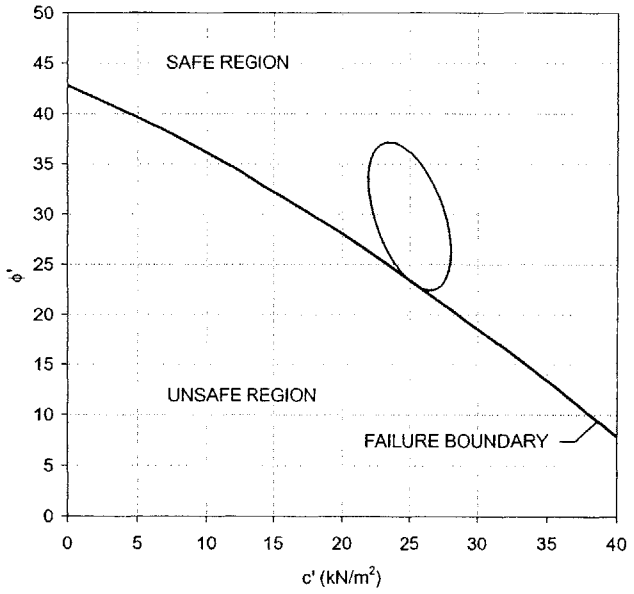

Figure D-7b. Dispersion Ellipse for ρ= -0.5

Figure D-8 shows the failure probability for different degrees of correlation.

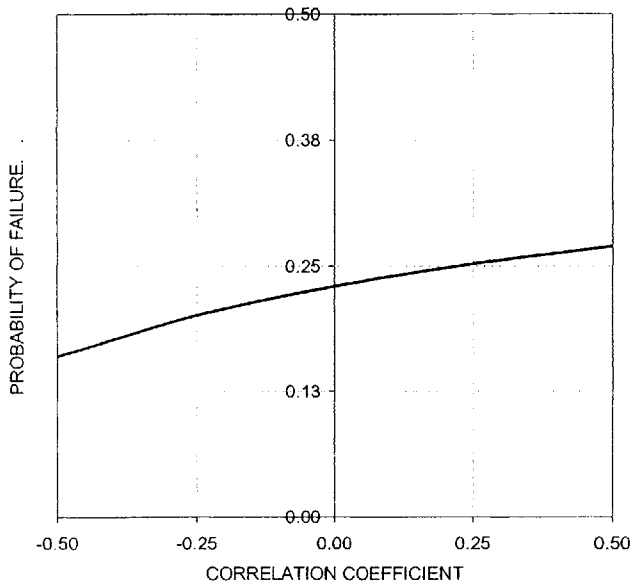

Figure D-8. Failure Probability for Different Correlation using SM Reliabilty

D-5.3. MONTE CARLO SIMULATION

Correlation between c' and ϕ' is included in the analysis using a triangular, or so-called Cholesky decomposition of the covariance matrix, $\underline{\Sigma}$, which is possible because the covariance matrix is symmetric, and positive definite.

$$\underline{\Sigma} = \underline{C}\underline{C}^T \qquad \text{(D-5)}$$

where $\underline{C}$ is a lower triangular matrix, the so-called Cholesky Matrix, and $\underline{C}^T$ is the transpose of $\underline{C}$. The Cholesky Matrix is given by:

$$\underline{C} = \begin{bmatrix} \sigma_{c'} & 0 \\ \rho\sigma_{\phi'} & \sigma_{\phi'}\sqrt{1-\rho^2} \end{bmatrix} \qquad \text{(D-6)}$$

Combinations of (c', ϕ') are simulated using:

$$\begin{bmatrix} c' \\ \phi' \end{bmatrix} = \begin{bmatrix} m_{c'} \\ m_{\phi'} \end{bmatrix} + \begin{bmatrix} \sigma_{c'} & 0 \\ \rho\sigma_{\phi'} & \sigma_{\phi'}\sqrt{1-\rho^2} \end{bmatrix} \begin{bmatrix} Z_1 \\ Z_2 \end{bmatrix} \qquad \text{(D-7)}$$

where Z_1 and Z_2 are standard Normal uncorrelated variables.

Figure D-9 shows the failure probability from Monte Carlo simulations for different degrees of correlation.

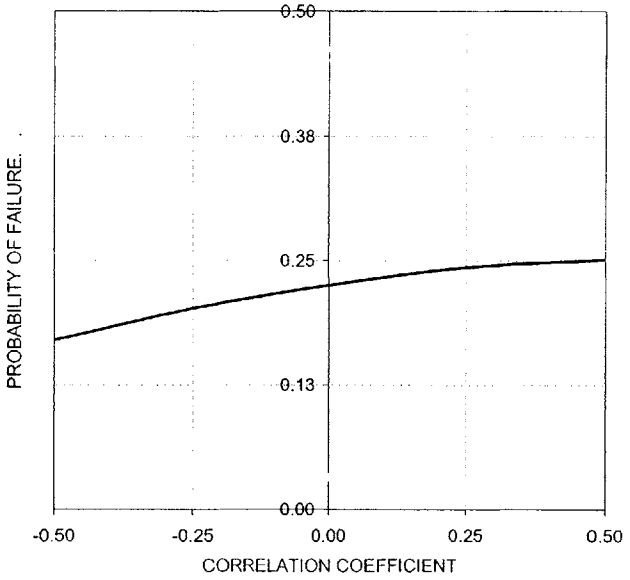

Figure D-9. Failure Probability for Different Correlation using Monte Carlo Simulations

Figures D-6, D-8 and D-9 show that correlation can have a significant influence on probabilities of failure, e.g. the failure probability for ρ= 0.5 is 1.5 times that when ρ= -0.5.

D-6. DISTRIBUTION OF PARAMETERS

In the following, we investigate the effects of Lognormal c' and ϕ', i.e $c' \sim LN(m_{\ln c'}, \sigma^2_{\ln c'})$ and $\phi' \sim LN(m_{\ln \phi'}, \sigma^2_{\ln \phi'})$ on slope reliability.

D-6.1. SECOND-MOMENT (SM) RELIABILITY INDEX

To estimate the second-moment reliability index, we transform the problem into Normal space by:

Transforming c' and ϕ' to Normal variables through the natural logarithm function. Since, $c' \sim LN(m_{\ln c'}, \sigma^2_{\ln c'})$ and $\phi' \sim LN(m_{\ln \phi'}, \sigma^2_{\ln \phi'})$, then $\ln c' \sim N(m_{c'}, \sigma^2_{c'})$ and $\ln \phi' \sim N(m_{\phi'}, \sigma^2_{\phi'})$, where:

$$m_{c'} = 2\ln(m_{\ln c'}) - \frac{1}{2}\ln(\sigma^2_{\ln c'} + m^2_{\ln c'}) \tag{D-7}$$

$$\sigma^2_{c'} = -2\ln(m_{\ln c'}) + \ln(\sigma^2_{\ln c'} + m^2_{c'}) \tag{D-8}$$

and similar Eqs. (D-7) and (8) relate $m_{\phi'}$ and $\sigma^2_{\phi'}$ to $m_{\ln \phi'}$ and $\sigma^2_{\ln \phi'}$.

Transforming the failure boundary, which in Normal space is given by:

$$F = \frac{e^{\ln c'}}{\gamma z \sin\alpha \cos\alpha} + \frac{\tan(e^{\ln \phi'})}{\tan\alpha} - m\left(\frac{\gamma_w \tan(e^{\ln \phi'})}{\gamma \tan\alpha}\right) \tag{D-9}$$

The second moment reliability index can then be obtained by transforming $\ln c'$ and $\ln \phi'$ into standard Normal variables, $c'^* = \frac{(\ln c' - m_{c'})}{\sigma_{c'}}$ and $\phi'^* = \frac{(\ln \phi' - m_{\phi'})}{\sigma_{\phi'}}$, and applying the iterative procedure shown in Figure D-1c, or using the techniques described in Chapter 5.

Figure D-10 shows the failure boundary and dispersion ellipse in transformed Normal space, and Figure D-11 shows this in standard Normal space.

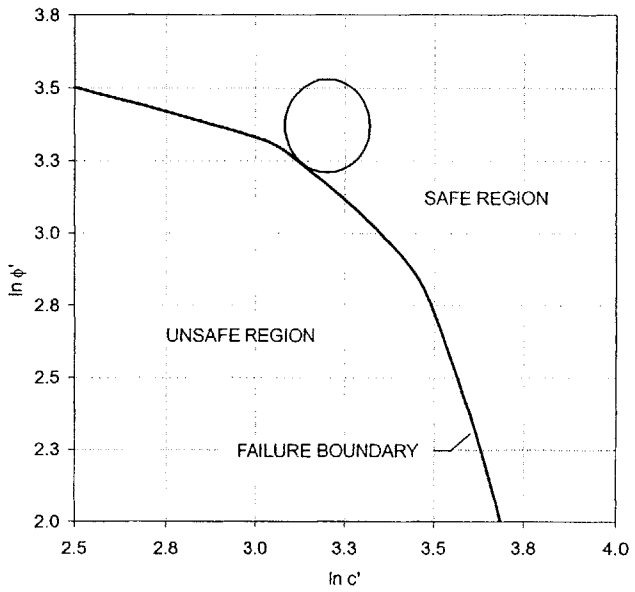

Figure D-10. Failure Boundary and Dispersion Ellipse in Normal Space

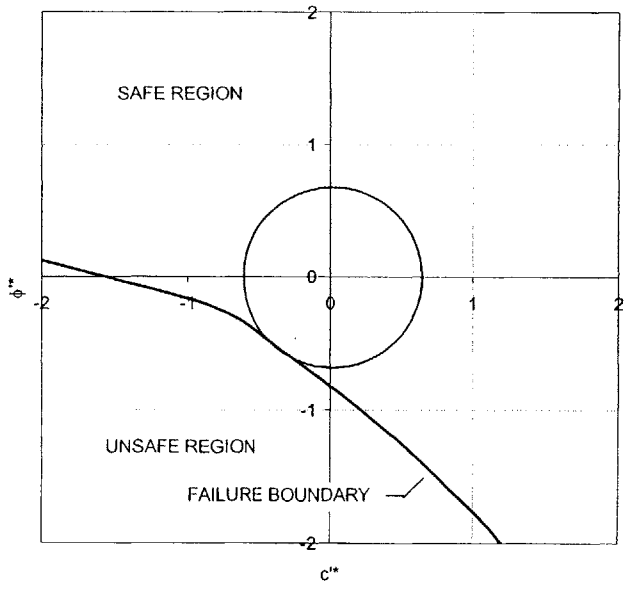

Figure D-11. Failure Boundary and Dispersion Ellipse in Standard Normal Space

We compute a reliability index $\beta = 0.656$ and the associated probability of failure is $P_f = \Phi(-\beta) = 0.255$.

D-6.2. MONTE CARLO SIMULATION

The exact probability of failure can be obtained by simulation from the appropriate Lognormal distributions of c' and ϕ'. We have simulated 20,000 (c', ϕ') and computed a probability of failure $P_f = P[F < 1] = 0.238$, from the empirical distribution shown in Figure D-12.

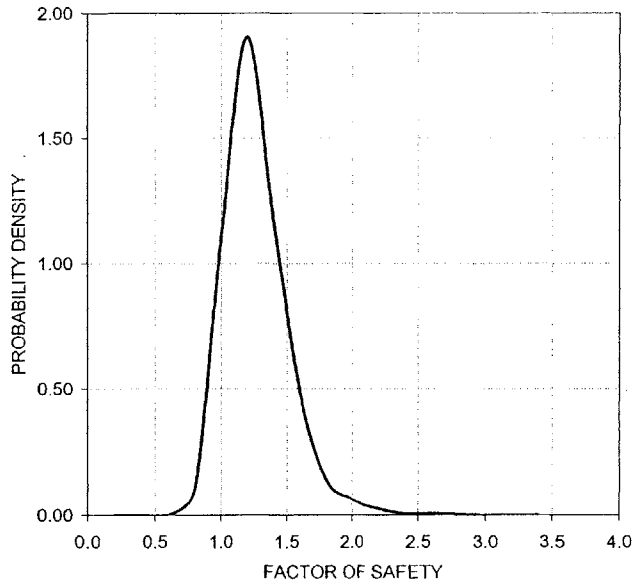

Figure D-12. Empirical probability density function of the factor of safety for Lognormal c' and ϕ'

Due to the non-linearity of the failure boundary (see Figure D-10) and the Non-Normal distribution of the Factor of Safety (see Figure D-12), there is a larger discrepancy between the results of SM analyses and Monte Carlo Simulations, than in the case of Normally distributed c' and ϕ'.

D-7. CONCLUSIONS

In this Appendix, different techniques were used to evaluate slope reliability. The results show that estimates of the probability of failure from FOSM and SM reliability techniques are in good agreement with those obtained using Monte Carlo simulations. This is because of the linear nature of the failure boundary, and the approximately normal distribution of the Factor of Safety. The agreement between the results is better when and ϕ' are Normally distributed than when they are Lognormally distributed.

In this example, the probability of failure for Lognormal c' and ϕ' is larger than that in the case of Normal c' and ϕ'. This, however, is a result that cannot be generalized and depends on the particular values of the means and standard deviations of c' and ϕ'.

The effect of correlation was investigated and we showed that this can be as important as the actual distributions of c' and ϕ'.

REFERENCES

Aleotti, P. and Chowdhury, R. 1999. Landslide Hazard Assessment: Summary Review and New Perspectives. Engineering Geology, Vol. 58. pp 21-44.

Anderson, M.G. and Howes, S. 1985. Development and Application of a Combined Soil Water-Stability Model. Quarterly Journal of Engineering Geology, Vol. 18. pp 236-255.

Anderson, M.G. and S. Howes, 1985. Development and application of a combined soil water-slope stability model, Q. J. Eng. Geol. London, Vol.18: pp. 225-236.

Anderson, S.A. and Sitar, N. 1995a. Shear Strength and Slope Stability in a Shallow Clayey Soil Regolith. Geological Society of America, Reviews in Engineering Geology, Volume X, W.C Haneberg and S.A. Anderson, editors, pp. 1-11.

Anderson, S.A. and Sitar, N. 1995b. Analysis of Rainfall-Induced Debris Flows. Journal of Geotechnical Engineering, ASCE, Vol. 121(7): 544-552.

Ang, A. H. and Tang W. H. 1975. Probability Concepts in Engineering Planning and Design, Vol. I - Basic Principles,. John Wiley and Sons Inc., New York.

Ang, A. H. and Tang W. H. 1984. Probability Concepts in Engineering Planning and Design. John Wiley and Sons Inc., New York, Vol. II, 562 pp.

Ashley, D.B.; Tse, E.C.; Einstein, H.H. 1979. "Advantages and Limitations of Adaptable Tunnel Design and Construction Methods", Proc. RETC, Chap. 57.

Australian Geomechanical Society. 2000. "Landslide Risk Management Concepts and Guidelines", Australian Geomechanics Society, Sub-Committee on Landslide Risk Management, Australian Geomechanics, Vol. 35, pp. 49-92.

Baecher, 1981. "Risk Screening for Civil Facilities", Massachusetts Institute of Technology, Dept.of Civil Eng. CER-81-9. 20 p.

Baecher, G.B. 1972. "Site Exploration: A Probabilistic Approach". Massachusetts Institute of Technology. Ph.D. Thesis, 515 p.

Baecher, G.B. 1978. "Analyzing Exploration Strategies". C.H. Dowding, (ed.) Site Characterization and Exploration, ASCE.

Baker, R.S. and Hillel, D. 1991. Observations of Fingering Behavior during Infiltration into Layered Soils. In: Timothy, J. and Shirmohammadi, A. (editors): Preferential Flow. pp. 87-99.

Barry, B. and Bechdol, M. 2000. Integrating Multisensor Data and RADAR texture Measures for Land Cover Mapping. Computers and Geosciences, Vol. 26, No. 4, pp. 411-421.

Bauer, A., and Calder, P.N., 1971. The influence and evaluation of blasting on stability. In: Stability in open pit mining, Brawner and Milligan, eds., Soc. Mining Engineers, AIME, N.Y., p. 83-94.

Baum, R.L. Savage, W.Z., Godt, J.W. 2002. TRIGRS; a Fortran program for transient rainfall infiltration and grid-based regional slope-stability analysis, Open-File Report - U. S. Geological Survey, OF 02-0424, p. 61.

Bear, J., 1972. Dynamics of Fluids in Porous Media, Elsevier, New York.

Bear, J., 1979. Hydraulics of Groundwater, McGraw-Hill, Inc., New York, 567 pp.

Bevan, K., 1979. A sensitivity analysis of the Penman-Montieth actual evapotranspiration estimates, Journal of Hydrology, 44: pp. 169-190.

Bevan, K.J. and M.J. Kirkby, 1979. A physically based, variable contributing area model of basin hydrology. Hydrological Sciences Bulletin 24, 1, pp. 43-69.

Bevan, K.J., Wood, E.F., Sivapalan, M., 1988. On hydrological heterogeneity-catchment morphology and catchment response. J. Hydrol. 100, 353-375.

Bishop, A. W. 1959. The Principle of Effective Stress. Tecknisk Ukeblad 39. pp. 859-863.

Bishop, A.W. and Morgenstern, N.R. 1960. Stability Coefficients for Earth Slopes. Geotechnique, Vol. 10. pp. 129-150.

Bishop, A.W., 1955. The use of the slip circle in the stability analysis of slopes. Geotechnique, 5:7-17.

Brabb, E.E. 1984. Innovative Approaches to Landslide Hazard and Risk Mapping. Proceedings of the Fourth International Symposium on Landslides, Toronto, Canada. Vol. 1.

Brabb, E.E.; Pampeyan, E.H. and Bonilla, M.G. 1972. Landslide Susceptibility in San Mateo County, California. U.S. Geological Survey, Miscellaneous Field Study Map. MF-360.

Brand, E.W; Premchitt, J. and Phillipson, H.B. 1984. Relationship Between Rainfall and Landslides in Hong Kong. Proceedings of the Fourth International Symposium on Landslides, Toronto. pp 377-384.

Bresler, E. and Dagan, G. 1983, Unsaturated flow in spatially variable fields. 2. Application of water flow models to various fields, Water Resource Res. 19, 413-420.

Bresler, E., Russo, D. and Miller, R. D. 1978, Rapid estimate of unsaturated hydraulic conductivity function, Soil Sci. Soc. Am. J. 42, 170-172.

Bromhead, E.N., 1997. Landslides in The Roughs, a site on the Lower Greensand Escarpment in South Kent. NEWTECH, (unpublished workshop discussion paper).

Brooks R.H. and Corey, A.T. 1966. Hydraulic Properties of Porous Media. Hydrology Paper No. 3, Fort Collins CO: Colorado State University.

Brooks, S.M. and K.S. Richards, 1994. The significance of rainstorm variations to shallow translational hillslope failure, Earth Surface Processes and Landforms, 19: pp. 85-94.

Burton, A and Bathurst, J.C. 1994. Modeling Shallow Landslide Erosion and Sediment Yield at the Basin Scale. In: International Workshop on Floods and Inundations Related to Large Earth Movements - Proceedings Preprint, International Association of Hydraulic Research - University of Trento, Trento, Italy. B7.1-B7-13.

Caine, N. 1980. The Rainfall Intensity-Duration Control of Shallow Landslides and Debris Flows. Geografiska Annaler, Series A, 62: 23-27.

Campbell, G.S. 1974. A Simple Method for Determining Unsaturated Conductivity from Moisture Retention Data. Soil Science, Vol. 113, No. 1: 61-88.

Campbell, R. H. 1975. Soil Slips, Debris Flows, and Rainstorms in the Santa Monica Mountains and Vicinity, Southern California. U.S. Geological Survey Professional Paper 851, Denver, CO. 51 p.

Cancelli, A. and Nova, R. 1985. Landslides in Soil Debris Cover Triggered by Rainstorms in Valtellina (central Alps, Italy). In: Sassa, K (editor). Proceedings of the Fourth International conference on Landslides, Tokyo. pp 267-272

Cannon, S. H. and Ellen, S. D. 1985. Rainfall Conditions for Abundant Debris Avalanches, San Francisco Bay Region, California. California Geology, Vol. 38, No. 12. pp. 267-272.

Carpenter, J.H. 1984. Landslide Risk Along Lake Roosevelt. MSc. Thesis, Massachusetts Institute of Technology, Cambridge, Massachusetts.

Carrara A., and Guzzetti F., (Editors). 1995. Geographical Information Systems in Assessing Natural Hazards, Kluwer Pub., Dordrecht, the Netherlands.

Carrara A., Cardinali M., Detti R., Guzzetti F., Pasqui V., and Reichenbach P., 1991. GIS Techniques and Statistical Models in Evaluating Landslide Hazard. Earth Surface Processes and Landforms, v. 16, 427-445

Carrara, A.; Publiese-Carratelli, E. and Merenda, L. 1977. Computer Based Data Bank and Statistical Analysis of Slope Instability Phenomena. Z. geomorph. N.F, Vol. 21, No. 2. pp 187-222.

Casadei, M. and W. E. Dietrich. 2003. Controls on Shallow Landslide width. in D. Rickermann and C. Chen, Debris-Flow Hazards Mitigation: Mechanics, Prediction, and Assessment. Proceedings of the Third International Conference on Debris Flows Hazards Mitigation, Davos Switzerland, 91-102p. Millpress, Rotterdam.

Casadei, M., W. E. Dietrich, and N. L. Miller. 2003. Testing a Model for Predicting the Timing and Location of Shallow Landslide Initiation in Soil Mantled Landscapes. Earth Surface Processes and Landforms, vol.28, no.9, pp.925-950.

Chandler, R.J. 1991. Slope Stability Engineering: Developments and Applications. Institution of Civil Engineers, Thomas Telford, London.

Chandler, R.J. and Hutchinson, J.N. 1984. Assessment of Relative Slide Hazard Within a Large, Pre-Existing Coastal Landslide at Ventnor, Isle of Wight. Proceedings of the Fourth International Symposium on Landslides, Toronto. pp 517-522.

Chen Z. and Li, S. 1998. Evaluation of Active Earth Pressure by the Generalized Method of Slices. Canadian Geotechnical Journal, Vol. 35 (4), pp. 591-599.

Chen, H, Lee, C. F., Law, K. T. 2004. Causative mechanisms of rainfall-induced fill slope failures, Journal of Geotechnical and Geoenvironmental Engineering, 130 (6), p. 593-602.

Chen, R.H., and Chameau, J.-L., 1982. Three-dimensional limit equilibrium analysis of slopes. Geotechnique, 32:31-40.

Cho, S. E., Lee, S. R. 2002. Evaluation of surficial stability for homogeneous slopes considering rainfall characteristics, Journal of Geotechnical and Geoenvironmental Engineering, 128 (9), p. 756-763.

Cholseky, B. 1924. Une Méthode de Résolution d'un Systême Défini d'Equations Lineaires. Bulletin Geodesique. 7:1 67-77.

Chowdhury, R N; Xu, D W. 1994. Slope system reliability with general slip surfaces. Soils and Foundations, vol.34, no.3, pp.99-105, Sep 1994

Chowdhury, R.N. 1980. Landslides as Natural Hazards; Mechanisms and Uncertainties, Geotechnical Engineering, 11 (2), p.135-180.

Christian, J.T., Ladd, C.C., and Baecher, G.B. 1994. Reliability and probability in stability analysis. Journal of Geotechnical Engineering Division, ASCE, 120: 1071-1111.

Cornell, C.A. 1971. First-Order Uncertainty Analysis of Soils Deformation and Stability. Proc. ICASPI, pp. 129-144.

Crosta, G. 1998. Regionalization of Rainfall Thresholds: An aid to Landslide Hazard Evaluation. Environmental Geology, Vol. 35. pp 124-130.

Crozier, M.J. 1992. Landslide Hazard Assessment: Theme Report. In: Proceedings of the Sixth International Symposium on Landslides, Christchurch, Vol. 1. pp 1843-1848.

Crozier, Michael J. 1999. Prediction of Rainfall-Triggered Landslides; A Test of the Antecedent Water Status Model. Earth Surface Processes and Landforms, 24 (9), p. 825-833.

Cruden, D. M. and Varnes D. J. 1996. Landslide Types and Processes. Landslides Investigation and Mitigation. Transportation Research Board, Special Report No. 247. Turner, A.K. and Schuster R.L. (editors). pp. 36-71.

Culligan, P J; Banno, K; Barry, D A; Steenhuis, T S; Parlange, J Y. 2002. Preferential flow of a nonaqueous phase liquid in dry sand. Journal of Geotechnical and Geoenvironmental Engineering, vol.128, no.4, pp.327-337, Apr 2002

Culligan, P.J.; Barry, D.A.; Parlange, J.-Y. 1997. Scaling Unstable Infiltration in the Vadose Zone. Canadian Geotechnical Journal, Vol. 34. pp. 466-470.

D.E., and J.-Y. Parlange. 1972. Wetting front instability in layered soil profile. Soil Sci. Soc. Am. Proc. 36:697-702.

Dagan, G. and Bresler, E. 1983. Unsaturated flow in spatially variable fields. 1. Derivation of models of infiltration and redistribution, Water Resource. Res. 19, 413-420.

Darcy, H. 1856. Dètermination des lois d'ècoulement de l'eau à travers le sable. p. 590-594. In Les Fontaines Publiques de la Ville de Dijon. Victor Dalmont, Paris.

Davis, A. M, Moore, J. M., Mason, P. J. 2000 A study of landslide hazard in S.E. Spain using integrated DEM, orthophotography and Landsat ETM imagery. Proceedings of the Fourteenth International conference on Applied geologic remote sensing, International Conference on Applied Geologic Remote Sensing, 14, p. 271-276.

Delacourt, C.; Carnec, C.; Fruneau, B.; Squarzoni, C. and Allemand, P. 2000. Geometrical and Dynamical Parameters of Several French Alps Landslides Revealed by Differential SAR Interferometry. Natural Hazards Workshop, 5-7 June, 200, Igls, Austria.

Dietrich, W.E. and Sitar, N. 1995. Geoscience and Geotechnical Engineering Aspects of Debris-Flow Hazard Assessment. Analysis of Rainfall-Induced Debris Flows. Journal of Geotechnical Engineering, ASCE, Vol. 120(6): 657-676.

Dillah, D. D. 1998, Uncertainty propagation and wetting front instability in unsaturated porous media, PhD Diss., Department of Civil and Environmental Engng, Polytechnic Univ., Brooklyn, NY.

Dirksen, C., J.B. Kool; P. Koorevaar and M.Th. van Genuchten. 1993. HYSWASOR - Simulation Model of Hysterica Water and Solute Transport in the Root Zone. In: D. Russo and G. Dagan (eds.), Water Flow & Solute Transport in Soils, pp. 99-122. Springer-Verlag, New York.

Ditlevsen, O. 1981. Uncertainty Modeling: With Applications to Multidimensional Civil Engineering Systems. McGraw Hill, New York.

Domenico, P.A. and F.W. 1990. Schwartz, Physical and Chemical Hydrogeology, John Wiley & Sons, N.Y.

Drake, N.A., Mackin, S. and Settle, J. 1999. Mapping Vegetation, Soils, and Geology in Semiarid Shrublands Using Spectral matching and Mixture Modeling of SWIR AVIRIS Imagery. Remote Sensing of the Environment, Vol. 68, No. 1, pp. 12-25.

Drake, N.A., Mackin, S. and Settle, J. 1999. Mapping Vegetation, Soils, and Geology in Semiarid Shrublands Using Spectral matching and Mixture Modeling of SWIR AVIRIS Imagery. Remote Sensing of the Environment, Vol. 68, No. 1, pp. 12-25.

Dubey, O.P. 1990. Modeling landcover and rainfall data for estimating ground water table fluctuations. Proceedings of the Asian Conference on Remote Sensing, Vol. 11, p. I.1.7.1-I.1.7.3.

Early, K.R.; Skempton, A.W. 1972. "Investigation of the Landslide in Walton's Wood, Staffordshire". Quarterly Jrnl. of Eng. Geol., Vol. 5, pp. 19-41.

Einstein H. H. 1988. Landslide Risk Assessment Procedure. Proceedings of the Fifth International Symposium on Landslides, Lausanne, Switzerland, A.A. Balkema, Rotterdam, Netherlands, Vol. 2, pp. 1075-1090.

Einstein H. H. 1988. Landslide Risk Assessment Procedure. Proceedings of the Fifth International Symposium on Landslides, Lausanne, Switzerland, A.A. Balkema, Rotterdam, Netherlands, Vol. 2, pp. 1075-1090.

Einstein, H. H. 2001, "Quantifying Uncertain Engineering Geologic Information", Invited Lecture 50th Geomechanics Colloquium and Felsbau, No. 5.

Einstein, H.H. 1995. "Risk and Risk Analysis in Rock Engineering", Keynote Lecture, Swedish Rock Mechanics Day, Stockholm.

Einstein, H.H. 1997. Landslide Risk: Systematic Approaches to Assessment and Management. In: Cruden, A. and Fell, R. (editors). Landslide Risk Assessment. Balkema, Rotterdam. pp 25-50.

Einstein, H.H. and Baecher, G.B. 1983. Probabilistic and Statistical Methods in Engineering Geology. Specific Methods and Examples. Part 1: Exploration. Rock Mechanics and Rock Engineering, Vol. 16, No. 39-72.

Einstein, H.H. and Karam, K.S. 2001. Risk Assessment and Uncertainties. Keynote Lecture. Proceedings of the International Conference on Landslides - Causes, Impacts and Countermeasures. Davos, Switzerland, 2001.

Einstein, H.H. Labreche, D.A., Markow, M.J., and Baecher, G.B. 1978. Decision Analysis Applied t Rock Tunnel Exploration. Engineering Geology, Vol. 12, pp 143-161.

Einstein, H.H.; Baecher, G.B. 1982. "Probabilistic and Statistical Methods in Engineering Geology, I. Problem Statement and Introduction to Solutions". Rock Mechanics. Suppl. 12, pp. 47-61.

Einstein, H.H.; Steiner, W.; Baecher, G.B. 1979, "Assessment of Empirical design Methods for Tunnels in Rock", Proc. Rapid Excavation and Tunnelling Conference.

Elachi, C. 1987. Introduction to the Physics and Techniques of Remote Sensing. John Wiley & Sons, Inc., New York.

El-Ramly, H. 2001. Probabilistic analyses of landslide hazards and risks: Bridging theory and practice. Ph.D. thesis, University of Alberta, Edmonton, Alta.

El-Ramly, H., Morgenstern, N.R., and Cruden, D. 2002. Probabilistic slope stability analysis for practice. Canadian Geotechnical Journal, 39: 665-683.

Endreny, T. A; Wood, E. F.; Lettenmaier, D. P. 2000. Satellite-derived digital elevation model accuracy; hydrological modeling requirements. Hydrological Processes, 14 (2), p. 177-194.

Fell, R. 1994. "Landslide Risk Assessment and Acceptable Risk". Canadian Geotechnical Journal, No. 31, pp. 261-272.

Fell, R. 1997. "Landslide Risk Management". Proc. Landslide Risk Assessment, Cruden, Fell (eds.) Balkema.

Fell, R., Hungr, O., Leroueil, S. and Reimer, W., 2000. Keynote Paper, - Geotechnical engineering of the stability of natural slopes and cuts and fills in soil. Procs., GeoEng2000, International Conference on Geotechnical and Geological Engineering in Melbourne, Australia, November, 2000, 104pp.

Ferretti, A.; Prati, C. and Rocca, F. 1999. Multibaseline In SAR DEM Reconstruction: The Wavelet Approach. IEEE Trans. Geosci. Remote Sensing, Vol. 37, No. 2, pp. 705-715.

Fourie, A.B. 1996. Predicting Rainfall-Induced Slope Instability. Proceedings of the Institute of Civil Engineers, Geotechnical Engineering, Vol. 119. pp 211-218.

Fredlund, D. G., Morgenstern, N. R. and Widger, R. A. 1978. The Shear Strength of Unsaturated Soils. Canadian Geotechnical Journal. Vol. 15 (3). pp. 313-321.

Fredlund, D.G. and Krahn, J. 1977. Comparison of Slope Stability Methods of Analysis. Canadian Geotechnical Journal. Vol. 14. No.3 pp. 429-439.

Fredlund, D.G. and Rahardjo, H. 1993. Soil Mechanics for Unsaturated Soils. John Wiley & Sons Inc., New York.

Fredlund, D.G., and Morgenstern, N.R. 1977. Stress state variables for unsaturated soils. Journal of the Geotechnical Engineering Division, Proceedings, American Society of Civil Engineering (GT5), 103: 447-466.

Fredlund, D.G., and Rahardjo, H. 1985. Theoretical context for understanding unsaturated residual soil behavior. Proceedings of the First International Conference on Geomechanics in Tropical Lateritic and Saprolitic Soils, Brazilia, Brazil, pp.295-306.

Fredlund, D.G. 1985. Soil mechanics principles that embrace unsaturated soils. Proceedings, 11th International Society for Soil Mechanics and Foundation Engineering, San Francisco, USA., Vol. 2, pp.465-473.

Fredlund, D.G. 1995. The scope of unsaturated soils mechanics: An overview. Proceedings, 1st International Conference on Unsaturated Soils, Paris, France, Vol. 3, pp.1155-1177.

Fredlund, D.G. 1997. From theory to the practice of unsaturated soil mechanics. Proceedings, 3rd Brazilian Symposium on Unsaturated Soils, Rio de Janeiro, Brazil

Freeze, A. and Cherry, J.A. 1979. Groundwater. Prentice Hall Inc.

Freeze, R. A. 1971. Three-dimensional, transient, saturated-unsaturated flow in a groundwater basin, Water Resources Research, 7(2): 347-366.

Freeze, R. A., 1972. Subsurface hydrology at waste disposal sites, IBM J. Res. Devel., 16(3): 117-129.

Freeze, R.A., and Witherspoon, P. A. 1968. Theoretical Analysis of Regional Ground Water Flow; [Part] 3, Quantitative Interpretations, Water Resources Research, 4 (3), p. 581-590.

Gardner, W.R. 1956. Calculation of Capillary Conductivity from Plate Outflow Data. Soil Science Society of America Proceedings, Vol. 20. pp. 317-320.

Geiser, F. 2000. Applicability of a General Effective Stress Concept to Unsaturated Soils. In: Unsaturated Soils for Asia. Rahardjo, Toll and Leong (editors). Balkema, Rotterdam.

Gentle, J. E. Cholesky Factorization. Numerical Linear Algebra for Applications in Statistics. Berlin: Springer-Verlag, pp. 93-95, 1998.

Geo-Slope International Ltd. 1998. SEEP/W for Finite Element Seepage Analysis. Vol. 4, Users Manual, Calgary, Alberta, Canada.

Gili, J.A.; Corominas, J. and Rius, J. 2000. Using Global Positioning Techniques in Landslide Monitoring. Engineering Geology, Vol. 55. pp. 167-192.

Glass, R. J.; Steenhuis, T. S.; Parlange, J. Y. 1987. Wetting Front Instability as a Rapid and Far-Reaching Hydrologic Process in the Vadose Zone. Journal of Contaminant Hydrology, 3 (2-4). pp. 207-226.

Glass, R. J.; Steenhuis, T. S.; Parlange, J. Y. 1989. Mechanism for Finger Persistence in Homogeneous, Unsaturated, Porous Media. Theory and Verification. Soil Science, 148 (1). pp. 60-70.

Glass, R.J., T.S. Steenhuis, and J.Y. Parlange. 1989c. Mechanism for finger persistence in homogeneous, unsaturated, porous-media- theory and verification. Soil Sci. 148:60-70.

Glass, R.J.; McConnel, V.S. and Thompson, M.E. 1991. Water Infiltration into Unsaturated Fractures; Gravity Driven Fingering. Eos, Transactions, American Geophysical Union, Vol. 72 (17).

Goel, N.S. and Norman, J.M. 1990. Instrumentation for Studying Vegetation Canopies for Remote Sensing in Optical and Thermal Infrared Regions. Remote Sensing Reviews, Vol. 5, No. 1, pp. 360.

Green, W. H. and Ampt, C. A. 1911. Studies in Soil Physics, I. Flow of Air and Water through Soils. Journal of Agricultural Science, Vol. 4. pp 1-24.

Guigner, N. and Franz, T. 1997. MODFLOW Manual. Waterloo Hydrogeologic, Inc.

Guzzetti F., 1993. Landslide Hazard and Risk by GIS-Based Multivariate Models. In: Reichenbach P., Guzzetti F., and Carrara A., (Editors), Abstracts, Proceed. Int. Workshop GIS in Assess. Nat. Hazards, Perugia, Sept. 20-22, 1993, pp. 83-91.

Hamilton, R. 1997. Report on Early Warning Capabilities for Geological Hazards. INDR Secretariat, Geneva.

Hansen A., 1984. Landslide hazard analysis. In: Brunsden D., and Prior D.B., (Editors), Slope instability. Wiley, New York, pp. 523-602.

Harleman, Donald R. F., 1977. Transport Processes In Water Quality Control, Massachusetts Institute of Technology.

Hasofer, A.M.; Lind, N.C. 1974. Exact and Invariant Second Moment Code Format. ASCE Journal of Engineering Mechanics, 100, No. EMI.

Hassan A. and Wolff. 2000. Effect of deterministic and probabilistic models on slope reliability index. Geotechnical Special Publication, vol.101, pp.194-208.

Hassan, A. 2001. Probabilistic Analyses of Landslide Hazards and Risks; Bridging Theory and Practice. PhD Thesis. University of Alberta, Edmonton, AB, Canada.

Hendrickx, J.M.H., L.W. Dekker, and O.H. Boersma. 1993. Unstable fronts in water repellent field soils. J. Environ. Qual. 22:

Hill, D. 1952. Channeling in Packed Columns. Chem. Eng. Sci., 1, 247-253.

Hillel, D., and R.S. Baker. 1988. A descriptive theory of fingering. Soil Sci. 146:51-56.

Ho, D.Y.F. and Fredlund, D.G. 1982. Increase in Shear Strength due to Soil Suction for Two Hong Kong Soils. Proceedings of the ASCE Geotechnical Conference Engineering and Construction in Tropical and Residual Soils. Honolulu, Jan. 1982, pp. 263-295.

Ho, K.; Leroi, E.; Roberds, W. 2000. "Quantitative Risk Assessment: Application, Myths and Future Direction". Proc. GeoEng 2000, Melbourne, Australia.

Hoeben, R. and Troch, P. A. 2000. Assimilation of active microwave observation data for soil moisture profile estimation. Water Resources Research, 36 (10), p. 2805-2819.

Hoek, E. and Bray, J. 1977. Rock Slope Engineering. Revised 2nd ed. London: Institution of Mining and Metallurgy.

Horton, R.E. 1933. The Role of Infiltration in the Hydrologic Cycle. Trans. American Geophysical Union, Vol. 14. pp 446-460.

Hutchinson, J.N. 1995. Landslide Hazard Assessment. In: Proceedings of the Sixth International Symposium on Landslides, Christchurch, Vol. 1. pp 1805-1842.

IUGS. (Working Group on Landslides, Committee on Risk Assessment). 1997. Quantitative Risk Assessment for Slopes and Landslides - The State-of-the-Art. Proc. Int'l. Workshop on Landslide Risk Assessment. Cruden, Fell (eds.), Balkema.

Iverson, R.M. 1991. Sensitivity of Stability Analyses to Groundwater Data. In: Bell, D.H. (editor) Landslides. Balkema, Rotterdam.

Iverson, R.M. 2000. Landslide Triggering by Rain Infiltration. Water Resources Research, 36 (7), p. 1897-1910.

Iverson, R.M. and Major, J.J. 1986. Groundwater Seepage Vectors and the Potential for Hillslope Failure and Debris Flow Mobilization. Water Resources Research, Vol. 22. pp 1543-1548.

Iverson, R.M., 1983. A model for creeping flow in landslides. Bull. Assoc. Engineering Geologists, 20:455-459.

Janbu, N. 1954. Application of Composite Slip Surface for Stability Analysis. Proceedings of European Conference on Stability of Earth Slopes, Stockholm, Sweden, pp. 43-90.

Janbu, N. 1973. "Slope Stability Computations," Embankment Dam Engineering, The Casagrande Volume, Wiley and Sons, NY, pp. 47-86.

Janbu, N., 1973. Slope stability computations. In, Hirschfeld and Poulos, eds., Embankment-Dam Engineering, John Wiley & Sons., N.Y., p. 47-86.

Jenson S.K., and Domingue J.O., 1988. Extracting Topographic Structure from Digital Elevation Data for Geographic Information System Analysis. Photogrammetric Engineering and Remote Sensing v. 54:11, pp. 1593-1600

Johnson, J. and Sitar, N. 1990. Hydrologic Conditions Leading to Debris Flow Initiation. Canadian Geotechnical Journal, Vol. 27. pp 789-801.

Johnson, K.A. and Sitar, N. 1989. Significance of Transient Pore Pressures and Local Slope Conditions in Debris Flow Initiation. Proceedings XII ICSMFE, Rio de Janeiro, Brazil, Vol. III, A.A. Balkema, Publishers, pp. 1619-1622.

Kahneman, D.; Slovic, P. and Tversky, A. 1982. Judgment Under Uncertainty: Heuristics and Biases. Cambridge, New York. Cambridge University Press.

Karam, K. S. 2000. On Rainfall Induced Landslides: A Deterministic Approach. MS Thesis. Massachusetts Institute of Technology.

Karam, K. S. 2005. Practical Geotechnical Risk Assessment. 11th International Conference of the IACMAG, Torino, Italy. 19-24 June 2005.

Keefer, D.K.; Wilson, R.C.; Mark, R.K.; Brabb, E.E.; Brown, W.M.; Ellen, S.D.; Harp, E.L.; Wieczorek, G.F.; Alger, C.S. and Zatkin, R.S. 1987. Real-Time Landslide Warning during Heavy Rainfall. Science, Vol. 238, No. 4829. pp-921-925.

Keeney, R.L.; Raiffa, H. 1976. Decision Analysis with Multiple Conflicting Objectives. John Wiley and Sons, New York.

Khalili, N. and Khabaz, M. H. 1998. A Unique Relationship for for the Determination of the Shear Strength of Unsaturated Soils. Geotechnique 48(5). pp. 681-687.

Kim, Y. and Huneycutt, B. 2000. Instrument characteristics and data products for NASA's next SAR mission. AAPG international conference and exhibition; abstracts, AAPG Bulletin, 84 (9), p. 1448.

Klute, A.: 1952, A numerical method for solving the flow equation for water in unsaturated materials, Soil Sci. 73, 105-116.

Kung, K.J.S. 1990. Preferential flow in a Sandy Vadose Zone. 1. Field Observation. Geoderma, 46. 51-58.

Lacasse, S., Nadim F. and Høeg, K. 2003. Risk Assessment in Soil and Rock Engineering. PanAm Conference, SARA, MIT, Cambridge, Mass., USA, June 2003.

Lacasse, S.; Nadim, F. 1996. "Uncertainty in Characterizing Soil Properties". ASCE Geotechnical Special Publication, No. 58.

Ladd, C.C. 1991. Stability Evaluation during Staged Construction. Journal of Geotechnical Engineering, ASCE, Vol. 117(4): 560-615.

Lambe, T.W. 1950. Capillary Phenomena in Cohesionless Soils. Published as a Separate. No. 4, American Society of Civil Engineers.

Lambe, T.W. and Whitman, R.V. Soil Mechanics. 1979. John Wiley & Sons Inc., New York.

Larsen, M.C. and Simon, A. 1992. A Rainfall Intensity Duration Threshold for Landslides in a Humid Tropical Environment, Puerto Rico. U.S. Geological Survey.

Leong, E.C. and Rahardjo, H. 1997a. Permeability Functions for Unsaturated Soils. Journal of Geotechnical and Geoenvironmental Engineering, Vol. 123, No. 12. pp 1118-1126.

Leong, E.C. and Rahardjo, H. 1997b. Review of Soil-Water Characteristic Curve Equations. Journal of Geotechnical and Geoenvironmental Engineering, Vol. 123, No. 12. pp 1106-1117.

Li, K S and White, W. 1987. Rapid evaluation of the critical slip surface in slope stability problems. International Journal for Numerical and Analytical Methods in Geomechanics, vol.11, no.5, pp.449-473, Oct 1987

Li, K S. and Lumb, P. 1987. Probabilistic design of slopes. Canadian Geotechnical Journal, vol.24, no.4, pp.520-535, Nov 1987

Lim, T.T.; Rahardjo, H.; Chang, M.F. and Fredlund, D.G. 1995. Effect of Rainfall on Matric Suction in Residual Soil Slopes. Canadian Geotechnical Journal. Vol. 33. No.4. pp 618-628.

Low, B. K. (2001). "Probabilistic slope analysis involving generalized slip surface in stochastic soil medium." Proc., 14th Southeast Asian Geotechnical Conf., December 2001, Hong Kong, pp.825-830, A.A.Balkema Publishers.

Low, B. K. and Wilson H. Tang (2004). "Reliability analysis using object-oriented constrained optimization." Structural Safety, Elsevier Science Ltd., Amsterdam, Vol. 26, No. 1, pp.69-89.

Low, B. K., Gilbert, R. B., and Wright, S. G. (1998). "Slope reliability analysis using generalized method of slices." J. Geotechnical and Geoenvironmental Engrg., 124(4): 350-362, ASCE, New York.

Low, B.K. (1996). "Practical probabilistic approach using spreadsheet." Geotechnical Special Publication No. 58, Proceedings, Uncertainty in the Geologic Environment: From Theory to Practice, Madison, Wisconsin, ASCE, Vol. 2, pp. 1284-1302. [PDF (239 kB)]

Low, B.K. (1997). "Reliability analysis of rock wedges." Journal of Geotechnical and Geoenvironmental Engineering, ASCE, New York, Vol. 123, No. 6, pp. 498-505.

Low, B.K. (2003). "Practical probabilistic slope stability analysis". Proceedings, Soil and Rock America 2003, 12th Panamerican Conference on Soil Mechanics and Geotechnical Engineering and 39th U.S. Rock Mechanics Symposium, M.I.T., Cambridge, Massachusetts, June 22-26, 2003.

Low, B.K. 1997. "Reliability Analysis of Rock Wedge". ASCE Journal of Geotechnical and Geoenvironmental Eng. Vol. 123, No. 6, pp. 498-505.

Low, B.K. and Phoon, K.K. (2002). "Practical first-order reliability computations using spreadsheet". Proceedings, Probabilistics In Geotechnics: Technical And Economic Risk Estimation, Graz, Austria, September 15-19, 2002, pages 39-46.

Low, B.K. and Wilson H. Tang (1997). "Efficient reliability evaluation using spreadsheet." J. Engrg. Mechanics, 123(7): 749-752, ASCE, New York.

Low, B.K. and Wilson H. Tang (1997). "Efficient reliability evaluation using spreadsheet." Journal of Engineering Mechanics, ASCE, Vol. 123, No. 7, pp. 749-752.

Low, B.K. and Wilson H. Tang (1997). "Reliability analysis of reinforced embankments on soft ground." Canadian Geotechnical Journal, Vol. 34, No. 5, pp. 672-685.

Low, B.K., Gilbert, R.B., and Wright, S.G. (1998). "Slope reliability analysis using generalized method of slices." Journal of Geotechnical and Geoenvironmental Engineering, ASCE, New York, Vol. 124, No. 4, pp. 350-362.

LPC. 1978. "Eboulements et chutes de pierres sur les routes. Méthode de Cartographie". Groupe d'Etudes des Falaises (GEF) Laboratoire Central des Ponts et Chaussées. Rapport de Recherche LPC No. 80, 63p.

Lumb, P. 1975. Slope Failures in Hong Kong. Quarterly Journal of Engineering Geology, Vol. VIII. pp 31-65.

Merenyi, E., Farrand, W.H., Stevens, L.E.M, Theodore, S. and Chhibber, K. 2000. Mapping Colorado River Ecosystem Resources in Glen Canyon; Analysis of Hyperspectral Low-Altitude AVIRIS Imagery. Proceedings of the Fourteenth International Conference on Applied Geologic Remote Sensing, Vol., 14, pp. 44-51.

Modaressi, A, and Abou-Bekr, 1994. A Unified Approach to Model the Behavior of Saturated and Unsaturated Soils. Computer Methods and Advances in Geomechanics, Proceedings of the Eighth International Conference on Computer Methods and Advances in Geomechanics. H.J. Siriwardane and M.M. Zaman (ed.), Balkema, 1507-1513, (1994)

Montgomery, D. R., W. E. Dietrich, and J. T. Heffner. 2002. Piezometric Response in Shallow Bedrock at CB1: Implications for Runoff Generation and Shallow Landsliding. Water Resources Research, Vol.38, No. 12, 1274.

Montgomery, D.R. and Dietrich, W.E. 1987. A Physically Based Model for the Topographic Control of Shallow Landsliding. Water Resource Research. Vol. 30. pp. 1153-1171.

Moore, I.D. and Grayson, R.B. 1991. Terrain-Based Catchment Partitioning and Runoff Prediction using Vector elevation data. Water Resources Research, Vol. 27, No. 6 pp 1177-1191.

Morgensterm, N.R., and Price, V.E., 1965. The analysis of the stability ot general slip surfaces. Geotechnique, 15:79-93.

Morgenstern, N. R. (1995). "Managing Risk in Geotechnical Engineering." Proc., Pan Am. Conf., ISSMFE.

Morgenstern, N.R. 1997. Towards Landslide Risk Assessment in Practice. In: Cruden, A. and Fell, R. (editors). Landslide Risk Assessment. Balkema, Rotterdam. pp 15-23.

Morgenstern, N.R. and de Matos, M.M. (1975) "Stability of Slopes in Residual Soils", Proceedings of the 5th Panamerican Conference on Soil Mechanics and Foundation Engineering, Vol. 3, pp. 369-384, Buenos Aires.

Morgenstern, N.R. and Price, V.E. 1965. The Analysis of the Stability of General Slip Surfaces. Geotechnique, Vol. 15, No. 1, pp. 79-93.

Nadim, F.; Lacasse, S. 1999. Probabilistic slope stability evaluation, Proc. 18th Annual Seminar on Geotechnical Risk Management, Hong Kong, 177-186, May 14.

Nash, J. C. 1990.The Choleski Decomposition. Compact Numerical Methods for Computers: Linear Algebra and Function Minimization, 2nd ed. Bristol, England: Adam Hilger, pp. 84-93.

New York State Department of Transportation. 1993. "Rock Slope Hazard Rating Procedure" (Draft). Soil Mechanics Bureau, Tech. Services, Div.

Ng, C. W. W., Shi, Q. 1998. Influence of rainfall intensity and duration on slope stability in unsaturated soils, The Quarterly Journal of Engineering Geology, 31, Part 2, p. 105-11.

Noverraz, F. 1984. "Cartographie de glissements de terrain, méthode de levé; objectif et fonction des cartes d'instabilité. Mouvements de Terrains". Association Française de Géographie Physique. Colloque de CAEN, pp. 217-223.

Oberg, A.L. and Sallfors, G. (1995) A Rational Approach to the Determination of the Shear-Strength Parameters of Unsaturated Soils, Unsaturated Soils. Proc. 1st Int. Conf. on Unsaturated Soils (UNSAT 95), Paris, France (ed. Alonzo, E.E. and Delage, P.), Rotterdam: Balkema, Vol. 1, pp. 151-158.

Okimura, T and Ichikawa, R. 1985. A Prediction Method for Surface Failures by Movements of Infiltrated Water in a Surface Soil Layer. Natural Disaster Science. Vol. 7. pp. 41-51.

O'Loughlin, E.M. 1986. Prediction of Surface Saturation Zones in Natural Catchments by Topographic Analysis. Water Resources Research, Vol. 22, pp 794 - 804.

Palmer, A.C., and Rice, J.R., 1973. The growth of slip surfaces in the progressive failure of over-consolidated clay. Proc. Roy. Soc. Lond., Ser. A, 332:527-548.

Parlange, J.Y., and D.E. Hill. 1976. Theoretical analysis of wetting instability in soils. Soil Sci. 122:236-239.

Paté, M.E. 1981. "Risk-Benefit Analysis for Construction of New Dams: Sensitivity Study and Real Case Application". Massachusetts Institute of Tech. Department of Civil Engineering. Research Report No. R81-26. 99p.

Peck, R.B. 1969. "Advantages and Limitations of the Observational Method in Applied Soil Mechanic". 9th Rankine Lecture, Géotechnique, Vol. 19, pp. 171-187.

Philip, J. R. 1969. Theory of Infiltration. Advances in Hydroscience, 5, p. 215-296.

Philip, J. R.: 1957, The theory of infiltration, 1. The infiltration equation and its solution, Soil Sci. 83, 345-357.

Pradel, D. and Raad, G. 1993. Effect of Permeability on Surficial Stability of Homogenous Slopes. Journal of Geotechnical Engineering, ASCE, Vol.119. pp 315-332.

Pratt, J.W.; Raiffa, H.; Schlaiffer, R. 1965. Introduction to Statistical Decision Theory, McGraw Hill.

Protopapas, A. L. and Bras, R. L. 1986, A model of plant growth and its relation to moisture and salinity transport in soil, Technical Report TR309, Ralph M. Parsons Lab., Mass. Inst. Of Technology., Cambridge.

Protopapas, A. L. and Bras, R. L. 1988, State-space dynamic hydrological modeling of soil-cropclimate interactions, Water Resource. Res. 24(10), 1765-1779.

Protopapas, A. L. and Bras, R. L. 1990, Uncertainty propagation with numerical models for flow and transport in the unsaturated zone, Water Resour. Res. 26(10), 2463-2474.

Protopapas, A.L. and Bras, R.L. 1991. The One-Dimensional Approximation for Infiltration in Heterogeneous Soils, Water Resources Research, 27 (6), p. 1019-1027.

R.K. Khanzode, D.G. Fredlund, and S.K. Vanapalli, 2000. A new test procedure to measure the soil-water characteristic curves using a small centrifuge. Asian Conference on Unsaturated Soils (UNSAT-ASIA 2000) From Theory to Practice, May 18-20, 2000, ed. H. Rahardjo, D.G. Toll and E.C. Leong. A.A. Balkema, Rotterdam, 2000, pp. 345-350.

Rahardjo, H.; Lim, T.T.; Chang, M.F. and Fredlund, D.G. 1995. Shear Strength Characteristics of a Residual Soil. Canadian Geotechnical Journal. Vol. 32. pp 60-77.

Rahardjo, H.; Lim, T.T.; Chang, M.F. and Fredlund, D.G. 1995. Shear Strength Characteristics of a Residual Soil. Canadian Geotechnical Journal. Vol. 32. pp 60-77.

Raiffa, H.; Schlaifer, R.L. 1964. Applied Statistical Decision Theory. Harvard Business School, Cambridge, Ma. See also: Pratt, J.W.; Raiffa, H.; Schlaiffer, R. 1965. Introduction to Statistical Decision Theory. McGraw Hill, New York.

REFERENCES

Reichenbach P., Guzzetti F, and Carrara A., (Editors), 1993. Abstracts. Proceed. Workshop on Geographical Information Systems in Assessing Natural Hazards, Perugia, 20-22 September 1993. CNR-IRPI, Perugia, 140 pp.

Reid, M.E. 1994. A Pore-Pressure Diffusion Model for Estimating Landslide-Inducing Rainfall. Journal of Geology, Vol. 102, No. 6, pp. 709-717.

Reid, M.E.; Neilsen, H.P. and Dreiss, S.J. 1988. Hydrologic Factors Triggering a Shallow Hillslope Failure. Bulletin of the Association of Engineering Geologists, Vol. 25, No. 3. pp 349-361.

Reid, M.E.; Neilsen, H.P. and Dreiss, S.J. 1988. Hydrologic Factors Triggering a Shallow Hillslope Failure. Bulletin of the Association of Engineering Geologists, Vol. 25, No. 3. pp 349-361.

Reid, M.E.; Neilsen, H.P. and Dreiss, S.J. 1988. Hydrologic Factors Triggering a Shallow Hillslope Failure. Bulletin of the Association of Engineering Geologists, Vol. 25, No. 3. pp 349-361.

Reid, M.R. and Iverson, M.R. 1992. Gravity Driven Groundwater Flow and Slope Failure Potential. 1. Effects of Slope Morphology, Material Properties and Hydraulic Heterogeneity. Water Resource Research, Vol. 28. pp 939-950.

Reutov, E. A.; Shutko, A. M. 1992. Estimation of the depth to a shallow water-table using microwave radiometry, International Journal of Remote Sensing, 13 (12), p. 2223-2232.

Rezaur, R. B., Rahardjo, H., Leong, E. C., Lee, T. T. 2003. Hydrologic behavior of residual soil slopes in Singapore, Journal of Hydrologic Engineering, 8 (3), p. 133-144.

Richards, L. A. 1931, Capillary induction of liquids through porous mediums, Physics 1, 318-333.

Ridley, A. M. and Burland, J. B. 1993. A new instrument for the measurement of soil moisture suction. Geotechnique, Vo. 43, No. 2. pp 321-324.

Rizo, V. and Tesauro, M. 2000. SAR Interfermotery and Field Data of Randazzo Landslide (Eastern Sicily, Italy). Phys. Chem. Earth (B), Vol. 25, No. 9. pp. 771-780.

Roberds, W.J.; Ho, K.; Leung, K.W. 1997. "An Integrated Methodology for Risk Assessment and Risk Management for Development Below Potential Natural Terrain Landslides". Proc. Int'l. Workshop on Landslide Risk Assessment, Cruden, Fell, (eds.), Balkema.

Roering,J.J., K. M. Schmidt, J. D. Stock, W. E. Dietrich and D. R. Montgomery. 2003. Shallow Landsliding, Root Reinforcement, and the Spatial Distribution of Trees in the Oregon Cost Range, Canadian Geotechnical Journal, v. 40 ,p. 237-253.

Rosenblueth, E. 1975. Point Estimates for Probability Moments. Proc. Nat. Acad. Sci., USA, 72, No.10. pp 3812-3814.

Rubin, J.; Steinhardt, R. and Reiniger, P. 1964. Soil Water Relations During Rain Infiltration: II. Moisture Content Profiles During Rains of Low Intensities. Proceedings of the American Society of Soil Sciences, Vol. 28. pp 1-5.

Russo, D. and Bouton, M.: 1992, Statistical analysis of spatial variability in unsaturated flow parameters, Water Resource. Res. 28(7), 1911-1925.

Sabins, F. F., Jr. Remote Sensing: Principles and Interpretation (New York: W.H. Freeman, 1986).

Schwartz, F.W. 1984. Modeling of Ground Water Flow and Composition. In: Hitchon, B. and Wallick, E., I. (editors), Proceedings of the First Canadian/American Conference on Hydrogeology; Practical Applications of Ground Water Geochemistry, p.178-188.

Singhroy, V. H.; Loehr, J. E., and Correa, A. C.. 2000. Landslide risk assessment with high spatial resolution remote sensing satellite data. IGARSS 2000; IEEE 2000 international geoscience and remote sensing symposium; Taking the pulse of the planet; the role of remote sensing in managing the environment; proceedings,

International Geoscience and Remote Sensing Symposium, Vol. 6, p. 2501-2503.
Sjoblom, K.J. 2000. The Mechanisms Involved During the Desaturation Process of a Porous Matrix. PhD Thesis, Massachusetts Institute of Technology.
Skempton, A. W. and DeLory, F. A. 1957. Stability of Natural Slopes in London Clay. Proceedings of the Fourth International Conference on Soil Mechanics and Foundation Engineering, Butterworths, London, Vol. 2. pp 378-381.
Skempton, A.W. and Hutchinson, J.M. 1969. Stability of Natural Slopes and Embankment Foundations. Proceedings of the Seventh International Conference on Soil Mechanics and Foundation Engineering, State-of-the-Art Volume. pp 291-340.
Soeters R., R.N., and van Westen C.J., 1991. Remote Sensing and Geographical Information Systems as Applied to Mountain Hazard Analysis and Environmental Monitoring. Proceed. 8th Thematic Conf. Geol. Remote Sensing (ERIM), Apr. 29-May 2, 1991, Denver, v. 2, 1389-1402
Stael v. Holstein, C.A.S. 1974. "A Tutorial in Decision Analysis". Readings in Decision Analysis. Howard, Matheson, Miller (eds.) SRI, Menlo Park.
Taylor, D.W. 1948. Fundamentals of Soil Mechanics. New York, Wiley.
Terlien M.T.J., van Westen C.J., and van Asch Th.W.J., 1995. The Use of Deterministic Models in Landslide Hazard Assessment. Carrara A., and Guzzetti F., (Editors), Geographical Information Systems in Assessing Natural Hazards, Kluwer Pub., Dordrecht, the Netherlands.
Terlien, Mark T. J. 1996. The Determination of Statistical and Deterministic Hydrological Landslide-Triggering Thresholds. Environmental Geology, Vol. 35, No. 3, pp. 124-130.
Terzaghi, K. 1936. The Shear Resistance of Saturated Soils. Proceedings of the First International Conference on Soil Mechanics and Foundation Engineering, Cambridge, MA, Vol. 1. pp 54-56.
Terzaghi, K. 1950. Mechanism of landslides. In: Paige. S. (editor). Application of Geology to Engineering Practice. Geological Society of America, Boulder, CO. pp. 83-123.
Terzaghi, K. 1961. "Engineering Geology on the Job and in the Classroom". Journal of the BSCE, April 1961.
Terzaghi, K. and Peck, R. B. 1967. Soil Mechanics in Engineering Practice. 2nd Edition, John Wiley & Sons Inc., New York.
Terzaghi, K., 1936. Critical height and factor of safety of slopes against sliding. 1st Internat. Conf. Soil Mech. etc. (reproduced in From Theory..... etc.)
Tindall, J.A. and Kunkel, J.R. 1999. Unsaturated Zone Hydrology for Scientists and Engineers, Prentice-Hall, Inc. New Jersey.
Toker, N. K. Modeling and Characterization of Effective Stresses in Unsaturated Soils. PhD Thesis in Civil and Environmental Engineering, Massachusetts Institute of Technology. To be published in 2006.
Toker, N.K. 2002. Improvements and Reliability of the MIT Tensiometer and Studies on Soil Moisture Characteristic Curves. MS Thesis, Massachusetts Institute of Technology.
Torres, R., W. E. Dietrich, D. R. Montgomery, K. Loague, and S. P. Anderson. 1998. Unsaturated Zone Processes and the Hydrologic Response of a Steep, Unchanneled Catchment. Water Resources Research, v. 34, p.1865-1879.
Transportation Research Board, 1994. Landslides Investigation and Mitigation. Special Report No. 247, V. Turner, R.L. Schuster (eds.).

Transportation Research Board. 1996. Landslides: Investigation and Mitigation. Special Report 247, Transportation Research Board.

UNESCO Working Party on World Landslide Inventory. 1991. "A Suggested Method for a Landslide Inventory". Bulletin of the Int'l. Assoc. of Eng. Geology, No. 43.

UNESCO Working Party on world Landslide Inventory. 1993. Multilingual Landslide Glossary, Canadian Geotechnical Society.

van Genuchten and Alves, 1982. "Analytical Solutions of the One- Dimensional Convective-Dispersive Solute Transport Equation," U.S. Department of Agriculture, Technical Bulletin No. 1661.

Van Genuchten, M. Th. 1980, A closed-form equation for predicting the hydraulic conductivity of unsaturated soils, Soil Sci. Soc. Am. J. 44, 892-898.

van Genuchten, M.Th., 1981. "Analytical solutions for chemical transport with simultaneous adsorption, zero-oder production and first-order decay," Journal of Hydrology, 49: 213-233. Elsevier Scientific Publishing Co., Amsterdam.

van Westen C.J., 1993. Application of Geographic Information Systems to Landslide Hazard Zonation. ITC-Publication, No. 15, ITC, Enschede, 245 pp.

Vanapalli, S.K. and D.G. Fredlund, 1999. Comparison of empirical procedures to predict the shear strength function for unsaturated soils. XI Asian Regional Conference, International Society for Soil Mechanics and Foundation Engineering, Seoul, August 16-20, 1999, ed. Sung-Wan Hong et al., A. A. Balkema, Vol. 1, pp. 93-96.

Vanapalli, S.K., and D.G. Fredlund. 1997. Interpretation of undrained shear strength of unsaturated soils in terms of stress state variables. 3rd Brazilian Symposium on Unsaturated Soils, April 21-25, ed. Sung-Wan Hong et al. Tacio de Campos & E.A. Vargas, Freitas Editora, pp. 35-45.

Vanapalli, S.K., Fredlund, D.G., and Pufahl, D.E. 1998. Unsaturated shear strength behavior of compacted soils in drained and undrained loading conditions. Proceedings of the Second International Conference on Unsaturated Soils, August 27-30, 1998, Beijing, International Academic Publishers, Vol. 1, pp. 161-166.

Vanapalli, S.K., Pufahl, D.E., and Fredlund, D.G. 1999. Relationship between soil-water characteristic curves and the as-compacted water content versus soil for a clay till. XI Pan-American Conference on Soil Mechanics and Foundation Engineering, Brazil, 1999. August 8-12, 1999, Vol. 2, pp. 991-998.

Vanmarcke, E.H.; Bohnenblust, H. 1982. "Methodology for Integrated Risk Assessment for Dams". MIT Research Report R-82-11.

Varnes, D.J. 1958. Landslide Types and Processes. Special Report 29, Landslides and Engineering Practice, Highway Research Board.

Varnes, D.J. 1984. "Landslide Hazard Zonation: A Review of Principles and Practice". Natural Hazards 3, UNESCO, 63 pp.

Varnes, D.J., 1982. Time-deformation relations in creep to failure of earth materials. Proc. 7th SE Asia Geotechnical Conf., Hong Kong. 107-130.

Veneziano, D.V. 1974. "Contribution to Second Moment Reliability". Dept. Report No. R74-33, Dept. of Civil Eng., MIT, Cambridge, MA.

Vogel, T., K. Huang, R. Zhang, and M.Th. van Genuchten. 1996. The HYDRUS code for simulating water flow, solute transport, and heat movement in variably-saturated porous media. Version 5.0. Research Rep. 140. USSL, Riverside, CA.

Wagner, W.; Lemoine, G. and Rott, H. 1999. A Method for Estimating Soil Moisture from ERS Scatterometer and Soil Data. Remote Sensing of the Environment, Vol. 79. pp. 191-207.

Wallace, K. 1975. The Analysis of Surface Infiltration into Earth Structures. Fourth Southeast Asian Conference on Soil Engineering, Kuala Lumpur.

Warrick, A.W., J.W. Biggar and D.R. Nielsen, 1971. Simultaneous solute and water transport for an unsaturated soil. Water Res. Res., 7 : 1216-1225.

Whitman, R.V., and Bailey, W.A., 1967. Use of computers for slope stability analysis. Jour. Soil Mech. Found. Engrs. Proc. ASCE, SM4:475-497.

Wieczorek G. F. 1998. Preparing a Detailed Landslide-Inventory Map for Hazard Evaluation and Reduction. Bulletin of the Association of Engineering Geologists, Vol XXI, No. 3. pp. 337-342.

Wieczorek, G. F. 1996. Landslide Triggering Mechanisms. Landslides Investigation and Mitigation. Transportation Research Board, Special Report No. 247. Turner, A.K. and Schuster R.L. (editors). pp. 76-87.

Wieczorek, G.F. and Sarmiento, J. 1988. Rainfall, Piezometric Levels, and Debris Flows near La Honda, California, in Storms between 1975 and 1983. In: Ellen, S. D. and Wieczorek, Gerald F. (editors), Landslides, Floods, and Marine Effects of the Storm of January 3-5, 1982, in San Francisco Bay region, California, U. S. Geological Survey Professional Paper, P 1434, pp. 43-62.

Wierenga, P.J and M.L. Brusseau. 1995. Water and contaminant transport in the vadose zone. Chapter 6. In Environmental Hydrology. Vijay Singh, ed. Kluwer Academic Publishers. :165-193.

Wierenga, P.J., D.R. Nielsen y R.M. Hagan. 1969. Thermal properties of a soil based upon field and laboratory measurements. Soil Sci. Soc. Am. Proc., 33: 354-360.

Wilkinson, P. L., Brooks, S. M., Anderson, M. G. 2000. Design and application of an automated non-circular slip surface search within a combined hydrology and stability model (CHASM). In: Brooks, S. M. (editor), McDonnell, R. A. (editor), Geocomputation in hydrology and geomorphology, Hydrological Processes, 14 (11-12), p. 2003-2017.

Wilson, R.C. and Wieczorek, G.F. 1995. Rainfall Thresholds for the Initiation of Debris Flows at La Honda, California. Environmental and Engineering Geoscience, Vol. 1, No. 1. pp. 11-27.

Wolff, W. 1996. Probabilistic slope stability in theory and practice. Uncertainty '96, Madison, WI, United States, July 31-Aug. 3, 1996. Geotechnical Special Publication, vol.58, pp.419-433.

Wolff, W. and Hassan, A. 1999. Search algorithm for minimum reliability index of earth slopes. J. Geotech. and Geoenviron. Eng., Vol. 125, No. 4.

Wong, H.N.; Ho, K.K.S.; Chan, Y.C. 1997. "Assessment of Consequences of Landslides". Proc. Int'l. Workshop on Landslide Risk Assessment, Cruden, Fells (eds.) Balkema.

Wu, T. H. 2003. Assessment of Landslide Hazard under Combined Loading. Canadian Geotechnical Journal. vol.40, no.4, pp.821-829.

Wu, T.H., Tang, W.H. and Einstein H.H. 1996. Landslide Hazard and Risk Assessment. In: Landslides Investigation and Mitigation. Transportation Research Board, Special Report No. 247. Turner, A.K. and Schuster R.L. (editors). pp. 106-128.

Wu, W. and Siddle, R.C. 1995. A Distributed Slope Stability Model for Steep Forested Basins. Water Resource Research. Vol. 31. pp. 2097-2110.

Wyler, E.; Bohnenblust, H. 1991. "Disaster Scaling, A Multi-Attribute Approach Based on Fuzzy Set Theory". Proc. Int'l. Conf. on Probabilistic Safety, Assessment and Management, Vol. 1.

Yao, T. and Hendrickx, J.M.H. 1996. Stability of Wetting Fronts in Dry Homogenous Soils under Low Infiltration Rates. Soil Science Society of America Journal, Vol. 60 (1). pp. 20-28.